FINAL REPORT

ANALYSIS AND DESIGN OF ECCENTRIC STIFFENERS PART OF MOMENT CONNECTIONS TO COLUMN FLANGES

Prepared for:

American Institute of Steel Construction

One Prudential Plaza, 130 E Randolph St, Chicago, IL 60601

Prepared By:

Department of Civil and Architectural Engineering

Lawrence Technological University

21000 West Ten Mile Road

Southfield, MI 48075

August 12, 2019

Keith J. Kowalkowski, PhD, PE, SE

Primary Investigator

Javier Alvarez Rodilla, EIT

Graduate Research Scholar

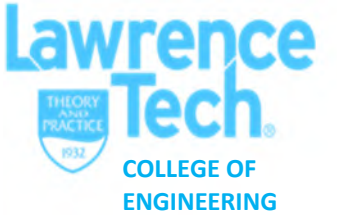

EXECUTIVE SUMMARY

This report contains a comprehensive summary of all the experimental and analytical work performed and all relative observations, conclusions and recommendations for the project entitled "Analysis and Design of Eccentric Stiffeners Part of Moment Connections to Column Flanges".

In the experimental investigations, forty column specimens were tested. The column specimens were relatively small wide-flange shapes and tested to mimic columns subjected to concentrated lateral forces that develop within moment connection. Three different test methods were used: (1) single compression in which a downward force was applied to the top flange of a column specimen from a hydraulic actuator, (2) double compression in which a downward force was applied to the top flange of a column specimen but with a support directly adjacent and at the bottom flange, and (3) single tension in which an upward force was applied to the top flange of a column specimen.

Four wide flange sizes were tested: W10X19, W10X39, W12X26, and W16X31. However, not all test methods were used with each column size. For each column size and test method performed for them, four column specimens were tested as part of a group of specimens:

- One test was performed without any stiffeners near midspan to establish a baseline capacity prior to the addition of any stiffeners.
- One test was performed with stiffeners directly under the concentrated load and therefore with an eccentricity of 0 in. This is referred to as the concentric stiffener condition.
- One test was performed with stiffeners placed horizontally from the applied load at a high eccentricity of either 4 in. or 6 in. (W16X31 only).
- One test was performed with stiffeners placed horizontally from the applied load at a low eccentricity of either 2 in. or 3 in. (W16X31 only).

For most single compression tests, the column specimen reached an ultimate load when web local crippling occurred directly under the applied load unless concentric stiffeners were used. For each section size tested under single compression, the load significantly increased when concentric stiffeners were placed in the column specimen in comparison to when the same size was tested without stiffeners. However, when eccentric stiffeners were used, there were negligible changes in

the load carrying capacity in comparison to the condition without stiffeners. Visual inspection and the results of Digital Image Correlation suggest that web local crippling is very concentrated directly under the load.

For most double compression tests, the column specimen reached a maximum load when web local crippling occurred directly under the applied load. This was true for column specimens tested without stiffeners and column specimens tested with eccentric stiffeners. This failure mechanism was unexpected since calculations from the AISC specification indicate that the column specimens should reach a load capacity governed by web compression buckling. For double compression tests with concentric stiffeners, the load increased substantially in comparison to the tests without stiffeners; much more than anticipated from calculations for the effective stiffener capacity.

For the single tension tests, most W12X26 and W16X31 column specimens failed in the welds from the loading plate to the column specimen due to excessive flange bending causing unequal weld stresses. Although flange bending was the expected governing limit state, the maximum load obtained during the test was much higher than that calculated. Similar to the compression tests, the use of eccentric stiffeners had a negligible influence on the load carrying capacity. Flange bending was local under the applied load and therefore, unequal weld stresses developed similar to the condition without stiffener. Tests with concentric stiffeners reached much higher loads.

Finite element models were developed for column specimens using the finite element software ABAQUS and by running a *STATIC RIKS analysis to study the post-buckling behavior. Initial models represented the experimental column specimens to verify/calibrate the methodology, such that the methodology could be adapted for larger column sizes more regularly used in practice. After several iterations, finite element models were developed for each test type with maximum load very similar to that of the experimental results. However, there were dissimilarities in the elastic stiffness. Web local crippling was observed in the single and double compression models initiating at loads close to the maximum loads from the experimental investigations. In single tension tests, the failure load was assumed when the ultimate stress was reached in the welds, which consistently occurred at loads similar to the failure loads obtained in the experimental tests. Some column specimens with eccentric stiffeners were modeled and similar to the experimental investigations, the results indicate that the maximum load with eccentric stiffeners are very similar to the no stiffener condition.

Finite element models were developed for larger column sizes more regularly used in practice. All test methods included the column sizes W14X68, W14X120, W14X176, W14X233, W24X131, and W24X229. For all test methods and each set of parameters, a group of four column specimens consisted of one modeled without stiffeners, one modeled with concentric stiffeners, one modeled with stiffeners at an eccentricity of 2 in. and one modeled with stiffeners at an eccentricity of 4 in. A summary of additional parameters for each test type is as follows:

- For single compression, each column size consisted of a group of specimens modeled with 3/8 in. stiffeners and simply supported at 5 ft. Additional groups were modeled using 3/4 in. stiffeners but only for W14X233 and W24X229. One additional group was modeled for W14X233 with 3/4 in. stiffeners and the column specimens simply supported at 3.5 ft.
- For double compression, a more *through force* was simulated from the top loading plate to the bottom reaction plate in comparison to the experimental investigations. Each column size was modeled with 3/8 in. stiffeners and 3/4 in. stiffeners. Therefore, there were two full groups for each column size.
- For single tension, each column size consisted of a group of specimens modeled with 3/8 in. stiffeners. For the fillet welds between the loading plate and the top flange of the column specimens, three weld sizes of 1/4 in., 9/16 in. and 7/8 in. were modeled for each column size using loading plate thickness of 3/4 in., 1 1/2 in. and 2 1/4 in., respectively. Therefore, there were three full groups for each column size.

The results of the larger column specimens showed that eccentric stiffeners are much more effective in comparison to the results of smaller column specimens tested experimentally. The influence of eccentricity on the *effective stiffener capacity* was studied using various section properties but the flange thickness developed the most consistent trends in the results. Recommendations for determining the effective stiffener capacity are derived for a variation of stiffener eccentricity and flange thickness and are the primary recommendations presented in this report. Final design equations are provided that utilize the ratio of eccentricity vs. flange thickness or the 'e / t_f' ratio. Eccentric stiffeners should not be considered effective if the flange thickness is less than 1/2 in. or if the eccentricity is greater than 4 in. due to limitations of this research.

For single compression tests and for specimens in the same test group, the highest load capacity was always obtained in the specimen with concentric stiffeners, the second highest in the specimens with stiffeners at a 2 in. eccentricity, the third highest in specimens with stiffeners at a 4 in. eccentricity, and the lowest in specimens without stiffeners. Therefore, there were clear trends in the results. However, for double compression tests, in some cases, concentric stiffeners were detrimental due to sudden stiffener buckling and eccentric stiffeners were less detrimental since they better assisted in bracing the web from crippling. It is believed that some stiffeners were too slender for the column specimen modeled. A recommendation for slenderness is provided in this document.

The results of this research show that methods for computing the capacity of wide flange sections when subjected to concentrated loads and for calculating the effective stiffener capacity of concentric stiffeners are questionable. These capacities need to be computed accurately to ensure that the total concentrated load capacity of members with eccentric stiffeners is computed accurately as well.

For compression tests, both experimental and analytical results show that the ultimate load is reached at a capacity close to or slightly less than that predicted for web local crippling. AISC equations for the limit state of web local yielding and web compression buckling are conservative. However, future research to enhance the equations for these limit states are recommended along with research to further study the effective stiffener capacity of concentric stiffeners.

For single tension tests, the limit state of flange bending usually under predicts the ultimate load capacity for the column specimen and therefore, the current AISC equation can be used conservatively. However, in some cases, weld failure was interpreted to occur at loads less than that predicted by flange bending and less than that predicted for the weld strength since flange bending was influencing the weld stress distribution regardless of weld size. It is recommended that a new method for considering flange bending be established that considers the weld strength simultaneously. Recommendations provided in this report for the influence of stiffener eccentricity are valid regardless of weld size.

A preliminary report was submitted to the AISC Research Advisory Committee on October 31, 2019 that focused on the experimental investigations and provided comprehensive details for each column specimen tested. Not all information from the preliminary report is repeated in this final report.

TABLE OF CONTENTS

LIST OF FIGURES

LIST OF TABLES

CHAPTER 1: INTRODUCTION AND BACKGROUND

1.1 Introduction

This report provides a summary of the experimental and analytical investigations performed as part of the project entitled "Analysis and Design of Eccentric Stiffeners Part of Moment Connections to Column Flanges". The project was sponsored by the American Institute of Steel Construction (AISC) and performed by the research team at Lawrence Technological University (LTU). As discussed later in this chapter, a preliminary report was submitted to the AISC Research Advisory Board on October 29, 2018. Some information from the preliminary report has been omitted in this final report.

This research project was primarily intended to study the influence of using eccentric stiffeners to reinforce columns part of moment connections. In these cases, beam flanges or flange plates deliver high concentrated forces to the column flanges, often requiring the use of column reinforcement. The test specimens tested were oriented horizontally with a concentrated load applied at the top flange and at mid length. The concentrated load was either an upward force simulating an attached member in tension or downward force simulating an attached member in compression. The test specimens will further be referred to as "column specimens".

When concentrated loads are applied to columns from moment connections, five capacity limit states are often calculated to evaluate the column member for its resistance to concentrated loads. However, the limit state of web panel zone shear is not studied as part of this research since columns are generally reinforced with doubler plates in lieu of stiffeners if the column does not have adequate capacity per this limit state. Therefore, four other limit states are analyzed in this research project.

Different limit states are considered if a single compression force is applied to one flange, if a single tension force is applied to one flange, if a double compression force is applied to both flanges simultaneously and the force on each side is directly adjacent to each other creating a through force, or if a double tension force is applied to both flanges simultaneously. Tension or compression refers to if the member connected, such as a plate or column flange, is subjected to a tensile or compressive axial force. Therefore, the force is perpendicular to the longitudinal axis of the steel member in question.

The AISC specification (AISC, 2016) does not distinguish between the single tension condition and the double tension condition since the same limit states are applicable. Therefore, the three conditions analyzed in this research are single tension, single compression, and double compression. The limit states that define resistance of a steel member to concentrated loads are summarized as follows per the AISC Specification for Structural Steel Buildings, Section J10 (AISC, 2016).

- Web local yielding – Limit state applies when a single concentrated tension force is applied to the column flange, when a single concentrated compression force is applied to the column flange, or when a double concentrated compression force is applied to the column flanges.
- Flange bending – Limit state applies when a single concentrated tension force is applied to the column flange and across the width of the flange (case for moment connections).
- Web local crippling – Limit state applies when a single or double concentrated compression force is applied to the column flange(s).
- Web compression buckling – Limit state applies when a double concentrated compression forces is applied to both column flanges simultaneously, causing a through compression force.

More detail regarding each limit state is discussed in the literature review of Chapter 2. In the event that the calculated applied force (demand) from the moment connection exceeds the capacity per the limit states listed above, stiffener plates and/or doubler plates are used to reinforce the column section. Usually, the use of stiffener plates is preferred but in some cases, interferences exist which disallow the stiffener plates to be "concentric" with the applied load. Due to the interferences, eccentric stiffeners are often proposed that are welded into the section (welded at flanges and web) but not in line with the concentrated force. Instead, the stiffeners are located at an eccentricity with respect to the location of the concentrated force.

In this research project, forty specimens were experimentally tested. Four different section sizes were tested (W10X19, W10X39, W12X26 and W16X31). However, not all section sizes were tested under the three different loading conditions of single tension, single compression, and double compression. For single compression, all four sizes were tested. For double compression and single tension, three of the four sizes were tested. For each test type and each section size, the following tests were performed and the four will be further referred to as the "test group":

- One test was performed without any stiffeners at midspan to get a baseline capacity prior to the addition of any stiffeners.
- One test was performed with stiffeners directly in line with the concentrated load and therefore with an eccentricity of 0 in. This is also referred to as the "concentric" stiffener condition.
- One test was performed with stiffeners at a high eccentricity, suggesting the stiffeners were placed in the column specimen horizontally from the applied load or at a distance away from the concentrated load along the longitudinal axis. For the W16X31 column specimen, the high eccentricity was equal to 6 in. and for other column specimens, the high eccentricity was equal to 4 in.
- One test was performed with stiffeners at a low eccentricity. For the W16X31 column specimen, the low eccentricity was equal to 3 in. and for other column specimens, the low eccentricity was equal to 2 in.

In addition to the experimental investigations, analytical investigations were performed in this research using the finite element method and the finite element program ABAQUS (2014). Finite element models were first developed for the experimental column specimens. Once the finite element models were calibrated using experimental data, the methodology was further used to evaluate eccentric stiffeners used in larger column specimens. The larger column sections chosen were W14X68, W14X120, W14X176, W14X233, W24X131, and W24X229. All of these column specimens were modeled with the test conditions of single compression, double compression, and single tension. In addition, for each "test group", four test specimens were analyzed with (1) no stiffeners, (2) concentric stiffeners, (3) stiffeners at a low eccentricity of 2 in., and (4) stiffeners at a high eccentricity of 4 in. Therefore, the loading conditions and stiffener eccentricity conditions utilized in the experimental investigations matched that of the analytical investigations. For some conditions, multiple test groups were utilized to study the influence of stiffener thickness, weld size from the loading plate to the top flange of the column specimen, and unbraced length. For instance, all double compression tests were first analyzed with 3/8 in. stiffeners and then reevaluated with 3/4 in. stiffeners.

This chapter will provide further background regarding the issues with eccentric stiffeners and origin of the research project. This chapter will also provide report objectives and a description of the report arrangement. Further chapters will describe the various test setups and test procedure, the column specimen details and test matrix, instrumentation for performing the tests, experimental results, the methodology for the analytical finite element models, analytical results, and conclusions and recommendations for practice and further research.

1.2 Background

Eccentric refers to an offset between the beam flange or flange plate, part of the column moment connection, with respect to a required stiffener as illustrated in Figure 1.2-1(b). Figure 1.2-1(a) demonstrates a condition where are stiffeners are "non-eccentric" or "concentric" in comparison to the beam flange or flange plate. Note that Figure 1.2-1(b) shows one demonstration of an eccentric stiffener in which one beam flange is offset the stiffener. It is possible to place the stiffener between the bottom beam flanges in which the stiffener would be eccentric to both beam flanges but at a smaller magnitude.

(a) Non-eccentric stiffener condition (b) Eccentric stiffener condition

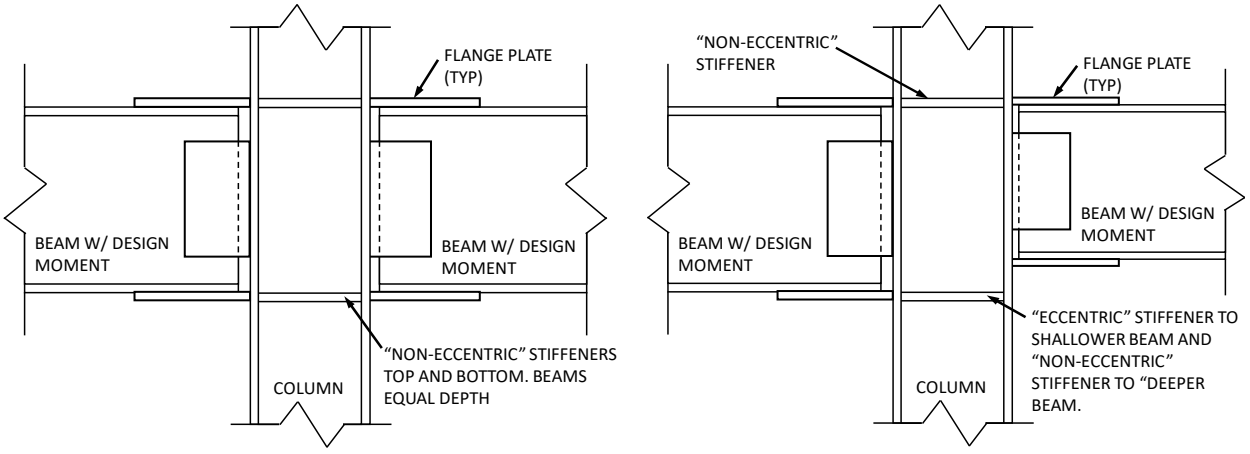

Figure 1.2-1: Example of non-eccentric stiffener vs. eccentric stiffener

When concentrated loads are applied perpendicular to a column flange, several concentrated load limit states have to be checked including those per Sections J10.1, J10.2, J10.3, and J10.5 of the AISC 360 Specification for Structural Steel Buildings (AISC, 2016). The limit states include flange bending, web local yielding, web local crippling, and web compression buckling, respectively. If

the capacity of any of these limit states is less than the computed applied load, AISC permits the use of full-depth transverse stiffeners to partially resist the concentrated loads. The lowest applicable capacity for the concentrated load limit states is used to define the member capacity without stiffeners and dictates the demands for column stiffeners. The required stiffener capacity is simplified and equal to the applied concentrated load minus the member capacity. Per Section J10.8 of the AISC specification (AISC, 2016), stiffeners are designed as tension or compression members, part of the connection.

Eccentric stiffeners may be necessary in lieu of concentric stiffeners for various scenarios. These cases occur frequently in design. In some cases, it is not feasible to place stiffeners in the column, adjacent to each beam flange that is applying the concentrated load due to the presence of multiple connections framing into the joint or other cases that would create interferences within the column boundaries. In general, it is not feasible to place two stiffeners very close to each other due to the welding that must occur on both sides of the individual stiffeners. Common cases that occur in practice when multiple stiffeners are theoretically required at slightly different elevations include:

- When beams are moment connected to both column flanges but are of different depths and per calculations, stiffeners are required for the concentrated loads being applied to both flanges.
- When beams are moment connected to both column flanges but the top of steel elevation is different on both sides and per calculations, stiffeners are required for the concentrated loads being applied on both sides.
- When the location of a stiffener for a moment connection to a column flange would interfere with a flange plate designed as part of a connection where a beam frames into a column web.

Figure 1.2-2 illustrates the three cases listed above. Figure 1.2-2(a) shows two beams of slightly different depths, with the same top of steel elevation and moment connected to the column flanges on either side. Figure 1.2-2(a) also shows the location of concentric column stiffeners required for each beam in dashed lines, emphasizing how close the required stiffeners would be to each other. Figure 1.2-2(b) shows a condition where two beams frame to the column at different top of steel elevations. Figure 1.2-2(c) shows a condition where two beams are moment connected to column flanges and an additional beam is moment connected and framing into a column web. In this case,

the flange plates used as part of the moment connection for the beam framing to the column web may also serve as stiffeners for the concentrated loads applied to the column flanges. However, the location of the flange plate is defined by the depth of the beam framing into a column web and therefore, this flange plate/stiffener is eccentric with respect to the beam to column flange moment connection. In all three cases, the location of all non-eccentric stiffeners may not be feasible due to the welding that must occur for each stiffener. In addition, it may not be necessary to have each stiffener if other stiffeners/flange plates are close to the proximity of the concentrated loads.

a) Beams with different depths

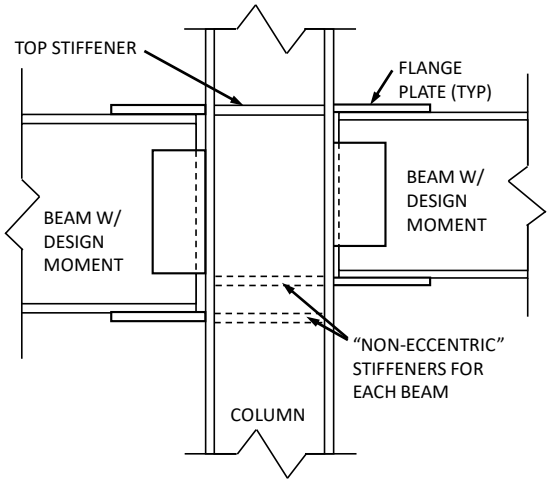

b) Beams with different top of steel elevations

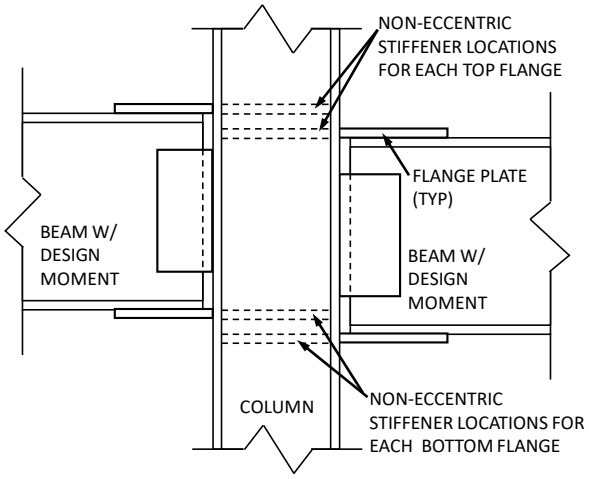

c) Moment connection to column web at different elevation

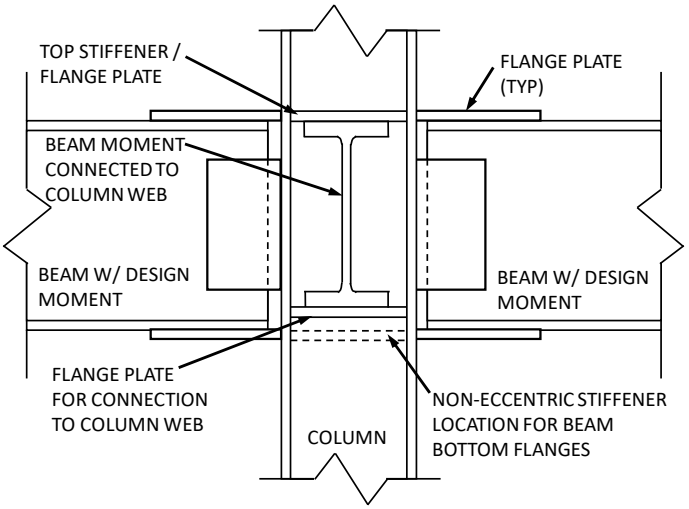

Figure 1.2-2: Non-eccentric stiffener locations and issues with proximity to other stiffeners

Although the AISC specification (AISC, 2016) provides some guidance on the design of column stiffeners, there is no assistance indicated in the specification for the design of or allowances associated with eccentric stiffeners. The only source available from AISC for the design of eccentric column stiffeners or alternate methods to reinforce the column is the AISC Design Guide 13 "Stiffening of Wide-Flange Columns at Moment Connections: Wind and Seismic Applications" (Carter, 1999). More specifically, Section 5.1 of the design guide discusses options for column stiffening for beams of differing depth and/or top of steel. The design guide shows multiple options if the beam flanges on opposite sides of the column are at different elevations. One option demonstrated in the design guide is the use of partial depth transverse stiffeners as shown in Figure 1.2-3(a) (Carter, 1999). Alternatively, it is possible to use sloping stiffeners as shown in Figure 1.2-3(b).

a) Option w/ partial depth transverse stiffeners b) Option w/ sloping stiffener at bottom flange

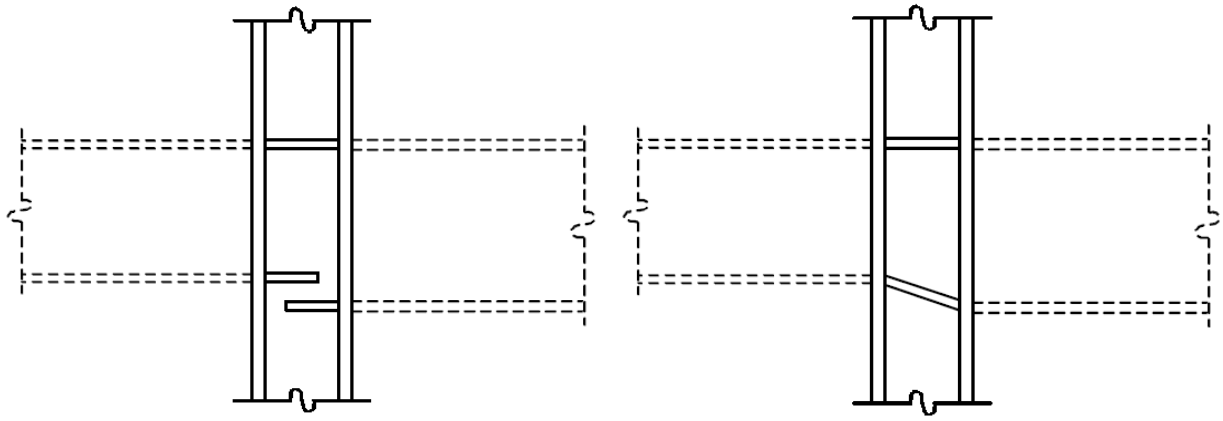

Figure 1.2-3: Stiffening options at offset beam flanges per Design Guide 13 (Carter, 1999)

A final option discussed in the design guide and frequently in this proposal is the use of one transverse stiffener that is adjacent to one beam flange and not the other or provide one transverse stiffener in between the two beam flanges. In either case, this creates a design eccentricity, '*e*', as shown in Figure 1.2-4. Research performed by Graham et al. (1959) suggests that transverse stiffeners with a 2 in. eccentricity provides approximately 65 percent of the strength of an identical transverse stiffener that is non-eccentric. In addition, it was recommended, "for design purposes, it would probably be advisable to neglect the resistant of stiffeners having eccentricity greater than 2 in. The required transverse stiffener area, width and thickness can be established by the same criteria as for concentric stiffeners, provided that the strength his reduced linearly from 100 percent at zero

eccentricity to 65 percent at 2 in. eccentricity". The research by Graham et al. (1959) will be discussed in more detail in Chapter 2.

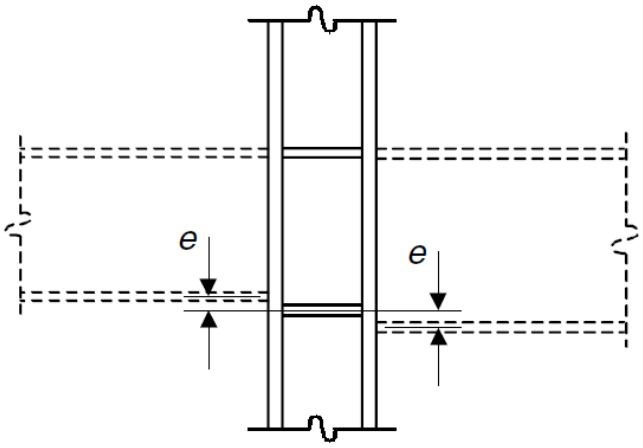

Figure 1.2-4: Stiffener option at eccentricity 'e' per AISC Design Guide 13 (Carter, 1999)

The recommendations provided by Graham et al. (1959) are contradictory to the information provided in this project's Request for Proposal (RFP) in regards to the motivation for performing this research project. The RFP indicates that many engineers do not limit eccentricity to 2 in. From verbal communication with the AISC Research Advisory Committee and from the RFP, "Other engineers and fabricators report considering stiffeners effective up to an eccentricity of 6 in." However, there is no evidence to suggest the stiffeners are actually effective at this magnitude of eccentricity or if any reduction factors apply with respect to the effective strength.

1.3 Research Objectives

The primary research objectives as discussed in this report are summarized as follows:

- Develop a comprehensive literature review of all previous research related to this topic including the development of concentrated load limit states currently used in practice, use of stiffeners to resist the effects of concentrated loads, eccentric stiffener use, and current codes and standards available for analyzing these conditions.
- From experimental testing, evaluate the effectiveness of eccentric stiffeners in comparison to the use of concentric stiffeners for eccentricities up to 6 in.
- Using finite element models, further evaluate the use of eccentric stiffeners for larger column

sizes than that of the experimental column specimens.

- Recommend effective capacities for eccentric stiffeners at a range of eccentricities and for a range of column sizes.
- Evaluate the accuracy of the concentrated load limit states as stated in the AISC specification using both experimental and analytical results.

The last objective listed above was not specifically stated as part of the project proposal. It was added after observing the experimental results of this research and deemed more critical after reviewing the analytical results of this research. The experimental results revealed that the equations for the concentrated load limit states usually underestimate the capacity of the column specimens and therefore, the limit states were evaluated in more detail using both experimental and analytical results.

1.4 Report Arrangement

Chapter 2 provides a literature review of prior research performed on steel members subjected to concentrated loads, analysis and design of concentric stiffeners, and analysis and design of eccentric stiffeners. This chapter will also outline the provisions in the AISC specification (AISC, 2016) and design guidelines relevant to the project along with the development of requirements in such provisions.

Chapter 3 summarizes the experimental investigations. A much more detailed description of the experimental investigations was provided in the preliminary report dated October 29, 2019. Chapter 3 includes the experimental test matrix and reasons the test matrix was selected, a description of the column specimens, test setups and instrumentation, load-displacement results that directly show the influence of eccentric stiffeners, a discussion of the experimental test behavior and conclusions from the experimental results.

Chapter 4 summarizes the methodology used for most of the finite element models. The discussion includes material properties, element types, loading conditions, boundary conditions, and analysis procedures.

Chapter 5 presents the analytical results of finite element models used to mimic the experimental

column specimens. These results were used to calibrate the finite element models for further analysis of larger column sections.

Chapter 6 focuses on studying larger column sections than the experimental column specimens and the influence of using eccentric stiffeners in more detail. This chapter discusses the failure modes associated with several finite element models and other failure mechanisms that influence the results and behavior. Recommendations for the design of eccentric stiffeners are formulated using the results in this chapter.

Chapter 7 studies the AISC specification (AISC, 2016) equations for predicting the limit states associated with wide-flange shapes when subjected to concentrated loads. In addition, the chapter evaluates calculations that are utilized for predicting the capacity of concentric stiffeners.

Chapter 8 provides a summary and conclusions for the entire research project. Recommendations are provided for the use of eccentric stiffeners in design. In addition, recommendations are provided for future research with an emphasis on modern studies used to evaluate the AISC limit states and equations traditional used for predicting the capacity of stiffeners.

Appendix A provides several photographs taken from the experimental investigations. All of these photographs were originally presented in the preliminary report. Appendix B shows the Welding Procedure Specification (WPS) used for the critical welds in the experimental investigations. Appendix C provides images from Digital Image Correlation (DIC), which was utilized as instrumentation during the experimental investigations. Appendix D provides the theoretical calculations for concentrated load limit states whenever applicable in this report. Appendix E provides screenshots of finite element models after initial yielding and at the failure load or shortly after to view the appearance after buckling.

1.5 Summary of Preliminary Report

A preliminary research report was submitted on October 29, 2019. Not all information from the preliminary report will be repeated in this report. A summary of the contents and information omitted or repeated is as follows:

- Chapter 1 of the preliminary report provided an introduction similar to this chapter. Some of the information was repeated in this chapter.

- Chapter 2 of the preliminary report provided a literature review. The literature review has been expanded as part of this report.
- Chapter 3 of the preliminary report focused on preliminary finite element models that were used in aid to select the experimental test matrix. These models will be discussed briefly and used for Chapters 3 and 4 of this report.
- Chapter 4 of the preliminary report focused on the experimental test matrix. Reasons for the selection of the test matrix were also provided. This information will be summarized in Chapter 3 of this report.
- Chapter 5 of the preliminary report discussed the column specimens, experimental test setup, and instrumentation. Most of this information is repeated within Chapter 3 of this report.
- Chapter 6 of the preliminary report summarized the experimental results. An abbreviated version of this information is provided in Chapter 3 of this report. All photographs of the experimental column specimens are provided in Appendix A of this report.
- Chapter 7 of the preliminary report provided a summary, conclusions, and preliminary recommendations from the experimental investigations. This has been superseded by the information provided in Chapter 8 of this report.
- Chapter 8 of the preliminary report provided recommendations for the analytical investigations and is superseded by the information included in the analytical chapters of this report.

CHAPTER 2: LITERATURE REVIEW

This chapter presents a comprehensive literature review of all prior research performed on steel members subjected to concentrated forces, analysis and design of concentric stiffeners, and design and analysis of eccentric stiffeners. This section will also outline the provisions in the AISC specification (AISC, 2016) and other design specifications relevant.

2.1 Concentrated Load Limit States

In a moment connection, the beam end moment is resolved at the column face with a resultant force couple in the beam flanges. One of the concentrated forces in the couple would be a compression force and the other one a tension force. The applied moment in the end of the beam (M_u per LRFD) may be accompanied by an applied axial force (P_u per LRFD). The beam's flange force is determined using Equation 2-1.

$$P_{uf} = \frac{M_u}{d_m} \pm \frac{P_u}{2} \quad (2\text{-}1)$$

Where:

P_{uf} = beam flange force, tension or compression (kip)

M_u = factored beam end moment (kip-in)

d_m = moment arm between the forces in the couple (in)

P_u = factored beam axial force if applicable (kips)

When concentrated loads are applied to columns from moment connections, four capacity limit states are often calculated to evaluate the column member for its resistance to concentrated loads. The limit states are web local yielding, flange bending, web local crippling, and web compression buckling. The mentioned limit states are described in the following subsections. For each limit state, the equations as presented in the current AISC specification (AISC, 2016) are provided along with background research that describe how these limit states and equations originated and evolved over time.

2.1.1 Web Local Yielding

Web local yielding is the compressive crushing or tension yielding of the beam web caused by a compressive or tensile force applied directly to the flange. This limit state applies for both single

and double concentrated forces. The nominal strength for the limit state of web local yielding is determined using Equations 2-2 or 2-3 (AISC, 2016). When the concentrated force is applied at a distance from the member end that is greater than the full nominal depth of the member, *d*, Equation 2-2 is used. When the concentrated force is applied at a distance from the member that is less or equal to the full nominal depth of the member, *d*, Equations 2-3 is used.

$$R_n = F_{yw} t_w (5k + l_b) \quad (2\text{-}2)$$

$$R_n = F_{yw} t_w (2.5k + l_b) \quad (2\text{-}3)$$

Where:

F_{yw} = specified minimum yield stress of the web material (ksi)

k = distance from outer face of the flange to the web toe of the fillet (in)

l_b = length of bearing (in)

t_w = thickness of web (in)

Per the AISC specification, when the calculated applied force exceeds the capacity of the column section per Equation 2-2 or 2-3, either a pair of transverse stiffeners or a doubler plate shall be provided. Note that the ASD and LRFD methods have different load combinations for applied loads and different safety factors applied to Equation 2-2 or 2-3. However, per the LRFD method, the resistance factor, ϕ, is taken as 1.0. This suggests that the limit state is not expected to cause a critical failure if the load is exceeded and the limit state may be present in the specification as a conservative check.

The web local yielding provisions (Equations 2-2 and 2-3) are intended to limit the extent of yielding in the web of a member into which a force is being transmitted. The provisions were derived by considering a stress zone that spreads out with a slope of 2:1 to the '*k* line' from experimental test results performed by Khabbaz and Jensen (1957). However, the analyses performed by Graham et al. (1959) indicated a distribution of force on a 2.5:1 slope to the column '*k* line'. It is assumed that within the width that the force is transmitted, that the stress is uniform. The entire width is equal to '$t + 5k$', where '*t*' is the thickness of the loading plate (or flange). This width, as well as the slope of 2.5:1, are conservative values from experimental evidence of Graham et al. (1959). Figure 2.1-1 illustrates how the force spreads in to the column assuming the applied load is in compression.

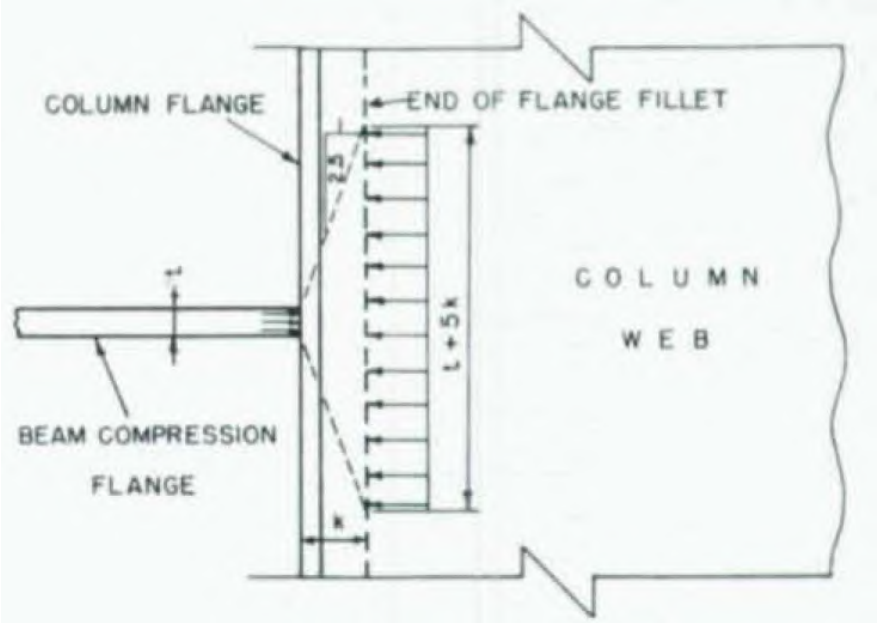

Figure 2.1-1: Idealized analysis of compression region of connection (Graham et al. 1959)

The original equation proposed by Graham et al. (1959) for web yielding is shown as Equation 2-4, which is equivalent to Equation 2-2, but with different variables.

$$Q_c = \sigma_y w(t + 5k) \quad (2\text{-}4)$$

Where:

Q_c = resistance supplied by column web (kip)

σ_y = specified yield stress of the web material (ksi)

w = column web thickness (in)

t = beam flange thickness (in)

Graham et al. (1959) stress distribution assumptions are based on the stress distribution theory by Parkes (1952), which demonstrated that most of the stress distribution on a loaded column occurs in the web at a distance k from the top flange rather than at the top of the column. Recent research by Hajjar et al. (2003) confirms that the web local yielding provisions provided by AISC and thus the findings by Graham et al. (1959) are reasonable and slightly conservative in calculating the need for column stiffening.

2.1.2 Web Local Crippling

Web local crippling represents a buckling of the web directly under the flange on the side of the concentrated load and is caused by a single compressive concentrated force or the compressive component of double concentrated forces (both sides may be compression but in some cases, one side is compression and the other is tension). Similar to web local yielding, the calculations for web local crippling are dependent on whether or not the concentrated force is close to the end of the column section or not. When the concentrated compressive force is applied at a distance from the member end that is greater than or equal to *d/2*, Equation 2-5 (AISC, 2016) is used to calculate the capacity.

$$R_n = 0.8{t_w}^2 \left[1 + 3\left(\frac{l_b}{d}\right)\left(\frac{t_w}{t_f}\right)^{1.5}\right]\sqrt{\frac{EF_{yw}t_f}{t_w}}Q_f \quad (2\text{-}5)$$

When the concentrated compressive force is applied at a distance from the member that is less than *d/2*, two equations are used depending on the l_b/d ratio. When the l_b/d ratio is less than or equal to 0.2, Equation 2-6 is used. Else, Equation 2-7 is used.

$$R_n = 0.40{t_w}^2 \left[1 + 3\left(\frac{l_b}{d}\right)\left(\frac{t_w}{t_f}\right)^{1.5}\right]\sqrt{\frac{EF_{yw}t_f}{t_w}}Q_f \quad (2\text{-}6)$$

$$R_n = 0.40{t_w}^2 \left[1 + \left(\frac{4l_b}{d} - 0.2\right)\left(\frac{t_w}{t_f}\right)^{1.5}\right]\sqrt{\frac{EF_{yw}t_f}{t_w}}Q_f \quad (2\text{-}7)$$

Where:

d = full nominal depth of the member (in)

Q_f = 1.0 for wide-flange sections

t_f = thickness of the loaded flange (in)

F_{yw} = specified minimum yield stress of the web material (ksi)

E = elastic modulus of the steel (ksi)

l_b = length of bearing (in)

t_w = thickness of web (in)

Per the AISC specification, when the calculated applied force exceeds the capacity of the column section per Equation 2-5, 2-6, or 2-7, either a transverse stiffener, a pair of transverse stiffeners, or a

doubler plate extending at least three quarters if the depth of the web shall be provided. Per the LRFD design method, the resistance factor, ϕ, is taken as 0.75, which is the same resistance factor taken for fracture limit states in the AISC specification (AISC, 2016). This suggests that the limit state is concerning and a failure may cause catastrophic failure of the structure or the calculations are less conservative and there are too many uncertainties with the calculations.

The first researchers used the term "web crippling" to describe the phenomenon that is nowadays known as web local yielding. It was not until the first edition of the AISC LRFD Specification (AISC, 1986), that the term web local crippling was differentiated from web local yielding. Web local crippling is defined as crumpling of the web into buckled waves directly beneath the load, which is more common in slender webs, whereas web local yielding is yielding of that same area in more compact webs (AISC, 2016).

Equations 2-5 and 2-6 were developed by Roberts (1981). An experimental and theoretical investigation on web crippling in slender plate girders subjected to localized edge loading was carried out. Twenty-six girders of varying depth, web thickness and flange thickness were tested in a hydraulic testing machine. For all girders tested, out of plane deformations on the web were noticed close to the maximum load. The profile for the more slender plates had an S-shape, indicating the formation of three yield lines on the web. One yield line was adjacent to the top flange and the other two at the points of maximum deflection. In girders with thicker webs, the two upper yield lines tended to merge into one adjacent to the top flange. Figure 2.1-2 shows illustrations of the web deformations for three of the specimens tested.

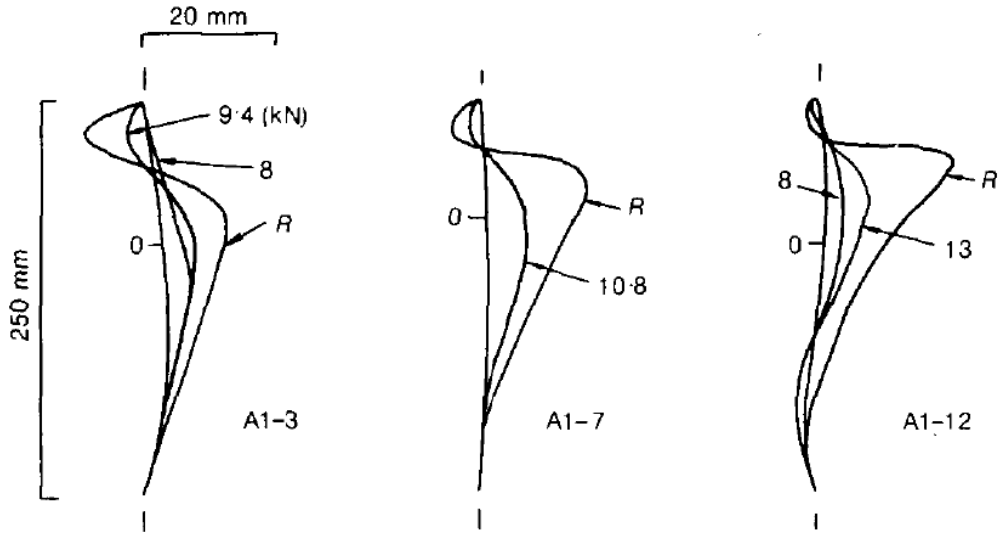

Figure 2.1-2: Web profiles after testing (Roberts, 1981)

Roberts (1981) original yield mechanism used to simulate the behavior of the webs is illustrated in Figure 2.1-3. Dimensions α and β define the position of the assumed yield lines in the web and plastic hinges in the flange and θ defines the deformation of the web just before collapse. M_w, σ_w, M_f, and σ_f are the plastic moments and yield stress of the web and flange, respectively. Equation 2-8 describes the collapse load, P_u, over the web length, η, that is assumed to have yielded.

$$P_u = \frac{4M_f}{\beta} + \frac{4\beta M_w}{\alpha cos\theta} + \frac{2cM_w}{\alpha cos\theta} - \frac{2\eta M_w}{\alpha cos\theta} \quad (2\text{-}8)$$

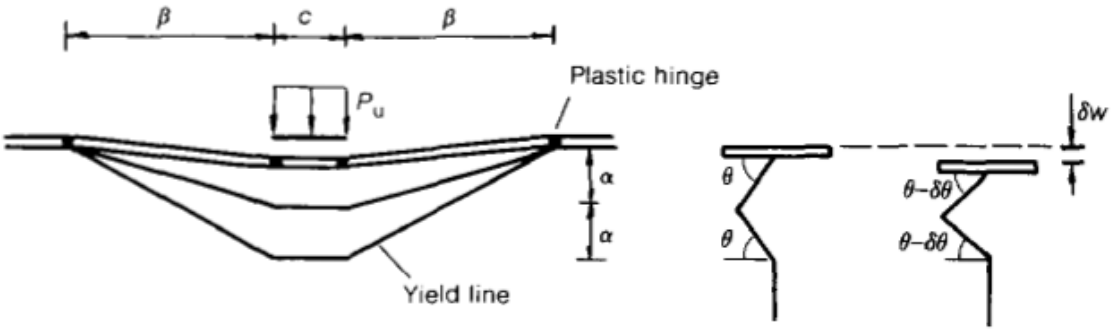

Figure 2.1-3: Assumed web crippling yield mechanism (Roberts, 1981)

Equation 2-8 results in Equation 2-9 through some additional assumptions and is similar to what is used in the current AISC Specification (AISC, 2016). Equation 2-9 provides a lower bound solution from the available test data (Roberts, 1981).

$$P_u = 0.5{t_w}^2 \left[1 + 3\left(\frac{c}{d}\right)\left(\frac{t_w}{t_f}\right)^{1.5}\right]\sqrt{\frac{E\sigma_w t_f}{t_w}} \quad (2\text{-}9)$$

From Equation 2-9, the influence of the loaded length, *c,* diminishes rapidly with increasing flange thickness. When the length of bearing to depth ratio, c/d, becomes large, it is impractical to assume that the flange remains flat between the two inner plastic hinges. Thus, it is recommended that the ratio, *c / d,* is less than or equal to 0.2 for the assumptions to be valid. For girders with relatively thick flanges, where the spread of the plastic hinges in the flange is restricted by vertical web stiffeners, the use of this equation tends to underestimate the collapse load. However, it tends to predict a collapse load below the load when web bending begins. Therefore, it is a good serviceability check for such girders.

Roberts (1981) also proposed Equation 2-10, which assumes that in practice, web panels of web girders are often subjected to edge loading and combined bending. The bending stress is taken into account by the term σ_b.

$$P_u = 0.5{t_w}^2 \left[1 + 3\left(\frac{c}{d}\right)\left(\frac{t_w}{t_f}\right)^{1.5}\right]\sqrt{\frac{E\sigma_w t_f}{t_w}}\sqrt{1 - \left(\frac{\sigma_b}{\sigma_w}\right)^2} \quad (2\text{-}10)$$

Equation 2-10 successfully predicted the collapse load for the available test data. However, further experimental results were required for girders with thicker webs to ascertain the applicability of the equation.

Roberts (1981) set the basis for Equations 2-11 and 2-12, which were used in the first AISC LRFD Specification (1986). Equation 2-11 was used when the compressive force to be resisted is applied at a distance from the member end greater than or equal to *d*/2. Otherwise, the second equation was used. However, more experimental analysis was needed for girders with thicker webs, and a solution had to be found to overcome the limitation of $c/d \leq 0.2$ by Roberts (1981). The term *N*, refers to length of bearing, which is the same as the term *c* in Roberts (1981) equations and l_b in the current AISC Specification (2016).

$$R_n = 135{t_w}^2 \left[1 + 3\left(\frac{N}{d}\right)\left(\frac{t_w}{t_f}\right)^{1.5}\right]\sqrt{\frac{F_{yw} t_f}{t_w}} \quad (2\text{-}11)$$

$$R_n = 68{t_w}^2 \left[1 + 3\left(\frac{N}{d}\right)\left(\frac{t_w}{t_f}\right)^{1.5}\right]\sqrt{\frac{F_{yw}t_f}{t_w}} \qquad (2\text{-}12)$$

Elgaaly and Salkar (1991) studied the behavior of webs of rolled and built-up beams subjected to in-plane and eccentric compressive edge loads. Members with thicker webs and longer bearing lengths were studied to compliment the results by Roberts (1981). Rolled shapes were tested under load which was applied either on the top flange and at the center of the beam or under the bottom flange at the ends of the beam. The effect of small eccentricity of the load with respect to the plane of the web was also investigated through experimental testing and computer analysis. The sections studied were rolled beams ranging from W12 to W21. The ratio of the bearing length to the beam depth, *N/d*, varied from 0.2 to 0.6. The tests were carried out in a Baldwin Testing Machine and the load was applied through thick steel plates. Two rollers were used as supports and bearing stiffeners were placed over the supports.

From the test results, a difference in the failure mode between stocky and slender webs was observed. The stockier webs yielded before crippling and the slender webs underwent web crippling before yielding. In all tests performed on rolled shapes, the former mode of failure was observed; yield lines under the load or over the support were observed before crippling occurred. The out-of-plane deformations in the web were observed near or at failure. It was also noticed that the height of the circular yield line observed on the web under the load increased with the increase in the *N/d* ratio.

Elgaaly and Salkar (1991) indicated from observations of the behavior of the specimens near and at failure, one cannot justify the classification of web yielding and web crippling as two separate failure modes. Hence, only the web crippling Equations 2-11 and 2-12 from the first edition of the LRFD AISC (1986) were checked based on the test results. The constant of 135 was derived by Galambos using some 89 test results from 122 reported by Elgaaly in 1983 (Elgaaly and Salkar, 1991). In the derivation, Galambos assumed that the dead and live loads were of the same magnitude. Based on the derivation by Galambos and assuming a strength reduction factor of 0.75, the reliability index was calculated to be equal to 2.7. Hence, it was concluded that Equation 2-11 could be applied to rolled shapes as well as built-up sections.

The constant of 68 in Equation 2-12 was derived by Galambos using some 29 test results from 69 reported by Elgaaly in 1983 (Elgaaly and Salkar, 1991) and using the assumption that bearing stiffeners over the supports can be omitted in member with relatively stocky webs. Based on the derivation by Galambos and assuming a strength reduction factor of 0.75, the reliability index was calculated as 2.5. Elgaaly and Salkar (1991) indicated that Equation 2-12 was conservative when longer bearing lengths were used at the ends of the members and it should be modified based on their experimental results. Based on this recommendation, Equation 2-12 was changed to Equation 2-13 for the condition when $N/d > 0.2$ which is very similar to Equation 2-7 used in the current AISC specification (AISC, 2016).

$$R_n = 0.40{t_w}^2 \left[1 + \left(\frac{4N}{d} - 0.2\right)\left(\frac{t_w}{t_f}\right)^{1.5}\right]\sqrt{\frac{EF_{yw}t_f}{t_w}} \qquad (2\text{-}13)$$

2.1.3 Flange Bending

Flange bending occurs from a single concentrated tension forces and the tensile component of double-concentrated forces applied to the column section flange through a plate welded across the flange. This limit state does not have to be checked if the length of loading across the member flange is less than $0.15b_f$, where b_f is the member flange width. The limit state of flange bending is calculated using Equation 2-14 (AISC, 2016). If the concentrated force is located within $10t_f$ of the end of the member, then R_n per Equation 2-14 shall be reduced by 50%.

$$R_n = 6.25F_{yf}{t_f}^2 \qquad (2\text{-}14)$$

Where:

F_{yf} = specified minimum yield strength of the flange (ksi)

t_f = thickness of the loaded flange (in)

Equation 2-14 fundamentally relates to the plastic capacity of a steel plate subjected to weak axis bending. The weak axis plastic section modulus of a steel plate with a width, b, and a thickness, t, is equal to $Z_y = bt^2 / 4$. Per the AISC specification, Section J10 (AISC, 2016), when the calculated applied concentrated force exceeds the capacity per Equation 2-14, a pair of transverse stiffeners are required. The resistance factor for the LRFD method, ϕ, per the specification is 0.9, which is a typical factor used for a yielding limit state and the plastic moment capacity of a beam or plate

element and is usually associated with uncertainties with the material properties of the steel.

Graham et al. (1959) indicated that the effective length of the column flange for flange local bending is $12t_f$ and the column flange is assumed to be fixed at the ends of this length. Therefore, yield lines form in the column flange at $6t_f$ in each direction from the point of the applied concentrated force. Figure 2.1-4 shows a visual representation of the flange bending region assumed by Graham et al. (1959). The author uses '*c*' to define the flange properties as opposed to '*f*'. An additional $4t_f$ is needed in the column flange to simulate the fixed end condition of this model (AISC, 2016), and consequently, a total of $10t_f$ is needed on each side of the column flange to develop the full flange bending strength given by Equation 2-14. Due to the absence of applicable research in this topic, a 50% reduction has been introduced for cases where the concentrated force is applied within $10t_f$ from the end of the member.

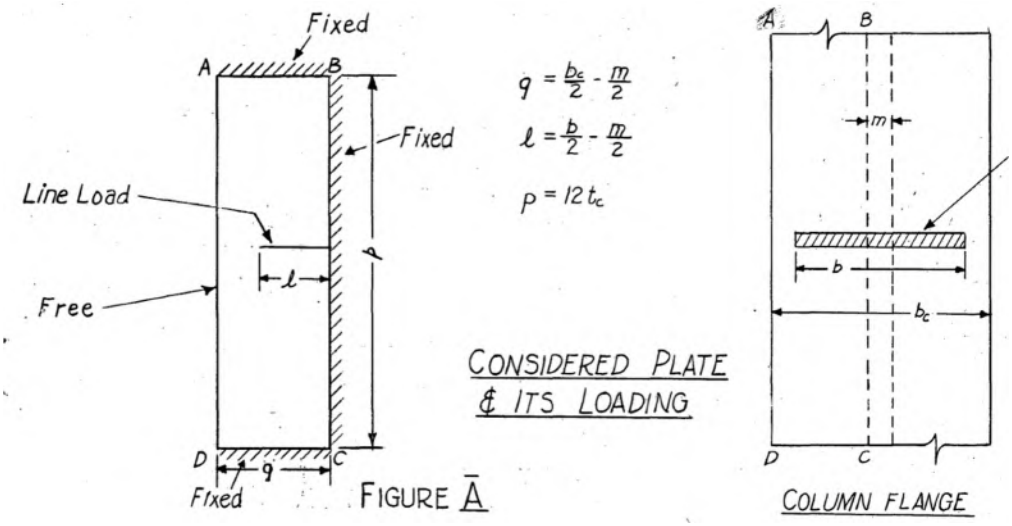

Figure 2.1-4: Action of the column flange in the tension region (Graham et al., 1959)

Originally, Equation 2-14 was developed to provide a lower bound to the force required for weld fracture, which would take place due to stress concentrations that develop in the weld (uneven stress distribution) from flange bending (Graham et al., 1959). Equation 2-14 is a modification from the original equation proposed by Graham et al. (1959) describing weld fracture due to flange bending. Equation 2-15 shows the original equation.

$$Q_t = \sigma_y t m + 7\sigma_y {t_c}^2 \qquad (2\text{-}15)$$

Where:

σ_y = specified minimum yield stress of the flange (ksi)

t_c = thickness of the loaded flange (in)

t = column web thickness (in)

m = distance $2k_1$ (in)

k_1 = distance from the center of the section to the end of the fillet on the flange (in)

The first term in Equation 2-15 represents the strength provided by the rigid portion of the flange just above the web and the second term describes the force in the column section flange when plastic moment is applied. The first term was removed from the original equation to give Equation 2-14. The factor of 7 was originally denoted by c_1. However, it was found that for wide flange columns and beams used in practical connections, c_1 varied from 7 to 10 (Graham et al., 1959). At first, a factor of 7 was chosen for c_1 to be conservative. It was later modified to 6.25 in the LRFD Specification (Hajjar et al., 2003).

Recent research on welds with minimum Charpy V-notch strength requirements showed that weld fracture is no longer the failure mechanism when the strength given by Equation 2-14 is exceeded. In fact, it was found that the strength provided by Equation 2-14 is consistently less than the force required to bend the tips of the flanges of typical columns sections by 1/4 in. (Hajjar et al., 2003; Prochnow et al., 2000). Thus, proving that the provisions given by AISC for flange bending are reasonable and conservative in calculating the need for column stiffening. Equation 2-16 was proposed for flange local bending in connections consisting of wide-flange girders framing into wide-flange columns with fully-restrained connections (Hajjar et al., 2003). Per the authors, Equation 2-16 provides superior test-to-predicted ratios as compared to current provisions.

$$R_n = (0.8 + 5.9t_{cf}^2)F_{yc} \quad (2\text{-}16)$$

Where:

t_{cf} = thickness of the column flange (in)

F_{yc} = minimum specified yield strength of the column (ksi)

The mentioned deformation of 1/4 in. on the flange tips is within the acceptable limits in ASTM A6/A6M, and if the deformation is exceeded, this level could influence other aspects of the

performance of the member, such as flange local buckling. Although this deformation could also occur under compressive forces, it is well established that flange local bending is checked only for tensile forces since the original failure mode was weld fracture. Hence, it is not necessary to check flange bending for compressive forces (AISC, 2016).

2.1.4 Web Compression Buckling

Web compression buckling may occur when a pair of concentrated compressive forces are applied to both flanges of the column section and across from each other. The applied force that is compared to the limit state is the force that transfers through the column web. The available strength for the limit state of web compression buckling is calculated using Equation 2-17 (AISC, 2016). When a pair of concentrated compressive forces to be resisted is applied at a distance from the member end that is less than $d / 2$, R_n per Equation 2-17 shall be reduced by 50%.

$$R_n = \left(\frac{24{t_w}^3\sqrt{EF_{yw}}}{h}\right) Q_f \qquad (2\text{-}17)$$

Where:

h = clear distance between flanges less the fillets (d - 2k) (in)

Q_f = 1.0 for wide-flange sections

F_{yw} = specified minimum yield stress of the web material (ksi)

E = elastic modulus of the steel (ksi)

t_w = thickness of web (in)

Per the AISC specification, when the calculated applied force exceeds the capacity of the column section per Equation 2-17, a single transverse stiffener, a pair of transverse stiffeners, or a doubler plate extending the full depth of the web is required. The resistance factor for the LRFD method, ϕ, per the specification is 0.9, which is a typical factor used for a buckling limit state per Chapter E of the specification (AISC, 2016).

Timoshenko (1936) derived Equation 2-18, which describes the theoretical elastic buckling stress of a plate in his book "Theory of Elastic Stability".

$$F_{cr} = \frac{k\pi^2 E}{12(1-\mu^2)(b/t)^2} \qquad (2\text{-}18)$$

Where:

k = constant depending on type of stress, edge support conditions, and aspect ratio of the plate

E = elastic modulus of the steel

μ = Poisson's ratio

b/t = width to thickness ratio

Chen, Newlin, and Oppenheim (Salmon and Johnson, 1996) have treated web buckling in a column member as a plate subject to equal and opposite concentrated loads as shown in Figure 2.1-5. The elastic buckling load, P_{cr}, assuming simply supported boundary conditions and having a large a/h ratio is described in Equation 2-19 where the variable 'k' from Equation 2-18 is assumed 4.

$$P_{cr} = \frac{4\pi^2 E t^3}{12(1-\mu^2)h} = \frac{33{,}400t^3}{h} \qquad (2\text{-}19)$$

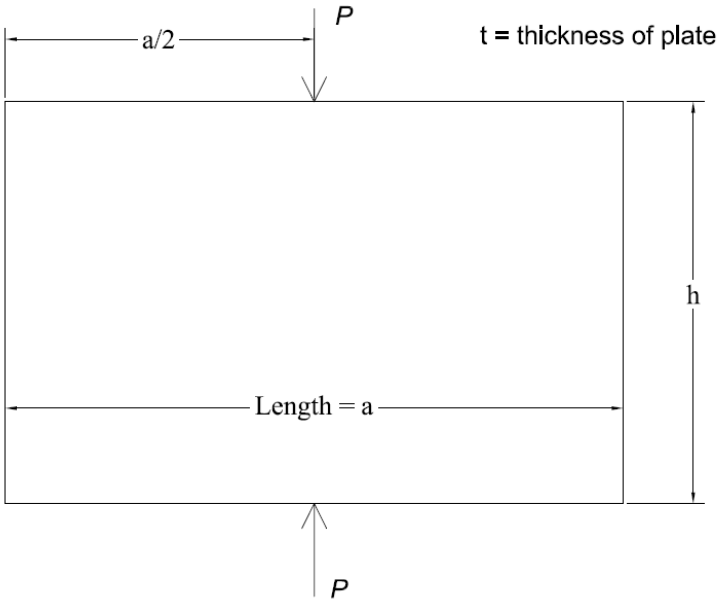

Figure 2.1-5: Plate subject to equal and opposite concentric concentrated loads (Salmon and Johnson, 1996)

If the rotational restraint provided by the column flanges were the fully fixed condition, the buckling strength would be theoretically twice as large as that given by Equation 2-19 (Salmon and Johnson, 1996). Experimental work by several authors concluded that the increase in effective degree of fixity at the loaded edge should be accounted for in practical design by making the strength proportional to the square root of the yield stress. Thus, Equation 2-20 was derived (Salmon and

Johnson, 1996).

$$P_{cr} = \frac{33{,}400t^3}{h}\sqrt{\frac{F_{yw}}{36}} = \frac{5570t^3\sqrt{F_{yw}}}{h} \quad (2\text{-}20)$$

The coefficient of 5570 was adjusted to 4100 in the first edition of the LRFD AISC Specification (1986), representing a lower bound from all experimental results. The equation was later rewritten as Equation 2-17 as in the current AISC Specification (2016).

2.2 Historical Research on Web Stiffeners

Prior to 1959, limited research was performed on beam-to-column moment connections and the influence of concentrated loads applied to the column flange. In general, there was no solidified design guidelines and research to provide clear conclusions and recommendations for the influence of concentrated forces. In particular, information regarding the criteria for column stiffening was missing.

Graham et al. (1959) conducted research on interior beam-to-column connections with the main purpose to understand the behavior of moment connections, with and without stiffeners, as well as the rotational capacity of these connections. Full-scale tests for two-way and four-way connections were performed. Two-way connection tests resembled conditions existing in a tier building where two beam sections were attached to both flanges of the column. Four-way connections included two beams connected to both sides of the column web with the two beams connected to the flanges. Thirteen (13) tests were carried out. Table 2.2-1 summarizes the test matrix (Graham et al, 1959).

Table 2.2-1: Full scale two and four-way connection tests by Graham et al. (1959)

	Column Shape	Beam Shape		Stiffener	
		Flange	Web	Type	Dimension
Two Way Connection	8 WF 31	12 WF 36	-	None	-
	8 WF 67				
	12 WF 65				
	12 WF 99				
	8 WF 31			±	3.9" x 7/16"
	12 WF 40			±	3.9" x 1/4"
	8 WF 31			± ±	5/16" x 22"
	12 WF 40			± ±	5/16" x 22"
	12 WF 40			Tee Stiffener	ST6 WF 32.5"x22"
	8 WF 31			Doubler Plate	5/16" x 20"
Four Way Connection	12 WF 65	16 WF 36	16 WF 36	None	-
	12 WF 40	16 WF 36	12 WF 27	± ± ±	1/2" thick
	12 WF 40	16 WF 36	16 WF 36	Tee Stiffener	ST6 WF 32.5"x22"

±	Horizontal plate stiffener, at level of tension and compression flanges
± ±	Vertical stiffeners at toes of column flanges
± ± ±	Horizontal plates that served as top plate and as seat plate

After examining the experimental behavior and results, Graham et al. (1959) realized that the full-scale test could have been performed on a smaller scale. Three different test types were carried out in order to determine column web buckling criterion, connection tension criterion, and effectiveness of eccentric stiffeners under compression. For the last tests, stiffeners at different eccentricities were added to the column. These tests were far simpler and quicker than full-scale tests such as those represented in Table 2.2-1. The length of all specimens was 3 ft., except for the eccentric stiffener tests in which the length of the specimens was 4 ft.

Double compression tests simulated the forces that would transfer from the compression flange of a beam to the web of the column. The test consisted of a "column stub" in which the web was subjected to compression by applying force at the flanges between two square bars, which were the same width as the flange of the beam section being simulated. An illustration of the test setup from Graham et al. (1959) is shown in Figure 2.2-1. The column stub was then tested in a 300 kip universal testing machine. A total of 11 double compression tests were carried out. According to the tests results and observations, yielding of the web began first directly underneath the bar, and then continued into the web until the beam failed by buckling. At a load representing 20% of the

overall column capacity, flange bending was witnessed.

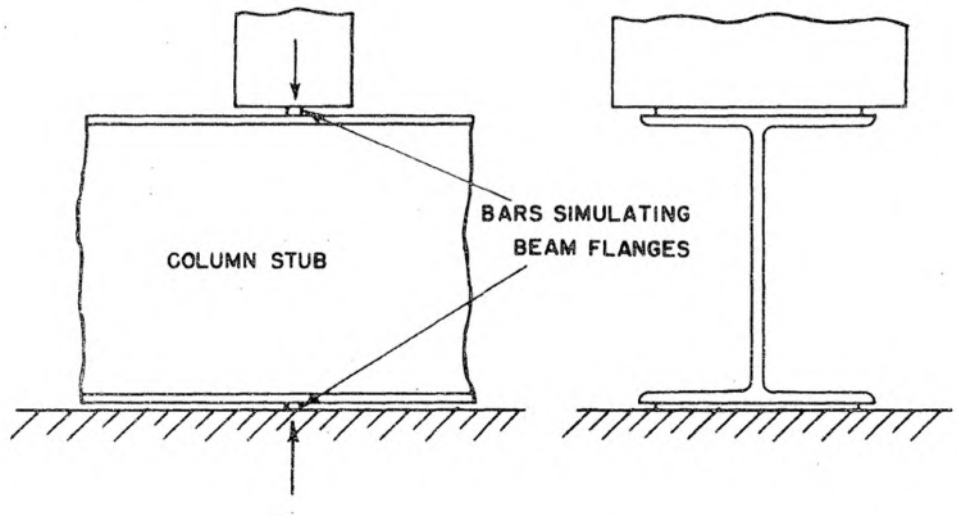

Figure 2.2-1: Double compression test performed by Graham et al. (1959)

In addition to double compression tests, double tension tests were performed to simulate the application of load to the column flange from beam flanges subjected to tension. The test consisted of a column stub being pulled by two equal plates, grove welded to the flanges of the column. Figure 2.2-2 illustrates the double tension test setup. The size of the plates mimicked beam sections. The specimen was then tested in an 800 kip universal testing machine. Eleven (11) double tension tests were carried out. Yield lines were first noted in the column fillet beneath the loading plate and then continued into the column web or on the column flange. The failure modes were either crack in the weld or crack in the column web/fillet below the flange and due to excessive straining close to the column fillet or at the center of the weld as a result of the outward yielding of the column flanges (flange bending).

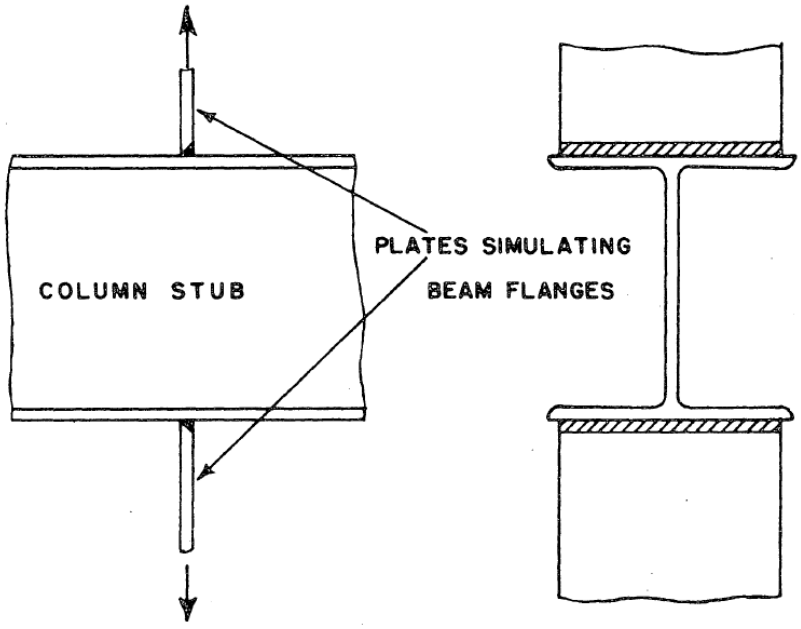

Figure 2.2-2: Double tension test performed by Graham et al. (1959)

In four-way connections, where the flange-connected and web-connected beams are of different depths, their bottom flanges are not always in-line. A third test was carried out to determine the degree of stiffening in this situation, where the stiffener was eccentric to the other compression loads. Two column sizes were used, W12X40 and W14X61 (per modern nomenclature), with stiffeners at 0 in. (concentric), 2 in., 4 in., and 6 in. of eccentricity. Eleven (11) specimens were tested in a 300-kip universal testing machine under double compression. Both series of tests showed a fast decline in the effectiveness of stiffeners at higher eccentricities. The stiffeners with 2 in. eccentricity provided approximately 65% of the effective load capacity of concentric stiffeners (calculated as capacity of specimens with stiffeners minus capacity of specimens with no stiffeners), whereas the stiffeners at 4 in. provided 20% effectiveness and at 6 in., the effects were negligible. Figure 2.2-3 shows a representation of a column stub with an eccentric stiffener from Graham et al. (1959).

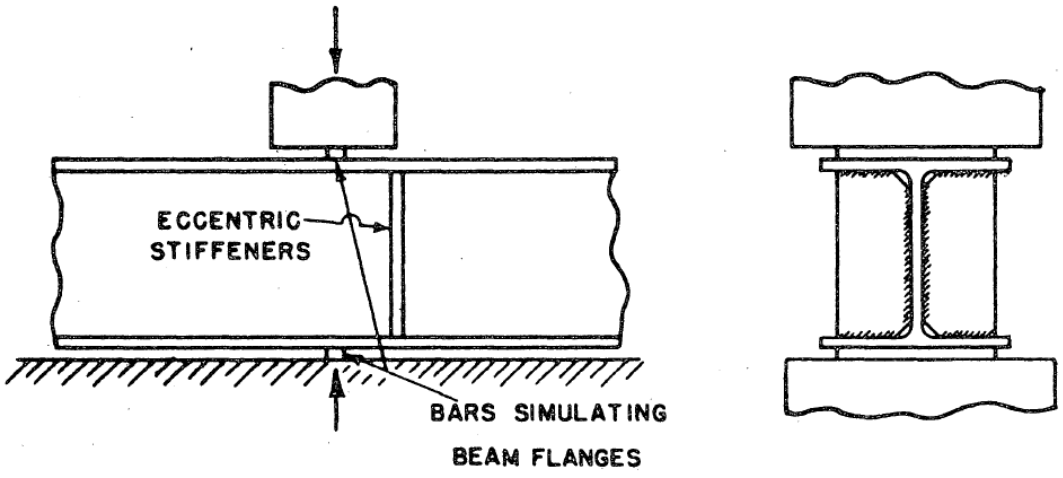

Figure 2.2-3: Double compression tests with eccentric stiffeners from Graham et al. (1959)

Despite the limited testing performed on eccentric stiffeners (5 per wide-flange section, 2 sections), Graham et al. (1959) observed and concluded that the influence of stiffeners at eccentricities higher than 2 in. has very little influence on the concentrated load resistance of the column. Graham et al. (1959) recommended to neglect the influence of stiffeners at higher eccentricities and to consider stiffeners of eccentricities of 2 in. or less as 60% effective as compared to concentric stiffeners. Table 2.2-2 summarizes the results for all three simulated connection tests.

Table 2.2-2: Simulated connection tests results by Graham et al. (1959)

	Column Shape	Loading Bar/Plate		Failure Load (kips)	Method of Failure
		Width	Thickness		
Compression Criterion Tests	8 WF 48	7"	1/2"	137	
	8 WF 58			202.5	
	10 WF 66			175.7	
	10 WF 72			190	
	12 WF 40			102.5	
	12 WF 65			143	
	12 WF 85			247.5	
	14 WF 61			137.5	
	14 WF 68			164	
	14 WF 84			221	
	14 WF 103			250	
Tension Criterion Tests	8 WF 31	7"	3/4"	100	Crack in column fillet
	8 WF 31	7"	7/16"	95	Crack in center of weld
	12 WF 65	8 1/2"	5/8"	149	"
	14 WF 68	8 1/2"	5/8"	167	"
	14 WF 84	11 1/2"	7/8"	212	"
	12 WF 65	8 1/2"	5/8"	82	Crack in column fillet
	14 WF 84	11 1/2"	7/8"	125	Crack in center of weld
	12 WF 65	8 1/2"	1 1/2"	189	"
	14 WF 68	8 1/2"	1 1/2"	199	"
	8 WF 67	7 1/2"	3/4"	256	Crack at outside of weld
	14 WF 176	11 1/2"	7/8"	444	"
Eccentric Stiffener Tests	**Column Shape**	**Stiffener**		**Eccentricity (in)**	**Failure Load (kips)**
	12 WF 40	3 3/4" x 1/4" x 10 3/4"		0	172
		"		2	146
		"		4	113
		3 3/4" x 1/4" x 10 3/4" + 3" x 1/4" x 8" Tee		4	116
		3 3/4" x 1/4" x 10 3/4"		6	104
		None		-	102.5
	14 WF 61	4 1/4" x 3/8" x 12 1/2"		0	282
		"		2	232.5
		"		4	167.6
		"		6	142.8
		None		-	137.5

Johnson (1959) published a research paper in the *British Welding Journal* titled "Compressive and Tensile Loading Tests on Joists with Web Stiffeners". The project addressed the design of web stiffeners in detail. An attempt to formulate a simple rule for the design of web stiffeners was made. Simple compression and tension tests were carried out on 12 in. long specimens of either 10X8X55 RSJ or 8X8X45 BFB with concentric stiffeners (in line with the applied load). A total of 18 tests with the applied load in compression and 4 tests with the applied load in tension were carried out. The stiffeners were welded to the members with different welding procedures, different sizes, and different configurations. Load was applied with mild steel plates that were welded to the outer faces of the specimen flanges and in line with the stiffeners. After analyzing the tests, the following conclusions were made:

- If stiffeners are welded to the web and inner faces of the flanges of the beam, compressive stresses are induced which are probably higher in the web than in the stiffeners.
- It is recommended to provide lateral support to the stiffeners by welding them to the face of the web.
- There is not much benefit from stiffeners that are fabricated perfectly to fit within the section. Some imperfections will result in very similar behavior in comparison to the ideal condition.

Beedle and Christopher (1963) published a report with the main purpose to consolidate and discuss the results of some of the most important research studies of rigid moment connections. Rigid moment connections are designed to develop the full plastic moment of the connecting member. The inelastic rotation that occurs after M_p is reached at the ends of the beam permits redistribution of moment so that subsequently the plastic moment is reached at the center. Tests for welded beam-to-column connections were performed at Lehigh University. According to the test results, the presence of horizontal or vertical (turned sideways 90° and welded to the edge of the flanges only) stiffeners provide more strength to the moment connection and allows the beam to develop its moment capacity at the column flange. Similarly, according to test results at Cambridge University on moment connections bolted to the beam and welded to column, the presence of stiffeners help the connection develop the design moments, compared to the test without stiffeners where the column web buckled before developing the plastic moments. This concludes that transverse stiffeners provide additional strength in beam-to-column moment connections.

2.3 More Recent Experimental Investigations on Effectiveness of Web Stiffeners

Elgaaly and Salkar (1991) studied the design of built-up and rolled sections under in-plane compressive edge loading as well as the effect of load eccentricity with respect to the plane of the web. During the course of their investigation, the authors encountered stiffener failure in single compression tests in which local crippling occurred in the stiffeners. Research in this area was started by Elgaaly and Nunan (1989) at the University of Maine. Twenty-two W12x19 rolled sections were tested to study the effect of eccentricity on the maximum load. Two different load application methods were used, (1) with a patch plate and (2) with a cylindrical bar, both placed at a specified eccentricity from the plane of the web. Figure 2.3-1 shows the load application methods. The researchers found reduction in the web ultimate strength when the load was applied through a thick patch plate placed eccentric with respect to the plane of the web. Moreover, reductions occurred when the load was applied using a cylindrical roller, thus meaning that the eccentricity of the load with respect to the neutral axis of the steel member is directly related to the decrease in capacity.

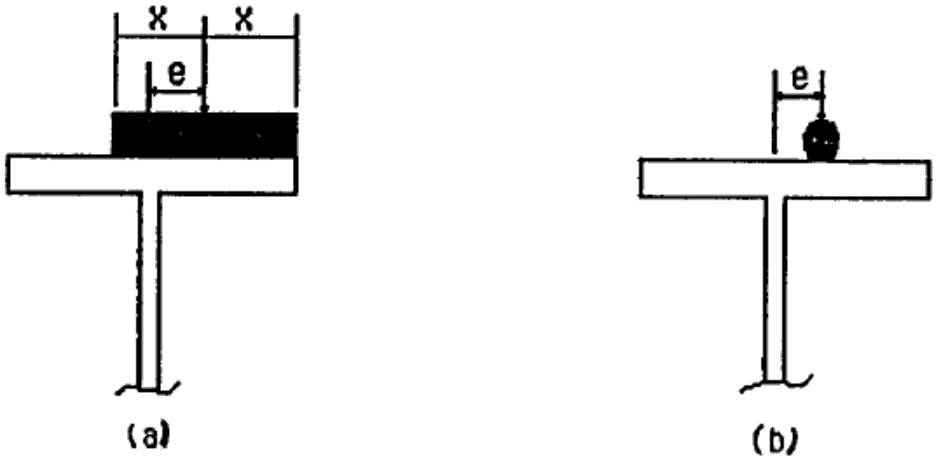

Figure 2.3-1: Load application methods (Elgaaly and Nunan, 1989)

Further research was carried out by Elgaaly and Sturgis (1989). Several rolled and built-up columns were tested. The parameters studied were the flange to web thickness ratio, t_f/t_w, the eccentricity of the load, e, and the panel aspect ratio, b/d (where b represents the distance between supports and d is the depth of the member). The authors concluded that the web ultimate strength decreases with an increase in e, increases with an increase in t_f/t_w, and that the panel aspect ratio did

not significantly affect the web strength.

Salkar (1992) performed seventeen (17) experimental tests on W16X26 rolled sections with a length to depth ratio (*b/d*) of 2.3. Three methods of load application on the top flange were considered; (1) loading though a plate, (2) loading through a wide flange section (meaning that a wide flange section was placed on the member under study to apply the force), and (3) loading through a roller. Details of the 17 tests conducted by Salkar (1992) are summarized in Table 2.3-1.

Table 2.3-1: Tests on webs with intermediate load-bearing stiffeners (Salkar, 1992)

Test No.	t_w (in)	t_f/t_w	b_f/t_f	d/t_w	t_s/t_w	d_s/d	N/d	e_1 (in)	F_{yw} (ksi)	F_{ys} (ksi)	P_{tst} (kips)	Load Application Method
1	0.262	1.23	17.2	59.9	0.653	0.50	0.303	0	48	55	161.1	Patch plate
2	0.254	1.24	17.4	61.5	0.673		0	0.5	49	55	107.0	Roller
3	0.262	1.22	17.2	59.9	0.653		0.303		46	55	161.6	Patch plate
4	0.249	1.29	17.2	62.8	0.695		0	0	47	53	114.0	Roller
5	0.253	1.36	16.0	61.8	0.961		0.304		49	48	169.1	Patch plate
6	0.250	1.26	17.5	62.5	0.972		0	0.5	52	48	120.0	Roller
7	0.260	1.31	16.2	60.3	0.935		0.304		48	48	161.0	Patch plate
8	0.255	1.27	17.0	61.3	0.949		0	0	47	48	144.0	Roller
9	0.256	1.31	16.5	61.0	1.230		0.303		49	47	175.2	Patch plate
10	0.251	1.29	17.0	62.5	1.250		0	0.5	49	47	127.5	Roller
11	0.258	1.27	16.8	60.8	1.220			0	50	47	148.8	Roller
12	0.264	1.29	16.1	59.2	1.190				44	49	150.0	Roller
13	0.253	1.34	16.2	61.8	0.676	0.75			47	45	126.0	Roller
14	0.263	1.29	16.1	59.4	0.932				46	48	153.6	Roller
15	0.263	1.28	16.3	59.4	1.180				46	48	164.0	Roller
16	0.262	1.26	16.7	59.6	0.920			0.5	46	48	132.1	Roller
17	0.255	1.29	16.7	61.3	0.945		0.303	0	47	48	145.3	I-Section W4x13

In Table 2.3-1, P_{tst} refers to the test failure load, F_{yw} and F_{ys} refer to the yield stress of the web and stiffener material, respectively, d_s is depth of stiffener, t_s is thickness of stiffener, N represents the width of loading (assumed 0 for the roller condition), and e_1 refers to the eccentricity of load with respect to the plane of stiffener. Three modes of failure were observed; web crippling below the stiffener, local stiffener crippling, and global stiffener crippling. Web crippling was only seen in the specimens with half-depth stiffeners, whereas the specimens with deep stiffeners failed by global stiffener crippling.

2.4 Analytical Investigations on Effectiveness of Web Stiffeners

Sherbourne (1978) published the paper "Computer Simulation of Column Webs in Structural Steel Connections" which focused on analyzing the stability of column webs in beam-column moment connections. Analytical studies were performed with the finite element method. With this investigation, an attempt was made to quantify the effects of significant geometric parameters such as the stiffener size and shape and the width and thickness of the web and flanges. The finite element models used the displacement approach on the minimization of the total potential energy of the system. A variable mesh geometry, with smaller elements grouped near the load and along the direction of the load was used to accurately simulate the load distribution and element displacement. Elements in the flanges and web stiffeners had different thicknesses from that of the web. The loads were always applied at nodal points. The mesh geometry and boundary conditions used in this finite element model are illustrated in Figure 2.4-1.

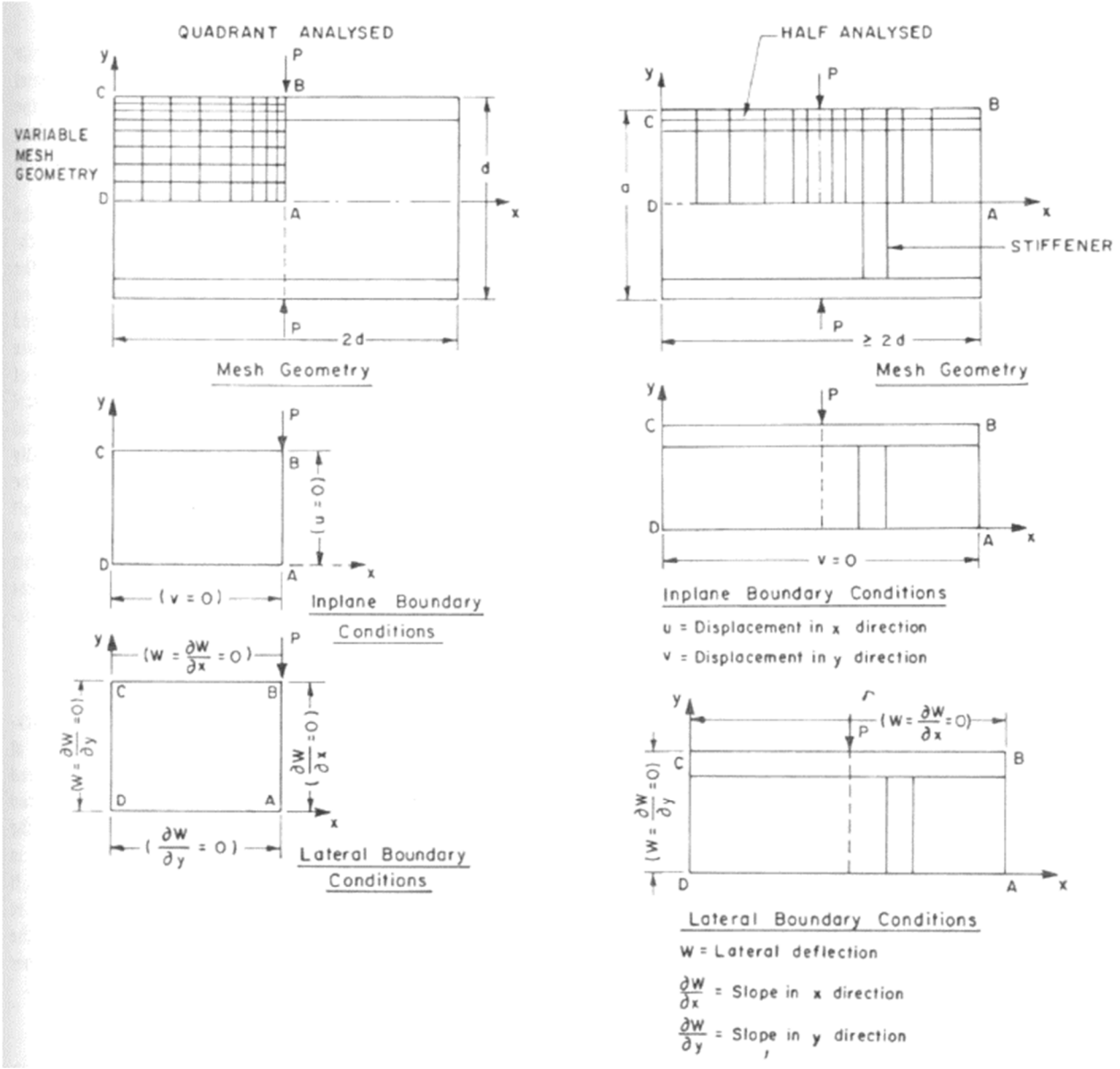

Figure 2.4-1: Mesh geometry and boundary conditions for FEM by Sherbourne (1978)

Sherbourne (1978) found that the web thickness has a direct influence on the buckling load and behavior of the column. A relationship exists between the two basic problems, which determine the behavior of the column web, which are excessive yielding and elasto-plastic buckling of the web under non-uniform stress. To study the transitional behavior for a given wide flange section, Sherbourne (1978) gradually increased the web thickness to change the failure mechanism from buckling to yielding. He defined an ideal section as one that would promote buckling and yielding at the same load. The results for two wide flange sections are shown in Figure 2.4-2.

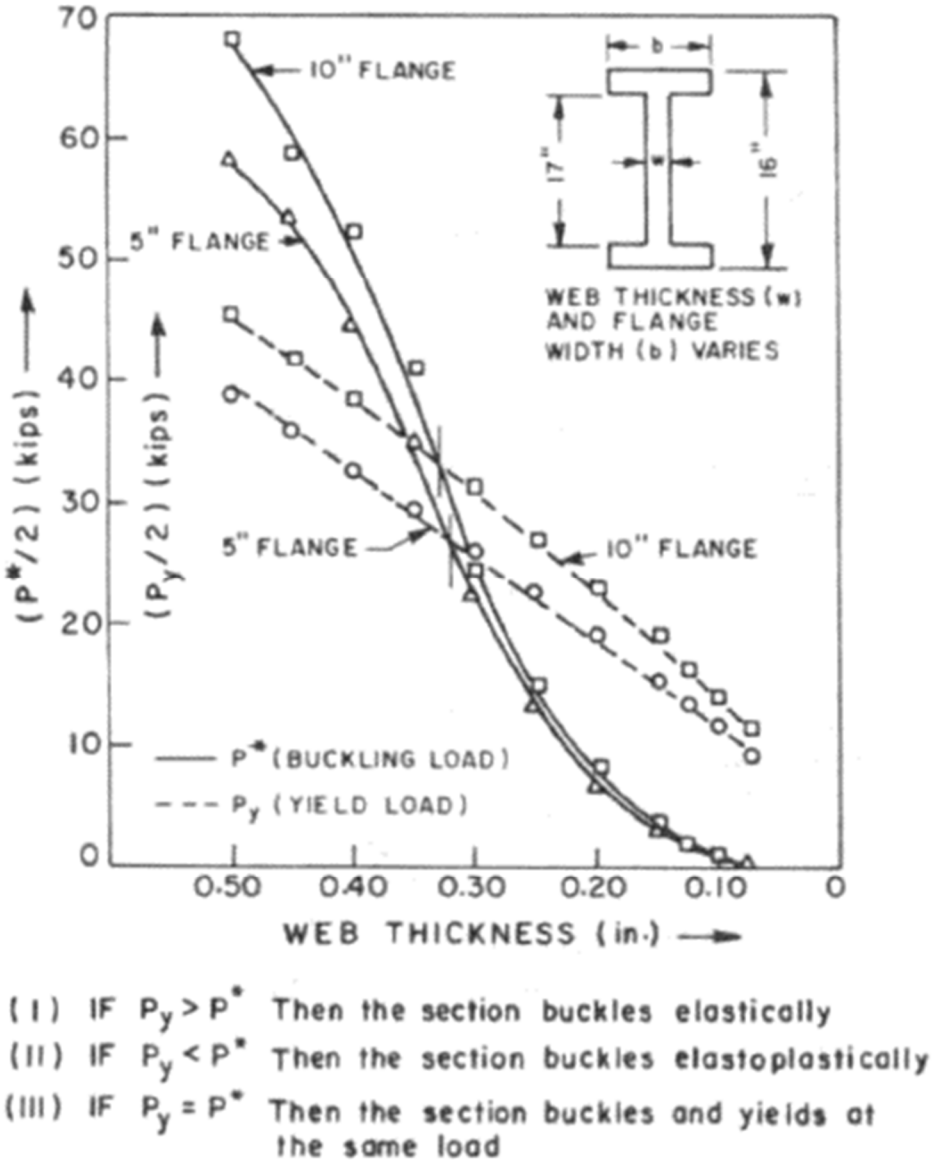

Figure 2.4-2: Variation of buckling load with column web thickness by Sherbourne (1978)

The analytical results showed that the flange width does not have a significant influence on the buckling load compared to the variation of the web thickness. Nonetheless, an increase in the flange width increases the buckling load slightly. From the finite element models, for thicker webs, increasing the flange width has a considerable influence as compared to the case with thinner webs.

Analytical tests on wide flange sections with concentric and eccentric stiffeners were also performed. The author verified that transverse stiffeners essentially increase the horizontal load that can be applied to the column flange from moment connections and that the location and size of them

play an important role in the load carrying capacity. The study consisted of two different test series with two different stiffener sizes. The first series had a stiffener with a thickness equal to the flange thickness and the second series had a stiffener with a thickness equal to half the thickness of the flange. Figure 2.4-3 illustrates the eccentricities studied and the location of the load. The column sections studied ranged from W12X14 to W14X95 (using modern nomenclature). In general, the effectiveness of the stiffeners decreases very rapidly as the eccentricity increased. For the first test series, the effectiveness of the stiffeners located at an eccentricity of 25% of half the column depth ranged between 50% and 75% of that for concentric stiffeners. For the second test series, the results showed that the load capacity decreases dramatically compared to the results from the previous series. Nevertheless, the load capacity reduction percentage is similar to the results with thicker stiffeners.

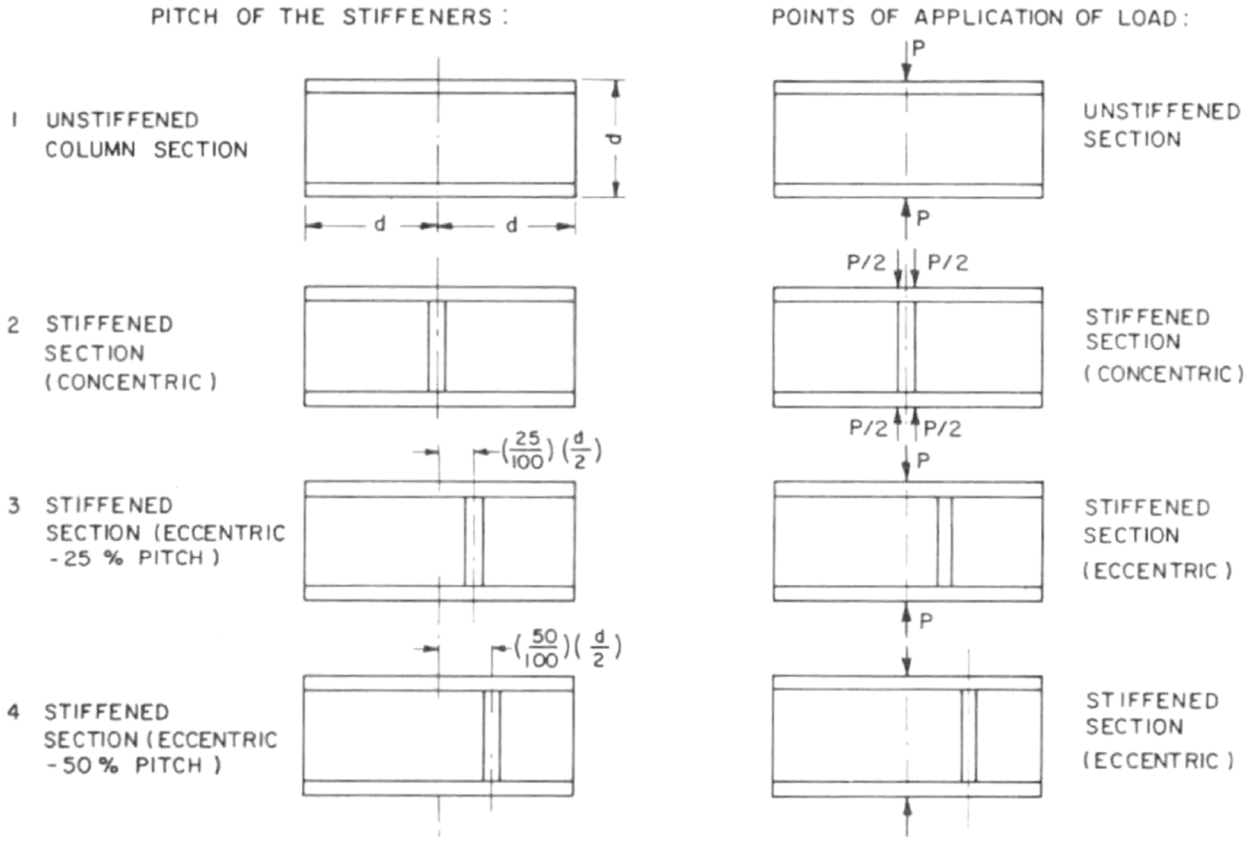

Figure 2.4-3: Stiffener conditions for tests performed by Sherbourne (1978)

The finite element model approach was validated by comparing the results with the experimental tests performed by Graham et al. (1959). Sherbourne (1978) decided to use the full scale two way connection test results of the following column shapes; W8X31, W12X65 and W12X40 which were connected to a W12X36 beam section (the first two tests without stiffeners, and the last one with two stiffeners concentric with both top and bottom flanges of the beam section) to compare findings. The estimates from the analytical approach for the maximum load that causes buckling load were within 30% of the experimental results. Moreover, the estimates for the yield load were in most cases within 10% of those from the finite element analysis. The predicted results compared fairly well with the experiments, attesting to the validity of the modeling technique. Sherbourne (1978) believed that the formulation used for his research may be further improved by including non-linear geometric behavior and employing sophisticated and large numbers of finite elements.

Norwood (2018) published a thesis entitled "Effect of Continuity Plate Eccentricity on the Performance of Welded Beam-to-Column Connections". The main objective was to expand on the eccentric stiffener design guidelines as well as to provide a new design equation for determining beam-to-column connection capacities for configurations having eccentricities. Norwood (2018) developed 12 finite element models to investigate the influence of eccentricity with different beam depths. The column sections analyzed were W14x132 and W21x147 and both were modeled with the same wide flange sections attached, with these beams selected to vary the connection eccentricity (eccentricity created by the difference in between the location of the bottom flanges of the connected beams). Figure 2.4-4 shows the basic configuration of the models developed by Norwood (2018). The models for each column size had a different eccentricity condition, varying from 0 in. to 6 in. of eccentricity.

Norwood's analytical results were then compared with the full-scale test results by Graham et al. (1959) to validate the finite element models. Without geometric imperfections, the finite element models significantly overestimated the measured sub-capacity given by Graham et al. (1559), while the simulations considering imperfections were able to reasonably estimate the maximum sub-capacity.

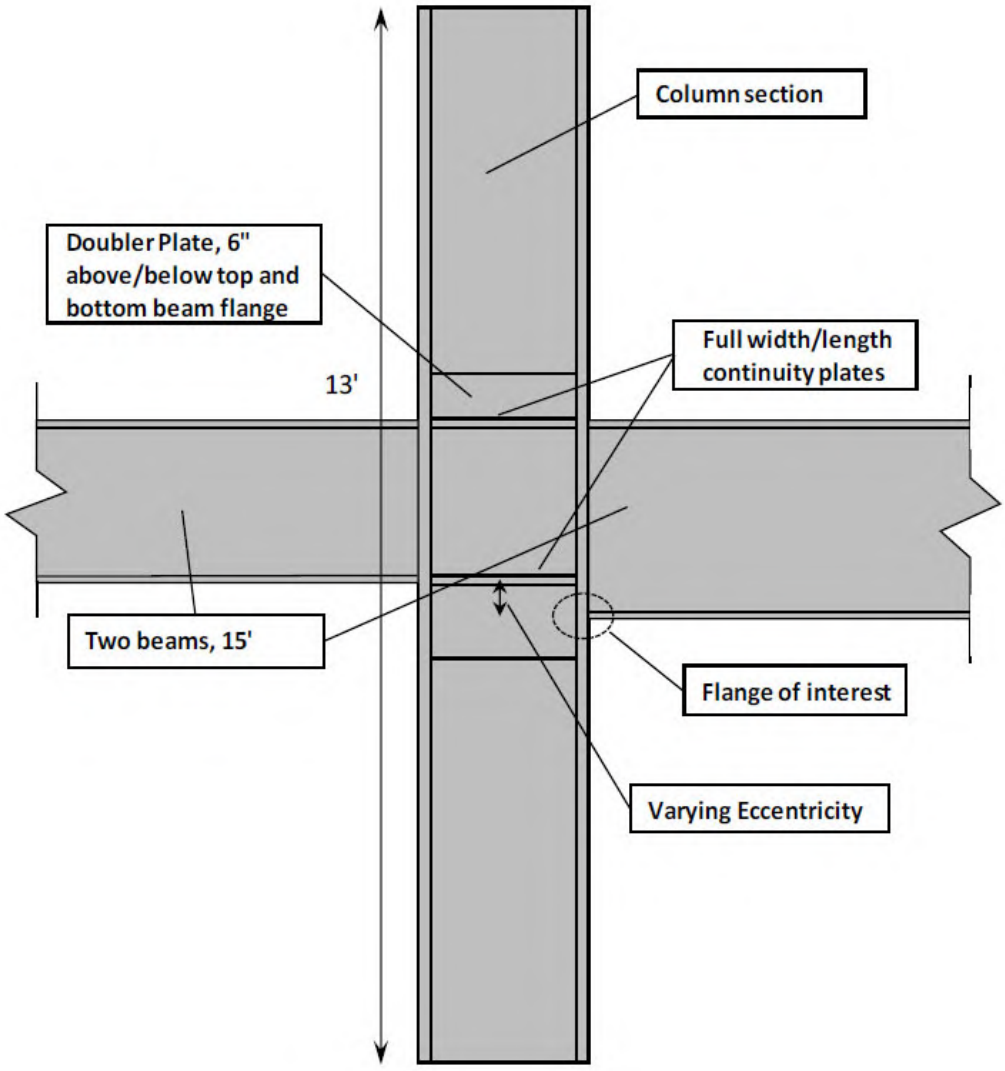

Figure 2.4-4: Basic configuration of the connections modeled by Norwood (2018)

From the research by Hajjar et al. (2003), the different limit states applicable to the connection shown in Figure 2.4-4 are flange local bending (FLB), web local yielding (WLY), web local crippling, web compression buckling, and web panel zone shear (PZ). Table 2.4-1 summarizes the results of the different connection configurations selected by Norwood. 'R_u' represents the capacity for each test and '$\phi R_n/R_u$' represents the theoretical capacity vs. demand ratios for the unstiffened condition and for different theoretical limit states. Ratios less than 1.0 indicate that the limit state has been exceeded and that transverse stiffeners are required to prevent FLB. From Table 2.4-1, the web panel zone shear limit state significantly controls over other limit states and doubler plates

should be required per AISC (2016), which increases resistance to the WLY limit state as well.

Table 2.4-1: Beam-column configurations design summary (Norwood, 2018)

Column	Beam 1	Beam 2	Eccentricity (in)	ØRn/Ru FLB	ØRn/Ru WLY	ØRn/Ru PZ
W14x132	W12x96	W12x96	0.0000	0.45	0.44	0.24
W14x132	W16x100	W16x77	0.2750	0.45	0.44	0.27
W14x132	W14x82	W12x96	1.6450	0.54	0.52	0.27
W14x132	W18x106	W16x77	2.0200	0.48	0.47	0.28
W14x132	W16x89	W12x96	4.1250	0.51	0.49	0.26
W14x132	W18x86	W12x96	5.8300	0.53	0.51	0.27
W21x147	W12x96	W12x96	0.0000	0.56	0.49	0.37
W21x147	W16x100	W16x77	0.2750	0.56	0.50	0.41
W21x147	W14x82	W12x96	1.6450	0.67	0.59	0.39
W21x147	W18x106	W16x77	2.0200	0.60	0.54	0.42
W21x147	W16x89	W12x96	4.1250	0.63	0.56	0.38
W21x147	W18x86	W12x96	5.8300	0.66	0.57	0.38

It is important to note that the flange local bending (FLB) limit state is somewhat arbitrarily defined in the specifications based on subjective effects of column flange deformations. Early research by Graham et al. (1959) featured an equation developed for the FLB limit state, which was initially used as an indicator of weld fracture. However, research by Prochnow et al. (2000) found that the equation is generally conservative. Therefore, Norwood (2018) used a limit state for FLB in Table 2.4-1 that is similar to that recommended by Prochnow et al. (2000), which is based on a ¼ in. column flange deformation. Norwood (2018) used an allowable deformation for an individual flange of 1/8 in. The thought behind this slight modification is that each flange could separate 1/8 in. in opposite directions and reach the 1/4 in. total allowable deformation. This approach was also used in another research project by Lee et al. (2002).

The finite element analysis was performed using the commercial finite element program ABAQUS (2014). Four-noded linear shell elements with reduced integration (S4R in ABAQUS) were used as well as a cyclic nonlinear kinematic material hardening model based on the plastic strain behavior of A572 Gr. 50 steel. Norwood (2018) used a mesh size of 0.5 in. near the connection while a mesh size of 3 in. was used away from the connection region. Figure 2.4-5 shows the boundary conditions used for the two-way moment connection models.

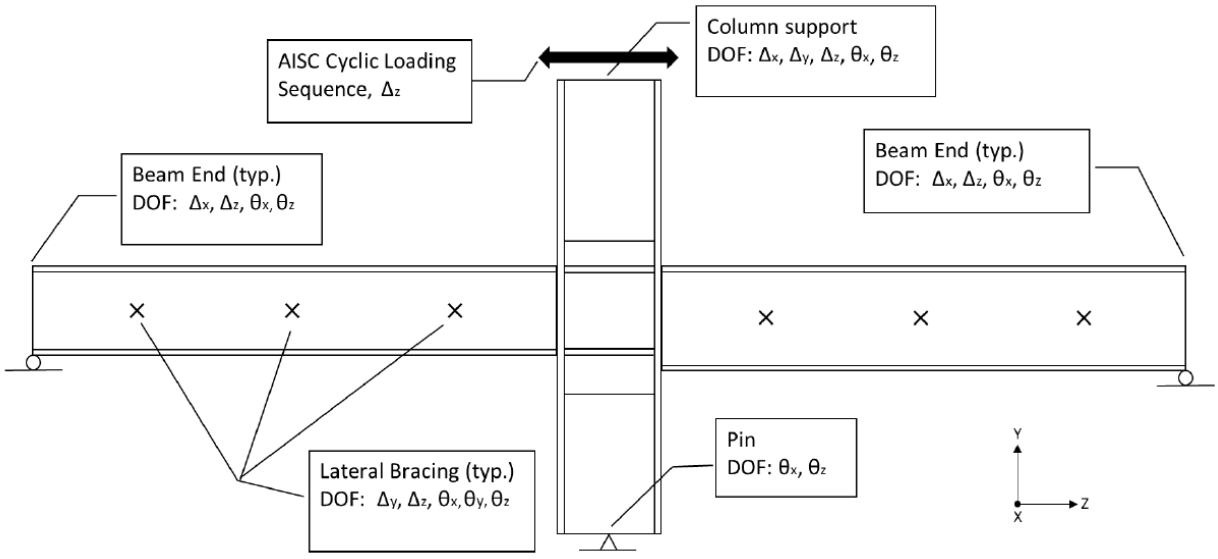

Figure 2.4-5: Boundary conditions for two-way moment connections (Norwood, 2018)

The validations tests included W12x40 and W14x61 column stub specimens similar to the ones used by Graham et al. (1959) and tested in double compression. Norwood (2018) considered geometric imperfections in the validations tests to be able to match the results by Graham et al. (1959). Imperfections were introduced at 100%, 50%, and 10% of the maximum fabrication tolerance allowed with a 10% imperfection providing the most accurate results compared to the experimental results. Table 2.4-2 illustrates the results of the W14x61 and W12x40 validation models with a percent error to show a direct comparison between the analytical and experimental results. All results compare favorably with the exception of the W12X40 tested without stiffeners. For this case, the analytical result provided by Norwood (2018) is not in line with the remaining results in the table.

Table 2.4-2: Comparison of results from Graham et al (1959) and Norwood (2018)

Column Section	Eccentricity (in)	Graham et al. Failure Load (kip)	10% Imperfection Failure Load (kip)	Percent Error (%)
W12x40	0	172.00	171.41	0.34%
W12x40	2	146.00	152.29	4.31%
W12x40	4	113.00	112.71	0.25%
W12x40	6	104.00	103.84	0.15%
W12x40	NS	102.50	130.84	27.45%
W14x61	0	282.00	272.74	3.28%
W14x61	2	232.50	231.63	0.37%
W14x61	4	167.60	166.28	0.79%
W14x61	6	142.80	143.14	0.24%
W14x61	NS	137.50	143.33	4.24%

During the analytical tests, it was noticed that significant column flange yielding took place prior to the flange local bending (FLB) limit state. Thus, an additional failure mode of flange local yielding (FLY), which indicates complete yielding of the column flange section, was taken into account to determine the capacity of the column section.

The analytical results from Norwood's research are shown in Figures 2.4-6 and 2.4-7. In a similar way to previous research, increasing the level of eccentricity between the beam flange and the transverse stiffener results in a decrease in resistance to concentrated forces. However, the results showed that eccentric stiffeners were more effective than the recommended values from previous research. For the FLY limit state, there was a 90% decline in stiffener participation with eccentricities from 0 to 2 in. However, the stiffener was found to maintain that 10% increase in capacity up to 4 in. of eccentricity. On the other hand, for the FLB limit state, the stiffener contribution was found to be in between a 50-60% increase in capacity at 2 in. of eccentricity. The stiffener contribution fell to 10% at 4 in. of eccentricity. Moreover, more compact sections receive less contribution from transverse stiffeners regardless of the limit state. This is shown in Figures 2.4-6 and 2.4-7, which describe the added column capacity versus eccentricity for both W21X147 and W14X132 column sections and both FLY and FLB limit states. The W14X132 section is less compact than the W21X147 section with a width-to-thickness ($b/2t_f$) ratio of 7.15 and 5.44 respectively.

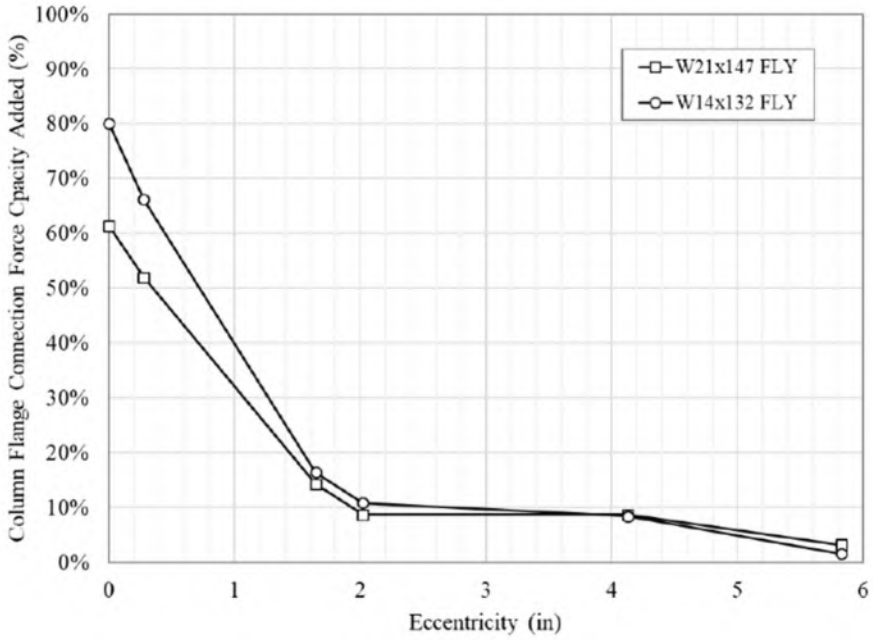

(a)

Figure 2.4-6: Effectiveness of stiffener eccentricity for the different width-to-thickness ratios for FLY limit state (Norwood, 2018)

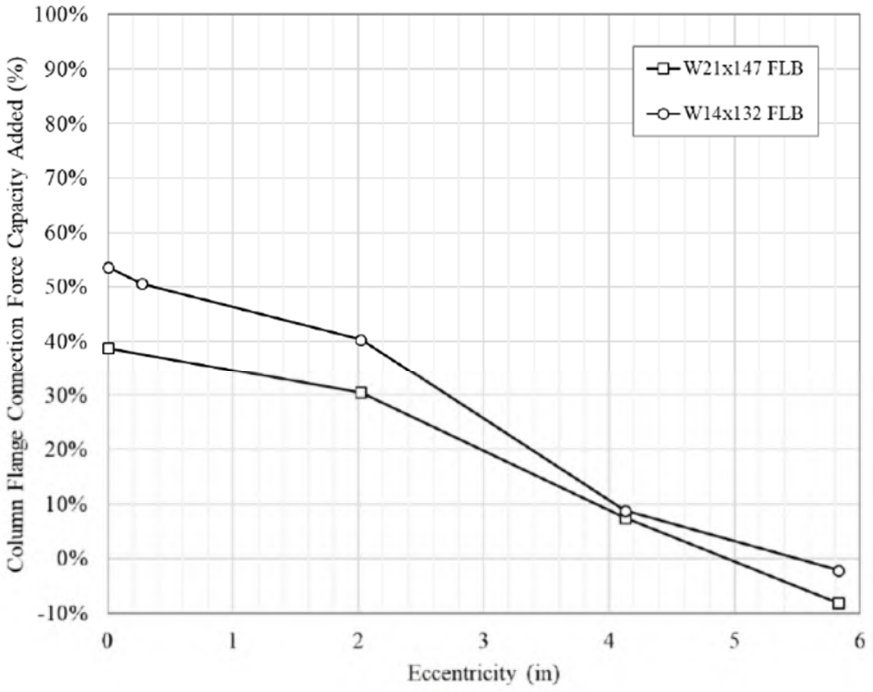

(b)

Figure 2.4-7: Effectiveness of stiffener eccentricity for the different width-to-thickness ratios for FLB limit state (Norwood, 2018)

Equation 2-21 is a representation of the equation by Carter (1999) in which the capacity of stiffeners is reduced by 35% at 2 in. of eccentricity. Beyond 2 in. of eccentricity, Carter (1999) recommends that no contribution shall be taken into account. From analytical results, Norwood (2018) proposed Equation 2-22 for determining concentrated load capacities in beam-to-column connections for stiffener eccentricities up to 4.5 in.

$$\emptyset R_{n,ecc} = \emptyset R_{n,FLB} + R_{u,st}(1 - 0.175e) \quad 0in. \leq e \leq 2in. \tag{2-21}$$

$$\emptyset R_{n,ecc} = \emptyset R_{n,FLB} + R_{u,st}(-0.039(e^2 + e - 25)) \quad 2in. \leq e \leq 4.5in. \tag{2-22}$$

Where:

$\phi R_{n,ecc}$ = resulting connection capacity (kip)

$\phi R_{n,FLB}$ = column capacity to resist FLB (kip)

$R_{u,st}$ = required strength of the stiffeners (kip)

e = stiffener eccentricity (in)

Salkar et al. (2015) studied web crippling under patch loading and the use of partial-depth stiffeners. Chapter J of the 2010 AISC Specification (AISC, 2010) requires the use of either single or double-sided half-depth (minimum) transverse web stiffeners or web doubler plates when the web crippling strength is less than the design concentrated load. However, research by Salkar et al. (2015) clearly showed that web crippling could still occur in webs having half-depth stiffeners. A finite element analysis was performed and then validated by comparing it to the experimental results previously performed by Salkar (1992).

A finite element analysis was performed by Salkar (2015) to study the stiffened web behavior and to conduct a parametric study to analyze the effect of various parameters (N, d_s, t_s, and e_1) on the stiffened web. Three dimensional eight-node isoparametric shell elements with six degrees of freedom per node were used to discretize the specimens. For material nonlinear analysis, an elastic-plastic model was used. The hardening modulus selected was 1,000 ksi (about 3.5% of the elastic modulus). The mesh was made up of 216 shell elements and 705 nodes. The average ratio of the experimental test capacity from Salkar (1992) to the finite element analysis failure load was 1.017, thus validating the accuracy of the finite element model. The finite element results show strength

increases with t_s (thickness of stiffener) up to an optimum value of t_s. This optimum value was always found to be close to the thickness of the web. The crippling strength of the beam increased by 15% when d_s (depth of stiffener) was increased from 0.5d to 0.75d. Eccentric loading through a plate did not have an effect on the stiffened web crippling effect, whereas eccentric loading through a roller or an I-beam reduced the stiffened web strength considerably. Lastly, the magnitude of the ratios t_f / t_w and t_f / t_s are directly related to the web crippling strength reduction caused by eccentric loading. These conclusions are applicable for rolled beams and for the parameters N/d up to 0.3, e_1 up to 0.5 in., and d_s/d value up to 0.75.

Salkar (2015) used the results of the parametric study to develop a formula to predict the stiffened web capacity, P_u, as shown in Equation 2-23. This equation is valid only if the ratio of the width of stiffener (front to back) to its thickness does not exceed $0.56(E/F_{ys})^{0.5}$.

$$P_u = K + F_{ys} t_s b_s (R) \left(2d_s / d\right)^X \tag{2-23}$$

Where:

$$K = 0.80 t_w^2 \left\{1 + 3\left(N/d\right)\left(t_w/t_f\right)^{1.5}\right\}\left(EF_{yw}t_f/t_w\right)^{0.5} \tag{2-24}$$

$$R = 2e_1 \left\{\left(t_f/t_w\right)^{0.5}\left(t_f/t_s\right)^{0.5}/1.55 - 1\right\} + 1 \tag{2-25}$$

$$X = 0.50\left(d/d_s\right) \tag{2-26}$$

b_s = twice the width of the front or back stiffener

Salkar (2015) gave recommendations to change the provision given in the 2010 AISC Specification (AISC, 2010) for calculating the stiffened web strength. It was recommended that webs shall be provided with a minimum three-quarter depth web stiffeners for eliminating the web crippling limit state and that the stiffener thickness be approximately the thickness of the web to maximize the web strength. The present AISC Specification (AISC, 2016) recommends the use of half-depth stiffeners to eliminate the web crippling limit state, but it does not provide any direct formula to evaluate the stiffened web strength due to the addition of a half stiffener. The proposed equation provides a means for evaluating stiffened web crippling strength.

2.5 Additional Beam-Column Reinforcement Research

In the 1990's, due to an atmosphere of reduced construction activity, minimizing construction, fabrication, and erection costs was a priority. Transverse stiffeners and doubler plates are very expensive to use. "It is the labor involved in cutting, profiling, and welding transverse stiffeners and web doubler plates that is predominant in their cost" (Carter, 1999). Several authors such as W. A. Thornton (Thornton, 1992), Bill Dyker (Dyker, 1992), Barry L. Barger (Barger, 1992), and David T. Ricker (Ricker, 1992) published reports in *Modern Steel Construction* in a special report on "How Design Engineers Can Cut Fabrication Costs". The mindset was to abolish the use of transverse stiffeners and doubler platers by increasing the column sizes and reducing costs at the same time. Some of the statements are as follows:

- "Column weights can be increased … without increasing costs because the stiffeners and the doubler plates will tend to increase erection costs" (Thornton, 1992).
- "Perhaps a slight increase in the unit weight of a column would offset all the costs associated with stiffeners" (Dyker, 1992).
- "Consider using a heavier column shaft or high strength steel to eliminate the need of column stiffeners" (Ricker, 1992).

Despite the efforts to reduce the use of transverse stiffeners, AISC Design Guide 13 "Stiffening of Wide-Flange Columns at Moment Connections: Wind and Seismic Applications" (Carter, 1999) was published. More information from this design guide was provided earlier in this chapter and is also provided later in this chapter.

In search of new solutions for the concentrated load problem in moment connections, Tawaga (2005) took a different approach. Instead of using stiffener plates, the author proposed a new stiffening method to meet some architectural needs. This new method used bolted channels as an alternative to traditional stiffeners and doubler plates. The channels were intended to eliminate transverse stiffeners and allow ducting inside of the joint. This approach also eliminated the drawbacks related to welding. The research was based on finite element simulations to examine the strength of the connection. According to the author, tensile loads predicted and obtained from tests

indicate that stiffening with channels improves the yield strength of the specimen without stiffeners by 53%-104%, depending on the channel stiffener thickness. Although this research excluded instability characteristics in the compression zone, the proposed method of stiffening with channels was found to be satisfactory for strengthening both the column web against shear forces and the flanges against tension forces. However, the proposed channels did not provide large stiffening effects to resist shear in the column-web panel zone.

A decade later, Tawaga (2014) investigated bolted beam-to-column connections stiffened with steel member assemblies instead of channel stiffeners. The primary objective of this study was to find a stronger solution to the previous research with channel stiffeners that would provide larger stiffening effects on the column-web yielding and panel-zone shear. For instance, the assemblies used for the study were composed of steel angles and plates as illustrated in Figure 2.5-1.

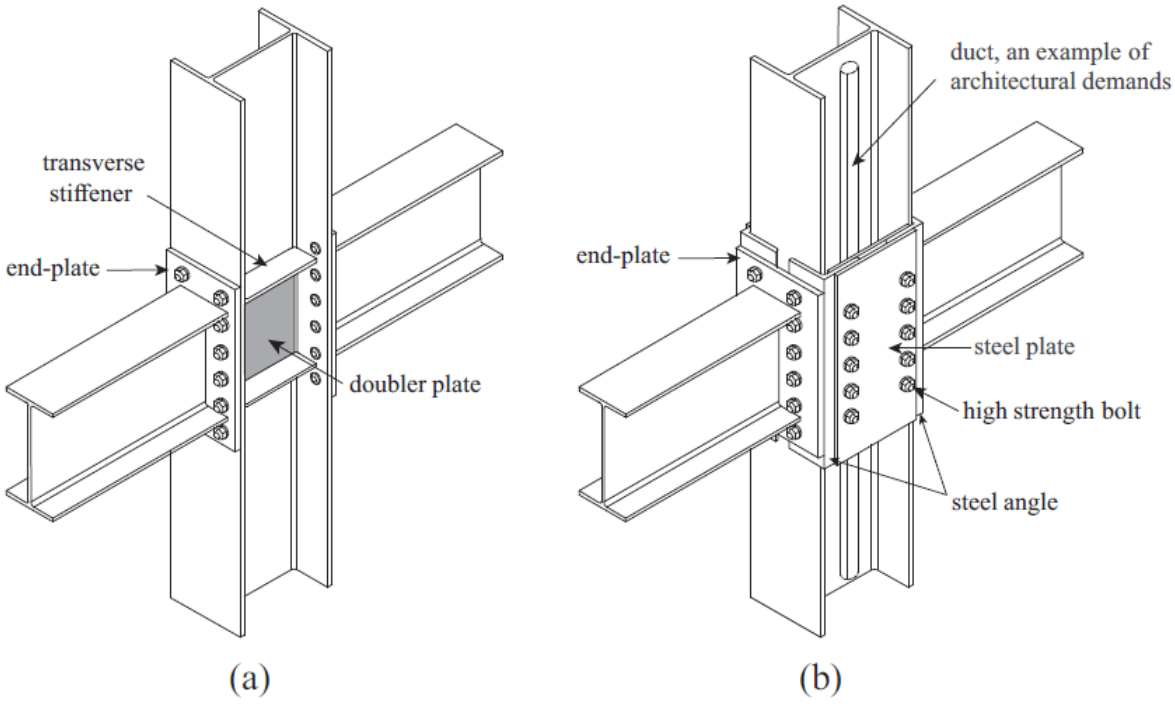

Figure 2.5-1: Beam-to-column end plate moment connections: (a) typical connection with stiffeners and (b) proposed bolted joint with side angles

Local tensile strength was first evaluated based on the yield line theory. Then local compressive strength was also evaluated. To acknowledge the stiffening method efficiency, three local tensile tests and one cyclic load test were carried out. The test results turned to match with the calculated

values for the strength of the connection, thus revealing the new proposed method to be effective.

2.6 Current Code Provisions/Recommendations for Eccentric Stiffener Design

There are several steel construction specifications used throughout the world. Some of the most recognized entities in terms of steel construction are the American Institute of Steel Construction (AISC), the European Commission, the Canadian Institute of Steel Construction (CISC), and the Building Center of Japan. Each of them have different rules and regulations. A review of these specifications reveal limited details on stiffener design for concentrated loads and even less detail for the design of eccentric stiffeners to resist concentrated loads. The following subsections summarize all information found from various specifications on the design of eccentric stiffeners. The applicability of such specifications other than that published by AISC to this research project is somewhat uncertain.

2.6.1 American Institute of Steel Construction (AISC)

The AISC "Specification for Structural Steel Buildings" (AISC, 2016) is the current specification used in the United States and provides some guidance on the design of column stiffeners as tension or compression members. However, the specification and the Steel Construction Manual (AISC, 2017) do not provide information in regards to eccentric stiffener design.

The only source available from AISC for the design of eccentric column stiffeners or alternate methods to reinforce the column is the AISC Design Guide 13 "Stiffening of Wide-Flange Columns at Moment Connections: Wind and Seismic Applications" (Carter, 1999). More specifically, Section 5.1 of the design guide discusses options for column stiffening for beams of differing depth and/or top of steel. This was discussed in Chapter 1 of this report and summarized here for completeness. The design guide shows several options if transverse stiffening is required to resist concentrated forces. One option described in the design guide is the use of partial-depth transverse stiffeners as shown in Figure 2.6-1(a) (Cater, 1999). However, it is usually more cost effective to reduce the amount of stiffeners, thus, partial-depth transverse stiffeners can be replaced with sloping stiffeners as shown in Figure 2.6-1(b) (Carter 1999).

a) Option w/ partial depth transverse stiffeners b) Option w/ sloping stiffener at bottom flange

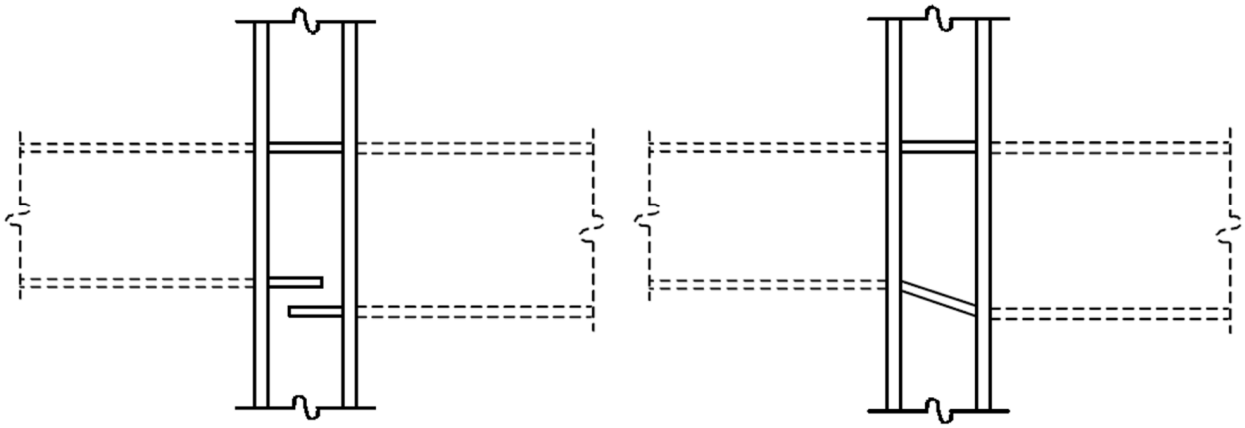

Figure 2.6-1: Stiffening options at offset beam flanges per Design Guide 13 (Carter, 1999)

Another option described in the design guide is the use of full-depth eccentric stiffeners as shown in Figure 2.6-2. These stiffeners create an eccentricity '*e*' between the beam flanges or flange plates and the column stiffener. The recommendations by Graham et al. (1959) were used to formulate the criteria for eccentric stiffener design. The design guide indicates that the effective capacity of eccentric stiffeners should be 100% of the concentric stiffener capacity at 0 in. eccentricity and should decrease to 65% of the concentric stiffener capacity at a 2 in. eccentricity. Interpolation can be used between 0 in. and 2 in.

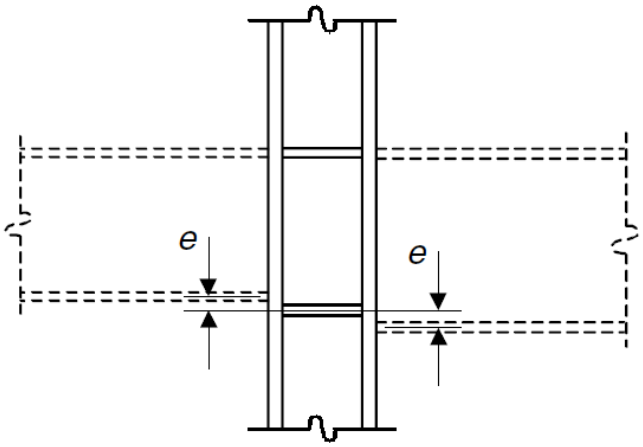

Figure 2.6-2: Stiffener option at eccentricity 'e' per AISC Design Guide 13 (Carter, 1999)

2.6.2 Eurocode 3: Design of Steel Structures

The Eurocodes are ten European standards that indicate design rules that must be followed per the European Union. They were established by the European Committee for Standardization upon request of the European Commission. Eurocode 3 refers to the design of steel structures and describes how to design steel structures using the limit state design method.

EN 1993-1-1 (2005) provides general rules for buildings. In particular, Section 5 explains the structural analysis to follow in design. There are certain requirements that involve stiffeners in this section. In a uniform member, where a transverse force that exceeds 10% of the shear resistance of the cross section is applied to the web at the plastic hinge location, web stiffeners should be provided within a distance along the member of h / 2 from the plastic hinge location (where h is the height of the cross section).

EN 1993-1-5 (2006) Section 9 gives design rules for stiffeners in plated structures which supplement the plate buckling rules. From Section 9.3, focused on shear design, the rigid end post should comprise of two double-sided transverse stiffeners that form the flanges of a short beam of length h_w. These stiffeners can be eccentric up to a maximum distance of $0.1\ h_w$. Figure 2.6-3 shows a rolled section forming an end post. The eccentricity is represented by '*e*'.

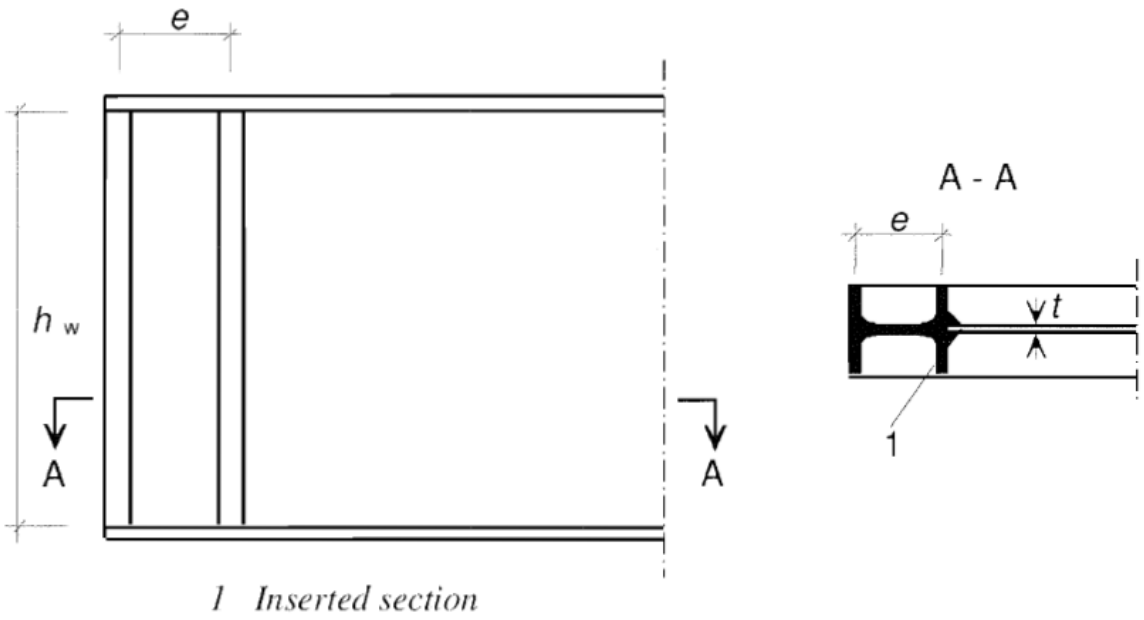

Figure 2.6-3: Rolled section forming an end-post (EN 1993-1-5, 2006)

Section 9.4 (EN, 2006) focuses on transverse loads. Transverse stiffeners are used to provide resistance against shear and transverse loads if the resistance of an unstiffened web is insufficient. The code itself does not provide rules for the design of eccentric stiffeners, but if single sided or other "asymmetric stiffeners" are used, the resulting eccentricity has to comply with Sections 6.3.3 or 6.3.4 of EN 1993-1-1. Sections 6.3.3 and 6.3.4 provide different guidelines to verify the resistance to lateral-torsional buckling of different members. The code also states that if the stiffeners are assumed to provide lateral restraint to the compression flange, they have to comply with the stiffness and strength criteria in the design for torsional buckling.

Eurocode 8 (EN, 2004) refers to the design of structures for earthquake resistance and describes how to design structures in seismic zones using the limit state design method. In particular, Section 6.6.4 focuses on beam to column connections. Stiffeners are used to help reach the required degree of overstrength taking into account the moment of resistance and the shear force of the beams connected to the column. However, there are no details on the design of these stiffeners. Section 6.8 focuses on frames with eccentric bracings and provides design and detailing rules for the frames with eccentric bracings to allow seismic links to dissipate energy by the formation of plastic bending and/or shear mechanisms. Design criteria for full-depth web stiffeners for the seismic links is provided, yet it does not apply to the design of stiffeners to resist transverse loads.

2.7 Summary of Literature Review

This chapter provided a literature review of historical and recent experimental and analytical research regarding beam-to-column moment connections and transverse stiffeners used to reinforce the column section. In addition, this review provided some examples on previous studies carried out specifically on eccentric stiffeners, which is the focus of this research. This chapter outlined the provisions in the AISC specification (AISC, 2016) with respect to limit states associated with concentrated forces along with the development of requirements in such provisions.

In general, there have been limited experimental tests performed previously regarding eccentric stiffener design. There are very limited tests that have been performed when the applied load to the member in question is tension instead of compression. Therefore, there is very limited studies of flange bending and how it influences the stresses that develop in the welds under both eccentric and concentric loading. Although it is recognized that the original flange bending equations were

developed to avoid stress concentrations in the weld.

Graham et al. (1959) tested two beam sections with a range of eccentricities for a total of 10 tests. These tests are not sufficient to assign design capacities for eccentric stiffeners in comparison to the design capacities of concentric stiffeners. Further experimental studies by Salkar (1992) and analytical studies by Sherbourne (1978), Carter (1999), and Norwood (2018), etc. showed that more analyses need to be performed regarding the influence of eccentricity with both experimental and analytical research. All the mentioned studies show that the effective capacity of stiffeners located at a certain eccentricity of the applied load is reduced compared to concentric stiffeners and the "effective stiffener capacity" is very low at eccentricities as small as 4 in. Sherbourne (1978) showed that there are many parameters affecting the effectiveness of eccentric stiffeners. Moreover, the effective capacity of eccentric stiffeners as recommended by Graham et al. (1959) seems conservative compared to analytical studies by Norwood (2018) when larger sections were modeled. Therefore, more in depth research needs to be done on different sections with varying properties in order to understand and provide recommendations for the design of eccentric stiffeners.

There is little guidance in the AISC specification (2016) for the design of stiffeners in general. The AISC specification indicates that stiffeners in tension should be designed as tension members and stiffeners in compression should be designed as compression members. The design equations for stiffener capacity do not properly consider the different limit states associated with concentrated loads. For buckling limit states, one must consider how the stiffeners brace the column web and allow more of the load to spread into the web as the stiffener shares the load. The analytical studies performed by Norwood (2018) propose a design equation for determining connection capacities, extending to the effect of eccentric stiffeners. However, Norwood's study assumes that flange local yielding or flange local bending is always the governing limit state. However, this is not always the case since in many occasions, web local crippling or web compression buckling are the governing limit states.

The AISC "Specification for Structural Steel Buildings" (AISC, 2016) does not provide information regarding eccentric stiffener design. The only source available from AISC for the design of eccentric column stiffeners or alternate methods to reinforce the column is the AISC Design Guide 13 "Stiffening of Wide-Flange Columns at Moment Connections: Wind and Seismic Applications"

(Carter, 1999). The use of eccentric stiffeners should appear in the specification or in the Steel Construction Manual (AISC, 2017).

Eurocode 3 and specifically, the document EN 1993-1-5 "General rules – Plated structural members" provides guidelines used by the European Union for the design of column stiffeners. However, this code lacks information regarding the design of eccentric stiffeners. Instead, the code states that if "other asymmetric" stiffeners are used, the resulting eccentricity should comply with certain rules for torsional buckling. Overall, there is limited assistance for the design of eccentric stiffeners outside of AISC.

CHAPTER 3: EXPERIMENTAL INVESTIGATIONS

3.1 Chapter Description

As mentioned in Chapter 1, a preliminary report was submitted to the AISC Research Advisory Board on October 29, 2018. This chapter will present a summary of the information provided in that report which focused on the experimental investigations. Some information is repeated in more detail than other information as deemed appropriate by the research team.

3.2 Experimental Test Matrix

A detailed description of how the test matrix was selected is provided in the preliminary report. In general, the experimental column specimens were selected such that their predicted capacities would be below the capacity of the hydraulic actuator, while still providing a range of sections that would fail at different load magnitudes. In addition, sections were selected to theoretically have capacities dictated by different concentrated load limit states. As discussed in this chapter, the failure modes associated with the column specimens were not always in line with the predicted limit state.

Prior to performing the experimental investigations, column specimens were modeled using the finite element method and the finite element program ABAQUS (2014). In these studies, the steel material was assumed to behave elastic-perfectly plastic and column specimens were subjected to single compression, double compression, and single tension. In addition, the column specimens were modeled with and without concentric stiffeners at midspan. The conditions with stiffeners always resulted in higher capacities than the conditions without stiffeners and column sizes were selected to ensure the load did not exceed the capacity of the hydraulic actuator of 220 kips. Figures 3.2-1 and 3.2-2 shows two models of W16X31 column specimens subjected to single compression loading at midspan. Figure 3.2-1 shows the results with no stiffeners at midspan and Figure 3.2-2 shows the results with concentric stiffeners on both sides of the column specimen. Similar finite element models were developed for a W16X31 column specimens subjected to double compression.

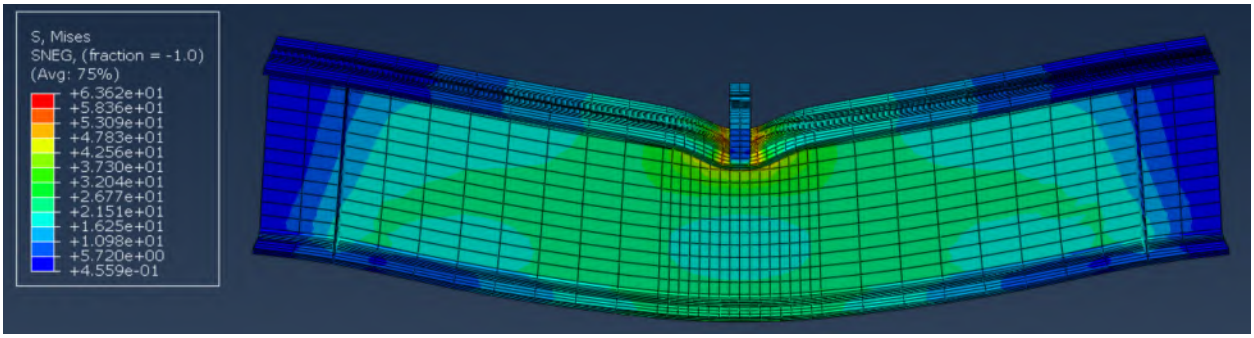

Figure 3.2-1: W16X31 loaded in single compression without midspan stiffeners

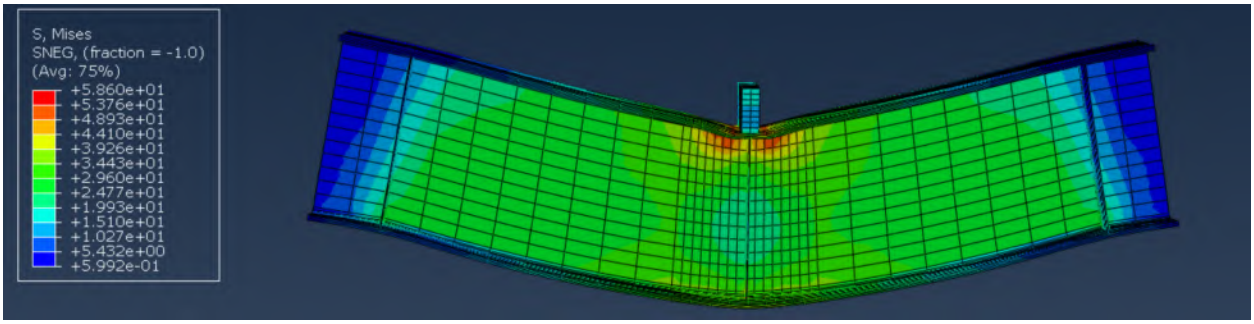

Figure 3.2-2: W16X31 loaded in single compression with midspan stiffeners

As an example output from the analytical investigations, the load-displacement results of the four aforementioned finite element models are shown in Figure 3.2-2. Since the material properties of the actual column specimens would likely have a yield stress higher than 50 ksi and since the stress-strain curve will not be elastic-perfectly plastic, the research team found it impractical to test the W16X31 in double compression with stiffeners on both sides since the load carrying capacity was higher than 220 kips from the finite element model. Because of this, the research team experimentally tested the W16X31 in double compression with stiffeners on one side of the web only after consulting with the AISC Research Advisory Committee.

Additional studies were performed on members subjected to single tension and further studies were performed on a W10X19 column specimen in order to evaluate buckling of the web under double compression load. In all, the finite element investigations revealed that sizes equal to or smaller than a W16X31 should be tested in double compression. Sizes comparable or smaller to a W16X31 should be tested in single compression and single tension. It was later revealed to the research team that the capacity of the hydraulic actuator in tension (upward force) was limited to 145 kips, which is discussed in more detail later in this chapter.

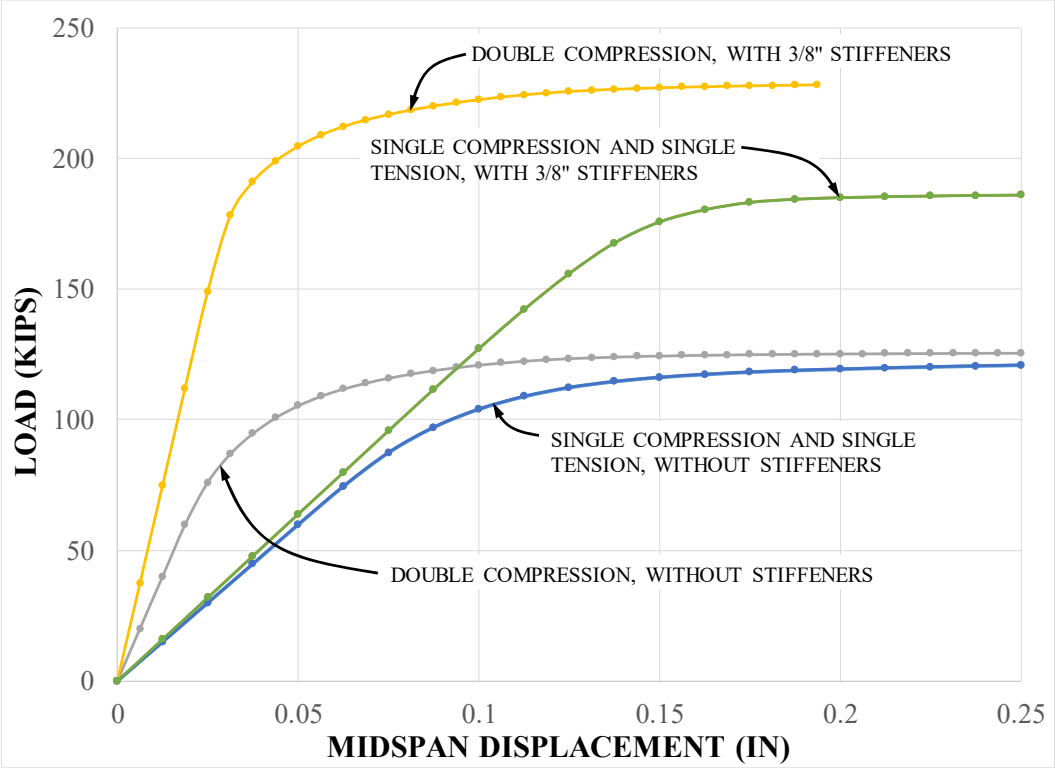

Figure 3.2-3: Load-displacement results of W16X31 finite element models

The sizes were chosen to have a variation in the predicted limit state that defines capacity under concentrated loads. These limit states include web local yielding, web compression buckling, and flange bending (AISC, 2016). The research team was unable to find a reasonable column section that the capacity would be governed by the limit state of web local crippling per the equations in the AISC specification, Section J10 (AISC, 2016) assuming nominal capacities (note that web local crippling uses the lowest resistance factor when using the LRFD design method and can control in design. However, it never controls for nominal capacities before the resistance factors are applied). As an example, a W16X31 was chosen since the equations for the limit states showed it would reach its capacity by flange bending in a single tension test, web yielding in a single compression test, and web compression buckling in a double compression test.

Finally, the research team evaluated the proportioning of various wide flange shapes in an attempt to relate the geometry of smaller shapes to the geometry of larger shapes and to ensure a range of proportions upon testing. Three different ranges were considered for the flange slenderness ($b_f / 2t_f$) and three different ranges were considered for the web slenderness (h/t_w) as shown in Table

3.2-1. The ranges included approximately the same amount of wide-flange members per range. The concept was that if a smaller column is tested, similar behavior under concentrated loads could be expected for a larger column in the same range knowing the required load to cause equivalent deformations would be higher (note that the results in Chapter 6 contradict this concept).

Table 3.2-1: Ranges of slenderness for the flange and web for proportioning study

Range #	$\lambda_f = b_f / 2t_f$	$\lambda_w = h / t_w$
1	2.38 – 4.65	5.66 – 22.0
2	4.71 – 6.31	22.3 – 37.8
3	6.35 – 8.74	38.2 – 53.0

In all, four different column specimen sizes were selected that would; (a) fail by the ideal limit state associated with the test method per the AISC specification (AISC, 2016), (b) be within a different group associated with the ranges of λ_f and λ_w, and (c) not be too large such that the maximum load would not exceed the capacity of the hydraulic actuator.

Forty (40) column specimens were tested. As mentioned, three different test methods were used: (1) single compression in which a downward force was applied to the top flange of a column specimen from a hydraulic actuator, (2) double compression in which a downward force was applied to the top flange of a column specimen but with a support directly adjacent and at the bottom flange, and (3) single tension in which an upward force was applied to the top flange of a column specimen. The four wide flange sizes were W10X19, W10X39, W12X26, and W16X31. However, not all test methods were used with each column size with the exception of the W16X31 and W12X26. For each column size and test method performed for them, four column specimens were tested as part of a "test group":

- One test was performed without any stiffeners near midspan to establish a baseline capacity prior to the addition of any stiffeners.
- One test was performed with stiffeners directly under the concentrated load and therefore with an eccentricity of 0 in. This is also referred to as the "concentric" stiffener condition.
- One test was performed with stiffeners at a high eccentricity, in that they were placed in the column specimen horizontally from the applied load. For W16X31 column specimens, the

high eccentricity was equal to 6 in. and for other column specimens, the high eccentricity was equal to 4 in.

- One test was performed with stiffeners at a low eccentricity, similar to the high eccentricity condition. For W16X31 column specimens, the low eccentricity was equal to 3 in. and for other column specimens, the low eccentricity was equal to 2 in.

The experimental test matrix is shown in Table 3.2-2. The nomenclature of each specimen includes the column specimen size, the test type, and the magnitude of stiffener eccentricity for each test if applicable. For the test types, 'SC' represents single compression, 'DC' represents double compression, and 'ST' represents single tension.

The largest shape selected was the W10X39 whose dimensions best serve that of a common column section. Preliminary calculations using AISC, Section J10 (AISC, 2016) indicated that the concentrated load capacity of this column size would not exceed the actuator capacity under single compression load with stiffeners concentric under the load. However, this column size was not used for double compression since the finite element studies performed on a W16X31 indicated the load would be higher than the capacity of the hydraulic actuator. Similarly, the W10X19 was not tested in single tension since the flange slenderness is small and flange bending was not expected to be the governing limit state.

For each test, the eccentricity of the stiffeners from the application of load is shown in Table 3.2-2. An 'NA' means that no stiffeners were used and '0' means concentric stiffeners were used. Originally, it was proposed to test at a high eccentricity of 6 in. and a low eccentricity of 3 in. for all column sizes. However, after performing tests on a W16X31, negligible changes were found in the results when a 6 in. eccentricity was used in comparison to the tests without stiffeners. With the approval of the AISC Research Advisory Committee, the high eccentricity value was changed to 4 in. and the low eccentricity value was changed to 2 in. for other column specimen sizes. If results at 6 in. were still of interest, the results could be extrapolated once a relationship between eccentricity and effective stiffener capacity is obtained.

Table 3.2-2: Full experimental test matrix for all column specimens

Nomenclature	Size	Test	Eccentricity (in)
W10X39-ST-NA	W10X39	Single Tension	NA
W10X39-ST-E4	W10X39	Single Tension	4
W10X39-ST-E2	W10X39	Single Tension	2
W10X39-ST-E0	W10X39	Single Tension	0
W12X26-ST-NA	W12X26	Single Tension	NA
W12X26-ST-E4	W12X26	Single Tension	4
W12X26-ST-E2	W12X26	Single Tension	2
W12X26-ST-E0	W12X26	Single Tension	0
W16X31-ST-NA	W16X31	Single Tension	NA
W16X31-ST-E6	W16X31	Single Tension	6
W16X31-ST-E3	W16X31	Single Tension	3
W16X31-ST-E0	W16X31	Single Tension	0
W10X19-SC-NA	W10X19	Single Compression	NA
W10X19-SC-E4	W10X19	Single Compression	4
W10X19-SC-E2	W10X19	Single Compression	2
W10X19-SC-E0	W10X19	Single Compression	0
W10X39-SC-NA	W10X39	Single Compression	NA
W10X39-SC-E4	W10X39	Single Compression	4
W10X39-SC-E2	W10X39	Single Compression	2
W10X39-SC-E0	W10X39	Single Compression	0
W12X26-SC-NA	W12X26	Single Compression	NA
W12X26-SC-E4	W12X26	Single Compression	4
W12X26-SC-E2	W12X26	Single Compression	2
W12X26-SC-E0	W12X26	Single Compression	0
W16X31-SC-NA	W16X31	Single Compression	NA
W16X31-SC-E6	W16X31	Single Compression	6
W16X31-SC-E3	W16X31	Single Compression	3
W16X31-SC-E0	W16X31	Single Compression	0
W10X19-DC-NA	W10X19	Double Compression	NA
W10X19-DC-E4	W10X19	Double Compression	4
W10X19-DC-E2	W10X19	Double Compression	2
W10X19-DC-E0	W10X19	Double Compression	0
W12X26-DC-NA	W12X26	Double Compression	NA
W12X26-DC-E4	W12X26	Double Compression	4
W12X26-DC-E2	W12X26	Double Compression	2
W12X26-DC-E0	W12X26	Double Compression	0
W16X31-DC-NA	W16X31	Double Compression	NA
W16X31-DC-E6	W16X31	Double Compression	6
W16X31-DC-E3	W16X31	Double Compression	3
W16X31-DC-E0	W16X31	Double Compression	0

3.3 Column Specimens

All column specimens were 6 ft. in total length. They were all supported near the ends by rollers at a specific span length. All single compression tests had the column specimen simply supported at 5 ft. with the exception of three W10X19 tests in which the span was reduced to 4 ft. due to the presence of lateral-torsional buckling witnessed during the first test performed on a W10X19 column specimen. The double compression tests were all supported at 5 ft. and with an additional support (reaction plate) located directly under the concentrated load from the actuator.

Single tension tests were initially designed to have a span of 4 ft. and initial tests were performed on a W12X26 with a span of 4 ft. However, due to a fabrication error, these tests were later voided and all tests that are further discussed in this report were tested with a span of 4.5 ft. The fabrication error was related to the location of bearing stiffeners as discussed in more detail in the preliminary report.

All welding for stiffeners and loading plates (for single tension only) was performed at the welding shop at Woodhaven High School in Woodhaven, Michigan. Critical stiffeners were located near the location of the applied load (near midspan). For these stiffeners, the welds were made with flux-cored arc welding per the request of the AISC Research Advisory Committee with a Welding Procedure Specification (WPS) reviewed by members of AISC. The WPS is included in Appendix B of this report.

For most column specimens, stiffeners were located on both sides of the web, with a total depth equal to the depth between column flanges minus 1/16 in. The width of the stiffeners allowed them to extend to the edge of the flange to the nearest 1/16 in. At the flange-web junctions, 1/2 in. corner cuts were fabricated.

Bearing stiffeners were used for most tests at the supports to ensure concentrated load failure mechanisms were not developed at the support reactions. Welding for these stiffeners were not assumed as critical and therefore, the research team allowed a welding procedure convenient to the welder. A description of the bearing stiffeners used for each test is summarized as follows:

- For double compression tests, no bearing stiffeners were used since all of the load was assumed to pass through the web to the bottom support reaction, opposite the applied load

from the actuator.

- For single tension tests, bearing stiffeners were located near each support and on both sides of the web for all cases. Due to fabrication errors, the stiffeners were offset the supports slightly in all cases. However, none of the test results reported in Chapter 6 seem to be influenced by local deformations due to the concentrated reactions at the supports.
- For single compression tests, the research team used either one stiffener at each support or two stiffeners at each support, depending on the expected capacity of the column specimen in relation to the concentrated reactions at the ends.

For W10X39, W12X26, and W16X31 column specimens, all stiffeners were 3/8 in. and welded to both flanges and web on both sides using 1/4 in. welds. For the W10X19 column specimens, all stiffeners were 1/4 in. and welded to both flanges and web on both sides using 3/16 in. welds.

Column specimens fabricated for single tension tests were fabricated with a 7/8 in. loading plate attached to them, which would later be connected to elements of the test setup with bolts. All plates were attached to the column specimens with 3/8 in. fillet welds on both sides. Per the request of the AISC Research Advisory Committee, these welds were made with flux-cored arc welding with the WPS shown in Appendix B.

Photographs of W10X39-ST column specimens prior to testing are shown in Figures 3.3-1 to 3.3-4. The low and high eccentricity values are labeled in Figures 3.3-3 and 3.3-4, respectively. The end bearing stiffeners are located on both sides of the web and at 6 in. from the edge of the column, meaning they are 5 ft. apart.

Figure 3.3-1: Photograph of W10X39-ST-NA (no stiffeners at midspan) prior to testing

Figure 3.3-2: Photograph of W10X39-ST-E0 (no eccentricity) prior to testing

Figure 3.3-3: Photograph of W10X39-ST-E2 (eccentricity = 2 in.) prior to testing

Figure 3.3-4: Photograph of W10X39-ST-E4 (eccentricity = 4 in.) prior to testing

3.4 Summary of Material Properties

All column specimens were made from A992 steel. Several uniaxial tension tests were performed on samples taken from the column specimen web and flanges to evaluate the material properties. These properties are summarized in Section 4.3 when discussing the finite element model of the experimental column specimens. All stiffener plate material was specified to be A36 steel from the material supplier. However, uniaxial tension tests from this material revealed that not all stiffeners were of this grade. Instead, some were believed fabricated from A572 Gr. 50. This is evident from the clear distinction in some of the stress-strain results. After further inspection, it was determined from documentation from the material received that some plates were A36 and some "met the requirements of A36 and A572 Gr. 50". All single tension loading plates were 7/8 in. and fabricated from A36 steel. Note that only the loading plates for single tension were welded to the column specimens. The loading plates for compression were not welded to the column specimens but were instead considered as part of the test frame and were utilized for multiple tests.

3.5 Experimental Test Setups

All experimental research was performed in the Structural Testing Center (STC) at Lawrence Technological University (LTU). Experimental testing was performed using a load frame and 220-kip hydraulic actuator located in the STC as shown in Figure 3.5-1. Elements of the test setup shown in the figure were used for either the single or double compression test setups.

Figure 3.5-1: Photograph of test frame and 220 kip actuator in the STC

3.5.1 Single Compression Test Setup

Single compression tests were performed by supporting the column specimens 5 ft. on center and with a load applied at midspan. Figure 3.5-2 shows a photograph of the complete test setup with a column specimen located under the hydraulic actuator. Figure 3.5-3 shows a full schematic of the test setup identifying the key features. The support located directly under the column specimen in Figure 3.5-3 is utilized for double compression tests only and will be discussed in more detail in Section 3.5.2.

At each end, the column specimens were supported by 3 in. rollers and a support frame available to the research team prior to initiating the project. These elements are identified in Figure 3.5-3. Schematics of the end support condition, which include details for the lateral support frame, are shown in Figures 3.5-4 and 3.5-5. The welding for the lateral support frame was performed at the welding shop in Woodhaven High School, Woodhaven MI. As shown in Figure 3.5-4, the lateral

support frame was designed to resist twisting of the column specimen at the supports and completely brace it for lateral torsional buckling. This frame was found to be very effective in resisting translation as column specimens were noticeably bearing against the shim plates upon testing. The lateral support frame consisted of rectangular HSS sections. At each support, there were four vertical members and two diagonal members. All HSS sections were welded to a common bottom plate (56.875 in. long). The bottom plate was connected to the existing support frame with bolts. As shown in Figure 3.5-5, the bottom plate was fabricated with a grove to support the 3 in. roller.

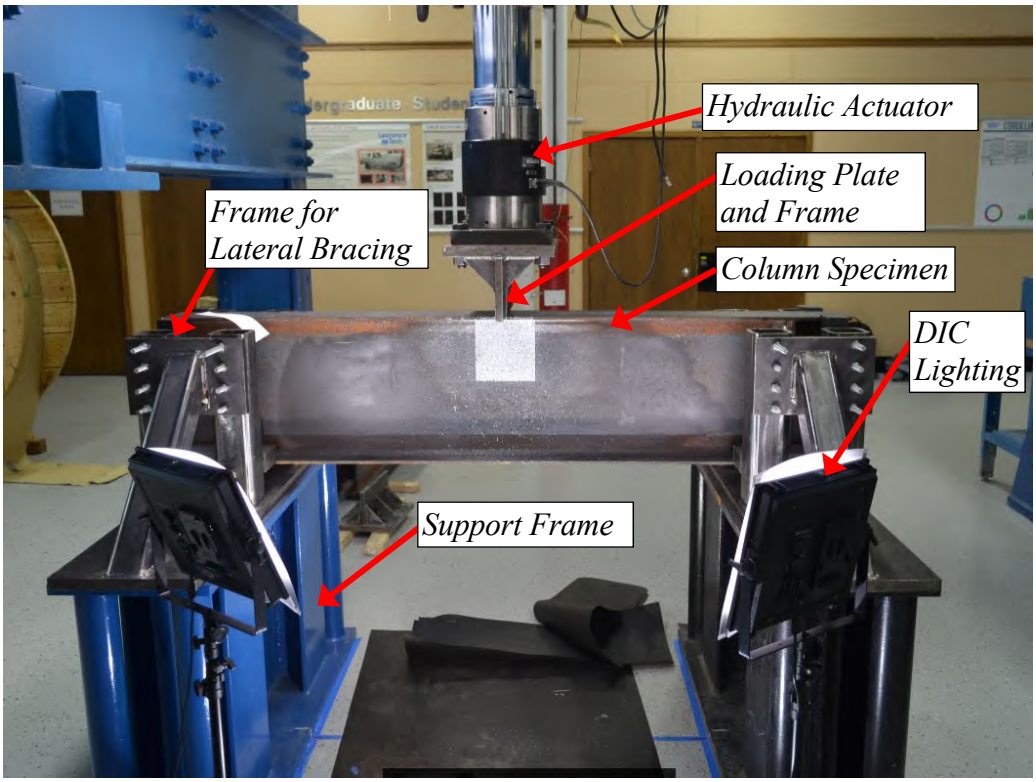

Figure 3.5-2: Photograph of test setup for single compression tests

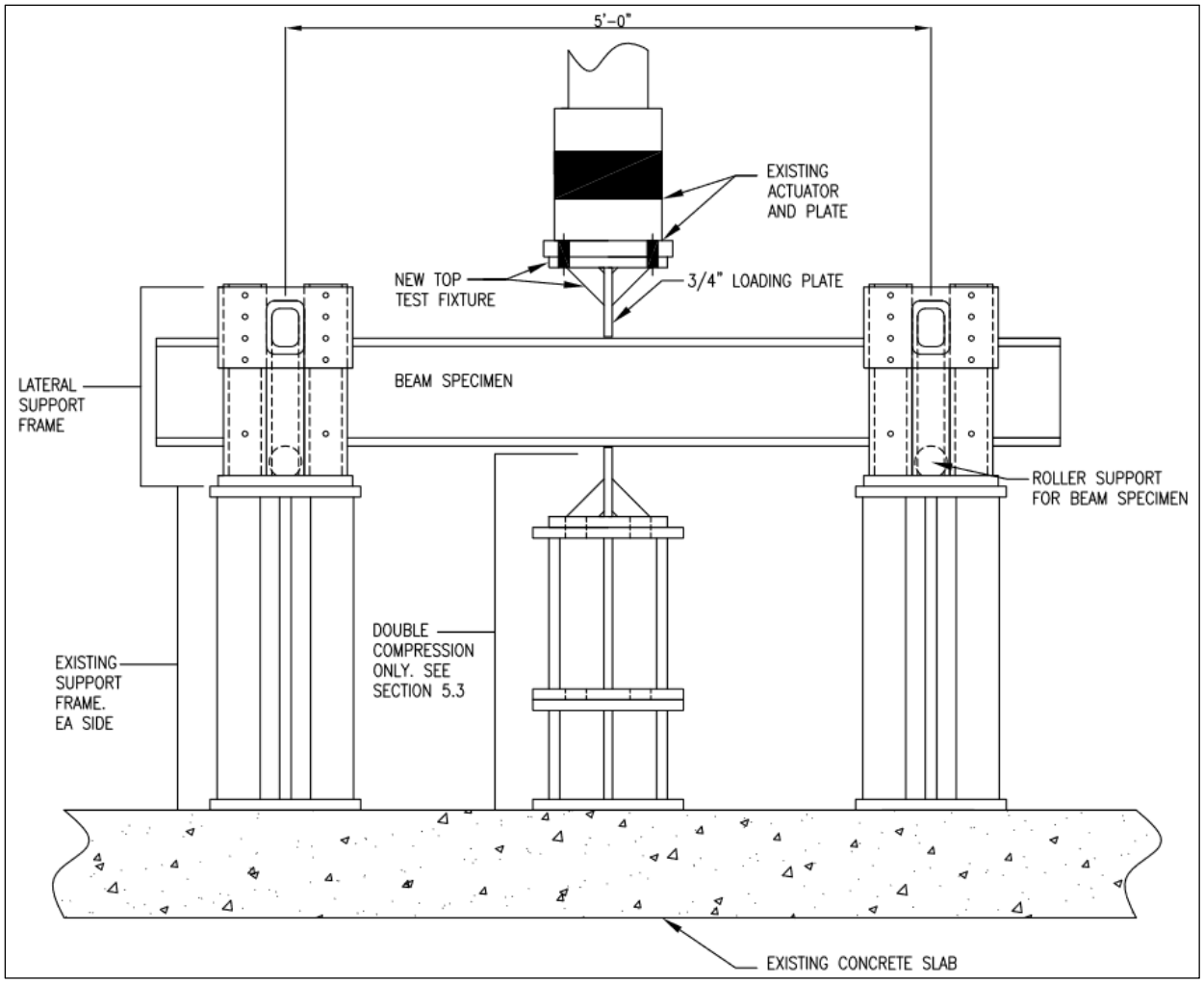

Figure 3.5-3: Illustration of test setup for single compression

At the top of the lateral support frame, the diagonal braces were welded to a 1 in. plate that was bolted to two vertical HSS sections. Bolts were used in lieu of welds in order to use the bolt holes for dual purposes. The bolt holes were also used to connect to shim plates. Column specimens tested had different flange widths and depth and the test setup had to be able to resist lateral translation for any size member considered. Therefore, holes were fabricated in the vertical HSS sections to allow the shim plates to be located at different elevations for different column depths. Various size shim plates were fabricated from 1/16 in. to 1 in. The shim plates were fabricated with holes that matched the spacing of the holes on the vertical HSS members. To connect the shim plates to the vertical HSS sections and back plates, 5/8 in. threaded rods were used with nuts.

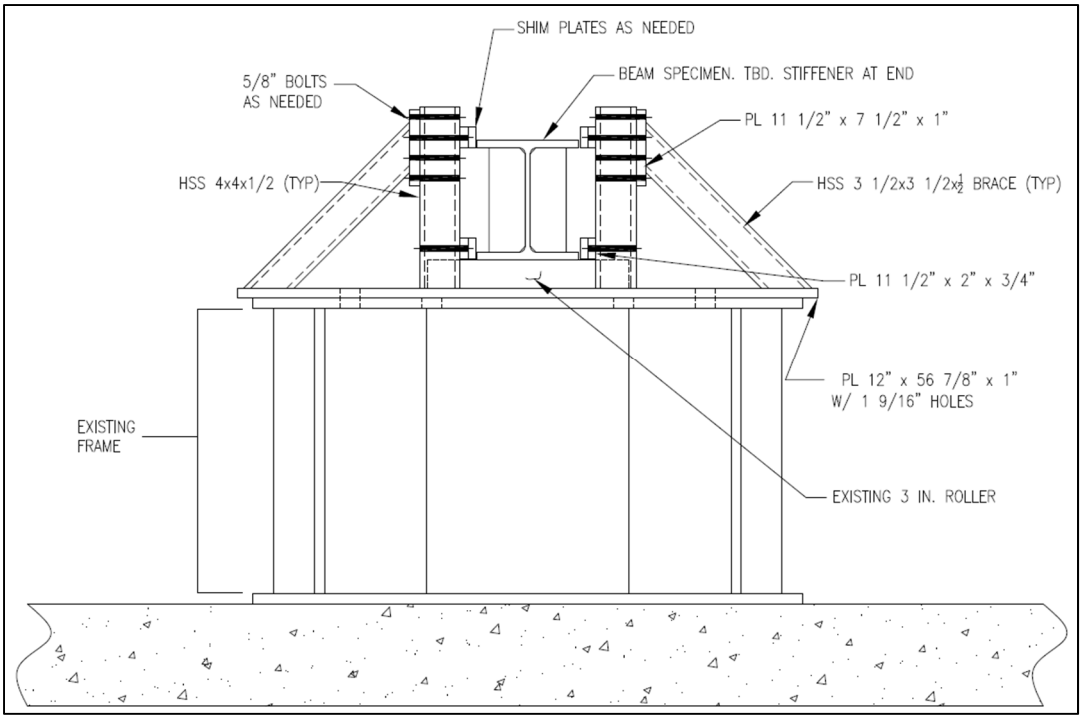

Figure 3.5-4: Elevation of end support details

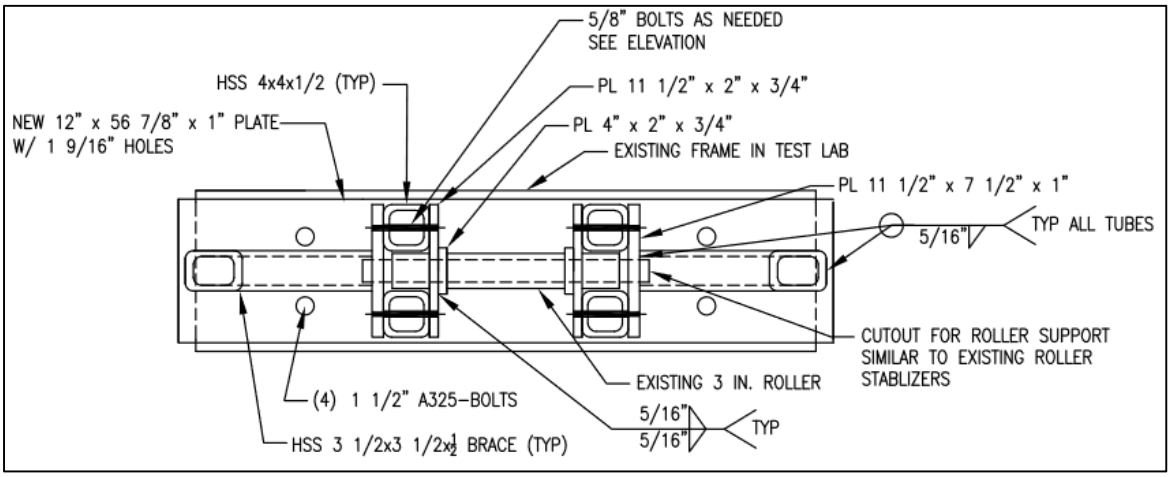

Figure 3.5-5: Plan view of end support details

Column specimens were loaded in single compression from the hydraulic actuator located in the STC. Figure 3.5-2 showed the test fixture above the column specimen. The element subjected to compression and applying the concentrated load is shown as the loading plate and is part of the test fixture. Further details are shown in Figures 3.5-6 and 3.5-7. The research team studied the thickness of the loading plate during the preliminary finite element studies and found that a 3/4 in. plate fabricated from A36 steel should be adequate. Upon testing, the center of the plate was found to

indent minimally as concentrated stresses resulted from resistance of the column specimen web. Therefore, the plate was periodically cut during testing in 1/2 in. increments to straighten it. To avoid buckling of the plate and twisting of the plate at the weld, triangular stiffeners were used for support. The test fixture was bolted to a plate that was already connected to the hydraulic actuator.

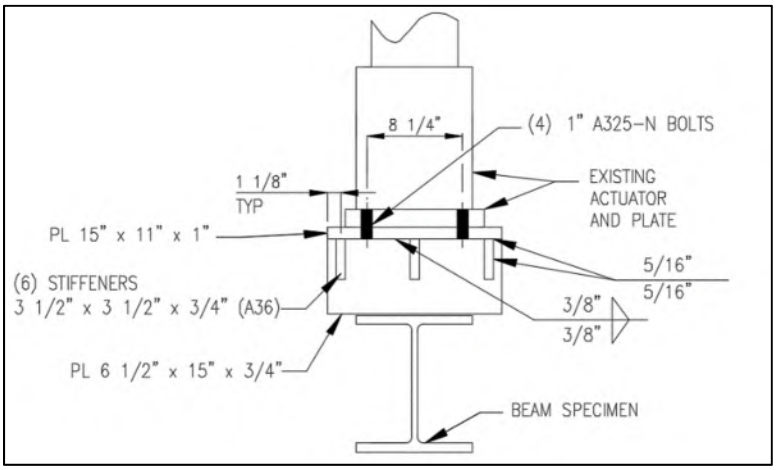

Figure 3.5-6: Elevation view of top test fixture attached to actuator

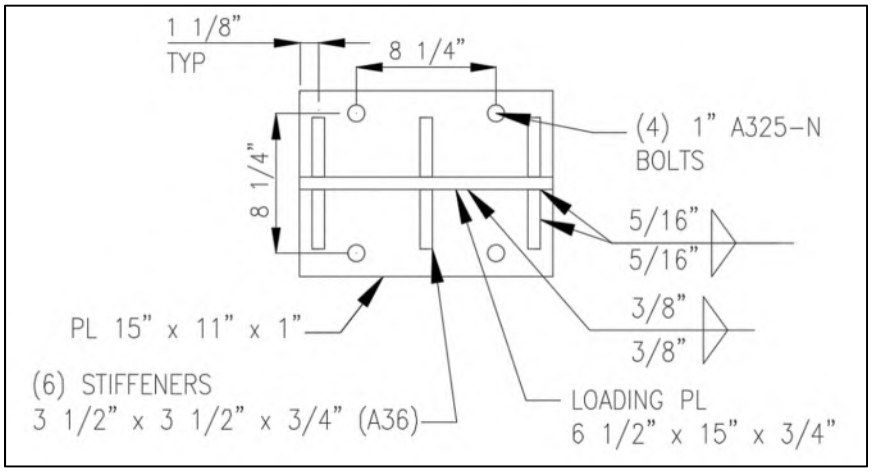

Figure 3.5-7: Plan view of top test fixture

3.5.2 Double Compression Test Setup

The double compression setup was similar to the single compression setup but with an additional support directly below the column specimen and in line with the applied load. Similar to the loading plate on the top, a 3/4 in. bottom reaction plate was set to bear directly to the bottom flange when subjected to loading from the top loading plate; simulating a through force through the web of the column specimen. The location of the bottom support is shown in Figure 3.5-3. Upon testing, the

research team found that more deformations occurred near the top flange as opposed to the bottom flange. Theoretically, if the load from the top was equal to the load transferred to the bottom, the amount of deformations at the top and bottom flange would be the same. After reviewing the tests in more detail, it was found that elastic displacements in the column specimen and loading plates allowed the column specimen to rotate slightly at the ends, suggesting that some of the force from the actuator was transferred to the end supports. Although load cells were not used to measure the amount of force transferred to the bottom support, the research team still feels that the majority of the force was indeed transferred to the bottom reaction plate.

Figure 3.5-8 shows a side elevation schematic of the test setup at midspan, in line with the hydraulic actuator. The bottom support frame includes an existing frame that was already available in the STC and a test fixture that includes the bottom loading plate. Figure 3.5-9 shows a plan view of the bottom support frame. The new test fixture for the bottom support consisted of a base plate that was bolted to the existing frame. The loading plate and stiffeners were similar to that used for the top test fixture. All new plate material was specified to be A36.

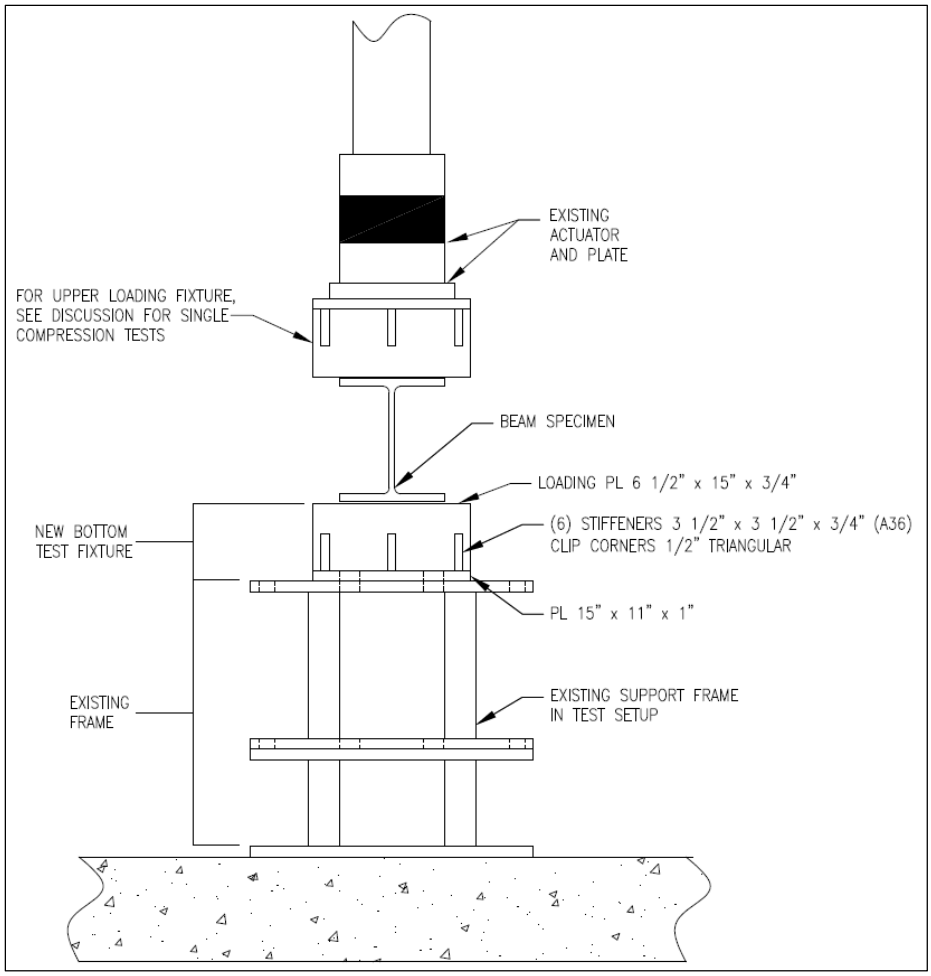

Figure 3.5-8: Side elevation of test setup at midspan emphasizing bottom support frame

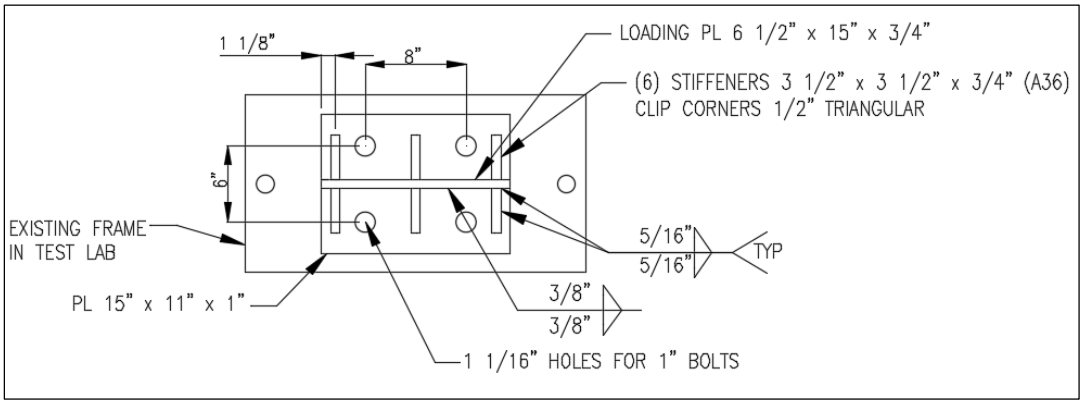

Figure 3.5-9: Plan view of bottom test fixture used for double compression

3.5.3 Single Tension Test Setup

The test setup for single tension was more rigorous than the test setup for single compression. To avoid drilling holes into the floor of the STC and to provide a strong reaction support, a special reaction frame was designed, constructed and attached to the existing test frame in the STC. Figure 3.5-10 shows a photograph of the test setup identifying the key features.

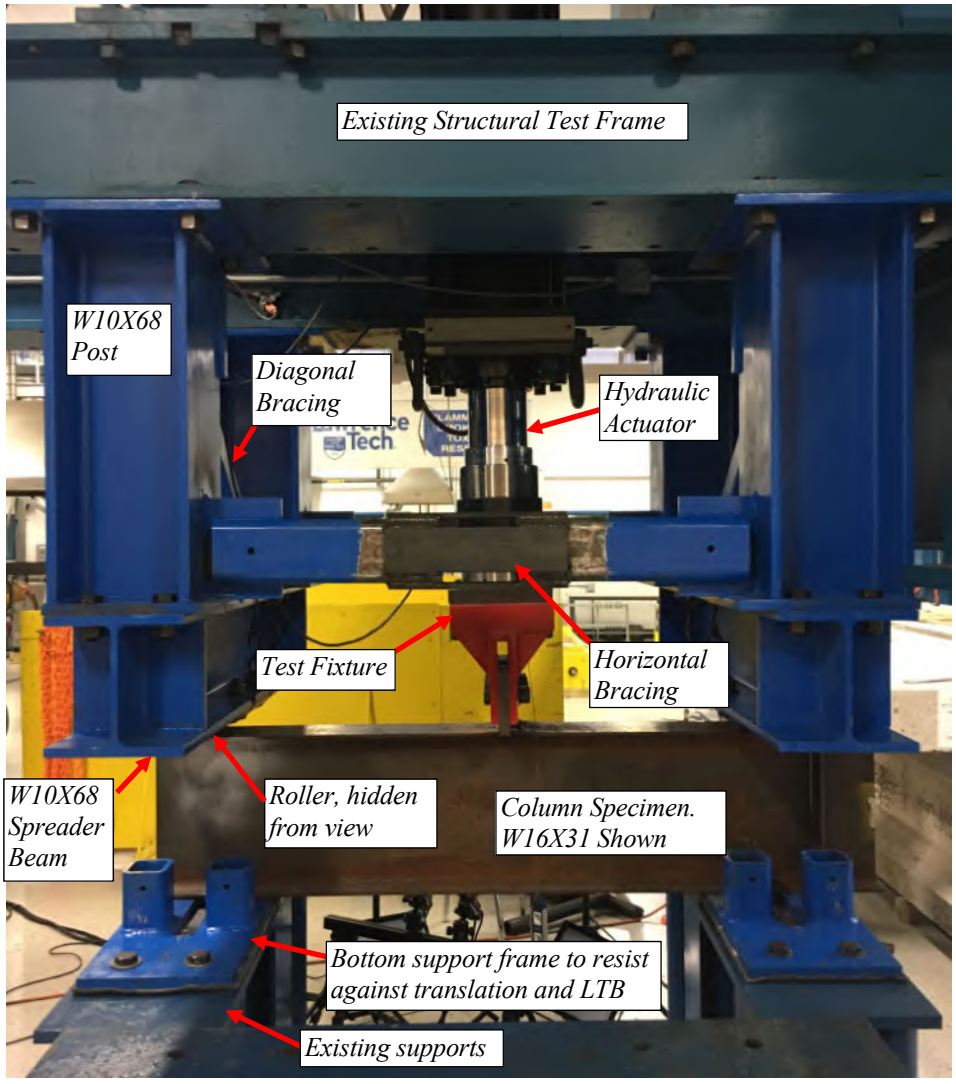

Figure 3.5-10: Photograph of single tension test setup

Figure 3.5-11 shows an illustration of the test setup in elevation along with a full perspective of the test setup in relation to the existing structural test frame. As shown, the hydraulic actuator was not centrally located on the structural test frame. Although possible to move the actuator, the amount of work allocated was not justified. Since the reaction frame would interfere with elements of the

structural test frame, the column specimens could not be supported at 5 ft. on center, which was used for the compression testing. Instead, the test setup was designed to support the column specimen at 4 ft. on center, which was later increased to 4.5 ft. for reasons discussed in the preliminary report.

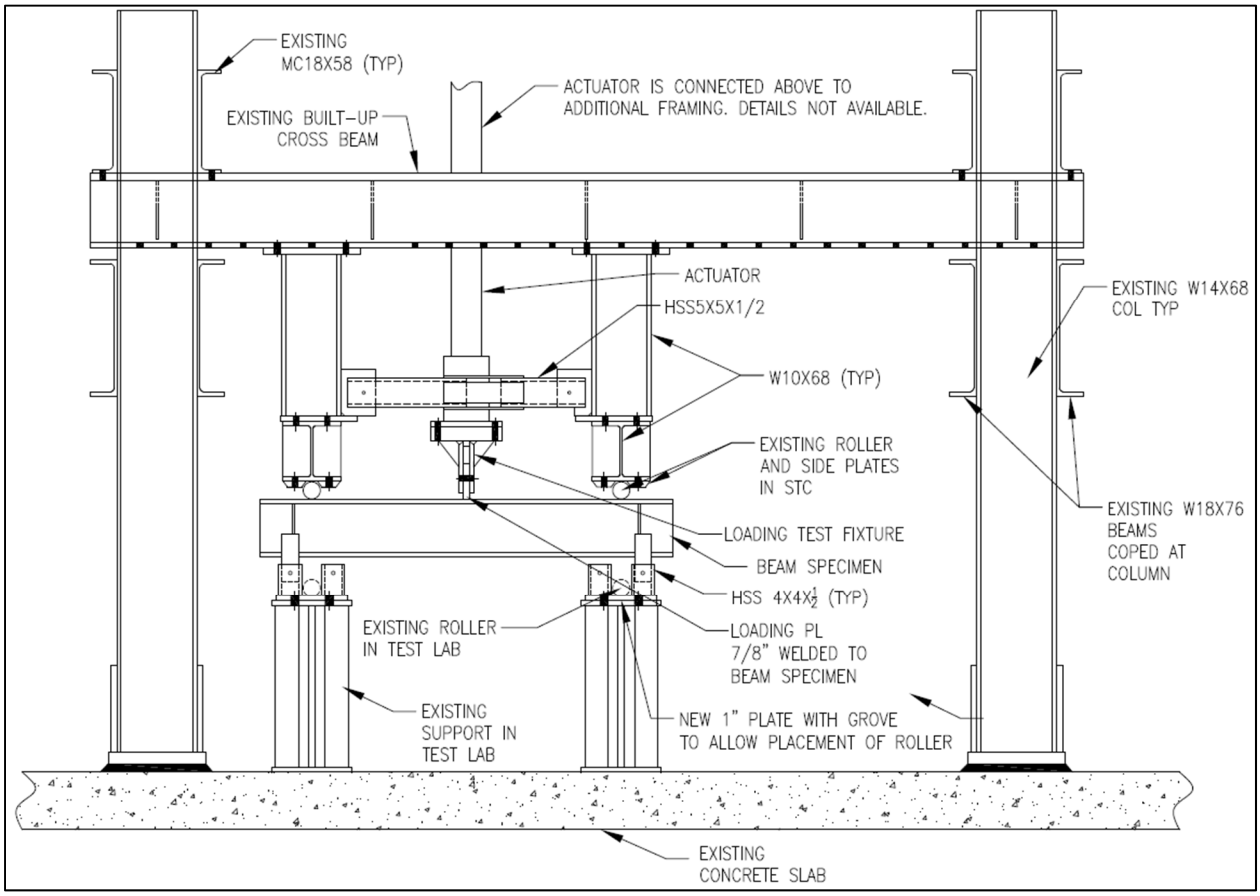

Figure 3.5-11: Single tension test setup in relation to structural test frame

Holes in the crossbeam of the existing structural test frame were prefabricated and the new column posts were attached to the test frame using these holes. However, the actuator was not evenly spaced between holes. Instead, it was offset by approximately 2 in. The actuator was attached to the center of the column specimen but the spans on either side of midspan to the end supports were slightly different.

Figure 3.5-12 shows another elevation of the test setup, zoomed in in comparison to Figure 3.5-11. Figure 3.5-12 identifies each critical element of the test setup and the location of all welding. Dimensions for the elements of the test setup are not shown for clarity. All welding was performed at Woodhaven High School in Woodhaven, MI except for the welding from the horizontal and

diagonal bracing to the gusset plates, which was performed within the STC.

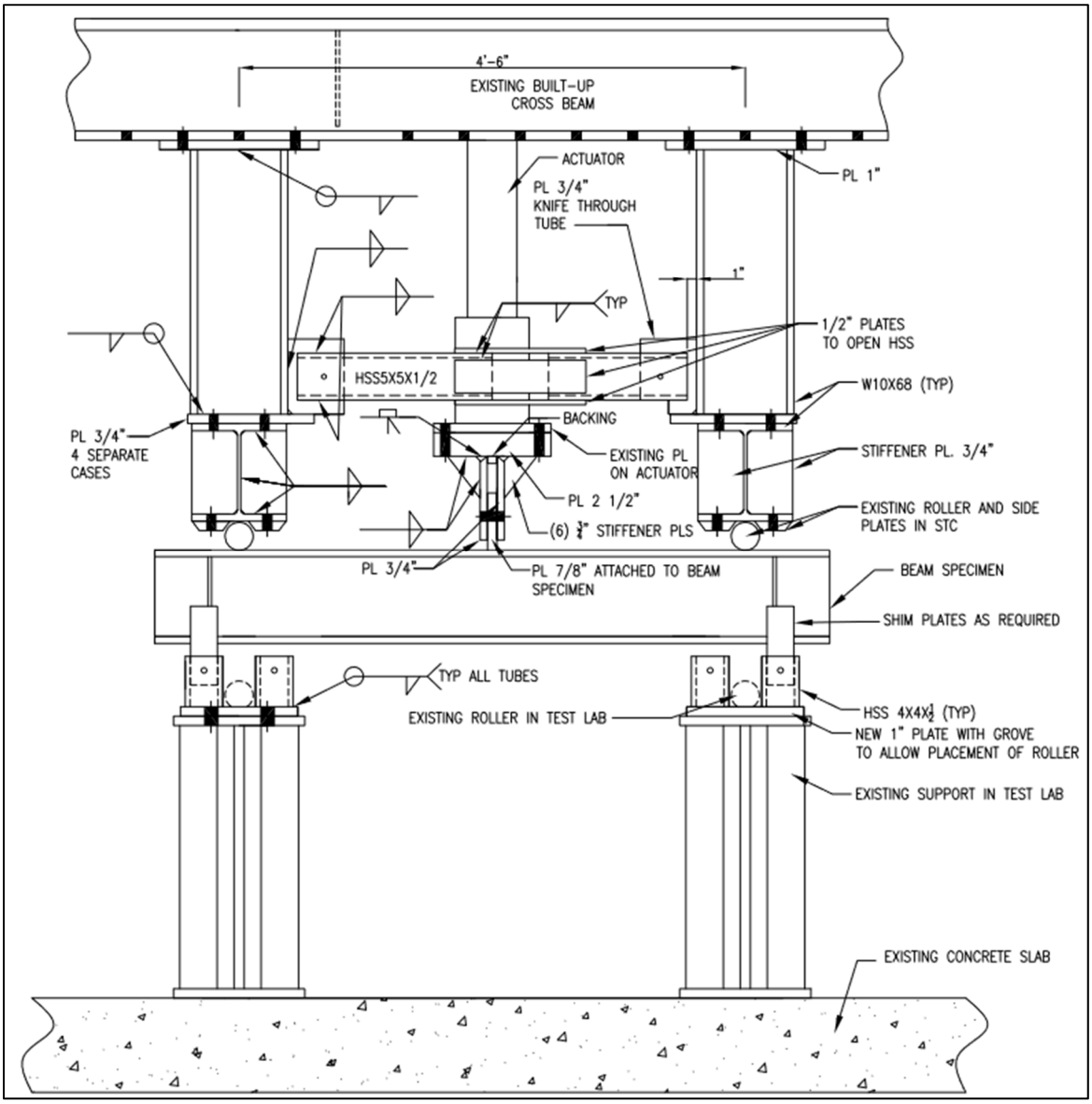

Figure 3.5-12: Elevation view of test setup emphasizing elements of reaction frame

Figure 3.5-13 shows a side view of the loading condition at the hydraulic actuator, emphasizing the details of the test fixture and connection to the hydraulic actuator. Figure 3.5-14 shows a side view at the support condition, which provides details for the W10X68 spreader beam and diagonal bracing.

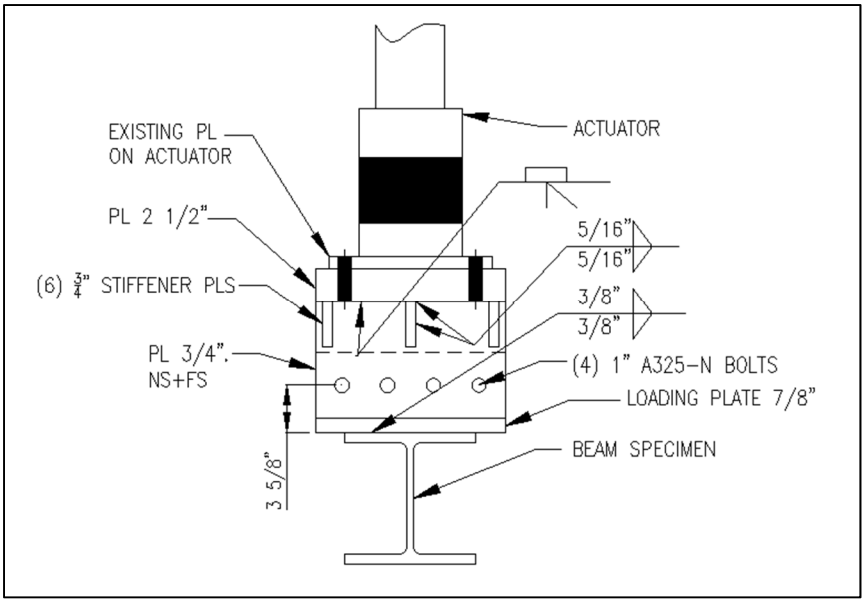

Figure 3.5-13: Side view at test setup at actuator (loading) condition

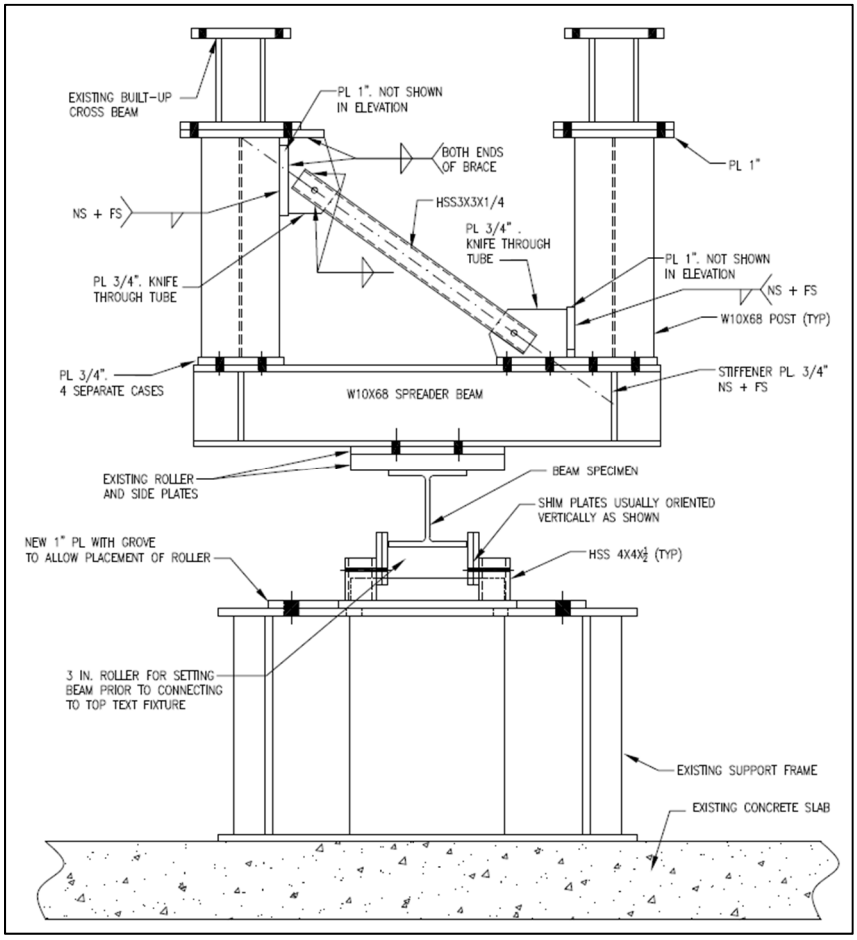

Figure 3.5-14: Side view of test setup at support condition

All new steel consisted of HSS rectangular sections, plates, bolts, and wide flanges. All plates were specified as A36 steel, although it is unknown if the steel supplier provided this grade or provided a grade that met the requirements of A36 steel. All wide flanges were W10X68 sections made from A992 steel. All HSS sections were A500 Gr. 50 with a minimum yield stress of 50 ksi. All bolts used as part of the test setup were 1 in. diameter and of grade A325. All welds were made using E70XX electrodes and with details shown in the drawings.

To temporarily support the column specimen and allow the actuator to come down to an elevation and evenly pick up the column specimen, the existing support frames used for the compression setup were also used for the tension setup. A bottom plate was fabricated to sit on the support frames that was fabricated with a notch to allow bottom rollers to sit in the notch. Depending on the size of the column specimen tested, shim plates were inserted between the existing support frame and the bottom plate as shown in Figure 3.5-12. On each plate, four HSS tubes were welded with a length of 5.375 in. These tubes were used to support shim plates inserted between the tubes and the bottom flange of the column specimen. In this single tension setup, the bottom flange was the compression flange and the bottom shim plates provided lateral support to resist twisting of the flange and lateral translation.

At the supports and in line with the spreader beams, the top flange of the column specimen was designed to bear on rollers. The rollers were set in between two plates that were beveled on both sides. These plates were already fabricated prior to initiating the research project. The beveled plates were connected to a W10X68 spreader beam, named as it spreads to two different vertical posts. The 5 ft. spreader beams are best illustrated in Figure 3.5-14.

On each end, the spreader beams were bolted to 3/4 in. plates. Each of four plates had different dimensions and hole geometry in order to accommodate connections to diagonal and horizontal bracing. In addition, between the bolts, the spreader beams were reinforced with 3/4 in. stiffener plates on either side of the web and directly in line with the posts above. The spreader beams were connected to 3/4 in. plates with either 4 bolts or 8 bolts, again depending on the braces that were coming into the joint. The 3/4 in. plates were welded to W10X68 posts. Each post was approximately 4 ft. long and welded to 1 in. plates at the top. The 1 in. plates were bolted to beams of the existing structural test frame located within the STC. Each one of the top plates had different

dimensions to accommodate connections for the diagonal bracing. Four bolts were used to connect each of these plates to the crossbeam of the structural test frame. The top plates were fabricated with oversized holes to allow more tolerance when connecting to the existing structural test frame.

Two different brace types were used. Along the length of the column specimen, horizontal HSS5X5X1/2 sections were used to disallow lateral movement between the bottom of the posts upon loading of the column specimen. If these braces were not used, the roller supports would translate with respect to each other and flexural stresses would develop in the posts. The braces had to be cut and spliced to allow the test frame to "open up" 6 in. and increase the span of the column specimen from 4 ft. to 4 ft. 6 in. In the opposite direction, diagonal braces of size HSS3X3X1/4 were used. All braces were knifed and welded to 3/4 in. gusset plates. Holes were fabricated into the plates and the HSS members to install an erection pin, meant to temporarily support the brace prior to welding. The gusset plates were welded to the top or bottom plates and either directly to the column flange or to additional plates that were installed and welded to each column flange.

The test fixture that is attached to the actuator and connection to the column specimen was shown in Figures 3.5-12 and 3.5-13. The test fixture was thoroughly analyzed with detailed calculations using the AISC specification (AISC, 2016). The primary elements of the test fixture include a 2 1/2 in. plate, two 3/4 in. side plates, a backing bar, and triangular stiffeners. The 2 1/2 in. plate was directly connected to the actuator with bolts. As described in Section 3.4, single tension specimens were fabricated with a top loading plate of 7/8 in. welded to the column specimens. In order to ensure that the loading plate was in line with the actuator, it was necessary to connect the loading plate to two 3/4 in. side plates with four 1 in. A325 bolts. The side plates were welded to the base plate (2 1/2 in. plate) using complete joint penetration (CJP) groove welds. A common 1 in. plate was cut and inserted to serve as backing for the CJP welds on both sides. Six ¾ in. triangular stiffeners were installed to keep the two side plates free from distortion and plumb. This setup proved to be efficient for all tests performed as no distress was found in the test fixture or the 1 in. bolts.

Figure 3.5-15 shows a photograph of the test setup from the side, which includes a W10X39 column specimen. This photograph was taken after testing a column, thus the column has already been lowered and shim plates removed. Elements of the reaction frame are visible in the photograph.

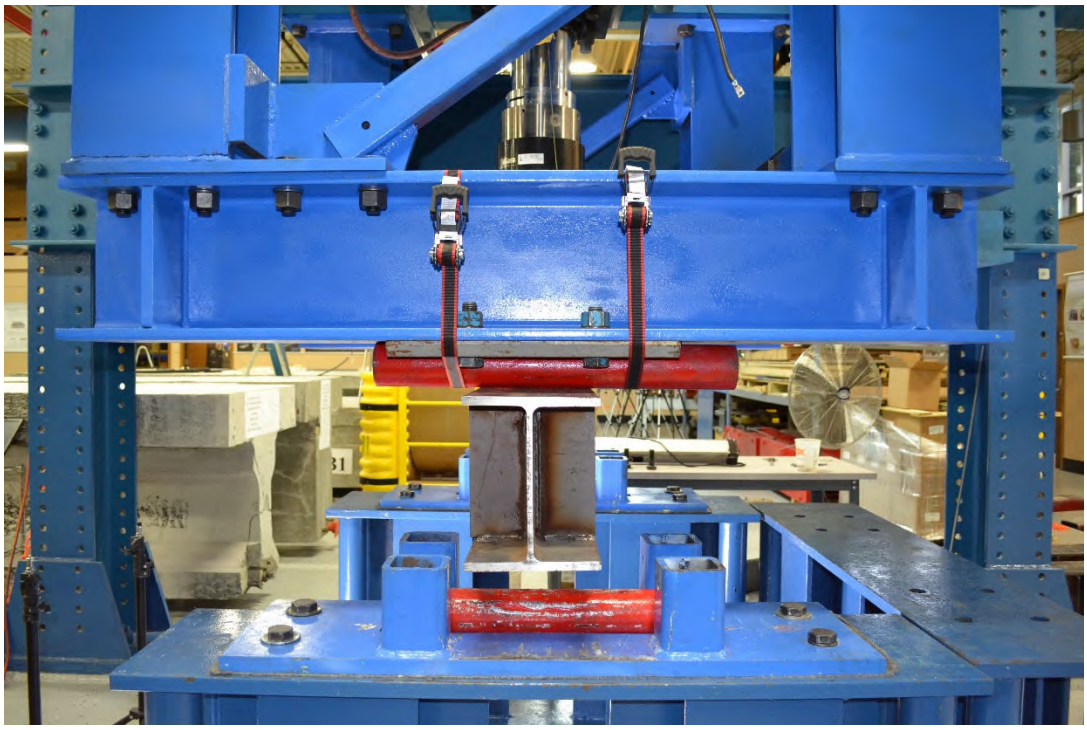

Figure 3.5-15: Side photograph of reaction frame

3.5.4 Digital Image Correlation

Digital Image Correlation (DIC) was idealized in this project as the primary form of instrumentation. DIC is capable of developing a three-dimensional strain state that allows the identification of heavy stresses and hence, modes of failure. DIC is also capable of tracking the displacement at various points in all three directions simultaneously.

As shown in Figure 3.5-16, a dual camera, 3D DIC system, was set up in front of the wide flange column section. The camera resolution is 5M pixels (2560 x 1920). A pair of Navitar 25mm, f/1.8-16 mm lens was used to capture the image of the object. Internal discussion and preliminary testing was utilized to determine the best locations for the two cameras. The two cameras were placed 9.5 in. away from each other using an optical rail. For each test, the distance from the optical rail to the test specimen was 7 in. The angle between the two cameras axis was set as 25 degree. Two 3200-5600 lux high power LED lamps with polarizer were used to illuminate the test specimen.

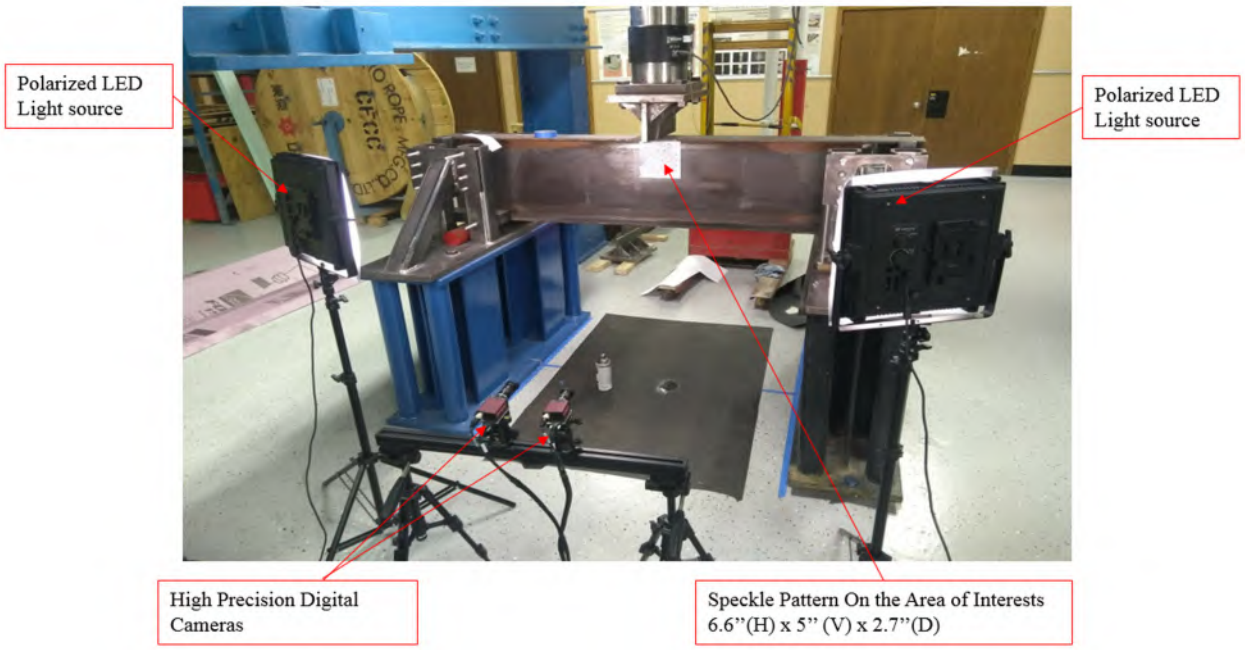

Figure 3.5-16: Test setup for DIC Instrumentation

The column specimens were painted with spackle paint directly underneath the top loading plate in all cases and on the front side only. The research team relied on symmetry in double compression tests as paint was not applied near the bottom reaction plate. Paint was applied to the web, bottom of the top flange, and when stiffeners were present, on one side closest to applied load and across the thickness. When a concentric stiffener was used, the stiffener was always painted on one side only and across the thickness. The cameras were angled to capture the strains on all faces that were painted. It was also assumed that if stiffeners existed on the backside, the strains in the stiffener and adjacent web would be similar to that captured on the front side.

To obtain better results, only a small area was painted for each test. In the setup, a maximum dimension of 6 in. long was covered by 2048 pixels. This gives a ratio of 0.075 mm/pixel. Commonly, within each subset, 3-6 speckles are needed. In this case, a subset size of 39 pixels was used which results in subset size of 3 mm in real dimensions. According to this subset size, the average speckle size should be 0.5 mm. to 1 mm. in length or (0.25 mm^2 - 1 mm^2 in area).

The speckles were applied using spray paint. Prior to applying the speckle, the areas were sanded using sand paper to obtain results that are more accurate. This was also necessary since the mill scale on the column specimen had a tendency to peel off once significant yielding was identified.

Sanding increased the reliability of the paint layer on the surface of the column specimen. After the surface preparation was complete, a white color spray was used to create background for the speckles. White color creates a favorable contrast for the speckles and reduced reflection through the shiny surface of the column specimen. Then, the black colored speckles are sprayed on the white background as shown in Figure 3.5-17.

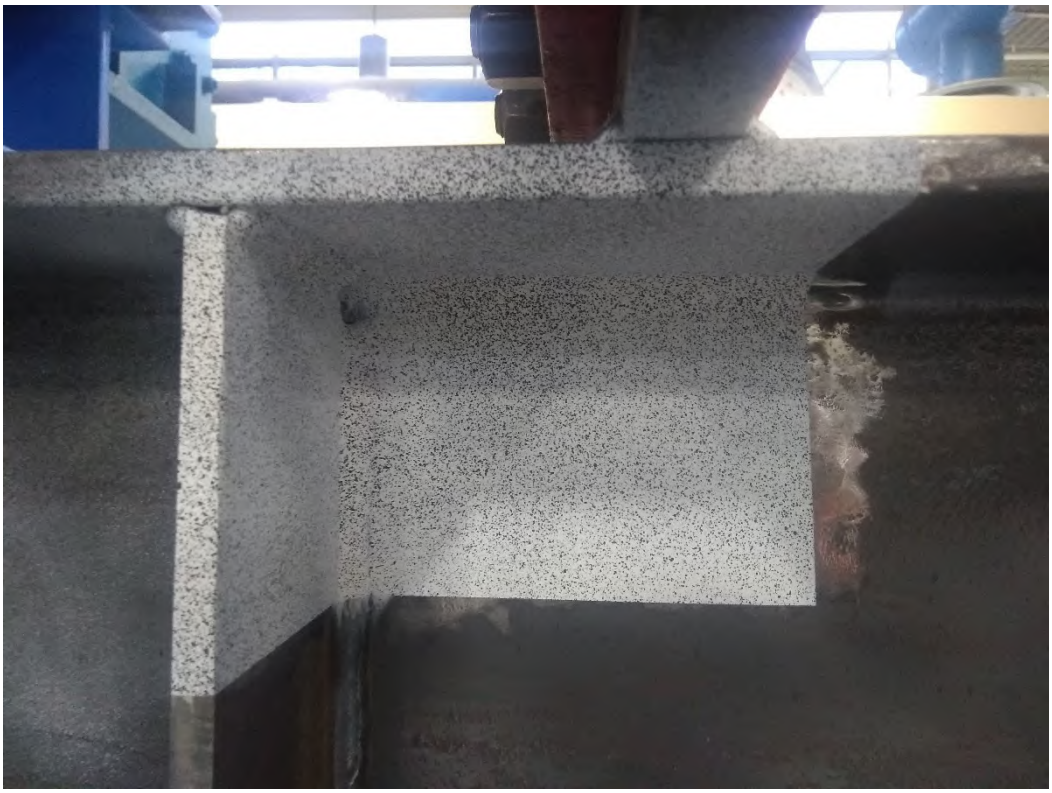

Figure 3.5-17: Speckle Pattern Ready for Testing

Details involving the procedure for calibration and the static test are included in the preliminary report. After the DIC setup & speckle pattern are optimized for the test, it was then required to calibrate the 3-dimensional DIC system for intrinsic parameters (optical parameters & distortions) and extrinsic parameters (relative position of the cameras). The static test was performed to provide information about the correct speckle sizing, calibration and physical status (flatness, roughness etc.) before applying the actual test load.

The DIC data is not discussed significantly with the experimental results. However, the DIC screenshots were idealized for confirmation of experimental behavior when necessary and generally confirmed the results assumed and viewed during the tests. DIC screenshots are provided in

Appendix C of this report and more can be provided upon request.

The DIC processing time was extensive as it took approximately two hours to process each test. In addition, more time was allocated to review the processed data and provide the screenshots. However, new technology has evolved that allows the user to view the results in real time. Therefore, although the processing time for this project was extensive, the use of DIC in future steel research has several benefits over traditional strain gauges.

DIC screenshots were provided for multiple strain types and at load magnitudes specified by the primary investigator. A description of the load magnitudes that correspond to screenshots taken from the DIC software are as follows:

- The condition of the web, flange, and stiffener is shown at a load magnitude slightly above that predicted for web local yielding (AISC, 2016) for the column section without stiffeners. The objective was to analyze how much local yielding occurs in the web of the column as well as the amount of bending that occurs in the flange for the column specimen without stiffeners and compare it to the spread of yielding that occurs in the columns specimens with stiffeners.
- For the column specimen without stiffeners, a screenshot is taken at the maximum load capacity. The load capacity was reached during web local crippling for all compression tests and right before a weld fracture for the majority of the single tension tests. For compression tests, the DIC screenshots start showing the crippling effect, where it occurs and strain levels associated with it. For tension tests, the amount of bending that occurs in the flange, which is directly linked to the stresses in the weld, is evaluated. The other three column specimens part of the test group are also evaluated using DIC at this same load magnitude to compare conditions with and without stiffeners. In the event where a column specimen with stiffeners reached a capacity lower than the capacity of the corresponding column specimen without stiffeners, DIC was used to evaluate the column specimen at its individual capacity.
- All column specimens are shown at a load level between the two aforementioned conditions.
- Finally, all column specimens are shown at their respective capacity if a capacity was not defined by a previous condition. In the case where the actuator reached its capacity prior to

the column specimen reaching its capacity, the strain conditions at the actuator capacity are provided instead.

As an example, some of the results of the W12X26 tests subjected to single compression (W12X26-SC) are provided herein. The results are provided for the four specimens at a load of 59 kips and at a load of 78.2 kips. This represents a load slightly higher than the theoretical web local yielding limit state for the column without stiffeners and the load corresponding to the capacity of the column specimen without stiffeners, respectively. The results are shown for strain in the y-direction, which corresponds to the direction of the applied load. The results of all four specimens are shown at 59 kips in Figure 3.5-18 and at 78.2 kips in Figure 3.5-19.

(a) W12X26-SC-NA

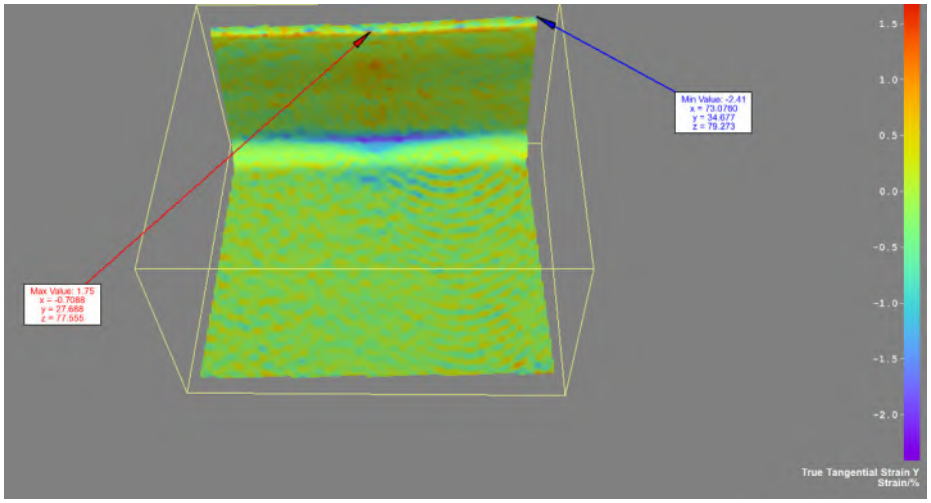

(b) W12X26-SC-E4

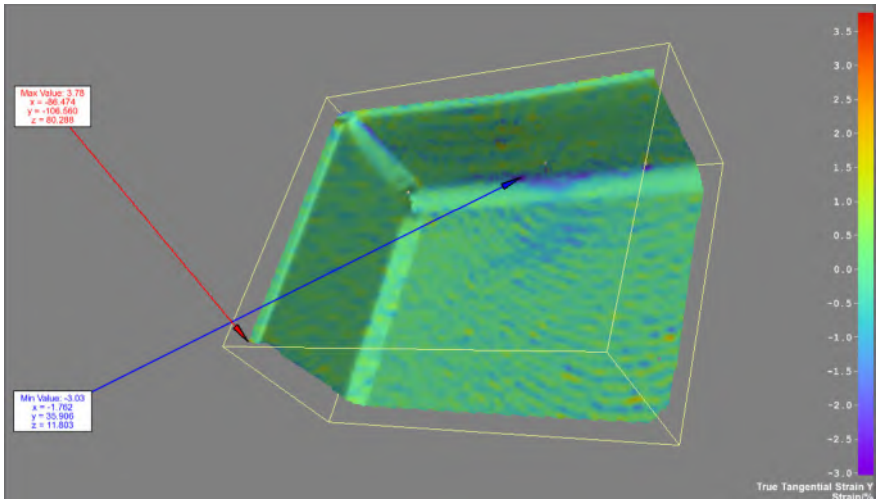

(c) W12X26-SC-E2

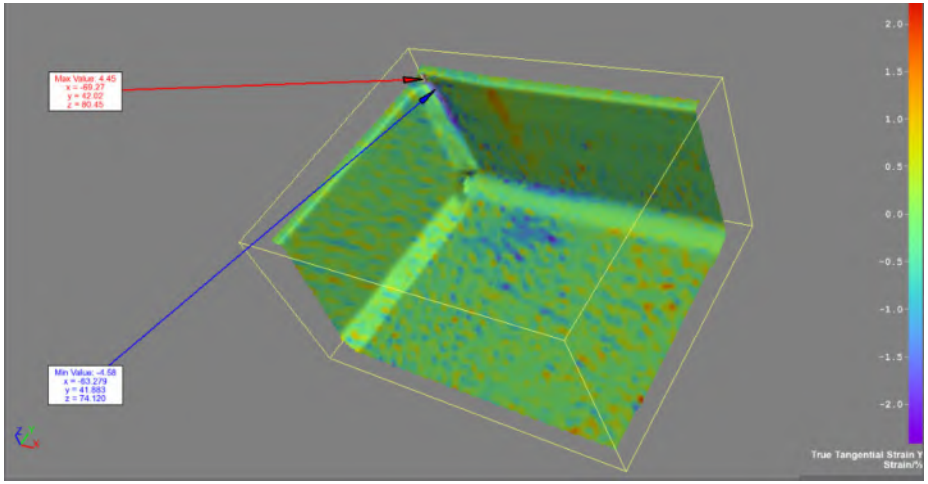

(d) W12X26-SC-E0

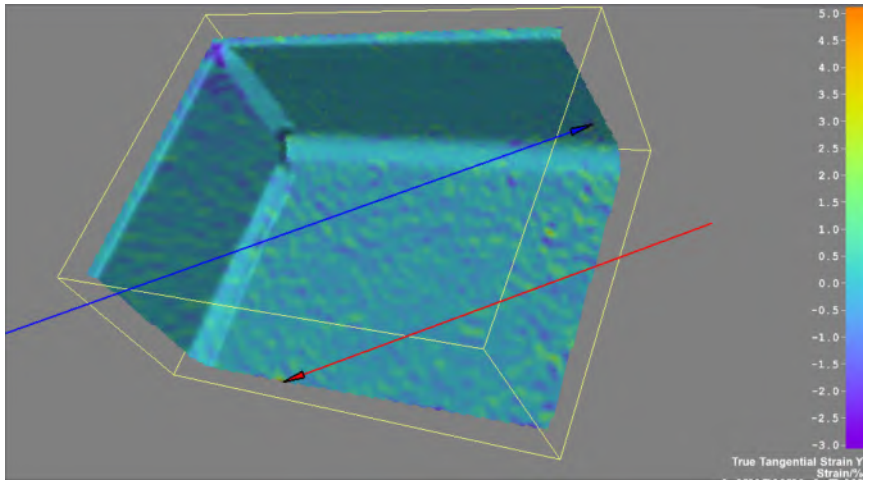

Figure 3.5-18: DIC Vertical (Y) strain for W12X26-SC column specimens at 59 kips

(a) W12X26-SC-NA

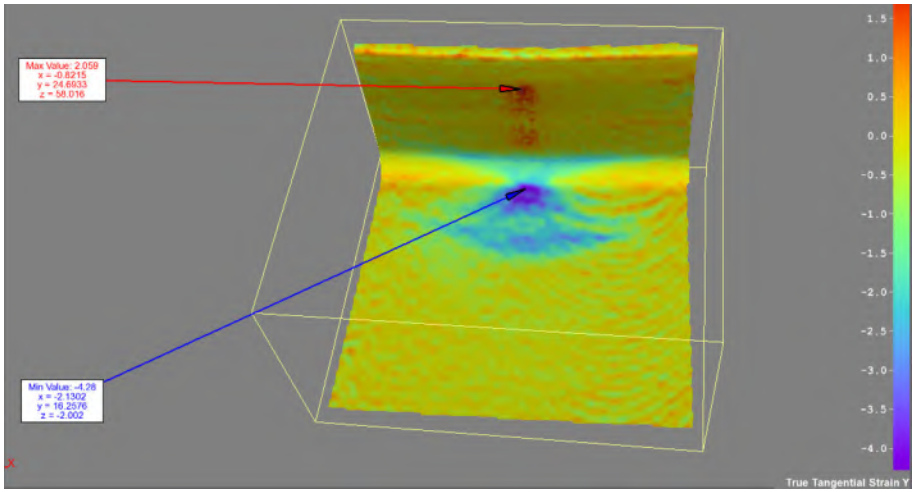

(b) W12X26-SC-E4

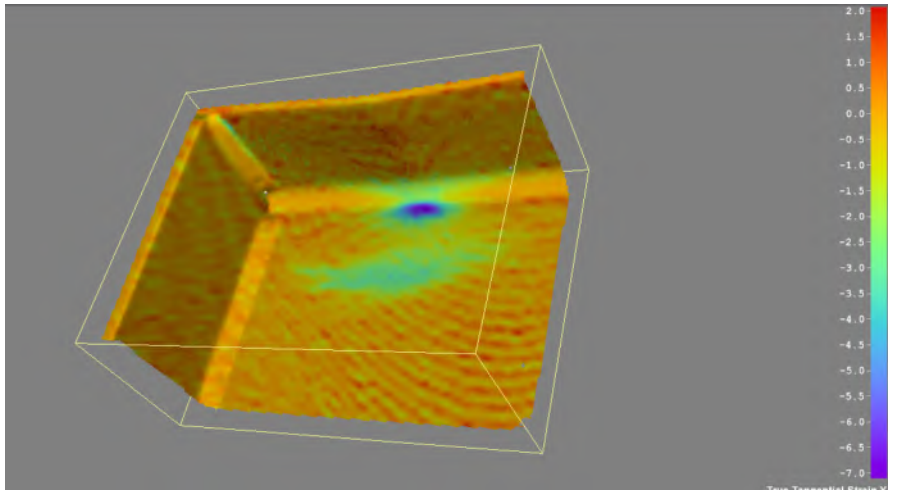

(c) W12X26-SC-E2

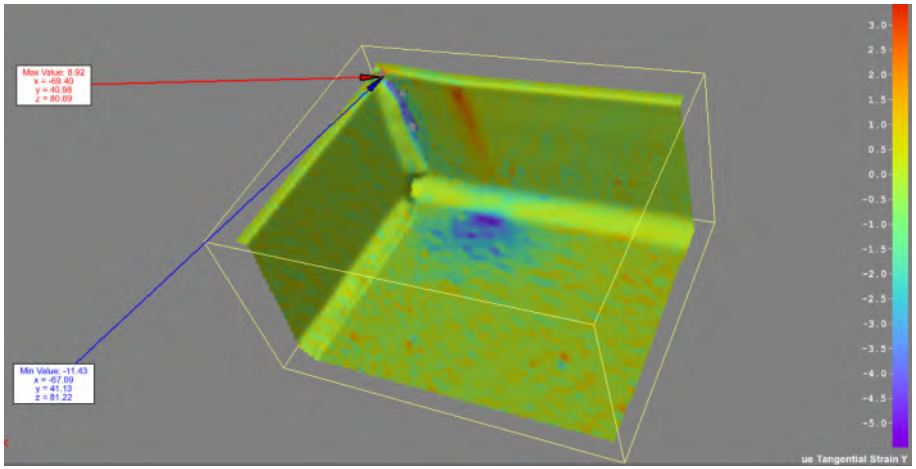

(d) W12X26-SC-E0

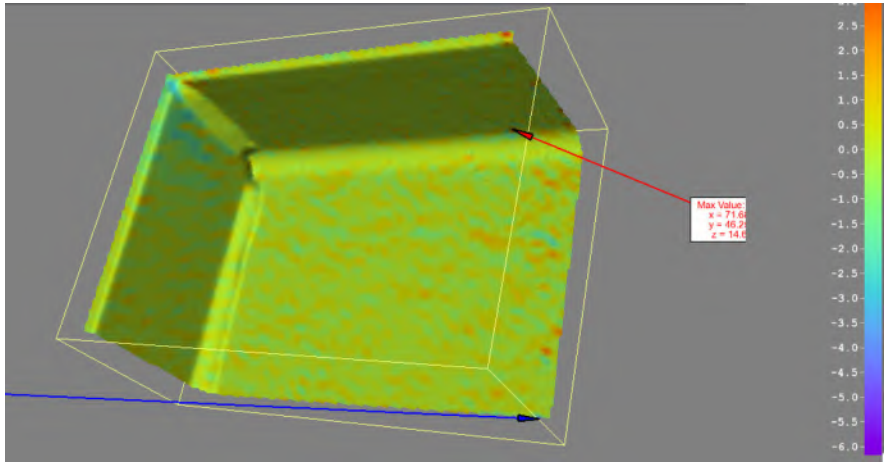

Figure 3.5-19: DIC Vertical (Y) strain for W12X26-SC column specimens at 78.2 kips

3.5.5 Other Instrumentation

Limited additional instrumentation was used as part of the experimental investigations since analysis of the test results was very dependent on the applied load and results from DIC. Each test was videotaped so that each test may be inspected afterwards. The hydraulic actuator is equipped with a load cell that was used to measure the applied load at any point during the test. In addition, the actuator stroke displacement is tracked in inches. Prior to initiating the test procedure, both the actuator and the displacement readings were zeroed using the computer attached to the hydraulics. All load and displacement test data was recorded every 0.1 seconds.

Note that if similar experiments are performed in the future, it is recommended to keep track of the displacement at the bottom of the steel member using a displacement transducer. The total displacement measured by the stroke of the actuator incorporated both flexural deformations and local deformations from concentrated loads. Measuring the displacement at the bottom of the column specimen would provide knowledge on the amount of flexural deformations vs. local deformations that occur during the test.

In addition, if double compression tests are performed in the future, it is recommended to install a load cell within the bottom support frame to determine the amount of load transferred to the bottom support. The research team assumes that most of the load from the hydraulic actuator transferred to the bottom support. However, some load was transferred to the end supports as evident by the end rotations and lack of symmetry in the deformations near the top flange as opposed to the bottom flange.

3.6 Experimental Procedure

Single and Double Compression Experimental Procedure

The test procedure for the experimental investigations was fairly systematic. Prior to the initiation of loading, the load and displacement readings were zeroed. Three student researchers worked in unison to ensure that the recording of the test data initiated at the same time. The instrumentation that needed to be initiated in unison included; recordings of the load and displacement data from the hydraulic actuator on one computer, the initiation of the DIC software on another computer, and the video camera.

Each test was performed in displacement control. The loading rate for the test was 0.05 in/min. Loading was paused randomly to evaluate the condition of the column specimen in the setup or if a sudden noise occurred that alarmed the research team. For most compression tests, the test was considered complete when the maximum load was obtained and the load started to decrease significantly with an increase in vertical displacement. A sudden decrease in load indicated that a buckling failure mechanism had occurred and the column "failed". The research team did not have a set criteria to how much the load needed to decrease but allowed enough overall displacement so the mechanism that caused failure would be easily visible on the column specimen after the test was complete. Usually, the mode of failure was web local crippling for both the single compression and double compression tests, which always occurred in the web near the flange with the applied load. Some columns failed by lateral-torsional buckling and specimens with concentric stiffeners appeared to fail by inelastic buckling of the stiffeners. One test was considered complete when the capacity of the actuator was reached and no more load could be applied.

Single Tension Experimental Procedure

The test procedure for the single tension tests was similar to the test procedure used for the compression tests. The column specimens were attached to the top test fixture using bolts and the specimen had to be raised using the hydraulic actuator prior to initiating the test, such that the specimen came into contact with the top rollers. Three researchers once again simultaneously initiated the instrumentation for collecting the data during the test. The test rate was set as 0.05 in/min.

The single tension tests were considered complete when one of the two events occurred: (1) the actuator capacity was reached or (2) when the weld from the loading plate (see Section 3.3) to the column specimen failed. Weld failure generally occurred for column specimens without stiffeners or when eccentric stiffeners were used. One column specimen reached a capacity when the weld from the eccentric stiffener to the column specimen top flange failed which upon further loading, caused a fracture through the web of the column specimen directly under the concentrated load (the flange separated from the web). For all three column specimen sizes, the capacity of the actuator was reached when concentric stiffeners were used. In addition, for all W10X39 column specimens, the capacity of the hydraulic actuator was reached. As mentioned earlier in this report, the research

team was under the impression that the capacity of the actuator was 220 kips in both tension and compression and upon testing, found that the actuator capacity in tension (upwards) was 145 kips instead. Therefore, the behavior and strain distribution before reaching the capacity were studied using DIC.

3.7 Experimental Results

As stated earlier in this report, much more detail regarding observations and experimental behavior for each column specimen was provided in the preliminary report dated October 29, 2018. This section and the following subsections provide an abbreviated version presenting the results and providing a discussion of the results.

For each test, photographs were taken of the test specimens before each test and several photographs were taken after each test that show the deformed state of the test specimens. All photographs are provided in Appendix A with some shown in the following subsections for demonstration purposes. In addition, each test was videotaped from the front side and all videos may be provided upon request. Finally, as mentioned in Section 3.5.4, the DIC data was processed with screenshots at loads magnitudes of interest. Screenshots are provided in Appendix C.

For each test, load-displacement plots were generated. The load represents the load recorded from the hydraulic actuator and the displacement represents the stroke of the actuator. In the following subsections, the four tests as part of a set (one without stiffeners, one with concentric stiffeners, and two with eccentric stiffeners) are plotted together to further understand the influence of eccentric stiffeners. In addition, theoretical (or nominal) capacities associated with concentrated load limit states are also shown on the figures for the wide-flange section in question and without stiffeners. These are represented with horizontal lines labeled '*FB*' for flange bending, '*WLY*' for web local yielding, '*WCR*' for web local crippling and '*WCB*' for web compression buckling. The theoretical capacities are computed in Appendix D.

3.7.1 Single Compression Test Results

Sixteen (16) experimental column specimens were tested in single compression. This includes four wide-flange sizes and four tests per size. A discussion of the results is separated by wide-flange size and therefore 'test set' in this section.

A summary of all the results from the single compression tests are provided in Table 3.7-1. The results in the table only include the 'Test Capacity' which is the maximum load recorded during the test and the 'Effective Stiffener Capacity'. The effective stiffener capacity is equal to the capacity of the test with stiffeners minus the result of the corresponding test without stiffeners. As shown, some test results have negative effective stiffener capacities; indicating that a test with eccentric stiffeners had less capacity than the corresponding test without stiffeners.

In addition, the tables list the capacities for web local yielding (*WLY*) and web local crippling (*WCR*) for the column specimen without stiffeners, which are both limit states associated with this test method. Since they are assumed to contribute to an overall capacity with stiffeners, they are shown as one value for the test set. In addition, the theoretical 'Stiffener' capacity is provided assuming the stiffeners are concentric. The theoretical stiffener capacity was computed as discussed in Section 3.8.

The "Theoretical Capacity" varies for each type of test depending on the stiffener condition. For columns without stiffeners, the theoretical capacity represents the capacity of the lowest computed limit state associated with the test method. For all columns sizes, web local yielding controlled. For columns with concentric stiffeners, the theoretical capacity is the lowest computed limit state in addition to the concentric stiffener capacity. For column specimens with eccentric stiffeners, the corresponding theoretical capacity is unknown as it is related to the primary objective of this research project. Therefore, the theoretical capacity is blank.

Table 3.7-1: Single compression theoretical capacities and test results

Column Specimen	Eccentricity (in)	WLY (k)	WCR (k)	Stiffener (k)	Theoretical Cap. (k)	Test Capacity (k)	Effect. Stiff Capacity (k)
W16X31-SC-NA	NA	75	103.4	62.5	75	112.4	-
W16X31-SC-E6	6				-	99.3	-13.1
W16X31-SC-E3	3				-	111.2	-1.2
W16X31-SC-E0	0				137.5	176.8	64.4
W12X26-SC-NA	NA	52.5	74.7	76.9	52.5	78.2	-
W12X26-SC-E4	4				-	79.2	1
W12X26-SC-E2	2				-	87.1	8.9
W12X26-SC-E0	0				129.4	148.3	70.1
W10X19-SC-NA	NA	58.1	88.2	27.0	58.1	69.6	-
W10X19-SC-E4	4				-	57.4	-12.2
W10X19-SC-E2	2				-	70.6	1
W10X19-SC-E0	0				85.1	103.3	33.7
W10X39-SC-NA	NA	102.2	143.6	97.6	102.2	131	-
W10X39-SC-E4	4				-	132.9	1.9
W10X39-SC-E2	2				-	142.3	11.3
W10X39-SC-E0	0				199.8	198.1	67.1

Some observations from Table 3.7-1 are as follows:

- For all tests without stiffeners and with concentric stiffeners, the maximum load exceeded the theoretical capacities for the tests with one exception. The results were very similar for W10X39-SC-E0.
- The maximum loads obtained for all specimens with eccentric stiffeners were similar to the results of the corresponding specimens without stiffeners. There were no clear trends in the results. However, the 'low eccentricity' condition always resulted in a higher capacity than the 'high eccentricity' condition. Therefore, it is believed that as eccentricity decreases, load carrying capacity increases.
- The maximum loads for columns without stiffeners were close to the maximum loads computed for web local crippling with the exception of the W10X19. For this case, lateral-torsional buckling was also witnessed during the test as discussed later in this section. It is believed that this effect influenced the capacity results.
- For column specimens with concentric stiffeners, there was a significant increase in capacity in comparison to the condition without stiffeners. In addition, the effective stiffener capacity results compared well with the theoretical stiffener capacities.

W16X31 Single Compression Tests

The four W16X31 column specimens had four different stiffener conditions near the application of the point load: (1) one column was tested without stiffeners, (2) one column was tested with concentric stiffeners (eccentricity = 0 in.), (3) one column was tested with a high eccentricity of 6 in., and (4) one column was tested with a low eccentricity of 3 in. Photographs of these experimental column specimens are provided in Appendix A from Figure A-1 to Figure A-16.

The load-displacement relationships for all four column specimens are shown together in Figure 3.7-1. From the AISC specification, Section J10 (AISC, 2016), the web local yielding capacity was calculated as 75 kips using a yield stress of 55 ksi. This was assumed the governing limit state prior to initiating the test. Three of the four column specimens reached a capacity between 99.3 kips and 112.4 kips. However, the column specimen with the low eccentricity and high eccentricity condition reached a lower capacity than the column specimen without stiffeners. This is a dissimilar relationship in comparison to other test sets evaluated in this research but indicates that eccentric stiffeners have a negligible influence on the concentrated load capacity of the column specimens.

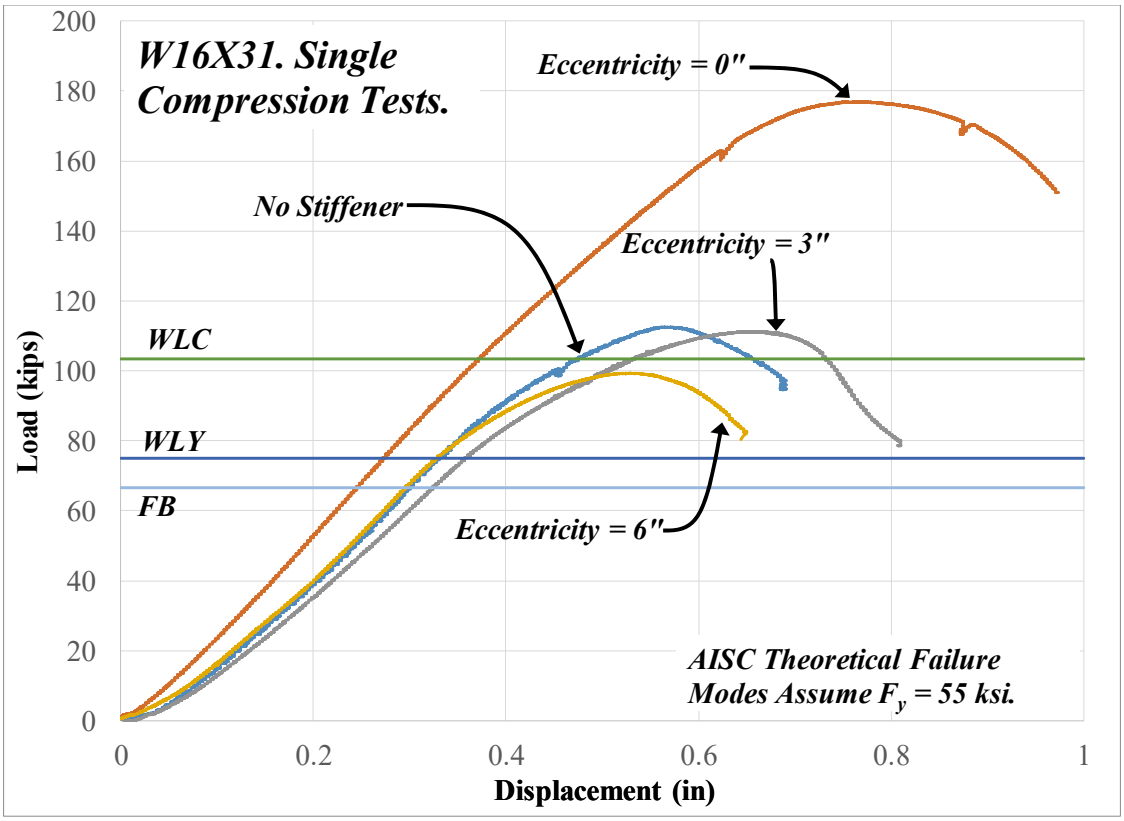

Figure 3.7-1: Load-displacement results of W16X31-SC column specimens

Figure 3.7-1 indicates that the load capacity and stiffness of column specimens with eccentric stiffeners are similar to the results of the column specimen without stiffeners. In the concentric stiffener condition, the load increased substantially in comparison to the other conditions and the elastic stiffness of the load-displacement relationship increased slightly. Since the column specimens were simply supported, it is assumed that the elastic stiffness is primarily influenced by flexural properties, which are assumed equal for all column specimens. However, since displacement was measured at the top of the column specimen, the total displacement is influenced by flexural deformations and local deformations in the flange and web that occur near the location of the concentrated load. These observations further demonstrate how ineffective the eccentric stiffeners are in comparison to concentric stiffeners since the elastic stiffness is very similar to the condition without stiffeners, suggesting that local deformations are approximately equal.

Figure 3.7-1 also shows that three of the column specimens failed at a capacity close to the predicted capacity for web local crippling (103.4 kips) which was the mode of failure identified from visual inspection of these column specimens. When the results are looked at in more detail, non-

linear behavior does initiate near the limit state of web local yielding. However, there is still a much higher capacity after the calculated value for this limit state.

Similar behavior was observed during the tests for the condition without stiffeners and the conditions with eccentric stiffeners. For all of these cases, yielding started in the column web directly beneath the loading plate. Yielding was seen to continue through the web by means of "strain lines" radiating from the mentioned point. Yielding continued through the web until the column specimens failed by web local crippling. In all three cases, the crippling effect was noticed at about ¼ the depth of the web from the top flange. For the case with a low eccentricity, it appeared that the "bulge", representing significant out-of-plane displacement of the web, was smaller in area. However, this did not influence the load carrying capacity significantly. Figure 3.7-2 demonstrates that web crippling is the mode of failure and governs the final capacity of the column specimens as excessive out-of-plane deformations develop in the web under the load. Figure 3.7-2(a) shows the case without stiffeners, Figure 3.7-2(b) shows the case with stiffeners at an eccentricity of 6 in. and Figure 3.7-2(c) shows the case with stiffeners at an eccentricity of 3 in. As shown, although all three specimens exhibit web local crippling, as the stiffeners become more concentric, the local area of out-of-plane displacement decreases. Results in this research show that although the eccentric stiffeners do not have much of an influence on the load-carrying capacity, they do assist with the post-buckling behavior of the column specimens.

(a) W16X31-SC-NA (b) W16X31-SC-E6 (c) W16X31-SC-E3

Figure 3.7-2: Load-displacement results of W16X31-SC column specimens

W16X31-SC-E0 represents the W16X31 column specimen with concentric stiffeners. Overall, the test behavior of this column specimen was significantly different from the behavior of the other column specimens in the test set. Yielding was first noticed at a much higher load. Strain lines in the column web radiating from the stiffener welds were noticed at a load of 150 kip. Yielding continued through the web and the stiffeners upon further loading. Slight flange bending on the front side of the column was first noticed at a load of 160 kip. As shown from Figure 3.7-1, the load capacity of this column specimen was significantly higher than that of the other column specimens. The total capacity was 176.8 kips, which was much higher than the capacity of the column specimen without stiffeners of 112.4 kips. The effective stiffener capacity from the test compared well to the predicted theoretical capacity from Table 3.7-1.

Figure 3.7-3(a) shows the column specimen after completion of the test. In addition to the presence of stiffener buckling, Figure 3.7-3(a) also shows patterns of strain lines in the web. These strain lines were found on both sides of the column specimen and in horizontal and vertical patterns. The final test condition is shown with the final test condition of the column without stiffeners in

Figure 3.7-3(b) and the condition with eccentric stiffeners at 3 in. in Figure 3.7-3(c). The vertical strain lines in the web from the concentric stiffener condition are not identified in the other two conditions. In addition, there are no signs of stiffener buckling for the 3 in. eccentric stiffener condition and in general, the stiffeners do not appear nearly as engaged in sharing the load.

Near the completion of the test, W16X31-SC-E0 eventually showed signs of lateral-torsional buckling in combination with stiffener buckling. However, this phenomenon occurred well after significant yielding had occurred to elements of the column specimen and is not considered to contribute to the mode of failure.

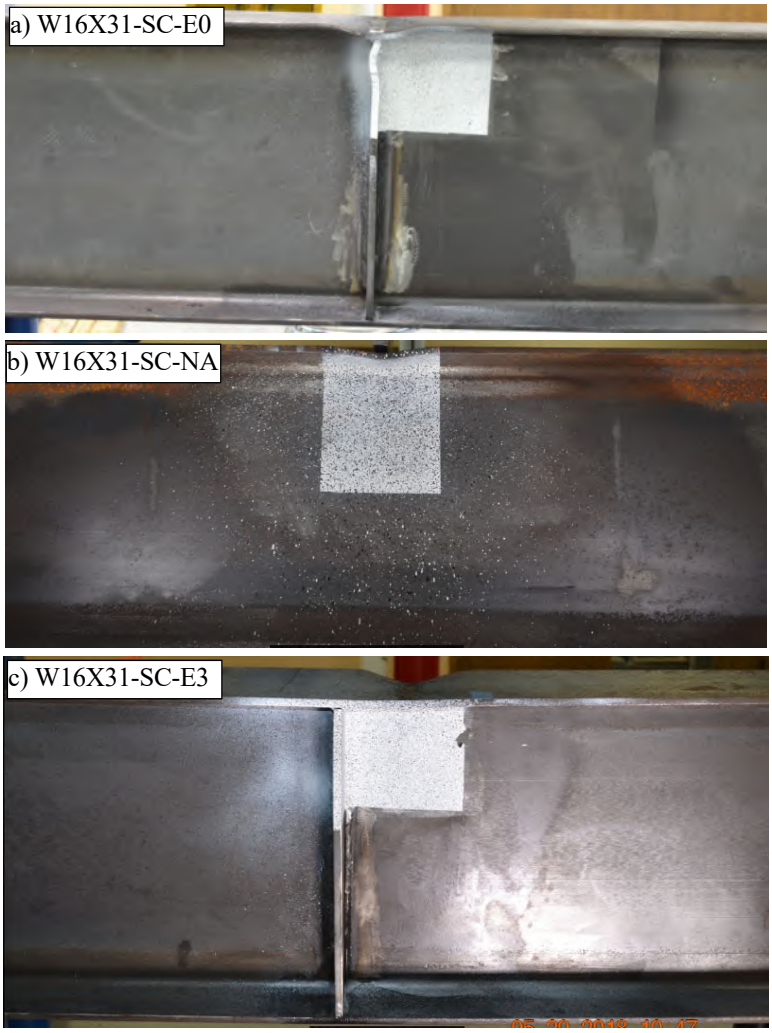

Figure 3.7-3: Condition of W16X31-SC column specimens after testing

W12X26 Single Compression Tests

The four W12X26 column specimens had four different stiffener conditions near the application of the point load but the conditions were slightly different than the W16X31 column specimens: (1) one column was tested without stiffeners, (2) one column was tested with concentric stiffeners (eccentricity = 0 in.), (3) one column was tested with a high eccentricity of 4 in., and (4) one column was tested with a low eccentricity of 2 in. Photographs of these experimental column specimens are provided in Appendix A from Figure A-54 to Figure A-70.

The load-displacement relationships for all four column specimens are shown in Figure 3.7-4. For all four specimens, the data was adjusted so that the displacement increased from zero when the load started to noticeably increase. The column specimen with no stiffener reached a capacity of 78.2 kips. Both specimens with high and low eccentricity conditions reached a slightly higher capacity of 79.2 kips and 87.0 kips, respectively. The column specimen with concentric stiffeners reached a significantly higher capacity of 148.2 kips (almost twice the capacity of others).

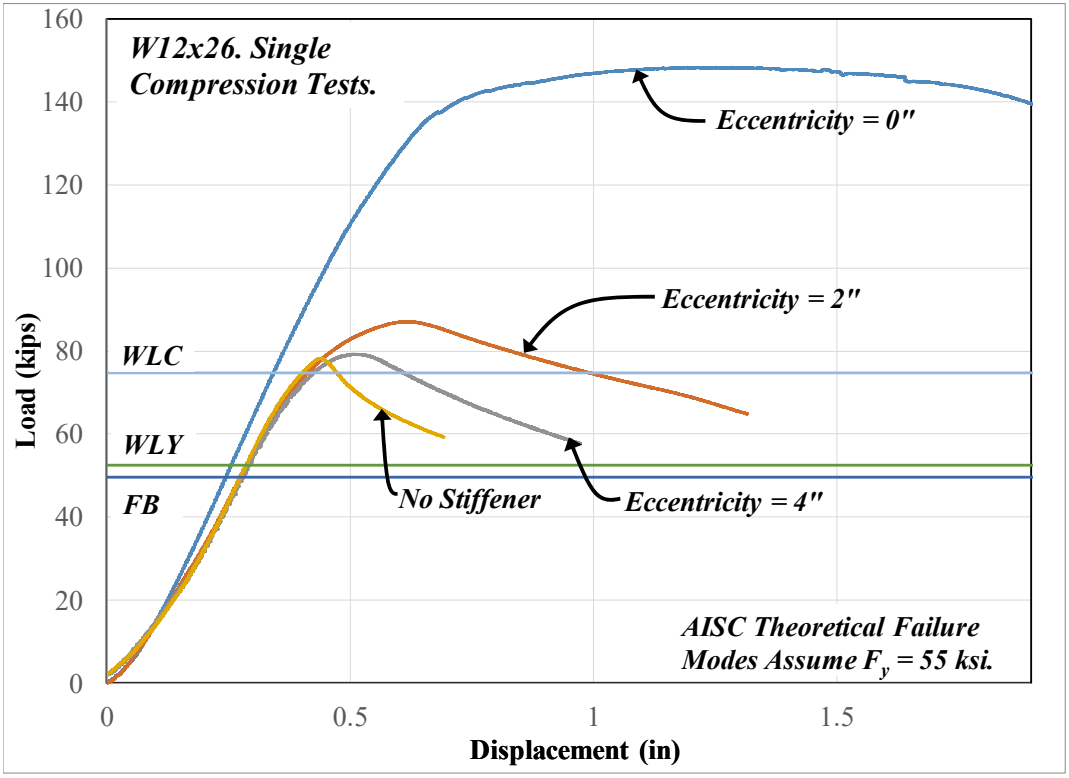

Figure 3.7-4: Load-displacement results of W12X26-SC column specimens

Figure 3.7-4 indicates that the load capacity and stiffness of column specimens with eccentric stiffeners are very similar to the result without stiffeners. The results of this test set relate well to the overall observations found during the experimental investigations. The maximum load of the column specimen with a low eccentricity of 2 in. increased slightly in comparison to the condition without stiffener but for the concentric stiffener condition, the load increased substantially in comparison to the other conditions and the elastic stiffness of the load-displacement relationship moderately increased. These observations further demonstrate how ineffective the eccentric stiffeners are in comparison to concentric stiffeners since the elastic stiffness is very similar to the condition without stiffeners suggesting that local deformations are approximately equal.

Figure 3.7-4 shows nominal capacities for the limit states of web local crippling (*WLC*), web local yielding (*WLY*), and flange bending (*FB*) per the AISC specification, Section J10 (AISC, 2016). Although flange bending is not a limit state considered for compression tests per the AISC specification (AISC, 2016), significant flange bending was witnessed during the compression tests and therefore, the capacity was calculated and shown on the graphs to compare to the non-linear behavior found in the load-displacement results. The results show that three of the columns failed at a capacity close to the predicted capacity for web local crippling (74.7 kips), which was the mode of failure identified from visual inspection of these column specimens. When the results are looked at in more detail, non-linear behavior does initiate near the limit state of web local yielding. However, the column specimens reach much higher loads after the calculated value for this limit state and significant non-linear behavior is not witnessed in the load-displacement relationship until web crippling initiates.

Similar to the load-displacement relationships, the experimental behavior witnessed for the column specimens with eccentric stiffeners was similar to the condition without stiffeners. In all three cases, yielding was first seen in the column web beneath the loading plate and continued through the web by means of strain lines radiating from the mentioned point until the column reached its maximum load and suddenly failed (due to load decreasing) by web local crippling. For W16X31-SC-E2, strain lines were also found radiating from the stiffener weld. At a load within 60% of the load capacity, a modest amount of bending of the column flanges underneath the applied load was noticed. For all three column specimens, signs of lateral-torsional buckling occurred near

the completion of the test as shown in the photographs of Appendix A.

Figure 3.7-5 shows the condition of W12X26-SC-NA after testing, which provides a good representation of the deformed state of all three aforementioned column specimens after testing. Figure 3.7-5 shows that web local crippling is the failure mechanism of the column specimen. This failure mode governed the final capacity of the column specimen as excessive out-of-plane deformations developed in the web under the loads. When crippling was first noticed in the web, the load started to drop suddenly with a further increase in vertical displacement. This is a characteristic of a buckling failure mode. Figure 3.7-5 also identifies the horizontal and vertical strain lines that appeared in the web.

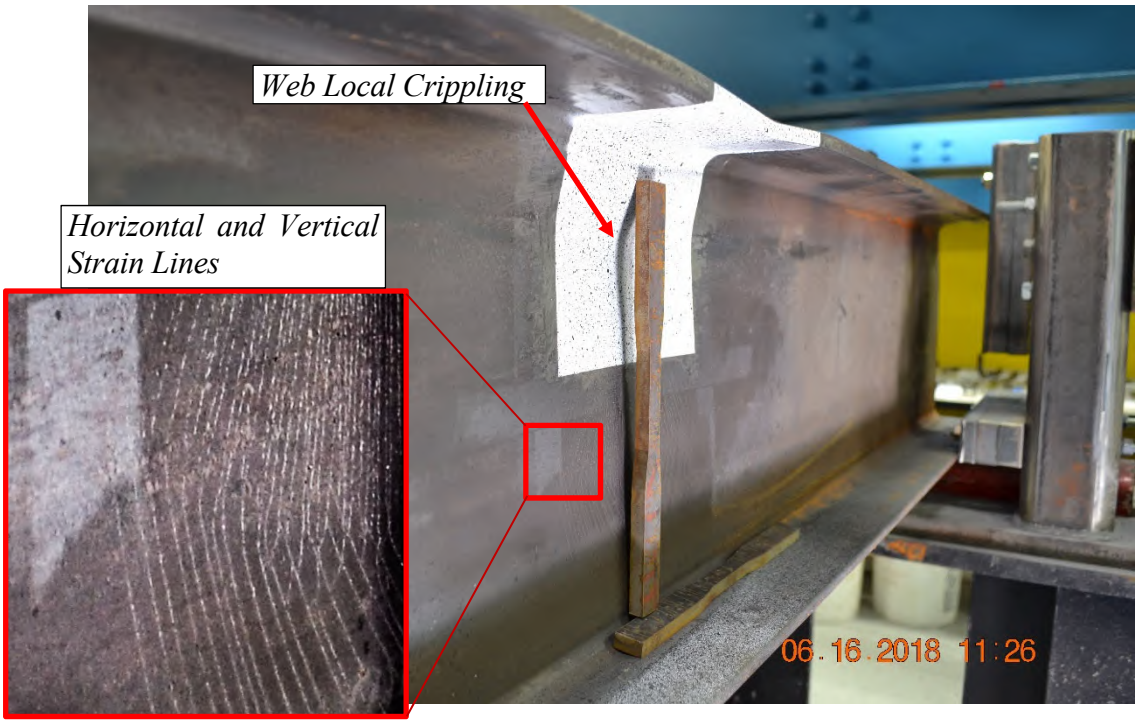

Figure 3.7-5: W12X26-SC-NA after testing emphasizing web crippling

W12X26-SC-E0 represents a W12X26 column specimen, tested in single compression, and with concentric stiffeners at midspan. As shown in Figure 3.7-4, this column specimen resulted in slightly higher elastic stiffness and significantly higher load carry capacity. Yielding was first identified at a much higher load as well. Large horizontal and vertical strain lines in the web were identified at a load of 130 kips. The research team also noticed yielding on the bottom face of the bottom flange by means of large strain lines and mill scale peeling off. The total capacity of W12X26-SC-E0 was

148.3 kips and the capacity of the column specimen without stiffeners of 79.2 kips. The effective stiffener capacity was therefore 70.1 kips. This was close to the calculated stiffener capacity of 76.9 kips assuming F_y = 39 ksi for the stiffeners. Figure 3.7-6 shows a close-up elevation view of the column specimen. As demonstrated, the front stiffener buckled locally on the top and close to the concentrated load. Since significant yielding clearly occurred prior to buckling, the failure mode is best described as inelastic stiffener buckling. In addition to the presence of stiffener buckling, Figure 3.7-6 also shows local flange buckling and shows significant patterns of strain lines in the web and mill scale peeling off. These strain lines are much more dramatic than the strain lines seen for the column specimen without stiffeners from Figure 3.7-5.

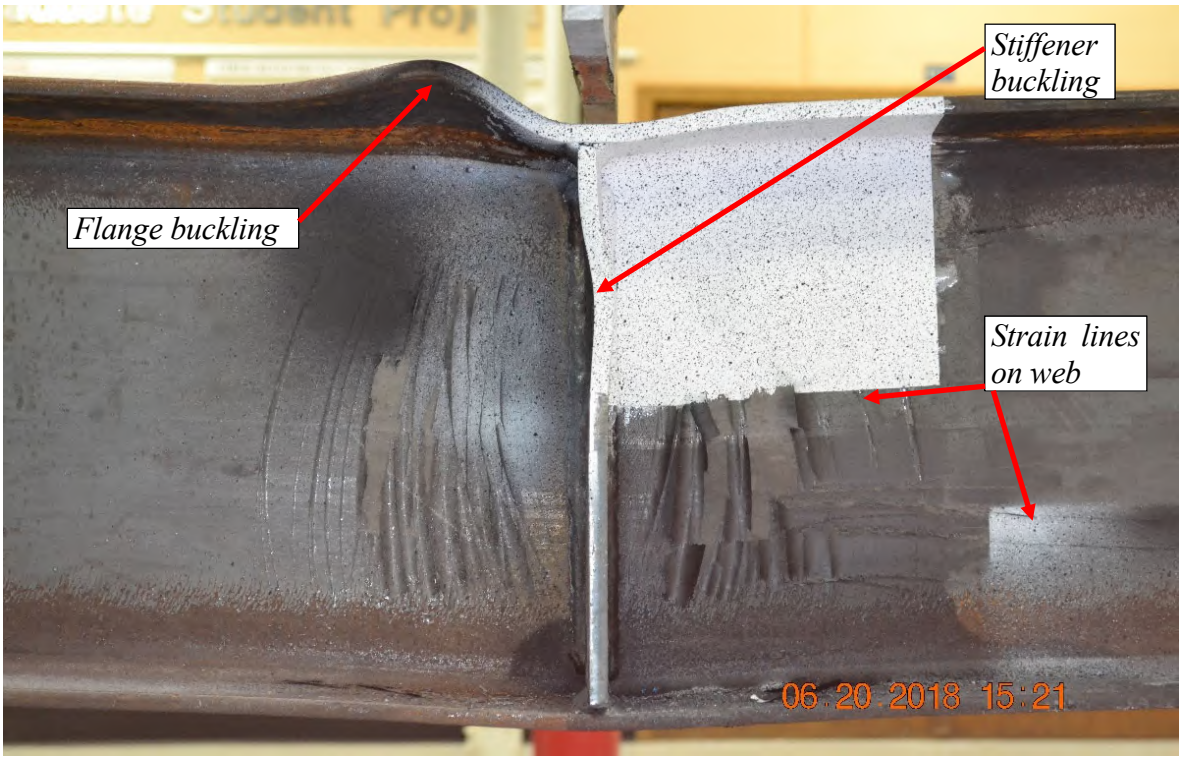

Figure 3.7-6: Close-up view of front side of W12X26-SC-E0 after testing

Overall, the results of the W12X26-SC test set are similar to the results of the W16X31-SC test set. Therefore, for the single compression test method, the columns without concentric stiffeners reached a maximum load when web crippling occurs. For these column sizes, eccentric stiffeners do not significantly change the load carrying capacity or the mode of failure. Using concentric stiffeners is effective to resist against concentrated loads since it disallows web crippling of the web and the stiffeners inherently share the load more effectively with the local web area.

W10X19 Single Compression Tests

Four W10X19 column specimens were tested in single compression. They had four different stiffener conditions near the application of the point load: (1) one column specimen was tested without stiffeners, (2) one column specimen was tested with concentric stiffeners (eccentricity = 0 in.), (3) one column was tested with a high eccentricity of 4 in., and (4) one column was tested with a low eccentricity of 2 in. Photographs of these experimental column specimens are provided in Appendix A from Figure A-17 to Figure A-36.

All column specimens were supposed to be simply supported at 5 ft. However, due to the presence of lateral-torsional buckling during the first test, the span was reduced to 4 ft. for the three remaining tests. The column specimen with a high eccentricity of 4 in. was the only specimen tested at 5 ft. However, it is assumed based on the results with a low eccentricity of 2 in. that the high eccentricity condition would have similar results to the column specimen without stiffeners if it were supported at 4 ft. All columns underwent some lateral-torsional buckling with an example shown in Figure 3.7-7. Calculations in the AISC specification (AISC, 2016) for the flexural capacity of this column revealed that lateral-torsional buckling would occur at an unbraced length of 4 ft. or 5 ft. When selecting the experimental test matrix, the research team overlooked this possibility but also felt the plate from the hydraulic actuator would provide enough friction for lateral support of the compression flange.

Figure 3.7-7: Side view of W10X19-SC-E0 after testing showing lateral-torsional buckling

For this test group only and for all column specimens tested at 4 ft., the research team slightly prevented the column specimens from lateral-torsional buckling by bracing the loading plate to the top flange to avoid lateral motion. In order to do so, two small steel plates were attached to the loading plate at a distance equal to the top flange width with two 8 in. high strength c-clamps, as shown in Figure 3.7-8.

`a) Isometric View b) Side view

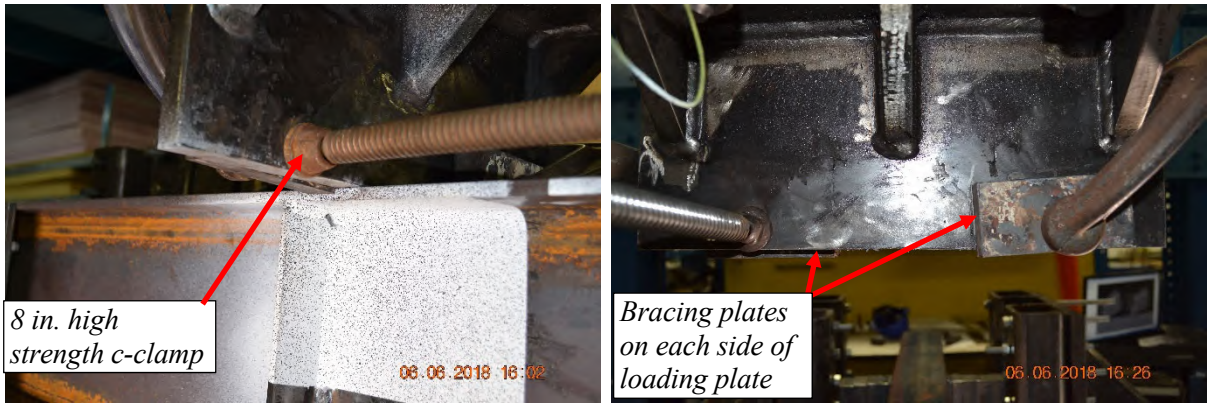

Figure 3.7-8: Method used to brace W10x19 specimens against lateral-torsional buckling

The load-displacement relationships for all four column specimens are shown together in Figure 3.7-9. For all four specimens, the data was adjusted so that the displacement increased from zero when the load started to noticeably increase. The column specimen with a high eccentricity of 4 in. failed due to lateral-torsional buckling at a load of 57.3 kips, which was much less than the column specimen without stiffeners. The column specimen without stiffeners reached a maximum capacity of 69.5 kips. Similarly, the column specimen with a low eccentricity of 2 in. reached a capacity of 70.5 kips. The column specimen with concentric stiffeners failed at a much higher capacity of 103.3 kips. Although the data for W10X19-SC-E4 should not be further used for comparisons, the relationships found for this test set are similar to that for other single compression test sets. In general, steel columns *without* concentric stiffeners fail by web crippling and for this column size, combined with lateral-torsional buckling. The influence of eccentric stiffeners is negligible on the load carrying capacity. For the concentric stiffener, the load increased substantially in comparison to the other conditions and the elastic stiffness of the load-displacement relationship slightly increased.

Figure 3.7-9 also indicates nominal capacities for the limit states described in the AISC specification, Section J10 (AISC, 2016), which are web local crippling (*WLC*), web local yielding (*WLY*), and flange bending (*FB*). The reason for plotting the flange bending capacity was discussed earlier in this section. The results show that for the eccentric stiffener condition and the no stiffener condition that the change in the load-displacement curve from elastic to plastic behavior is near the predicted capacity for flange bending (53.6 kips). From visual inspection of the tests, flange bending was very substantial for these column specimens. For the column specimen with concentric stiffeners, the load-displacement curve indicates inelastic behavior close to the predicted capacity for web local crippling (91.1 kips).

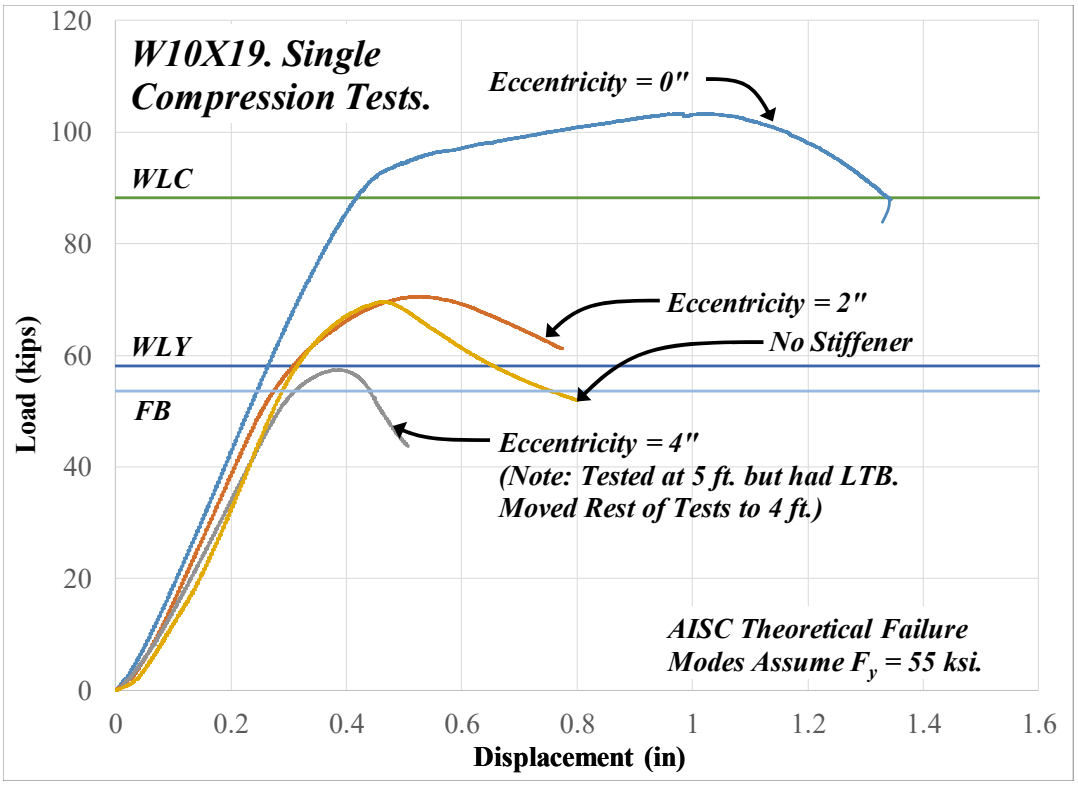

Figure 3.7-9: Load-displacement results of W10X19-SC column specimens

The specimen with the high eccentricity of 4 in. (W10X19-SC-E4) will not be discussed further since it had a higher span and showed additional signs of lateral-torsional buckling. However, the experimental behavior of W10X19-SC-NA and W10X19-SC-E2 were very similar. In both cases, yielding began first in the column web beneath the loading plate and in the top flange directly underneath the loading plate. Yielding continued through the web by means of "strain lines" radiating from beneath the loading plate. For W10X19-SC-E2, strain lines were also found to radiate from the stiffener weld on the backside of the column specimen. Deformations continued in the webs until the column specimens failed by web crippling. For both specimens, the crippling effect embraced a much larger *relative* area of the web compared to the localized "bulge" identified in the W16X31-SC tests. In summary, the experimental behavior of the column specimen without stiffeners was very similar to the behavior of the column specimen with stiffeners at a 2 in. eccentricity.

The test behavior of this column specimen with concentric stiffeners was significantly different than the behavior of the other column specimens in the test set. Slight flange bending on both sides

of the column was first noticed at a load of 75 kips which represents a load already higher than the capacity of other column specimens. Large horizontal and vertical strain lines in the column web were noticed at a load of 90 kips. Yielding continued through the web and flanges by means of mill scale peeling off. As shown in Figure 3.7-9, the load capacity of this column specimen was significantly higher than that of the other column specimens. The total capacity was of 103.2 kips, which was much higher than the capacity of the column specimen without stiffeners of 69.5 kips. The effective stiffener capacity is therefore 33.7 kips. This was close to the calculated stiffener capacity of 27 kips assuming F_y = 39 ksi for the stiffeners.

Figure 3.7-10 (b) shows a close-up elevation of this column specimen, which is compared to the condition of W10X19-SC-E2 shown in Figure 3.7-10 (a). This figure alone demonstrates the amount of load resisted by the concentric stiffeners in comparison to the condition with eccentric stiffeners. The stiffeners on both sides of the column specimen showed signs of excessive yielding as evident from the removal of mill scale on the surface. In addition, one stiffener buckled slightly on the top. Finally, the web strain lines are much more pronounced for the condition with concentric stiffeners. Therefore, the stiffeners not only aid in sharing the concentrated load, but they also brace the web from web crippling and allow more force to transfer into the web of the column specimen.

a) Condition with 2 in. eccentric stiffener

b) Condition with concentric stiffener

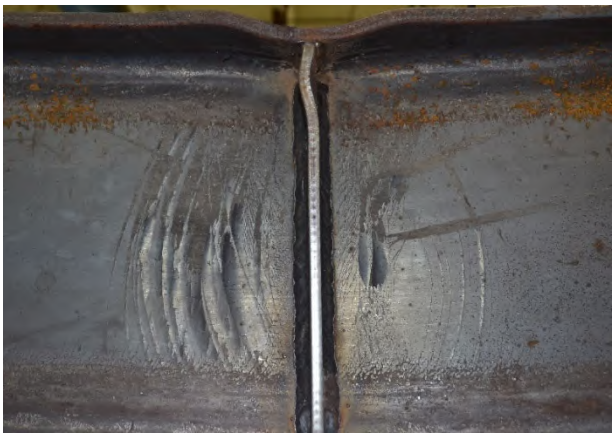

Figure 3.7-10: Comparison of web condition with eccentric and concentric stiffeners

W10X39 Single Compression Tests

Four W10X39 column specimens were tested in single compression. The four column specimens had four different stiffener conditions near the application of the point load: (1) one column was tested without stiffeners, (2) one column was tested with concentric stiffeners (eccentricity = 0 in.), (3) one column was tested with a high eccentricity of 4 in., and (4) one column was tested with a low eccentricity of 2 in. Photographs of these experimental column specimens are provided in Appendix A from Figure A-37 to Figure A-53.

The load-displacement relationships for all four column specimens are shown in Figure 3.7-11. The column specimen with no stiffener reached a capacity of 131 kips. Both specimens with high and low eccentricity conditions reached a slightly higher capacity of 132.9 kips and 142.3 kips, respectively. The column specimen with concentric stiffeners reached the highest capacity of 198.1 kips. Comparisons between the different specimens are in line with the general observations found in this research. The load capacity and stiffness of column specimens with eccentric stiffeners are very similar to the results of the column specimens without stiffeners. In this case, the maximum load obtained for the column specimen with a low eccentricity of 2 in. was noticeably higher than the condition without stiffener. Since this was the largest column size studied, it provides some confidence that eccentric stiffeners are effective for typical column sizes used in practice. In the concentric stiffener condition, the load significantly increased in comparison to the other conditions. Dissimilar to other test sets in single compression, the elastic stiffness of the W10X39 specimen with concentric stiffeners was not noticeably higher than that of other W10X39 column specimens.

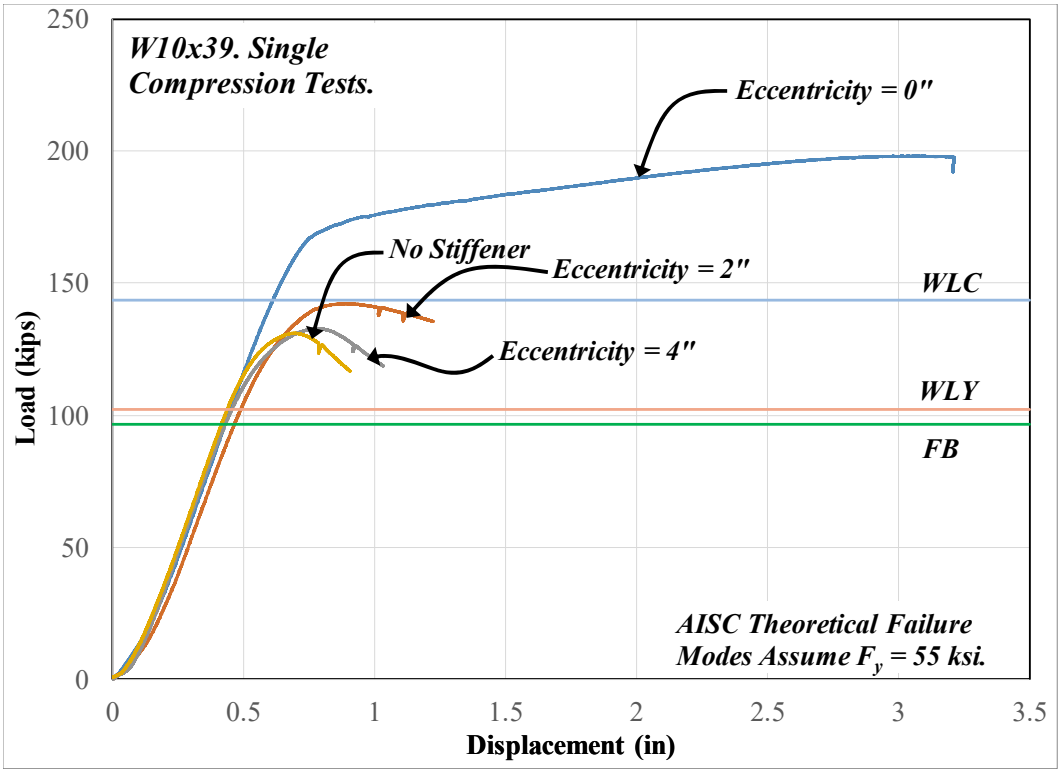

Figure 3.7-11: Load-displacement results of W10X39-SC column specimens

Figure 3.7-11 also indicates nominal capacities for the limit states described in the AISC specification, Section J10 (AISC, 2016), which are web local crippling (*WLC*), web local yielding (*WLY*), and flange bending (*FB*). In the eccentric stiffener condition and the no stiffener condition, the change in the load-displacement curve from elastic to plastic behavior is near the predicted capacity of web local yielding. However, there is a much higher capacity after the calculated value for this limit state.

Similar to other single compression test sets discussed in this section, the experimental behavior of column specimens with eccentric stiffeners was very similar to the condition without stiffeners. In general, all tests were performed successful in that the column specimens reached a capacity governed by a concentrated load failure mechanism. Yielding began first in the column web directly beneath the loading plate. Some flange bending was also witnessed for each test. Strain lines were noticed in the area of the web under the concentrated load. Yielding continued in this area of the web until all column specimen failed by web crippling. However, per Figure 3.7-11, all three of these column specimens reached a capacity lower than the predicted value for web local crippling.

In general, for all W10X39 tests, the web seemed more engaged in carrying load in comparison to other column specimen sizes. Figure 3.7-12 shows W10X39-SC-NA after completion of the test on both sides of the column specimen, which demonstrates the web crippling failure mode.

Figure 3.7-12: W10X39-SC-NA after testing emphasizing web crippling

At the completion of W10X39-SC-E2, a crack was found on the top weld for the front stiffener, which is believed due to excessive flange bending and concentrated stresses that develop on one side of the weld. Overall, the results of the test indicate some benefit in using stiffeners at a low eccentricity, yet there is a limited increase in capacity in comparison to the concentric stiffener condition.

The test behavior of the column specimen with concentric stiffeners (W10X39-SC-E0) was significantly different that the behavior of the other column specimens in the test set. Yielding was first noticed at a much higher load. Horizontal and vertical strain lines in the column web were noticed at a load of 150 kips. At a load of 175 kips, large strain lines radiating from the stiffener weld to the web were noticed. As the load increased, more strain lines appeared and propagated along the length of the specimen, more so than any other column specimen tested in single

compression. Flange bending and stiffener inelastic buckling were also noticed towards the end of the test.

Figure 3.7-13 shows the W10X39-SC-E0 column specimen at the completion of the test. This figure alone demonstrates the amount of load resisted by the concentric stiffeners. The stiffeners on both sides of the column specimen showed signs of excessive yielding. In addition, the stiffener on the front side buckled locally on the top, near the concentrated load. Since significant yielding occurred prior to buckling, the failure mode can best be described as inelastic stiffener buckling. In addition to the presence of stiffener buckling, Figure 3.7-13 also shows patterns of strain lines in the web and flange local buckling in the top flange. As discussed in Section 7.5, the maximum load results in an internal moment greater than the plastic moment for the column specimen and therefore, in design, the stiffeners clearly would have served and intended purposes.

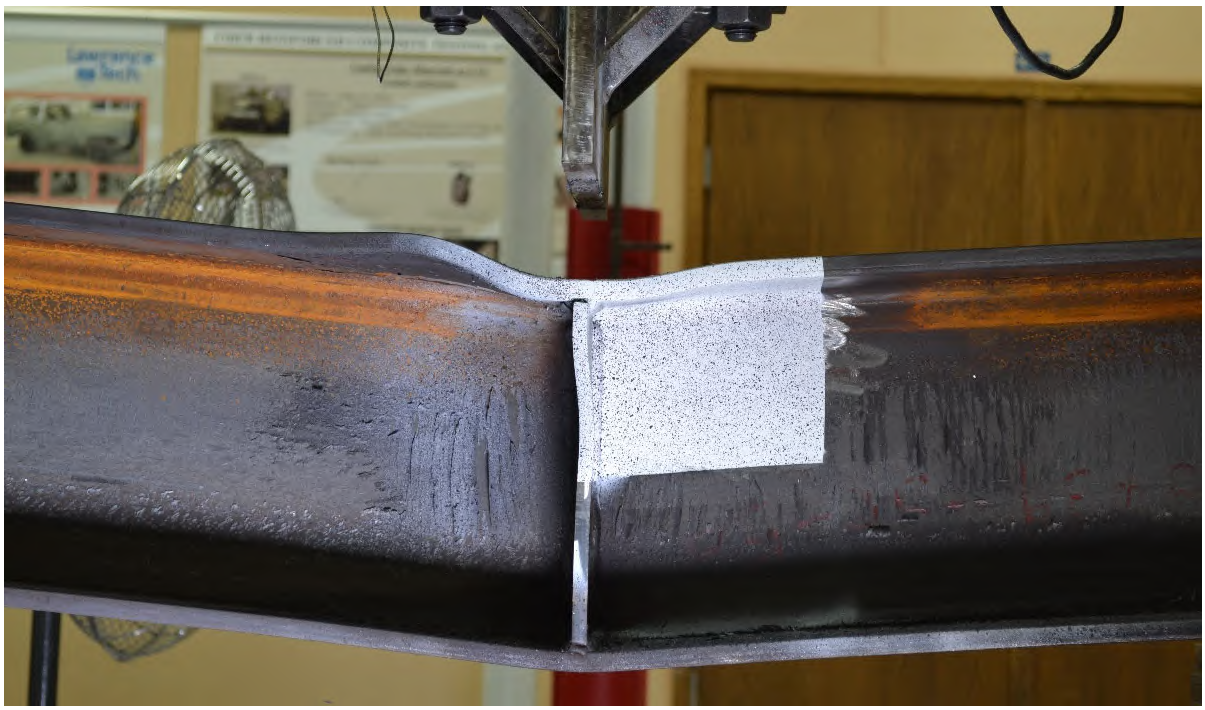

Figure 3.7-13: Elevation of W10X39-SC-E0 after testing

3.7.2 Double Compression Tests

Twelve (12) experimental column specimens were tested in double compression. This includes three wide-flange sizes and four tests per size from the four stiffener conditions. A discussion of the results is separated by wide-flange size and therefore 'test set' in this section.

A summary of all the results from the double compression tests is provided in Table 3.7-2. The results in the table include the 'Test Capacity', which is the maximum load recorded during the test, and the 'Effective Stiffener Capacity'. The effective stiffener capacity is equal to the capacity of the test with stiffeners minus the result of the corresponding specimen without stiffeners in the same test set. Specimen W12X26-DC-E0 reached a load equal to the load of the hydraulic actuator of 220 kips and therefore, its capacity is uncertain but at least 134 kips.

In addition, the tables list the capacities for web local yielding (*WLY*), web compression buckling (WCB) and web local crippling (*WCR*) for the column specimen without stiffeners, which are all limit states applicable for this test method. Since they are assumed to contribute to an overall capacity with stiffeners, they are shown as one value for the test set. In addition, the theoretical 'Stiffener' capacity is provided assuming the stiffeners are concentric using Equation 3-1 of Section 3.8. Note that only one stiffener was used for the W16X31-DC test set (as opposed to stiffeners on both side of the web) since preliminary investigations revealed that a W16X31 with two concentric stiffeners would exceed the actuator capacity. The final "Theoretical Capacity" varies for each type of test depending on the stiffener condition, which was discussed for the single compression tests in Section 3.7.1.

Table 3.7-2: Double compression theoretical capacities and test results

Column Specimen	Eccentricity (in)	WLY (k)	WCB (k)	WCR (k)	Stiffener (k)	Theoretical Cap. (k)	Test Capacity (k)	Effect. Stiff Capacity (k)
W16X31-DC-NA	NA	75	44.3	103.4	31.1	44.3	119.7	-
W16X31-DC-E6	6					Research	117.4	-2.3
W16X31-DC-E3	3					Research	121.1	1.4
W16X31-DC-E0	0					75.4	163.2	43.5
W12X26-DC-NA	NA	52.5	34	74.7	76.9	34	86.4	-
W12X26-DC-E4	4					Research	90.6	4.2
W12X26-DC-E2	2					Research	110.9	24.5
W12X26-DC-E0	0					110.9	220 **	+ 134
W10X19-DC-NA	NA	58.1	53.7	88.2	27	53.7	78.5	-
W10X19-DC-E4	4					Research	84.4	5.9
W10X19-DC-E2	2					Research	88	9.5
W10X19-DC-E0	0					80.7	180	101.5

** reached actuator capacity

Some observations from Table 3.7-2 are as follows:

- The theoretical equations provided by AISC (2016) for the limit states associated with double compression indicated that web compression buckling should have controlled for all column sizes when stiffeners are not present. In all cases without stiffeners and eccentric stiffeners, the load-carrying capacity of the column specimens was much higher than the predicted value. In addition, all capacities were higher than the theoretical capacity for web local yielding. The final capacities related better to the capacity predicted by web local crippling, which was observed as the failure mode associated with most of the tests.
- The maximum loads obtained for all specimens with eccentric stiffeners were usually close to the results of the corresponding specimens without stiffeners. There were no clear trends in the results. However, the 'low eccentricity' condition always resulted in a higher capacity than the 'high eccentricity' condition. For the W12X26 test set, there was one significant increase in load carrying capacity when the low eccentricity condition was tested. However, the effective stiffener capacity of 24.5 kips was still much lower than the effective stiffener capacity for the column specimen with concentric stiffeners which is unknown but at least 134 kips.
- For column specimens with concentric stiffeners, there was a significant increase in capacity in comparison to the condition without stiffeners. The increase in capacity was more

pronounced in comparison to the single compression tests. In addition, the effective stiffener capacities were much higher than the computed theoretical values. This is dissimilar from the single compression test results. It is hypothesized that single compression tests fail as a combination of the effects from concentrated loads, shear and flexure. However, the double compression tests primarily fail by the concentrated load effect and the stiffeners have a greater relative influence in bracing the web buckling modes of failure.

W16X31 Double Compression Tests

Four W16X31 column specimens were tested in double compression with four different stiffener conditions near the application of the point load: (1) one column was tested without stiffeners, (2) one column was tested with a concentric stiffener (eccentricity = 0 in.), (3) one column was tested with a high eccentricity of 6 in., and (4) one column was tested with a low eccentricity of 3 in. For the latter three, only one stiffener was used on one side of the web as discussed earlier in this section. Photographs of these experimental column specimens are provided in Appendix A from Figure A-71 to Figure A-87.

The load-displacement relationships for all four column specimens are shown together in Figure 3.7-14. For all four specimens, the data was adjusted so that the displacement increased from zero when the load started to noticeably increase. Three of the four test specimens reached a capacity between 117 kips and 121 kips. Therefore, the results directly indicate that eccentric stiffeners with the magnitudes of eccentricity used have no influence on the load-carrying capacity. For the high eccentricity condition, the maximum load slightly decreased in comparison to the condition without stiffeners. This comparison is likely influenced by imperfections in the test setup and the column specimens themselves.

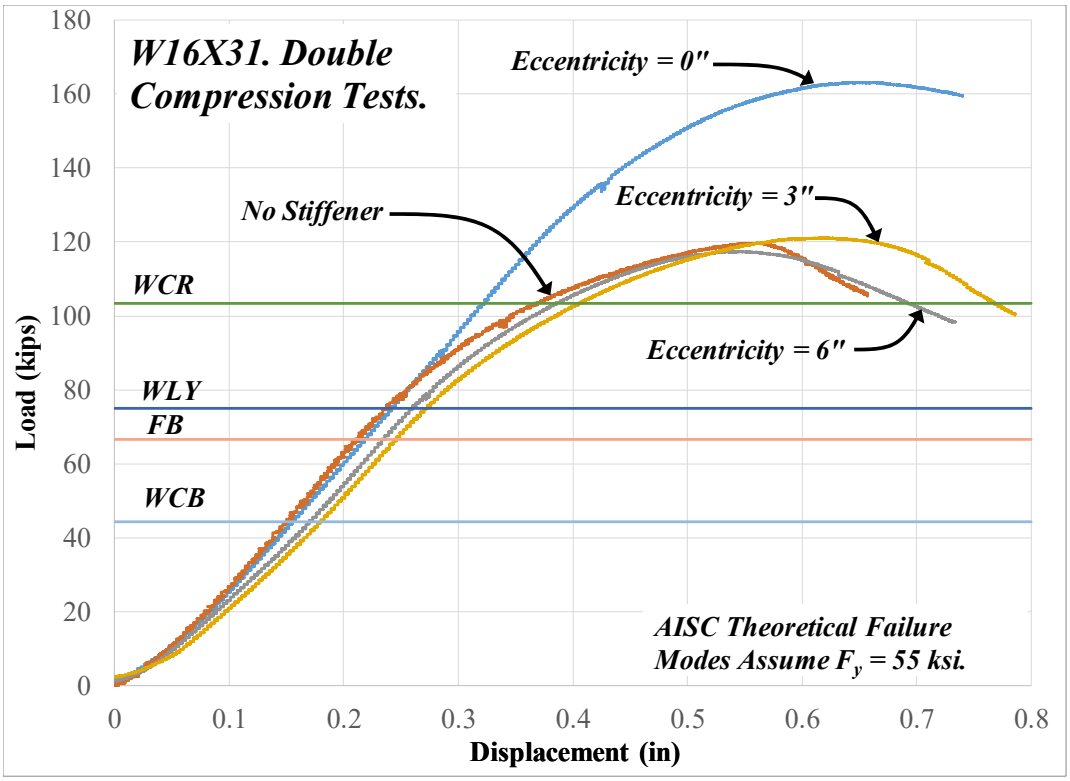

Figure 3.7-14: Load-displacement results of W16X31-DC column specimens

For all four column specimens, the research team found that in general, more deformations occurred near the top flange as opposed to the bottom flange. Theoretically, if the load from the top was equally transferred to the bottom, the amount of deformations at the top and bottom flange would be identical. After reviewing the tests in more detail, it was found that elastic displacements in the column specimen and loading plates allowed the column to rotate at the ends, suggesting that some of the force from the actuator was transferred to the end supports. In addition and for this group of double compression specimens only, there may have been a gap less than 1/16 in. between the bottom of the bottom flange and the top of the bottom loading plate. This resulted in some small vertical displacement prior to engaging the bottom support and therefore causing some of the concentrated load to be reacted directly at the end supports.

Figure 3.7-14 also shows nominal capacities for the limit states of web local crippling (*WCR*), web local yielding (*WLY*), web compression buckling (*WCB*), and flange bending (*FB*) per the AISC specification, Section J10 (AISC, 2016). Reasons for including flange bending in the analysis were discussed in Section 3.7-1. The results show that three of the columns failed at a load slightly higher

than the predicted capacity for web local crippling (103.4 kips) which was the mode of failure identified from visual inspection of these column specimens. When results are evaluated in more detail, non-linear behavior does initiate near the limit state of web local yielding. However, the column specimens were able to achieve a much higher capacity than that defined by this limit state. In addition, the equations in the AISC (2016) specification suggest that web compression buckling is the governing limit state when no stiffeners are present. The load capacities vastly exceeded the capacity computed per this limit state. However, a lack of web compression buckling may be influenced by not obtaining a true through force from the top to bottom plates.

Similar experimental behavior was observed during the test for the condition without stiffeners and the conditions with eccentric stiffeners. In addition, similar to the single compression tests, yielding began in the column web beneath the top loading plate. Yielding continued through the web by means of horizontal and vertical strain lines radiating from the mentioned point. The presence of strain lines for W16X31-DC-NA was very limited and localized compared to other tests carried out by the research team. For all three of these specimens, more local deformations occurred near the top flange as opposed to the bottom flange. At a load near 70% of the load capacity, modest bending of the column flanges underneath the load was noticed. Eventually, all three of the aforementioned column specimens failed by web crippling towards the top of the column specimen. When crippling was first noticed in the web, the load started to drop suddenly with a further increase in vertical displacement, which is a characteristic of a buckling failure mode. For W16X31-DC-E3, which is the column specimen with stiffeners at a low eccentricity, the research team noticed that after the maximum load was reached, the load decreased less suddenly in comparison to the test without stiffeners. Figure 3.7-15 shows a demonstration of the deformed state of the column specimens. Figure 3.7-15 (a) shows an elevation view of W16X31-DC-E6. Strain lines are identified in the web near the top flange. Figure 3.7-15 (b) shows a side view that emphasizes that web crippling occurs at the maximum load as excessive out-of-plane deformations occur in the web.

a) Elevation View

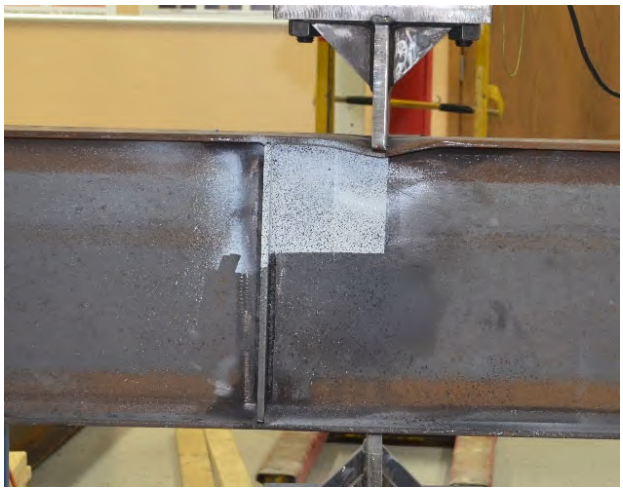

b) Side View

Figure 3.7-15: Elevation and side view of W16X31-DC-E6 after testing

For the concentric stiffener condition from Figure 3.7-14, the load increased substantially in comparison to the other conditions and the elastic stiffness of the load-displacement relationship increased slightly. Concentric stiffeners help to transfer the load through from the top to bottom flange plates, avoiding excessive local deformations. The elastic stiffness of the concentric stiffener condition is higher since the stiffeners immediately engage after loading. This further demonstrates how ineffective the eccentric stiffeners are in comparison to concentric stiffeners. The experimental behavior of W16X31-DC-E0 was noticeably different than the behavior of other column specimens in the test set. Strain lines initiated in the web starting near the location of both the top and bottom loading plates at a load of 85 kips. Yielding continued through the web and the stiffener by means of strain lines and mill scale peeling off. Flange bending was noticed on the side of the column specimen without stiffener. Stiffener yielding was observed on the opposite side. From Figure 3.7-14, the load capacity of this column specimen was significantly higher than that of the other column specimens. The total capacity was 163.2 kips which was much higher than the capacity of the column specimen without stiffener of 119.7 kips. The effective stiffener capacity it therefore 43.5 kips. A photograph of the test specimen from the front (stiffener) side is shown in Figure 3.7-16. The figure indicates that the mill scale peeled off the front of the stiffener, which suggest that yielding occurred and the stiffener shared a significant amount of load during the test.

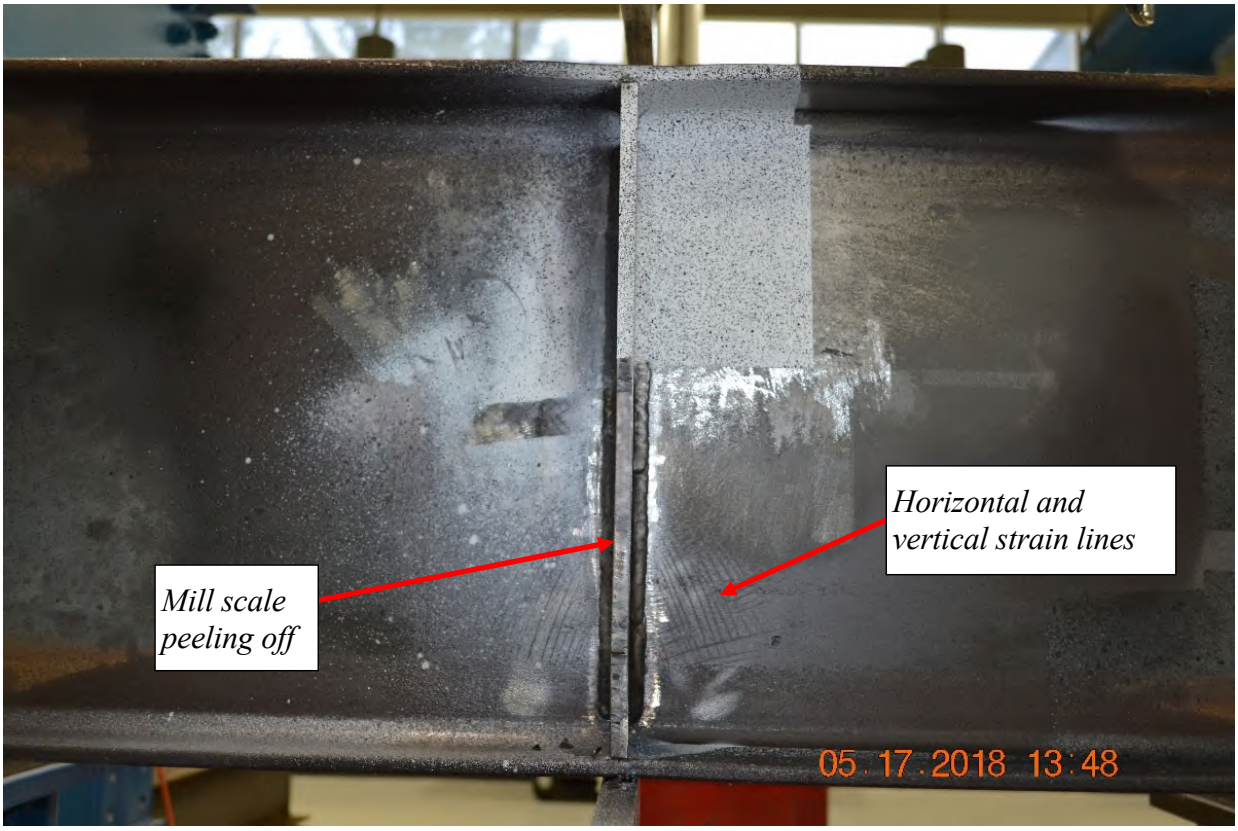

Figure 3.7-16: Elevation of W16X31-DC-E0 after testing

W10X19 Double Compression Tests

Four W10X19 column specimens were tested in double compression with four different stiffener conditions near the application of the point load: (1) one column was tested without stiffeners, (2) one column was tested with concentric stiffeners (eccentricity = 0 in.), (3) one column was tested with a high eccentricity of 4 in, and (4) one column was tested with a low eccentricity of 2 in. Dissimilar from the W16X31-SC test set, all column specimens with stiffeners had them on both sides of the web. In addition, the stiffeners were 1/4 in. as opposed to 3/8 in. Photographs of the experimental column specimens are provided in Appendix A from Figure A-88 to A-107.

All tests were continuously supported with two equal spans of 2.5 ft. each. To brace the top flange and alleviate the influence of lateral-torsional buckling, the research team used a similar method as used for the W10X19-SC test set. Figure 3.7-8 showed the steel plates and c-clamps that were used. Although lateral-torsional buckling should not contribute to the failure mechanism in the double compression tests, there was some signs of it near the maximum load as shown in the figures

of Appendix A.

The load-displacement relationships for all four column specimens are shown together in Figure 3.7-17. Three of the four column specimens reached a capacity between 78.5 kips and 87.8 kips. The column specimens with the low and high eccentricity condition reached a slightly higher capacity that the column specimen without stiffeners. In addition, as eccentricity decreased, the load carrying capacity increased. However, the load carrying capacity of the column specimen with concentric stiffeners was far higher than any of the other conditions, which again suggests that eccentric stiffeners are not nearly as effective as concentric stiffeners. The effective stiffener capacity of the column specimen with concentric stiffeners was 101.5 kips and the effective stiffener capacities of the conditions with eccentric stiffeners was less than 10% of that.

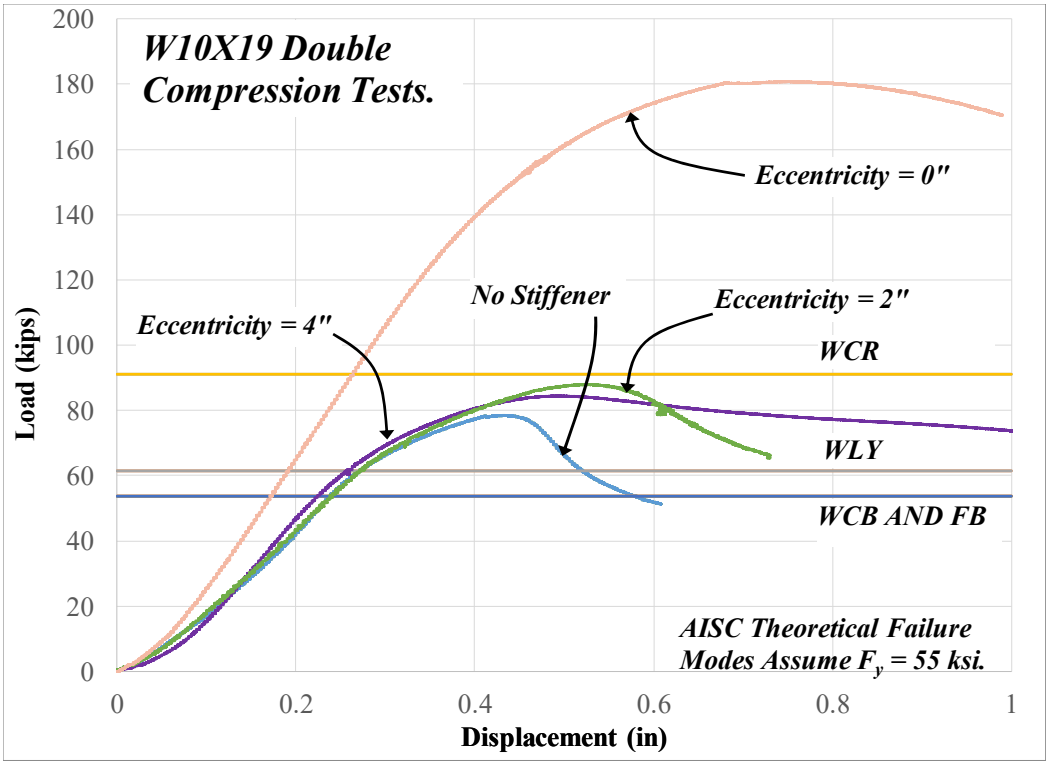

Figure 3.7-17: Load-displacement results of W10X19-DC column specimens

Figure 3.7-17 clearly demonstrates that the capacity and elastic stiffness of column specimens with eccentric stiffeners are similar to the results of the column specimen without stiffeners. However, the post-buckling behavior after the maximum load is reached is noticeably different, particularly for this test set. As mentioned, in the concentric stiffener condition, the effective

stiffener capacity was more than 100 kips, which was much higher than that predicted from theoretical stiffener capacities that were manually computed. The elastic stiffness of the load-displacement relationship substantially increased for the concentric stiffener condition in comparison to the other three column specimens. This further demonstrates how ineffective the eccentric stiffeners are in comparison to concentric stiffeners since the local deformations that occur under a certain load are approximately the same as the condition without stiffeners.

Figure 3.7-17 also shows nominal capacities for the limit states of web local crippling (*WCR*), web local yielding (*WLY*), web compression buckling (*WCB*), and flange bending (*FB*) per the AISC specification, Section J10 (AISC, 2016). The results show that three of the column specimens failed at a capacity slightly lower than the predicted capacity for web local crippling (88.2 kips), which was the mode of failure identified from visual inspection of these column specimens. When results are looked at in more detail, non-linear behavior does initiate near the limit state of web local yielding. However, there is still a much higher capacity after the calculated value for this limit state. All column specimens also reached a capacity well beyond the theoretical capacity for web compression buckling, which per the AISC specification should have been the governing limit state.

Similar to the W16X31-DC test set, the experimental behavior of the column specimens with eccentric stiffeners was similar to the behavior of the column specimen without stiffeners. For all three cases, yielding began in the column web directly beneath the top loading plate. Yielding continued through the web, which was identified by horizontal and vertical strain line patterns that eventually encompassed the entire depth of the web. Yielding continued until the column specimens failed by web crippling. Although deformations were found near the bottom reaction plate, the effects of concentrated loads were more evident under the top loading plate and the web crippling effect was more concentrated near the top loading plate. For the W10X19-DC-E2 test, substantial flange bending occurred in both the top and bottom flanges and therefore, it is assumed that more load was directly transferred from the top to bottom loading plates.

To demonstrate the mode of failure and deformed state after testing and for these three column specimens, Figures 3.7-18 and 3.7-19 show two photographs of W10X19-DC-E4 after testing. Figure 3.7-18 shows an elevation of the backside. Horizontal and vertical strain lines are identified over the entire depth of the web. Figure 3.7-18 also shows that significant flange bending occurred

during the test. Figure 3.7-19 shows a better representation of the web crippling effect as a straight part is placed up next to the web. The out-of-plane deformations that occur in the web were well pronounced in this column specimen.

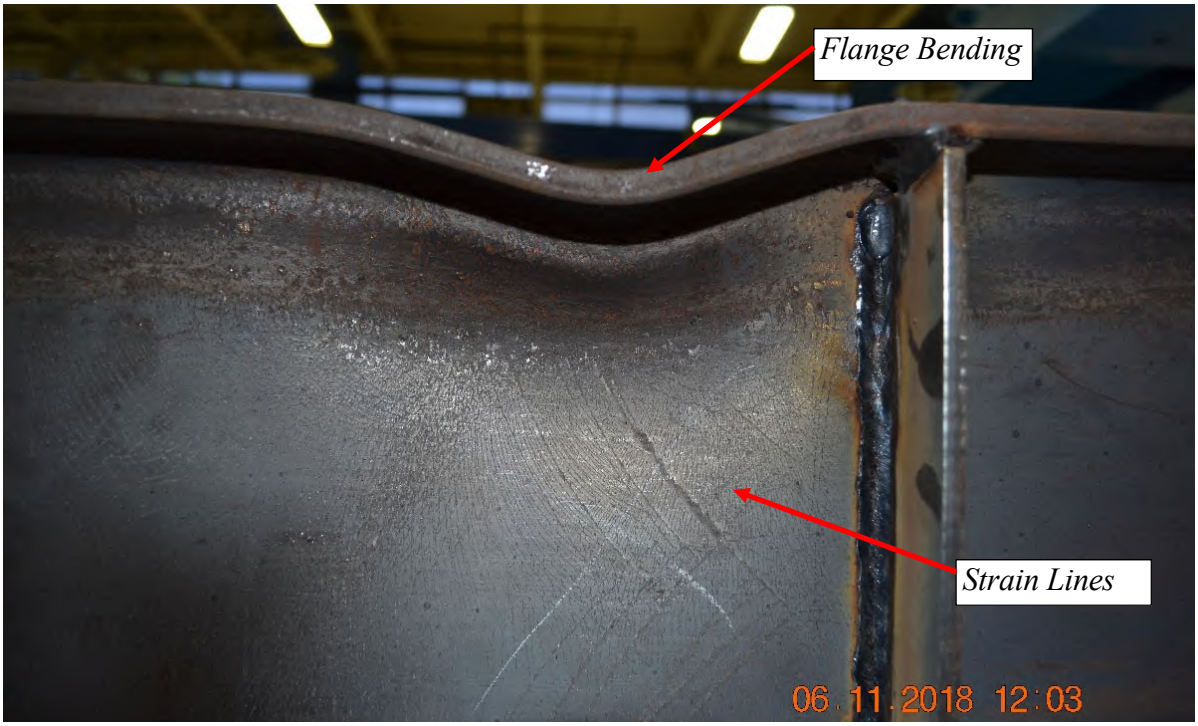

Figure 3.7-18: Close-up view of W10X19-DC-E4 after testing

Figure 3.7-19: W10X19-DC-E4 after testing emphasizing web crippling

As discussed earlier in this section, the column specimen with concentric stiffeners reached a far higher capacity than any of the other column specimens. The research team believes there are several reasons that concentric stiffeners provide a much higher effective capacity than predicted in the double compression test. First, the concentric stiffeners immediately engage once the load is applied and provide a direct force transfer to the bottom plate. In addition, they brace the web of the column specimen from buckling effectively, eliminating this mode of failure all together. Finally, they allow more of the web to be engaged in resisting the concentrated load in comparison to that interpreted from a web local yielding check using the AISC (2016) specification.

For the column specimen with concentric stiffeners, strain lines in vertical and horizontal patterns were noticed on the web and on both sides of the stiffeners. Slight flange bending on both the top and bottom flanges was first noticed at 177 kips. At the end of the test, the stiffener on the front side of the column specimen buckled locally near the top loading plate. On the backside, the stiffener plate buckled under the top loading plate and above the bottom reaction plate. This is demonstrated in Figure 3.7-20. Horizontal and vertical strain lines are localized in the web near the top and bottom plates, which is also visual in Figure 3.7-20.

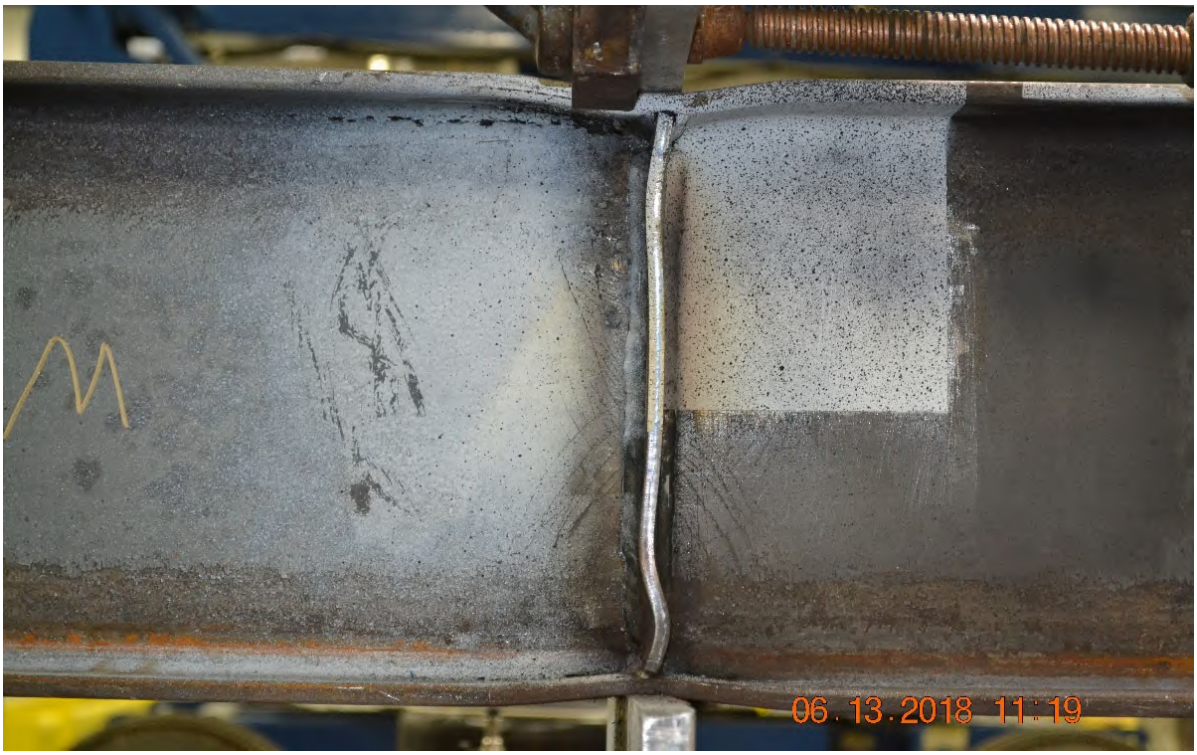

Figure 3.7-20: Back view of W10X19-SC-E0 after testing showing stiffener buckling

W12X26 Double Compression Tests

Four W12X26 column specimens were tested in double compression with four different stiffener conditions near the application of the point load: (1) one column specimen was tested without stiffeners, (2) one column specimen was tested with concentric stiffeners (eccentricity = 0 in.), (3) one column specimen was tested with a high eccentricity of 4 in., and (4) one column specimen was tested with a low eccentricity of 2 in. Photographs of the column specimens are shown in in Appendix A from Figures A-108 to A-122. All column specimens were continuously supported with two equal spans of 2.5 ft. each.

The load-displacement relationships for all four column specimens are shown in Figure 3.7-21. The relationships between the column specimen without stiffeners, with eccentric stiffeners, and with concentric stiffeners are very similar to the relationships for the W10X19-DC test set. The column specimen without stiffener reached a capacity of 86.4 kips. The specimens with high and low eccentricity conditions reached higher capacities of 90.6 kips and 110.9 kips, respectively. The column specimen with concentric stiffeners reached the maximum capacity of the hydraulic actuator of 220 kips, without showing significant signs of failure. Therefore, for the low eccentricity condition, there is a notable increase in capacity but not nearly to the same level as for the concentric stiffener condition. Although the capacity of the condition with concentric stiffeners is uncertain, it is certain that the effective stiffener capacity of the condition with low eccentricity is less than 20% of the effective stiffener capacity when concentric stiffeners are used. In addition, the elastic stiffness of the concentric stiffener condition is slightly higher than the other conditions. For the other three conditions, the elastic stiffness was very similar, which further demonstrates how ineffective the eccentric stiffeners are in comparison to concentric stiffeners.

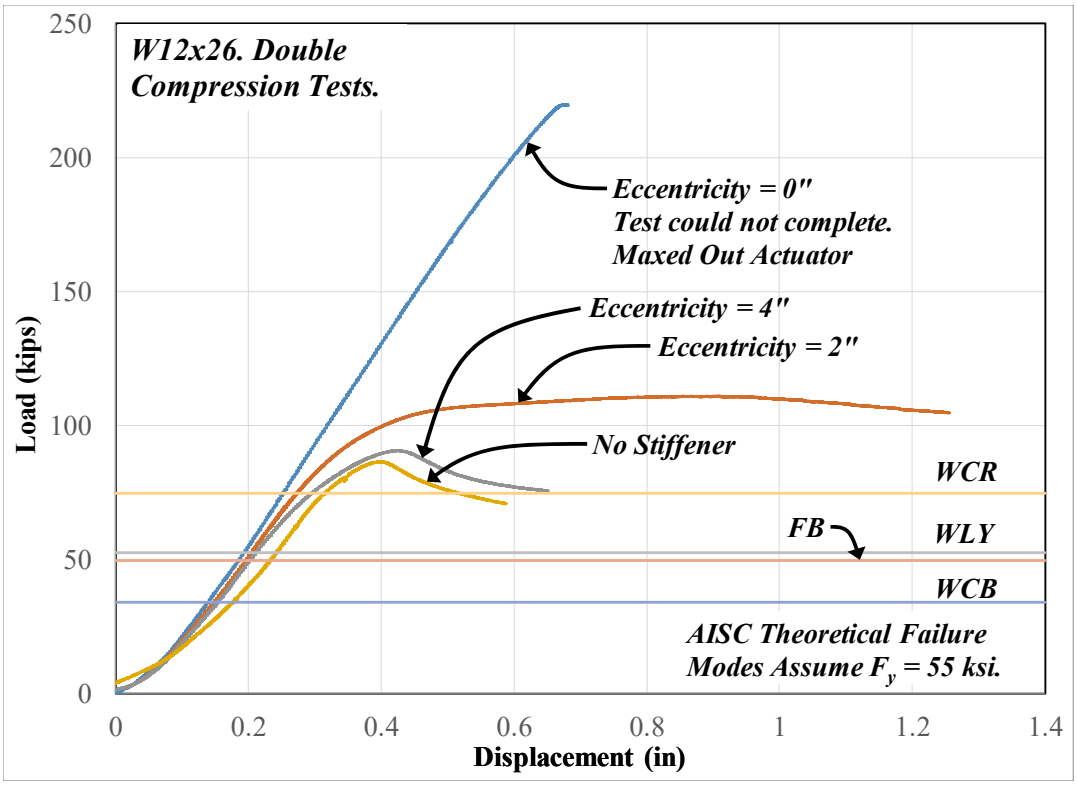

Figure 3.7-21: Load-displacement results of W12X26-DC column specimens

Figure 3.7-21 also shows nominal capacities for the limit states of web local crippling (*WCR*), web local yielding (*WLY*), web compression buckling (*WCB*), and flange bending (*FB*) per the AISC specification, Section J10 (AISC, 2016). The results show that the high eccentricity and no stiffener cases failed at a capacity slightly higher than the predicted capacity for web local crippling (74.7 kips), which was the mode of failure identified from visual inspection of these column specimens. For all specimens, the load carrying capacity was much higher than that predicted from web local yielding and web compression buckling.

The experimental behavior of W12X26-DC-NA and W12X26-DC-E4 were very similar. Again, this shows that for the high eccentricity condition, the stiffeners have very minimal influence in resisting the concentrated forces. Yielding first began in the column web beneath the top loading plate. Strain lines in horizontal and vertical patterns were seen on the web under the load. Yielding continued through the web until the column reached its maximum load and suddenly failed by web crippling. In a similar way to other double compression tests, more deformations were seen near the top flange as compared to the bottom flange. For W12X26-DC-E4, significant flange bending was

noticed on the top flange, whereas on the bottom flange, yielding was noticed but no significant deformations developed in comparison to the top flange.

The load capacity of W12X26-DC-E2 was noticeably higher (24.5 kips) than the condition without stiffener. In this test, both the top and bottom flanges appeared to be engaged suggesting a through force. Yielding still began in the column web beneath the top loading plate. Yielding continued through the web by means of strain lines radiating from the mentioned point until the column specimen failed by web local crippling. At the conclusion of the test, substantial flange bending in both the top and bottom flanges was found. This is illustrated in Figure 3.7-22. However, the column specimen still failed by web crippling that was more concentrated towards the top flange as demonstrated in Figure 3.7-23.

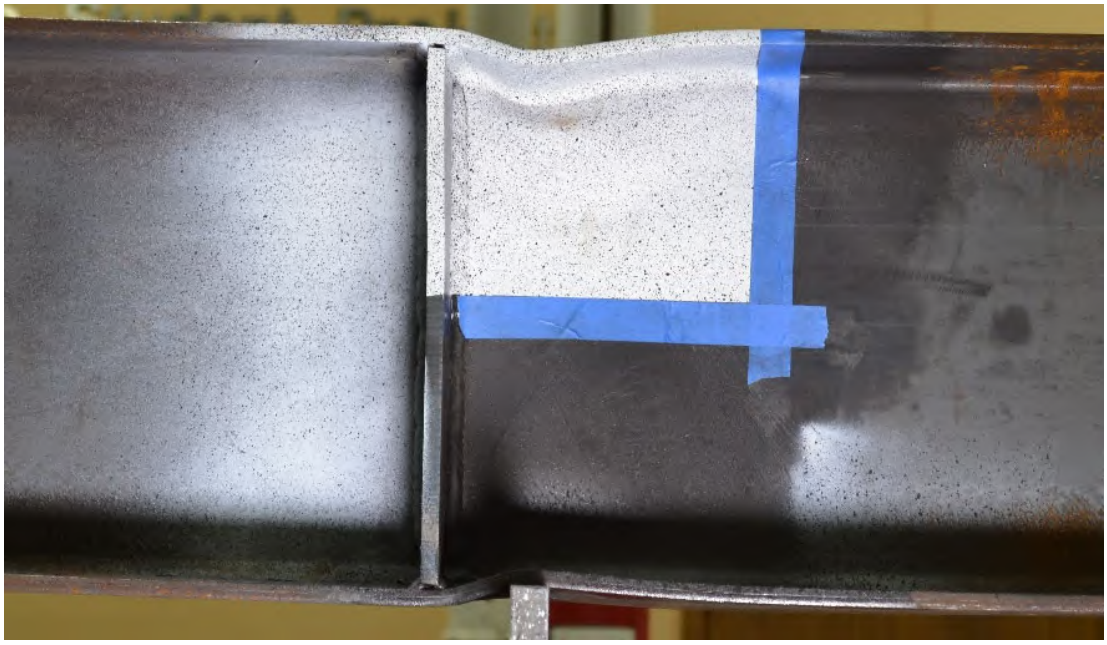

Figure 3.7-22: Elevation view of W12X26-DC-E2 after testing

Figure 3.7-23: W12X26-DC-E2 after testing emphasizing web crippling

The test behavior of the column specimen with concentric stiffeners (W12X26-DC-E0) was significantly different from the behavior of the other column specimens in the test group. As shown in Figure 3.7-21, the column specimen reached the maximum capacity of the actuator of 220 kips which was already much higher than the anticipated from theoretical calculations using the AISC specification (2016). Yielding was identified in the stiffeners during the test by means of mill scale peeling off. Strain lines were then noticed in the web and in both the top and bottom flanges. The effective stiffener capacity was higher than 134 kips, which represents the difference between the capacity of the column specimen when the actuator capacity was reached minus the capacity of the column specimen without stiffeners. The theoretical stiffener capacity was computed as 73 kips assuming F_y = 39 ksi for the stiffeners.

Figure 3.7-24 shows the column specimen after testing. The deformations in the column specimen are not as pronounced as other double compression specimens with concentric stiffeners. However, there are signs of mill scale peeling off the stiffeners and some strain lines are identified in the web.

Figure 3.7-24: Close-up view of W12X26-DC-E0 after testing

3.7.3 Single Tension Tests

Twelve (12) experimental column specimens were tested in single tension. This includes three wide-flange sizes and four tests per size. A discussion of the results is separated by wide-flange size and therefore 'test set' in this section.

The column specimen sizes were chosen assuming that the capacity of the hydraulic actuator was equal to 220 kips as it was the only capacity listed on the actuator. However, it was later discovered that this was the capacity of the hydraulic actuator only when a downward force was applied. Prior to this research project, the actuator had never been used for an upward force and no one from the faculty and staff at LTU realized the actuator was calibrated for a lower capacity if an upward force was applied. After encountering a maximum load of approximately 140 kips during one of the tests, documentation was obtained that verified a difference in calibrated actuator capacity when an upward force is applied.

A summary of all the results from the single tension tests are provided in Table 3.7-3. The results in the table include the 'Test Capacity', which is the maximum load recorded during the test, and the 'Effective Stiffener Capacity'. The effective stiffener capacity is equal to the capacity of the test with stiffeners minus the result of the corresponding test without stiffeners in the same test set. All specimens that reached the actuator capacity are listed with a capacity of 144 kips (actuator capacity

145 kips but about 1 kip in actuator prior to zeroing) although the true capacity of these column specimens is unknown.

In addition, the tables list the capacities for web local yielding (*WLY*) and flange bending (*FB*) for the column specimen without stiffeners, which are limit states associated with this test method. Since they are assumed to contribute to an overall capacity with stiffeners, they are shown as one value for the test set. In addition, the theoretical 'Stiffener' capacity is provided assuming the stiffeners are concentric using Equation 3-1. The final "Theoretical Capacity" varies for each type of test depending on the stiffener condition as discussed in Section 3.7-1.

Table 3.7-3: Single tension theoretical capacities and test results

Column Specimen	Eccentricity (in)	WLY (k)	FB (k)	Stiffener (k)	Theoretical Cap. (k)	Test Capacity (k)	Effect. Stiff Capacity (k)
W16X31-ST-NA	NA	76.9	66.6	62.5	66.6	127	-
W16X31-ST-E6	6				Research	125.5	-1.5
W16X31-ST-E3	3				Research	129	2
W16X31-ST-E0	0				159.7	144 **	+ 17
W12X26-ST-NA	NA	54.1	49.6	76.9	49.6	79.2	-
W12X26-ST-E4	4				Research	115.1	35.9
W12X26-ST-E2	2				Research	133.7	54.5
W12X26-ST-E0	0				122.6	144 **	+ 65
W10X39-ST-NA	NA	104.4	96.6	97.6	96.6	144 **	-
W10X39-ST-E4	4				Research	144 **	NA
W10X39-ST-E2	2				Research	144 **	NA
W10X39-ST-E0	0				194.2	144 **	NA

** reached actuator capacity

Since all four W10X39 column specimens reached the capacity of the hydraulic actuator, limited observations can be made using Table 3.7-3. However, some observations from Table 3.7-3 using the other two column sizes and with respect to AISC limit states are as follows:

- The theoretical equations provided by AISC (2016) for the limit states of flange bending and web local yielding significantly underestimate the load carrying capacity of the column specimens; even for the condition without stiffeners. Even though all W10X39 column specimens reached the capacity of the hydraulic actuator, the equations provided in AISC show that they should not have prior to failure.
- As discussed in this section, flange bending is problematic in tension tests since it creates

uneven stresses in the weld that connects the loading plate to the column. However, these test results indicate that the equation underestimates the capacity even for the W12X26 column specimen that failed prematurely as discussed later in this section.

- From the W16X31-ST test set, eccentric stiffeners do not have a significant influence on the concentrated load capacity of the column specimen. However, the 'low eccentricity' condition resulted in a slightly higher capacity than the 'high eccentricity' condition. The W16X31 column specimen had a low eccentricity condition of 3 in. for all three test methods and all three test methods reveal that even at a 3 in. eccentricity, the stiffeners have negligible influence on the results.
- The W12X26 specimen without stiffeners (W12X26-ST-NA) seemed to fail prematurely as discussed later in this section and it is alleged that the capacity at the high eccentricity condition should have been very similar to the capacity without stiffeners. However, there is a notable increase in the capacity when the low eccentricity condition was tested, which is a similar relationship found for the double compression tests performed on this column size. Overall, it appears that for the column sizes tested, when a 2 in. eccentricity is used, there is a noticeable increase in effective stiffener capacity in comparison to when a 3 in. or 4 in. eccentricity is used.
- However, for column specimens with concentric stiffeners, there is a significant increase in capacity in comparison to the condition without stiffeners and it is assumed that if the specimens were tested to their true capacity, that similar relationships would be obtained as found for the compression specimens.
- In general, the load carrying capacity results of the single tension tests are not as valuable as the compression tests. However, similar conclusions regarding the influence of eccentric vs. concentric stiffeners are found in the results. Further investigations that evaluate the influence of eccentric vs. concentric stiffeners are done analytically in this report.

W16X31 Single Tension Tests

Four W16X31 column specimens were tested in single tension. The four column specimens had four different stiffener conditions near the application of the point load: (1) one column specimen was tested without stiffeners, (2) one column specimen was tested with concentric stiffeners (eccentricity

= 0 in.), (3) one column specimen was tested with a high eccentricity of 6 in., and (4) one column specimen was tested with a low eccentricity of 3 in. As discussed in Section 3.5.3, the column specimens were simply supported at 4.5 ft. Photographs of the experimental column specimens are shown in Appendix A from Figure A-123 to A-141.

The load-displacement relationships for all four column specimens are shown together in Figure 3.7-25. For all four specimens, the data was adjusted so that the displacement increased from zero when the load started to noticeably increase. This occurred at higher recorded displacements in comparison to the compression specimens due to gaps in bolt holes at the connection near the hydraulic actuator. Once the bolts were fully engaged, linear elastic behavior was identified in the test results.

Three of the four column specimens reached a capacity between 125 kips and 129 kips. The test capacity for the column specimen with stiffeners at a high eccentricity was slightly less than for the column specimen without stiffeners and the test capacity for the column specimen with stiffeners at a low eccentricity was slightly higher than for the column specimen without stiffeners. However, all three test capacities were very similar and in general, eccentric stiffeners have no influence on the load carrying capacity for this column size and these magnitudes of eccentricity. The results of the column specimen with concentric stiffeners are discussed later in this section.

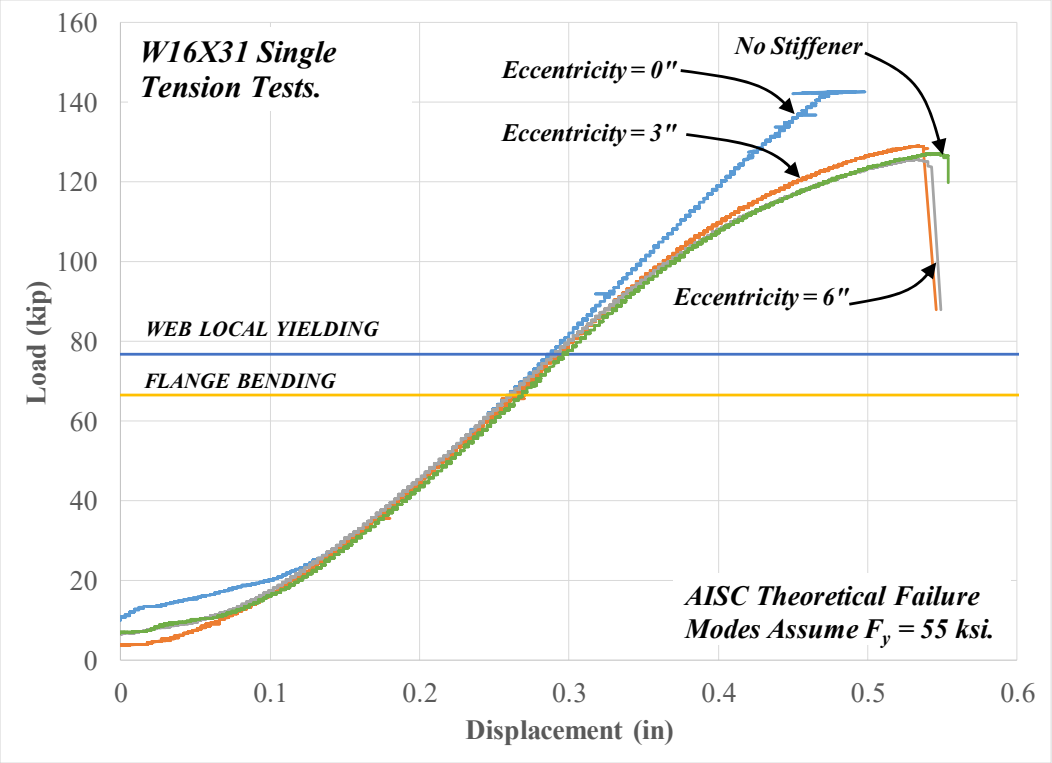

Figure 3.7-25: Load-displacement results of W16X31-ST column specimens

Under close inspection of the results in Figure 3.7-25, the elastic stiffness of the column specimen with concentric stiffeners (eccentricity = 0 in.) is slightly higher than for the other conditions. However, the differences are not as pronounced as was generally identified for the compression specimens. Since the column specimens were simply supported, it is assumed that the elastic stiffness is primarily influenced by flexural properties, which are assumed equal for all column specimens. However, some local deformations do occur in the web, welds, and flange near the location of the applied load.

Figure 3.7-25 also shows nominal capacities for the limit states of web local yielding (*WLY*) and flange bending (*FB*) per the AISC specification, Section J10 (AISC, 2016) which are the only two limit states associated with this test method. Non-linear behavior does initiate near the limit state of web local yielding for the column specimens without concentric stiffeners. However, the column specimens reach a much higher capacity than that computed for this limit state and for flange bending, which was the governing failure mechanism as described herein.

For the three column specimens without concentric stiffeners, some yielding was identified in the web as evident by strain lines and verified using DIC test data recorded for the column specimens. Therefore, web local yielding did occur and influenced the non-linear test behavior from Figure 3.7-25. However, the deformations that occurred in the web were not nearly as significant as found for the compression specimens. Flange bending was also noticed in the top flange and the edge of the loading plate failed to remain plane when this occurred. All three of the column specimens eventually failed due to rupture in the weld between the loading plate and the top flange of the column. The weld failure occurred as a loud and sudden event with minimal warning. The weld failure was primarily due to excessive flange bending, which creates concentrated stresses in localized areas of the weld. Due to flange bending, the outside tips of the flange move with the loading plate since the localized stiffness of the flange is smaller near the tips. At the center of the flange, the flange is less prone to move with the plate since the web on the backside of the flange resists it. The deformations in the flange create higher stresses in the welds near the center of the flanges as the stiff loading plate translates vertically. The weld therefore fractures near the center due to higher stresses. Visual inspection of the test and the load-displacement behavior show that eccentric stiffeners do not effectively resist flange bending, and therefore, uneven stresses still develop in the welds.

Figure 3.7-26 shows an elevation of W16X31-ST-E6 after testing and identifies the presence of yielding that occurred in the web and flange. Figure 3.7-26 also identifies the approximate 'width' of flange bending. It is assumed that yield lines form in the flange within this width where significant out-of-plane deformations occur in the flange. For this column specimen, the eccentric stiffeners were not found within this effective width and therefore, do not resist the flange bending effect. Figure 3.7-27 shows a close up of the weld fracture and demonstrates that the center of the weld fractured and for this column specimen, weld at the end of the length remained intact.

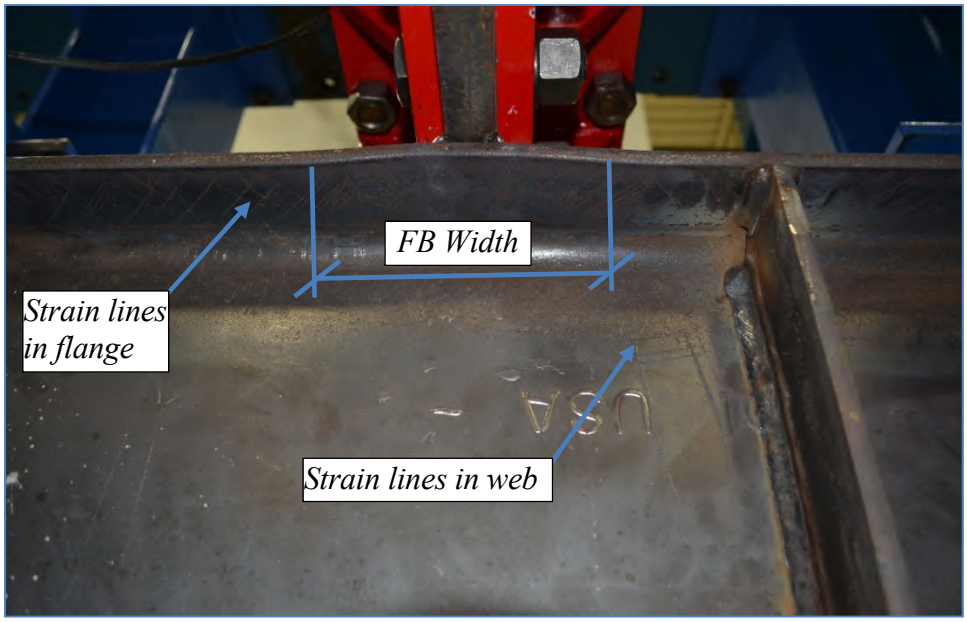

Figure 3.7-26: Close-up view of W16X31-ST-E6 after testing from back side

Figure 3.7-27: Weld fracture of W16X31-ST-E6 after testing

The column specimen with concentric stiffeners (W16X31-ST-E0) reached the capacity of the hydraulic actuator of 144 kips, which was only 18 kips higher than the condition without stiffener. However, there were no signs of yielding or other significant deformations when the capacity was reached and it is assumed that the load capacity comparisons in single tension would be similar to the results in single compression and significant differences would exist between the actual capacity of the specimen with concentric stiffeners in comparison to other specimens. Minor strain lines were noticed after testing on the bottom face of the bottom flange, just underneath the stiffeners. The

primary difference in the concentric stiffener condition is that load is transferred directly to the stiffeners, which stiffen the flange from bending. The entire weld will develop more uniform deformations and therefore, more uniform stress across the width of the flange. It is believed that the maximum capacity of the connection would be closer to the nominal capacity of the welds themselves, which is computed as 185 kips using Section J2 of the AISC (2016) specification.

W12X26 Single Tension Tests

Four W12X26 column specimens were tested in single tension. The four column specimens had four different stiffener conditions near the application of the point load: (1) one column specimen was tested without stiffeners, (2) one column specimen was tested with concentric stiffeners (eccentricity = 0 in.), (3) one column specimen was tested with a high eccentricity of 4 in., and (4) one column specimen was tested with a low eccentricity of 2 in. Photographs of the experimental column specimens are shown in Appendix A from Figure A-163 to A-175.

The load-displacement relationships for all four column specimens are shown together in Figure 3.7-28. Similar to the W16X31-ST test set, the data was adjusted so that the displacement increased from zero when the load started to noticeably increase. The column specimen without stiffeners (W12X26-ST-NA) seemed to fail prematurely by weld fracture at a load of 79.2 kips. The research team believes that there was a defect on the weld. When failure started, the sound was not nearly as pronounced (loud) as for the other column specimens when weld fracture occurred. In addition, only a small length of the weld initially failed. Then, the load gradually reduced as more and more of the weld fractured during the test. After testing the W16X31-ST test set, the research team expected the maximum load obtained for W12X26-ST-E0 to be very close to the maximum load obtained for W12X26-ST-E4.

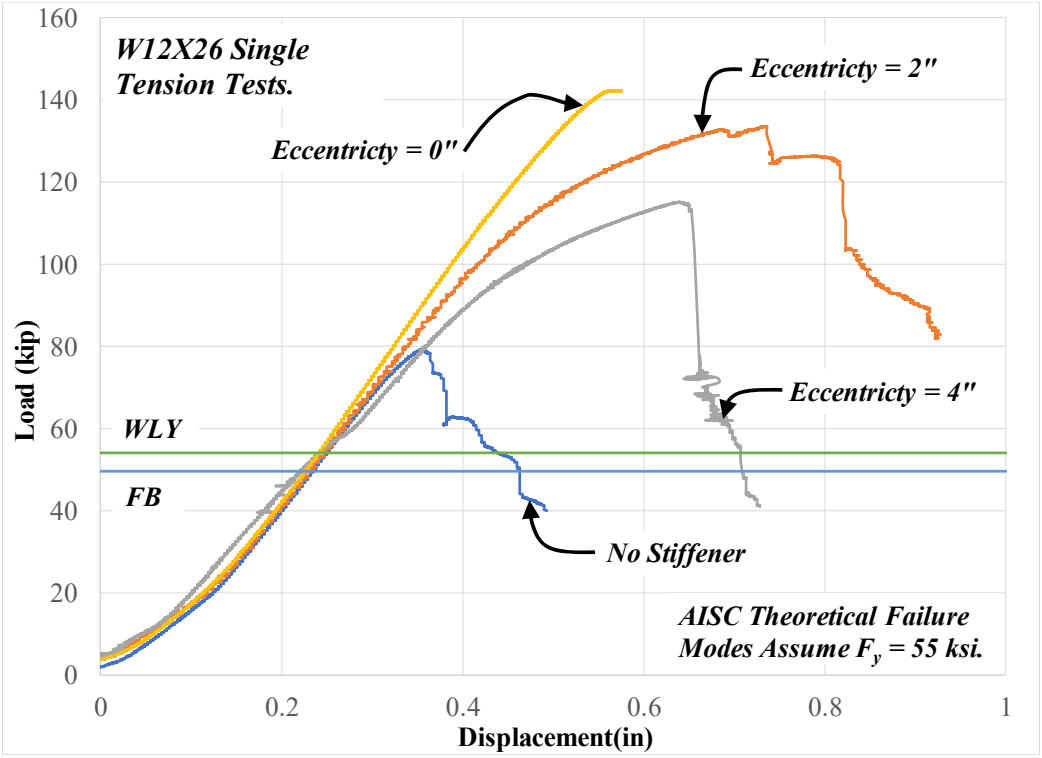

Figure 3.7-28: Load-displacement results of W12X26-ST column specimens

The column specimen with stiffeners at a high eccentricity also failed by weld fracture, but at much higher load of 115.1 kips. The sudden failure was similar to the sudden failure that occurred for three of the W16X31-ST column specimens. Meanwhile, the column specimen with stiffeners at a low eccentricity failed at a higher load and is described as a different failure mechanism. Instead of failure occurring in the weld from the loading plate to the top flange, failure occurred in the weld between the stiffener plate and the top flange and then a crack propagated in the web directly below the top fillet. This is shown in Figure 3.7-29. The maximum load obtained for this column specimen was 133.7 kips, approximately 18.5 kips higher than the maximum capacity obtained for the high eccentricity condition. The experimental behavior of these column specimens will be discussed in more detail later in this section.

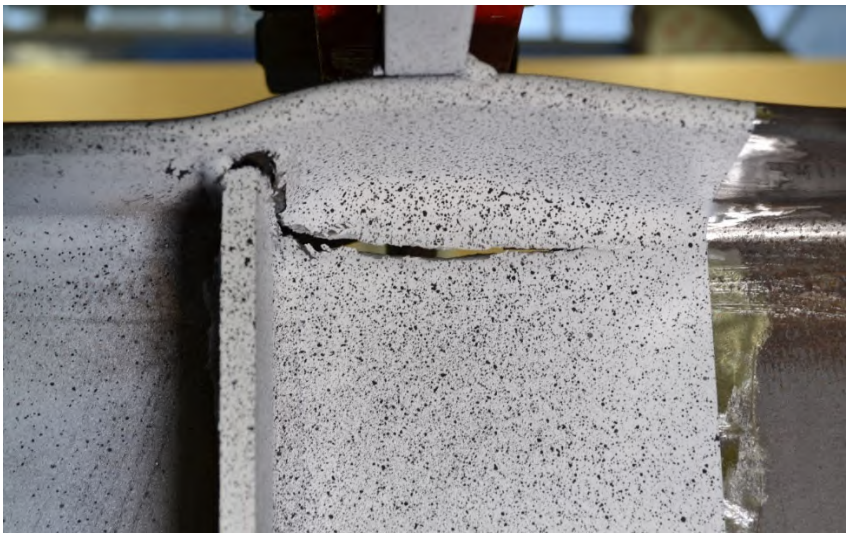

Figure 3.7-29: W12X26-ST-E2 after testing emphasizing web fracture

From Figure 3.7-28, all four column specimens had similar elastic behavior during a portion of the applied tests. The test with concentric stiffeners had the highest elastic stiffness and maintained elastic behavior until the actuator capacity was reached. Since the column specimens were simply supported, it is assumed that the elastic stiffness is primarily influenced by flexural properties, which are assumed equal for all column specimens. However, some local deformations do occur in the web, welds, and flange near the location of the applied load.

Figure 3.7-28 also shows nominal capacities for the limit states of web local yielding (*WLY*) and flange bending (*FB*) per the AISC specification, Section J10 (AISC, 2016), which are the only two limit states associated with this test method. All specimens failed at loads significantly higher than predicted per these limit states even though flange bending appeared to be associated with the failure mechanism for three column specimens as described herein.

As mentioned, column specimen W12X26-ST-NA appeared to fail prematurely by weld fracture. No signs of yielding in the web were noticed by the research team during and after the test. At a load close to failure, flange bending and strain lines on the top flange were noticed near the concentrated load. It is assumed for this column specimen that flange bending contributed to the failure mode but a local defect in the weld was still the primary reason for the premature failure. A photograph of the failed weld is shown in Figure 3.7-30 and its appearance is noticeably different from other weld failures such as that shown in Figure 3.7-27.

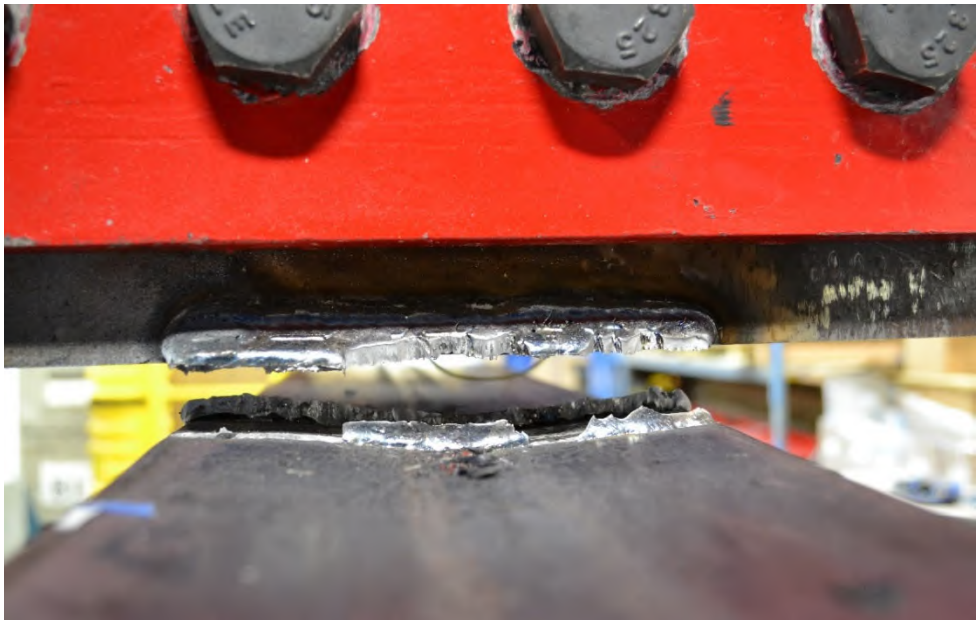

Figure 3.7-30: Weld fracture of W12X26-ST-NA

For specimen W12X26-ST-E4, the research team did not find any abnormalities with the test setup, test procedure, or any other abnormal events that occurred during the test. Similar to W16X31-ST column specimens, yielding began in the column web beneath the loading plate as identified by the presence of strain lines and mill scale peeling off. Yielding was also identified in the top flange and significant flange bending near the tips was noted. The column specimen failed by weld rupture in between the loading plate and the top flange. This weld failure was mainly due to excessive flange bending, which creates excessive localized stresses in the weld. From Figure 3.7-28, the column specimen did not sustain the maximum load for a long time, but rather a dramatic and quick failure occurred due to sudden failure of the weld.

For column specimen W12X26-ST-E2, yielding also began in the column web underneath the applied load. Strain lines parallel to the direction of the applied load were identified in the web. The column specimen reached its capacity when a failure occurred at the weld between the top flange and the inside face of the stiffener. Then, the crack propagated from the weld into the web and below the concentrated load. For reference, a few tension tests performed by Graham et al. (1959) also failed by web fracture just below the fillet but it is uncertain if the crack initiated in a stiffener weld.

The column specimen W12X26-ST-E0 with concentric stiffeners reached the maximum capacity of the actuator at 144 kips and similar conclusions were drawn as for the W16X31-ST test set.

During the test, the research team did notice transverse strain lines across the web from the supports (reference Figures A-172 and A-173). Strain lines were also noticed after testing on the bottom face of the bottom flange just underneath the stiffener. No signs of yielding were noticed in the welds or on the top flange near the applied load. From Figure 3.7-28, the column specimen demonstrated elastic behavior until the maximum load was reached. The different behavior of this column specimen compared to the equivalent column specimens with eccentric stiffeners or without stiffeners further emphasize how ineffective eccentric stiffeners are in comparison to concentric stiffeners. As described in the discussion of the W16X31-ST test set, the primary difference in the concentric stiffener condition is that load is transferred directly to the stiffeners, which stiffen the flange from bending. The entire weld will develop more uniform deformations and therefore, more uniform stress across the width of the flange. It is believed that the maximum capacity of the connection would be closer to the nominal capacity of the welds themselves, which is computed as 217 kips using Section J2 of the AISC (2016) specification.

W10X39 Single Tension Tests

Four W10X39 column specimens were tested in single tension. The four column specimens had four different stiffener conditions near the application of the point load: (1) one column specimen was tested without stiffeners, (2) one column specimen was tested with concentric stiffeners (eccentricity = 0 in.), (3) one column specimen was tested with a high eccentricity of 4 in., and (4) one column specimen was tested with a low eccentricity of 2 in. Photographs of the experimental column specimens are shown in Appendix A from Figure A-142 to A-159.

For this test set, all four column specimens reached the maximum capacity of the hydraulic actuator. In comparison to other column specimens, the W10X39 specimens have a significantly higher capacity expected with respect to the limit states associated with concentrated loads and the result of them all reaching a capacity greater than 144 kips was not a surprise after performing the tests on W12X26 and W16X31 column specimens. Some yielding by means of strain lines and mill scale peeling off was noticed in the column specimens without concentric stiffeners. However, none of the four column specimens showed significant signs of deformation that would lead too failure.

Overall, the results of this test set was a disappointment in this research project. As mentioned earlier in this section, there was no visible indication that would suggest that the upward capacity

was lower than the downward capacity for the hydraulic actuator. The research team decided to complete all tests and try to identify as efficiently as possible, the influence of using eccentric vs. concentric stiffeners. From visual inspection of each test, the research team did notice slightly different experimental behavior for the column specimen with concentric stiffeners (W10X39-ST-E0) in comparison to that of the other column specimens.

The load-displacement relationships for all four column specimens are shown together in Figure 3.7-31. Figure 3.7-31 indicates that all column specimens reached the same maximum capacity when the test halted and minimal non-linear behavior was found in the test results once the load was fully engaged.

Figure 3.7-31 also shows nominal capacities for the limit states of web local yielding (*WLY*) and flange bending (*FB*) per the AISC specification, Section J10 (AISC, 2016), which are both applicable for this test method. The capacity of 144 kips is significantly higher than the capacities of the limit states computed. Under further inspection of the load-displacement results, it does appear that some non-linear behavior initiates near the computed limit state for web local yielding for the column specimen without stiffener (W10X39-ST-NA) and the column specimen with stiffeners at a high eccentricity (W10X39-ST-E4).

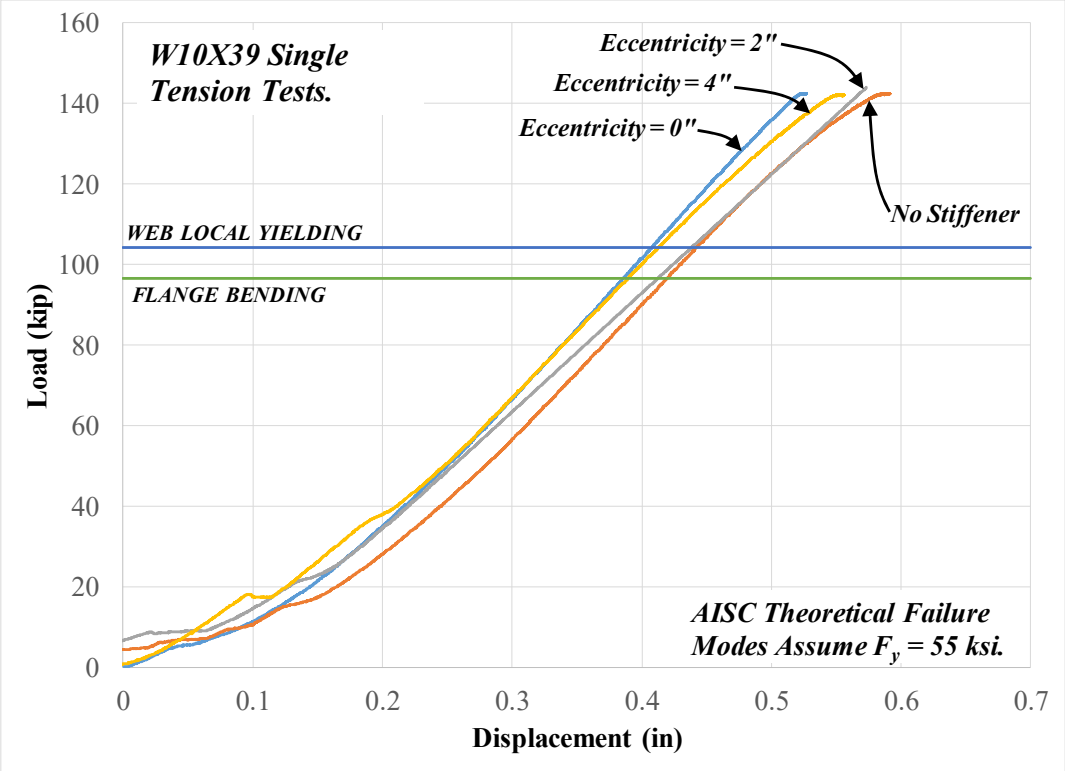

Figure 3.7-31: Load-displacement results of W10X39-ST column specimens

An elevation of W10X39-ST-NA is shown in Figure 3.7-32. For this test and the tests with eccentric stiffeners, some yielding did occur in the web directly beneath the loading plate. In addition, strain lines parallel to the direction of the applied load were identified in the webs. Some flange bending occurred during the tests as well. However, for all three column specimens, the welds from the loading plate to the top flange remained intact as demonstrated in Figure 3.7-33.

The experimental behavior of the column specimen with concentric stiffeners (W10X39-ST-E0 was noticeably different from the experimental behavior of the other column specimens. No signs of yielding were noticed by the research team underneath the concentrated load in the web or stiffener. In addition, no signs of flange bending of the top flange was identified. There were some strain lines found at the bottom of the bottom flange and shown in Figure 3.7-34. Although none of the W10X39-ST specimens failed, it is assumed that if a true capacity was reached for all column specimens, similar conclusions would be made for this test set as made for other test sets part of this research project.

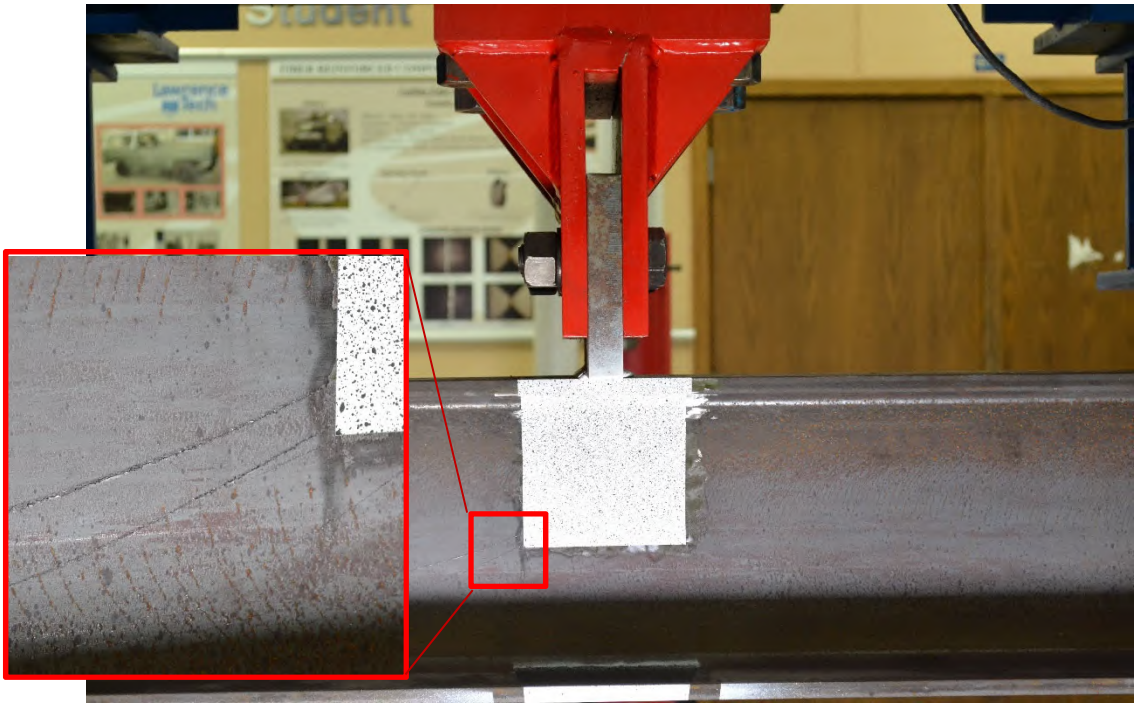

Figure 3.7-32: Close up view of W10X39-ST-NA after testing

Figure 3.7-33: Weld condition of W10X39-ST-E4 after testing (Side 1)

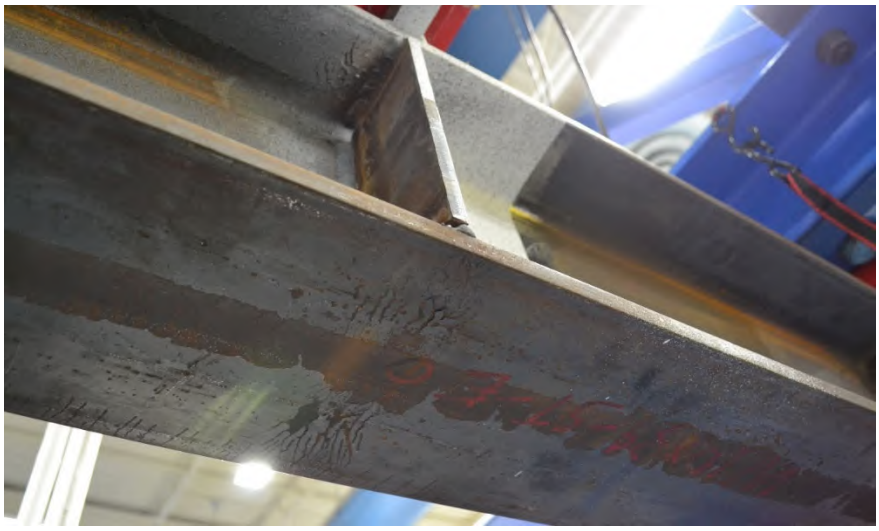

Figure 3.7-34: Bottom view of W10X39-ST-E0 after testing

3.8 Further Evaluation of AISC Limit States and Stiffener Capacity

The experimental results presented in this chapter suggest that using eccentric stiffeners is not an efficient way to resist the effects of concentrated loads in comparison to the use of concentric stiffeners. However, only small column specimen sizes were tested and these conclusions are evaluated in more detail using analytical models later in this report. The results of using larger column specimens show that eccentric stiffeners can be effective in resisting the loads while validating the observations derived in this chapter as well.

The experimental results also suggest that the equations presented in the AISC specification (2016) for the limit states associated with concentrated loads are suspect. Therefore, the research team studied these limit states in more detail as the project progressed. Comparisons of the load carrying capacities and the theoretical capacities using the limit states specified using the AISC specification were provided in Tables 3.7-1, 3.7-2, and 3.7-3.

For the theoretical capacities from the aforementioned tables, the assumed bearing length for compression tests is 0.75 in. and the assumed bearing length for single tension tests is 0.875 in., which represent the thickness of the loading plates. Note that for the single tension tests, the bearing length could be assumed wider for web local yielding since the load is transferred through welds that are centered farther apart than 0.875 in. For each listed theoretical capacity, an expected yield stress of 55 ksi is assumed (ANSI/AISC, 2010), which compares well to an average value from the results

of material properties shown in Section 4.3. The assumed elastic modulus is 29000 ksi.

As shown in Table 3.7-2, all double compression tests without stiffeners resulted in a much higher capacity than the predicted capacity for web compression buckling. As described in previous sections of this chapter, this failure mechanism was not witnessed at all during the tests. Instead, web local crippling was witnessed near the top flange for all column specimens tested without stiffeners and all column specimens with eccentric stiffeners. As mentioned earlier in this report, it is uncertain how much load was actually transferred through the web to the reaction plate directly below since the bottom flange did not bend as prominently as the top flange. However, most of load is still assumed to transfer to the bottom support simulating a double compression condition. If future studies are performed per this test method, this can be monitored with additional load cells. In the finite element analyses presented in Section 6.6, a true through force was simulated for larger column specimens.

The limit state of web local yielding is applicable for all test methods per the AISC specification (AISC, 2016). With the exception of W10X19-SC-E4, which appeared to fail primarily by lateral-torsional buckling, all test results were found higher than calculated per this limit state. For column specimens without stiffeners, the actual tested capacity was anywhere from 20% (for W10X19-SC-NA which still seemed to be influenced by lateral-torsional buckling) to 65% higher than that predicted for web local yielding. This includes column specimens tested in single compression, double compression, and single tension.

For the single tension tests (ref. Table 3.7-3), all column specimens without stiffeners were expected to fail by the limit state of flange bending from the AISC specification, Section J10 (AISC 2016). The research team learned a great deal with respect to this limit state in this research and it is understood that the equations were derived as a lower bound to ensure weld fracture does not occur (Graham et al. 1959). All column specimens including those with stiffeners either; failed at loads higher than the predicted capacity, or reached the actuator capacity, which was still much higher than that predicted by the limit state of flange bending. The results show that the equation in the AISC specification for flange bending is probably too conservative. However, the research was performed with only one plate thickness applying the concentrated load (7/8 in.) and only one weld size was used to connect the flange plates to the column specimen (3/8 in.). A more parametric study is

performed in Section 6.7 using finite elements to evaluate the true capacity of column specimens subjected to single tension that considers a variation of shapes, plate thickness, and weld size.

As shown from the values in Table 3.7-1 and 3.7-2, the results of column specimens without stiffeners and the results of column specimens with eccentric stiffeners reached a capacity similar to the capacity predicted by the limit state of web local crippling. One clear exception was the results of column specimens in the W10X19-SC test set, which the experimental behavior suggested the test results were influenced by lateral-torsional buckling. Without including this test set and the concentric stiffener column specimens, ratios of the load carrying capacity to the maximum load predicted from the equation for web local crippling are summarized in Table 3.8-1. All capacities were within 21% of that predicted from web local crippling with the exception of W12X26-DC-E2. Therefore, these results combined with the observed mode of failure suggest that the web local crippling equation reasonably predicts the load carrying capacity of wide-flange column.

Table 3.8-1: Comparison of test capacity to web local crippling

Column	Test	Eccent. (in)	WCR (k)	Test Capacity (k)	Test Capacity / WCR
W10X19	DC	NA	88.2	78.5	0.89
		4		84.4	0.96
		2		88.0	1.00
W12X26	DC	NA	74.7	86.4	1.16
		4		90.6	1.21
		2		110.9	1.48
	SC	NA	74.7	78.2	1.05
		4		79.2	1.06
		2		87.1	1.17
W10X39	SC	NA	143.6	131.0	0.91
		4		132.9	0.93
		2		142.3	0.99
W16X31	DC	NA	103.4	119.7	1.16
		6		117.4	1.14
		3		121.1	1.17
	SC	NA	103.4	112.4	1.09
		6		99.3	0.96
		3		111.2	1.08

The theoretical stiffener capacities were calculated and shown in Tables 3.7-1, 3.7-2, and 3.7-3. The capacities was determined assuming a yield stress of 39 ksi for the stiffener material. Uniaxial tension tests were performed on specimens fabricated from the stiffener material. All stiffeners were specified to be A36 steel and the research team believes that most were. However, differences in the stress-strain curves suggest that some stiffeners were A572 Gr. 50 and the steel supplier noted that they met the requirements for A36 steel. The theoretical stiffener capacity was determined using Equations 3-1 and 3-2.

$$R_n = 2 \; x \; F_y \; x \; b_s \; x \; t_s \tag{3-1}$$

$$b_s = b_{fb} / 2 - t_{wb} / 2 - ½ \tag{3-2}$$

Where:

R_n = nominal stiffener capacity

F_y = yield stress of the stiffener assumed to be 39 ksi

b_s = width of the stiffener

t_s = thickness of stiffener

b_{fb} = width of the column specimen

t_{wb} = thickness of the web of the column specimen

All stiffeners extended to the outside edge of the column specimen flanges with the exception of some of the column specimens in the W12X26-ST test set. The '*2*' in Equation 3-1 is for two stiffeners. Column specimens part of the Test Set W16X31-DC had stiffeners on one side of the web only and therefore, the '*2*' was omitted in the calculation. The '*1/2*' in Equation 3-2 is for 1/2 in. corner clips specified for all stiffeners. Equation 3-1 assumes the capacity of the stiffener is governed by gross yielding (yield stress times area at top of stiffener).

Members of the AISC Research Advisory Committee previously noted that Equation 3-1 may not be appropriate for stiffeners subjected to compression. Instead, it was recommended to use the AISC Specification, Section J7 (AISC, 2016). However, after reviewing the differences in Section J7, the research team finds it appropriate to use Equation 3-1 since stiffener capacity is associated with sharing the load as the web yields and the vertical strain in the web and stiffeners will be similar. To evaluate and dissipate buckling of the stiffeners, all passed a recommended slenderness limit defined by Equation 3-3.

$$\lambda_s = b_s / t_s \leq \lambda_r = 0.56*sqrt(E / F_y) \quad (3\text{-}3)$$

Where:

λ_s = actual slenderness of the stiffener for a local buckling check

λ_r = slenderness limit to ensure that elastic local bucking of the stiffener does not occur.

The limit for λ_r is recommended for plate elements subjected to axial compression and supported on one edge per Table B4.1a from the AISC specification (AISC, 2016).

Table 3.8-2 shows a comparison between the effective stiffener capacity for concentric stiffeners vs. the theoretical stiffener capacity computed using Equation 3-1. Note that all single tension tests with concentric stiffeners reached the actuator capacity and therefore, the effective stiffener capacity must be higher. In addition, for one double compression test, the actuator reached its capacity and the effective stiffener capacity could not be measured. Therefore, the effective stiffener capacities include a '+' indicating the capacity is greater than this value. Note that all W10X39 column specimens tested in single tension reached the actuator capacity and therefore, the effective stiffener capacity is listed as 'NA'. The values are shown along with a ratio of the effective vs. predicted capacity.

Table 3.8-2: Calculated vs. effective stiffener capacity

Nomenclature	Theoretical Stiffener Capacity (k)	Effective Stiffener Capacity (k)	Ratio	Notes
W10X39-ST-E0	97.6	NA	NA	All Specimens Reached Actuator Cap.
W12X26-ST-E0	76.9	+ 65	NA	Reached Actuator Cap.
W16X31-ST-E0	62.5	+ 17	NA	Reached Actuator Cap.
W10X19-SC-E0	27.0	33.7	1.25	
W10X39-SC-E0	97.6	67.1	0.69	
W12X26-SC-E0	76.9	70.2	0.91	
W16X31-SC-E0	62.5	64.4	1.03	
W10X19-DC-E0	27.0	101.5	3.76	
W12X26-DC-E0	76.9	+ 134	1.74	Reached Actuator Cap.
W16X31-DC-E0	31.1	43.5	1.40	One-Sided Stiffener

As shown in Table 3.8-2, traditional methods for predicting the capacity of stiffeners were reasonable for members subjected to single compression. The ratios range between 0.69 and 1.25. Note that the ratios are discussed again with analytical results in Section 7.5 and the low value of 0.69 is a result of the W10X39 column specimen reaching significant shear and flexural

deformations. Therefore, the effective stiffener capacity is uncertain with respect to the concentrated load effect.

As shown in Table 3.8-2, traditional methods for predicting the stiffener capacity of columns subjected to double compression underestimate the true capacity. The ratio is 1.47 for the column specimen with a stiffener on one side of the web only and range from 1.74 to 3.76 for the two sided stiffener condition. However, the 1.74 ratio is limited by the capacity of the actuator and if the column specimen was allowed to reach its true capacity, the ratio would be higher. It is proposed that the stiffeners do not just share the load but also assist in spreading the load more effectively into the web of the column specimen. In addition, the stiffeners support the web efficiently against buckling failure modes since no web local crippling could be identified during the concentric stiffener tests.

3.9 Conclusions from Experimental Tests

Conclusions presented in the following subsections are sorted by test type. The conclusions are the same as presented in the preliminary report dated October 29, 2018. They are repeated here since they are based on experimental results only. The conclusions are somewhat repeated in Section 8.1 but are also influenced by the results of the analytical investigations.

3.9.1 Conclusions from Single Compression Tests

The following are the primary conclusions from the single compression tests:

- The load carrying capacity of column specimens without stiffeners is governed by the limit state of web local crippling. The capacity is generally close to the values calculated for web local crippling per the equations in the AISC specification, Section J10 (AISC, 2016).
- When column specimens are tested without stiffeners, the capacity is much higher than that predicted by the AISC specification for web local yielding. However, from visual inspection of the column specimens, yielding of the web does occur prior to reaching the load carrying capacity. In general, web local yielding does not dictate capacity since the column specimen can sustain further loading.
- Most tests exhibited significant flange bending. This is not a limit state considered by the AISC specification for compression loading. However, yielding of the flange influences the

non-linear behavior of the load-displacement results.

- Tests with concentric stiffeners generally failed by inelastic buckling of the stiffeners in combination with inelastic lateral-torsional buckling. The load carrying capacity of column specimens with concentric stiffeners was much higher than the load carrying capacity of other column specimens in the test group. This suggests that lateral-torsional buckling did not significantly contribute to the failure mechanism as all column specimens in a group would theoretically have the same capacity under this limit state.
- Traditional methods for calculating the effective capacity of concentric stiffeners are fairly accurate for single compression tests.
- Columns tested with stiffeners at a high eccentricity (6 in. for W16X31 and 4 in. for other column specimens) reach a load capacity very similar to the load capacity of the column specimen without stiffeners. In most cases, the results were slightly higher than the column without stiffeners but in one case (not including column specimen that failed by lateral torsional buckling), the load was actually lower.
- Columns tested with stiffeners at a low eccentricity (3 in. for W16X31 and 2 in. for other columns) showed some improvement in load capacity in comparison to the columns without stiffeners. The percent increase in load was between 0% and 17%. However, the results were inconsistent and no clear relationships could be derived to determine the effectiveness of eccentric stiffeners.
- Even though the load capacity did not increase substantially for columns tested with stiffeners at a low eccentricity, the stiffeners did assist in the post-buckling behavior of the columns since the high load was maintained for a much higher displacement. For the columns without stiffeners, the load decreased more suddenly.

For all test groups, the effective stiffener capacity was calculated as the capacity of the column with stiffeners minus the capacity of the column without stiffeners. The effective stiffener capacity of the column specimens with eccentric stiffeners was compared to the capacity of the column specimens with concentric stiffeners. The primary conclusion from this evaluation is as follows:

- The effective stiffener capacity for columns with eccentric stiffeners was between 0%-18%

of the effective stiffener capacity for columns with concentric stiffeners. Therefore, with the column specimen sizes tested, eccentric stiffeners should not be relied on to resist the effects of single compression loads applied to column flanges. Larger sections will be evaluated in the analytical portion of this research to evaluate this conclusion in more detail.

3.9.2 Conclusions from Double Compression Tests

The following are the primary conclusions from the double compression tests:

- Column specimens without stiffeners did not fail by web compression buckling as predicted by the AISC specification. Instead, all reached a load carrying capacity at a limit state best described as web local crippling near the top flange where the load was applied. The web local crippling capacity was close to that calculated using the equations in the AISC specification even though web and flange yielding was also witnessed prior to reaching the capacity.
- Web yielding did occur but this did not constitute a method of failure for the column specimen. Web yielding and flange bending appeared to have a minimal influence on the load-displacement relationship. It's probable that inelastic behavior influenced the final capacity of the column specimens. However, the overall load carrying capacity was much higher than that predicted for web local yielding and web compression buckling. In addition, the non-linear behavior from the load-displacement relationships initiated at loads higher than that predicted by web local yielding.
- For the W16X31 column specimen with one concentric stiffener, the calculated (theoretical) effective stiffener capacity was noticeable less than the actual effective stiffener capacity obtained from testing. When two concentric stiffeners were used with the W12X26 and W10X19 column specimens, the effective stiffener capacity from testing was substantially higher than the calculated stiffener capacity.
- Traditional methods for calculating the effective capacity of concentric stiffeners underestimates the effective strength for double compression conditions.
    - This still needs to be analyzed but it is believed that concentric stiffeners in a double compression test have three effects: (1) share the load with the web, (2) stabilize the web allowing more load, and (3) allow the load to spread to more width of the web

than predicted from web local yielding of $5k + l_b$.

Since the effective stiffener capacity of concentric stiffeners was so much higher than the calculated effective stiffener capacity, the test results of the effective stiffener capacity of eccentric stiffeners will be compared in the following bullet points to the calculated effective stiffener capacity. Conclusions from the tests performed with eccentric stiffeners are as follows.

- Column specimens tested with stiffeners at a high eccentricity (6 in. for W16X31 and 4 in. for other columns) reach a load capacity very similar to the load capacity of the column specimens without stiffeners. The capacity increased by 0% to 7.5% of the tests without stiffeners. The effective capacity of the eccentric stiffeners were anywhere from 0% to 22% of the calculated capacity of concentric stiffeners.
- Column specimens tested with stiffeners at a low eccentricity (3 in. for W16X31 and 2 in. for other columns) showed limited improvement in capacity in comparison to the columns without stiffeners. The increase in capacity was anywhere from 1% to 28% of the columns without stiffeners. The effective stiffener capacity ranged from 5% to 35% of the calculated concentric stiffener capacity. Two tests came out to approximately 35% which is still much lower than that implied in the AISC Design Guide 13 (Carter, 1999) which assumes as high as 65%. The effective capacity of eccentric stiffeners at a low eccentricity was much less than the tested effective stiffener capacity of concentric stiffeners (3% to 12%).
- Similar to single compression tests, even though the load did not increase substantially for column specimens with stiffeners at a low eccentricity, the stiffeners assisted in the post-buckling behavior of the columns since the high load was maintained for a longer displacement.

The primary conclusion from the tests on eccentric stiffeners as part of double compression tests is as follows:

- Eccentric stiffeners should not be relied on to resist the effects of double compression loads applied to column flanges for the column specimens tested. The recommendations in the AISC Design Guide 13 (Carter, 1999) are inappropriate for this loading condition. Larger sections will be evaluated in the analytical portion to evaluate this conclusion in more detail.

3.9.3 Conclusions from Single Tension Tests

The following are the primary conclusions from the single tension tests:

- All test results of column specimens without stiffeners reached a capacity higher than calculated for the limit state of flange bending. This is true for all column specimens including the column specimen that failed prematurely. For column specimens without stiffeners, all test capacities were at least 50% higher than that predicted from flange bending. For the W16X31 column specimen, the test results were 90% higher.
- Although the test results suggest that the capacity is much higher than predicted from the flange bending equations, inspection of the results suggest that this limit state still influences capacity significantly since flange bending creates unequal stresses in the weld from the loading plate to the flange of the column specimens. Weld failures did not occur in concentric stiffener conditions since the flange was not able to bend.
- The test results suggest that the capacity of members in single tension are much higher than that predicted from the limit state of web local yielding.
- When concentric stiffeners are used, the capacity of the column specimen increases significantly. However, the true differences in capacity are uncertain since the true capacity could not be measured experimentally.

The following conclusions with respect to eccentric stiffeners will focus on the results of W16X31 column specimens for reasons described in this section.

- The use of eccentric stiffeners at a high eccentricity and in a single tension test does not alter the capacity of the column specimen. For the case of the W16X31 column specimen, the capacity actually decreased slightly.
- The use of eccentric stiffeners at a low eccentricity and in single tension test appears to slightly increase the capacity of the column specimen. However, for the W16X31 column specimen, the increase was only 1% in comparison to the test without stiffeners. For the W12X26 column specimen tests, there is a noticeable increase in the capacity when a 2 in. eccentricity is used in comparison to a 4 in. eccentricity.

- Overall, the trends in the load carry capacity results for column specimens tested in single tension appear similar to the trends of the compression tests. The use of eccentric stiffeners at an eccentricity of 2 in. or more does not nearly provide the effective capacity obtained when using concentric stiffeners since the deformations in the members due to concentrated loads are too localized.

CHAPTER 4: METHODOLOGY FOR ANALYTICAL FINITE ELEMENT MODELS

This chapter and subsequent chapters discuss the analytical investigations that were used to further analyze column specimens subjected to concentrated loads. All analytical studies were performed using the finite element method and the finite element program ABAQUS (ABAQUS, 2014). ABAQUS was chosen due to its unique meshing capabilities, variation of element types, and non-linear geometric and material performance.

This chapter discusses common methodology used for most finite element models. The discussion includes material properties, element types, loading conditions, boundary conditions, and analysis procedures. In addition, Section 4.1 provides a brief summary of the preliminary investigations that were performed before the experimental investigations. Additional modeling features used for specific finite element models are discussed with the individual finite element models later in the report. Note that for single tension tests, additional methodology is discussed in Section 5.4 with the models of the experimental column specimens since careful attention was necessary for modeling the welds from the loading plate to the column specimen.

Chapter 5 presents the analytical results of finite element models used to mimic the experimental column specimens. Additional modeling assumptions and analysis assumptions are discussed in Chapter 5 since the finite element calibration was performed using the experimental column specimens. The final methodology discussed in this chapter was derived through trial and error of studying the experimental column specimens and therefore, Chapter 5 has analysis assumptions that contradict the specific methods discussed in this chapter.

In the analytical investigations, the influence of using eccentric stiffeners vs. concentric stiffeners is studied using a similar methodology as used for the experimental column specimens in which column specimens were analyzed without stiffeners, with concentric stiffeners and with stiffeners at multiple eccentricities. Chapter 6 will focus on studying larger sections than the experimental column specimens and the influence of using eccentric stiffeners in more detail. The larger sections represent typical sections used for column design in larger buildings.

Chapter 7 specifically studies the AISC (2016) limit states for predicting the capacity of wide-flange shapes when subjected to concentrated loads. The experimental results of this research have

raised questions about the calculations that are currently in place for flange bending, web crippling, web local yielding and web compression buckling and it was previously recommended to use the finite element methodology to study the accuracy of these equations in more detail.

4.1 Preliminary Investigations

The preliminary investigations summarized in this section were discussed in detail in a preliminary report submitted by the research team to the AISC Research Advisory Committee. However, they were critical in the development of the experimental research program and for the initiation of the new finite element models and therefore, summarized briefly in this section.

Column specimens were analyzed under the loading conditions studied in this research (single tension, single compression, and double compression). Column specimens were analyzed with end bearing stiffeners and with and without stiffeners under concentrated loads. Models for the preliminary investigations were analyzed using a static-stress simulation using the *STATIC option in ABAQUS (ABAQUS, 2014). In addition, some models were analyzed using an eigenvalue buckling analysis using the *BUCKLE option in attempt to capture the failure mechanisms of web local crippling and web compression buckling.

The two main objectives of the preliminary analytical investigations were: (1) to determine the columns sizes to be used in the experimental investigations by comparing the load capacity of the column to the capacity of the actuator of 220 kips, and (2) to simulate the different modes of failure in the finite element models as predicted by the AISC specification (AISC, 2016).

The preliminary finite element studies focused on two section sizes; (1) W16X31 and (2) W10X19. Since the conclusions for these two column sizes were very similar, the research team did not consider other column sizes for the finite element models. Both column sizes were analyzed with and without stiffeners and both were subjected to single compression and double compression loading conditions. The finite element models included the column specimens themselves, concentric stiffeners at midspan when applicable, bearing stiffeners near the supports, and loading plates. The column specimens and loading plates were modeled with C3D8 solid elements (ABAQUS, 2014) and bearing and concentric stiffeners were modeled with S4 shell elements. These element types are discussed in more detail in Section 4.3. Loading plates included the top loading

plate for all test methods and the bottom reaction plate for double compression tests. Finite element investigations were also performed to model some single tension tests. However, the welds from the loading plate to the top flange were not considered.

Screenshots of finite element models of W16X31 column sections are shown in Figures 4.1-1, 4.1-2, and 4.1-3 for a single compression test, a double compression test, and a single tension test, respectively. In Figure 4.1-3, S4 shell elements are used for the loading plate to demonstrate how different modeling assumptions were attempted during the preliminary investigations.

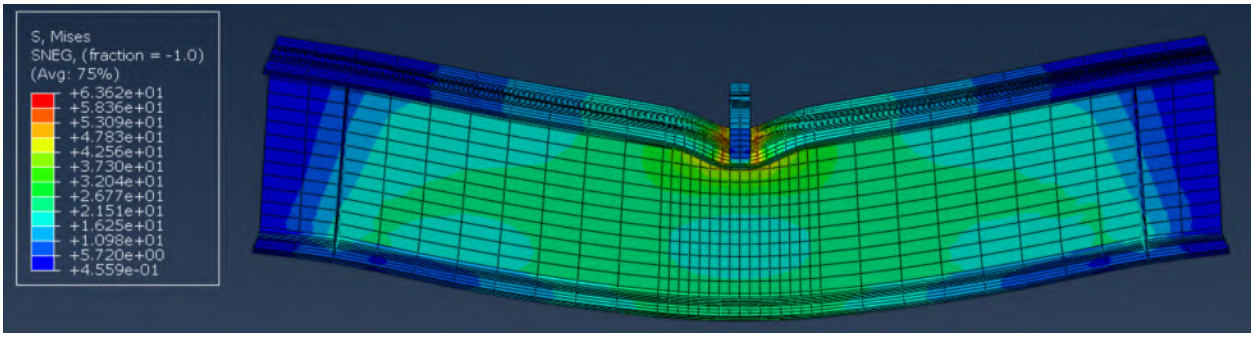

Figure 4.1-1: W16X31 loaded in single compression without midspan stiffeners

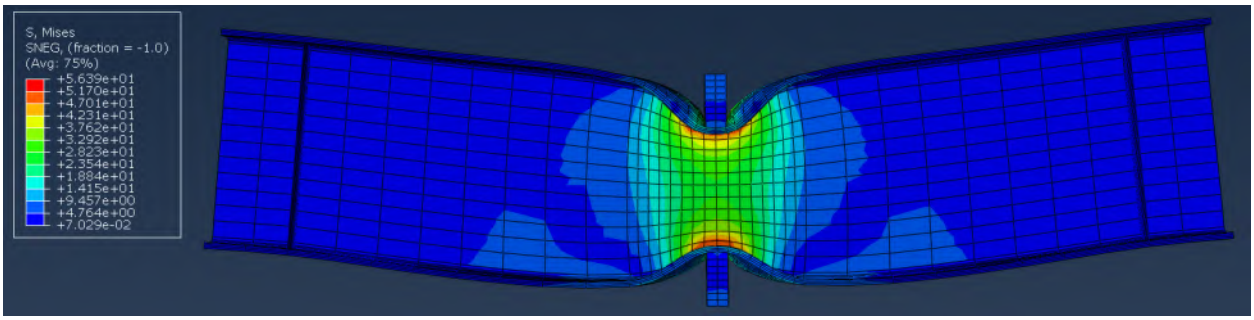

Figure 4.1-2: W16X31 loaded in double compression without midspan stiffeners

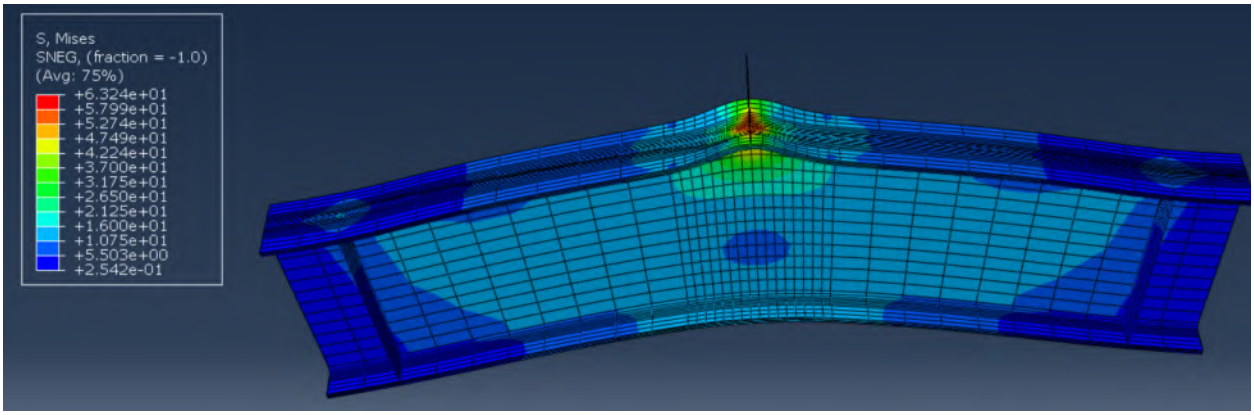

Figure 4.1-3: W16X31 loaded in single tension and with shell elements for loading plate

Some conclusions drawn from the preliminary investigations were as follows:

- The loading plate dimensions and stiffness are crucial factors in predicting the deformations that develop in the column specimen. The loading plates are best modeled with solid elements.
- Stiffeners can be modeled with S4 shell elements as the concentrated load is properly distributed into the stiffeners from the top flange.
- Capturing web crippling using a post-buckling analysis is cumbersome but critical for future investigations.
- A finer mesh is desired near the loading plate to allow deformations to occur in the loading plate and to attach the weld elements directly to the column flange and loading plate when performing single tension tests.

4.2 Model Parts and Element Types

Similar to the preliminary investigations, all finite element models included the column specimens themselves, concentric stiffeners at midspan when applicable, bearing stiffeners near the supports when applicable, and loading plates. Loading plates include the top loading plate for all test methods and the bottom reaction plate for double compression tests. Bearing stiffeners were included for all single tension and single compression tests. They were not used for any double compression tests.

All steel plates were modeled using either solid elements or shell elements. Solid elements were chosen to model the column specimen due to the presence and significance of the fillet region of the column specimens. The fillet dimensions could not be accounted for accurately if shell elements were utilized. Different solid elements were considered including Types C3D8, C3D8R, and C3D8I (ABAQUS, 2014), but in the end, C3D8I was selected for most conditions and was also used for the loading plates. C3D8I is an eight-node three-dimensional continuum element with three degrees of freedom per node and enhanced by incompatible modes to improve its bending behavior. The primary effect of the modes is to eliminate the parasitic shear stresses that cause the response of regular first-order displacement elements to be too stiff in bending as well as eliminate the artificial stiffening due to Poisson's effect in bending (ABAQUS, 2014).

Four-node linear shell elements of Type S4 (ABAQUS, 2014) were used to model the stiffeners. These elements are general-purpose shell elements and have six deformation degrees of freedom per node (three displacements and three rotations). A screenshot showing the cross-section of a finite element model of a W16X31 column specimen is shown in Figure 4.2-1. An isometric view is shown in Figure 4.2-2. Finer meshes were used near the application of the concentrated load and coarser meshes were used away from the concentrated load since less local deformations were anticipated near the supports.

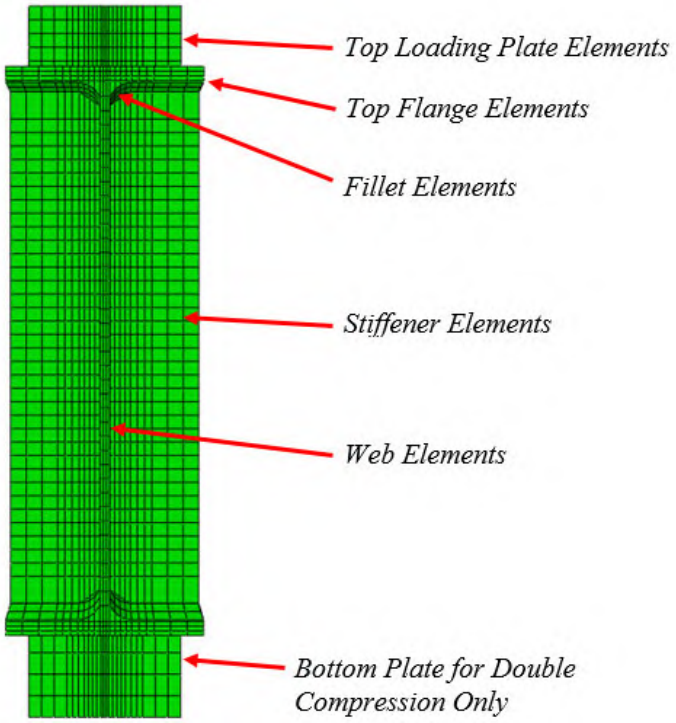

Figure 4.2-1: Cross-section of the finite element model of a W16X31 column specimen

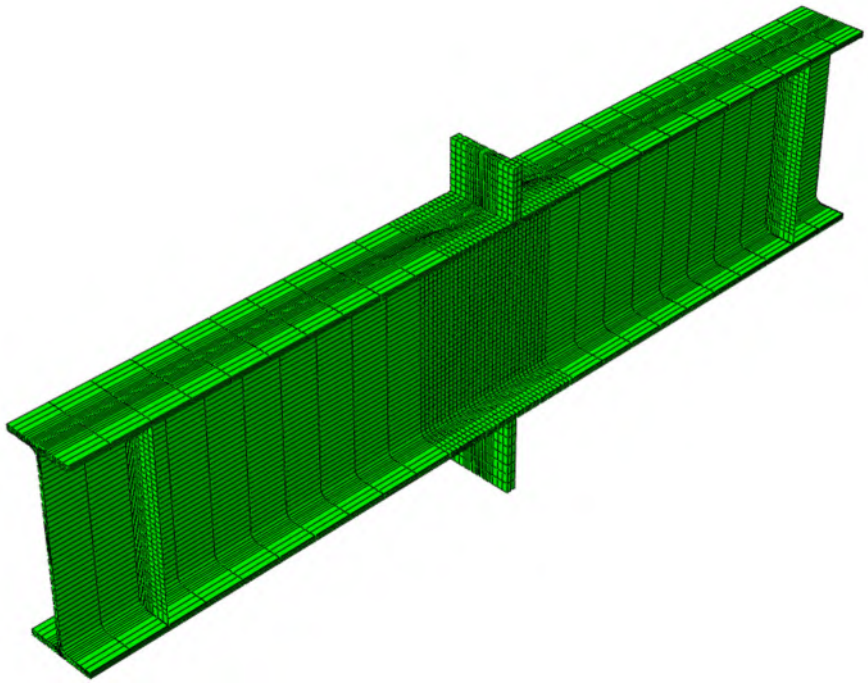

Figure 4.2-2: Isometric view of finite element model of W16X31 column specimen

For single tension tests, the finite element models also included the welds from the loading plate to the top flange of the column specimens. From the experimental results, it was determined that these welds are a critical element for properly predicting the failure mechanism of the column specimens. Thus, the welds were modeled as diligently as possible. A discussion of the elements used for the welds is provided with the analytical results of single tension tests in Section 5.4.

4.3 Material Properties

Once the experimental tests were complete, uniaxial tension samples were fabricated from the webs and flanges of the column specimens at areas away from the concentrated loads at midspan. For the experimental column specimens, the material properties used in ABAQUS were derived from tension tests conducted on these samples using ASTM E8/E8M-09 (ASTM, 2009). The samples were typically taken from the top of the web on the column edge due to the lack of inelastic deformations in this particular region of the column specimen. The samples were then reshaped with a water jet machine in accordance with ASTM E8/E8M-09. The specimens were tested in uniaxial tension with an Instron 8502A tensile testing machine. An Instron strain gage extensometer was used to obtain strain readings. The tests were conducted using a displacement rate control of 0.03

in/min.

Column specimens were obtained that were assumed fabricated from a larger column. This was evident by markings on the column specimens when received at LTU, which represent a serial number of the initial longer column. Therefore, the same material properties were assumed for the same column size (e.g. all W16X31 column specimens with the same serial numbers were assumed to have the same material properties). Table 4.3-1 summarizes the material properties of all the column sections tested experimentally. The sections with the same serial numbers were assumed to have the same material properties and in the table, the material properties are not repeated for the same serial numbers. For each column specimen with the same serial number, at least two samples were tested, and the average stress-strain curves were used in the finite element models.

Table 4.3-1: Material properties of all experimental column specimens

Column Specimen			Serial Number	Average Values from Stress-Strain Curve					
				E (ksi)	σ_y (ksi)	σ_u (ksi)	ε_{sh} (ksi)	ε_y (ksi)	ε_u (ksi)
W16X31	SC	NS	B128447-401	34100	53.0	70.0	0.0150	0.0016	0.0130
		E6	B139471-104	30687	48.4	65.1	0.0180	0.0016	0.1667
		E3	B139471-401	32291	54.2	69.2	0.0140	0.0017	0.1436
		E0	B139471-104						
	DC	NS	B139471-403	30037	52.5	68.5	0.0143	0.0018	0.1907
		E6	B139471-104						
		E3	B139471-104						
		E0	B139471-403						
	ST	NS	B139471-403						
		E6	B139471-104						
		E3	B139471-104						
		E0	B139471-401						
W10X19	SC	NS	1804015	30864	52.7	65.8	0.0360	0.0017	0.1367
		E4	1804015						
		E2	1804015						
		E0	19DCE0	33000	57.0	69.1	0.0180	0.0010	0.0869
	DC	NS	1804015						
		E4	19DCE0						
		E2	19DCE0						
		E0	19DCE0						
W12X26	SC	NS	2711927	30531	56.0	68.7	0.0270	0.0018	0.1692
		E4	2711927						
		E2	1707668	28987	59.4	73.4	0.0240	0.0020	0.1743
		E0	1707668						
	DC	NS	26DCNS	33224	52.6	66.7	0.0223	0.0016	0.1780
		E4	2807677	30145	55.3	66.4	0.0280	0.0018	0.1590
		E2	2807677						
		E0	2807677						
	ST	NS	2807677						
		E4	2711927						
		E2	2807677						
		E0	2807677						
W10X39	SC	NS	39SCE2	30899	52.6	66.5	0.0220	0.0017	0.1719
		E4	39SCE2						
		E2	39SCE2						
		E0	39SCE2						
	ST	NS	39STNS	30600	52.4	67.0	0.1960	0.0017	0.1823
		E4	39STNS						
		E2	39STNS						
		E0	39STNS						

The stress-strain relationships were idealized and implemented into the finite element program using the *ELASTIC and *PLASTIC keywords (ABAQUS, 2014). Idealization of a measured stress-strain curve is demonstrated in Figure 4.3-1. A straight line is used to predict elastic behavior and define the elastic modulus. Yielding of the material is idealized as a straight line with a stress equal to the yield stress of the material and the line is drawn from the yield strain to the assumed strain at the onset of strain hardening. The strain hardening profile was idealized using selected points along the curve all the way up to the ultimate stress. A fourth order polynomial trend line was used on top of the original stress-stress curve to obtain the most accurate idealization. The stress-strain relationship was not modeled after the ultimate stress was reached and it is assumed that material failure would occur in the model when this stress is reached.

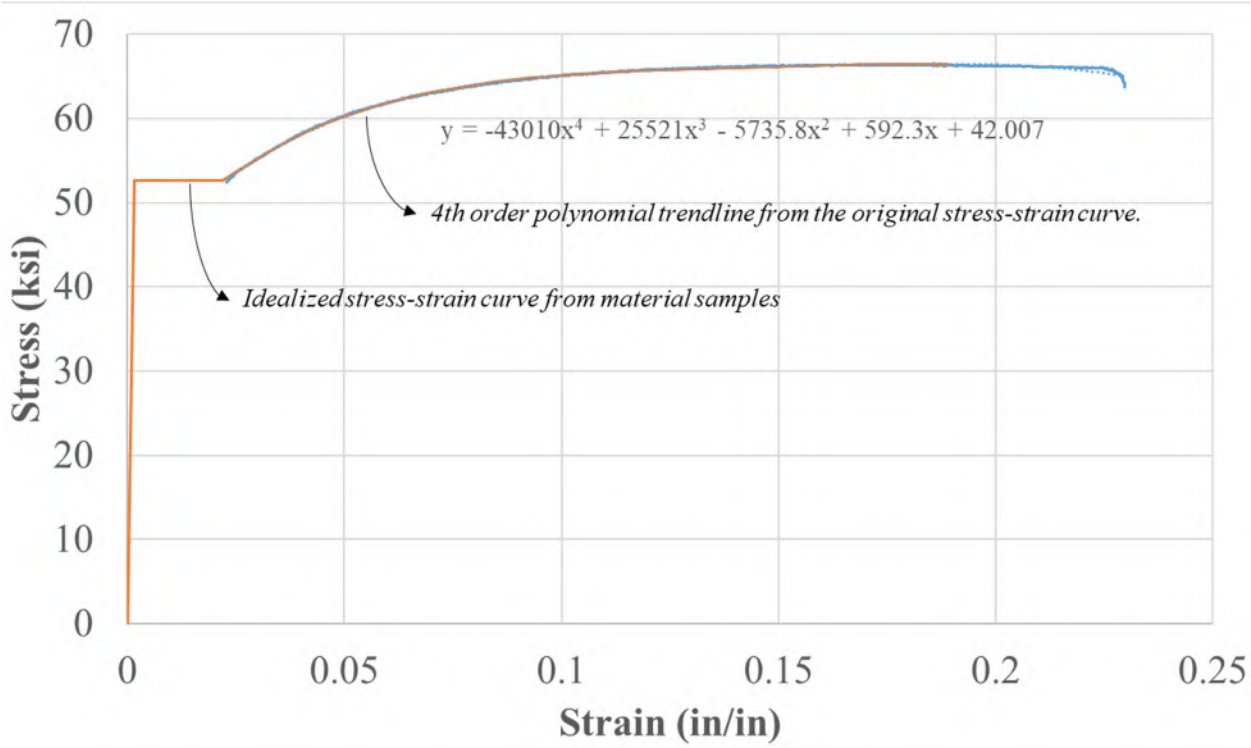

Figure 4.3-1: Idealized stress-strain curve for the W10X39-SC-E2 material properties

Note that the actual stress-strain curves were utilized for the finite element modeling of the experimental column specimens. However, further finite element studies were performed with the minimum material properties for steel grades as specified in the AISC Steel Construction Manual (AISC, 2016), since in practice, it is anticipated that these are the properties available. For instance,

for A992 steel, the minimum yield stress of 50 ksi, minimum ultimate stress of 65 ksi, and elastic modulus of 29000 ksi were used to develop recommendations for practice. Figure 4.3-2 demonstrates how the stress-strain curves derived from the experimental investigations were modified to develop stress-strain curves with the minimum properties specified for A992 steel.

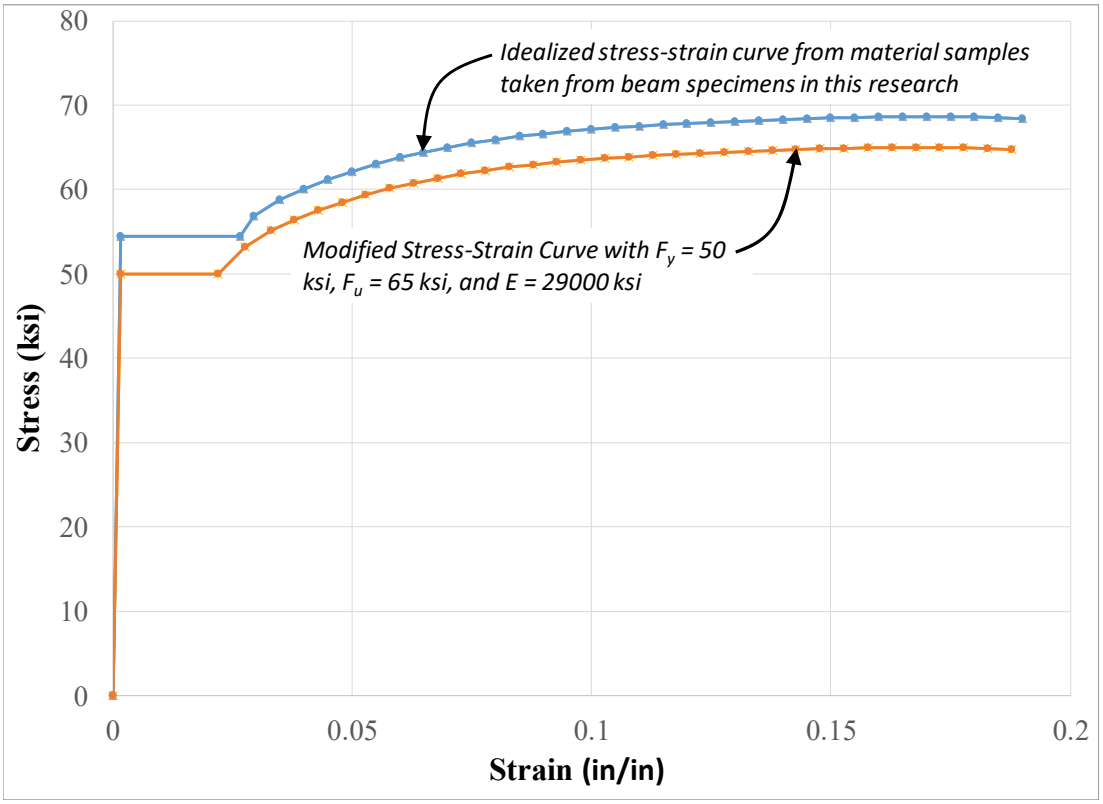

Figure 4.3-2: Idealized strain curve used for further analytical studies

In the experimental investigations, the research team found diverse results for uniaxial tension tests performed on samples fabricated from stiffener plates. After further investigation of the material order, the steel supplier indicated that some stiffeners met the properties of A36 but other stiffeners met the properties for A36 and A572 Gr. 50.

The stress-strain curves shown in Figure 4.3-3 are idealizations of typical stress-strain curves taken from stiffener plate samples. The research team assumes that the curve with yield stress less than 50 ksi is for A36 steel and the other curve is for A572 Gr. 50 steel.

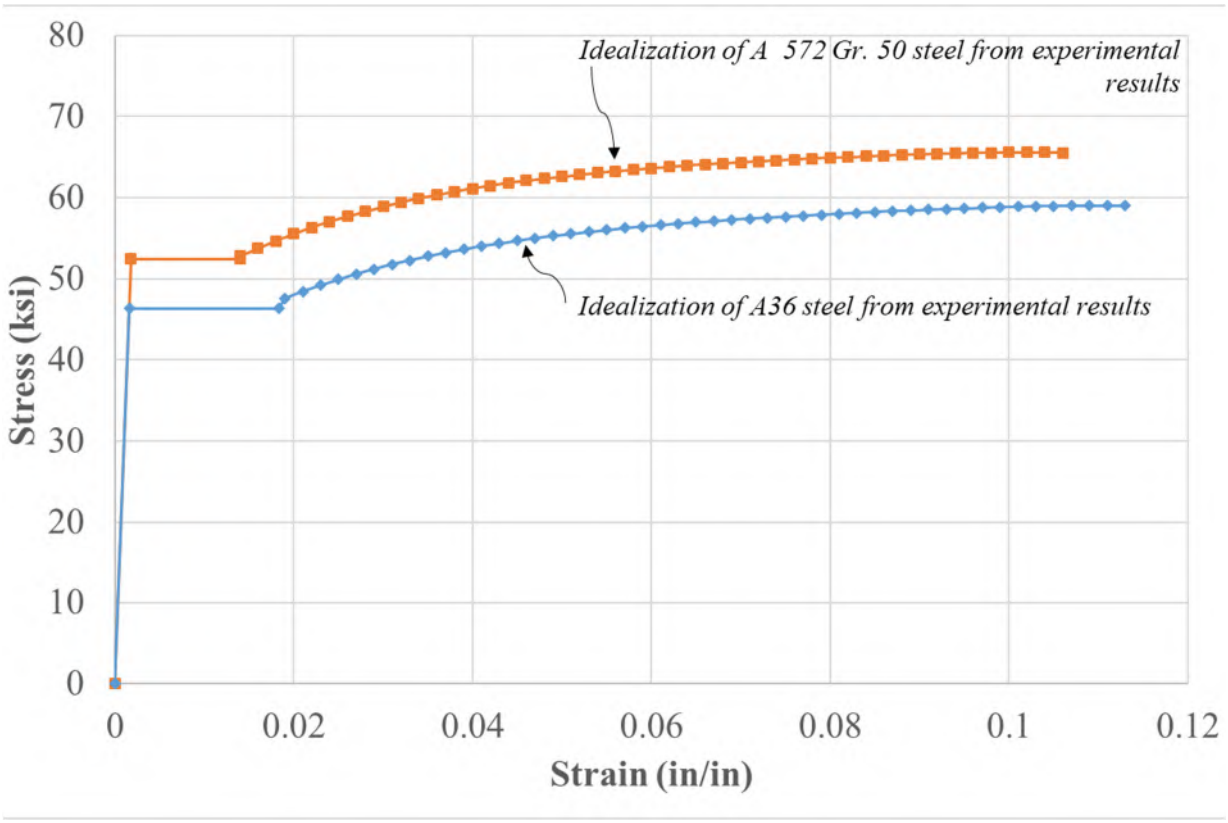

Figure 4.3-3: Idealized stress-strain curve for stiffener plate material

4.4 Boundary Conditions and Constraint Equations

The connection in between the stiffeners and the wide flange section (shell-to-solid connection) was modeled by extending the elements of the stiffeners one-element thickness into the solid section and connecting the nodes on the stiffeners to the intersecting nodes on the solid sections. This connection type allowed additional fixity between the shell and solid elements. In reality, the two-sided welds provide fixity between plates and this modeling approach provided a more realistic boundary condition in comparison to just connecting the stiffeners to the nodes on the face of the column specimens.

All experimental column specimens and additional column specimens of larger size were assumed to react against roller supports to simulate the experimental testing condition as discussed in Chapter 3. For the compression tests, the roller supports were located under the column specimen and for the single tension tests, the roller supports were located above the column specimen. For the compression specimen models, the specimens were consistently simply supported at 5 ft. On each

side and underneath the bearing stiffeners if applicable, the nodes along the width of the flange were fixed vertically (DOF 2).

The top of the loading plate was allowed to deform in plane. However, the center of the top plate was fixed in the transverse (horizontal) directions (DOF 1 and 3). Loading was applied by specifying a displacement boundary condition (DOF 2) using the *BOUNDARY option (ABAQUS, 2014). This is an optional method that forces a displacement while computing the required load to obtain such displacement and is easier to control in the finite element model as opposed to the *LOAD option which applies a specific load. This was controlled by the center node on the top the top loading plate. One node was used as the control node such that ABAQUS would provide one loading force required to produce a given displacement. Other nodes on the top surface of the top plate were slaved to the control node in the vertical direction (DOF 2) using the *EQUATION option such that the entire surface moved in the vertical direction together for each increment of displacement. Figure 4.4-1 shows an isometric view of the finite element model of a W10X39 and shows schematics to represent the boundary conditions.

The dimensions of the loading plates were deemed critical for the study. During the preliminary investigations, the depth of the loading plate seemed relatively insignificant. However, the experimental behavior showed that a minimum depth for the plate was needed to let the model develop higher stresses near the center of the plate when it contacts the column specimen since the loading plate was more restricted at the middle, adjacent to the column specimen web. During the experimental investigations, localized yielding was spotted near the center of the loading plate. Deformations of the loading plate were also required to simulate the effects of flange bending, particularly during the single tension tests.

For the larger column sections discussed in Chapter 6, some additional steps were required to model the loading plate. Due to the high strength of the column sections, the loading plate was found to buckle when the same thickness and strengths were used. The research team decided that the plate thickness for all models was to remain the same in order to avoid adding another variable to the analytical investigations. To avoid buckling of the plate, the center of the plate and through the depth was fixed for longitudinal translation (DOF 3). In addition, the strength of the plate was increased as needed to ensure that failure occurred in the column specimen instead of developing excessive

inelastic deformations in the loading plate. This is discussed in more detail in Chapter 6. Similarly, for double compression tests and for larger sections, more steps were needed to model the bottom loading plate. The bottom loading plate was constrained in the transverse directions so that it could only deform in plane, and it was constrained to have the same displacement as the top loading plate but in opposite directions, simulating a true through force. For smaller sections, the bottom reaction plate was fixed as it was in the experimental investigations.

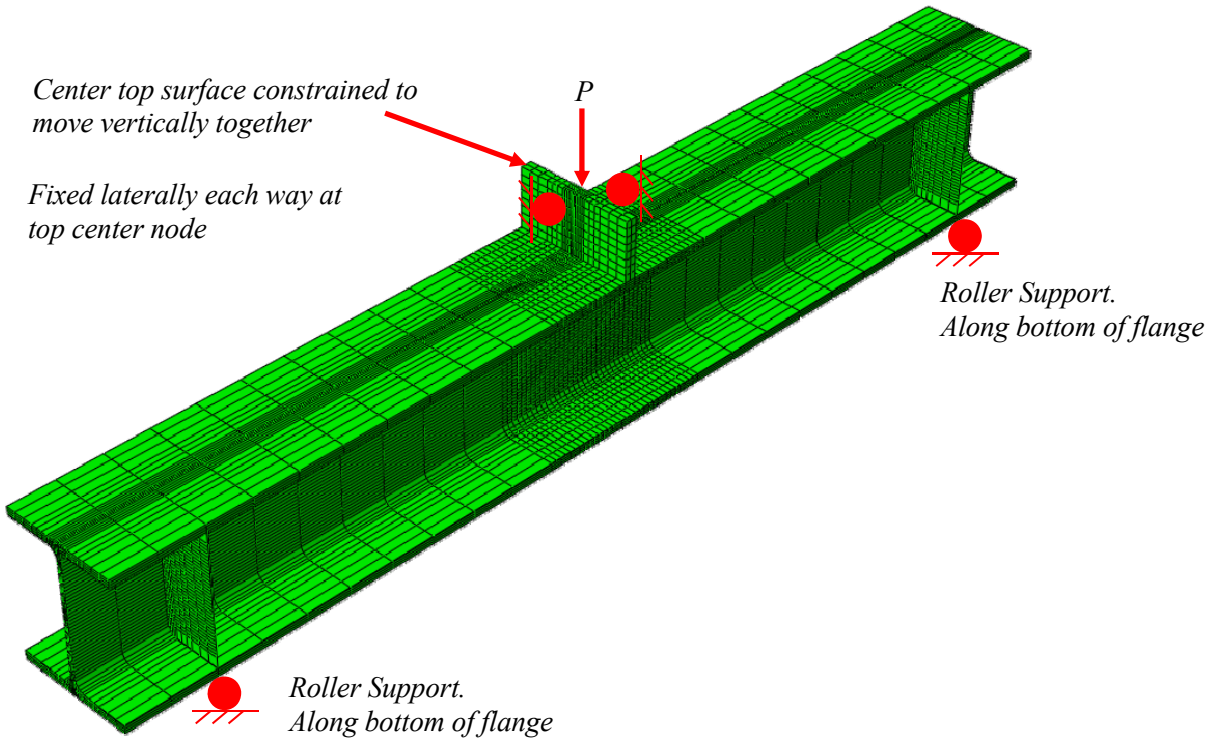

Figure 4.4-1: Isometric view of finite element model showing boundary conditions

As mentioned earlier in this chapter, additional steps were required in single tension tests to model the welds, which includes additional steps to constrain the welds to nodes part of the column specimen and loading plate. These details are discussed in Section 5.4.

4.5 Analysis Procedure

Multiple procedures were evaluated to simulate and analyze the deformations and stresses that develop in the finite element results. The column specimens were initially modeled as perfectly straight and symmetric with respect to geometry, boundary conditions and loading. Therefore, a buckling mode of failure was not expected analytically even though it was witnessed experimentally

for the compression tests.

For all the single tension tests, buckling was not as much of a concern and therefore, the column specimens were modeled without imperfections. A gradual applied load can be modeled in ABAQUS using the *STATIC analysis procedure (ABAQUS, 2014), which represents a general static analysis option. However, the *STATIC RIKS analysis option, which was also used for the single and double compression tests, was found to be more realistic when simulating the failure mechanisms and stress distributions in the column specimens. A *STATIC RIKS analysis is generally used to predict geometrically nonlinear collapse of a structure but more realistic results were obtained when using this option for the single tension tests. Section 4.5.2 explains the *STATIC RIKS analysis in detail.

Both the single compression and double compression experimental tests were found to experience web local crippling. Thus, in order to simulate a buckling failure mechanism, additional steps were required. Buckling modes under consideration in this research include web local crippling, web compression buckling, stiffener buckling and potentially local flange buckling.

First, an eigenvalue analysis was carried out in ABAQUS, which simulates a buckled shape. In the eigenvalue analysis, the finite element software identified multiple buckling or "mode" shapes for the particular column specimen. Section 4.5.1 gives more detail on the eigenvalue analysis. The eigenvalue analysis does not account for non-linear material properties, nor the appropriate load-displacement behavior simulated from the applied load from the actuator. Therefore, the research team simulated the actual behavior of the column specimens considering buckling in a static-stress analysis. To do this, an imperfection was specified in ABAQUS using the *IMPERFECTION option, which represented a small percentage of the buckled shape determined from the eigenvalue analysis. Section 4.5.2 gives more insight on the imperfection included in the finite element model. After the imperfection was specified, a static-stress analysis was performed using the *STATIC RIKS (ABAQUS, 2014) option to capture the post-buckling behavior.

4.5.1 Eigenvalue Analysis

The research team used an eigenvalue analysis in ABAQUS with the aim to simulate the buckled shape seen during the experimental test results. Eigenvalue analysis is generally used to estimate the critical buckling loads of stiff structures. Even when the response of a structure is non-linear

before collapse, a general buckling analysis can provide useful estimates of collapse mode shapes (ABAQUS, 2014).

ABAQUS offers either the Lanczos or the subspace iteration eigenvalue extraction methods. Both extraction methods provide valid solutions. The only difference between the two methods is the duration of the iteration process, which depends on the problem size. After several trial studies, the subspace iteration method was chosen since the analysis time is faster when only a few mode shapes are desired. For all single compression tests, the second mode shape was chosen for specifying an imperfection since it always showed the best representation of web crippling seen during the experimental results. Figure 4.5-1 shows the second mode shape of the W16X31 column specimen subjected to single compression. The contours represent the resultant displacement in the column specimen. ABAQUS scales the mode shape results such that the maximum resultant magnitude of displacement is 1.0.

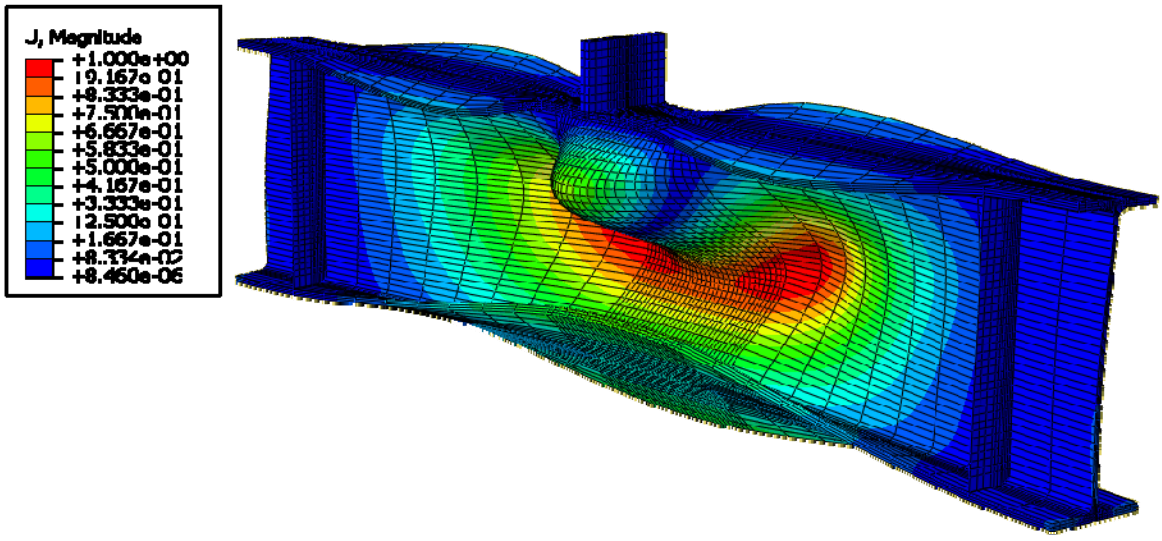

Figure 4.5-1: Second mode shape of W16X31 subjected to single compression

4.5.2 Static-Stress Analysis

A *STATIC RIKS analysis is generally used to predict geometrically non-linear collapse of a structure. As mentioned in Section 4.5, the eigenvalue analysis does not account for non-linear material properties, nor the appropriate load-displacement behavior simulated from the applied load from the actuator. Therefore, it was more appropriate and accurate to simulate the actual behavior of the column specimens considering buckling in a static-stress analysis. The *STATIC RIKS

analysis is capable of generating a crippling effect on the column specimen and it is the most appropriate analysis procedure for the compression tests. The program requires an increment in arc length along the static equilibrium path in scaled load-displacement space, which creates the out-of-plane deformations along the length in the direction of the load applied.

To resemble the experimental test results using finite element models and develop feasible comparisons between the finite element results and the experimental results, the research team included an "imperfection" in the analysis model using the *IMPERFECTION option (ABAQUS, 2014). Imperfections were not used in the single tension models since buckling or crippling effects were not expected. In reality, no column is perfectly straight. Instead, all steel columns are fabricated with allowable tolerances of the cross-section as specified by ASTM A6/A6M (ASTM, 2017) and the AISC Code of Standard Practice (AISC, 2016). For each column specimen, the mode shape from the eigenvalue analysis that best represented the shape of the column specimen during experimental results was identified. The same mode shapes selected for the experimental column specimens were also used for larger column sections. The imperfection was specified in the static-stress analysis as a percentage of the mode shape from the corresponding eigenvalue analysis.

During the analytical studies using the experimental column specimens, the research team calibrated a consistent imperfection (consistent percentage of buckled shape) such that the analytical results consistently compared to the maximum load and post buckling behavior of the experimental results. An imperfection as high as 30% of the buckled shape was used to evaluate the analytical procedure but was much higher than that anticipated in practice since it would imply an out-of-plane displacement of 0.3 in. Different imperfections were attempted but in the end, an imperfection of 0.001% of the buckled shape proved to provide the best analytical results in comparison to the experimental results for various column specimens. As discussed in this chapter and Chapter 5, this was not necessarily the case for all column specimens. However, it was the most consistent and therefore, often used for the "final" analytical analysis of each column specimen evaluated and for further investigations of larger column sizes.

Figure 4.5-2 shows the load-displacement results for finite element models of a W10X39 column specimen tested in single compression and without stiffeners for various imperfection assumptions. The analytical results are shown with the experimental results. There are discrepancies between the

analytical and experimental results with respect to elastic stiffness and displacement in general, which was consistent for all column specimens evaluated. Section 4.6 provides a further evaluation of the analytical elastic stiffness.

As shown in Figure 4.5-2, as the imperfection increases, the maximum load obtained from the analytical model decreases. This is common for applications involving a critical buckling load that as the member becomes less straight to begin with, buckling occurs at a lower load and out-of-plane deformations initiate more substantially. From Figure 4.5-2, the cases with no imperfection and with an imperfection of 0.001% provided the best comparative results in comparison to experimental data. It was more realistic to use the results with an imperfection of 0.001% as the final analytical results for this column specimen since specifying a small imperfection is more realistic.

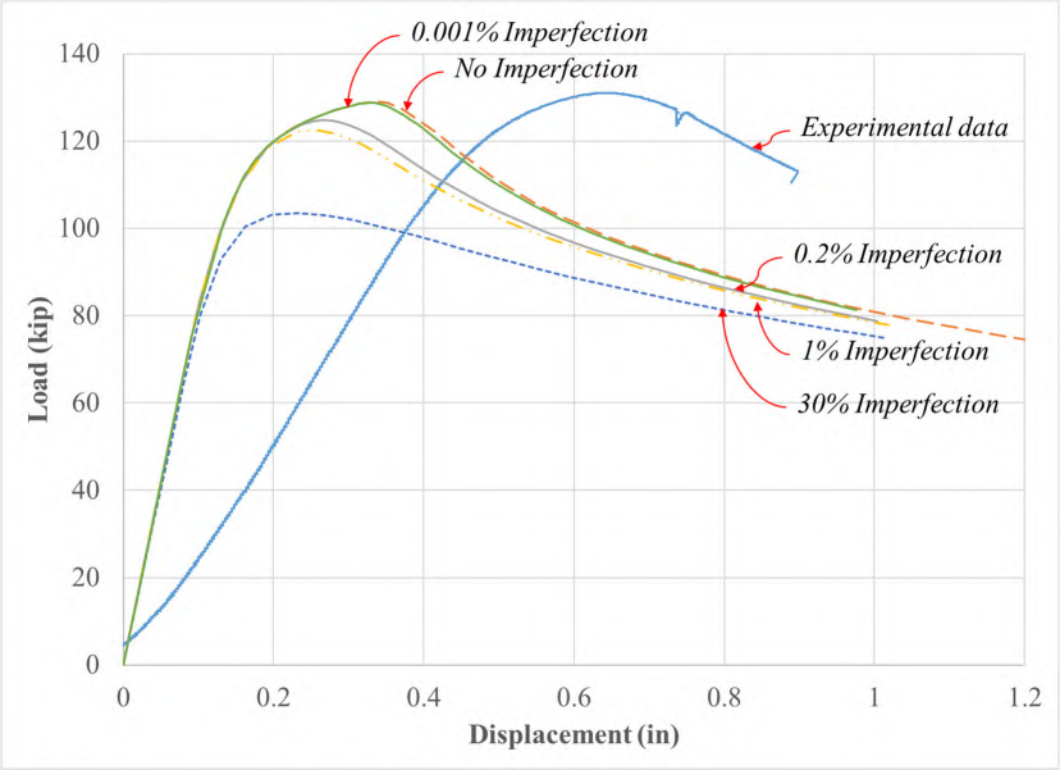

Figure 4.5-2: Load-displacement comparison between experimental and analytical results for the W10X39-SC-NA column specimen

An additional analysis was performed on member with concentric stiffeners to evaluate if the imperfection of 0.001% provided the best fit for the load-displacement results. The research team found that the load-displacement results using imperfections of 0.001% and 0.2% were identical to the results obtained using strictly a *STATIC RIKS analysis without imperfections. Figure 4.5-3

compares the experimental and analytical results for the W10X39-SC-E0 column specimen with an imperfection of 0.001% and without imperfection. Figure 4.5-4 compares the experimental and analytical results for the W12X26-SC-E0 column specimen with an imperfection of 0.2% and without imperfection. After this study, it was determined that it was not necessary to include the *IMPERFECTION option in the models with concentric stiffeners.

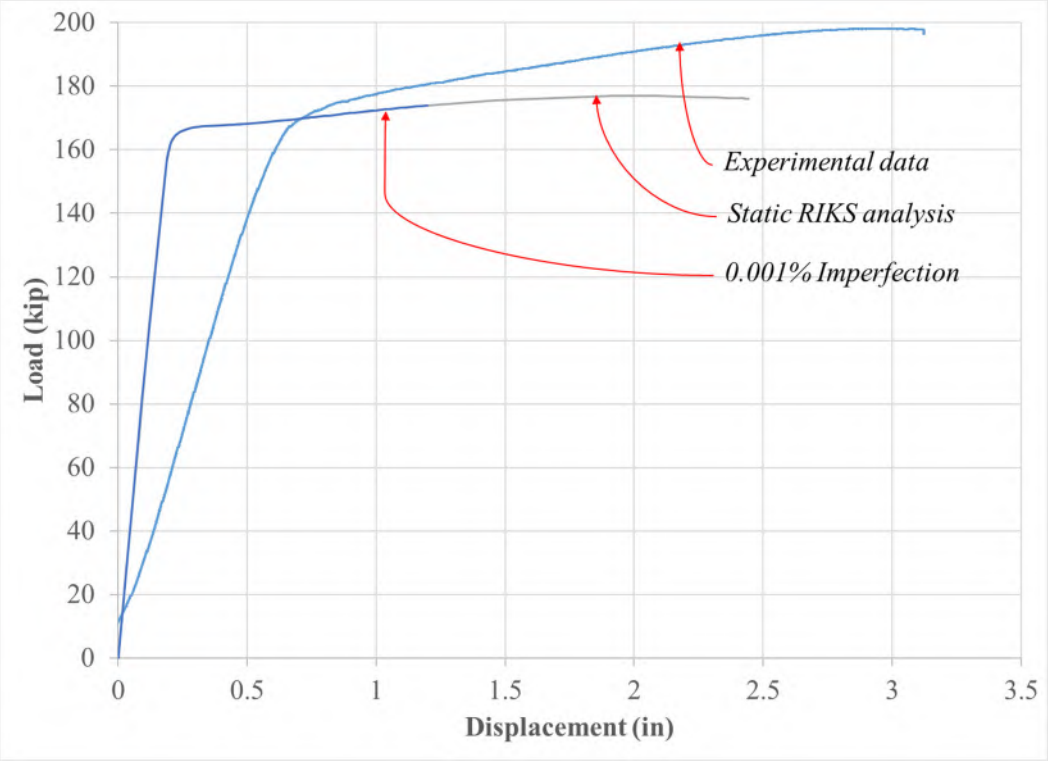

Figure 4.5-3: Comparison of analytical and experimental load-displacement relationships for the W10X39-SC-E0 column specimen

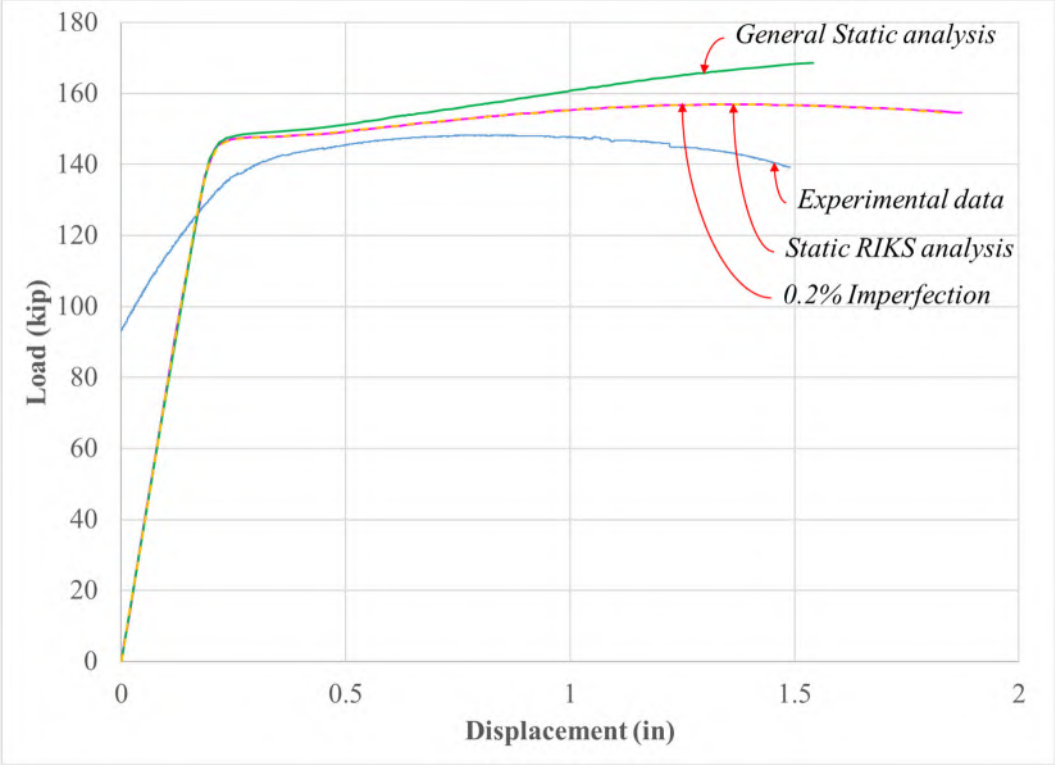

Figure 4.5-4: Comparison of analytical and experimental load-displacement relationships for the W12X26-SC-E0 column specimen

4.6 Further Evaluation of Analytical Column Stiffness

As discussed in Section 4.5.2, the analytical column specimen results compare well with the experimental results when using an imperfection of 0.001%. This is evident by the evaluation of the load-displacement behavior when crippling occurs and this comparison was usually found consistent for all column specimens evaluated. However, significant discrepancies are identified in the elastic portion of the load-displacement behavior, which makes the analytical models questionable. After reviewing the models repeatedly with respect to material properties, boundary conditions, and loading conditions, the LTU research team could not identify any flaws in the analytical models and therefore questioned the displacement that was measured during the experimental investigations.

The experimental displacement is a measurement of the change in position of the actuator and is therefore related to the stroke of the actuator upon testing. At the time of developing the experimental research program, this displacement measurement was assumed adequate to develop load-displacement relationships since accurate displacement readings were not necessary as the primary focus of the research was to identify maximum loads and evaluate the mode of failure under

concentrated load. The analytical models primarily account for relative deformations that occur in the column specimen itself since a limited amount of vertical height was used for the loading plate and the columns was directly vertically supported at the location of the end rollers. Several factors could influence the measurements of the actuator position that are not accounted for in the analytical models. For instance, several parts of the test setup were subjected to compression including the actuator itself, the compression plate, the end roller supports and a small carpet that existed under the end supports to protect the floor.

Two studies were performed to evaluate if the analytical models were indeed a good representation of the actual deformations that occur in the column specimens. One study was performed experimentally and the other was performed analytically.

For the experimental study, string pots were connected to the bottom of a column specimen as shown in Figure 4.6-1. A W10X39 column specimen that was originally tested as a single tension member was used for this study and the string pots were connected to the tension loading plate; still attached to the column specimen. This single tension member did not fail when the maximum actuator capacity was reached as described in Section 3.7.3 and limited plastic deformations were found in the member. One string pot was attached to each side of the loading plate and hence, assumed attached on both sides of the bottom flange. However, comparisons between the analytical displacements and the experimental displacements were still not favorable. The elastic stiffness compared better in comparison to the displacement obtained from the hydraulic actuator. However, the discrepancies still left concerns regarding how the analytical models were developed.

Figure 4.6-1: String pots attached to column specimen for measuring elastic displacement

For the analytical study, displacements found in ABAQUS were compared with theoretical displacements. The amount of displacement that occurs in the column specimen at midspan and at the top flange includes the flexural deformations, the shear deformations, and the local deformations due to the concentrated loads. The research team had no methods to predict the local deformations that occur due to the concentrated load. Therefore, these deformations were temporarily removed from the finite element model by constraining all nodes in the cross-section directly under the concentrated load (midspan) to have the same vertical displacement when subjected to loading. At the end supports, the nodes in the cross-section were not constrained. However, it was assumed that the end stiffeners would provide enough stiffness to keep the cross-section plane and local deformations at the concentrated reaction would be minimal. The analytical results were compared to theoretical predictions in the elastic range only.

Figure 4.6-2 shows the finite element results at a maximum load of 130.5 kips. An evaluation of the load displacement relationship reveals that this was the last load increment in which the column was still behaving elastic. Note that an imperfection was not specified in this model and since the vertical displacement of the center nodes were specified to be the same, no web crippling occurred during the analysis. In Figure 4.6-2, the displacement is amplified to 10X the actual displacement and the stress distribution shown by the contours represents longitudinal stresses.

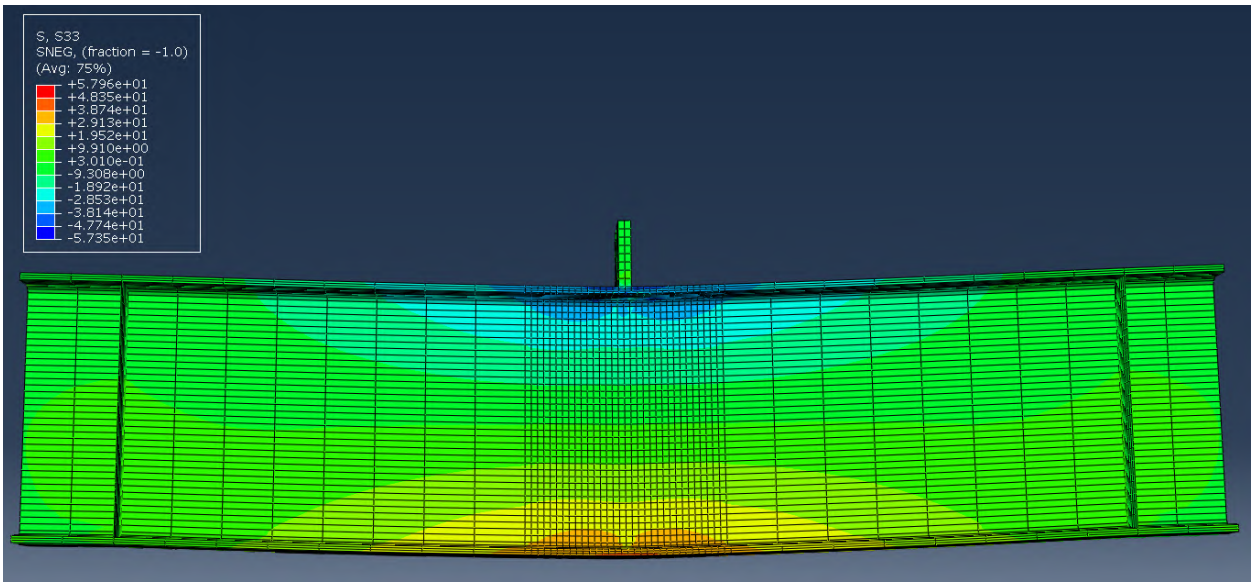

Figure 4.6-2: Finite element model of W16X31 column specimen at a load of 130.5 kips

At a load of 130.5 kips, the vertical displacement at the bottom of the column specimen in the finite element model was *0.0964 in*. A vertical displacement at the center of the column due to flexure was calculated using the theoretical flexural displacement of $PL^3 / (48EI)$. However, in a short column, shear deformations are significant. To account for shear and flexural deformations, the finite element software program RISA-3D was used to model the W16X31 section using multiple frame elements. First, shear deformations were optioned to not be included in RISA-3D and the displacement at midspan was equal to the flexural displacement calculated as 0.054 in. Then, shear deformations were optioned to be included and the total displacement under the point load was *0.096 in.*, which matched the results of the finite element model. A screenshot of the RISA-3D model is shown in Figure 4.6-3. The deflected shape matches the deflected shape of the finite element model.

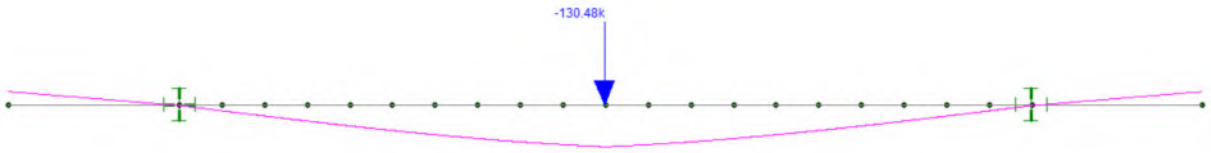

Figure 4.6-3: RISA-3D model of a W16X31 column specimen at a load of 130.48 kips

All variables that created discrepancies between the analytical and experimental displacements are uncertain. However, the analytical/theoretical studies discussed in this section indicate that the finite element models are adequately predicting the elastic stiffness and displacement results.

CHAPTER 5: ANALYTICAL MODELS OF EXPERIMENTAL COLUMN SPECIMENS

5.1 Analytical Test Matrix for Experimental Column Specimens

Finite element models were developed for various experimental column specimens (W16X31, W12X26, W10X19, and W10X39) and for conditions under which they were tested (single and double compression and single tension). Column specimens were modeled with or without stiffeners. However, not all forty (40) experimental column specimens were considered for this phase of the research since the primary objective was to calibrate the finite element models using experimental results. Instead, a reduced test analytical matrix is shown in Table 5.1-1. The nomenclature used to describe each column specimen is discussed in Section 3.2.

Table 5.1-1: Analytical test matrix for experimental column specimens

Column Specimen Nomenclature
W10X19-DC-E0
W10X19-DC-NA
W12X26-DC-E0
W12X26-DC-NA
W12X26-DC-E4
W16X31-DC-NA
W10X39-SC-E0
W10X39-SC-NA
W12X26-SC-E0
W12X26-SC-NA
W12X26-SC-E4
W12X26-ST-E0
W12X26-ST-E4
W16X31-ST-E0
W16X31-ST-NA

In Table 5.1-1, the specimens are ordered in the order that they will be discussed in this chapter. The selection of the column specimens to analyze was somewhat random. However, the research team believed that analyzing column specimens without stiffeners and with concentric stiffeners would be adequate to calibrate all features of the finite element models. In addition, for each test type and for a W12X26 column specimen, an analysis was done with stiffeners at an eccentricity of 4 in. to identify if there are any issues with the finite element models with the eccentric condition.

The subsequent sections will discuss the results of each test type. Section 5.2 discusses the results of the double compression tests. Section 5.3 discusses the results of the single compression tests and Section 5.4 discusses the results of the single tension tests. For each compression test, the results of the specimens are discussed individually. The discussion is somewhat repetitive between similar specimens but the research team wants to relay that each column specimen was analyzed thoroughly to justify the use of the finite element models for larger column sections. Screenshots of the finite element models at or slightly after the maximum load are provided in Appendix E.

5.2 Double Compression Tests

This section provides a detailed discussion of the finite element models that replicated the column specimens subjected to a double compression force. Three column sizes were tested experimentally with and without stiffeners; (1) W10X19, (2) W12X26, and (3) W16X31. The following column specimens were used to perform the comparative analytical studies:

- W10X19-DC-NA
- W10X19-DC-E0
- W12X26-DC-NA
- W12X26-DC-E0
- W12X26-DC-E4
- W16X31-DC-NA

Note that the W12X26 column specimen with concentric stiffeners (W12X26-DC-E0) reached the capacity of the hydraulic actuator. However, it was still used as part of the analytical investigations to evaluate if the elastic stiffness remained relatively constant until the capacity of the actuator was reached and used to evaluate the analytical performance of the stiffeners when subjected to compression loading.

All double compression tests were modeled with the column specimens supported at 5 ft. No bearing stiffeners were used in any double compression tests since they were not used for experimental investigations. Material properties of each column size were imputed into the finite element models as discussed in Section 4.3. A loading plate was used above the column at midspan as discussed in Section 4.2. In addition, a bottom reaction plate was used below the column at

midspan to simulate the double compression condition. The nodes at the bottom of the reaction plate were fixed for translation in all three directions.

After several trial studies, the most accurate results were obtained by modeling the column specimens with an imperfection of 0.001% and using the *STATIC RIKS analysis (ABAQUS, 2014) as discussed in Section 4.5.2. All screenshots of finite element models shown in the following subsections represent finite element models with this imperfection. However, results using other imperfections are shown on the load-displacement results, which were all used to eventually select the 0.001%.

5.2.1 W10X19-DC-NA

A finite element model was developed for W10X19-DC-NA, which represents the W10X19 column specimen tested in double compression and without stiffeners at midspan. The analytical results of this column specimen compare reasonably well to experimental results. However, the results are not as favorable as for other column specimens discussed later in this chapter.

Figure 5.2-1 shows a screenshot of the finite element model while it was still behaving elastic. The deformations are scaled to 1X (i.e. actual scale) which is common for all finite element screenshots of single and double compression tests. As concluded during the experimental investigations, the stresses are high in the flange and web directly underneath the loading plate and near the bottom reaction plate. The load causes slight flange bending on the top flange, which increases more substantially near the tips of the flange.

Figure 5.2-2 shows the finite element model after inelastic deformations initiate in the web. Only the top half of the column specimen is shown. The grey area indicates stresses beyond 65.8 ksi. As inelastic deformations initiate, the stresses in the web are slightly offset on both faces of the web, emphasizing the web crippling effect as seen during the experimental investigations. Most of the inelastic deformations are localized under the top flange and limited inelastic deformations occur near the bottom flange. However, compared to other column specimen sizes, the W10X19 column specimen exhibited higher stresses near the bottom loading plate.

In a similar manner to the experimental tests, the research team continued loading the column specimen after the maximum load had been reached to analyze the post-buckling behavior and the

inelastic deformations in the specimen. Figure 5.2-3 shows a screenshot of the finite element model after the maximum load was reached and after web crippling occurred. The shape of the column specimen is very similar to that seen from the experimental test of this column specimen as shown in Figure 5.2-4. Significant flange bending and crippling in the web underneath the loading plate take place.

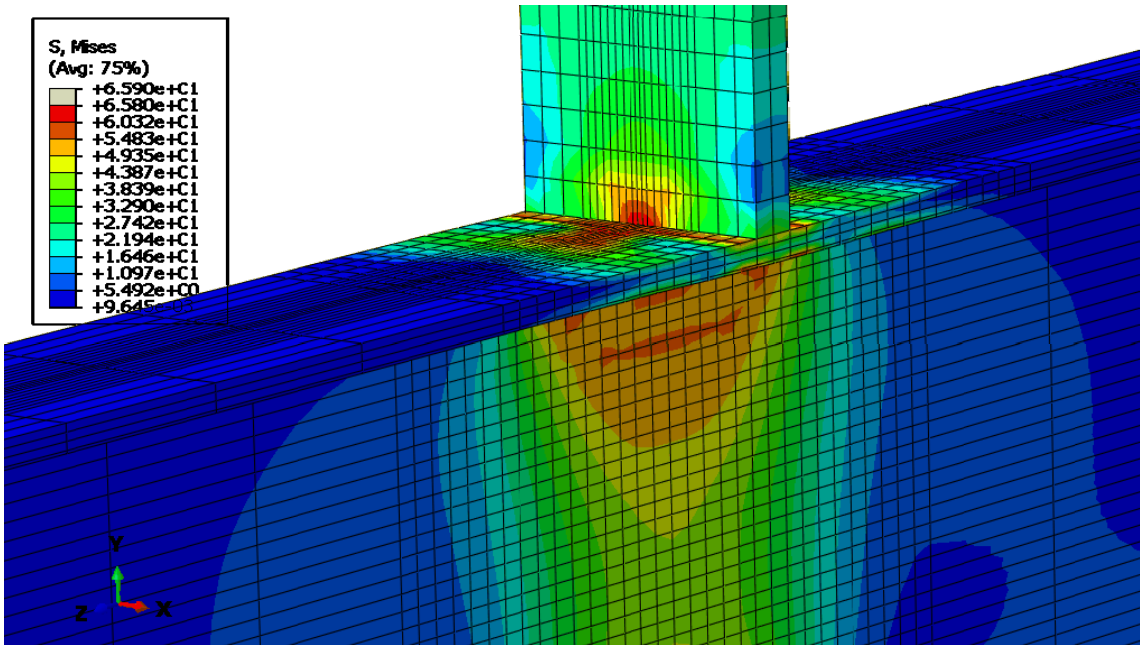

Figure 5.2-1: Finite element model of W10X19-DC-NA during elastic behavior

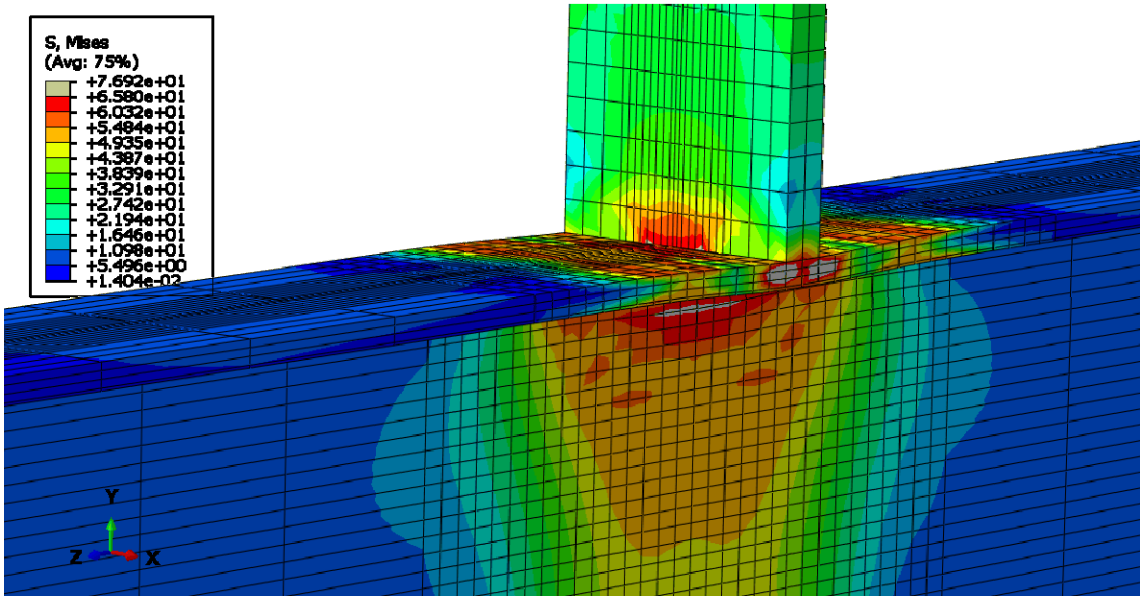

Figure 5.2-2: Finite element model of W10X19-DC-NA during inelastic behavior

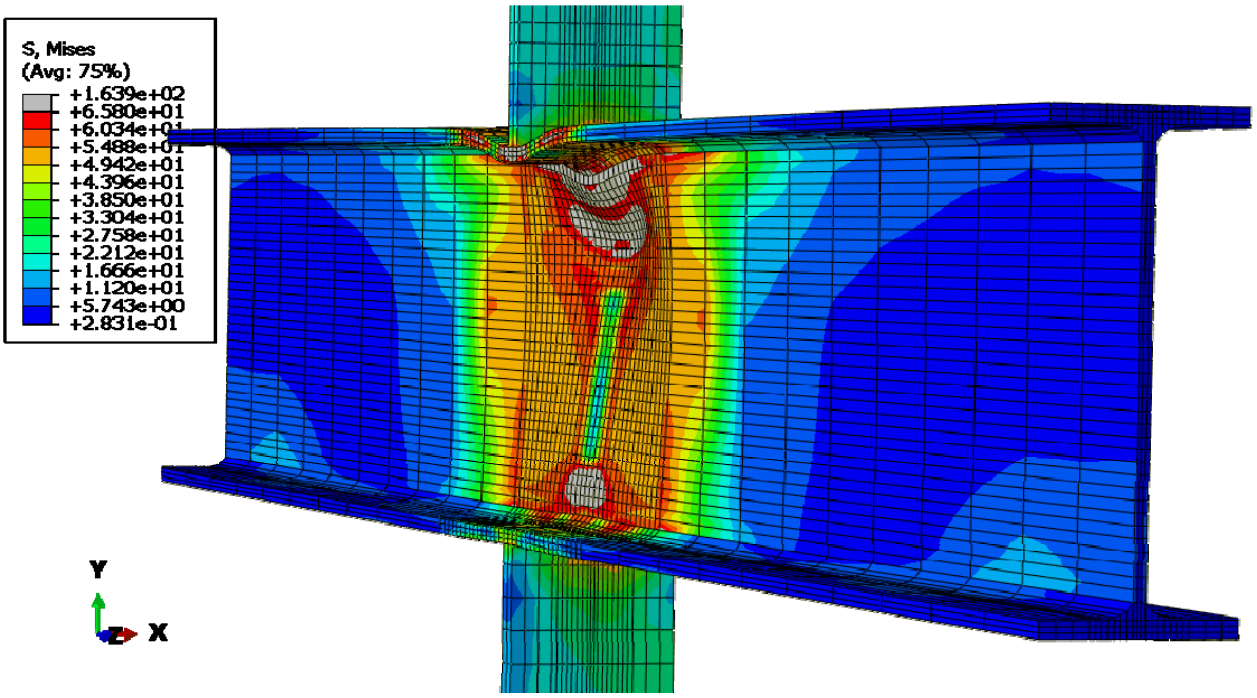

Figure 5.2-3: Finite element model of W10X19-DC-NA emphasizing web crippling

Figure 5.2-4: W10X19-DC-NA after testing emphasizing web crippling

In the final analytical study selected with an imperfection of 0.001%, failure occurred at a maximum load of 87.1 kips, which compared relatively well to the maximum load obtained from the experimental results of 78.5 kips. Although there is noticeable difference in maximum load, it is believed that the experimental column specimen was more influenced by imperfections in comparison to other column specimens since the cross-sectional elements are relatively small. In addition, the experimental column specimen showed some signs of lateral-torsional buckling at failure. The failure mode and stress distribution in the flanges and web compare well with the behavior witnessed during the experimental test in that the stresses were concentrated in the web under the loading plate. This produced web crippling and more out-of-plane deformation occurred in the web near the top loading plate as opposed to the bottom loading plate.

The analytical and experimental load-displacement results are compared in Figure 5.2-5. The figure shows the analytical results for various imperfections. The linear portion of the load-displacement relationship always varied between the analytical and experimental results. As explained in Section 4.6, the research team proved that the analytical elastic stiffness was indeed accurate and therefore, there are no concerns moving forward with this discrepancy. Figure 5.2-6 shows comparative results after shifting the experimental displacement such that the maximum loads occurred at approximately the same displacement, which allows an improved illustration to study the behavior near the maximum load. From this comparison, the analytical results using an imperfection of 0.001% provided the best match for the shape of the experimental results and the analytical results using an imperfection of 0.2% provided the best comparison for maximum load.

An additional analytical result is provided in Figures 5.2-5 and 5.2-6 in which an imperfection of 0.001% of the first mode shape from the eigenvalue analysis was used in lieu of the second mode shape, which was typically used. These types of studies proved that using the second mode shape from the eigenvalue analysis provides the best analytical results in comparison to the experimental results.

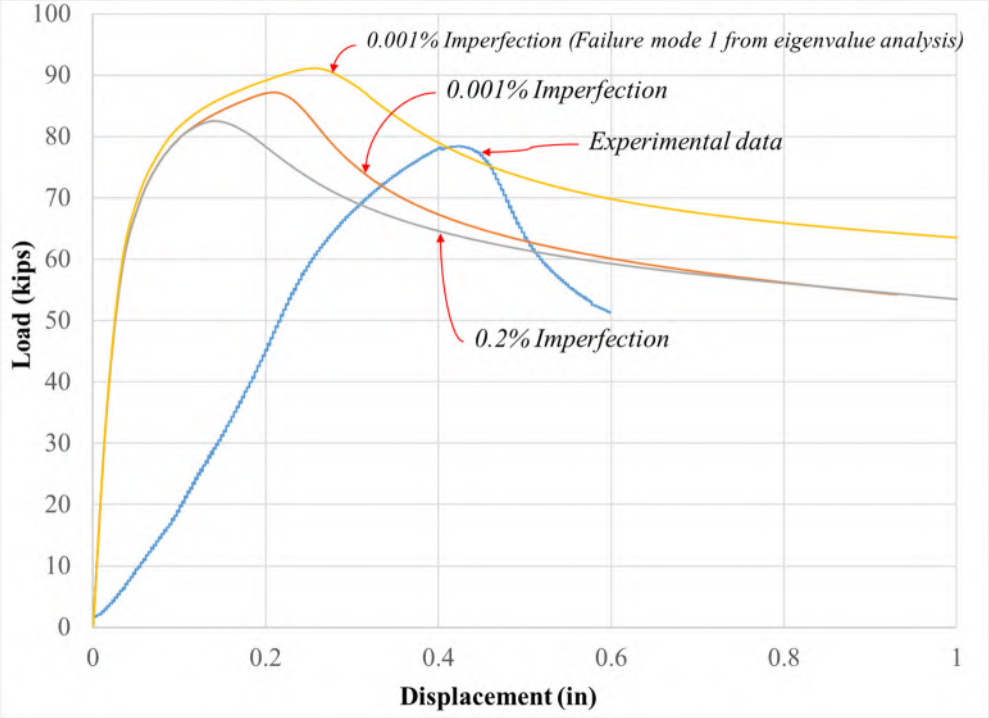

Figure 5.2-5: Comparison of analytical and experimental load-displacement relationships for the W10X19-DC-NA column specimen

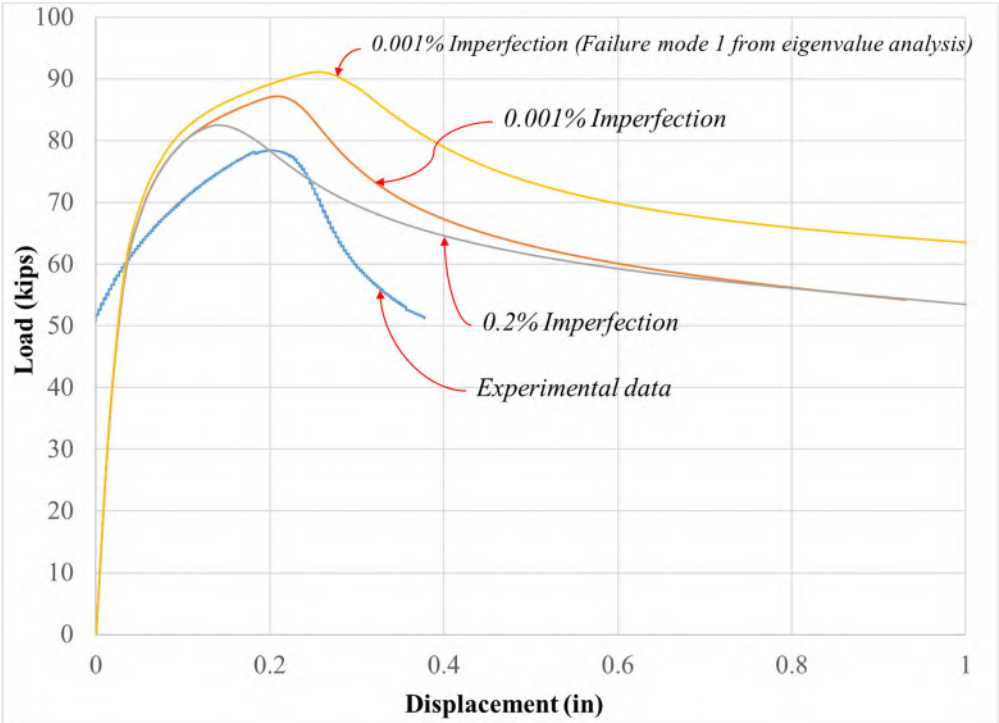

Figure 5.2-6: Comparison of analytical and experimental load-displacement relationships for the W10X19-DC-NA column specimen after shifting experimental displacement

5.2.2 W10X19-DC-E0

A finite element model was developed for W10X19-DC-E0, which represents the W10X19 column specimen tested in double compression and with concentric stiffeners at midspan. In general, the analytical results summarized in this section compare well with the experimental results when using the same analysis assumptions as used for W10X19-DC-NA.

Figure 5.2-7 shows a screenshot of the finite element model during elastic behavior. Stress concentrations are visible directly under the top loading plate and above the bottom reaction plate. The stresses are only slightly higher near the top plate in comparison to the bottom plate. This implies that not all of the force is reacted at the bottom support, but instead is also transferred to the end supports. However, the stresses in the top and bottom halves of the column are more similar in comparison to the equivalent analysis of the column specimen without stiffeners (W10X19-DC-NA) due to the presence of the concentric stiffeners and their ability to distribute the applied load through the member.

Stresses are well distributed through the stiffeners, which verifies the stiffeners are performing their intended purpose of sharing the concentrated load. Stresses in the stiffener are slightly higher at the top and bottom and near the tips of the flanges. A more uniform stress distribution exists near the center of the depth of the stiffener. This behavior is due to relative stiffness. The flanges are subjected to weak axis bending and the stiffener near the tip of the flange is therefore subjected to higher stresses since it takes the entire load (per unit length) from the loading plate above. Near mid-depth, the web and stiffeners develop approximately the same strain increment under loading and therefore have more uniform stresses. In addition, the load is more distributed in the web near mid-depth with respect to width.

Figure 5.2-8 shows the finite element model after inelastic deformations initiate. The grey area indicates stresses greater than 65.8 ksi. Inelastic deformations are shown to initiate in the flange close to the fillet in both the top and bottom of the column specimen. Higher stresses are also found in the web near the fillet. As witnessed during the experimental investigations, the top flange near the loading plate appears to be subjected to slightly more inelastic deformations.

Figure 5.2-9 shows a screenshot of the finite element model when the Von Mises stress reached its maximum magnitude and significant inelastic deformations occurred. This is also after the

maximum load was reached in the model. Failure was assumed to occur in the web portion under the load and in the stiffener as significant bending and buckling takes place at these two locations as they reach very high stresses.

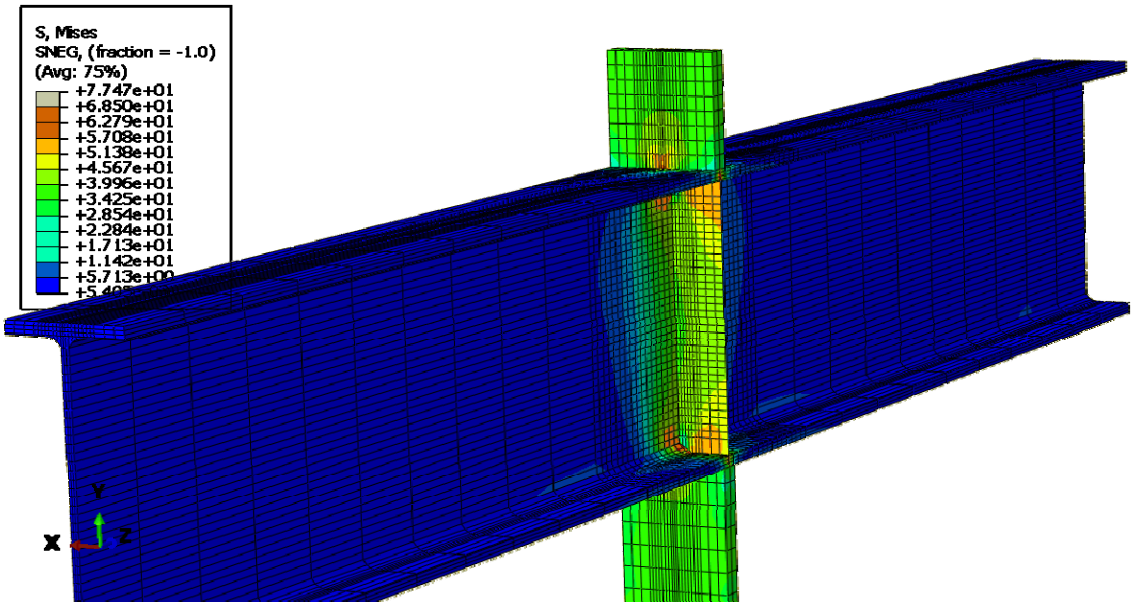

Figure 5.2-7: Finite element model of W10X19-DC-E0 during elastic behavior

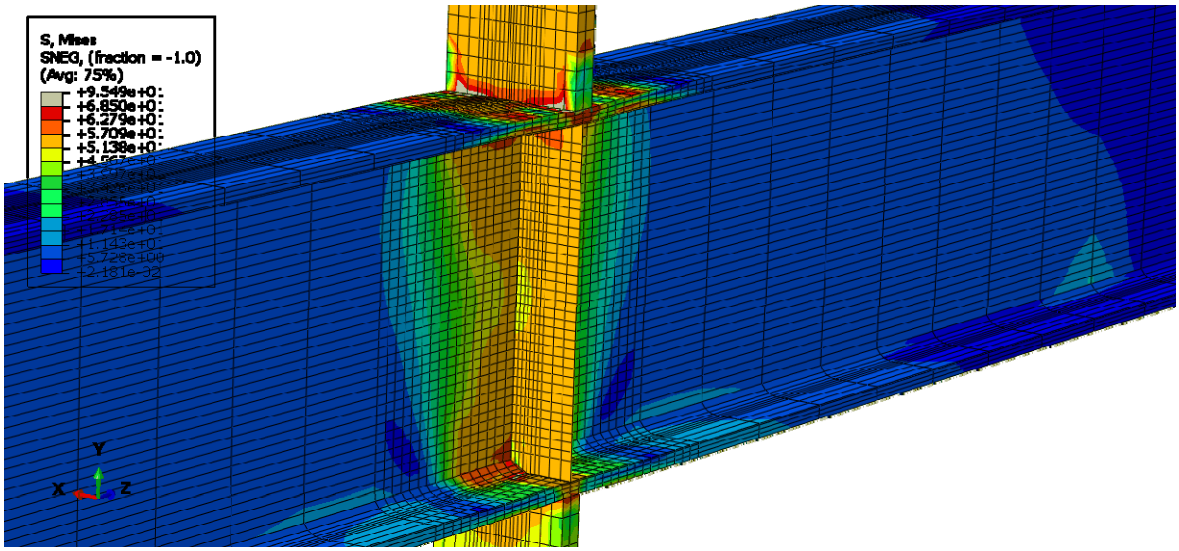

Figure 5.2-8: Finite element model of W10X19-DC-E0 during inelastic behavior

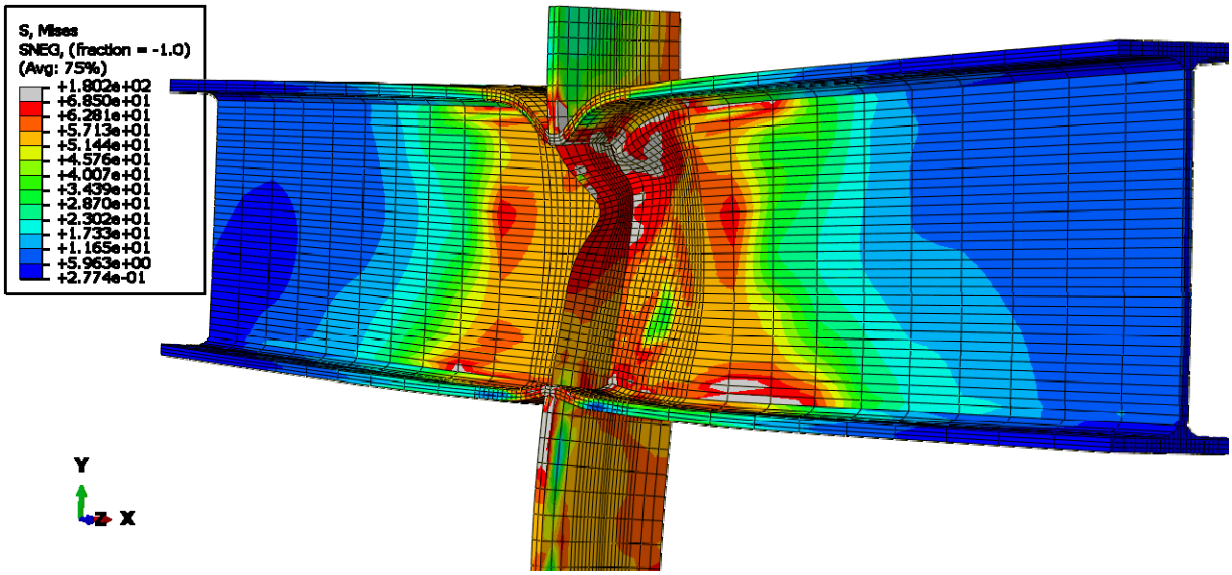

Figure 5.2-9: Finite element model of W10X19-SC-E0 near maximum load

The analytical maximum load of 184 kips is very close to the experimental load capacity of 180 kips. In addition, the failure mode and stress distribution in the stiffener, web, and flanges compare well to the behavior of the column specimen during experimental testing. The stresses were concentrated under the applied load and eventually, web yielding and stiffener buckling occurred.

The analytical and experimental load-displacement results are compared in Figure 5.2-10 after shifting the experimental displacement such that the maximum loads occurred at approximately the same displacement. The final analytical results are labeled "Static RIKS Analysis". The linear portion of the load-displacement relationship always varied between the analytical and experimental results. As explained in Section 4.6, the research team proved that the analytical elastic stiffness was indeed accurate and therefore, there are no concerns moving forward with this discrepancy.

During the calibration process, two different types of analysis options were used to study the column specimens particularly when concentric stiffeners were used; (1) a general *STATIC analysis, and (2) a *STATIC RIKS analysis (ABAQUS, 2014). The load-displacement results using both analytical analysis options are provided in Figure 5.2-10. As previously explained in Section 4.5.2, a *STATIC RIKS analysis is generally used to predict geometric non-linear collapse of a structure and it proved to provide more realistic results. In the *STATIC RIKS analysis, the column specimen reached a maximum load and then the load started to decrease, similar to the experimental behavior, which indicates a non-linear failure mechanism. In the general *STATIC analysis, the

load increased until the maximum stress-state was achieved and then the analysis terminated.

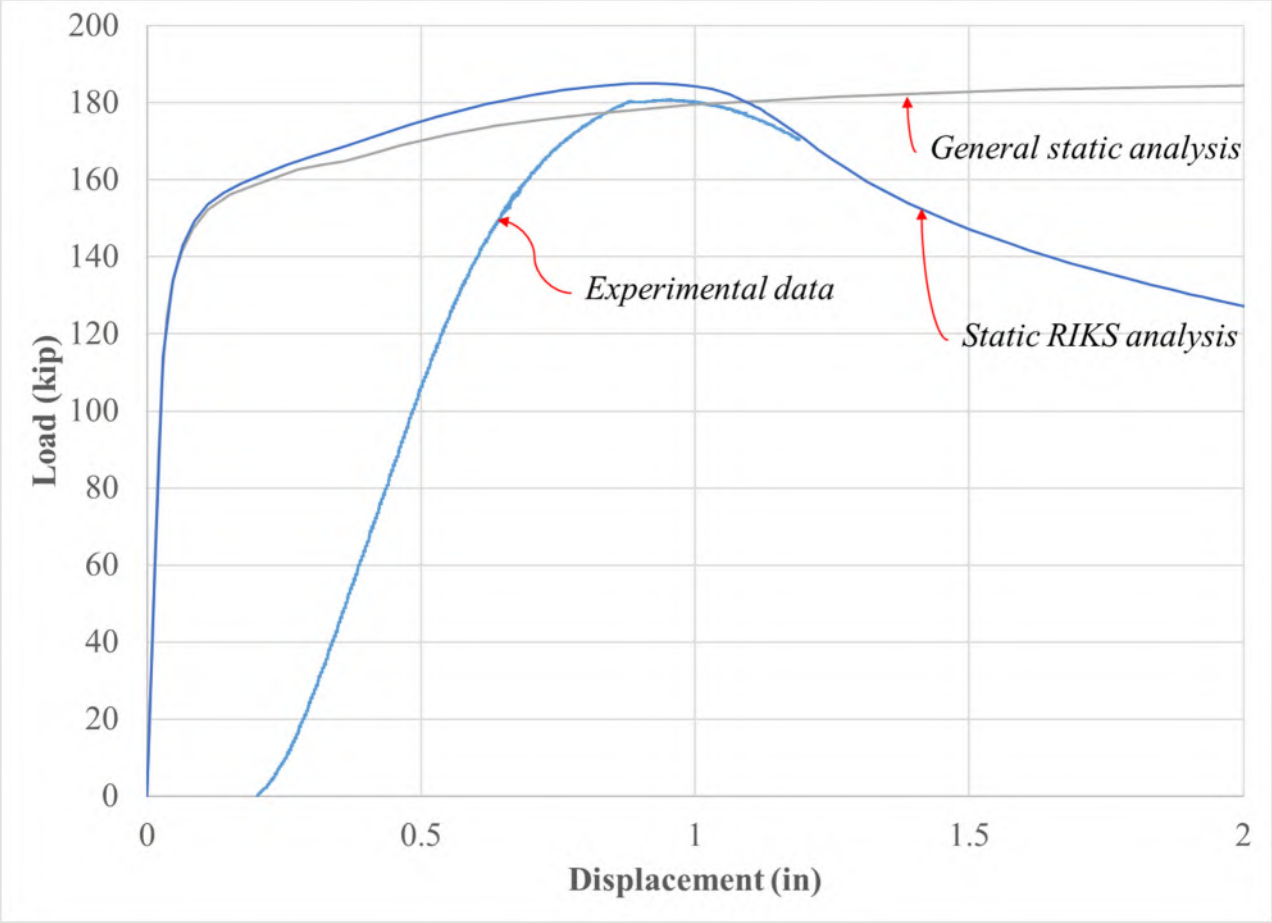

Figure 5.2-10: Comparison of analytical and experimental load-displacement relationships for the W10X19-DC-E0 column specimen

5.2.3 W12X26-DC-NA

A finite element model was developed for W12X26-DC-NA, which represents the W12X26 column specimen tested in double compression and without stiffeners at midspan. In general, the analytical results for this column specimen compare well with the experimental results.

Figure 5.2-11 shows a screenshot of the finite element model while it was still behaving elastic. As witnessed during the experimental investigations, stresses are higher in the flange and web near the top loading plate in comparison to the bottom loading plate. Under further loading, stress concentrations continue to develop in the web under the top loading plate and as inelastic deformations occur in the web, the top flange is subjected to flange bending.

Figure 5.2-12 shows the finite element model after inelastic deformations initiate in the web. The grey area indicates stresses greater than 66.9 ksi. As inelastic deformations progress, the stresses are different in both faces of the web, emphasizing that web crippling is occurring. The out-of-plane deformations in the web are more significant near the top flange as opposed to near the bottom flange.

In a similar manner to the experimental tests, the research team continued loading the column specimen after the maximum load had been reached to analyze the post-buckling behavior and the inelastic deformations in the column specimen. Figure 5.2-13 shows a screenshot of the finite element model after reaching the maximum load and after web crippling occurred. The failure shape shown is very similar to the failure shape witnessed during the experimental test for this particular column specimen as shown in Figure A-110 of Appendix A. Significant flange bending and crippling in the web underneath the loading plate took place.

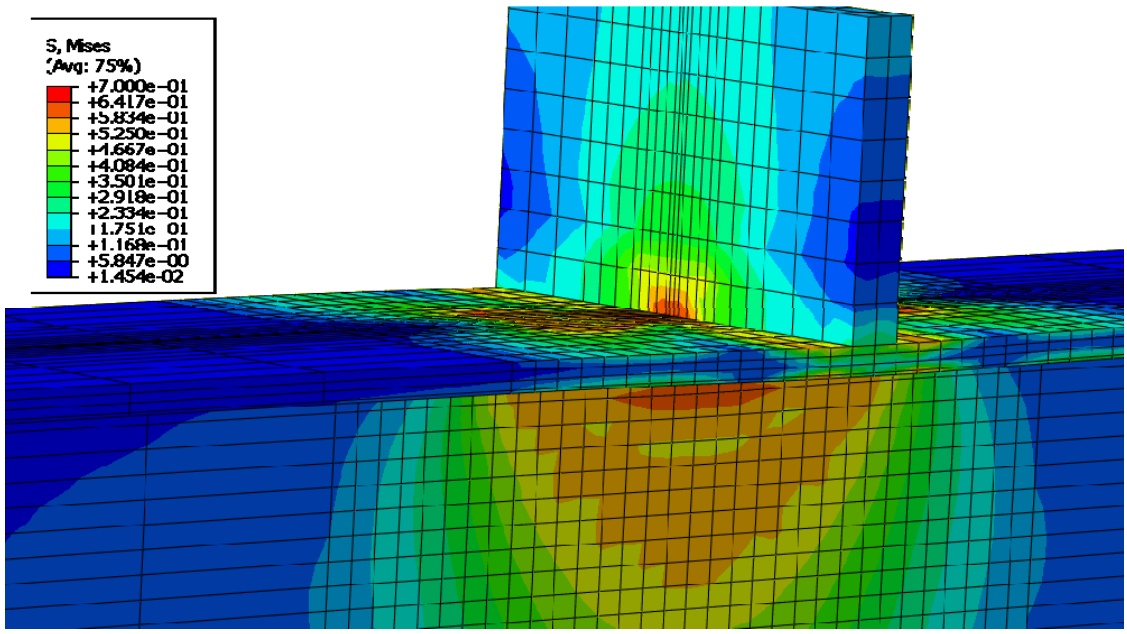

Figure 5.2-11: Finite element model of W12X26-DC-NA during elastic behavior

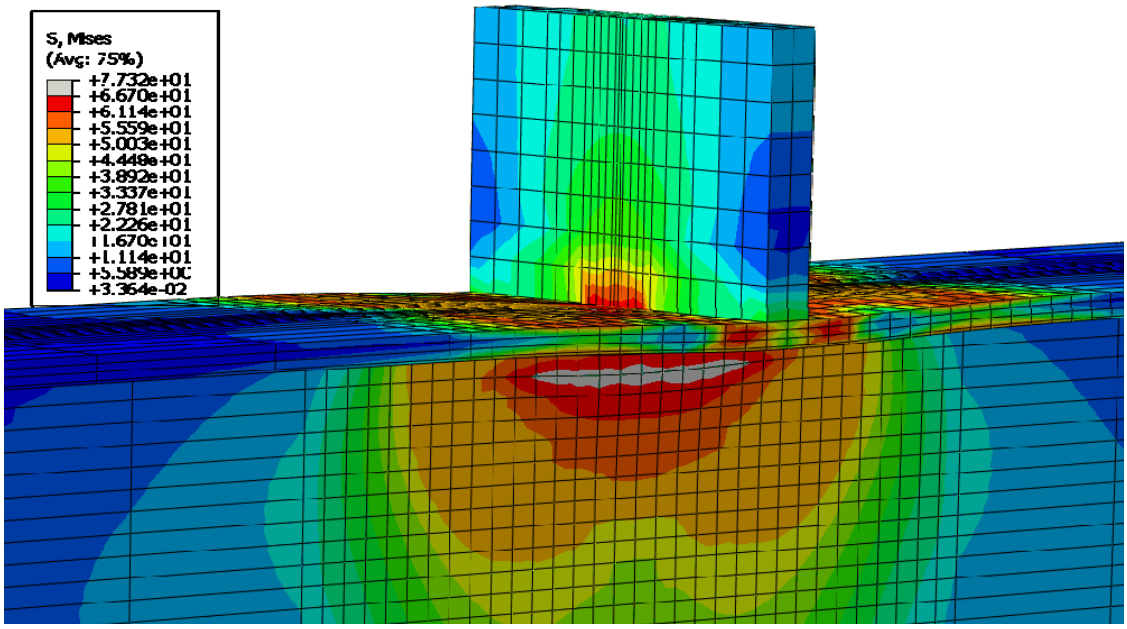

Figure 5.2-12: Finite element model of W12X26-DC-NA during inelastic behavior

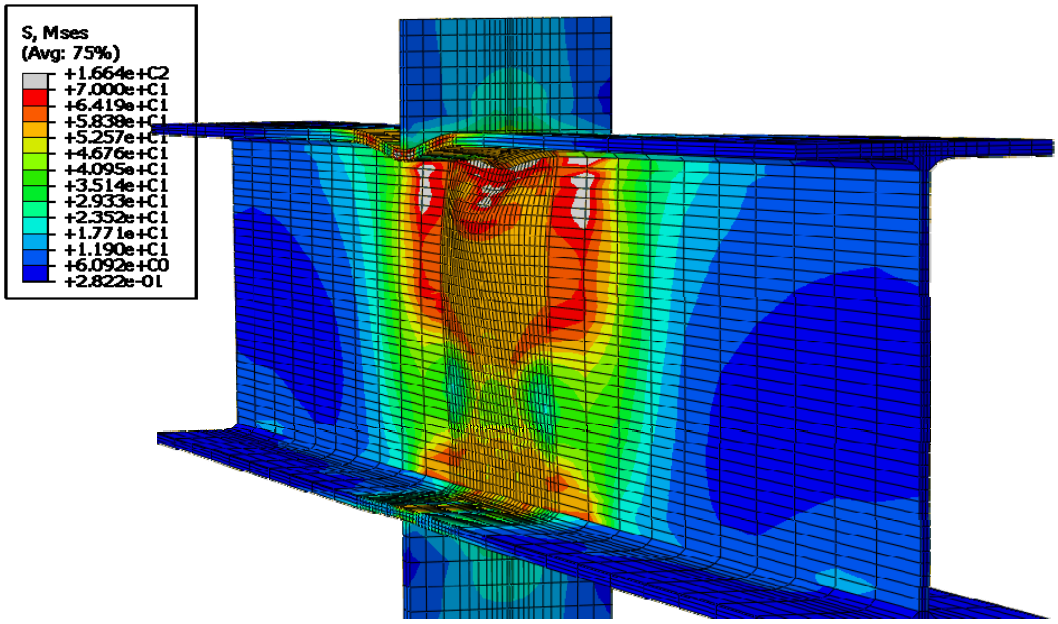

Figure 5.2-13: Finite element model of W12X26-DC-NA after web crippling occurred

The analytical results compare well to the experimental results. The predicted analytical capacity of 87.9 kips compares favorably to the experimental capacity of 86.3 kips. In addition, the failure mode and stress distribution in the flanges and web compares well with the behavior witnessed during the experimental test in that the stresses were concentrated in the web under the top loading plate, which produced the web crippling effect.

The analytical and experimental load-displacement results are compared in Figure 5.2-14 after shifting the experimental displacement such that the maximum loads occurred at approximately the same displacement. Two analysis were performed with either a 0.2% imperfection or a 0.001% imperfection. As shown in Figure 5.1-14, the analytical results compare well with the experimental results when an imperfection equal to 0.001% of the buckled shape from the eigenvalue analysis is used.

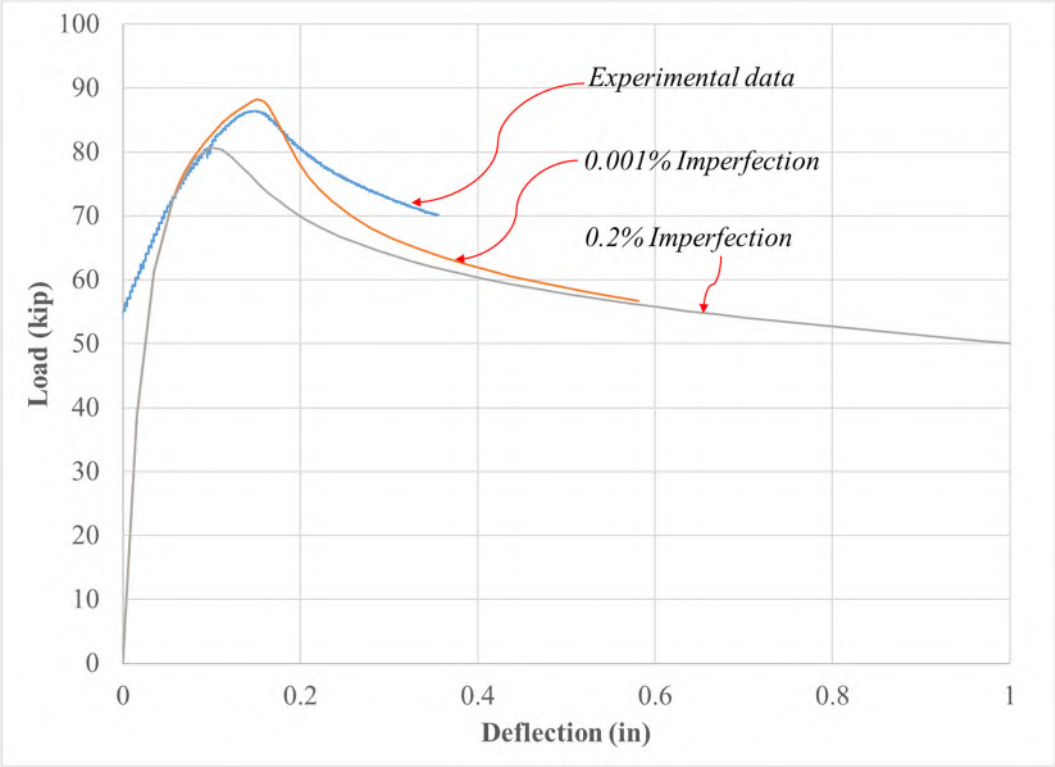

Figure 5.2-14: Comparison of analytical and experimental load-displacement relationships for the W12X26-DC-NA column specimen

5.2.4 W12X26-DC-E0

A finite element model was developed for W12X26-DC-NA, which represents the W12X26 column specimen tested in double compression and with concentric stiffeners at midspan. Once again, in general, the analytical results for this column specimen compare well with the experimental results.

Figure 5.2-15 shows a screenshot of the finite element model while it was behaving elastic. Stresses are slightly higher near the top loading plate in comparison to the bottom reaction plate. The stresses in the web are relatively uniform through the depth of the member, which is dissimilar to

the analytical results of the equivalent column specimen without stiffeners (W12X26-DC-NA). The presence of concentric stiffeners and their axial load capacity allows the load to effectively transfer though the web of the member. The stress distribution in the stiffeners is somewhat uneven as more stress is concentrated near the flanges of the column specimen.

Figure 5.2-16 shows the finite element model after the column specimen initiates inelastic behavior. The grey area indicates stresses greater than 66.3 ksi. Inelastic deformations are shown to initiate in the flange region close to the fillet in both the top and bottom of the column specimen. Figure 5.2-17 shows the finite element model under further loading and when the column specimens exhibits further inelastic deformations. As further inelastic deformations develop, there are more differences in the stress distribution near the top of the column specimen in comparison to the bottom of the column specimen. This suggests that as higher load/displacement is applied, a higher percentage of the load is transferred to the end supports.

Figure 5.2-18 shows a screenshot of the finite element model after reaching the maximum load and after stiffener buckling occurred. Significant flange bending is also identified in Figure 5.2-18. The experimental test column did not reach a maximum load prior to reaching the capacity of the hydraulic actuator. However, the stiffener buckling shown in the analytical results was witnessed during other experimental tests with concentric stiffeners such as the W10X19-DC-E0 column specimen.

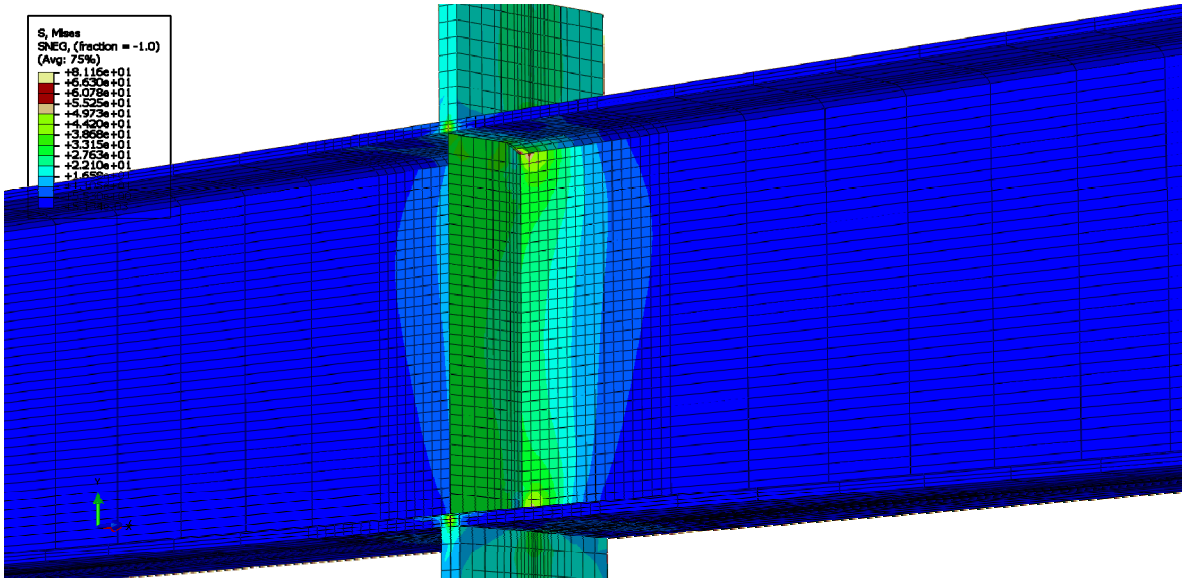

Figure 5.2-15: Finite element model of W12X26-DC-E0 during elastic behavior

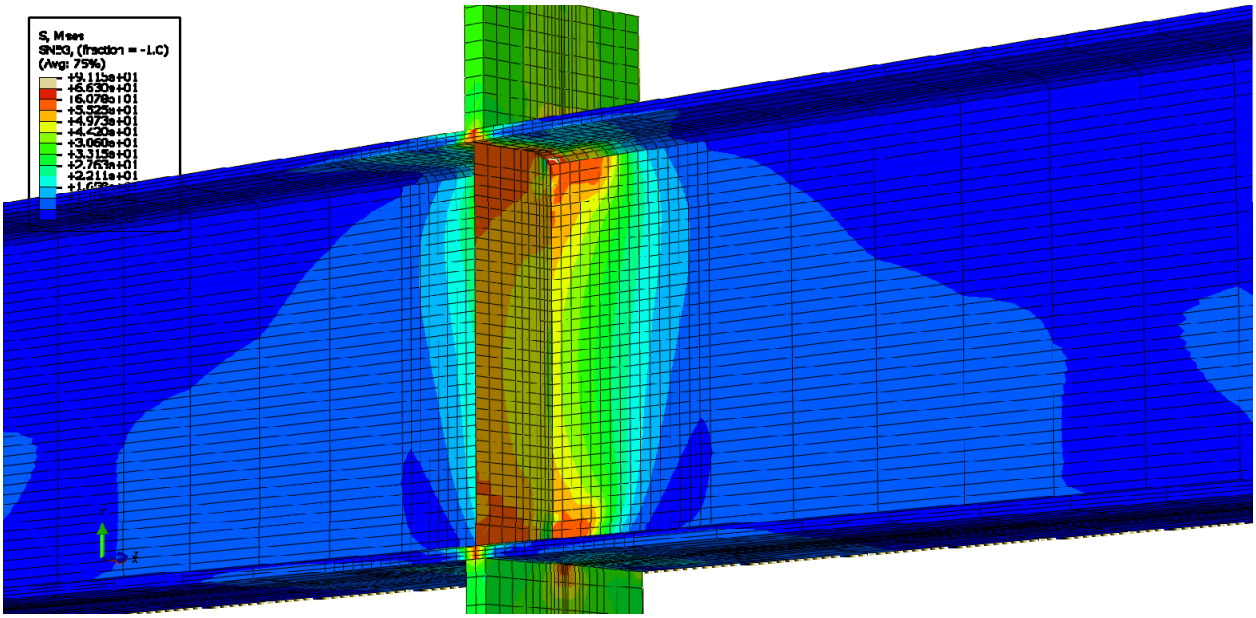

Figure 5.2-16: Finite element model of W12X26-DC-E0 during inelastic behavior

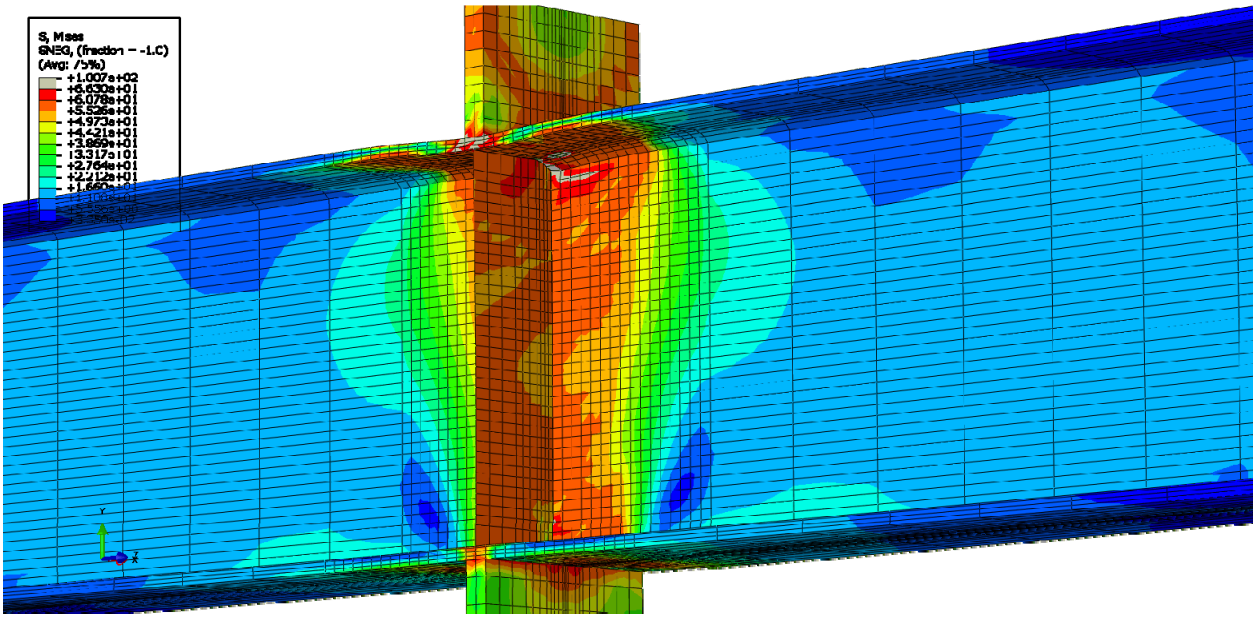

Figure 5.2-17: Finite element model of W12X26-DC-E0 with more inelastic behavior

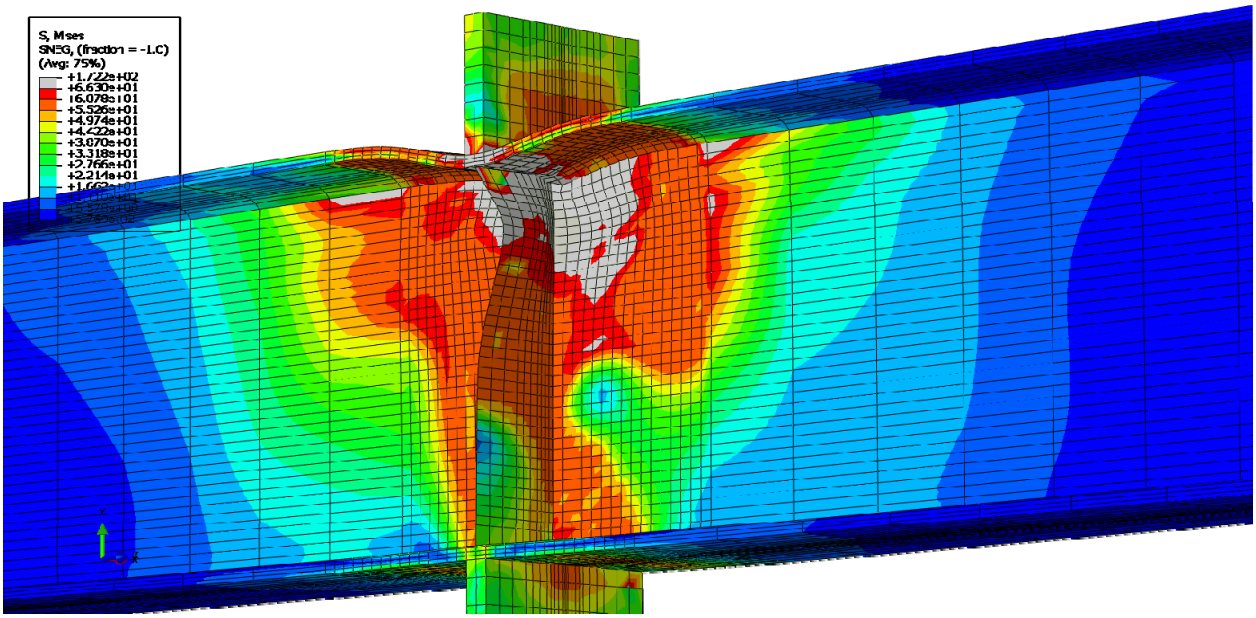

Figure 5.2-18: Finite element model of W12X26-DC-E0 after stiffener buckling

Figure 5.2-19 shows a comparison of the load-displacement experimental and analytical results. The experimental test reached the maximum capacity of the loading actuator at 220 kips. The linear portion of the load-displacement relationship is different between the analytical and experimental results as discussed in Section 4.6. The elastic stiffness for both analytical and experimental results is also shown with straight lines starting at the origin. For this column specimen analysis, two different analysis methods were evaluated during the calibration process; (1) a general *STATIC analysis and (2) a *STATIC RIKS analysis (ABAQUS, 2014). As explained in Section 4.5.2, a *STATIC RIKS analysis is generally used to predict geometric non-linear collapse of a structure and it is assumed to provide more realistic results since it was able to capture stiffener buckling. From the experimental results, the column specimen starts showing inelastic behavior at around 175 kips, which compares relatively well to 160 kips from the analytical results.

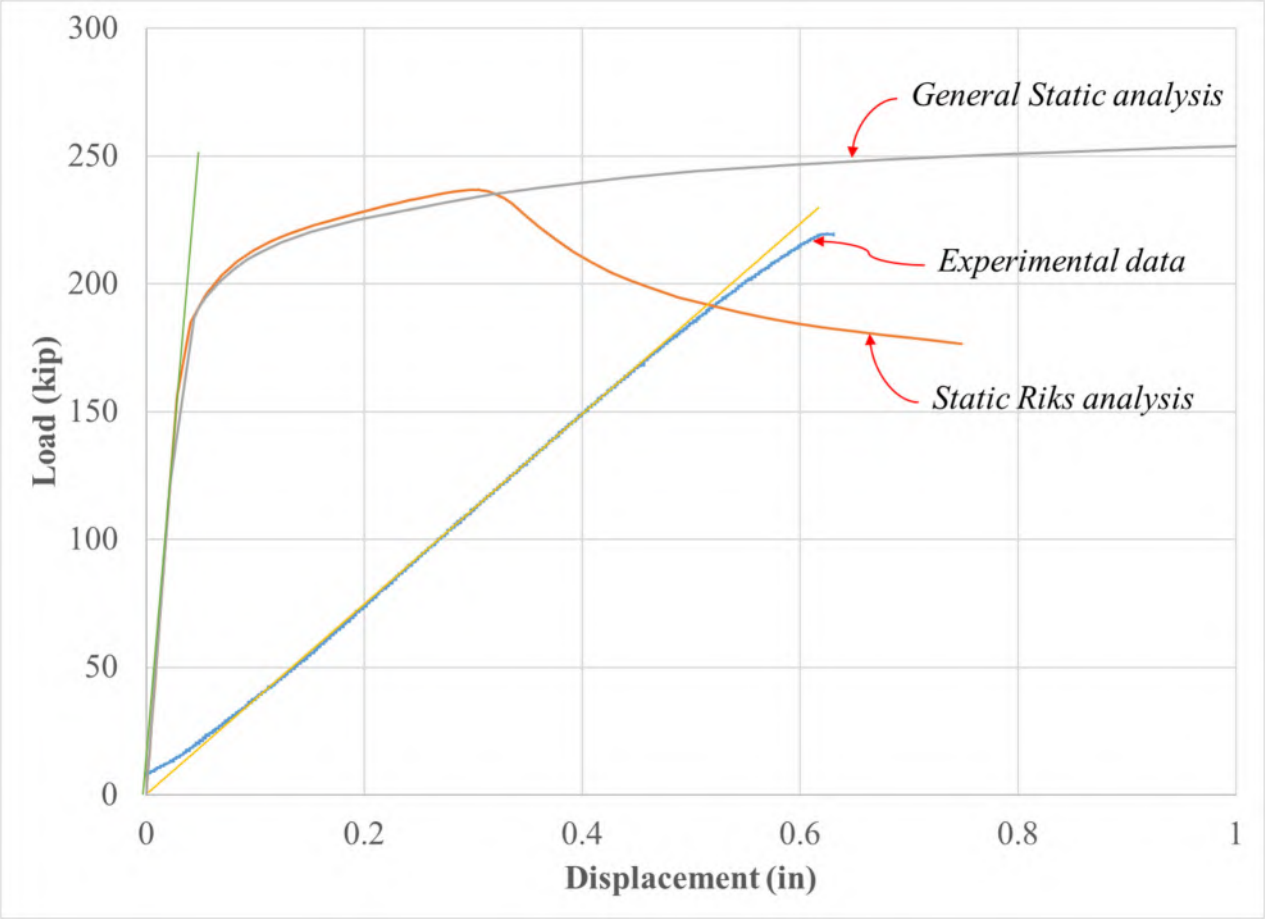

Figure 5.2-19: Comparison of analytical and experimental load-displacement relationships for the W12X26-DC-E0 column specimen

5.2.5 W12X26-DC-E4

A finite element model was developed for W12X26-DC-E4, which represents the W12X26 column specimen tested in double compression and with stiffeners 4 in. eccentric from the location of the applied load.

Figure 5.2-20 shows a screenshot of the finite element model while it was still behaving elastic. Similar to conclusions made during the experimental results, the eccentric stiffeners appear ineffective in sharing the concentrated load. The stresses are concentrated in the web and flanges near the top loading plate and bottom reaction plate. Similar to other double compression tests, the stresses are slightly higher near the top loading plate in comparison to near the bottom reaction plate, suggesting that some of the load is transferred to the end supports even when the model is behaving elastic. In the concentric stiffener analysis from Section 5.2.4, the stiffeners provided a more direct

force transfer from the top to bottom plates, particularly when behaving elastic. As further load is applied, stress concentrations increased in the web adjacent to both plates.

Figure 5.2-21 shows the finite element model after inelastic deformations initiate. The grey area indicates stresses beyond 66.3 ksi. As inelastic deformations initiate, the web stresses are different on both faces of the web, indicating that web crippling is occurring similar to the finite element model without stiffeners as discussed in Section 5.2.3. In addition, the concentrated stresses are more localized near the top loading plate as opposed to the bottom reaction plate. The results imply that failure occurs in the web underneath the top loading plate.

Similar to the experimental tests, the analytical models were loaded after crippling occurred to analyze the post-buckling behavior and the inelastic deformations that develop in the column specimen. Figure 5.2-21 shows a screenshot of the finite element model after web crippling occurred. The failure shape is very similar to the failure shape for the same column size without stiffener (W12X26-DC-NA), which further supports the conclusion that eccentric stiffeners are ineffective in sharing the concentrated load. Significant flange bending and crippling in the web underneath the loading plate are clearly visible in Figure 5.2-22.

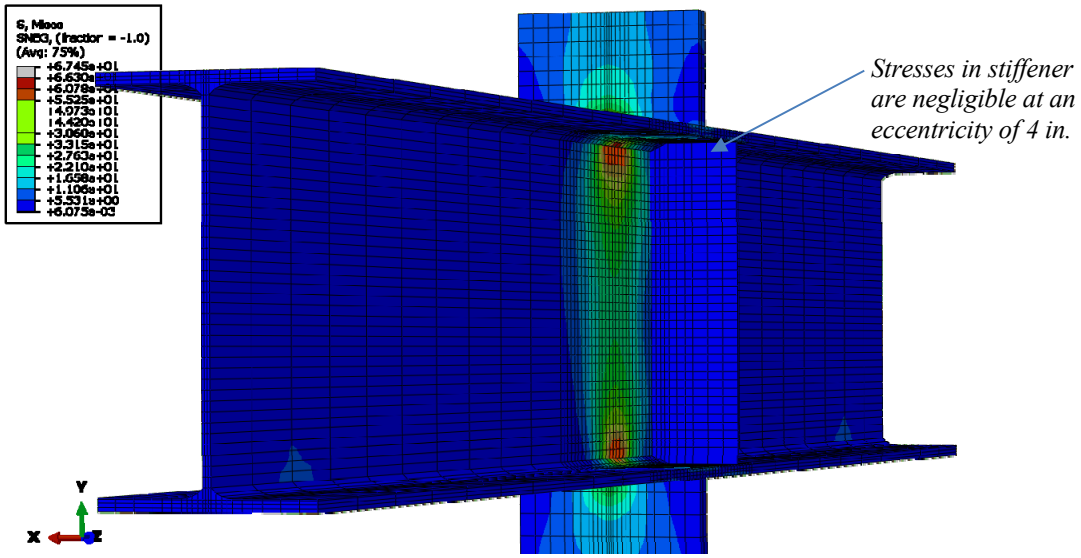

Figure 5.2-20: Finite element model of W12X26-DC-E4 during elastic behavior

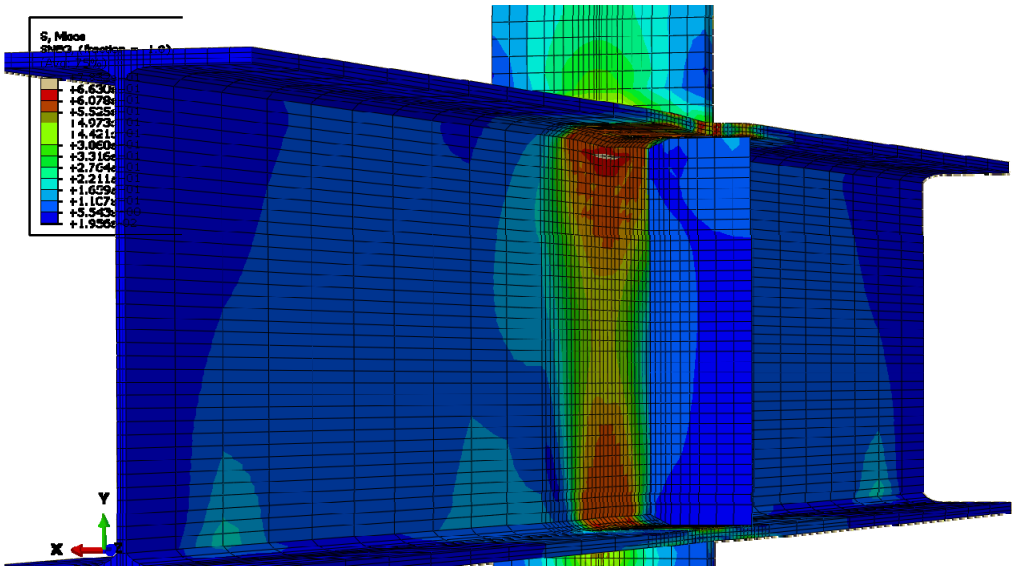

Figure 5.2-21: Finite element model of W12X26-DC-E4 during inelastic behavior

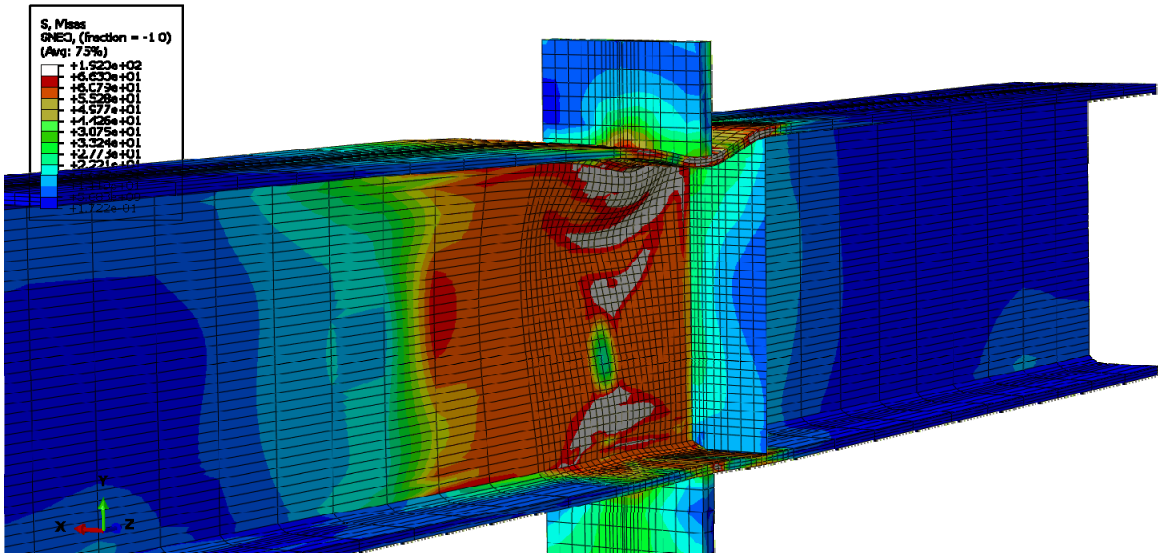

Figure 5.2-22: Finite element model of W12X26-DC-E4 after web crippling

The results of the finite element model compare fairly well to the experimental results. The predicted analytical capacity of 99.4 kips is relatively close to the experimental load capacity of 90.5 kips. In addition, the failure mode and stress distribution in the flanges and web compare well with the behavior witnessed during the experimental test in that the stresses were concentrated in the web under the loading plate producing web crippling.

The analytical and experimental load-displacement results are compared in Figure 5.2-23 after shifting the experimental displacement such that the maximum loads occur at approximately the

same displacement even though only a small shift was necessary for this column specimen. The analytical results are labeled “Static RIKS Analysis”. The shapes of the load-displacement curves is noticeably different between the analytical and experimental results. For the analytical condition, it appears that more inelastic deformations occur prior to web crippling but when it occurs, both cases suggest a sudden decrease in load.

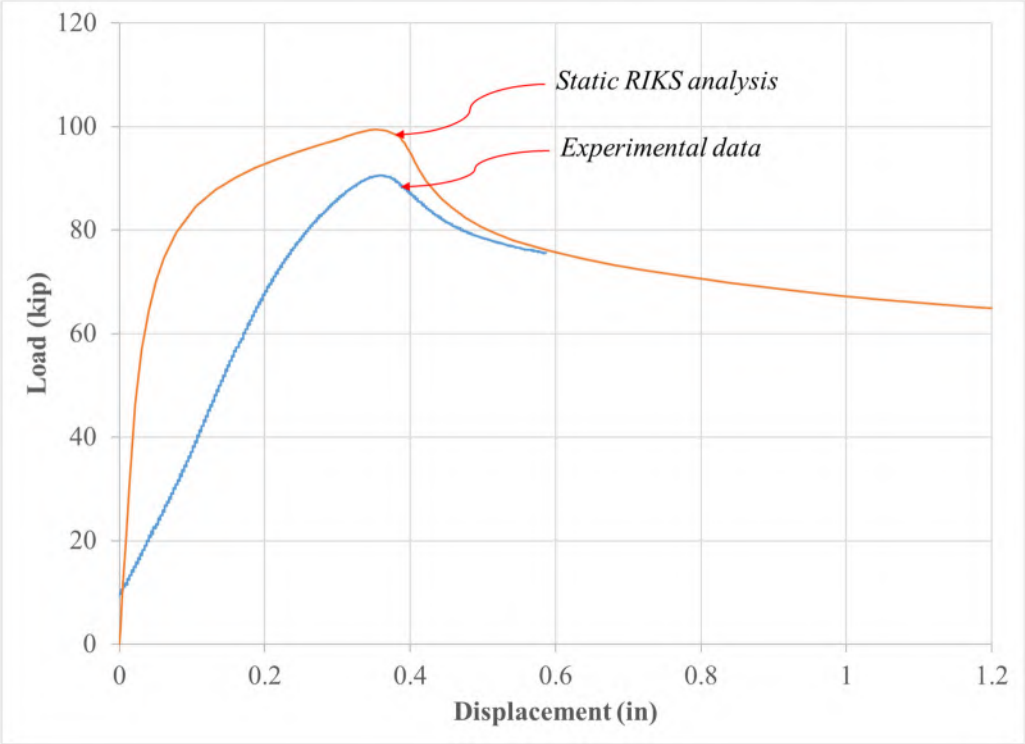

Figure 5.2-23: Comparison of analytical and experimental load-displacement relationships for the W12X26-DC-E4 column specimen

5.2.6 W16X31-DC-NA

A finite element model was developed for W16X31-DC-NA, which represents the W16X31 column specimen tested in double compression and without stiffeners at midspan. Figure 5.2-24 shows a screenshot of the finite element model while it was still behaving elastic. As concluded during the experimental investigations, the stresses are higher in the flange and web directly under the applied load and higher near the top loading plate as opposed to the bottom reaction plate.

Figure 5.2-25 shows the finite element model after inelastic deformations initiate in the web. The grey area indicates stresses greater than 68.3 ksi. As inelastic deformations initiate, the stresses in the web are slightly offset in both faces of the web, which indicates that web crippling is occurring.

The column specimen was loaded after the maximum load was reached to analyze the post-buckling behavior and the inelastic deformations in the specimen. Figure 5.2-26 shows a screenshot of the finite element model beyond the maximum load and after web crippling occurred. The failure mode and deformed shape are very similar to that witnessed during the experimental investigations for this particular column specimen. Significant flange bending and crippling in the web underneath the loading plate are clearly visible in Figure 5.2-26.

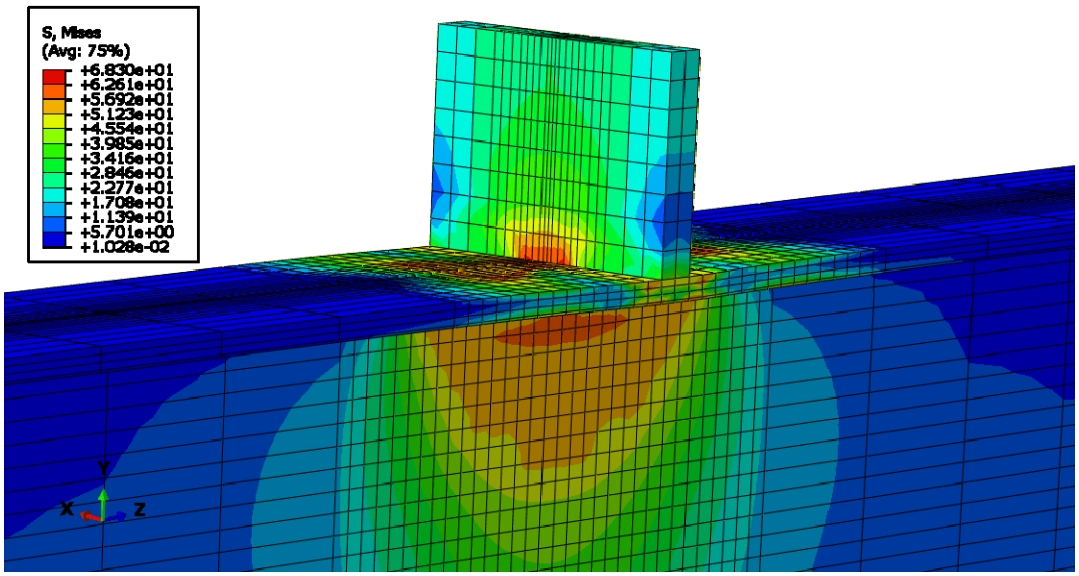

Figure 5.2-24: Finite element model of W16X31-DC-NA during elastic behavior

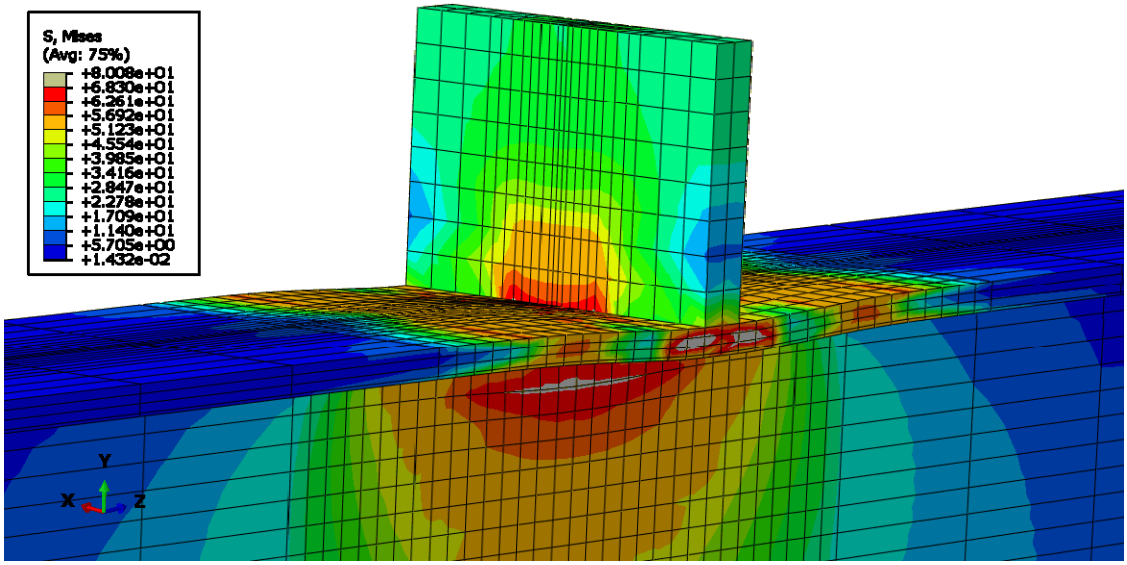

Figure 5.2-25: Finite element model of W16X31-DC-NA during inelastic behavior

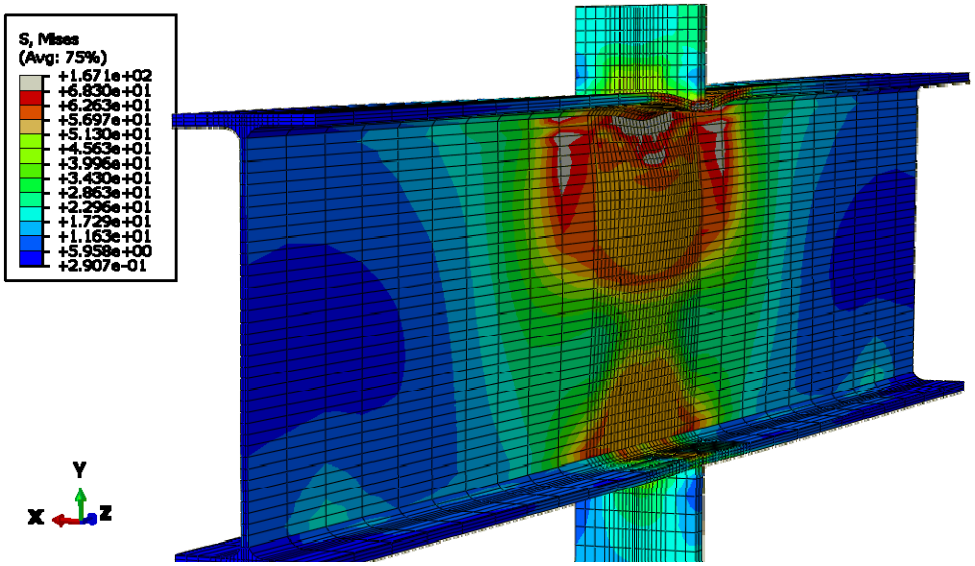

Figure 5.2-26: Finite element model of W12X26-DC-NA showing web crippling

The results of the finite element model compare well to the experimental results. The predicted analytical capacity of 115 kips compares well to the experimental capacity of 121 kips. In addition, the failure mode and stress distribution in the flanges and web compare well with the behavior witnessed during the experimental investigations in that the stresses were concentrated in the web under the loading plate, producing web crippling.

The analytical and experimental load-displacement results are compared in Figure 5.2-27 after shifting the experimental displacement such that the maximum loads occurred at approximately the same displacement. Three analyses were performed overall with different imperfection conditions. As shown in Figure 5.2-27, the analytical results compare well with the experimental results when an imperfection equal to 0.001% of the buckled shape from the eigenvalue analysis is used.

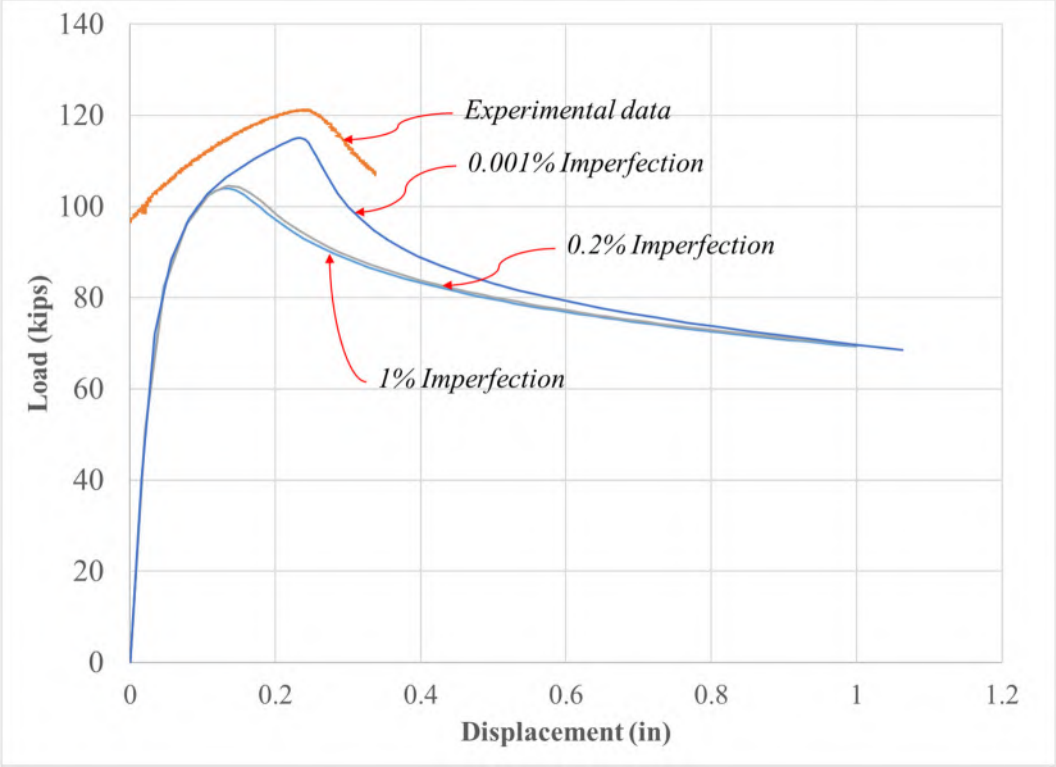

Figure 5.2-27: Comparison of analytical and experimental load-displacement relationships for the W16X31-DC-NA column specimen

5.3 Single Compression Tests

This section provides a detailed discussion of the finite element models developed to represent the experimental column specimens subjected to single compression. Four column sizes were tested experimentally. However, only two sizes were utilized for the analytical investigations. Overall, the following column specimens were evaluated analytically and discussed in the following subsections:

- W10X39-SC-NS
- W10X39-SC-E0
- W12X26-SC-NS
- W12X26-SC-E0
- W12X26-SC-E4

The methodology discussed in Chapter 4 was used for all column specimens. All single compression tests were modeled with the column specimens simply supported at 5 ft. For all models,

bearing stiffeners were used at each end support and on both sides of the column specimen.

Similar to the double compression tests, the best results were obtained by modeling the column specimens with an imperfection of 0.001% of the buckled shape from the eigenvalue analysis and using the *STATIC RIKS analysis option (ABAQUS, 2014). For models without concentric stiffeners, the finite element screenshots represent models with these conditions as the final analytical models used for the column specimens. However, for the analytical models of columns specimens with concentric stiffeners, the experimental results did not show buckling in the web under the load and therefore, no imperfection was specified in the finite element models.

5.3.1 W10X39-SC-NA

A finite element model was developed for W10X39-SC-NA, which represents the W10X39 column specimen tested in single compression and without stiffeners at midspan. Figure 5.3-1 shows a screenshot of the finite element model while it was still behaving elastic and scaled to a deformation of 1X (actual scale, which is used for all finite element screenshots of single compression models). The stresses are higher in the flange and web directly under the concentrated load. There is also signs of flange bending under the elastic load, which is similar to that witnessed during the experimental investigations.

Figure 5.3-2 shows the finite element model after inelastic deformations initiate under the loading plate, including in the top flange and the web near the fillet. The grey area indicates stresses beyond the ultimate stress, which was specified as 66.5 ksi. Similar to that discussed for the double compression tests, the stresses in the web are slightly offset on both faces, which indicates web crippling is occurring.

Figure 5.3-3 shows a screenshot of the finite element model after web crippling occurred and after the maximum load was reached. The deformations shown are very similar to the deformations witnessed during the experimental test of this column specimen as shown in Figure A-39 of Appendix A. Significant flange bending and crippling in the web underneath the loading plate take place.

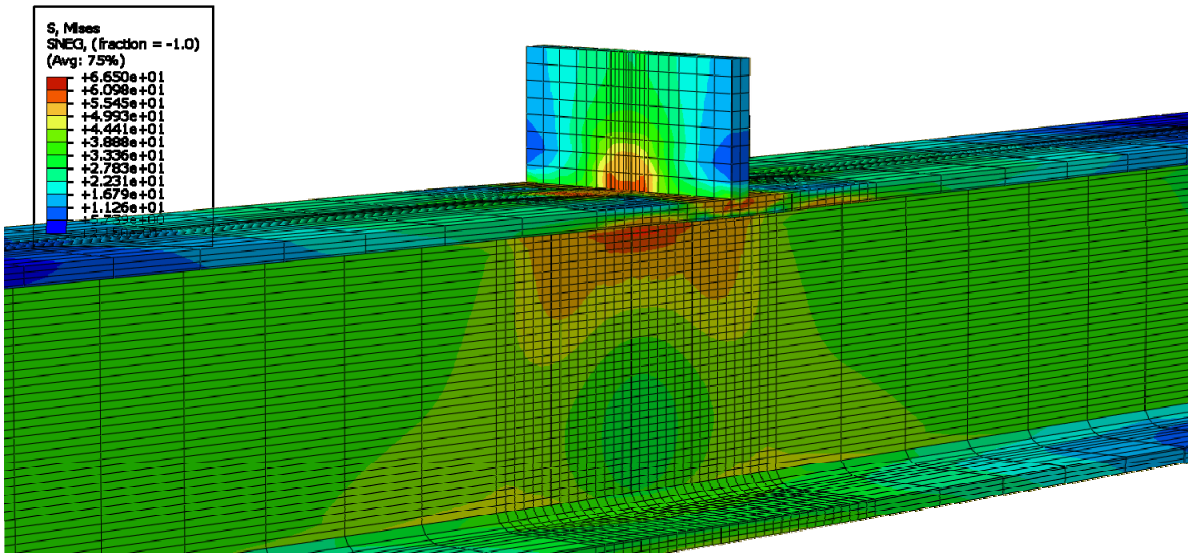

Figure 5.3-1: Finite element model of W10X39-SC-NA during elastic behavior

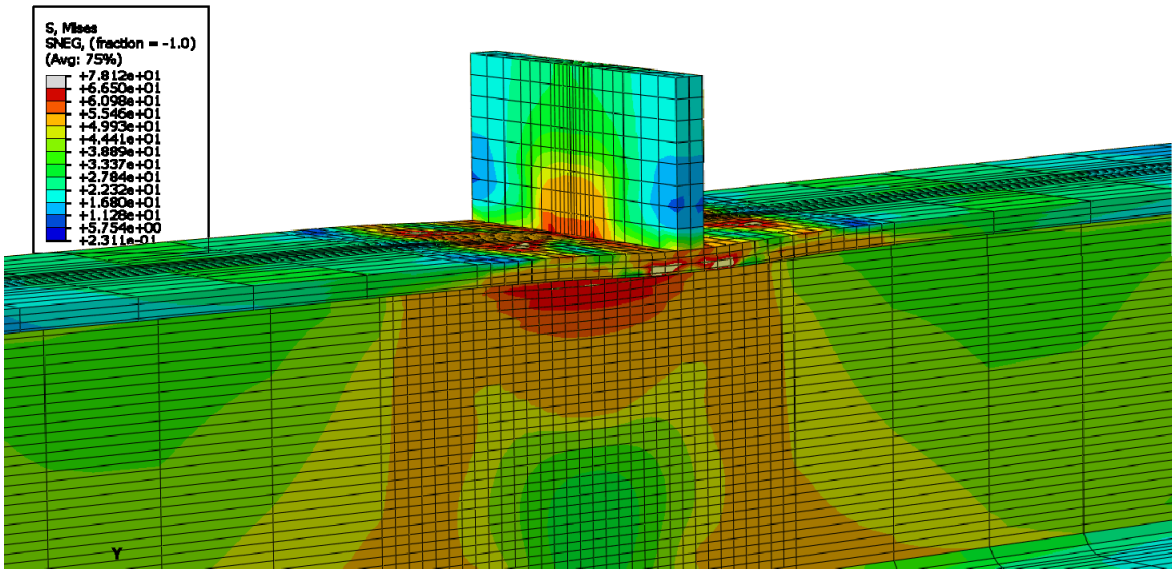

Figure 5.3-2: Finite element model of W10X39-SC-NA during inelastic behavior

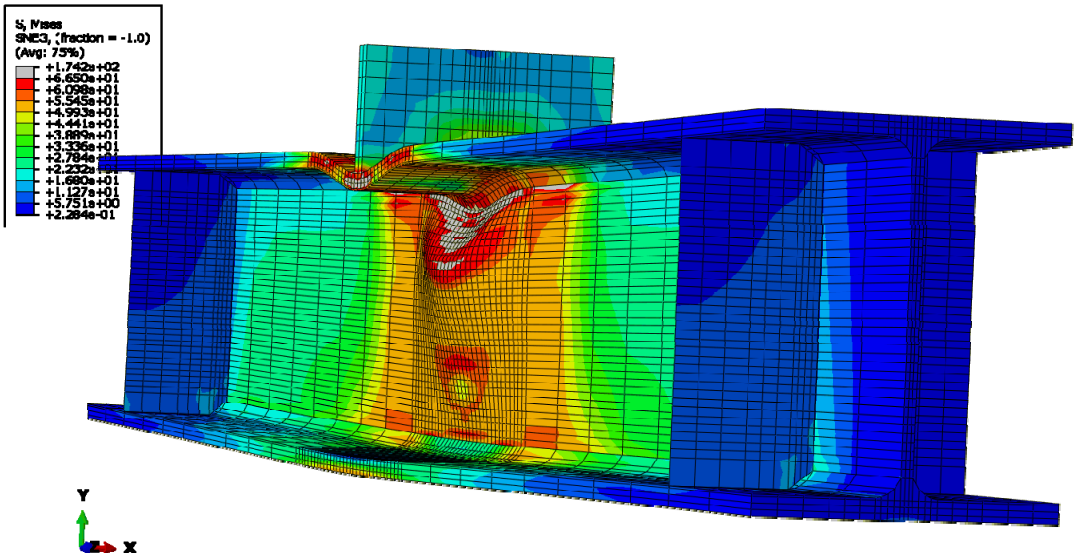

Figure 5.3-3: Finite element model of W10X39-SC-NA after web crippling occurs

The analytical results compared well with the experimental results for this column specimen. The predicted analytical capacity of 128.8 kips is close to the experimental capacity of 130.9 kips. In addition, the failure mode and stress distribution in the flanges and web compares well to the conditions witnessed during the experimental test.

The analytical and experimental load-displacement relationships are compared in Figure 5.3-4. Overall, five analytical models were developed for this column specimen; each with a different imperfection condition. The linear portion of the load-displacement relationship is significantly different between analytical and experimental results, which was discussed in Section 4.6. Figure 5.3-5 shows comparative results after shifting the experimental displacement, which shows the maximum loads for the analytical and experimental results at approximately the same displacement. In Figures 5.3-4 and 5.3-5, the analytical results obtained without imperfection and with imperfections of 0.001%, 0.2%, 1%, and 30% are shown. The results with no imperfection and the results with an imperfection of 0.001% compare well with the experimental results. However, only one imperfection condition is utilized for further studies of larger column sections and using a 0.001% imperfection provided good consistency between the analytical and experimental results for all single compression tests without concentric stiffeners.

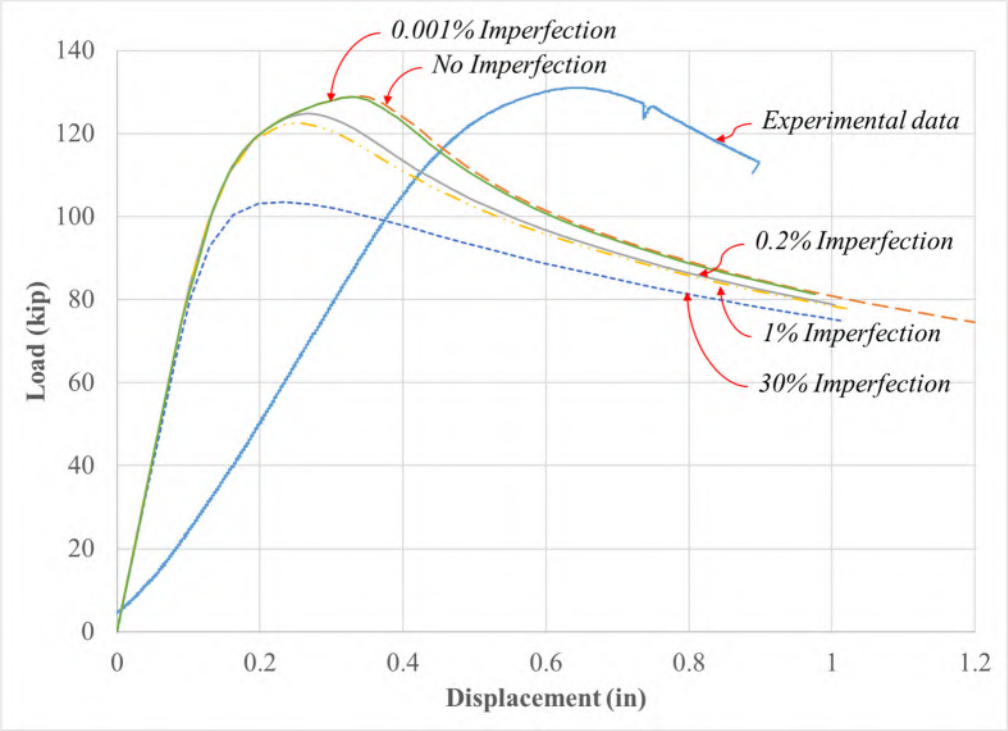

Figure 5.3-4: Comparison of analytical and experimental load-displacement relationships for the W10X39-SC-NA column specimen

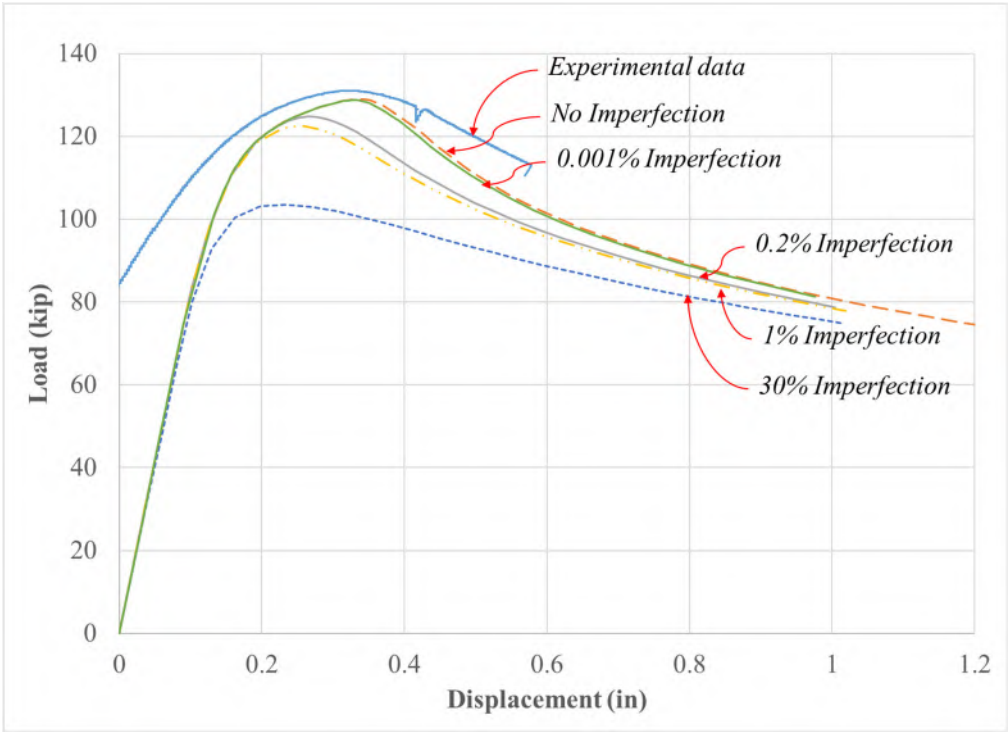

Figure 5.3-5: Comparison of analytical and experimental load-displacement relationships for the W10X39-SC-NA column specimen after shifting experimental displacement

5.3.2 W10X39-SC–E0

A finite element model was developed for W10X39-SC-E0, which represents the W10X39 column specimen tested in single compression and with concentric stiffeners. In general, the analytical results compared fair with the experimental results and there are some discrepancies discussed in this section.

Figure 5.3-6 shows a screenshot of the finite element model when behaving elastic. Stresses are slightly concentrated near the top loading plate. However, in comparison to the W10X39 column specimen without stiffeners, the stresses are better distributed through the depth of the web and significant stresses are also observed in the stiffeners, indicating they serve the intended purpose of sharing the concentrated load. As further load is applied, stresses become more concentrated in the web near the top loading plate, in the top flange near to the applied load, and in the top of the stiffeners.

Dissimilar from the analytical models of double compression specimens with concentric stiffeners, significant flange bending of the top flange on both sides of the applied load was seen in the finite element results. Figure 5.3-7 shows the finite element model after inelastic deformations initiate. The grey area indicates stresses greater than 66.5 ksi. Inelastic deformations are shown to initiate in the top flange close to the applied load and in the fillet of the wide flange section.

Figure 5.3-8 shows the finite element model at the maximum stress state and after significant inelastic deformations occurred. Both the top and bottom flanges are subjected to significant inelastic deformations. The screenshot is shown after reaching the maximum load. However, a clear buckling mode of failure is not visible.

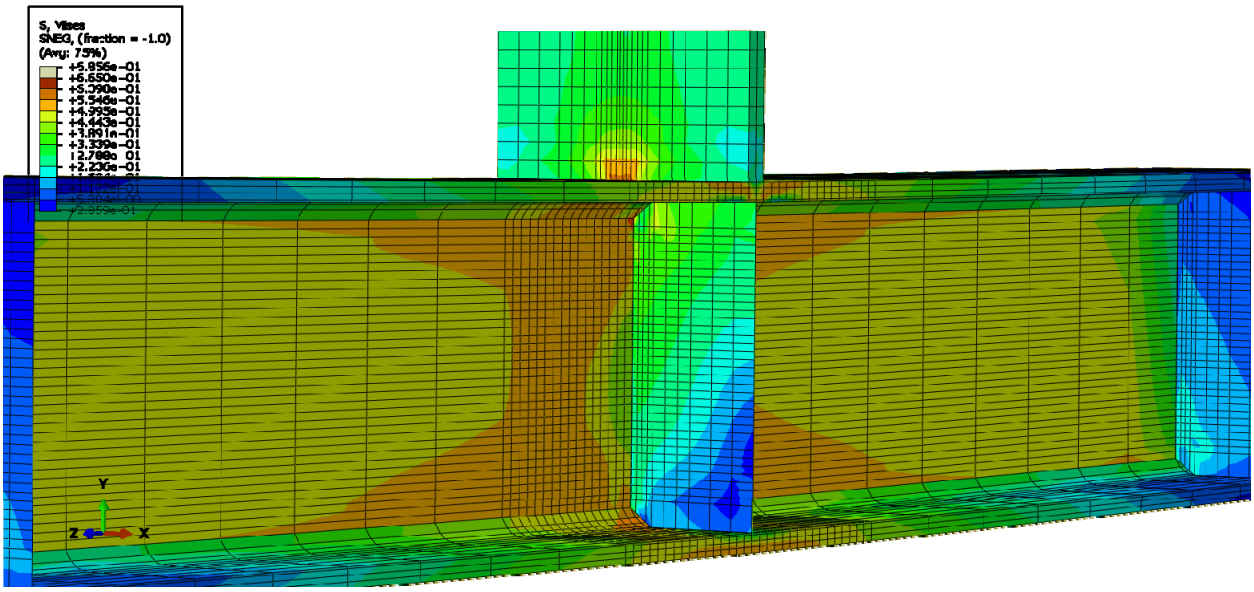

Figure 5.3-6: Finite element model of W10X39-SC-E0 during elastic behavior

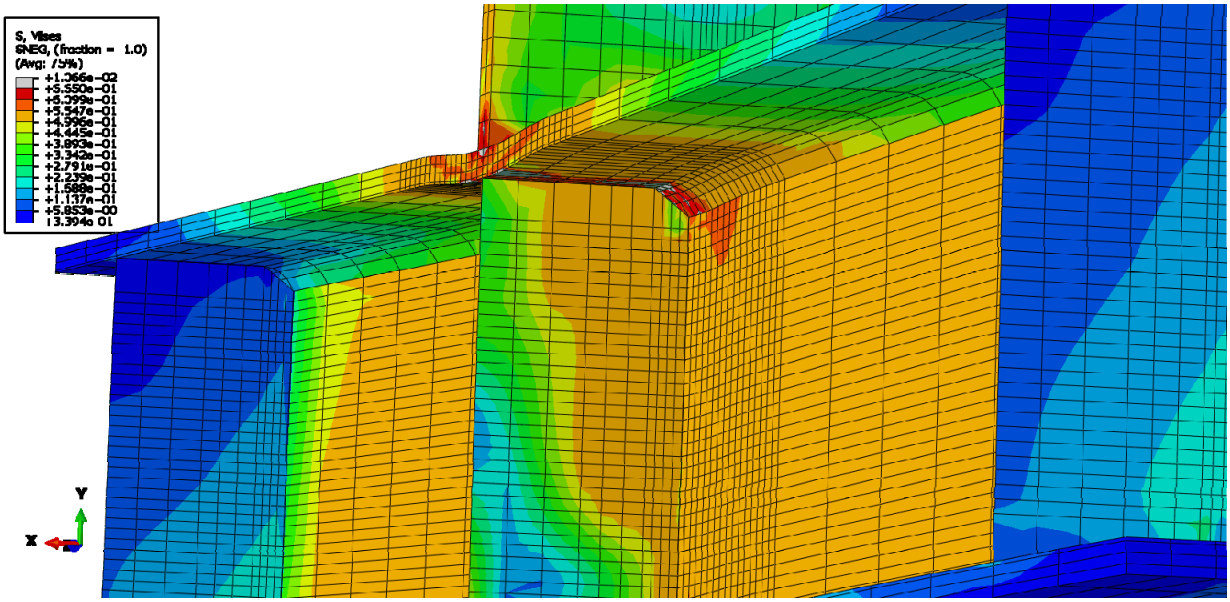

Figure 5.3-7: Finite element model of W10X39-SC-E0 during inelastic behavior

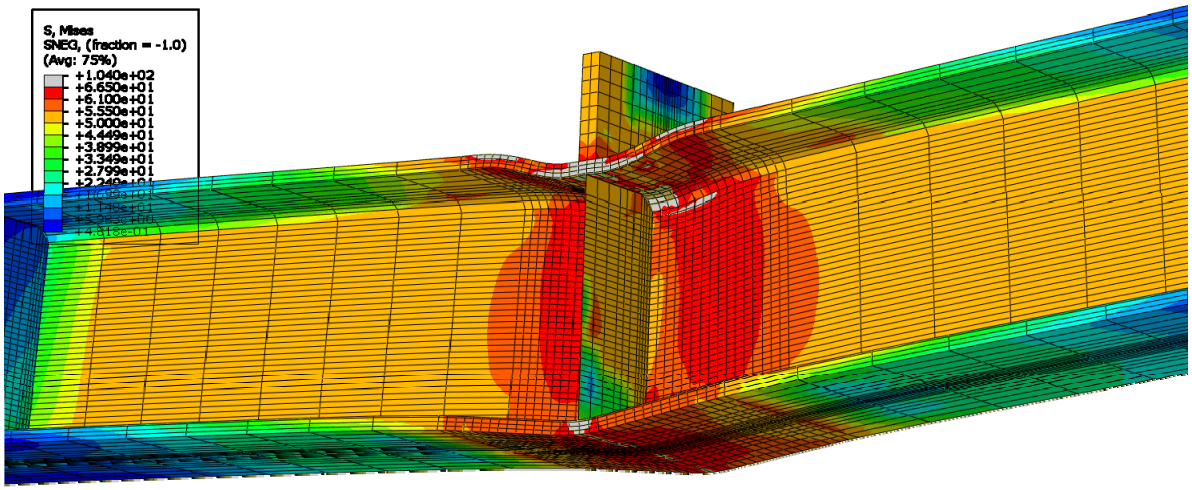

Figure 5.3-8: Finite element model of W10X39-SC-E0 after maximum load

Comparisons between the experimental and analytical results showed some similarities but some discrepancies as well. At the maximum load obtained, the distribution of stresses compares well with the experimental results as evident by the spread of yielding seen in the experimental column specimen as shown in Figure A-52 of Appendix A. Figure 5.3-9 shows a comparison between the analytical and experimental load-displacement results. The predicted analytical capacity of 176 kips is significantly lower than the experimental capacity of 198 kips.

As shown in Figure 5.3-9, both the experimental and analytical column specimens initiate inelastic deformations at approximately the same load. Both results reach a high amount of displacement without signs of buckling. Two different analysis assumptions were used for the analytical investigations; a *STATIC RIKS analysis (ABAQUS, 2014) without imperfection and with an imperfection of 0.001% of the buckled shape determined from the eigenvalue analysis. The results with and without imperfections yielded the same results in this case.

After completion of the analytical results discussed in Chapter 6 and after evaluating the concentrated load limit states in Chapter 7, the results of this column specimen was understood in more detail. In either the analytical or the experimental condition, concentric stiffeners allow the column specimen to reach a failure mode associated with shear and flexural stresses and therefore, the column specimen should have been calibrated using a different approach. This is dissimilar from all of the other experimental column specimens tested in single compression.

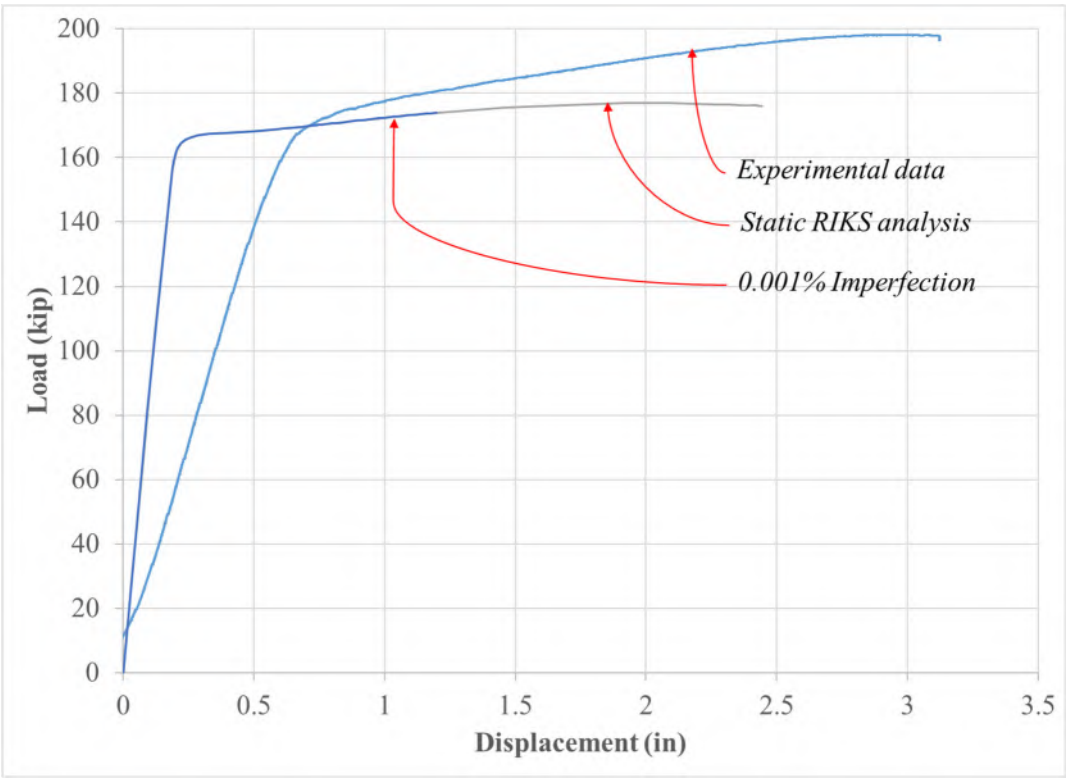

Figure 5.3-9: Comparison of analytical and experimental load-displacement relationships for the W10X39-SC-E0 column specimen

5.3.3 W12X26-SC-NA

A finite element model was developed for W12X26-SC-NA, which represents the W12X26 column specimen tested in single compression and without stiffeners at midspan. Figure 5.3-10 shows a screenshot of the finite element model while it was still behaving elastic. The stresses are higher in the flange and web directly under the concentrated load. There is also signs of flange bending under a low load, which was similar to that witnessed during the experimental test of this column specimen. Also, compared to W10X39-SC-NA discussed in Section 5.3.1, the stresses are more concentrated under the applied load.

Figure 5.3-11 shows the finite element model after inelastic deformations initiate under the loading plate, including in the top flange and the web near the fillet. The grey area indicates stresses beyond 68.5 ksi. The stresses in the web are slightly offset on both faces, which indicates web crippling is occurring.

Figure 5.3-12 shows a screenshot of the finite element model after web crippling occurred and after the maximum load was reached. The deformations shown are very similar to the deformations witnessed during the experimental test of this column specimen as shown in Figure A-56 of Appendix A. Significant flange bending and crippling in the web underneath the loading plate took place.

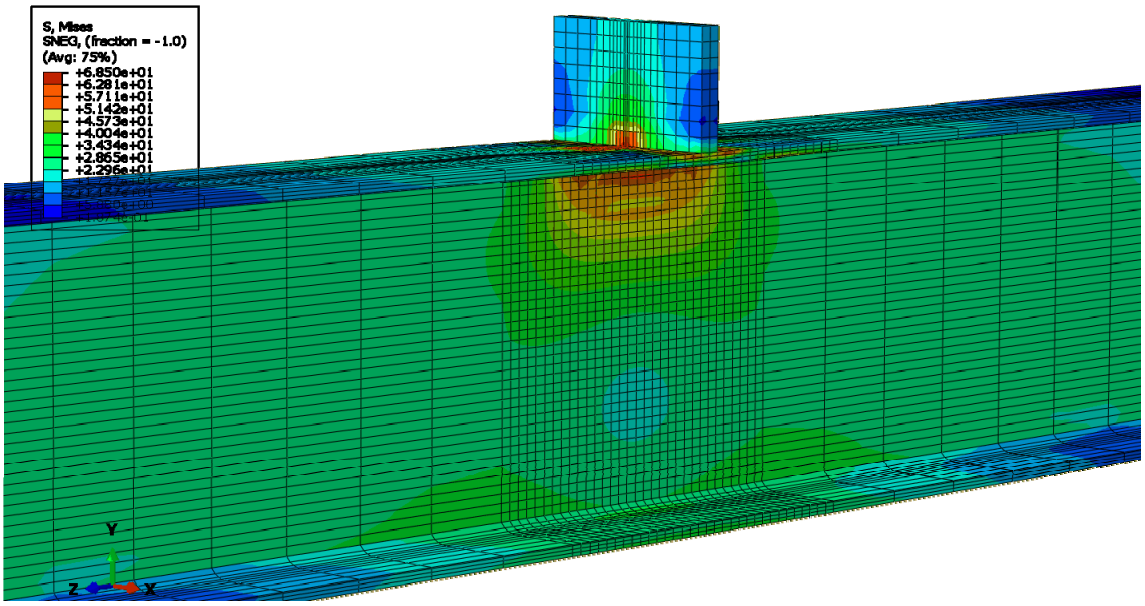

Figure 5.3-10: Finite element model of W12X26-SC-NA during elastic behavior

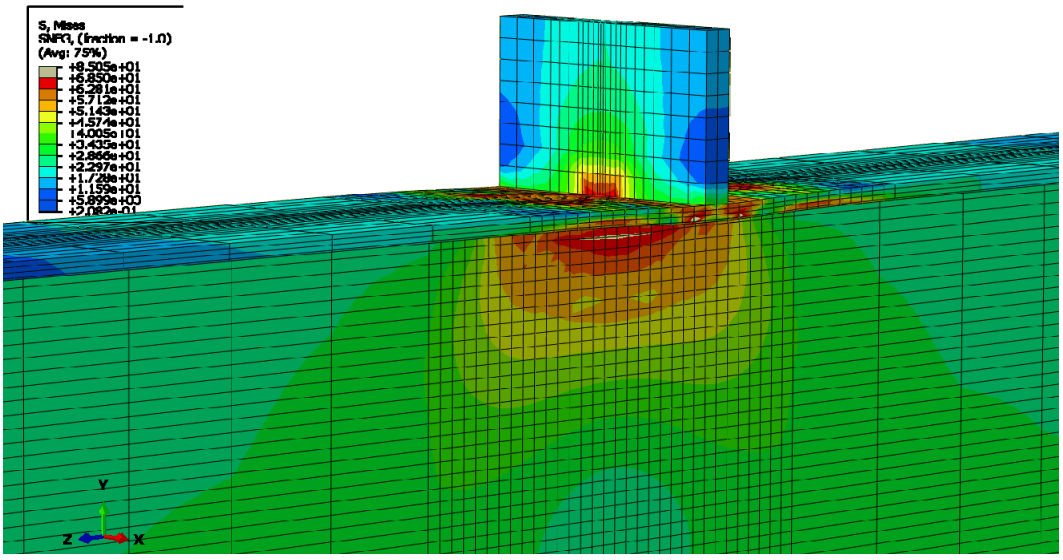

Figure 5.3-11: Finite element model of W12X26-SC-NA during inelastic behavior

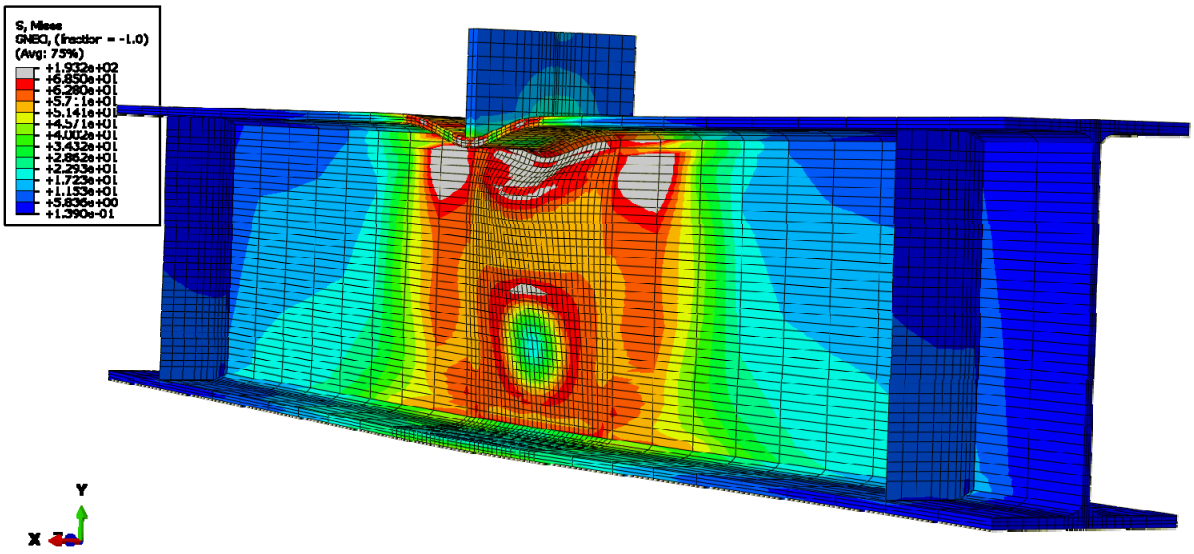

Figure 5.3-12: Finite element model of W12X26-SC-NA after web crippling

The results of the finite element model compare well to the experimental results. The predicted analytical capacity of 83.1 kips is very similar to the experimental capacity of 78.8 kips. In addition, the failure mode and stress distribution in the flanges and web compare well with the behavior of the experimental column specimen in that the stresses were concentrated in the web under the loading plate and crippling was the mode of failure.

The analytical and experimental load-displacement results are compared in Figure 5.3-13 after shifting the experimental displacement such that the maximum loads occurred at approximately the same displacement. Two analyses were performed overall with two different imperfection conditions. The elastic portion of the load-displacement relationship varies between the analytical and experimental results as discussed in Section 4.6. For this particular column specimen, the results with an imperfection of 0.2% were more accurate than the results for an imperfection of 0.001%. In fact, the maximum load predicted with this imperfection was 78.8 kips which matched the experimental results. This could be due to imperfections in the experimental tests or due to fabrication imperfections. However, to be consistent with the remaining column specimens, an imperfection of 0.001% was used for the final analysis. In either case, the maximum load and the shape of the curves near the maximum load are very similar.

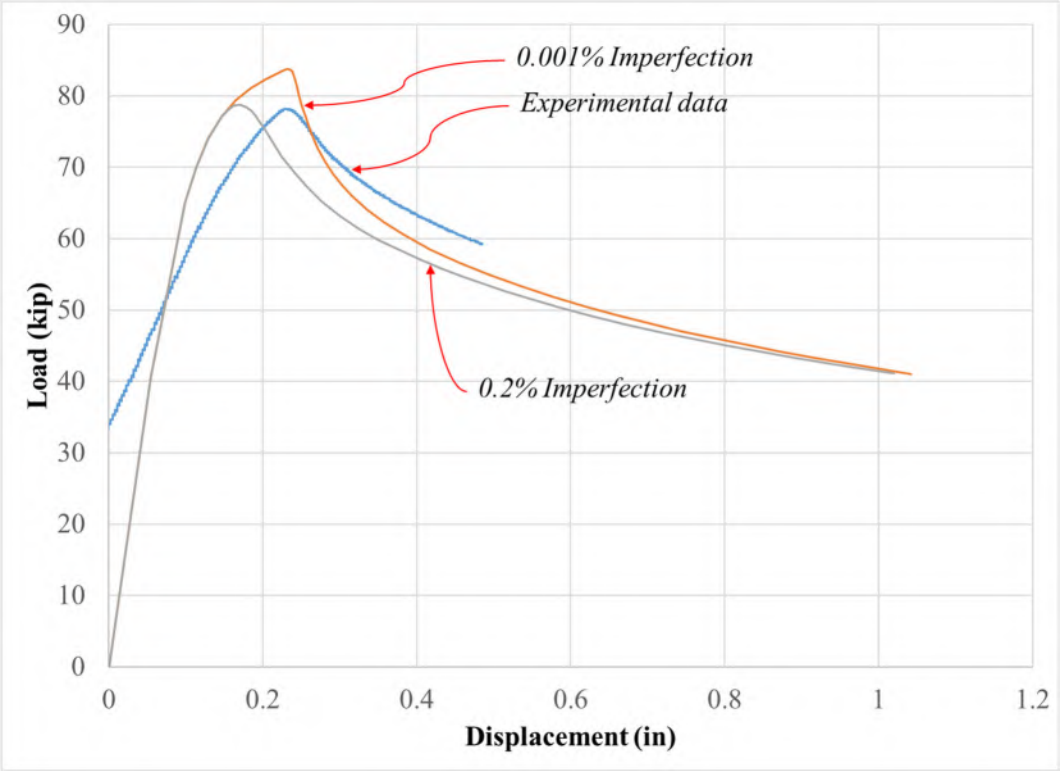

Figure 5.3-13: Comparison of analytical and experimental load-displacement relationships for the W12X26-SC-NA column specimen

5.3.4 W12X26-SC-E0

A finite element model was developed for W12X26-SC-E0, which represents the W12X26 column specimen tested in single compression and with concentric stiffeners at midspan. The analytical results compared relatively well with the experimental results but there are some discrepancies discussed in this section.

Figure 5.3-14 shows a screenshot of the finite element model while it was behaving elastic. As shown in the figure, the stresses are slightly higher near the top loading plate in comparison to near the bottom flange at midspan. However, the stress distribution looks extensively different in comparison to the stress distribution found for the equivalent column without stiffeners as shown in Figure 5.3-10. The results demonstrate how the stiffeners engage to share the concentrated load and the load is gradually transferred to the column specimen through the connections at the column web and bottom flange.

As further load is applied, the stress concentrations increase in the web adjacent to the loading plate, in the top flange near the applied load, and in the top of the stiffeners. Stresses in the stiffener are non-uniform at the top and bottom due to bending of the flanges. Figure 5.3-15 shows the finite element model after inelastic deformations initiate. The grey area indicates stresses greater than 73.4 ksi. Inelastic deformations are shown to initiate in the flange region close to the applied load and in the fillet of the wide flange section.

Figure 5.3-16 shows a screenshot of the finite element model after significant inelastic deformations have occurred and after the maximum load was reached. Both the top and bottom flanges are subjected to significant inelastic deformations and the top flange appears to be exhibiting local buckling. Similar deformations were observed on the experimental test for this particular column specimen as shown in Figure A-68 of Appendix A.

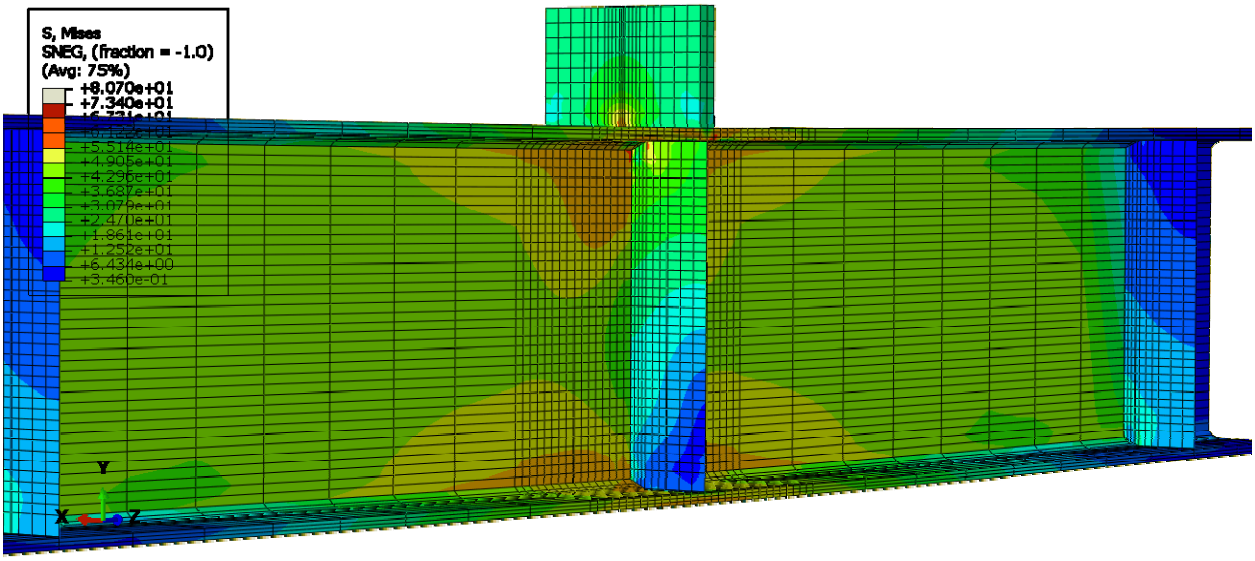

Figure 5.3-14: Finite element model of W12X26-SC-E0 during elastic behavior

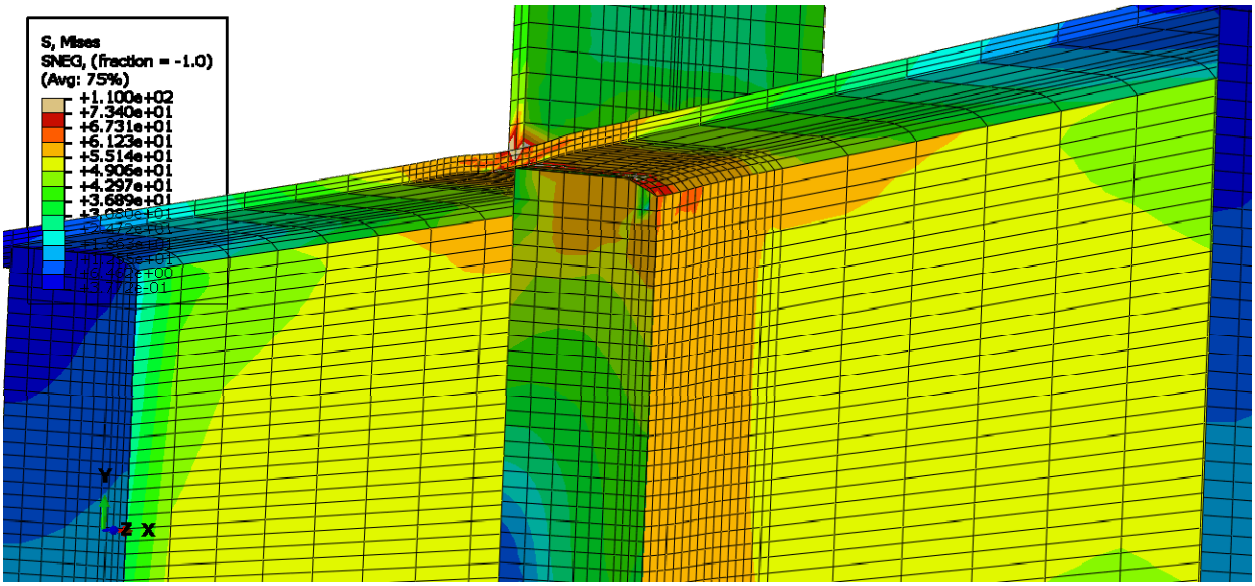

Figure 5.3-15: Finite element model of W12X26-SC-E0 during inelastic behavior

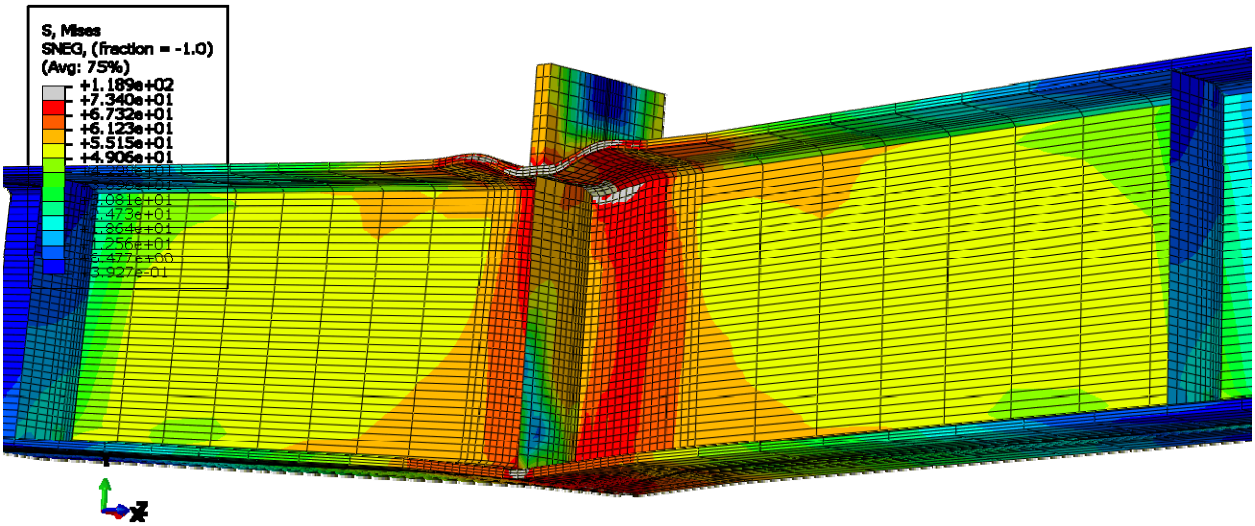

Figure 5.3-16: Finite element model of W12X26-SC-E0 after the maximum load

The analytical and experimental load-displacement results are compared in Figure 5.3-17 after shifting the experimental displacement. The predicted analytical capacity of 156.9 kips compared favorably to the experimental capacity of 148.2 kips. Both curves show that inelastic deformations initiate at approximately the same magnitude of load. Higher loads are maintained for high displacements until the load starts to gradually decrease. Three different analysis procedures were used to evaluate this particular column specimen analytically; (1) a general *STATIC analysis, (2) a *STATIC RIKS analysis without imperfection and (3) a *STATIC RIKS analysis with imperfection.

The two *STATIC RIKS analyses yielded almost identical results and are plotted on top of each other in Figure 5.3-17.

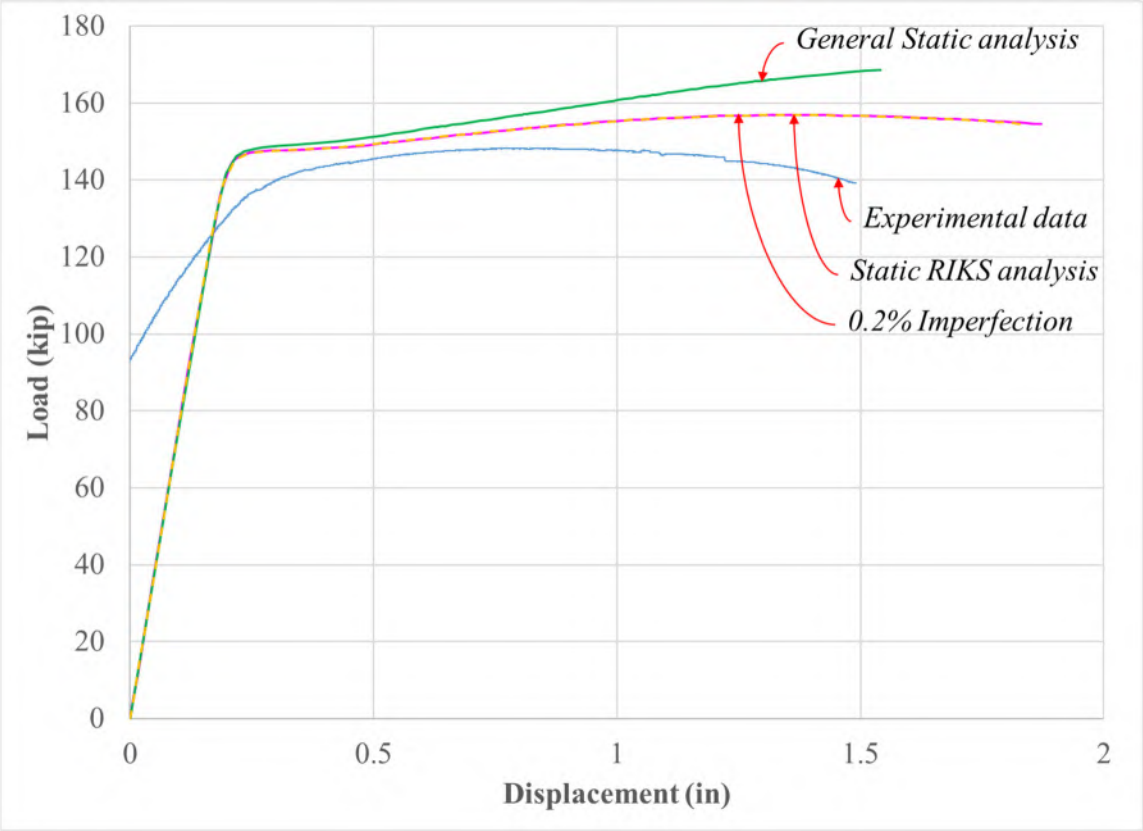

Figure 5.3-17: Comparison of analytical and experimental load-displacement relationships for the W12X26-SC-E0 column specimen

5.3.5 W12X26-SC-E4

A finite element model was developed for W12X26-SC-E4, which represents the W12X26 column specimen tested in single compression and with stiffeners on either side of the column specimen, 4 in. eccentric from the concentrated load. This study was used specifically to evaluate the effects of eccentric stiffeners on the analytical results for single compression tests. Figure 5.3-18 shows a screenshot of the finite element model while it was still behaving elastic. Similar to the experimental results, the research team found the eccentric stiffeners to be ineffective. The stresses are localized on the web and flange under the applied load. In a similar manner to the analysis of W12X26-SC-NA, the stresses are not well distributed through the depth of the web.

Figure 5.3-19 shows the finite element model after inelastic deformations initiate. The grey area indicates stresses beyond 68.5 ksi. As inelastic deformations initiate, the web stresses are different in both faces of the web, indicating that web crippling has occurred. High inelastic deformations are localized under the concentrated load implying that failure occurs within the web underneath the loading plate.

The research team continued loading the analytical column specimen after the maximum load was reached to analyze the post-buckling behavior and the inelastic deformations in the specimen. Figure 5.3-20 shows a screenshot of the finite element model near the end of the analysis and after web crippling and the maximum load occurred. The shape of the column specimen is similar to the shape of the equivalent column specimen analyzed without stiffeners (W12X26-SC-NA), which further supports the conclusion that eccentric stiffeners are ineffective. Significant flange bending and crippling in the web underneath the loading plate are both observed in Figure 5.3-20 and limited stresses are seen in the stiffener plate.

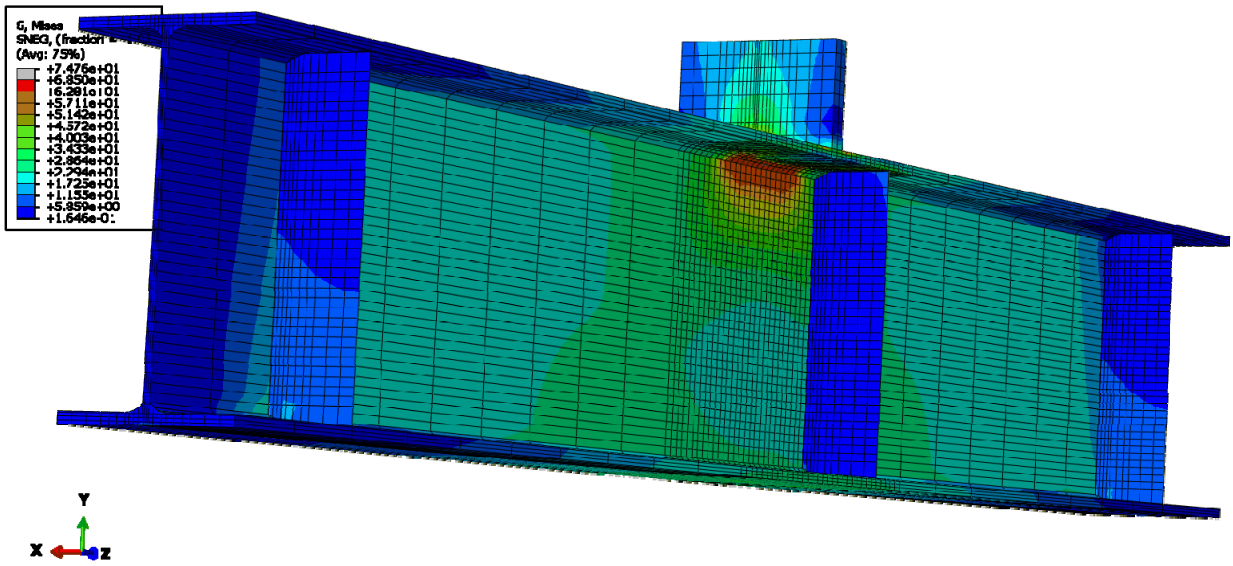

Figure 5.3-18: Finite element model of W12X26-SC-E4 during elastic behavior

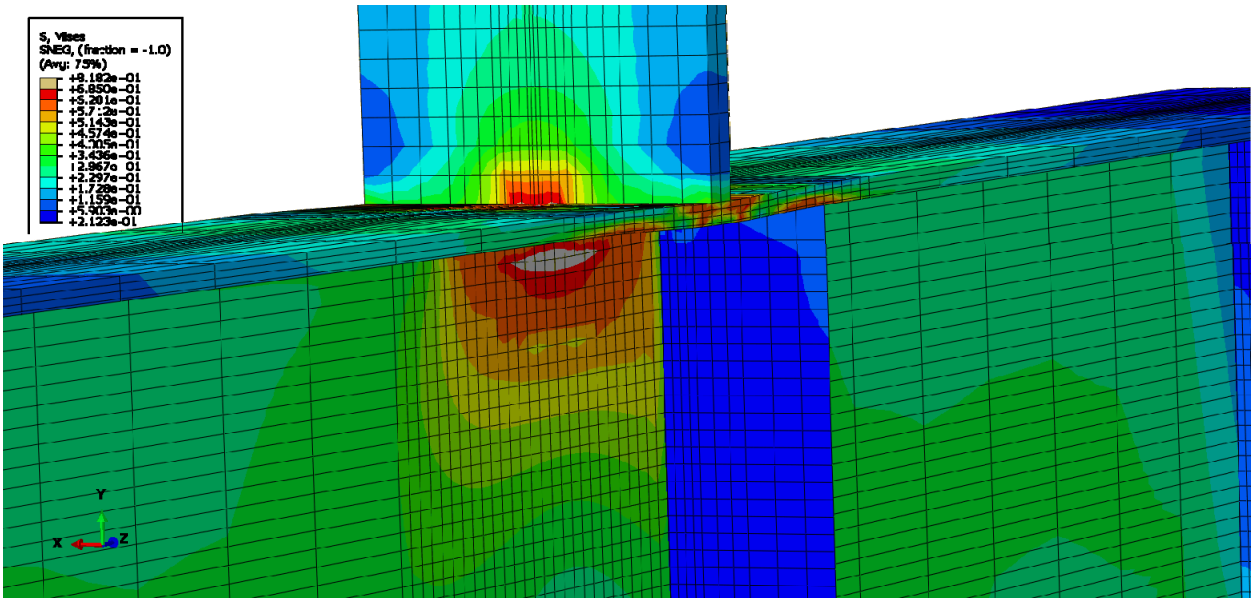

Figure 5.3-19: Finite element model of W12X26-SC-E4 during inelastic behavior

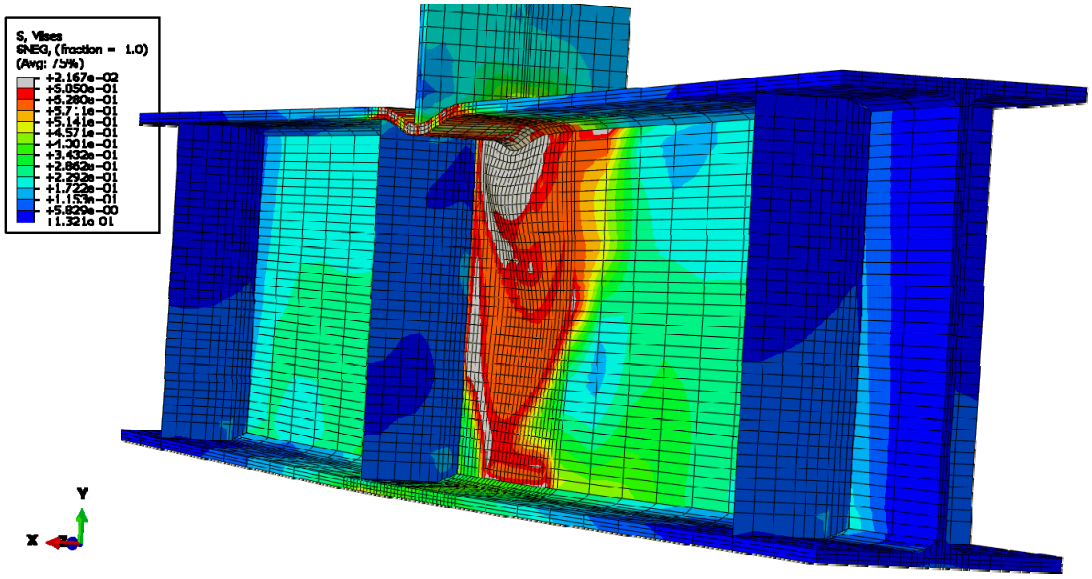

Figure 5.3-20: Finite element model of W12X26-SC-E4 after web crippling

In comparison to other column specimens analyzed in this chapter, the analytical results do not compare as well to the experimental results. The failure mode and stress distribution in the flanges and web compare well with the behavior witnessed during the experimental test in that the stresses were concentrated in the web under the loading plate producing web crippling. However, the analytical capacity of 95.8 kips is noticeably higher than the experimental load capacity of 79.1 kips.

The analytical and experimental load-displacement results are compared in Figure 5.3-21. In both the experimental and analytical load-displacement relationships, the column specimens reached a maximum load and then sudden failure occurred, similar to the behavior of column specimens without stiffeners. For the eccentric stiffener cases, the research team used the STATIC RIKS analysis in ABAQUS with no imperfection. This was later reevaluated with an imperfection of 0.001% but there was minimal change.

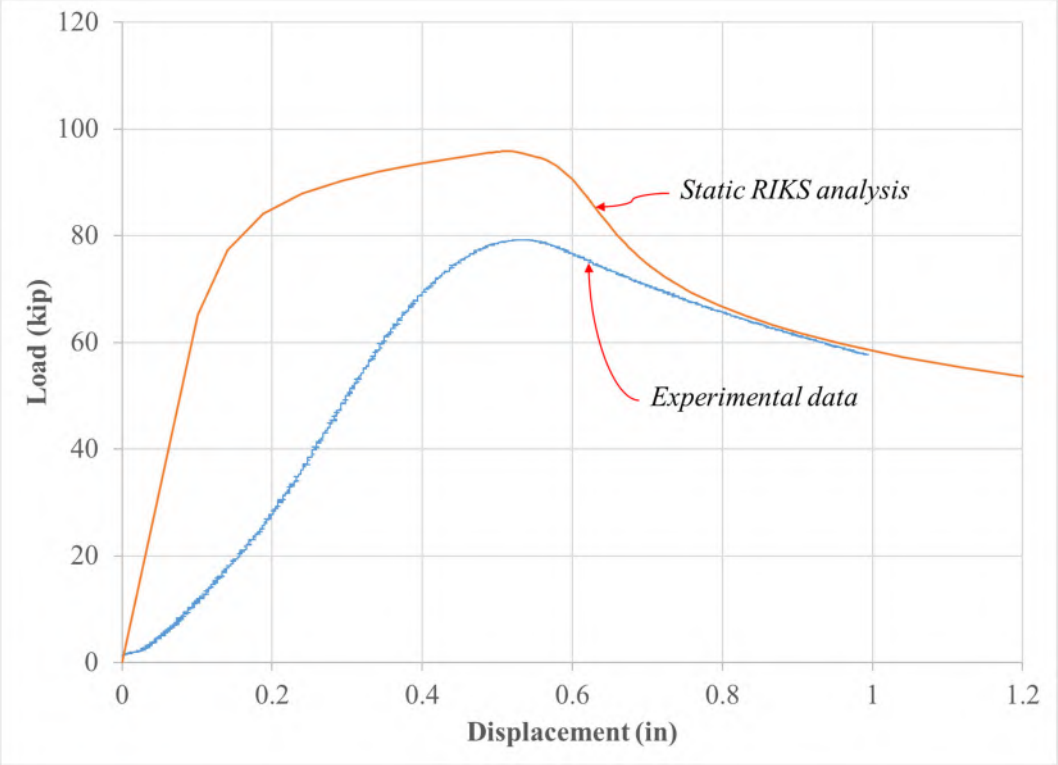

Figure 5.3-21 Comparison of analytical and experimental load-displacement relationships for the W12X26-SC-E4 column specimen

5.4 Results of Single Tension Tests

The section summarizes the finite element models that were developed to represent the column specimens subjected to single tension. There were minimal experimental investigations to compare to for this test condition. Three column sizes were tested experimentally; (1) W10X39, (2) W12X26, and (3) W16X31. However, the W10X39 single tension tests all reached the capacity of the hydraulic actuator. In addition, the W12X26 single tension member without stiffeners (W12X26-ST-NA) fractured prematurely due to defects in the welds. Therefore, the following column specimens were used to perform the comparison studies and to validate the finite element modeling approach for further studies:

- W16X31-ST-NA
- W12X26-ST-E4
- W16X31-ST-E0
- W12X26-ST-E0

Note that the W16X31 and W12X26 columns with concentric stiffeners (W16X31-ST-E0 and W12X26-ST-E0) also reached the capacity of the hydraulic actuator. However, they were evaluated to confirm the elastic stiffness remains relatively constant to when the capacity of the hydraulic actuator was reached and to evaluate the analytical performance of the stiffeners when subjected to tension loading. It is assumed that the behavior of the experimental W12X26-ST-E4 column specimen would be very similar to a condition without stiffeners since all tests performed in this research and with these column sizes indicated that an eccentricity greater than 2 in. is ineffective in resisting concentrated forces.

Additional modeling details are required in the single tension tests in comparison to the compression tests. The primary addition is the welds from the loading plate to the top flange of the column specimen. Welding details are described in Section 5.4.1. These details are critical since the experimental results showed that if failure occurred in the single tension tests, it occurred in the welds due to an uneven stress distribution.

In addition to adding welds, the column specimens were simply supported at 4.5 ft. in lieu of 5 ft. and end boundary conditions were enforced at the top of the column specimens in lieu of the

bottom to match the experimental test condition. Although experimentally, the end stiffeners were slightly off the location of the end supports, they were assumed located directly at the supports in the analytical models, which is assumed a negligible difference. The loading plate was modeled as 3/4 in., which was also used during the experimental investigations.

5.4.1 Welding Details for Single Tension Tests

The experimental results indicated that failure of single tension tests without concentric stiffeners occurred at the welds from the column specimens to the loading plates. It was concluded from observation that the welds failed due to an uneven stress distribution and the capacity at failure was significantly less than theoretical calculations for the weld strength using the entire weld length. Uneven weld stresses were caused by bending of the flanges under load, which caused less deformation in the weld at the ends as opposed to near the center of the welds. The center of the weld was subjected to significantly higher deformations with the column web directly adjacent. When concentric stiffeners were utilized, the welds did not fail, as the flanges did not significantly bend under the applied load and thus allowed the weld deformations and stresses to be uniform along the length.

These experimental observations indicated that proper modeling of the welds was critical in the analytical research. However, as discussed in this section, modeling the true behavior of welds is cumbersome with respect to geometry and material properties.

The welds from the loading plate to the column specimen were specified to be flux-core fillet welds with a size of 3/8 in. In order to model the geometry of the welds, a finer mesh was used for the loading plate and the column specimen in the vicinity where the plate elements interact with the weld. A screenshot of the finite element model at the weld location is shown in Figure 5.4-1.

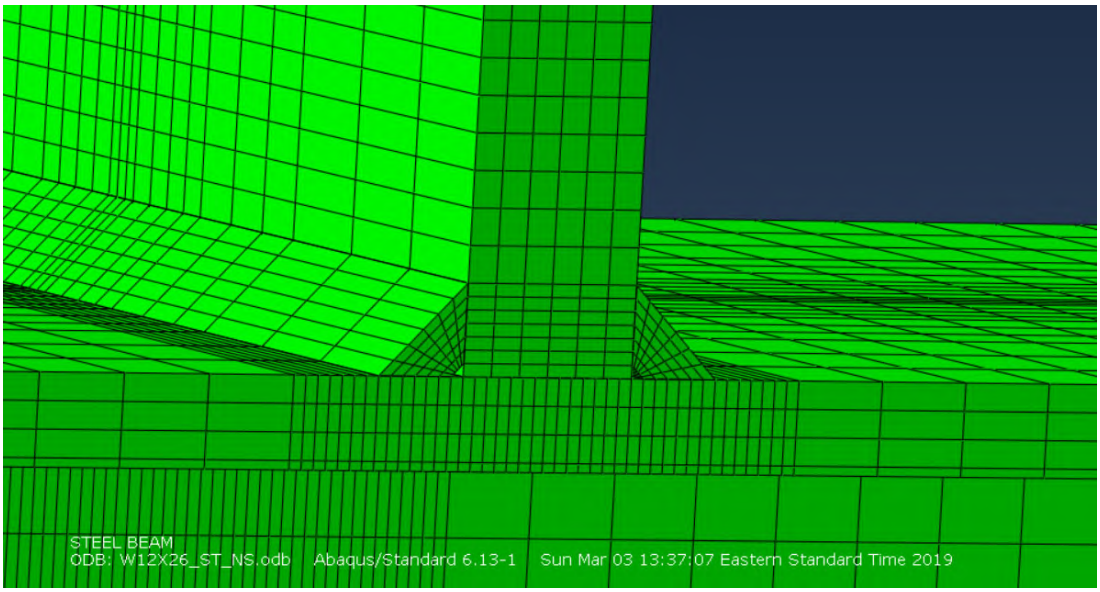

Figure 5.4-1: Finite element model of single tension tests at weld detail

Design calculations for fillet welds assume that the geometry is triangular. However, welds will fuse with the base metal and become slightly "bumpy". Modeling the true geometry of the welds is not feasible. In addition, the mechanical behavior during arc welding requires the knowledge of thermal history of the components and the constitutive behavior of the materials. In general, there is no way to predict the exact shape of the welds on the column specimens or the welds that would be present in the field. The welds were modeled with C3D8 elements (ABAQUS, 2014). These elements are three-dimensional continuum elements with three degrees of freedom per node. The elements are cubic and arranged together in a triangular pattern with a slight gap at the apex. The welds became finer near the center of the width of the member to match the mesh used for the flange of the column.

The nodes used for the boundaries of the welds (where they are assumed to contact the plate elements) were not specified as the same as the nodes on the plate elements even though the coordinates were identical. To provide compatibility between the welds and the connecting flange and plate, each node on the welds that connect to the plate elements was constrained (slaved) to a node on the plate elements by ensuring the displacements in all three directions (x, y, and z) were the same. This was the simplest approach to ensure that the welds interacted with the flange and plate. The constraint condition was inputted into ABAQUS using several constraint equations.

Another critical assumption in effectively modeling the behavior of the weld is the material model. In a static-stress analysis using finite elements, the most critical properties of the elements relates to properties from the stress-strain curve, which includes assumptions for the elastic modulus, elastic limit, plastic strains vs. stress, and the ultimate stress. Weld material properties are often measured using ANSI/AWS B4.0 "Standard Methods for Mechanical Testing of Welds" (ANSI/AWS, 2007). The research team performed uniaxial tension tests to obtain the stress-strain relationships for the wide flange column specimens and stiffener plates but did not test the welds for the properties in question using ANSI/AWS B4.0. Therefore, a literature review was performed to identify material properties that have been measured in the past. However, very limited prior research was available to confidently predict the fundamental stress-strain properties of the weld material used in this research.

Several researchers have reported the yield and ultimate stress of weld materials. For instance, Bowman and Quinn (1994) reported weld-metal tension test results on welds made with Atom Arc E7018 Alpha, low hydrogen, 3/16-in diameter electrodes. They reported than on average, the yield stress was 57.8 ksi, the yield strain was 0.0019 in/in, the tensile strength was 69 ksi and the maximum elongation was 37.8%. However, full stress-strain relationships were not reported in this work.

Kartal et al. (2007) evaluated weld metal mechanical properties utilizing novel tensile testing methods and using digital image correlation (DIC). In this study, local stress-strain behavior in the weld zone of a 316H stainless steel pipe with a girth weld was investigated by tensile tests of specimens machined from the pipe. A photograph that shows how the tension specimens were fabricated from the area of the girth weld is shown in Figure 5.4-2.

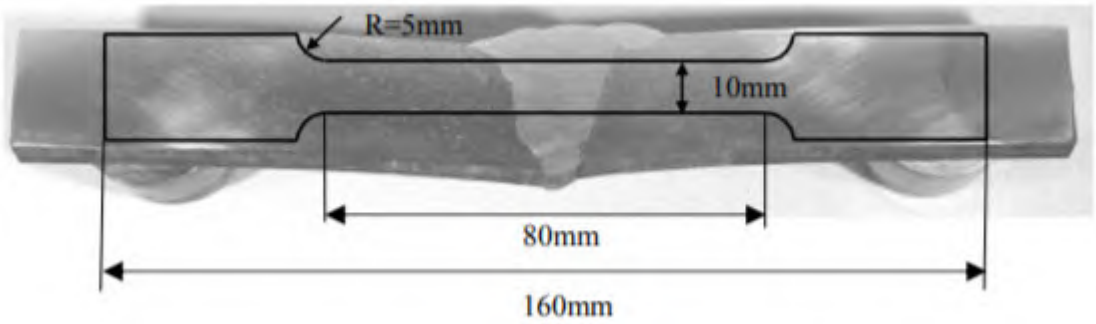

Figure 5.4-2: Weld-metal tension test coupon from Kartal et al. (2007)

The electrode strength used in this study was not provided in the paper. Typically, in structural steel design, the design weld (electrode) strength, F_{EXX}, is assumed 70 ksi, which relates well to the tests performed by Bowman and Quinn (1994). A plot of the experimental results from Kartal et al. (2007) is shown in Figure 5.4-3. The circles identify the results of the weld material. After converting the units, the ultimate stress of the weld material is approximately 82 ksi (567 MPA reported in the paper). The graph shown was overlaid using Microsoft Excel and the units were converted to Imperial units. The resulting elastic modulus was found to be approximately 29,000 ksi and non-linear behavior initiated at approximately 50 ksi.

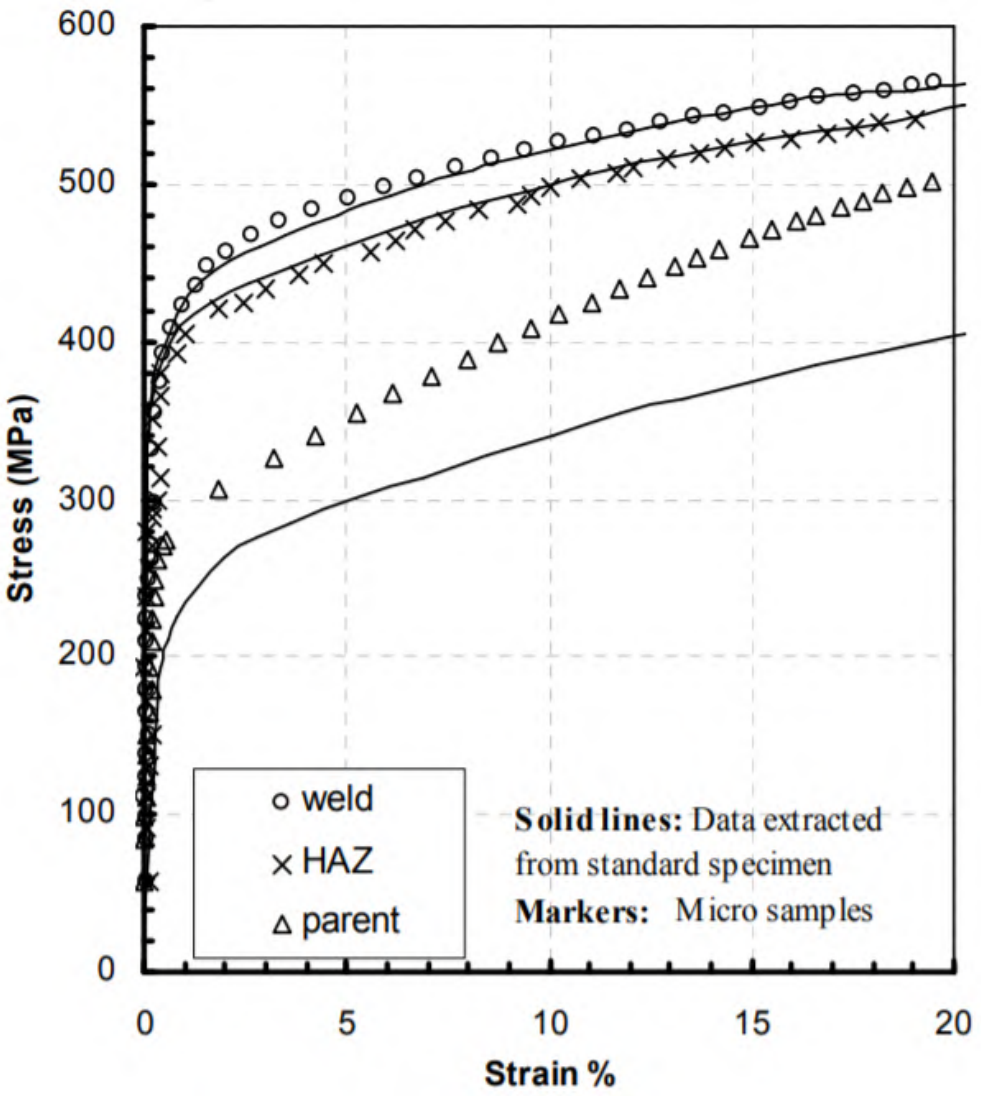

Figure 5.4-3: Tension test results from Kartal et al. (2007) using DIC

Again, other researchers reported basic material properties but very limited information was found to define the full-stress strain relationship. Keinänen and Chauhan (2013) reported weld stress-strain material properties and curves that predicted a maximum ultimate stress of 78 ksi. However, the curves shown did not appear as realistic as that obtained by Kartal et al. (2007). Of all the information found in the literature, the data and information obtained from Kartal et al. (2007) appeared the most useful for this research project and was therefore used for the analytical investigations.

5.4.2 W16X31-ST-NA

The development and initial calibration of the finite element models of single tension tests focused on the W16X31 shape without stiffeners. This column size yielded the most beneficial results for single tension tests performed in this research. The load-displacement results of the specimen without stiffeners, the specimen with stiffeners at an eccentricity of 3 in. and the results of the specimen with stiffeners at an eccentricity of 6 in. were all very similar, thus providing confidence in the results.

After several trial attempts, the research team settled on using C3D8 elements (ABAQUS, 2014) for all elements (except stiffeners), which is dissimilar to the C3D8I elements used for the compression specimens. Stiffeners were modeled with S4 shell elements. Both of these element types have been discussed in this report.

Figure 5.4-4 shows a screenshot of the finite element model while it was still behaving elastic. The deformations are scaled at 1X (actual scale). As concluded during the experimental investigations, the weld stresses are much higher and concentrated near the center of the weld. As load is applied, the flanges will bend near the ends, and therefore less deformation develops in the weld itself. In contrast, the center of the weld is restricted by the stiffness of the web adjacent to it and therefore, deformation is more concentrated in the weld itself. Figure 5.4-5 shows the finite element model after inelastic deformations initiate in the weld. The grey area indicates stresses beyond 70 ksi, chosen arbitrarily to emphasize where significant inelastic deformations occur. As inelastic deformations initiate, the weld stresses become more uniform along the length. However, the stresses are still higher near the center of the weld as opposed to near the edges.

Failure or fracture of the weld itself cannot be visually represented in the finite element model. Instead, the model will continue to load the column as more and more of the elements reach stresses at or beyond (due to stress risers) the ultimate stress. To indicate when failure occurs in the weld, the research team identified when the Von Mises stress exceeded the ultimate stress, which was specified as 82.4 ksi. Therefore, this magnitude was specified as an upper limit for the contours and a grey area suggests that the stress was exceeded. Figure 5.4-6 shows a screenshot of the finite element model when a portion of the weld stress exceeds 82.4 ksi. The results imply that failure

occurs at the center of the weld and where it connects to the loading plate. In the final analytical study selected, this occurred at a load magnitude of approximately 122 kips which compared reasonably well to the maximum load obtained during the experimental results of 127 kips.

Another method that can be used to predict when the maximum load is reached is to evaluate the maximum plastic strain, which was specified in the material model to be approximately 0.2 in/in when the ultimate stress was first reached. PEEQ is the ABAQUS name for the equivalent plastic strain. It is a scalar measure of all the components of equivalent plastic strain at each position in the model (ABAQUS, 2014). Figure 5.4-7 shows the PEEQ distribution in the model at the same increment of load, which confirms that the maximum stress and plastic strain state was captured at this increment in implies that at approximately this load magnitude, failure would occur.

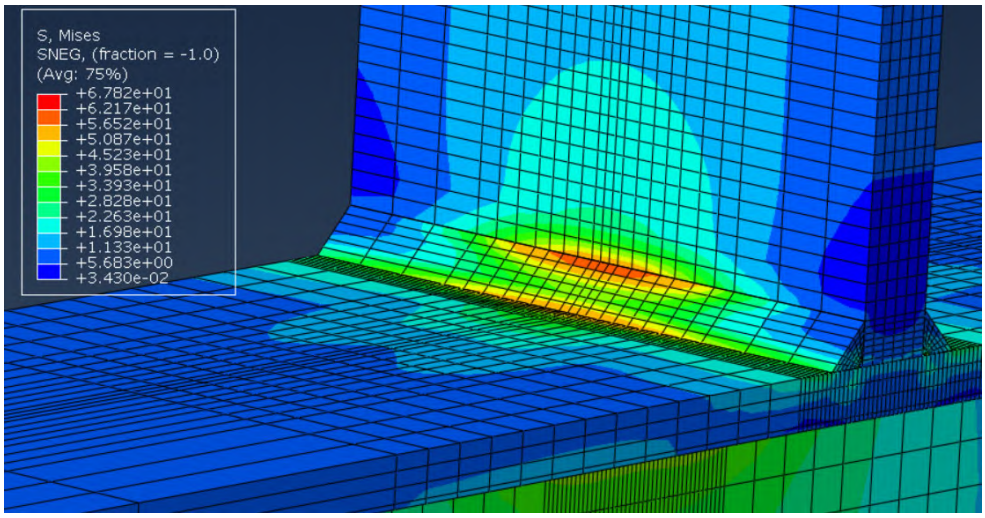

Figure 5.4-4: Finite element model of W16X31-ST-NA during elastic behavior

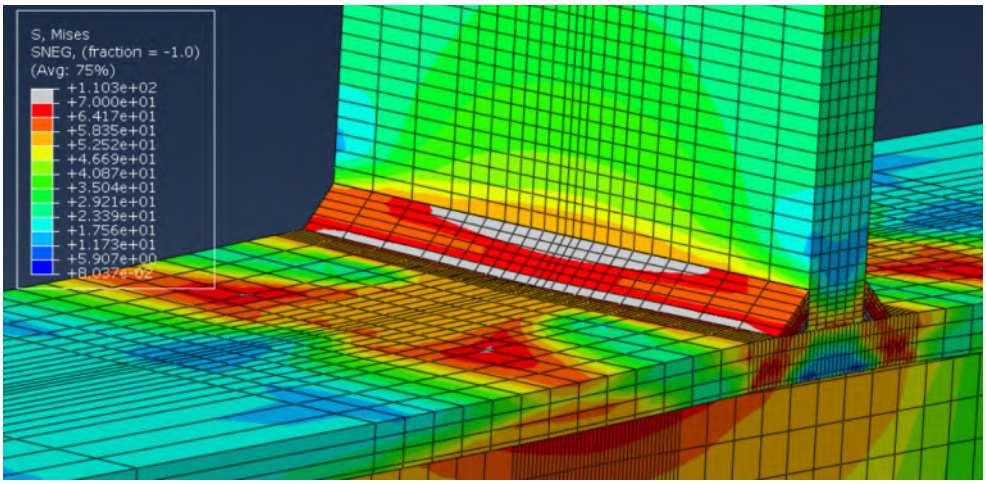

Figure 5.4-5: Finite element model of W16X31-ST-NA during inelastic behavior

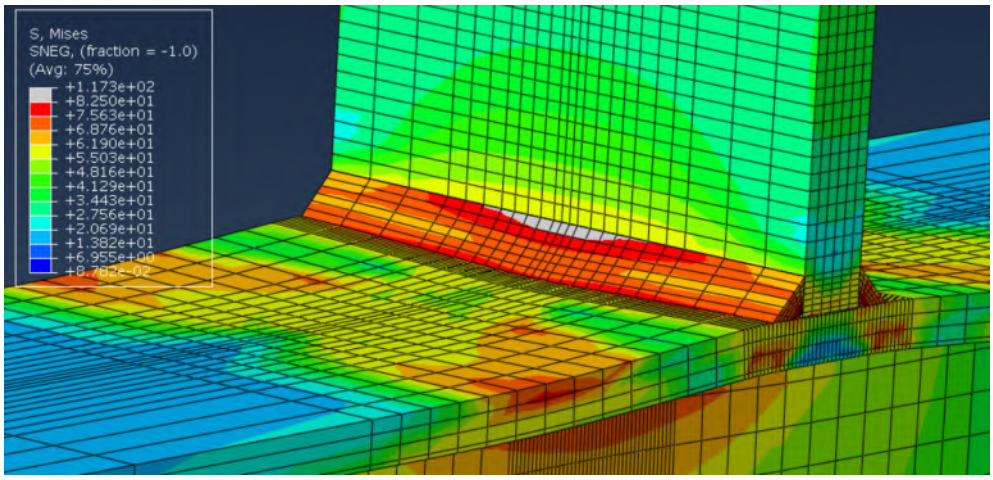

Figure 5.4-6: Finite element model of W16X31-ST-NA at assumed failure load of 122 kips

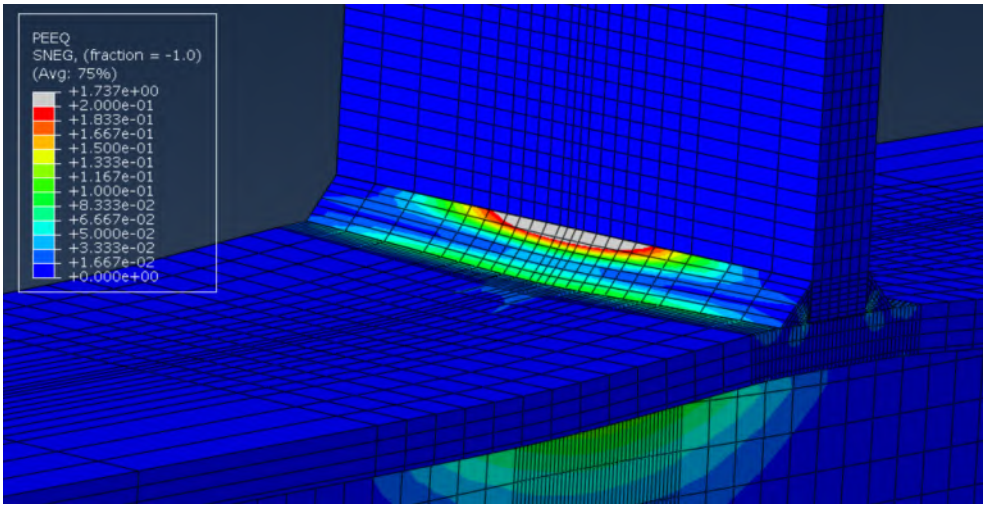

Figure 5.4-7: Plastic strains within W16X31-ST-NA at assumed failure load of 122 kips

The results of the finite element model compare well to the experimental results for some details but compare unfavorably for other details. In the methods used, the predicted analytical capacity of 122 kips compares favorably to the experimental capacity of 127 kips. In addition, the stress distribution in the weld compares well with the behavior assumed during the experimental investigations in that the weld stresses were concentrated in the center of the weld and failure seemed to occur where the weld connects to the loading plate. However, the overall load-displacement relationships between the analytical results and experimental results did not compare as well.

For the single tension tests, the loading plate was connected to the hydraulic actuator using a bolted connection as shown with the experimental test setup in Figure 3.5-13. Prior to obtaining linear elastic behavior, the bolts needed to fully engage in the bolt holes. To perform comparisons between the experimental and analytical results, the elastic portion of the load-displacement curve was shifted as if it imitated at the origin (0 in., 0 kip.). A linear portion of the load-displacement relationship was used to calculate the elastic stiffness of the column specimen. From this, a line with this stiffness was drawn from the origin as shown in Figure 5.4-8. Then, a constant amount of displacement was subtracted from the experimental displacements until the elastic portion of the load-displacement results overlaid the straight line. This is also shown in Figure 5.4-8. The research team assumes that if the connections were fully engaged at the initiation of the test that the curve would follow the straight line shown.

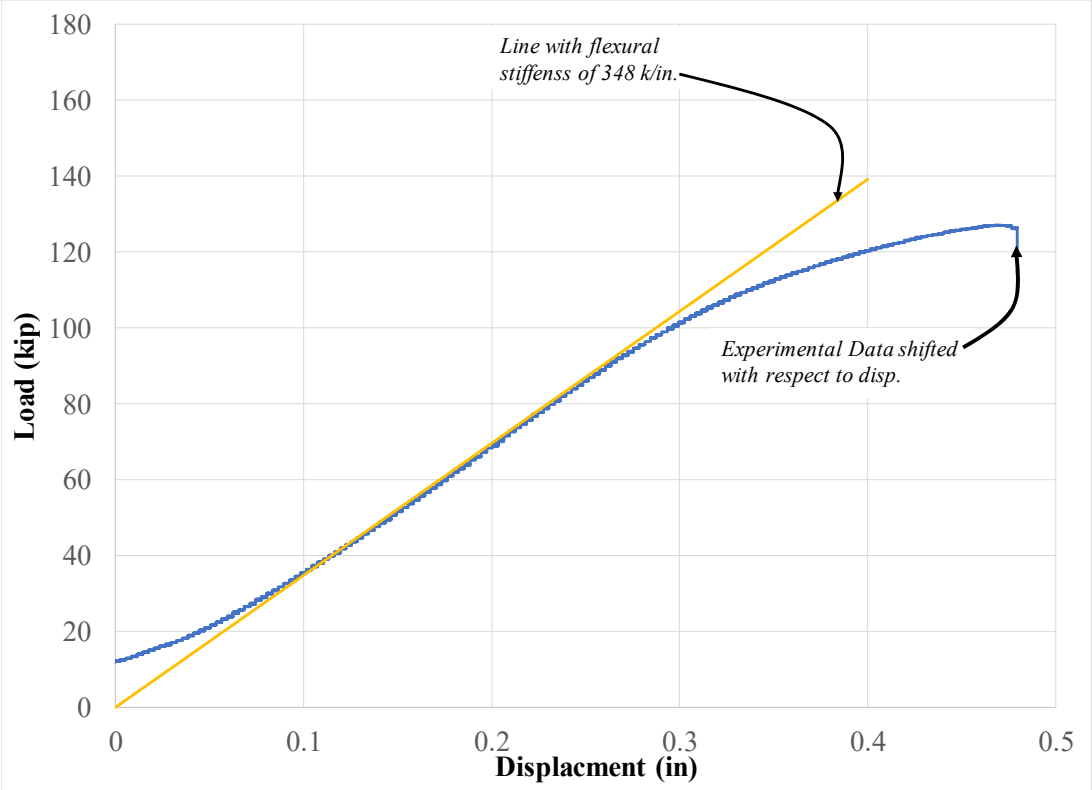

Figure 5.4-8: Shifting of the load-displacement curve to account for movement in connections

Despite the efforts to evaluate the load-displacement results from the origin, the overall load-displacement relationship of the analytical column specimen had some discrepancies. Comparative results are shown in Figure 5.4-9. Note that several trial attempts were utilized to acquire the analytical comparisons in Figure 5.4-9 and some of the trial attempts are presented and discussed herein.

The line marked "Analytical results up to assumed fracture state" is the "final" analysis that will be compared with experimental results and was plotted to the assumed point when the weld failed and 122 kips. These results were obtained with the finite element model shown in Figures 5.4-4 to 5.4-7. The analytical studies of compression tests revealed that the elastic stiffness of the experimental column specimens vastly differentiated from the analytical elastic stiffness. In Section 4.6, the research team proved that the analytical elastic stiffness was indeed accurate in comparison to theoretical predictions and therefore, there are no concerns moving forward with the discrepancy. However, for this single tension comparison, inelastic behavior appears to initiate

at a much lower load in the analytical column specimen. An additional straight line was drawn in Figure 5.4-9 to represent the elastic stiffness of the analytical column specimen, which helps identify when inelastic deformations initiate. Significant inelastic deformations initiated in the analytical model at approximately 80 kips and non-linear behavior initiated in the experimental model at approximately 95 kips. In addition, inelastic deformations appears to be more prominent in the analytical models until failure.

The research team spent a significant amount of time to identify/explain the aforementioned discrepancies. Since the weld material models were determined from prior research, this was further evaluated assuming that yielding could be occurring at a lower weld stress than in reality. Therefore, the weld was modeled as linear elastic with the load-displacement results shown by the grey curve in Figure 5.4-9 which is identified as "Analytical results with elastic weld only". However, this only changed the results slightly since significant inelastic deformations were also occurring in the column specimen web directly underneath the load as shown in Figure 5.4-10. Figure 5.4-10 shows the plastic strain distribution in the column specimen when the weld was modeled as elastic only. Significant tension yielding occurs in the web directly under the load.

After observing the evidence in Figure 5.4-10, one final concern in the analytical models was that the aspect ratio of the web elements near the weld location was too high. The web elements were thin in width in comparison to height, which was dissimilar to the weld and flange elements. Therefore, one final study was performed to evaluate the influence of the aspect ratio. The models used to perform the compression tests were used to perform single tension tests by moving the end supports to the top of the column and at a distance of 4.5 ft. apart and by displacing the loading plate up instead of down. The same material properties for the plate and column specimen (same as for compression tests with W16X31) were implemented into this new model. Welds were not included in this study. The results are shown by the green line in Figure 5.4-9, which is identified as "Web analyzed with courser mesh". The load-displacement results were similar and the amount of load for a given displacement was slightly lower. Therefore, the discrepancies between the experimental and analytical results were not due to the element aspect ratio. In addition, in the courser mesh, significant plastic deformations were still found in the web directly underneath the loading plate.

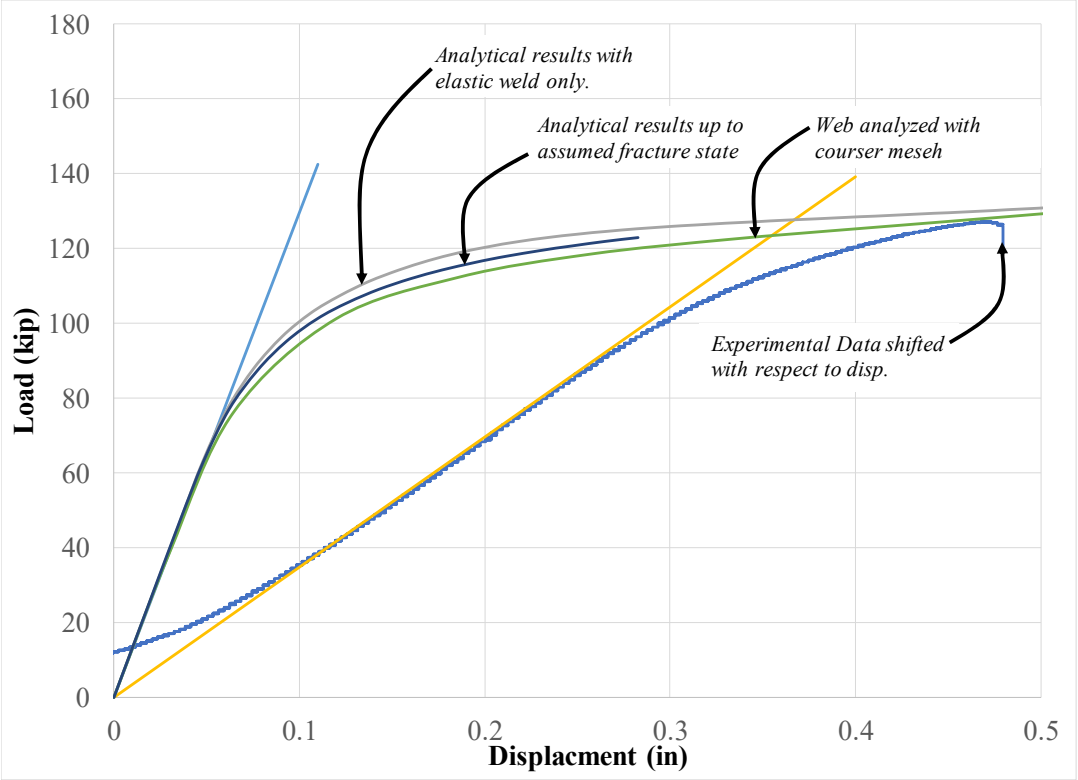

Figure 5.4-9: Comparison of analytical and experimental load-displacement relationships for the W16X31-ST-NA column specimen

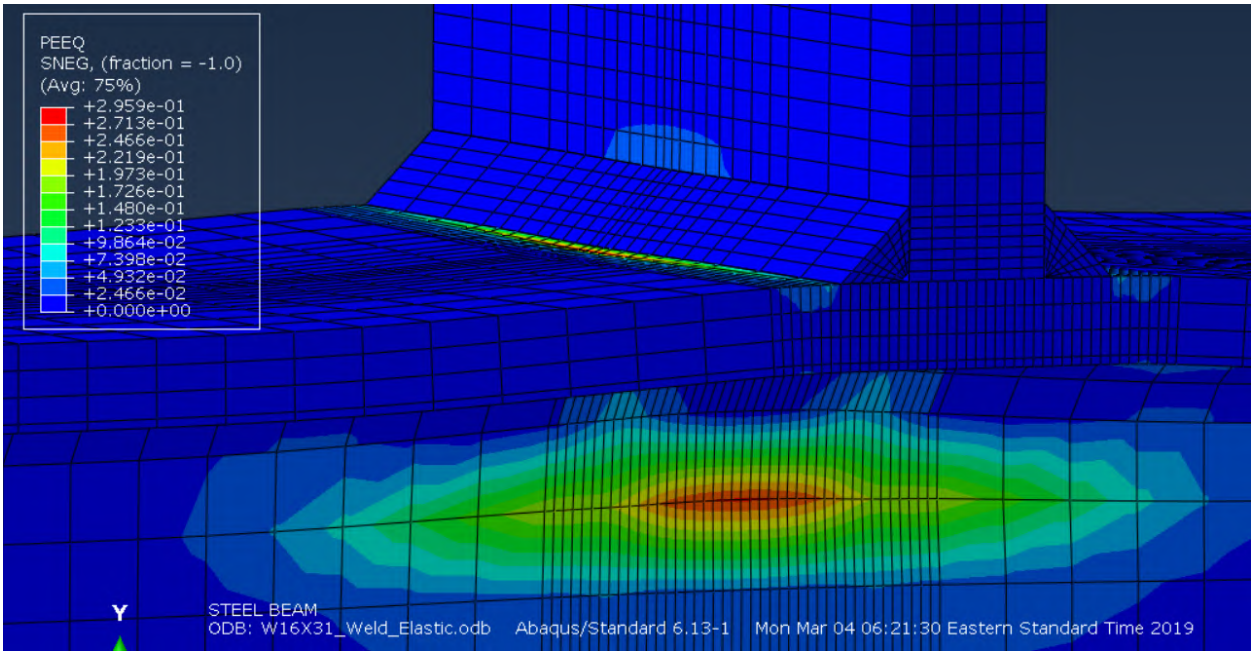

Figure 5.4-10: Plastic strains in web of W16X31-ST-NA when modeling the weld elastic

After performing the analytical investigations on single tension tests and evaluating all evidence in the results, the research team once again found that the behavior of the finite element model is similar with respect to weld stresses and maximum load capacity. Similar conclusions were obtained in the compression models. However, there are discrepancies with respect to the overall load-displacement behavior, which again is similar to the compression tests. The research team decided to move forward and use the general assumptions and inputs for future studies since the effects of flange thickness, stiffener location, and material properties can still be directly evaluated with the current model assumptions.

5.4.2 W12X26-ST-E4

As mentioned several times in this report, the W12X26 column specimen without stiffeners failed prematurely, and therefore could not be used to perform a similar study as described in Section 5.4.1. Instead, a similar study was performed for the W12X26 column specimen with stiffeners at an eccentricity of 4 in. Since the experimental results show that at this eccentricity, the stiffeners have negligible influence on the results, it was anticipated that the conclusions derived in this section would be similar to the conclusions derived for the W16X31-ST-NS analysis discussed in Section 5.4.1. Material properties for the column specimen were implemented into ABAQUS based on uniaxial tension tests that were performed on specimens fabricated from the W12X26 sections.

Figure 5.4-11 shows a screenshot of the finite element model at a load of 41 kips and while the column specimen was still behaving elastically. Similar to the studies performed on the W16X31 column specimen, the weld stresses are concentrated near the center of the weld yielding the same conclusions as discussed in Section 5.4.1. In addition, significant stresses are identified in the web of the column specimen directly underneath the load and fillets. At this magnitude of load, the stiffeners appear to have no influence on the performance of the column specimens as the stress distribution appears as a mirror image from the column centerline.

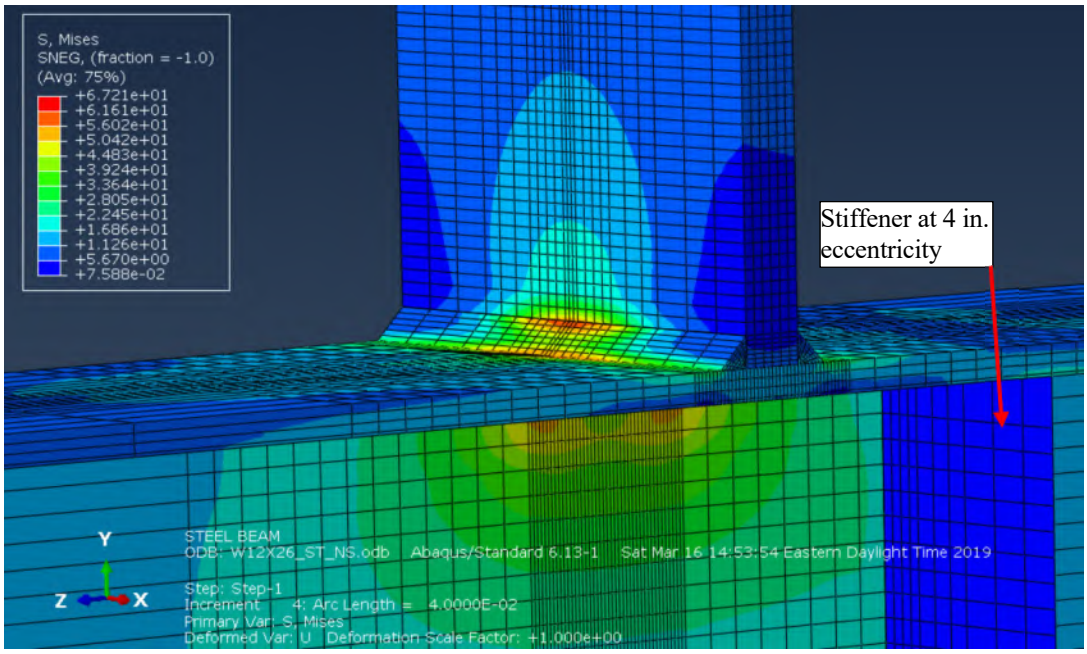

Figure 5.4-11: Finite element model of W12X26-ST-E4 while remaining elastic

Figure 5.4-12 shows the stress distribution in the column specimen while it was behaving inelastic and at a load of 85 kips. The stress contours for the Von Mises stress distribution were set to range to 65 ksi. Therefore, any grey areas have a Von Mises stress higher than 65 ksi. The stresses are relatively uniform in the welds where they connect to the column flange but are still higher at the center where they interact with the loading plate. The stresses in the web of the column specimen have exceeded the yield stress, thus indicating that tension yielding of the web has also occurred.

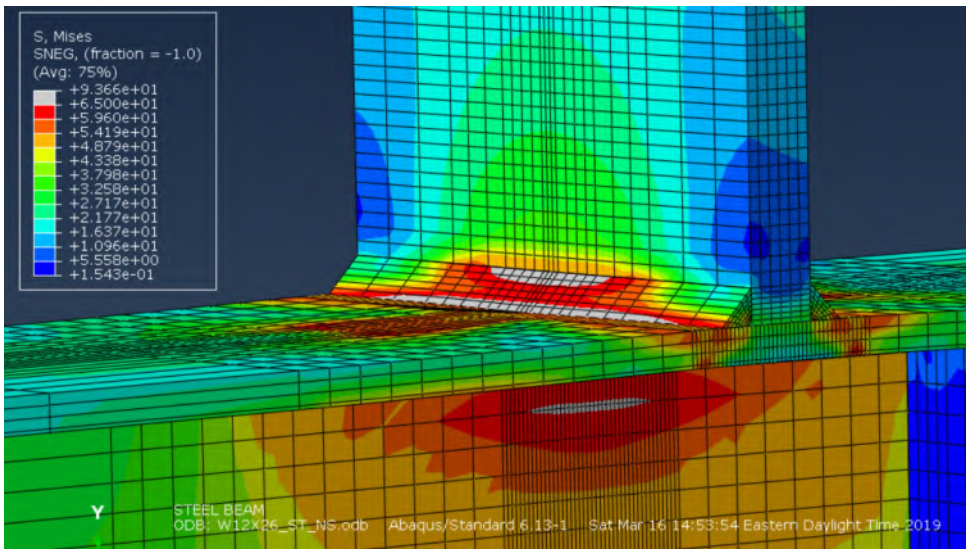

Figure 5.4-12: Finite element model of W12X26-ST-E4 while behaving inelastic

To identify when failure occurs in the weld, the research team evaluated when the Von Mises stress exceeded the ultimate stress, which was specified as 82.4 ksi. Therefore, this magnitude was specified as an upper limit for the contours and a grey area suggests that the stress was exceeded. Figure 5.4-13 shows a screenshot of the finite element model when a portion of the weld stress exceeds 82.4 ksi. Note that in the column specimen, there were "spots" where this stress level was exceeded but failure was identified in the weld during the experimental test. In the final analytical study selected, this occurred at a load of approximately 111 kips which compared reasonably well to the maximum load obtained during the experimental investigations of 114 kips. The results in Figure 5.4-13 show high weld stresses, significant web local yielding and significant bending of the flange at this load magnitude.

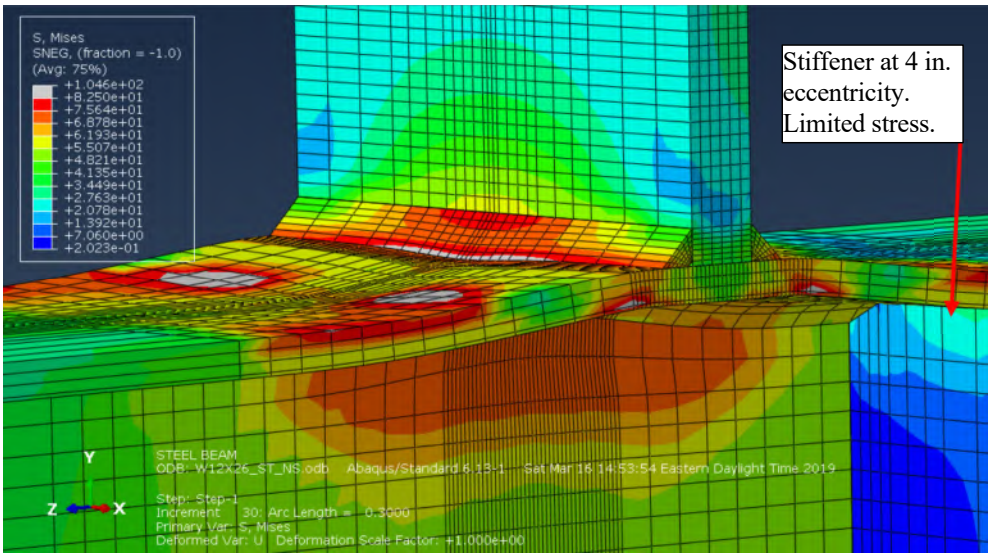

Figure 5.4-13: Finite element model of W12X26-ST-E4 at assumed failure load of 111 kips

This finite element model provides an additional piece of evidence of how stiffeners at this eccentricity and for this column size do not assist in resisting the effects of the concentrated load. Figure 5.4-14 shows the stress distribution from above the column specimen. The stress profile is very close to a mirror image on either side of the concentrated load. In fact, there are very small differences even though Figure 5.4-13 shows that a small amount of force transfers to the top of the stiffeners since some stress is seen in the stiffener.

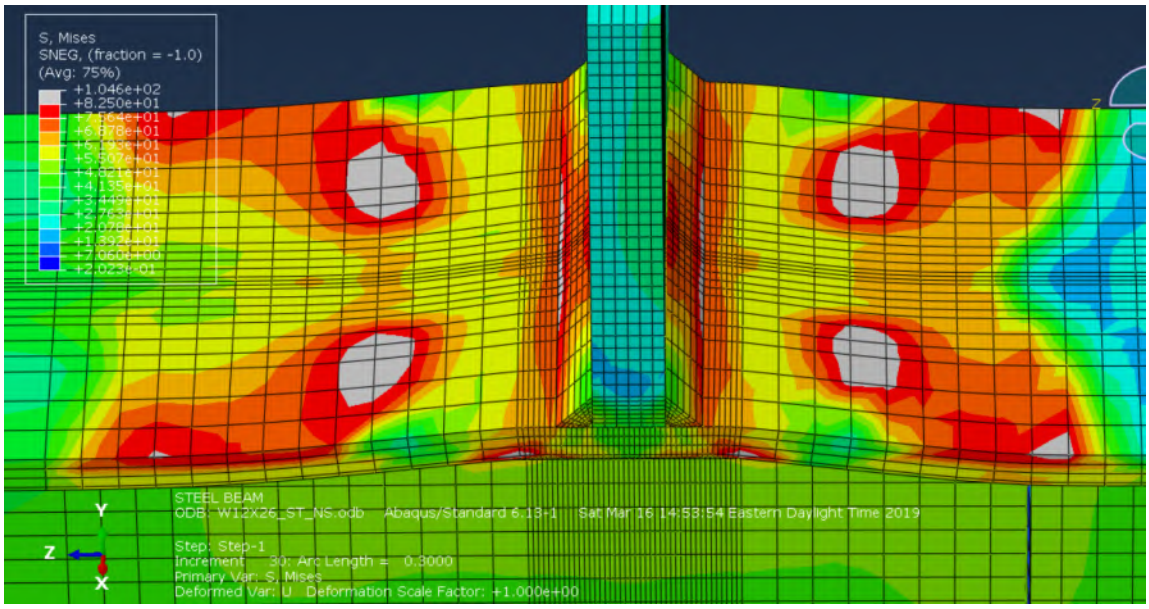

Figure 5.4-14: W12X26-ST-E4 at load of 111 kips, showing stress distribution from top

The load-displacement relationship of the analytical column specimen was compared to the experimental results. In order to perform the comparison, a linear portion of the experimental load-displacement curve was used to determine the elastic flexural stiffness. Due to a shift in the displacement at around 60 kips (assumed slip in test setup), the portion of the curve used to determine the elastic stiffness was from an applied load of 61 kips to 79 kips. Then, a straight line was drawn from the origin and the experimental displacement was adjusted such that the elastic portion of the results overlapped the straight line. This line is then further used to identify when nonlinear behavior initiates after that. From the data, it appears that non-linear behavior initiated experimentally at about 87 kips.

The aforementioned experimental results are shown with the analytical results in Figure 5.4-15. Both the experimental and analytical results are shown with straight lines from the origin that have the same flexural stiffness as the elastic portions of the load-displacement results.

The observations are similar as for W16X31-ST-NA. Although the maximum load obtained analytically compares well with the maximum load obtained experimentally, non-linear behavior appears to initiate at a lower load in the analytical results. In addition, more inelastic displacement occurs prior to reaching the assumed load-carrying capacity.

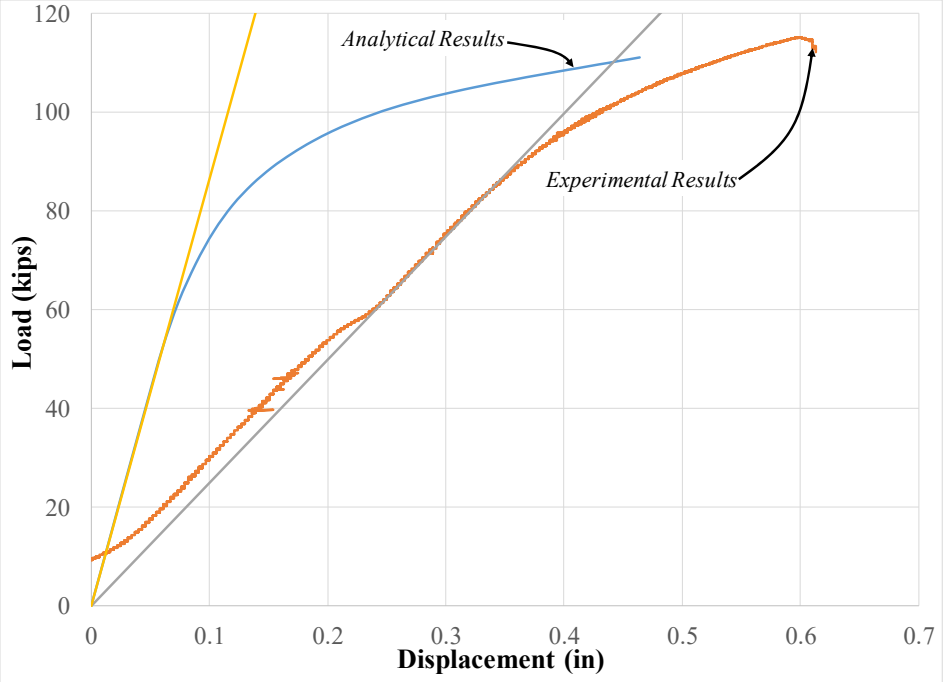

Figure 5.4-15: Comparison of analytical and experimental load-displacement relationships for the W12X26-ST-E4 column specimen

All observations made when comparing the experimental and analytical results were similar to the observations made for the W16X31 column specimen. Therefore, there is consistency in the analytical results for the single tension analytical models without concentric stiffeners. After evaluating all evidence in the results, the research team once again found that the behavior of the finite element models is similar with respect to weld stress behavior and maximum load capacity and can be used for further studies.

5.4.3 W16X31-ST-E0

A finite element model was developed for W16X31-ST-E0, which represents the W16X31 column specimen tested in single tension and with stiffeners on either side of the column specimen underneath the applied concentrated load. This study was used specifically to study the effect of concentric stiffeners on the analytical results for single compression tests and to validate the modeling technique for single tension tests with stiffeners so that larger columns sections could be studied. This particular column size yielded the most beneficial results for single tension tests performed in this research, thus providing confidence in the results.

Figure 5.4-16 shows a screenshot of the finite element model while it was still behaving elastically. The deformations are scaled at 1X (actual scale). Even with the concentric stiffeners, Figure 5.4-16 shows that the weld stresses are higher and concentrated near the center of the weld. In comparison to the single tension tests without stiffeners, the stiffeners provide enough stiffness to avoid excessive deformations in the flanges and thus, avoid excessive unequal stresses along the length of the weld. Figure 5.4-17 shows the finite element model after inelastic deformations initiate in the weld. The grey area indicates stresses beyond 70 ksi, chosen arbitrarily to emphasize where significant inelastic deformations occur. As inelastic deformations initiate on the top flange, the weld stresses become more uniform along the length. However, the stresses are still higher near the center of the weld as opposed to near the edges. It is also worth noting that there is a stress concentration on the flange near the stiffener plates.

To indicate when failure occurs in the weld, the research team identified when the Von Mises stress exceeded the ultimate stress, which was specified as 82.4 ksi. Therefore, this magnitude was specified as an upper limit for the contours and a grey area suggests that the stress was exceeded. Figure 5.4-18 shows a screenshot of the finite element model when a portion of the weld stress exceeds 82.4 ksi. The screenshot also shows significant inelastic deformations on the flange region connected to the concentric stiffener, meaning that this region could potentially fail. However, more significant deformations occur near the center of the weld where it connects to the loading plate and, therefore, it was assumed by the research team that failure occurred at this location. In the finite element model, this occurred at a load magnitude of 157.5 kips.

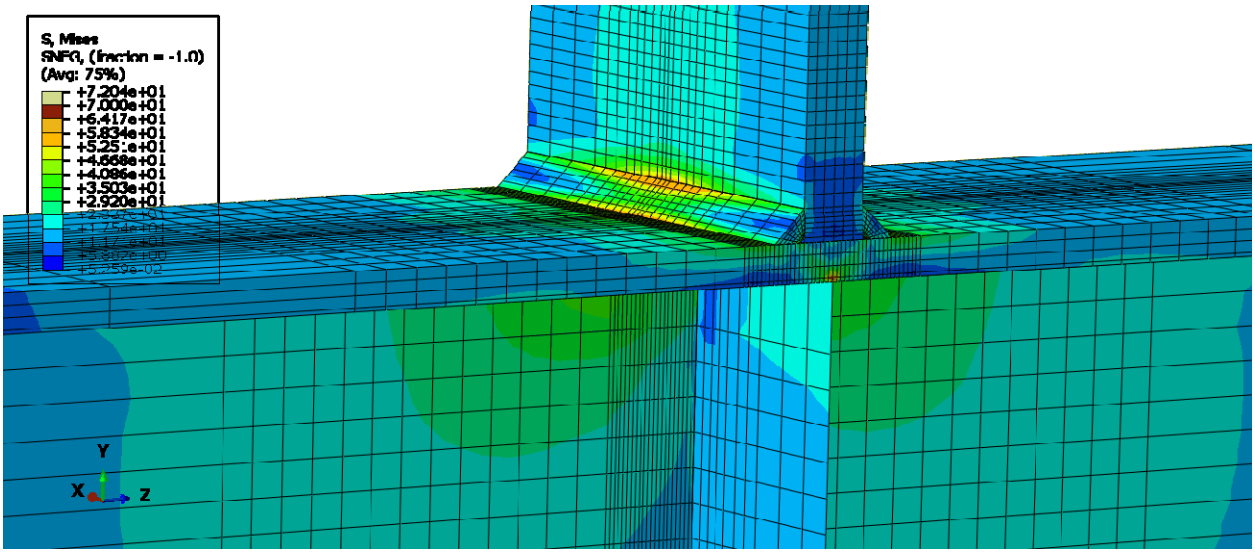

Figure 5.4-16: Finite element model of W16X31-ST-E0 while remaining elastic

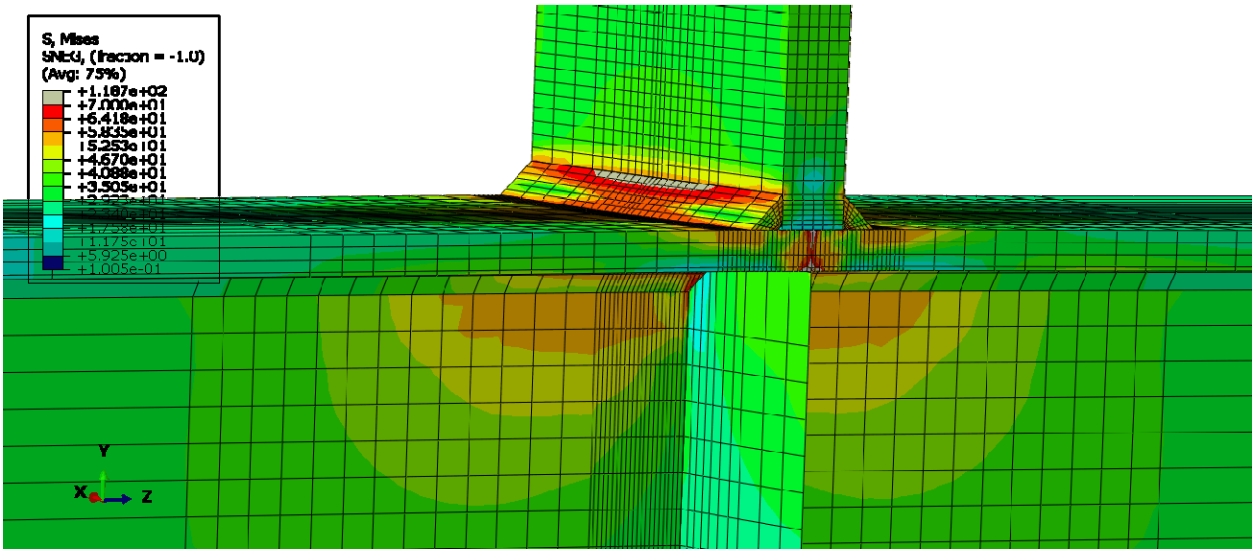

Figure 5.4-17: Finite element model of W16X31-ST-E0 while behaving inelastic

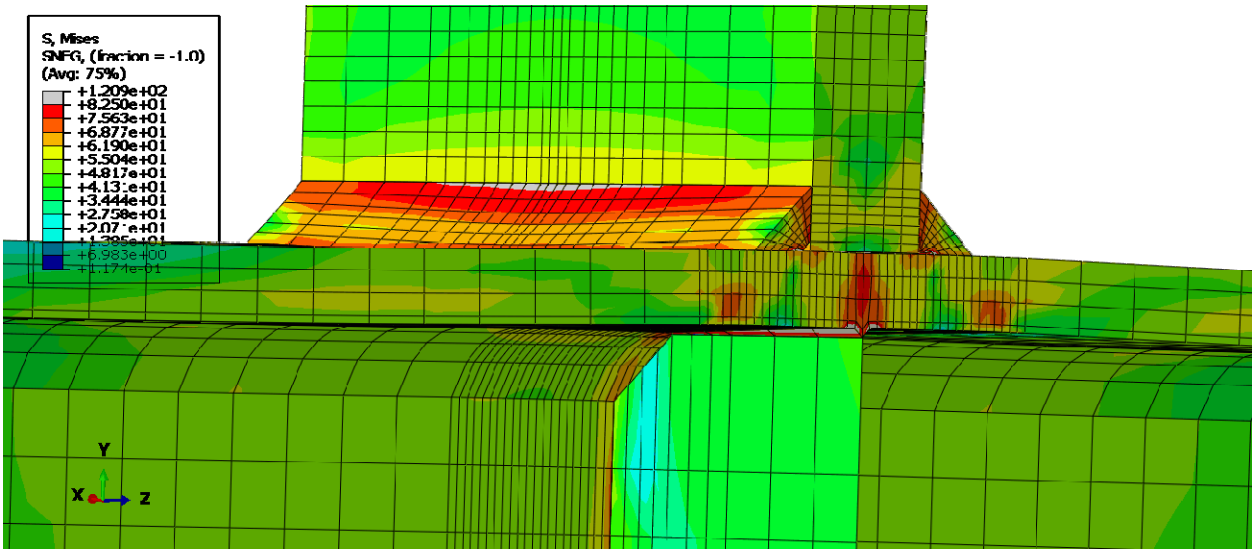

Figure 5.4-18: Finite element model of W16X31-ST-E0 at assumed failure load of 157.5 kip

The load-displacement relationship of the analytical columns specimen was compared to the experimental results. In order to perform the comparison, a linear portion of the experimental load-displacement curve was used to determine the elastic flexural stiffness. The portion of the curve used to determine the elastic stiffness was from an applied load of 60 kip to 100 kips. This line was then further used to identify when nonlinear behavior initiates after that. From the data, it appears that nonlinear behavior initiated experimentally at approximately 120 kips. Nonlinear behavior initiated analytically at approximately 100 kips.

The aforementioned experimental results are shown with the analytical results in Figure 5.4-19. Both results are shown with straight lines from the origin that have the same flexural stiffness as the elastic portions of the load-displacement results. The analytical test reaches it maximum load capacity shortly after inelastic behavior initiates.

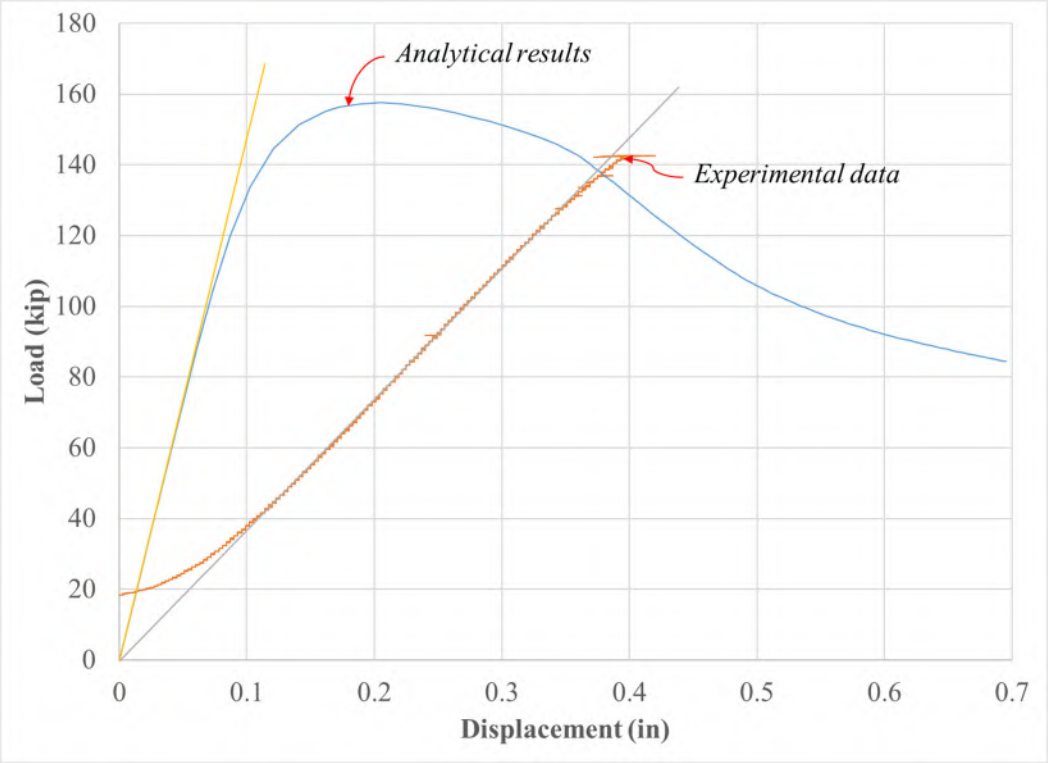

Figure 5.4-19: Comparison of analytical and experimental load-displacement relationships for the W16X31-ST-E0 column specimen

All observations made when comparing the experimental and analytical results were similar to the observations made for the W16X31-ST-NA column specimen. Therefore, there is consistency in the analytical results for the single tension analytical models.

5.4.4 W12X26-ST-E0

A finite element model was developed for W12X26-ST-E0, which represents the W12X26 column specimen tested in single tension and with stiffeners on either side of the column specimen underneath the applied concentrated load. Similar to W16X31-ST-E0, the experimental column specimen reached the maximum capacity of the hydraulic actuator and the conclusions derived for this section are similar to those derived in Section 5.4.3.

Figure 5.4-20 shows a screenshot of the finite element model while it was still behaving elastically. The deformations are scaled at 1X (actual scale). As concluded during the experimental investigations, the weld stresses are higher and concentrated near the center of the weld but they are not as pronounced as for the no stiffener condition. In comparison to the single tension tests without

stiffeners, the stiffeners provide enough stiffness to avoid excessive deformations in the flanges and thus, avoid "excessive" unequal stresses along the length of the weld. Figure 5.4-21 shows the finite element model after inelastic deformations initiate in the weld. The grey area indicates stresses beyond 70 ksi, chosen arbitrarily to emphasize where significant inelastic deformations occur. As inelastic deformations initiate on the top flange, the weld stresses become more uniform along the length. However, the stresses are still higher near the center of the weld as opposed to near the edges.

Figure 5.4-22 shows a screenshot of the finite element model when a portion of the weld stress exceeds 82.4 ksi. The screenshot also shows significant inelastic deformations on the flange region connected to the concentric stiffener. However, more significant deformations occur on the center of the weld where it connects to the loading plate and, therefore, it is assumed that failure occurs at this location. In the finite element model, this occurred at a load magnitude of 155 kips.

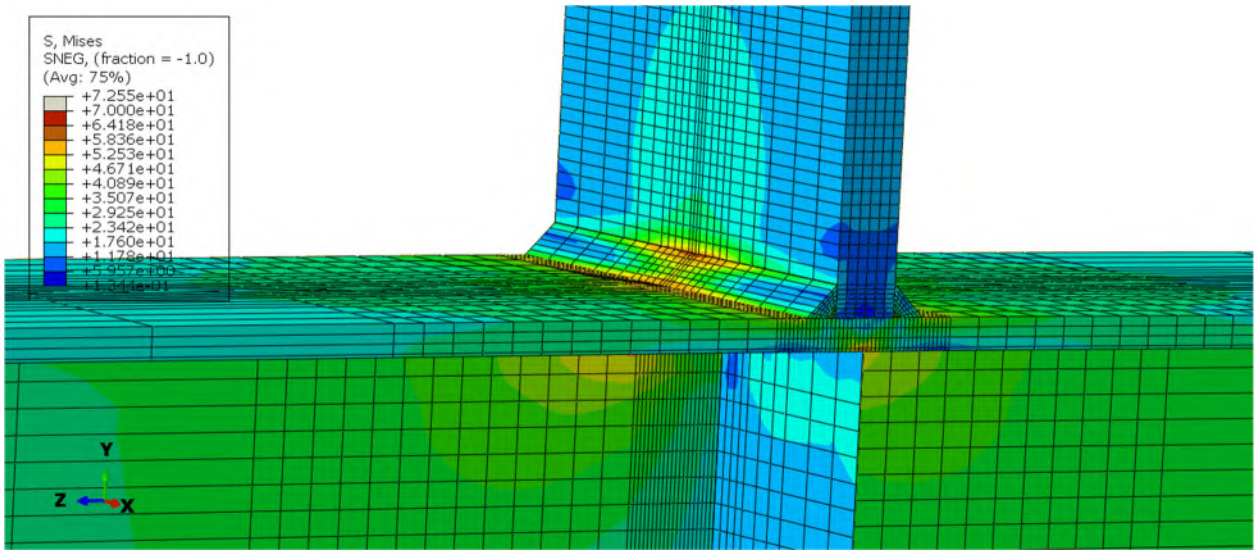

Figure 5.4-20: Finite element model of W12X26-ST-E0 while remaining elastic

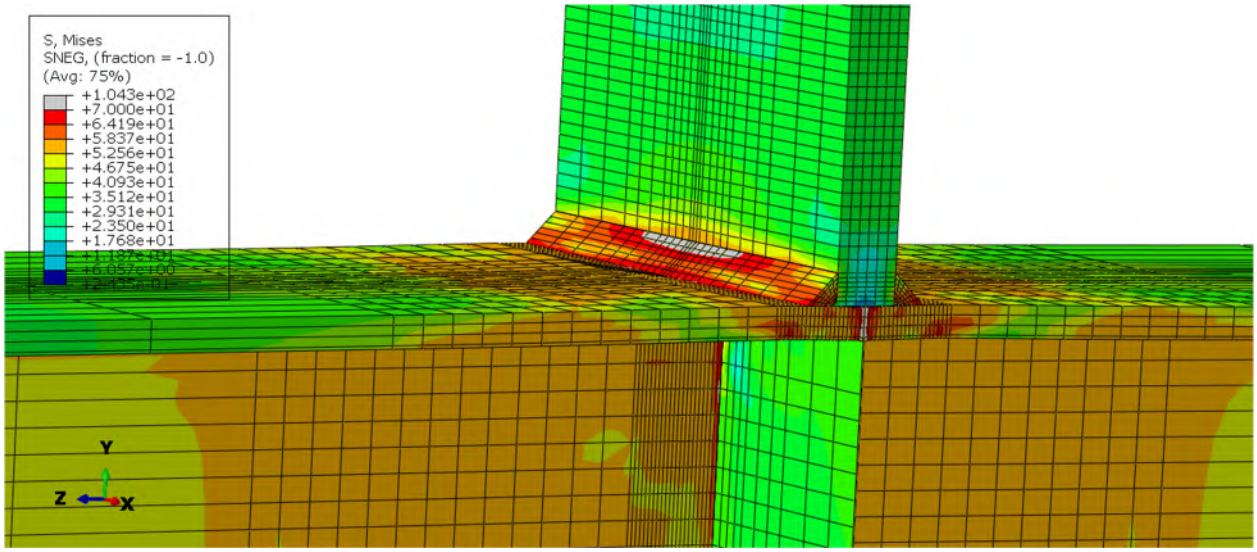

Figure 5.4-21: Finite element model of W12X26-ST-E0 while behaving inelastic

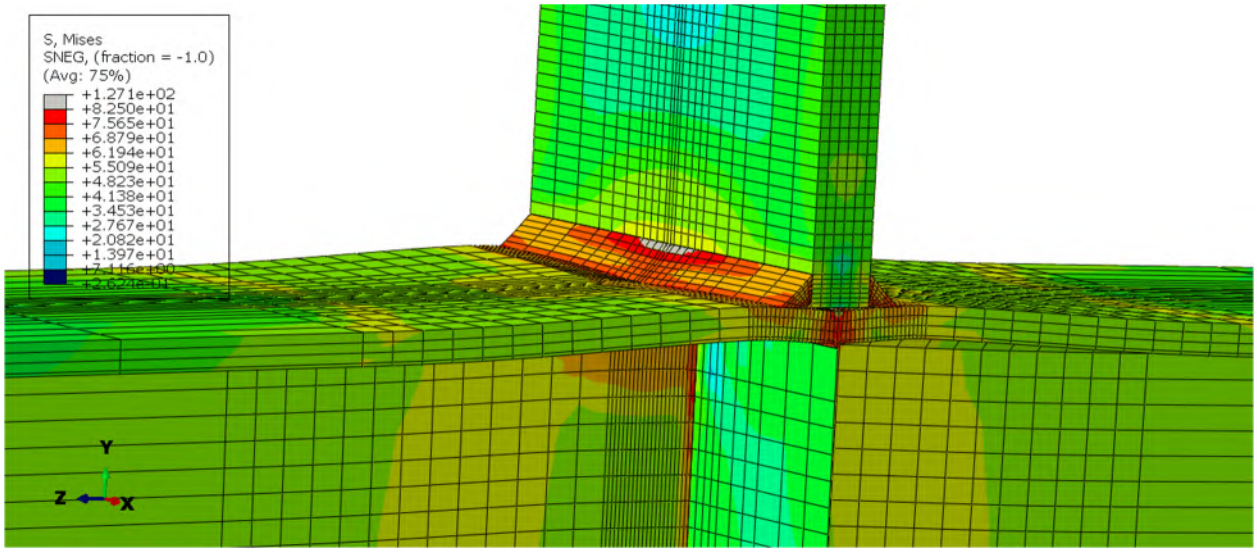

Figure 5.4-22: Finite element model of W12X26-ST-E0 at assumed failure load of 155 kip

The load-displacement relationship of the analytical columns specimen was compared to the experimental results. In order to perform the comparison, a linear portion of the experimental load-displacement curve was used to determine the elastic flexural stiffness. The portion of the curve used to determine the elastic stiffness was from an applied load of 60 kip to 100 kips. This line was the further used to identify when nonlinear behavior initiates after that. From the data, it appears that nonlinear behavior initiated experimentally at approximately 120 kips, which compared well with the analytical results.

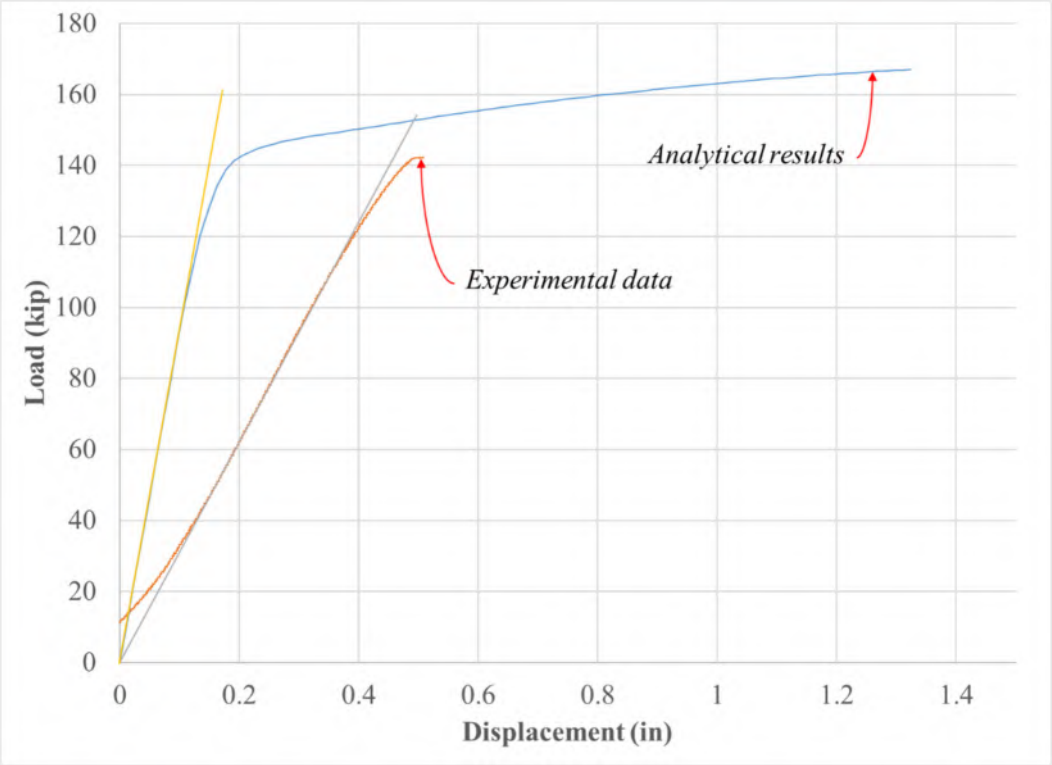

Figure 5.4-23: Comparison of analytical and experimental load-displacement relationships for the W12X26-ST-E0 column specimen

5.5 Summary of Analytical Models of Column Specimens

Table 5.5-1 provides the % error between the experimental results and the finite element results with no imperfection and imperfections of 0.001% and 0.2%. Both single compression and double compression models with stiffeners were only modeled using a *STATIC RIKS analysis without imperfections as explained in Section 4.5.2. Similarly, all tension tests were modeled without imperfection since buckling or crippling effects were not expected as stated in Section 4.5.2. All single and double compression tests without stiffeners were modeled with imperfections of 0.001% and 0.2%. Regardless of the imperfection conditions, all maximum loads obtained analytically were close to the maximum loads obtained in the experimental results, which reaffirms that the methodology used for the finite element modeling are valid and are acceptable for larger sections.

In Table 5.5-1, the column specimens that reached the maximum load capacity of the hydraulic actuator have a "+" sign next to the maximum load, meaning that the actual maximum load is higher than the magnitude shown.

Some conclusions from the analytical investigations presented in this chapter were as follows:

- The *STATIC RIKS analysis was consistently generating failure mechanisms and shapes similar to those witnessed in the experimental tests.
- In general, an imperfection of 0.001% usually gave more accurate results compared to an imperfection of 0.2% for the column sections without stiffeners. However, this conclusion is not firm since in some cases, a 0.2% imperfection gave more accurate results. Either way, in reality, there is a significant difference between 0.001% and 0.2% and the primary conclusion is *only a small imperfection is required in the finite element models*.
- The imperfection was crucial in the tests without stiffeners since the actual imperfections in the column sections played an important role in determining the load capacity of the section when a buckling mode was expected. In tests with stiffeners, the imperfection was found negligible since the stiffeners negated the influence in the actual condition.
- There were significant differences in the elastic stiffness of the analytical vs. experimental results. Reasons are not fully understood but the experimental displacement includes all deformations that could occur in all elements of the test setup, whereas the analytical displacement only considers deformations in the column specimen and portions of the top and bottom loading plates.
- For single tension tests, there are stress concentration in the welds attaching the loading plate to the top flange.
    - For tests without concentric stiffeners, the stress concentration is very uneven along the length of the weld due to excessive flange bending.
    - For tests with concentric stiffeners, the stresses are still not uniform along the length. However, the condition is more favorable in comparison to the condition without concentric stiffeners.

Table 5.5-1: Comparison between experimental vs. analytical results

Column Specimens	Experimental	Static Riks Analysis		0.001% Imp.		0.2% Imp.	
	Max. Load (k)	Max. Load (k)	% Err.	Max. Load (k)	% Err.	Max. Load (k)	% Err.
W10X19-DC-E0	180	184	2.22	-	-	-	-
W10X19-DC-NA	78.5	-	-	87.1	10.96	82.5	5.10
W12X26-DC-E0	220+	236.7	7.59	-	-	-	-
W12X26-DC-NA	86.3	-	-	87.9	1.85	80.7	6.49
W12X26-DC-E4	90.5	99.4	9.83	-	-	-	-
W16X31-DC-NA	121	-	-	115	4.96	105	13.22
W10X39-SC-E0	198	176	11.11	-	-	-	-
W10X39-SC-NA	130.9	-	-	128.8	1.60	125.6	4.05
W12X26-SC-E0	148.2	156.9	5.87	-	-	-	-
W12X26-SC-NA	78.8	-	-	83.1	5.46	78.8	0.00
W12X26-SC-E4	79.1	95.8	21.11	-	-	-	-
W12X26-ST-E0	142.5+	155	8.77	-	-	-	-
W12X26-ST-E4	114	111	2.63	-	-	-	-
W16X31-ST-E0	142.5+	157.5	10.53	-	-	-	-
W16X31-ST-NA	127	122	3.94	-	-	-	-

CHAPTER 6: FURTHER ANALYTICAL STUDIES TO EVALUTE ECCENTRICITY

6.1 Introduction

Analytical investigations were performed to further evaluate the influence of eccentricity on the effective stiffener capacity using larger columns specimens in comparison to the smaller column specimens tested experimentally. The column specimens were subjected to single tension, single compression and double compression. For the double compression tests, the models were adjusted such that both top and bottom plates simulate a true through force, compared to the previous analytical phase where the bottom plate was a reaction. This was achieved by constraining the bottom loading plate to move at the same rate as the top loading plate but in an opposite direction.

The quantity of analyses performed was proposed in the preliminary report. However, the amount of tests performed increased substantially during the analytical studies performed in this research. In the preliminary report, it was recommended to perform 16 analytical models of column specimens in single compression, 16 in double compression, and 16 in single tension. The 16 models for each test method included 4 column sizes and 4 analyses per size. However, the scope was adjusted as discussed in Section 6.2 to include 34 models in single compression, 42 models in double compression and 72 models in single tension.

Dissimilar from the experimental results, the analytical results presented herein suggest there is some benefit in utilizing eccentric stiffeners when concentric stiffeners are not feasible and when the larger column sections are used. Variables associated with this study are vast and can include the section size, magnitude of eccentricity, stiffener thickness, loading plate thickness and width, column unsupported length, and weld size when single tension tests are modeled. The study presented in this chapter focuses on the first two variables of section size and magnitude of eccentricity. For single tension tests, a variety of weld sizes and loading plate thickness is also evaluated. All stiffeners had a 3/8 in. thickness, all columns were 6 ft. long and all loading plates for compression tests had a thickness of 1 in. and a width equal to the width of the column size evaluated.

6.2 Analytical Test Matrix

The basic analytical test matrix is provided in Table 6.2-1. The nomenclature shown in the table is for an analysis set of four specimens. For each analysis set: (1) one model was analyzed with no stiffeners near the concentrated load, (2) one was analyzed with concentric stiffeners, (3) one was analyzed with stiffeners at a 2 in. eccentricity for the concentrated load, and (4) one was analyzed with stiffeners at a 4 in. eccentricity for the concentrated load. The nomenclature used for each individual model is similar to that used for the experimental column specimens and includes the column size, the test method, and the magnitude of eccentricity (NA for no stiffener, E0 for concentric stiffener, E2 for a 2 in. eccentricity, and E4 for a 4 in. eccentricity). For the single tension tests, one additional nomenclature variable is used to represent the weld thickness from the loading plate to the top flange of the column specimens. For double compression and single compression tests, the additional nomenclature variable represents the stiffener thickness as it varied as discussed later in this section.

Table 6.2-1: Analytical test matrix for evaluating influence of eccentricity

Nomenclature	Test Type	Column Size	Stiff. 't_s' (in)	Unsupported Length (ft)	Plate 't' (in)	Weld (in)
W24X131-SC-3/8	Single Compression	W24X131	3/8	5	1	NA
W24X229-SC-3/8		W24X229	3/8	5	1	NA
W14X68-SC-3/8		W14X68	3/8	5	1	NA
W14X120-SC-3/8		W14X120	3/8	5	1	NA
W14X176-SC-3/8		W14X176	3/8	5	1	NA
W14X233-SC-3/8		W14X233	3/8	5	1	NA
W24X229-SC-3/4		W24X229	3/4	5	1	NA
W14X233-SC-3/4		W14X233	3/4	5	1	NA
W14X233-SC-3/4(2)		W14X233	3/4	3.5	1	NA
W24X131-DC-3/8	Double Compression	W24X131	3/8	NA	1	NA
W24X229-DC-3/8		W24X229	3/8	NA	1	NA
W14X68-DC-3/8		W14X68	3/8	NA	1	NA
W14X120-DC-3/8		W14X120	3/8	NA	1	NA
W14X176-DC-3/8		W14X176	3/8	NA	1	NA
W14X233-DC-3/8		W14X233	3/8	NA	1	NA
W24X131-DC-3/4		W24X131	3/4	NA	1	NA
W24X229-DC-3/4		W24X229	3/4	NA	1	NA
W14X68-DC-3/4		W14X68	3/4	NA	1	NA
W14X120-DC-3/4		W14X120	3/4	NA	1	NA
W14X176-DC-3/4		W14X176	3/4	NA	1	NA
W14X233-DC-3/4		W14X233	3/4	NA	1	NA
W24X131-ST-1/4	Single Tension	W24X131	3/8	5	3/4	1/4
W24X229-ST-1/4		W24X229	3/8	5	3/4	1/4
W14X68-ST-1/4		W14X68	3/8	5	3/4	1/4
W14X120-ST-1/4		W14X120	3/8	5	3/4	1/4
W14X176-ST-1/4		W14X176	3/8	5	3/4	1/4
W14X233-ST-1/4		W14X233	3/8	5	3/4	1/4
W24X131-ST-9/16		W24X131	3/8	5	1 1/2	9/16
W24X229-ST-9/16		W24X229	3/8	5	1 1/2	9/16
W14X68-ST-9/16		W14X68	3/8	5	1 1/2	9/16
W14X120-ST-9/16		W14X120	3/8	5	1 1/2	9/16
W14X176-ST-9/16		W14X176	3/8	5	1 1/2	9/16
W14X233-ST-9/16		W14X233	3/8	5	1 1/2	9/16
W24X131-ST-7/8		W24X131	3/8	5	2 1/4	7/8
W24X229-ST-7/8		W24X229	3/8	5	2 1/4	7/8
W14X68-ST-7/8		W14X68	3/8	5	2 1/4	7/8
W14X120-ST-7/8		W14X120	3/8	5	2 1/4	7/8
W14X176-ST-7/8		W14X176	3/8	5	2 1/4	7/8
W14X233-ST-7/8		W14X233	3/8	5	2 1/4	7/8

For each analysis set, Table 6.2-1 indicates the test method, the column size, the thickness of the stiffener, the unsupported length as one additional test set was performed with an unsupported length of 3.5 ft. in lieu of 5 ft., the thickness of the loading plate, and the weld size used in the models for single tension tests. Overall, six column sizes were selected for the analytical investigations. This includes four different W14 column sizes, which will be critically evaluated to investigate the influence of 'stockiness' on the eccentric stiffener results. As size of the W14 increases, the flange thickness increases and the slenderness of the flange ($b_f / 2t_f$) and the slenderness of the web (h / t_w) both decrease. Per conversations with the AISC Research Advisory Committee, it is also necessary to evaluate large W24 sections that are used as columns in more seismic prone regions. Therefore, and additional 2 column sizes were selected with one size almost twice the weight of the other size.

For the single tension tests, a weld size of 1/4 in. was originally selected. However, it was determined that for most column sizes, the 1/4 in. weld fails at a load close to the theoretical weld capacity. In addition, the stresses across the width of the flange were uniform suggesting minimal flange bending. Therefore, additional weld sizes of 9/16 in. and 7/8 in. were added to the test matrix. For each weld size, a different loading plate thickness was also used to ensure failure does not occur in the base metal prior to the weld (it was later decided to model the plates as elastic only negating this possibility). For the smaller weld size of 1/4 in., a 3/4 in. thickness loading plate was used, for the 9/16 in. weld, a 1 1/2 in. thick loading plate was used, and for a weld size of 7/8 in., a 2 1/4 in. thick loading plate was used.

Initially, all single and double compression tests were performed with 3/8 in. stiffeners. However, this thickness was determined too small to properly evaluate larger column sizes based on the behavior of the column specimens. Therefore, models were studied with 3/4 in. stiffeners as well. The studies with 3/8 in. are still utilized to evaluate most of the single compression results and to directly evaluate the influence of stiffener thickness in the double compression results.

One test set (W14X233-SC-3/4) was evaluated with an unbraced length of 3.5 ft. instead of 5 ft., which was used for the experimental investigations. Reasons are discussed in Section 6.5.6.

6.3 Material Properties

For the analytical investigations presented in this chapter, the research team used minimum material properties that are assumed in the AISC Steel Construction Manual (AISC, 2017) for A992 steel. These include a minimum yield stress of 50 ksi, a minimum ultimate stress of 65 ksi, and an elastic modulus of 29000 ksi. To determine a realistic stress-strain relationship that includes these properties, uniaxial tension tests performed on samples fabricated from the column specimens were utilized. Figure 6.3-1 demonstrates how the stress-strain curves derived from the experimental investigations were modified to develop similar stress-strain curves with the minimum properties specified for A992 steel. For all analytical models presented in this chapter, the curve labeled as "Modified Stress-Strain Curve" was used for all column specimens.

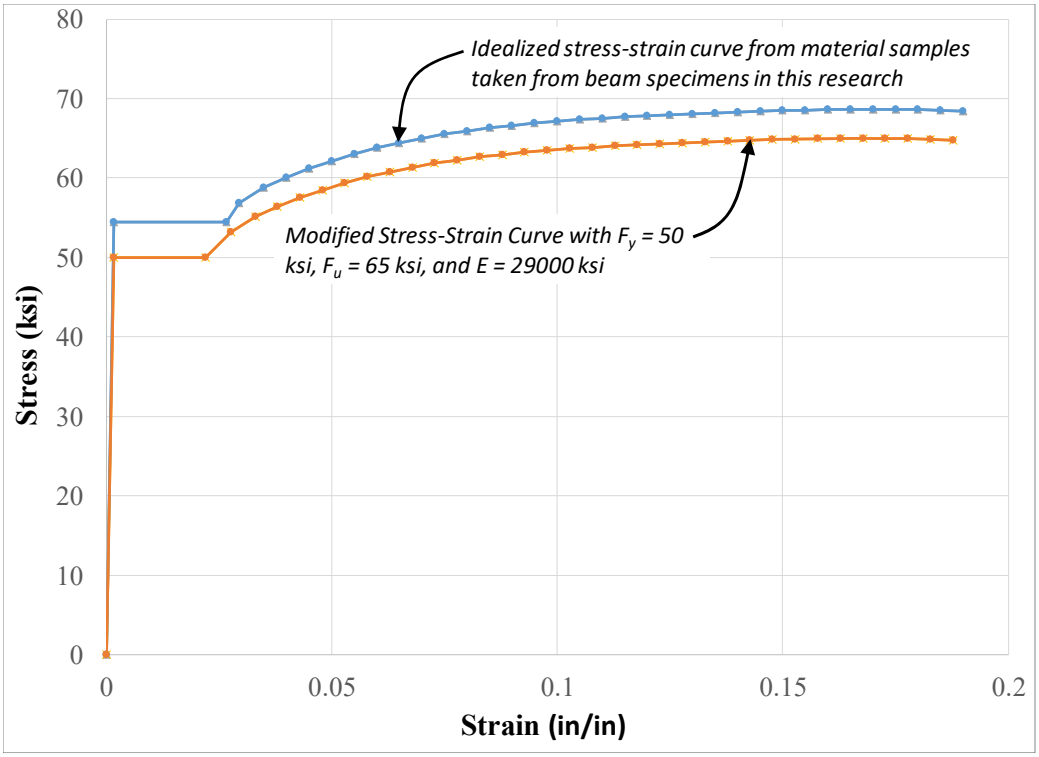

Figure 6.3-1: Idealized strain curve used for analytical studies

In the experimental investigations, the research team found diverse results for uniaxial tension tests performed on samples fabricated from stiffener plates. After further inspection of the material order, the steel supplier indicated that some stiffeners met the properties for A36 but other stiffeners met the properties for A36 and A572 Gr. 50. To avoid another parameter in the research, all

stiffeners were modeled with the same material properties as the experimental column specimens as shown in Figure 6.3-1.

6.4 Modeling Changes from Experimental Column Specimens

Initial analytical investigations with larger column specimens revealed that the loading plate did not have adequate capacity to deliver the loads necessary to generate a concentrated load failure mechanism. When load was applied, significant yielding occurred in the loading plate. The thickness of the loading plate and material properties are other potential variables in the analytical study. The research team decided that variation in the loading plate is not as critical as other variables including the column size, stiffener eccentricity, and stiffener thickness. In addition, it is assumed in design that what loads the column will be evaluated elsewhere when the entire moment connection is evaluated. Therefore, the loading plate was modeled elastic only and with an elastic modulus of 29000 ksi. The elastic behavior allowed the loading plates to deform as the column specimen flanges and/or welds deformed but disallowed them from being the source of failure.

For larger column specimens, the loading plates started to buckle elastically under high loads, which dictated the load capacity within the models. Therefore, the center nodes within the loading plate were fixed along the longitudinal axis of the column specimens to prevent this from occurring as illustrated in Figure 6.4-1.

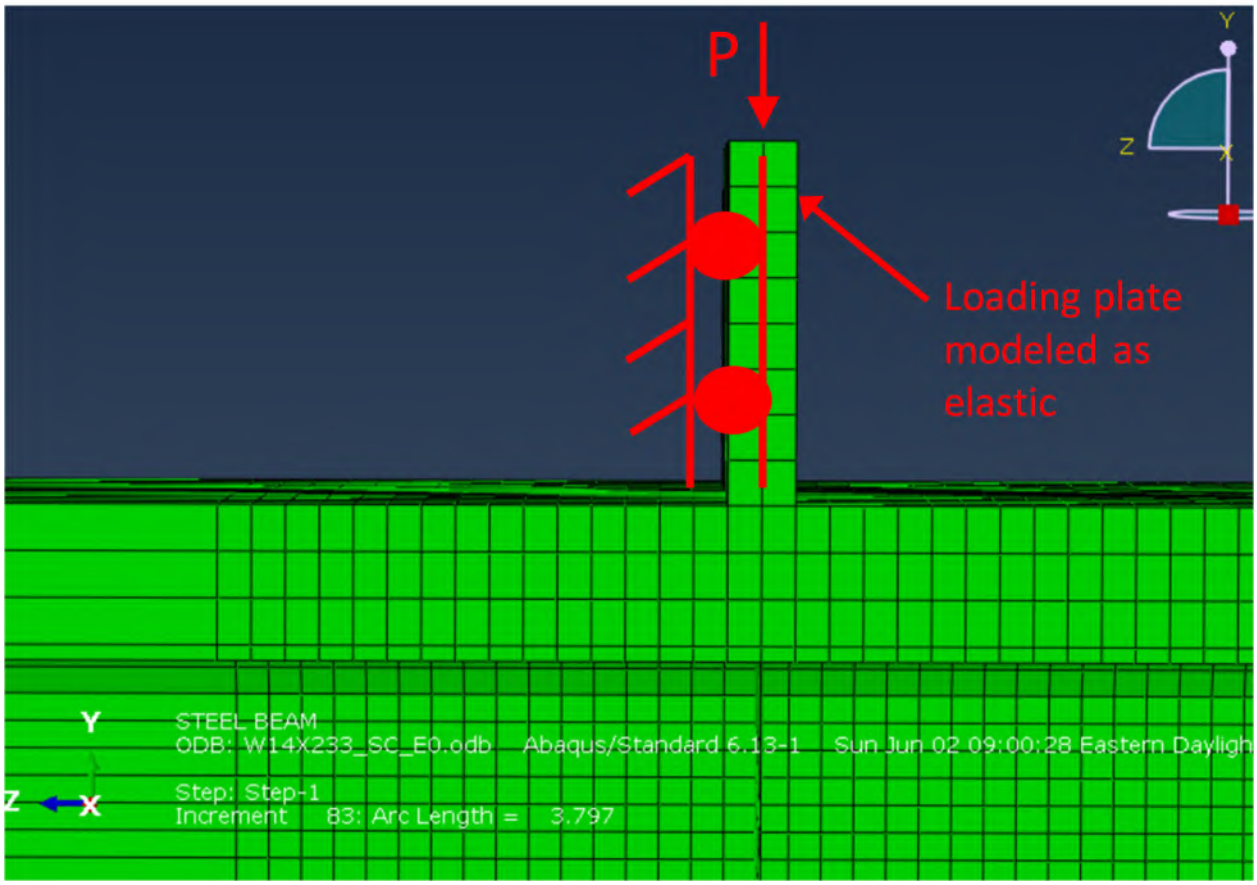

Figure 6.4-1: Additional boundary condition used for loading plate

In the finite element models of the experimental column specimens subjected to a compression loading condition, the research team used C3D8I elements to model the column size and loading plate, which are eight-node three-dimensional continuum elements with three degrees of freedom per node and enhanced by incompatible modes to improve its bending behavior (ABAQUS, 2014). However, for specific models of larger column specimens, the finite element program had issues converging to a solution under higher loads due to severe distortions of the elements. The models in a way were "stuck" at higher loads and the next increment of the analysis could not complete. In general, the higher the load capacity, the more susceptible the models were in being "stuck". For instance, when modeling a W14X120 column specimen in single compression, the models with no stiffeners and stiffeners at an eccentricity of 4 in. were able to finish. However, the models with concentric stiffeners and with an eccentricity of 2 in. were stuck at higher loads. Significant time was dedicated to observe the results and identify the cause of this behavior. In one trial evaluation,

all cubic elements for a W14X233 with concentric stiffeners were changed to Type C3D8R, which is an 8-node linear brick, reduced integration with hourglass control element (ABAQUS, 2014). When using this element type in lieu of C3D8I, the analysis was able to complete. To study the accuracy of using this element type, the W14X68 model with 2 in. eccentricity was evaluated with type C3D8R and C3D8I elements. The load-displacement results of the two analytical models near the highest load are shown in Figure 6.4-2. In Figure 6.4-2, the grey line is the result with C3D8I elements and the orange line is the result with C3D8R elements. As shown, the results using either element type are very similar with respect to load capacity and trends in the load-displacement behavior. For consistency, all models were evaluated using C3D8R elements for all loading conditions.

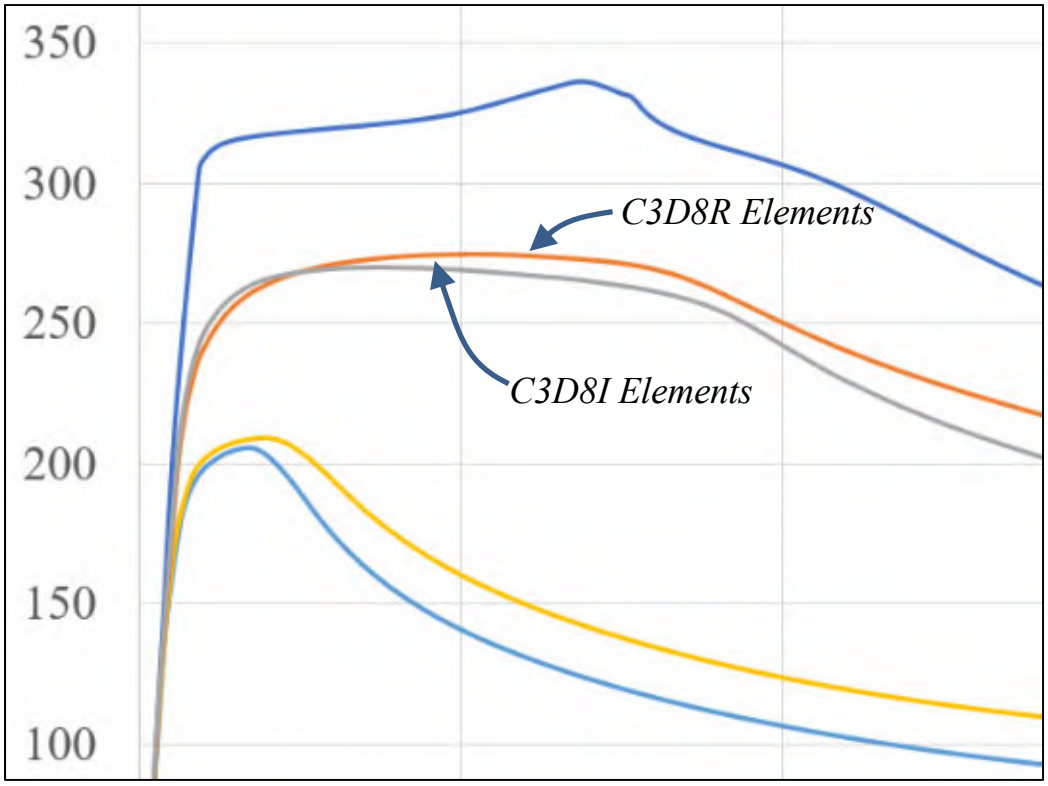

Figure 6.4-2: Comparison of using C3D8I vs. C3D8R for specimen W14X68-SC-E2-3/8

In the experimental investigations of double compression tests, load was applied to the column from a top loading plate that was connected to the hydraulic actuator. A bottom reaction plate was placed below the bottom flange and these conditions were meant to simulate a through force. However, the experimental tests and the analytical investigations of these column specimens

revealed that not all the force is transferred directly through the column specimen and instead, some of the load is transferred to the end supports. Thus, a true double compression test was not achieved. For the analytical investigations of larger column specimens, this was mitigated by enforcing that the bottom loading plate moves equal and opposite the top loading plate. More specifically, one node on the bottom reaction plate was specified to have an equal and opposite displacement as one node on the top loading plate using a constraint equation. All nodes on the top surface of the top reaction plate were specified to have equal displacements and all nodes on the bottom surface of the bottom reaction plate were specified to have the equal displacements. Moreover, the center nodes within the bottom loading plate were fixed along the longitudinal axis in a comparable way to the top loading plate to prevent elastic buckling from occurring (see Figure 6.4-1).

6.5 Analytical Results of Single Compression Tests

This section discusses all the results associated with analytical finite element models of single compression tests. Overall, the performance of each analytical model was diverse and was dependent on the column size, stiffener eccentricity condition, and stiffener thickness. This section will not go into detail regarding the performance of each column specimen but instead provides general observations regarding the behavior of various models and provides the important results associated with each model. Screenshots of all models are provided in Appendix E. Theoretical capacities for the analytical column specimens and for the limit states of web local yielding, web local crippling and for 3/8 in. stiffeners (AISC, 2016) are provided in Appendix D.

6.5.1 Failure Mechanisms and Screenshots

All analytical column specimens without stiffeners reached their capacity when web crippling occurred in the web. However, in some cases, the web crippling behavior (out-of-plane behavior) was similar to the web crippling that occurred for the experimental column specimens and in other cases, web crippling was only observed in a very small area directly under the load. Regardless, there was a decrease in load for a given displacement when web crippling occurred. Depending on the column size, significant yielding was also observed before buckling and contributed significantly to the mode of failure. The results of the experimental column specimens presented in Chapter 3 revealed that most column specimens reached a capacity at a load close to the theoretical web local crippling capacity. This was also true for some of the column specimens evaluated analytically as

shown in Table 6.5-3, which is discussed later in Section 6.5.3. However, as the column specimens became larger, more yielding occurred prior to crippling and the final capacity was found between the theoretical capacities for web local yielding and web local crippling. Since crippling did eventually occur, the failure mode for these specimens is best described as inelastic web local crippling.

Figure 6.5-1 shows a screenshot of W14X68-SC-NA, which reached a maximum load of 232 kips. This result was very close to the theoretical capacity for web local crippling, computed as 234 kips. The contours represent the resultant magnitude of displacement at each point in the column specimen and is used to demonstrate the out-of-plane displacement of the web with the vertical displacement of the loading plate. In Figure 6.5-1, the vertical displacement of the loading plate is approximately 1.5 in.

Figure 6.5-2 shows a screenshot of W14X233-SC-NA, which reached a maximum load of 966 kips. This is between the theoretical capacities for web local yielding of 508 kips and web local crippling of 1495 kips. In Figure 6.5-2, the contours represent the resultant magnitude of displacement at each point in the column specimen (similar to Figure 6.5-1). At this point in the analysis, the vertical displacement of the loading plate is 1.5 in., which is the same as shown for W14X68-SC-NA in Figure 6.5-1. However, at this magnitude of displacement, there is no indication of web local crippling. Figure 6.5-3 shows the Von Mises stress distribution at the same magnitude of displacement and demonstrates that significant yielding has occurred primarily under the load but also along the length of the column specimen in the web from shear. Directly under the load, the Von Mises stress reached the ultimate stress of 65 ksi. Therefore, for stockier columns, the maximum load is controlled by the stress state and not exclusively web local crippling. In Section 6.5.6, this column specimen size (W14X233) is used to evaluate the influence of the unsupported length since significant shear and flexural deformations were identified in this model and models with stiffeners. Figure 6.5-4 shows the column specimens at a displacement of the loading plate of approximately 3 in. when the web starts to cripple locally under the applied load.

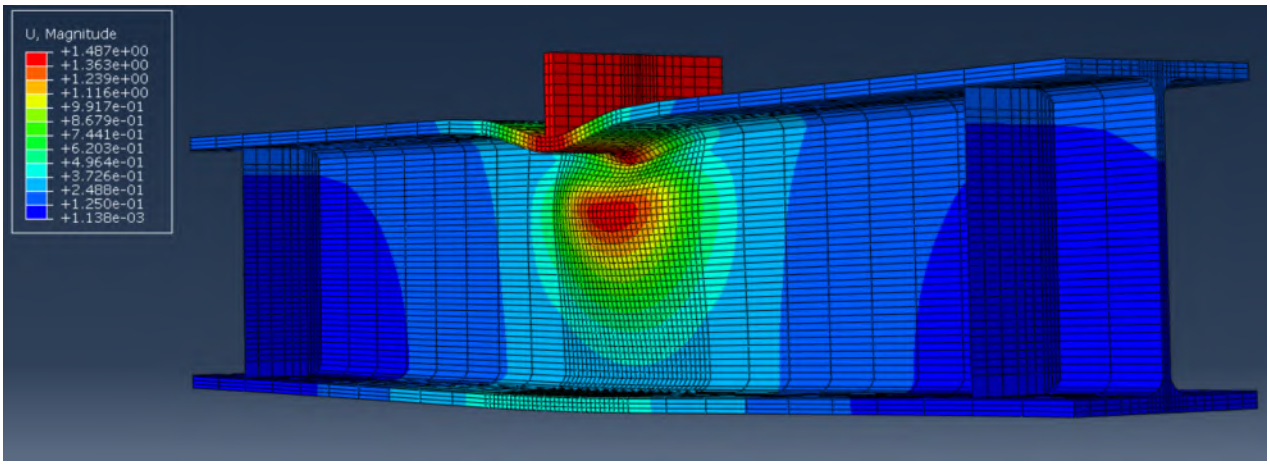

Figure 6.5-1: W14X68-SC-NA at displacement of 1.5 in. emphasizing web crippling

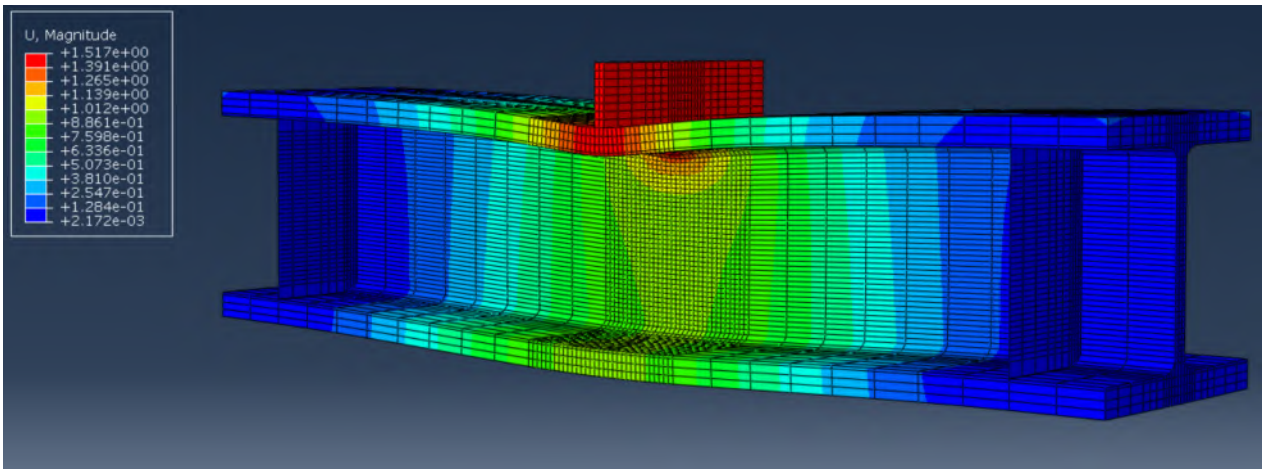

Figure 6.5-2: W14X233-SC-NA at displacement of 1.5 in.

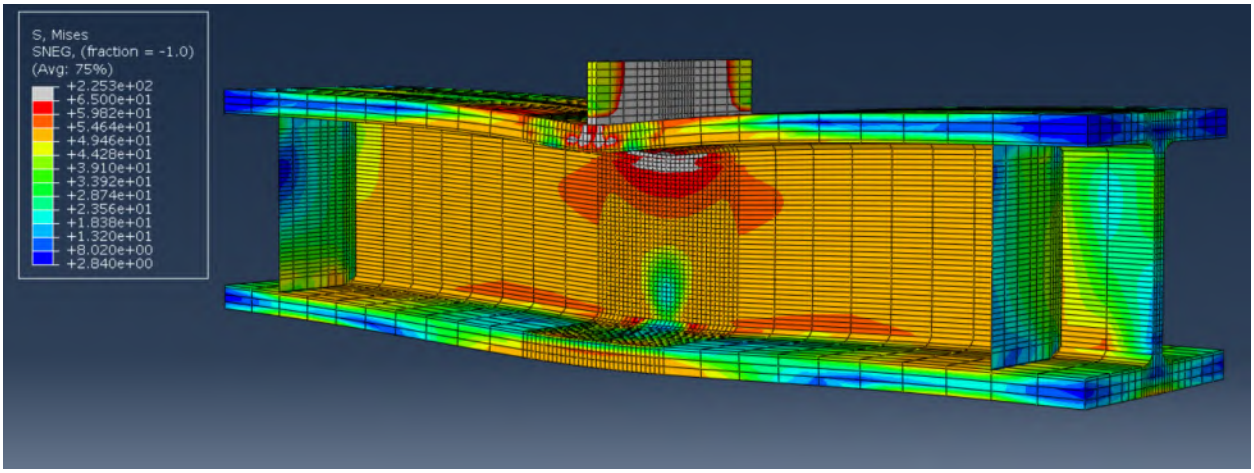

Figure 6.5-3: Stress distribution within W14X233-SC-NA at displacement of 1.5 in.

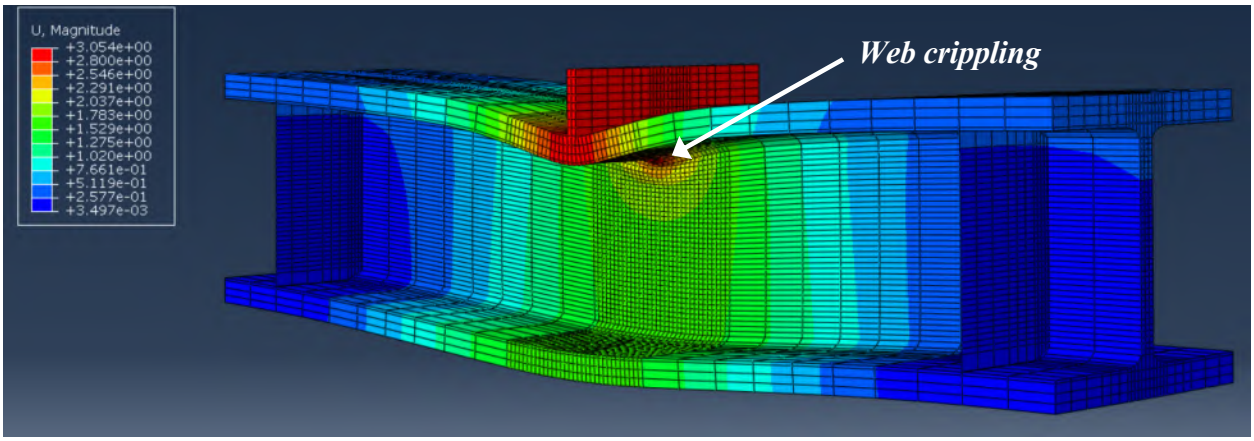

Figure 6.5-4: W14X233-SC-NA at displacement of 3 in. emphasizing eventual web crippling

The maximum load for analytical column specimens with concentric stiffeners was generally reached when a failure mode occurred in the stiffeners. In most cases, buckling occurred in the stiffeners. In some cases, buckling of the stiffener appeared instantaneous causing a 'swift' decrease in load. An example of this condition is shown for W24X131-SC-E0 in Figure 6.5-5. The contours in Figure 6.5-5 represent the resultant magnitudes of displacement and help demonstrate that buckling of the stiffener controlled the maximum load that was obtained. The sudden decrease in load is shown with load-displacement curves for this column specimen later in this section. On the contrary, stiffener buckling for other column specimens occurred more gradually and after a significant amount of yielding occurred in the column specimen. An example is shown for W14X233-SC-E0 in Figure 6.5-6. Another observation in the results shown in Figures 6.5-5 and 6.5-6 is that stiffener buckling occurred near the top for W24X131-SC-E0 and near mid height for W14X233-SC-E0.

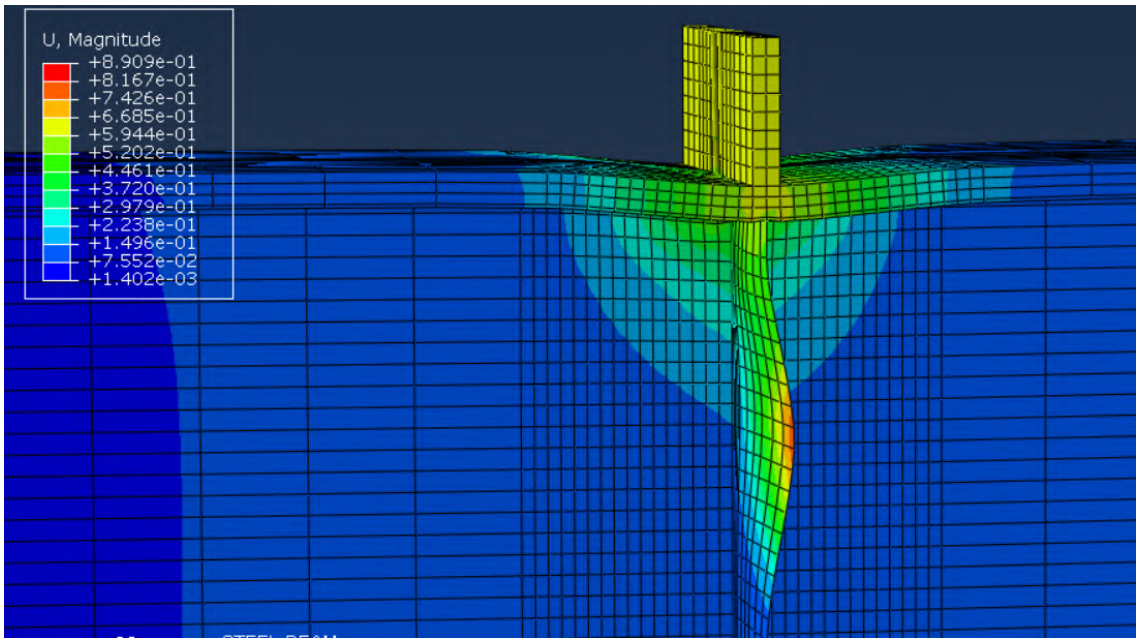

Figure 6.5-5: Stiffener buckling that occurred for W24X131-SC-E0

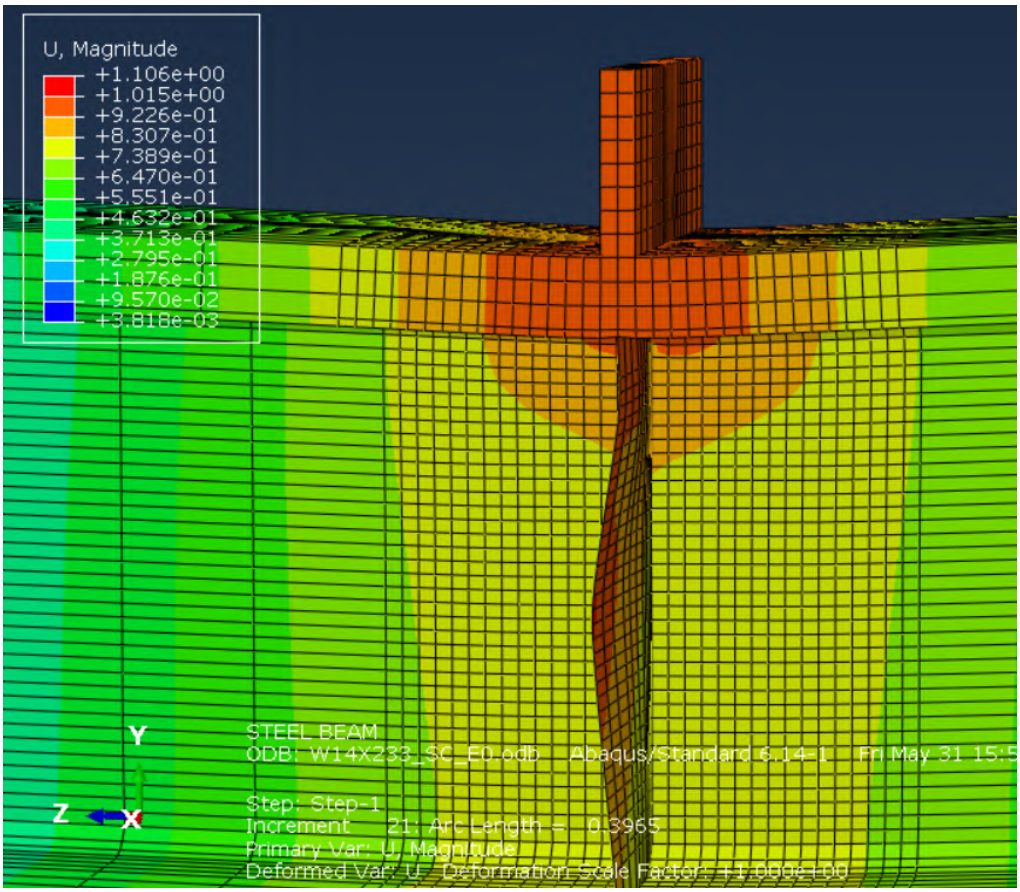

Figure 6.5-6: Eventual stiffener buckling that occurred for W24X131-SC-E0

For analytical column specimens with eccentric stiffeners, the maximum load was generally governed by a combination of a failure mode associated with the column specimen itself and buckling and/or bending of the stiffener. General observations used to describe the performance of each analytical column specimen varied for each case and will not be provided individually. Figure 6.5-7 shows a screenshot of W24X131-SC-E2, which has stiffeners eccentric at 2 in. From Figure 6.5-7, stiffener buckling occurred, which controlled the maximum load obtained from the analysis. However, for this same column specimen, web local crippling eventually occurred upon further displacements and directly under the load as shown in Figure 6.5-8.

Figure 6.5-9 shows a screenshot of W24X131-SC-E4, which has stiffeners eccentric at 4 in., after web local crippling occurred. In this case, stiffener buckling did not occur prior to web local crippling. However, after web crippling occurred, the stiffener started to bend as more deformations occurred in the column specimen. This is a similar observation as witnessed from the experimental column specimens as web local crippling generally occurred prior to the stiffeners engaging in resisting the deformations.

For larger column sections with eccentric stiffeners, significant yielding occurred in the stiffeners and column section prior to reaching a maximum load. In all cases, the stiffeners showed some signs of buckling or yielding but the overall failure mode is not described with one type of mechanism. Therefore, the failure modes associated with column specimens with eccentric stiffeners are quite diverse and will not be described individually. Instead, the effective stiffener capacities will be compared to the equivalent concentric stiffener capacities in Sections 6.5.3 and 6.5.4. More discussion regarding the experimental behavior of the column specimens and associated failure modes can be provided upon request.

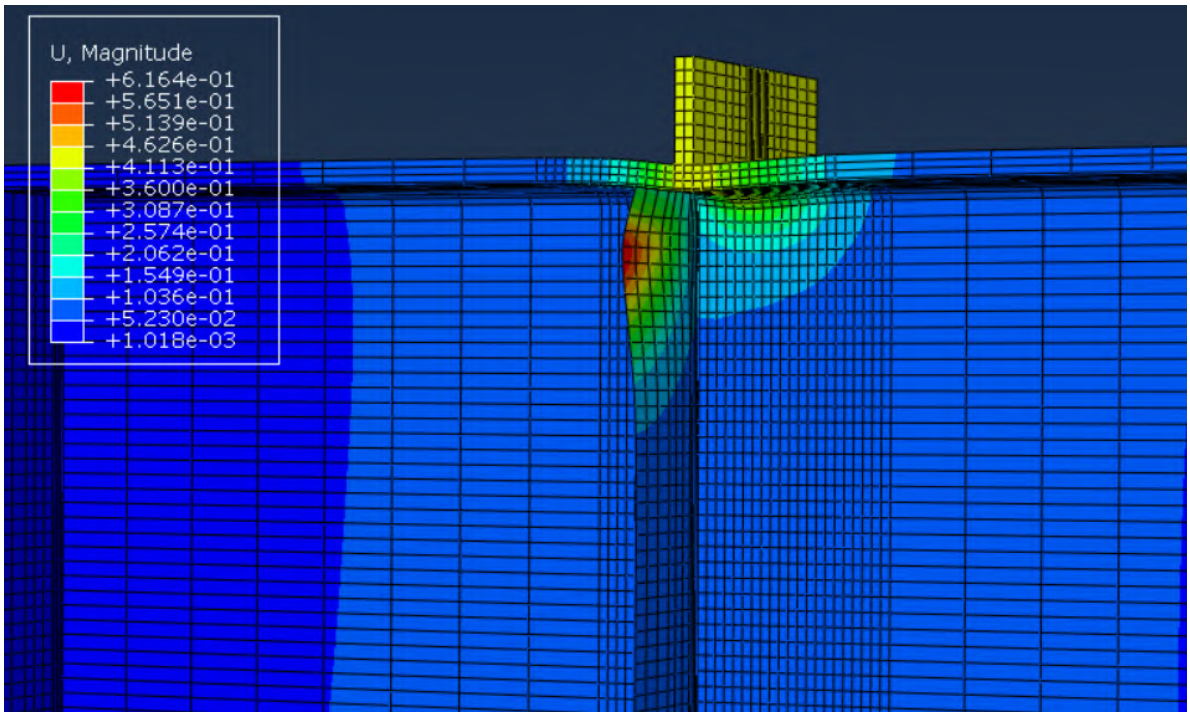

Figure 6.5-7: Buckling of eccentric stiffener for W24X131-SC-E2

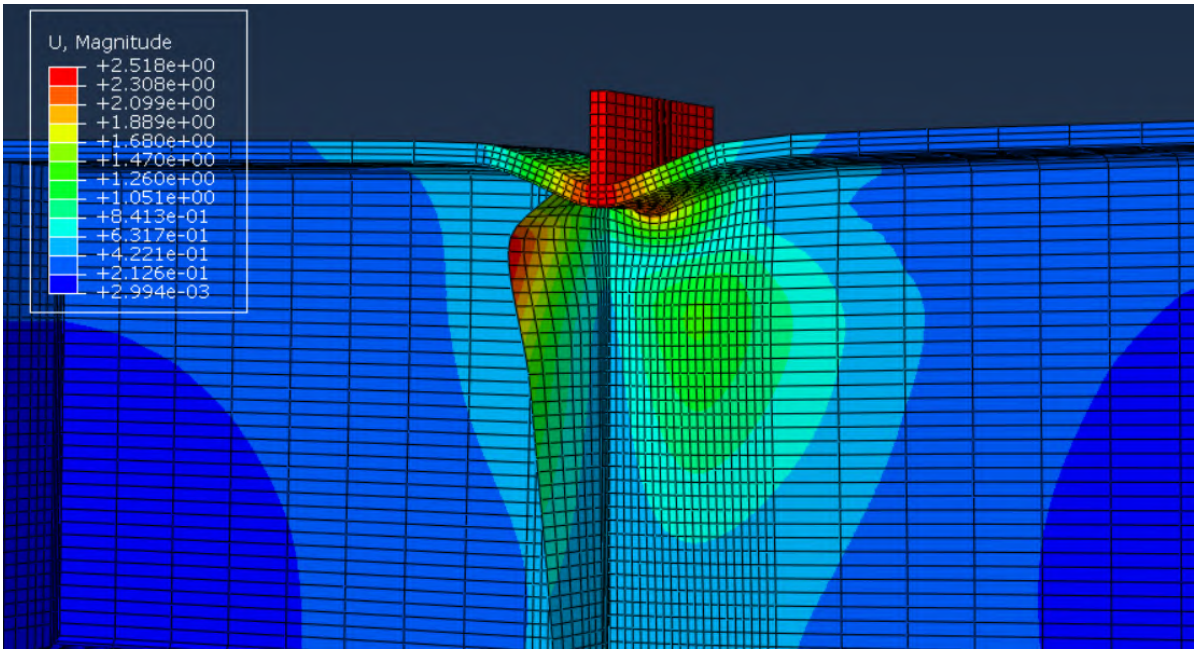

Figure 6.5-8: Web local crippling after stiffener buckling for W24X131-SC-E2

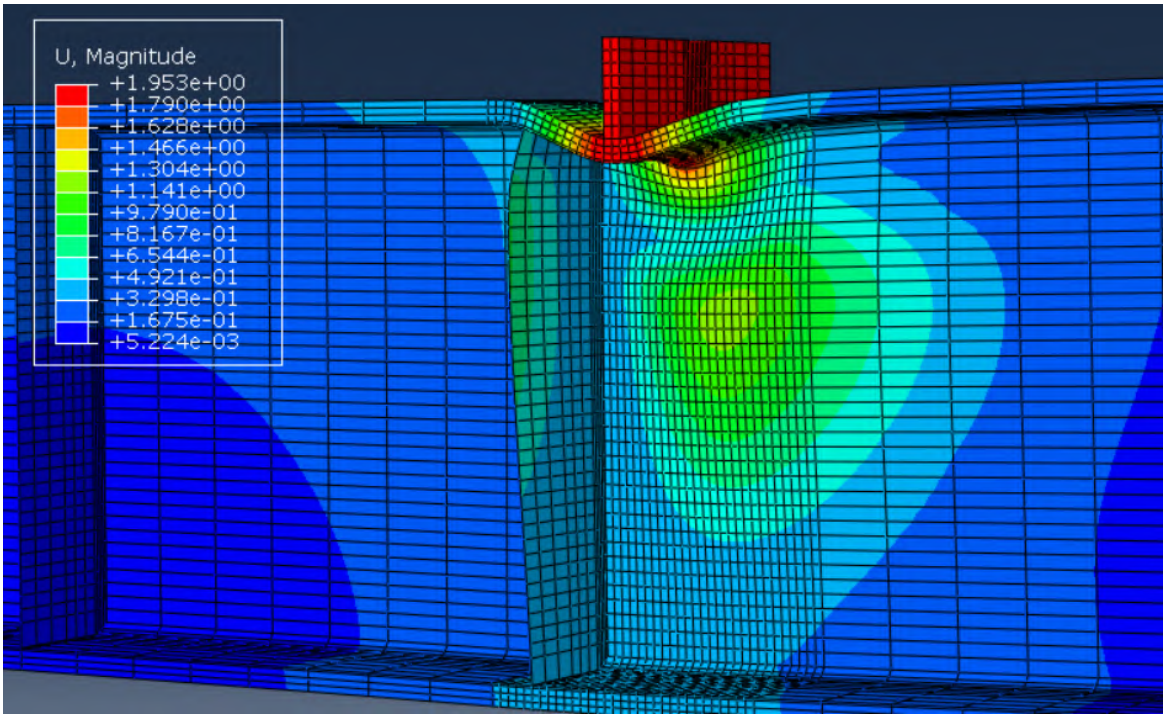

Figure 6.5-9: Web local crippling that occurred for W24X131-SC-E3

6.5.2 Load-Displacement Results

Figures 6.5-10 to 6.5-15 show the load-displacement results for all analytical column specimens subjected to single compression and with a stiffener thickness of 3/8 in. The results are plotted for each 'group' of specimens. For instance, Figure 6.5-10 shows the results for four W14X68 column specimens with the different aforementioned stiffener conditions.

The results in Figure 6.5-10 for the W14X68 column specimens are similar to the results found for the experimental column specimens. For the no stiffener condition, some non-linear behavior occurs and then suddenly the load starts to decrease as web local crippling occurs as shown in Figure 6.5-1. The load-displacement results of the analytical model with a stiffener eccentricity of 4 in. is similar. The maximum load obtained is slightly higher than the condition without stiffener and web local crippling occurs. However, the post-crippling performance of the column specimen is enhanced since the stiffener takes more apparent load after crippling occurs. All of these traits are similar to the experimental results. However, for the 2 in. eccentricity condition, there is a significant increase in load-capacity and significant yielding occurs in the column specimen prior to stiffener buckling combined with web local crippling occurring. This behavior is similar to the behavior of

W24X131-SC-E2 as shown in Figure 6.5-8. The increase in capacity at an eccentricity of 2 in. is more pronounced in comparison to the experimental column specimens. The column specimen with no eccentricity was able to reach high loads with significant yielding in the column specimen prior to stiffener buckling occurring.

On the contrary, from Figure 6.5-13, the load-displacement results of all four W14X233 column specimens are similar. In all cases, the column specimens showed significant non-linear behavior prior to either web crippling or stiffener buckling occurring. This was emphasized in the discussion of Figure 6.5-2 to 6.5-4. The increase in load capacity when stiffeners are used is relatively small compared to capacity of the column specimen without stiffeners. This column size will be evaluated in Section 6.5.4 using thicker stiffeners and in Section 6.5.5 using a reduced unsupported length of 3.5 ft. in lieu of 5 ft.

In general, the load-displacement results of other column specimen and comparisons associated with the influence of using eccentric and concentric stiffeners are 'in between' the results shown in Figure 6.5-10 and 6.5-13. Note that the final capacity of W14X120-SC-E0 was estimated from Figure 6.5-11 since the analysis terminated prematurely. The maximum load was estimated as 502 kips.

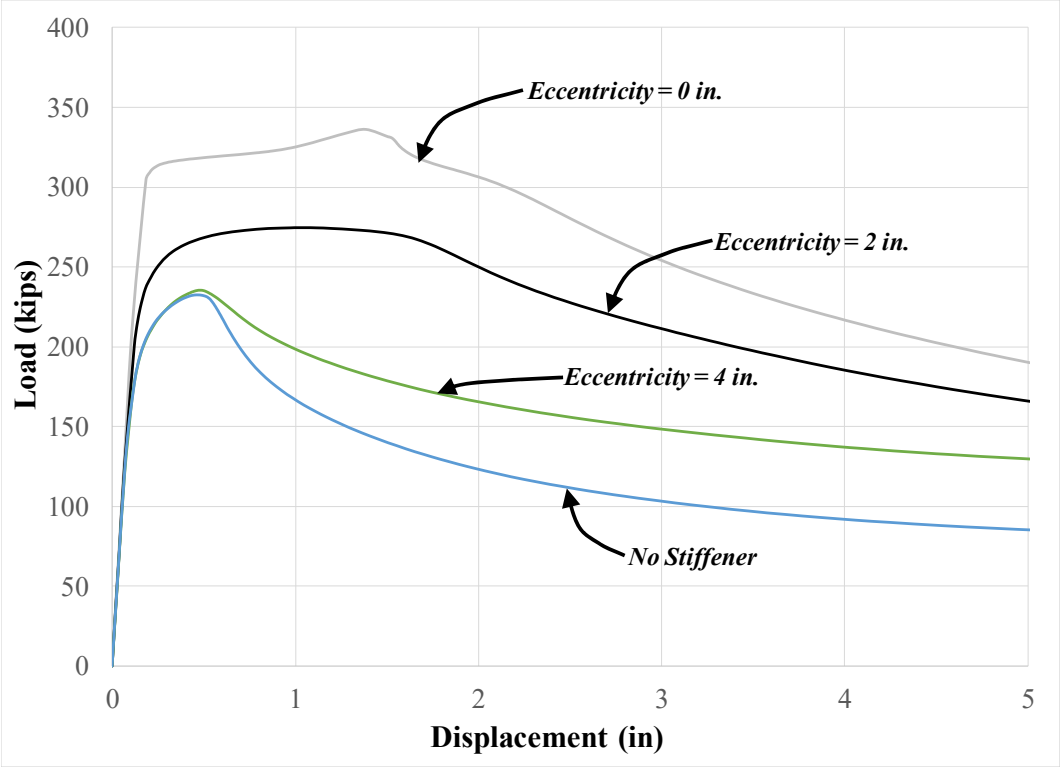

Figure 6.5-10: Load-displacement results of W14X68-SC-3/8 specimens

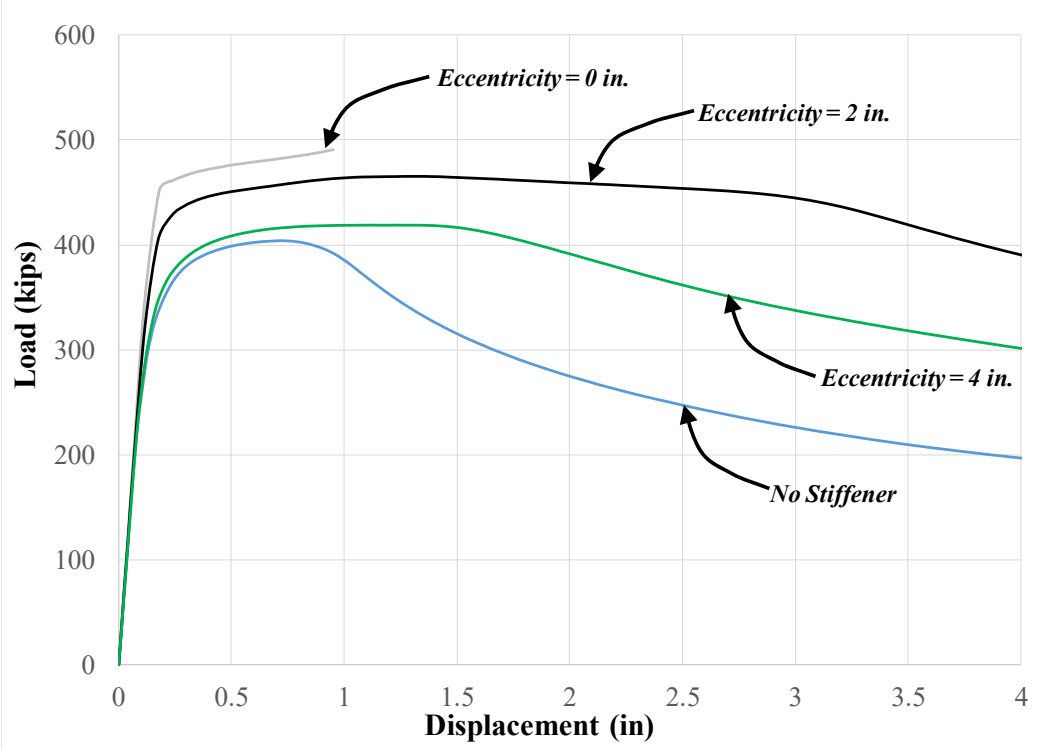

Figure 6.5-11: Load-displacement results of W14X120-SC-3/8 specimens

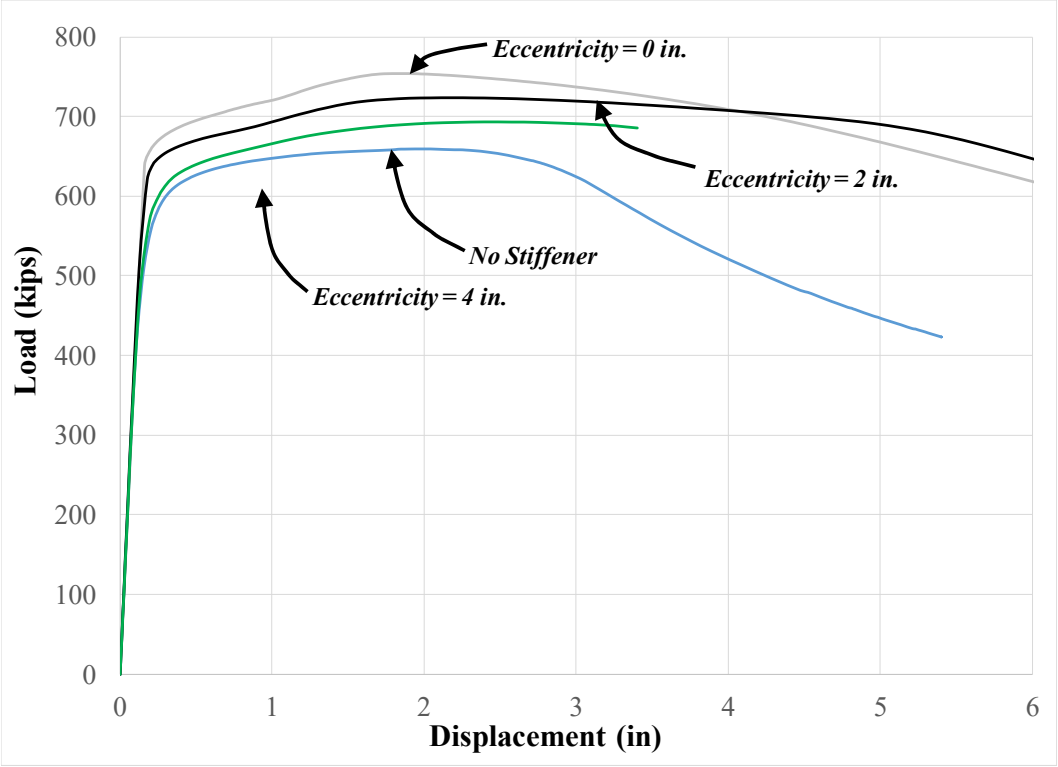

Figure 6.5-12: Load-displacement results of W14X176-SC-3/8 specimens

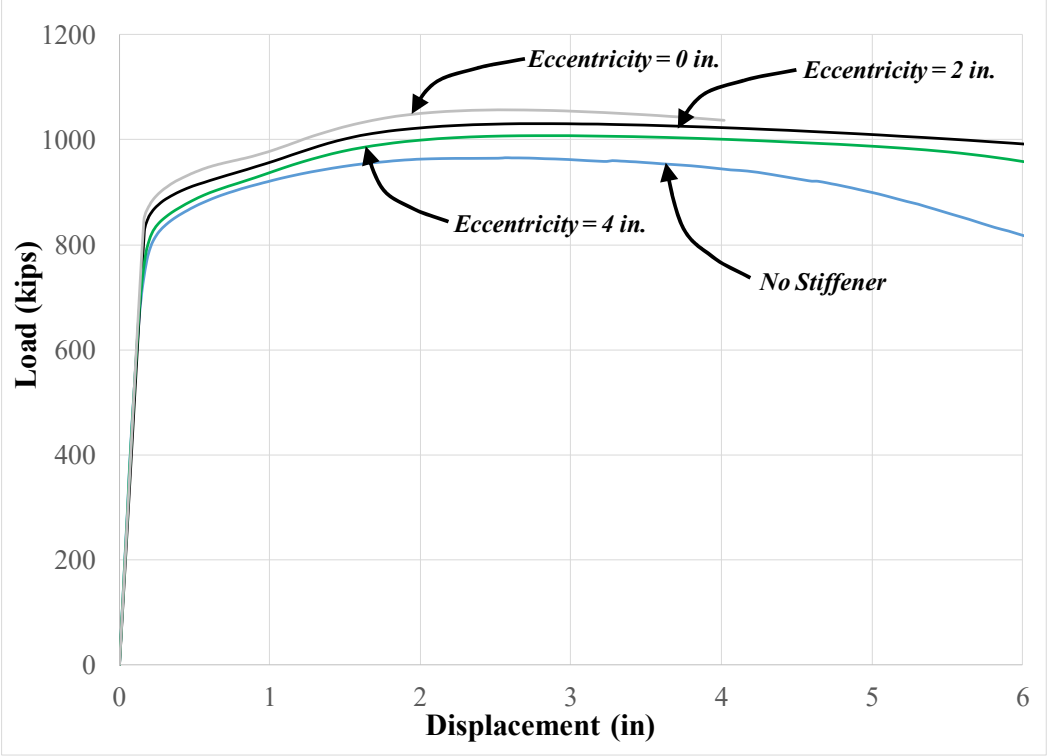

Figure 6.5-13: Load-displacement results of W14X233-SC-3/8 specimens

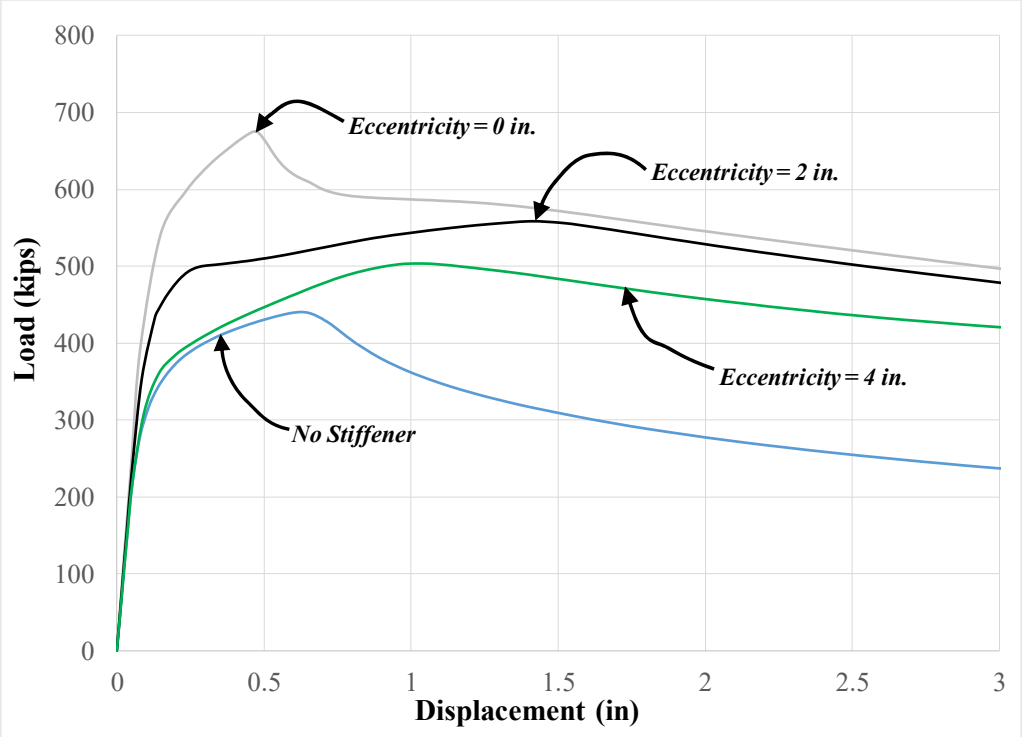

Figure 6.5-14: Load-displacement results of W24X131-SC-3/8 specimens

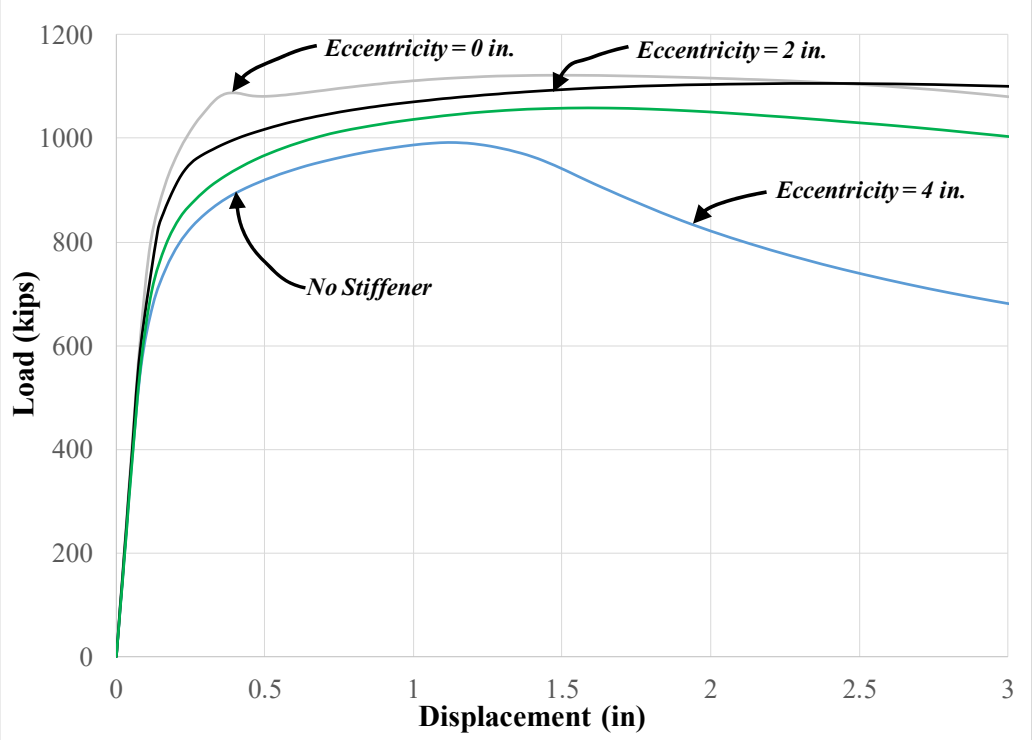

Figure 6.5-15: Load-displacement results of W24X229-SC-3/8 specimens

6.5.3 Primary Results of Single Compression Tests

Table 6.5-1 provides the primary results of all analytical models with no stiffeners and when 3/8 in. stiffeners are used. Results with 3/4 in. stiffeners are presented in Section 6.5.5. The table provides general information for the analysis model including the column size, the stiffener condition and the stiffener thickness '*t*'. All of these specimens were tested with an unsupported length between supports of 5 ft., which is a variable discussed later in this section and Section 6.5.6. Table 6.5-1 also shows the theoretical capacities for the limit states of web local yielding (WLY) and web local crippling (WCR) along with the theoretical concentric stiffener capacity from Equation 3-1. WLY and WCR are used to compare to the results of the analytical column specimens without stiffeners and the concentric stiffener capacity is used to compare to the results of the effective stiffener capacity for the analytical column specimen with concentric stiffeners.

The primary results in Table 6.5-1 include the maximum load (Max Load) obtained for each analysis. For all cases with stiffeners, an analytical "Effective Stiffener Capacity" is listed, which represents the difference between the maximum load obtained for that analysis and the result of the corresponding column specimen without stiffeners. Finally, the effective stiffener capacities of column specimens with eccentric stiffeners are shown as a percentage of the effective stiffener capacity of the corresponding analysis with concentric stiffeners. This is shown in the table under "% Conc. Stiffener" and represents the primary result of the analytical investigations.

Table 6.5-1: Primary results for single compression tests with 3/8 in stiffeners

General Info			Theoretical Calculations				Results		
Column Size	Stiff. Eccent. (in)	Stiffener t (in)	WLY (k)	WCR (k)	WCB (k)	Stiff (k)	Max Load (k)	Eff. Stiff. Cap. (k)	% Conc. Stiffener
W24X131	NA	3/8	244	465	297	199.7	440.4	-	-
W24X131	0	3/8					675.9	235.5	-
W24X131	2	3/8					558.7	118.3	50.2
W24X131	4	3/8					502.9	62.5	26.5
W24X229	NA	3/8	571	1234	1187	196.4	992.2	-	-
W24X229	0	3/8					1122.3	130.0	-
W24X229	2	3/8					1106.7	114.5	88.0
W24X229	4	3/8					1058.3	66.1	50.8
W14X68	NA	3/8	152	234	182	147.7	232.3	-	-
W14X68	0	3/8					335.9	103.5	-
W14X68	2	3/8					274.5	42.1	40.7
W14X68	4	3/8					235.2	2.9	2.8
W14X120	NA	3/8	249	456	520	219.4	404.1	-	-
W14X120	0	3/8					502.0	97.9	-
W14X120	2	3/8					465.1	61.0	62.3
W14X120	4	3/8					418.9	14.8	15.1
W14X176	NA	3/8	428	896	1452	233.4	659.5	-	-
W14X176	0	3/8					754.0	94.5	-
W14X176	2	3/8					723.4	64.0	67.7
W14X176	4	3/8					693.4	33.9	35.9
W14X233	NA	3/8	508	1495	2832	232.5	965.7	-	-
W14X233	0	3/8					1056.7	91.0	-
W14X233	2	3/8					1030.6	64.9	71.4
W14X233	4	3/8					1008.2	42.5	46.7

For analytical column specimens without stiffeners, Table 6.5-1 shows that the maximum load is very close to the theoretical capacity for web local crippling when column specimens have more slender webs (W14X68 and W24X131). However, for the remaining column specimens, the maximum load was found between the theoretical capacities for web local yielding and web local crippling. This comparison relates well with the failure modes viewed in the analytical models. Comparisons between the theoretical capacity of column stiffeners and the effective stiffener capacity of column specimens with concentric stiffeners varies significantly and needs to be evaluated in more detail. However, these stiffeners had relatively high slenderness (b/t) ratios and

local buckling was not considered in the calculations.

Table 6.5-1 demonstrates that the maximum loads for column specimens with stiffeners are always higher than the equivalent condition without stiffeners. However, for specimens with eccentric stiffeners, the 'percent of concentric effective stiffener capacity' (shown as '% Conc. Stiffener' in table) varies significantly and the results are highly dependent on column size. Dissimilar from the results of experimental column specimens, the percentages themselves are usually significant. However, the experimental column specimens had relatively small flanges and high h / t_w ratios in comparison to the analytical column specimens. Based on the results and relationships presented in Table 6.5-1, a technique must be derived that idealizes the column size to predict appropriate effective stiffener capacities when eccentric stiffeners are used. This is dissimilar from the recommendations in AISC Design Guide 13 (Carter, 1999) which gives recommendations based on eccentricity alone regardless of the column size.

For instance and for a W24X229, when stiffener eccentricity is 2 in., the effective stiffener capacity is 88% of the concentric stiffener condition and when the eccentricity is 4 in., the effective stiffener capacity is 51% of the concentric condition. In contrast and for a W14X68; when stiffener eccentricity is 2 in., the effective stiffener capacity is 41% of the concentric stiffener condition and when the eccentricity is 4 in., the effective stiffener capacity is 3% of the concentric condition. Therefore, the results are highly dependent on column size and more rigorous studies are required to identify appropriate relationships between the column size, magnitude of eccentricity, and the effective stiffener capacity.

For the single compression tests, factors that influence the effective stiffener capacity at various eccentricities are hypothesized as the flange thickness (or '*k*' dimension) and the slenderness of the web (h / t_w) ratio. These two geometric properties are evaluated in Section 6.5.4 in order to identify relationships to the analytical results. However, the geometric properties would also have to be related to the magnitude of eccentricity.

Prior to recommending a relationship, the research team evaluated if the trends in "% Conc. Stiffener" are linear with respect to stiffener eccentricity. The "Conc. Stiffener" results from Table 6.5-1 are shown graphically in Figure 6.5-16 along with two results using ¾ in. stiffeners, which are discussed in more detail in Section 6.5.5. The result of the concentric stiffener case is used for the

relationships as well, which is always equal to 100%. In summary, the curves in Figure 6.5-16 are hypothesized as appropriate relationships for the influence of eccentricity on effective stiffener capacities and for the various column sizes evaluated, considering stiffener thickness.

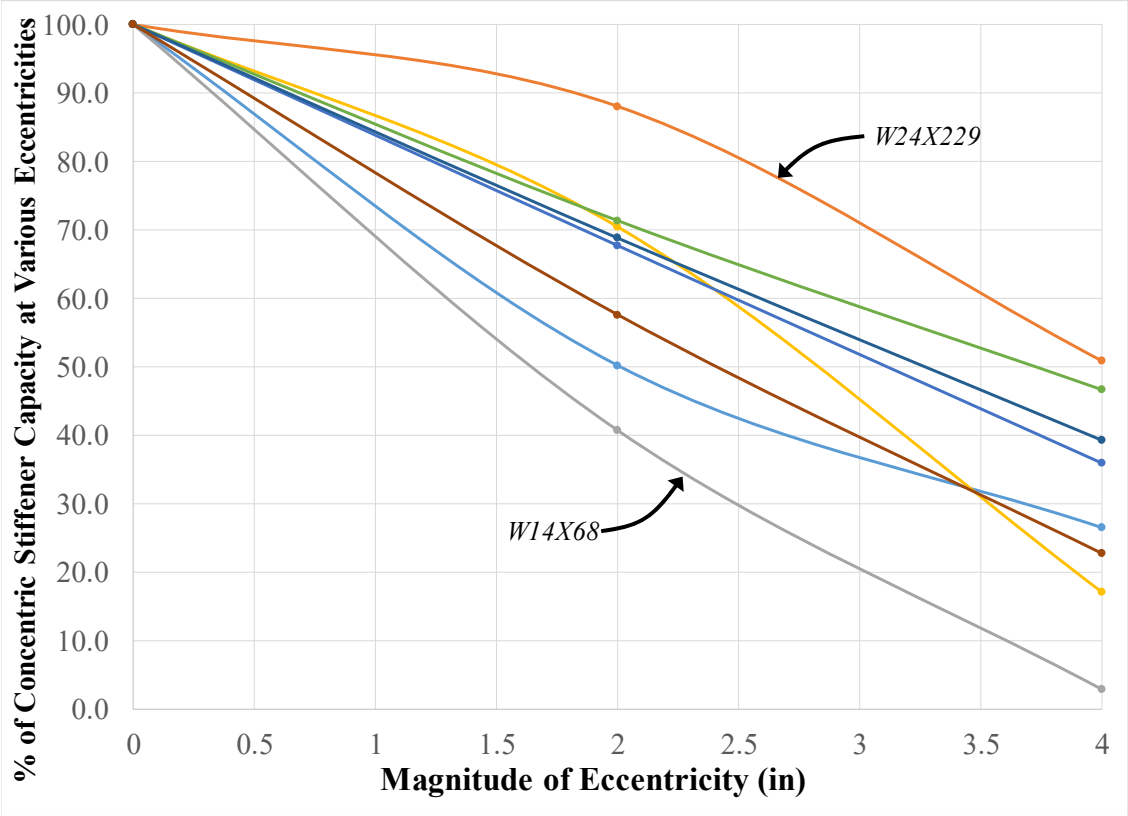

Figure 6.5-16: Influence of eccentricity on effective stiffener capacity

In general, if the curves presented in Figure 6.5-16 are straight lines, interpolation could be used to determine the effective stiffener capacity at any eccentricity. If the curves are concave down, the use of interpolation or a linear equation to define the influence of eccentricity would be conservative. However, if the curves are concave up, interpolation or the use of a linear equation to define eccentricity would be unconservative. The relationships presented in Figure 6.5-16 are inconsistent. For some cases, the curves are concave down (e.g. W24X229 with 3/8 in. stiffeners). In other cases, they are concave up (e.g. W14X68) and in some cases, the curves are almost straight lines (e.g. W14X233 with 3/8 in. stiffeners). However, for the conditions in which the curves are concave up, if straight lines are drawn from the values at eccentricities of 0 in., 2 in., and 4 in., these straight lines would compare well to the curves presented. Therefore, it is recommended to develop relationships for 2 in. and 4 in. of eccentricity and the use of a linear equation, which is developed in Section 6.8.

6.5.4 Influence of Geometric Properties on Effective Stiffener Capacity

In Section 6.8, the research team demonstrates the development of linear equations recommended for practice that accounts for the effects of stiffener eccentricity. However, initial studies were performed that evaluate section properties and how they affect the "% Conc Stiffener" results at individual eccentricities. These studies are presented in this section for the single compression tests and aided the development of the final recommendations.

This section evaluates the influence of geometric properties on the effective stiffener capacity results for the single compression tests. More specifically, the influence of flange thickness and the influence of web slenderness (h / t_w) are evaluated vs. the "Conc. Stiffener" results for column specimens with eccentric stiffeners. Aided with experimental results, it was hypothesized that both geometric properties have an influence on the effective stiffener capacity. However, the results of the single compression tests reveal that columns with higher h / t_w ratios can have significantly higher "% Conc. Stiffener" results in comparison to column specimens with lower h / t_w ratios. For instance, the 'percentage' results for W24X229 specimens are higher than that for W14X233 specimens. This is true when 3/8 in. stiffeners are used per Table 6.5-1 and when 3/4 in. stiffeners are used as presented in Section 6.5.5. However, as discussed in Section 6.5.1, the comparative results for the W14X233 column specimens were significantly influenced by shear and flexure. Therefore, relationships using h / t_w are inconclusive. Figure 6.5-17 demonstrates the comparisons between the "% Conc. Stiffener" and the h / t_w ratios for various column specimens and when the stiffener eccentricity is 2 in. The plot is shown in scatter format. The closed blue circles present analytical column specimen results when 3/8 in. stiffeners are used and the open circles represent the experimental results (does not include W16X31 results since eccentricities studied were 3 in. and 6 in.). As shown in Figure 6.5-17, the results are sporadic and no clear relationships exist between the web slenderness and the effective stiffener capacity results. In general, as web slenderness increases, the 'percentage' results decrease. However, as presented later in this section, it is more intuitive to use the flange thickness and develop relationships with effective stiffener capacities.

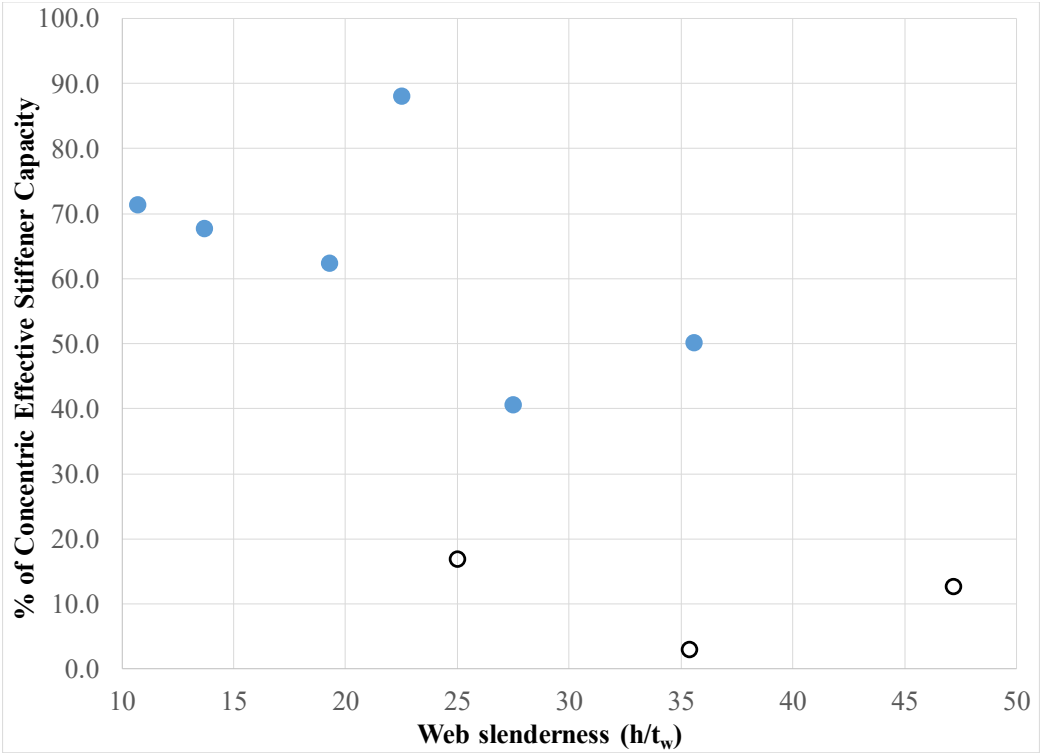

Figure 6.5-17: Comparison of web slenderness and effective stiffener capacity

For the results of column specimens with stiffeners at 2 in. eccentricity, Figure 6.5-18 shows relationships between the flange thickness and the "% Conc. Stiffener" results. The closed blue circles represent results of analytical column specimens and the open circles represent experimental results. Figure 6.5-18 demonstrates a 'better' relationship between this geometric property and the analytical results as opposed to the web slenderness. No clear trend can be established using the results as the analytical models reveal that there are many factors that influence the failure modes and maximum load results. However, the results do show that in general, as flange thickness increases, the percentage results increase as well, and conservative relationships between flange thickness and effective stiffener capacity can be established for the practicing engineer. A conservative straight line equation is plotted with the results, which could be used to predict the effective stiffener capacity when stiffeners are 2 in. eccentric (superseded by studies in Section 6.8). If the flange thickness is less than 0.5 in., it is recommended that stiffeners shall not be permitted to be eccentric. If the flange thickness is greater than 2 in. and the eccentricity is 2 in., the effective stiffener capacity shall be limited to 80% of the effective stiffener capacity of the concentric case. The straight line equation shall be used if the flange thickness is between 0.5 in. and 2 in.

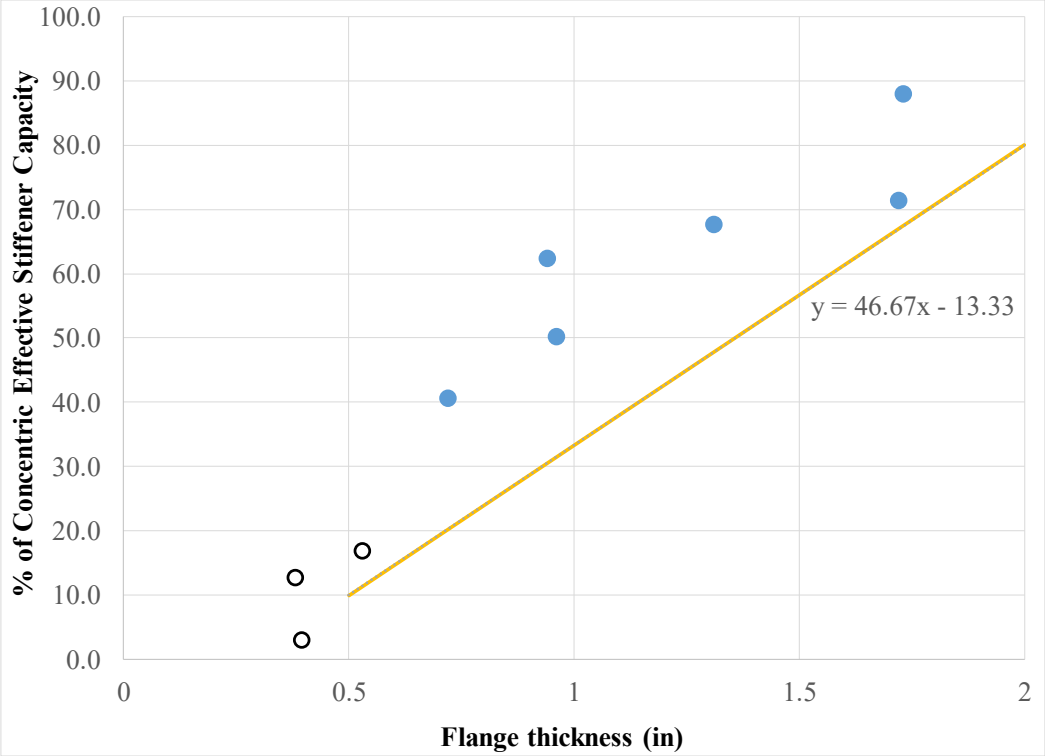

Figure 6.5-18: Effective stiffener capacity vs. flange thickness with 2 in. eccentricity

Similarly and for the results of column specimens with a 4 in. eccentricity, Figure 6.5-19 shows relationships between the flange thickness and the "% Conc. Stiffener" results. Again, the trends show that as flange thickness increases, the percentage results increase and conservative relationships can be established for the practicing engineer. A different straight line equation is proposed between a flange thickness of 0.65 in. and 2 in. Per this relationship, when the stiffener eccentricity is 4 in., the minimum flange thickness shall be 0.65 in. in lieu of 0.5 in.

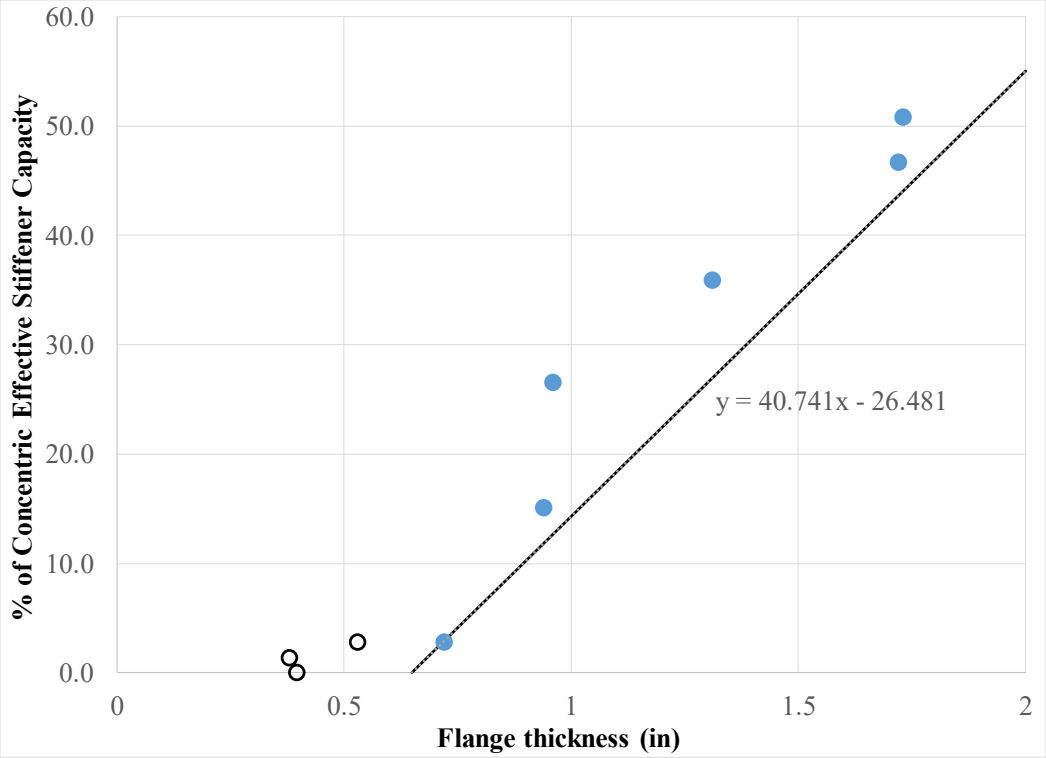

Figure 6.5-19: Effective stiffener capacity vs. flange thickness with 4 in. eccentricity

6.5.5 Evaluation of Stiffener Thickness on Single Compression Results

This section evaluates the influence of stiffener thickness on the analytical results of column specimens subjected to single compression. Evaluating multiple stiffener thickness was not considered in the scope of work from the recommendations proposed in the preliminary report. However, after reviewing the analytical results and studying the behavior of the column specimens, it was decided that some test sets should be re-evaluated choosing a stiffener thickness of 3/4 in. For instance, Figure 6.5-13 indicates that the W14X233-SC-3/8 column specimens only have a small relative increase in maximum load when 3/8 in. stiffeners were used. All four of the W14X233-SC-3/8 column specimens had similar load-displacement behavior without any signs of sudden buckling and it is believed that stresses resulting from the concentrated load, flexure and shear all significantly contributed to the maximum load obtained. In addition, for multiple column sizes, the stiffeners buckled which dictated the maximum load that could be obtained. Therefore, some analyses using thicker stiffeners is necessary, in which stiffener buckling is not expected.

Two larger column sizes, W14X233 and W24X229, were analyzed with 3/4 in. stiffeners. The load displacement results for the W14X233-SC-3/4 column specimens are shown in Figure 6.5-20 and the load-displacement results for the W24X229-SC-3/4 are shown in Figure 6.5-21. Note that the results for the "No Stiffener" condition are the same as presented in Figures 6.5-13 and 6.5-15, respectively.

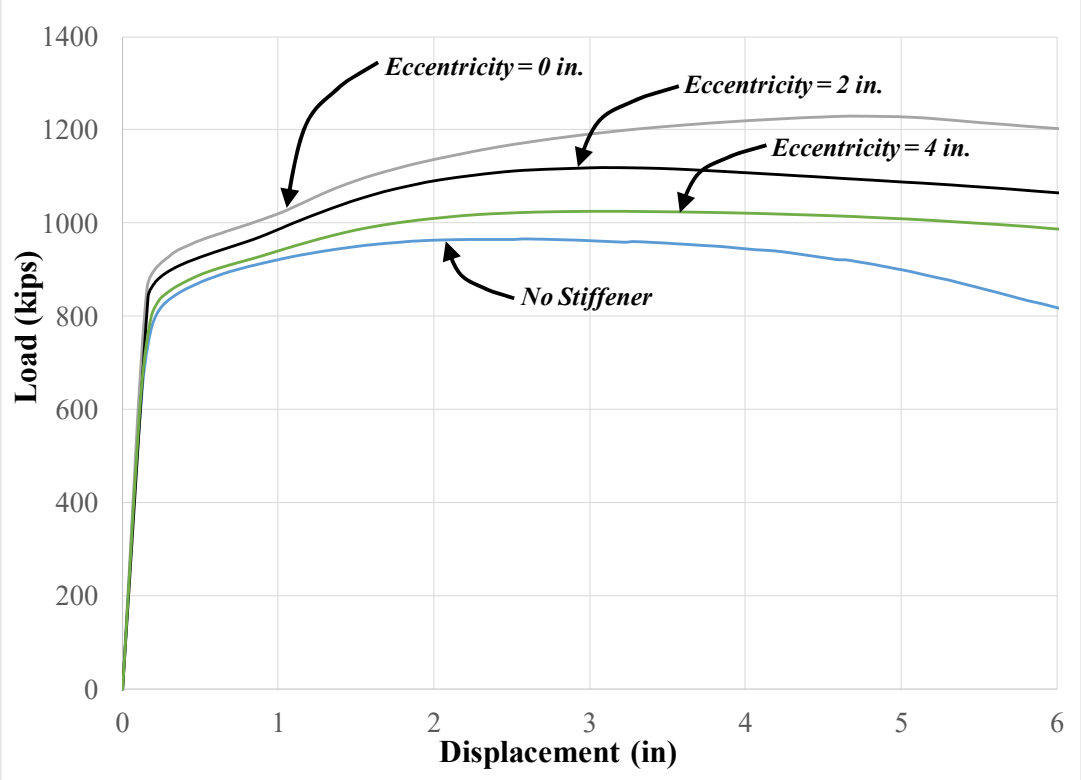

Figure 6.5-20: Load-displacement results for the W14X233-SC-3/4 test set

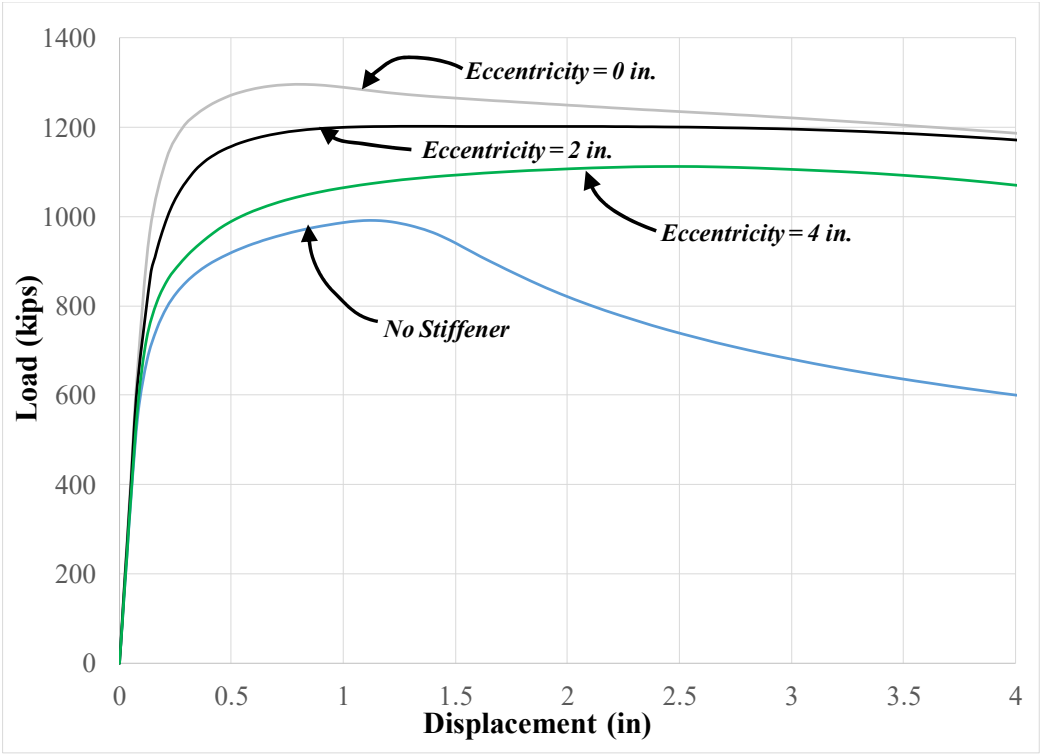

Figure 6.5-21: Load-displacement results for the W24X229-SC-3/4 test set

The load-displacement results in Figures 6.5-20 and 6.5-21 indicate similar behavior in comparison to Figures 6.5-13 and 6.5-15, respectively. However, there is an increase in effective stiffener capacity when comparing the individual eccentricity conditions. A summary of the results is provided in Table 6.5-2. The results of the column sizes when using 3/8 in. stiffeners and 3/4 in. stiffeners are shown together. A description of the primary results was provided for Table 6.5-1. As shown in Table 6.5-2, an increase in stiffener thickness increases the effective stiffener capacity for both column sizes and all stiffener eccentricity conditions. However, the "% Conc. Stiffener" result decreases with an increase in stiffener size. This result was surprising and causes concerns with the straight line relationships provided in Figure 6.5-18 and 6.5-19. However, an increase in the applied load itself causes even higher shear and flexural stresses, which are contributing to the maximum load obtained. Final recommendations are derived in Section 6.8 and will incorporate the use of 3/4 in. stiffeners.

Table 6.5-2: Comparison of primary results with 3/8 in. and 3/4 in. stiffeners are used

General Info			Results		
Column Size	Stiff. Eccent. (in)	Stiffener t (in)	Max Load (k)	Eff. Stiff. Cap. (k)	% Conc. Stiffener
W24X229	NA	3/8	992.2	-	-
W24X229	0	3/8	1122.3	130.0	-
W24X229	2	3/8	1106.7	114.5	88.0
W24X229	4	3/8	1058.3	66.1	50.8
W24X229	NA	3/4	992.2	-	-
W24X229	0	3/4	1296.8	304.6	-
W24X229	2	3/4	1201.8	209.6	68.8
W24X229	4	3/4	1111.8	119.6	39.3
W14X233	NA	3/8	965.7	-	-
W14X233	0	3/8	1056.7	91.0	-
W14X233	2	3/8	1030.6	64.9	71.4
W14X233	4	3/8	1008.2	42.5	46.7
W14X233	NA	3/4	965.7	-	-
W14X233	0	3/4	1230.2	264.5	-
W14X233	2	3/4	1118.1	152.4	57.6
W14X233	4	3/4	1025.8	60.2	22.7

Figure 6.5-22 shows the W14X233-SC-E0-3/4 column specimen at a maximum vertical displacement of the loading plate of approximately 4 in. At this point, the column stiffeners showed no signs of buckling and the shear deformations that developed in the column specimen are very significant. The contours represent the Von Mises stress and any grey area indicates the Von Mises stress is greater than the yield stress of 50 ksi. The entire web of the column between the load points has yielded from shear and the top and bottom flange have yielded from flexure at midspan. Therefore, the maximum load is clearly not explicit to a concentrated load effect.

Stiffener thickness is studied directly using the results of double compression tests. The double compression tests are not influenced by shear and flexural stresses and deformations that could not be avoided in the single compression tests.

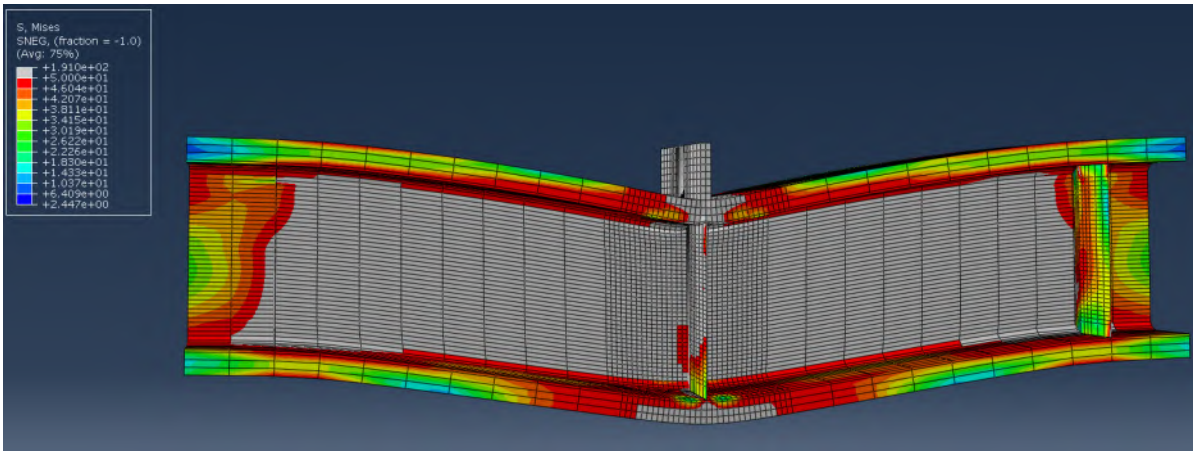

Figure 6.5-22: Von Mises stress distribution in W14X233-SC-E0-3/4 at 4 in. displacement

6.5.6 Evaluation of Unsupported Length on Single Compression Results

This section briefly investigates the influence of unsupported length on the analytical results of column specimens subjected to single compression. In the single compression tests, reducing the unsupported length reduces the flexural stresses that develop in the analytical models. However, if the analytical models are subjected to the same maximum load, the shear forces will be the same and therefore, stresses associated with shear in the cross-section cannot be reduced. As shown in Figure 6.5-22, the shear deformations and stress distribution are significant for column specimens evaluated in this research, more so that the flexural deformations. Therefore, shortening the unsupported length is not expected to have a significant influence on the maximum loads obtained.

To provide one trial evaluation, one test set of W14X233 specimens was evaluated with an unsupported length of 3.5 ft. in lieu of 5 ft. The stiffener thickness of 3/4 in. was used. The load-displacement results of this test set are shown in Figure 6.5-23. In addition, a screenshot of the finite element model with concentric stiffeners is shown in Figure 6.5-24. In Figure 6.5-24, the contours represent the Von Mises stress distribution and are shown when the vertical displacement of the loading plate was approximately 3 in.

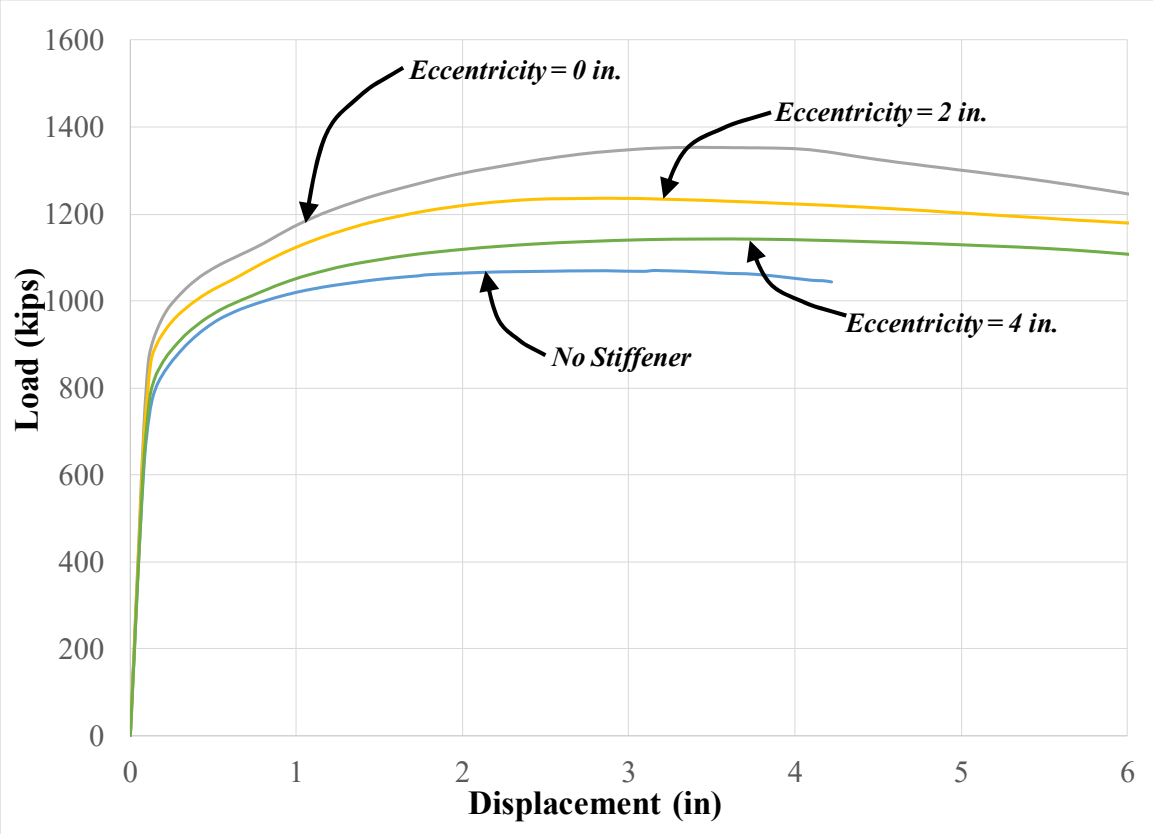

Figure 6.5-23: Load-displacement results of W14X233-SC-3/4, unsupported length of 3.5 ft.

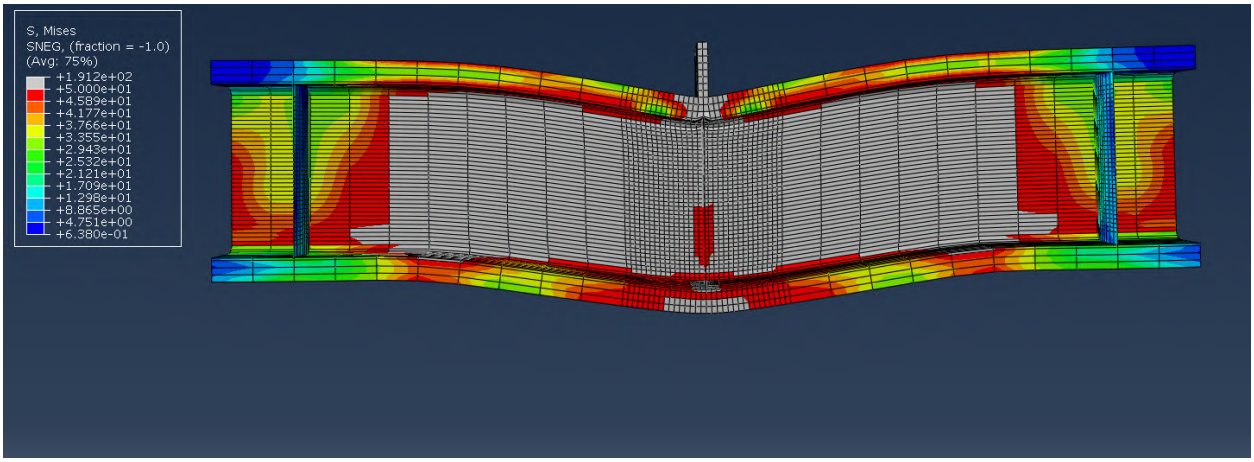

Figure 6.5-24: Von Mises stress distribution in W14X233 with unsupported length of 3.5 ft.

The primary results of the analytical models are compared in Table 6.5-3. The results include two test sets of W14X233-SC-3/4 column specimens that had the same eccentricity conditions and same stiffener thickness when stiffeners were used. However, one test set was performed with an unsupported length of 5 ft. and the other was performed with an unsupported length of 3.5 ft. As shown in Table 6.5-3, column specimens with the shorter length of 3.5 ft. resulted in a higher maximum load than the equivalent column specimens with a length of 5 ft. In addition, the effective stiffener capacity was always slightly higher than the equivalent condition with a length of 5 ft. Therefore, flexure does have a small influence on the concentrated load results for single compression tests. However, for the column specimens with eccentric stiffeners, the "% Conc. Stiffener" results are very similar at an unsupported length of 5 ft. and 3.5 ft. Therefore, the most important result of this research is not significantly influenced by the unsupported length.

Table 6.5-3: Comparison of primary results with 5 ft. and 3.5 ft. unsupported lengths

General Info				Results		
Column Size	**Stiff. Eccent. (in)**	**Stiffener t (in)**	**Unsupported Length (ft)**	**Max Load (k)**	**Eff. Stiff. Cap. (k)**	**% Conc. Stiffener**
W14X233	NA	0.75	5	965.7	-	-
W14X233	0	0.75	5	1230.2	264.5	-
W14X233	2	0.75	5	1118.1	152.4	57.6
W14X233	4	0.75	5	1025.8	60.2	22.7
W14X233	NA	0.75	3.5	1069.6	-	-
W14X233	0	0.75	3.5	1353.8	284.2	-
W14X233	2	0.75	3.5	1236.8	167.2	58.8
W14X233	4	0.75	3.5	1142.1	72.5	25.5

6.6 Analytical Results of Double Compression Tests

This section discusses all the results associated with analytical finite element models of double compression tests. The performance of each analytical model was diverse and was dependent on the column size, stiffener eccentricity condition, and stiffener thickness. This section will not go into detail regarding the performance of each column specimen but instead provides general observations regarding the behavior of various models and provides the important results associated with each model. Screenshots of all models are provided in Appendix E. Theoretical capacities for analytical column specimens and for the limit states of web local yielding, web crippling, web compression buckling and for 3/8 in. and 3/4 in. stiffeners (AISC, 2016) are provided in Appendix D.

In addition to the test matrix provided in Table 6.2-1, it was deemed appropriate to model the W16X31 column specimen but with the modifications for double compression described in Section 6.4 in order to simulate a true through force. The W16X31 was an experimental column specimen tested in double compression. However, it was originally modeled analytically in Chapter 5 assuming the same boundary conditions as in the experimental investigations and not with a 100% through force. The additional study will validate if the conclusions derived during the experimental investigations are valid if 100% of the force is transferred directly through the web of the column specimen.

The research team developed analytical models using 3/8 in. stiffeners at first, but decided to use 3/4 in. stiffeners due to the very disperse and inconsistent results provided by the smaller stiffener plates. This is further discussed in Section 6.6.5. All model descriptions, results and conclusions prior to Section 6.6.5 are based on column sections modeled with 3/4 in. stiffeners unless stated otherwise.

6.6.1 Failure Mechanisms and Screenshots

All analytical column specimens without stiffeners reached their capacity when web compression buckling took place. The overall behavior of the analytical models was different compared to the experimental column specimens. The variations were due to the modeling changes that were applied as explained in Section 6.4. All *experimental results* in double compression without stiffeners showed signs of web local crippling, similar to the single compression results, due to the uneven load distribution in between both top and bottom loading plates. The modified *analytical models* showed signs of the theoretical failure mechanism of web compression buckling that would occur due to a compression force equally applied to both top and bottom loading plates. Most analytical models experienced significant yielding of the column specimen and eventually the column failed by some form of inelastic buckling. In the analytical results of column specimens without stiffeners, inconsistent buckling modes occurred which is dependent on the h / t_w ratio. As discussed in Salmon and Johnson (1996), plate buckling may occur in multiple half sine waves, which is dependent on the plate thickness, unsupported length, boundary conditions, and effective width. However, for web compression buckling, the effective width subjected to compression and the boundary conditions are uncertain. Buckled shapes with one and two half sine waves were observed. This is further discussed

in Section 7.3, which describes web compression buckling more detail.

Figure 6.6-1 shows a screenshot of the modified analytical model of W16X31-DC-NA. The contours represent the resultant magnitude of the displacement at each point in the column specimen and they are used to demonstrate the out-of-plane displacement of the web with the vertical displacement of the loading plates. In Figure 6.6-1, the vertical displacement of the loading plate is approximately 1.5 in. The failure shape shown is web compression buckling, which is slightly more pronounced near the bottom loading plate. Figure 6.6-2 shows a screenshot of the same column specimen tested per the methods described in Chapter 5 where load was applied to the top flange only. Even though the failure shapes might appear similar, the stress distributions were found more concentrated near the top flange in Figure 6.6-2 as opposed to the concentrated stresses more mirrored at both flanges for the results in Figure 6.6-1.

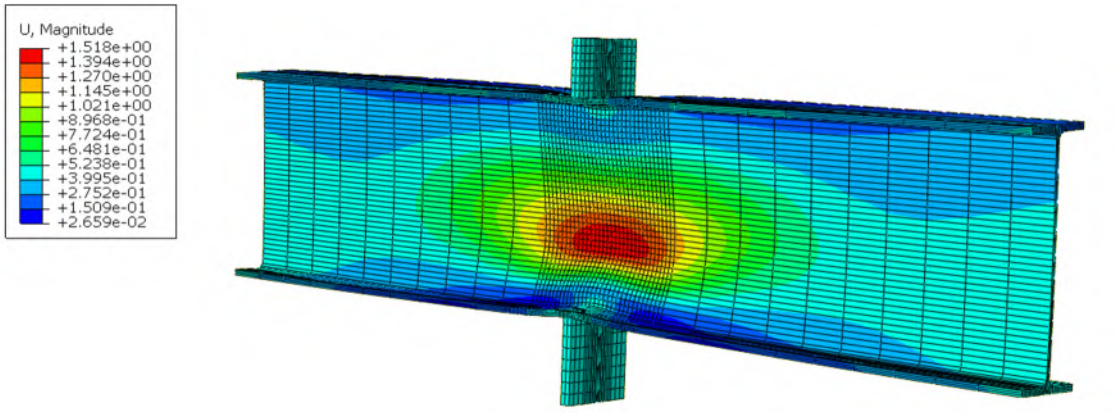

Figure 6.6-1: W16X31-DC-NA at displacement of 1.5 in. with web compression buckling

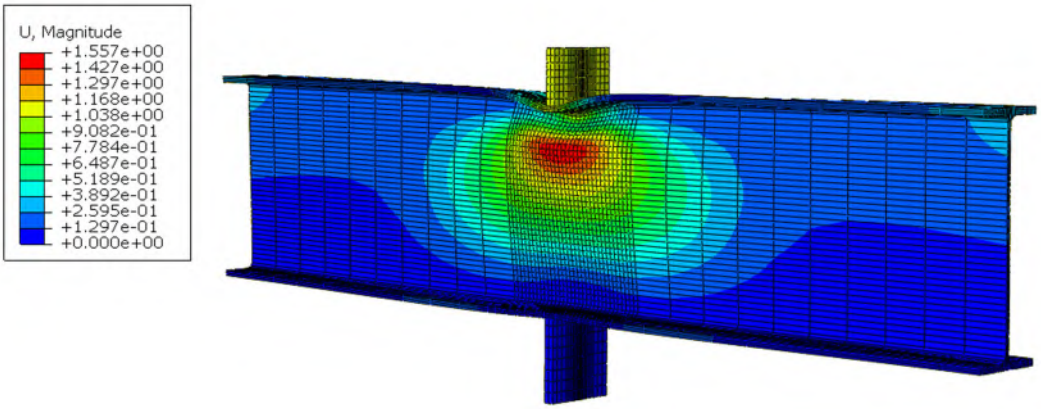

Figure 6.6-2: W16X31-DC-NA with load on top only and at a displacement of 1.5 in.

Figure 6.6-3 shows a screenshot of W14X68-DC-NA, which reached a maximum load of 274 kips. This result surpassed the theoretical load capacity for web compression buckling, computed as 181.5 kips, and it also surpassed the theoretical load capacity for web crippling computed as 233.9 kips. The contours represent the resultant magnitude of displacement at each point in the column specimen and they are used to demonstrate the out-of-plane displacement of the web with the vertical displacement of the loading plate. In this particular case the analytical column specimen buckled with two half sine waves in the web and under the applied load. However, most of the analytical models buckled in the web with one half sine wave as shown for the W24X229 column specimen in Figure 6.6-4.

Figure 6.6-4 shows a screenshot of W24X229-DC-NA, which reached a maximum load of 1041 kips. This magnitude is slightly lower than the theoretical capacity of web compression buckling of 1187 kips and much higher that the theoretical capacity of web local yielding of 571 kips. It is believed that in this condition, *inelastic* web compression buckling represented the governing failure mechanism. In AISC (2016), most buckling checks consider some form of elastic buckling and some form of inelastic buckling, particularly when using Chapter E of the specification. However, the limit state of web compression buckling alone per Section J10.5 does not consider the two conditions independent.

In Figure 6.6-4, the contours represent the resultant magnitude of displacement at each point in the column specimen (similar to Figure 6.5-3). At this point in the analysis, the vertical displacement of the loading plate is 1.5 in., which is the same as shown for W14X68-DC-NA in Figure 6.6-3. In this particular column specimen, the maximum out-of-plane displacement occurred at the center of the web in between both loading plates and the top half is a mirror image of the bottom half. Figure 6.6-5 shows the Von Mises stress distribution at the same magnitude of displacement and demonstrates that significant yielding has occurred primarily on the web. In general, for column sections with stockier webs, more yielding occurred prior to the inelastic web compression buckling and the out-of-plane deformation is not as significant as for members with thinner webs.

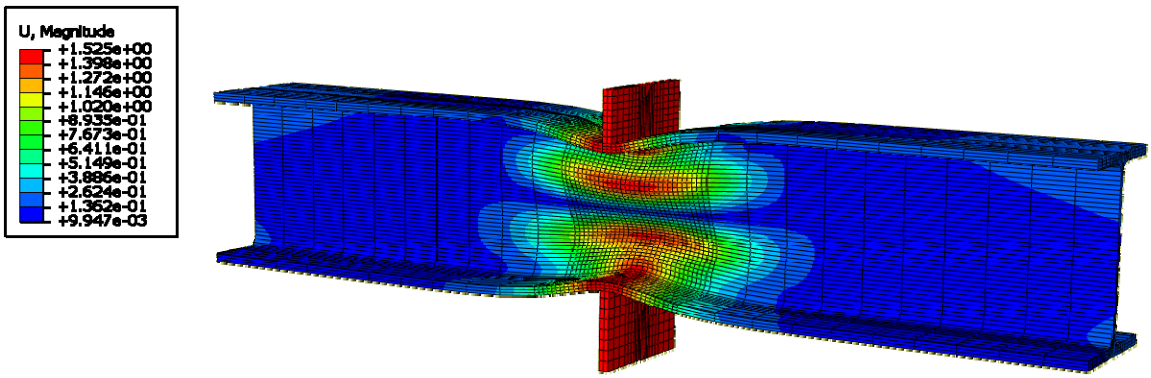

Figure 6.6-3: W14X68-DC-NA at displacement of 1.5 in. emphasizing the "S" buckled shape on the web

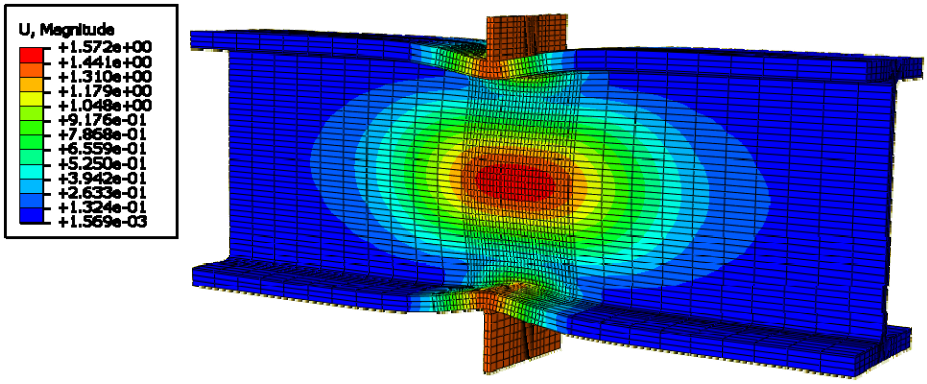

Figure 6.6-4: W24X229-DC-NA at displacement of 1.5 in. with web compression buckling

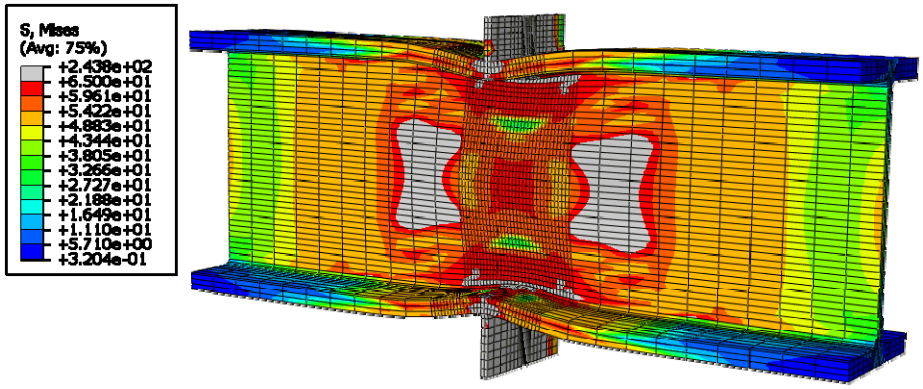

Figure 6.6-5: Stress distribution within W24X229-DC-NA at displacement of 1.5 in.

The maximum load for analytical column specimens with concentric stiffeners was generally reached when a failure mode occurred in the stiffeners. In most cases, buckling occurred in the stiffeners. Stiffener buckling generally occurred "suddenly" as there was a rapid decrease in load for a given displacement. The buckled shapes of the stiffeners on each column section varied

arbitrarily. In some cases the buckling behavior differed on both front and back stiffeners on the same section. An example of this is shown in Figures 6.6-6 and 6.6-7, which show the front and back of the W24X131-DC-E0 column section. The contours represent the resultant magnitude of displacement at each point in the column specimen and are used to demonstrate the out-of-plane displacement of the web and stiffeners with the vertical displacement of the loading plate. Figure 6.6-6 and 6.6-8 show that stiffener buckling occurred near the top and bottom flanges for W24X131-DC-E0-3/4. However, Figure 6.6-7 shows that on the opposite side of W24X131-DC-E0-3/4, stiffener buckling occurred in three half sine waves. This is also the condition for W24X229-DC-E0-3/4 on one side as shown in Figure 6.6-8. The failure modes witnessed in this research are intriguing and could be used as a guide for future research. Further discussion regarding the use of concentric stiffeners is provided in Section 7.5.

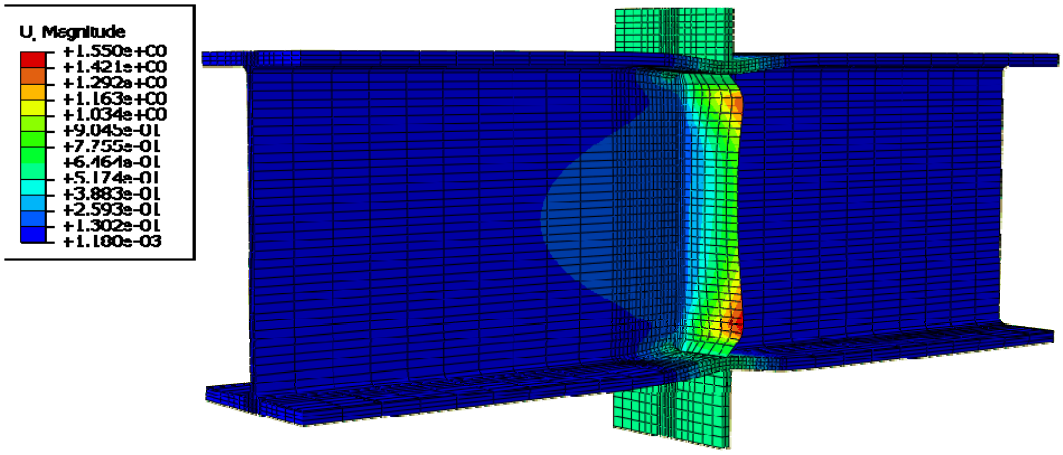

Figure 6.6-6: Stiffener buckling that occurred for W24X131-DC-E0-3/4

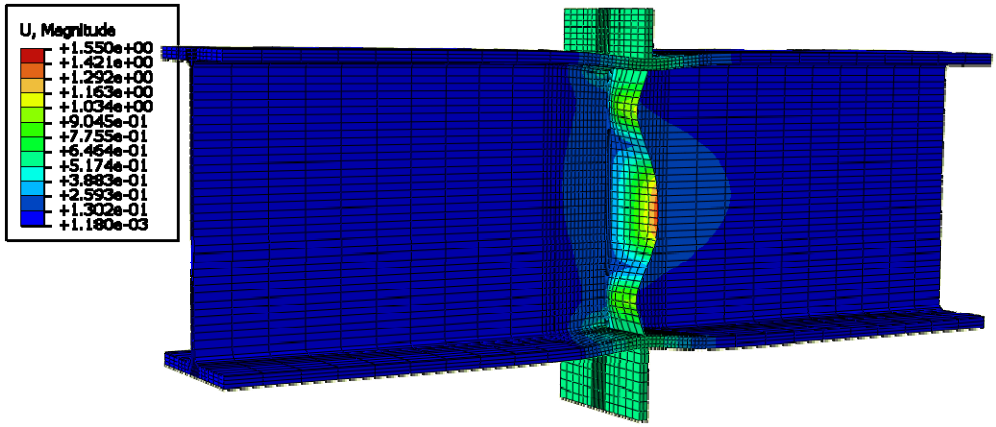

Figure 6.6-7: Stiffener buckling on the opposite of W24X131-DC-E0-3/4

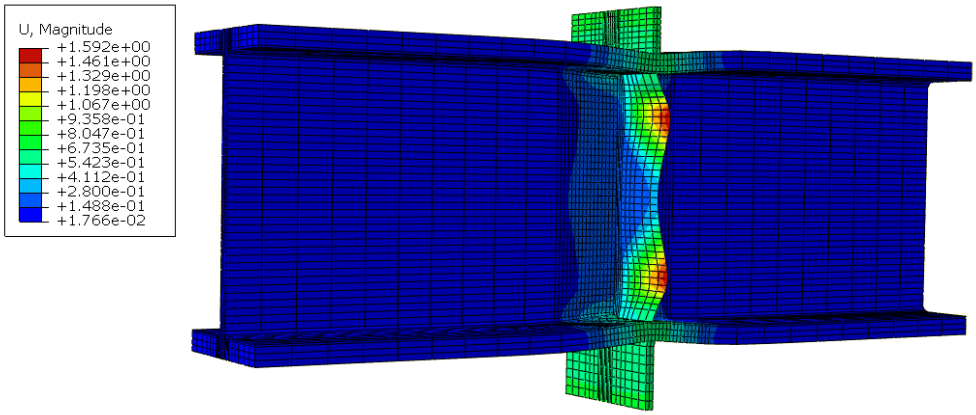

Figure 6.6-8: Stiffener buckling that occurred for W24X229-DC-E0-3/4

For analytical column specimens with eccentric stiffeners, the maximum load was generally governed by a combination of a failure mode associated with the column specimen itself and buckling and/or bending of the stiffener. General observations used to describe the performance of each analytical column specimen varied for each case and will not be provided individually.

Figure 6.6-9 shows a screenshot of W24X131-DC-E2-3/4, which has stiffeners eccentric at 2 in. From Figure 6.6-9, stiffener buckling occurred. However, for this same column specimen, web compression buckling eventually occurred upon further displacements and directly under the loads as shown in Figure 6.6-10. After web compression buckling occurred, the load started to decrease.

Figure 6.6-11 shows a screenshot of W24X131-DC-E4-3/4, which has stiffeners eccentric at 4 in. In this case, stiffener buckling and web compression buckling take place simultaneously. As more deformations take place, both the stiffener and the web continue to deform in an inelastic way.

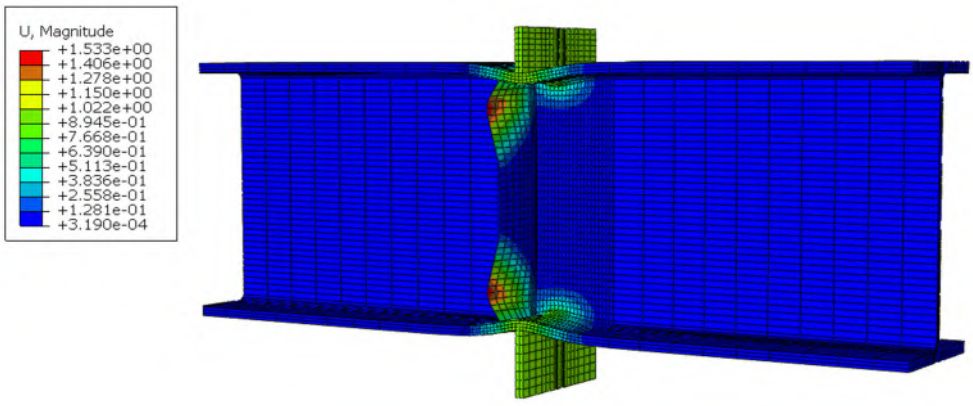

Figure 6.6-9: Initial buckling of stiffener for W24X131-DC-E2-3/4

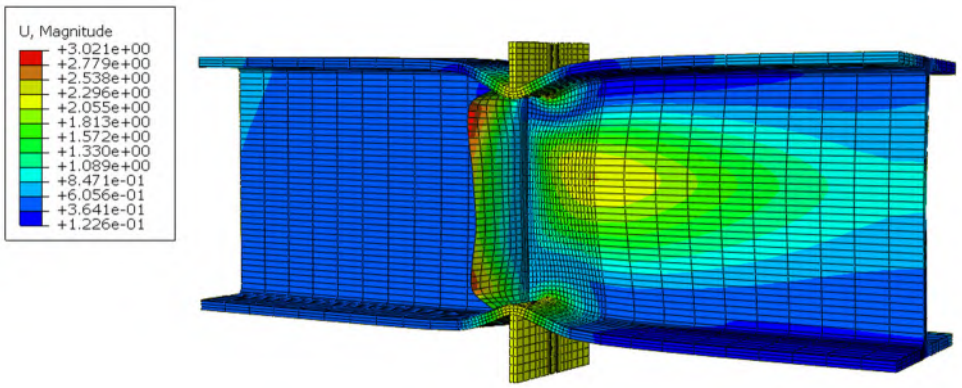

Figure 6.6-10: Web compression buckling after stiffener buckling for W24X131-DC-E2-3/4

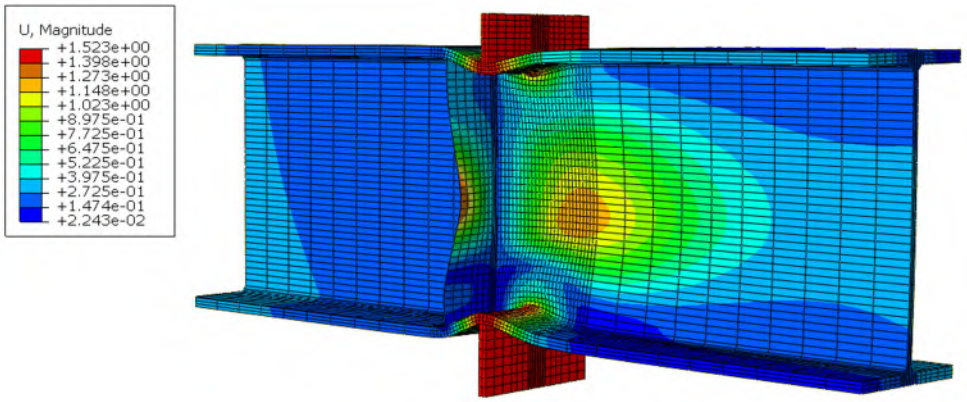

Figure 6.6-11: Web compression buckling and stiffener buckling for W24X131-DC-E4

More discussion regarding the experimental behavior of the column specimens and associated failure modes can be provided upon request. The remainder of this section is dedicated to the load-displacement results of the analytical column specimens and the effective stiffener capacities when concentric and eccentric stiffeners are utilized.

6.6.2 Load-Displacement Results

All load-displacement results described in this section are for analytical column specimens using 3/4 in. stiffeners. Section 6.6.5 provides more insight on not including the results when 3/8 in. stiffeners are used. Figures 6.6-12 to 6.6-17 show the load-displacement results for all analytical column specimens subjected to double compression and with a stiffener thickness of 3/4 in. The results are plotted for each 'group' of specimens. For instance, Figure 6.6-12 shows the results for four W14X68 column specimens with the different stiffener conditions.

The results in Figure 6.6-12 for the W14X68 column specimens are similar to the results found for the experimental column specimens in terms of relative load capacity, meaning that the condition with concentric stiffener reached the highest load capacity and as the eccentricity increased, the load capacity decreased accordingly. However, there are discrepancies in the overall behavior compared to the experimental results of smaller column sections. In the experimental results, only some non-linear behavior occurred prior to the load started to decrease. On the other hand, for pure double compression tests and with larger column sections, significant yielding occurs in the column specimen prior to the sudden drop in load caused by stiffener buckling combined with web compression buckling.

For the column specimens with concentric stiffeners, the maximum load was always governed by stiffener buckling. In Figure 6.6-12 and for W14X68-DC-E0-3/4, the sudden drop in load represents the stiffener buckling. However, for "stockier" columns sections such as W14X233-DC in Figure 6.6-15, stiffener buckling occurred at a load that was less than or slightly greater than the column specimen without stiffeners. For column specimens with eccentric stiffeners, in some cases, the stiffeners were found to brace the column specimen from buckling, allowing the maximum load to be maintained for higher magnitudes of displacement, such as in Figure 6.6-17 for the W24X229-DC-3/4 column specimen. In other cases, web compression buckling was still found to govern depending on the dimensions of the column specimen and magnitude of eccentricity.

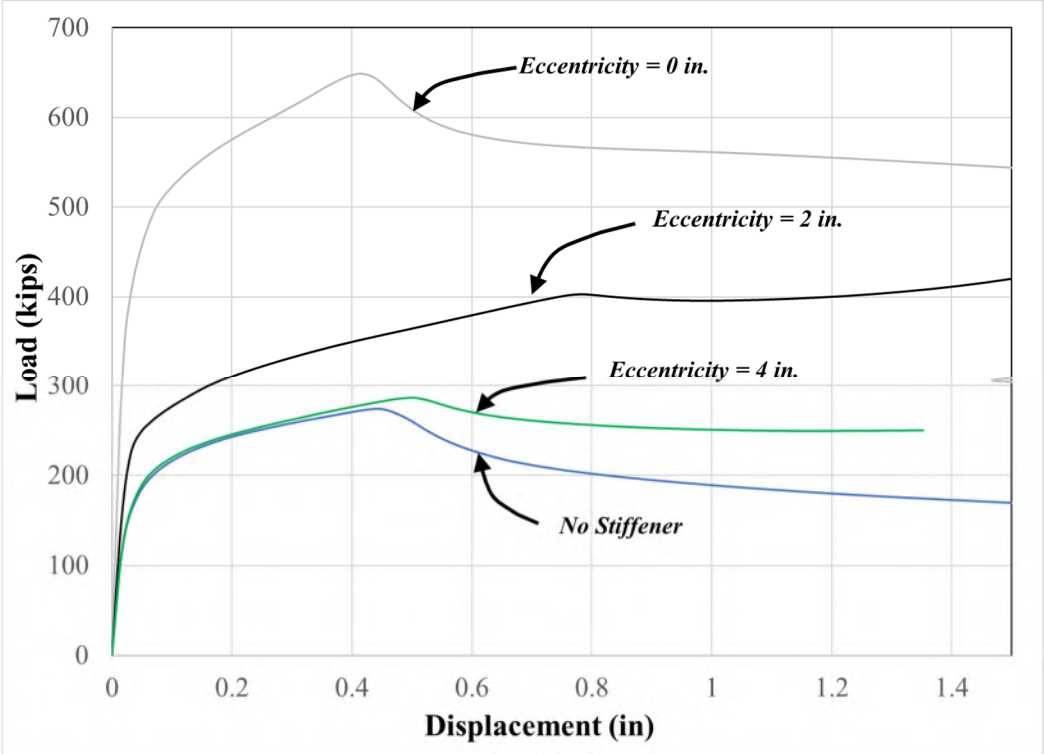

Figure 6.6-12: Load-displacement results of W14X68-DC-3/4 speciemens

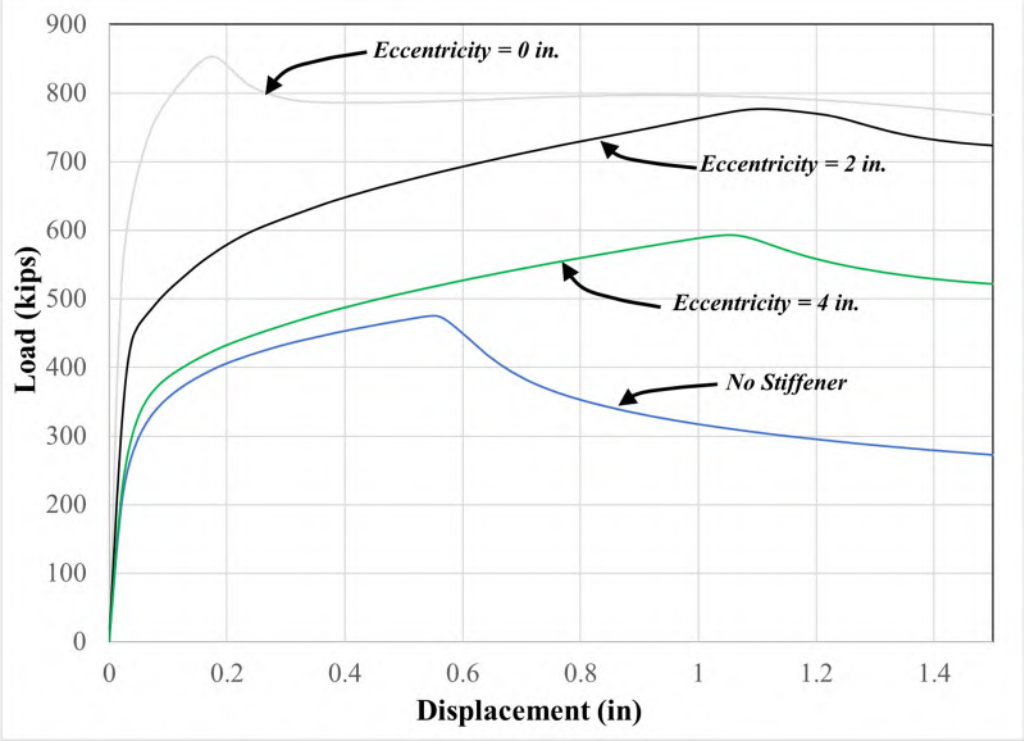

Figure 6.6-13: Load-displacement results of W14X120-DC-3/4 specimens

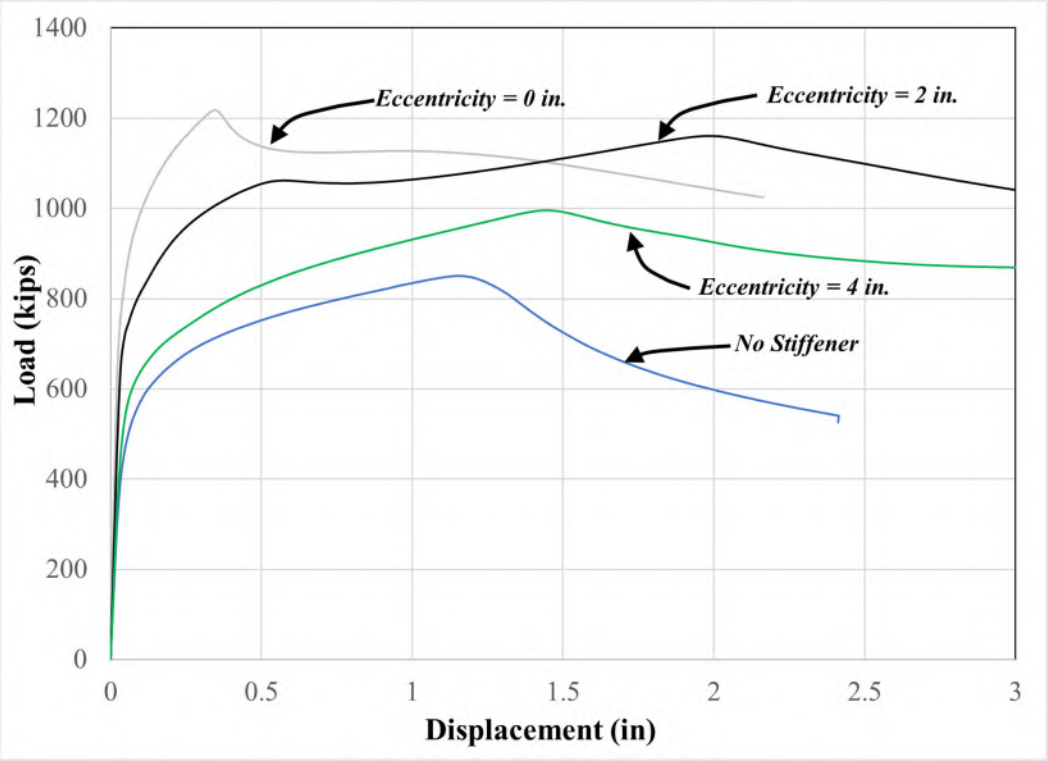

Figure 6.6-14: Load-displacement results of W14X176-DC-3/4 specimens

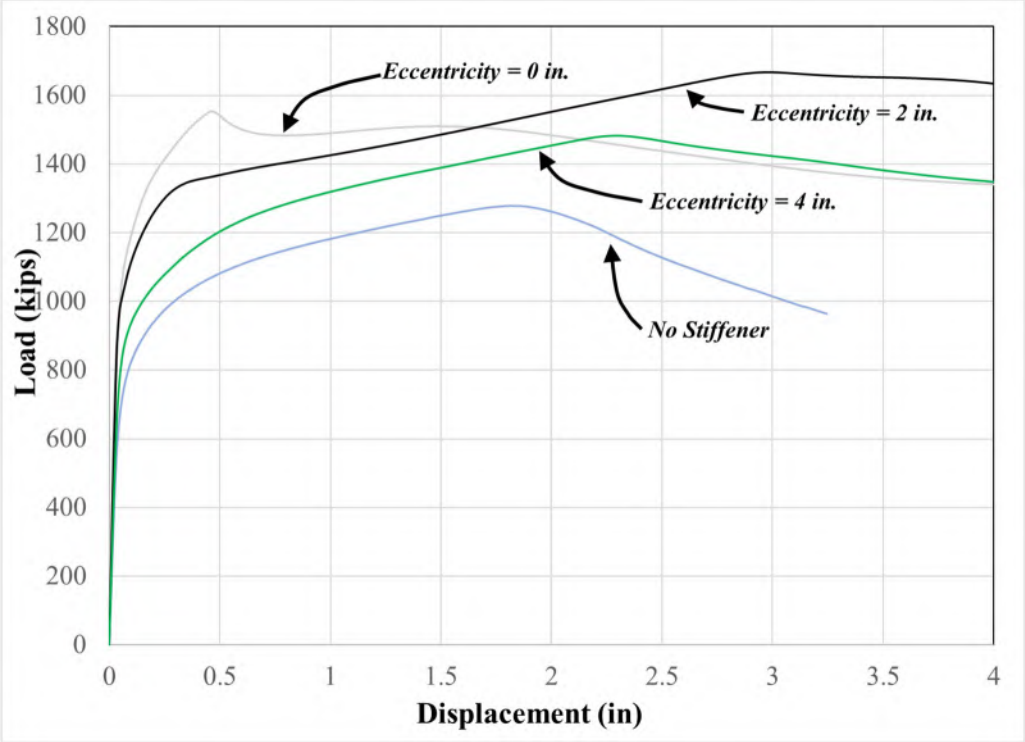

Figure 6.6-15: Load-displacement results of W14X233-DC-3/4 specimens

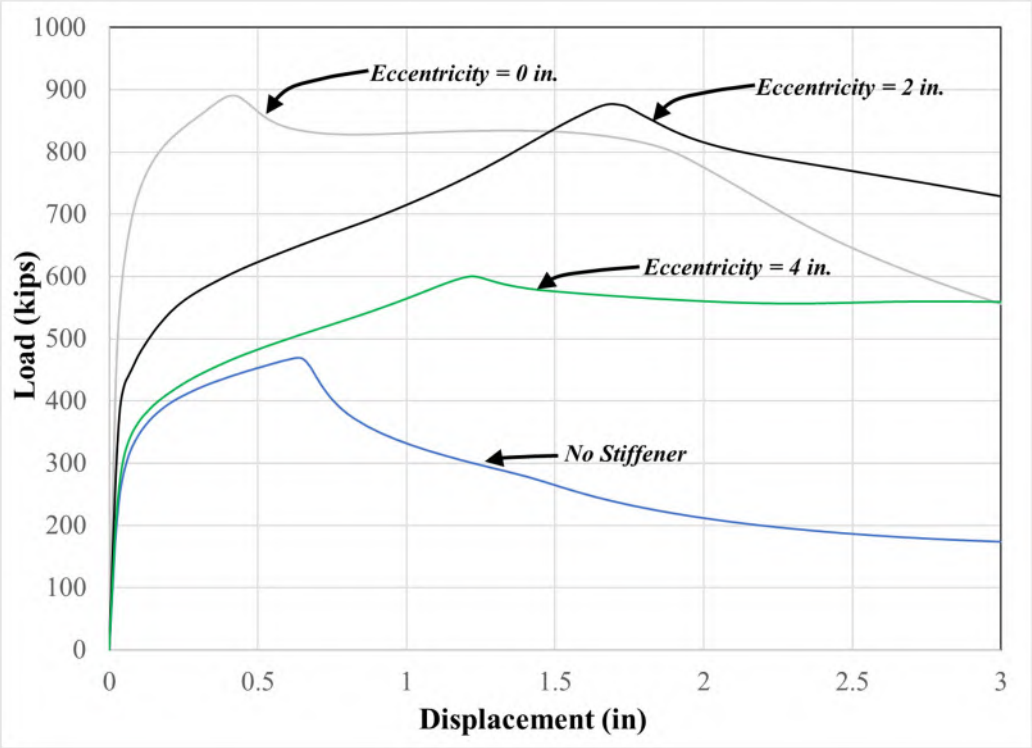

Figure 6.6-16: Load-displacement results of W24X131-DC-3/4 specimens

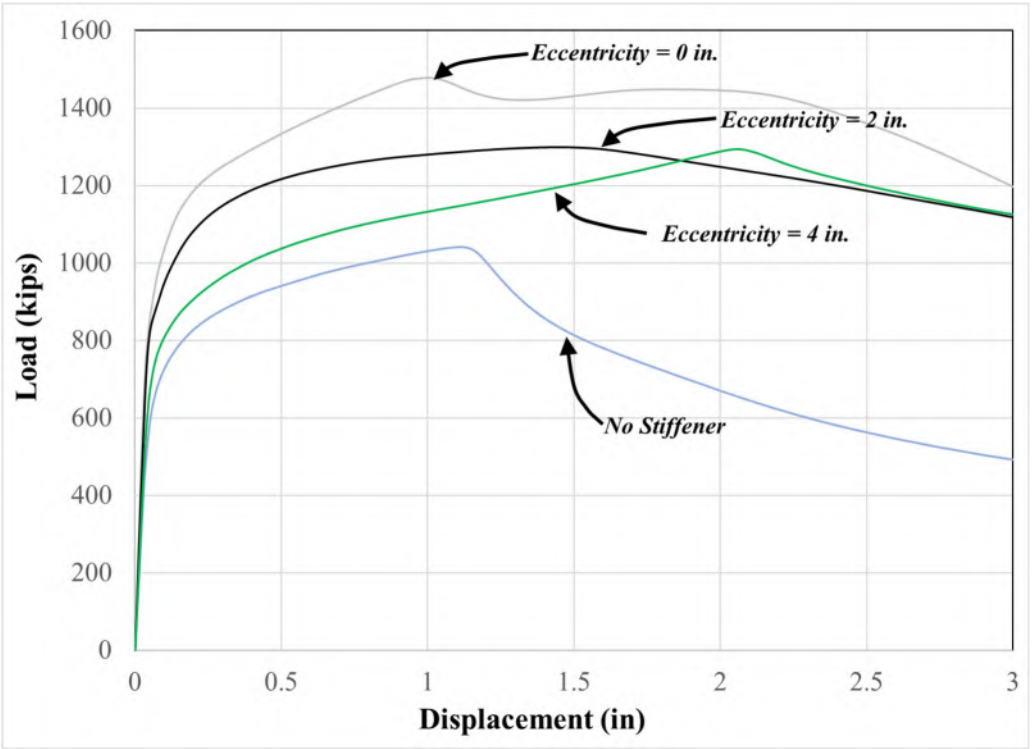

Figure 6.6-17: Load-displacement results of W24X229-DC-3/4 specimens

6.6.3 Primary Results of Double Compression Tests

Analytical models for column sections tested in double compression were developed without stiffeners and with smaller and bigger stiffeners of 3/8 in. and 3/4 in. thickness, respectively. The results for the analytical models with a smaller thickness of 3/8 in. are shown in Section 6.6-5.

Table 6.6-1 shows all the primary results of all analytical models with no stiffeners and when 3/4 in. stiffeners are used. The table provides general information for the analysis model including the column size, the stiffener condition and the stiffener thickness 't'. Table 6.6-1 also shows the theoretical capacities for the limit states of web local yielding (*WLY*), web local crippling (*WCR*), and web compression buckling (*WCB*) along with the theoretical concentric stiffener capacity from Equation 3-1. *WLY*, *WCR*, and *WCB* are used to compare to the results of the analytical column specimens without stiffeners, and the concentric stiffener capacity is used to compare to the results of the effective stiffener capacity for the analytical column specimen with concentric stiffeners.

Table 6.6-1 lists the primary results, which includes the maximum load obtained for each analysis. For all cases with stiffeners, an analytical "Effective Stiffener Capacity" is listed which represents the difference between the maximum load obtained for that analysis and the result of the corresponding column specimen without stiffeners. Finally, the effective stiffener capacities of column specimens with eccentric stiffeners are shown as a percentage of the effective stiffener capacity of the corresponding analysis with concentric stiffeners. This is shown in the table under "% Conc. Stiffener" and represents the primary result of these analytical investigations.

Table 6.6-1: Primary results for double compression tests with 3/4 in. stiffeners

General Info			Theoretical Capacities				Results		
Column Size	Stiff. Eccent. (in)	Stiffener 't' (in)	WLY (k)	WCR (k)	WCB (k)	Stiff (k)	Max Load (k)	Effective Stiff (k)	% Conc. Stiffener
W24X131	NA	NA	244	464.6	297	400	469.0	-	-
W24X131	0	3/4					890.8	421.8	-
W24X131	2	3/4					876.8	407.7	96.7
W24X131	4	3/4					601.1	132.1	31.3
W24X229	NA	NA	571	1234	1187	392	1040.8	-	-
W24X229	0	3/4					1478.1	437.3	-
W24X229	2	3/4					1298.7	257.9	59.0
W24X229	4	3/4					1293.5	252.7	57.8
W14X68	NA	NA	152	233.9	182	296	274.0	-	-
W14X68	0	3/4					648.7	374.6	-
W14X68	2	3/4					460.8	186.8	49.9
W14X68	4	3/4					286.9	12.8	3.4
W14X120	NA	NA	249	455.9	520	438	475.8	-	-
W14X120	0	3/4					853.7	377.8	-
W14X120	2	3/4					777.0	301.2	79.7
W14X120	4	3/4					593.1	117.3	31.0
W14X176	NA	NA	428	896	1452	466	849.9	-	-
W14X176	0	3/4					1217.9	368.0	-
W14X176	2	3/4					1160.5	310.6	84.4
W14X176	4	3/4					995.0	145.1	39.4
W14X233	NA	NA	508	1495	2832	466	1278.7	-	-
W14X233	0	3/4					1554.6	275.9	-
W14X233	2	3/4					1666.2	387.5	140.4
W14X233	4	3/4					1483.3	204.6	74.1

For analytical column specimens without stiffeners, Table 6.6-1 shows that in most cases the maximum load is very close to the theoretical capacity for web local crippling. When column specimens have more slender webs (W14X68 and W24X131), the web compression buckling theoretical capacity underestimates the maximum load of the specimens and, in contrast, the web compression buckling equation for the stockier members (W14X120, W14X176, and W14X233) overestimates the load capacity. This comparison does not relate well to the failure modes observed in the analytical models presented in Section 6.6.1 since web compression buckling appeared to be the governing failure mode.

Table 6.6-1 demonstrates that the maximum loads for column specimens with stiffeners are always much higher than the equivalent condition without stiffeners. For specimens with eccentric stiffeners, the "% Conc. Stiffener" results vary significantly and the results are highly dependent on the column size. Eccentric stiffeners at 2 in. of eccentricity provided a capacity as high as 140% of the concentric stiffener condition for the W14X233 column specimen, and as low as 50% percent for the W14X68 column specimen. The W14X233 was the only column specimen, which reached its highest capacity with eccentric stiffeners. Reasons are unclear. However, for the concentric condition, the stiffeners share the load, yield and then stiffener buckling occurs instantaneously causing a drop in load prior to the web of the column specimen being subjected to significant stresses. When a smaller stiffener thickness of 3/8 in. was used, the effect was even more dramatic, in the sense that the load capacity of the specimen without stiffeners was higher than the capacity of the member with 3/8 in. concentric stiffeners. When eccentric stiffeners are used, the stiffeners themselves develop some curvature and therefore, partially negate the effect of sudden buckling.

Dissimilar from the results of experimental column specimens, the percentages themselves are very significant. Most of them higher than the original 60% capacity for the 2 in. eccentricity case recommended by Graham et al. (1959). Based on the results and relationships presented in Table 6.6-1, a technique must be derived that idealizes the column size to predict appropriate effective stiffener capacities when eccentric stiffeners are used. This is dissimilar from the recommendations in AISC Design Guide 13 (Carter, 1999) which gives recommendations based on eccentricity alone regardless of the column size.

For instance and for a W24X131, when the stiffener eccentricity is 2 in., the effective stiffener capacity is 97% of the concentric stiffener condition and when the eccentricity is 4 in., the effective stiffener capacity is 31% of the concentric stiffener condition. In contrast, for a W14X68, when stiffener eccentricity is 2 in., the effective stiffener capacity is 50% of the concentric stiffener condition and when the eccentricity is 4 in., the effective stiffener capacity is 3% of the concentric stiffener condition (very similar to experimental column specimens with 4 in. eccentricity). Therefore, the results are highly independent on column size and more rigorous studies are required to identify appropriate relationships between the column size, magnitude of eccentricity, and the stiffener effective capacity.

For the double compression tests, factors that influence the effective stiffener capacity at various eccentricities are hypothesized as the flange thickness (or '*k*' dimension) and the slenderness of the web (h / t_w) ratio. These two geometric properties are evaluated in Section 6.6.4 in order to identify relationships to the analytical results.

Prior to recommending a straight-line equation that is dependent on stiffener eccentricity as described for single compression in Section 6.5.3, justification using analytical results is necessary. The "% Conc. Stiffener" results from Table 6.6-1 are shown graphically in Figure 6.6-18. The results of the concentric stiffener case is used for the relationships as well, which is always equal to 100%. In summary, the curves in Figure 6.6-18 are hypothesized as appropriate relationships for the influence of eccentricity on effective stiffener capacities and for the various column sizes evaluated, considering stiffener thickness. As a general rule, the effective stiffener capacity for eccentric stiffeners is always lower than the concentric stiffener capacity. However, the W14X233 column specimen reached a higher capacity with 2 in. eccentric stiffeners as described earlier in this section.

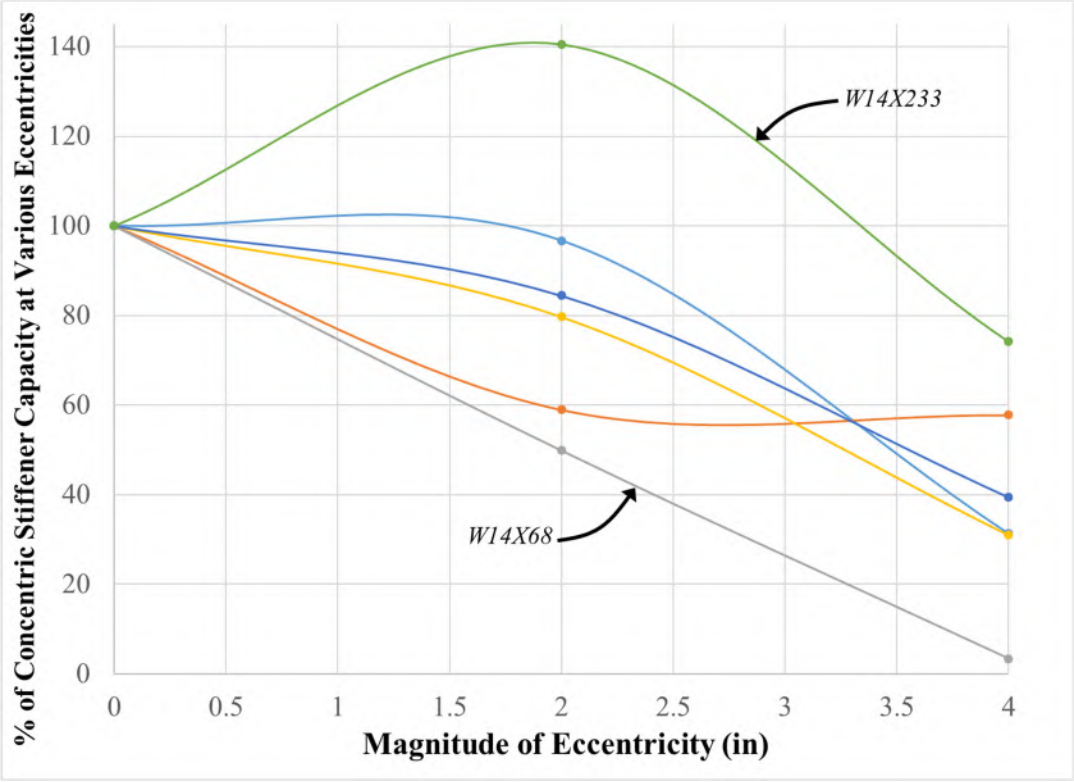

Figure 6.6-18: Influence of eccentricity in effective stiffener capacity

In general, if the curves presented in Figure 6.5-16 are straight lines, interpolation could be used to determine the effective stiffener capacity at any eccentricity. If the curves are concave down, the use of interpolation would be conservative. However, if the curves are concave up, interpolation would be unconservative. The relationships presented in Figure 6.6-18 are inconsistent. For some cases, the curves are concave down (e.g. W24X131). In other cases, they are concave up (e.g. W24X229) and in some cases, the curves are almost straight lines (e.g. W14X68). The result of the W24X229 is concerning but the other 5 column sizes have favorable results.

6.6.4 Influence of Geometric Properties on Effective Stiffener Capacity

This section evaluates the influence of geometric properties on the effective stiffener capacity results for the double compression tests. More specifically, the influence of flange thickness and the influence of web slenderness (h / t_w) are compared to the "% Conc. Stiffener" results for column specimens with eccentric stiffeners.

Initially, aided with experimental results, it was hypothesized that both geometric properties have an influence on the effective stiffener capacity. As discussed in Section 6.5.4 and for the single compression results, limited relationships could be derived using the h / t_w ratios of the different column sections. For the double compression tests, the results are further inconclusive. Figure 6.6-19 relates the "% Conc. Stiffener" results to the h / t_w ratios for various column specimens and when the stiffener eccentricity is 2 in. (in blue circles) and 4 in. (in black triangles). The plot is shown in scatter format. As shown in Figure 6.6-19, the results are sporadic and no clear relationships exist between the web slenderness and the effective stiffener capacity results. In general, as web slenderness increases, the 'percentage' results decrease. However, at a 2 in. eccentricity, the column specimen with the highest web slenderness had the second highest "% Conc. Stiffener" result. Therefore, the relationships are inconclusive.

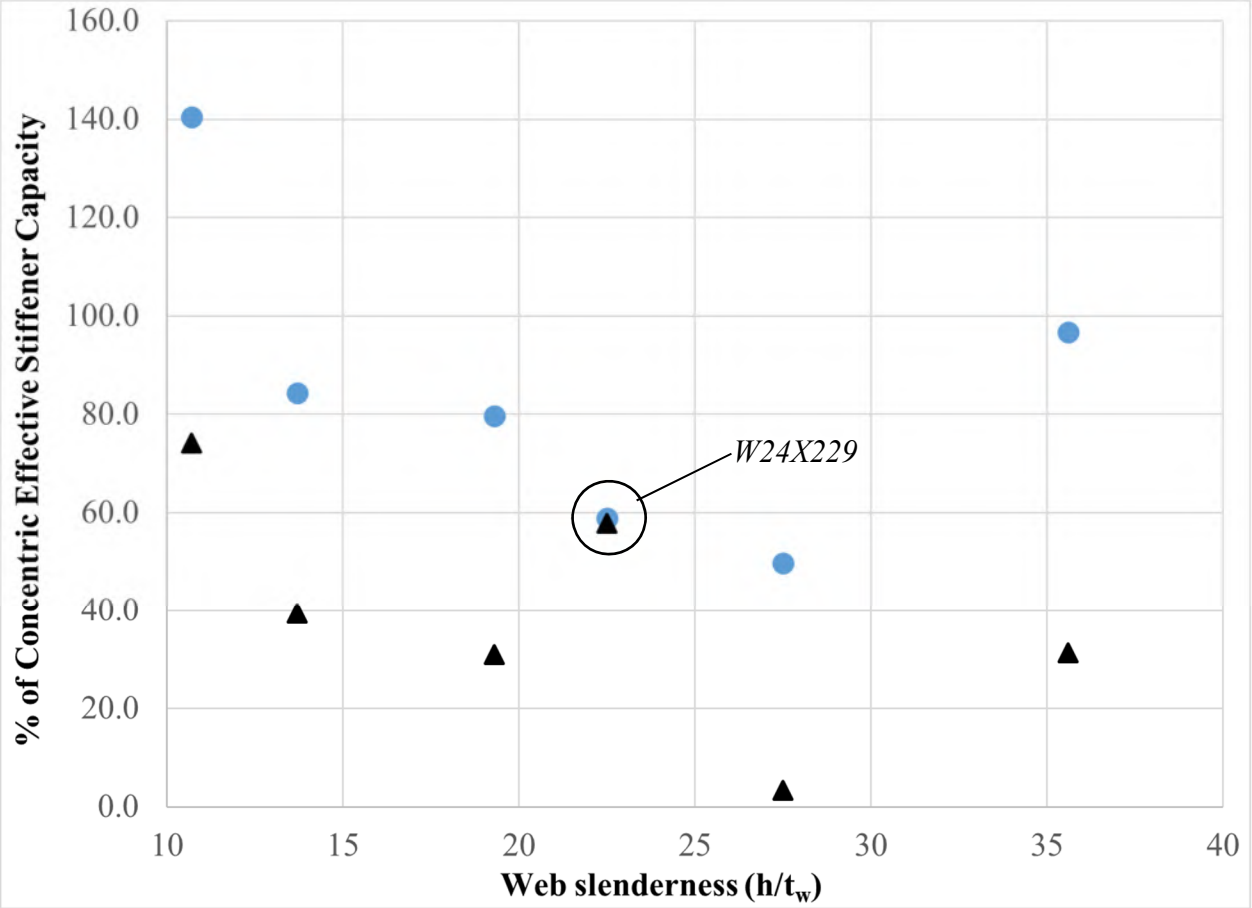

Figure 6.6-19: Comparison of web slenderness and effective stiffener capacity

For the results of columns specimens with stiffeners at 2 in. eccentricity, Figure 6.6-20 shows relationships between the flange thickness and the % Conc. Stiffener" results. The analytical column specimen results are represented with blue circles. Figure 6.6-20 demonstrates a 'better' relationship between this geometric property and the analytical results as opposed to the web slenderness. No clear trend can be established using the results as the analytical models reveal that there are many factors that influence the failure modes and maximum load results. However, the results do show that in general, as flange thickness increases, the percentage results increase as well and conservative relationships between flange thickness and effective stiffener capacity can be established for the practicing engineer.

The same straight line equation from Figure 6.5-18 for the single compression results is plotted within Figure 6.6-20. This line could be used as a conservative design methodology that determines the effective stiffener capacity of eccentric stiffeners in comparison to that of concentric stiffeners

considering various flange thickness. However, there is a point underneath the proposed equation. Therefore, a modified conservative equation is represented with a dashed line in which all results are above. If the flange thickness is less than 0.5 in., it is recommended that stiffeners shall not be permitted to be eccentric. If the flange thickness is greater than 2 in. and the eccentricity is 2 in., the effective stiffener capacity shall be limited to 70% of the effective stiffener capacity of the concentric case. These recommendations are superseded by the studies performed in Section 6.8 but were used in part of the development of Section 6.8.

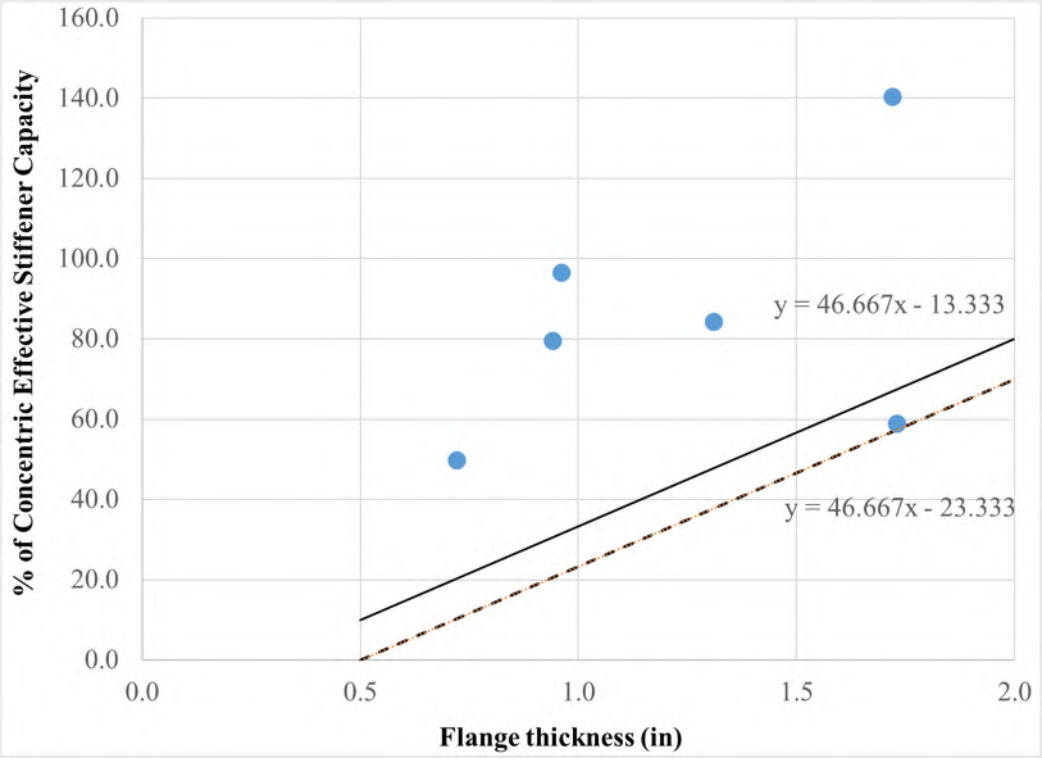

Figure 6.6-20: Effective stiffener capacity vs. flange thickness with 2 in. eccentricity

The relationships between the flange thickness and the "% Conc. Stiffener" results for column specimens with eccentric stiffeners at 4 in. are shown in Figure 6.6-21. Again, the trends show that as flange thickness increases, the percentage results increase and conservative relationships can be established for the practicing engineer. The same straight line equation as proposed for the single compression tests in Figure 6.5-19 is shown in Figure 6.6-21. Per this relationship, when the stiffener eccentricity is 4 in., the minimum flange thickness shall be 0.65 in. in lieu of 0.5 in. And, if the flange thickness is greater than 2 in. and the eccentricity is 4 in., the effective stiffener capacity shall be limited to 55% of the effective stiffener capacity of the concentric case.

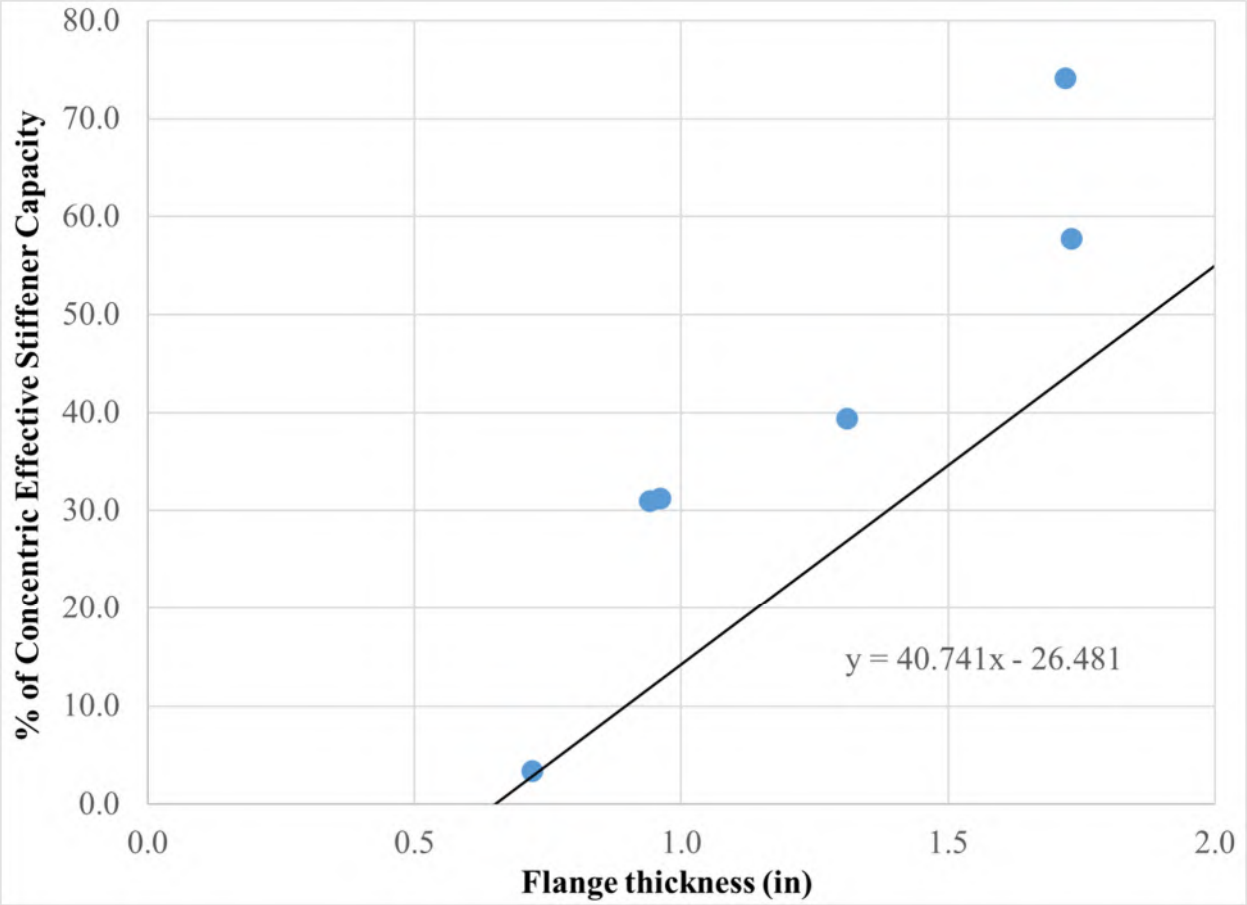

Figure 6.6-21: Effective stiffener capacity vs. flange thickness with 4 in. eccentricity

The two proposed relationships established using Figure 6.6-20 and Figure 6.6-21 for 2 in. eccentricity and 4 in. eccentricity, respectively, could be used for any magnitude of eccentricity and any column size. Again, these recommendations are superseded by Section 6.8, which accounts for all column specimen results for all test methods.

6.6.5 Influence of Geometric Properties on Effective Stiffener Capacity

This section evaluates the influence of stiffener thickness on the analytical results of column specimens subjected to double compression. Multiple stiffener thickness were not considered in the scope of work from the recommendations proposed in the preliminary report. However, after reviewing the analytical results and studying the behavior of the column specimens for 3/8 in. stiffeners, it was decided that all tests should be re-evaluated choosing a stiffener thickness of 3/4 in. For the double compression tests, the results using 3/4 in. stiffeners are considered primary but the results using 3/8 in. stiffeners are available and therefore presented herein.

Table 6.6-2 shows the primary results for single compression tests with 3/8 in. stiffeners. The different columns presented in Table 6.6-2 are described in detail in Section 6.6.3.

Table 6.6-2: Primary results for double compression tests with 3/8 in. stiffeners

General Info			Theoretical Capacities				Results		
Column Size	**Stiff. Eccent. (in)**	**Stiffener 't' (in)**	**WLY (k)**	**WCR (k)**	**WCB (k)**	**Stiff (k)**	**Max Load (k)**	**Effective Stiff (k)**	**% Con. Stiffener**
W24X131	NA	NA	243.5	464.6	297	200	938.1	-	-
W24X131	0	3/8					1226.8	288.8	-
W24X131	2	3/8					1354.2	416.1	144.1
W24X131	4	3/8					1189.9	251.8	87.2
W24X229	NA	NA	571.2	1234	1187	196	2081.6	-	-
W24X229	0	3/8					2297.9	216.3	-
W24X229	2	3/8					2434.8	353.2	163.3
W24X229	4	3/8					2338.8	257.2	118.9
W14X68	NA	NA	151.5	233.9	182	148	548.1	-	-
W14X68	0	3/8					893.4	345.3	-
W14X68	2	3/8					737.6	189.5	54.9
W14X68	4	3/8					537.5	-10.6	-3.1
W14X120	NA	NA	249.3	455.9	520	219	951.7	-	-
W14X120	0	3/8					1195.9	244.2	-
W14X120	2	3/8					1218.9	267.2	109.4
W14X120	4	3/8					1127.8	176.1	72.1
W14X176	NA	NA	427.5	896	1452	233	1699.8	-	-
W14X176	0	3/8					1845.1	145.3	-
W14X176	2	3/8					1949.6	249.8	171.9
W14X176	4	3/8					1875.5	175.7	120.9
W14X233	NA	NA	508.3	1495	2832	233	2557.4	-	-
W14X233	0	3/8					2511.9	-45.5	-
W14X233	2	3/8					2766.9	209.4	-460.5
W14X233	4	3/8					2755.1	197.7	-434.7

The results for 3/8 in stiffeners are very inconsistent and do not compare well with the studies performed up to this point. For most column specimens, eccentric stiffeners at an eccentricity of 2 in. reach a higher capacity than concentric stiffeners. In most cases, concentric stiffeners provide some extra load capacity compared to the column section without stiffeners. However, the most surprising result is that when the W14X233 column specimen is analyzed with 3/8 in. stiffeners, the column specimen reaches a lower capacity that the corresponding column specimen without

stiffeners. This is explicitly studied in Section 7.5. However, as shown earlier in Table 6.6-1, when 3/4 in. stiffeners are used, they are not slender and the load always increases resulting in a positive effective stiffener capacity.

Overall, the results in Table 6.6-2 are very sporadic and difficult to comprehend. Stiffener buckling is very critical in the double compression condition and it can be very problematic if the stiffeners are too slender, particularly in the concentric condition. Further studies and recommendations regarding stiffener slenderness are provided in Section 7.5. Since the stiffener slenderness is insufficient, it is cumbersome to develop relationships between stiffener eccentricity and effective stiffener capacity. However, the results in Table 6.6-2 do not negate the usefulness of the straight line equations presented in Figures 6.6-20 and 6.6-21 that relate flange thickness to "% Conc. Stiffener" results. With the exception of the W14X233 test group, which has negative answers for the aforementioned reasons, no results in Table 6.6-2 indicate that the straight line equations would not be conservative and therefore, they could still be utilized.

6.7 Analytical Results of Single Tension Tests

This section summarizes all the results of the analytical finite element models of single tension tests. This section will not go into detail regarding the performance of each column specimen but instead, demonstrates how each model was analyzed with respect to load capacity and elastic stiffness, provide general observations regarding the behavior of various models and provide the important results associated with each model along with recommendations for design practice. Screenshots of all models are provided in Appendix E. Theoretical capacities for the analytical column specimens and for the limit states of web local yielding, flange bending and for yielding of the 3/8 in. stiffeners (AISC, 2016) are provided in Appendix D.

6.7.1 Analytical Test Matrix for Single Tension Tests

Table 6.7-1 provides a summary of the analytical test matrix for the larger column specimens subjected to single tension. Overall, 72 analytical column specimens were analyzed in single tension (6 column sizes x 3 weld/loading plate thickness x 4 stiffener eccentricity conditions).

Table 6.7-1: Analytical test matrix for single tension testing of larger column specimens

Variable	Matrix
Column Sizes	W14X68, W14X120, W14X176, W14X233, W24X131, W24X229
Weld Sizes	1/4 in., 9/16 in., 7/8 in.
Loading Plate Thick.	3/4 in., 1 1/2 in., 2 1/4 in. (respectively)
Eccentricity Conditions	NA, 0 in., 2 in., 4 in.

Similar to the compression studies, the column specimen sizes included a W14X68, W14X120, W14X176, W14X233, W24X131, and W24X229. Initially, all column specimens were analyzed with 1/4 in. fillet welds and a loading plate with a thickness of 3/4 in. However, this proved insufficient for larger column specimens since failure occurred at very similar loads regardless of the eccentricity condition. For instance, the failure load for the W24X229 column specimen modeled without stiffeners was equal to 263 kips and the failure load for the W24X229 column specimen modeled with concentric stiffeners was equal to 263.5 kips. The failure loads with eccentric stiffeners was found between these two values. In all four cases, the failure load was dictated by limitations in the weld strength itself and not significantly influenced by local deformations that develop in the column specimens when subjected to concentrated loads. Therefore, the column specimens were further modeled with weld sizes of 9/16 in. and later with weld sizes of 7/8 in. To ensure failure occurred in the weld and not limitations of the base metal, the loading plates were increased in thickness to 1 1/2 in. and 2 1/4 in., respectively. It was later decided to model the loading plates as elastic only which further ensured that failure would not be influenced by significant deformations in the loading plate.

For conditions with stiffeners, all stiffeners were modeled with a 3/8 in. thickness. At this time, it is uncertain if analyzing one stiffener size is sufficient to develop recommendations. Larger stiffener thickness was considered. However, analyzing the 72 conditions as part of the text matrix shown in Table 6.7-1 was time consuming and since stiffener buckling is not an issue for the single tension tests, the stiffener thickness did not seem as critical as opposed to other parameters.

For each fillet weld size from the loading plate to the column specimen, a special finite element mesh was developed to ensure the nodes at the boundaries of the fillet welds matched the nodal locations on the column specimen flange and loading plate. Nodes on the boundaries of the fillet welds were slaved to nodes on either the loading plate and column specimen flange using constraint

equations as discussed in Section 5.4. Figure 6.7-1(a) shows a side profile of a W24X131 column specimen at the loading plate when 1/4 in. fillet welds were modeled. Figure 6.7-1(b) shows the W24X131 modeled with 7/8 in. fillet welds.

(a) 1/4 in. weld, 3/4 in. loading plate (b) 7/8 in. welds, 2 1/4 in. loading plate

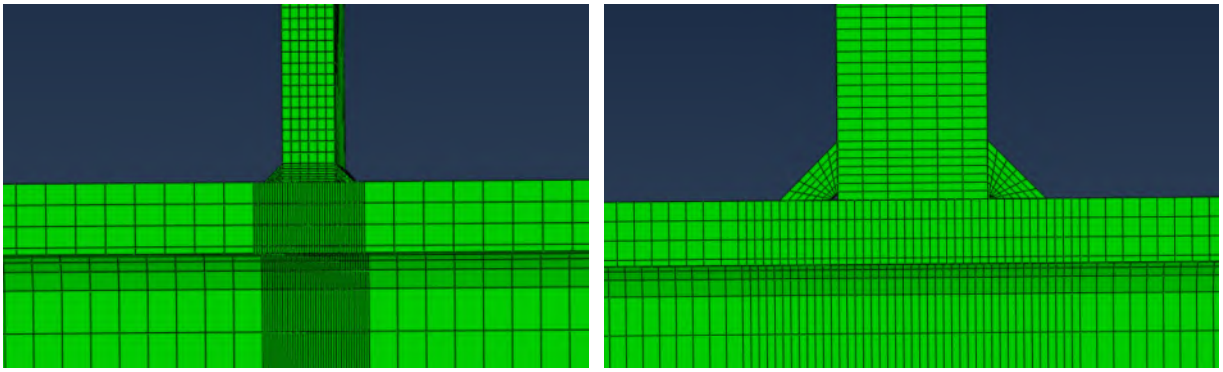

Figure 6.7-1: Demonstration of weld mesh used for single tension specimens

6.7.2 Analysis Assumptions and Results Evaluated

Finite element models for the experimental column specimens analyzed in single tension were discussed in Section 5.4. Similar to these models, weld failure was assumed to occur when the stress in the weld exceeded the ultimate stress of 82.4 ksi. Each model was visually inspected in ABAQUS (2014) to identify when this occurs by plotting the Von Mises stresses as contours and setting the maximum limit to 82.4 ksi. Therefore, anything grey in the model represented a stress greater than 82.4 ksi. For consistency, the research team assumed failure occurred when the grey area barely passed one layer of elements either at the top of the weld or at the bottom of the weld. This is demonstrated in Figures 6.7-2 and 6.7-3. In Figure 6.7-2, a W24X131 is modeled with 1/4 in. welds and failure was assumed to occur in the top of the weld where it connects to the loading plate. In Figure 6.7-3, a W24X131 is modeled with 7/8 in. welds. Initially and while the column specimen was behaving elastic, high weld stresses were concentrated near the top of the weld similar to Figure 6.7-2 but failure never occurred. As the flanges started to bend, stresses became more concentrated at the bottom of the weld.

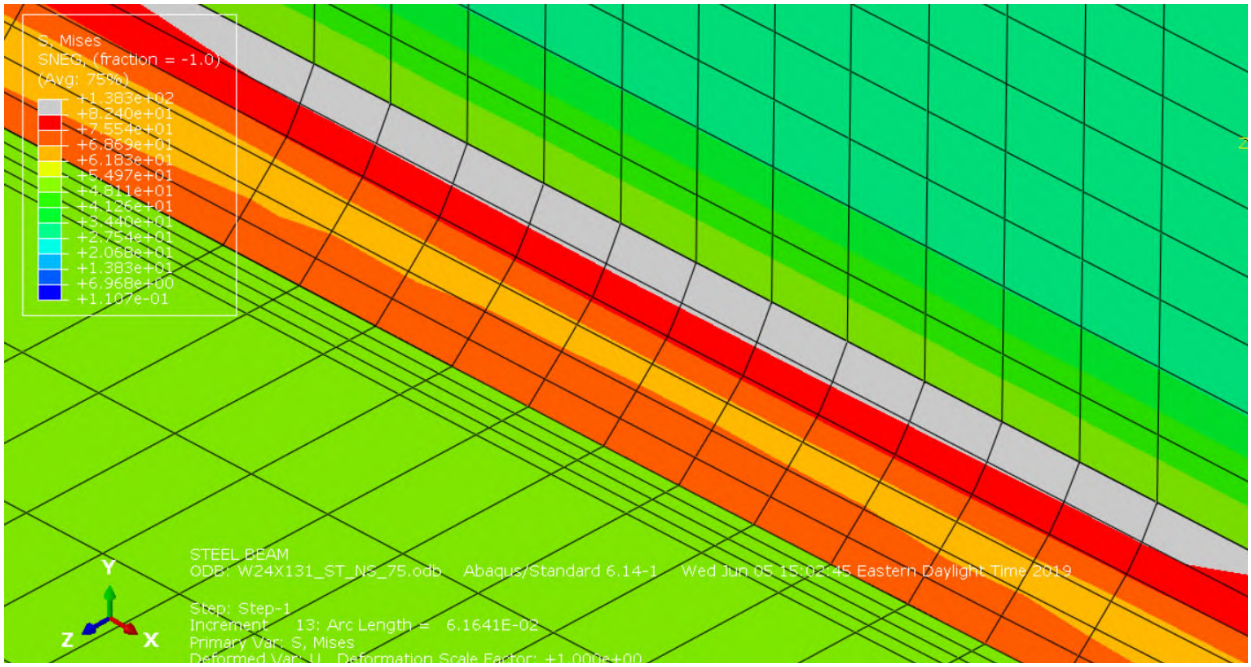

Figure 6.7-2: Stress distribution assumed at "failure" for W24X131 with 1/4 in. welds

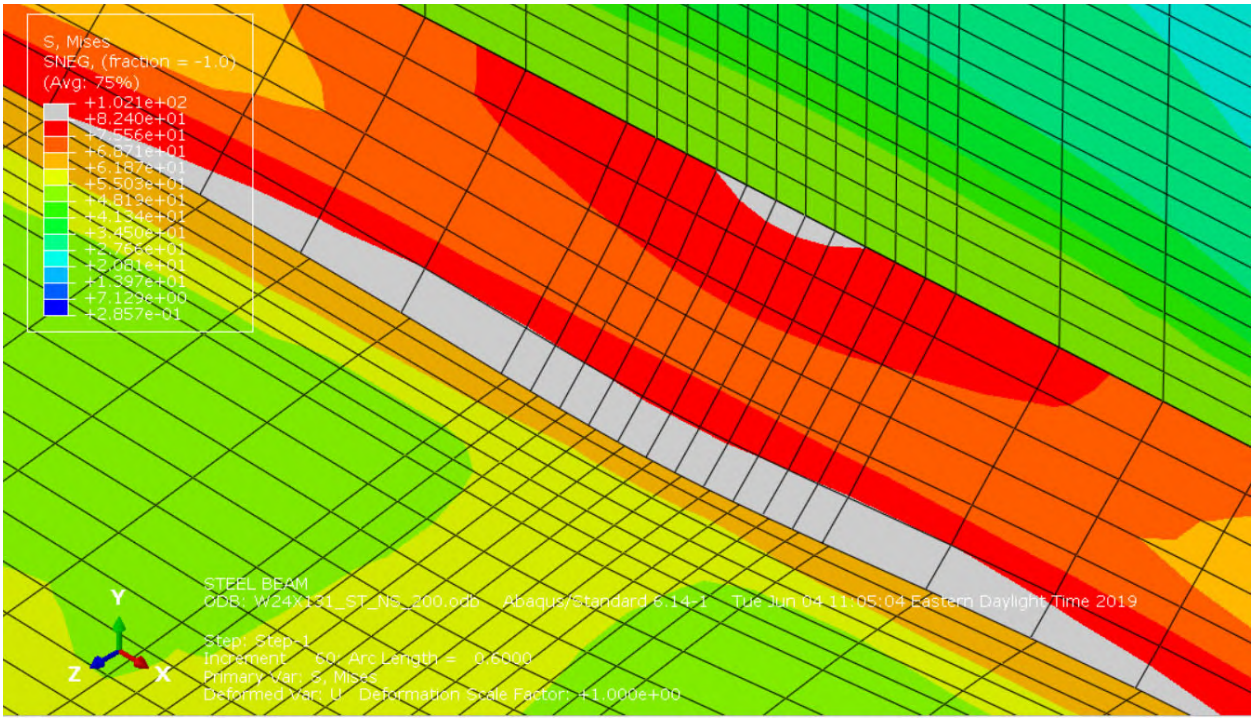

Figure 6.7-3: Stress distribution at assumed "failure" for W24X131 with 7/8 in. welds

All column specimens modeled with 1/4 in. welds reached an assumed failure load with a stress contour pattern similar to that shown in Figure 6.7-2. In addition, larger column sections (e.g. W14X233 and W24X229) always reached an assumed failure load with contours similar to that shown in Figure 6.7-2, regardless of weld size. In most of the other conditions, failure was assumed to occur with stress contours similar to that shown in either Figure 6.7-2 or 6.7-3. In limited conditions, the stress contours never demonstrated a failure in the weld since the ultimate stress was never exceeded. Instead, the column specimens exhibited significant displacements and maximum loads were governed by the shear and flexural stresses that developed in the column specimen. This only occurred when 7/8 in. welds were modeled and with stiffeners at an eccentricity of 0 in. or 2 in.

The failure or maximum loads of the individual column specimens were compared within a test group. A test group consisted of four column specimens with the same column size and weld details but with four different eccentricity conditions for the stiffeners. However, there were questions regarding the sensitivity and consistency of the results with respect to the assumed weld failure load. This was especially true when larger column specimens were modeled with small welds and the maximum loads were very similar regardless of the eccentric condition. Therefore, the results of the elastic stiffness and "effective elastic stiffness" were also evaluated and were found to be more beneficial when studying the effects of stiffener eccentricity as opposed to the maximum load.

Herein, "effective elastic stiffness" represents the change in elastic stiffness from the elastic stiffness results when stiffeners are used in comparison to the elastic stiffness when stiffeners are not used. Analyzing stiffness provides information regarding force that is directly transferred into the stiffeners considering eccentricity. It is important to recognize that the elastic stiffness considers flexural and shear deformations that occur in the column, elastic elongation of the loading plate and local deformations that occur in the column specimen from the concentrated load effect. If stiffeners are not present, more local deformations occur in the column specimen directly underneath the load due to the concentrated load effect. If concentric stiffeners are used, the local deformations are minimized. Since the failure load is often limited by weld capacity, the failure load results are often very similar for specimens in the same test group. However, there was always a significant difference in elastic stiffness and therefore, analyzing this provides stronger evidence regarding the effects of eccentricity.

Additional load capacities are discussed in Section 6.7.5 that are dependent on the theoretical plastic moment capacity of the column section and the theoretical shear capacity. Since the stress-strain curves used in the finite element models are not limited to the yield strength, the moment in the column could exceed the theoretical plastic moment capacity and the internal shear in the column could exceed the theoretical shear capacity. However, the theoretical capacities can be used as target. If the internal moment exceeds the plastic moment capacity, then the effects of concentrated loads are more negligible since the column specimen can reach loads beyond what they would be designed for in practice.

6.7.3 Finite Element Screenshots

As discussed frequently in the remainder of this report, welds connecting the loading plate to the top flange of the column specimen were not capable of developing a uniform stress across the width of the weld unless large column specimens were modeled with concentric stiffeners. As weld size decreased, flange thickness increased or the flange slenderness ($b_f / 2t_f$) decreased and the stiffeners became more concentric, the weld stresses became more uniform across the width of the flange. For instance, Figure 6.7-4 shows the weld stress distribution when a W24X229 column specimen is modeled with concentric stiffeners and 1/4 in. welds. Of all conditions, this developed the most uniform weld stress when failure is assumed to occur. The column size has a flange thickness very close to that of a W14X233. However, the flange slenderness is noticeably smaller. As shown in Figure 6.7-4, the weld stresses are almost perfectly uniform across the entire width. In contrast, Figure 6.7-5 shows the finite element model of the W14X68 column specimen modeled without stiffeners and 9/16 in. welds. Flange bending is much more pronounced and causes non-uniform stresses in the welds and a localized failure.

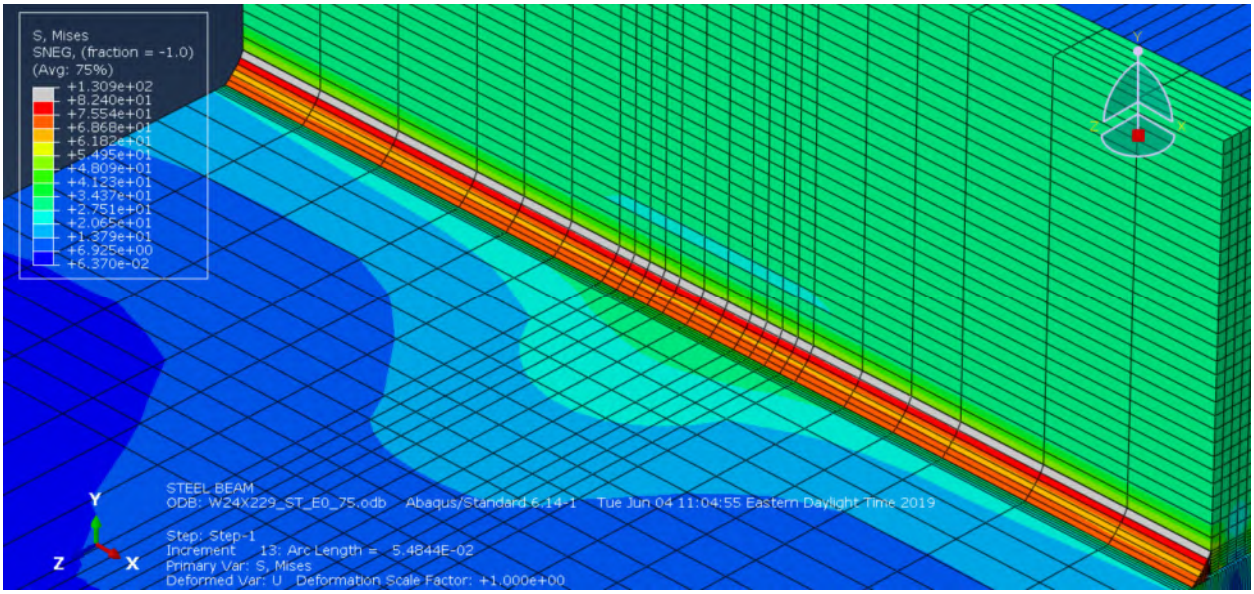

Figure 6.7-4: Finite element model of W24X229 with ¼ in. welds and concentric stiffeners

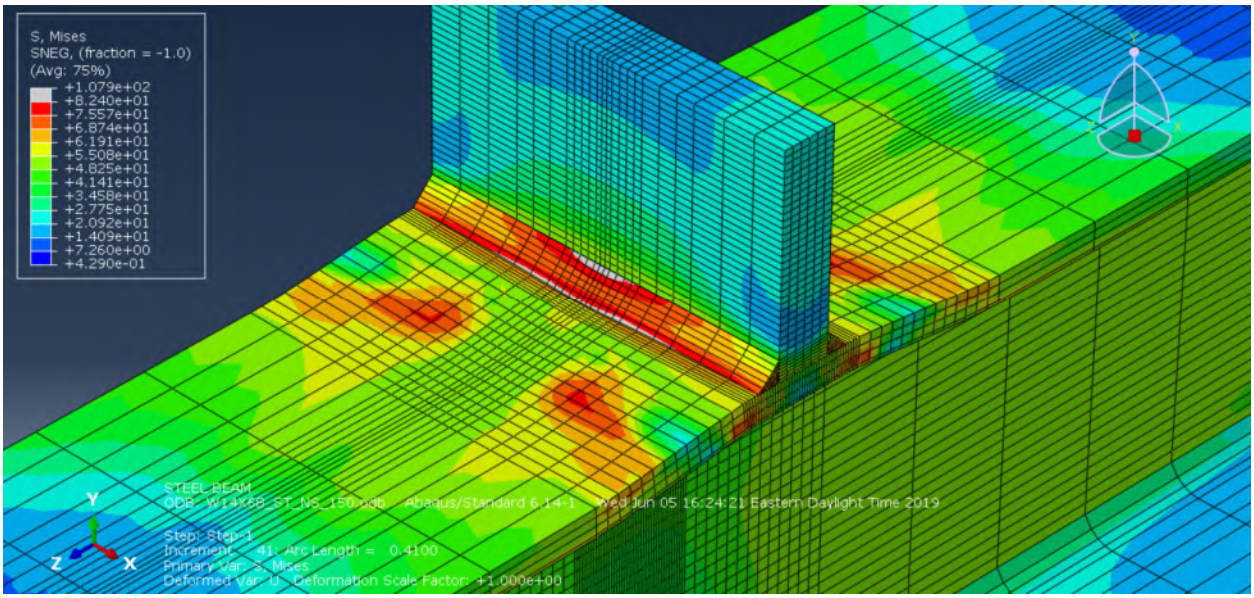

Figure 6.7-5: Finite element model of W14X68 with 9/16 in. welds and without stiffeners

A general description of the deformed shape of other column specimens at the assumed failure load was usually in between the two conditions shown in Figure 6.7-4 and 6.7-5. The influence of stiffener eccentricity varied significantly for the column specimens since welds of different thickness resulted in models that performed substantially different. In some cases, the weld size and stiffener eccentricity was "sufficient" and the maximum load was not governed but failure that occurs in the welds but instead, a maximum load was obtained and governed by shear and flexural

stresses/deformations.

The influence of eccentricity is pronounced using the results of a W14X68 modeled with 9/16 in. welds. The elastic stiffness and maximum load changed substantially between the four column specimens analyzed. Figures 6.7-6 to 6.7-9 shows the finite element results at approximately 180 kips with no stiffeners, stiffeners at an eccentricity of 4 in., stiffeners at an eccentricity of 2 in., and concentric stiffeners. The contours are scaled to the yield stress of 50 ksi and anything greater than 50 ksi indicates yielding in the column specimen or stiffeners. In Figure 6.7-6, the results show that significant yielding occurs in the web of the column specimen when no stiffener are used. Figure 6.7-7 shows that at a 4 in. eccentricity, some yielding still occurs and only a small portion of the load is transferred into the stiffeners. Figures 6.7-8 shows that at a 2 in. eccentricity, the stiffeners are becoming more engaged in resisting a portion of the load and the stresses in the web are decreasing at the same load magnitude of 180 kips. From Figure 6.7-9 and for the concentric condition, the stiffeners are fully engaged and there is no yielding in the web of the column specimen.

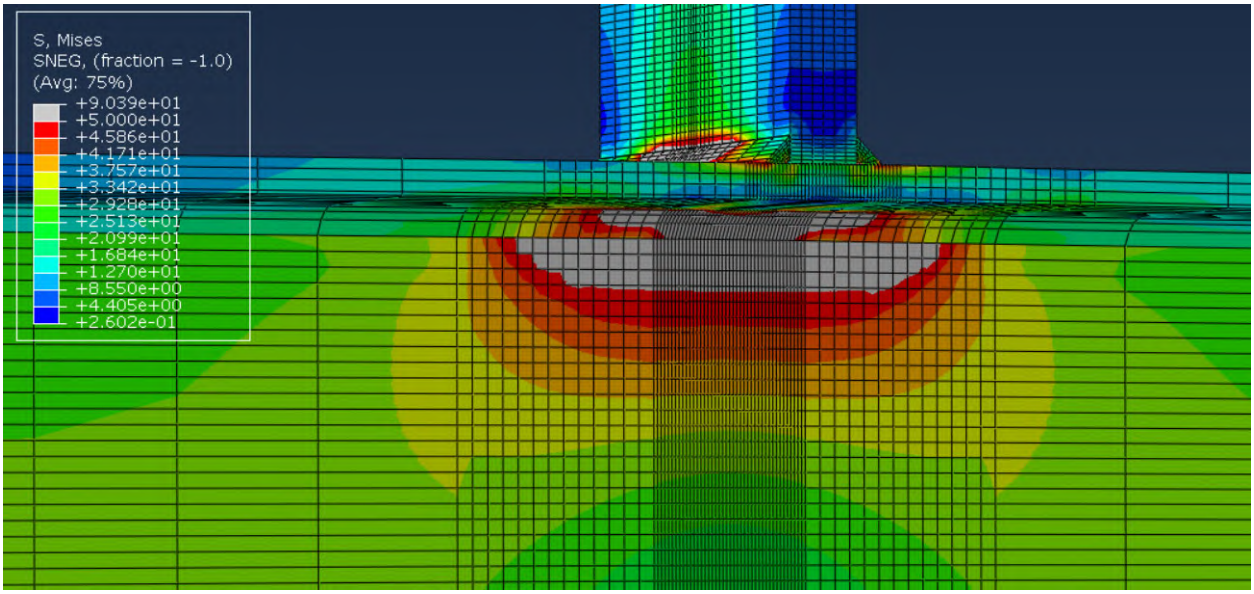

Figure 6.7-6: ST model of W14X68 with 9/16 in. welds, no stiffeners and at a load of 180 kips

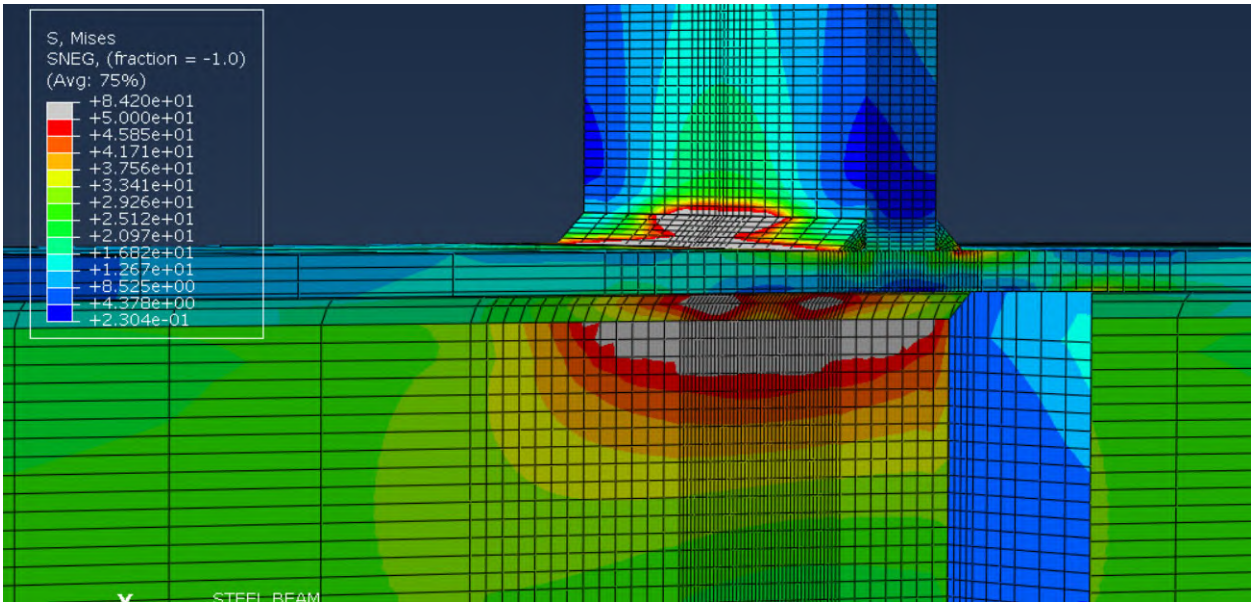

Figure 6.7-7: ST model of W14X68 with 9/16 in. welds, stiffeners at 4 in. eccentricity and at a load of 180 kips

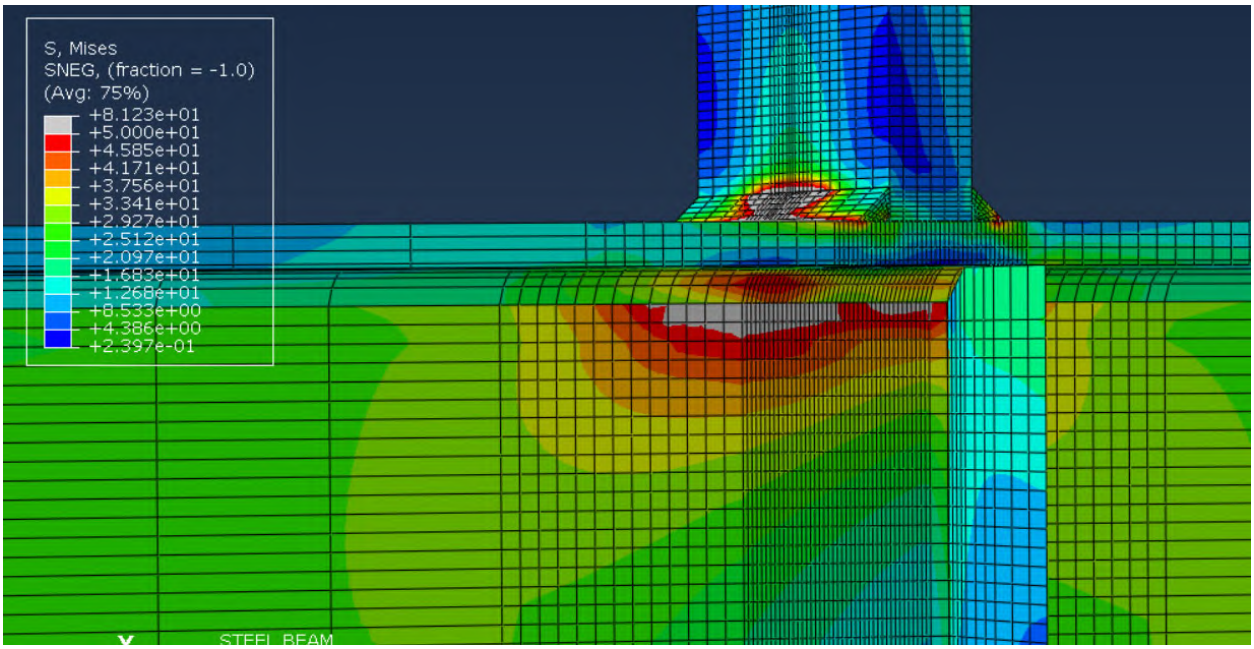

Figure 6.7-8: ST model of W14X68 with 9/16 in. welds, stiffeners at 2 in. eccentricity and at a load of 180 kips

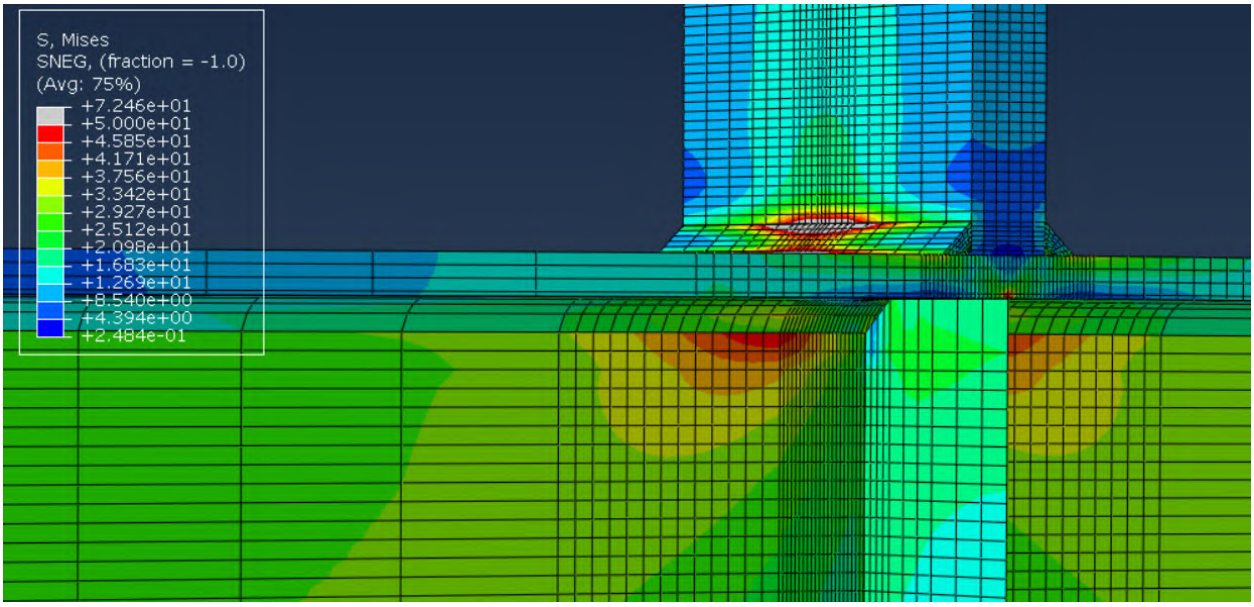

Figure 6.7-9: ST model of W14X68 with 9/16 in. welds, concentric stiffeners and at load of 150 kips

Figures 6.7-10 to 6.7-13 show the stress distribution at the individual failure loads for the aforementioned column specimens. The deformed shape is scaled to 5X for clarity. Significant flange bending is identified in Figure 6.7-10 for the no stiffener condition and failure occurred in the top of the weld. Figure 6.7-13 shows limited flange bending. In addition, significant shear yielding is developing in the web of the column specimen, which dictated the capacity of some of the column specimen models. Figures 6.7-11 and 6.7-12 show deformations and stresses in between that shown in Figures 6.7-10 and 6.7-13 when eccentric stiffeners are used.

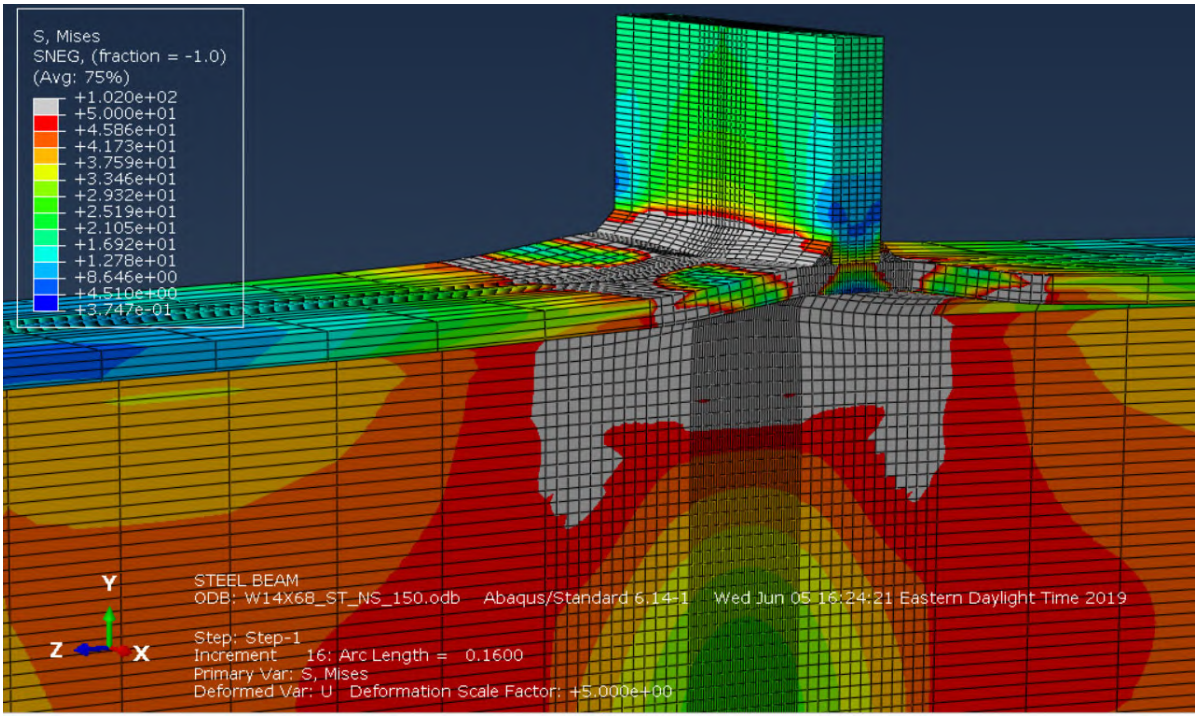

Figure 6.7-10: ST model of W14X68 with 9/16 in. welds, no stiffeners and at failure load

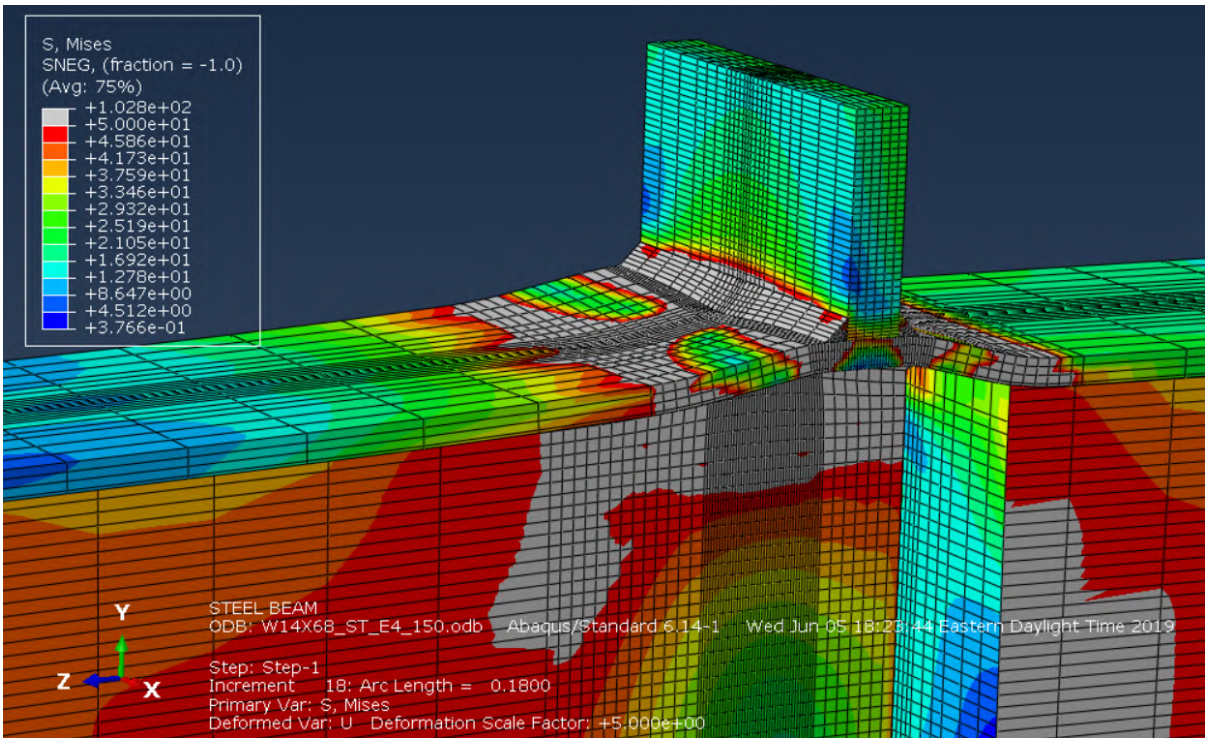

Figure 6.7-11: Single tension model of W14X68 with 9/16 in. welds, stiffeners at 4 in. eccentricity and at failure load

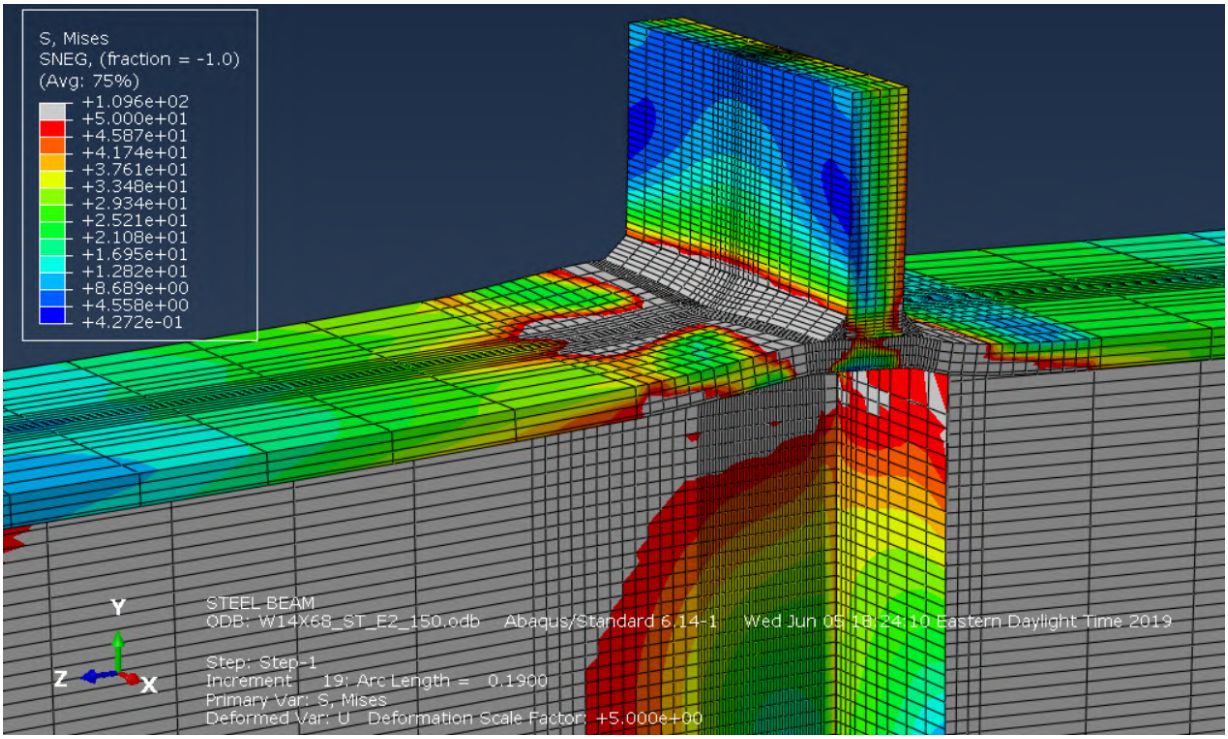

Figure 6.7-12: Single tension model of W14X68 with 9/16 in. welds, stiffeners at 2 in. eccentricity and at failure load

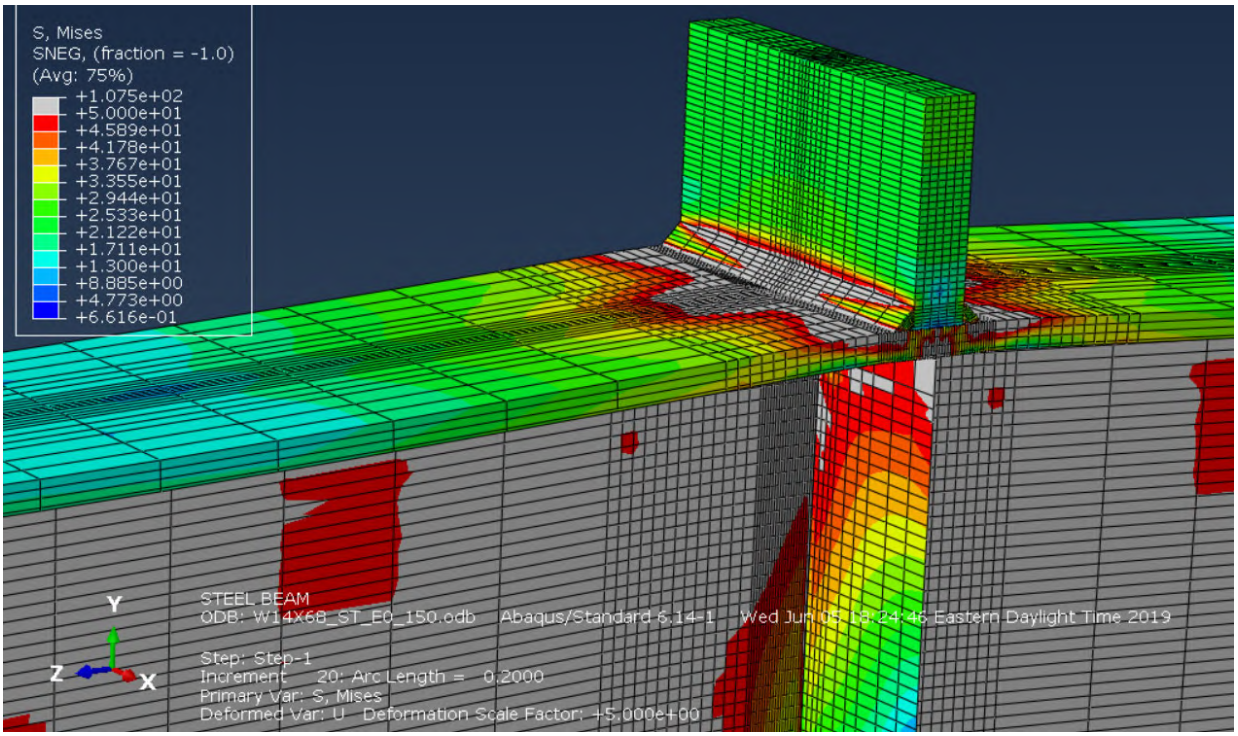

Figure 6.7-13: Single tension model of W14X68 with 9/16 in. welds, concentric stiffeners and at failure load

Other test groups exhibited similar trends as load was initially transferred into the stiffeners as shown in Figure 6.7-6 to 6.7-9 and at the failure load as shown in Figures 6.7-10 to 6.7-13. However, when larger sections were modeled with smaller weld sizes, the influence of stiffener eccentricity is minimal since the load carrying capacities are all similar. Figure 6.7-14 shows the W24X229 column specimen modeled with 1/4 in. welds and no stiffeners and at the assumed failure load. The shape of the column specimen and weld stresses are very similar to that with concentric stiffeners, which was shown in Figure 6.7-4. These trends and the influence of weld size makes the recommendations for the design of eccentric stiffeners complicating for the tension loading condition. However, in all test groups, the influence of stiffener eccentricity is more pronounced when evaluating the elastic stiffness as discussed in more detail in Sections 6.7-5 and 6.7-6.

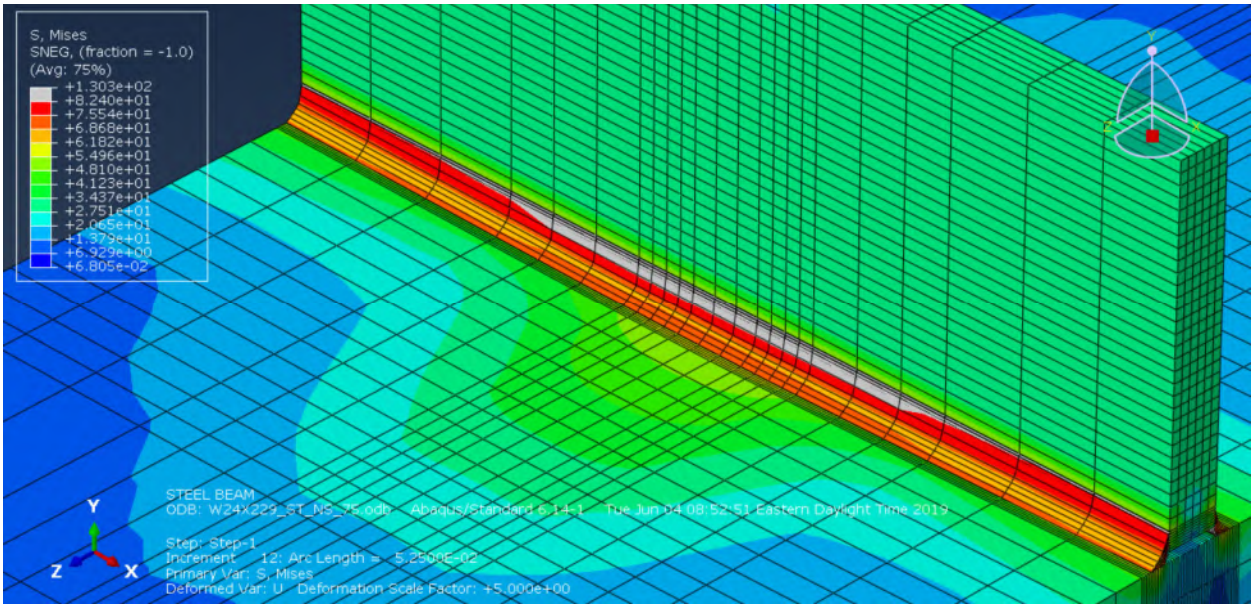

Figure 6.7-14: Single tension model of W24x229 with 1/4 in. welds and no stiffeners

6.7.4 Load-Displacement Results

Load-displacement relationships for the analytical models subjected to single tension are presented in this section. When performing the *STATIC RIKS analysis in ABAQUS (2014), after weld failure was assumed to occur, the load would eventually decrease with an increase in displacement. For instance, Figure 6.7-15 shows the finite element load-displacement results for the W24X131 column specimen modeled with 9/16 in. welds and with the results plotted well after weld failure is

assumed to occur. It is, however, more appropriate to plot the load-displacement relationships to when weld failure is assumed to occur as described in Section 6.7.2. In comparison to Figure 6.7-15, Figure 6.7-26 discussed later shows the same curves for the W24X131 modeled with 9/16 in. welds, up to when weld failure is assumed to occur.

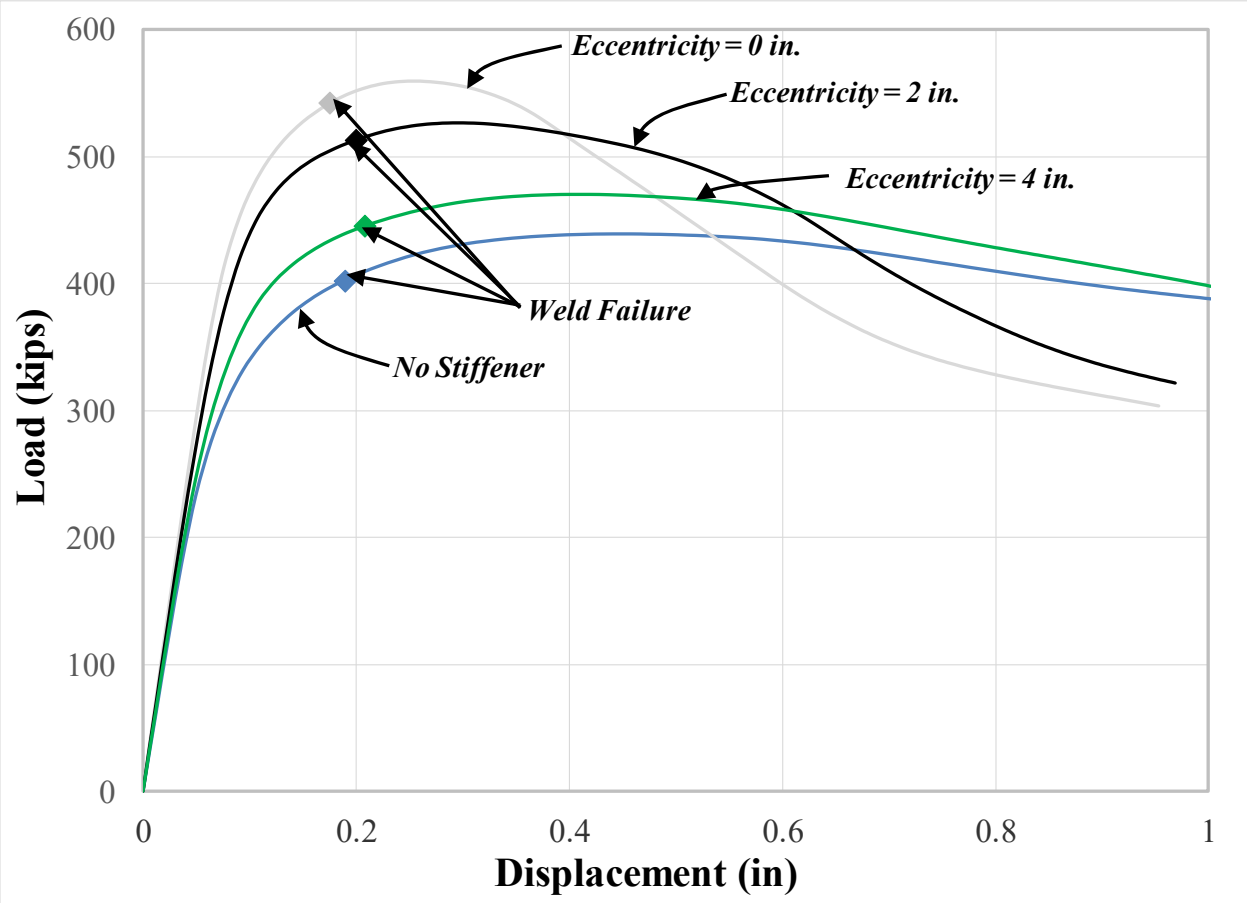

Figure 6.7-15: Load-displacement results of W24X131 plotted after weld failure occurs

Figures 6.7-16 to 6.7-21 show the load-displacement relationships for all analytical column specimens subjected to single tension and modeled with 1/4 in. welds from the 3/4 in. loading plate to the top flange of the column specimen. The results are plotted for each individual test group consisting of the same column size and different stiffener eccentricity conditions. For instance, Figure 6.7-16 shows the results for four W14X68 column specimens with the different aforementioned stiffener conditions. When 1/4 in. welds are modeled, the influence of eccentricity is the most pronounced for this test group in comparison to larger column sections.

The load-displacement results further demonstrate that when using a 1/4 in. weld and when a larger column size is modeled, the maximum load is governed significantly by limitations in the weld capacity. Figure 6.7-21 shows the results for the four W24X229 column specimens and the resulting failure loads are almost identical. For all test groups, stiffener condition has more of a direct influence on the elastic stiffness as opposed to the maximum load. As the concentrated load is applied, load is shared with the stiffeners. The more concentric the stiffeners are, the less local deformations develop in the column specimen due to the concentrated load effect.

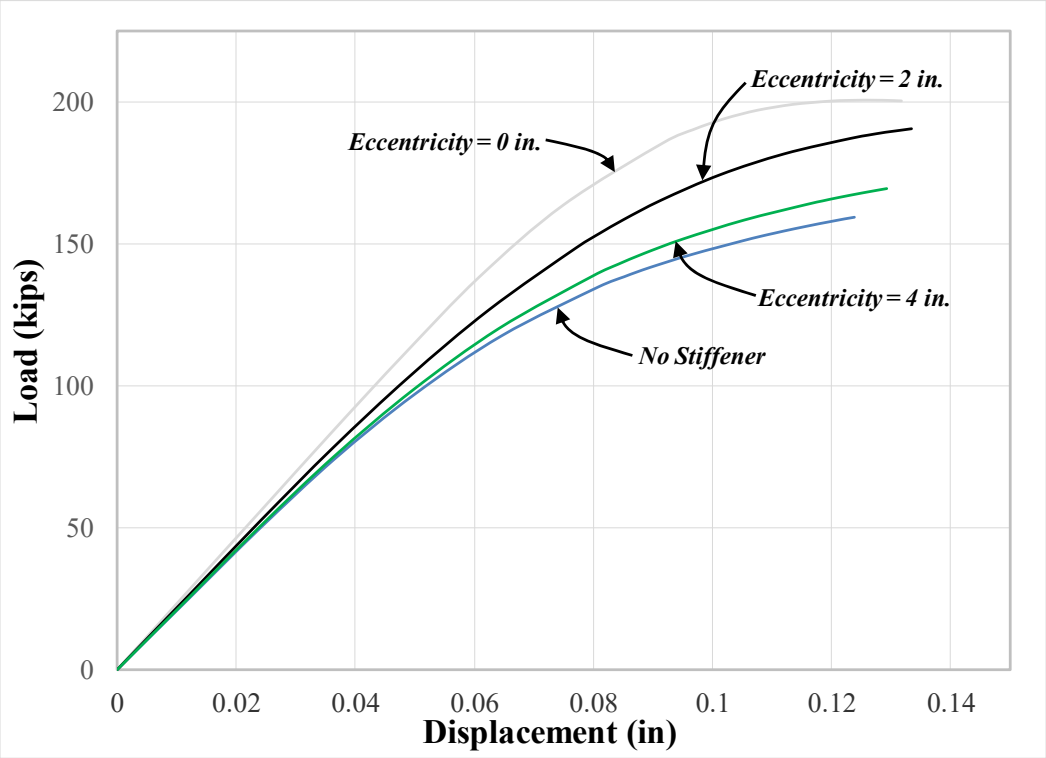

Figure 6.7-16: Load-displacement results of W14X68-ST-1/4 specimens

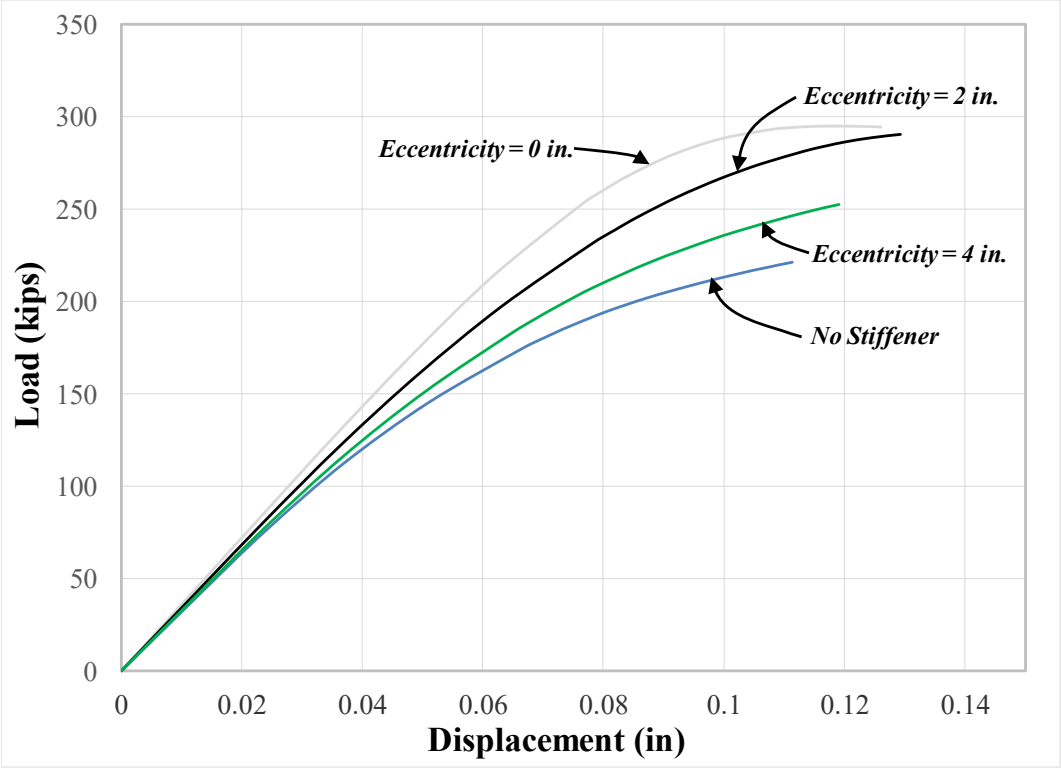

Figure 6.7-17: Load-displacement results of W14X120-ST-1/4 specimens

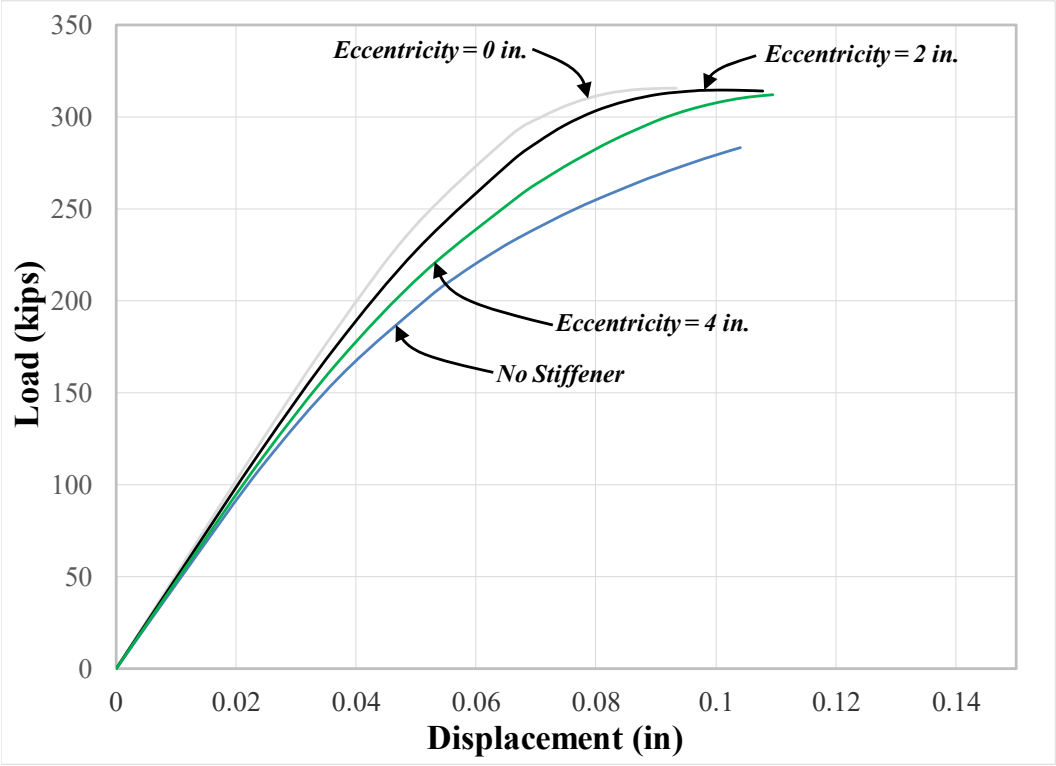

Figure 6.7-18: Load-displacement results of W14X176-ST-1/4 specimens

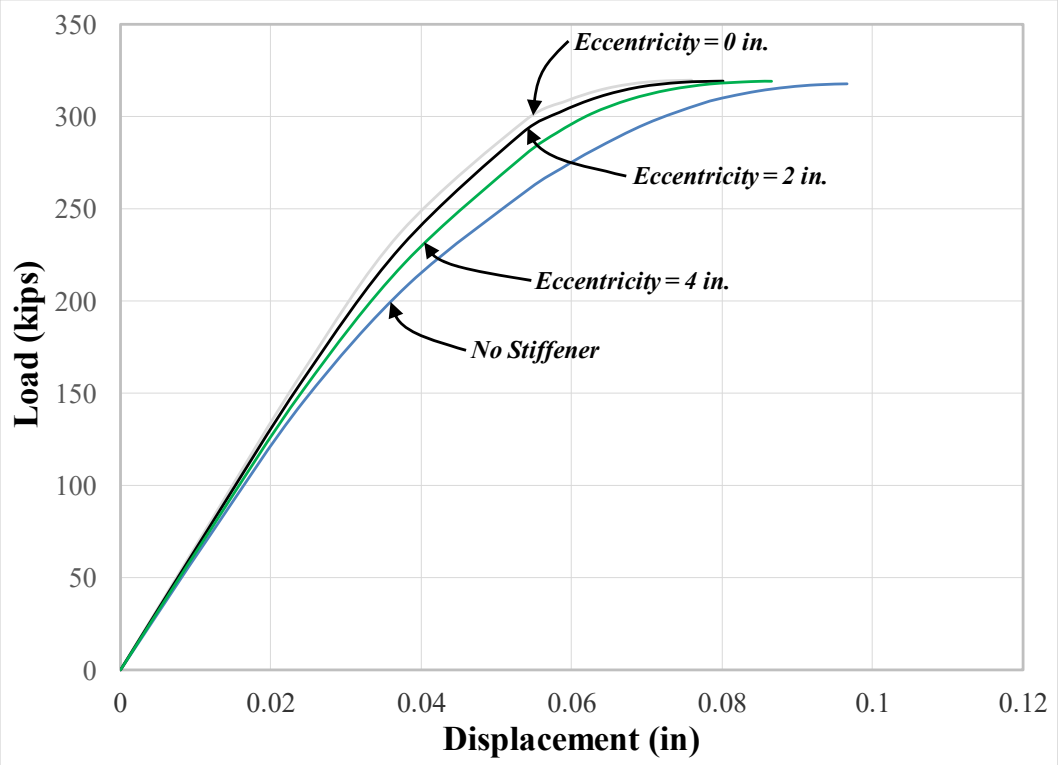

Figure 6.7-19: Load-displacement results of W14X233-ST-1/4 specimens

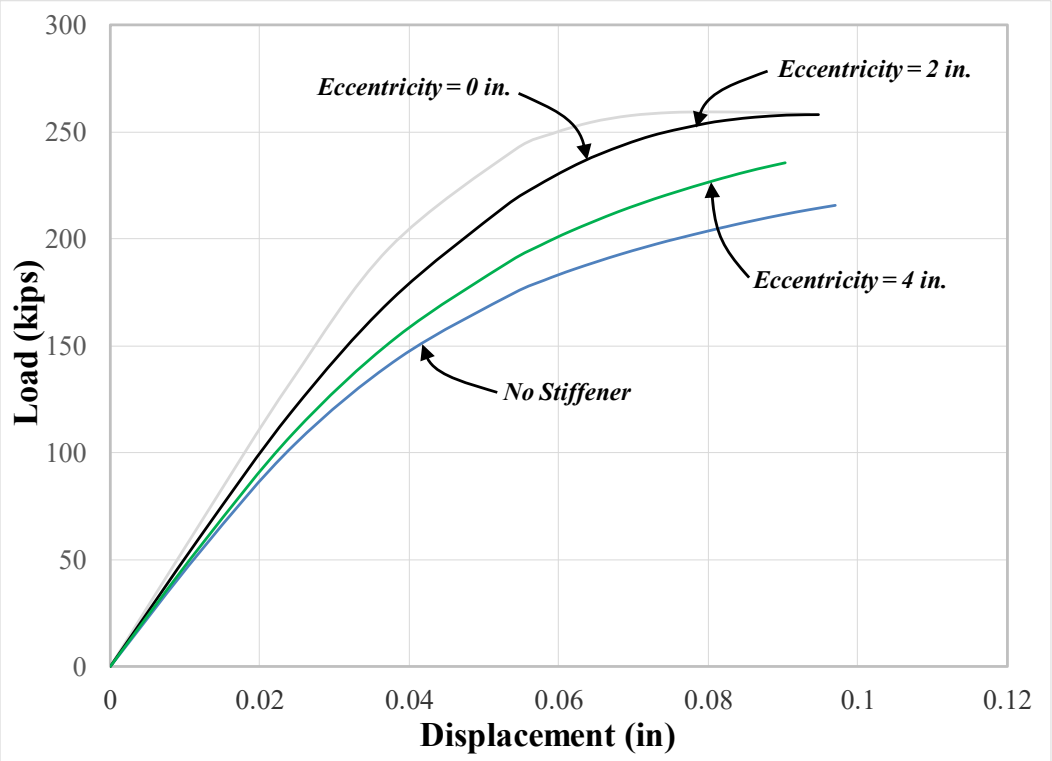

Figure 6.7-20: Load-displacement results of W24X131-ST-1/4 specimens

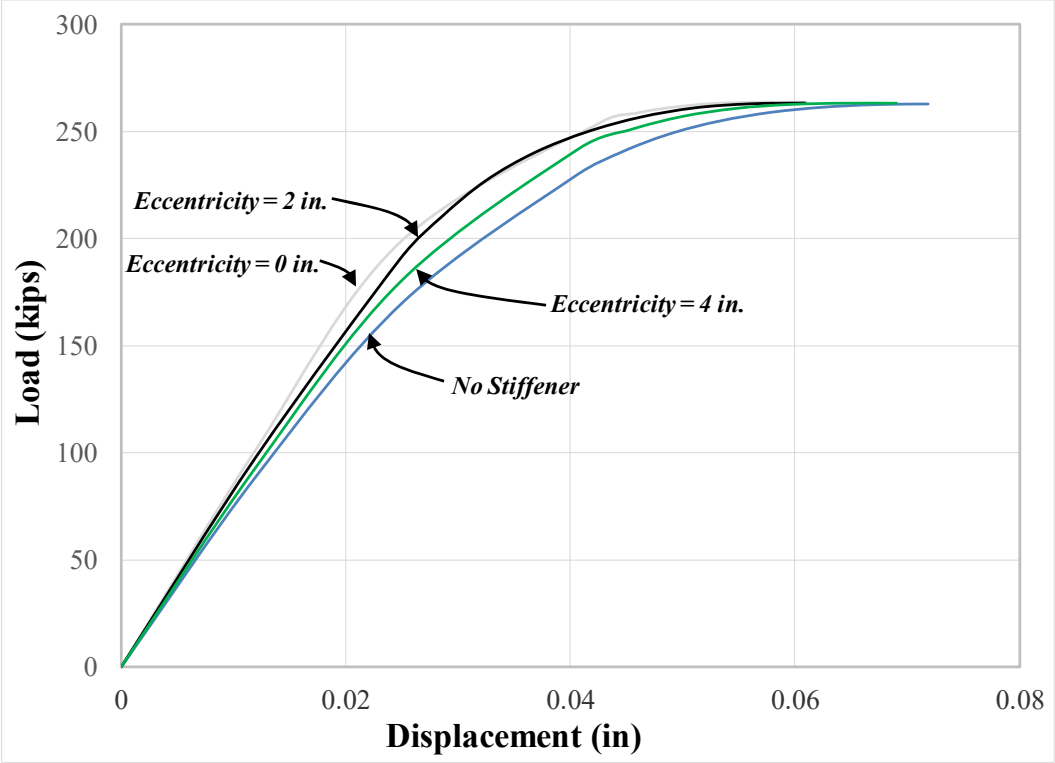

Figure 6.7-21: Load-displacement results of W24X229-ST-1/4 specimens

Figures 6.7-22 to 6.7-27 show the load-displacement results for all analytical column specimens subjected to single tension and modeled with 9/16 in. welds from the 1 1/2 in. loading plate to the top flange of the column specimen. Similar to the results with 1/4 in. welds, there are noticeable changes in elastic stiffness when comparing the results of different stiffener eccentricity conditions within a test group.

In contrast to results with 1/4 in. welds, the maximum loads for all column specimens significantly increased. In addition, there is more of a separation between the maximum loads for specimens within test group except for the largest column specimen sizes of W14X233 and W24X229. Finally, in comparison to the results with 1/4 in. welds, all column specimens were able to reach a higher overall displacement prior to weld failure.

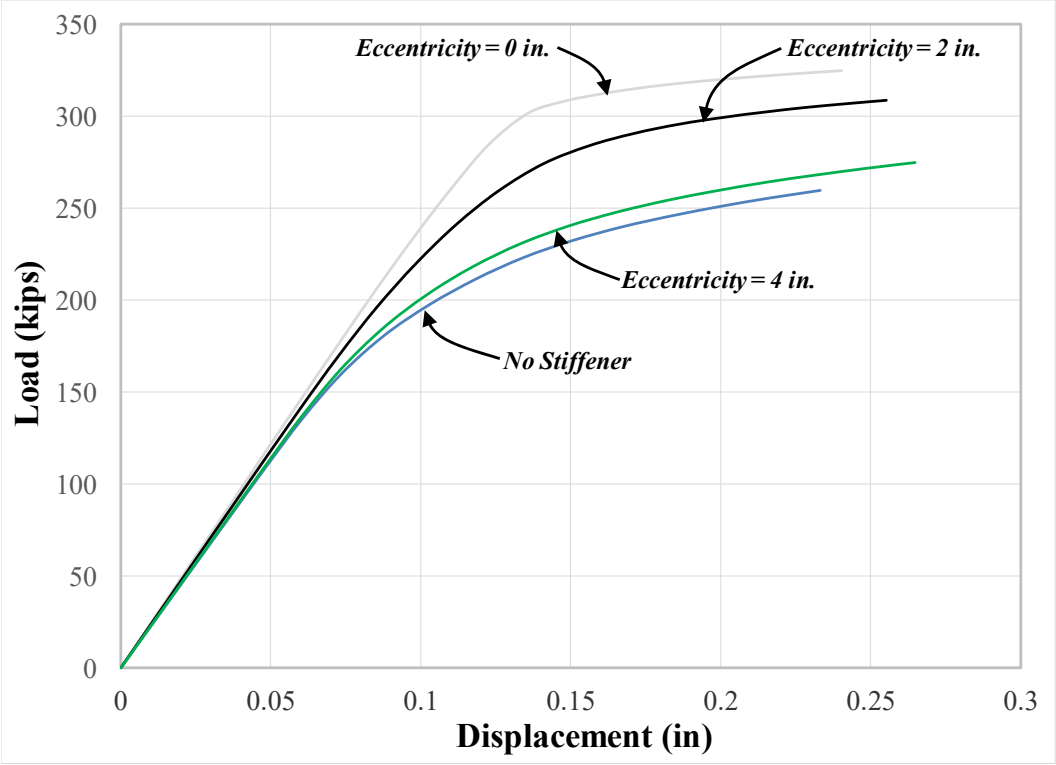

Figure 6.7-22: Load-displacement results of W14X68-ST-9/16 specimens

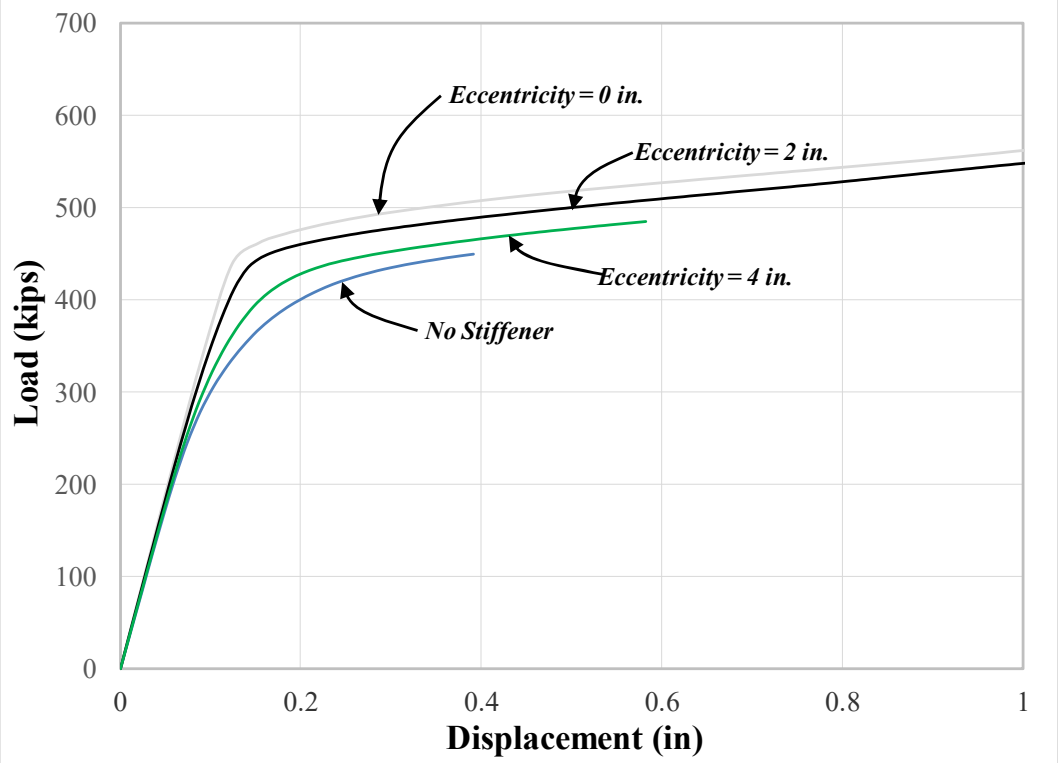

Figure 6.7-23: Load-displacement results of W14X120-ST-9/16 specimens

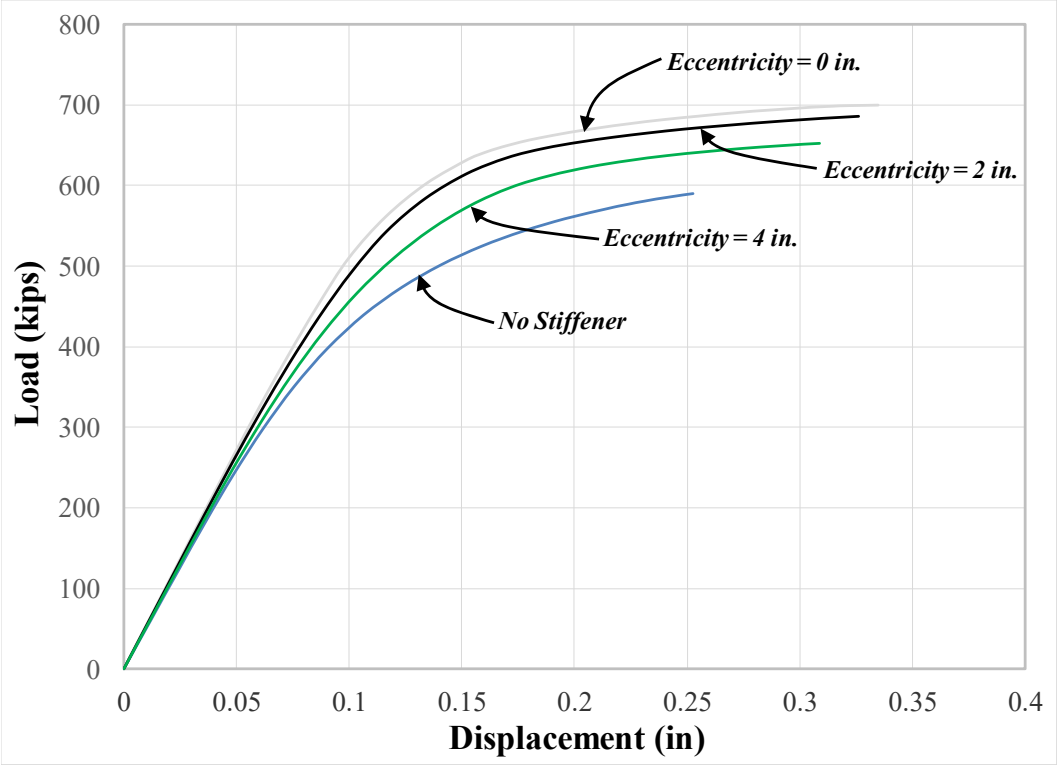

Figure 6.7-24: Load-displacement results of W14X176-ST-9/16 specimens

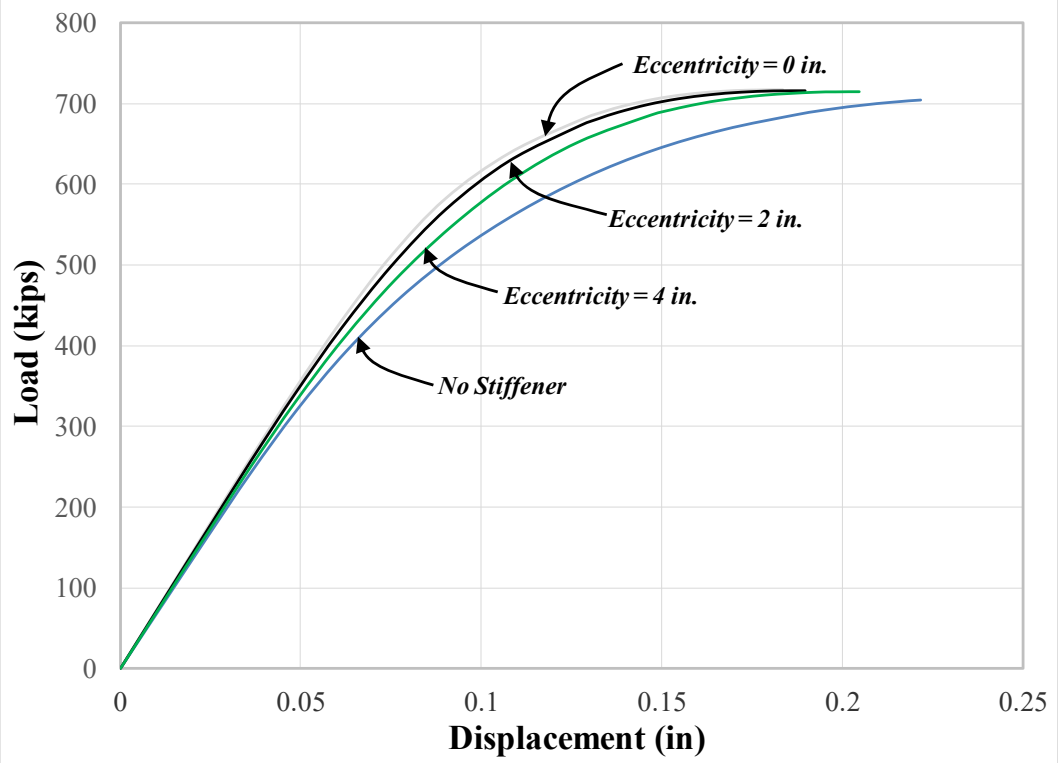

Figure 6.7-25: Load-displacement results of W14X233-ST-9/16 specimens

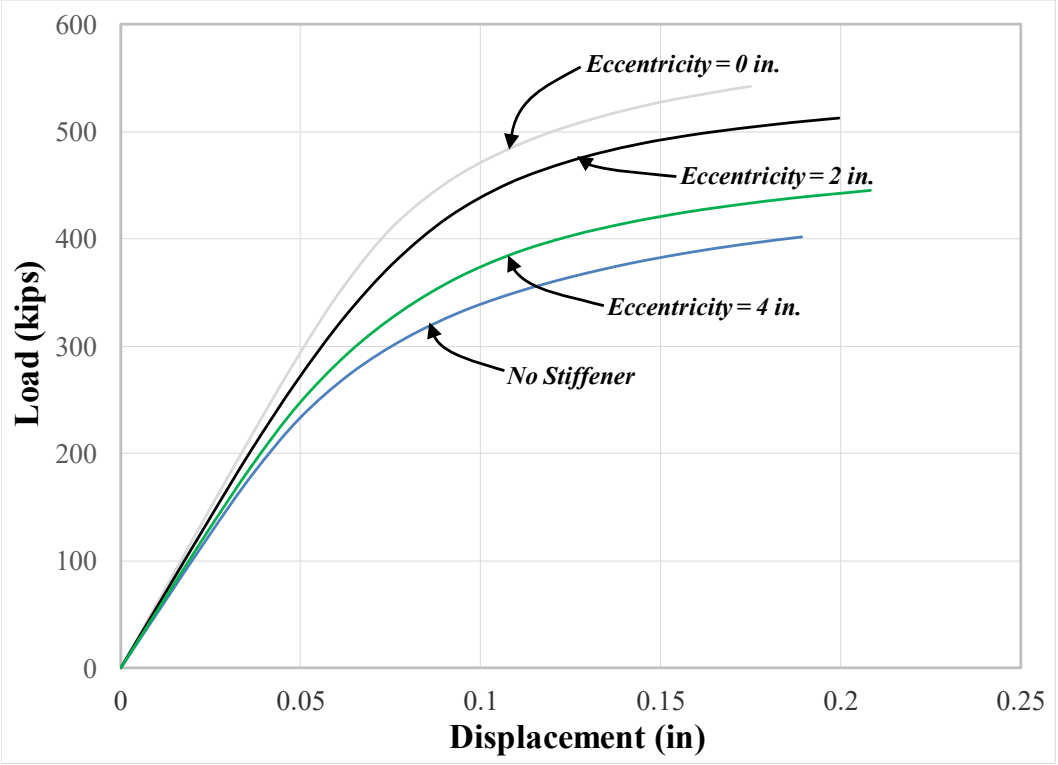

Figure 6.7-26: Load-displacement results of W24X131-ST-9/16 specimens

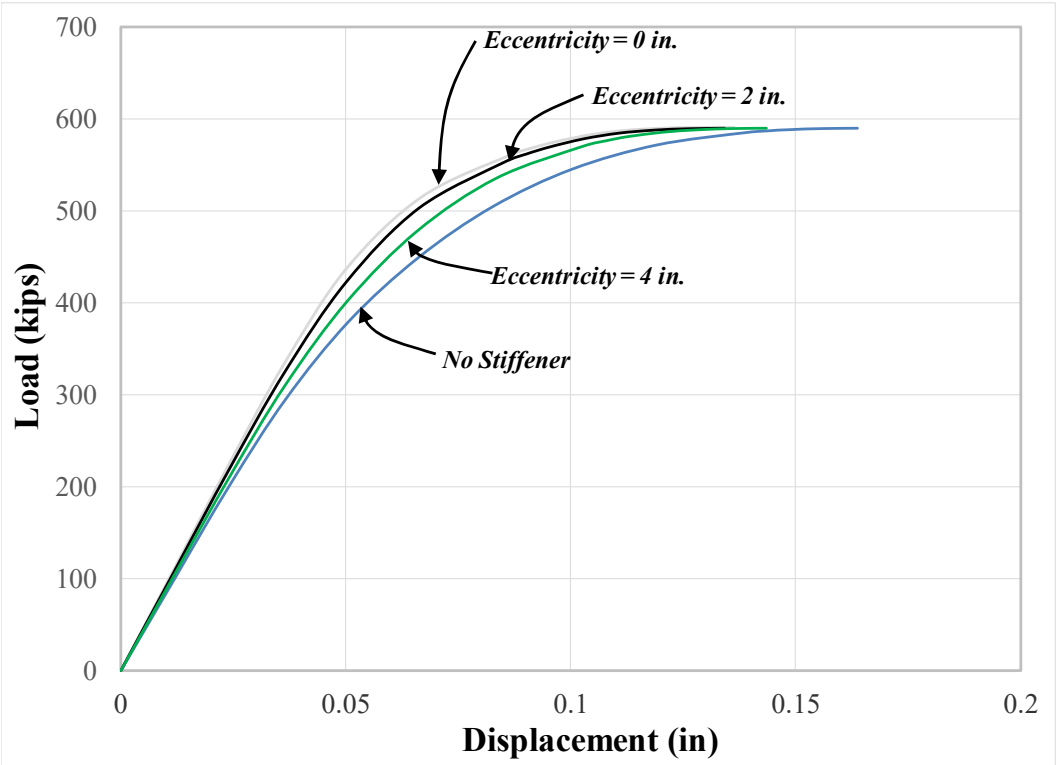

Figure 6.7-27: Load-displacement results of W24X229-ST-9/16 specimens

Figure 6.7-23 shows the four W14X120 column specimens modeled with 9/16 in. welds. In the models with concentric stiffeners and stiffeners at an eccentricity of 2 in., the weld size and stiffener conditions are "sufficient" as the column specimen is able to exhibit significant flexural and shear deformations prior to failure. Figure 6.7-28 shows the Von Mises stress distribution in the column specimen modeled with concentric stiffeners and at the assumed failure load. The deformed shape is scaled to 5X. The contours are scaled to the yield stress of 50 ksi. As shown in Figure 6.7-28, a significant portion of column section has yielded. The maximum load was found to correspond to an internal moment less than the plastic moment capacity for the column specimen, M_p, of 883 k-ft. Therefore, failure occurs prior to reaching this plastic limit. The maximum load better compared to the load required to reach the shear capacity, computed theoretically as 514 kips (theoretical shear capacity = 257 kips, multiply by 2 for applied load) and therefore, the stiffeners allowed failure to occur in shear as shown by the high stresses in the web in Figure 6.7-28.

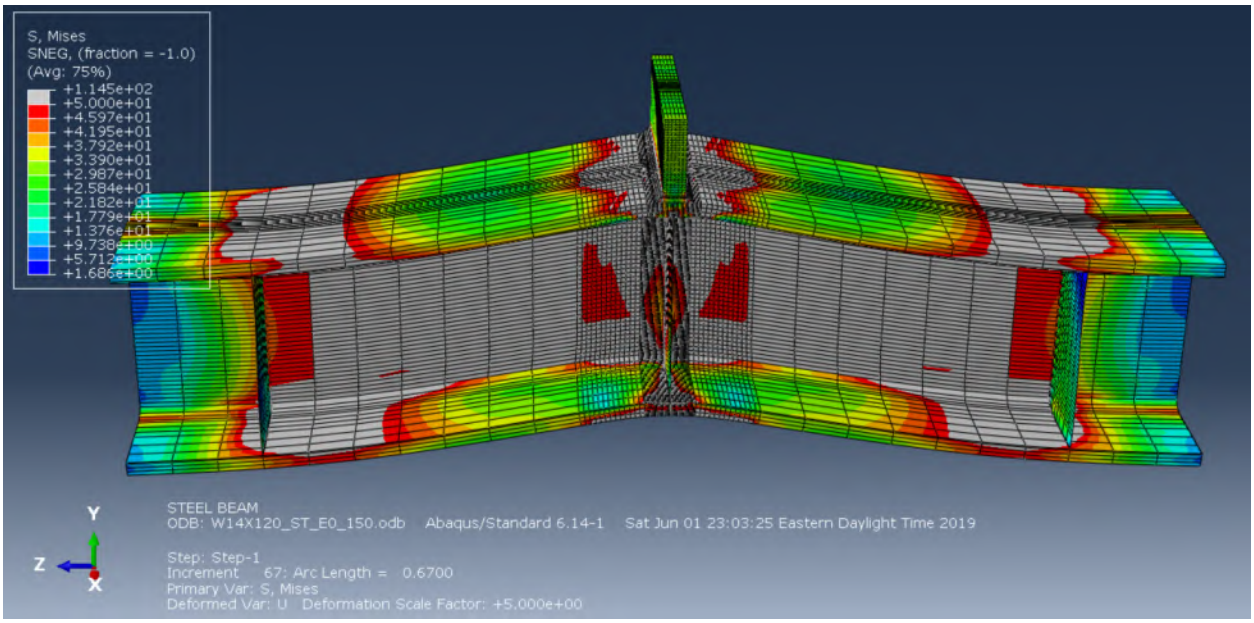

Figure 6.7-28: Stress distribution in W14X120 column specimen with 9/16 in. welds and concentric stiffeners

Figures 6.7-29 to Figure 6.7-34 show the load-displacement results for all analytical column specimens subjected to single tension and modeled with 7/8 in. welds from the 2 1/4 in. loading plate to the top flange of the column specimen. In comparison to the equivalent models with 9/16 in. welds, all failure loads increased as expected. There are clear trends between the stiffener condition and the maximum load and elastic stiffness. As stiffeners are added and become more concentric,

the maximum load always increased. As noted on Figures 6.7-29 to 6.7-31, in some cases, the method used to predict weld failure as described in Section 6.7-2 never occurred. Instead, the column specimens reached significant inelastic deformations and shear and flexural stresses. The weld size and stiffener condition were "sufficient" in allowing the column specimens to achieve this.

Figure 6.7-33 indicates that the W24X131 column specimen was the most influenced by the stiffener condition when 7/8 in. welds were modeled. The maximum load required to reach the theoretical plastic moment capacity was computed as 1233 kips and the maximum load required to reach the theoretical shear capacity was computed as 889 kips. Therefore, the column specimens reached a capacity governed by the concentrated load effect combined with uneven weld stresses. The results for the W14X233 and W24X229 column specimens show that the failure loads are still approximately equal regardless of the stiffener condition. Therefore, the maximum load is still governed by limitations in the weld capacity.

An observation of all finite element models and load-displacement results reveals there are many factors influencing the relationships between stiffener eccentricity and the maximum load obtained. However, as discussed, there are more distinct trends in the elastic stiffness. Therefore, recommendations and analysis will initially be performed based on elastic stiffness and checked and evaluated using changes in the assumed failure loads.

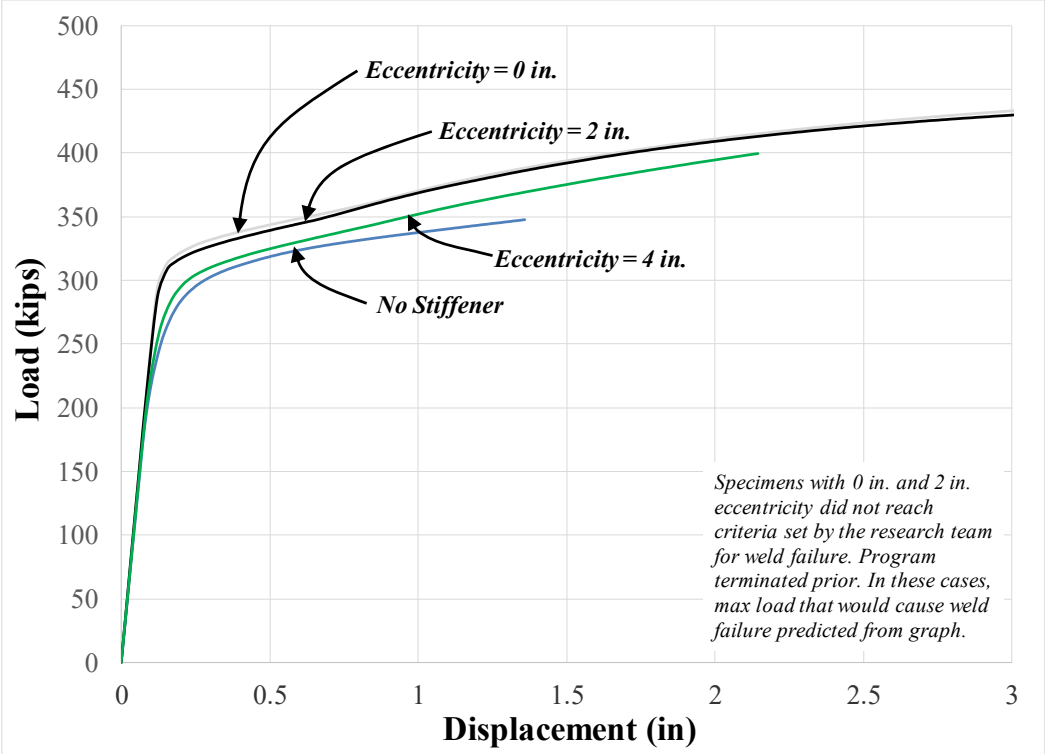

Figure 6.7-29: Load-displacement results of W14X68-ST-7/8 specimens

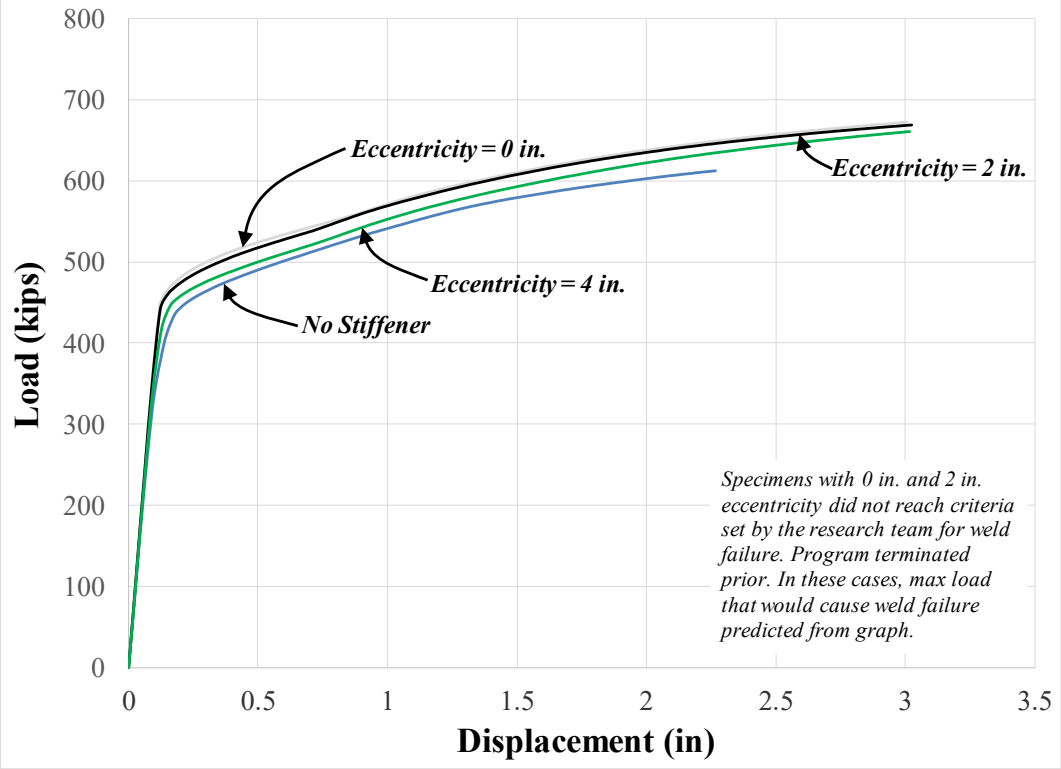

Figure 6.7-30: Load-displacement results of W14X120-ST-7/8 specimens

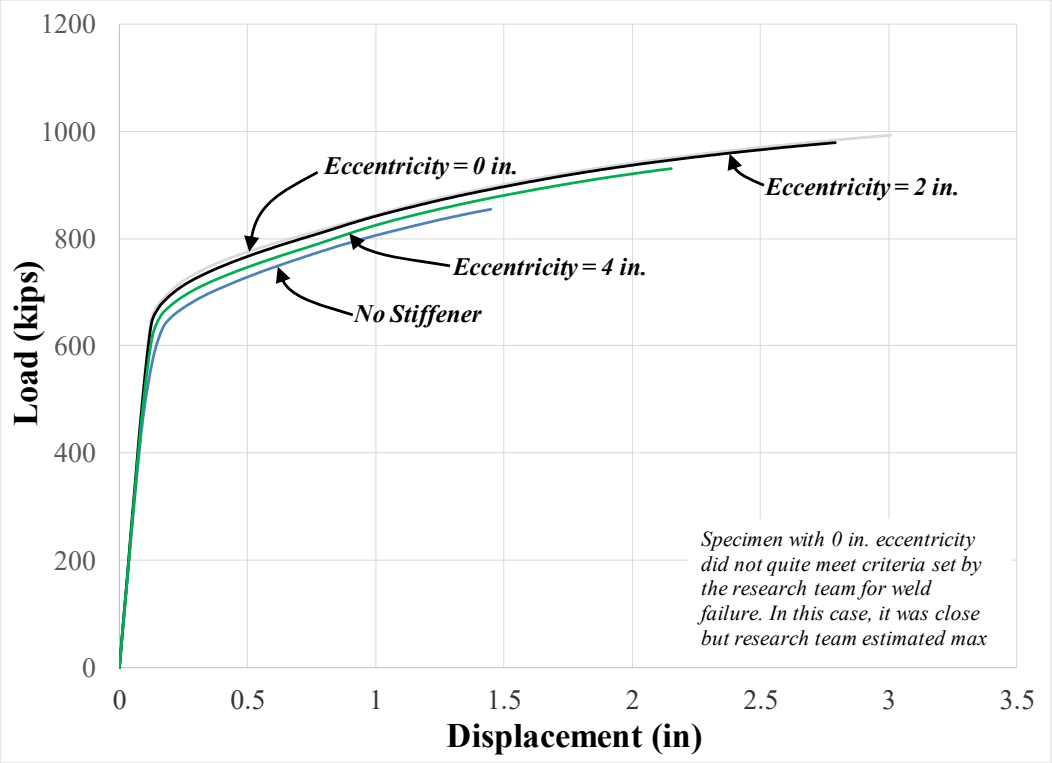

Figure 6.7-31: Load-displacement results of W14X176-ST-7/8 specimens

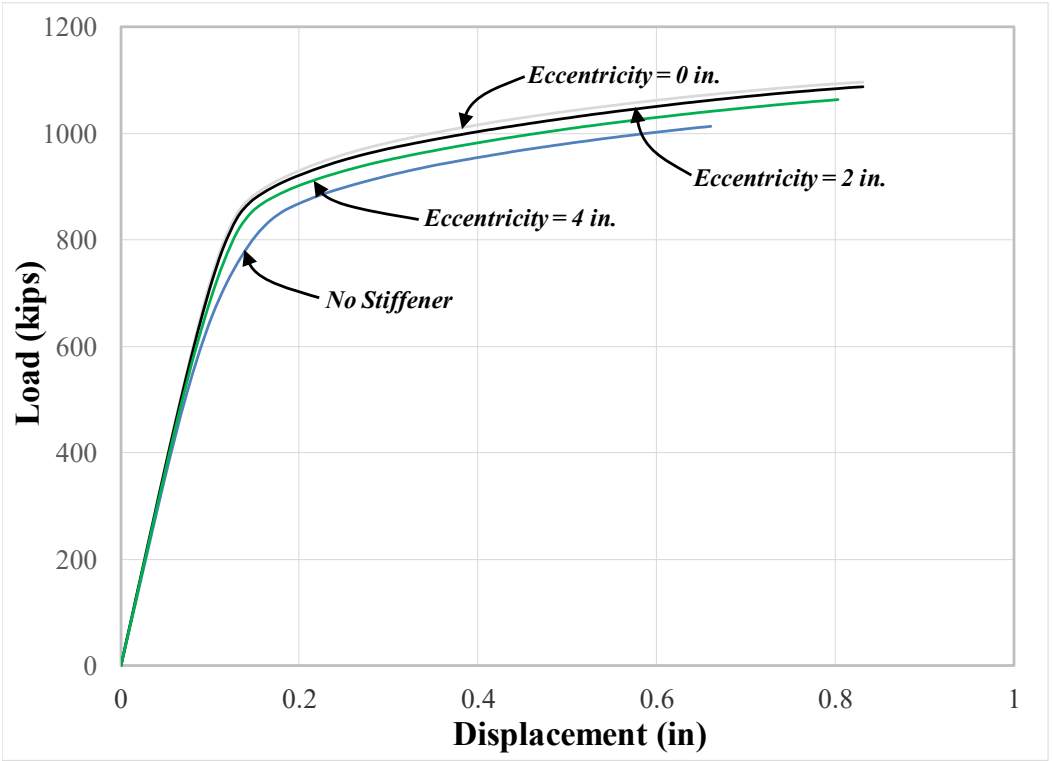

Figure 6.7-32: Load-displacement results of W14X233-ST-7/8 specimens

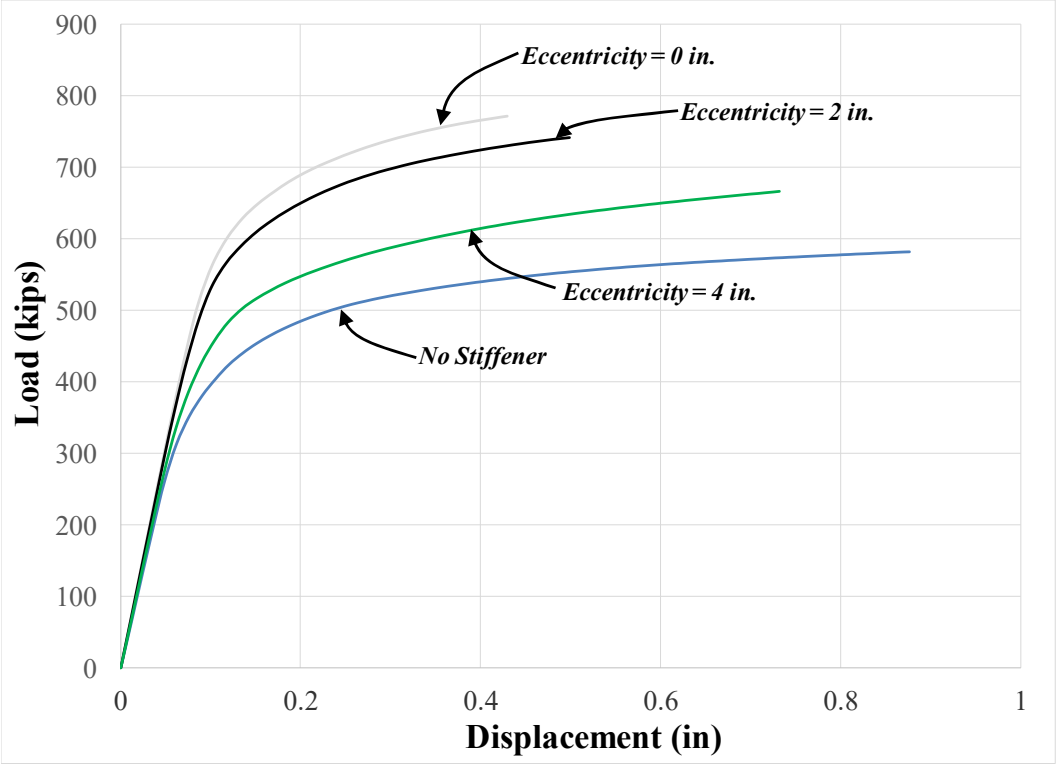

Figure 6.7-33: Load-displacement results of W24X131-ST-7/8 specimens

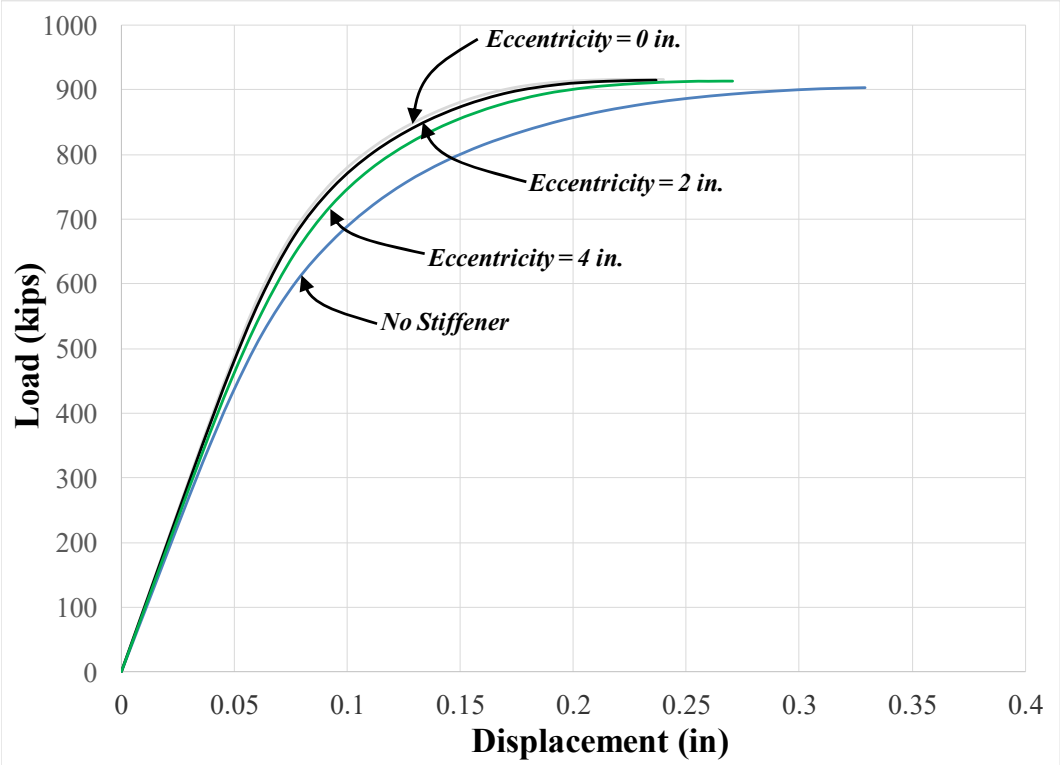

Figure 6.7-34: Load-displacement results of W24X229-ST-7/8 specimens

6.7.5 Primary Analytical Results

Several analytical results are presented in this section in table format. The failure loads are compared to a number of potential theoretical capacities in this section and the following section. The theoretical capacities are summarized in Table 6.7-2 and are described as follows:

- *WC* - theoretical weld capacity of the fillet welds from the loading plate to the column section flange, which is discussed more in the following paragraph.
- *Cap from M_p* - the maximum load that would be obtained assuming that the theoretical plastic moment governed and equal to Equation 6-1.

  $$Cap\ from\ M_p = (F_y * Z_x / 12) * 4 / L \quad (6\text{-}1)$$

  Where: F_y = yield stress, Z_x = plastic section modulus, and L = unsupported length
- *Cap from V_n* - the maximum load that would be obtained assuming that the theoretical shear yielding capacity governed and equal to Equation 6-2.

  $$Cap\ from\ V_n = 0.6 * F_y * d * t_w * 2 \quad (6\text{-}2)$$

  Where: F_y = yield stress, d = total depth of section, and t_w = web thickness
- *FB* - flange bending capacity from Equation 2-14 (see Appendix D).
- *WLY* - web local yielding capacity from Equation 2-3 (see Appendix D). The bearing length, l_b, is assumed equal to the loading plate thickness.

Table 6.7-2 shows the theoretical weld capacity (WC) and was initially calculated using Section J2 of the AISC specification (AISC, 2016) per Equation 6-3. Some adjustments to Equation 6-3 were made for the analytical column specimens as discussed in the following paragraph.

$$R_n = 0.707\ x\ 0.6\ x\ 1.5\ x\ 2\ x\ b_f\ x\ w\ x\ F_{exx} \quad (6\text{-}3)$$

Where:

0.707 = factor to account for failure across throat of fillet weld

0.6 = factor to account for failure of fillet weld in shear

1.5 = factor to account for loading transverse with respect to longitudinal axis of weld

2 = accounts for two welds

b_f = assumed length of weld across column specimen flange

w = weld thickness

F_{exx} = filler metal classification strength (AISC, 2016) assumed 82.4 ksi as discussed in Section 5.4.1 and used for all finite element models

For the analytical results, the weld capacity calculated per Equation 6-3 was always higher than the maximum load obtained in the models. Therefore, a modified weld capacity was calibrated for the analytical models and used in Table 6.7-2 for *WC*. Table 6.7-3, discussed later, shows that the maximum loads for all four analytical models of W24X229 column specimens subjected to single tension and modeled with 1/4 in. welds were very similar regardless of the stiffener condition. It is assumed that the column size and resistance to flange bending is stiff relative to the weld size and uniform stresses are achieved in the weld when failure occurs. The theoretical weld capacity using Equation 6-3 was computed as 343.3 kips. However, the maximum load for the analytical model of the W24X229 column specimens with concentric stiffeners was 263.6 kips. This was considered the stiffest condition that would generate a uniform weld stress. Reasons for the discrepancy were not studied in detail. However, all theoretical capacities computed per Equation 6-3 were multiplied by 0.77 (263.6/343.3) to calculate a modified weld capacity. For all column specimens with concentric stiffeners, the resulting modified weld strengths compared well to the capacities of the analytical models and therefore, the modification seemed appropriate for these studies.

A quick observation of the numbers in Table 6.7-2 reveals that the capacity based on M_p never governs over the capacity from shear using an unbraced length of 5 ft. Therefore, when significant deformations develop in the column specimens, it will be assumed that shear yielding governs over yielding from flexure but all failure mechanisms are partially contributing to the overall stress state.

Table 6.7-2: Various theoretical load capacities for the column specimens

Column Size	Plate t (in)	Weld (in)	WC (k)	Cap. From M_p (k)	Cap. From V_n (k)	FB (k)	WLY (k)
W24X131	3/4	1/4	260	1233	889	288	244
W24X229	3/4	1/4	264	2250	1498	935	571
W14X68	3/4	1/4	201	383	349	162	151
W14X120	3/4	1/4	296	707	513	276	249
W14X176	3/4	1/4	316	1067	757	536	427
W14X233	3/4	1/4	320	1453	1027	924	508
W24X131	1 1/2	9/16	584	1233	889	288	266
W24X229	1 1/2	9/16	593	2250	1498	935	607
W14X68	1 1/2	9/16	453	383	349	162	167
W14X120	1 1/2	9/16	665	707	513	276	271
W14X176	1 1/2	9/16	711	1067	757	536	459
W14X233	1 1/2	9/16	720	1453	1027	924	548
W24X131	2 1/4	7/8	908	1233	889	288	289
W24X229	2 1/4	7/8	923	2250	1498	935	643
W14X68	2 1/4	7/8	704	383	349	162	183
W14X120	2 1/4	7/8	1035	707	513	276	294
W14X176	2 1/4	7/8	1106	1067	757	536	488
W14X233	2 1/4	7/8	1120	1453	1027	924	589

The primary analytical results for column specimens subjected to single tension and modeled with 1/4 in. welds are shown in Table 6.7-3. The primary analytical results with 9/16 in. welds are shown in Table 6.7-4 and the primary results with 7/8 in. welds are shown in Table 6.7-5. In the tables, the theoretical weld capacity (*WC*) is shown with the results. The tables list all the primary results, which includes the failure load (Capacity) assumed for each analysis. For all cases with stiffeners, an analytical "Effective Stiffener Capacity" is listed which represents the difference between the maximum load obtained for that analysis and the result of the corresponding column specimen without stiffeners. The effective stiffener capacities of column specimens with eccentric stiffeners are shown as a percentage of the effective stiffener capacity of the corresponding analysis with concentric stiffeners. This is shown in the tables under the first column labeled "% Conc. Stiffener".

For reasons described in Sections 6.7-2 and 6.7-3, similar comparisons are performed with the elastic stiffness. The elastic stiffness is shown under the column labeled "Stiffness" and was computed as the change in load divided by the change in total displacement during the elastic portion

of the load-displacement relationship. The column "Eff. Stiffness" represents the effective elastic stiffness, which is the change in stiffness when stiffeners are used in comparison to the corresponding model without stiffeners. Although several effects influence the total displacement that occurs at the top of the loading plate, this parameter provides some representation of the amount of load that is transferred into the stiffeners and especially provides some indication of the change in load transferred into the stiffeners when eccentric stiffeners are modeled. The effective stiffener stiffness of column specimens with eccentric stiffeners are shown as a percentage of the effective stiffener stiffness of the corresponding model with concentric stiffeners. This is shown in the tables under the second column labeled "% Conc. Stiffener".

Table 6.7-3: Primary results of ST specimens modeled with 1/4 in. welds

Column Size	Stiff. Cond	Mod WC (k)	Capacity (k)	Eff. Stiff. Cap. (k)	% Conc. Stiffener	Stiffness (k/in)	Eff. Stiffness. (k/in)	% Conc. Stiffener
W24X131	NA	259.6	215.6	-	-	4213	-	-
W24X131	E0	259.6	258.2	42.7	-	5511	1298	-
W24X131	E2	259.6	257.9	42.3	99.1	4904	692	53.3
W24X131	E4	259.6	235.4	19.9	46.5	4447	235	18.1
W24X229	NA	263.6	263.0	-	-	6801	-	-
W24X229	E0	263.6	263.5	0.5	-	7987	1186	-
W24X229	E2	263.6	263.2	0.2	29.8	7663	862	72.7
W24X229	E4	263.6	263.1	0.1	22.1	7227	426	35.9
W14X68	NA	201.2	159.4	-	-	2078	-	-
W14X68	E0	201.2	200.4	40.9	-	2322	244	-
W14X68	E2	201.2	190.6	31.1	76.0	2180	102	42.0
W14X68	E4	201.2	169.4	10.0	24.4	2101	23	9.6
W14X120	NA	295.8	221.3	-	-	3171	-	-
W14X120	E0	295.8	294.7	73.4	-	3608	437	-
W14X120	E2	295.8	290.6	69.3	94.4	3411	241	55.0
W14X120	E4	295.8	252.6	31.3	42.7	3253	82	18.8
W14X176	NA	315.9	283.5	-	-	4529	-	-
W14X176	E0	315.9	315.5	32.0	-	5109	579	-
W14X176	E2	315.9	314.3	30.8	96.4	4916	387	66.7
W14X176	E4	315.9	312.1	28.6	89.5	4702	173	29.8
W14X233	NA	319.9	317.9	-	-	5979	-	-
W14X233	E0	319.9	319.6	1.7	-	6661	682	-
W14X233	E2	319.9	319.3	1.5	87.1	6485	506	74.2
W14X233	E4	319.9	319.1	1.2	70.2	6244	265	38.9

Table 6.7-4: Primary results of ST specimens modeled with 9/16 in. welds

Column Size	Stiff. Cond	Mod WC (k)	Capacity (k)	Eff. Stiff. Cap. (k)	% Conc. Stiffener	Stiffness (k/in)	Eff. Stiffness. (k/in)	% Conc. Stiffener
W24X131	NA	584.0	402.3	-	-	5045	-	-
W24X131	E0	584.0	542.0	139.7	-	5984	939	-
W24X131	E2	584.0	512.8	110.5	79.1	5649	604	64.3
W24X131	E4	584.0	445.2	42.9	30.7	5266	221	23.5
W24X229	NA	593.0	589.7	-	-	8341	-	-
W24X229	E0	593.0	591.0	1.3	-	9345	1004	-
W24X229	E2	593.0	590.5	0.8	59.3	9106	765	76.2
W24X229	E4	593.0	590.4	0.7	50.3	8732	391	39.0
W14X68	NA	452.7	259.5	-	-	2261	-	-
W14X68	E0	452.7	324.7	65.2	-	2432	171	-
W14X68	E2	452.7	308.4	48.9	75.0	2364	102	59.9
W14X68	E4	452.7	275.0	15.5	23.7	2287	25	14.9
W14X120	NA	665.5	449.5	-	-	3497	-	-
W14X120	E0	665.5	621.0	171.5	-	3794	297	-
W14X120	E2	665.5	562.1	112.6	65.7	3702	205	68.9
W14X120	E4	665.5	485.2	35.7	20.8	3570	73	24.5
W14X176	NA	710.7	590.4	-	-	5053	-	-
W14X176	E0	710.7	699.5	109.1	-	5453	400	-
W14X176	E2	710.7	685.7	95.3	87.3	5346	293	73.2
W14X176	E4	710.7	652.3	61.8	56.7	5185	132	33.0
W14X233	NA	719.8	704.4	-	-	6754	-	-
W14X233	E0	719.8	716.7	12.3	-	7221	468	-
W14X233	E2	719.8	715.8	11.4	92.7	7118	364	77.9
W14X233	E4	719.8	714.8	10.4	84.9	6945	191	40.8

Table 6.7-5: Primary results of ST specimens modeled with 7/8 in. welds

Column Size	Stiff. Cond	Mod WC (k)	Capacity (k)	Eff. Stiff. Cap. (k)	% Conc. Stiffener	Stiffness (k/in)	Eff. Stiffness. (k/in)	% Conc. Stiffener
W24X131	NA	908.4	581.9	-	-	5470	-	-
W24X131	E0	908.4	772.2	190.3	-	6258	788	-
W24X131	E2	908.4	742.1	160.2	84.2	6125	655	83.2
W24X131	E4	908.4	666.2	84.3	44.3	5750	280	35.5
W24X229	NA	922.5	903.4	-	-	9038	-	-
W24X229	E0	922.5	916.0	12.6	-	9935	897	-
W24X229	E2	922.5	915.1	11.7	92.4	9804	766	85.4
W24X229	E4	922.5	913.2	9.8	77.3	9476	438	48.8
W14X68	NA	704.2	347.9	-	-	2389	-	-
W14X68	E0	704.2	436.0	88.1	-	2511	122	-
W14X68	E2	704.2	431.0	83.1	94.3	2502	113	92.7
W14X68	E4	704.2	399.5	51.6	58.6	2424	36	29.1
W14X120	NA	1035.2	612.9	-	-	3701	-	-
W14X120	E0	1035.2	678.0	65.1	-	3942	241	-
W14X120	E2	1035.2	674.0	61.1	93.9	3915	215	89.0
W14X120	E4	1035.2	661.1	48.2	74.0	3795	95	39.3
W14X176	NA	1105.6	855.0	-	-	5331	-	-
W14X176	E0	1105.6	994.0	139.0	-	5683	353	-
W14X176	E2	1105.6	978.6	123.6	89.0	5640	310	87.8
W14X176	E4	1105.6	930.0	75.0	54.0	5497	166	47.2
W14X233	NA	1119.7	1013.0	-	-	7193	-	-
W14X233	E0	1119.7	1095.6	82.6	-	7578	384	-
W14X233	E2	1119.7	1087.6	74.6	90.3	7531	338	87.9
W14X233	E4	1119.7	1063.9	50.9	61.7	7393	199	51.9

Primary observations from the data presented in Tables 6.7-3 to 6.7-5 are as follows:

- The weld size and loading plate thickness have a significant influence of the failure load results. The failure load always increased when all parameters remain constant and only the weld size and loading plate thickness changed.
- The failure load results when using 1/4 in. are often less than or close to the flange bending capacity and web local yielding capacity from Table 6.7-2. However, when 7/8 in. welds are modeled, the capacities for all column specimen sizes are significantly higher than the capacities calculated per these limit states. This observation demonstrates that the calculations for web local yielding and flange bending underestimate a "true" capacity since they can be well exceeded.

- However, weld failure is influenced by the effects of flange bending. If concentric stiffeners are used, flange bending is minimized and higher loads are obtained. For all weld sizes and all column specimen sizes, there was always at least some increase in load when concentric stiffeners were used. From the results, it appears that the weld capacity and the influence of flange bending should be analyzed simultaneously in practice.
- As discussed in Section 6.7-3, for a group of specimens of the same column size and weld thickness, the lowest failure load was always assumed in the specimen without stiffeners, the second lowest in the specimen with stiffeners at a 4 in. eccentricity, the third with stiffeners at a 2 in. eccentricity and the highest with concentric stiffeners.

Figure 6.7-35 provides a comparison between the failure loads and the maximum load corresponding to the theoretical shear capacity (shear capacity x 2) for column specimens with concentric stiffeners. This figure is used to demonstrate how the analyses meant to evaluate the concentrated load effects are influenced by other failure limit states. As the weld size becomes thicker, the results show that eventually the effects of shear and flexure govern the maximum load, particularly for W14 column sections.

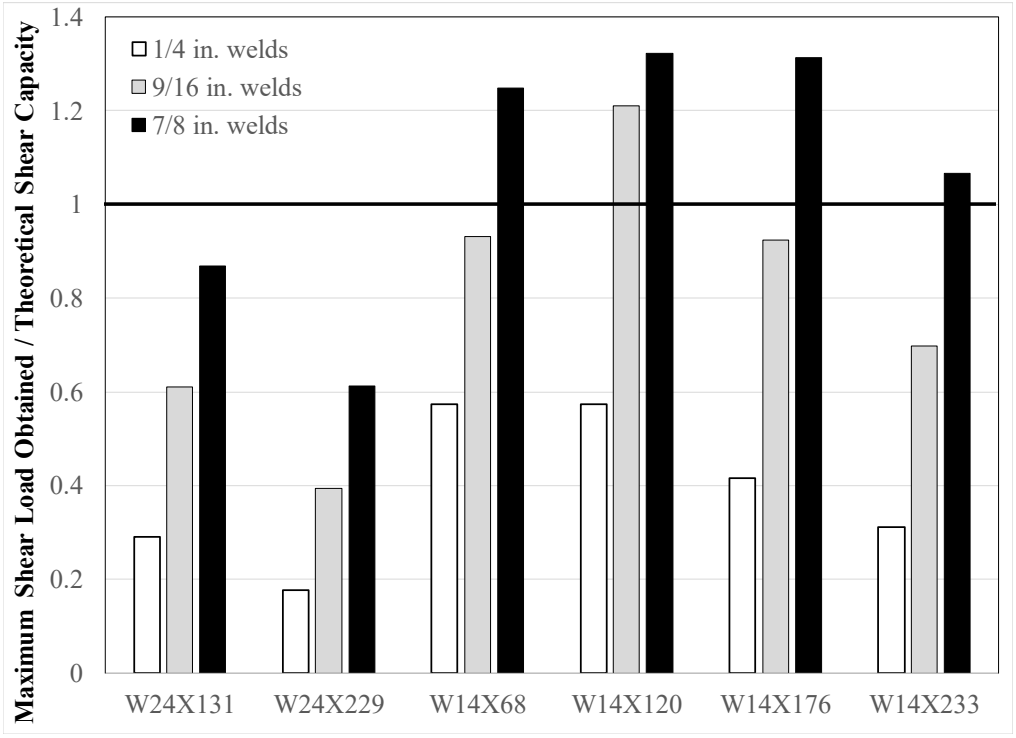

Figure 6.7-35: Ratios of failure loads vs. theoretical shear yielding capacity loads

The results in Tables 6.7-3 to 6.7-5 show that the change in elastic stiffness is valuable for evaluating the single tension test results since there are more consistent trends in the results as opposed to the failure load. For instance, for a W14X233 column specimen modeled with concentric stiffeners, the elastic stiffness when using 7/8 in. welds was 7578 k/in, which compares relatively well to the results of 7221 k/in and 6661 k/in when using 9/16 in. and 1/4 in. welds, respectively. The failure load when modeling with 7/8 in. welds was 1097 kips as opposed to 717 kips and 320 kips when using 9/16 in. welds and 1/4 in. welds, respectively. In addition, the results of "% of Conc. Stiffener" are much more sporadic when evaluating the failure load results as opposed to the elastic stiffness results. For instance, as column size gets larger, the "% Conc. Stiffener" result (for the elastic stiffness) always increases when using 1/4 in. welds and 9/16 in. welds for eccentricities of 2 in. and 4 in. These trends are not as consistent when modeling with 7/8 in. welds. However, when this weld size is used with 2 1/4 in. plates, one weld is located directly above the stiffeners when a 2 in. eccentricity is modeled. Trends in the results, with respect to an increase in "% Conc. Stiffener" results as column size gets larger, are similar to other weld sizes when the stiffener eccentricity is 4 in.

6.7.6 Influence of Column Dimensions on Effectiveness of Eccentric Stiffeners

Similar to the compression tests, the analytical research focuses on two eccentricities of 2 in. and 4 in. Recommendations for computing the effective stiffener capacity for eccentric stiffeners were provided with the single compression test results in Section 6.5.4. These recommendations are superseded by recommendations in Section 6.8. Currently, it is proposed to provide final recommendations for the practicing engineer that are valid for any type of loading condition. Therefore, the straight-line equations that are shown graphically with the results in Figures 6.5-18 and 6.5-19 will be compared to the elastic stiffness results of the single tension tests. To justify that the linear relationships can be used for single tension tests, the "% of concentric stiffener" results for the elastic stiffness from Tables 6.7-3 to 6.7-5 are shown graphically as curves for each column size/weld size combination in Figure 6.7-36. The result of the concentric stiffener case is used for the relationships as well, which is always equal to 100%. In summary, the curves in Figure 6.7-36 are hypothesized as appropriate relationships for the influence of eccentricity on effective stiffener capacities and for the various column sizes and weld thickness modeled. The individual curves are

not labeled to avoid clutter. Results with 1/4 in. welds are shown in black, results with 9/16 in. welds are dashed, and results with 7/8 in. welds are shown as light grey.

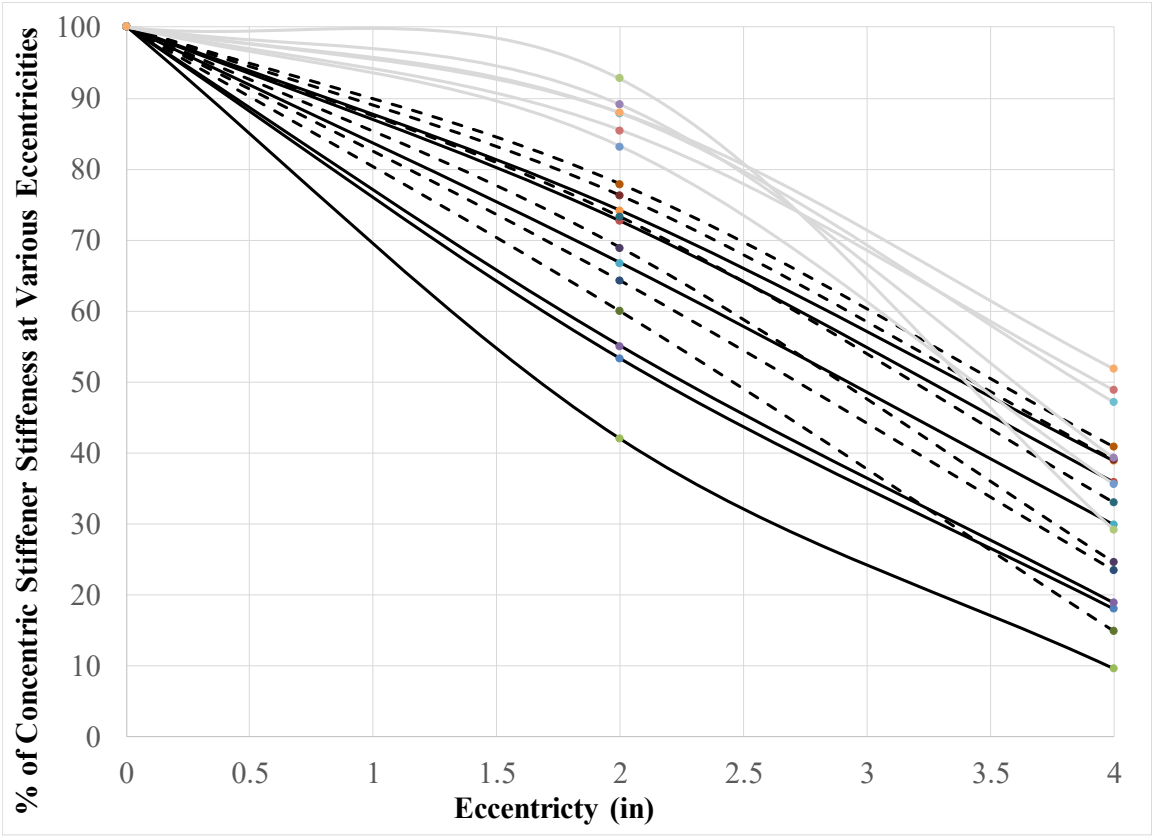

Figure 6.7-36: Influence of eccentricity on effective stiffener capacity for ST tests

If the curves presented in Figure 6.7-36 are straight lines, interpolation can be used to determine the effective stiffener capacity at any eccentricity. If the curves are concave down, the use of interpolation is conservative, which was the case whenever 7/8 in. welds were modeled. However, if the curves are concave up, interpolation is unconservative. The results in Figure 6.7-36 show that the use of interpolation is usually conservative particularly when using larger welds. The use of interpolation is sometimes unconservative if modeling with ¼ in. welds but if straight lines were plotted instead of the curves shown, the straight lines would almost fit directly on the curves for all cases that are concave up. Therefore, the use of interpolation or a straight line expression to account for eccentricity should be acceptable.

For concentrated tension loads, factors that influence the effective stiffener capacity at various eccentricities are hypothesized as the flange thickness (or '*k*' dimension) and the flange slenderness

($b_f / 2t_f$). Figure 6.7-37 shows the flange slenderness results vs. "% Concentric Stiffener Effective Stiffness" when stiffeners are modeled at an eccentricity of 2 in. Figure 6.7-38 shows the flange slenderness results vs. "% Concentric Stiffener Effective Stiffness" when stiffeners are modeled at an eccentricity of 4 in. Results when using a weld size of 1/4 in. are shown as circles, results when using a weld size of 9/16 in. are shown as triangles and results when using a weld size of 7/8 in. are shown as squares (consistent for Figures 6.7-37 to 6.7-42). In general, the results in Figures 6.7-37 and 6.7-38 indicate that as flange slenderness decreases, the percentage results increase. However, the trends are not clear and recommendations for design cannot be derived using the results. For instance, the flange slenderness of the W14X120 is higher than that of the W14X68. Yet, the percentage results of the W14X120 are significantly higher and therefore, stiffener eccentricity is not as detrimental. The results of the W14X233 column specimen and the results of the W24X229 column specimen are very similar even though the W14X233 is 21% more 'slender' than the W24X229. The flange thickness of the W14X233 and the W24X229 are almost identical. The results of the W14X120 column specimen are very similar to the results of the W24X131 column specimen and the flange thickness of these two column sizes are almost identical as well. Therefore, flange slenderness alone should not be used to predict the influence of eccentric stiffeners. The flange slenderness has some influence on the results but the flange thickness is the most influential parameter evaluated that influences the effectiveness of eccentric stiffeners, which was a conclusion drawn from the single compression test results as well.

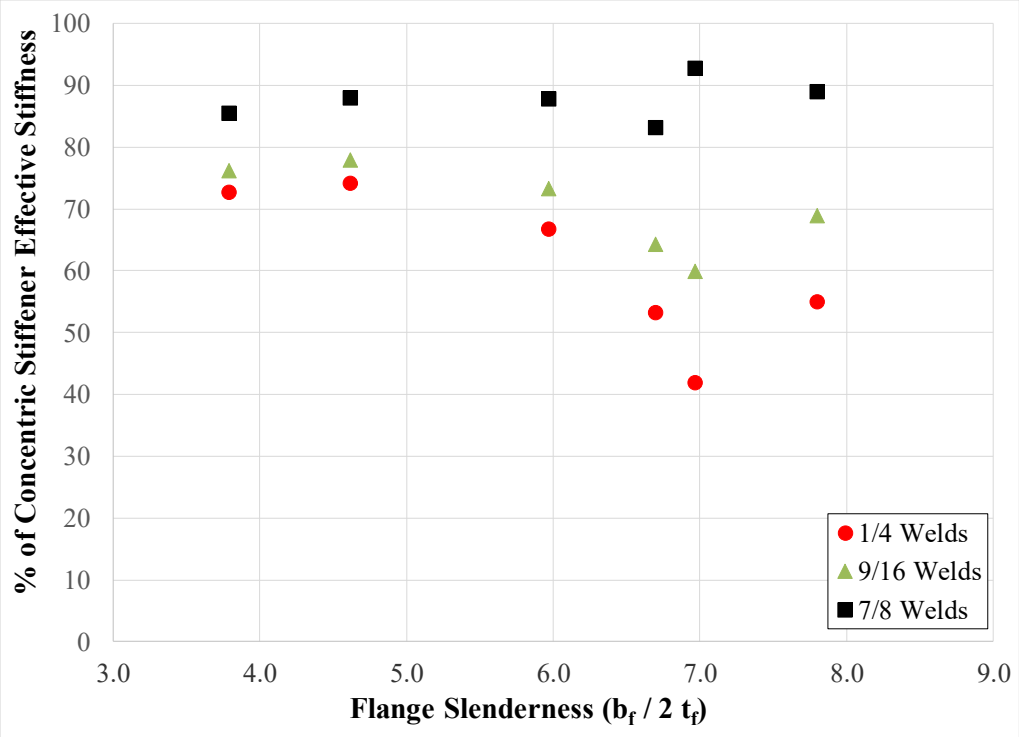

Figure 6.7-37: % of concentric stiffener stiffness vs. flange slenderness when modeling with a 2 in. eccentricity

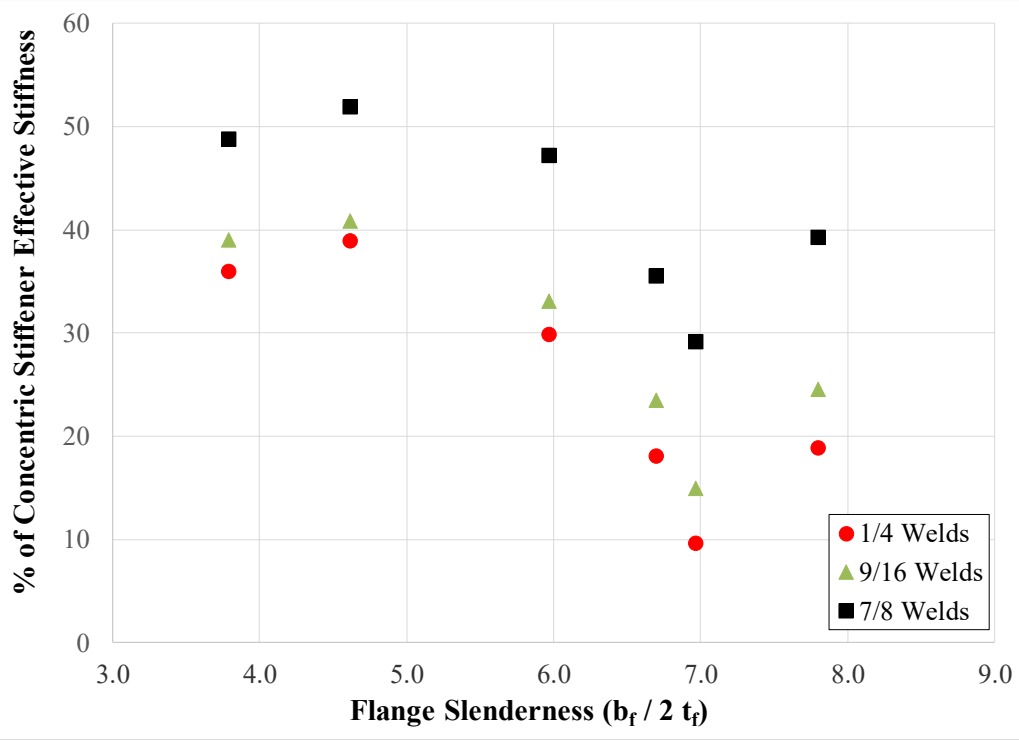

Figure 6.7-38: % of concentric stiffener stiffness vs. flange slenderness when modeling with a 4 in. eccentricity

Figure 6.7-39 shows relationships between the "% Concentric Stiffener Effective Stiffness" and flange thickness when stiffeners were modeled with an eccentricity of 2 in. When a weld size of 7/8 in. is used, the influence of flange thickness is inconclusive. It is alleged that due to the presence of the 2 1/4 in. loading plate, one weld is located directly above the stiffeners and therefore, load is transferred directly into the eccentric stiffener plate. However, for weld sizes of 1/4 in. and 9/16 in., as flange thickness increases, the percentage results increase as well. In Section 6.5-4 and from the results of single compression tests, straight-line equations were presented to establish a relationship between flange thickness and "% of concentric stiffener capacity" that could be used for design. The relationship for a 2 in. eccentricity is shown as Equation 6-4.

$$\% \text{ of concentric stiffener capacity} = 46.7t_f - 13.3 \quad (6\text{-}4)$$

The relationship of Equation 6-4 is plotted within Figure 6.7-39 as a straight line and in terms of "% of concentric stiffener stiffness". The results show that this equation and the relationship defined by it may be too conservative for single tension and a new relationship equation may be proposed that is less conservative. However, in the final recommendations presented for this research, it is beneficial to provide final recommendations that are valid for all loading scenarios.

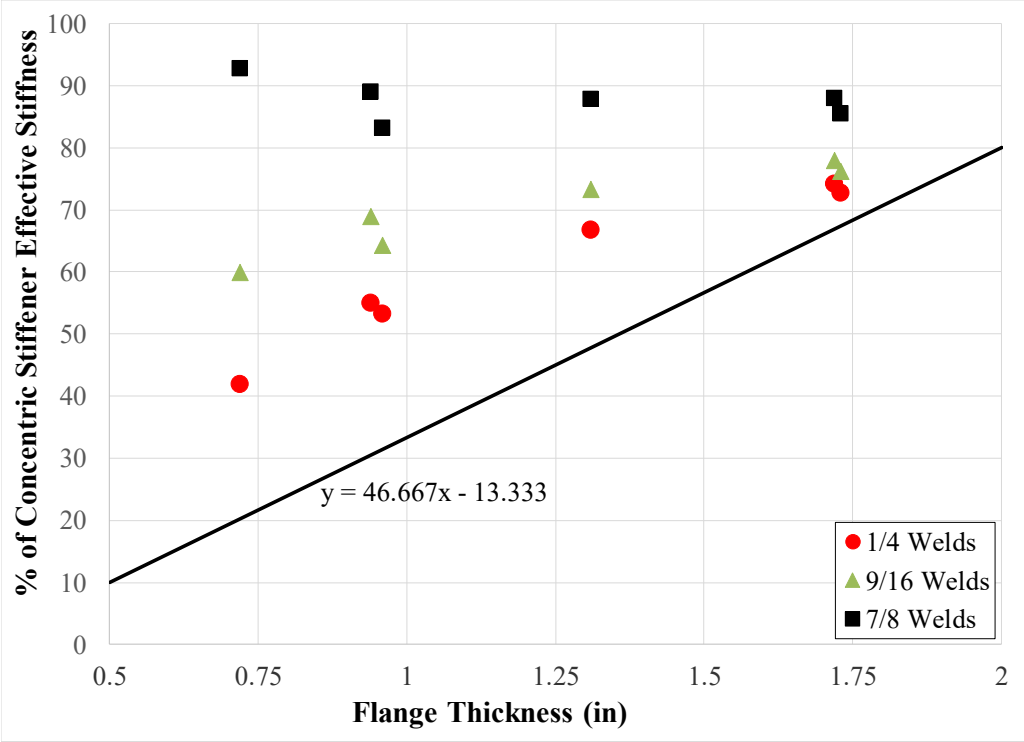

Figure 6.7-39: % of concentric stiffener stiffness vs. flange thickness with 2 in. eccentricity

Figure 6.7-40 shows relationships between the "% Concentric Stiffener Effective Stiffness" and flange thickness when stiffeners were modeled with an eccentricity of 4 in. Similar to the results obtained when the eccentricity is 2 in., the "percent" results increase with an increase in weld size and loading plate thickness. However, there are clearer trends in the influence of flange thickness and on the percent results. Equation 6-5 provides the original equation developed in Section 6.5-4 for the relationship between flange thickness and "% of concentric stiffener capacity" when the stiffener eccentricity is 4 in.

$$\% \text{ of concentric stiffener capacity} = 40.74t_f - 26.5 \quad (6\text{-}5)$$

The relationship of Equation 6-4 is plotted within Figure 6.7-40 as a straight line and in terms of "% of concentric stiffener stiffness". However, some of the percent results are below this line when larger column specimens were modeled with 1/4 in. and 9/16 in. welds. Therefore, a new relationship is suggested by Equation 6-6, which is conservative for almost all cases. Equation 6-6 is also shown in Figure 6.7-40 as a straight line and only one result falls just under this line. Dissimilar from Equation 6-5, Equation 6-6 is valid for a flange thickness of 0.5 in. and greater, which is consistent with the relationship established at an eccentricity of 2 in. per Equations 6-4.

$$\% \text{ of concentric stiffener capacity} = 30t_f - 15 \quad (6\text{-}5)$$

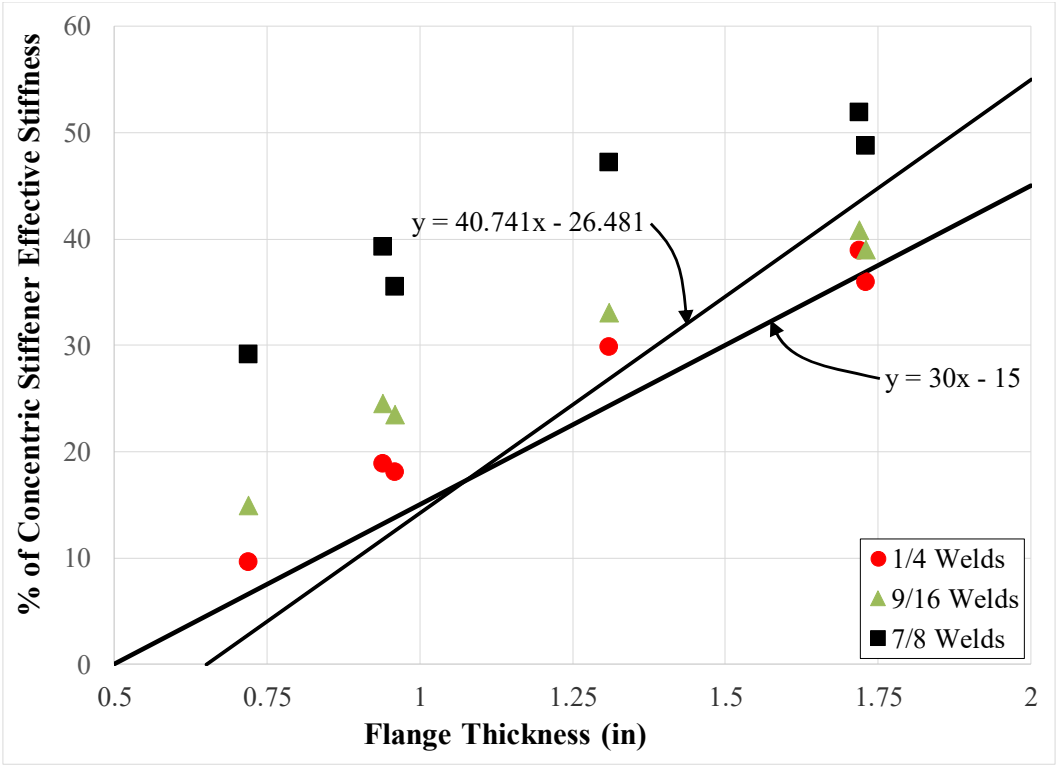

Figure 6.7-40: % of concentric stiffener stiffness vs. flange thickness with 2 in. eccentricity

Figure 6.7-41 shows relationships between the "% of concentric stiffener capacity" (as opposed to stiffness) and flange thickness when stiffeners were modeled with an eccentricity of 2 in. As mentioned, the results obtained for failure load are not as favorable with respect to trends and consistency as the results obtained for elastic stiffness primarily due to limitations in the weld capacity. However, the relationship defined by Equation 6-4 is plotted as a straight line on Figure 6.7-41 and most percent results are above this line, suggesting that the relationship is conservative. The only two exceptions in Figure 6.7-41 are for the W24X229 (flange thickness 1.73 in.) modeled with 1/4 in. welds and 9/16 in. However, per Tables 6.7-3 and 6.7-4, the effective stiffener capacities are very low since very similar results were obtained for this column section regardless of the stiffener condition. Since the results of effective stiffener capacity are very small, the percent results are very sensitive to rounding and interpretation/error of the failure load results.

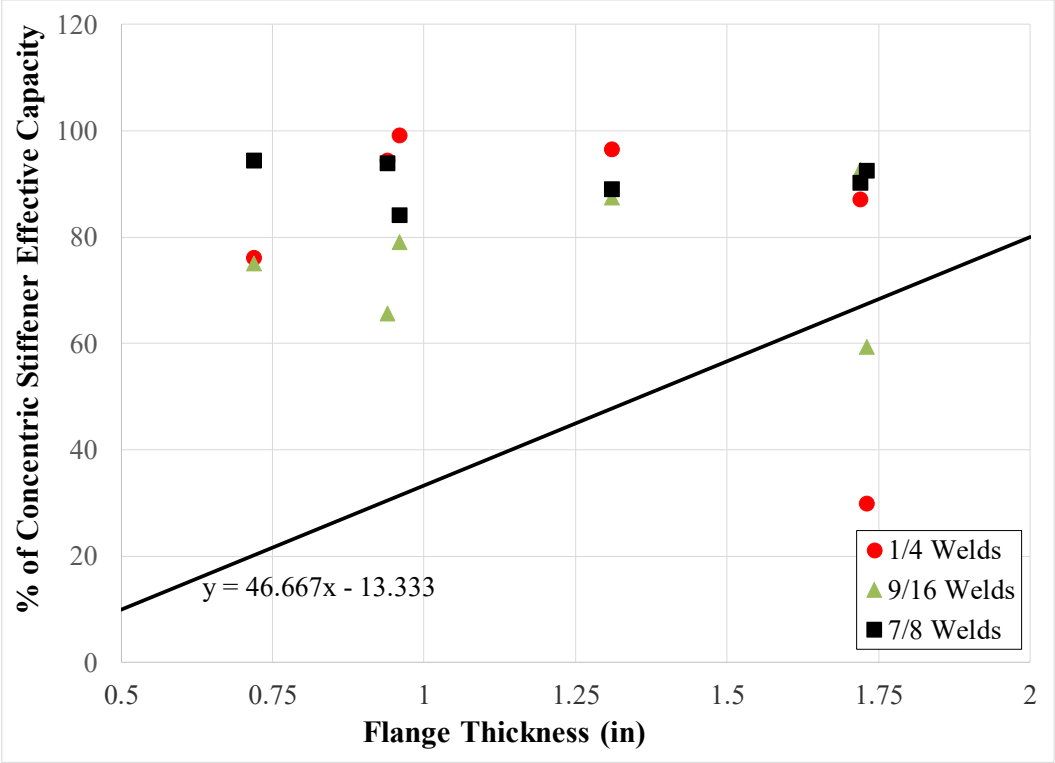

Figure 6.7-41: % of concentric stiffener capacity vs. flange thickness with 2 in. eccentricity

Figure 6.7-42 shows relationships between the "% of concentric stiffener capacity" and flange thickness when stiffeners were modeled with an eccentricity of 4 in. As shown in Figure 6.7-42, in general, as flange thickness increases, the percent results increase as well. However, the results are more sporadic than the effective stiffness results and therefore, it is favorable to use the stiffness results to define recommendations.

The two different relationships defined by Equations 6-5 and 6-6 are shown as straight lines on Figure 6.7-42 and expressed in terms of capacity in lieu of stiffness. Only one result is shown below these relationships, which represents the W24X229 column specimen modeled with ¼ in. welds. However, as mentioned, for this test group, all four results were small and the "% of concentric stiffener capacity" results were sensitive.

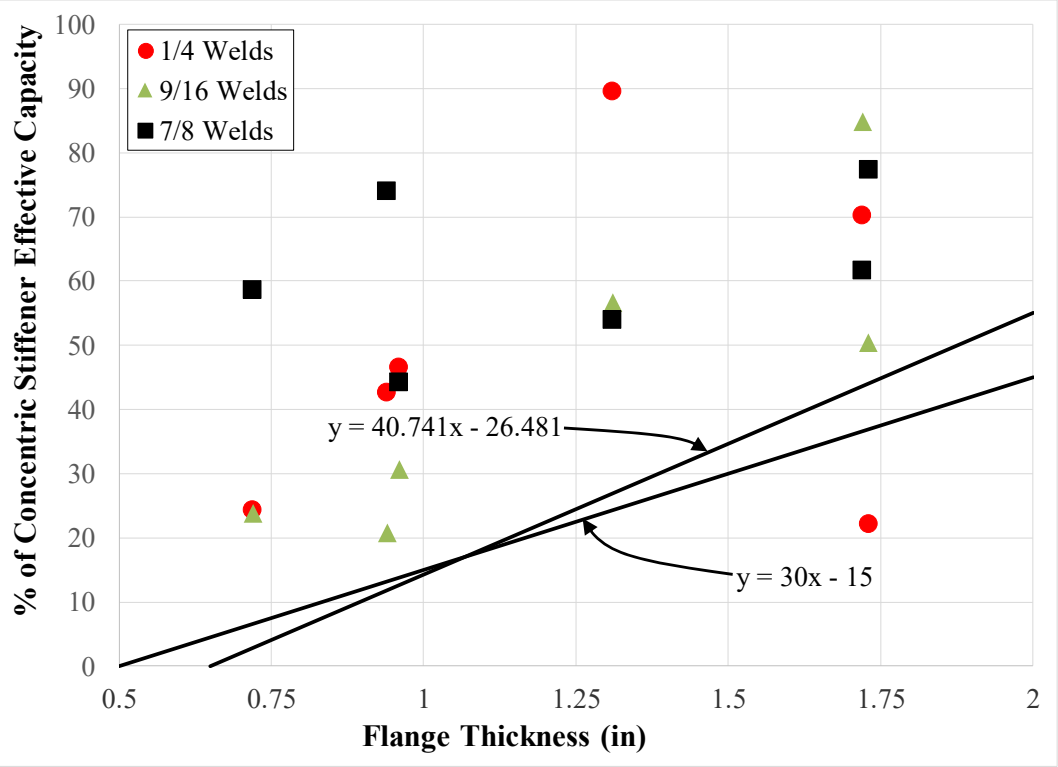

Figure 6.7-42: % of concentric stiffener capacity vs. flange thickness with 4 in. eccentricity

All of the recommended straight line expressions (Equations 6-4 to 6-6) are superseded by the recommendations provided in Section 6.8. However, the results of all loading conditions reveal that it is beneficial to use relationships valid from a flange thickness of 0.5 in. to 2.0 in. for a range of eccentricities up to 4 in. It is also recommended to ensure relationships are valid for both the maximum load obtained and the effective stiffness for all studies performed.

6.8 Effects of Stiffener Eccentricity for all Test Methods

Final recommendations for defining relationships between stiffener eccentricity and effective stiffener capacity are derived in this section. The final recommendations considered all experimental and analytical testing performed in the research.

This research project has indicated that it is inappropriate to develop a relationship between just stiffener eccentricity and effective stiffener capacity. Instead, the section cross-section has a significant role on how effective the stiffeners are at various eccentricities. In Sections 6.5.4, 6.6.4 and 6.7.6, it was identified that for all three test methods, that the most influential parameter of the cross-section that should be utilized to incorporate the cross-section is the flange thickness. The

slenderness of the web and flange influence the results as well, but the flange thickness is the dominant variable and conservative recommendations can be established using the flange thickness that are valid for all slenderness ratios.

In Sections 6.5.4, 6.6.4, and 6.7.6, conservative relationships were developed that related to the flange thickness to the "% Conc. Stiffener" results. These relationships were straight line equations dependent on flange thickness at specific eccentricities. The idea was that an effective stiffener capacity could be calculated at an eccentricity of 2 in. and 4 in. and interpolation could be used for eccentricities in between. However, with assistance from the AISC Research Advisory Committee, it is more appropriate to provide final recommendations in regression form and utilizing the ratio of stiffener eccentricity vs. the flange thickness or the 'e / t_f' ratio.

For the analytical single tension tests and as discussed in Section 6.7.6, it was concluded that the elastic stiffness provided more consistent trends to define relationships between eccentricity and the amount of load transferred to the stiffeners as opposed to the maximum load. It was also determined that if the elastic stiffness is used in lieu of the maximum load, recommendations would generally be conservative for the maximum load. For the single compression tests discussed in Section 6.5.4, it was concluded that relationships could be developed for the influence of stiffener eccentricity and flange thickness directly for the maximum load or effective stiffener capacity. Therefore, elastic stiffness was not considered a variable to study. However, the double compression test results were more sporadic for reasons described in Section 6.6. Therefore, one final study was performed that evaluated the effective elastic stiffness and how it was affected by stiffener eccentricity and flange thickness. The effective elastic stiffness was computed as the difference between the elastic stiffness for models with stiffeners and the equivalent model without stiffeners. For models with eccentric stiffeners, the "% of Conc. Stiffener" results were computed as the effective elastic stiffness of models with eccentric stiffeners divided by the effective elastic stiffness of models with concentric stiffeners. These results are not provided in table format but a similar procedure was followed for single tension tests in Section 6.7.5.

Figure 6.8-1 shows the results of effective elastic stiffness when using either 3/8 in. stiffeners or 3/4 in. stiffeners and either with a 2 in. eccentricity or a 4 in. eccentricity (4 conditions). The results in Figure 6.8-1 are very influential in understanding the effects of flange thickness and eccentricity

on the effective elastic stiffness. The relationships between flange thickness and "% Conc. Stiffener" results are fairly linear for all four conditions analyzed. However, the results would generally fall under the straight line equations derived in Section 6.5.4 which are also shown in Figure 6.8-1. After reviewing the results, it was found that the "% Conc. Stiffener" results are significantly higher when using the maximum load in lieu of elastic stiffness. Therefore, it is too conservative to use the stiffener stiffness for the double compression tests. However, the results provide move confidence that there are favorable relationships between eccentricity, flange thickness and effective stiffener capacity. The results are always slightly higher when 3/8 in. stiffeners are used by the trends are very similar regardless of the stiffener size.

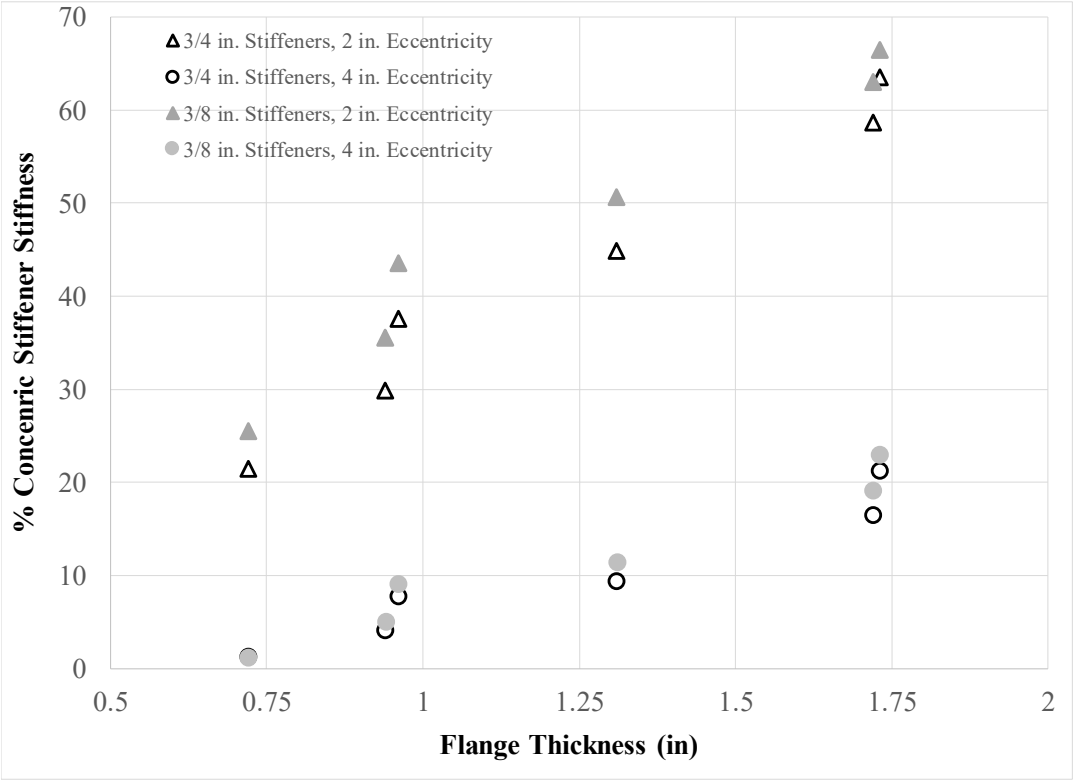

Figure 6.8-1: For double compression models, relationship between effective elastic stiffness and flange thickness

Figure 6.8-2 provides all of the "% Conc. Stiffener" results obtained in this research, either experimentally or analytically. The figure uses both the eccentricity and flange thickness in the form of the 'e / t_f' ratio and plots the results of this ratio vs. either the "% Conc. Stiffener" results in terms of elastic stiffness (analytical results only) or the "% Conc. Stiffener" results in terms of maximum load obtained. Therefore, Figure 6.8-2 is a comprehensive output of the research performed to

identify appropriate relationships between the parameters and effective stiffener capacity that are valid or conservative for all test conditions (single tension, single compression, double compression).

The amount of data in Figure 6.8-2 is vast and the research team did not delegate a significant amount of time to properly distinguish between each data set (with respect to colors and shapes of the data points). A legend is used for each data set where:

Exp – Refers to a set of experimental results

Any – Refers to a set of analytical results

SC – Refers to single compression

DC – Refers to double compression

ST – Refers to single tension

Cap. - refers to a set of data that compares effective stiffener capacity

Stiff. – Refers to a set of data that compares effective elastic stiffness

In addition, the legend indicates whether the data set represents when stiffeners were modeled at a 2 in. eccentricity (2 in. Ecc) or a 4 in. eccentricity (4 in. Ecc). If applicable, the weld size or stiffener size is provided if these sizes vary for multiple data sets.

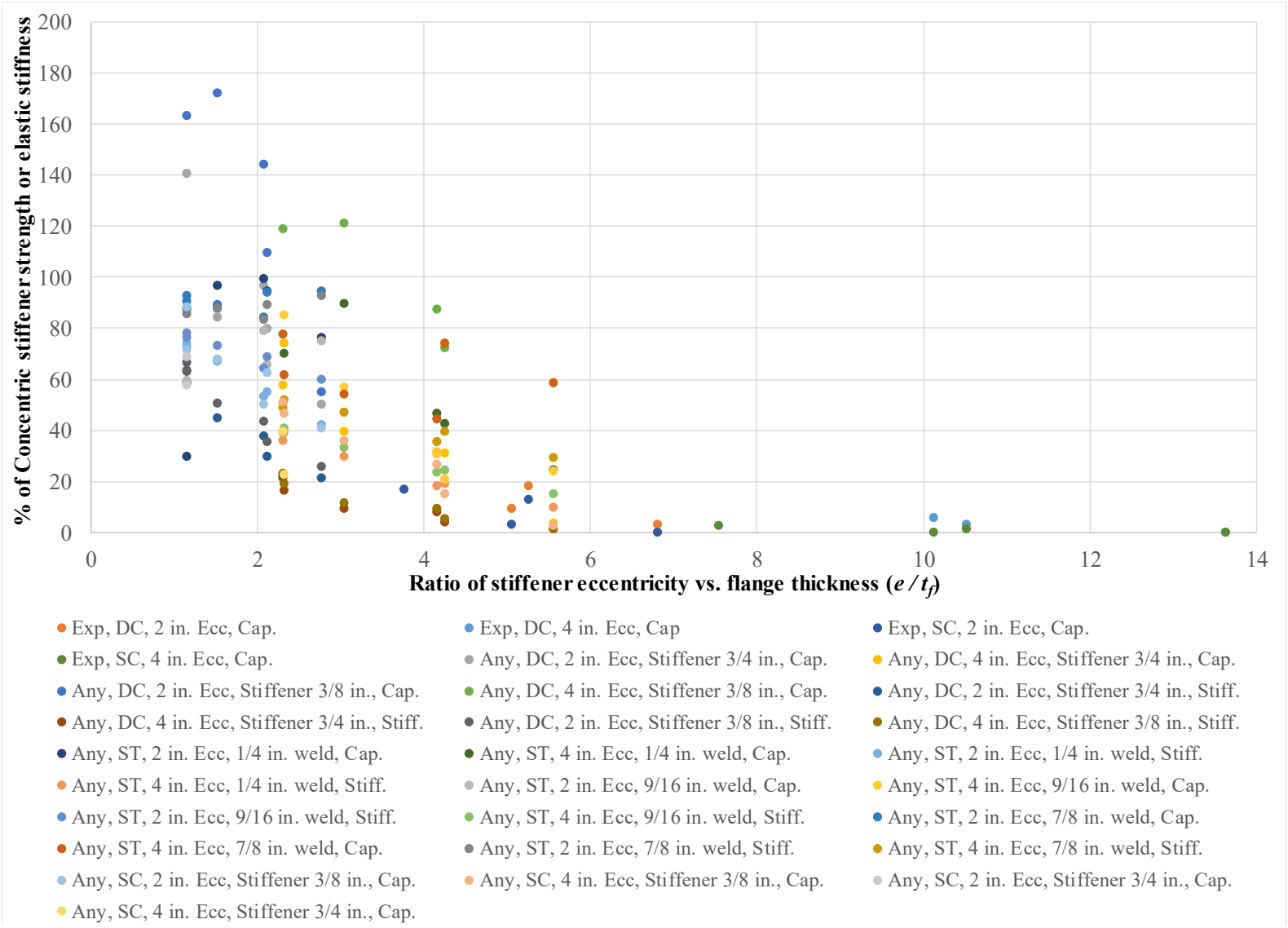

Figure 6.8-2: Relationships between "% Conc. Stiffener" results vs. e / t_f derived in research

Several data sets are provided in Figure 6.8-2 and it is cumbersome to differentiate and discuss them individually. However, under close observation, all data sets indicate that if the 'e / t_f' ratio increases, the "% of Conc. Stiffener" results always decrease. In Figure 6.8-2, 'e / t_f' ratios greater than 6.0 represent only experimental test results. One recommendation provided earlier in Section 6.5.4 is that eccentric stiffeners shall not be considered effective if the flange thickness is less than 0.5 in. In all cases where the 'e / t_f' ratio is greater than 6.0, the flange thickness is less than 0.5 and therefore, a relationship defined beyond 6.0 is not necessary. In addition, in Section 6.5.4, it was recommended that if a 4 in. eccentricity is present that the flange thickness shall not be less than 0.65 in. The ratio of 4 in. / 0.65 in. is approximately equal to 6.0. Therefore, final recommendations should have a maximum 'e / t_f' equal to 6.0.

Figure 6.8-3 is a reduction of Figure 6.8-2 after the removal of some data sets and after adjusting the y-axis to range from 0-100% and adjusting the x-axis to range from 0-6 in. Possible recommended design relationships are also shown in Figure 6.8-3 and will be discussed later in this section. All data sets that were obtained from double compression tests and relate the elastic stiffness to "% Conc. Stiffener" results were removed from the figure. These results showed clear trends from Figure 6.8-1 but using them seems too conservative since the "% Conc. Stiffener" results using the maximum load were always significantly higher. In addition, in Figure 6.8-3, the results of single tension tests with 1/4 in. welds were removed due to limitations of the weld strength and the "% of Conc. Stiffener" results were sensitive to very small differences in maximum load.

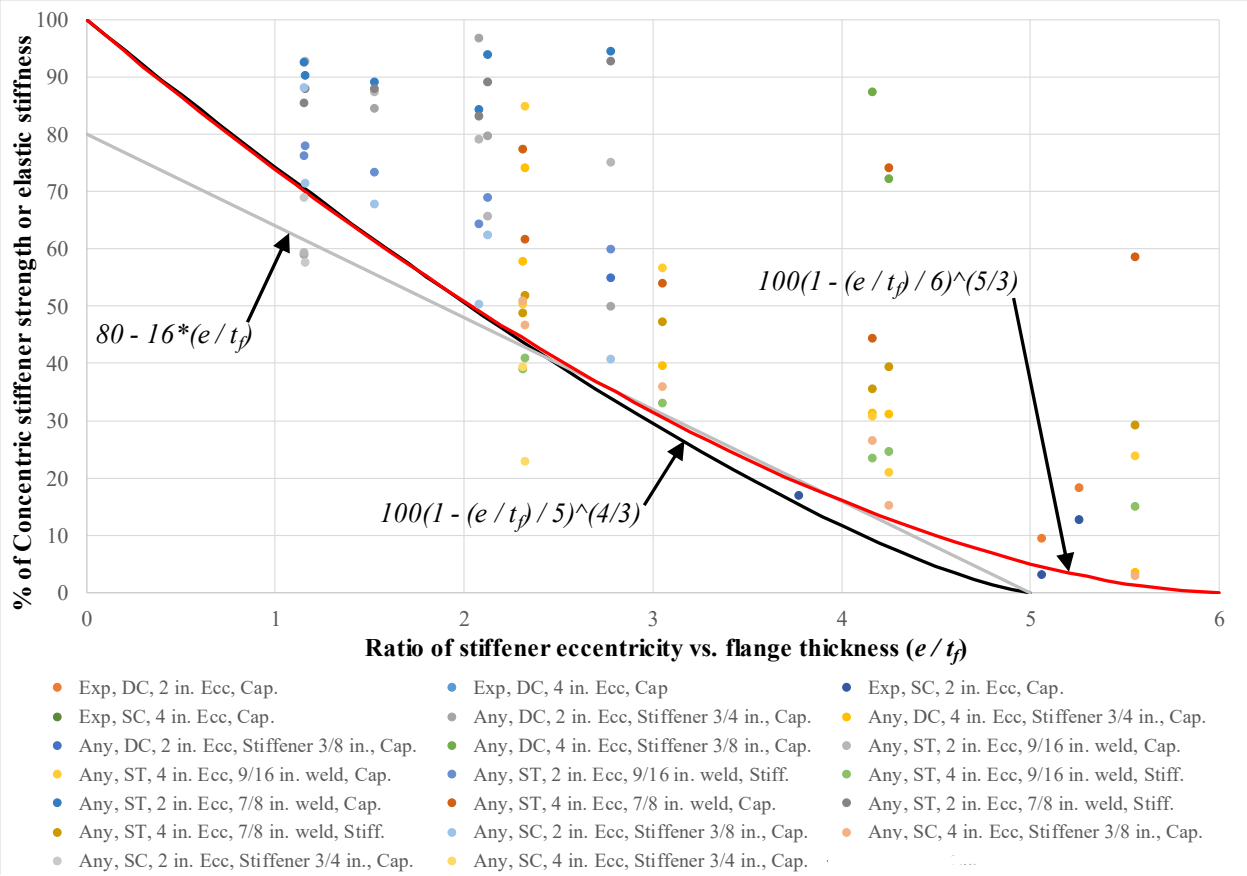

Figure 6.8-3: All data used to define relationship between e / t_f and % Conc. Stiffener results

Three possible relationships between the '*e / tf*' ratio and the "% of Conc. Stiffener" results are shown in Figure 6.8-3. This is includes a straight line expression, as shown by the grey line. In previous sections, straight lines were proposed with the results at specific eccentricities. However, it is logical to develop a relationship that suggests if the eccentricity is 0 in. (concentric stiffeners), that the capacity is 100% of the capacity of the concentric case. A conservative straight line expression could not be drawn with the results that originates at 100% and provides a maximum allowable '*e / tf*' of at least 5.0. Therefore, parabolic recommendations were established as well with one allowing a maximum '*e / tf*' of 5.0 (black curve) and one allowing a maximum '*e / tf*' of 6.0 (red curve). Both of these parabolic relationships indicate that if the eccentricity is 0 in., the effective stiffener capacity is 100% that of the concentric stiffener case. The curves "follow" each other until the '*e / tf*' ratio is greater than 3.0. In Section 8.5, a form of the latter equation will be provided for the final recommendation but if AISC prefers using a straight line expression, a form of the grey line in Figure 6.8-3 is recommended.

Overall, there is no theoretical evidence to support the design curves other than all results are close to or above the curves. After reviewing the results in Figure 6.8-3, one data point falls significantly under the recommended design relationships (at $e / t_f \approx 2.3$). This was the result from the analytical single compression test of the W24X229 column section modeled with ¾ in. stiffeners at an eccentricity of 4 in. The research team finds this result to be an outlier in the data and all remaining comparisons fall above the recommended design relationships or very close to them.

CHAPTER 7: FURTHER EVALUATION OF AISC LIMIT STATE CALCULATIONS

7.1 Introduction and Discussion

This chapter compares and discusses the experimental and analytical results of the column specimens without stiffeners and compare the results to the limit states associated with concentrated loads as specified in the AISC specification (AISC, 2016). Some specimens with stiffeners are also utilized to evaluate the effective stiffener capacities when concentric stiffeners are used. As stated several times in this report, the capacity associated with both analytical and experimental results was significantly higher than the *theoretical* capacity using the AISC limit state equations. The *theoretical* capacity is assumed as the governing (lowest) capacity per all limit states applicable for the loading condition (test method). Therefore, the results of this research question the limit state equations as presented in the specification.

A literature review for the limit states associated with concentrated loads was provided in Section 2.1. Primary research for developing the limit state equations was conducted by Graham et al. (1959) for web local yielding and flange bending and Roberts (1981) and Elgaaly and Salkar (1991) for web local crippling. Web compression buckling seems to be derived from fundamental plate buckling equations provided in Timoshenko (1936).

For most compression studies, the capacity of column specimens without stiffeners compared well with the theoretical calculations for the limit state of web local crippling. This was true for the experimental results and for the analytical results of smaller column specimens. For larger column specimens, the results were generally higher than that predicted for web local yielding and smaller than that predicted for web local crippling. For single tension specimens, the results are highly dependent on the weld size, which makes the study more complicating. However, when a relatively thick weld for the column size is used, the overall load capacity is generally much higher than that predicted for flange bending.

In the preliminary report, the research team recommended that the limit states associated with concentrated loads should be evaluated in more detail using more loading conditions (plates oriented along length of column and plates oriented flat on top of column specimen). However, after initiating the analytical investigations on larger column specimens, the research team decided it was necessary

to focus the analytical efforts on eccentric stiffeners since they are more effective using larger column sizes. Only limited time was available to study the concentrated load limit states in detail, which was not part of the original scope of the project. Therefore, this section only evaluates the analytical and experimental results previously shown in this report and initiates the discussion if the limit state equations should be reevaluated and if a comprehensive research project is justified.

7.2 Web Local Crippling/Yielding Studies using Single Compression Results

The limit states of web local crippling and web local yielding are studied in this section using all available results of single compression tests without stiffeners. These limit states will also be further studied using double compression tests in Section 7.3 and web local yielding will be studied using the single tension tests in Section 7.4. However, these two limit states will not be studied as rigorously in Sections 7.3 and 7.4 as opposed to this section.

Table 7.2-1 shows results for all experimental and analytical column specimens without stiffeners and tested in single compression. The experimental results are shaded in the table. The column size is shown with some important section dimensions along with the test capacity (*Test CAP).* In addition, the table shows the theoretical capacities for web local yielding (*WLY*) and web local crippling (*WCR*). Calculations for the theoretical capacities are provided in Appendix D and are nominal values prior to considering safety factors per LRFD or ASD design methods (AISC 2016). Finally, ratios of the theoretical web local yielding capacity to the test capacity (WLY/CAP) and the web local crippling capacity to the test capacity (WCR/CAP) are shown.

Table 7.2-1: Comparison of SC test capacities to theoretical capacities per AISC (2016)

				Test	Limit States		Ratios	
Col. Size	t_f (in)	t_w (in)	h / t_w	CAP (k)	WLY (k)	WCR (k)	WLY/CAP	WCR/CAP
W12X26	0.38	0.23	47.2	78.2	52.5	74.7	0.67	0.96
W10X19	0.395	0.25	35.4	69.6	58.1	88.2	0.83	1.27
W16X31	0.44	0.275	51.6	112.4	75	103.4	0.67	0.92
W10X39	0.53	0.315	25.0	131	102.2	143.6	0.78	1.10
W14X68	0.72	0.415	27.5	232.3	151.5	233.9	0.65	1.01
W14X120	0.94	0.59	19.3	404.1	249.3	455.9	0.62	1.13
W24X131	0.96	0.605	35.6	440.4	243.5	464.6	0.55	1.05
W14X176	1.31	0.83	13.7	659.5	427.5	896.0	0.65	1.36
W14X233	1.72	1.07	10.7	965.7	508.3	1495.0	0.53	1.55
W24X229	1.73	0.96	22.5	992.2	571.2	1234.0	0.58	1.24

The ratios in Table 7.2-1 are shown graphically for each column size in Figure 7.2-1. Bar graph format is used with the ratio for *WLY/CAP* shown next to the ratio for *WCR/CAP*. In Figure 7.2-1, a bolded line is shown at 1.0. In both Figure 7.2-1 and Table 7.2-1, the column sizes are arranged in ascending order by flange thickness, which related very well to trends in the test capacity.

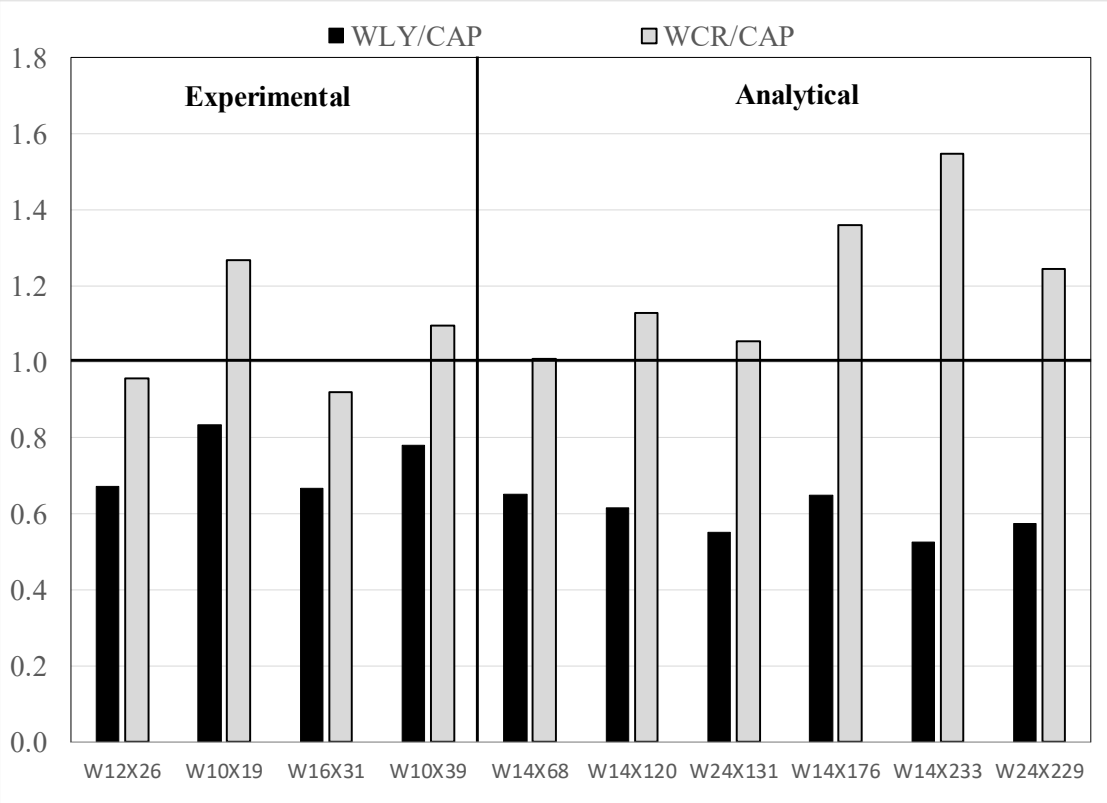

Figure 7.2-1: Ratios of theoretical capacities vs. single compression test capacities

As discussed in Chapter 3, it should be noted that the results for the capacity of the W10X19 column specimen were influenced slightly by lateral torsional buckling. Therefore, the bar graphs in Figure 7.2-1 should be a little lower than that shown.

All column specimens failed at a limit state best described as web local crippling. This is true for both the experimental and analytical results as discussed in previous chapters. Therefore, it is believed that the work performed by Roberts (1981) and the equations for this limit state shown in the AISC specification (AISC, 2016) are adequate. However, for larger column specimens, excessive yielding occurred prior to web local crippling, which is why the *WCR/CAP* ratios are noticeably higher than 1.0 in Figure 7.2-1. For the larger column sizes, inelastic web local crippling

occurred which is a combination of web local yielding and web local crippling.

All results in Figure 7.2-1 indicate that web local yielding is the controlling limit state as defined by the AISC specification (AISC, 2016) for all column sizes studied and because of this, should intuitively be related to the capacity of the specimen. For all results, the theoretical capacity for web local yielding under predicts the capacity of the column specimen. However, this may not warrant a change to the limit state for two reasons. First, yielding fundamentally is not a mechanism that causes failure but instead causes excessive deformations and allowing materials to yield and eventually reach an ultimate capacity is not always desirable. Second, the resistance factor using the LRFD design method is 1.0 as opposed to other limits such as web local crippling, which is 0.75 (AISC, 2016). It is therefore interpreted that exceeding the limit state of web local yielding is not that detrimental in design and instead, the limit state is included in Section J10 of the specification as a conservative check. Calculations indicate that web local yielding governs over web local crippling when nominal values (without resistance factors) are used for all wide flange sizes in the Steel Construction Manual (AISC, 2017) assuming the yield stress is 50 ksi. However, when resistance factors or the LRFD design method is used, this is not always the case.

Figure 7.2-2 shows the results in Figure 7.2-1 again but after incorporating the LRFD resistance factors, which only influenced the values for WCR/CAP. This graph is not meant to compare to experimental results but instead meant to show how the WLY/CAP and WCR/CAP ratios compare. For the column sizes in question, web local yielding would still govern in design but the bars are more comparable, particularly for the experimental column specimens.

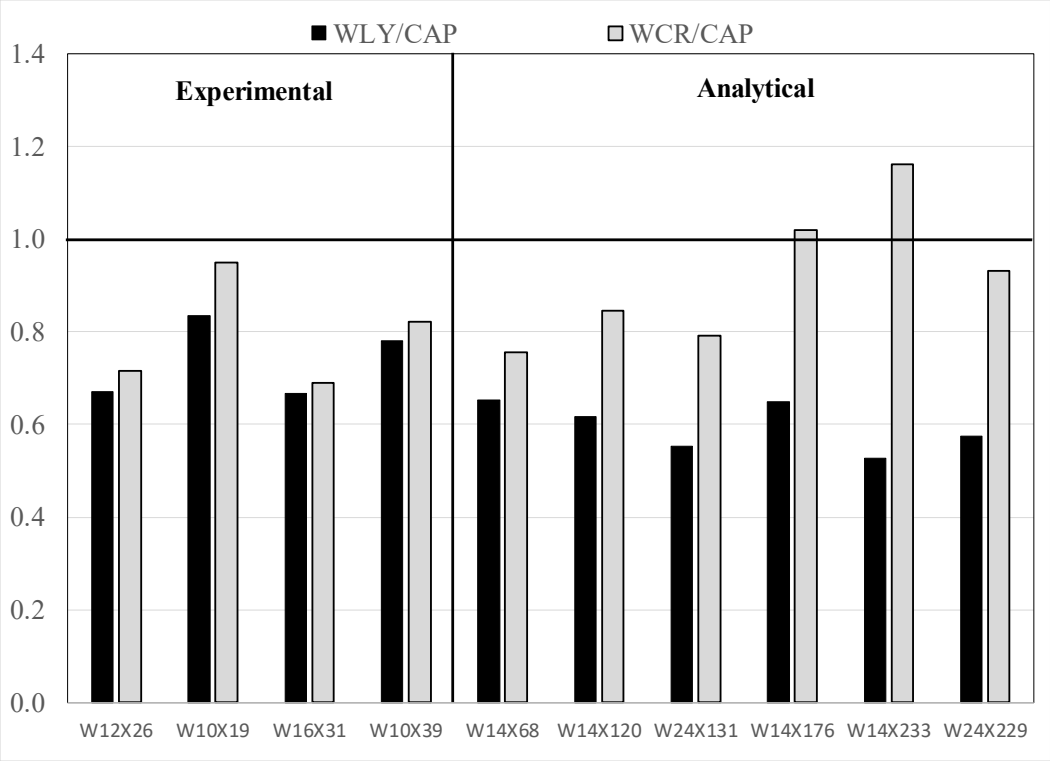

Figure 7.2-2: Ratios of LRFD design capacities vs. single compression test capacities

As mentioned earlier in this section, although the theoretical web local yielding capacity does not compare well to the test capacity, excessive yielding is not desired. In addition, for the larger column sections, it appeared from the finite element results that excessive yielding did occur prior to web local crippling, which always occurred and defined the maximum load that could be applied. Therefore, it is not recommended to remove the web local yielding equation but instead consider a modification after more studies are performed.

Figure 7.2-3 shows all load-displacement results of all column specimens, both analytically and experimentally with the applied loads *normalized* to the maximum load of the individual specimen in order for all results to be observed on the same plot. Therefore, the maximum normalized load for all column specimens is 1.0. The ratio of *WLY/CAP* is shown for each normalized load-displacement result as a horizontal line of the same color on the individual normalized load-displacement result.

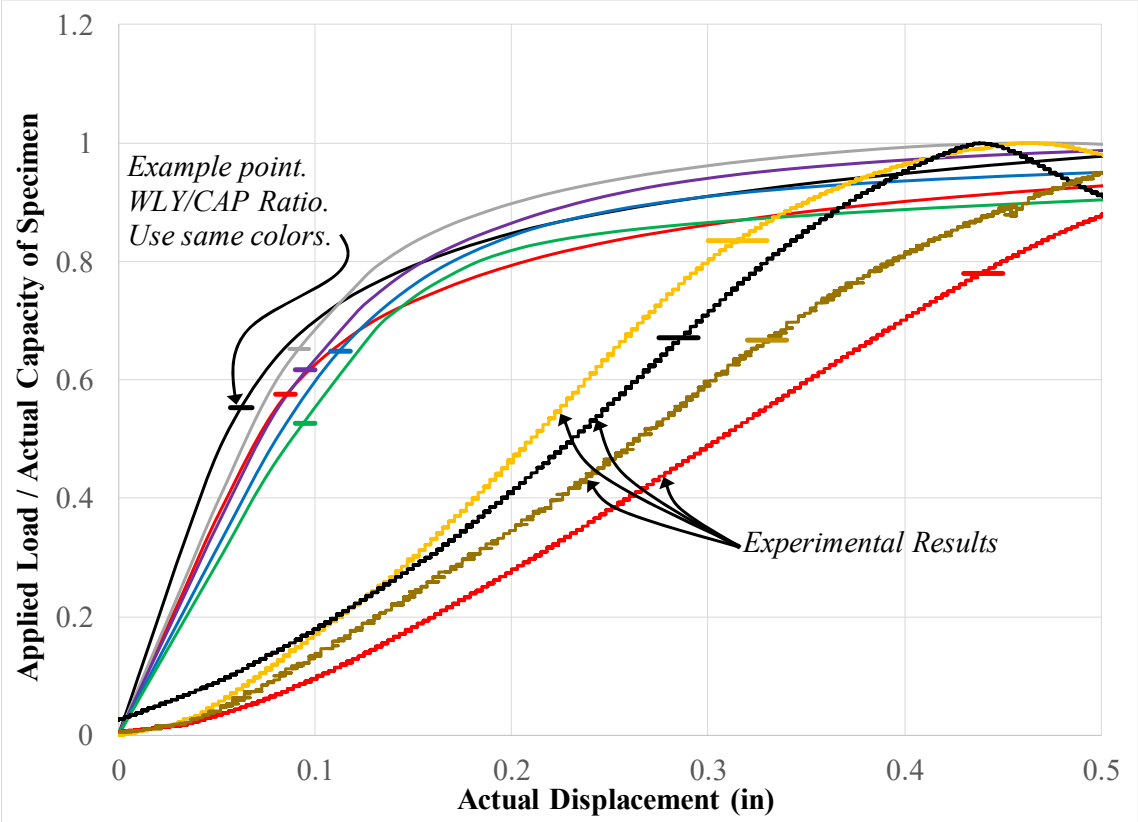

Figure 7.2-3: Observation of WLY/CAP ratios on normalized load-displacement results

From Figure 7.2-3, the analytical and experimental results both reveal that yielding or non-linear behavior in the load-displacement results initiates close to or above the predicted limit state of web local yielding and therefore, yielding is present in the specimens. This was also identified in the experimental results from DIC and the analytical results from the finite element models. However, the change in slope or tangent stiffness is usually not significant directly after initial yielding occurs and the load continues to increase significantly prior to failure. It appears that non-linear behavior is more pronounced directly after the web local yielding limit state is reached for deeper sections. For instance, the red line of the analytical column specimens represents the normalized results for the W24X229 column specimen and the black line of the analytical column specimens represents the normalized results for the W24X131 specimen.

Without performing rigorous studies, it is believed that the spread of yielding using the width assumed ($5k + l_b$) from Equation 2-2 is reasonable at first but as further load is applied, yielding initiates beyond this width and stresses begin to increase beyond the yield stress. Therefore,

"excessive" deformations do not occur right after web local yielding initiates. It is recommended that this limit state be evaluated in more detail to examine if the assumed width for web local yielding should be increased or if an additional factor can be added that recognizes that there is still reserve capacity prior to significant inelastic deformations occurring. This would include more experimental and analytical studies that consider different loading scenarios such as thicker plates, plates attached to the top flange but oriented longitudinally along the length of the specimen and plates laid flat (horizontal) on top of the flange of the column specimen.

In summary, it is recommended that the current provisions for web local crippling do appear accurate for single compression tests. More studies could be performed with more section sizes, loading conditions, and whether the section is end loaded vs. not end loaded. However, the work performed by Roberts (1981) appears adequate. Web local yielding should be studied in more detail and it is possible that one equation or design procedure could be incorporated that considers web local yielding and web local crippling simultaneously.

7.3 Web Compression Buckling Studies using Double Compression Results

In this section, experimental and analytical double compression results are utilized to study concentrated load limit states with a focus on evaluating the limit state of web compression buckling (AISC, 2016). The limit states of web local yielding and web local crippling are applicable for this loading condition as well. However, they were studied in Section 7.2 and the comments and conclusions made in Section 7.2 are still valid based on the results of the double compression tests as discussed herein.

All results for double compression tests without stiffeners are shown in Table 7.3-1. The experimental results are shaded in the table. The section sizes are ordered by flange thickness. Table 7.3-1 shows the column size with important dimensions along with the test capacity (*Test CAP*). In addition, the table shows the theoretical capacities for web local yielding (*WLY*), web local crippling (WCR), and web compression buckling (*WCB*). Calculations for the theoretical capacities are provided in Appendix D and are nominal values prior to considering safety factors per LRFD or ASD design methods (AISC, 2016). Ratios of the theoretical web local yielding capacity to the test capacity (*WLY/CAP*), web local crippling capacity to the test capacity (*WLY/CAP*), and web compression buckling to the test capacity (*WCB/CAP*) are shown.

Table 7.3-1: Comparison of DC test capacities to theoretical capacities per AISC (2016)

Column Information				Test CAP (k)	Ratio to SC CAP	Limit States			Ratios		
Col. Size	t_f (in)	t_w (in)	h / t_w			WLY (k)	WCR (k)	WCB(k)	WLY/CAP	WCR/CAP	WCB/CAP
W12X26	0.38	1.10	47	86.4	1.10	52.5	74.7	34.0	0.61	0.86	0.39
W10X19	0.4	1.13	35	78.5	1.13	58.1	88.2	53.7	0.74	1.12	0.68
W16X31	0.44	1.06	52	119.7	1.06	75.0	103.4	44.3	0.63	0.86	0.37
W14X68	0.72	1.18	28	274.0	1.18	151.5	233.9	181.5	0.55	0.85	0.66
W14X120	0.94	1.18	19	475.8	1.18	249.3	455.9	519.7	0.52	0.96	1.09
W24X131	0.96	1.06	36	469.0	1.06	243.5	464.6	296.6	0.52	0.99	0.63
W14X176	1.31	1.29	14	849.9	1.29	427.5	896.0	1452.0	0.50	1.05	1.71
W14X233	1.72	1.32	11	1278.7	1.32	508.3	1495.0	2832.0	0.40	1.17	2.21
W24X229	1.73	1.05	23	1040.8	1.05	571.2	1234.0	1187.0	0.55	1.19	1.14

Table 7.3-1 also compares the double compression test capacities to the single compression test capacities in the column labeled "Ratio to SC CAP". The comparison shows that the test capacity for double compression is always higher than that for single compression since all ratios are greater than 1.0. The results of the W14 specimens are significantly higher than the results of the W24 specimens. This is likely due to the results of the W14 single compression specimens being significantly influenced from shear and flexural stresses. This was discussed in detail in Section 6.5.6. These stresses are non-existent in the double compression tests, particularly for the analytical models. Further explanation regarding why the double compression test capacities are always higher has not been studied. However, the results appear to indicate similar patterns as witnessed for the single compression tests and therefore, similar conclusions are drawn with respect to the limit states of web local yielding and web local crippling.

Ratios presented Table 7.3-1 are shown graphically in Figure 7.3-1. Some of the *WCB/CAP* ratios were much higher than 1.0 and cut from the graph. In Figure 7.3-1, a bolded line is shown at 1.0.

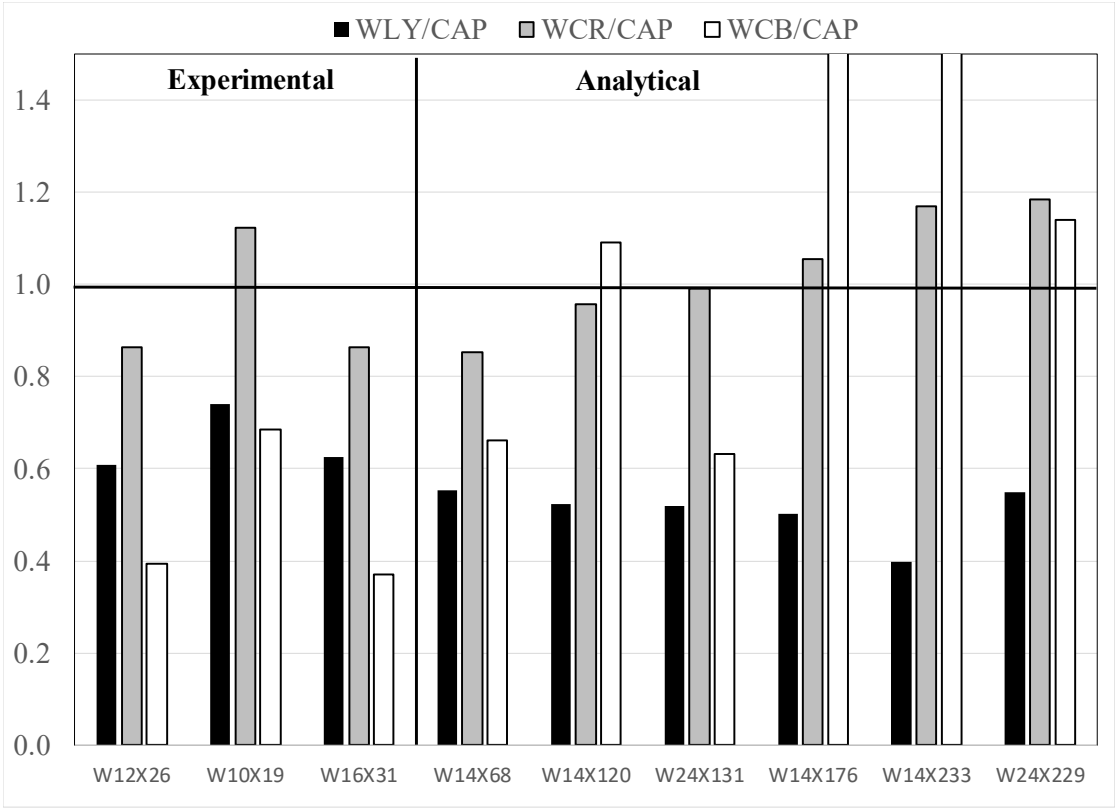

Figure 7.3-1: Ratios of theoretical capacities vs. single compression test capacities

As shown in Figure 7.3-1, web local yielding under predicts the actual capacity of the column specimen. However, as discussed for the single compression tests, some yielding of the web does occur prior to reaching the capacity. After reviewing the load-displacement graphs individually (as opposed to generating a figure similar to Figure 7.2-3), the change in tangent stiffness is not significant directly after initial yielding occurs and significant inelastic deformations do not occur until the maximum load is almost reached. Therefore, it is probable the calculations for the limit state of web local yielding are too conservative and should be looked at in more detail to observe the actual spread of yielding that occurs under concentrated loads.

All *experimental* double compression specimens failed by a limit state best described as web local crippling near the top loading plate as shown, for example, in Figure 3.7-15. In general, the maximum load for the test results compared best to the theoretical calculations for this limit state as shown in Figure 7.3-1 for both analytical and experimental specimens; even though the failure mode for some of the analytical models visually appeared as represent web compression buckling. All *WCR/CAP* ratios are within 0.8 and 1.2. Therefore, the theoretical capacity is within 80% and 120%

of the test capacity. As the sections got stockier (W14X176 and above), the theoretical capacity was often higher than the analytical test capacity. Instead, significant yielding of the column specimen occurred and eventually the columns failed by some form of inelastic buckling.

In the analytical results of column specimens without stiffeners, inconsistent buckling modes occurred which is dependent on the h / t_w ratio. As discussed in Salmon and Johnson (1996), plate buckling may occur in multiple half sine waves, which is dependent on the plate thickness, unsupported length, boundary conditions, and effective width. However, for web compression buckling, the effective width subjected to compression and the boundary conditions are uncertain.

As shown in Figure 7.3-2(a), the W14X68 analytical column specimen buckled with two half sine waves in the web and under the applied load. However, most of the analytical models buckled in the web with one half sine wave as shown for the W14X120 column specimen in Figure 7.3-2(b). Of all column specimens, the web compression buckling vs. test capacity compared best for the W14X120. The buckled shape of this specimen appears to be the correct for web compression buckling. At the same time, the W14X176 and W14X233 column specimens also buckled in one half sine wave and the theoretical web compression buckling capacity was well higher than the test capacity as shown in Figure 7.3-1.

(a) W14X68-DC-NA

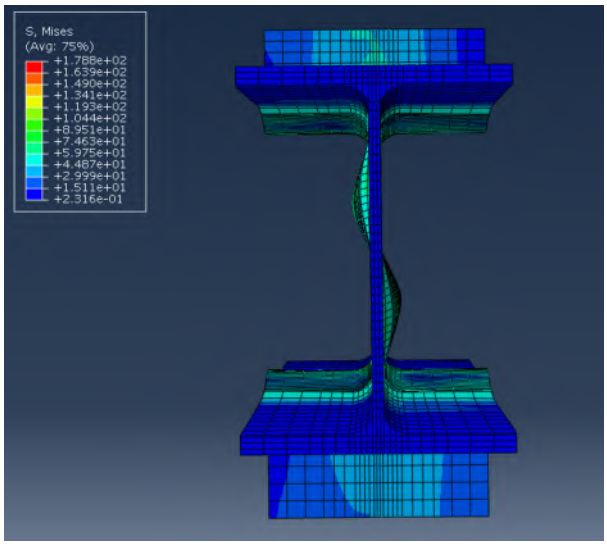

(b) W14X120-DC-NA

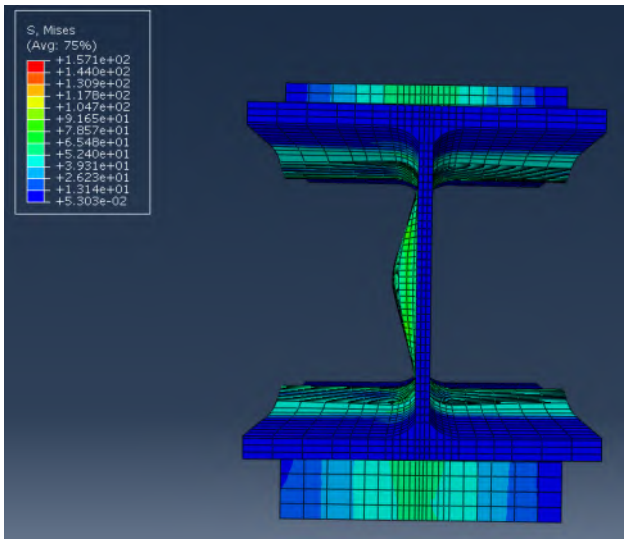

Figure 7.3-2: Buckled shape for W14 column specimens subjected to double compression

The literature review did not provide as much insight to the development of Equation 2-17 for web compression buckling as opposed to the development for other limit states. However, the buckled shapes in Figure 7.3-2 are intriguing and it is believed that more studies need to be performed to evaluate this limit state. In addition, the results in Figure 7.3-1 for the ratio of WCB/CAP are very sporadic in comparison to the results for WLY/CAP and WCR/CAP. Most importantly, when web compression buckling is supposed to control as for all of the experimental column specimens, the results show that the theoretical capacity is well exceeded. Therefore, this limit state is not well understood and a more rigorous experimental and analytical project is justified for evaluating this limit state in detail.

7.4 Flange Bending Studies using Single Tension Results

The results of the single tension tests are primarily utilized to evaluate the limit state of flange bending per Equation 2-14. The limit state of web local yielding is also applicable per this test method and will be discussed briefly. However, this limit state was primarily evaluated in Section 7.2.

As discussed in Section 6.7, the results of all single tension tests are highly dependent on the weld size and thickness of the attached plate. The combination of weld properties and steel section properties make a study for flange bending more complicating in comparison to studies for web local yielding, web local crippling and web compression buckling. Per the results in Section 6.7, regardless of the weld size, flange bending always has an influence on the ultimate capacity since the results with concentric stiffeners were always higher than the results without stiffeners suggesting that weak axis bending of the flange itself is influencing the results and causing non-uniform weld stresses across the width of the flange. When stiffeners were used, more uniform stresses could be obtained in the weld, allowing more load to be applied until the assumed failure. As weld size decreased, the relative capacities with and without stiffeners were closer.

The results of all single tension tests, both experimental and analytical and without stiffeners are provided in Table 7.4-1. All information within Table 7.4-1 will be discussed in the following paragraphs. There are only two experimental results available for this study since all W10X39-ST specimens reached the capacity of the hydraulic actuator. In addition, as discussed in Chapter 3, the column specimen W12X26-ST-NA seemed to fail prematurely due to an insufficient weld and

therefore, the results with stiffeners at a 4 in. eccentricity (W12X26-ST-E4) are used for this study.

Table 7.4-1: Comparison of ST test capacities to theoretical capacities per AISC (2016)

Column Specimen Information					Test CAP (k)	Limit States			Ratios		
Col. Size	t_f (in)	b_f (in)	$b_f / 2t_f$	Weld 'w' (in)		WC (k)	FB (k)	WLY (k)	WC/CAP	FB/CAP	WLY/CAP
W12X26	0.38	6.49	8.54	3/8	115.1	255.1	49.6	54.1	2.216	0.43	0.47
W16X31	0.44	5.53	6.28	3/8	127	217.4	66.6	76.9	1.711	0.52	0.61
W14X68	0.72	10	6.97	1/4	159.4	201.2	162.0	151.5	1.262	1.02	0.95
W14X68	0.72	10	6.97	9/16	259.5	452.7	162.0	167.0	1.745	0.62	0.64
W14X68	0.72	10	6.97	7/8	347.9	704.2	162.0	182.6	2.024	0.47	0.52
W14X120	0.94	14.7	7.8	1/4	221.3	295.8	276.1	249.3	1.337	1.25	1.13
W14X120	0.94	14.7	7.8	9/16	449.5	665.5	276.1	271.4	1.480	0.61	0.60
W14X120	0.94	14.7	7.8	7/8	612.9	1035.2	276.1	293.5	1.689	0.45	0.48
W24X131	0.96	12.9	6.7	1/4	215.6	259.6	288.0	243.5	1.204	1.34	1.13
W24X131	0.96	12.9	6.7	9/16	402.3	584.0	288.0	266.2	1.452	0.72	0.66
W24X131	0.96	12.9	6.7	7/8	581.9	908.4	288.0	288.9	1.561	0.49	0.50
W14X176	1.31	15.7	5.97	1/4	283.5	315.9	536.3	427.5	1.114	1.89	1.51
W14X176	1.31	15.7	5.97	9/16	590.4	710.7	536.3	458.6	1.204	0.91	0.78
W14X176	1.31	15.7	5.97	7/8	855.0	1105.6	536.3	489.7	1.293	0.63	0.57
W14X233	1.72	15.9	4.62	1/4	317.9	319.9	924.5	660.7	1.006	2.91	2.08
W14X233	1.72	15.9	4.62	9/16	704.4	719.8	924.5	700.9	1.022	1.31	0.99
W14X233	1.72	15.9	4.62	7/8	1013.0	1119.7	924.5	741.0	1.105	0.91	0.73
W24X229	1.73	13.1	3.79	1/4	263.0	263.6	935.3	571.2	1.002	3.56	2.17
W24X229	1.73	13.1	3.79	9/16	589.7	593.0	935.3	607.2	1.006	1.59	1.03
W24X229	1.73	13.1	3.79	7/8	903.4	922.5	935.3	643.2	1.021	1.04	0.71

Table 7.4-1 provides the column size with important column dimensions. In addition, the weld size, '*w*' is provided and for columns of the same size, each weld size represents at different analytical model. The capacity of the test, defined as the maximum load obtained experimentally when the weld failed or the maximum interpreted load when weld failure is assumed to occur analytically, as discussed in Section 5.4, is provided as "*Test CAP*". The theoretical capacities per AISC (2016) for the limit states of flange bending (*FB*) and web local yielding (*WLY*) are provided in Table 7.4-1. Calculations for the theoretical capacities are provided in Appendix D and are nominal values prior to considering safety factors per LRFD or ASD design methods (AISC, 2016).

Table 7.4-1 provides ratios of the theoretical web local yielding capacity to the test capacity (*WLY/CAP*) and the theoretical flange bending capacity to the test capacity (*FB/CAP*). In addition, the theoretical weld capacity (*WC*) is provided along with the *WC/CAP* ratio. The weld capacity and assumptions for it were discussed in Section 6.7.5. A theoretical capacity using Section J2 of the AISC specification (AISC, 2016) was used for the experimental *WC* and a modified weld capacity was used for the analytical *WC*.

The results in Table 7.4-1 show that web local yielding generally underestimates the ultimate capacity of the column specimen unless relatively smaller welds are used for the column size. Figure 7.4-1 graphically shows the results of *WLY/CAP* for all analytical specimens and all weld thickness. The results of this study indicate that when 1/4 in. welds are used, the capacity is limited by the weld and disallows the column specimen to fail by web local yielding. When larger welds are used, the column has much more capacity than the web local yielding limit and therefore, the column specimens never fail at a capacity close to the theoretical capacity for web local yielding.

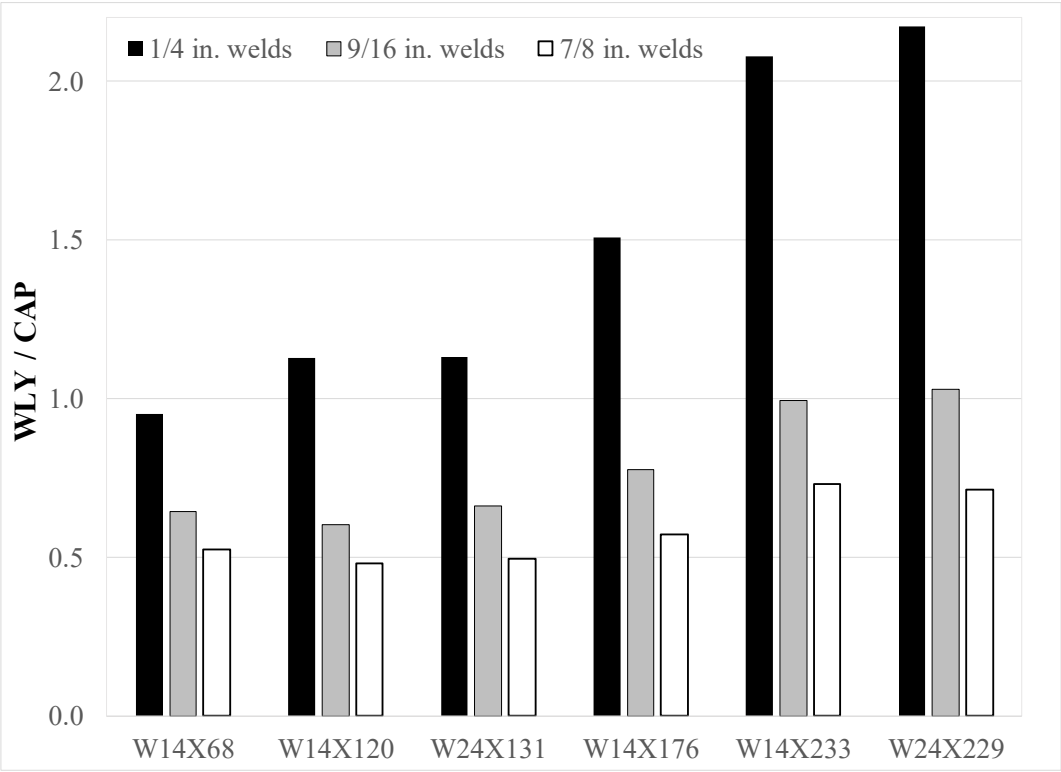

Figure 7.4-1: Comparisons of WLY/CAP ratios for different weld thickness

Similar to the single compression tests discussed in Section 7.2, yielding in the web was often found in the analytical models of column specimens prior to the capacity being reached. For instance, Figure 7.4-2 shows initial yielding in the W24X131 column specimen web when using 7/8 in. welds. The contours represent the Von Mises stress and are ranged to the yield stress of 50 ksi. Anything grey represents an area of the steel column with stresses greater than 50 ksi and therefore yielded. The applied load in Figure 7.4-2 is equal to 260 kips. Per Table 7.4-1, the web local yielding capacity was calculated as 288.9 kips. Therefore, the predicted capacity compares well to initial yielding. However, the column specimen and web can withstand significantly higher load. For instance, Figure 7.4-3 shows the stresses when the load is equal to 440 kips. This is still less than the maximum load obtained in the analysis when weld fracture was assumed to occur of 582 kips. The length '$5k + l_b$", which is the assumed width for web local yielding is estimated on the drawing. The comparison shows that the yield zone is wider than that predicted as more load is applied and stresses are still high just beyond the grey area. Although it is believed at this time that the web local yielding equations are too conservative, it is uncertain at this time what an acceptable amount of deformation would be in practice.

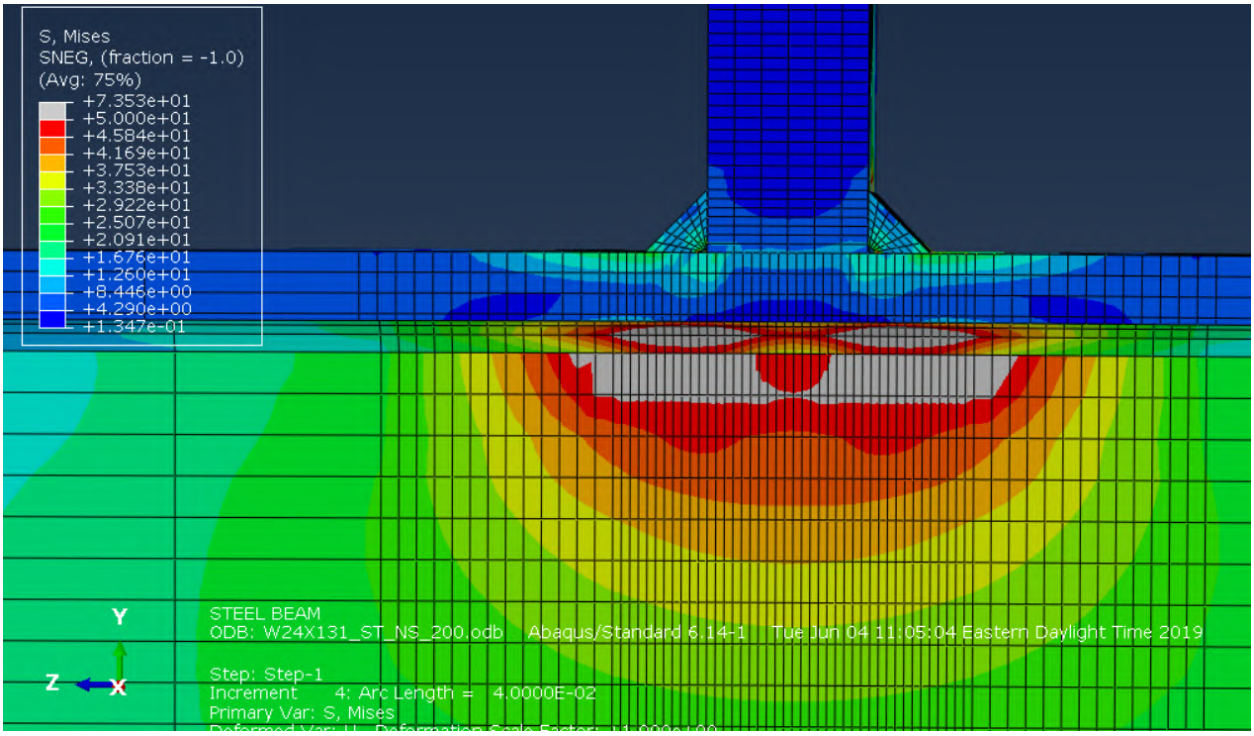

Figure 7.4-2: Initial yielding in web of W24X131 column specimen with load of 260 kips

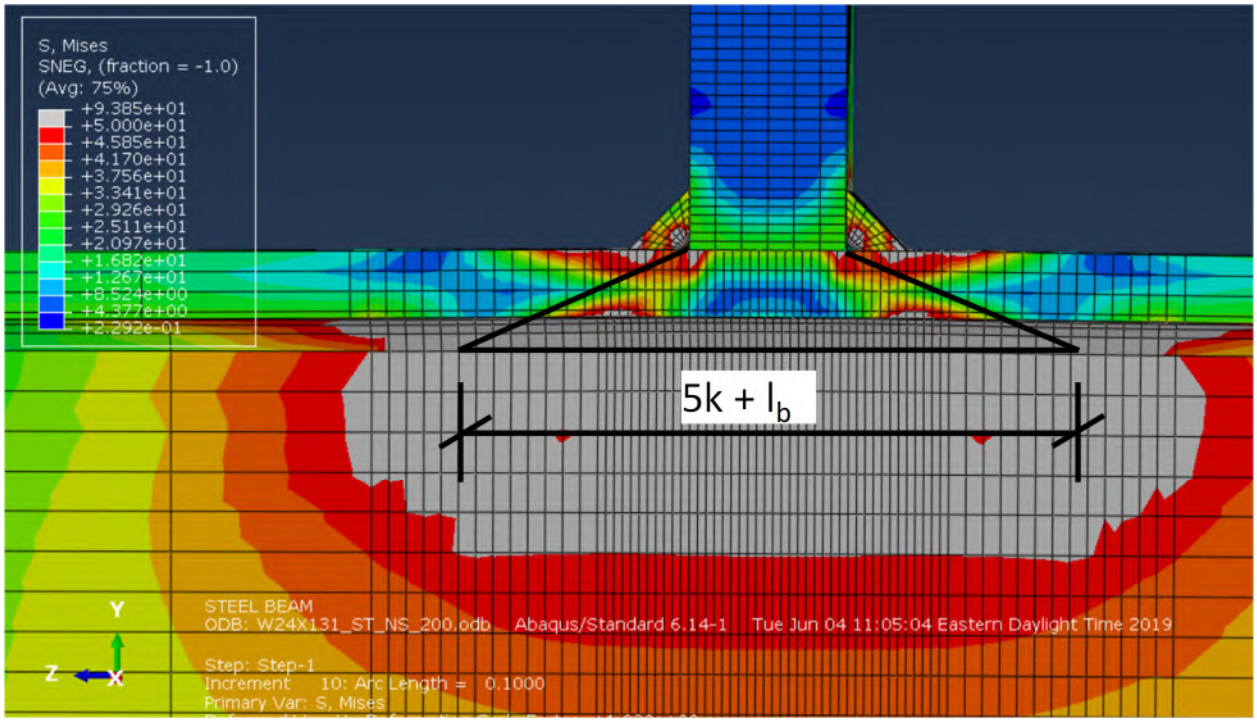

Figure 7.4-3: Spread of yielding in web of W24X131 column specimen with load of 440 kips

It is recommended to keep the limit state of web local yielding applicable for tension conditions in order to avoid excessive deformations of the column specimen. However, the equations and spread of yielding in the column specimen needs to be evaluated in more detail since the change in stiffness in the load-displacement results is not significant once yielding initiates in the web. When reviewing the results in detail, similar conclusions than that drawn from Figure 7.2-3 were also valid for the single tension results.

For the experimental column specimens, the theoretical capacities for flange bending and web local yielding are much lower than the test capacity. It is assumed that the weld size of 3/8 in. is "substantial" for these column sizes since significant deformations do not occur in the entire weld and the failure appears to be *dominated* by flange bending itself and not by limitations in the strength of the weld itself. This is applicable for *some but not all* of the analytical column specimens as well. For instance, for the W24X131 column specimen, when a 1/4 in. weld is used, failure appears to be controlled by limitations in the weld strength itself as more uniform weld stresses were found in the weld at the assumed failure. When a 7/8 in. weld is used, failure appears to be controlled by flange bending, which causes non-uniform stresses in the weld. Therefore, a weld size of 7/8 in. for this

column size is substantial. However, it is believed that if the weld size increased even more, a higher load would still be obtained. A comparison of the results when using these two weld sizes is shown in Figure 7.4-4. The contours are specified to range to the ultimate stress 82.4 ksi for the weld. Anything grey represents stress greater than 82.4 ksi. In Figure 7.4-4(a), uniform weld stresses exist across the column specimen flange when a 1/4 in. weld is modeled and limited flange bending is identified. However, Figure 7.4-4(b) shows that flange bending occurs more significantly at the maximum load when a 7/8 in. weld is modeled and weld stresses near the center of the weld are much higher than weld stresses towards the tips of the flanges.

a) W24X131 with 1/4 in. welds

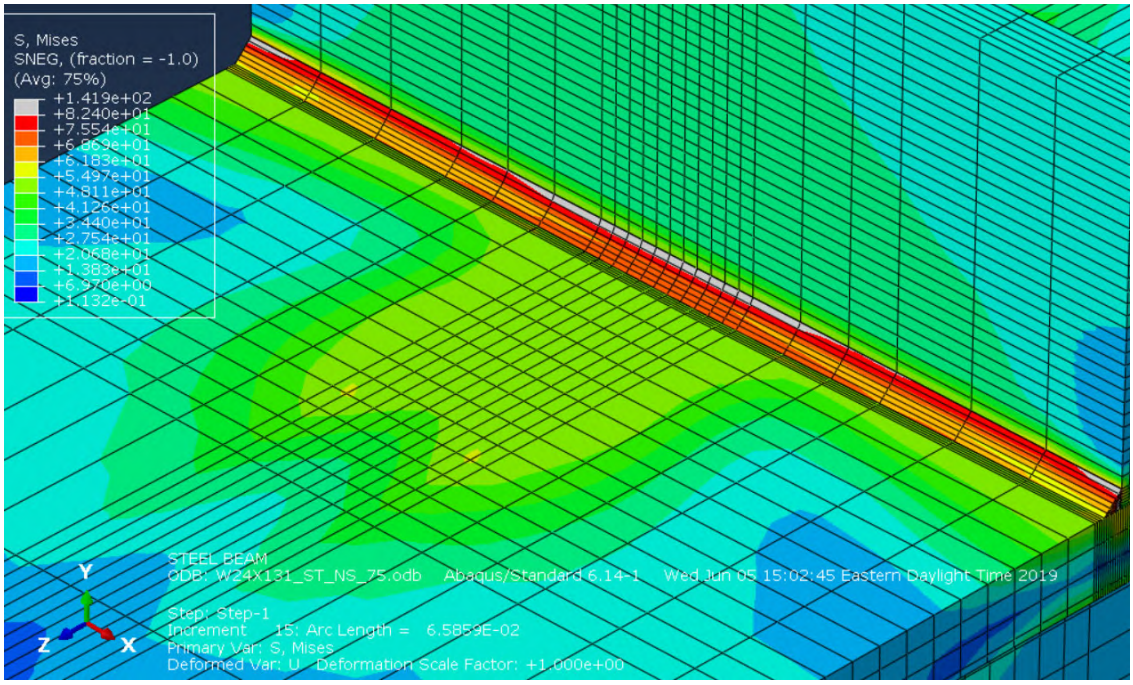

b) W24X131 with 7/8 in. welds

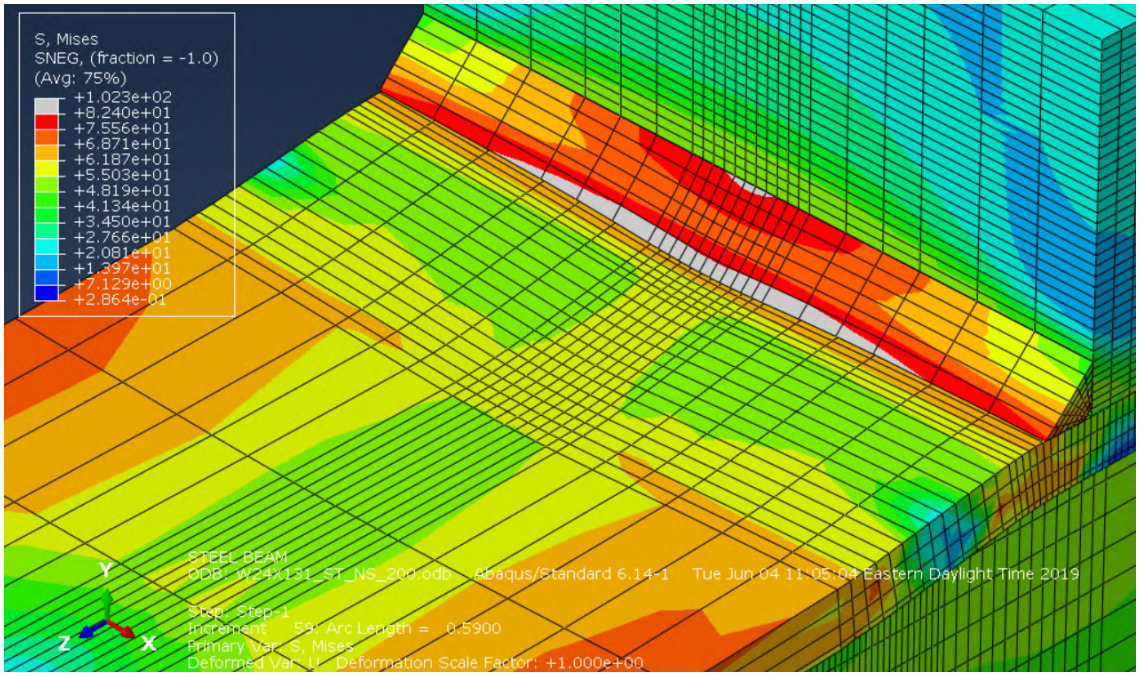

Figure 7.4-4: Weld stress distribution at failure for W24X131 analytical specimens

Fundamentally, the results in Table 7.4-1 show that as weld size increases, the capacity of the column specimen increases as well. This is expected but the trend shows a fundamental flaw with the flange bending equation. For instance, for a W14X68 column specimen, the theoretical capacity for flange bending was computed as 162 kips, which was slightly greater but compared well to the analytical test capacity of 159.4 kips when 1/4 in. welds were modeled. However, 162 kips is much lower than the analytical test capacities of 259.5 kips and 347.9 kips when 9/16 in. and 7/8 in. welds are modeled, respectively. Therefore, the theoretical capacity for flange bending is significantly exceeded even though the *effect* of flange bending still has an influence on the weld failure.

When the weld strength should control, flange bending influences the results even though there is nothing in the equations that would identify that. For instance, when the W24X131 column specimen was modeled using 1/4 in. welds, the theoretical capacity for flange bending was calculated as 288 kips, which does not control over the modified weld capacity of 259.6 kips. However, the capacity of the analytical model was 215.6 kips, which is less than both theoretical capacities. The reduction in weld strength is 17% *due to the influence* of flange bending but nothing in the AISC specification (2016) identifies this reduction. Therefore, following AISC (2016) would be unconservative.

The *FB/CAP* ratios from Table 7.4-1 are shown graphically for the analytical specimens in Figure 7.4-5. The results in Figure 7.4-5 further demonstrate that the flange bending equation alone does not accurately predict the capacity of the column specimens. When a weld size of 7/8 in. is modeled, the flange bending equation underestimates the capacity significantly when the column size is a W14X176 or smaller. When a weld size of 9/16 in. is modeled, the equation underestimates the capacity significantly when the column size is a W24X131 or smaller. In other cases, the capacities are comparable or the flange bending equation overestimates capacity. Again, if a relatively small weld size is used, it is intuitive to assume the weld size governs and values higher than 1.0 are expected for the *FB/CAP* ratio.

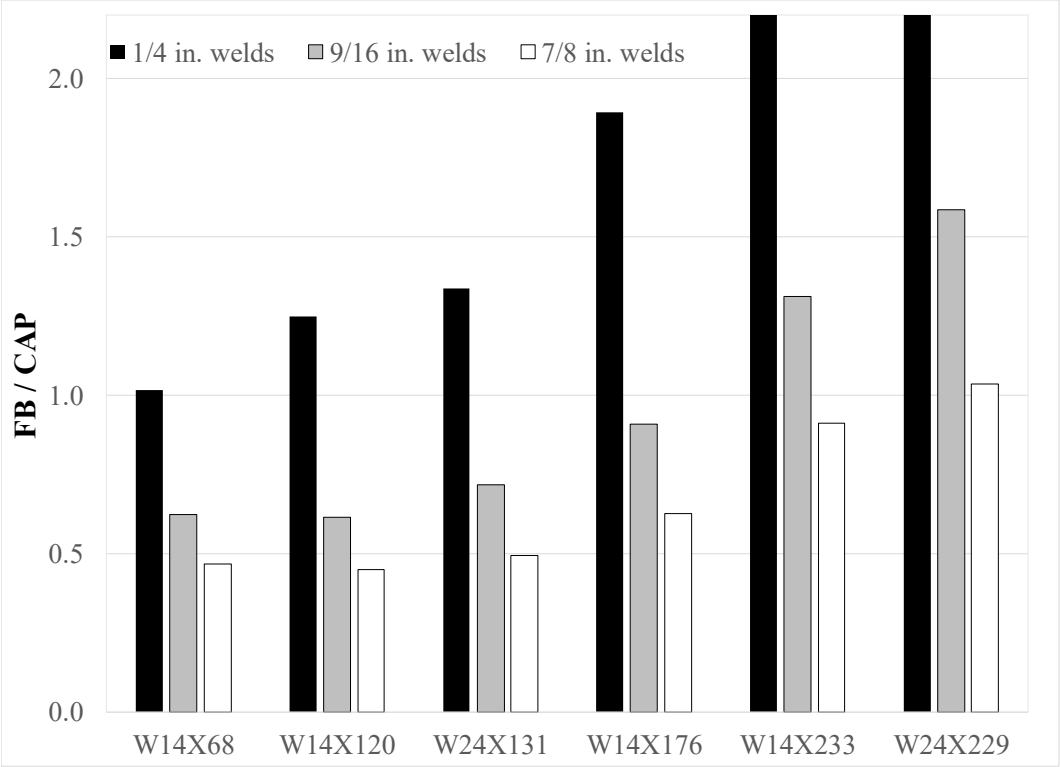

Figure 7.4-5: Comparisons of FB/CAP ratios for different weld thickness

Figure 7.4-6 shows ratios for the test capacity divided by the modified weld capacity. These ratios are opposite of the WC/CAP ratios given in Table 7.4-1. Both experimental results with 3/8 in. welds and analytical results with 1/4 in. welds are shown with black bars. The members are ordered by increasing flange thickness and other than the W14X68 vs. W14X120, they are also ordered by decreasing flange slenderness, $b_f / 2t_f$. In general, if the ratio is close to 1.0, then the weld stresses are assumed uniform across the width of the column flange when failure occurs. The research team has decided there is not enough experimental and analytical data at this time to establish recommended design procedures but the results in Figure 7.4-6 yield the following observations.

- For the experimental results, due to the presence of significant flange bending, weld failure generally occurs prior to the weld stresses becoming uniform.
- A weld thickness of 7/8 in. is still not substantial when a W24X229 column specimen is analyzed. Therefore, weld sizes that exceed 7/8 in. are appropriate for studying larger column sections.

- As weld size decreases, the weld stresses become more uniform at failure. However, all weld strengths are influenced by flange bending as no ratio is equal to 1.0.
- As flange thickness increases and flange slenderness decreases, the weld stresses become more uniform.
- Flange slenderness, $b_f / 2t_f$, is a variable in the studies combined with flange thickness. The flange thickness of the W24X229 and W14X233 column specimens are very similar but the results of W24X229 show more uniform stresses, which is a reflection of differences in slenderness. In addition, stresses in the W14X120 analytical model appear less uniform when 1/4 in. welds are used in comparison to stresses in the W14X68 model. The flange thickness of the W14X120 is noticeably bigger but the slenderness is larger as well.

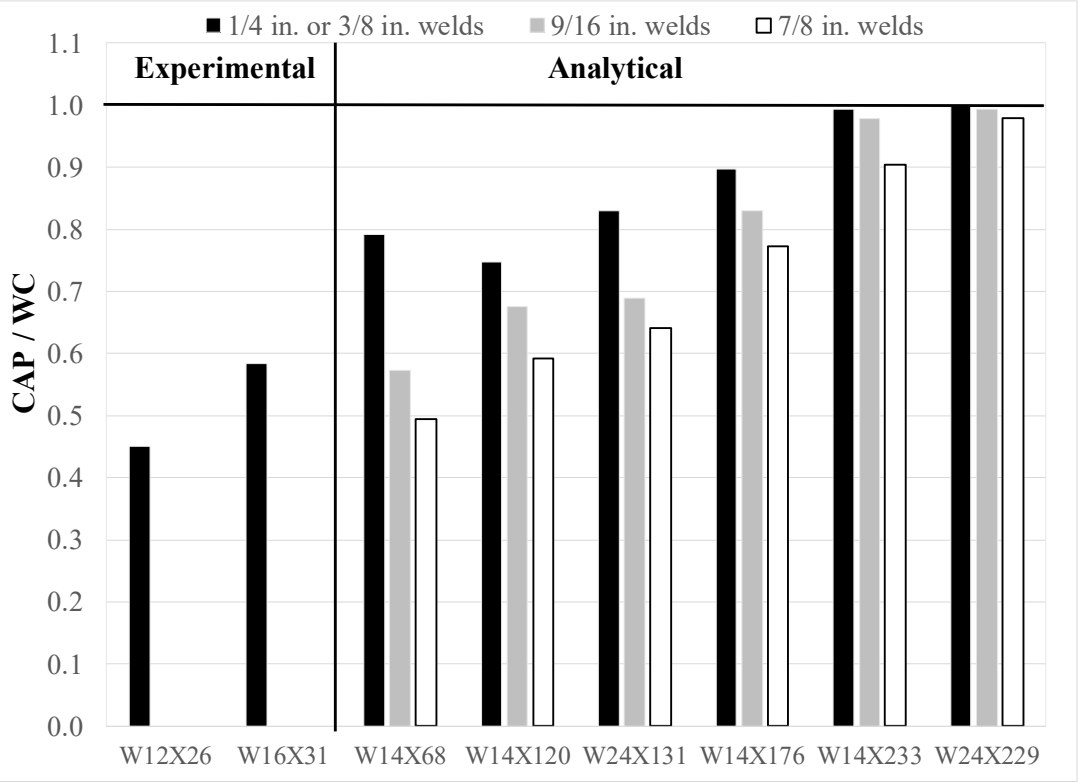

Figure 7.4-6: Comparisons of CAP/WC ratios for different weld thickness

Figure 7.4-6 provides the most influential evidence regarding the invalidity of the flange bending equation. In summary, the behavior of the finite element models clearly demonstrate that the final capacity for tension concentrated loads cannot be predicted from either the weld capacity or the

flange bending capacity alone. Instead, it is intuitive than any method used in practice should consider the two variables simultaneously. For instance, one possible procedure for estimating the true capacity when subjected to single tension is to compute the theoretical weld capacity and consider reduction factors that account for flange dimensions. More analytical and possibly experimental studies need to be performed to establish such a procedure.

One major limitation of the studies presented for single tension tests is that only fillet weld connections were investigated. However, moment connections often include partial or complete joint penetration groove welds. Finite element models of tension tests need to be developed that have weld material right at the end of the plate material and a review of the stress distribution in the plate and weld material should be studied as flange bending occurs for different column sections. Therefore, further studies are more diverse than just adding more column sizes and weld thickness.

7.5 Concentric Stiffener Studies

This section analyzes the effective stiffener capacity for concentric stiffeners. The results analyzed in this section are limited to analytical and experimental results previously presented in Chapters 7 and 3, respectively. No additional studies were performed to emphasize the results discussed in this section but this section justifies that more studies should be performed in future research.

All results for effective stiffener capacity and for concentric stiffeners only are provided in Table 7.5-1 for single compression (SC) tests, double compression (DC) tests, and single tension (ST) tests. The experimental results are shaded in the table. The table includes the weld size for single tension tests only. The thickness of the stiffener is provided along with the width of the stiffener, b_s, and the yield stress of the stiffener, F_{y_stiff}. As explained in Chapter 3, the stiffener yield stress for the experimental investigations was assumed 39 ksi. In the analytical models, all material including stiffeners were assumed to have a yield stress of 50 ksi. The width of an individual stiffener at the top flange, b_s, was calculated assuming that all stiffeners were connected at the web, corner clipped to connect to the flange and extended to the extreme edges of the flange. Different corner clips were used for the experimental and analytical models. In the experimental investigations, the corners were clipped 1/2 in. in all cases and the width of the stiffeners is computed per Equation 7-2. In the finite element models, the corners were assumed clipped to the edge of the fillet region and therefore, the width of the stiffener is calculated using Equation 7-3. The dimensions b_f, t_w, and k_1 in Equations

7-2 and 7-3 were taken from the AISC Steel Construction Manuel (AISC, 2017). Note, in Table 7.5-1, 'b_{sfull}' represents the full width of the stiffener without the corner clip and is used for the slenderness calculation discussed later.

$$b_s = b_f / 2 - t_w / 2 - ½ \quad (7\text{-}2)$$

$$b_s = b_f / 2 - k_1 \quad (7\text{-}3)$$

Table 7.5-1: Effective stiffener results for all column specimens with concentric stiffeners

Column Size	Loading	w (in)	t_s (in)	b_s (in)	F_{y_stiff} (ksi)	b_{sfull} (in)	b_s / t_s	λ_r	Theor. Stiff. Cap (k)	Effect. Stiff. Cap. (k)	Ratio
W16X31	SC	NA	3/8	2.13	39	2.63	7.01	15.27	62.2	64.4	1.03
W12X26	SC	NA	3/8	2.63	39	3.13	8.35	15.27	76.9	70.1	0.91
W10X19	SC	NA	1/4	1.39	39	1.89	7.54	15.27	27.0	33.7	1.25
W10X39	SC	NA	3/8	3.34	39	3.84	10.23	15.27	97.6	67.1	0.69
W16X31	DC	NA	3/8	2.13	39	2.63	7.01	15.27	31.1	43.5	1.40
W12X26	DC	NA	3/8	2.63	39	3.13	8.35	15.27	76.9	134.0	1.74
W10X19	DC	NA	1/4	1.39	39	1.89	7.54	15.27	27.0	101.5	3.76
W24X131	SC	NA	3/8	5.33	50	6.15	16.39	13.49	199.7	235.5	1.18
W24X229	SC	NA	3/8	5.24	50	6.07	16.19	13.49	196.4	130.0	0.66
W14X68	SC	NA	3/8	3.94	50	4.79	12.78	13.49	147.7	103.5	0.70
W14X120	SC	NA	3/8	5.85	50	7.06	18.81	13.49	219.4	97.9	0.45
W14X176	SC	NA	3/8	6.23	50	7.44	19.83	13.49	233.4	94.5	0.40
W14X233	SC	NA	3/8	6.20	50	7.42	19.77	13.49	232.5	91.0	0.39
W24X229	SC	NA	3/4	5.24	50	6.07	8.09	13.49	392.8	304.6	0.78
W14X233	SC	NA	3/4	6.20	50	7.42	9.89	13.49	465.0	264.5	0.57
W24X131	DC	NA	3/8	5.33	50	6.15	16.39	13.49	199.7	144.4	0.72
W24X229	DC	NA	3/8	5.24	50	6.07	16.19	13.49	196.4	108.1	0.55
W14X68	DC	NA	3/8	3.94	50	4.79	12.78	13.49	147.7	172.7	1.17
W14X120	DC	NA	3/8	5.85	50	7.06	18.81	13.49	219.4	122.1	0.56
W14X176	DC	NA	3/8	6.23	50	7.44	19.83	13.49	233.4	72.6	0.31
W14X233	DC	NA	3/8	6.20	50	7.42	19.77	13.49	232.5	0.0	0.00
W24X131	DC	NA	3/4	5.33	50	6.15	8.20	13.49	399.4	421.8	1.06
W24X229	DC	NA	3/4	5.24	50	6.07	8.09	13.49	392.8	437.3	1.11
W14X68	DC	NA	3/4	3.94	50	4.79	6.39	13.49	295.3	374.6	1.27
W14X120	DC	NA	3/4	5.85	50	7.06	9.41	13.49	438.8	377.8	0.86
W14X176	DC	NA	3/4	6.23	50	7.44	9.91	13.49	466.9	368.0	0.79
W14X233	DC	NA	3/4	6.20	50	7.42	9.89	13.49	465.0	275.9	0.59
W24X131	ST	9/16	3/8	5.33	50	6.15	16.39	13.49	199.7	139.7	0.70
W24X229	ST	9/16	3/8	5.24	50	6.07	16.19	13.49	196.4	1.3	0.01
W14X68	ST	9/16	3/8	3.94	50	4.79	12.78	13.49	147.7	65.2	0.44
W14X120	ST	9/16	3/8	5.85	50	7.06	18.81	13.49	219.4	171.5	0.78
W14X176	ST	9/16	3/8	6.23	50	7.44	19.83	13.49	233.4	109.1	0.47
W14X233	ST	9/16	3/8	6.20	50	7.42	19.77	13.49	232.5	12.3	0.05
W24X131	ST	7/8	3/8	5.33	50	6.15	16.39	13.49	199.7	190.3	0.95
W24X229	ST	7/8	3/8	5.24	50	6.07	16.19	13.49	196.4	12.6	0.06
W14X68	ST	7/8	3/8	3.94	50	4.79	12.78	13.49	147.7	88.1	0.60
W14X120	ST	7/8	3/8	5.85	50	7.06	18.81	13.49	219.4	65.1	0.30
W14X176	ST	7/8	3/8	6.23	50	7.44	19.83	13.49	233.4	139.0	0.60
W14X233	ST	7/8	3/8	6.20	50	7.42	19.77	13.49	232.5	82.6	0.36

Theoretical stiffener capacities are calculated in Table 7.5-1 assuming the controlling limit state is compression or tension yielding at the top flange. This approach was used by the PI during years in practice. However, this approach may be conservative for some scenarios and unconservative for other scenarios. Concerns are as follows:

- The stress in the stiffener can reach stresses beyond the yield stress and therefore, withstand/share more force than assumed.
- The approach does not consider the weld strength from the stiffeners to the flange and web. It is assumed welds are present that meet or exceed the strength of the plate.
- If yielding is the controlling limit state, it may be more accurate to use the entire width of the stiffener as opposed to the reduced width after subtracting out the corner clip dimension.
- For compression tests, the stiffeners may bear on the flanges, depending on how well the stiffener fits within the flanges and a bearing stress capacity is higher than a yielding capacity.
- In compression tests, the stiffener may buckle prior to developing the yield stress in the stiffener. The slenderness of the stiffener is shown in Table 7.5-1 as b_s / t_s.

The theoretical capacity of the stiffener is computed per Equation 7-4. As discussed in Chapter 3, members of the AISC Research Advisory Committee previously noted that using Equation 7-4 may not be appropriate for stiffeners subjected to compression. Instead, it was recommended to use the AISC Specification, Section J7 (AISC, 2016) assuming a bearing limit state. However, after reviewing the differences in Section J7, the research team still feels it is appropriate to use Equation 7-4 since stiffener capacity is associated with sharing the load. As the web yields, the vertical strain in the web and stiffeners will be similar. Note that for the experimental W16X31 column specimen subjected to double compression, the value of '2' in Equation 7-4 is omitted since a stiffener was present on one side only as opposed to two sides.

$$R_n = 2 \, x \, F_{y\_stiff} \, x \, b_s \, x \, t_s \qquad (7\text{-}4)$$

For most compression tests with concentric stiffeners, the stiffeners showed signs of buckling when the maximum load was reached. Failure mechanisms of the column specimens were specified as stiffener buckling since once it occurred, there was a sudden decrease in load. Stiffener buckling

is shown for an experimental result in Figure 7.5-1 (W16X31-SC-E0) and an analytical result in Figure 7.5-2 (W14X176-SC-E0). The contours in Figure 7.5-2 show resultant displacement.

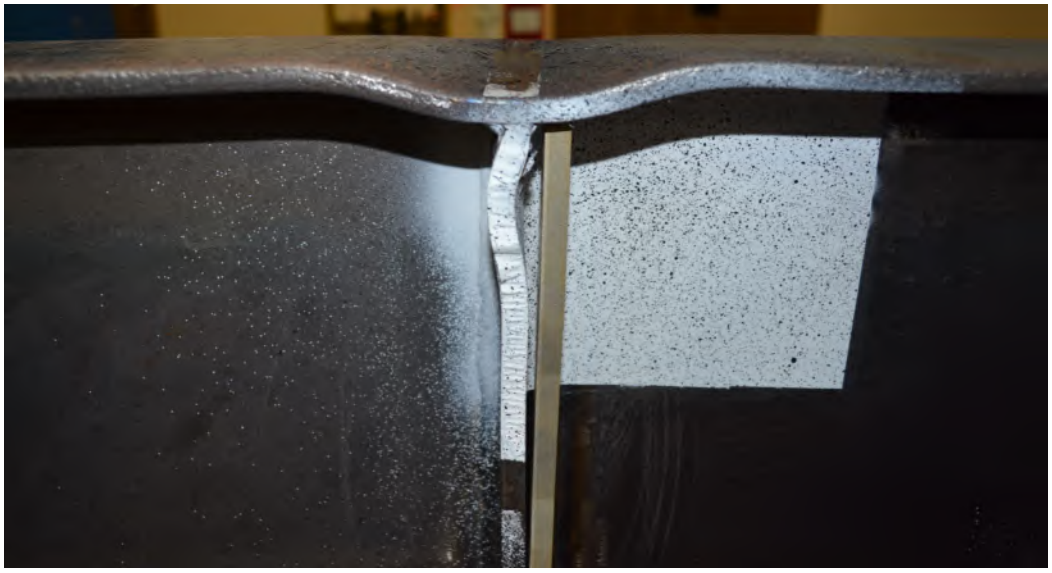

Figure 7.5-1: Local buckling of front stiffener of W16X31-SC-E0

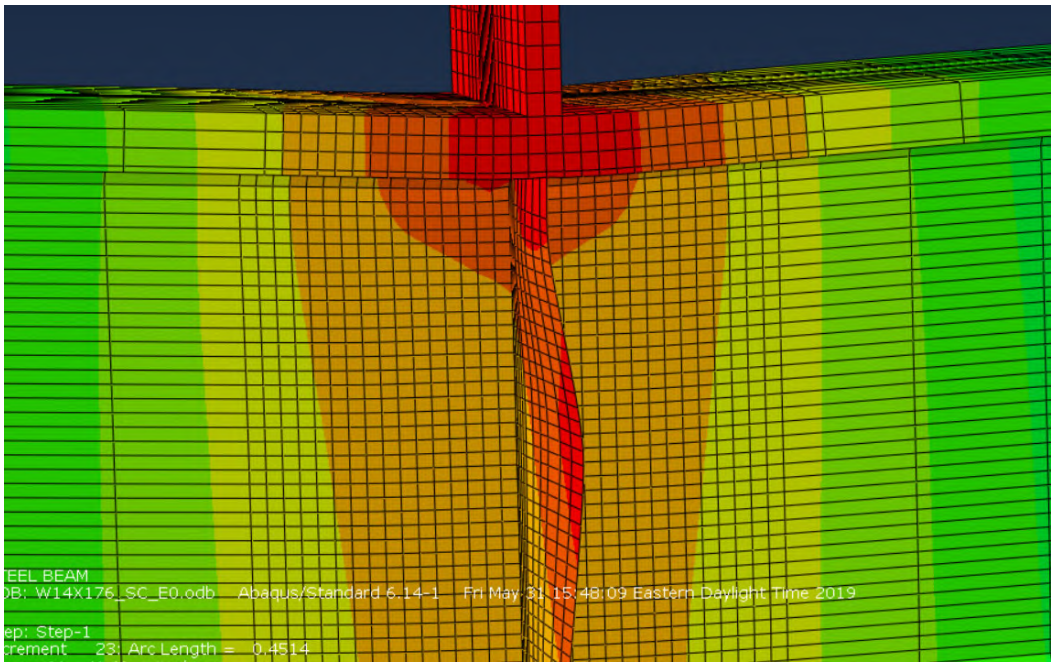

Figure 7.5-2: Local buckling of stiffener in analytical model of W14X176-SC-E0

In the experimental results, inelastic stiffener buckling was witnessed. This was evident from mill scale peeling off and verified with DIC results. In designing stiffeners for a maximum load based on yield stress, it is important to ensure that local buckling would not occur prior to yielding.

To do this using the AISC specification (2016), the slenderness ratio of the stiffener, λ_s, should not be greater than a slenderness limit, λ_r, which represents the maximum slenderness prior to elastic bucking of a compression element. This comparison is depicted in Equation 7-5. The limit for λ_r is recommended for plate elements subjected to axial compression and supported on one edge per Table B4.1a from the AISC specification (AISC, 2016).

$$\lambda_s = b_{sfull} / t_s \leq \lambda_r = 0.56*sqrt(E / F_{ystiff}) \quad (7\text{-}5)$$

Where:

λ_s = actual slenderness of the stiffener

λ_r = slenderness limit to ensure that elastic local bucking of the stiffener does not occur

b_{sfull} = full width of stiffener from face of web to tip of column specimen flange

It is more appropriate to use 'b_{sfull}' as opposed to 'b_s' for performing the slenderness check. The check is then more conservative and buckling is a mode of failure that occurs due to compressive stresses that develop over a length and not just at the locations of the corner clip. The compressive stresses in the stiffener are assumed fairly uniform through the depth of the stiffener for double compression tests and assumed to dissipate through the depth for single compression tests and therefore, it is not clear at this time if the slenderness limit per Equation 7-5, λ_r, is appropriate for single compression tests.

Slenderness values, λ_s, higher than the slenderness limit, λ_r, are shaded in Table 7.5-1 for compression tests only. As shown, all analytical column specimens with 3/8 in. stiffeners have "slender" stiffeners except for when a W14X68 column specimen is modeled. This would suggest that elastic stiffener buckling would occur prior to yielding and Equation 7-4 should not be utilized to predict the effective stiffener capacity. However, the results of the analytical models usually show that yielding still occurs prior to buckling. Figure 7.5-3 shows the normal (compressive) stresses in the stiffeners prior to the maximum load for the W14X176 column specimen subjected to single compression (a) and double compression (b). The contours are normalized to the yield stress of 50 ksi and anything black indicates a compressive stress greater than 50 ksi. The results clearly demonstrate that yielding is achieved in the stiffeners prior to buckling.

(a) W14X176-SC-E0 (b) W14X176-DC-E0

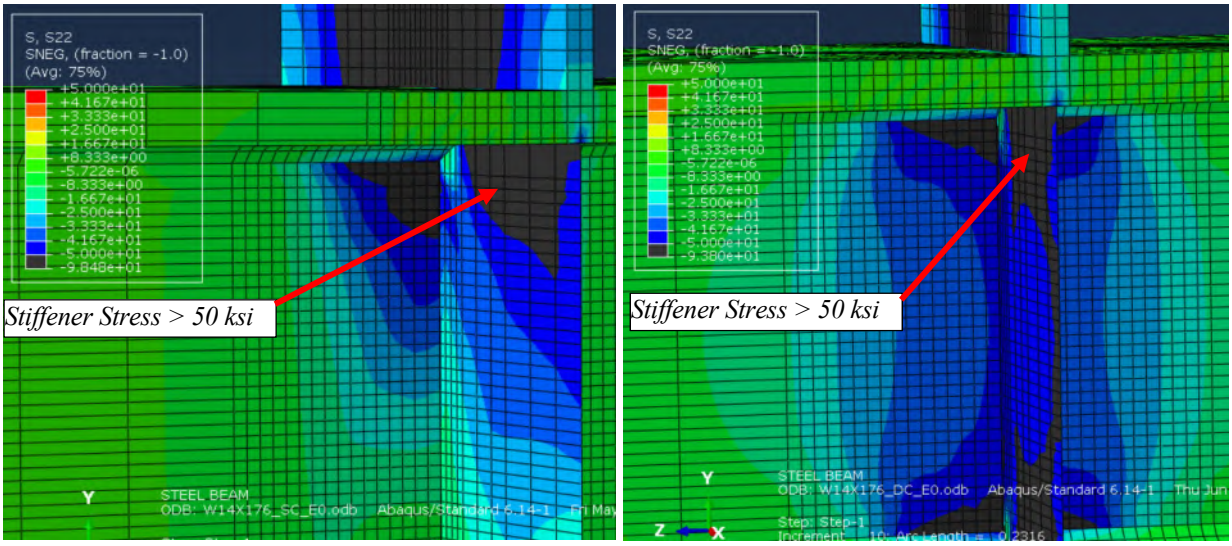

Figure 7.5-3: Stresses in stiffeners for W14X176 column specimens

In Table 7.5-1, the primarily test result is the effective stiffener capacity which is shown under the column labeled "Effective Stiff Cap". This is equal to the capacity of the test with concentric stiffeners minus the capacity of the corresponding test with no stiffeners. It is unclear how well this reflects the true capacity of the stiffeners since the true capacity is defined by a yield load or buckling load of the stiffener itself. However, in practice, stiffeners are designed for the difference between the applied load and the lowest concentrated load limit state. Therefore, the difference in the analytical results is related to design procedures and identifies what would be achieved if the stiffeners were added.

Table 7.5-1 provides a ratio for the effective stiffener capacity vs. the theoretical stiffener capacity. This will be further referred to as the *ESC/TSC* ratio. If the *ESC/TSC* results are close to 1.0, then Equation 7-4 provides a good estimate of the capacity. Several observations are identified from the results in Table 7.5-1 and described in the following paragraphs.

For the experimental results of single compression tests, the theoretical stiffener capacity compares well with the effective stiffener capacity. The ratios in Table 7.5-1 are between 0.7 and 1.25. However, no specific trends can be interpreted from the four results. In smaller sections, it is intuitive to assume that the stiffeners share more load since their relative stiffness increases in comparison to the web of the column specimen. The W10X39 column specimen is the most compact

of the four. The results of more compact or "stockier" sections are more influenced by the effects of flexure and shear for the single compression tests. Figure 3.7-11 provided the load-displacement results of all four W10X39-SC column specimens. The specimen with concentric stiffeners appeared to withstand significant flexural deformations prior to stiffener buckling. The maximum moment at midspan was equal to 248 kip-ft (P_{max} *x 5 ft / 4*) and the plastic moment, M_p, for the column specimen is equal to 235 k-ft (AISC, 2017). In this case, the concentric stiffeners dissipated the concentrated load effect and allowed the column specimens to reach design moments. Other column sections from Figure 3.7-11 failed at loads lower than the plastic moment due to the concentrated load effect. Therefore, the concentric stiffeners were beneficial but the true effective stiffener capacity is inconclusive.

From Table 7.5-1, the *ESC/TSC* results for experimental double compression tests show that stiffeners significantly enhance the concentrated load capacities. This was already discussed in detail in Chapter 3. It is believed that the stiffeners not only share the load but also brace the column web, disallowing crippling and therefore, the web is allowed to achieve a much higher stress while the stiffeners reach high stresses prior to buckling as well. It is also believed that as the stiffeners brace the web, yielding spreads in the web at a distance greater than the assumed width for the web local yielding limit state ($5k + l_b$).

For *analytical single compression tests* and when 3/8 in. stiffeners were modeled, the effective stiffener capacities compare reasonably well for three of the column specimen sizes and do not compare well for the larger W14 column sections. Instead, the *ESC/TSC* results are much lower than 1.0. These results are shown graphically in Figure 7.5-4 along with results using 3/4 in. stiffeners for two column specimen sizes. As described in Section 6.5, the results of the larger column sections were significantly influenced by the effects of shear and flexure. Studies were performed in Section 6.5.6 to evaluate the unsupported length and the results appeared to be more influenced by shear in lieu of flexure. The results of the larger column specimens are similar to the results of the W10X39 experimental column specimen in that the maximum load is not obtained from the concentrated load effect alone and therefore, the true concentric stiffener capacity cannot be measured. However, when larger stiffeners (3/4 in.) were utilized, the capacity of the column specimen did improve slightly, which is also depicted in Figure 7.5-4. This contradicts the conclusion that a capacity is not

influenced by the concentrated load effect. It is assumed that for the larger column specimens studied that the 3/8 in. stiffeners partially allow the specimen to reach its ultimate flexural/shear capacity and 3/4 in. stiffeners allow the specimen to achieve this capacity.

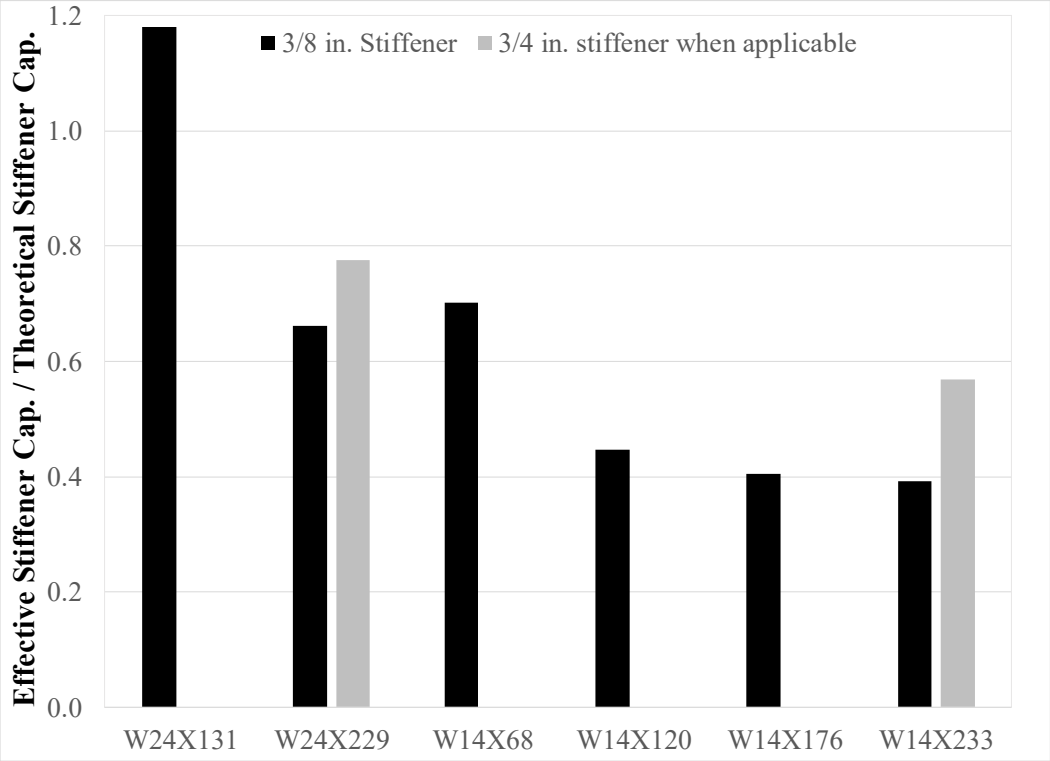

Figure 7.5-4: Effective stiffener capacities vs. theoretical stiffener capacities for SC tests

Table 7.5-1 shows that the *ESC/TSC* results are sporadic for the double compression analytical models. However, there are trends found in the data. As the section size gets bigger, the ESC/TSC ratios gets smaller. The results are shown graphically when using 3/8 in. stiffeners and 3/4 in. stiffeners in Figure 7.5-5. The results when using a 3/4 in. stiffener are always higher and closer to 1.0 and are therefore, more favorable. Therefore, the slenderness of the stiffener is a factor even though the finite element results show that stresses exceeding the yield stress are achieved when using 3/8 in. stiffeners. It is hypothesized that an optimum stiffener size can be derived for all column specimens that would achieve the theoretical effective stiffener capacity for all double compression tests.

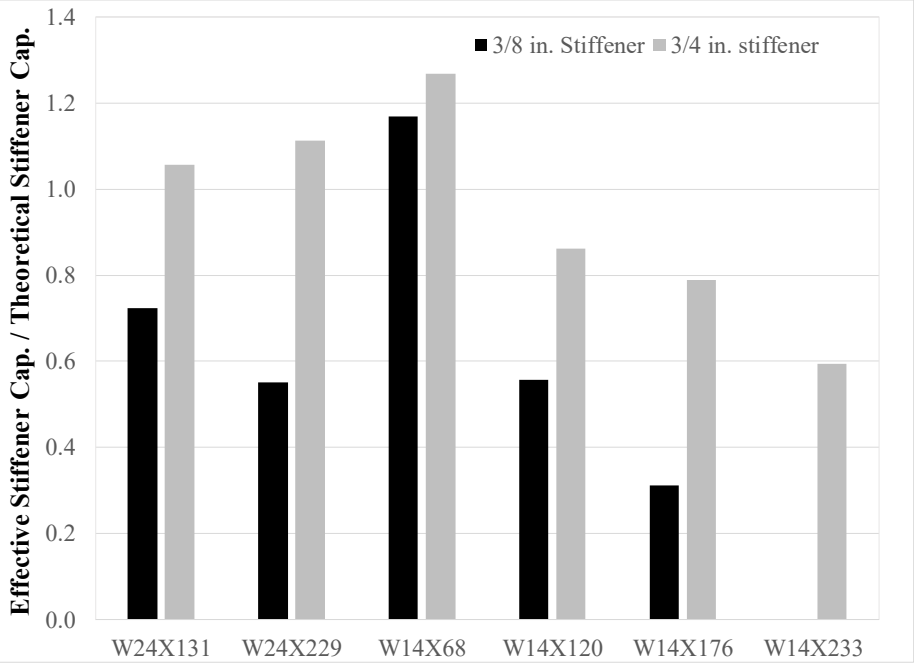

Figure 7.5-5: Effective stiffener capacities vs. theoretical stiffener capacities for DC tests

The most surprising result for the double compression tests, which was originally found in Table 6.6-2 is that when the W14X233 column specimen is analyzed with 3/8 in. stiffeners, the column specimen reaches a lower capacity that the corresponding column specimen without stiffeners. Under loading, the stiffeners share the load, yield and then stiffener buckling occurs instantaneously causing a drop in load prior to the web of the column specimen being subjected to significant stresses. When no stiffeners are used, the column specimen achieves significant stresses prior to web compression buckling occurring. Per Table 7.5-1, the stiffeners are calculated as slender when 3/8 in. stiffeners are used. However, when 3/4 in. stiffeners are used, they are not slender and the load does increase resulting in a positive effective stiffener capacity. Figure 7.5-6(a) shows the stress state of the column specimen without stiffeners when the maximum load is obtained in the analytical model. Figure 7.5-5(b) shows the stress state of the column specimen with 3/8 in. stiffeners when stiffener buckling is first noticed. In both cases, the contours show the normal (compressive) stresses in the vertical direction and are normalized to the yield stress of 50 ksi. Anything black represents a compressive stress higher than 50 ksi. When 3/8 in. stiffeners are utilized and buckle, the web of the column specimen is not as engaged as the condition without stiffeners. This comparison further demonstrates that although the yield stress does develop in 3/8 in. stiffeners, local buckling is still an issue and the stiffeners are detrimental to the concentrated load capacity of this column specimen.

(a) W14X233-SC-NA

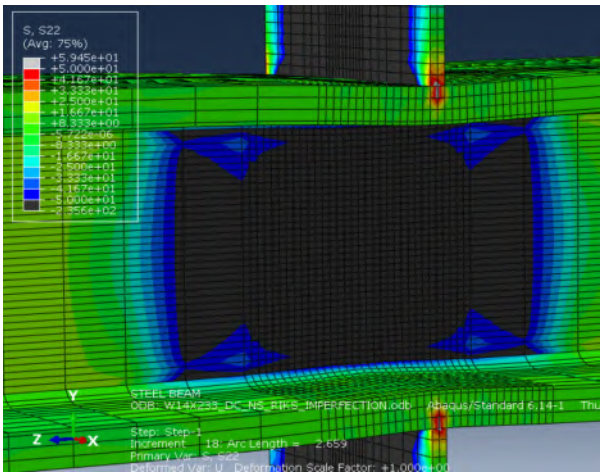

(b) W14X233-SC-E0 w/ 3/8 in. stiffeners

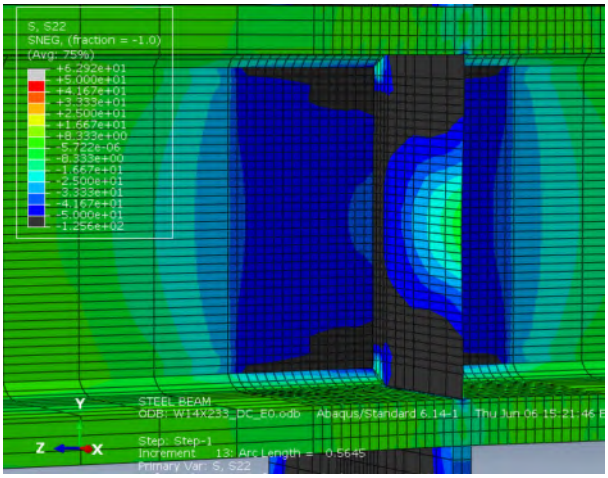

Figure 7.5-6: Stress distribution in W14X233 without stiffeners and with 3/8 in. stiffeners

In general, the results of the double compression analytical tests do not relate particularly well to the experimental results with respect to the ESC/TSC ratio. It is believed that for the analytical models that the webs are relatively thick in comparison to the stiffener dimensions and therefore, the stiffeners do not share the load as much. Regardless, the results in Figure 7.5-5 are inconclusive at this time and more studies are required to identify the true concentric stiffener capacity for various column sizes when subjected to double compression.

For the single tension tests, the effective stiffener capacity is not influenced by compression buckling but the true effective stiffener capacities are inconclusive since the weld capacity from the loading plate to the top flange was always found to control the results. The ESC/TSC results for the single tension tests are shown graphically in Figure 7.5-7. All ratios of effective stiffener capacity vs. theoretical stiffener capacity are less than 1.0. This suggests that weld failure, influenced by flange bending, always occurs prior to the stiffeners fully engaging. As weld size gets larger, the stiffeners are more engaged since the applied load is higher as well. In general, as weld size gets larger, the *ESC/TSC* results become closer to 1.0 as well.

In other cases, when the weld size is smaller, the column section without stiffeners was already adequate to develop near the full weld capacity, which resulted in low effective stiffener capacities, simply because they were not engaged significantly. Regardless, more studies need to be performed to establish the true effective stiffener capacity for tension tests. These studies will need to be performed without welds from the loading plate to the column flange or the welds need to be modeled

as elastic only. It is believed the theoretical stiffener capacity per Equation 7-4 is indeed adequate for tension concentrated load tests and therefore, only limited studies are required for verification. It may also be beneficial to perform these tests as double tension tests since flexure and shear stresses will not influence the results.

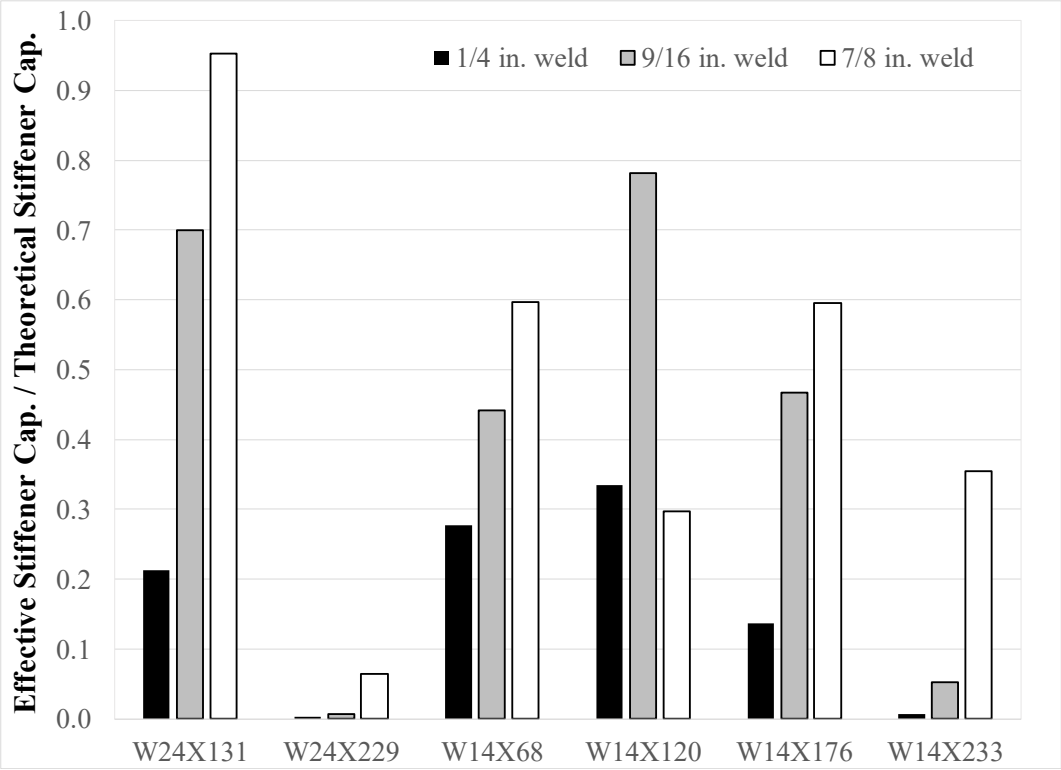

Figure 7.5-7: Effective stiffener capacities vs. theoretical stiffener capacities for ST tests

7.6 Further Development for Limit State Calculations

The results presented in this chapter reveal that the theoretical equations per the limit states associated with concentrated loads need to be evaluated in more detail. It is believed that this can only be accomplished with an additional comprehensive analytical and experimental research project that focuses on the limit states and the theoretical equations for eccentric stiffener capacity.

Analysis, observations and conclusions presented in this chapter are limited to the experimental and analytical investigations that were primary utilized to study the influence of eccentric stiffeners. A summary of the issues encountered are as follows:

1. Flange bending does occur when a tension concentrated load is applied to a column and influences the connection capacity. However, the equation presented in AISC (2016) for

flange bending underestimates the true capacity when the weld size is "substantial". The true capacity of the column specimen when subjected to tension concentrated loads needs to consider the effects of bending and the weld properties simultaneously. In addition, a new flange bending limit needs to be established when groove welds are used in lieu of fillet welds.

2. The results of double compression tests generally have capacities significantly higher than predicted for web compression buckling. It appears that the equations for web compression buckling are underdeveloped. Web compression buckling may occur in multiple half sine waves, which do not appear to be considered in the theoretical development of the equation. In addition, web compression buckling equations need to consider the width of the web subjected to compression stresses as currently, the length of bearing does not influence the theoretical capacity.

3. Test results generally indicate that capacities are higher than the theoretical equations for web local yielding. Web local yielding occurs but the column specimen has much more reserve capacity as yielding continues to spread longitudinally in the web under further loading and stresses exceed the yield stress when failure occurs. Large deformations are not desirable but new equations are recommended based on an amount of deformation that is acceptable.

4. Available equations for computing the eccentric stiffener capacity for concentric stiffeners are underdeveloped. It is believed that Equation 7-4 is adequate for single tension tests but some additional studies are recommended to verify this. However, it appears that stiffener buckling significantly influences the capacity for compression tests and studies need to be performed to identify an optimum stiffener thickness for various column sections to ensure that the web of the column specimen can adequately share the load with the stiffeners.

Previous work performed by other researchers have been promising in the development of the limit state equations. However, modern technology and in particular, the finite element method can really enhance understanding of the limit states.

This research project has shown that the calculations for the theoretical limit state of web local crippling compare well with the analytical and experimental results when web crippling occurs. This

is assuming that the web is relatively slender and therefore, studying this limit state in more detail is not recommended in comparison to other limit states. When larger column specimens were evaluated analytically, web crippling did occur but only after excessive yielding occurred first. The failure mode was described as inelastic web local crippling and the maximum load obtained analytically was less than that predicted per the theoretical equation.

The most important variable that needs to be studied in more detail is the section size. The analytical investigations presented in this research focused on only W24 and W14 members. However, column sizes and column sizes can still be much larger or have vast dimensions. Concentrated load limit states also have a major influence on plate girder design, which needs to be evaluated specially.

Further studies for Item 1 listed above are complicating. The results of this research have shown that the fillet weld size has a significant influence on the load capacity results when single tension tests are performed. A large comprehensive analytical test matrix will need to be established to develop relationships between weld size, flange dimensions, and concentrated load capacity. In addition, more tests need to be performed experimentally to verify the analytical results. One limitation from the research performed on single tension tests is that only fillet welds from the loading plate to the top flange were tested and modeled. However, it is common in moment connections to design with partial and complete joint penetration groove welds. These boundary conditions would influence the results and the relationships depicted in this research for single tension. Therefore, the test matrix to comprehensively study flange bending is vast.

For studying Item 2 listed above, the results of the experimental double compression tests are inconclusive since the load did not appear to completely transfer to the bottom reaction plate and web crippling near the loading plate always controlled for the failure mechanism. The analytical models simulated a through force and showed that a form of web compression buckling does occur. As mentioned, however, the limit state is underdeveloped at this time. Equations by Salmon and Johnson (1996) show that a buckling mode is influenced by the side and end boundary conditions and the unsupported length. However, there are several questions involving the buckling capacity for concentrated loads with respect to the boundary conditions, effective width, and the possibility of inelastic web compression buckling as opposed to elastic web compression buckling. In general,

the limit state should be studied significantly using finite elements in a comprehensive research project. Another factor not found in the current web compression buckling equation but found in other concentrated load limit states is the effect of bearing length. It is intuitive that if the plate is oriented longitudinally along the column section that the compression zone for buckling will be wider.

For studying Item 3, the spread of yielding needs to be studied in more detail with a relation to the amount of deformation that occurs under a given force. Models need to be developed for loading with a plate oriented longitudinally along the length of the column specimen and for loading from a horizontal flat plate. These loading conditions may significantly influence the results.

For studying Item 4, the design of web stiffeners is an additional variable that needs to be studied in more detail when concentrated loads are applied. This study will need to be performed after the concentrated load limit states have been further developed. As stated in this report, stiffeners not only share the load but also prevent a buckling mode from occurring in the web. However, the stiffeners themselves may buckle and be detrimental to the concentrated load effect. A large comprehensive test matrix will need to be established for several column sizes, multiple stiffener thickness, multiple weld sizes, and different loading conditions.

In future research, all limit states should be reevaluated for end loaded conditions as well. The limit states seem to be underdeveloped for end load conditions, particularly if the capacity is reduced by 50% in some cases with no transitional relationships. Another confusing aspect from the AISC (2016) limit states is the reduction of capacity for web local yielding when the applied load is within '*d*' from the end. Yet, there is a reduction for web local crippling and web compression buckling if the load is within '*d/2*' from the end (allows it to be closer for full capacity). It seems reasonable to assume that the full width for web local yielding should be used if the applied load is farther than '*d/2*' from the end since 2.5k is generally less than '*d/2*'.

CHAPTER 8: SUMMARY, CONCLUSIONS AND RECCOMENDATIONS

This chapter provides a brief summary of the work performed as part of this research project and primary conclusions and recommendations. Conclusions were presented for the experimental results in Section 3.9 and have been adjusted considering the new knowledge obtained from the analytical investigations. Final recommendations are provided in regards to the design of eccentric stiffeners and for future research.

8.1 Experimental Column Specimens

Forty column specimens were tested experimentally with a focus on the effects of stiffener eccentricity when subjected to concentrated loads. All experimental investigations were summarized in Chapter 3. A summary of the test matrix is as follows:

- Three concentrated load test methods: (1) single compression, (2) double compression, and (3) single tension.
- Four wide flange sizes: (1) W10X19, (2) W10X39, (3) W12X26, and (4) W16X31.
- Four stiffener eccentricity conditions in each test group: (1) one test performed with no stiffeners near midspan, (2) one test performed with concentric stiffeners, (3) one test performed with stiffeners at a low eccentricity of either 2 in. or 3 in. and (4) one test performed with stiffeners at a high eccentricity of 4 in. or 6 in.

Overall Behavior and Comparison to AISC Limit States:

Conclusions from the experimental results and regarding comparisons of the results to the AISC limit state equations are as follows:

- For compression loading conditions, the load carrying capacity of column specimens without stiffeners is governed by the limit state of web local crippling. The capacity is generally close to the values calculated for web local crippling per the equations in the AISC specification, Section J10 (AISC, 2016).
- For all loading conditions, the load carrying capacity is much higher than that predicted for web local yielding. Inelastic deformations occur in the web at loads close to that predicted for web local yielding. However, yielding will continue to spread in the web under further

loading and the initial amount of inelastic deformations are small when yielding first initiates.

- For a double compression loading condition, column specimens without stiffeners did not fail by web compression buckling and reached loads much higher than that predicted for web compression buckling per the AISC limit state equations.
- For a single tension loading condition, column specimens without stiffeners reached loads much higher than the predicted by the limit state of flange bending. All test results were at least 50% higher than that predicted for flange bending. However, inspection of the behavior and results indicate that bending of the flange influences the capacity significantly, causing uneven weld stresses and weld failure at loads much lower than that predicted for the weld strength predicted using the AISC specification.

Influence of Concentric Stiffeners:

The primary conclusions with respect to the influence of using concentric stiffeners in lieu of using no stiffeners in the column specimens are as follows:

- Single compression tests with concentric stiffeners usually failed by inelastic buckling of the stiffeners in combination with inelastic lateral-torsional buckling. The load carrying capacity of column specimens with concentric stiffeners was much higher than the load carrying capacity of other column specimens in the test group. Significant inelastic deformations were found in the W10X39 column specimen, which reached an internal moment higher than the plastic moment.
- In single compression tests results, traditional methods for calculating the effective capacity of concentric stiffeners are reasonable compared to test results.
- In double compression tests, the use of concentric stiffeners significantly increased the load carrying capacity. The effective stiffener capacities were much higher than that predicted using traditional equations and it is believed that for this loading condition that the stiffeners: (1) share the load with the web, (2) stabilize the web allowing more load, and (3) allow the load to spread to more width of the web than predicted from web local yielding.
- In single tension tests, concentric stiffeners reduce the influence of flange bending and allow a more uniform stress to develop in the welds from the loading plate to the top flange.

Influence of Stiffener Eccentricity:

The primary conclusions with respect to the influence of eccentricity on the effective stiffener capacity are as follows:

- All column specimens with eccentric stiffeners and subjected to a compression loading condition exhibited a failure mode best described as web local crippling, which was also the failure mode associated with column specimens without stiffeners.
- In compression tests, even though the load did not increase substantially for column specimens with eccentric stiffeners, the stiffeners assisted in the post-buckling behavior of the columns since the high load was maintained for a longer displacement in comparison to conditions without stiffeners.
- For all test methods, column specimens tested with stiffeners at a high eccentricity (4 in. or 6 in.) reach load capacities very similar to column specimens without stiffeners. For most column sizes tested, there is a very small and negligible influence on load capacity and stiffness as depicted from the load-displacement relationship.
- For all test methods, when a W16X31 is tested at a low stiffener eccentricity of 3 in., which is higher than the low eccentricity condition for other column specimens, there is a very small and negligible influence on load capacity and stiffness.
- For column specimens tested in single compression and with stiffeners at 2 in. eccentricity, there is a small increase in capacity and stiffness in comparison to the tests without stiffeners. The effective stiffener capacity was between 0% and 17% of the concentric stiffener condition. This is much lower than assumed using AISC Design Guide 13 (Carter, 1999).
- For column specimens tested in double compression and with stiffeners at 2 in. eccentricity, there is a small increase in capacity and stiffness in comparison to the tests without stiffeners. The effective stiffener capacity was between 9% and 18% of the concentric condition from the limited data available.
- From limited test data, column specimens tested in single tension and with stiffeners at an eccentricity of 2 in. showed some improvement in capacity in comparison to the condition with stiffeners at an eccentricity of 4 in.

8.2 Analytical Models of Experimental Column Specimens

Finite element models of the experimental column specimens were developed in order to verify/calibrate the finite element approach for studying larger column specimens. The methodology that describes the finite element modeling techniques was discussed in Chapter 4 and the results for the experimental column specimens were presented in Chapter 5. Relevant conclusions from these studies are as follows:

- Finite element models reasonably predict the ultimate load capacity of the column specimens when subjected to single compression and double compression loading conditions. The finite element models reached a maximum load that was governed by the limit state of web crippling when concentric stiffeners were not used and stiffener buckling when concentric stiffeners were used. These failure modes matched the experimental failure modes.
- The results showed a significant difference in the analytical displacement and experimental displacement results under a given load. More appropriate methods for measuring experimental displacement need to be utilized.
- In all loading cases, the *STATIC RIKS option for performing the analysis provides the most accurate results. For column specimens subjected to single or double compression, an imperfection of 0.001% (very small) simulates the most favorable results.
- For single tension members, utilizing the stress-strain curve presented by Kartal et al. (2007) and assuming failure occurred when the localized weld stress exceeded 82.4 ksi resulted in load capacities that consistently compared favorably to experimental results.

8.3 Analytical Studies of Larger Column Specimens

Larger experimental column specimens were evaluated analytically using the finite element approach and discussed in Chapter 6 with the results summarized in Sections 6.5-6.7. The analytical test matrix is summarized as follows:

- 34 models were used to study single compression, 42 models were used to study double compression, and 72 models were used to study single tension.
- Six column sizes were evaluated in all three loading conditions: (1) W14X68, (2) W14X120,

(3) W14X176, (4) W14X233, (5) W24X131, and (6) W24X229.

- Four stiffener eccentricity conditions in each test group: (1) one test performed with no stiffeners near midspan, (2) one test performed with concentric stiffeners, (3) one test performed with stiffeners at a low eccentricity of 2 in. and (4) one test performed with stiffeners at a high eccentricity of 4 in.
- For double compression, all conditions were analyzed with 3/8 in. stiffeners and 3/4 in. stiffeners. The analysis focused on models with 3/4 in. stiffeners.
- For single compression, tests were performed primarily with 3/8 in. stiffeners. The W14X233 and W24X229 column specimens were also evaluated with 3/4 in. stiffeners.
- The W14X233 was modeled with all stiffener conditions at an unsupported length of 3.5 ft. and the results were compared to the results at an unsupported length of 5 ft., which was used for all other column specimens.
- For single tension, all column specimens were tested with all four stiffener conditions and with three different fillet weld sizes of 1/4 in., 9/16 in., and 7/8 in.

Several conclusions are derived from the analytical results and some are dissimilar to that derived from the experimental results. Conclusions presented in this section focus on failure mechanisms and the influence of eccentricity. Further conclusions that discuss comparisons between the results and the AISC limit state equations are provided in Section 8.4. The primary conclusions are as follows:

Single compression loading:

- For column specimens with no stiffeners, the ultimate load is reached when a form of web crippling occurs. As the column section gets 'stockier', more yielding of the web is identified prior to the ultimate load being reached. Therefore, a form of inelastic web crippling is occurring at the maximum load.
- For column specimens with concentric stiffeners, the ultimate load is generally limited by stiffener buckling. Depending on the slenderness ratio of the stiffener, significant yielding in the stiffener may occur prior to stiffener buckling.

- For column specimens with eccentric stiffeners, the ultimate load is limited by web local crippling or a combination of stiffener buckling with web local crippling.
- In larger column sections, eccentric stiffeners are more effective in comparison to the column specimens analyzed experimentally. As flange thickness increases, the effects of eccentricity in stiffener design decreases.
- Trends in the analytical results show that stiffeners shall not be designed as eccentric if the flange thickness is less than 0.5 in.
- The web slenderness, h / t_w, does not have an influential relationship to the effective capacity of eccentric stiffeners.
- Eccentric stiffeners should not be utilized with eccentricities greater than 4 in. This is primarily due to limitations in the research performed but also due to trends in the results at different eccentricities.
- Using thicker stiffeners (3/4 in. as opposed to 3/8 in.) increases the effective stiffener capacity in all comparisons evaluated. However, the influence of eccentricity is similar with respect to percent decrease in effective stiffener capacity regardless of stiffener thickness.

Double compression loading:

- For column specimens with no stiffeners, a form of web compression buckling always occurred near the maximum load. Some column specimens showed two half-sine waves in the buckling mode.
- For column specimens with concentric stiffeners, the maximum load was always governed by stiffener buckling. In some cases, stiffener buckling occurred at a load that was less than or only slightly greater than the column specimen without stiffeners. This only occurred if the stiffeners were slender and the column specimen was more "stocky".
- For column specimens with eccentric stiffeners, in some cases, the stiffeners were found to brace the column specimen from buckling, allowing the maximum load to be maintained for high magnitudes of displacement. In other cases, web compression buckling was still found to govern, depending on the dimensions of the column specimen and magnitude of

eccentricity.

- With respect to load capacity, larger stiffeners were influenced more by the effects of eccentricity as opposed to smaller stiffeners. For the column sizes evaluated, the larger stiffeners are more realistic to be used in practice and should be used to provide recommendations regarding stiffener eccentricity.
- In larger column sections, eccentric stiffeners are more effective in comparison to the column specimens analyzed experimentally. As flange thickness increases, the effects of eccentricity in stiffener design decreases.

Single tension tests:

- In all test groups analyzed, the column specimen with concentric stiffeners resulted in the highest load, the column specimens with stiffeners at a 2 in. eccentricity resulted in the second highest load, the column specimen with stiffeners at a 4 in. eccentricity resulted in the third highest load, and the column specimen without stiffeners resulted in the lowest load. Therefore, there were consistent trends in the influence of stiffeners.
- As weld size decreases, eccentricity of the stiffener decreases, and the section gets "stockier", the effects of flange bending decreases and more uniform stresses develop in the weld.
- The results for effective stiffener capacities were generally at least 60% of that for concentric stiffeners when a 2 in. eccentricity is used unless the section size was large and the results were clearly governed by limitations in the weld.
- The relationships derived for single compression with respect to eccentricity, flange thickness and effective stiffener capacity are usually conservative for single tension members as well.
- Clearer trends are found between the stiffener eccentricity condition and the effective stiffener stiffness (change in elastic stiffness between column specimen with stiffeners vs. no stiffeners) and the same relationships used to define the influence of eccentricity vs. flange thickness that were originally derived using strength are valid for elastic stiffness as well.
- A consistent relationship found in the results regarding the influence of eccentricity was more

related to overall capacity as opposed to effective stiffener capacity. Regardless of weld size and assuming 3/8 in. stiffeners:

- The overall capacity of columns without stiffeners is at least 72% of the capacity of the corresponding columns with concentric stiffeners.
- The overall capacity of column specimens with stiffeners at an eccentricity of 2 in. is at least 90% of the overall capacity of the corresponding column with concentric stiffeners.
- The overall capacity of column specimens with stiffeners at an eccentricity of 4 in. is at least 78% of the overall capacity of the corresponding column with concentric stiffeners.

8.4 Further Analytical Studies to Evaluate AISC Limit State Equations

The results of this research questioned equations currently available for predicting the capacity of columns subjected to concentrated loads without stiffeners and then with concentric stiffeners. Without proper estimates of these capacities, the calculations for eccentric stiffeners are questionable as well. Chapter 7 exclusively evaluated the experimental and analytical results with a focus on comparisons to the AISC limit state equations and equations for predicting the effective stiffener capacity of concentric stiffeners. The primary conclusions are as follows:

- The equation used for the limit state of web local crippling appears adequate. There are no results developed in this research that would suggest otherwise and several results of compression tests reach a load capacity similar to the load capacity calculated per this limit state.
- The equation used for the limit state of web local yielding always under predicts the "web capacity" of column specimens. Initial yielding does occur near the predicted load but the web continues to yield under further loading and significant inelastic deformations do not occur until the applied load is significantly higher than that predicted per this limit state.
- The equation used for the limit state of web compression buckling under predicts the capacity of column specimens subjected to double compression. Web compression buckling does

occur as long as a through force is present but the equation should consider the width of loading as well as the influence of either elastic compression buckling vs. inelastic compression buckling.

- The equation used for the limit state of flange bending usually under predicts the capacity of column specimens subjected to a tension concentrated load. However, the effects of flange bending may be better accounted for if a new design approach is established for computing an effective weld strength that considers the effects of flange bending.
- Equations for the theoretical yield capacity of concentric stiffeners are a good estimate of the effective stiffener capacity for single compression and single tension loading conditions. For single compression, stiffeners should be designed as non-slender.
- In a double compression loading condition, using the theoretical yield capacity of concentric stiffeners appears conservative in most cases. However, as section sizes increase, concentric stiffeners may become ineffective if they have a high slenderness due to sudden buckling at loads below the capacity of the column specimen without stiffeners. Therefore, a minimum stiffener size should be used to avoid buckling and ensure the yield load can be obtained.

8.5 Recommendations for Eccentric Stiffener Design

Final recommendations from the findings of this research regarding the use of eccentric stiffeners in design are summarized in this section. The recommendations are limited to the column specimens evaluated in this research and should be expanded using additional section sizes, eccentricity conditions, and stiffener sizes and depths.

Recommendations are provided for computing the final effective stiffener capacity, 'R_{n_eff}', assuming a pair of full-depth transverse stiffeners. In this section, the actually eccentricity is denoted as 'e'. The effective stiffener capacity for concentric stiffeners is denoted 'R_{n_c}' and shall be computed using appropriate methods. A method governed by yielding of the stiffener is recommended based on the results of this research. Other recommendations are as follows:

- For all compression conditions, it is recommended that stiffeners pass the slenderness limit given by Equation 8-1. The results of double compression tests in which this slenderness was not passed were questionable.

  $\lambda_s = b_s / t_s \leq \lambda_r = 0.56*sqrt(E / F_{ystiff})$ (8-1)

- For the following conditions, eccentric stiffeners shall have no effective stiffener capacity, $R_{n\_eff} = 0$:
  - If the eccentricity, '*e*', is greater than 4 in.
  - If the flange thickness, 't_f', is less than 0.5 in.
  - If the ratio of 'e / t_f' is greater than 6.0.
- If these conditions pass, the effective stiffener capacity of eccentric stiffeners is computed as follows:

  $R_{n\_eff} = R_{n\_c} \, x \, (1 - (e / t_f) / 6)^{5/3}$ (8-2)

Note that if AISC prefers the straight line expression shown in Figure 6.8-3, some recommendations are rewritten as follows:

- For the following conditions, eccentric stiffeners shall have no effective stiffener capacity, $R_{n\_eff} = 0$:
  - If the eccentricity, '*e*', is greater than 4 in.
  - If the flange thickness, 't_f', is less than 0.5 in.
  - If the ratio of 'e / t_f' is greater than 5.0.
- If these conditions pass, the effective stiffener capacity of eccentric stiffeners is computed as follows:

  $R_{n\_eff} = R_{n\_c} \, (0.8 - 0.16(e / t_f))$ (8-3)

8.6 Recommendations for Future Research

Recommendations for future work with respect to concentrated load limit states are described in detail in Section 7.6 and summarized herein along with recommendations for future work with respect to eccentric stiffener design. Recommendations are as follows:

- Analyze more analytical column specimens of various sizes to study the influence of eccentric stiffeners in an effort to improve the recommendations from Section 8.5. Consider various stiffener thickness, magnitudes of eccentricity, different column section sizes, and stiffener depths.
- Evaluate the spread of yielding and inelastic deformations that develop in the web of column specimens when subjected to concentrated loads in more detail. Potentially redefine factors that are utilized in the web local yielding equation.
- Evaluate the limit state of web compression buckling in detail using both experimental (with 100% through force) and analytical research. This limit state should utilize an accurate width of the compression stress zone and mode of buckling failure.
- Evaluate the influence of flange bending on the weld capacity in detail when using fillet welds. Potentially redefine the approach for analyzing wide flange shapes when subjected to concentrated tension loads considering flange bending and weld capacity simultaneously.
- Evaluate the influence of flange bending when using partial penetration and complete joint penetration groove welds.
- Further develop design capacities and design procedures for concentric stiffeners and for various loading conditions. Propose new limitations for the slenderness ratio and overall capacities under various loading conditions.

REFERENCES

ABAQUS (2014). “ABAQUS/Standard User’s Manuals”, Version 6.14, Dassault Systems, 2014.

AISC (2017): “Steel Construction Manual”. American Institute of Steel Construction, Chicago, IL.

AISC (2016). “Specification for Structural Steel Buildings”. American Institute of Steel Construction, Chicago, IL.

AISC (1986): “Load and Resistance Factor Design Specification for Structural Steel Buildings”. American Institute of Steel Construction, Chicago, IL.

ANSI/AISC 341-10 (2010). “Seismic Provisions for Structural Steel Buildings”. American Institute of Steel Construction, Chicago IL.

ASTM A6 / A6M-17a (2017). “Standard Specification for General Requirements for Rolled Structural Steel Bars, Plates, Shapes, and Sheet Piling”, ASTM International, West Conshohocken, PA.

ASTM E8 / E8M-09 (2009). “Standard Test Methods for Tension Testing of Metallic Materials”, ASTM International, West Conshohocken, PA.

Barger, B.L. (1992). “What Designers Can Do to Reduce Fabrication Costs”. Modern Steel Construction, February 1992, pp. 31-32, AISC, Chicago, IL.

Beedle, L.S. and Christopher, R. (1963) “Tests of Steel Moment Connections”. Structural Engineers Association Proceedings, 1963, Reprint No. 251. Fritz Laboratory Reports. Paper 1308.

Bowman and Quinn (1994). "Examination of Fillet Weld Strength". Engineering Journal 31(3), pp. 98-108, American Institute of Steel Construction, Chicago IL

Carter (1999). “Design Guide 13: Wide-Flange Column Stiffening at Moment Connections”. American Institute of Steel Construction, Chicago, IL.

Dyker, W.G. (1992). “What Designers Can Do to Reduce Fabrication Costs” Modern Steel Construction, February., pp. 28-29, AISC, Chicago, IL.

Elgaaly. M. and Nunan, W. L. (1989): “Behavior of Rolled Section Web under Eccentric Edge

Compressive Loads". Journal of Structural Engineering, Vol. 115, No.7, July, 1989, ASCE.

Elgaaly, M. and Salkar, R. K. (1991): "Web Crippling Under Local Compressive Edge Loading". Department of Civil Engineering, University of Maine.

Elgaaly, M. and Sturgis, J. (1989): "Stability of Plates under Eccentric Edge Loads". Steel structures Journal: Proceedings of the sessions related to steel structures at Structures Congress '89, San Francisco Hilton, San Francisco, CA, May 1.

EN 1993-1-1 (2005) (English). Eurocode 3: Design of Steel Structures - Part 1-1: General Rules and Rules for Buildings". [Authority: The European Union Per Regulation 305/2011, Directive 98/34/EC, Directive 2004/18/EC].

EN 1993-1-5 (2006) (English). "Eurocode 3: Design of Steel Structures - Part 1-5: General Rules - Plated Structural Elements". [Authority: The European Union Per Regulation 305/2011, Directive 98/34/EC, Directive 2004/18/EC].

EN 1998-1 (2004) (English). "Eurocode 8: Design of Structures for Earthquake Resistance – Part 1: General Rules, Seismic Actions and Rules for Buildings" [Authority: The European Union Per Regulation 305/2011, Directive 98/34/EC, Directive 2004/18/EC].

Graham, J.D., Sherbourne, A.N., Khabbaz, R.N., and Jensen, C.D. (1959). "Welded Interior Beam-to-Column Connections". Report for AISC, AISC, Chicago, IL.

Hajjar et al. (2003): "Continuity Plate Detailing for Steel Moment-Resisting Connections". Article in Engineering Journal (New York), January 2003.

Johnson, L.G. (1959). "Compressive and Tensile Loading Tests on Joists with Web Stiffeners". British Welding Journal, September 1959.

Kartal et al. (2007). "Determination of Weld Metal Mechanical Properties Utilising Novel Tensile Testing Methods". Trans Tech Publications, Switzerland.

Keinänen and Chauhan (2013). "Computation of Welding Residual Stress in a Multi-pass Welded Mock-up Pipe". Conference Structural Mechanics in Reactor Technology. San Francisco, California, USA.

Khabbaz, R.N., Jensen, C.D. (1957). "Four-Way Welded Interior Beam Column Connections". Fritz

Laboratory Report No.233.13, Lehigh University.

Lee et al. (2002): “Column Stiffener Detailing and Panel Zone Behavior of Steel Moment Frame Connections”. Structural Engineering Report No. ST-01-3.2. Department of Civil Engineering, University of Minnesota, MN

Norwood, J. (2018): “Effect of Continuity Plate Eccentricity on the Performance of Welded Beam-to-Column Connections”. Thesis in partial fulfillment of the requirements for the degree if Master in Science in Civil Engineering, Department of Civil Engineering, University of Arkansas.

Parkes, E. W. (1952): “The Stress Distribution near a Loading Point in a Uniform Flanged Beam”. Engineering Department, University of Cambridge.

Prochnow et al. (2000): “Local Flange Bending and Local Web Yielding Limit States in Steel Moment-Resisting Connections”. Department of Civil Engineering, 500 Pillsbury Drive SE, University of Minnesota, MN

Riker, D.T. (1992). “Value Engineering and Steel Economy”. Modern Steel Construction, February, pp. 22-26, AISC, Chicago, IL.

Roberts, T. M. (1981): “Slender plate girders subjected to edge loading”. Proc. Institution of Civil Engineers, Part 2, 1981, 71, Sept., 805-819.

Salmon and Johnson (1996): “Steel Structures: Design and Behavior, Emphasizing Load and Resistance Factor Design” Fourth Edition, Prentice Hall, Upper Saddle River, NJ 07458, 1996.

Salkar (1992). “Strength and behavior of webs, with and without stiffeners, under local compressive in-plane and eccentric loads”.

Salkar et al.(2015). “Crippling of Webs with Partial Depth Stiffeners under Patch Loading”. Engineering Journal

Sherbourne A.N. and Jensen, C.D. (1957). “Direct Welded Beam Column Connections”. Fritz Laboratory Report No.233.12, Lehigh University.

Sherbourne, A.N. and Murthy, D.N.S. (1978). “Computer Simulation of Column Webs in Structural Steel Connections”. Computers and Structures Vol. 8. pp. 479-490.

Tagawa, H. and Gurel, S. (2005). “Application of Steel Channels as Stiffeners in Bolted Moment

Connections". Journal of Constructional Steel Research 61 (2005) 1650-1671.

Tagawa, H. and Liu, Y. (2014). "Stiffening of Bolted End-Plate Connections with Steel Member Assemblies". Journal of Constructional Steel Research 103 (2014) 190-199.

Thornton, W.A. (1992). "Designing for Cost Efficient Fabrication". Modern Steel Construction, February, pp. 12-20, AISC, Chicago, IL.

APPENDIX A: PHOTOGRAPHS OF EXPERIMENTAL COLUMN SPECIMENS

Table A-1: Index of photographs for experimental column specimens

Column Specimen	Figures	Starting Page
W16X31-SC-NA	A-1 to A-4	A-3
W16X31-SC-E6	A-5 to A-7	A-5
W16X31-SC-E3	A-8 to A-11	A-7
W16X31-SC-E0	A-12 to A-16	A-9
W10X19-SC-NA	A-17 to A-21	A-12
W10X19-SC-E4	A-22 to A-26	A-15
W10X19-SC-E2	A-27 to A-31	A-18
W10X19-SC-E0	A-32 to A-36	A-21
W10X39-SC-NA	A-37 to A-40	A-24
W10X39-SC-E4	A-41 to A-44	A-26
W10X39-SC-E2	A-45 to A-48	A-29
W10X39-SC-E0	A-49 to A-53	A-32
W12X26-SC-NA	A-54 to A-57	A-35
W12X26-SC-E4	A-58 to A-61	A-37
W12X26-SC-E2	A-62 to A-65	A-39
W12X26-SC-E0	A-66 to A-70	A-41
W16X31-DC-NA	A-71 to A-75	A-44
W16X31-DC-E6	A-76 to A-79	A-47
W16X31-DC-E3	A-80 to A-83	A-49
W16X31-DC-E0	A-84 to A-87	A-51
W10X19-DC-NA	A-88 to A-92	A-53
W10X19-DC-E4	A-93 to A-97	A-56
W10X19-DC-E2	A-98 to A-102	A-59
W10X19-DC-E0	A-103 to A-107	A-62
W12X26-DC-NA	A-108 to A-110	A-65
W12X26-DC-E4	A-111 to A-114	A-67
W12X26-DC-E2	A-115 to A-119	A-69
W12X26-DC-E0	A-120 to A-122	A-72
W16X31-ST-NA	A-123 to A-127	A-74
W16X31-ST-E6	A-128 to A-132	A-77
W16X31-ST-E3	A-133 to A-137	A-80
W16X31-ST-E0	A-138 to A-141	A-83
W10X39-ST-NA	A-142 to A-146	A-85
W10X39-ST-E4	A-147 to A-150	A-88
W10X39-ST-E2	A-151 to A-155	A-90
W10X39-ST-E0	A-156 to A-159	A-93
W12X26-ST-NA	A-160 to A-162	A-95
W12X26-ST-E4	A-163 to A-167	A-97
W12X26-ST-E2	A-168 to A-171	A-100
W12X26-ST-E0	A-172 to A-175	A-102

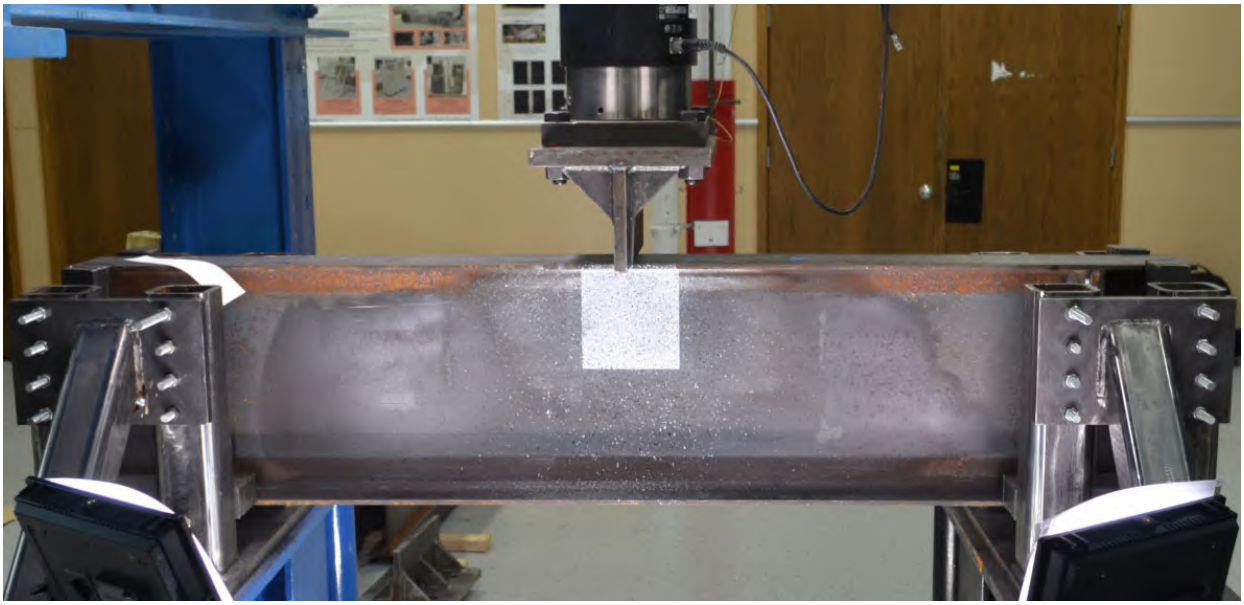

Figure A-1: Elevation of W16X31-SC-NA prior to testing

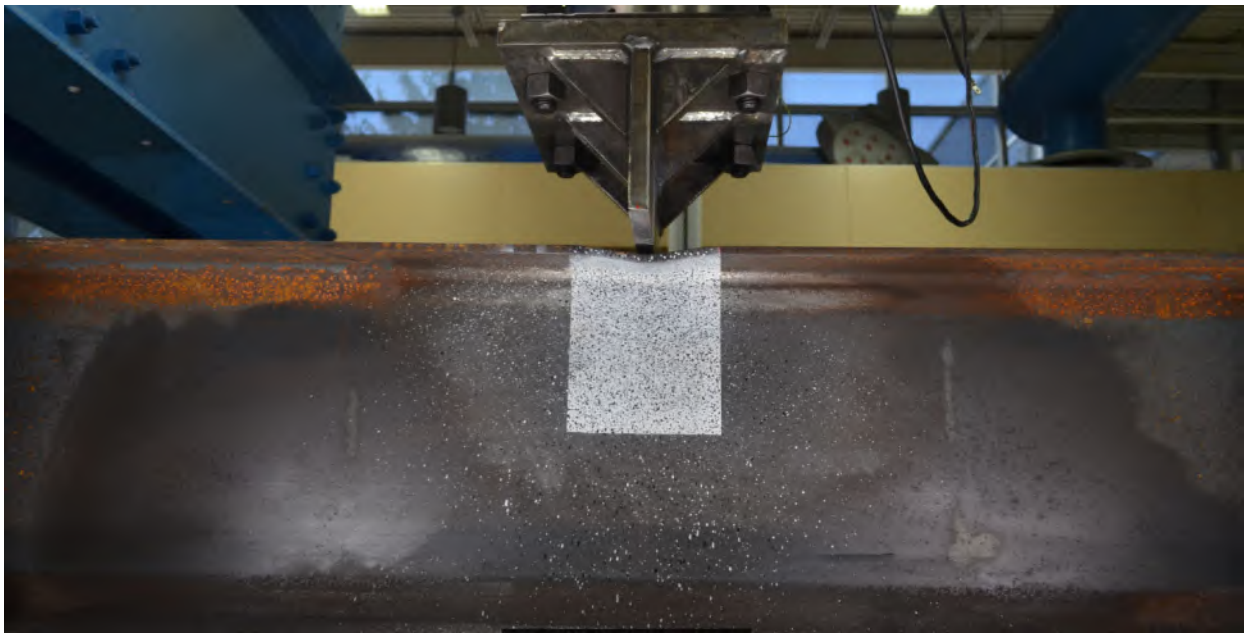

Figure A-2: Elevation of W16X31-SC-NA after testing

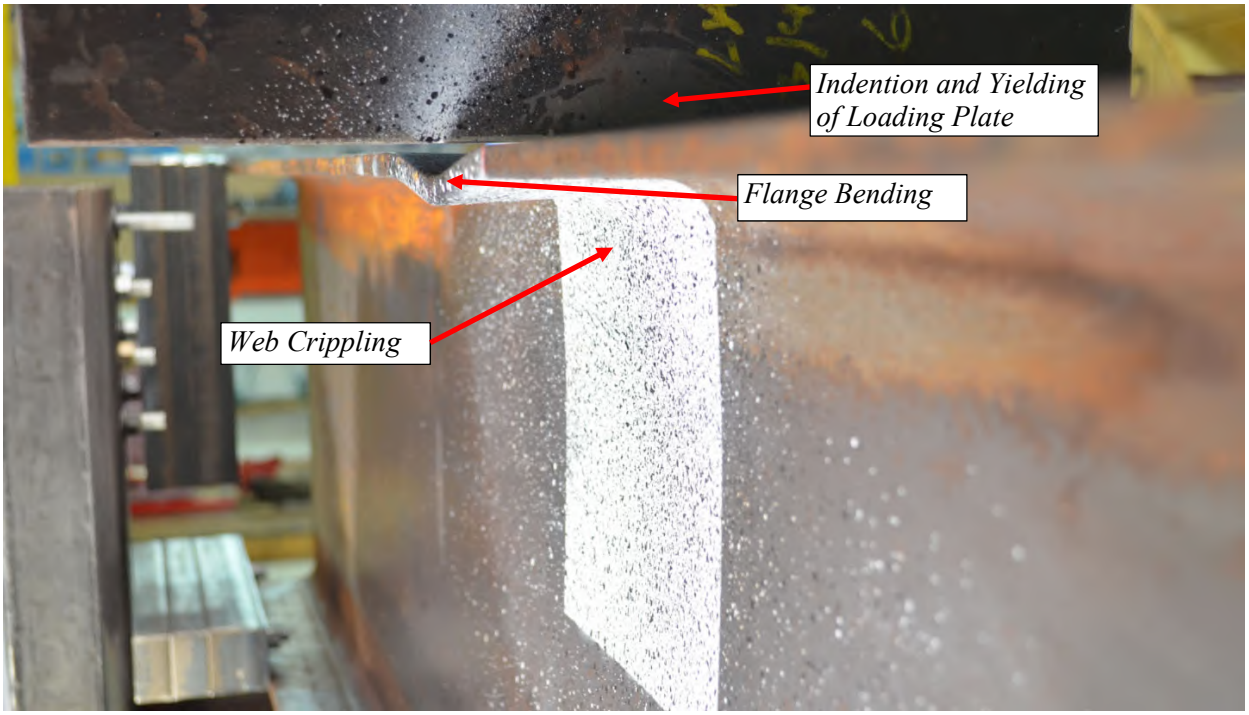

Figure A-3: W16X31-SC-NA after testing emphasizing flange bending

Figure A-4: W16X31-SC-NA after testing emphasizing web crippling

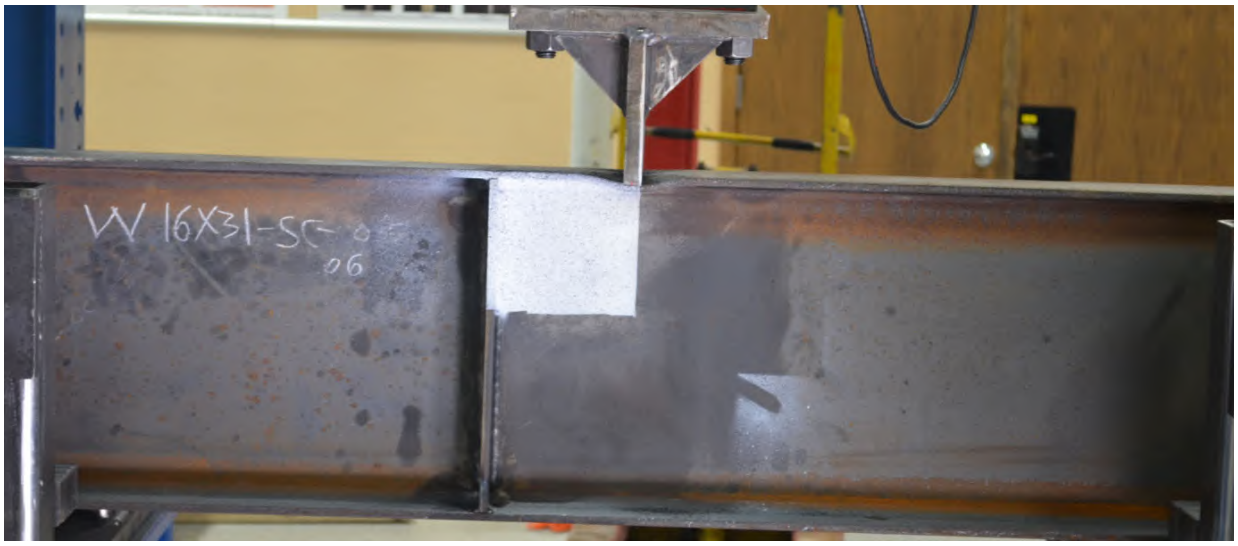

Figure A-5: Elevation of W16X31-SC-E6 after testing

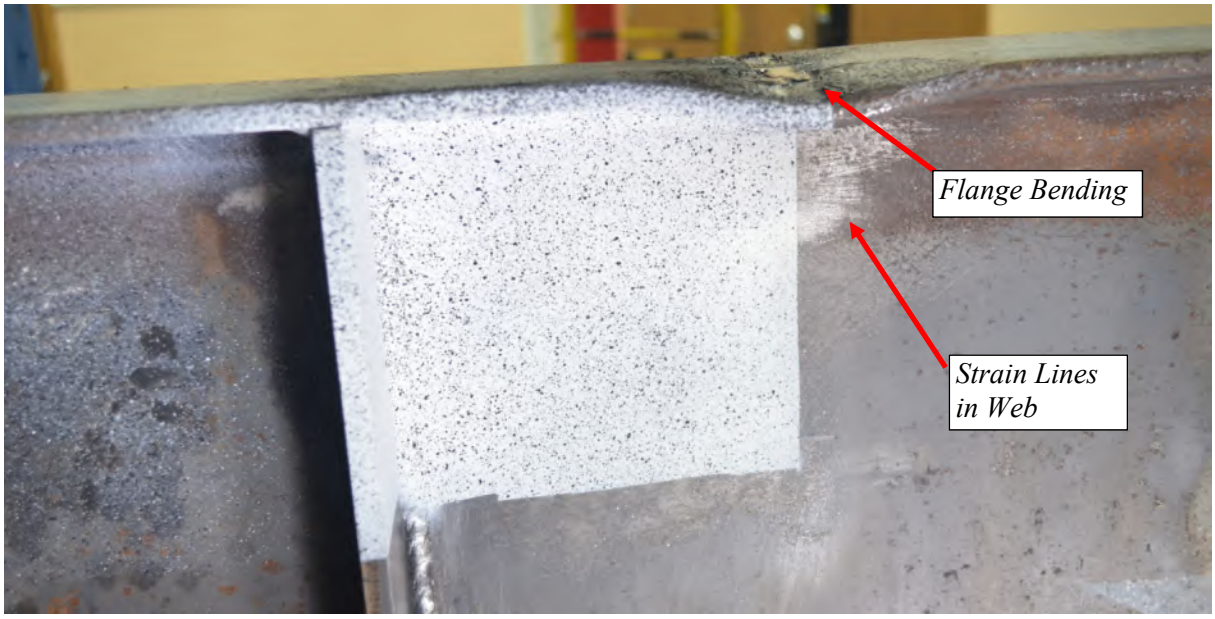

Figure A-6: W16X31-SC-E6 after testing with condition of flange and web

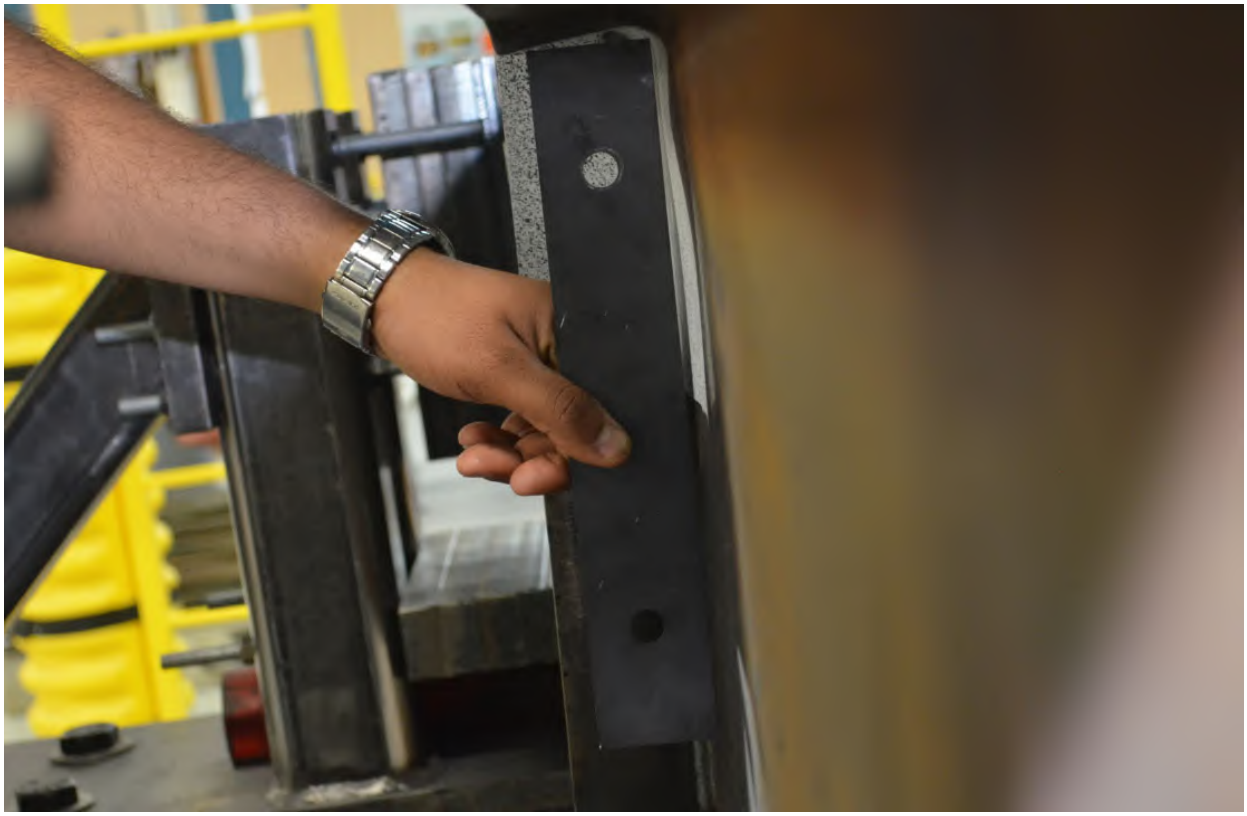

Figure A-7: W16X31-SC-E6 after testing emphasizing web local crippling

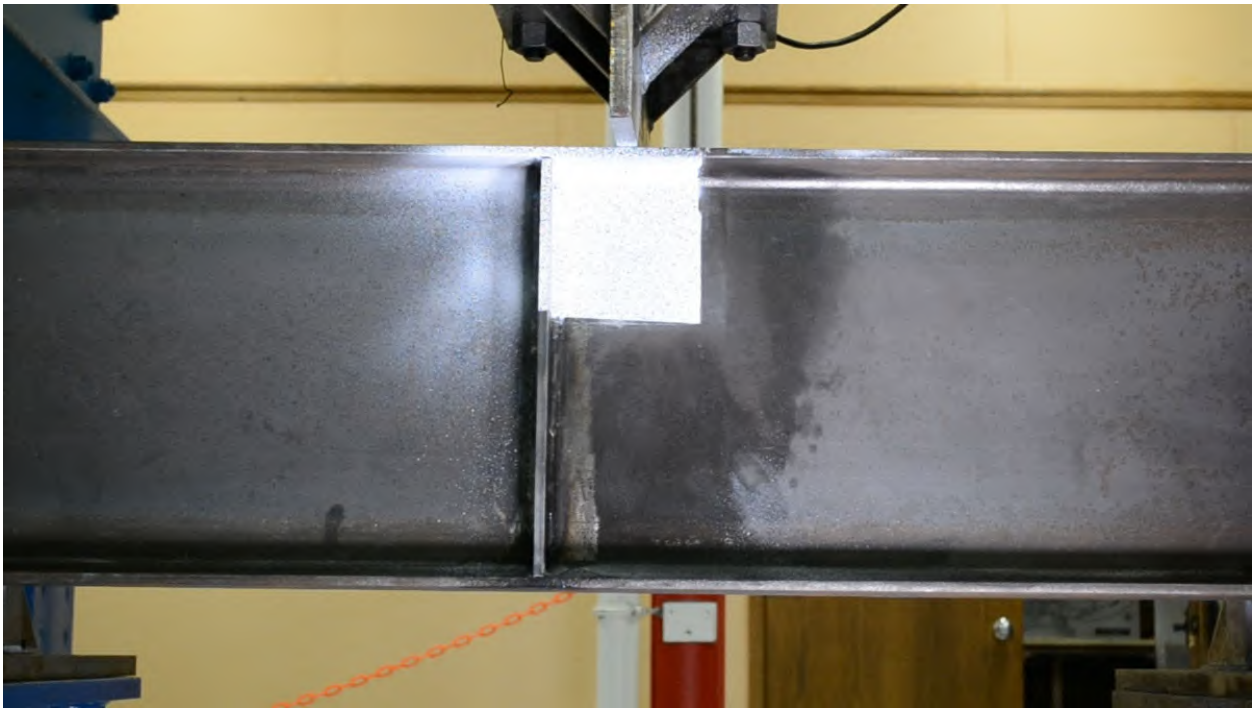

Figure A-8: Elevation of W16X31-SC-E3 prior to testing

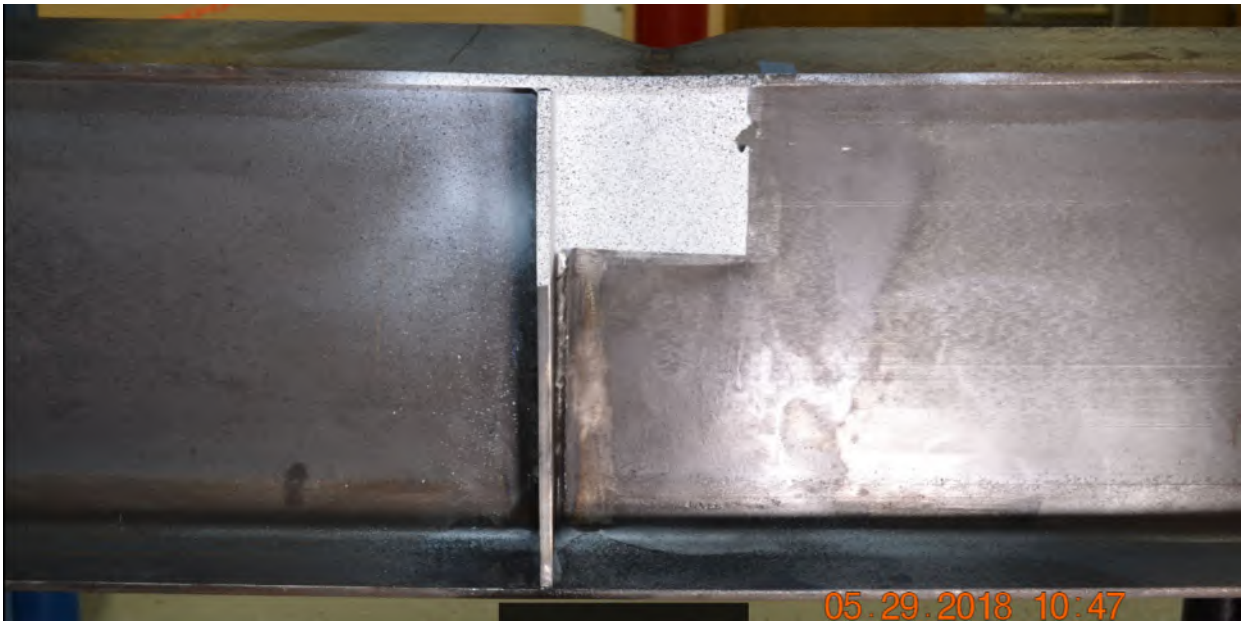

Figure A-9: Elevation of W16X31-SC-E3 after testing

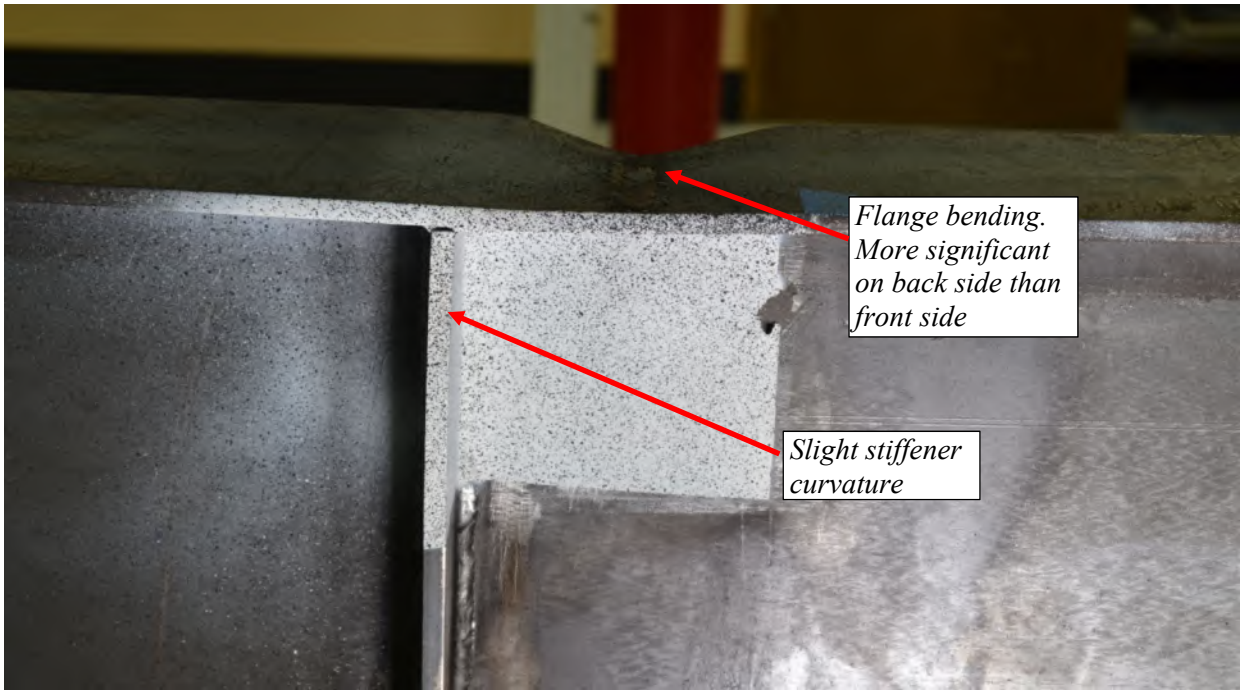

Figure A-10: Close-up view of W16X31-SC-E3 after testing

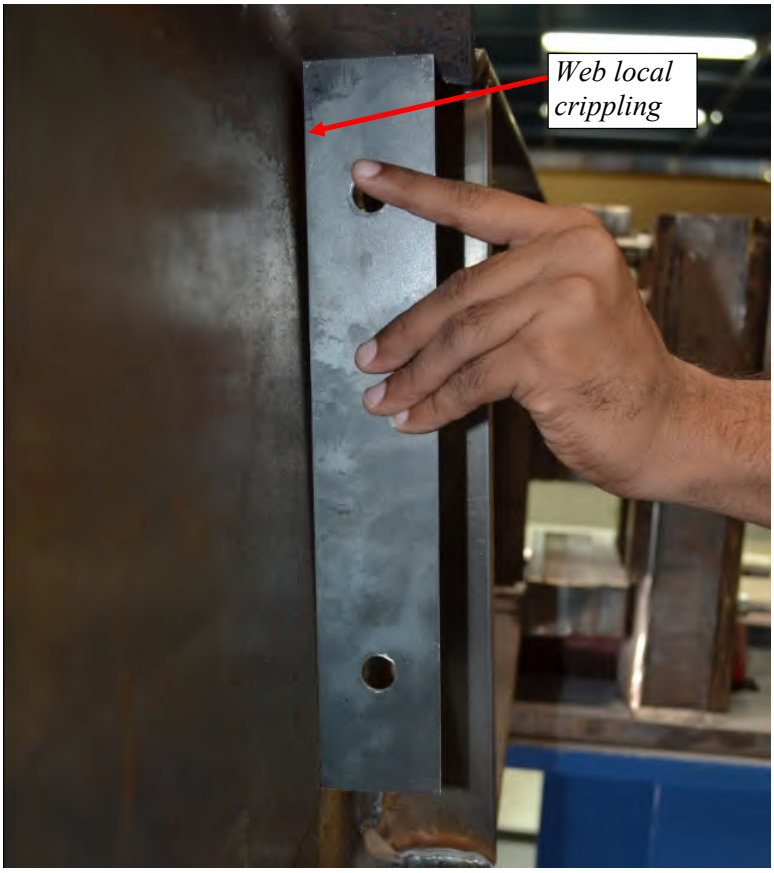

Figure A-11: W16X31-SC-E3 after testing emphasizing web crippling

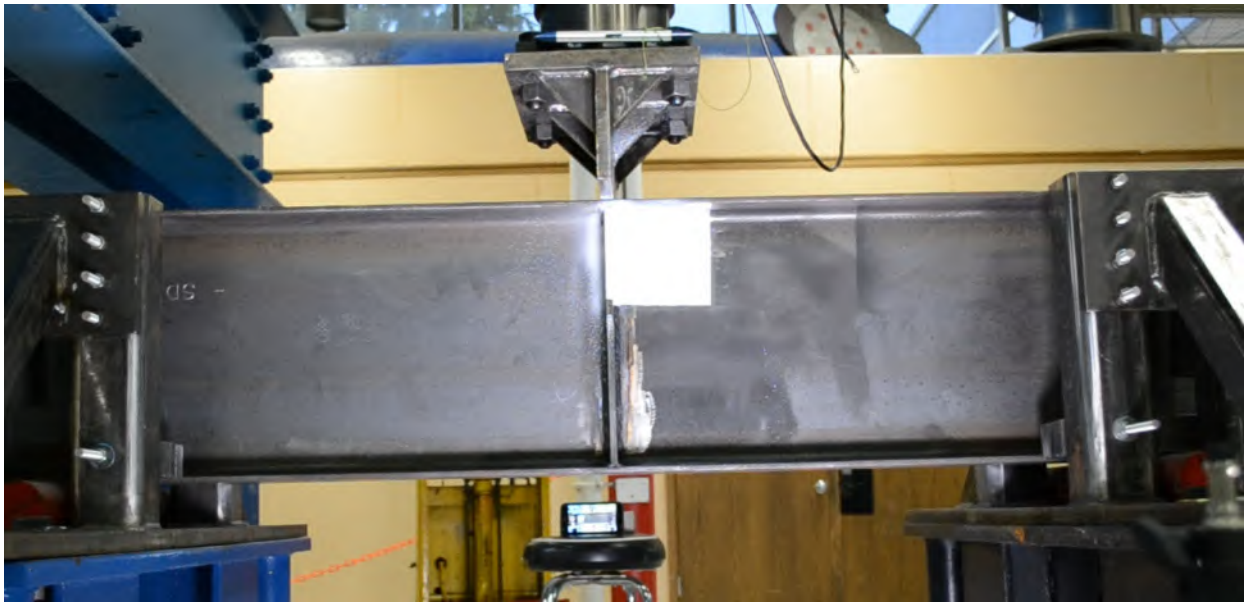

Figure A-12: Elevation of W16X31-SC-E0 prior to testing

Figure A-13: Elevation of W16X31-SC-E0 after testing

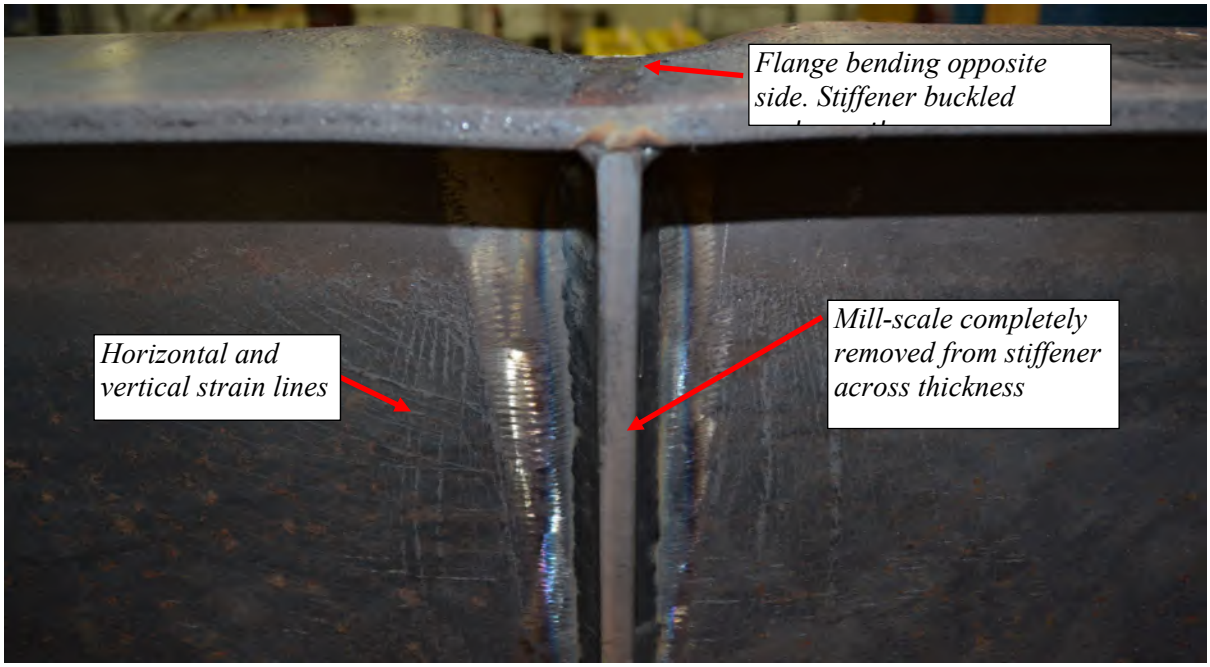

Figure A-14: Close-up view of backside of W16X31-SC-E0 after testing

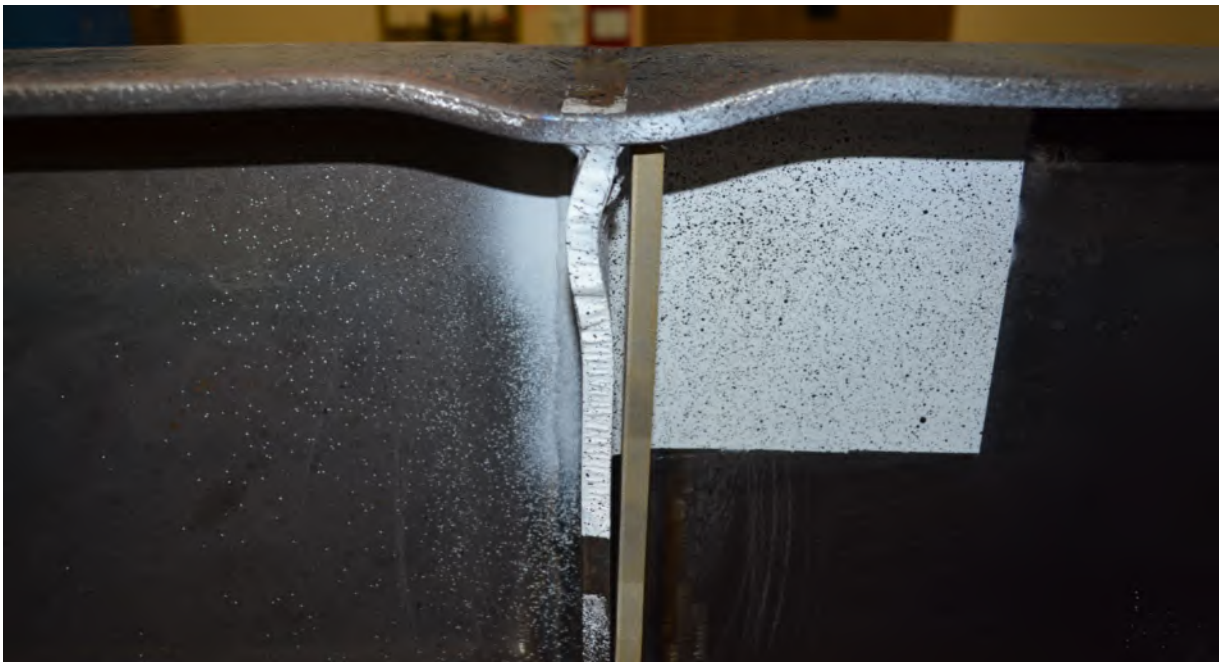

Figure A-15: Buckling of front stiffener of W16X31-SC-E0

Figure A-16: Side view of W16X31-SC-E0 after testing showing lateral-torsional buckling

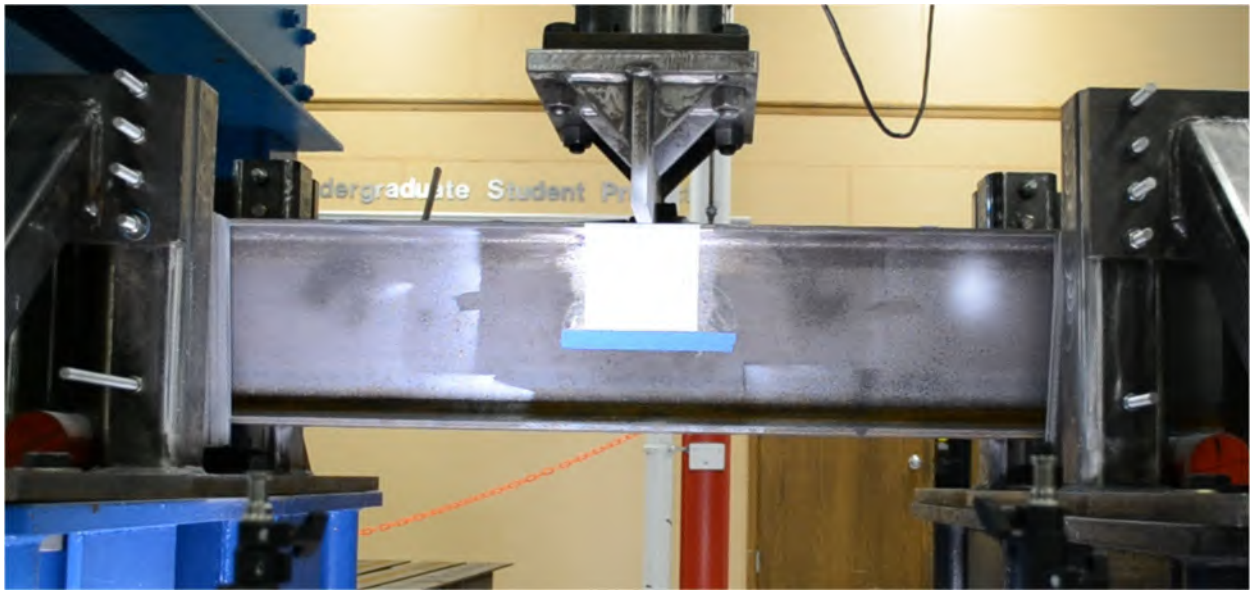

Figure A-17: Elevation of W10X19-SC-NA prior to testing

Figure A-18: Elevation of W10X19-SC-NA after testing

a) Bulge from front side of the specimen b) Bulge from back side of the specimen

Figure A-19: W10X19-SC-NA after testing emphasizing web crippling

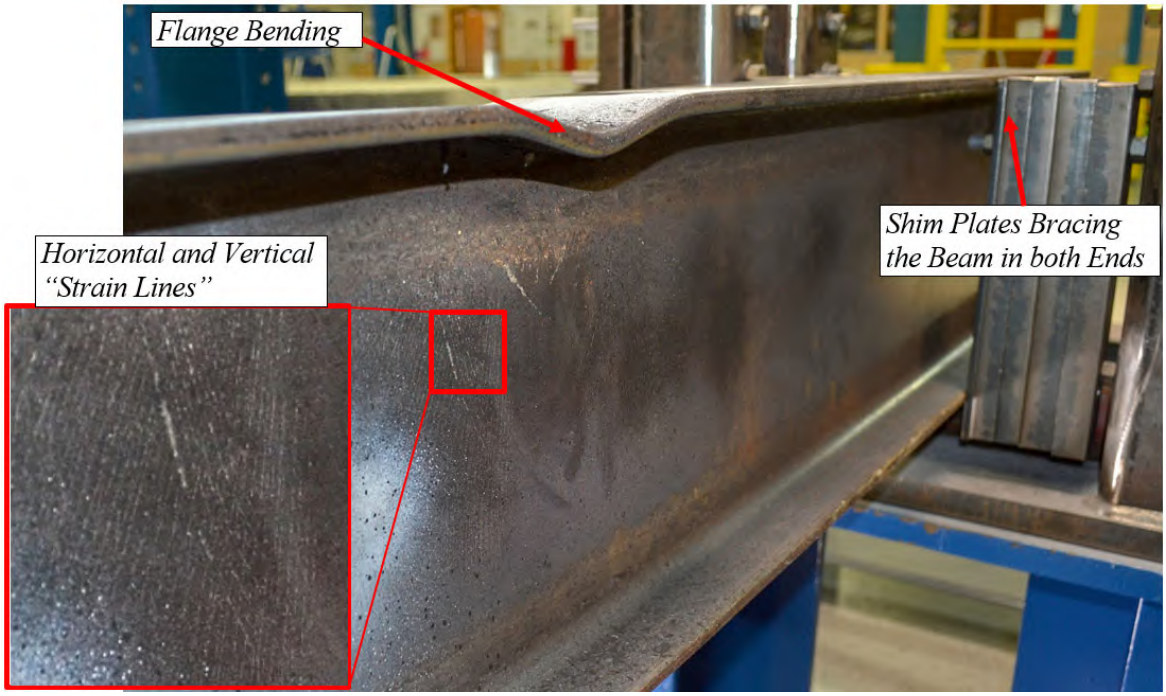

Figure A-20: W10X19-SC-NA after testing emphasizing flange bending

Figure A-21: Side view of W10X19-SC-NA after testing showing lateral torsional buckling

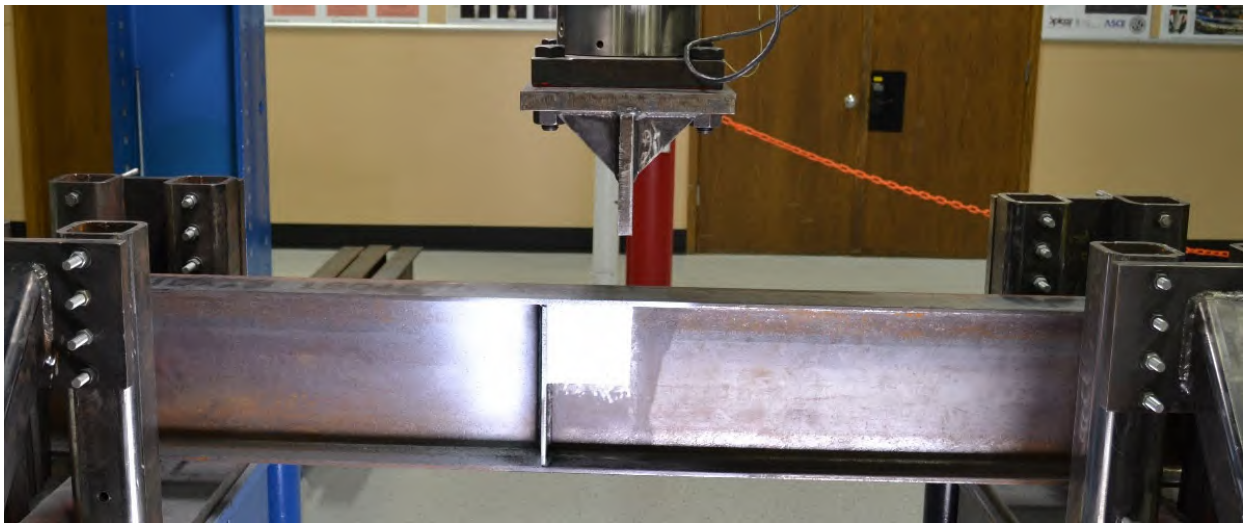

Figure A-22: Elevation of W10X19-SC-E4 prior to testing

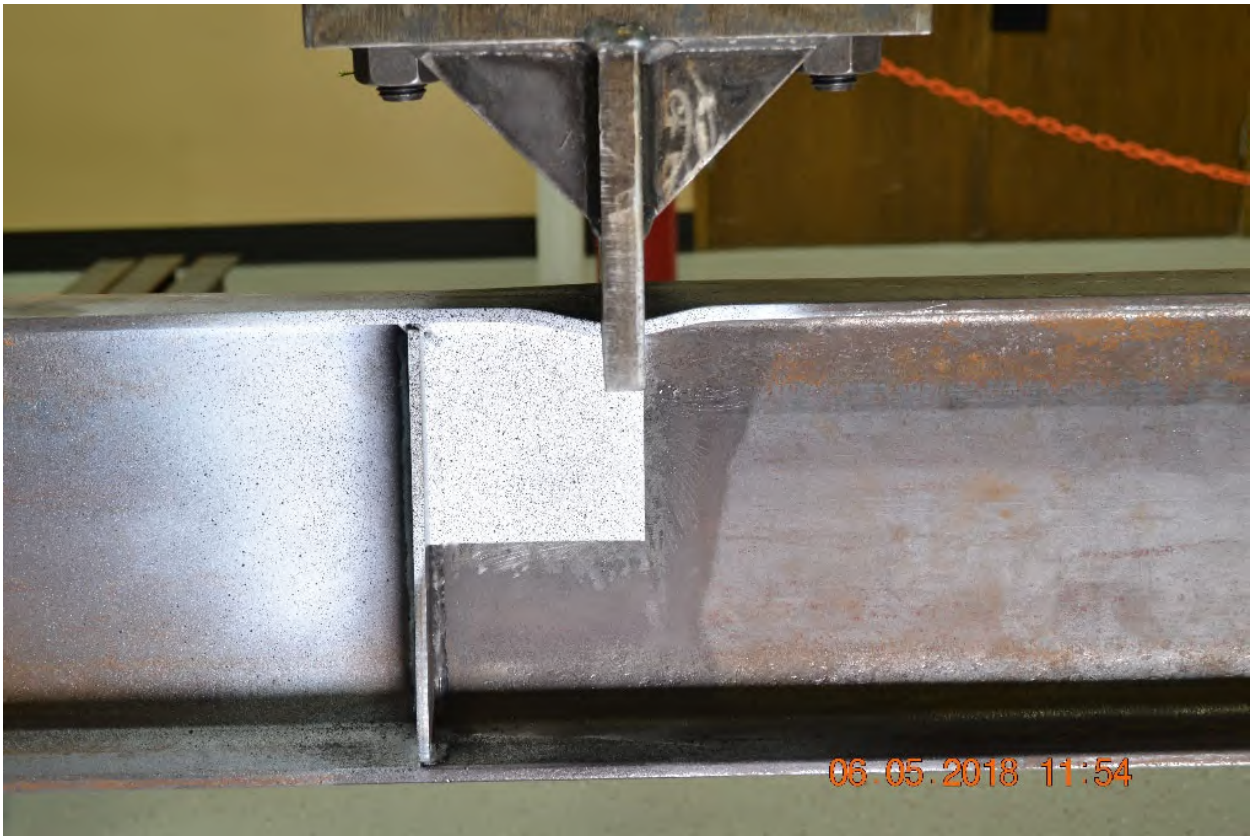

Figure A-23: Elevation of W10X19-SC-E4 after testing

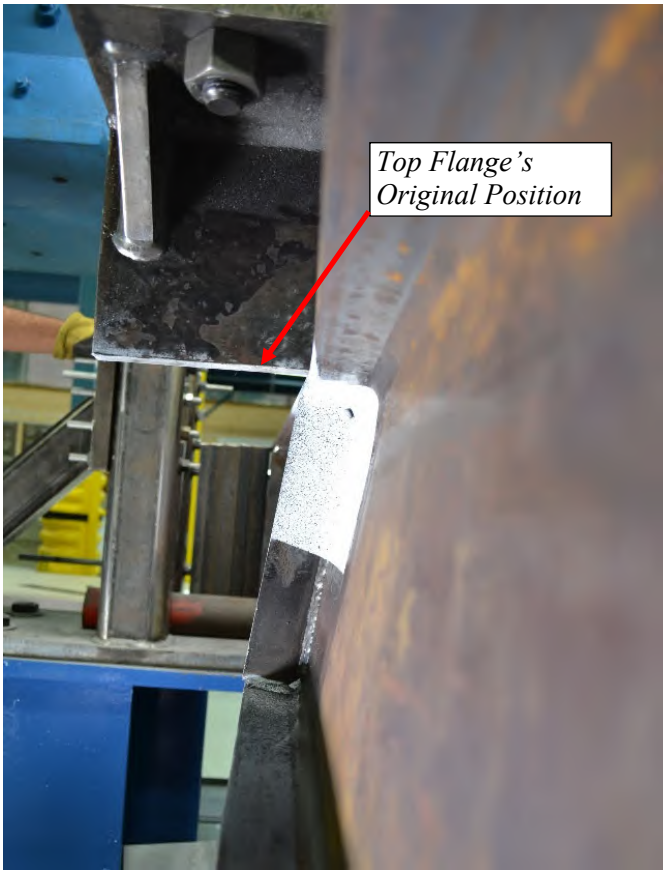

Figure A-24: W10X19-SC-E4 after testing emphasizing the twisting effect

Figure A-25: W10X19-SC-E4 after testing emphasizing flange bending and strain lines

Figure A-26: Side view of W10X19-SC-E4 after testing showing lateral-torsional buckling

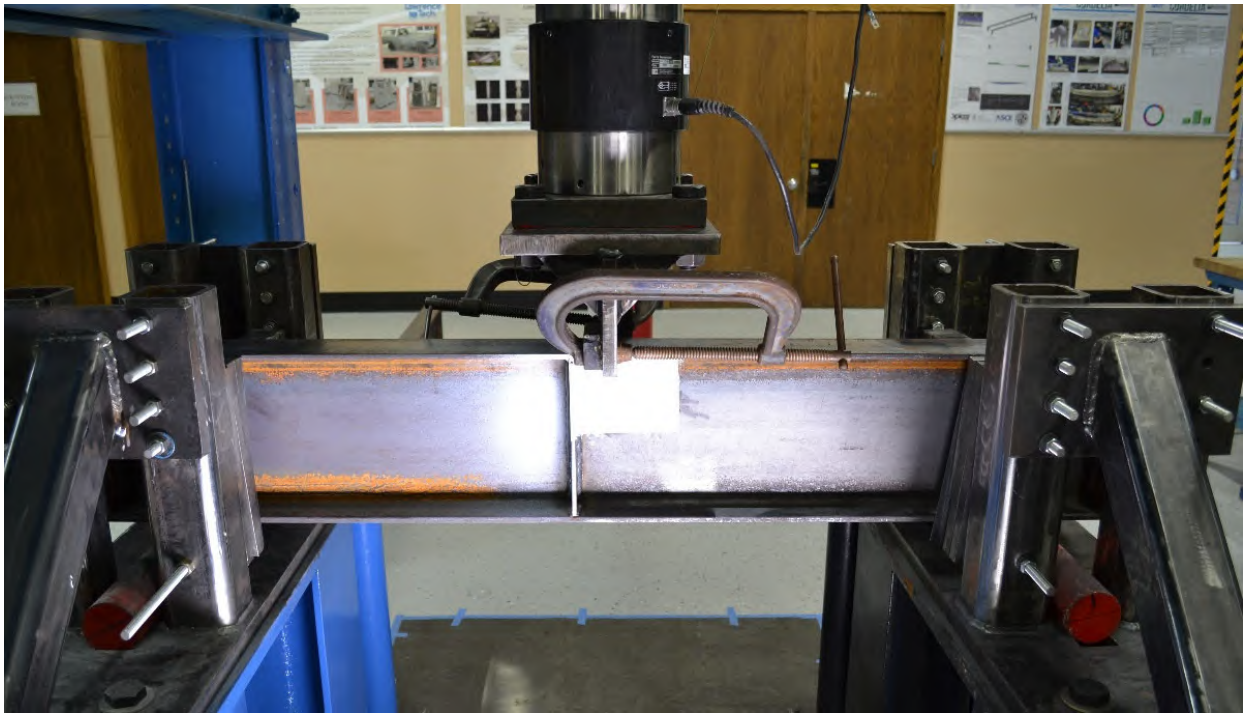

Figure A-27: Elevation of W10X19-SC-E2 prior to testing

Figure A-28: Elevation of W10X19-SC-E2 after testing

Figure A-29: Close up view of backside of W10X19-SC-E2 after testing

Figure A-30: W10X19-SC-E2 after testing emphasizing web crippling

Figure A-31: Side view of W10X19-SC-E2 after testing showing lateral-torsional buckling

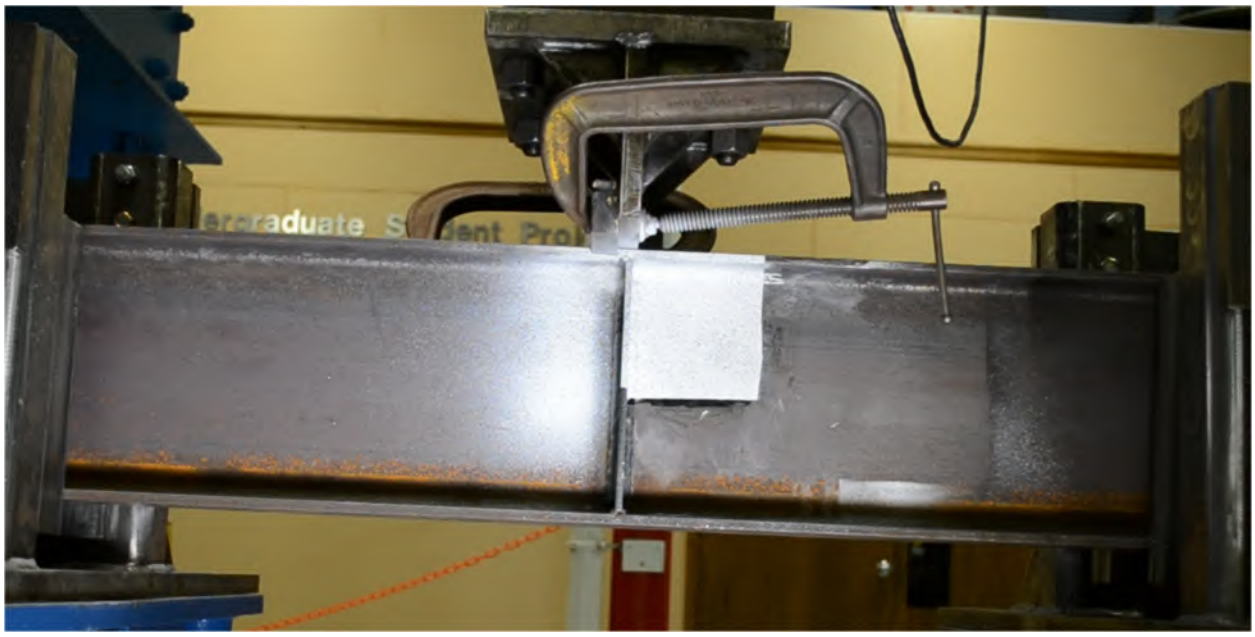

Figure A-32: Elevation of W10X19-SC-E0 prior to testing

Figure A-33: Close-up elevation of W10X19-SC-E0 after testing

Figure A-34: Close-up view of backside W10X19-SC-E0 after testing

Figure A-35: W10X19-SC-E0 after testing emphasizing flange and weld yielding

Figure A-36: Side view of W10X19-SC-E0 after testing showing lateral-torsional buckling

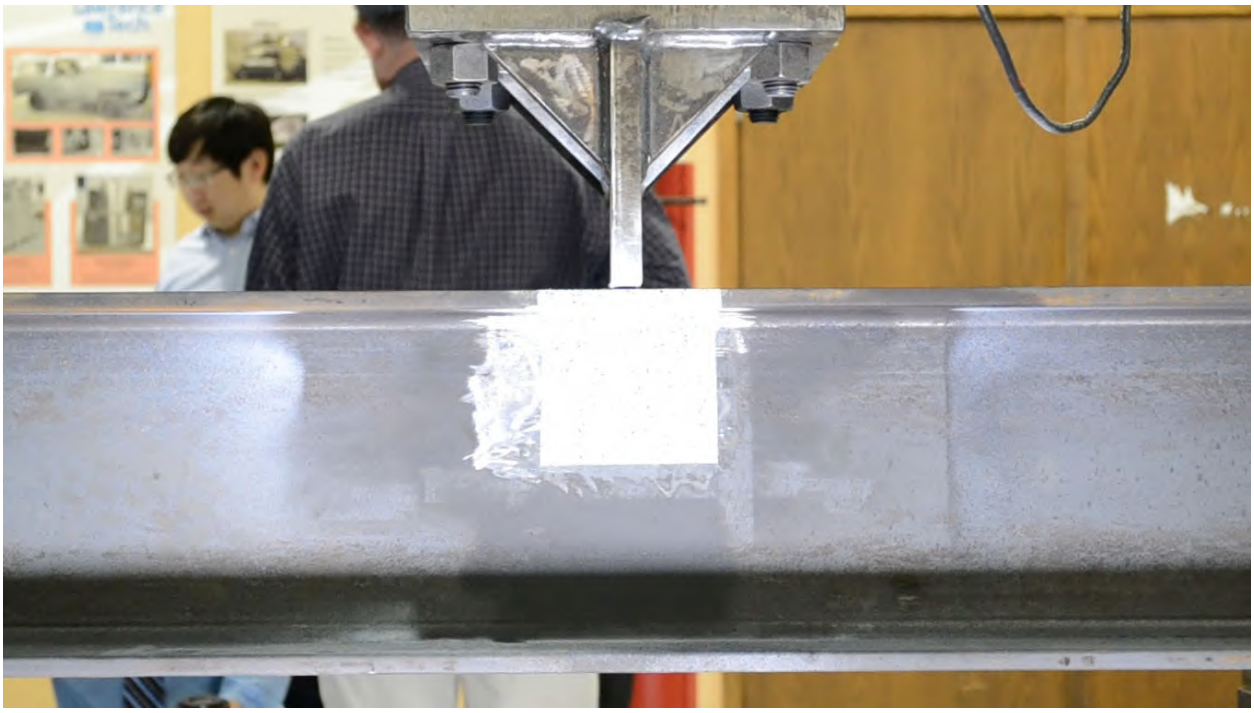

Figure A-37: Elevation of W10X39-SC-NA prior to testing

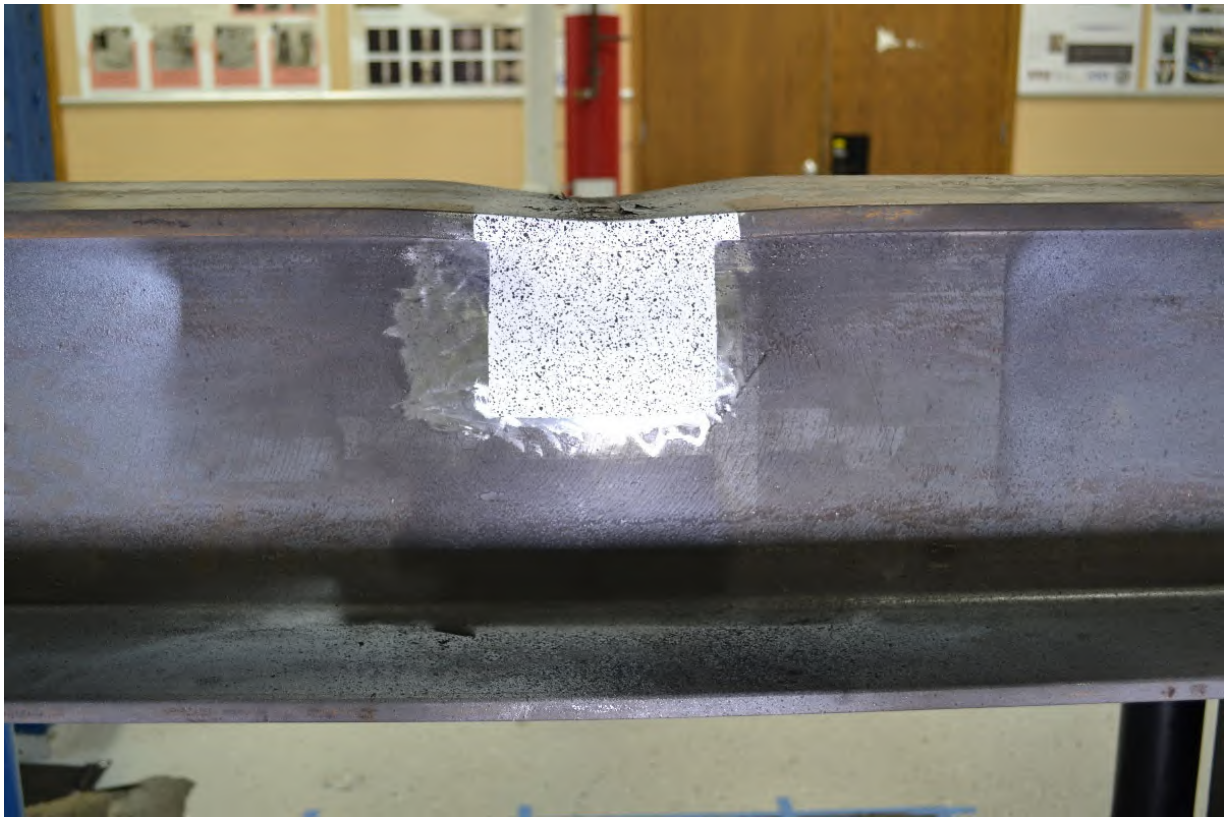

Figure A-38: Elevation of W10X39-SC-NA after testing

a) Bulge from front side of the specimen

b) Bulge from back side of the specimen

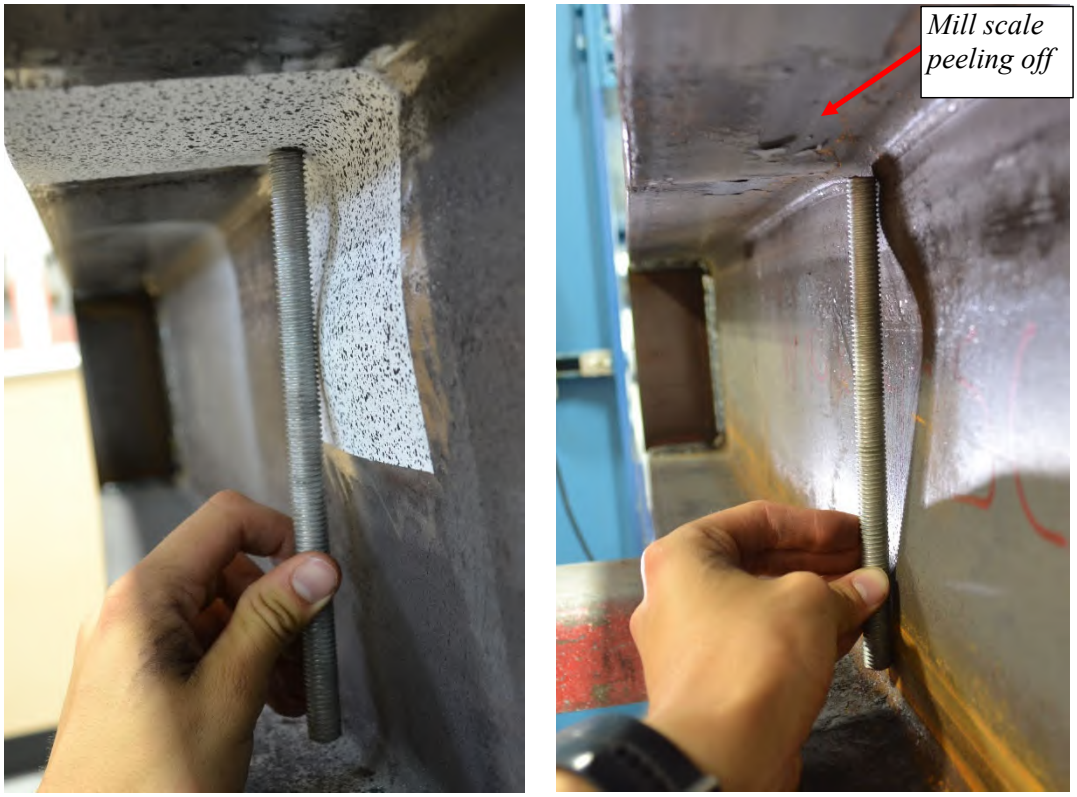

Figure A-39: W10X39-SC-NA after testing emphasizing web crippling

Figure A-40: Side view of W10X39-SC-NA after testing

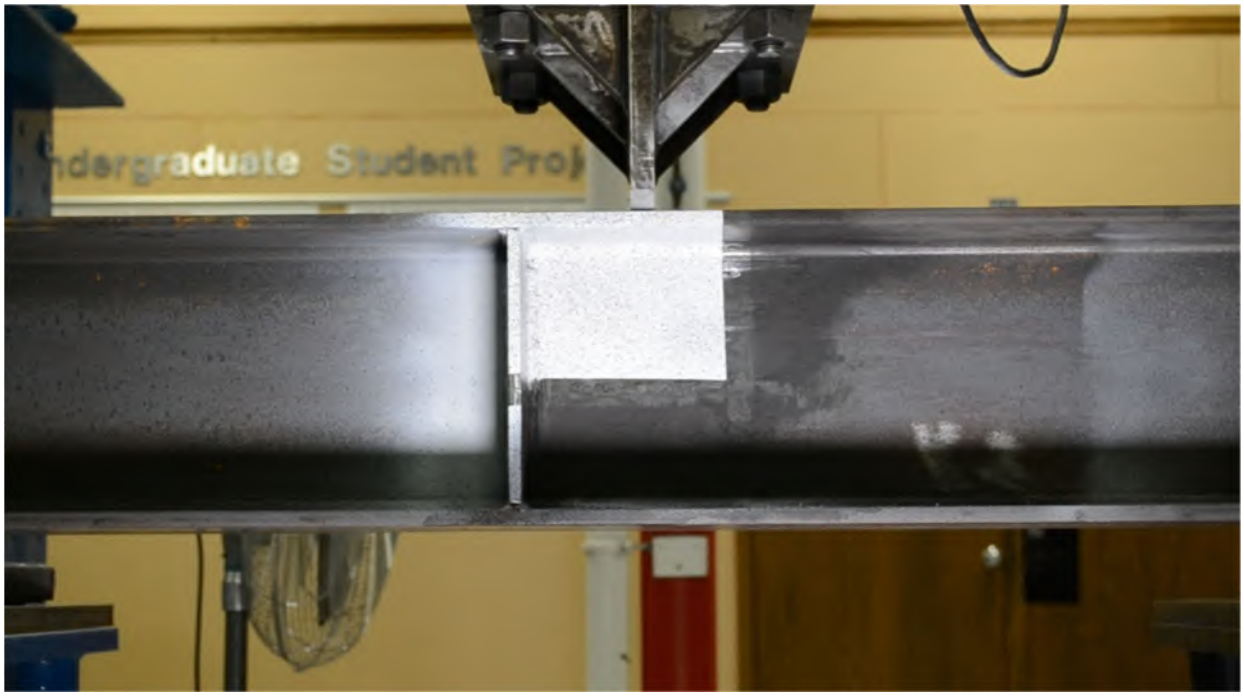

Figure A-41: Elevation of W10X39-SC-E4 prior to testing

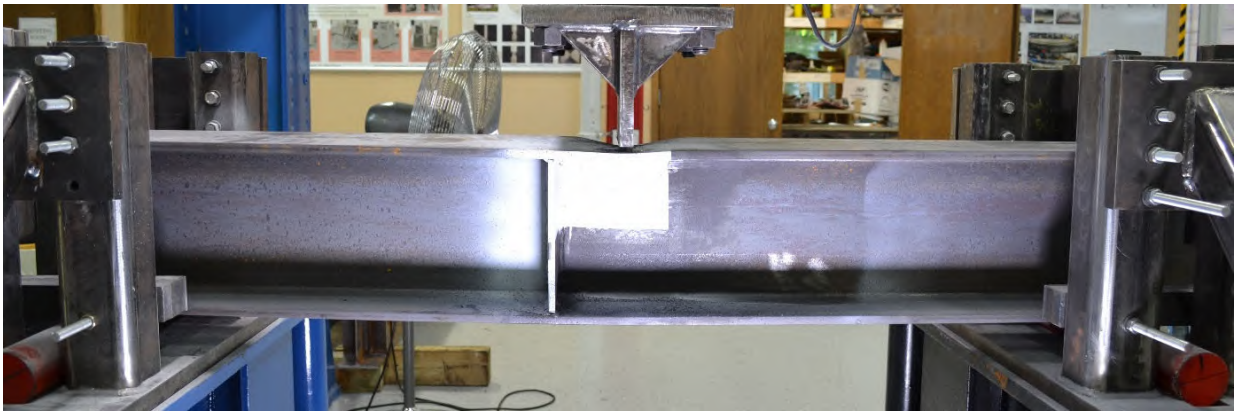

Figure A-42: Elevation of W10X39-SC-E4 after testing

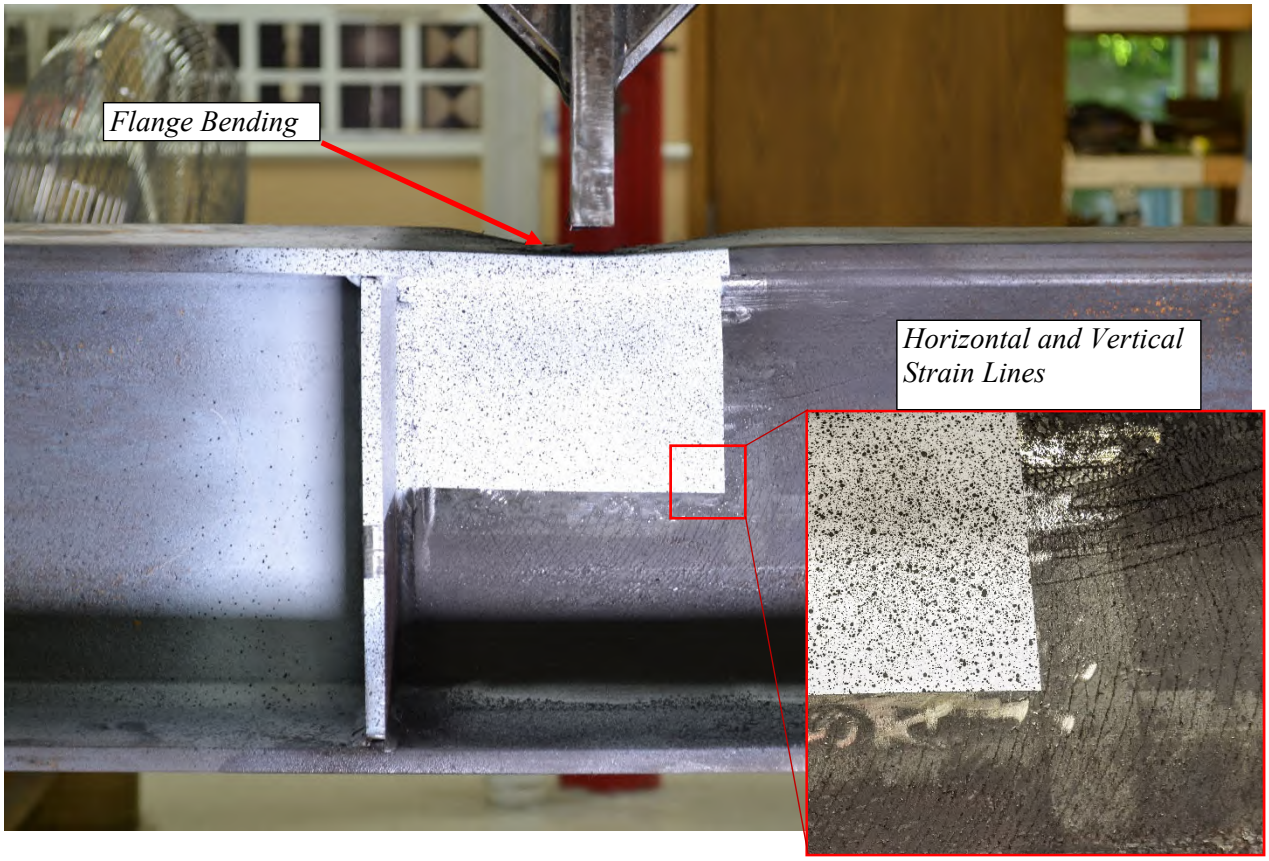

Figure A-43: Photo of W10X39-SC-E4 after testing with condition of flange and stiffener

a) Bulge from front side of the specimen

b) Bulge from back side of the specimen

Figure A-44: W10X39-SC-E4 after testing emphasizing web crippling

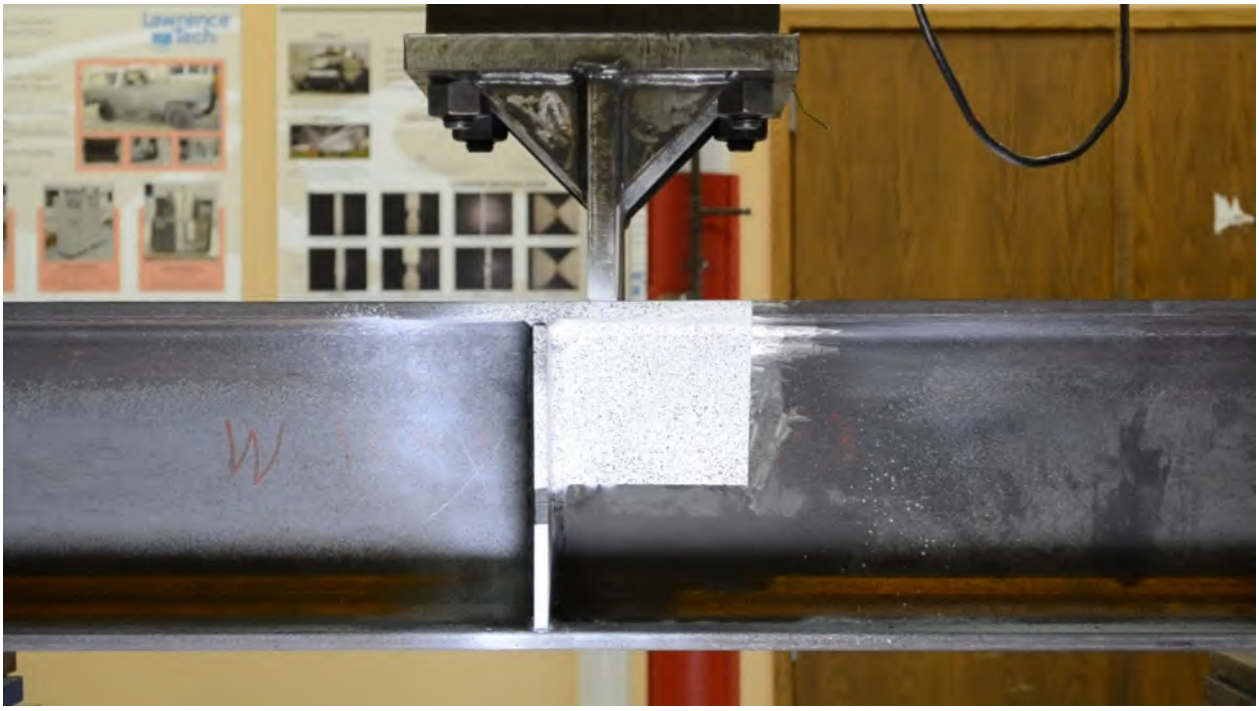

Figure A-45: Elevation of W10X39-SC-E2 prior to testing

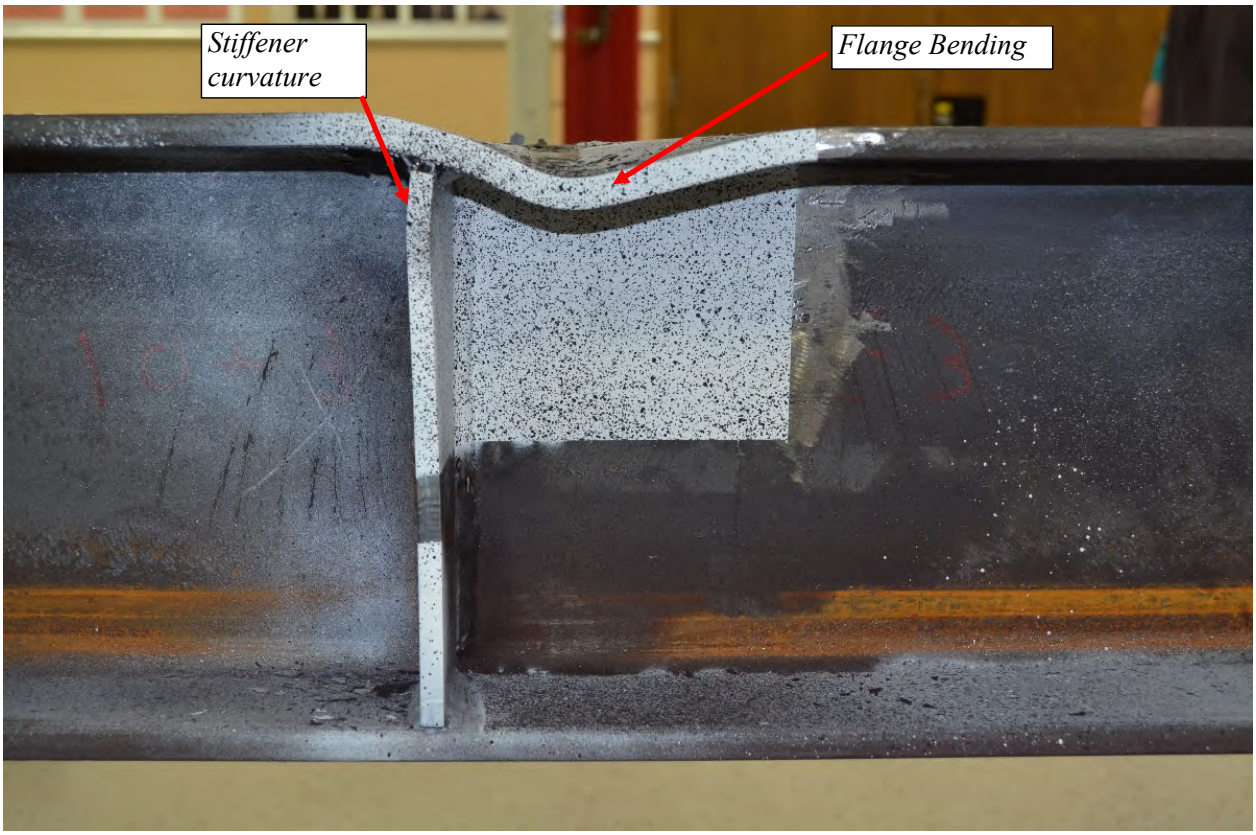

Figure A-46: Elevation view of W10X39-SC-E2 after testing

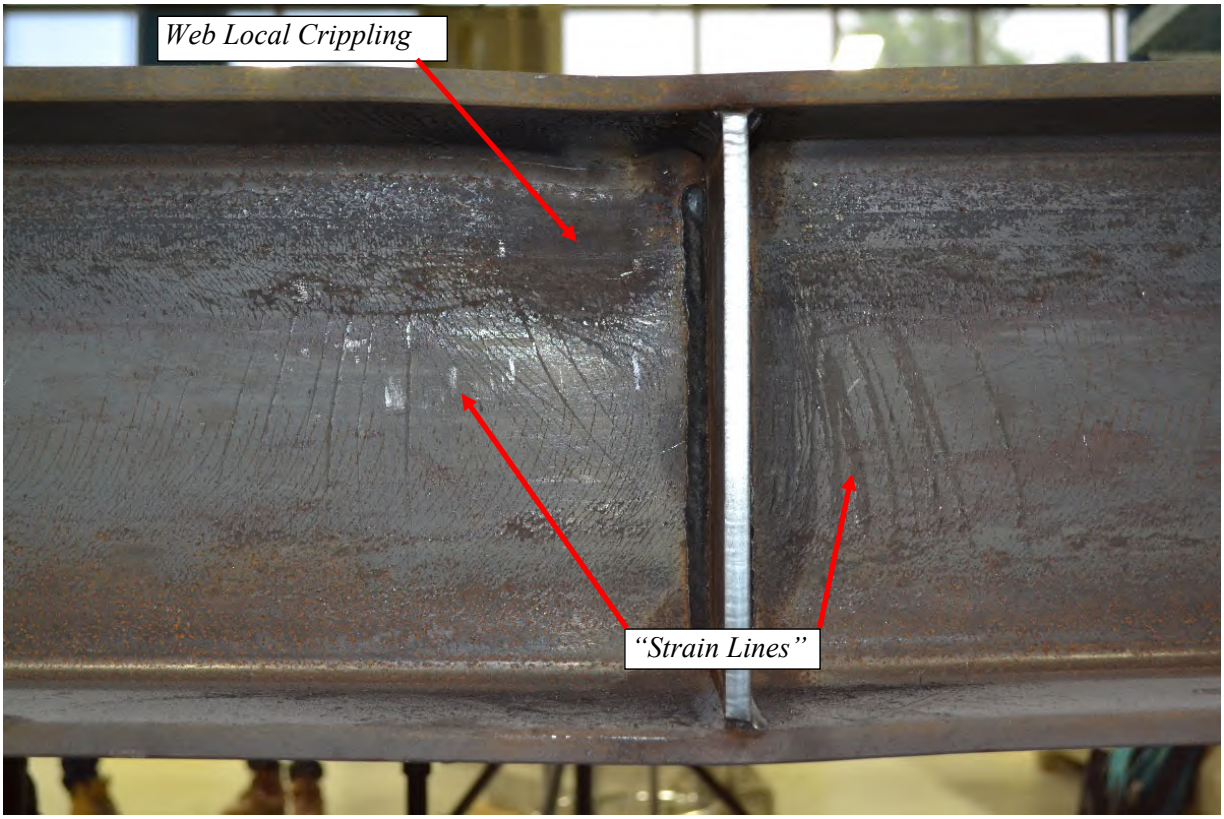

Figure A-47: Close up view of backside of W10X39-SC-E2 after testing

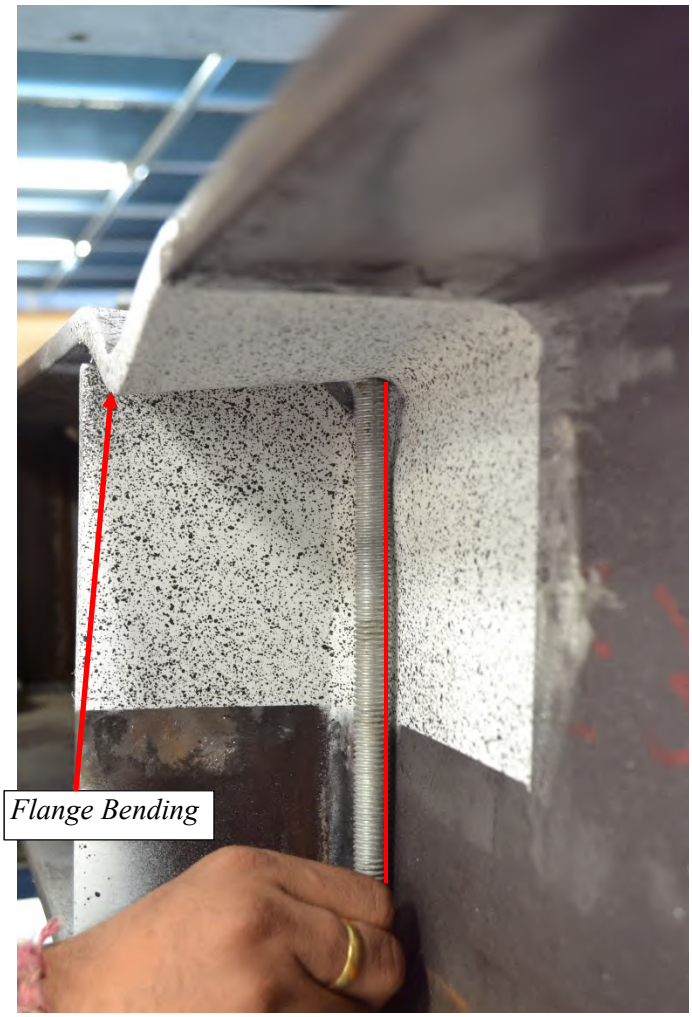

Figure A-48: W10X39-SC-E2 after testing emphasizing web crippling

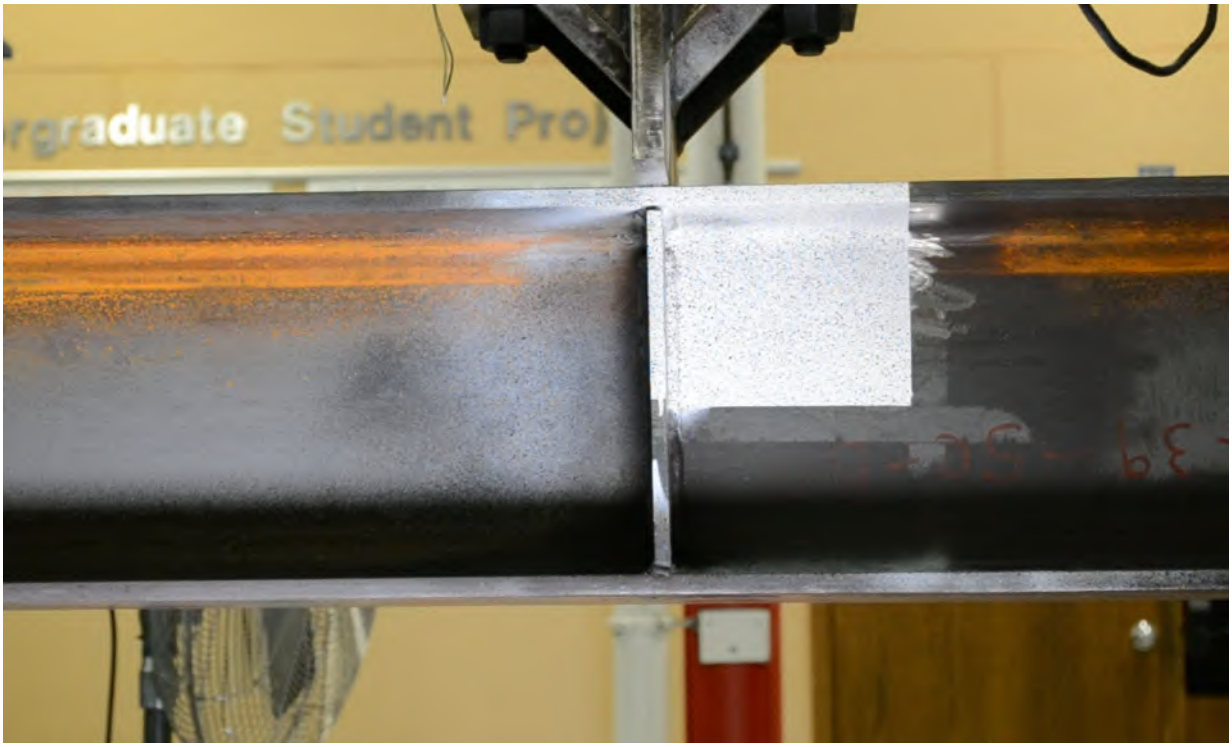

Figure A-49: Elevation of W10X39-SC-E0 prior to testing

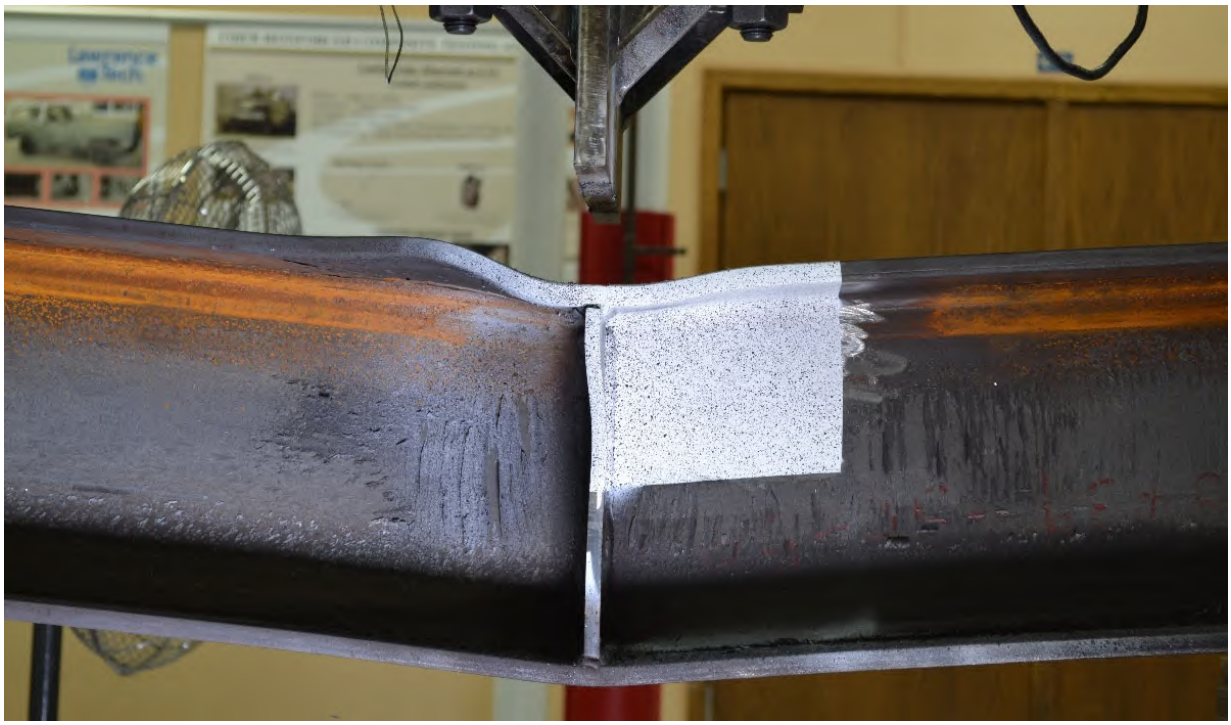

Figure A-50: Elevation of W10X39-SC-E0 after testing

a) Yielding from front side of the specimen

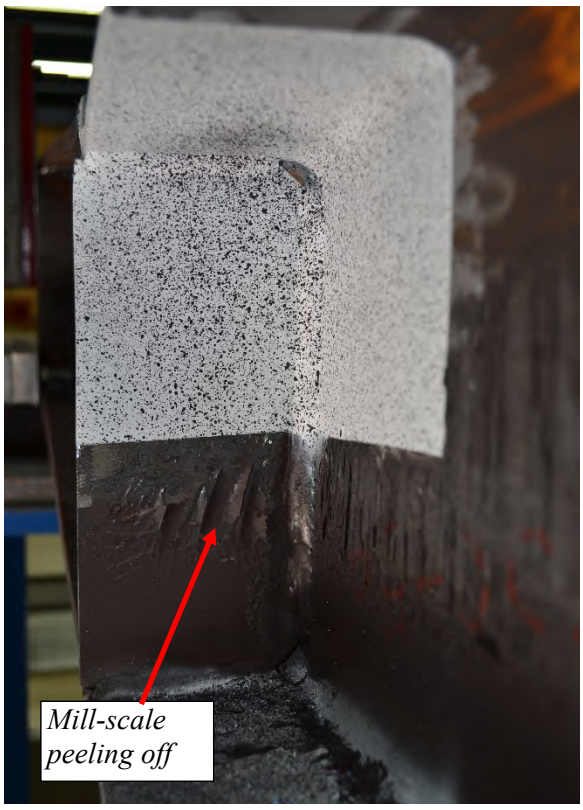

b) Yielding from back side of the specimen

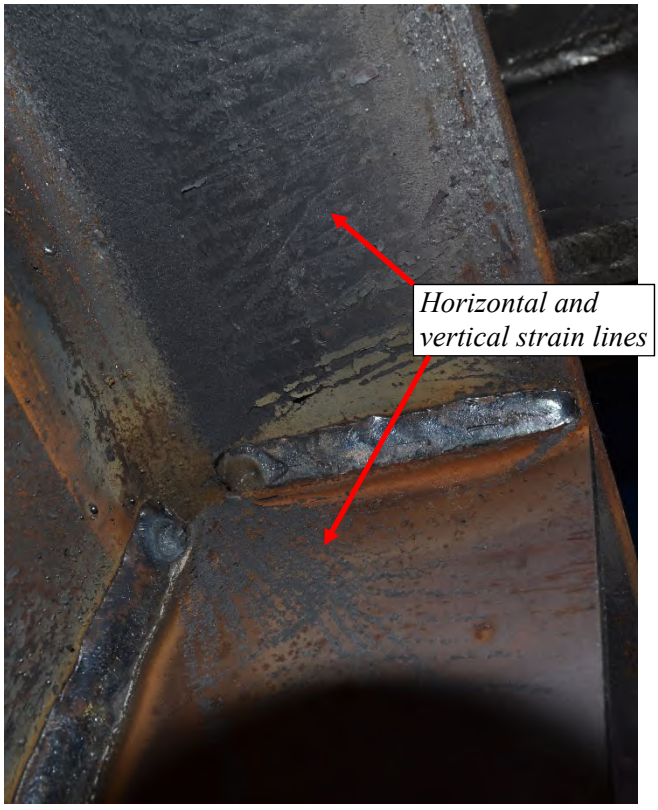

Figure A-51: W10X39-SC-E0 after testing emphasizing stiffener yielding

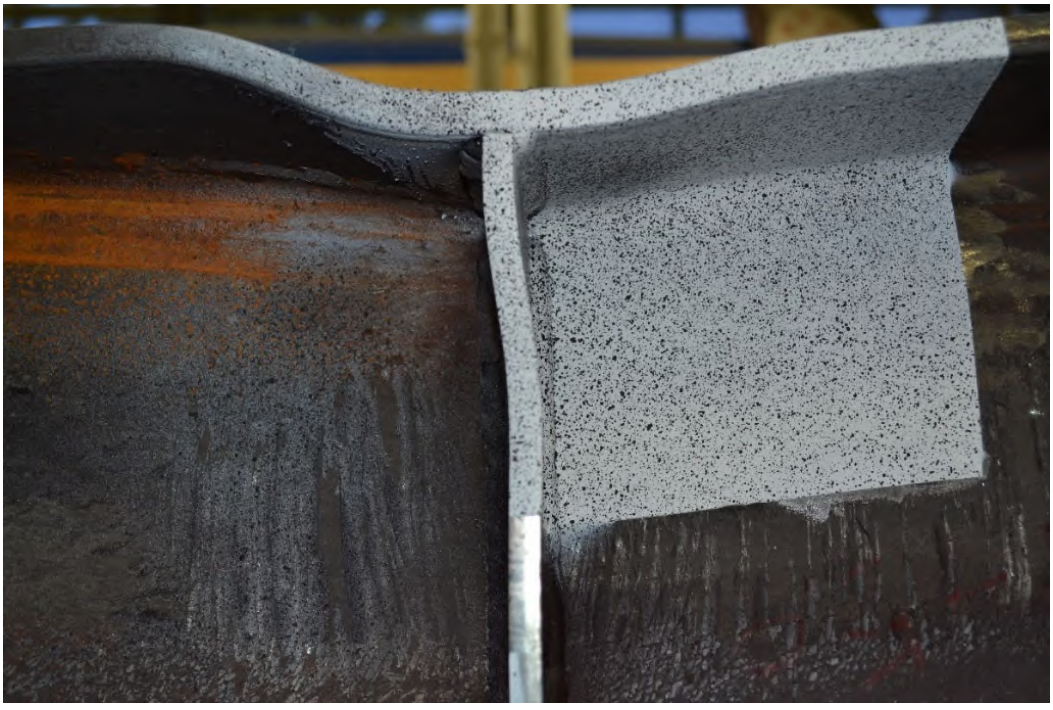

Figure A-52: Close-up view of W10X39-SC-E0 emphasizing buckling of front stiffener

Figure A-53: Side view of W10X39-SC-E0 after testing showing web strain lines

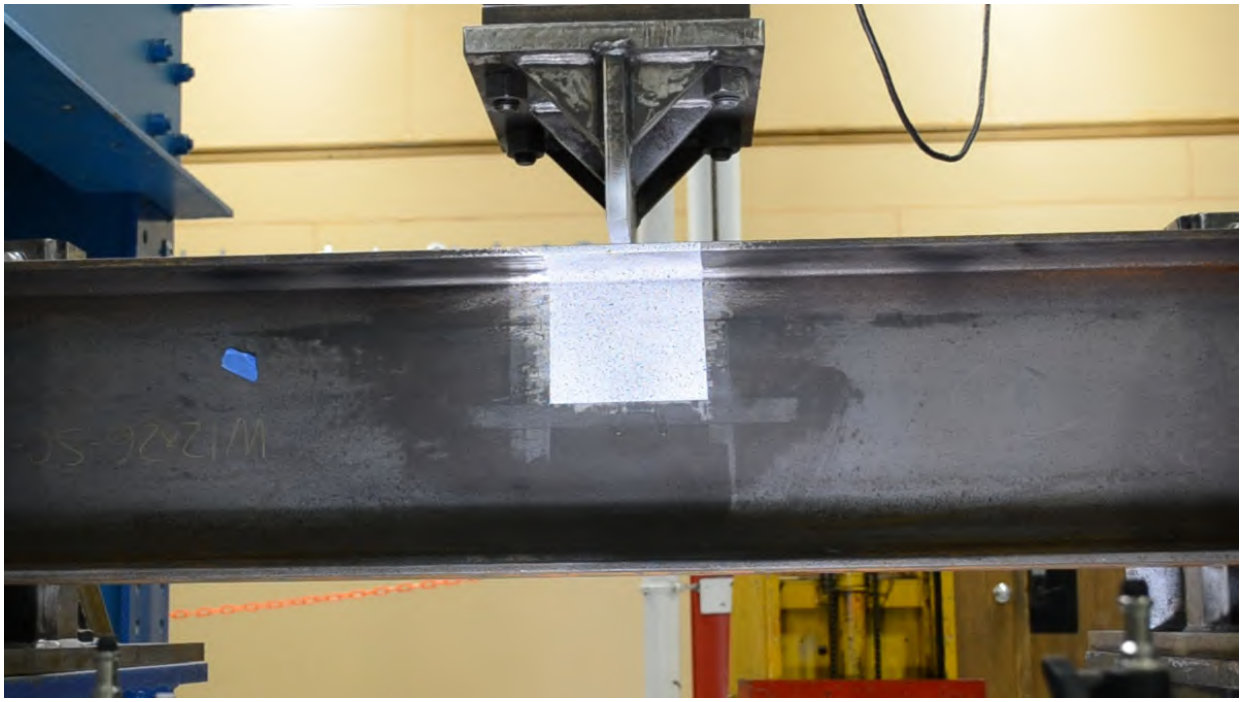

Figure A-54: Elevation of W12X26-SC-NA prior to testing

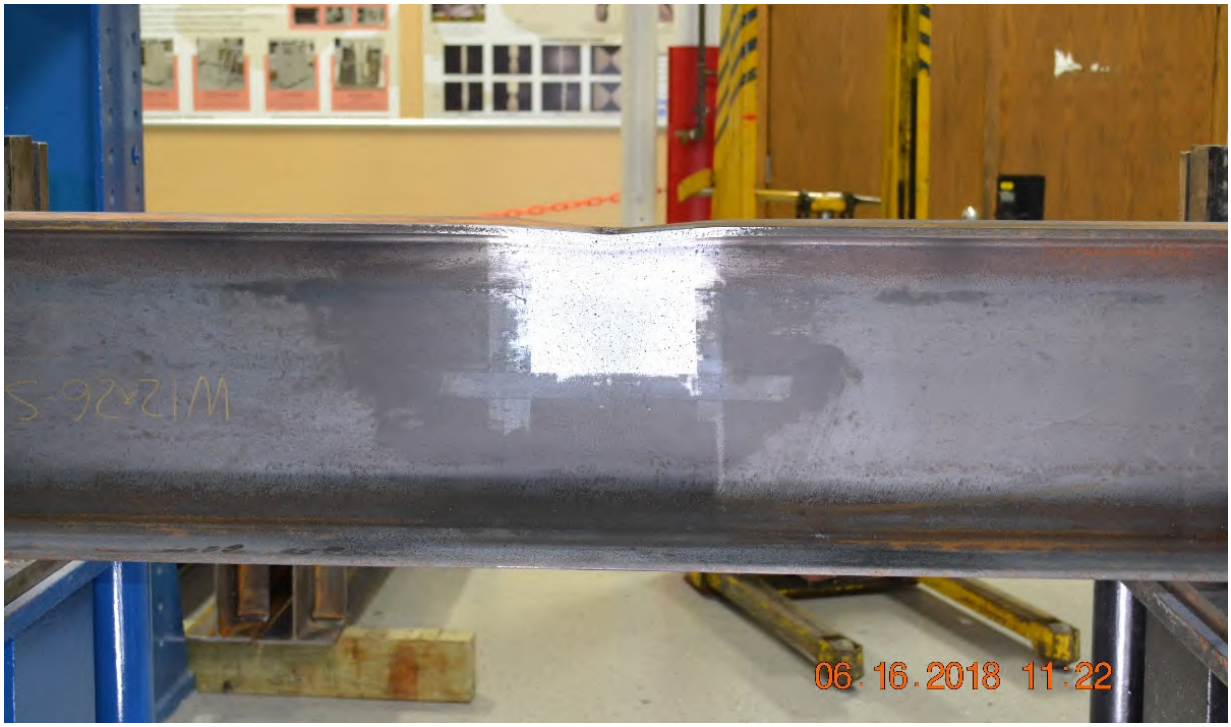

Figure A-55: Elevation of W12X26-SC-NA after testing

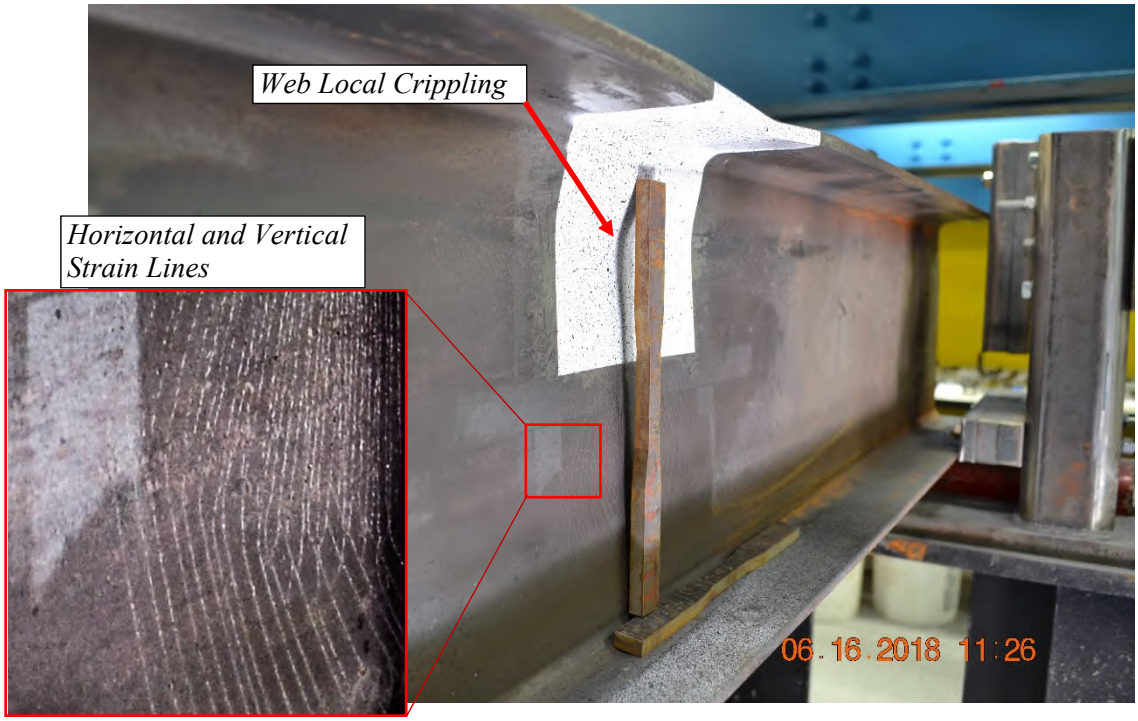

Figure A-56: W12X26-SC-NA after testing emphasizing web crippling

Figure A-57: Side view of W12X26-SC-NA after testing

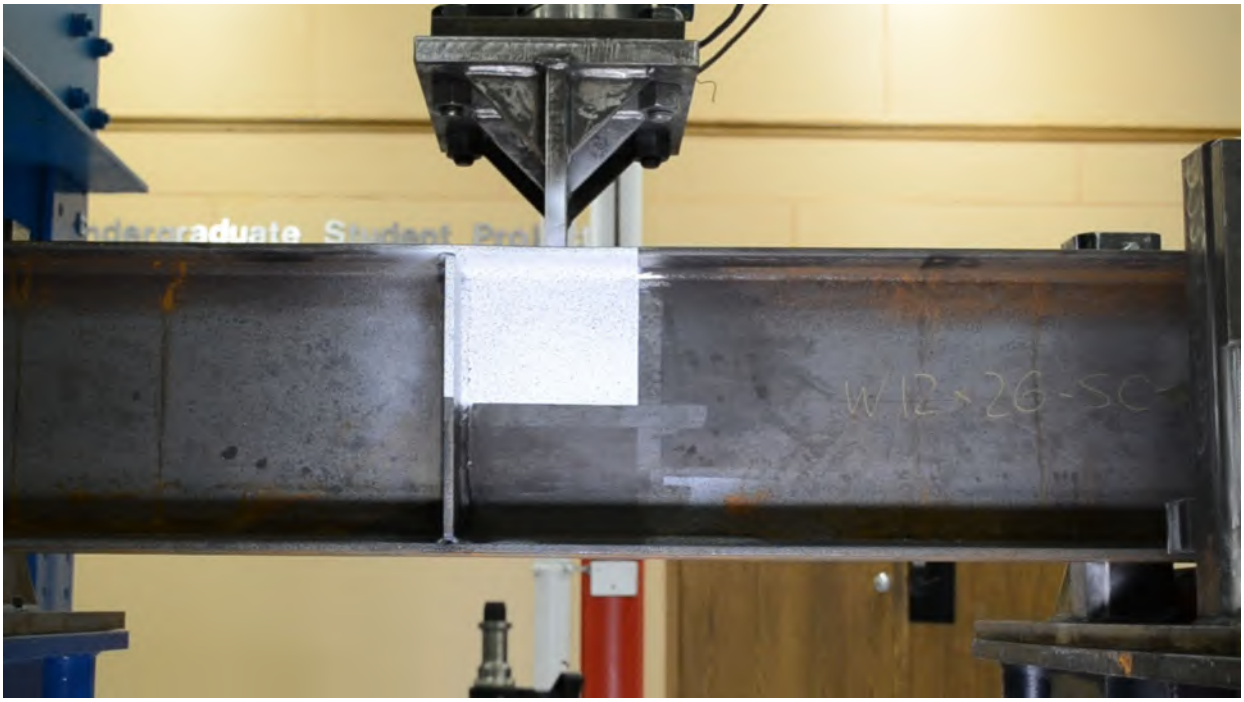

Figure A-58: Elevation of W12X26-SC-E4 prior to testing

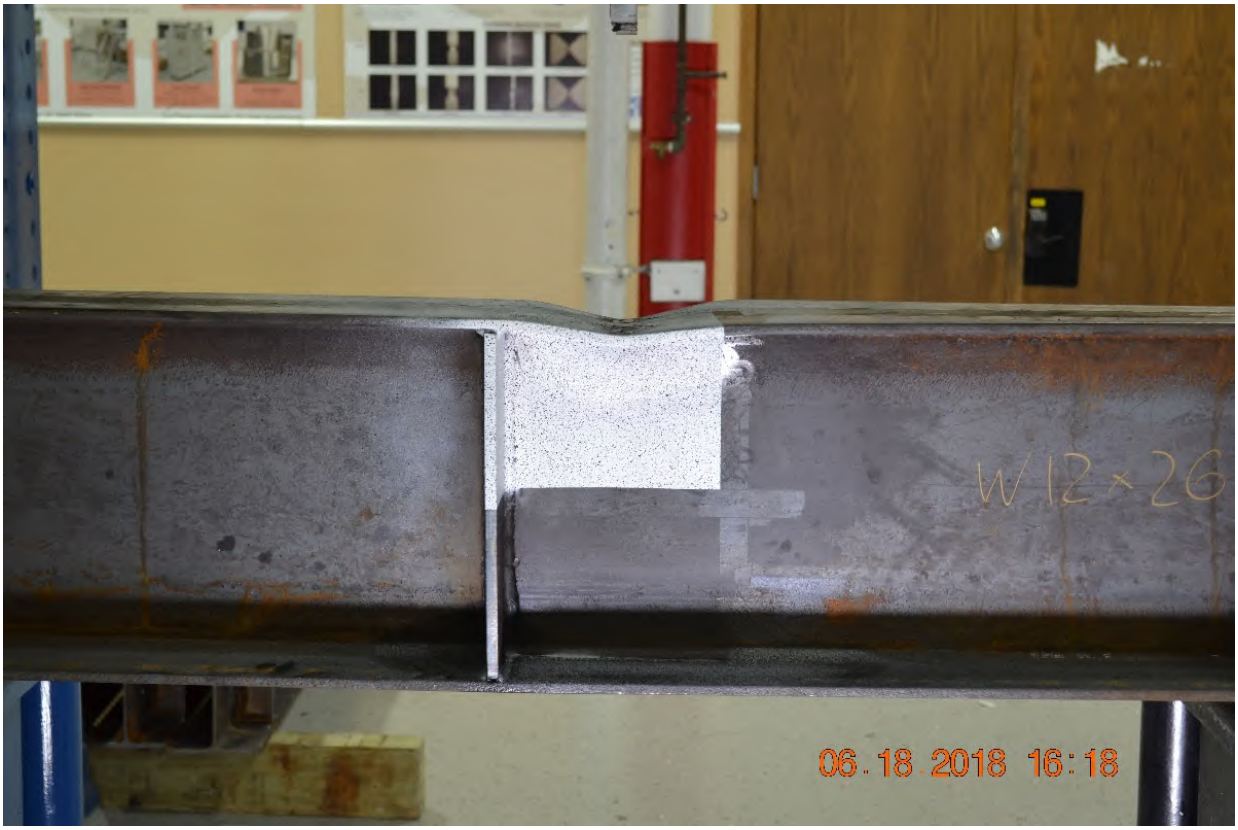

Figure A-59: Elevation of W12X26-SC-E4 after testing

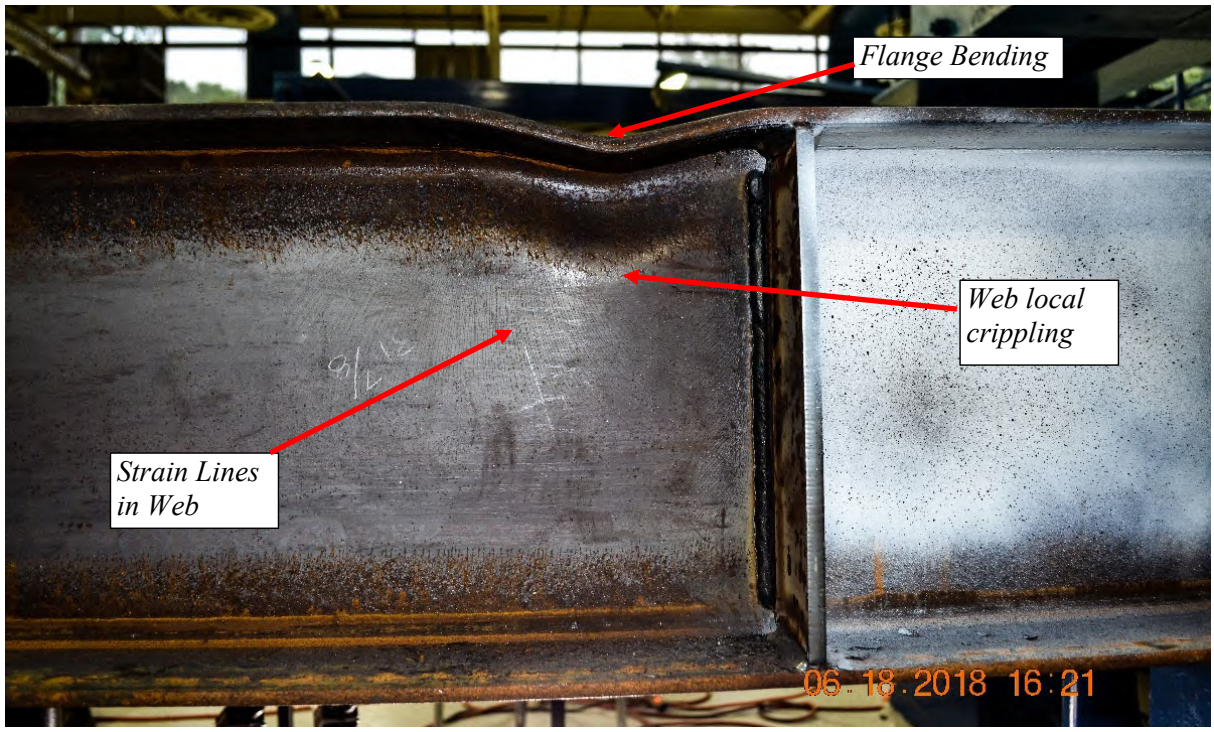

Figure A-60: Close-up of W12X26-SC-E4 after testing

Figure A-61: W12X26-SC-E4 after testing emphasizing web local crippling

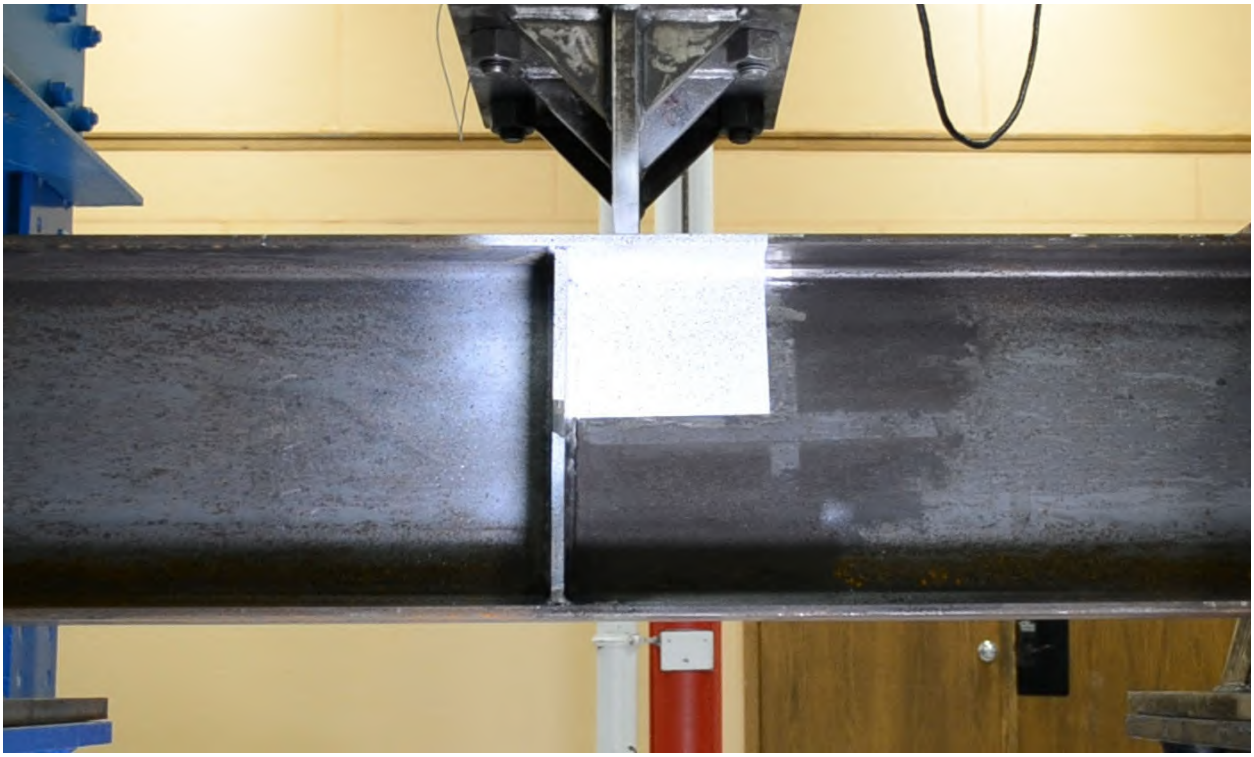

Figure A-62: Elevation of W12X26-SC-E2 prior to testing

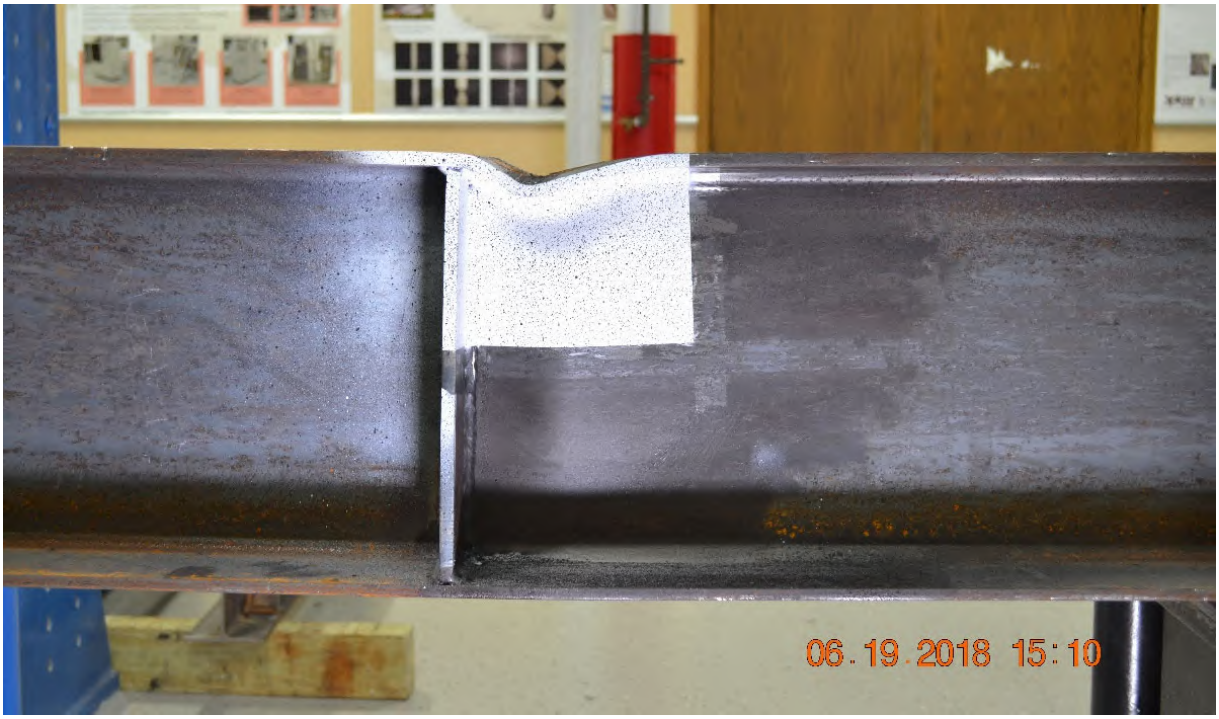

Figure A-63: Elevation of W12X26-SC-E2 after testing

a) Back side of the specimen

b) Front side of the specimen

Figure A-64: Close-up view of W12X26-SC-E2 after testing

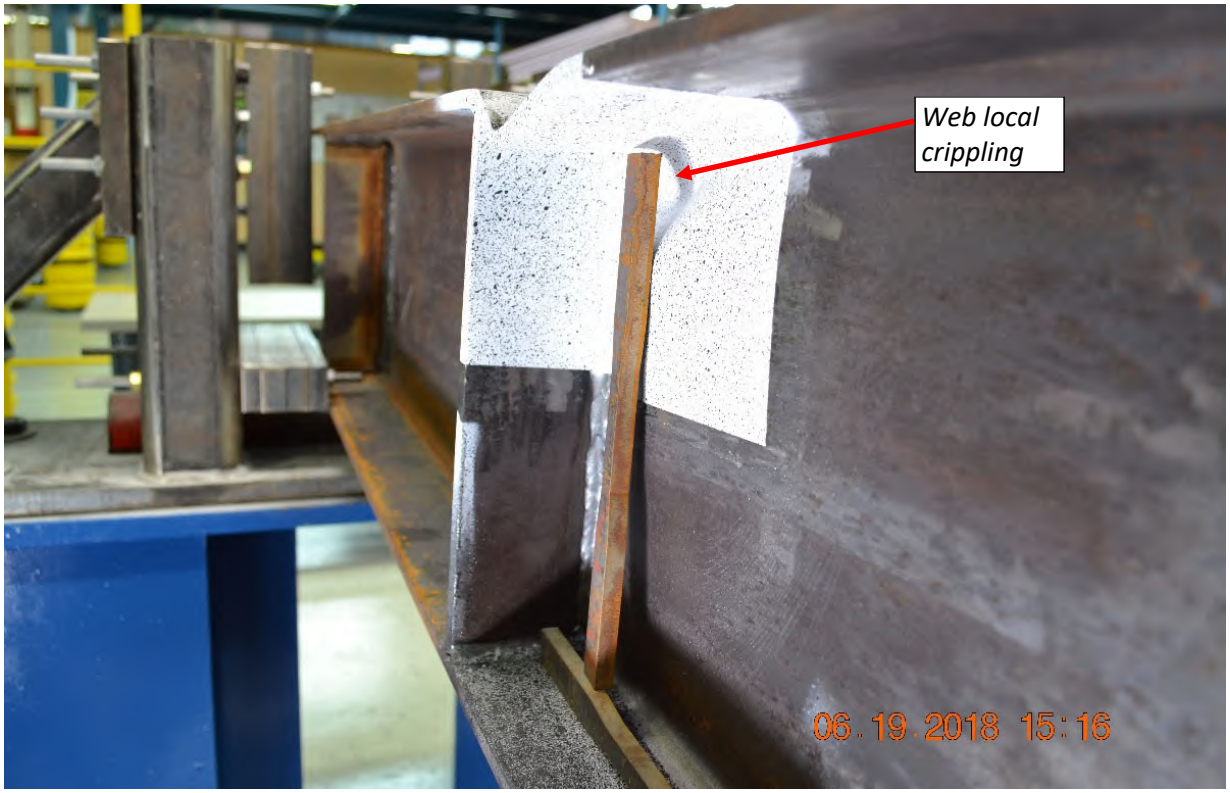

Figure A-65: W12X26-SC-E2 after testing emphasizing web crippling

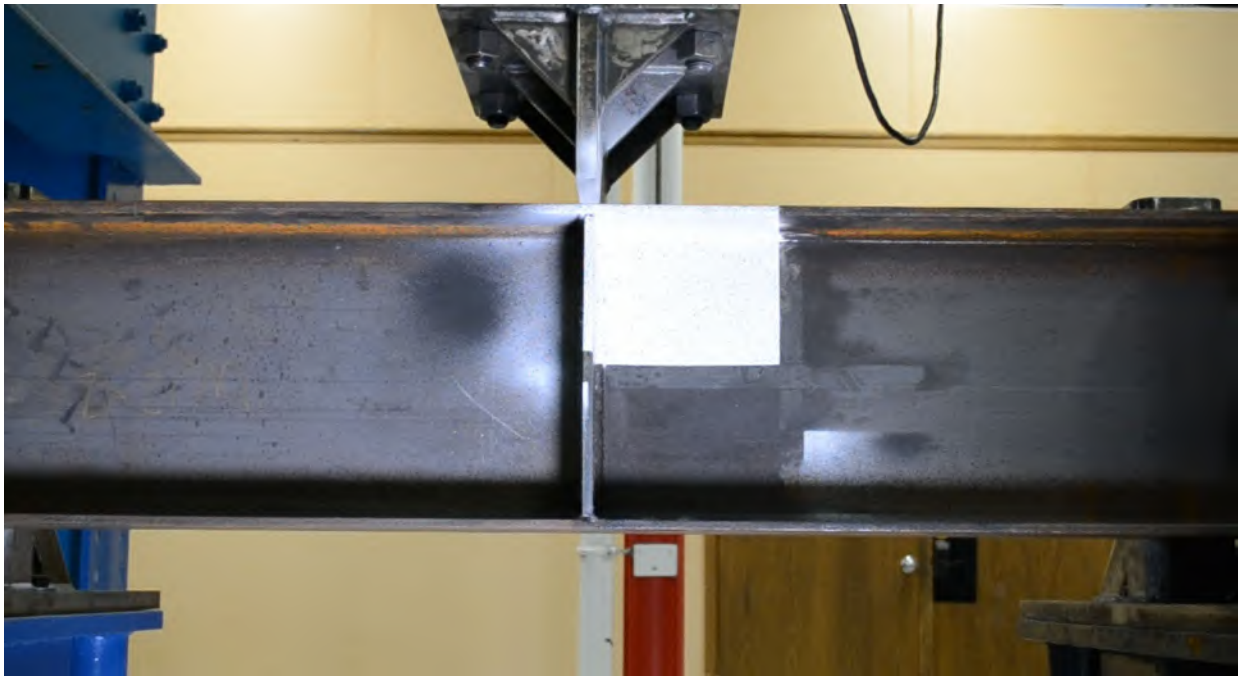

Figure A-66: Elevation of W12X26-SC-E0 prior to testing

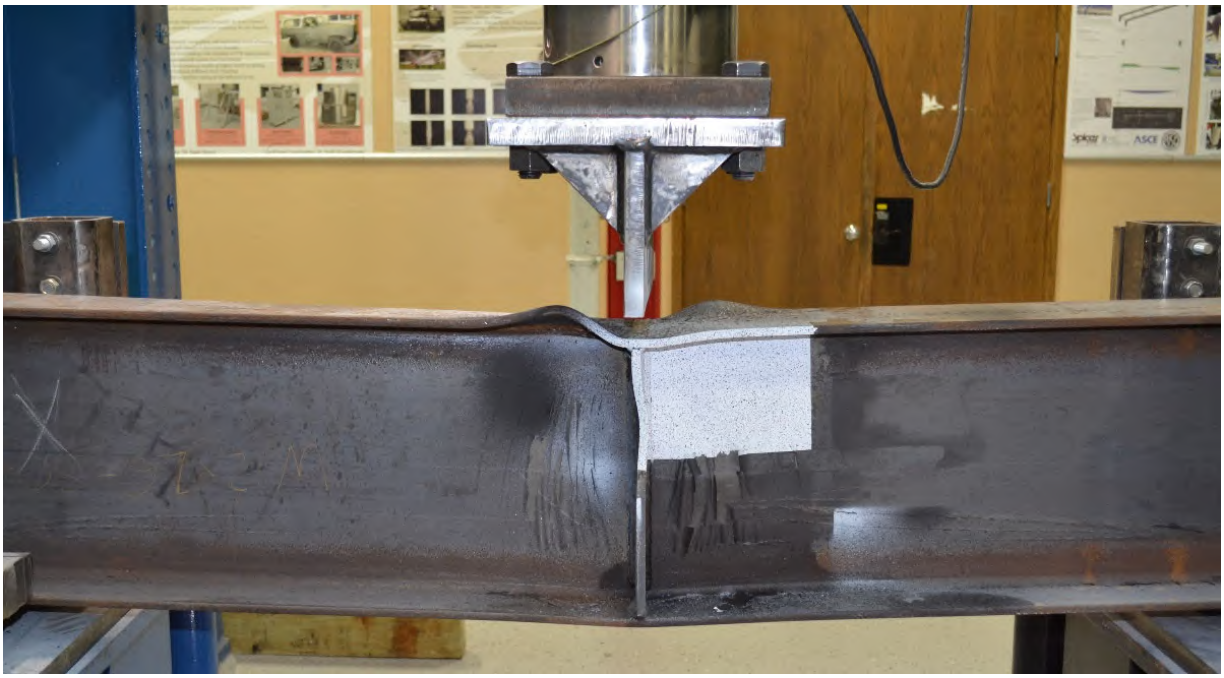

Figure A-67: Elevation of W12X26-SC-E0 after testing

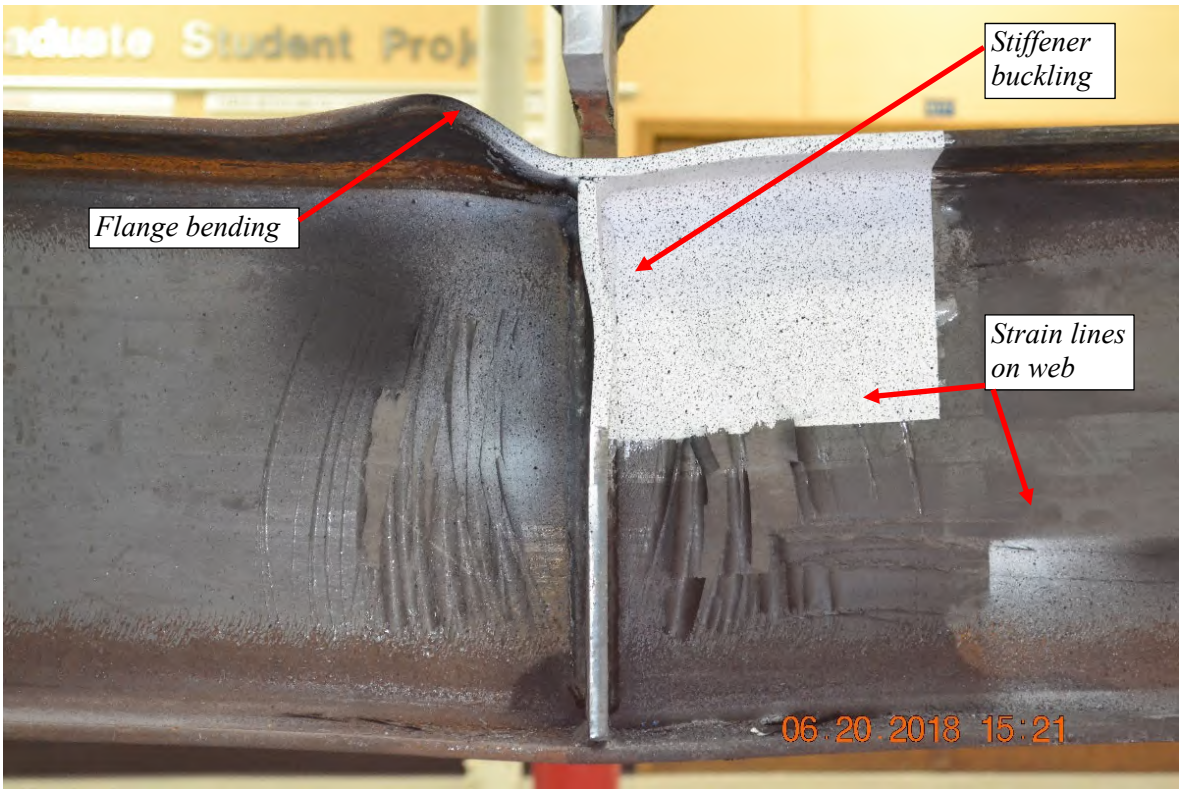

Figure A-68: Close-up view of front side of W12X26-SC-E0 after testing

Figure A-69: Side view of W12X26-SC-E0 after testing emphasizing yielding

Figure A-70: Bottom view of W12X26-SC-E0 after testing emphasizing yielding

Figure A-71: Elevation of W16X31-DC-NA prior to testing

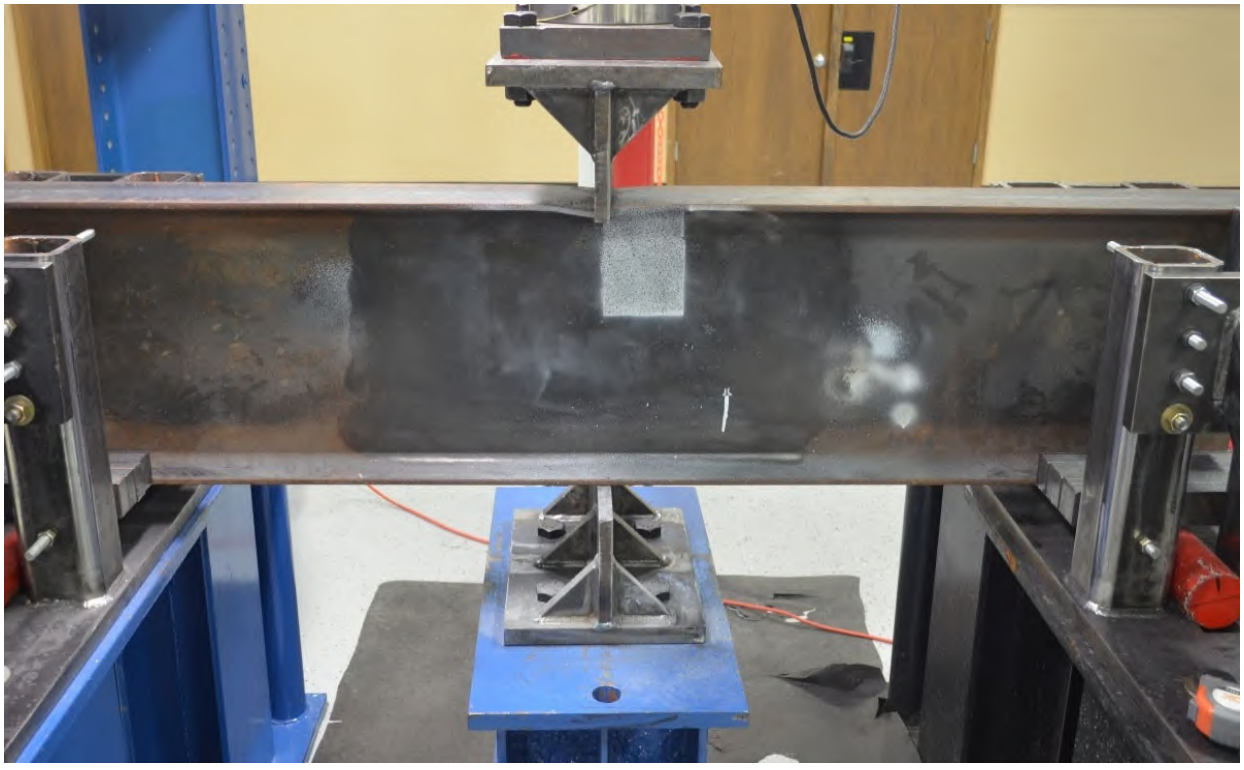

Figure A-72: Elevation of W16X31-DC-NA after testing

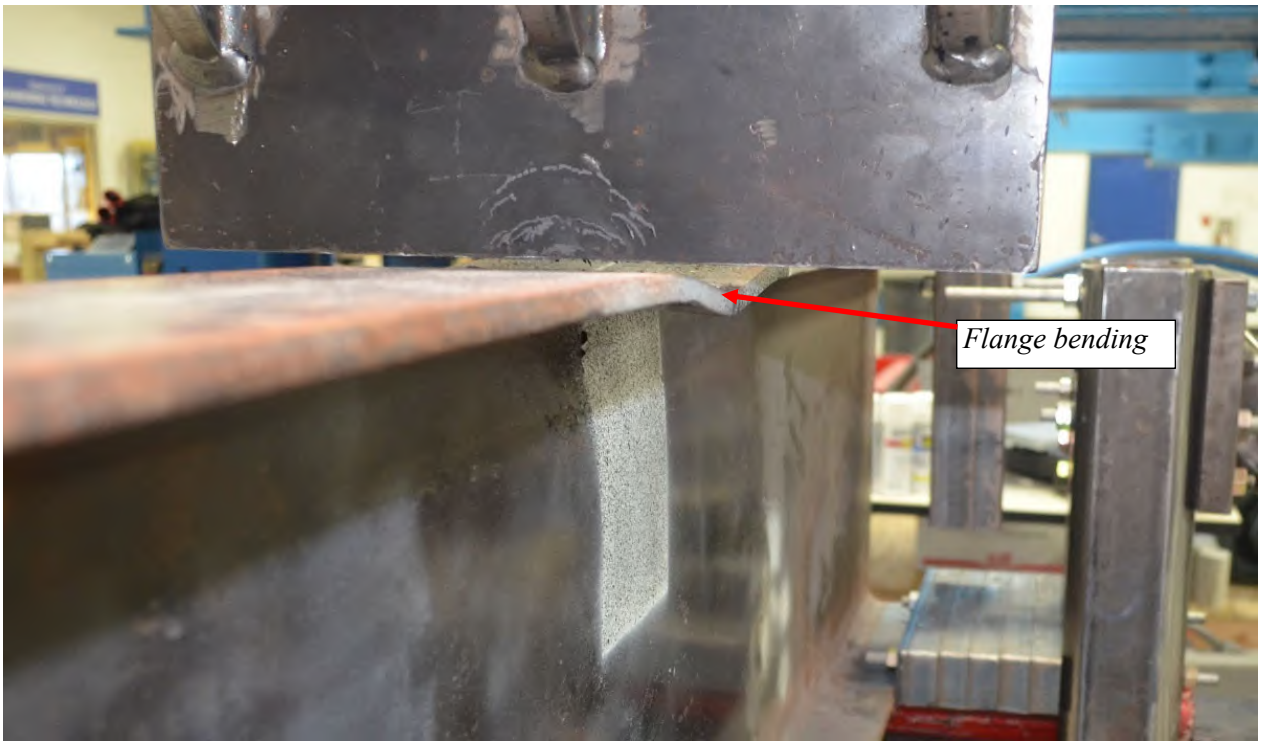

Figure A-73: W16X31-DC-NA after testing emphasizing flange bending

Figure A-74: W16X31-DC-NA after testing emphasizing web crippling

Figure A-75: W16X31-DC-NA after testing emphasizing web local yielding

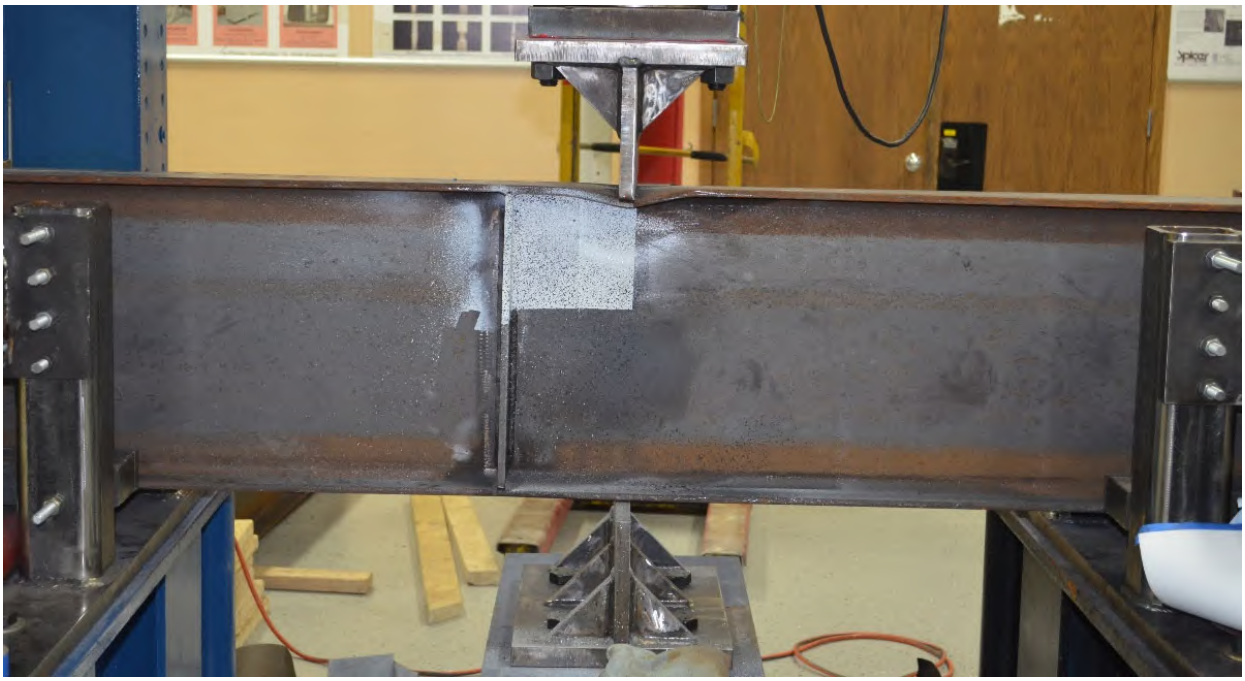

Figure A-76: Elevation of W16X31-DC-E6 after testing

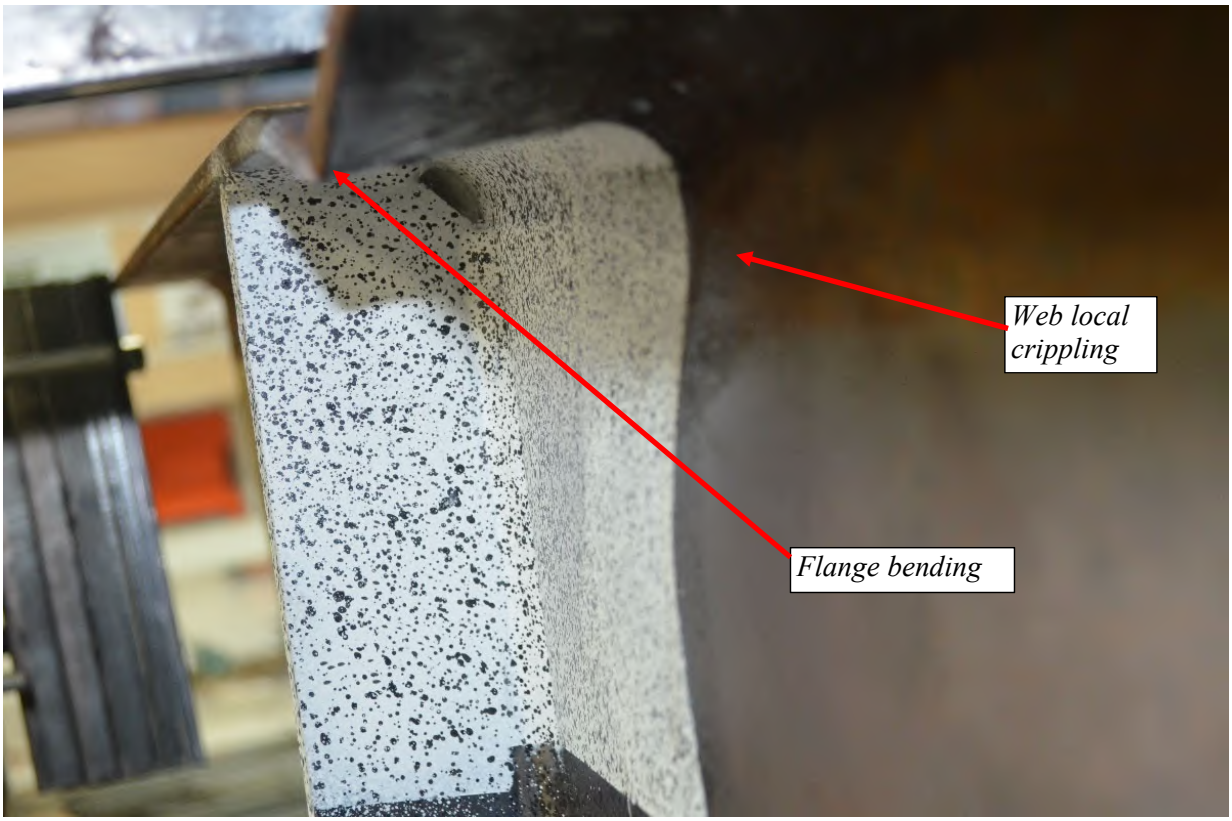

Figure A-77: Photo of W16X31-DC-E6 after testing with condition of flange and stiffener

Figure A-78: Condition of bottom loading plate after testing

Figure A-79: W16X31-DC-E6 after testing emphasizing web local crippling

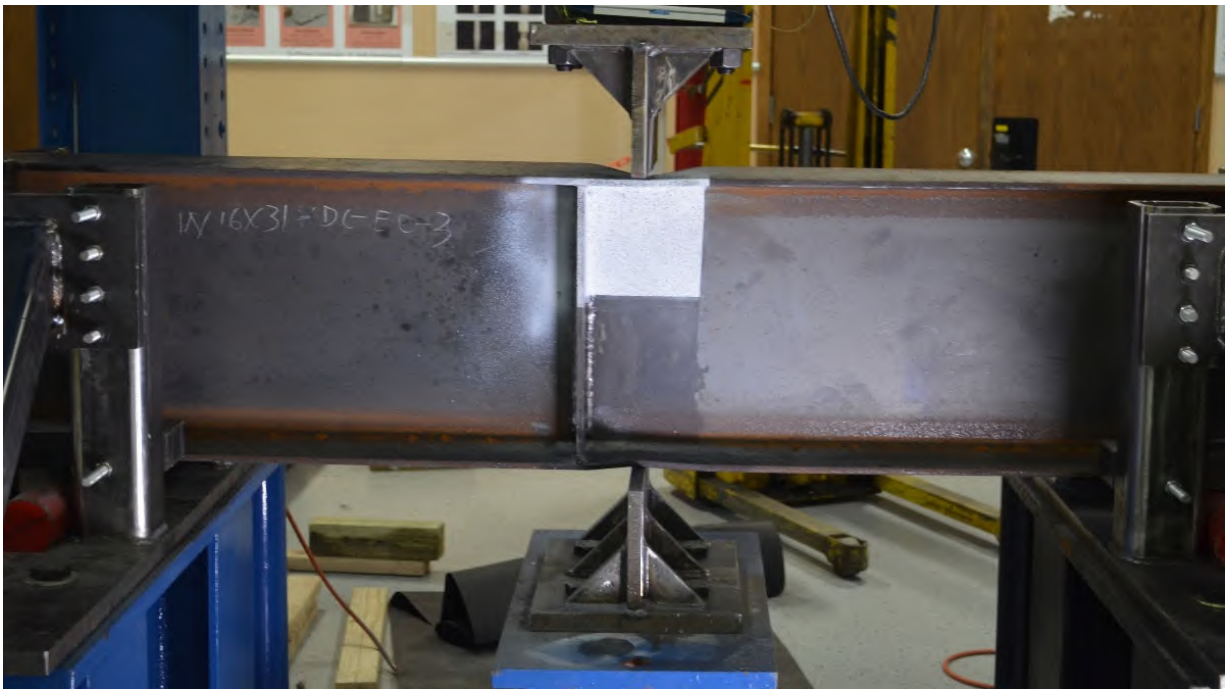

Figure A-80: Elevation of W16X31-DC-E3 after testing

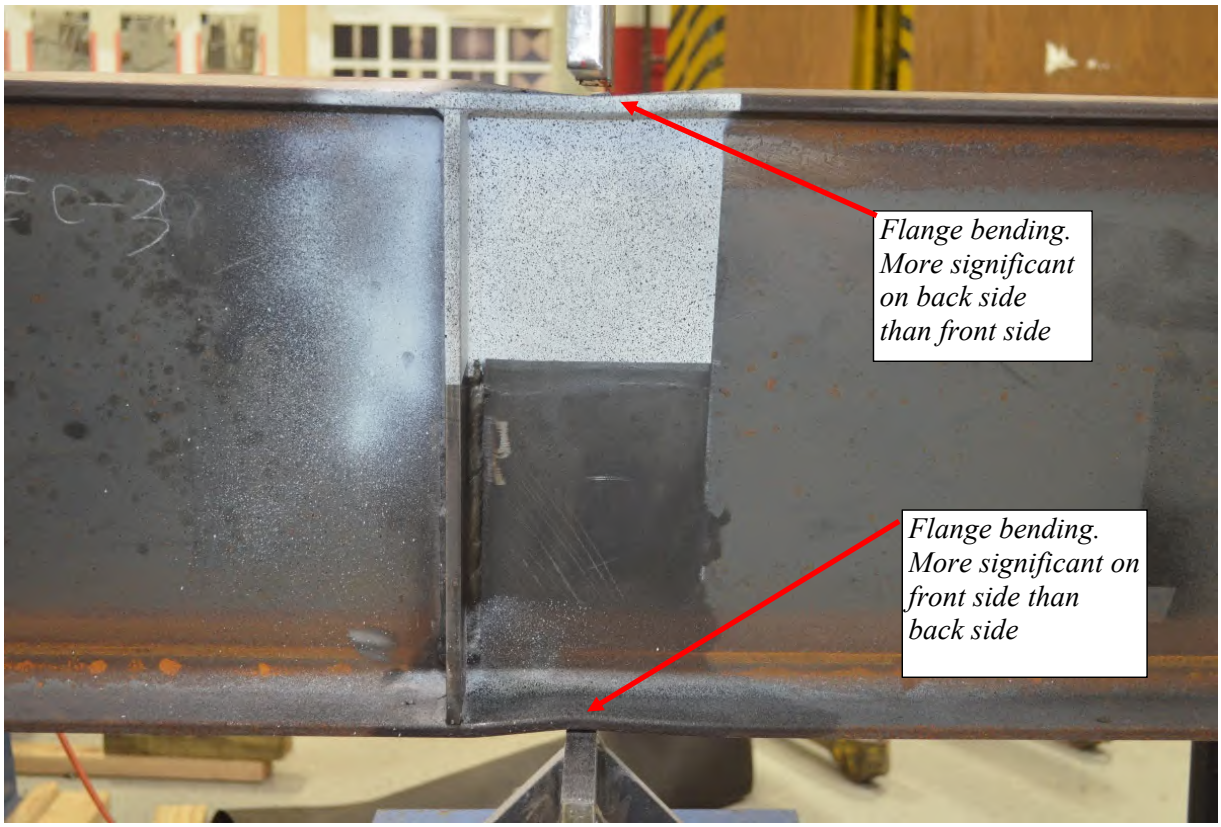

Figure A-81: Close up of W16X31-DC-E3 after testing

Figure A-82: Bottom flange to stiffener weld condition after testing

Figure A-83: W16X31-DC-E3 after testing emphasizing web crippling

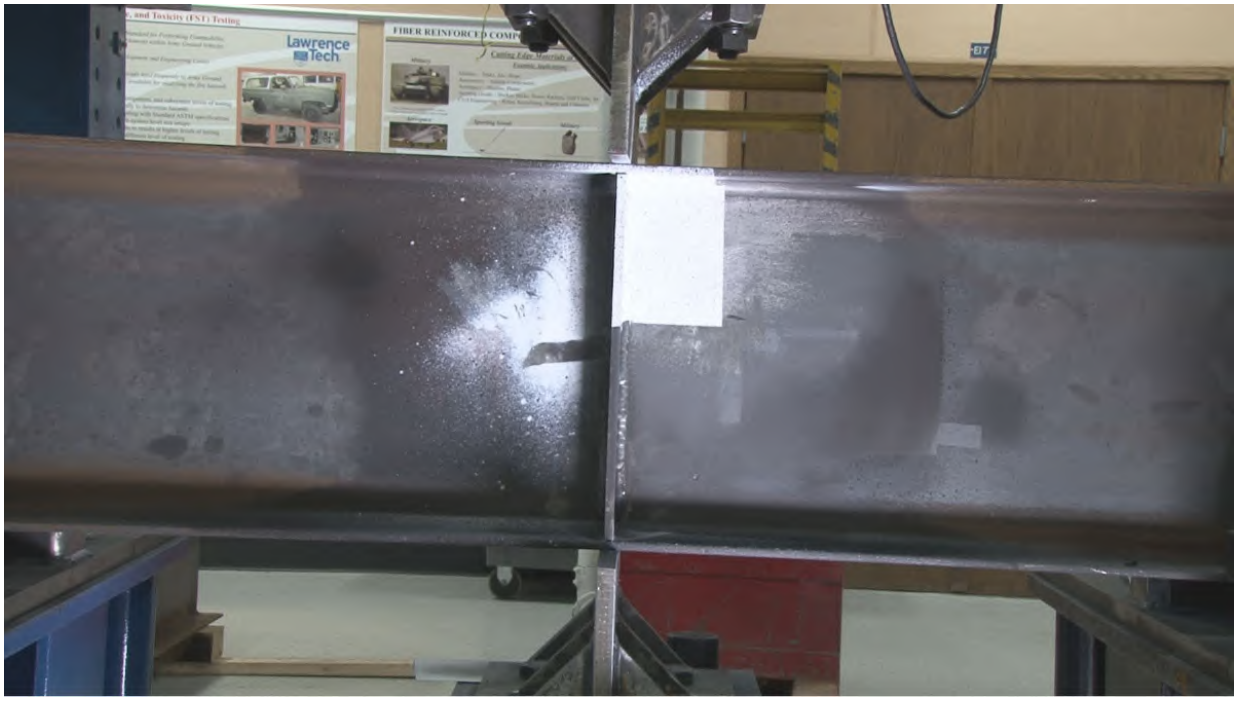

Figure A-84: Elevation of W16X31-DC-E0 prior to testing

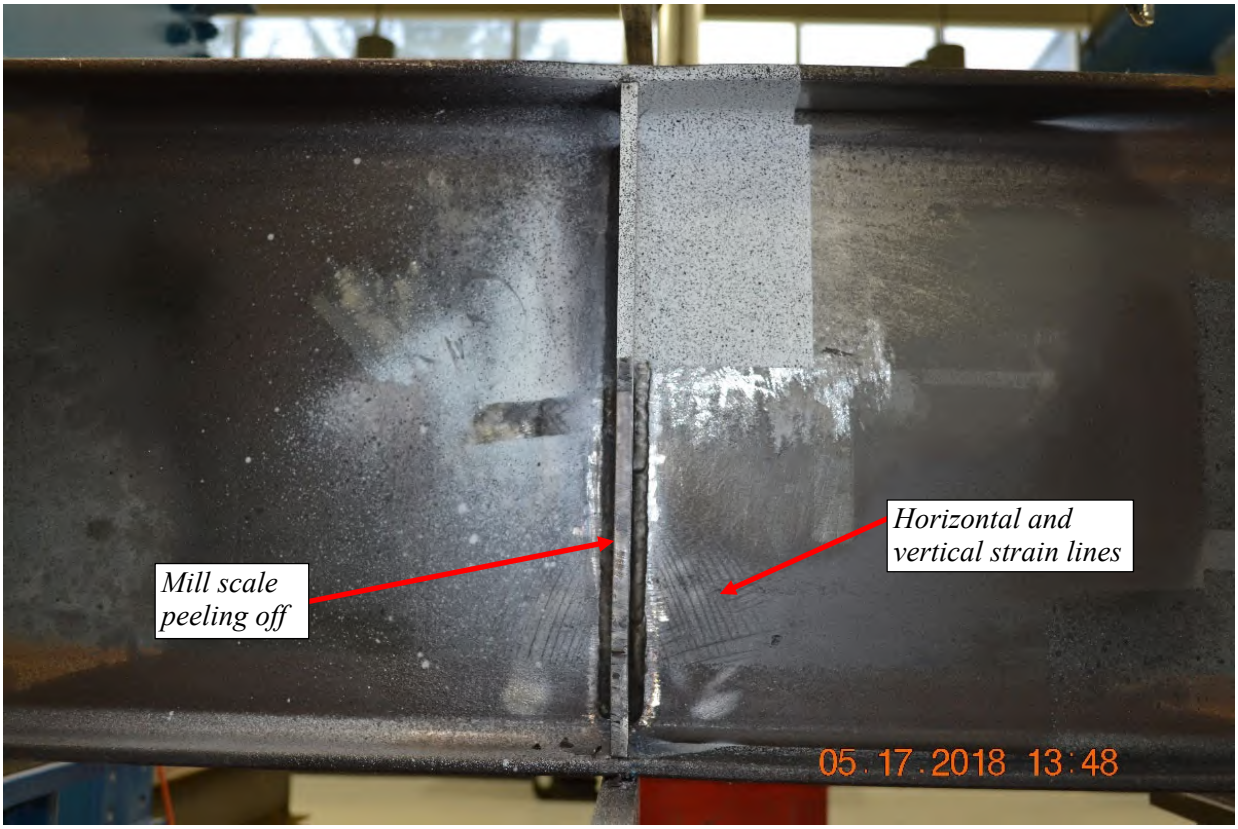

Figure A-85: Elevation of W16X31-DC-E0 after testing

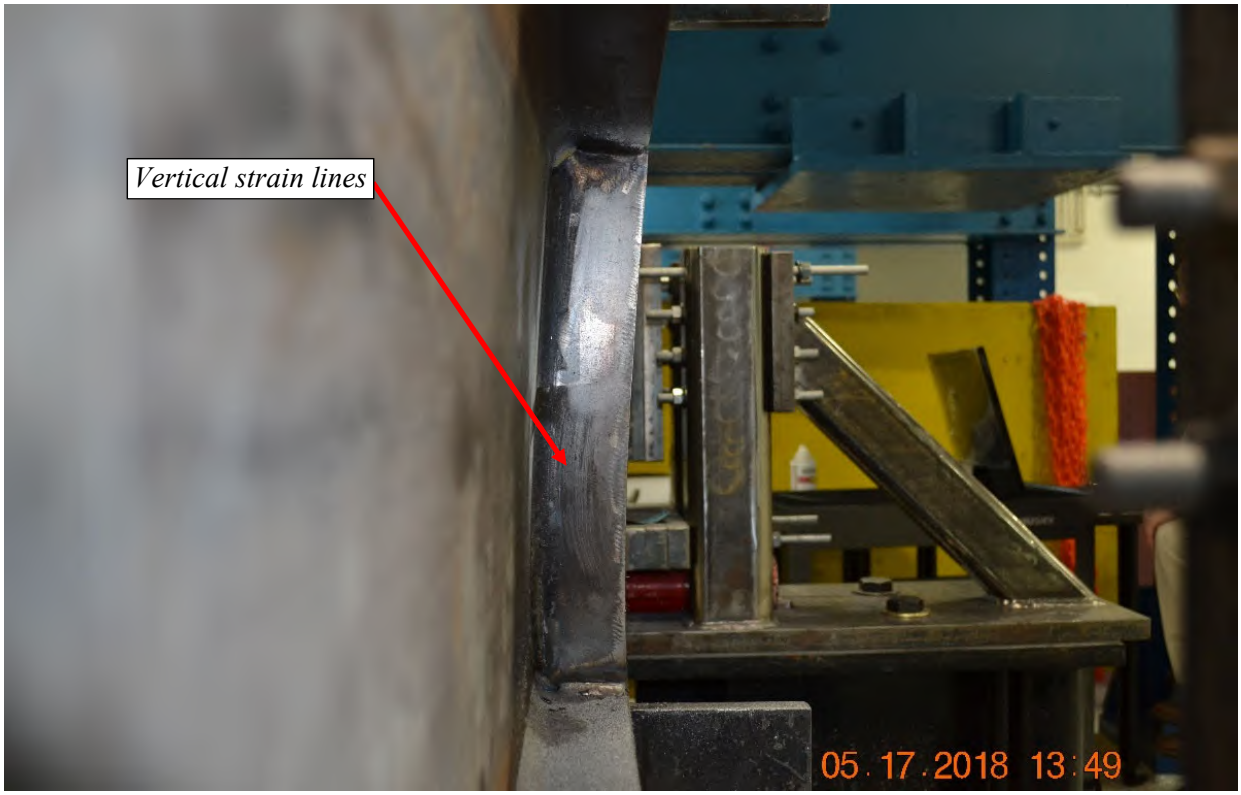

Figure A-86: Side view of W16X31-DC-E0 after testing

Figure A-87: Close-up of W16X31-DC-E0 emphasizing flange bending

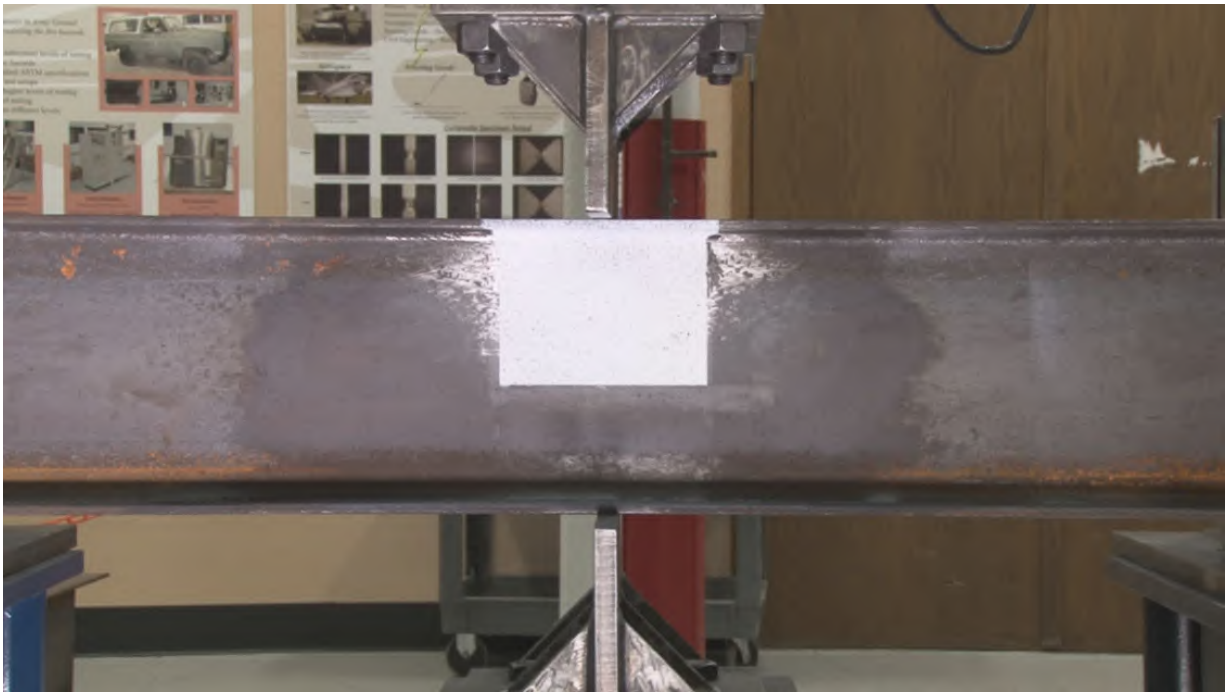

Figure A-88: Elevation of W10X19-DC-NA prior to testing

Figure A-89: Elevation of W10X19-DC-NA after testing

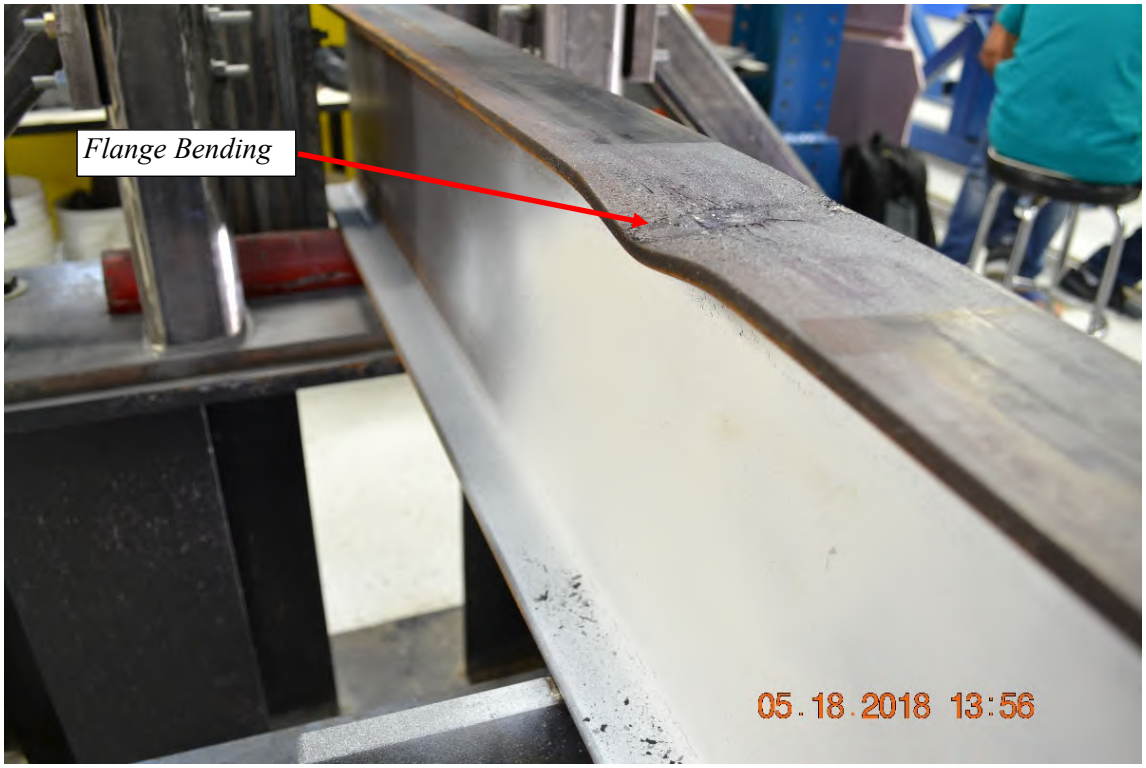

Figure A-90: W10X19-DC-NA after testing emphasizing flange bending

Figure A-91: W10X19-DC-NA after testing emphasizing web crippling

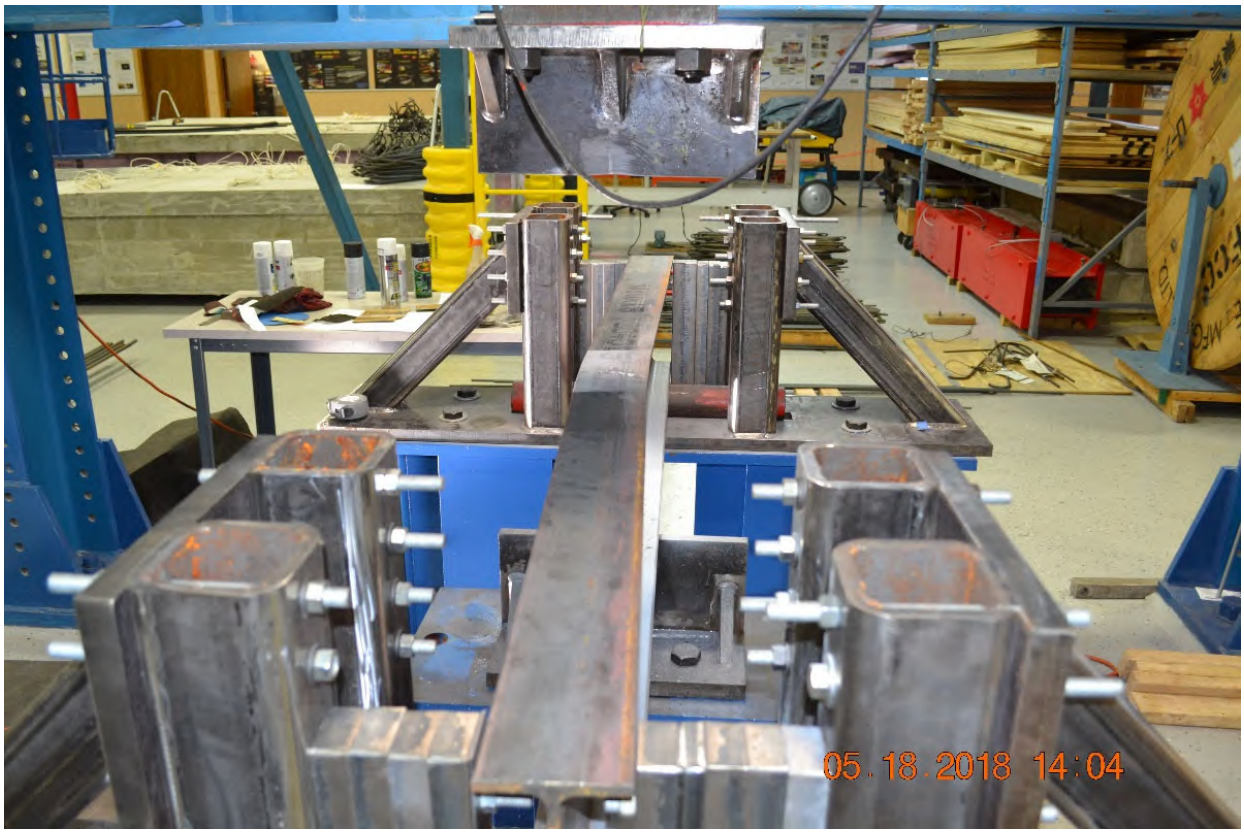

Figure A-92: Side view of W10X19-DC-NA after testing showing lateral translation

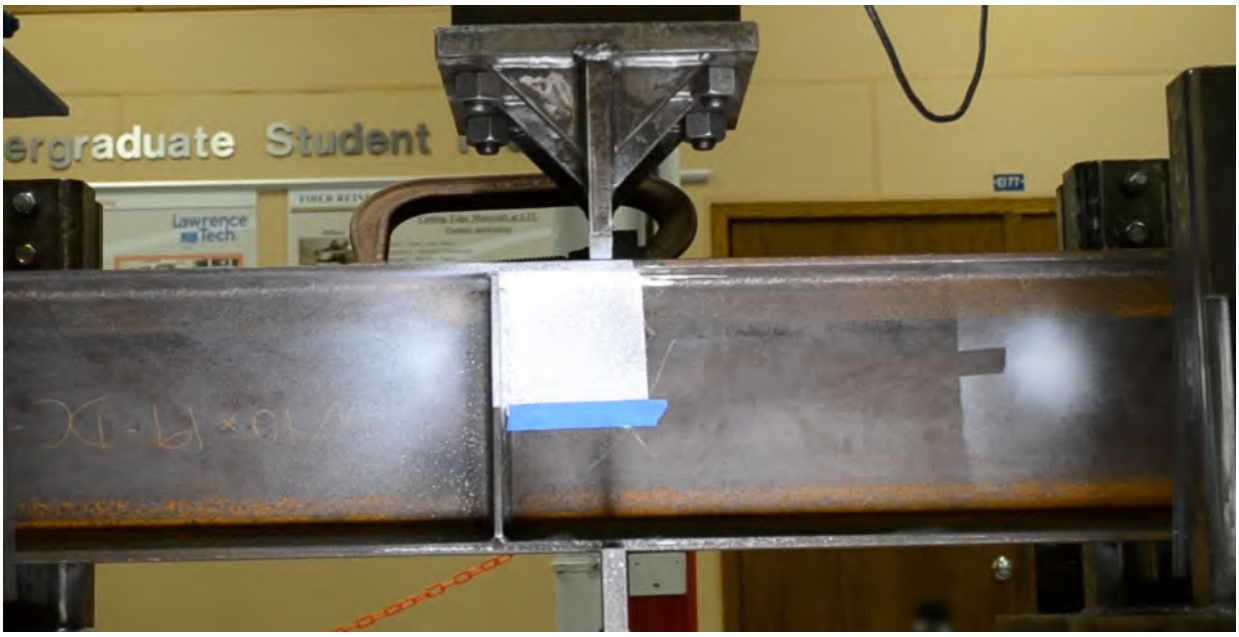

Figure A-93: Elevation of W10X19-DC-E4 prior to testing

Figure A-94: Elevation of W10X19-DC-E4 after testing

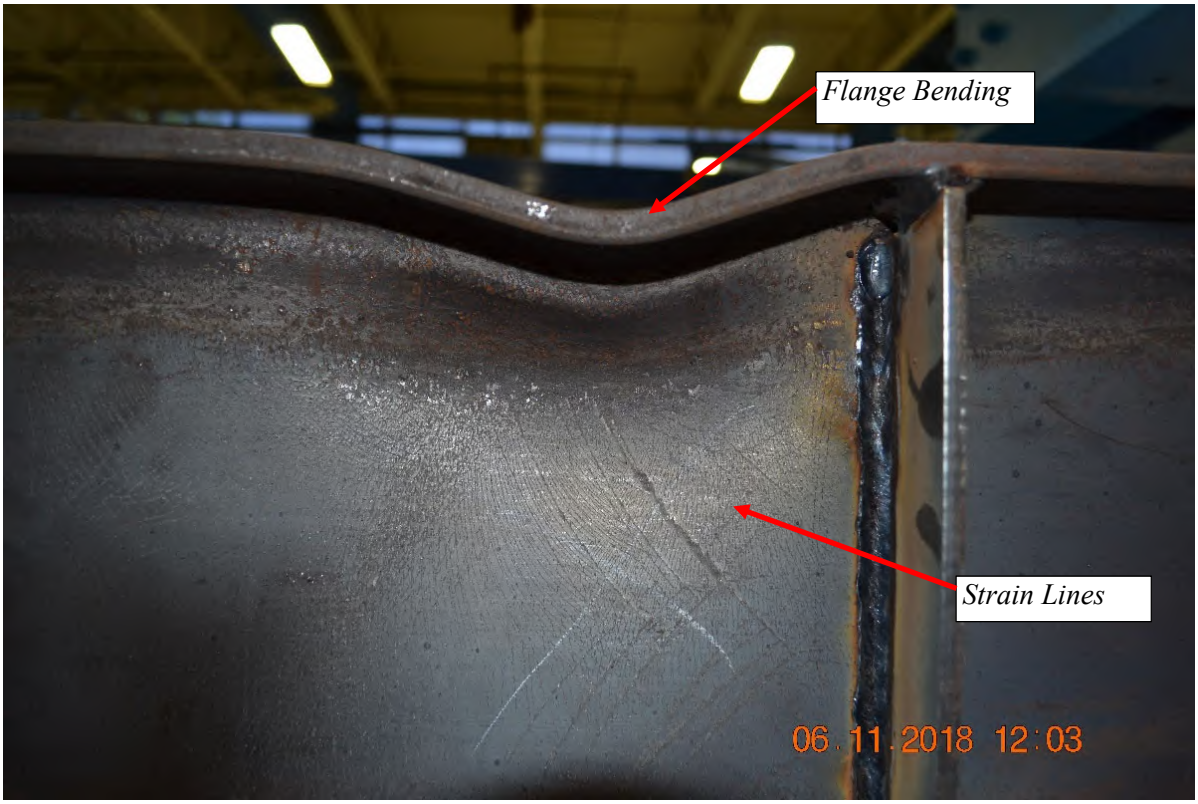

Figure A-95: Close-up view of W10X19-DC-E4 after testing

Figure A-96: W10X19-DC-E4 after testing emphasizing web crippling

Figure A-97: Side view of W10X19-DC-E4 after testing

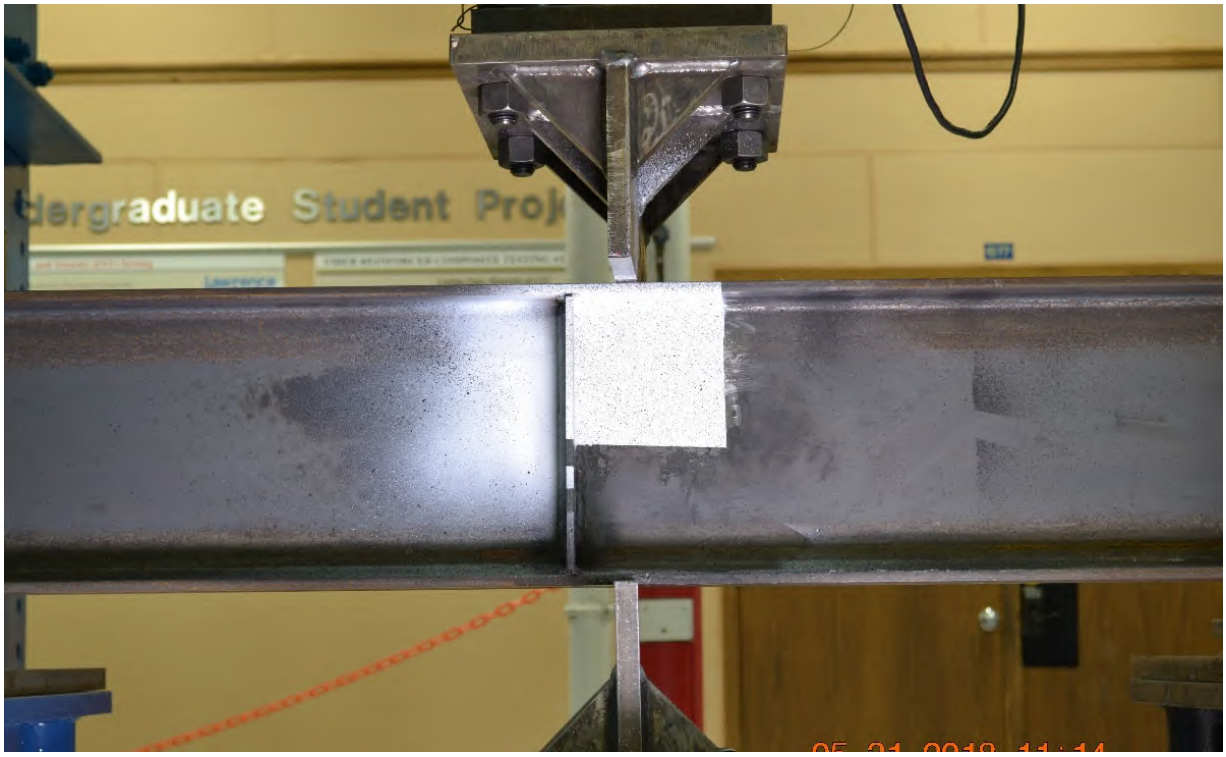

Figure A-98: Elevation of W10X19-DC-E2 prior to testing

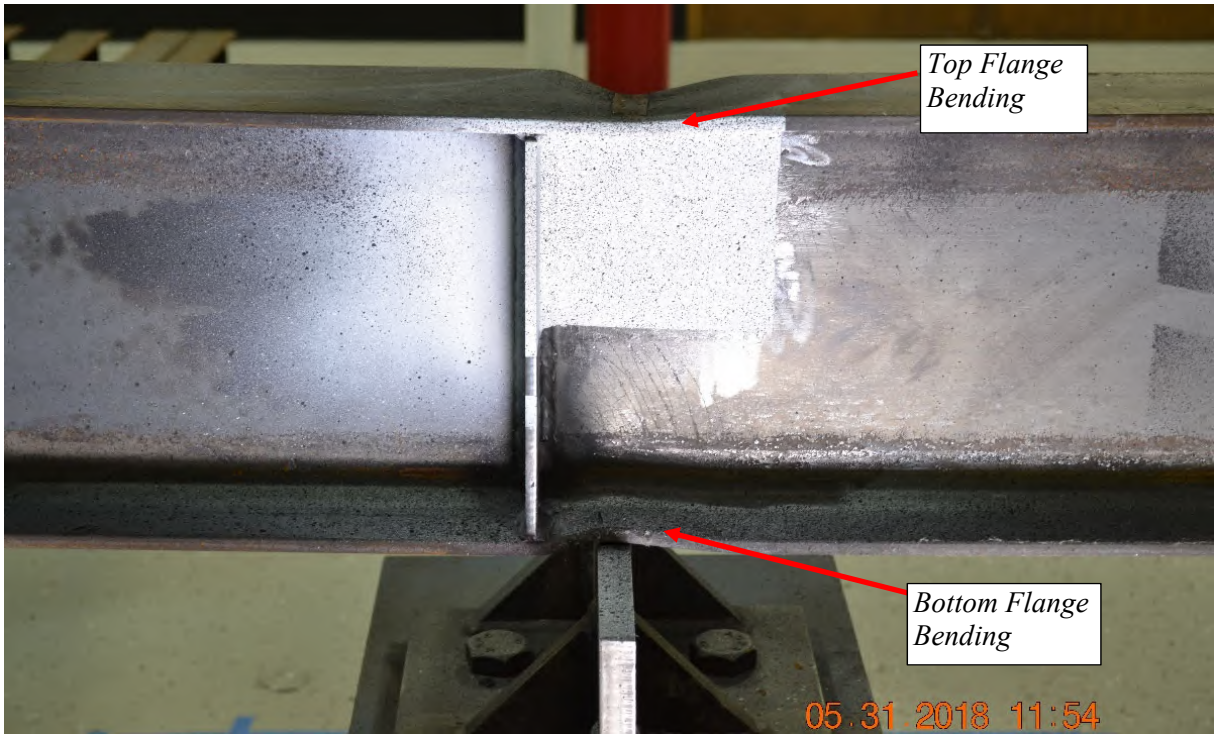

Figure A-99: Elevation of W10X19-DC-E2 after testing

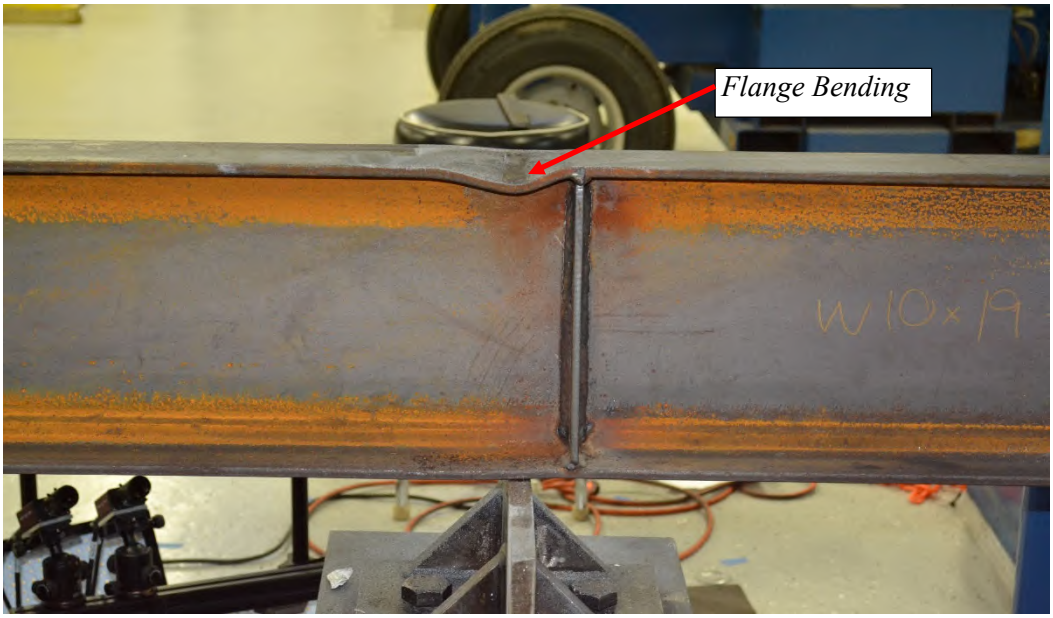

Figure A-100: Back view of W10X19-DC-E2 after testing

Figure A-101: W10X19-DC-E2 after testing emphasizing web crippling

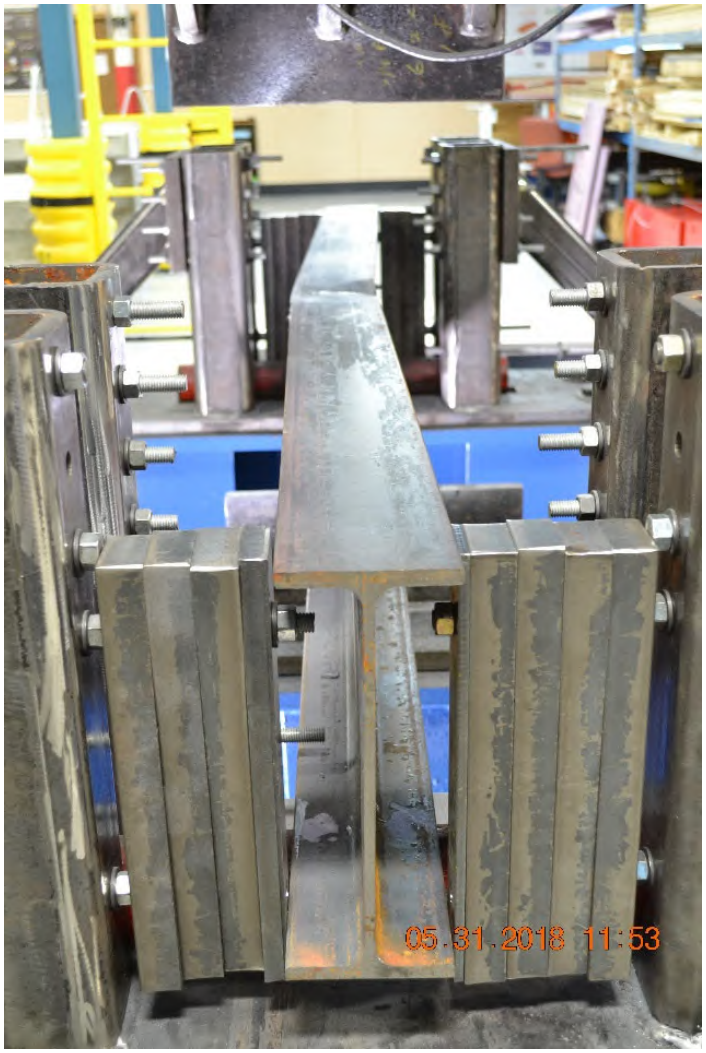

Figure A-102: Side view of W10X19-DC-E2 after testing showing lateral-torsional buckling

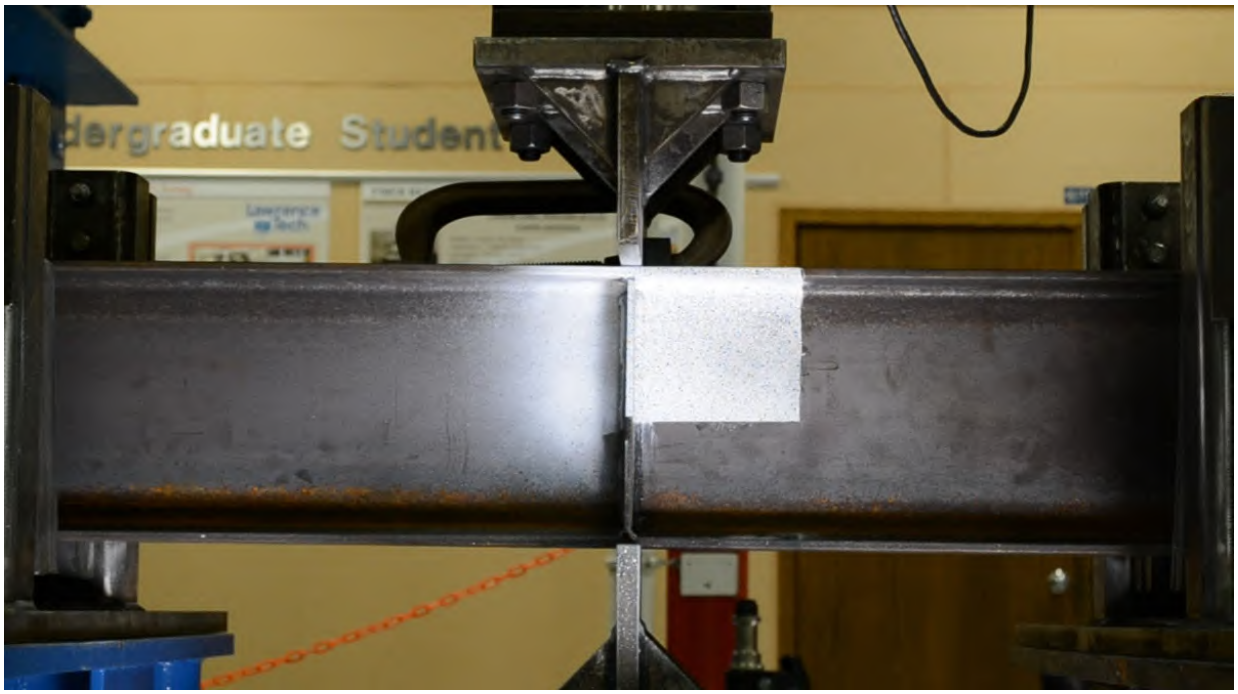

Figure A-103: Elevation of W10X19-SC-E0 prior to testing

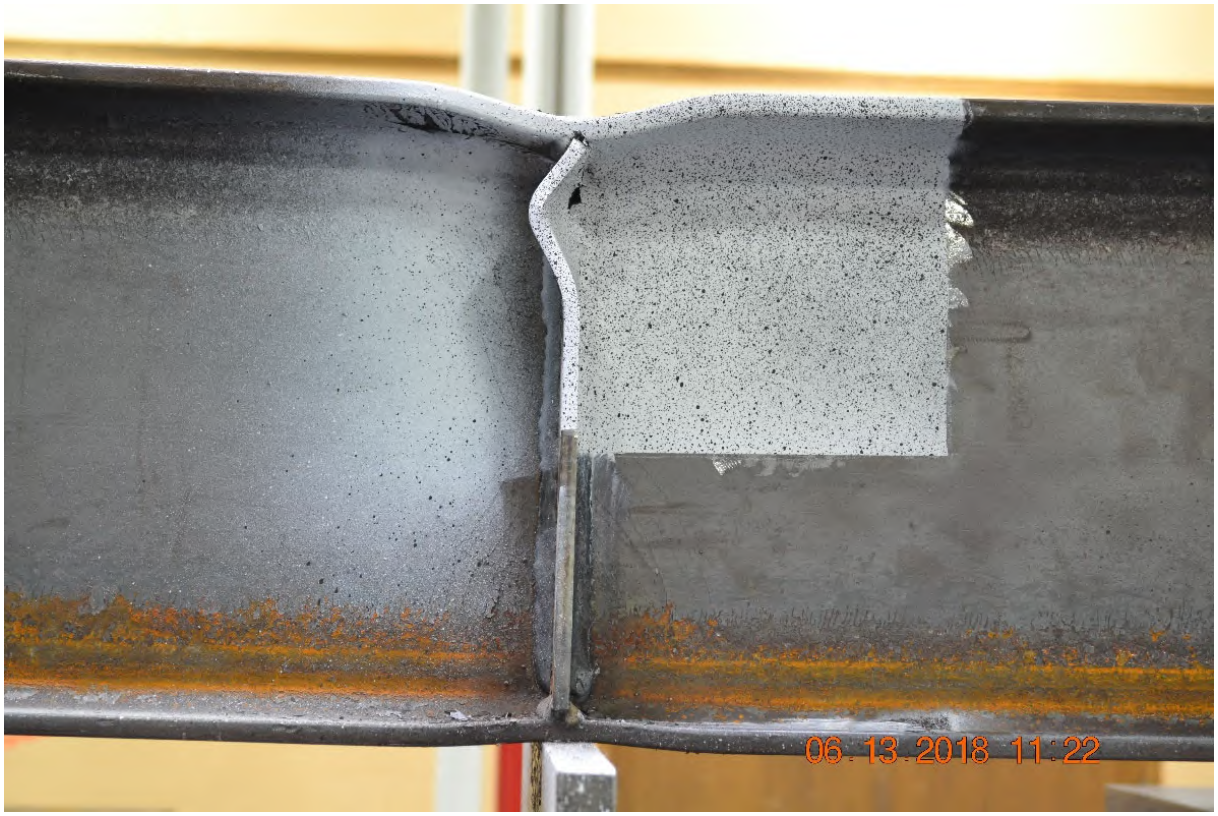

Figure A-104: Front view of W10X19-SC-E0 after testing

Figure A-105: Back view of W10X19-SC-E0 after testing

Figure A-106: W10X19-SC-E0 after testing emphasizing stiffener buckling

Figure A-107: Side view of W10X19-SC-E0 after testing showing the stiffener conditions

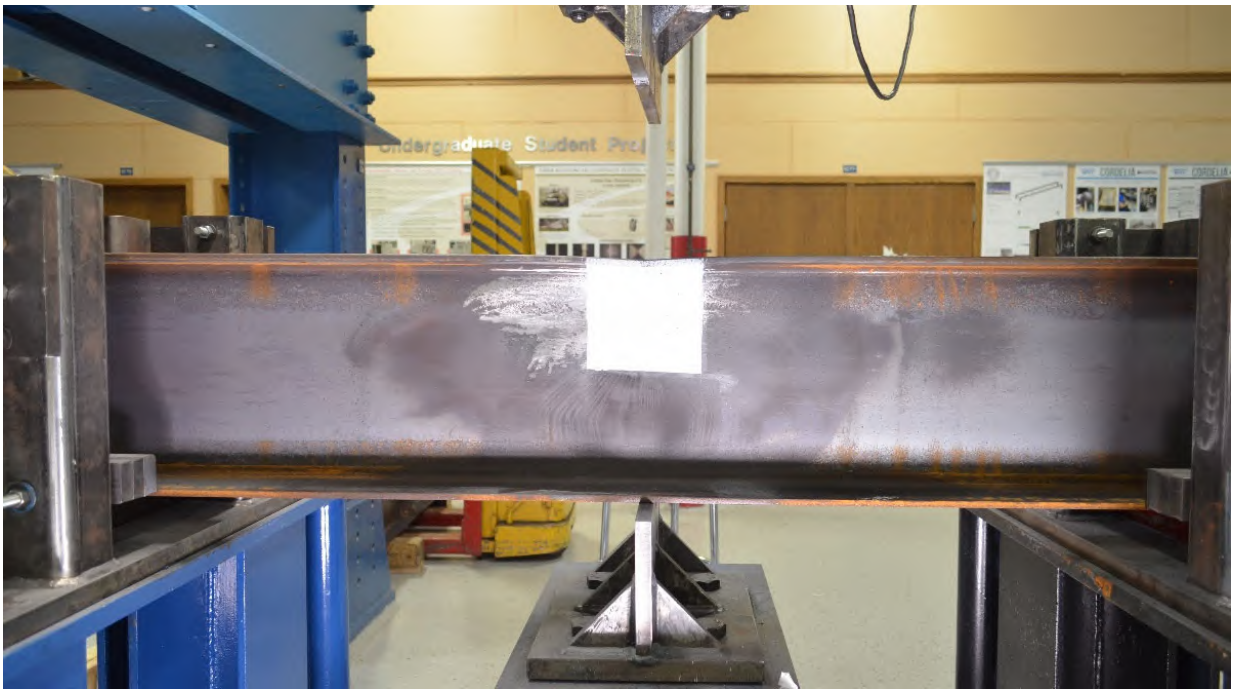

Figure A-108: Elevation view of W12X26-DC-NA after testing

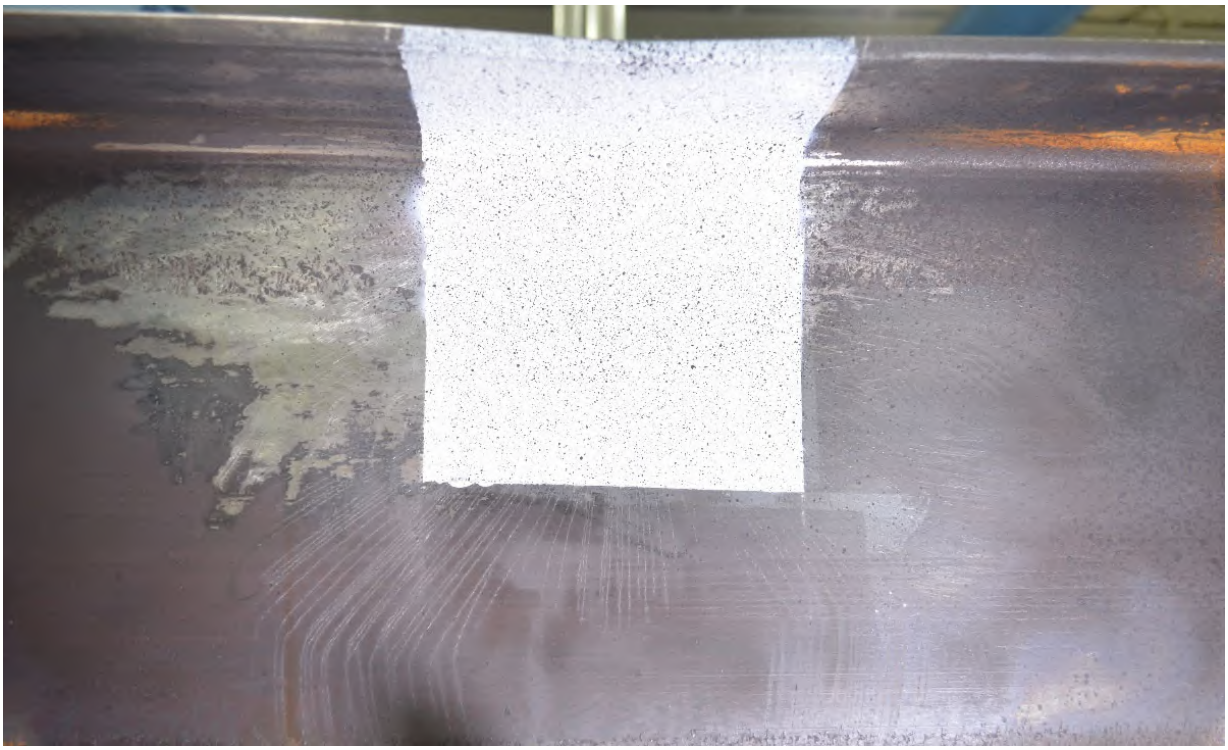

Figure A-109: Close-up view of W12X26-DC-NA after testing

Figure A-110: W12X26-DC-NA after testing emphasizing web crippling

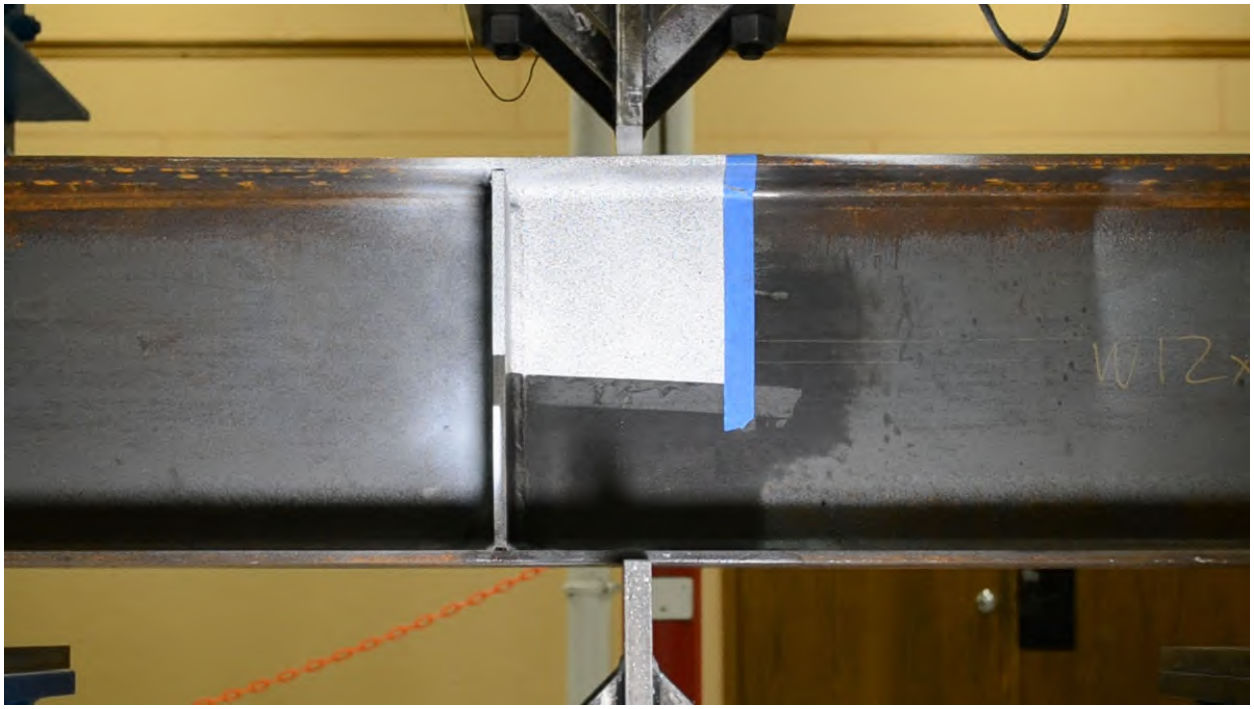

Figure A-111: Elevation of W12X26-DC-E4 prior to testing

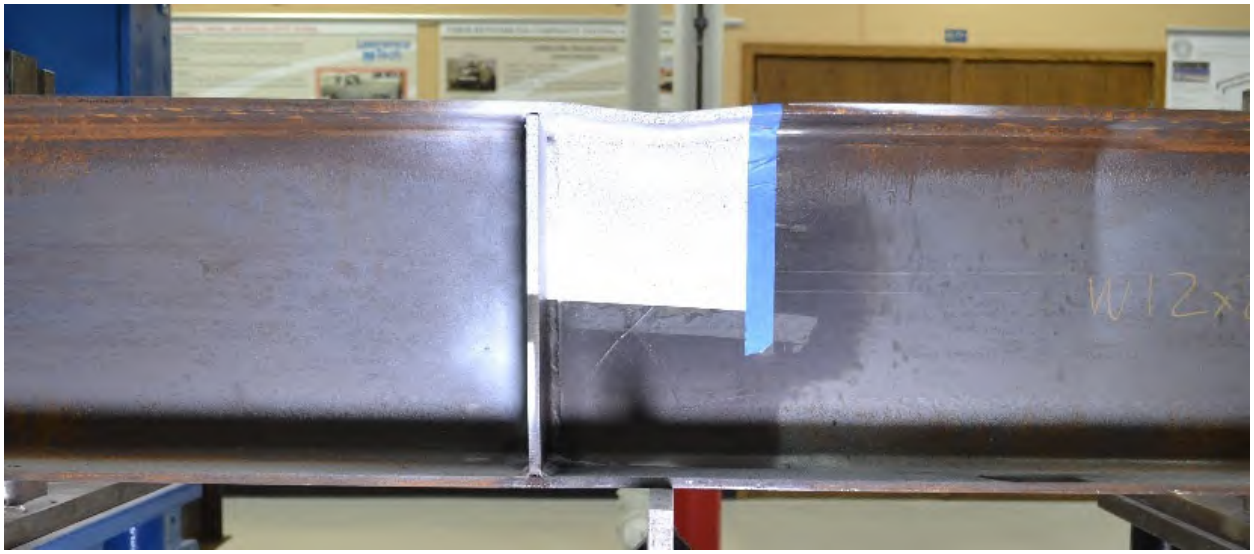

Figure A-112: Elevation of W12X26-DC-E4 after testing

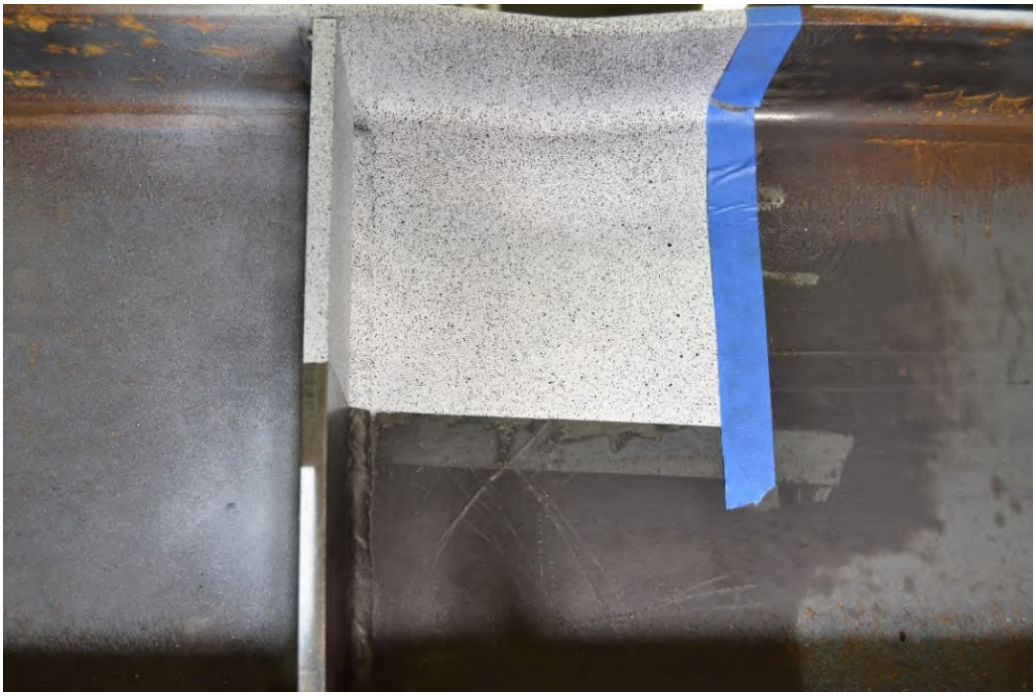

Figure A-113: Close-up of W12X26-DC-E4 after testing

Figure A-114: Side view of W12X26-DC-E4 after testing emphasizing web local crippling

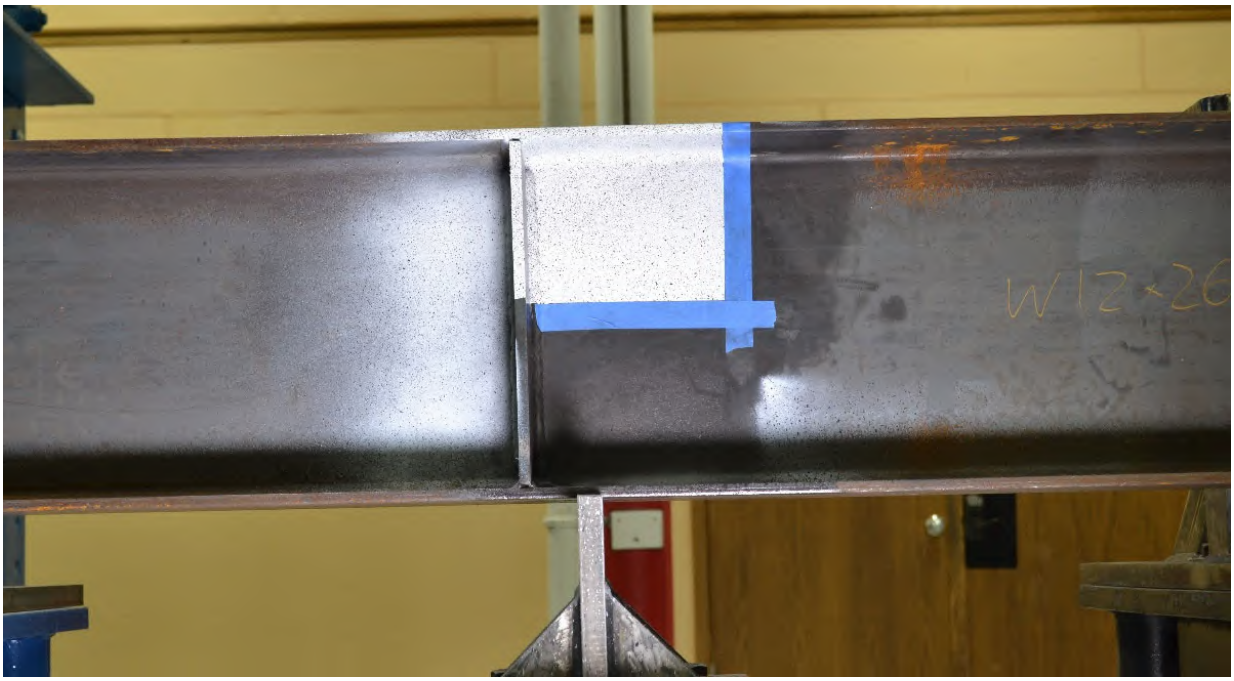

Figure A-115: Elevation of W12X26-DC-E2 prior to testing

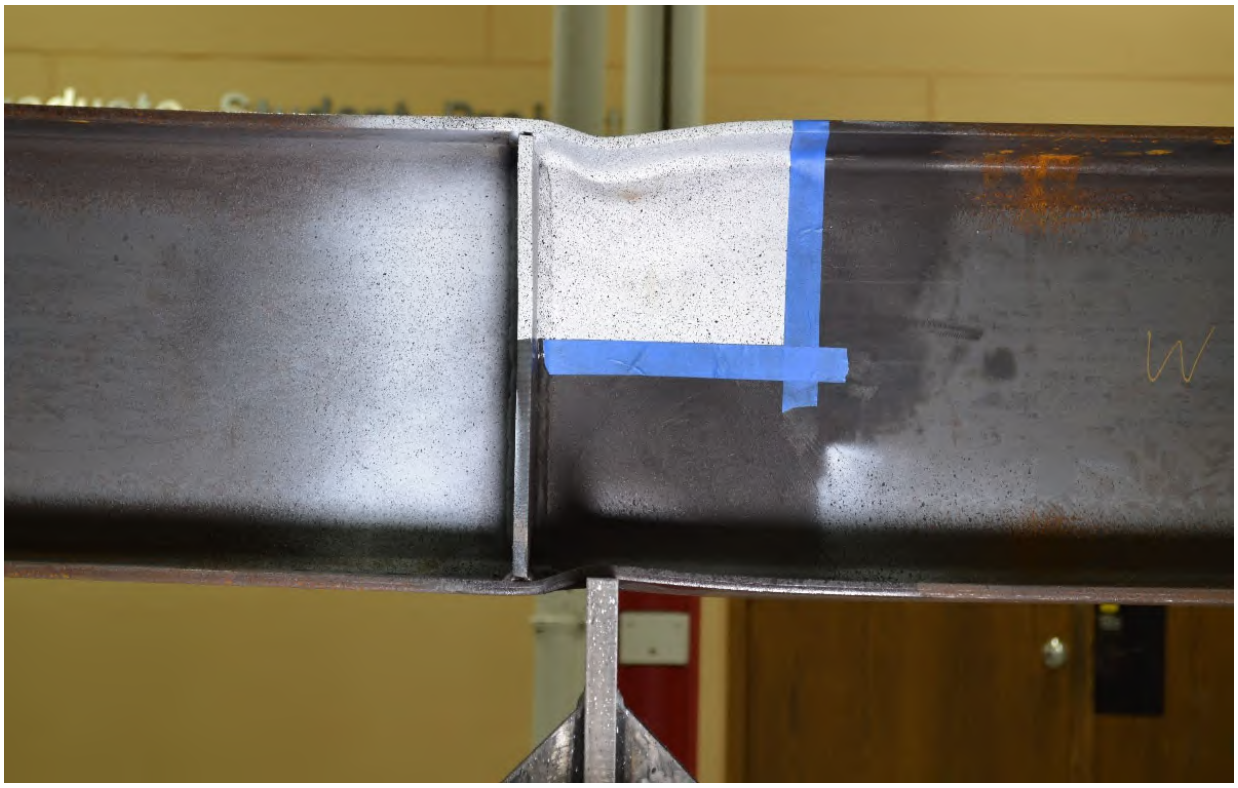

Figure A-116: Elevation view of W12X26-DC-E2 after testing

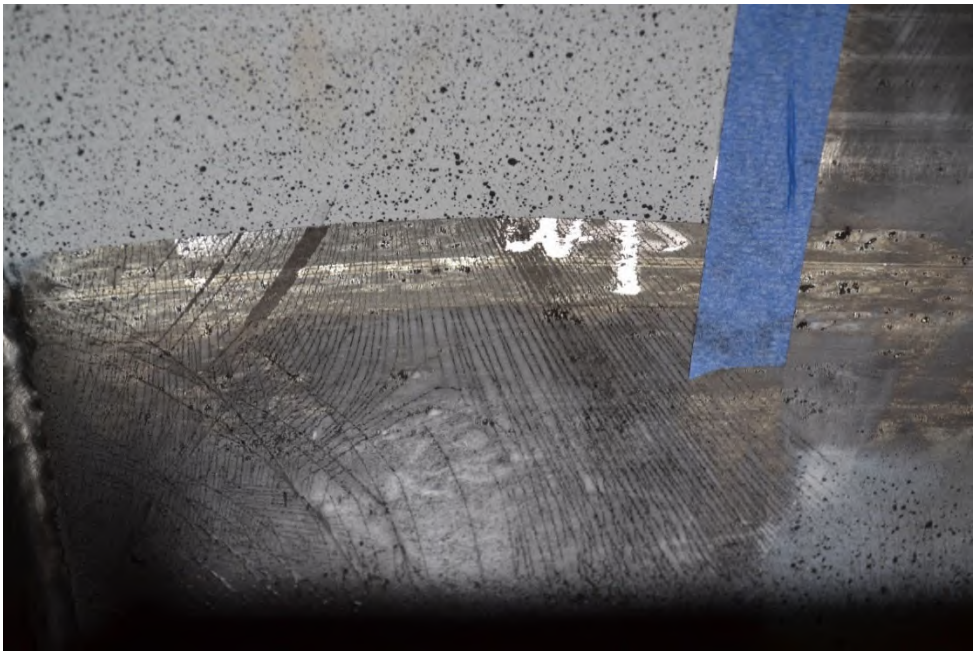

Figure A-117: Close-up view of W12X26-DC-E2 emphasizing the strain lines

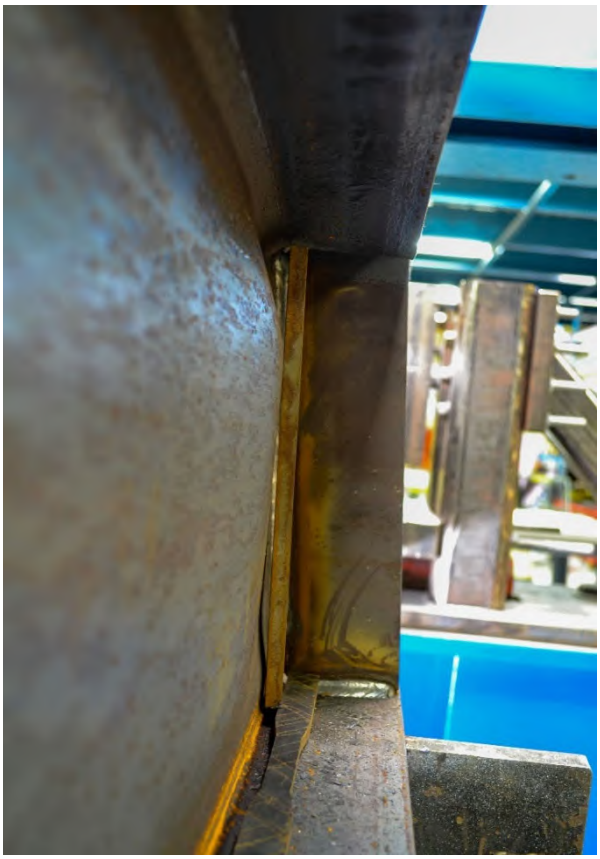

Figure A-118: W12X26-DC-E2 after testing emphasizing web crippling

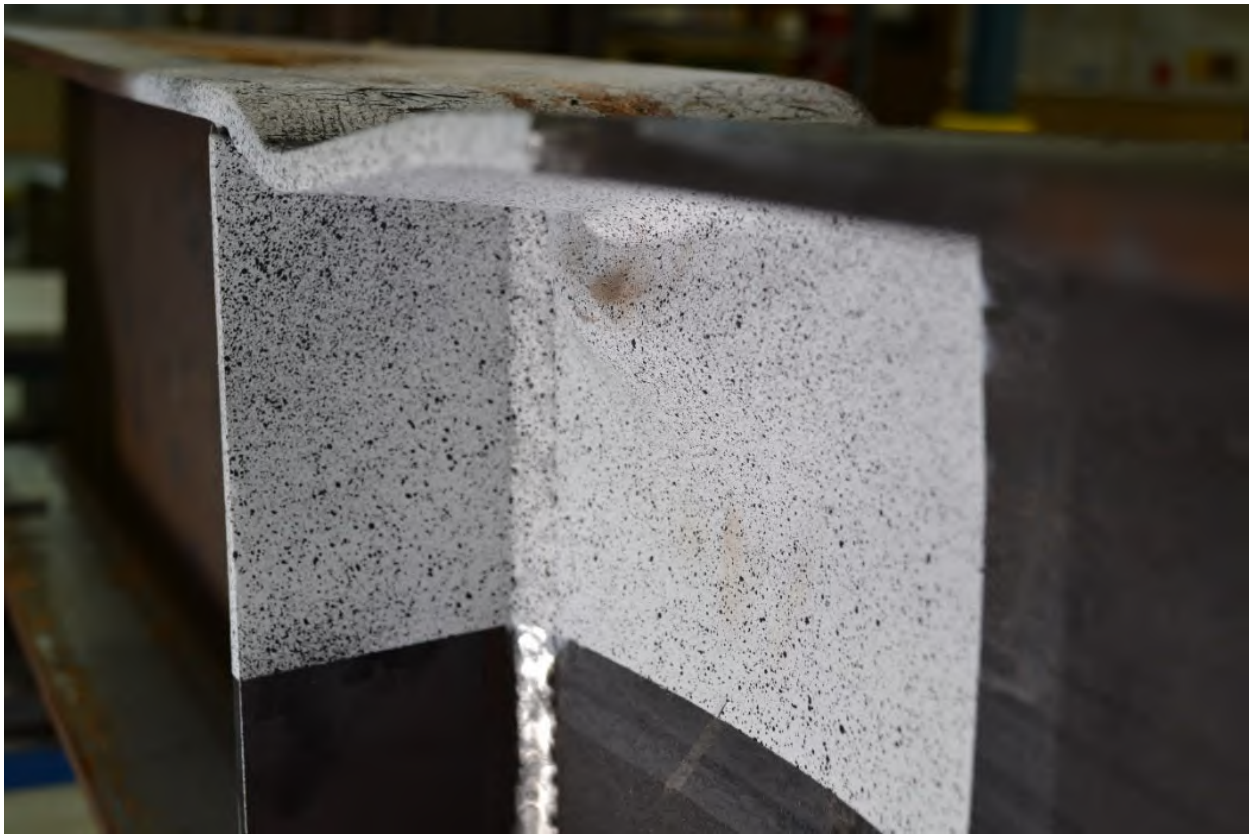

Figure A-119: W12X26-DC-E2 after testing further showing deformations near top flange

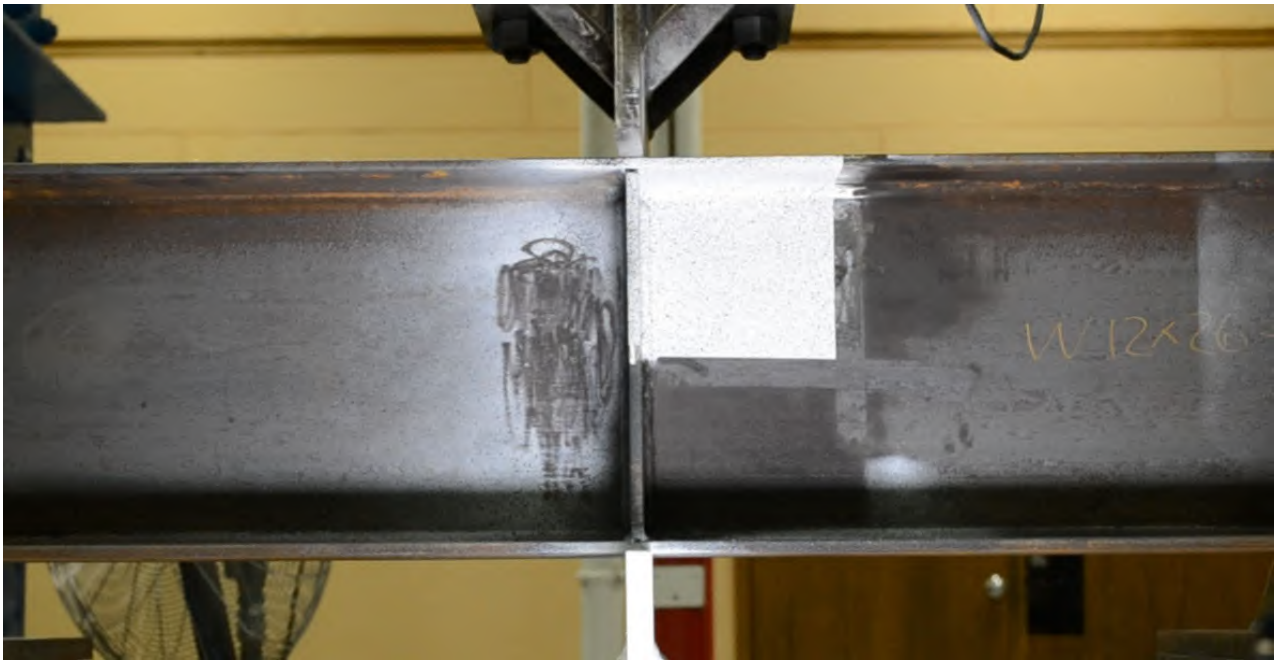

Figure A-120: Elevation of W12X26-DC-E0 prior to testing

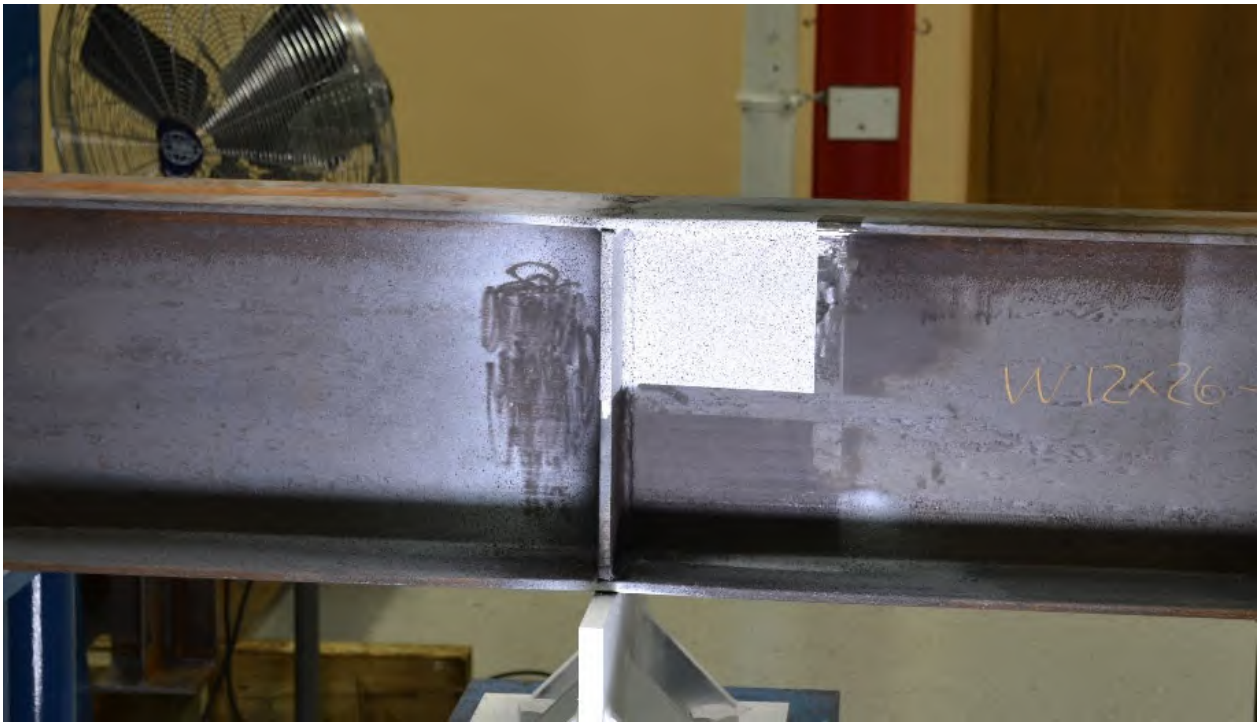

Figure A-121: Elevation of W12X26-DC-E0 after testing

Figure A-122: Close-up view of W12X26-DC-E0 after testing

Figure A-123: Elevation of W16X31-ST-NA prior to testing

Figure A-124: Elevation of W16X31-ST-NA after testing

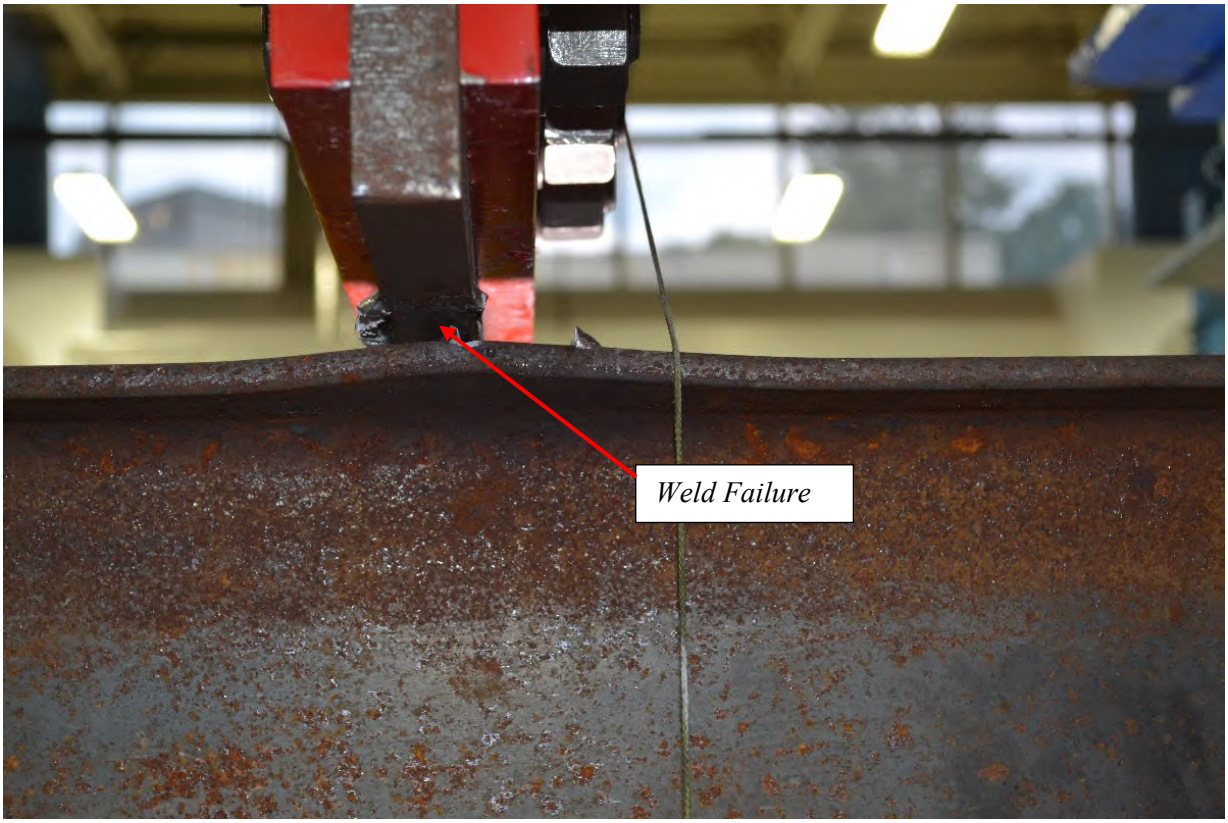

Figure A-125: Close-up view of W16X31-ST-NA after testing

Figure A-126: Weld fracture of W16X31-ST-NA after testing (Side 1)

Figure A-127: Weld fracture of W16X31-ST-NA after testing (Side 2)

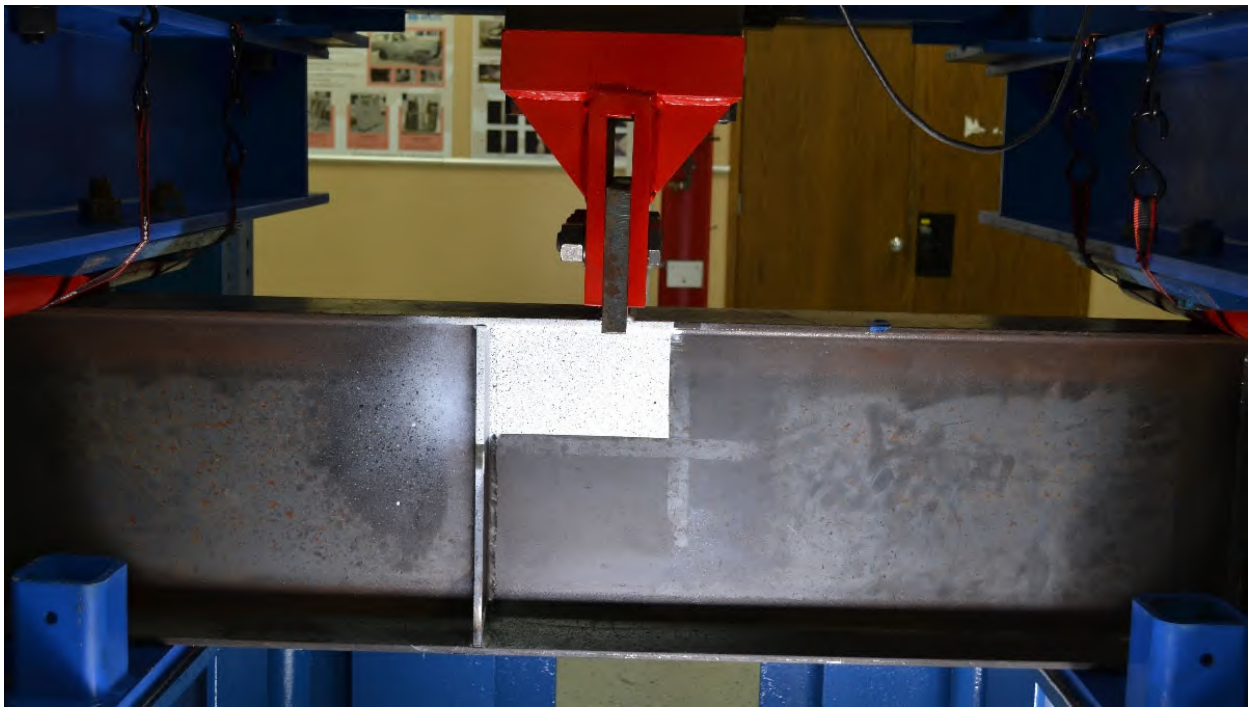

Figure A-128: Close up view of W16X31-ST-E6 prior to testing

Figure A-129: Close-up view of W16X31-ST-E6 after testing from front side

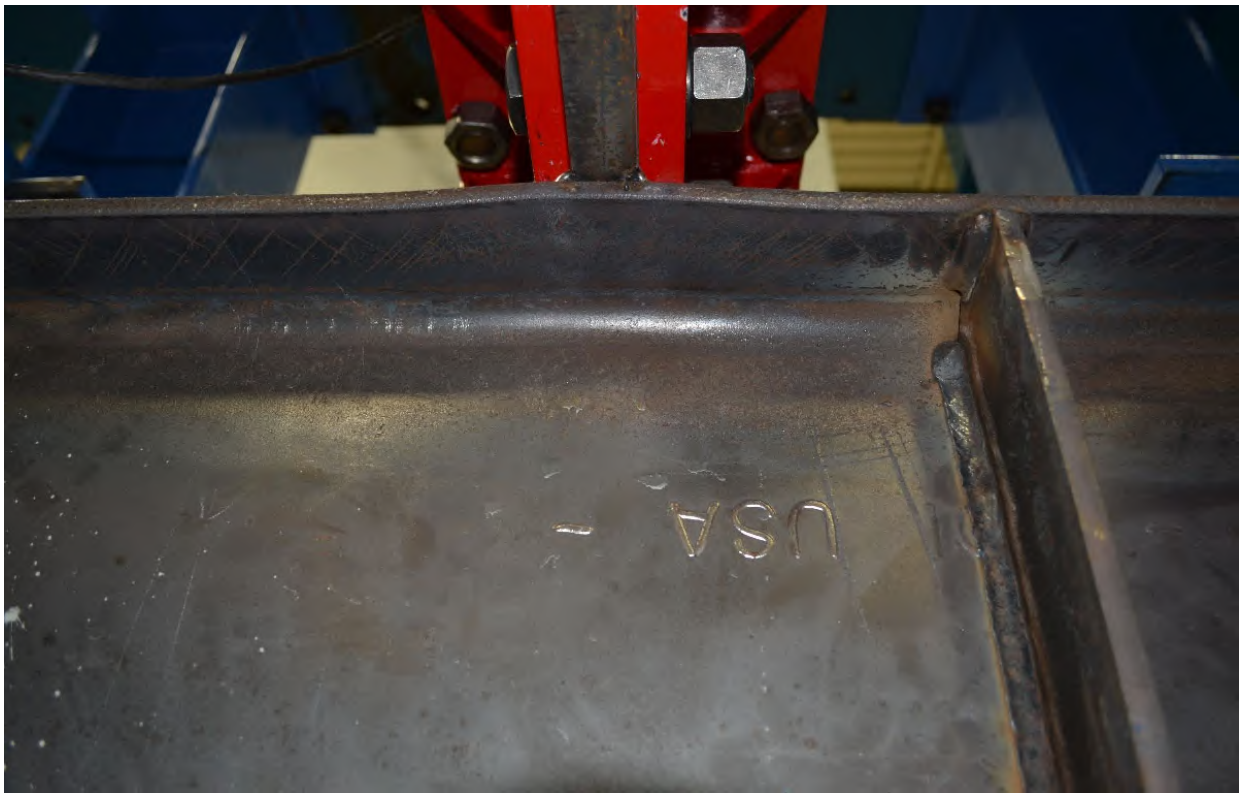

Figure A-130: Close-up view of W16X31-ST-E6 after testing from back side

Figure A-131: Weld fracture of W16X31-ST-E6 after testing (Side 1)

Figure A-132: Weld fracture of W16X31-ST-E6 after testing (Side 2)

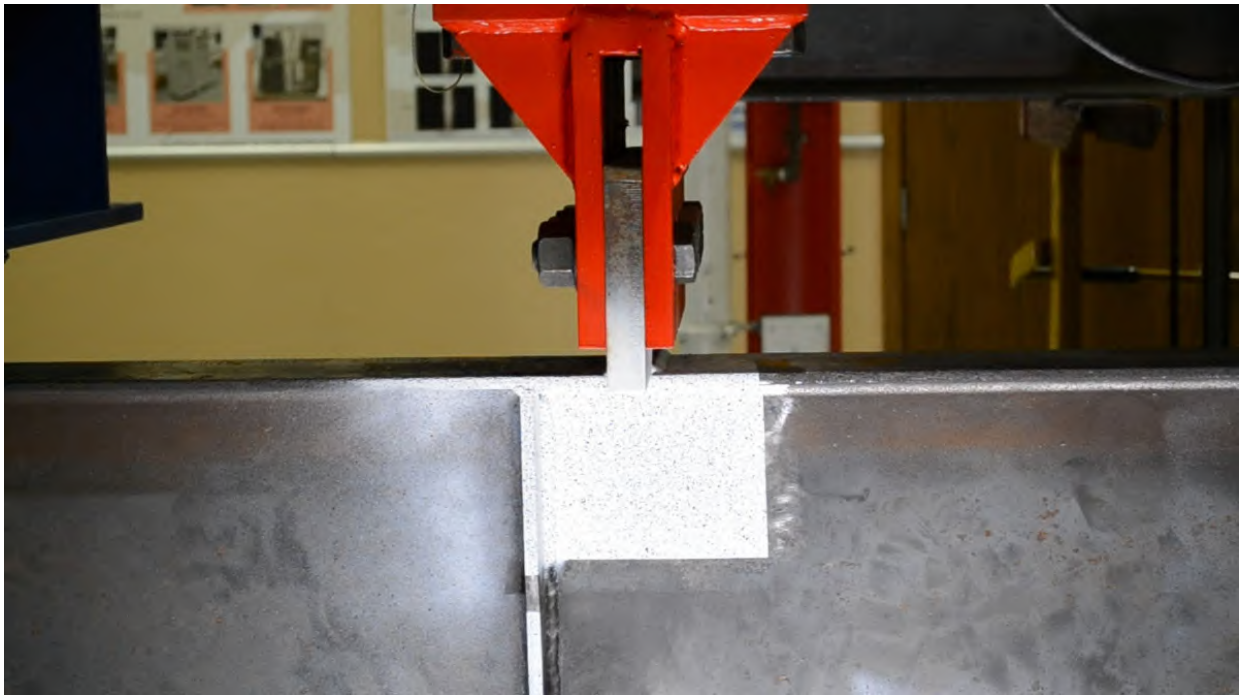

Figure A-133: Elevation of W16X31-ST-E3 prior to testing

Figure A-134: Elevation of W16X31-ST-E3 after testing

Figure A-135: Close-up view of W16X31-ST-E3 after testing

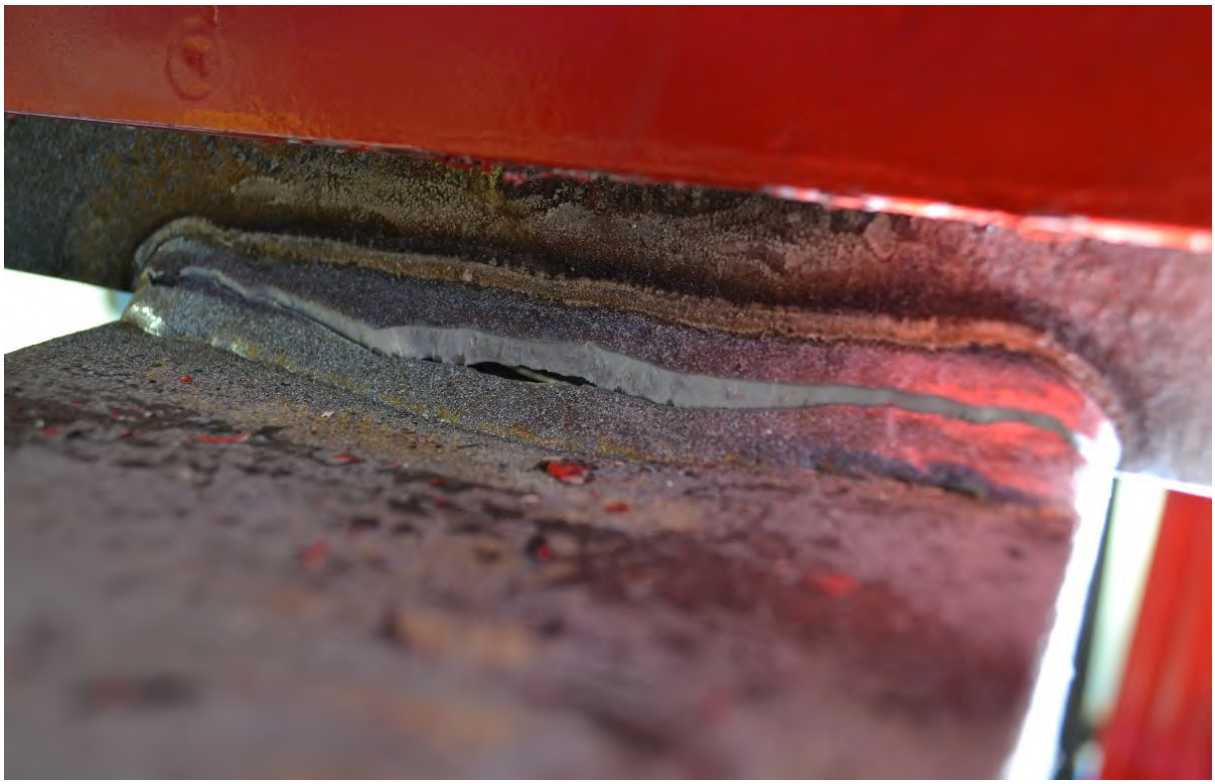

Figure A-136: Weld fracture of W16X31-ST-E3 after testing (Side 1)

Figure A-137: Weld fracture of W16X31-ST-E3 after testing (Side 2)

Figure A-138: Elevation of W16X31-ST-E0 prior to testing

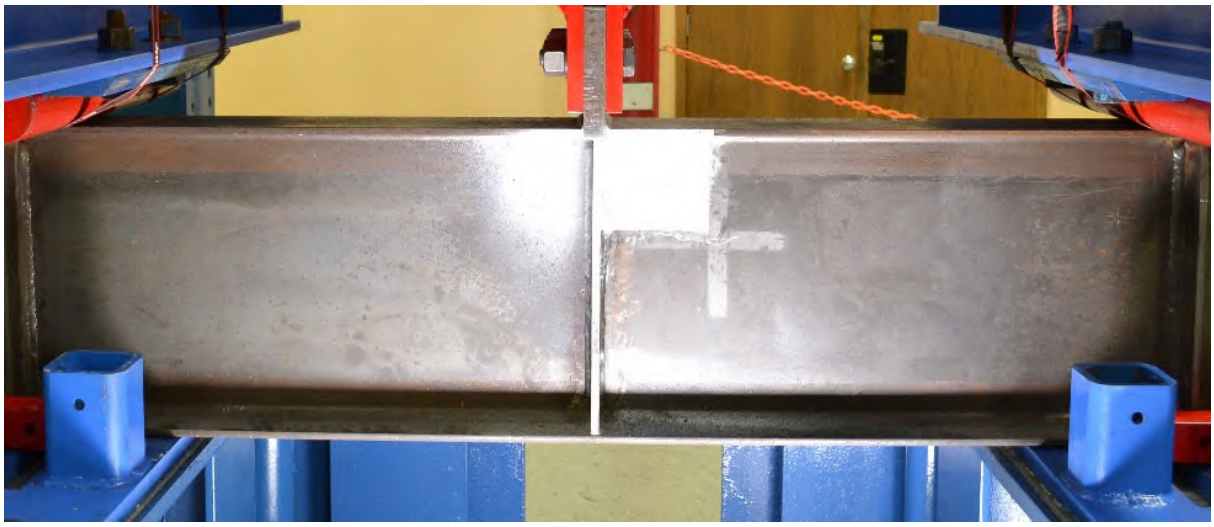

Figure A-139: Elevation of W16X31-ST-E0 after testing

Figure A-140: Weld condition of W16X31-ST-E0 after testing (Side 1)

Figure A-141: Weld condition of W16X31-ST-E0 after testing (Side 2)

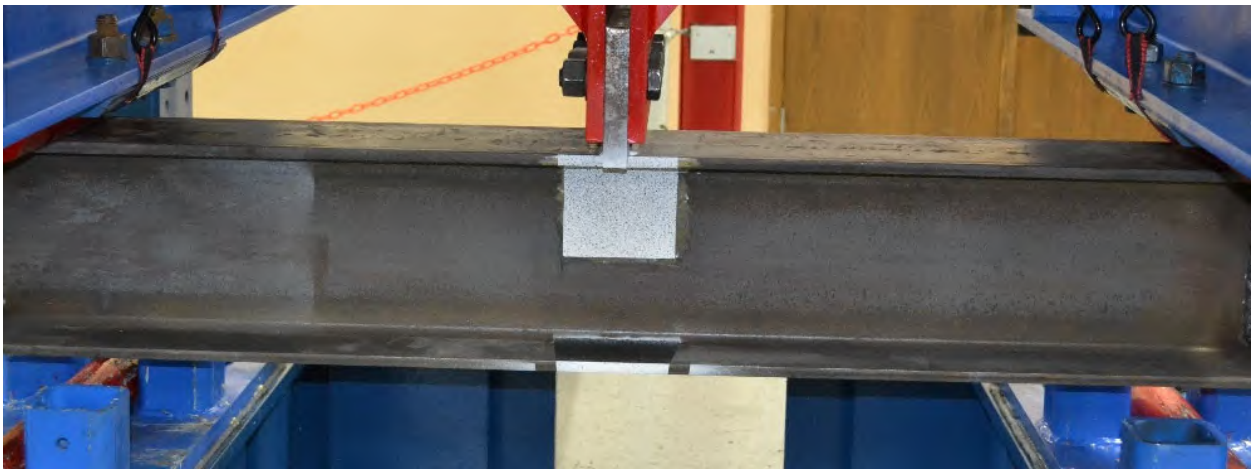

Figure A-142: Elevation of W10X39-ST-NA prior to testing

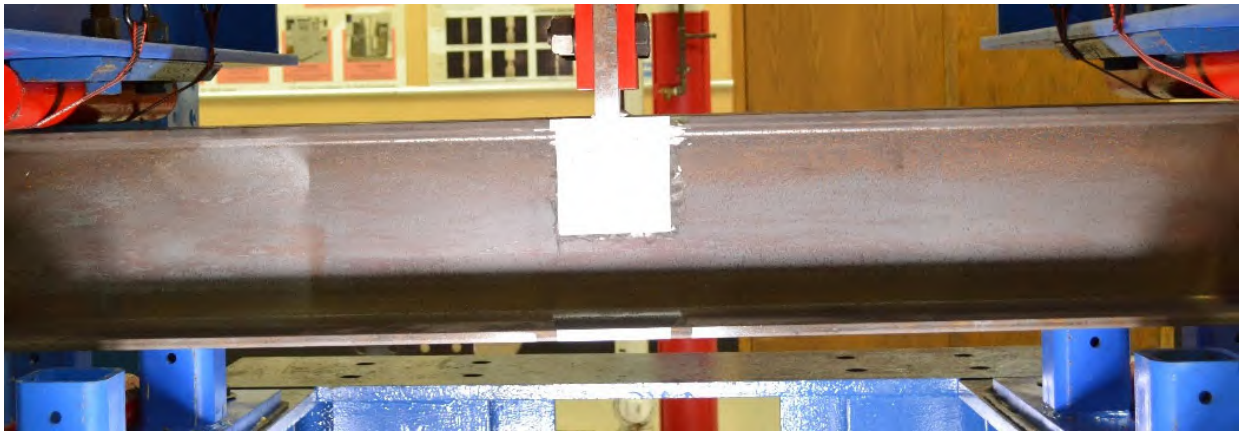

Figure A-143: Elevation of W10X39-ST-NA after testing

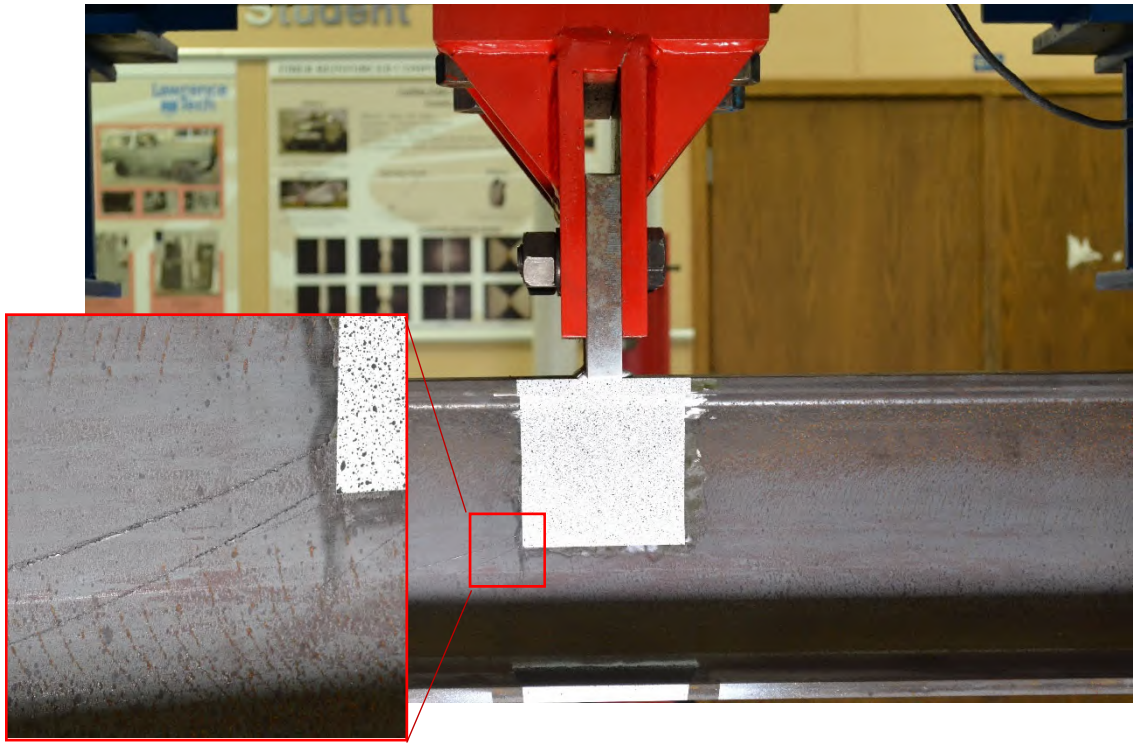

Figure A-144: Close up view of W10X39-ST-NA after testing

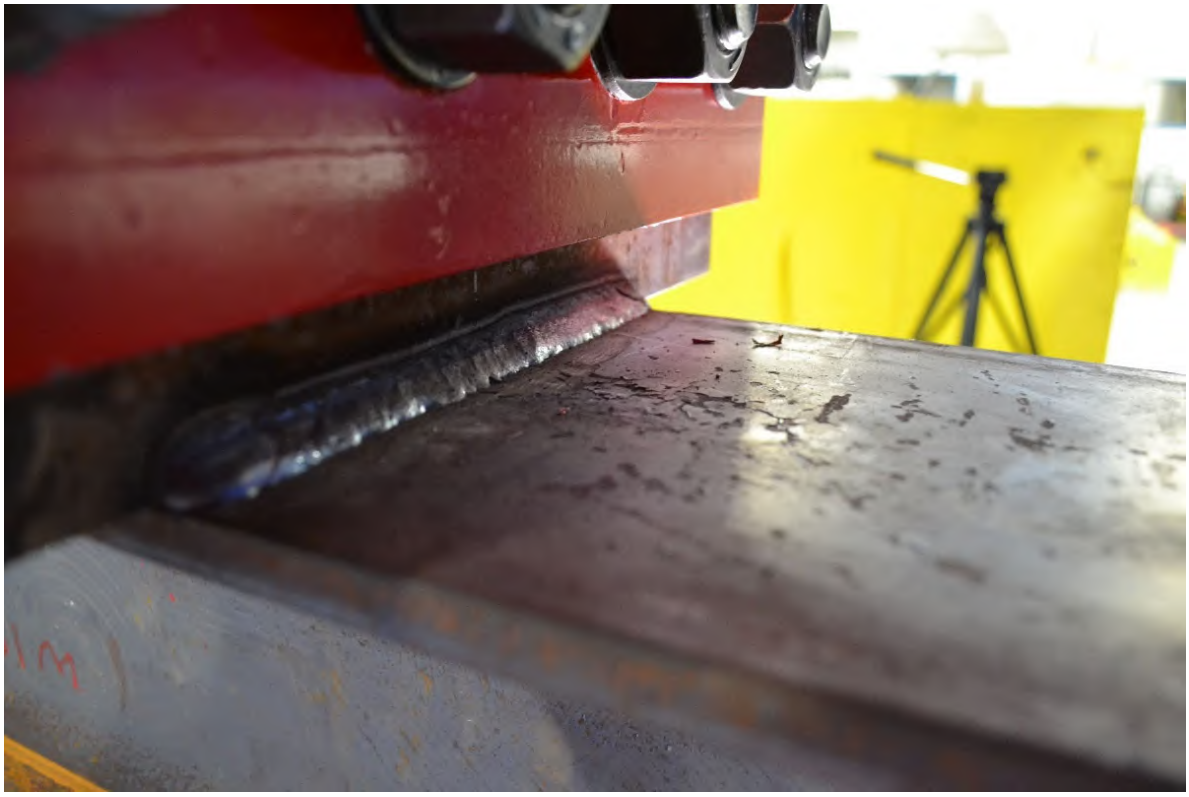

Figure A-145: Weld condition of W10X39-ST-NA after testing (Side 1)

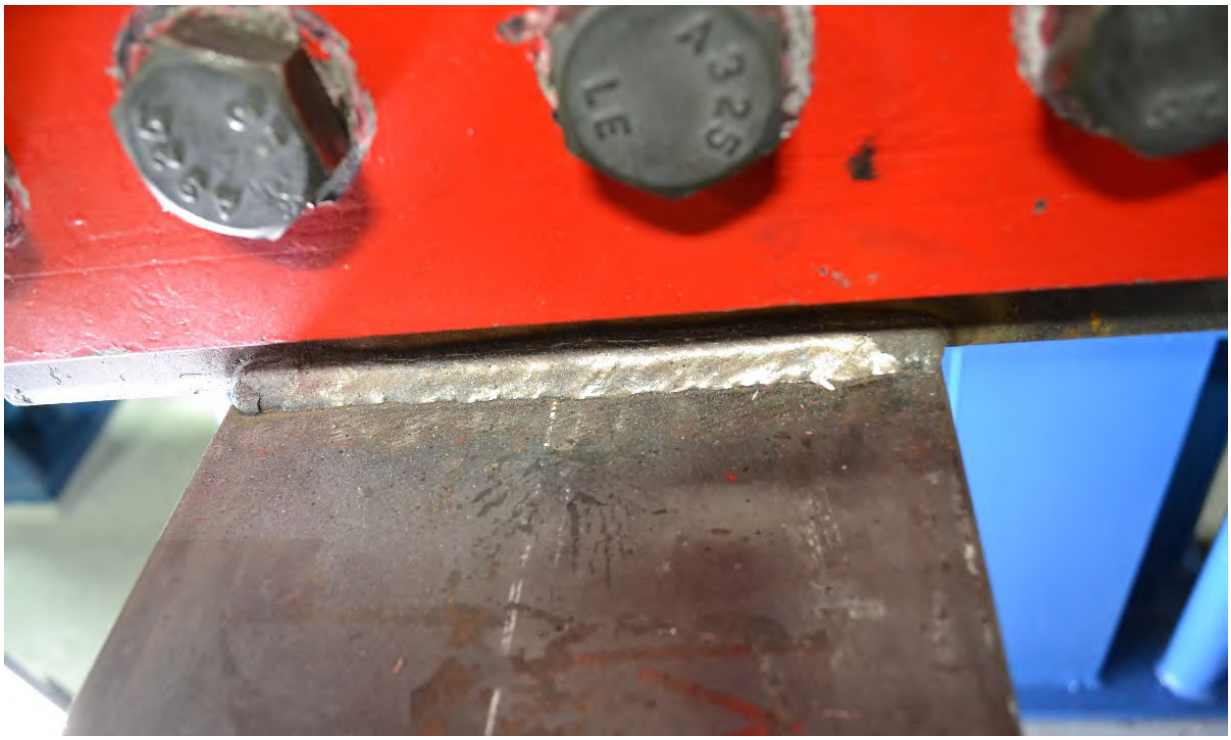

Figure A-146: Weld condition of W10X39-ST-NA after testing (Side 2)

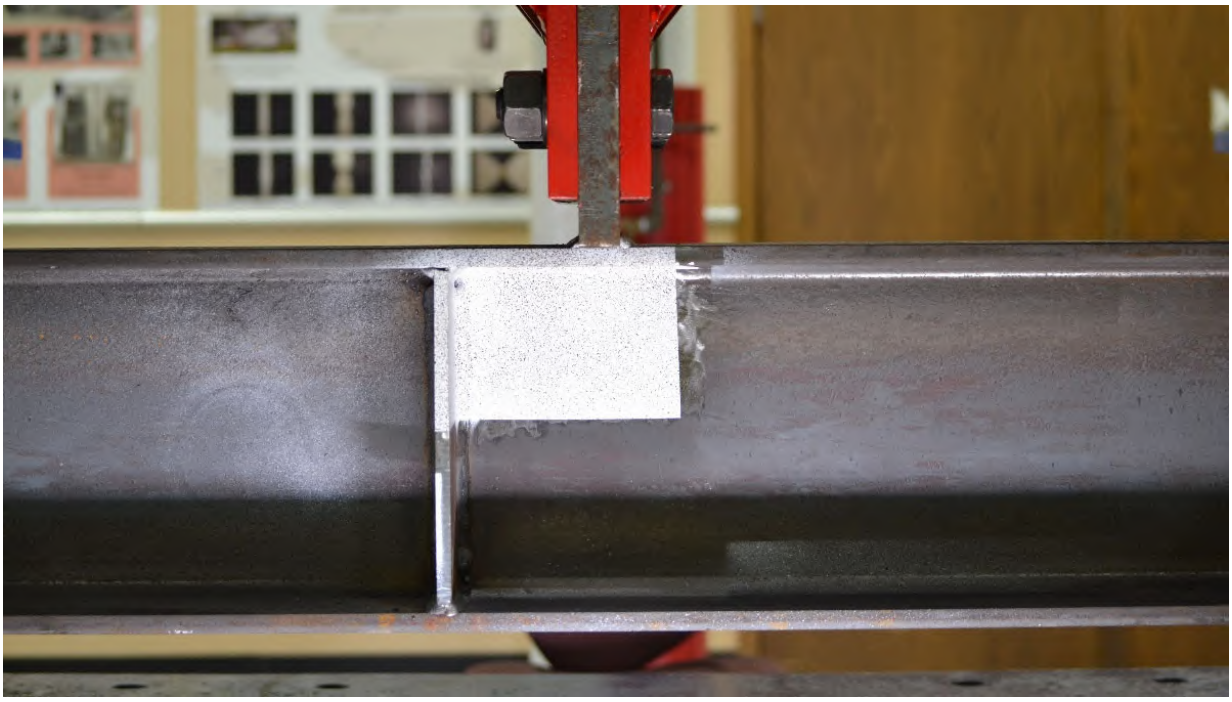

Figure A-147: Elevation of W10X39-ST-E4 prior to testing

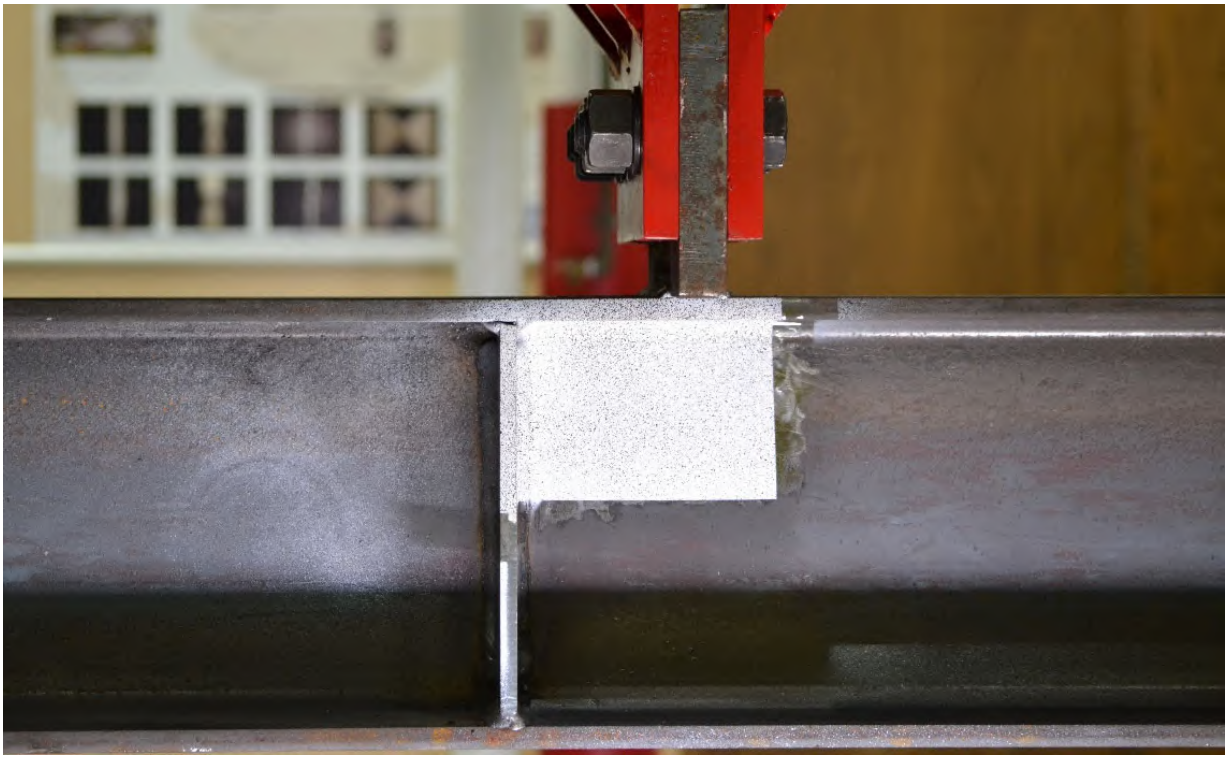

Figure A-148: Elevation view of W10X39-ST-E4 after testing

Figure A-149: Weld condition of W10X39-ST-E4 after testing (Side 1)

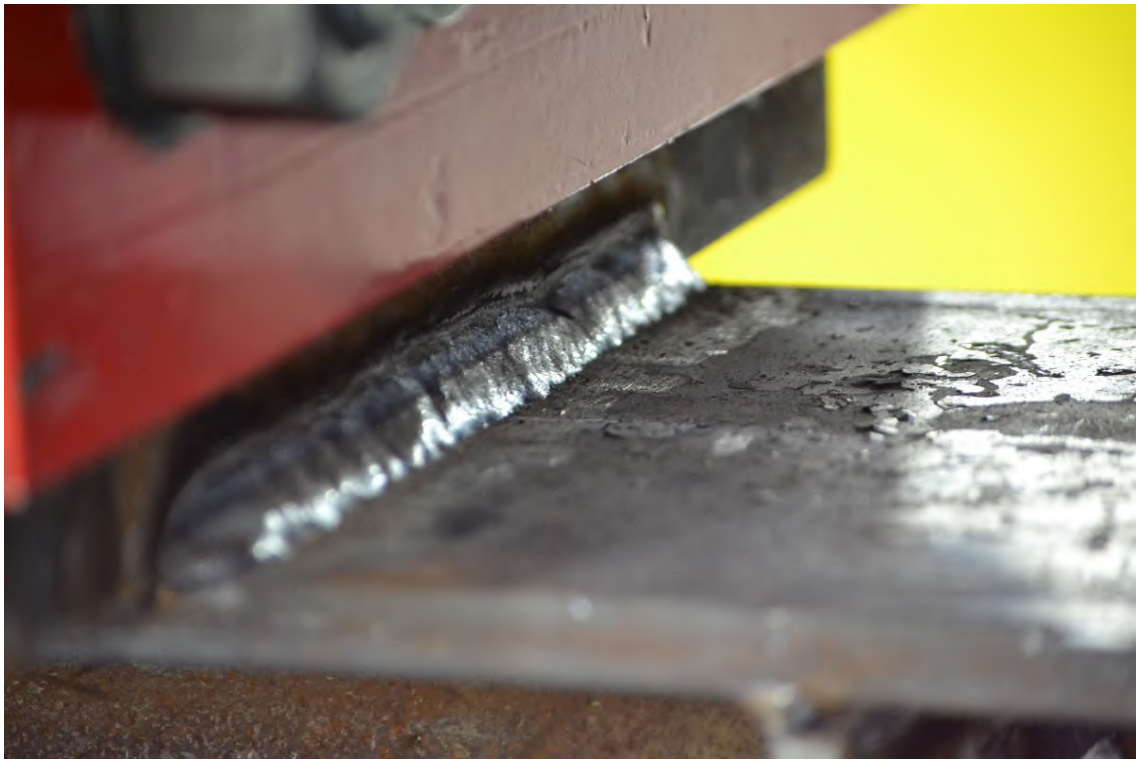

Figure A-150: Weld condition of W10X39-ST-E4 after testing (Side 2)

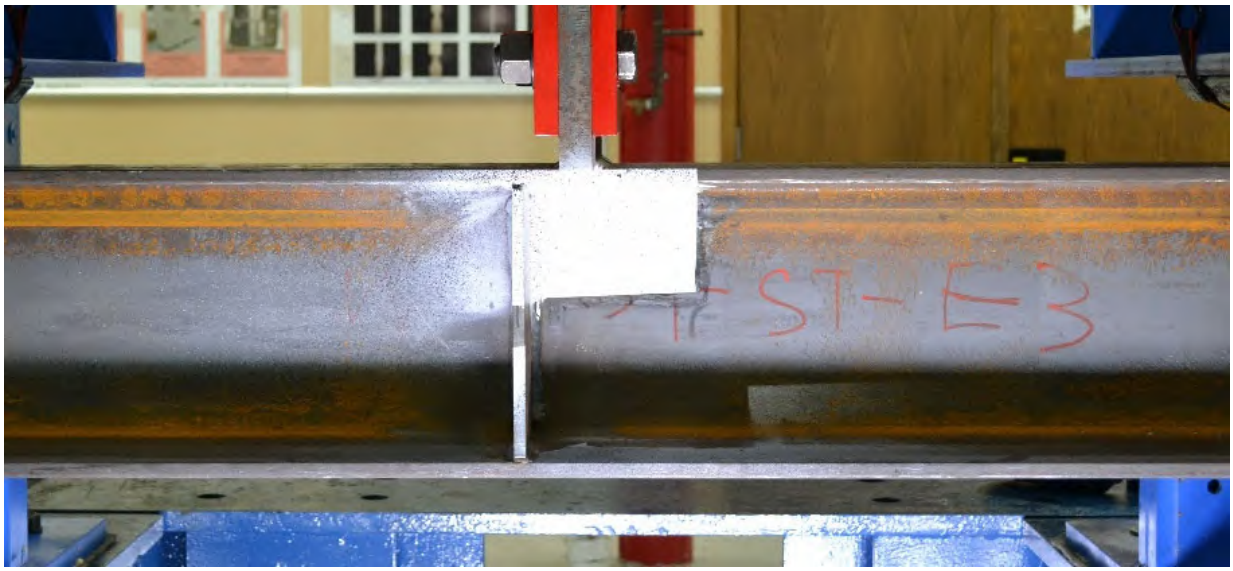

Figure A-151: Elevation view of W10X39-ST-E2 prior to testing

Figure A-152: Elevation view of W10X39-ST-E2 after testing

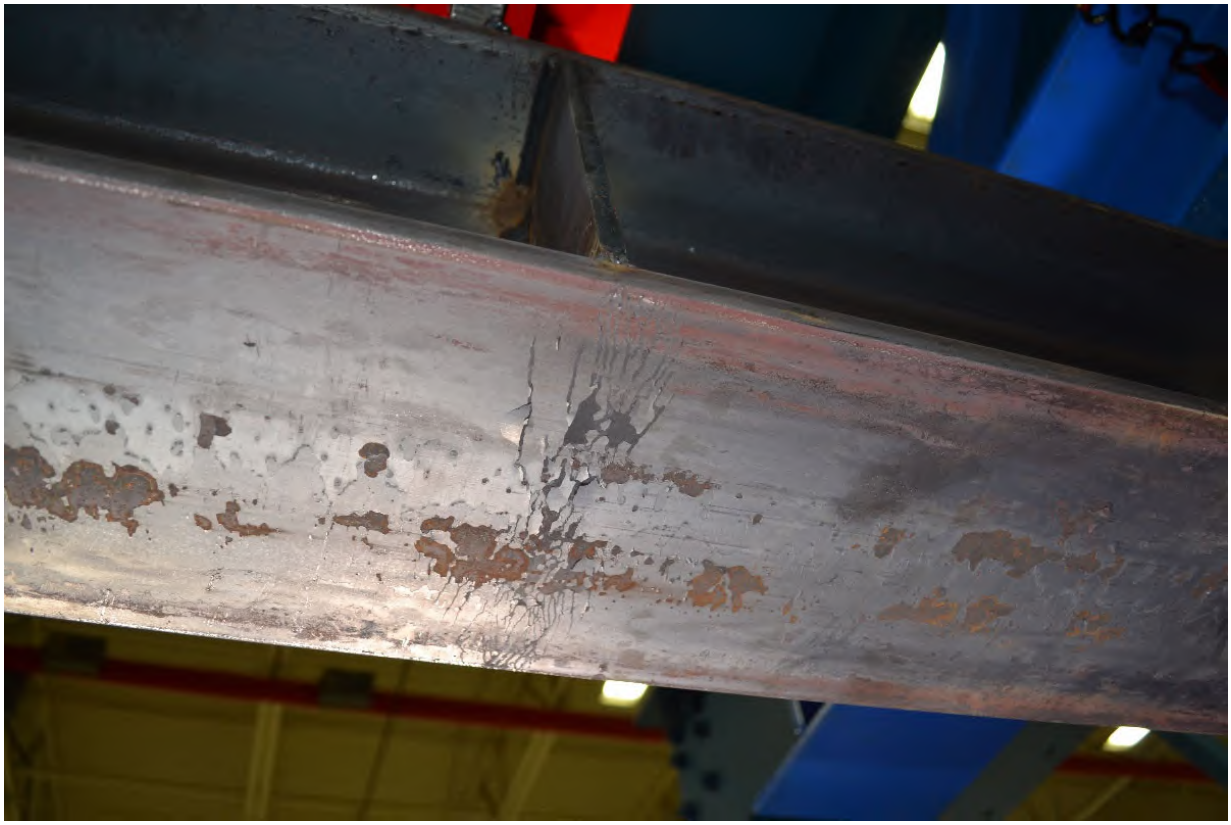

Figure A-153: Bottom view of W10X39-ST-E2 after testing

Figure A-154: Weld condition of W10X39-ST-E2 after testing (Side 1)

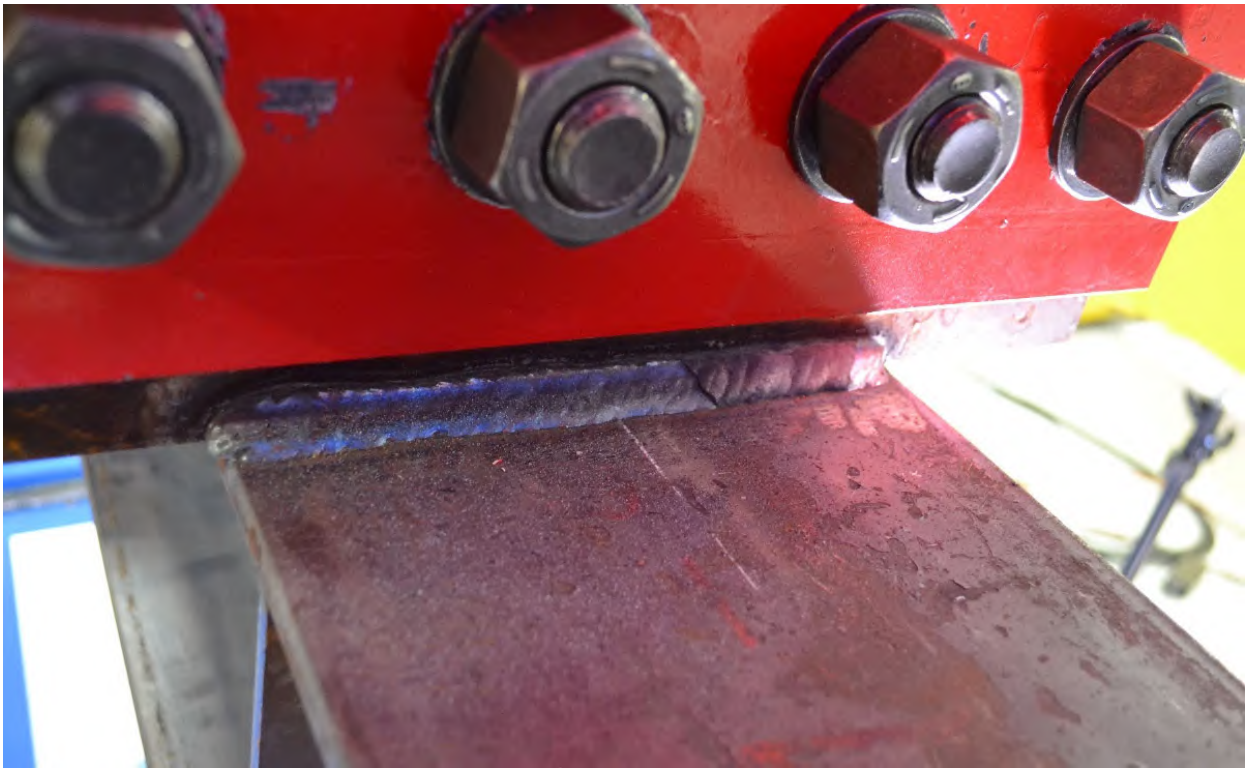

Figure A-155: Weld condition of W10X39-ST-E2 after testing (Side 2)

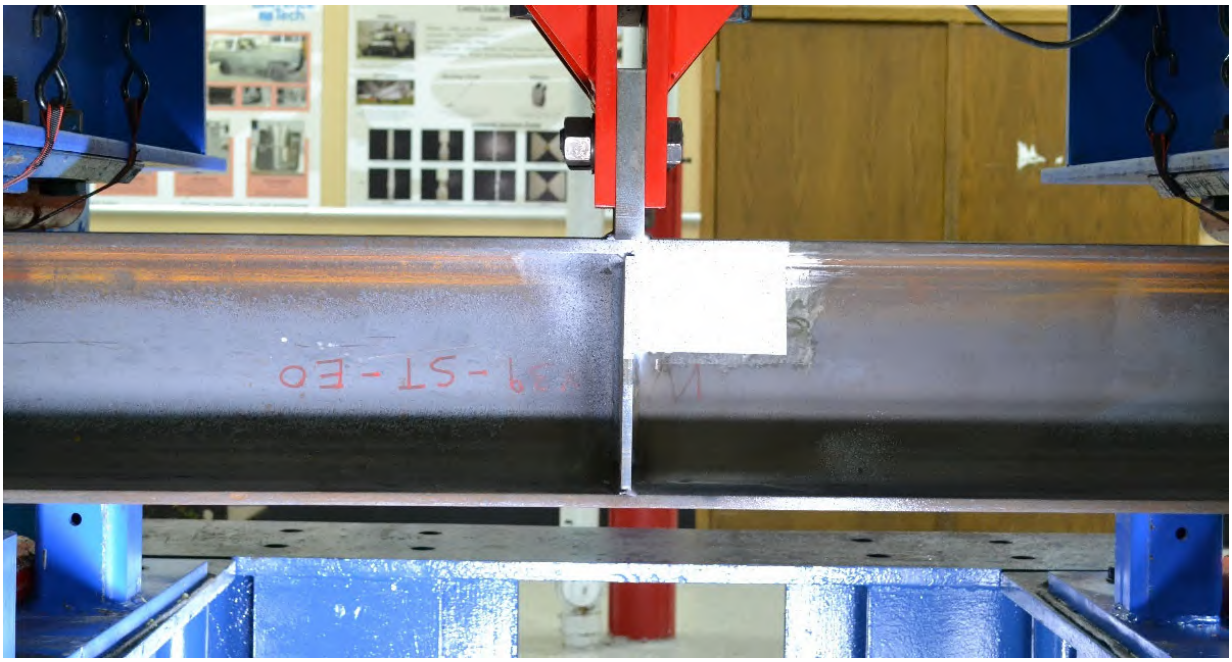

Figure A-156: Elevation of W10X39-ST-E0 prior to testing

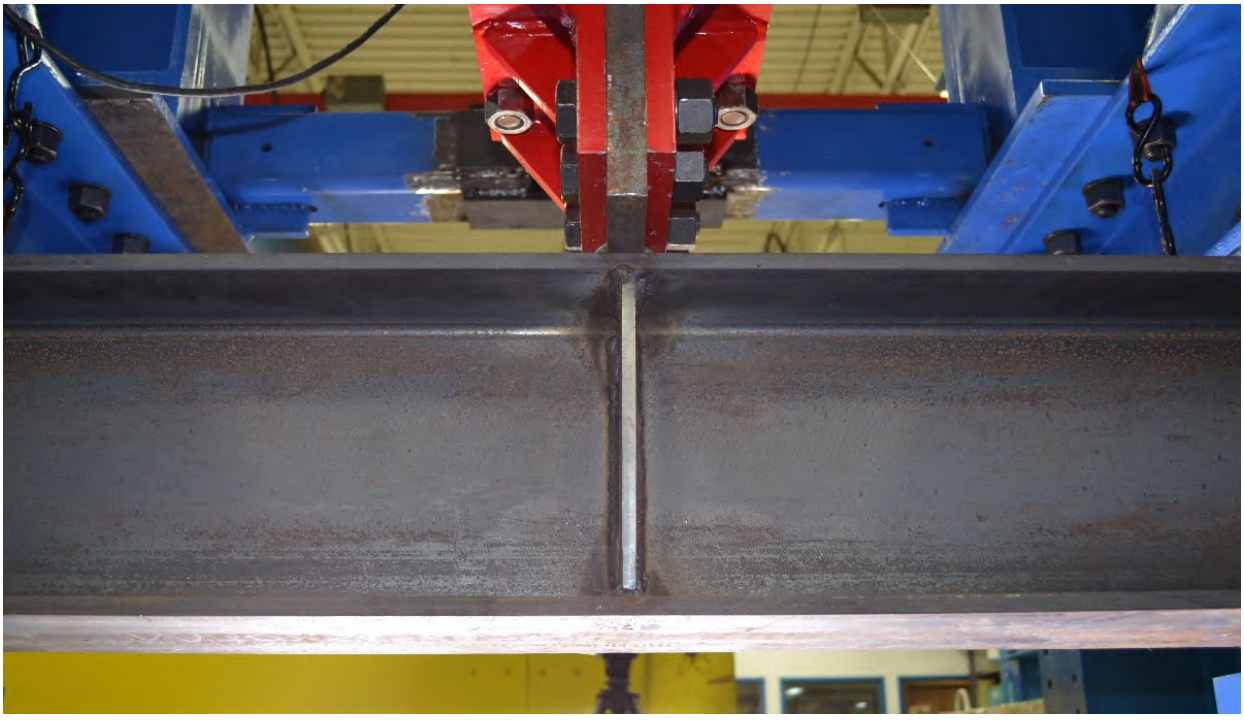

Figure A-157: Elevation view of W10X39-ST-E0 prior to testing

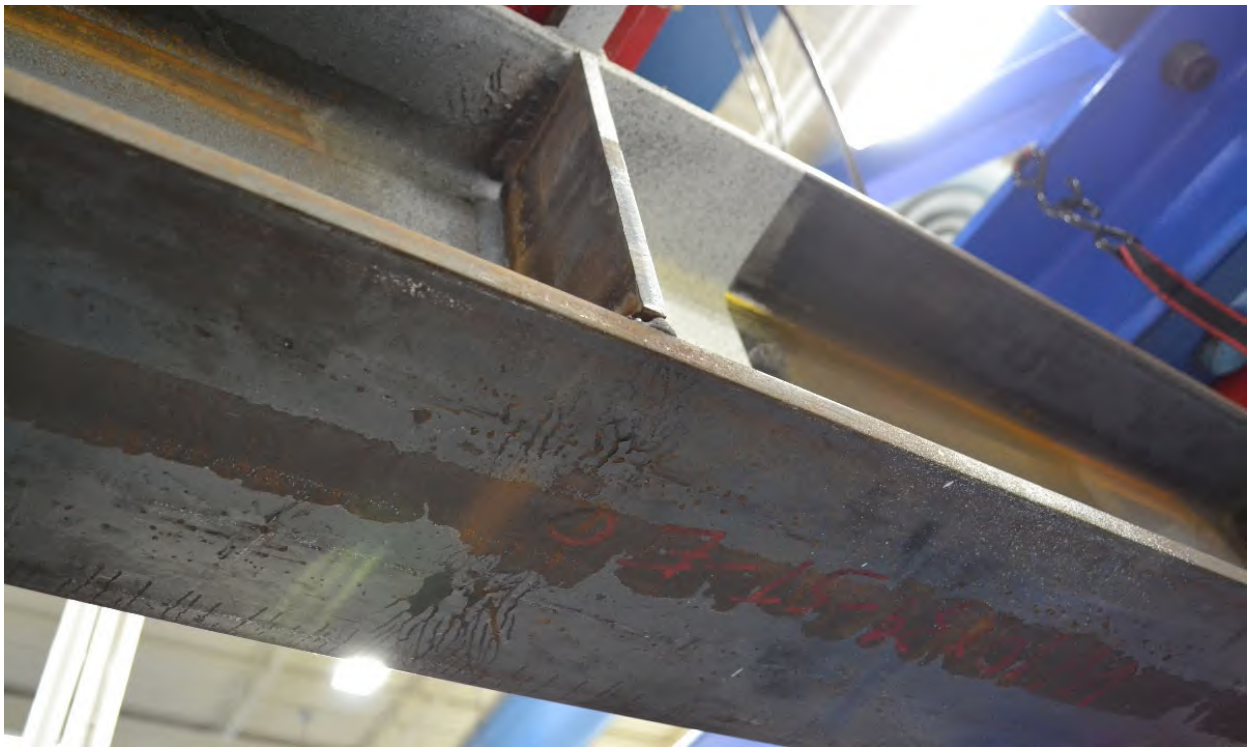

Figure A-158: Bottom view of W10X39-ST-E0 after testing

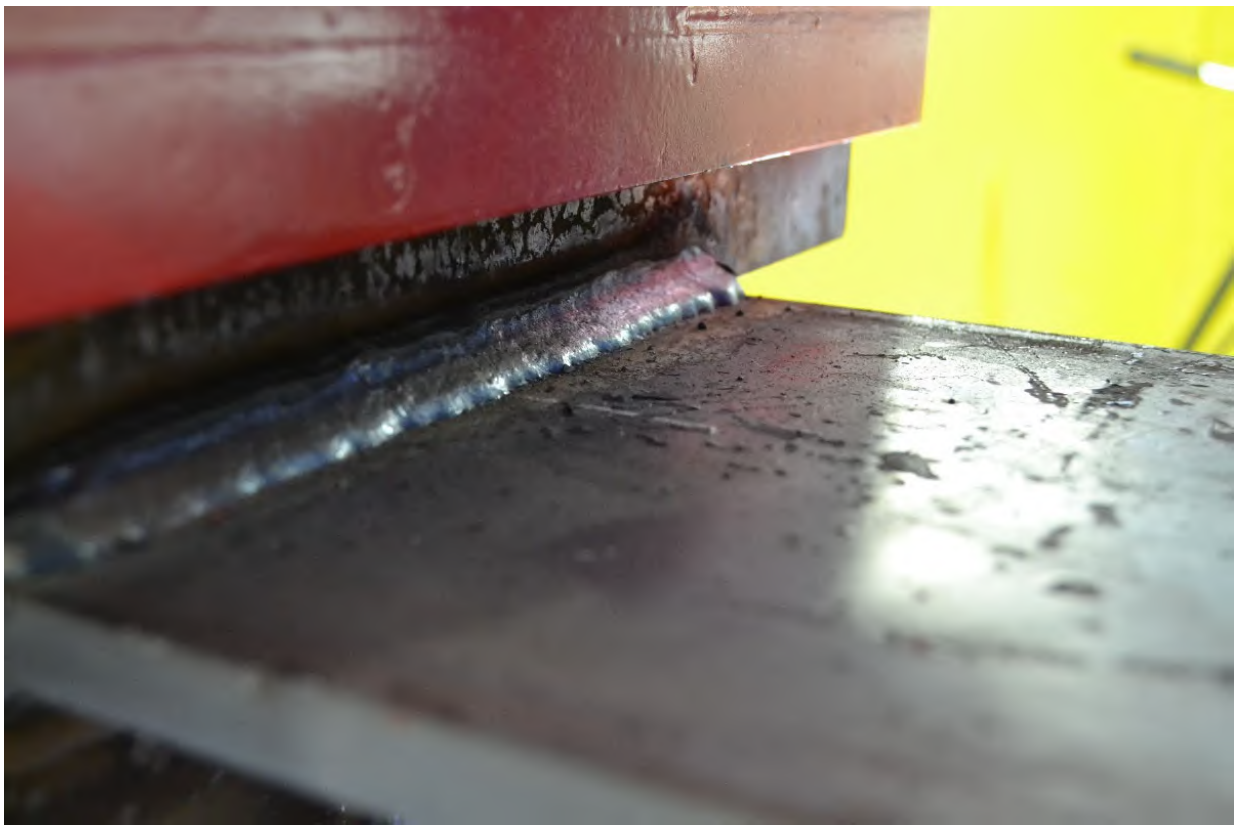

Figure A-159: Weld condition of W10X39-ST-E0 after testing

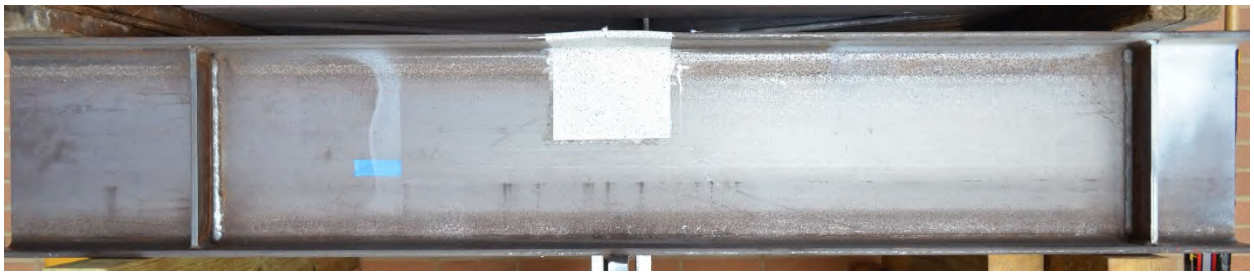

Figure A-160: Elevation view of W12X26-ST-NA after testing

Figure A-161: Side view of W12X26-ST-NA after testing emphasizing flange bending

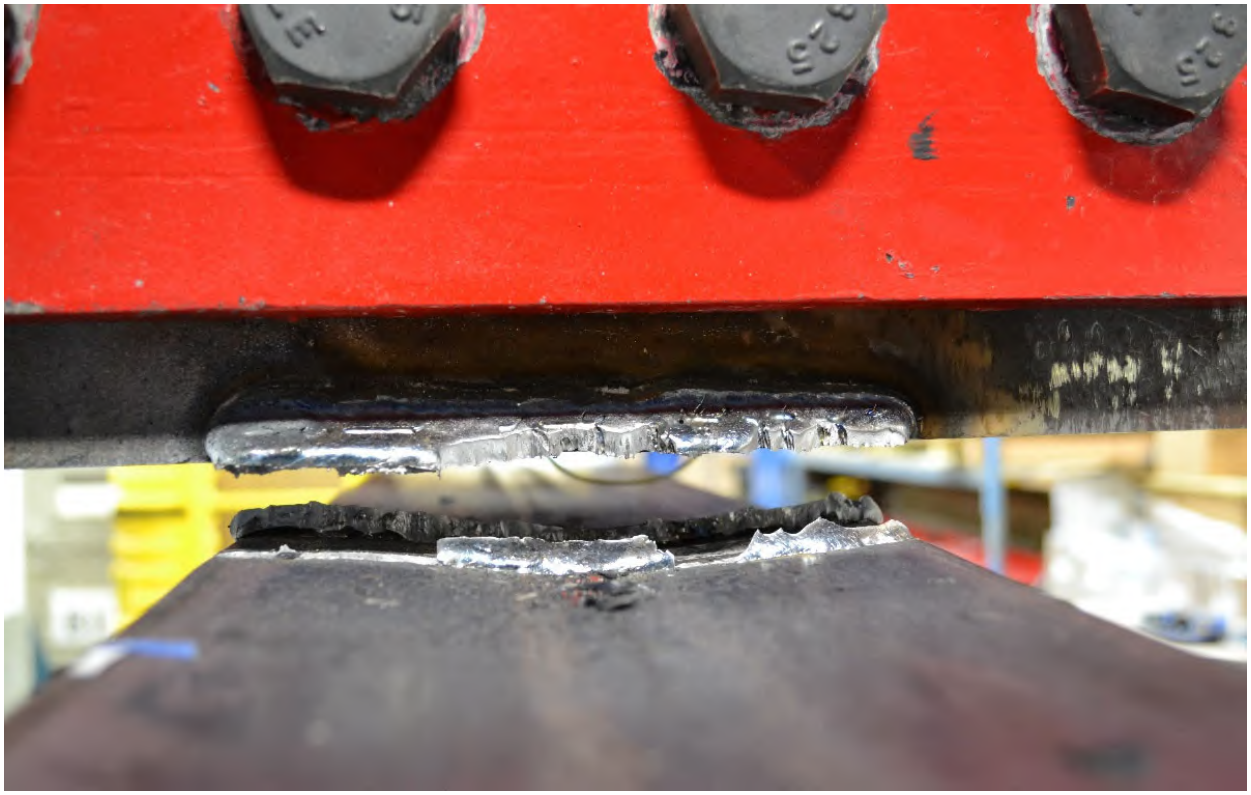

Figure A-162: Weld fracture of W12X26-ST-NA

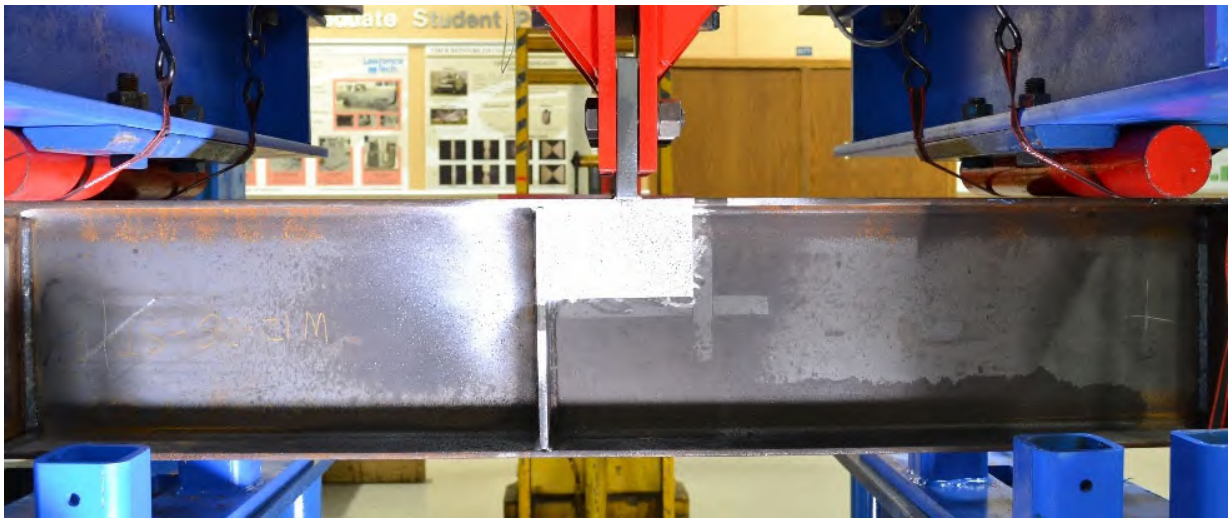

Figure A-163: Elevation view of W12X26-ST-E4 before testing

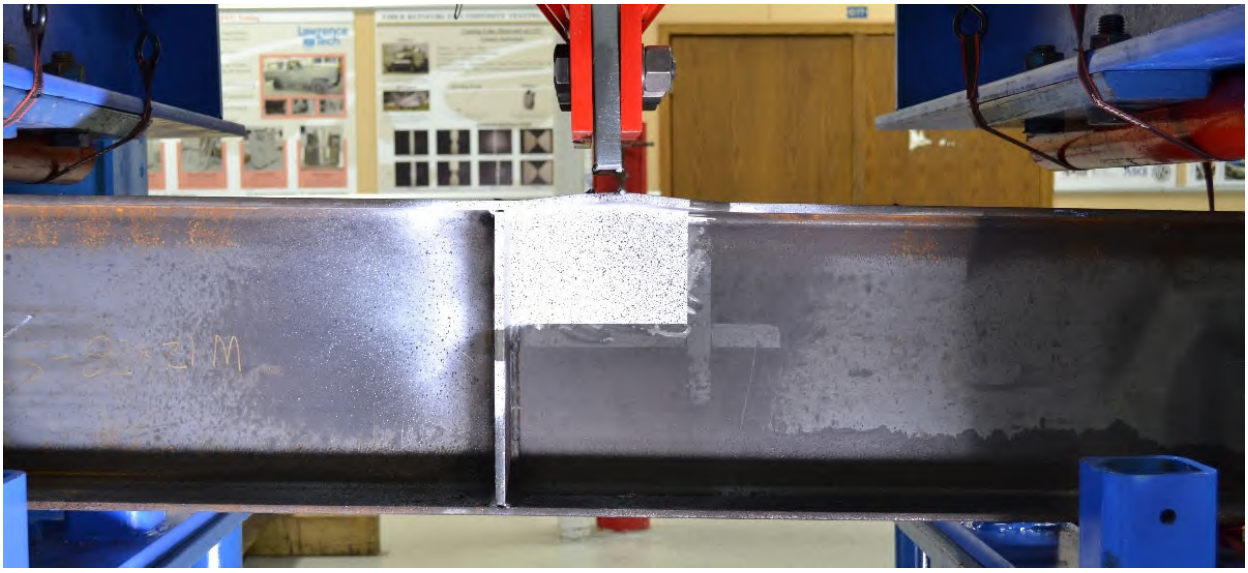

Figure A-164: Elevation view of W12X26-ST-E4 after testing

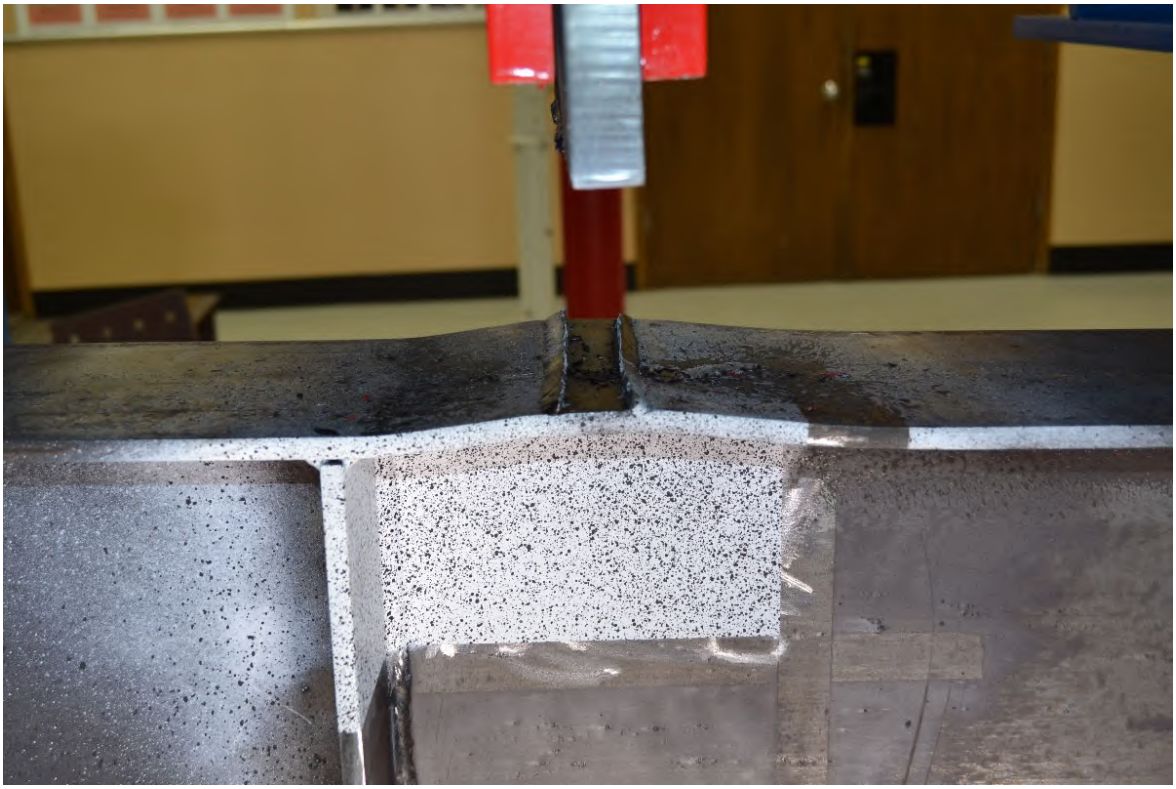

Figure A-165: Close-up view of W12X26-ST-E4 after testing

Figure A-166: W12X26-ST-E4 after testing emphasizing flange yielding

Figure A-167: Weld fracture of W12X26-ST-E4 after testing

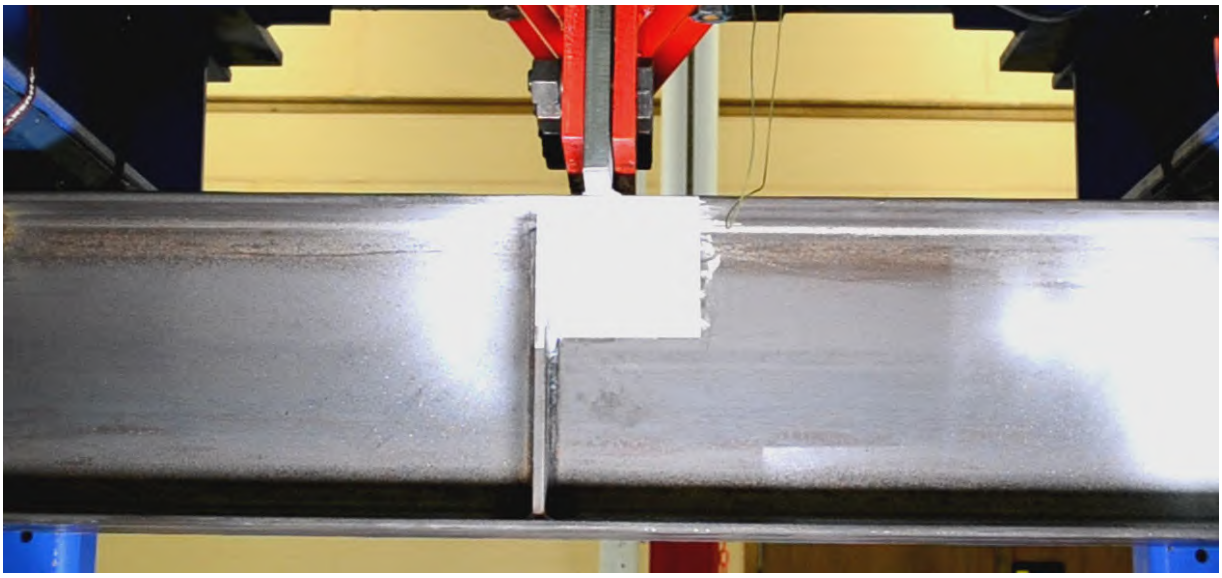

Figure A-168: Elevation view of W12X26-ST-E2 before testing

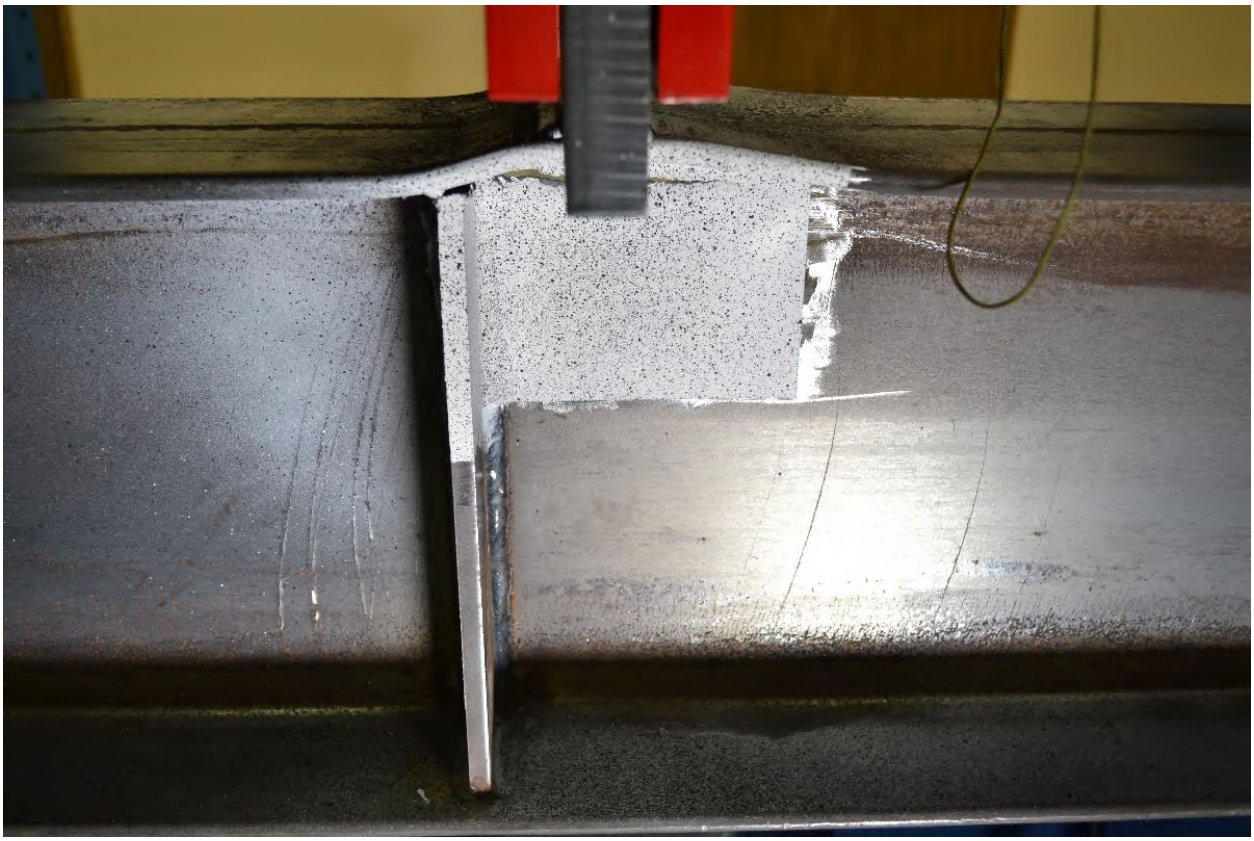

Figure A-169: Close-up view of W12X26-ST-E2 after testing

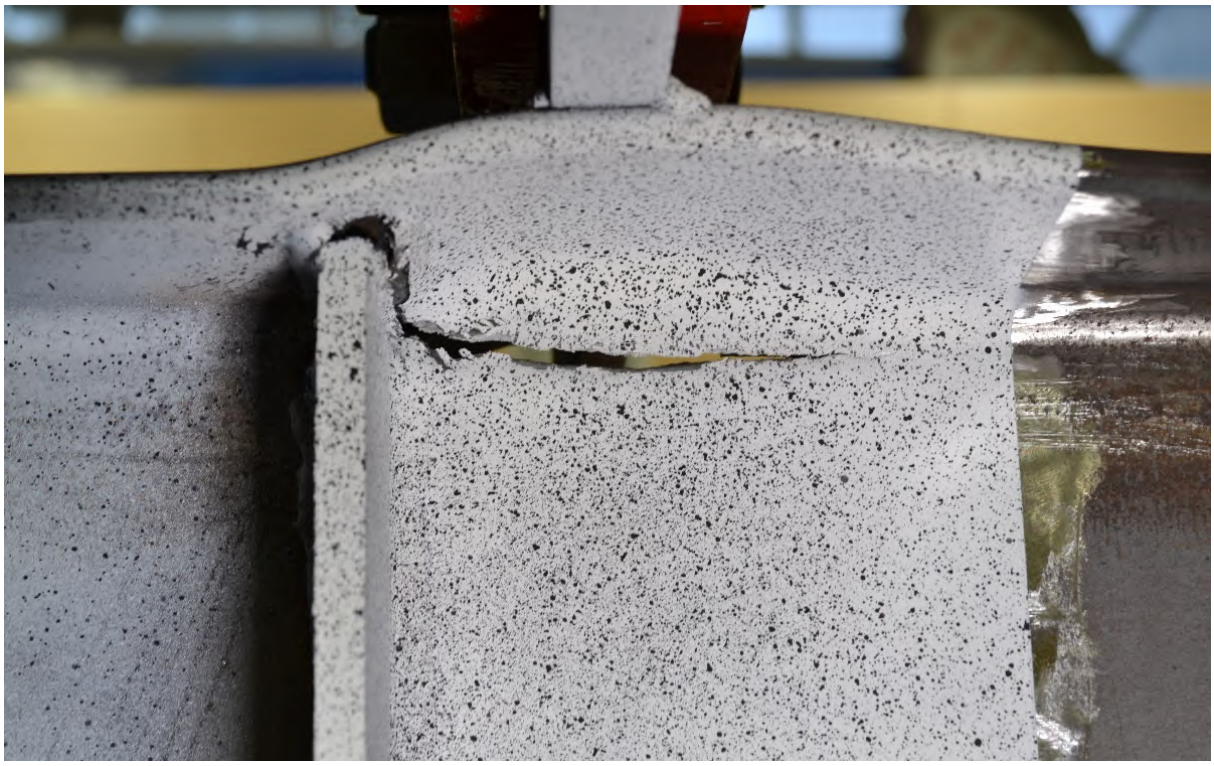

Figure A-170: W12X26-ST-E2 after testing emphasizing web fracture

Figure A-171: Top weld condition of W12X26-ST-E2 after testing

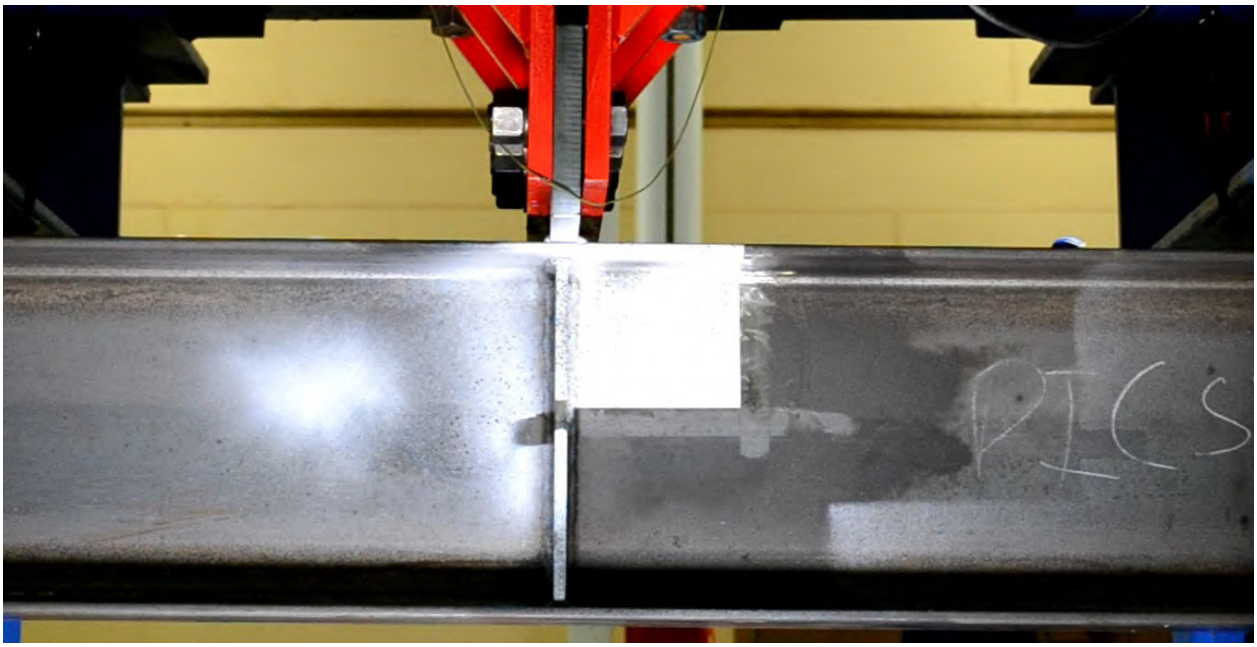

Figure A-172: Elevation of W12X26-ST-E0 before testing

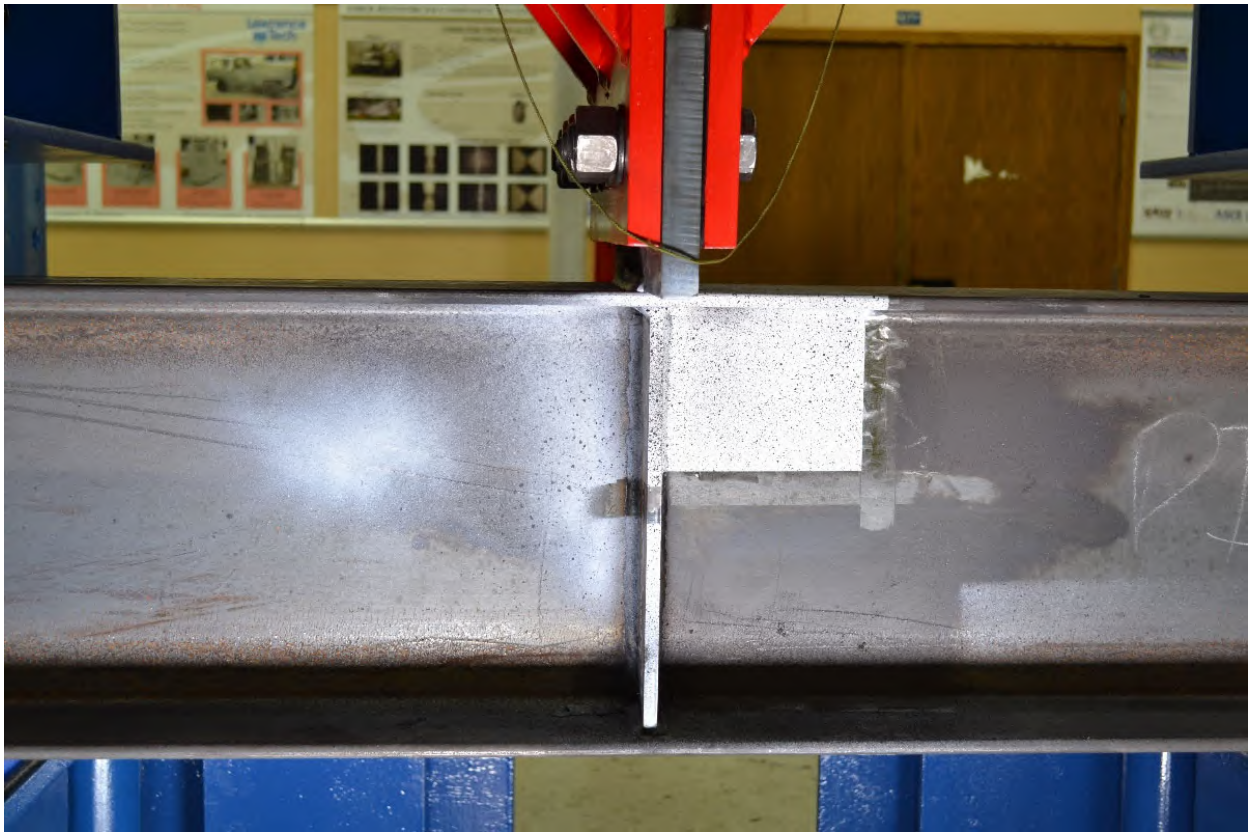

Figure A-173: Elevation view of W12X26-ST-E0 after testing

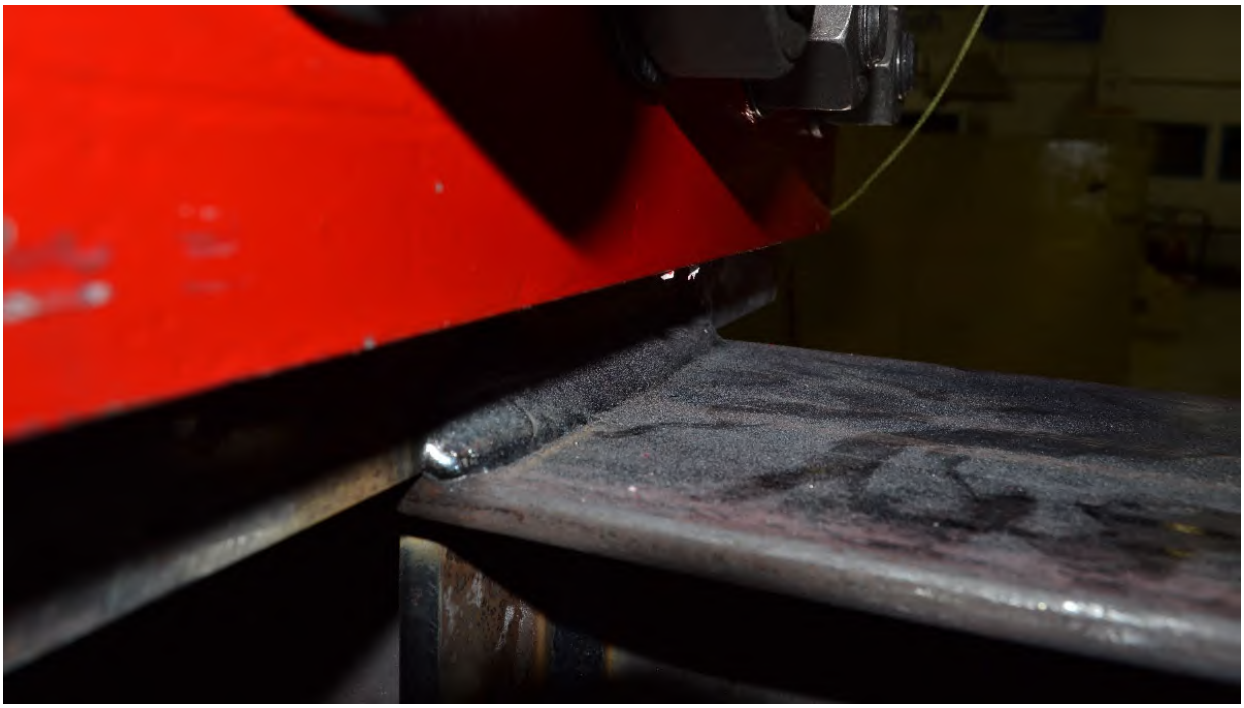

Figure A-174: Weld condition of W12X26-ST-E0 after testing (Side 1)

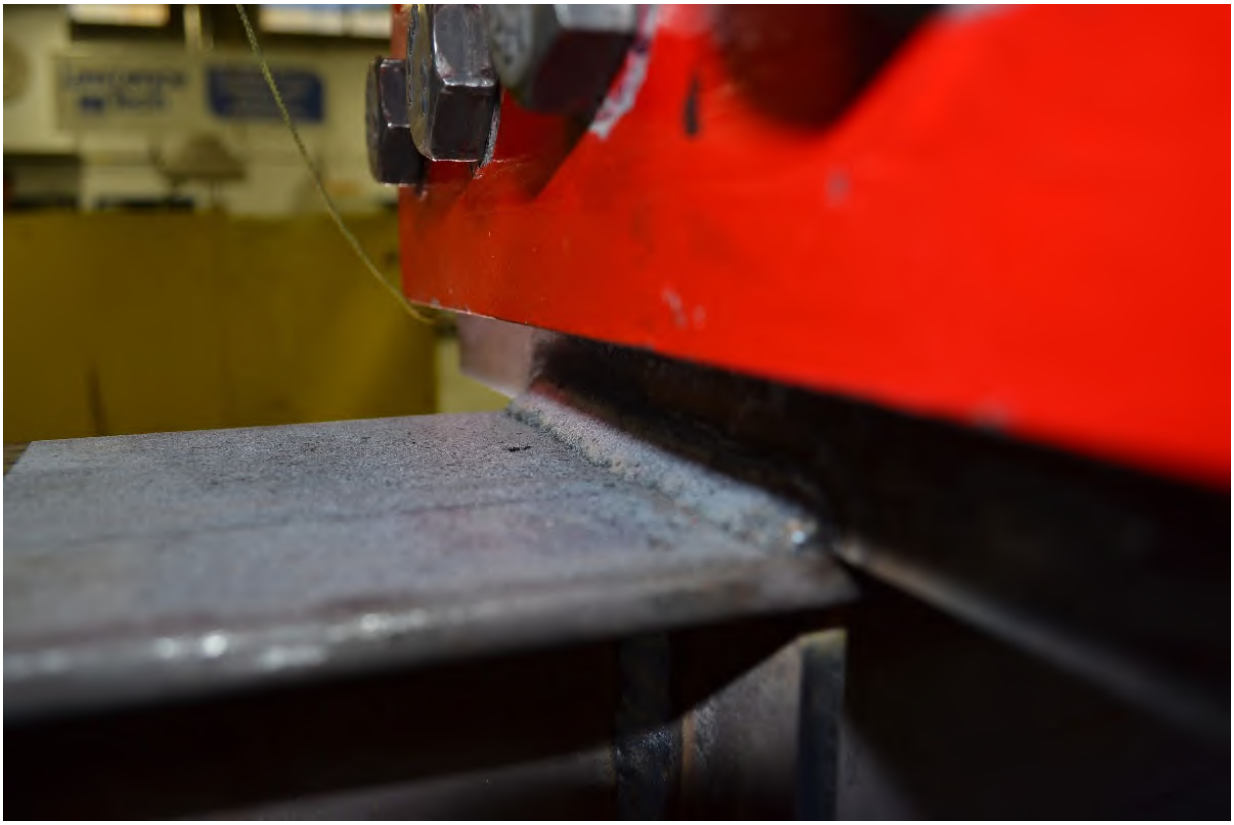

Figure A-175: Weld condition of W12X26-ST-E0 after testing (Side 2)

APPENDIX B: WELDING PROCEDURE SPECIFICATION (WPS)

Weld procedure used for weld connection from loading plates to top flange for single tension tests and for critical stiffeners near the concentrated load for all test methods.

WELDING PROCEDURE SPECIFICATION (WPS) Yes ■
PREQUALIFIED ____ QUALIFIED BY TESTING Salgat
or PROCEDURE QUALIFICATION RECORDS (PQR) Yes ☐

Identification # 11 Beams w/stiffeners
Revision ____ Date 4/12/2018 By ____
Authorized by ____ Date ____
Type—Manual ☐ Semiautomatic ■
Mechanized ☐ Automatic ☐

Company Name Woodhaven High School Welding for Lawrence Technical University
Welding Process(es) Flux-Cored Arc Welding
Supporting PQR No.(s) ____

JOINT DESIGN USED
Type:
Single ☐ Double Weld ■
Backing: Yes ☐ No ■
Backing Material:
Root Opening X ____ Root Face Dimension X ____
Groove Angle: X ____ Radius (J–U) X ____
Back Gouging: Yes ☐ No ■ Method ____

POSITION
Position of Groove: ____ Fillet: 2F
Vertical Progression: Up ☐ Down ☐

ELECTRICAL CHARACTERISTICS
Transfer Mode (GMAW) Short-Circuiting ■
Globular ☐ Spray ☐
Current: AC ☐ DCEP ■ DCEN ☐ Pulsed ☐
Power Source: CC ☐ CV ■
Other ____
Tungsten Electrode (GTAW)
Size: ____
Type: ____

BASE METALS
Material Spec. A36
Type or Grade ____
Thickness: Groove ____ Fillet 1/4"
Diameter (Pipe) ____

FILLER METALS
AWS Specification AWS A5.20, AWS 5.36,
AWS Classification Lincoln Ultracore 71A85

TECHNIQUE
Stringer or Weave Bead: Stringer
Multi-pass or Single Pass (per side) Single
Number of Electrodes 1
Electrode Spacing Longitudinal ____
Lateral ____
Angle ____
Contact Tube to Work Distance 3/4"
Peening NA
Interpass Cleaning: NA

SHIELDING
Flux ____ Gas 75%Argon/25%Co2
Composition ____
Electrode-Flux (Class) ____ Flow Rate 30CFH
Gas Cup Size 3/4

PREHEAT
Preheat Temp., Min. NA
Interpass Temp., Min. NA Max. ____

POSTWELD HEAT TREATMENT
Temp. NA
Time NA

WELDING PROCEDURE

Pass or Weld Layer(s)	Process	Filler Metals		Current		Volts	Travel Speed	Joint Details
		Class	Diam.	Type & Polarity	Amps or Wire Feed Speed			
1	FCAW	AWS A5.20	.045	DCEP	WFS 275-340	23-27		T-Joint, Double Fillet, 1/4" Leg Single Pass, 2F Position

APPENDIX C: SCREENSHOTS FROM DIGITAL IMAGE CORRELATION

Table C-1: Index of screenshots from Digital Image Correlation

Column Specimen	Figures	Starting Page	Column Specimen	Figures	Starting Page
W10X19-DC-E0	C-1 to C-5	C-3	W16X31-DC-E0	C-93 to C-97	C-49
W10X19-DC-E2	C-6 to C-10	C-5	W16X31-DC-E6	C-98 to C-101	C-51
W10X19-DC-E4	C-11 to C-15	C-8	W16X31-DC-NA	C-102 to C-105	C-54
W10X19-DC-NA	C-16 to C-19	C-10	W16X31-SC-E0	C-106 to C-110	C-56
W10X19-SC-E0	C-20 to C-24	C-12	W16X31-SC-E3	C-111 to C-114	C-59
W10X19-SC-E2	C-25 to C-29	C-15	W16X31-SC-E6	C-115 to C-118	C-61
W10X19-SC-E4	C-30 to C-33	C-17	W16X31-SC-NA	C-119 to C-122	C-63
W10X19-SC-NA	C-34 to C-37	C-19	W10X39-ST-E0	C-123 to C-124	C-65
W10X39-SC-E0	C-38 to C-41	C-21	W10X39-ST-E2	C-125 to C-126	C-66
W10X39-SC-E2	C-42 to C-46	C-23	W10X39-ST-E4	C-127 to C-128	C-67
W10X39-SC-E4	C-47 to C-51	C-26	W10X39-ST-NA	C-129 to C-130	C-68
W10X39-SC-NA	C-52 to C-55	C-28	W12X26-ST-E0	C-131 to C-133	C-69
W12X26-DC-E0	C-56 to C-59	C-30	W12X26-ST-E2	C-134 to C-136	C-70
W12X26-DC-E2	C-60 to C-64	C-32	W12X26-ST-E4	C-137 to C-139	C-72
W12X26-DC-E4	C-65 to C-69	C-35	W12X26-ST-NA	C-140 to C-141	C-73
W12X26-DC-NA	C-70 to C-73	C-37	W16X31-ST-E0	C-142 to C-144	C-74
W12X26-SC-E0	C-74 to C-78	C-39	W16X31-ST-E3	C-145 to C-147	C-76
W12X26-SC-E2	C-79 to C-83	C-42	W16X31-ST-E6	C-148 to C-149	C-77
W12X26-SC-E4	C-84 to C-88	C-44	W16X31-ST-NA	C-150 to C-151	C-78
W12X26-SC-NA	C-89 to C-92	C-47			

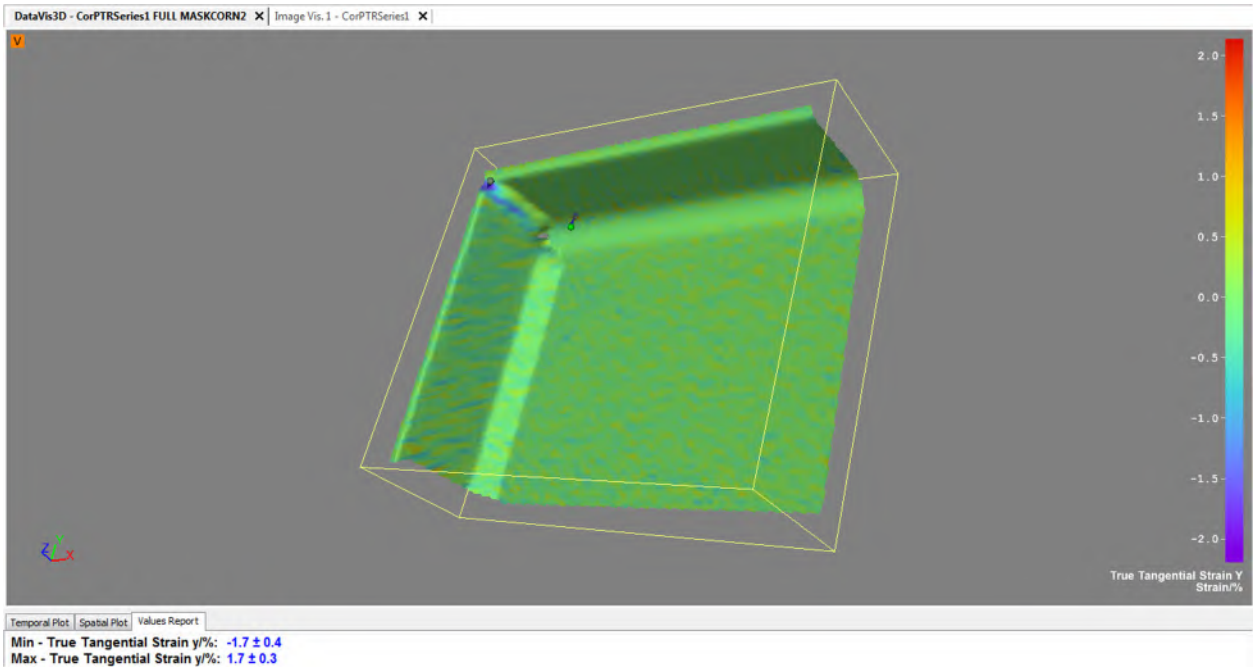

Figure C-1: W10X19-DC-E0 showing true tangential strain Y at a load of 63 kips

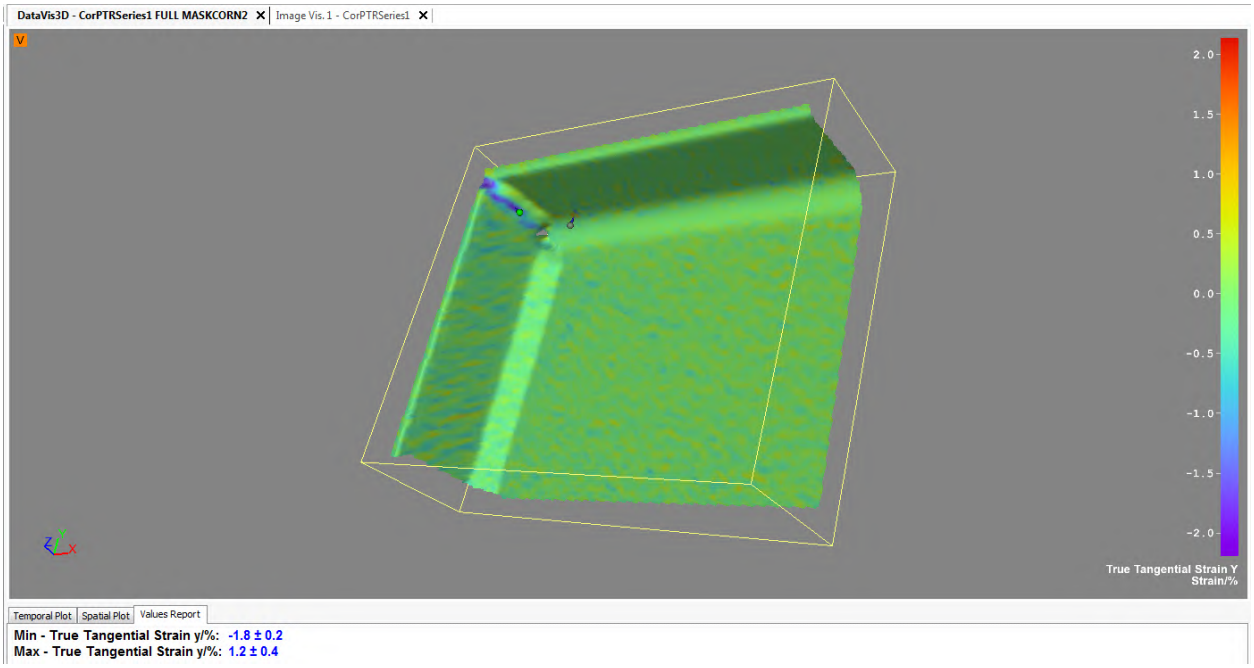

Figure C-2: W10X19-DC-E0 showing true tangential strain Y at a load of 71 kips

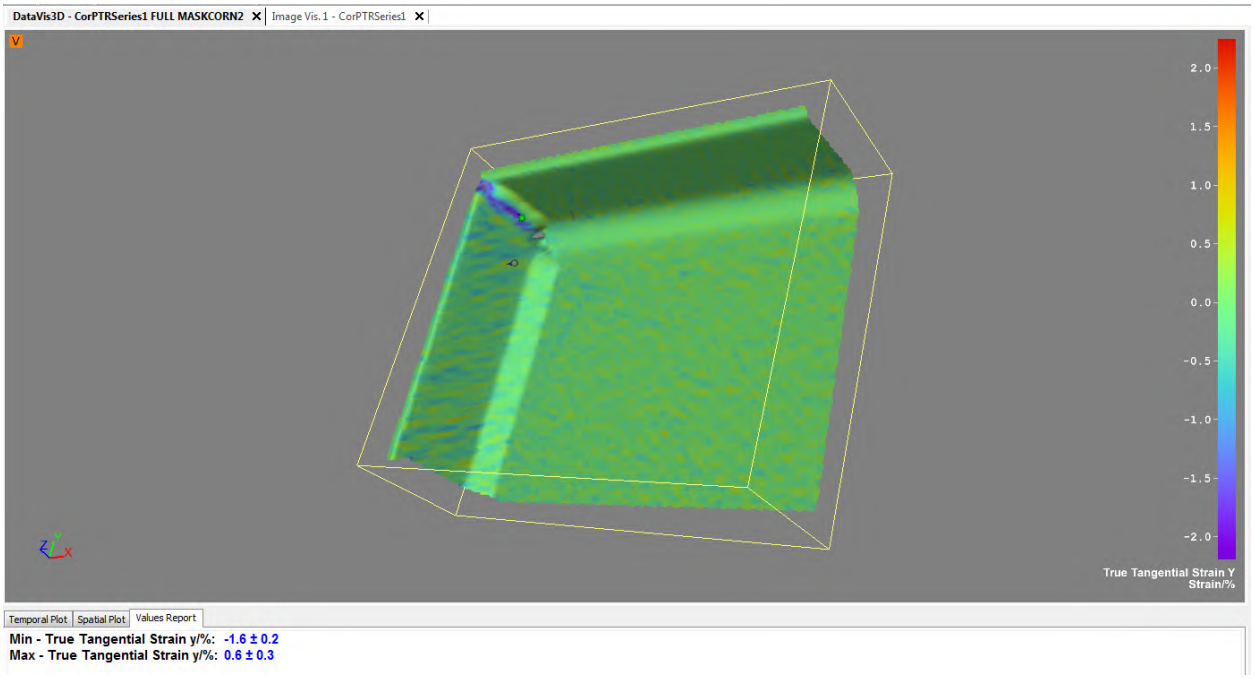

Figure C-3: W10X19-DC-E0 showing true tangential strain Y at a load of 78.5 kips

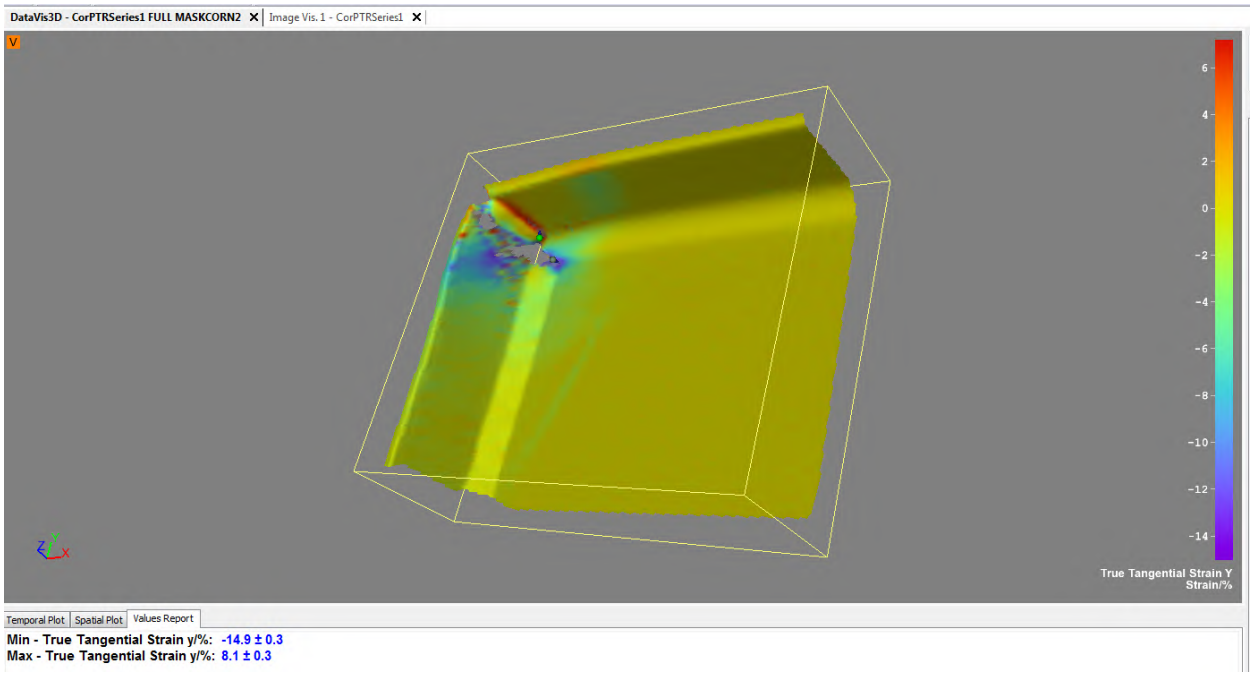

Figure C-4: W10X19-DC-E0 showing true tangential strain Y at its maximum load of 180 kips

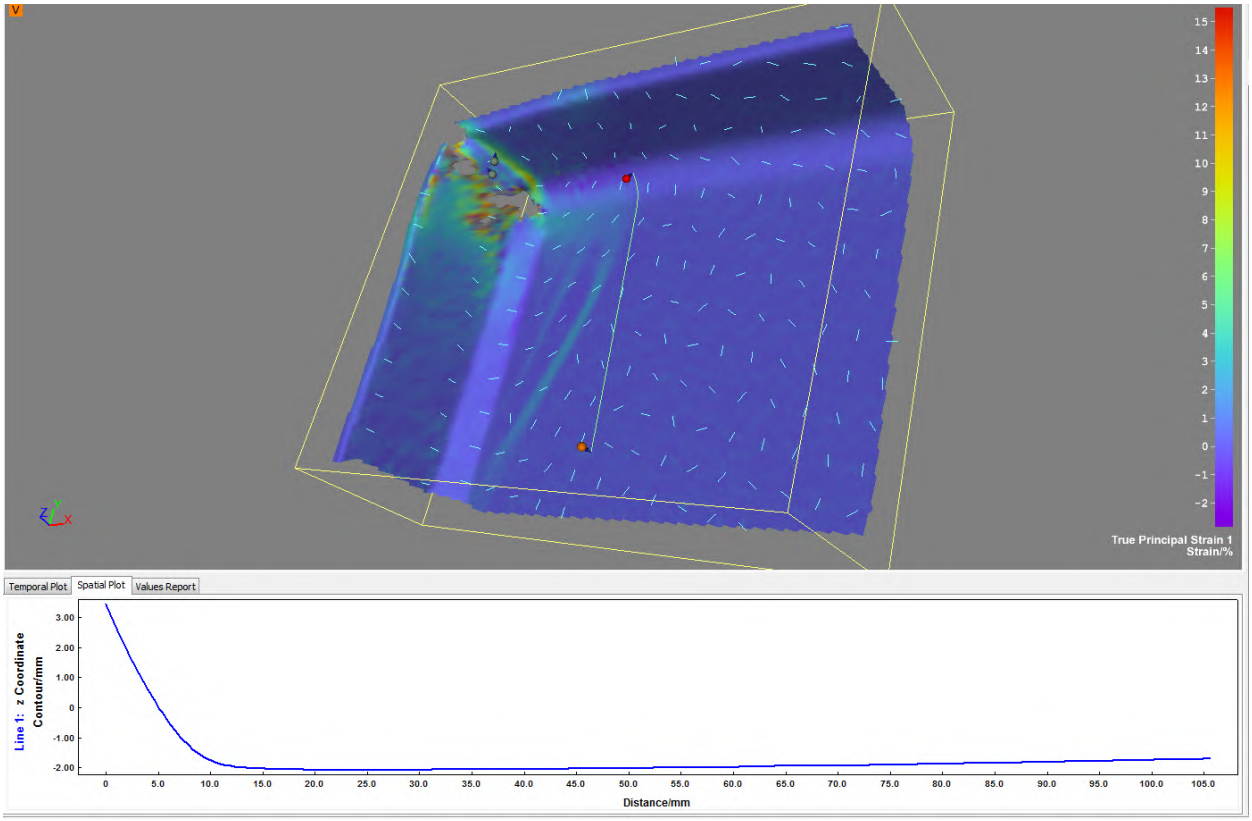

Figure C-5: W10X19-DC-E0 showing out of plane displacement at its maximum load of 180 kips

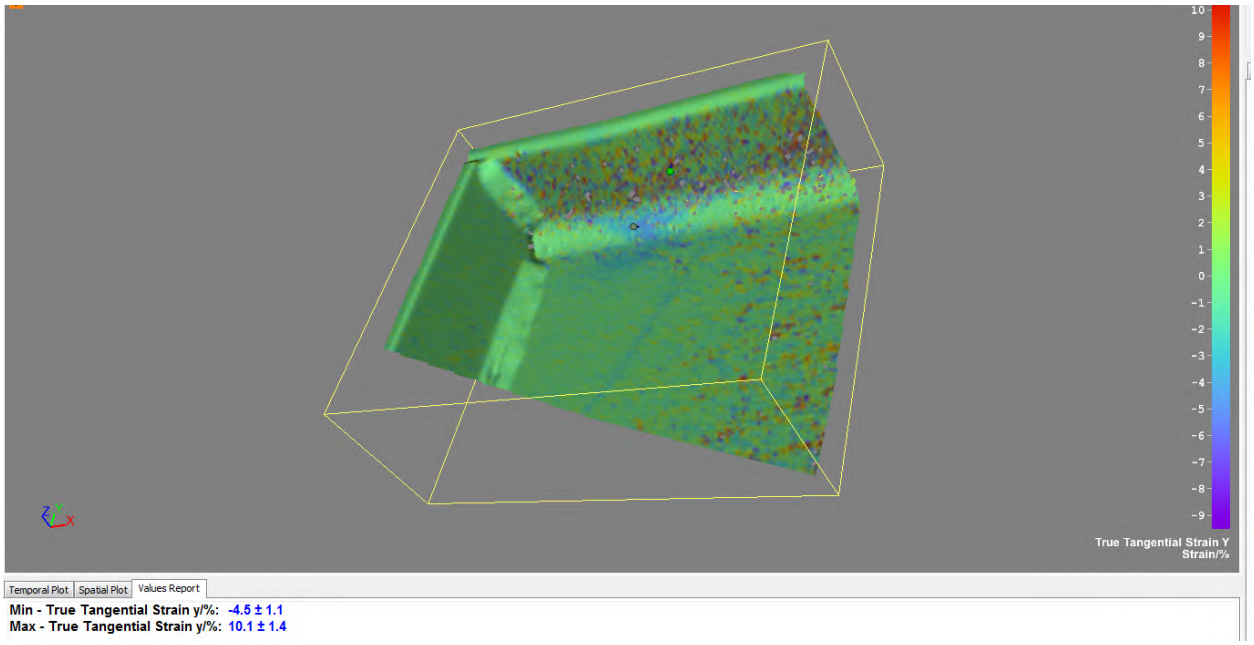

Figure C-6: W10X19-DC-E2 showing true tangential strain Y at a load of 63 kips

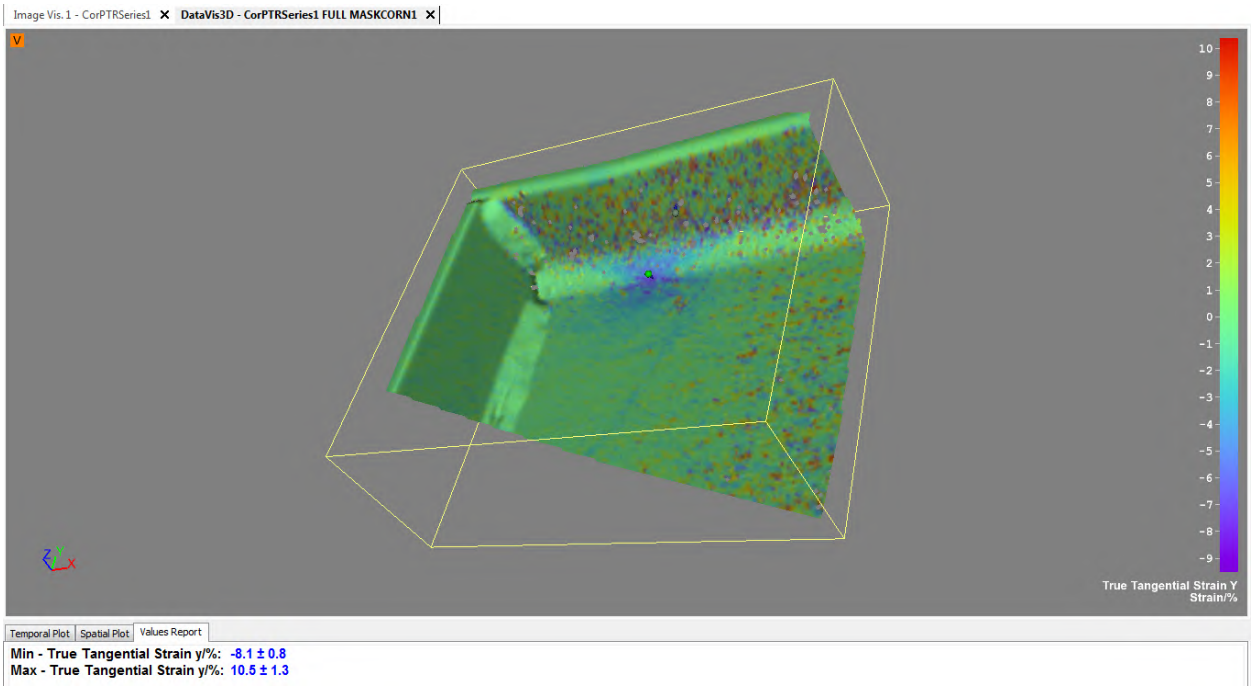

Figure C-7: W10X19-DC-E2 showing true tangential strain Y at a load of 71 kips

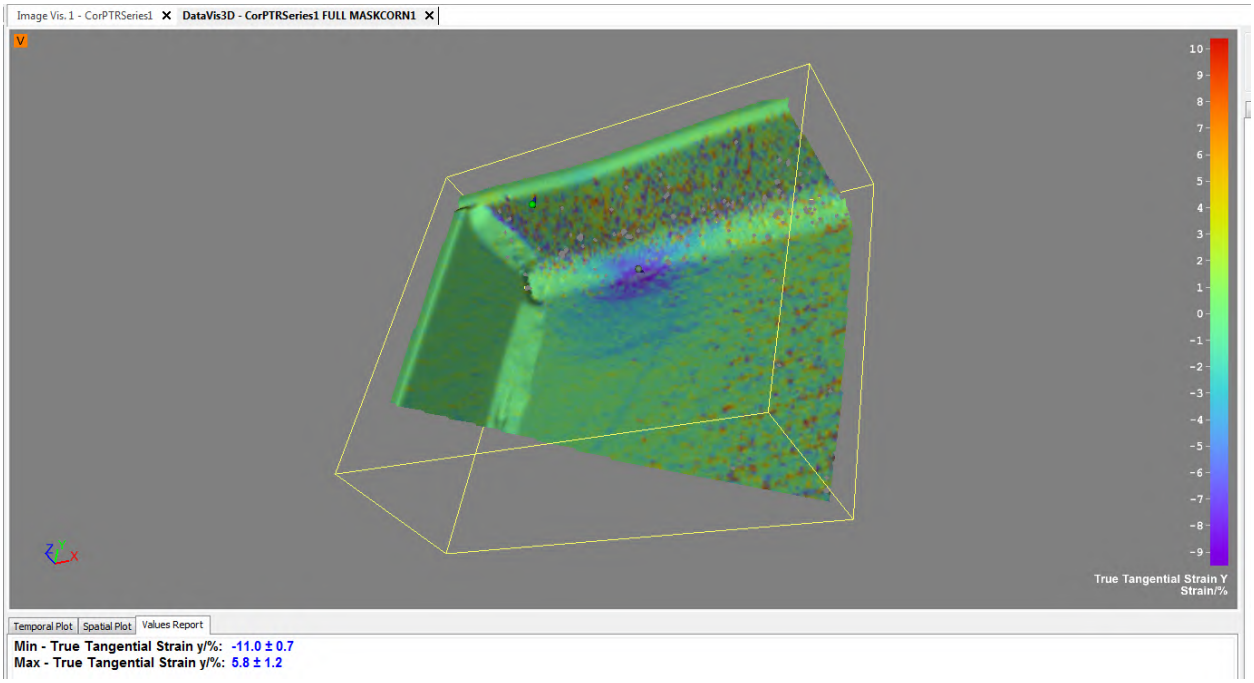

Figure C-8: W10X19-DC-E2 showing true tangential strain Y at a load of 78.5 kips

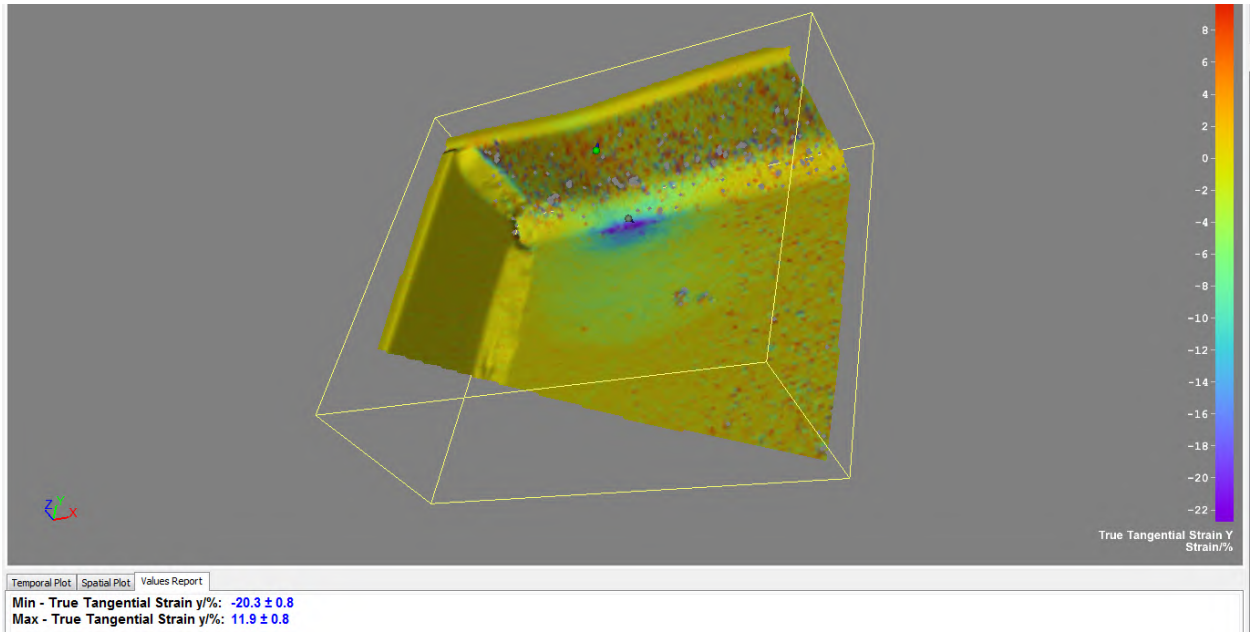

Figure C-9: W10X19-DC-E2 showing true tangential strain Y at its maximum load of 88 kips

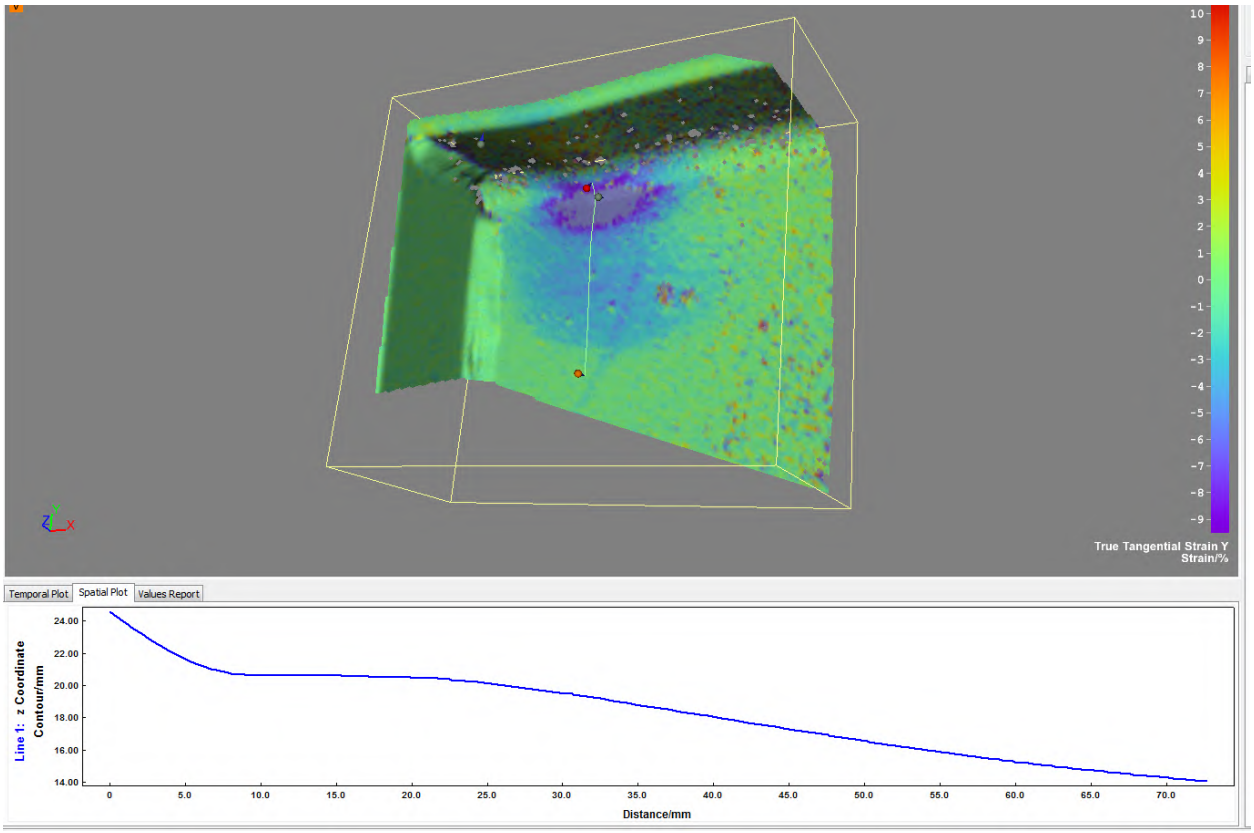

Figure C-10: W10X19-DC-E2 showing out of plane displacement at its maximum load of 88

kips

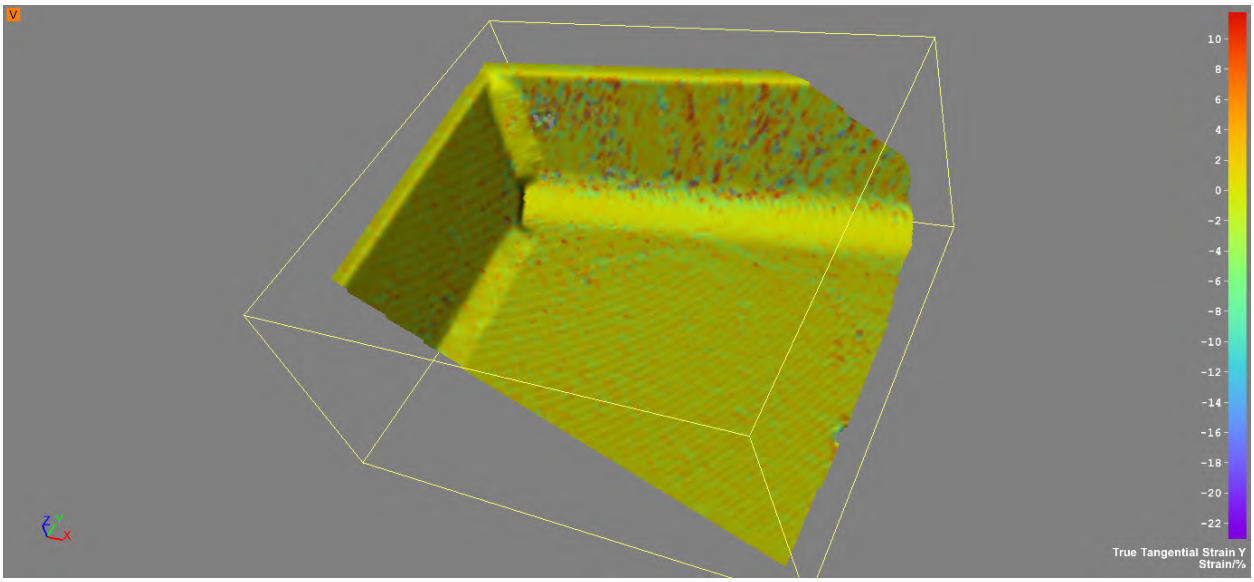

Figure C-11: W10X19-DC-E4 showing true tangential strain Y at a load of 63 kips

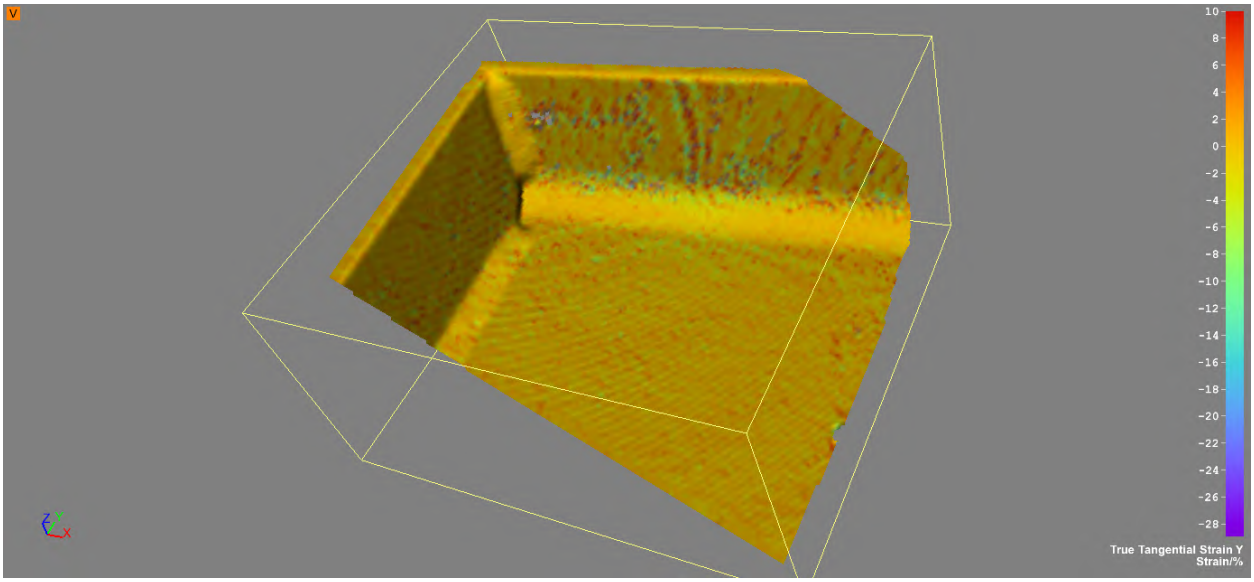

Figure C-12: W10X19-DC-E4 showing true tangential strain Y at a load of 71 kips

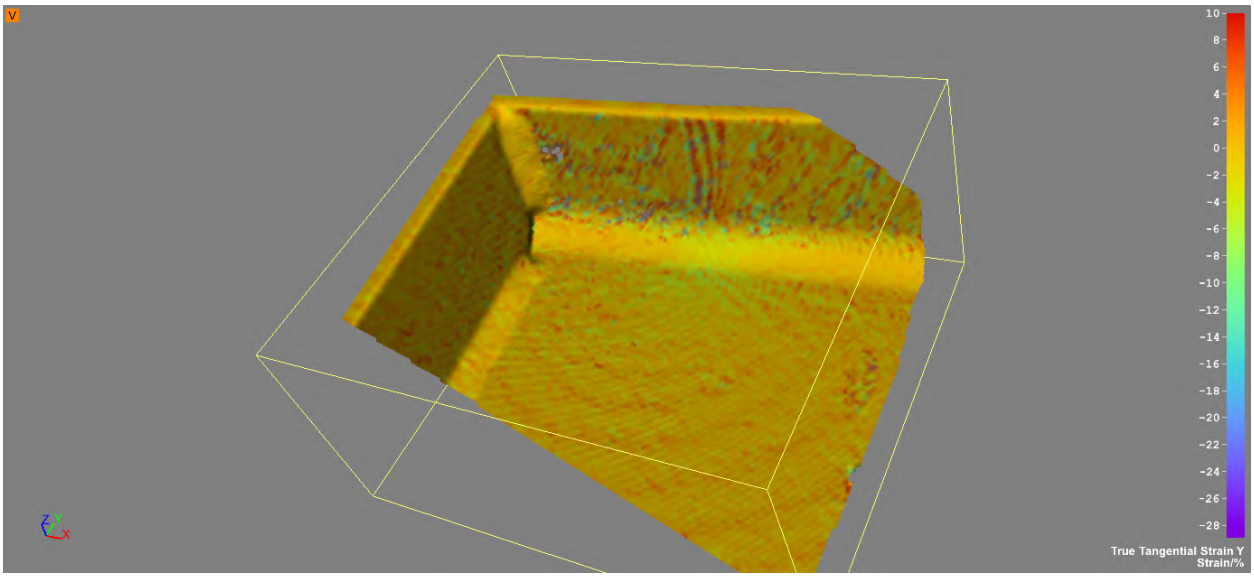

Figure C-13: W10X19-DC-E4 showing true tangential strain Y at a load of 78.5 kips

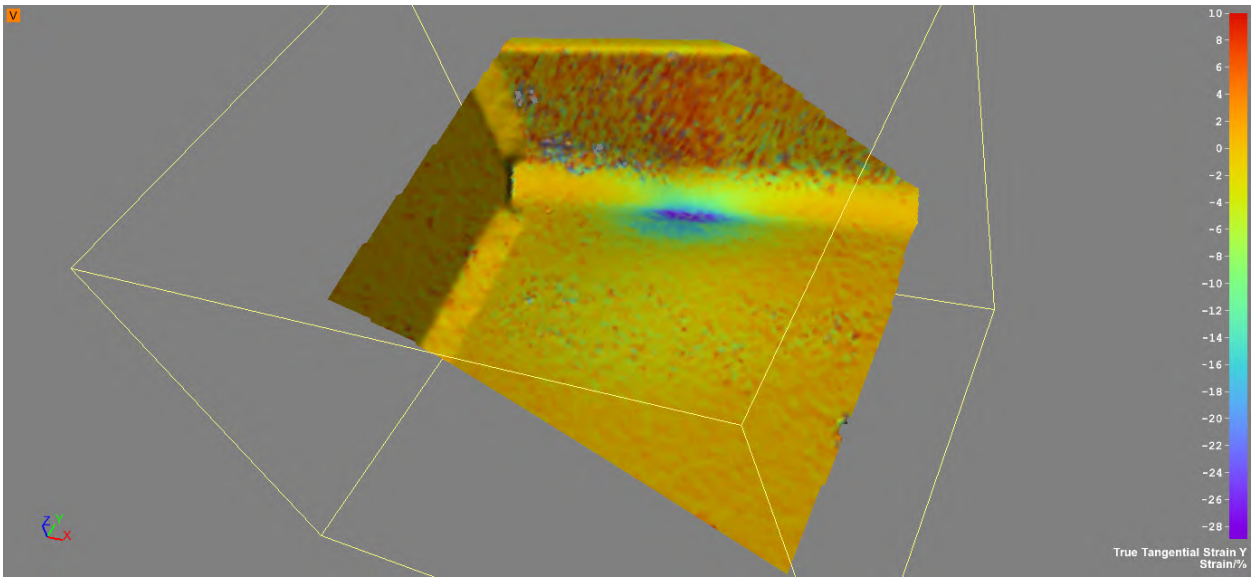

Figure C-14: W10X19-DC-E4 showing true tangential strain Y at its maximum load of 84.4 kips

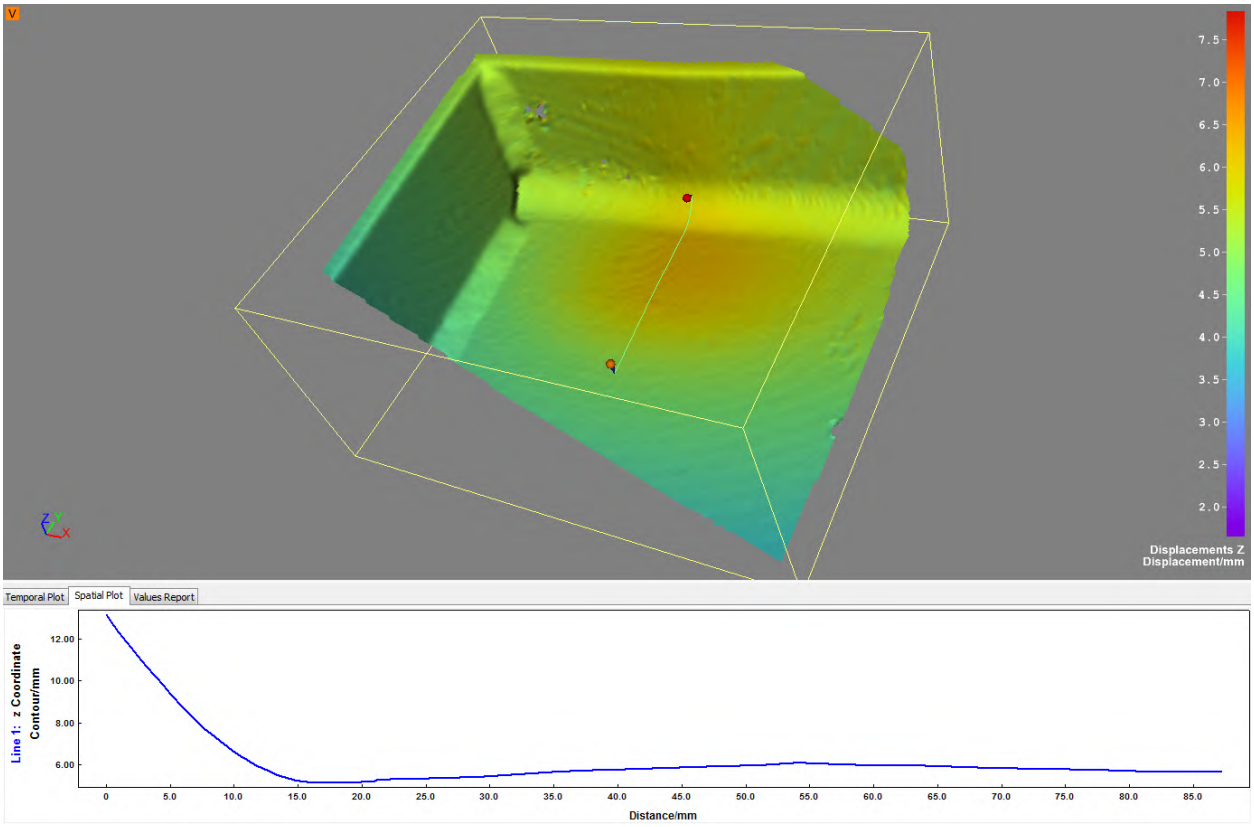

Figure C-15: W10X19-DC-E4 showing out of plane displacement at its maximum load of 84.4 kips

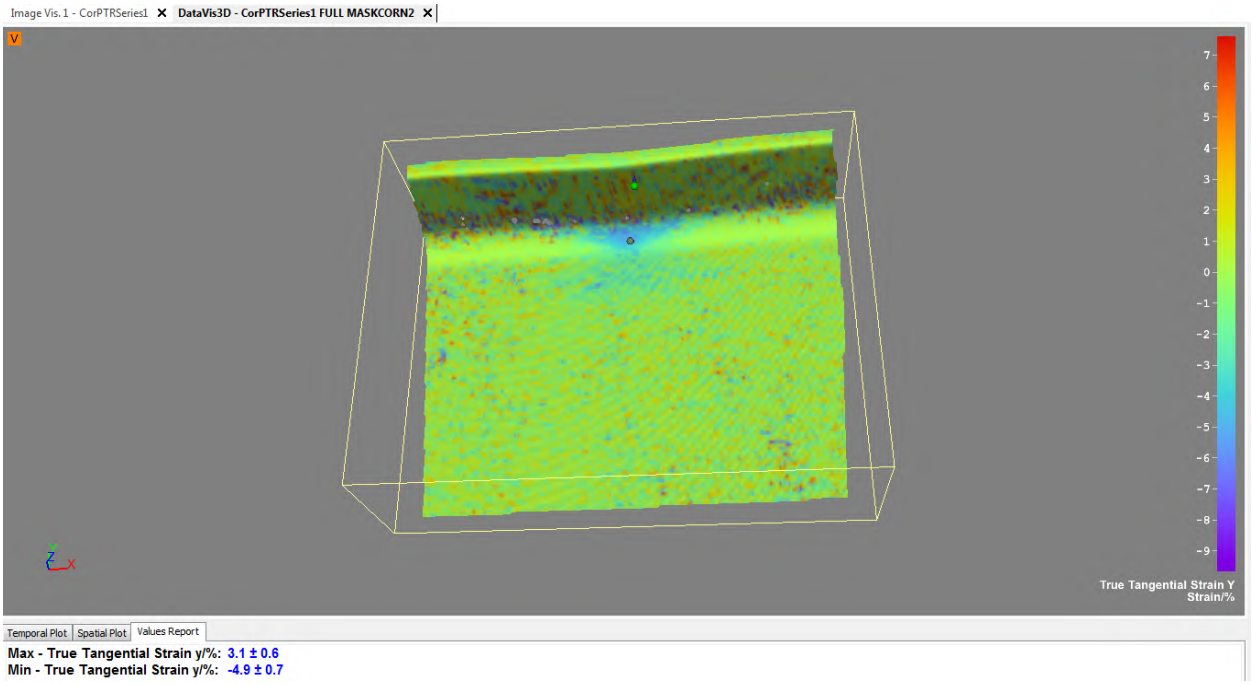

Figure C-16: W10X19-DC-NA showing true tangential strain Y at a load of 63 kips

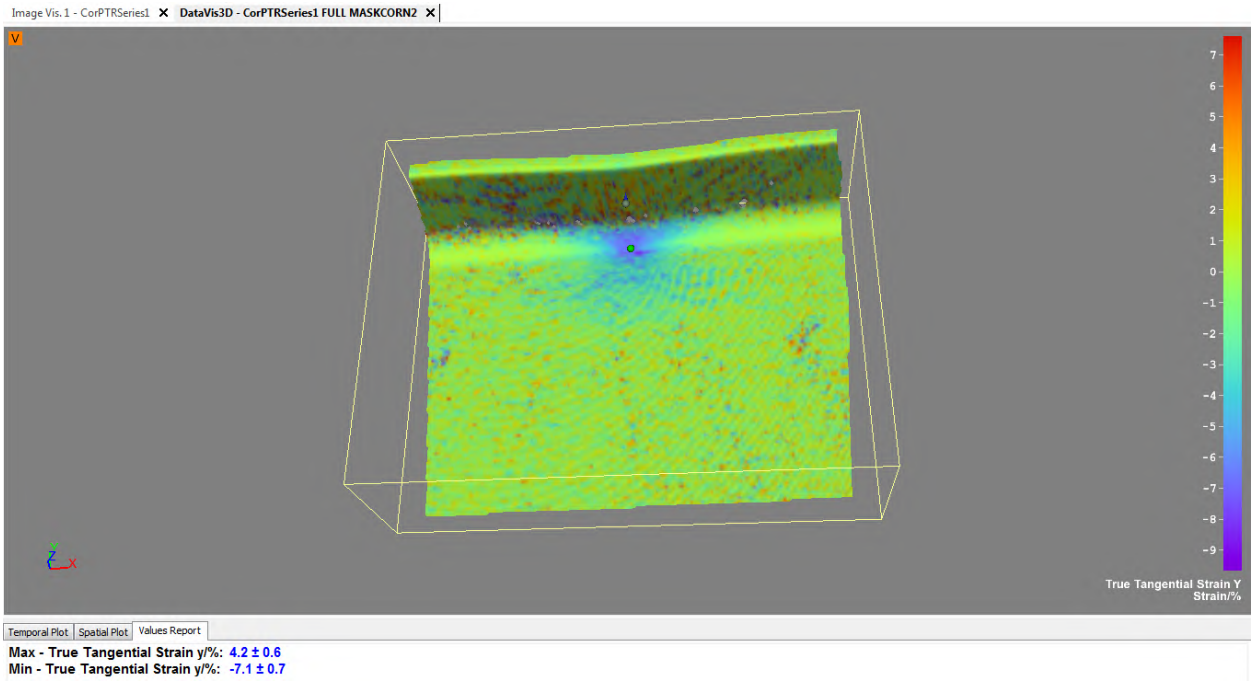

Figure C-17: W10X19-DC-NA showing true tangential strain Y at a load of 71 kips

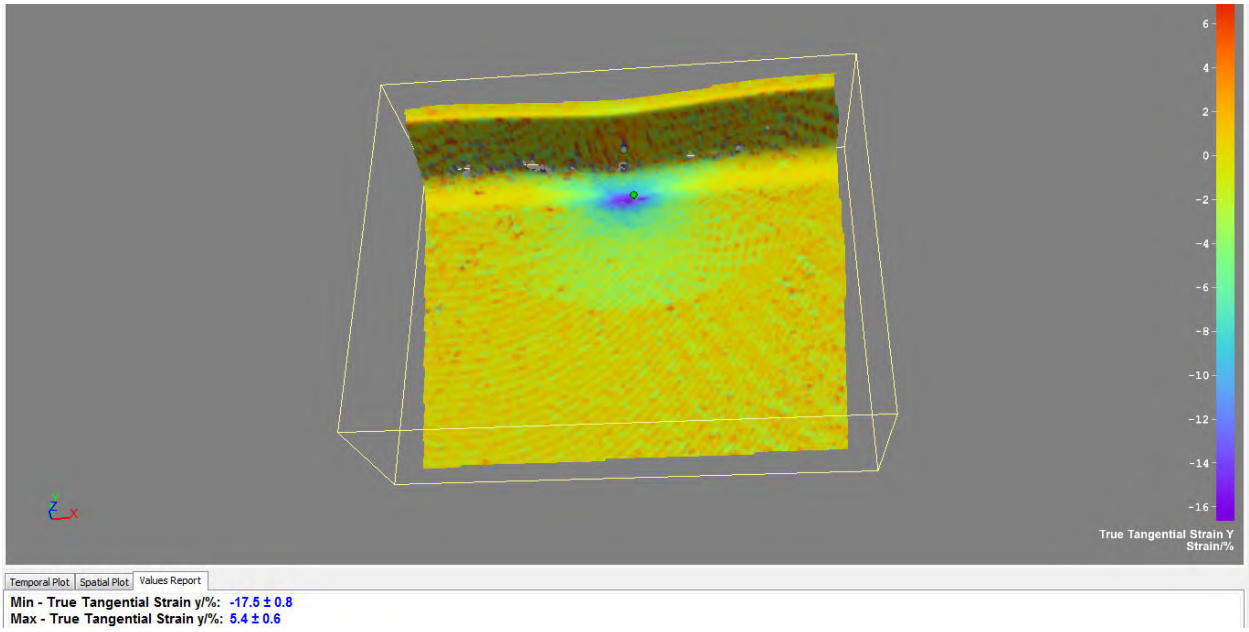

Figure C-18: W10X19-DC-NA showing true tangential strain Y at its maximum load of 78.5 kips

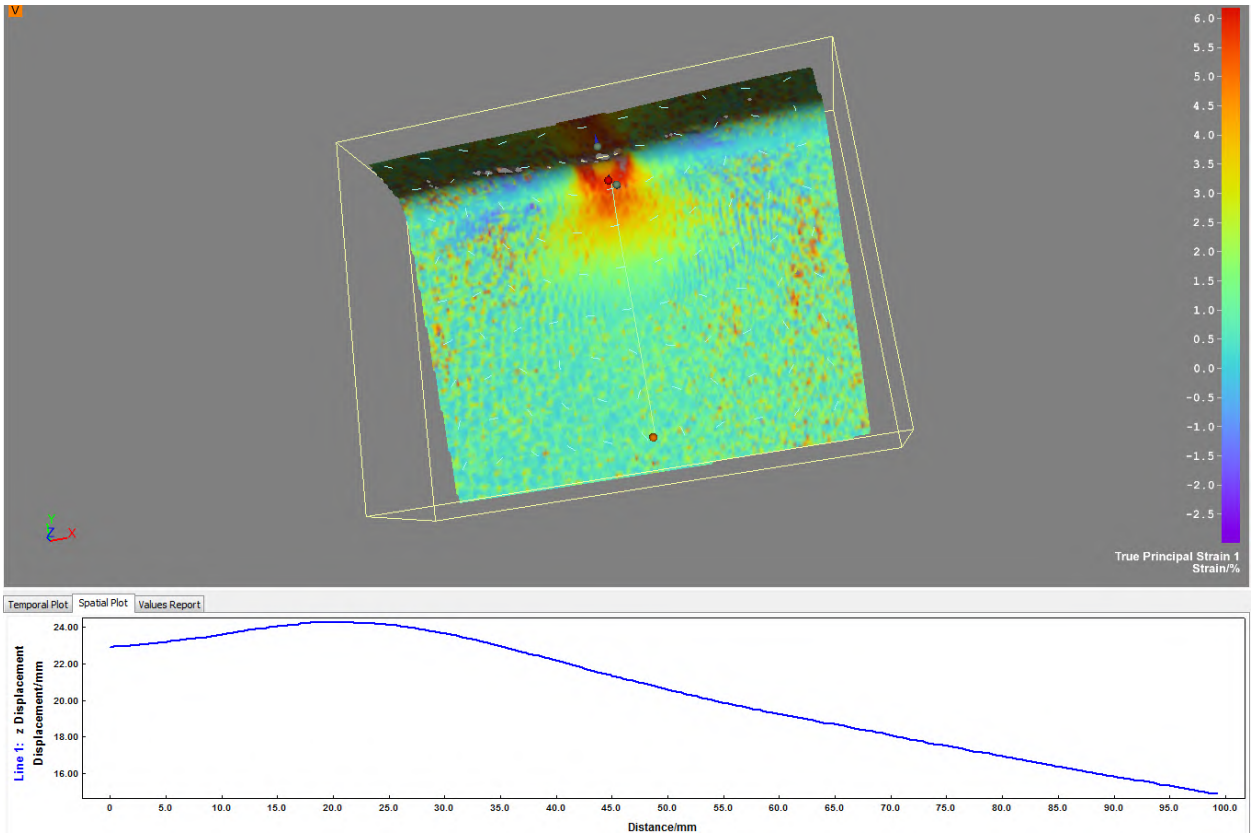

Figure C-19: W10X19-DC-NA showing out of plane displacement at its maximum load of

78.5 kips

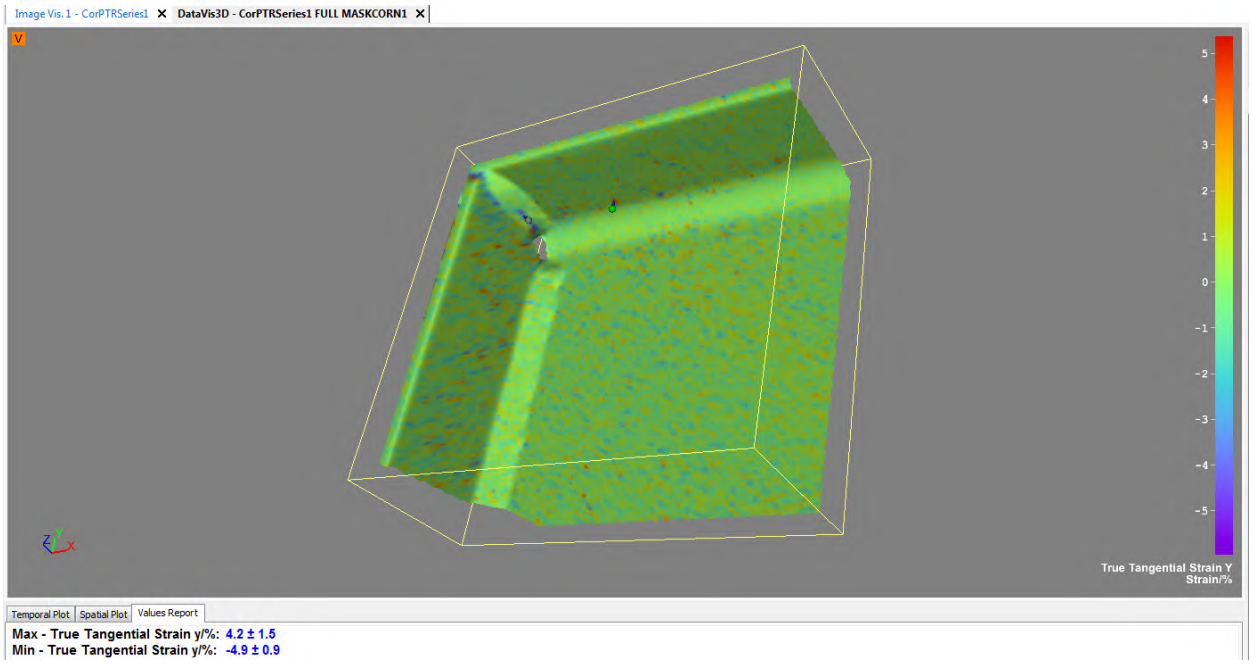

Figure C-20: W10X19-SC-E0 showing true tangential strain Y at a load of 63 kips

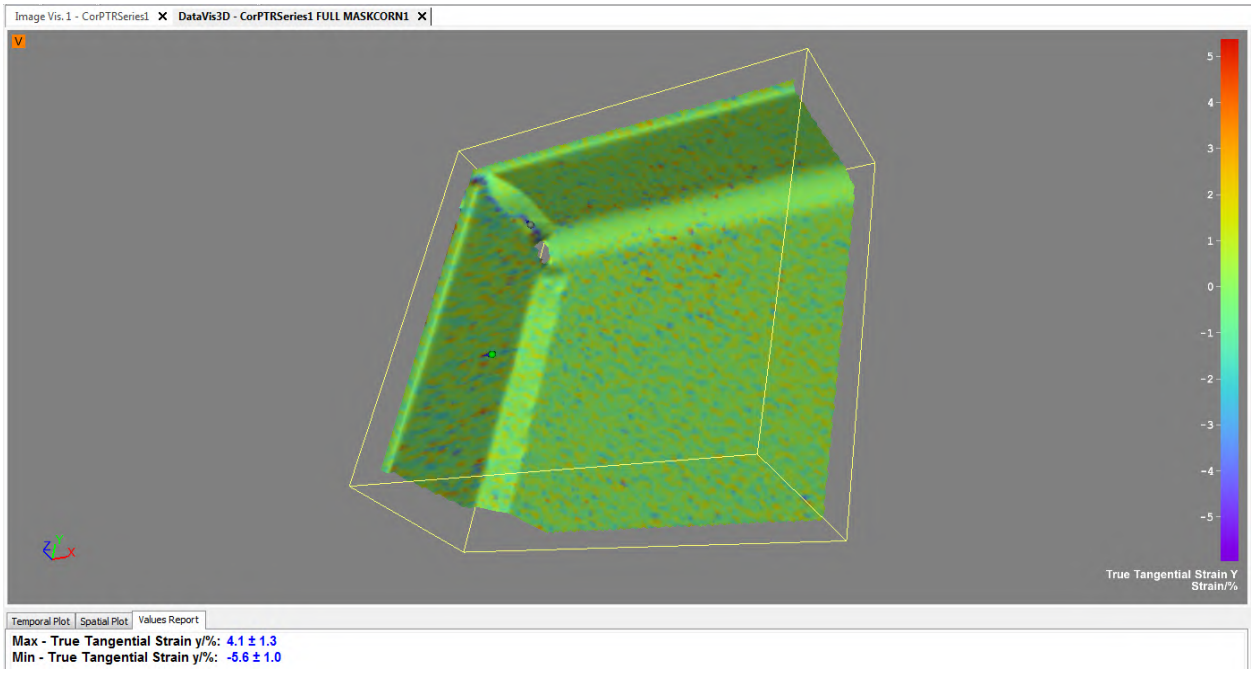

Figure C-21: W10X19-SC-E0 showing true tangential strain Y at a load of 66 kips

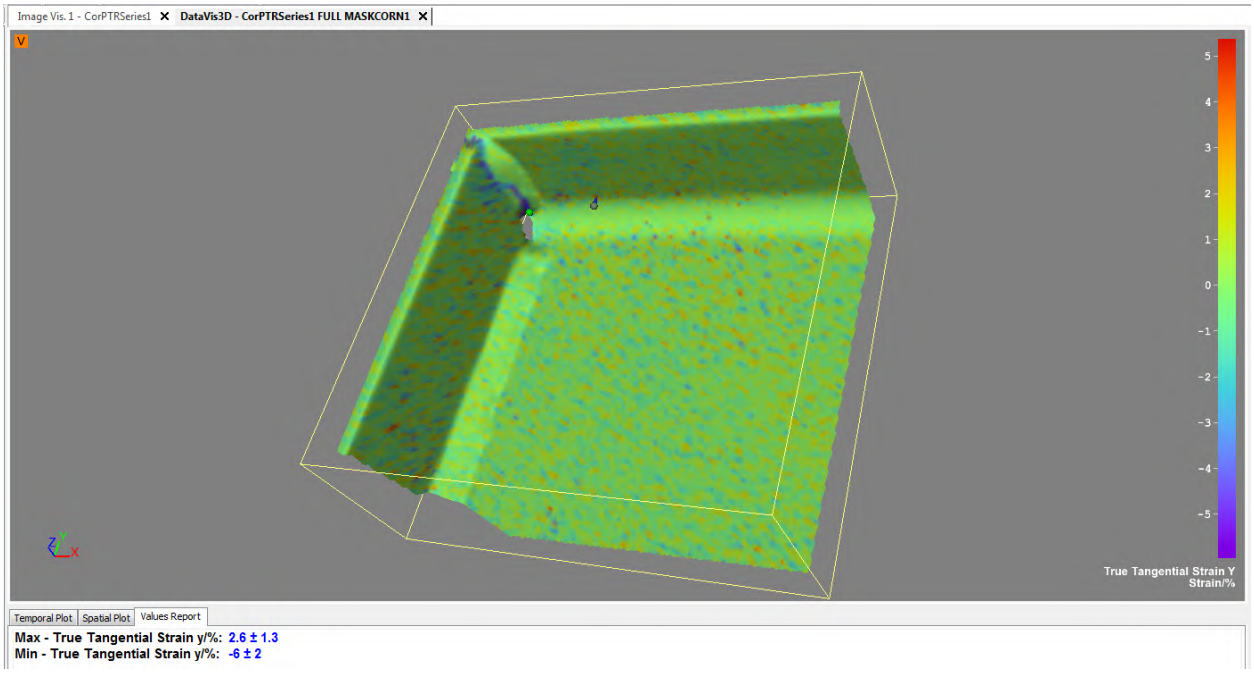

Figure C-22: W10X19-SC-E0 showing true tangential strain Y at a load of 69.6 kips

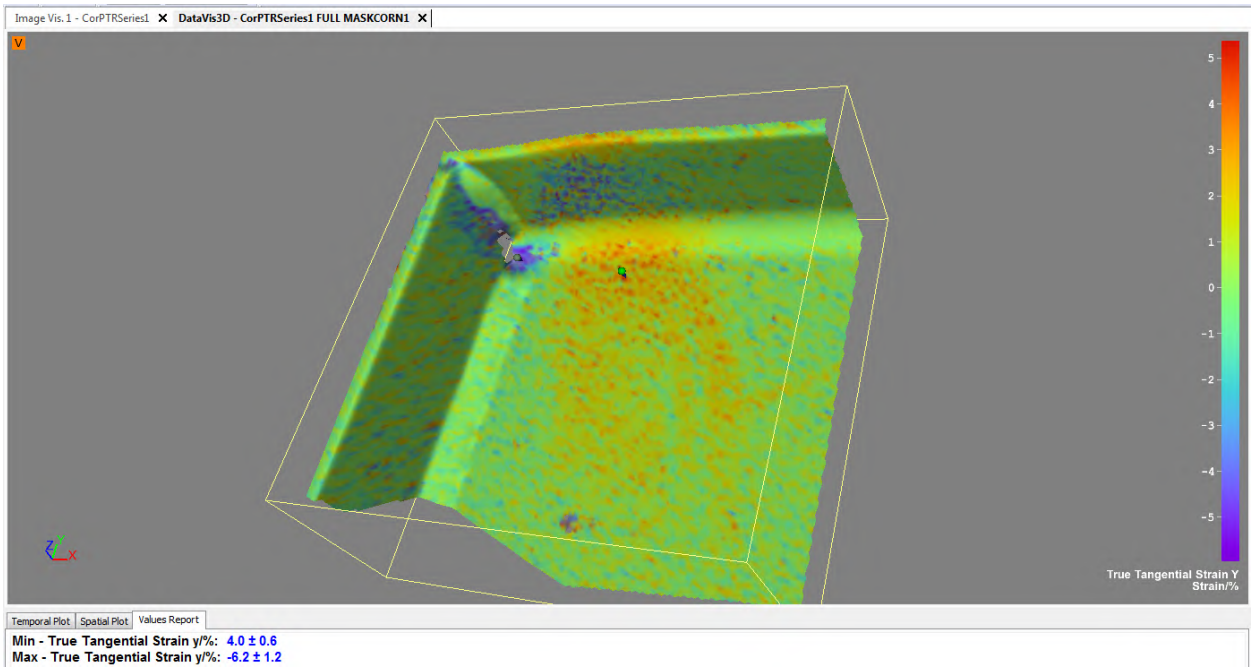

Figure C-23: W10X19-SC-E0 showing true tangential strain Y at its maximum load of 103.3 kips

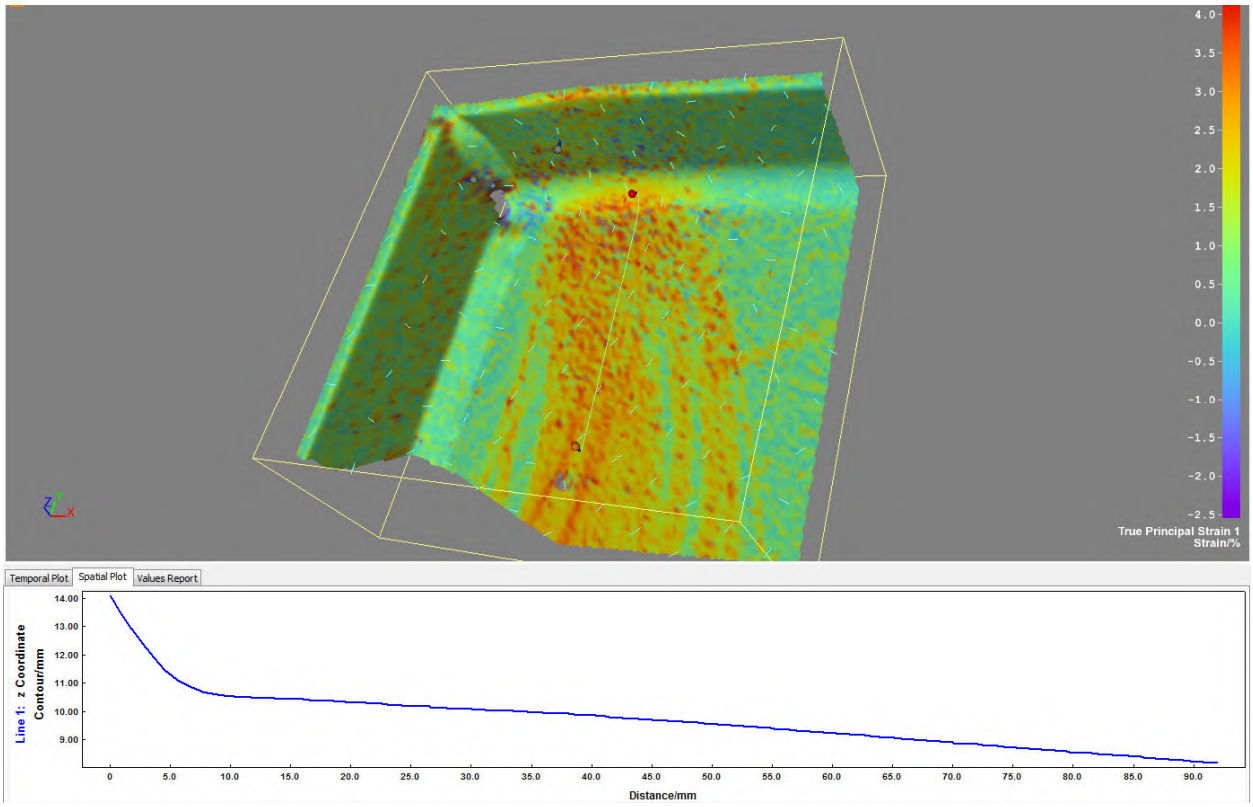

Figure C-24: W10X19-SC-E0 showing out of plane displacement at its maximum load of 103.3 kips

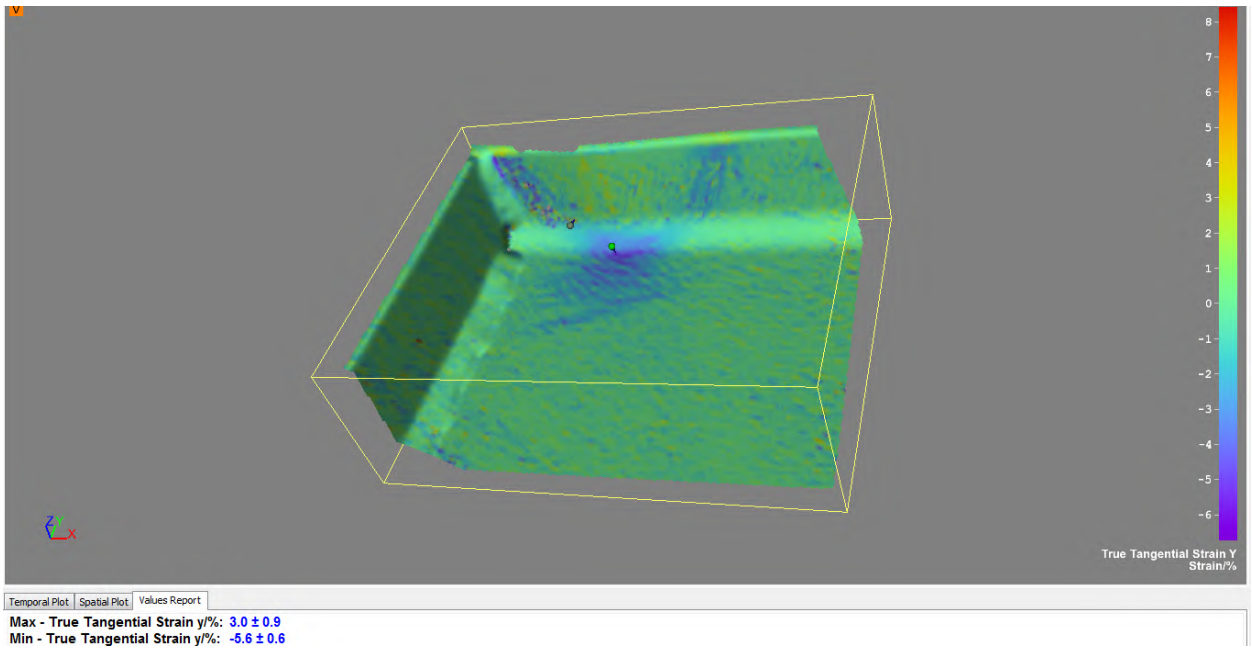

Figure C-25: W10X19-SC-E2 showing true tangential strain Y at a load of 63 kips

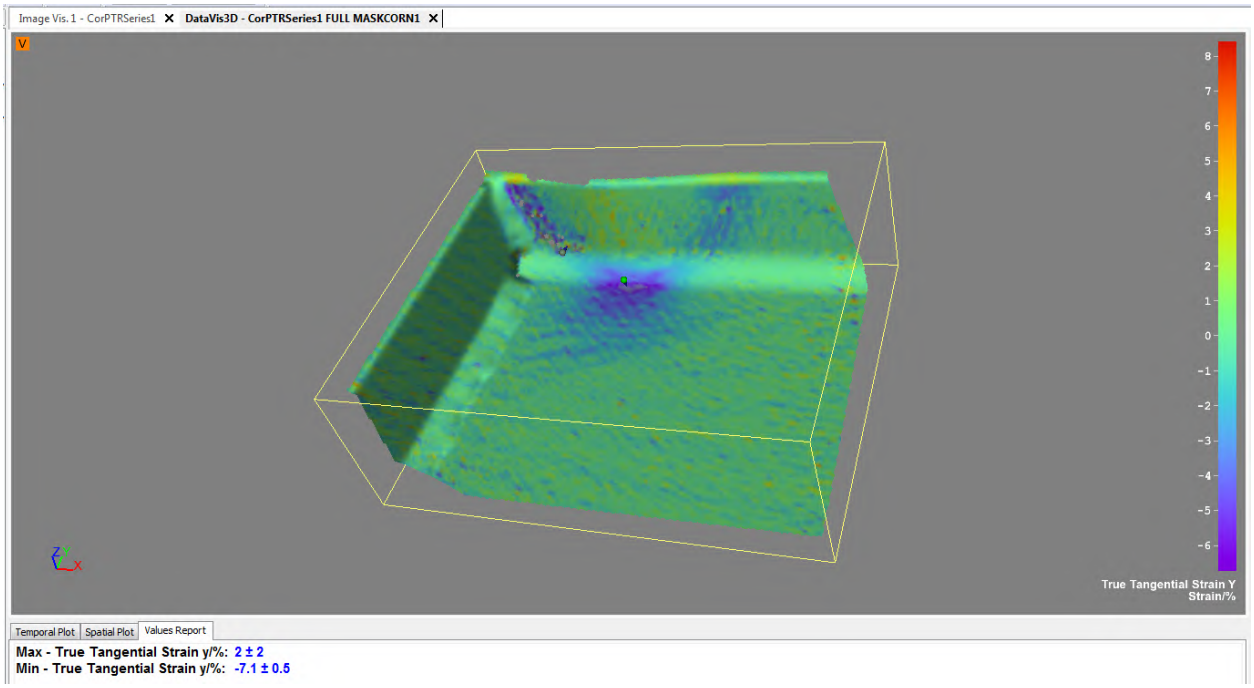

Figure C-26: W10X19-SC-E2 showing true tangential strain Y at a load of 66 kips

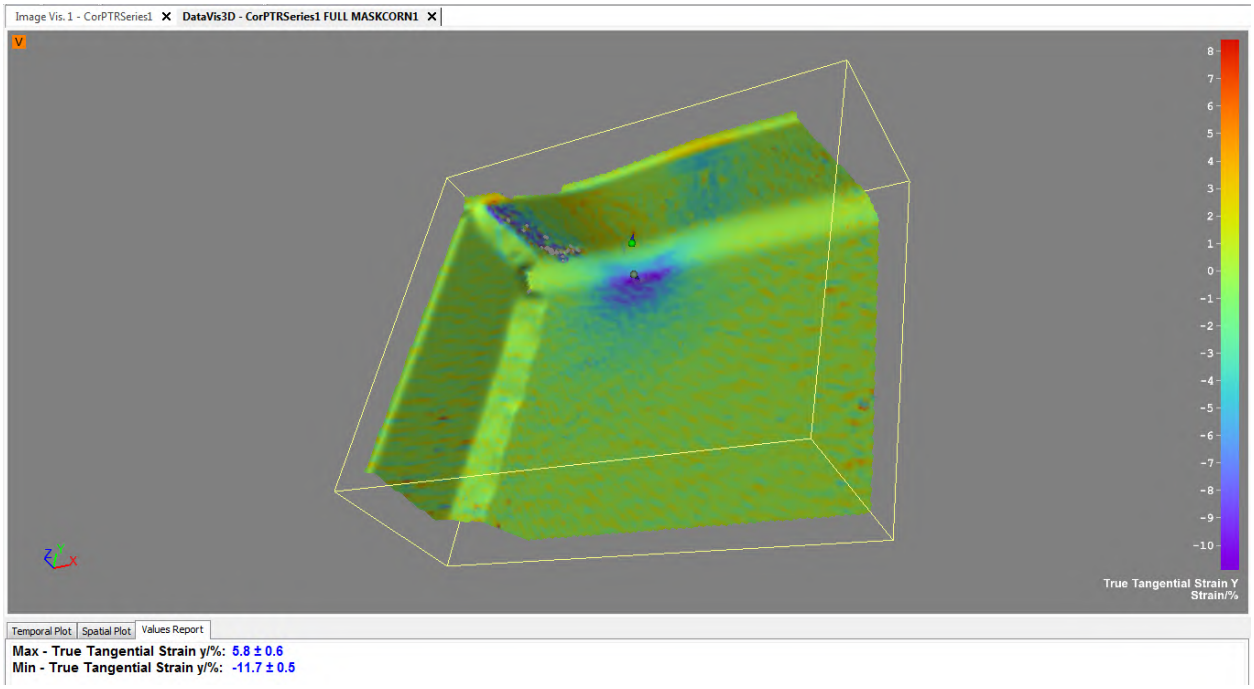

Figure C-27: W10X19-SC-E2 showing true tangential strain Y at a load of 69.6 kips

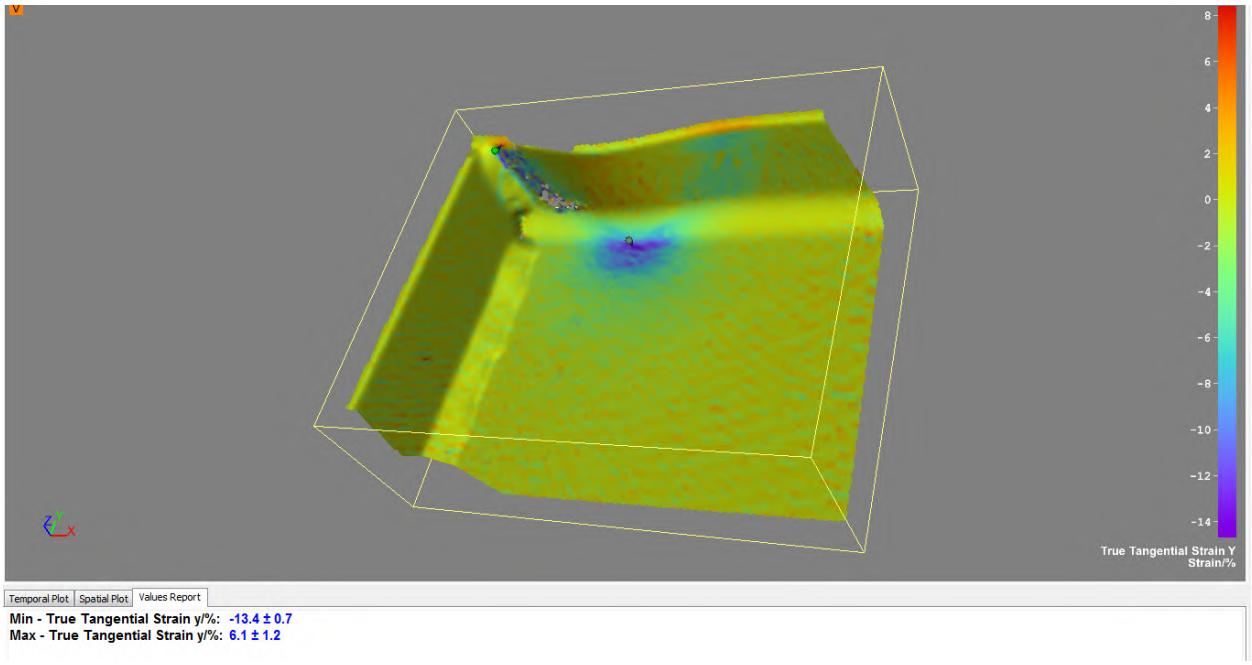

Figure C-28: W10X19-SC-E2 showing true tangential strain Y at its maximum load of 70.6 kips

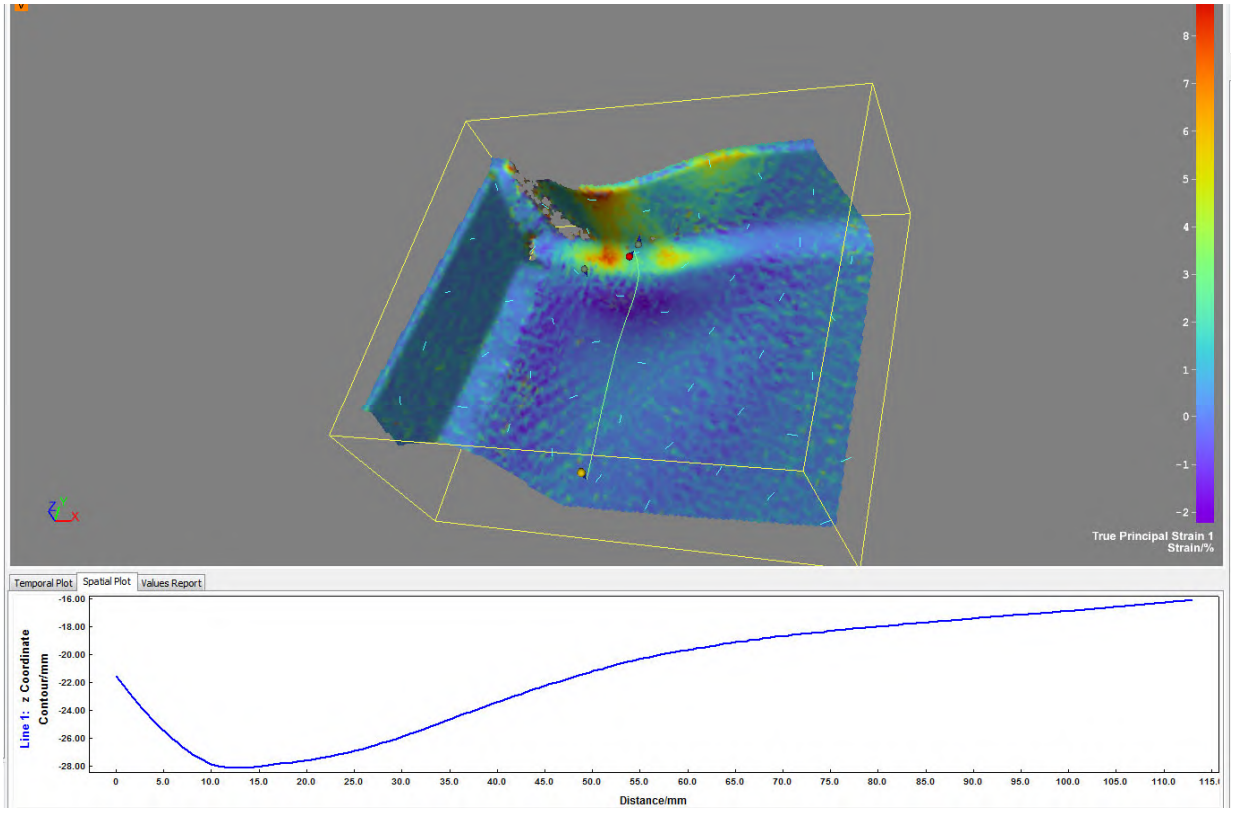

Figure C-29: W10X19-SC-E2 showing out of plane displacement at its maximum load of

70.6 kips

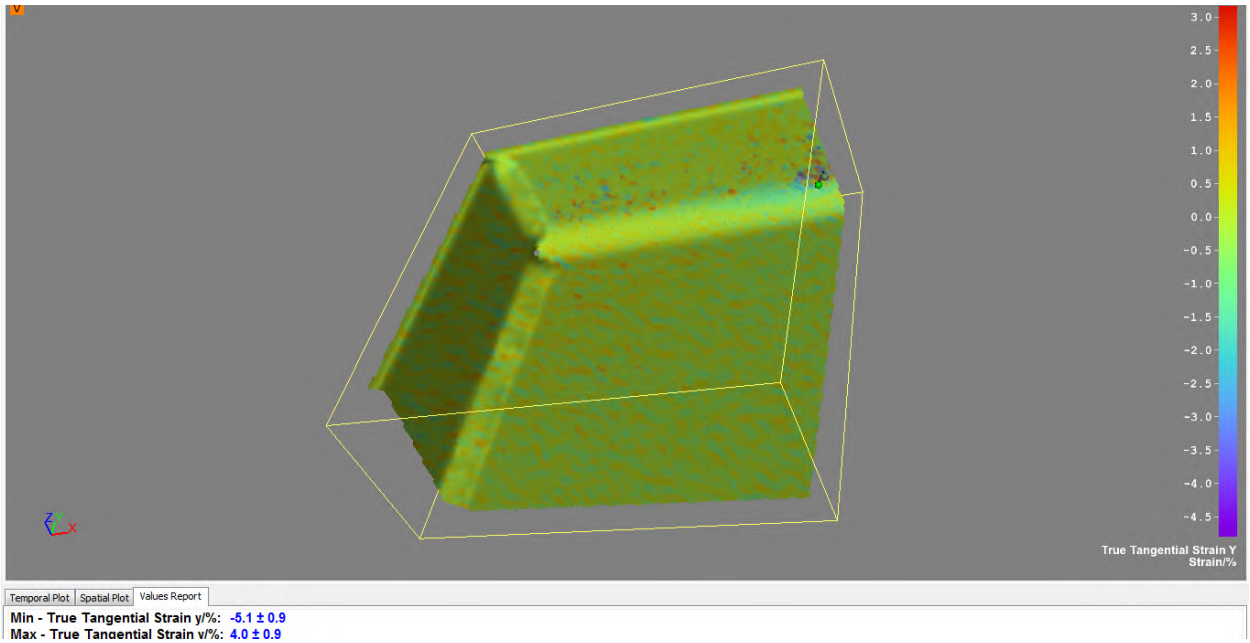

Figure C-30: W10X19-SC-E4 showing true tangential strain Y at a load of 40 kips

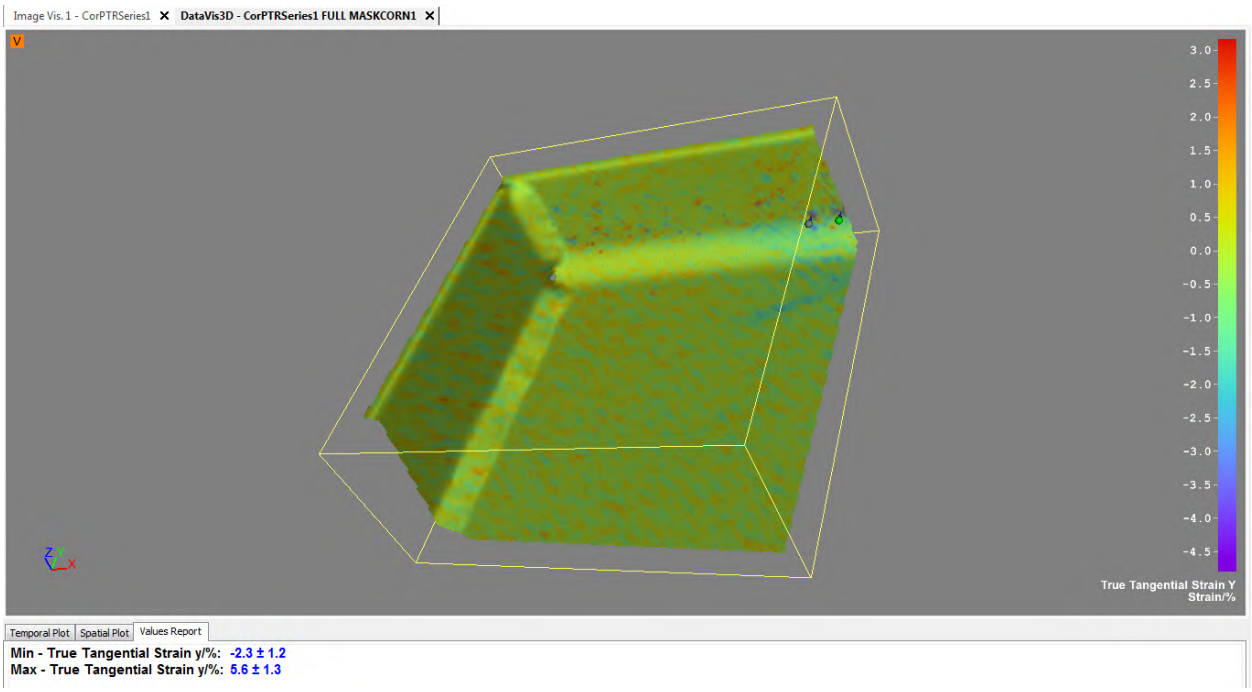

Figure C-31: W10X19-SC-E4 showing true tangential strain Y at a load of 50 kips

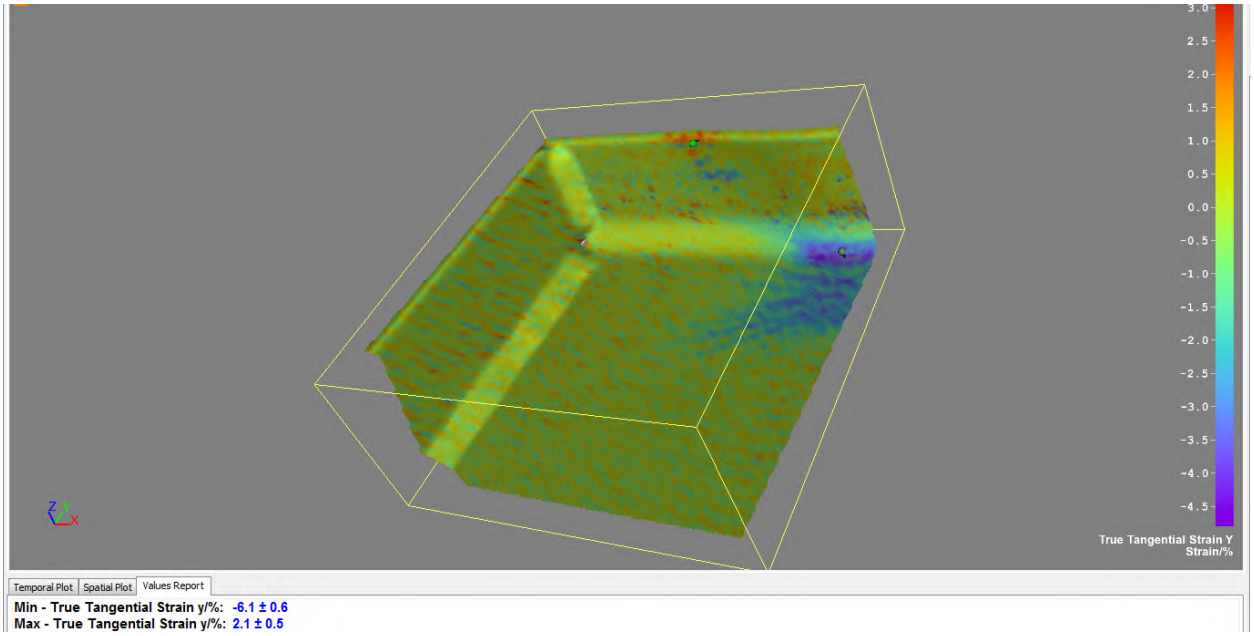

Figure C-32: W10X19-SC-E4 showing true tangential strain Y at its maximum load of 57.4 kips

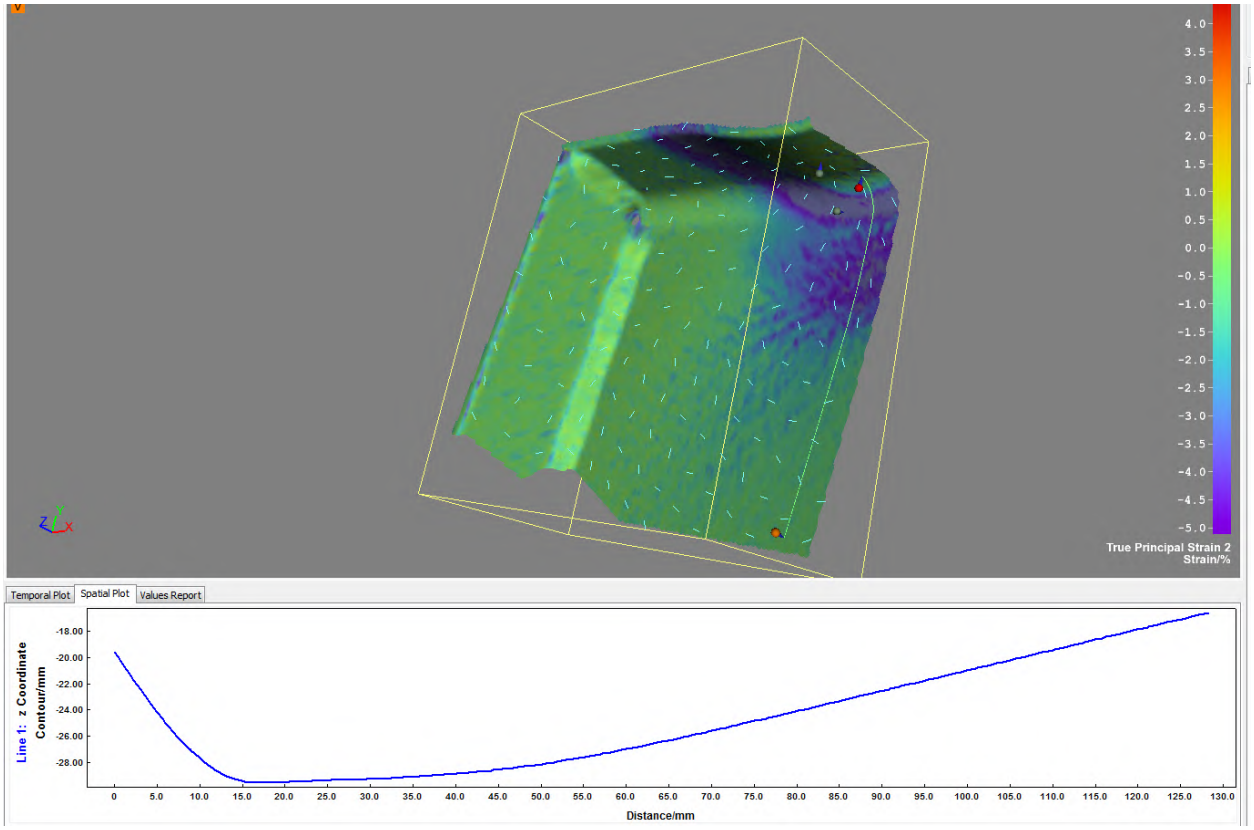

Figure C-33: W10X19-SC-E4 showing out of plane displacement at its maximum load of

57.4 kips

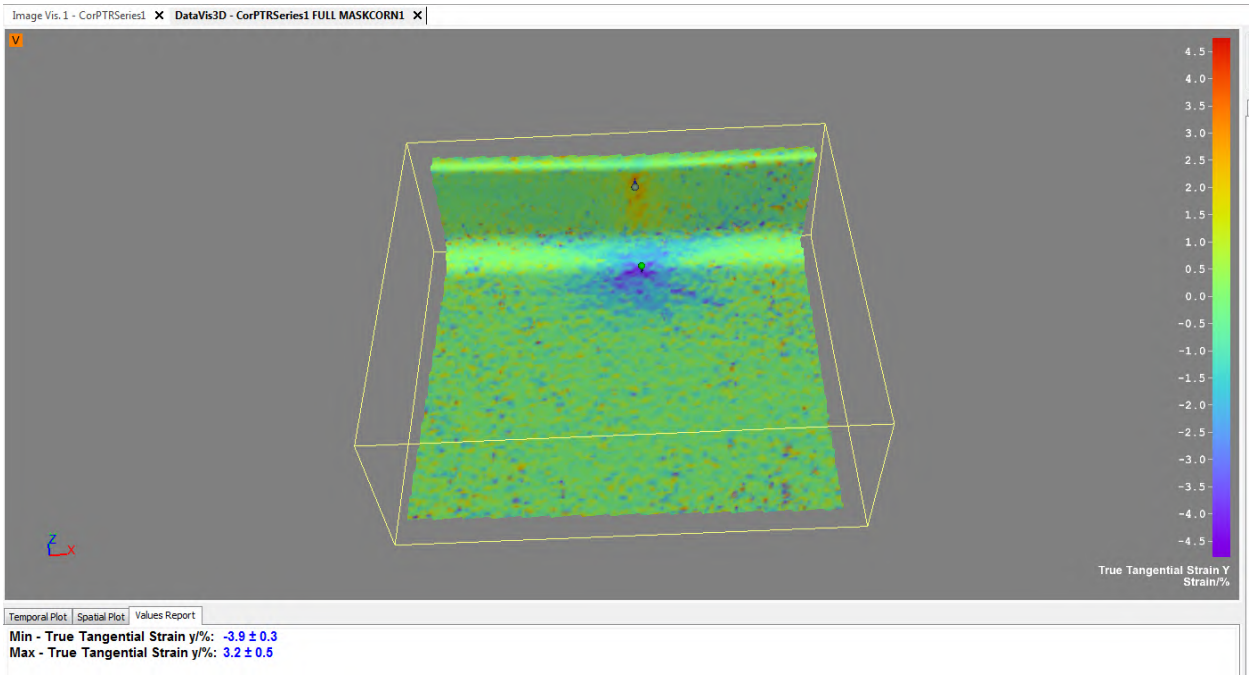

Figure C-34: W10X19-SC-NA showing true tangential strain Y at a load of 63 kips

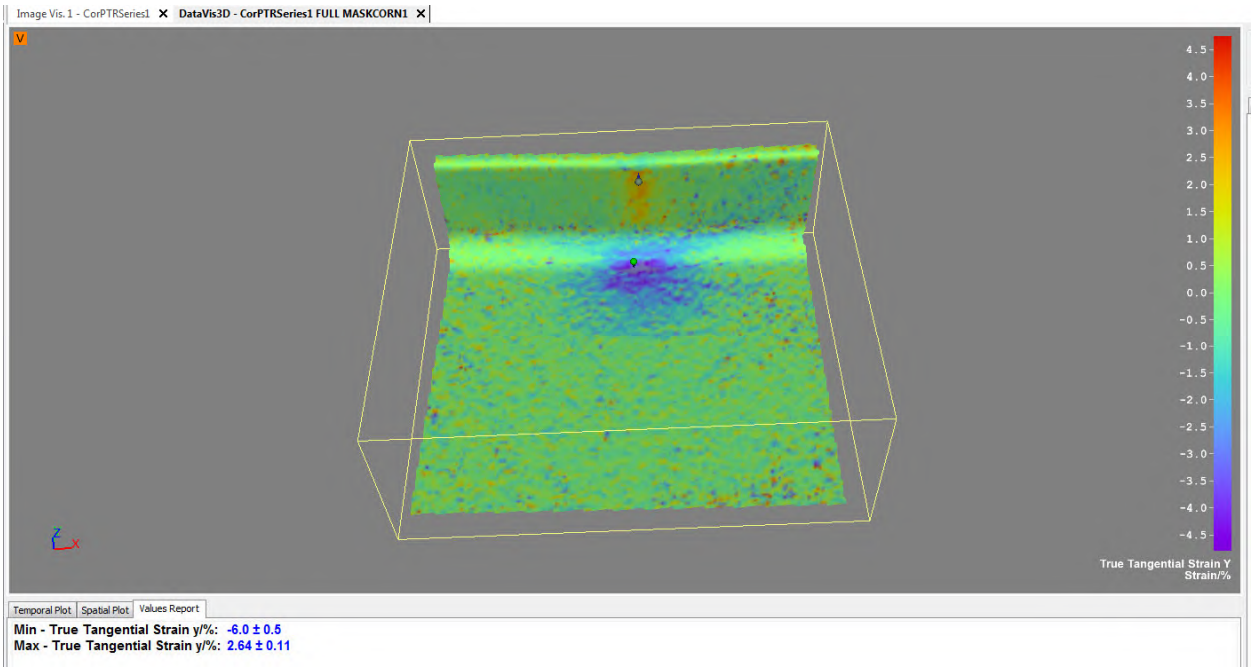

Figure C-35: W10X19-SC-NA showing true tangential strain Y at a load of 66 kips

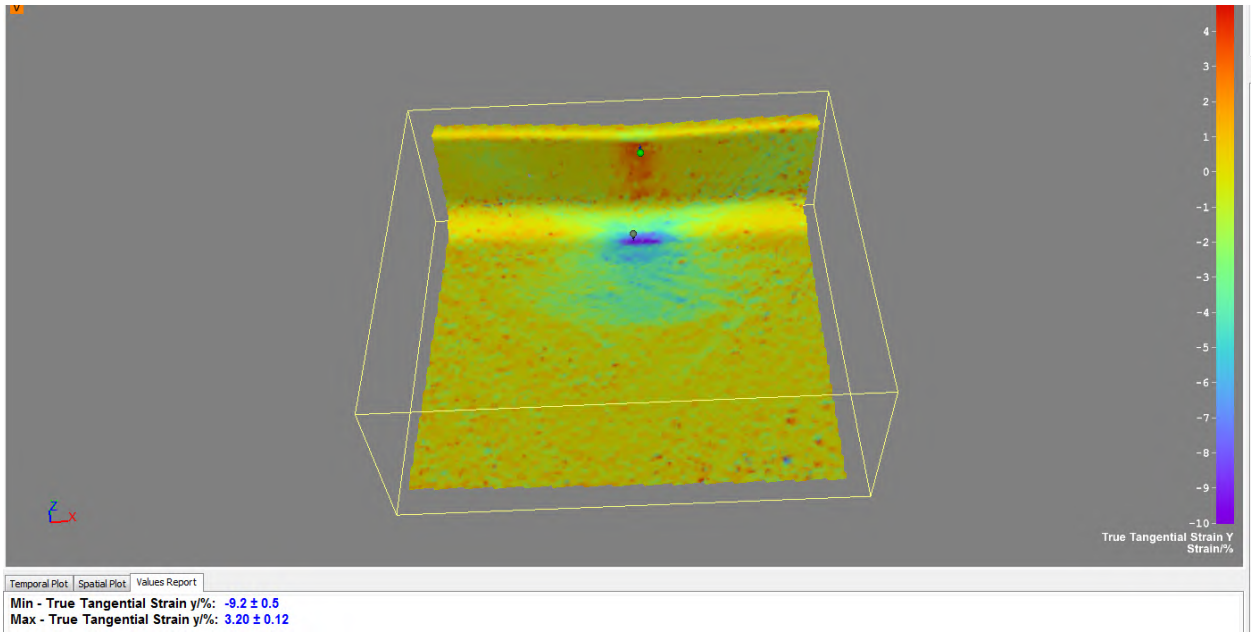

Figure C-36: W10X19-SC-NA showing true tangential strain Y at its maximum load of 69.6 kips

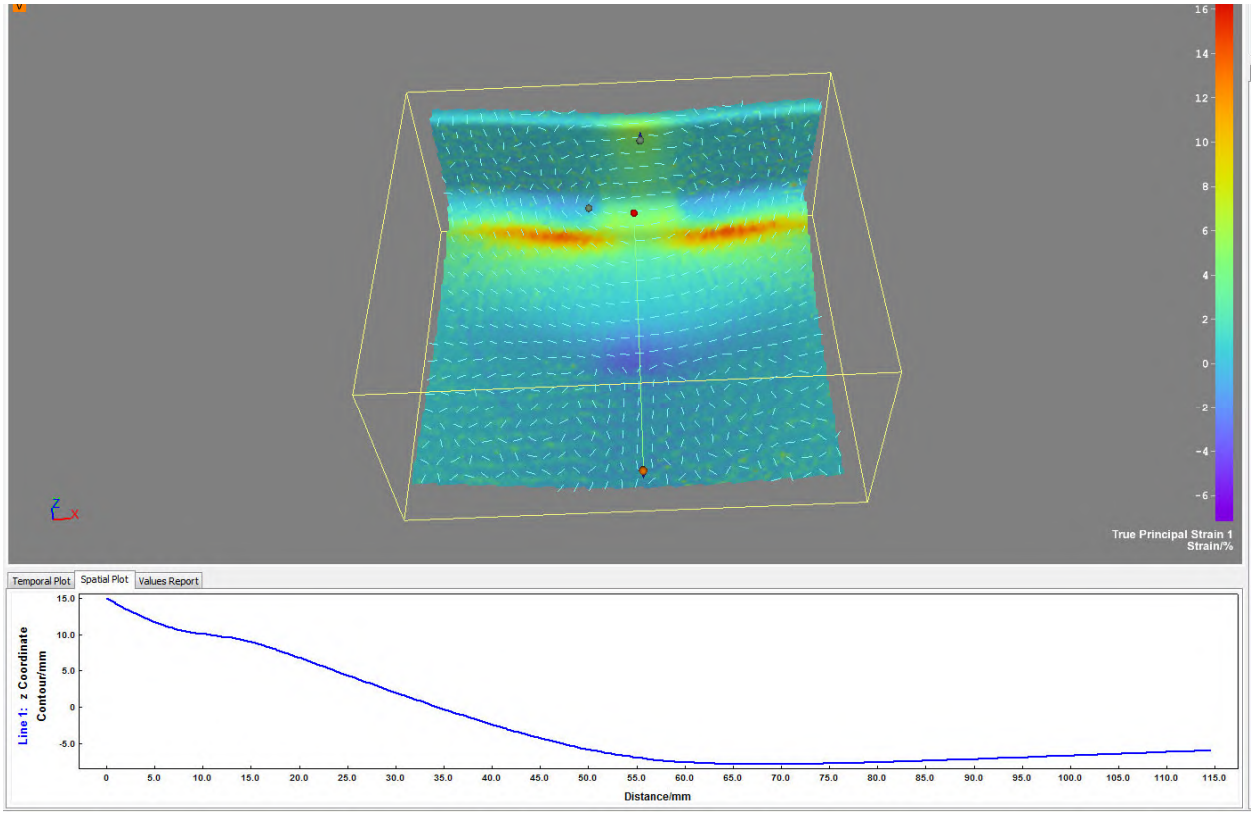

Figure C-37: W10X19-SC-NA showing out of plane displacement at its maximum load of 69.6 kips

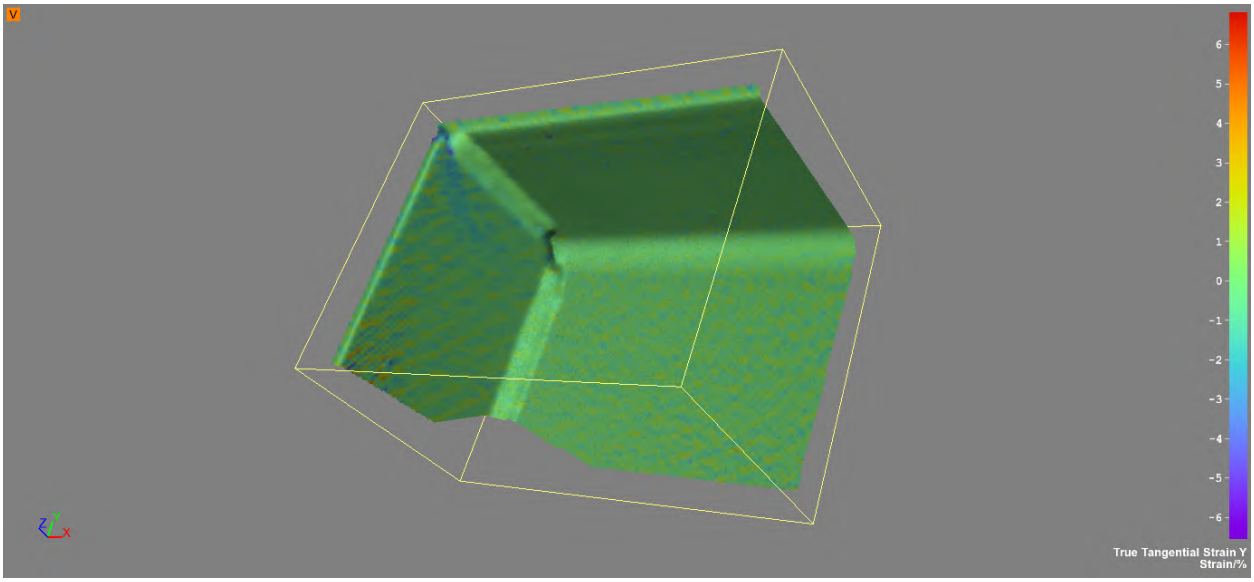

Figure C-38: W10X39-SC-E0 showing true tangential strain Y at a load of 111 kips

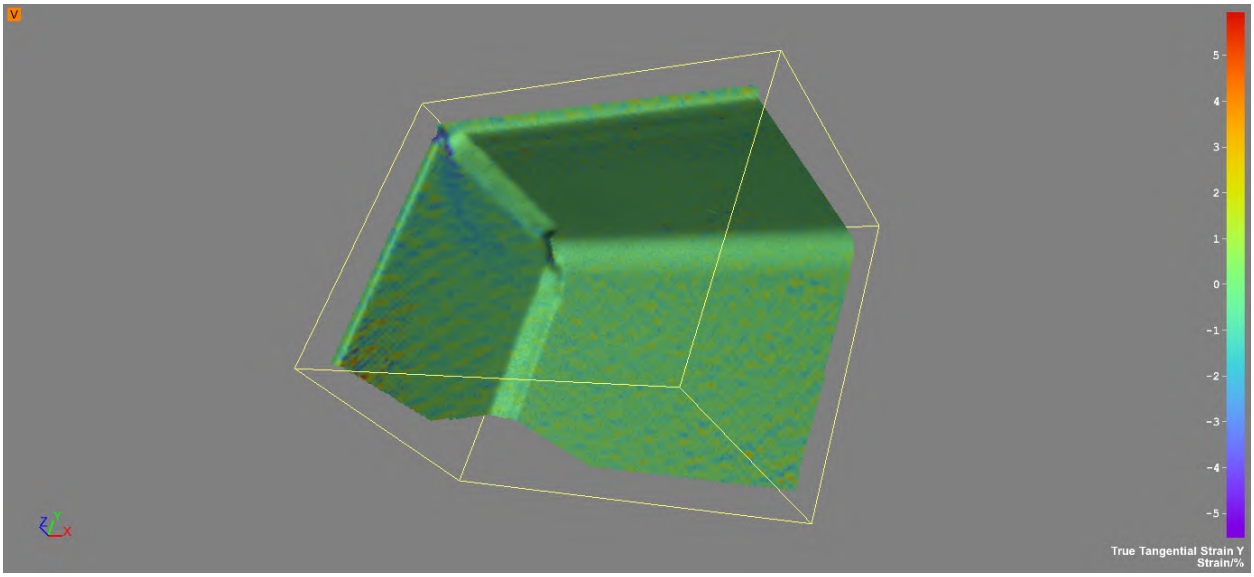

Figure C-39: W10X39-SC-E0 showing true tangential strain Y at a load of 121 kips

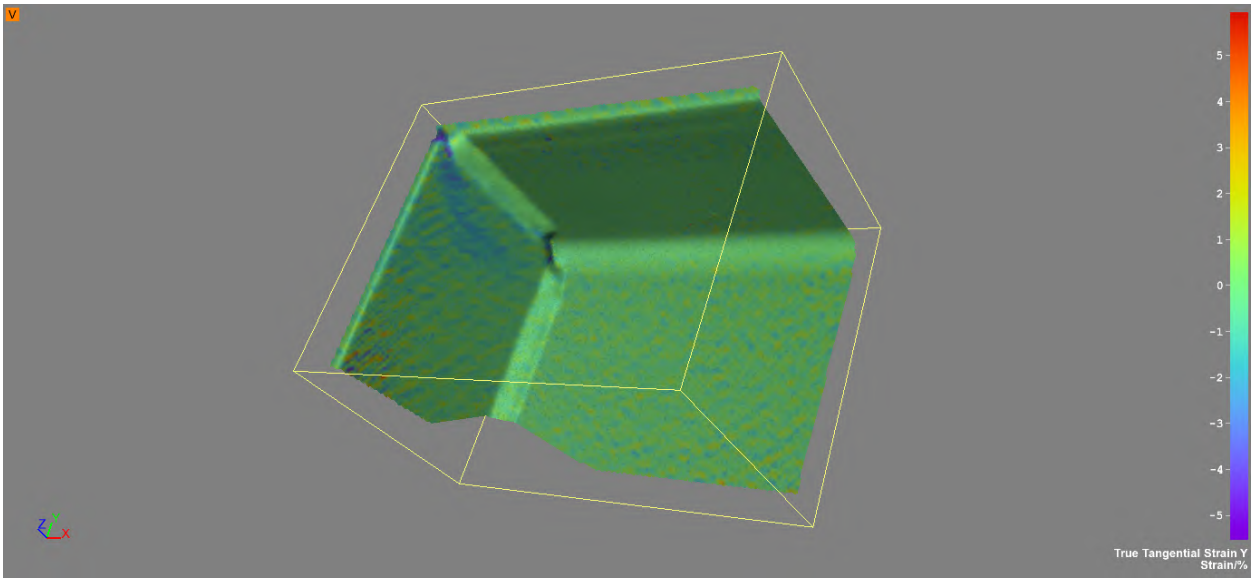

Figure C-40: W10X39-SC-E0 showing true tangential strain Y at a load of 131 kips

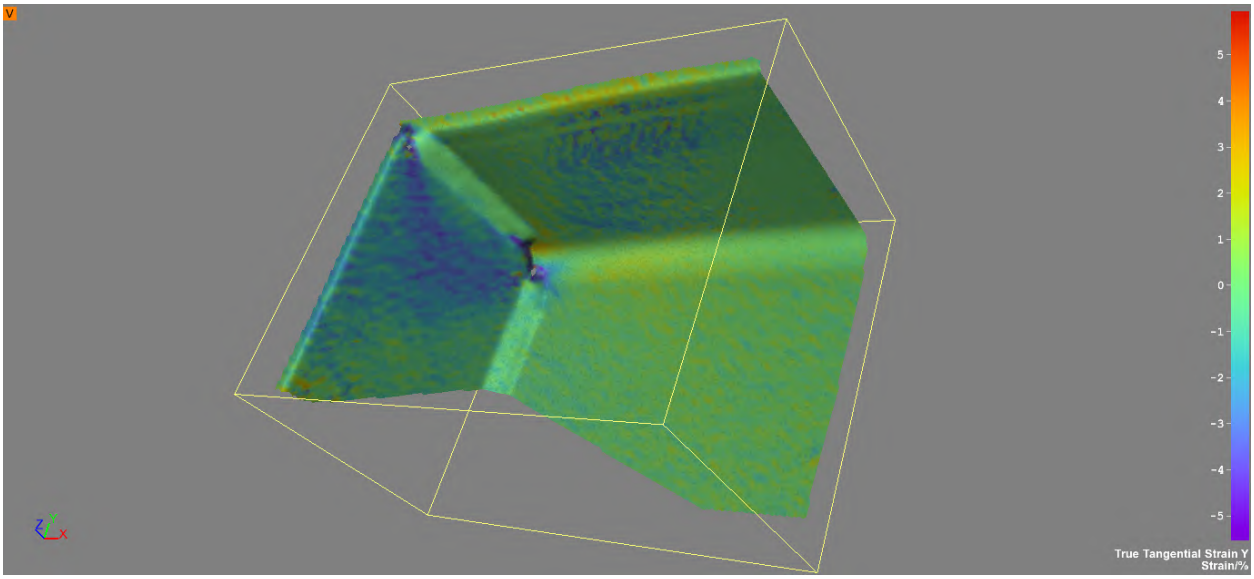

Figure C-41: W10X39-SC-E0 showing true tangential strain Y at its maximum load of 198.1 kips

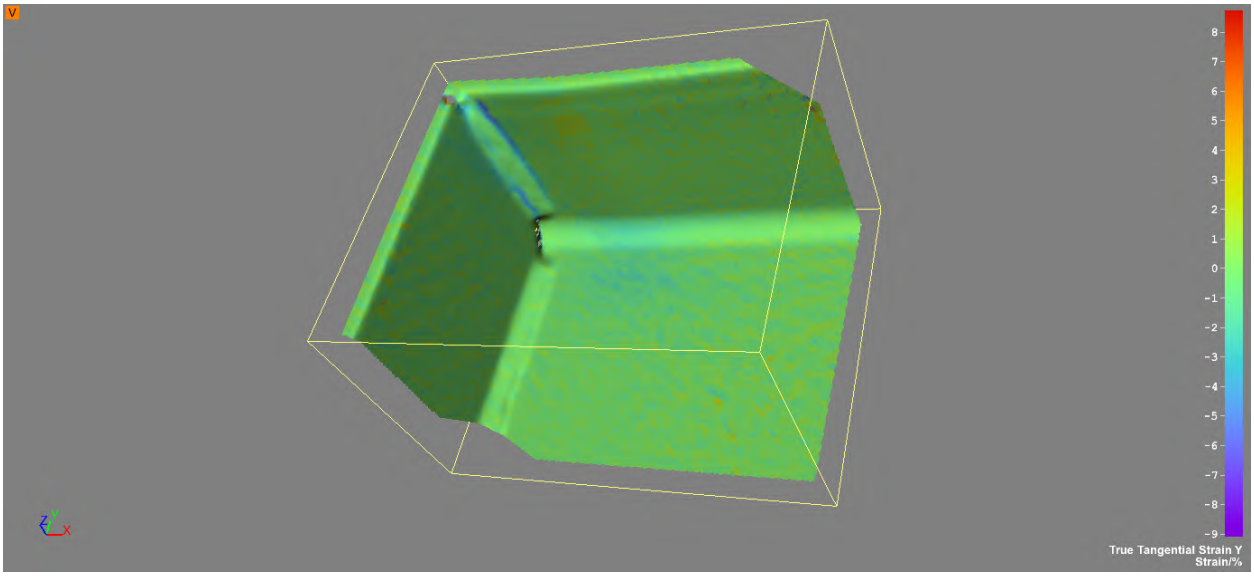

Figure C-42: W10X39-SC-E2 showing true tangential strain Y at a load of 111 kips

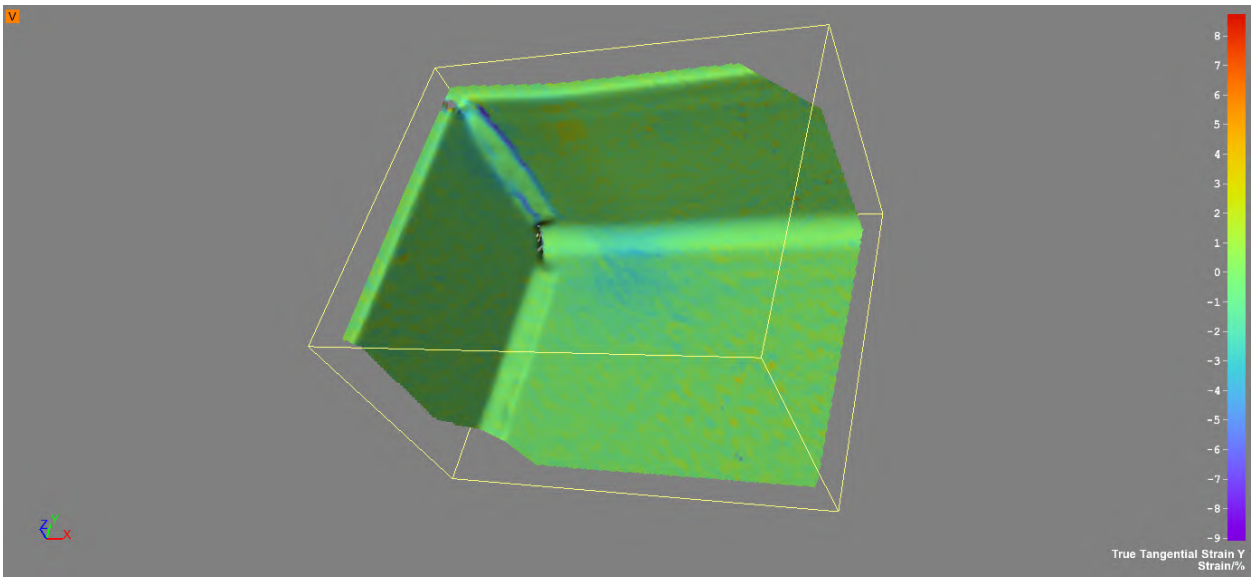

Figure C-43: W10X39-SC-E2 showing true tangential strain Y at a load of 121 kips

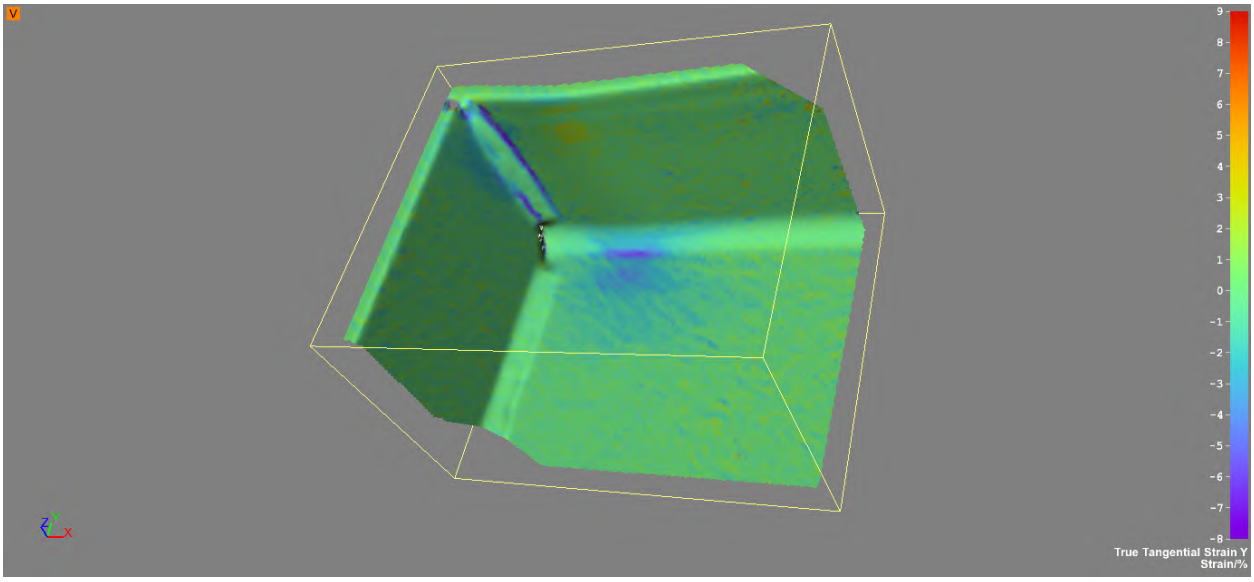

Figure C-44: W10X39-SC-E2 showing true tangential strain Y at a load of 131 kips

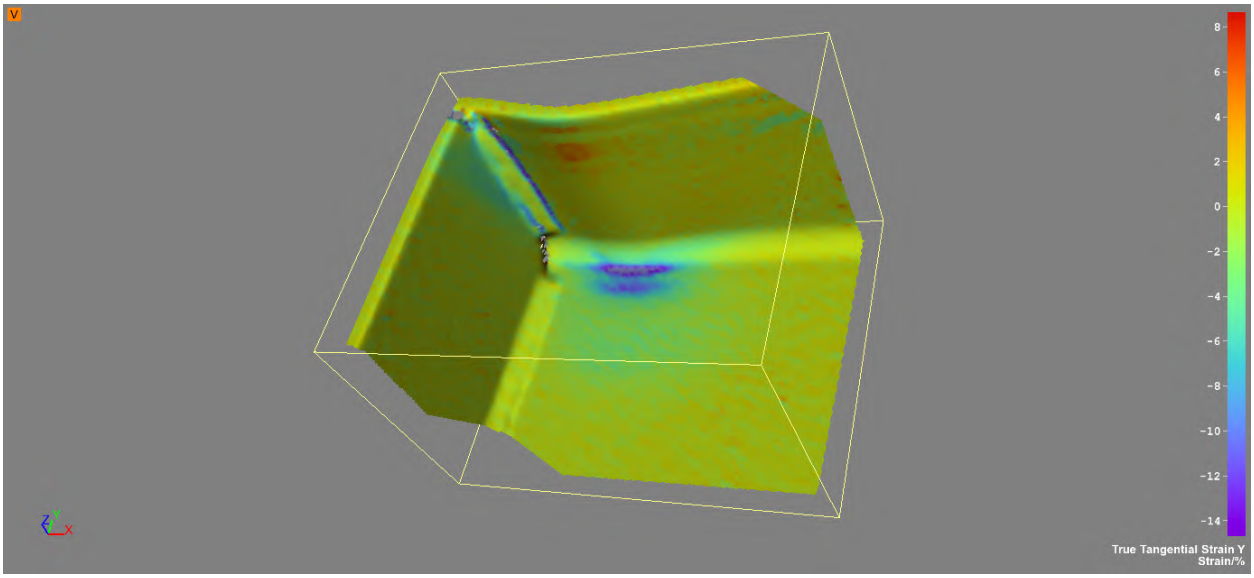

Figure C-45: W10X39-SC-E2 showing true tangential strain Y at its maximum load of 142.3 kips

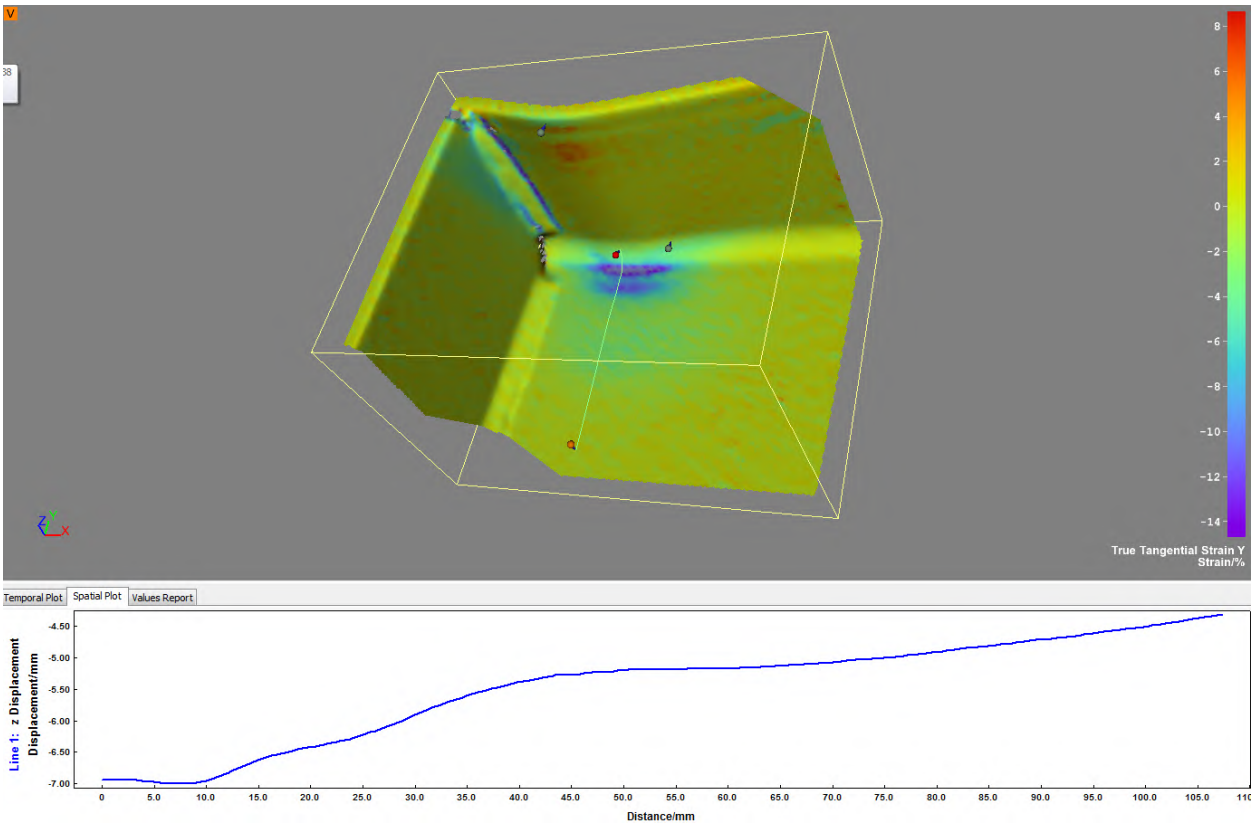

Figure C-46: W10X39-SC-E2 showing out of plane displacement at its maximum load of 142.3 kips

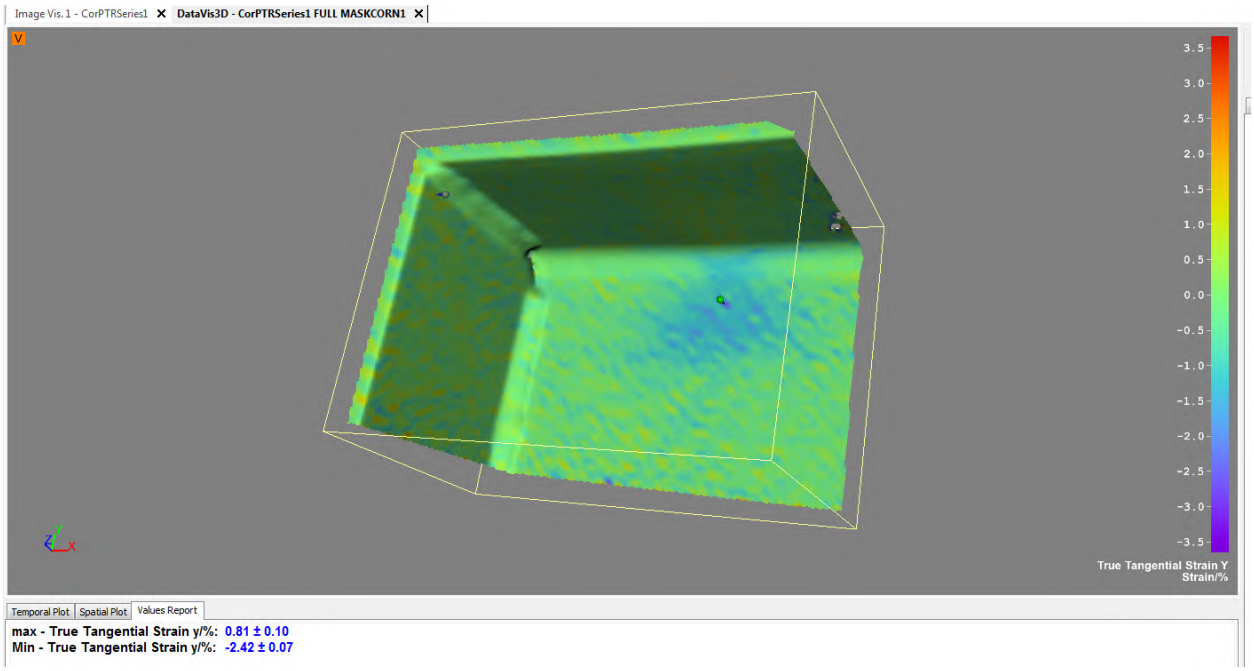

Figure C-47: W10X39-SC-E4 showing true tangential strain Y at a load of 111 kips

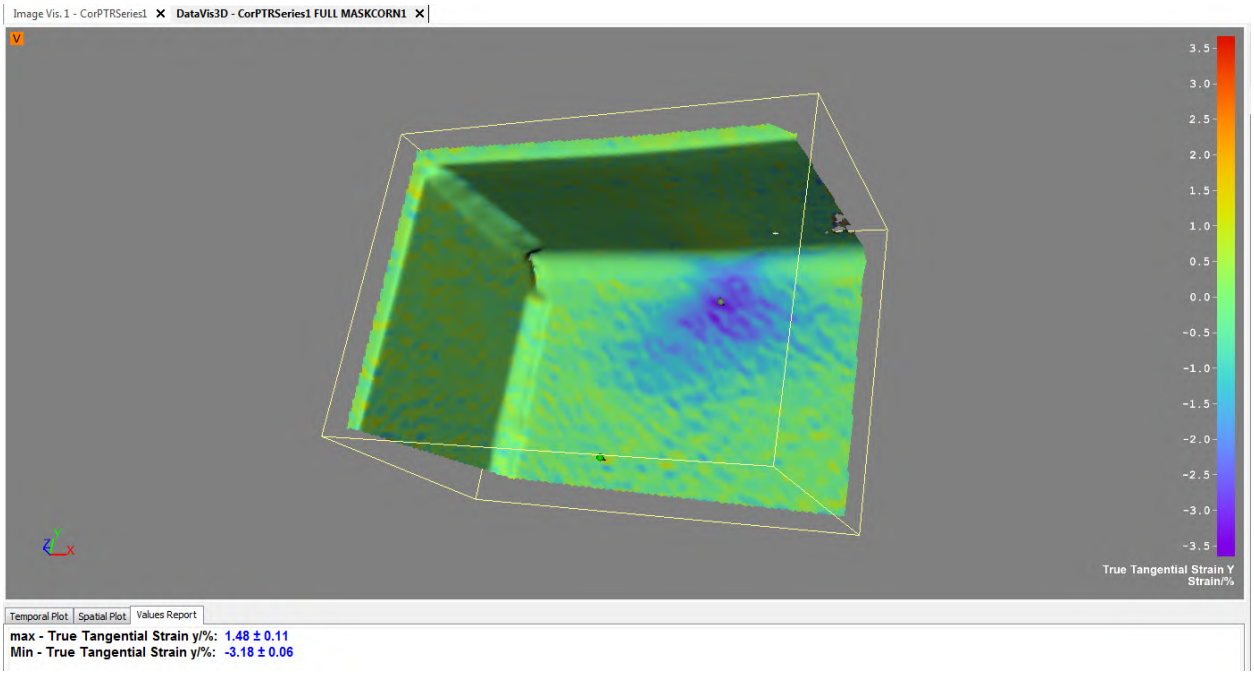

Figure C-48: W10X39-SC-E4 showing true tangential strain Y at a load of 121 kips

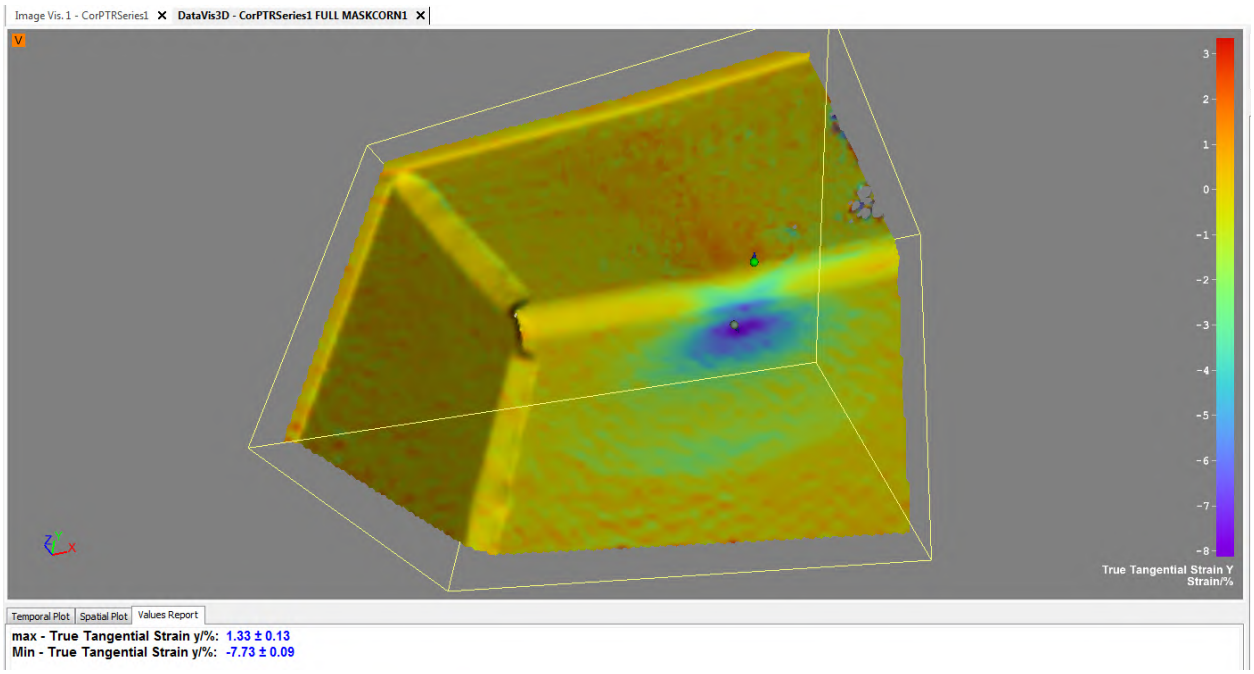

Figure C-49: W10X39-SC-E4 showing true tangential strain Y at a load of 131 kips

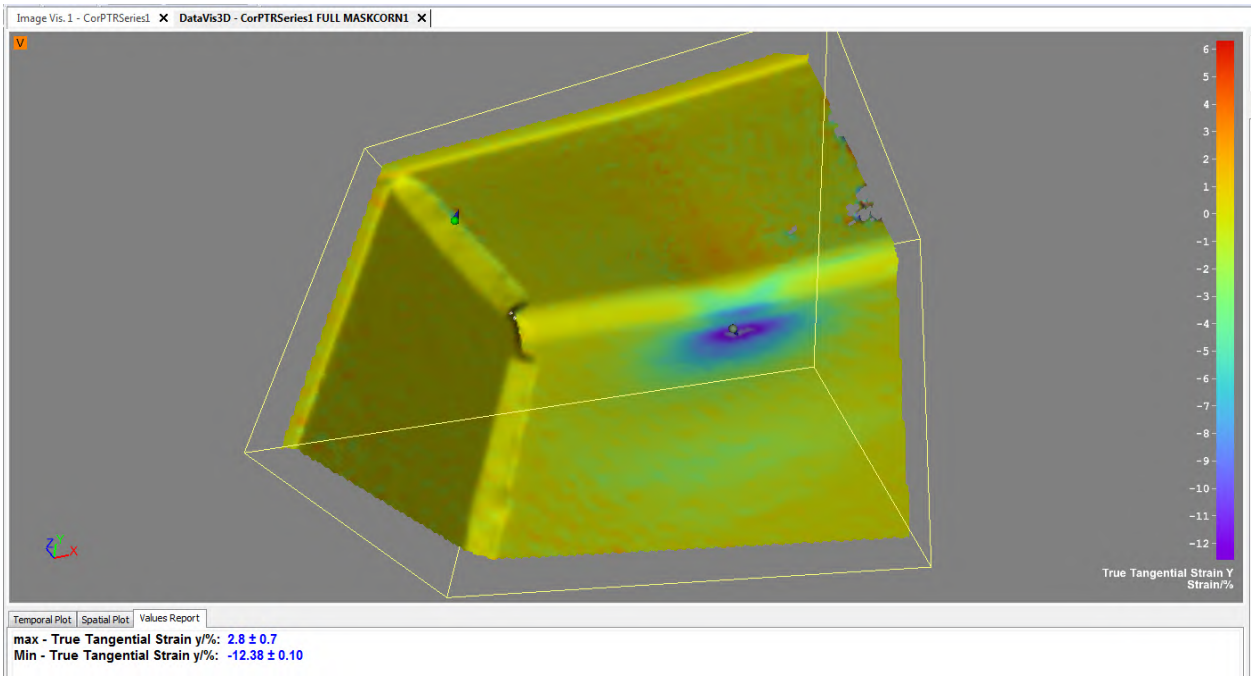

Figure C-50: W10X39-SC-E4 showing true tangential strain Y at its maximum load of 132.9 kips

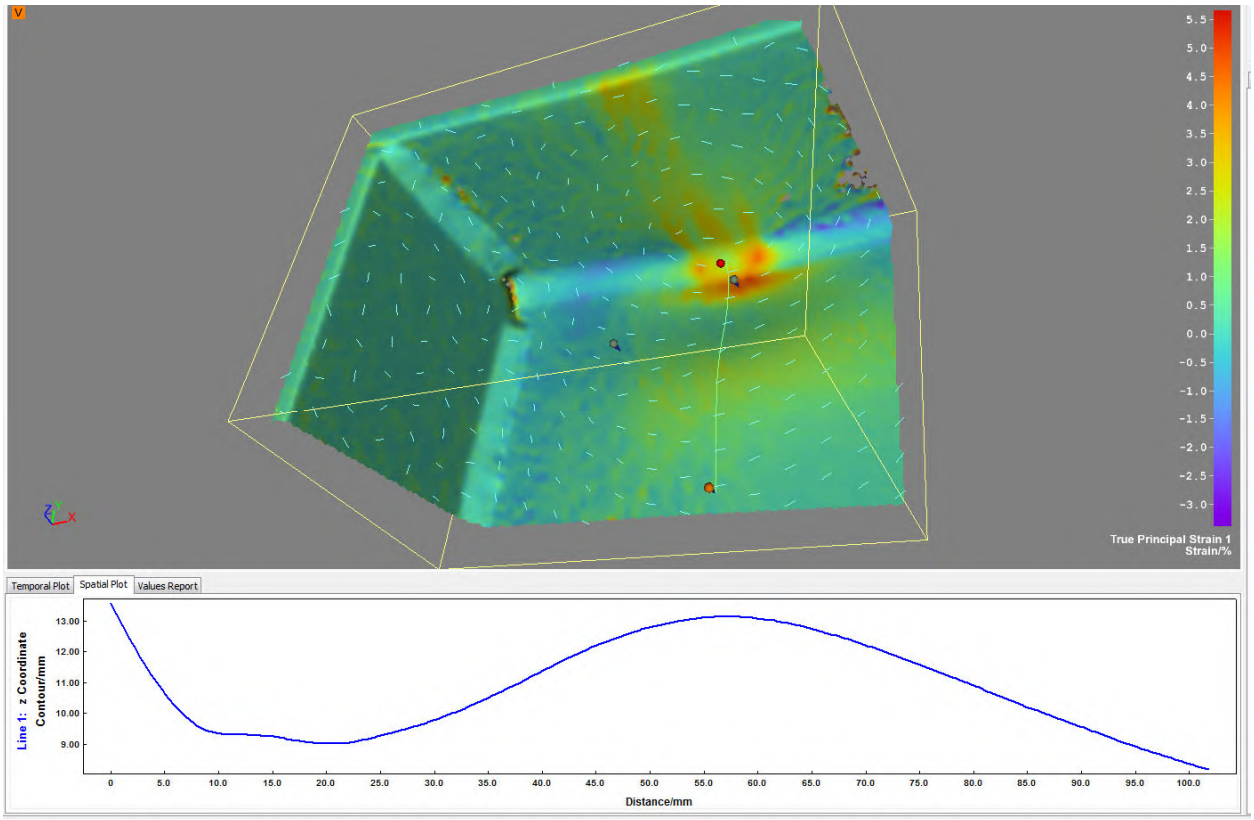

Figure C-51: W10X39-SC-E4 showing out of plane displacement at its maximum load of 132.9 kips

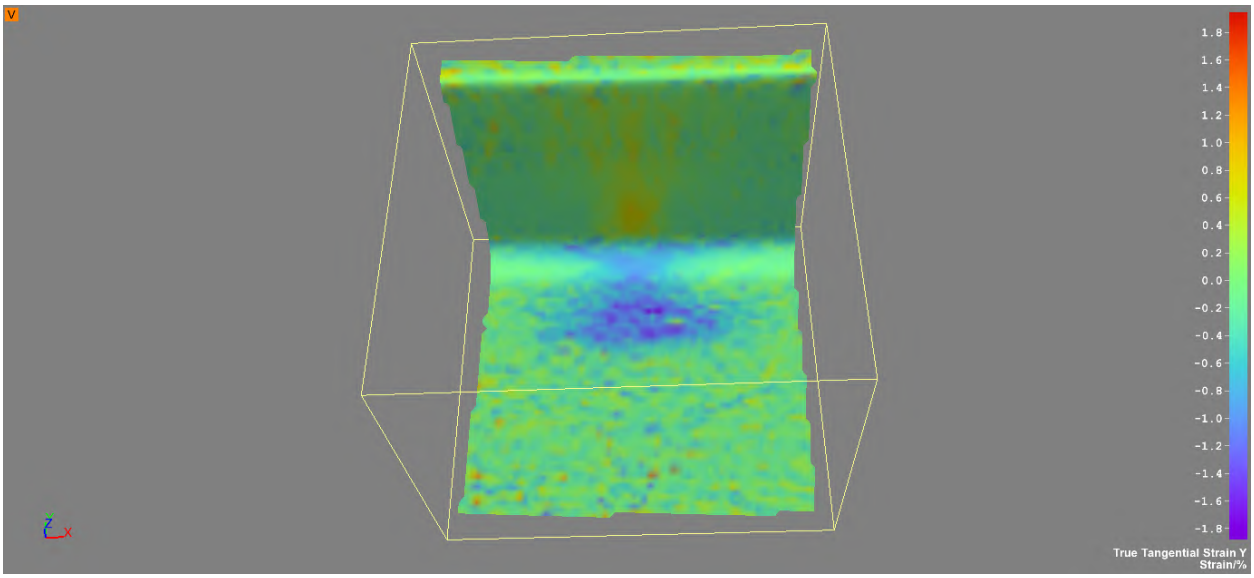

Figure C-52: W10X39-SC-NA showing true tangential strain Y at a load of 111 kips

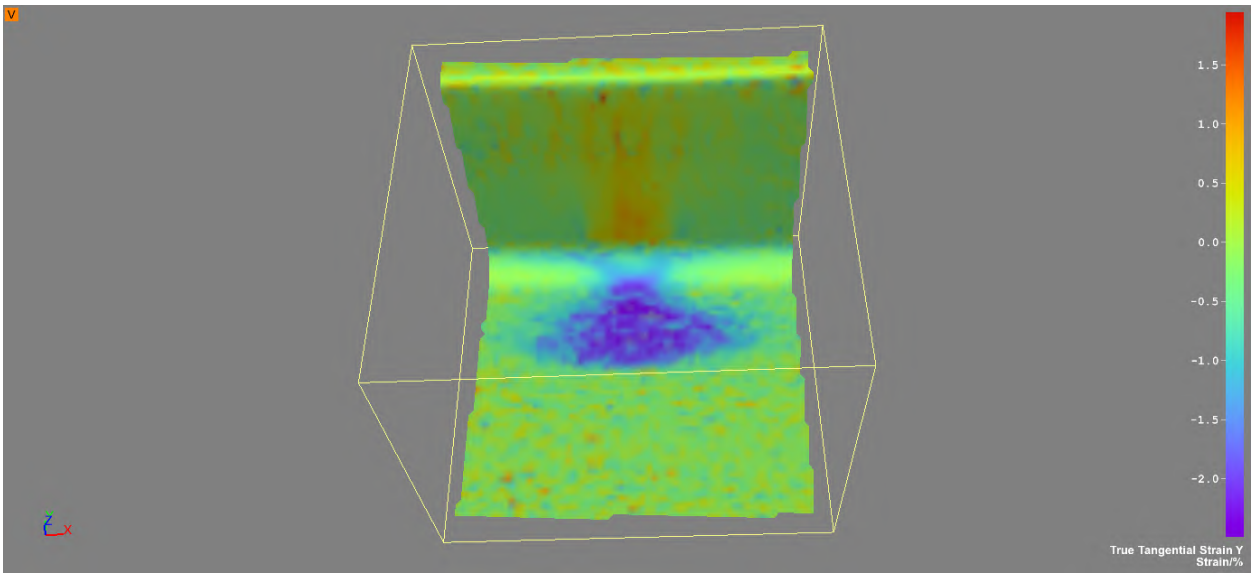

Figure C-53: W10X39-SC-NA showing true tangential strain Y at a load of 121 kips

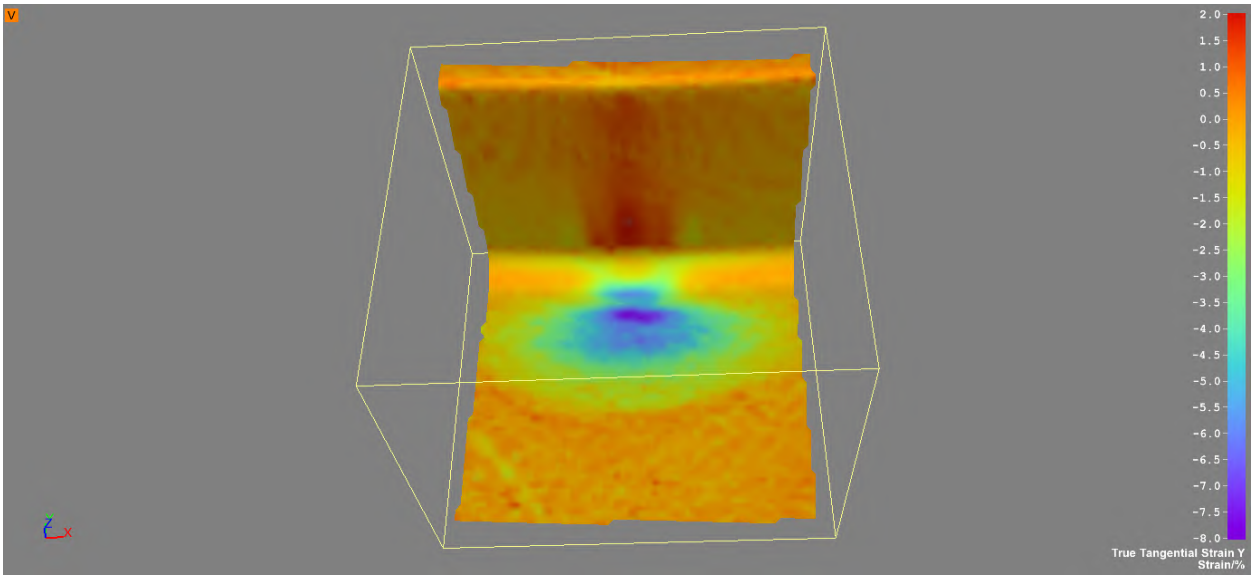

Figure C-54: W10X39-SC-NA showing true tangential strain Y at its maximum load of 131 kips

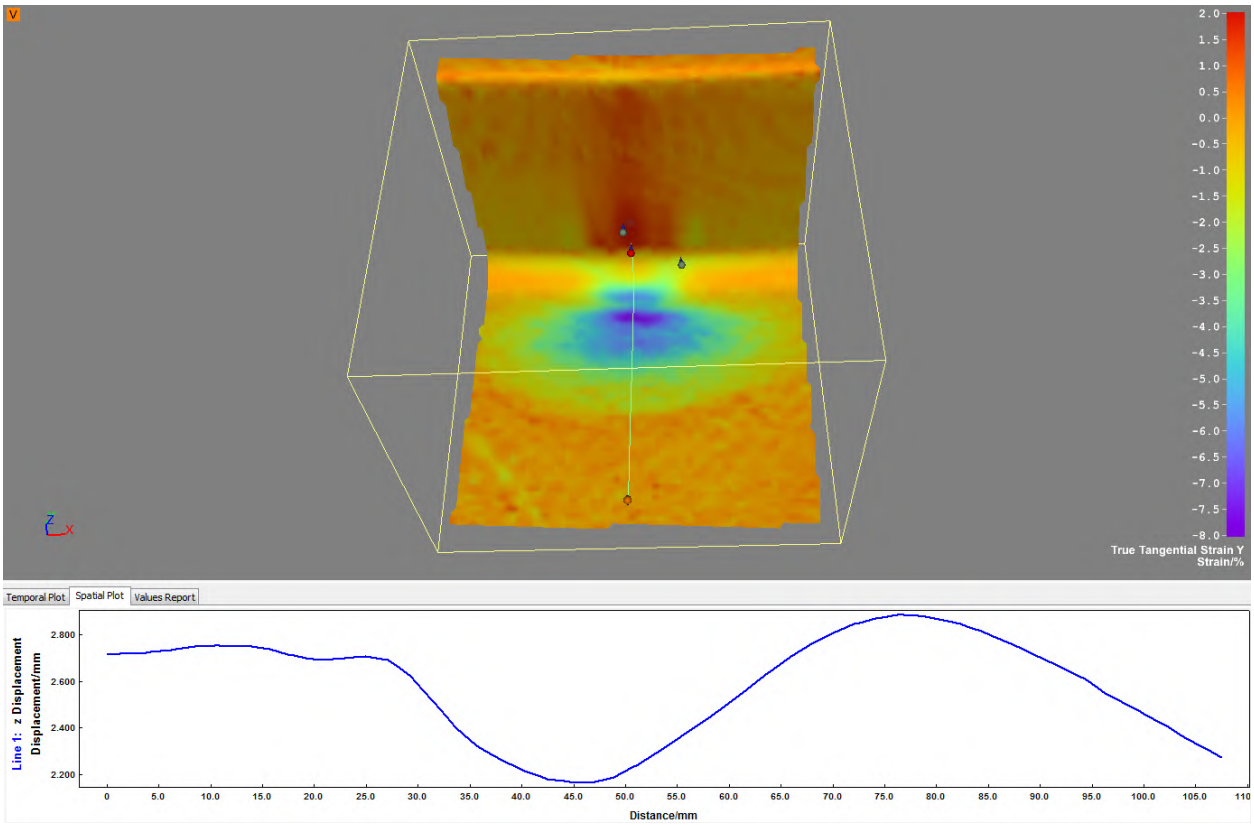

Figure C-55: W10X39-SC-NA showing out of plane displacement at its maximum load of 131 kips

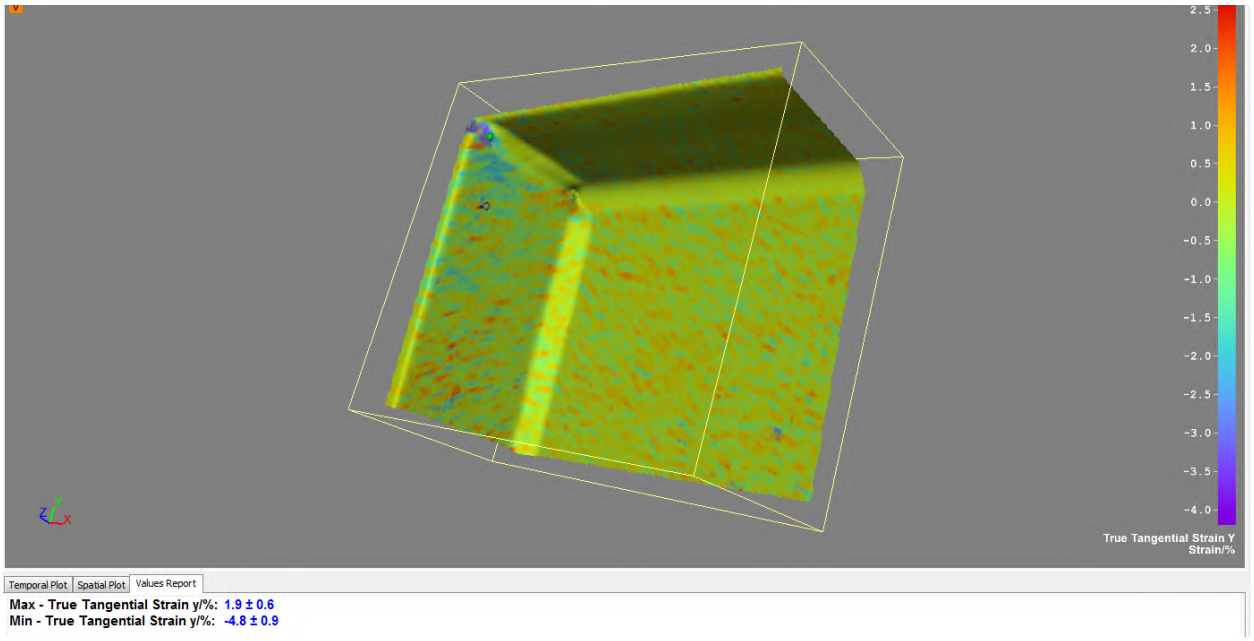

Figure C-56: W12X26-DC-E0 showing true tangential strain Y at a load of 59 kips

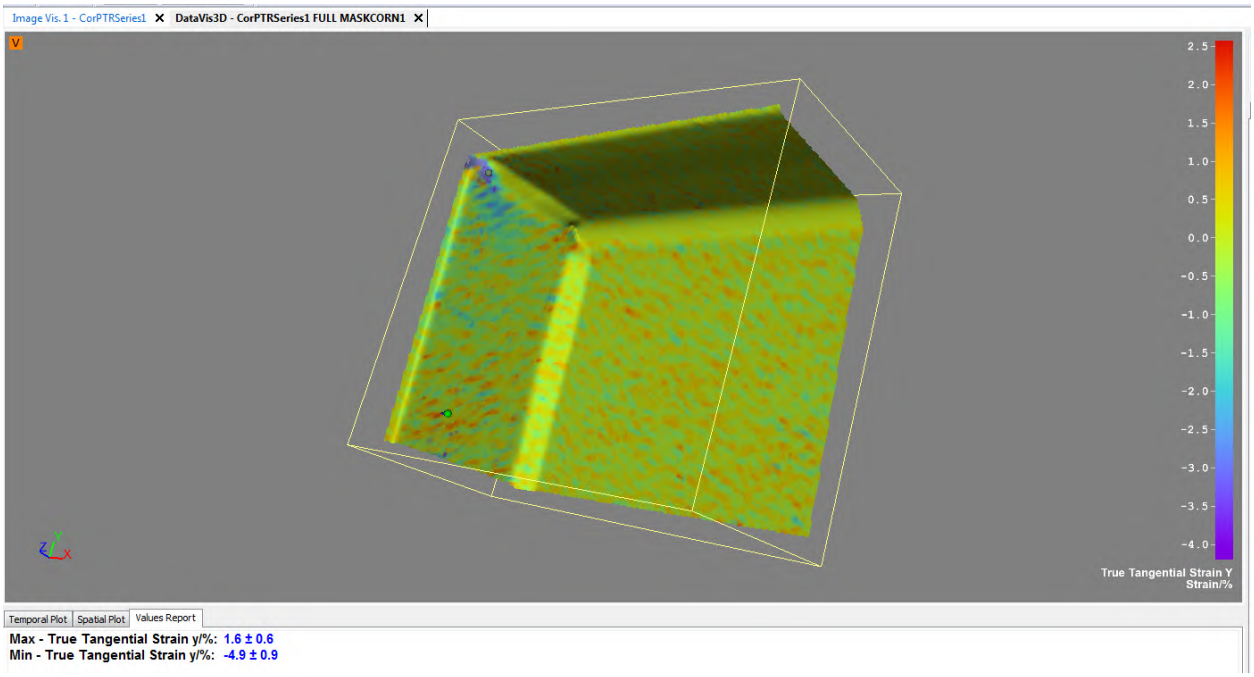

Figure C-57: W12X26-DC-E0 showing true tangential strain Y at a load of 70 kips

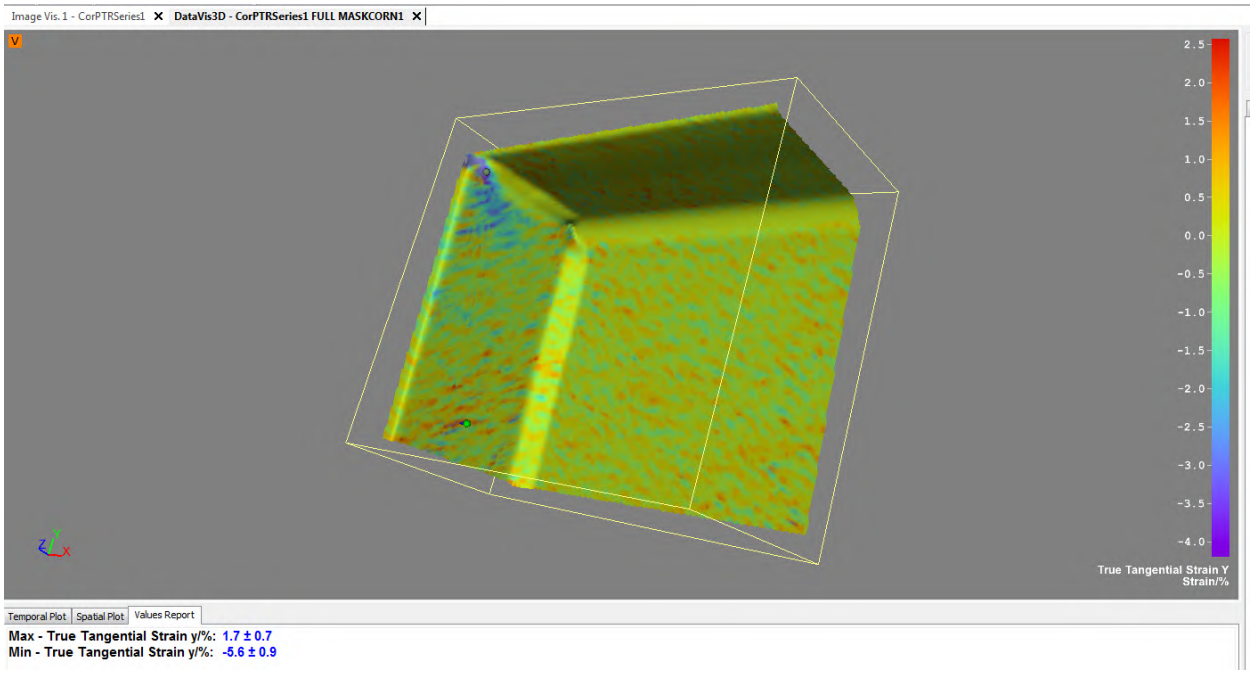

Figure C-58: W12X26-DC-E0 showing true tangential strain Y at a load of 86.4 kips

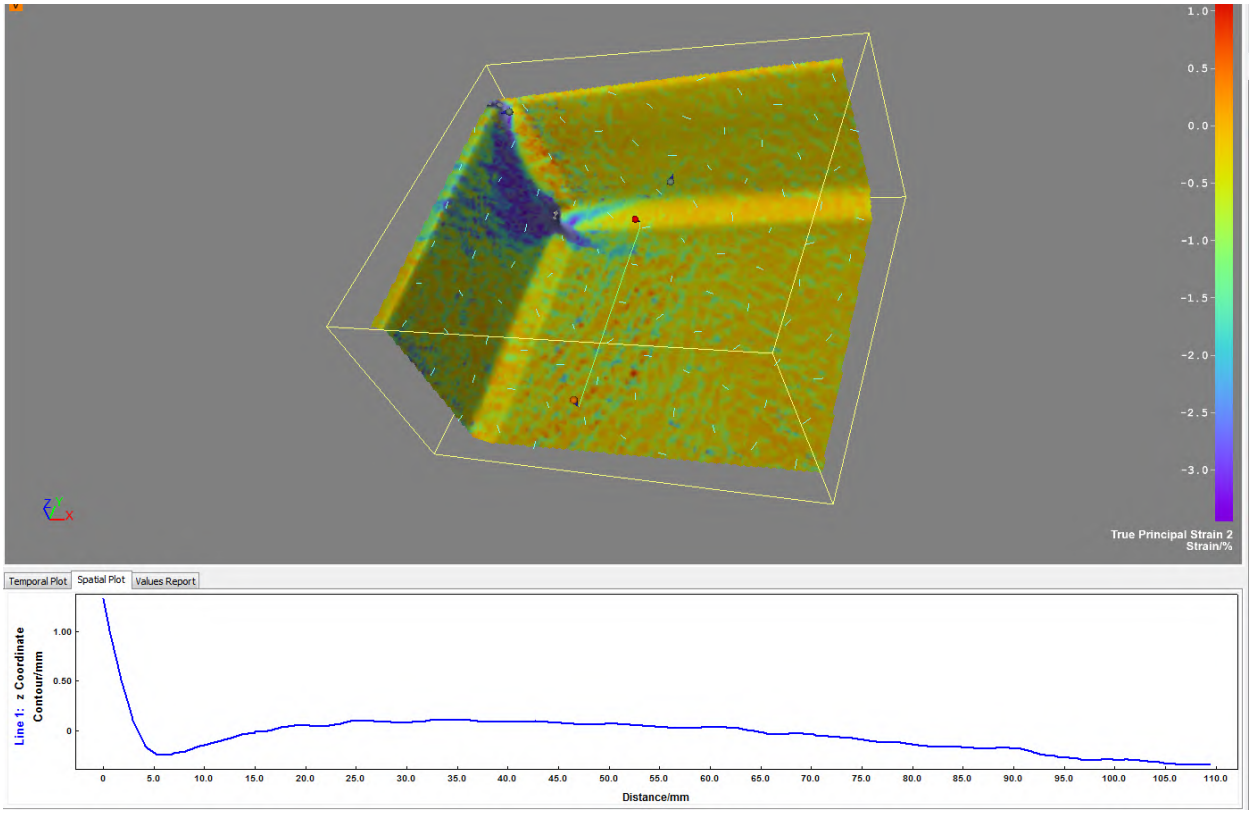

Figure C-59: W12X26-DC-E0 showing out of plane displacement at its maximum load of 220 kips

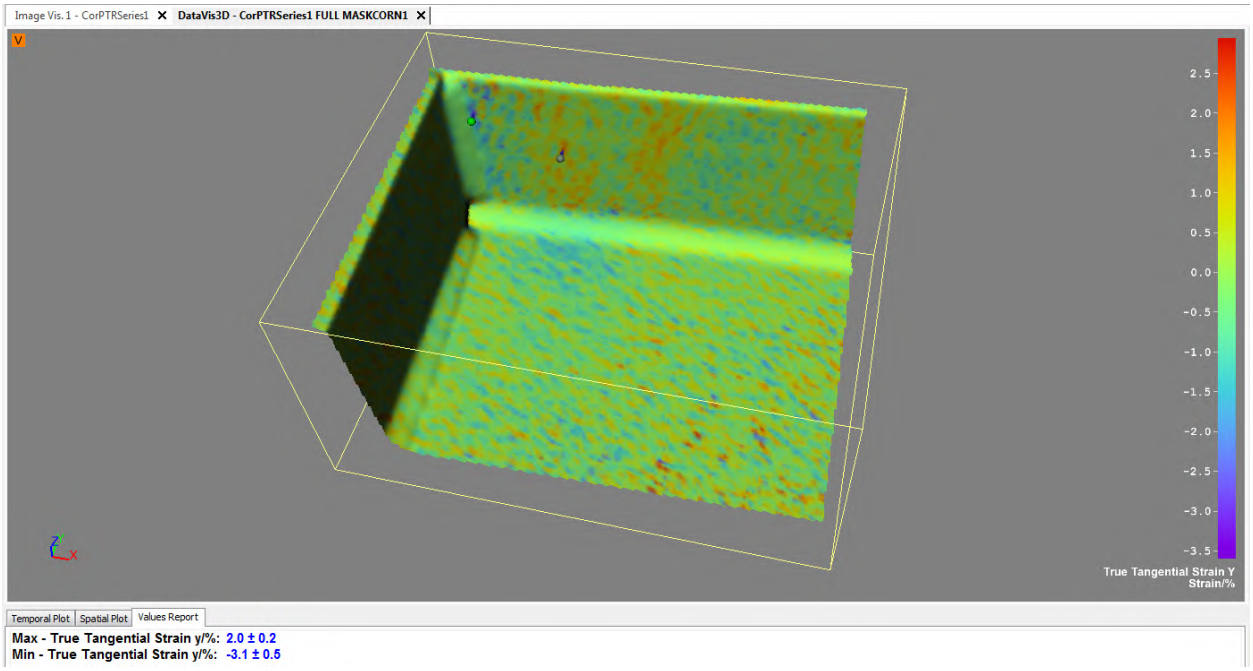

Figure C-60: W12X26-DC-E2 showing true tangential strain Y at a load of 59 kips

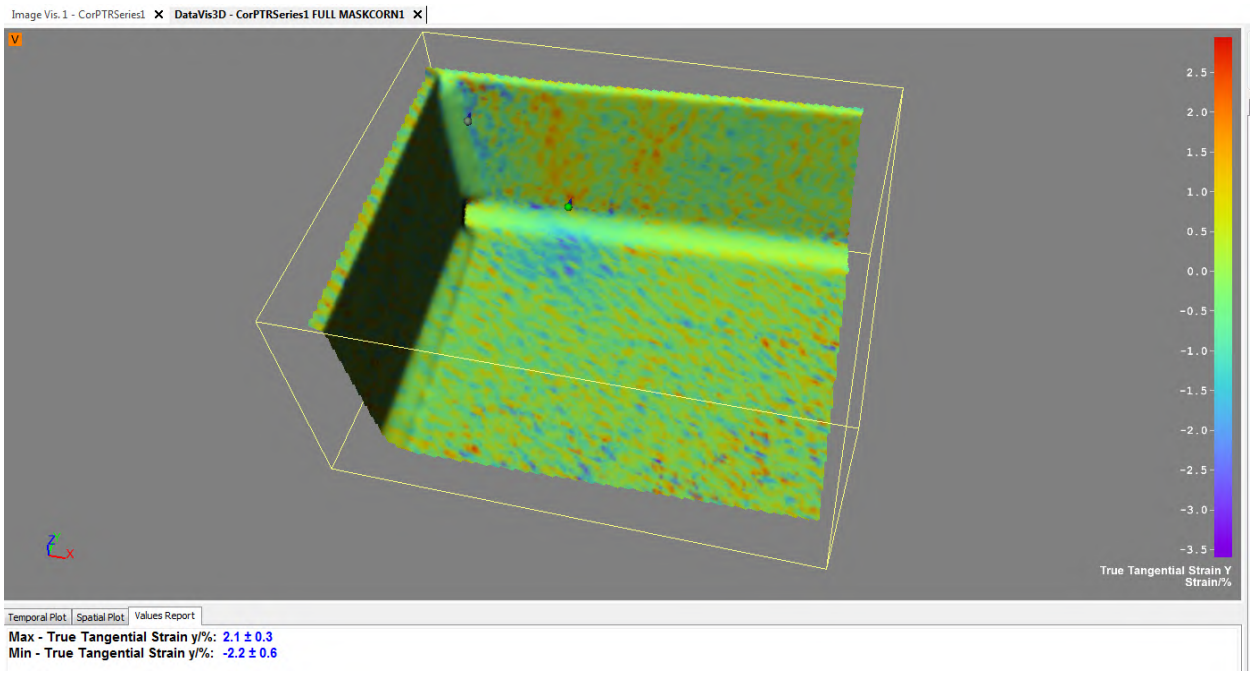

Figure C-61: W12X26-DC-E2 showing true tangential strain Y at a load of 70 kips

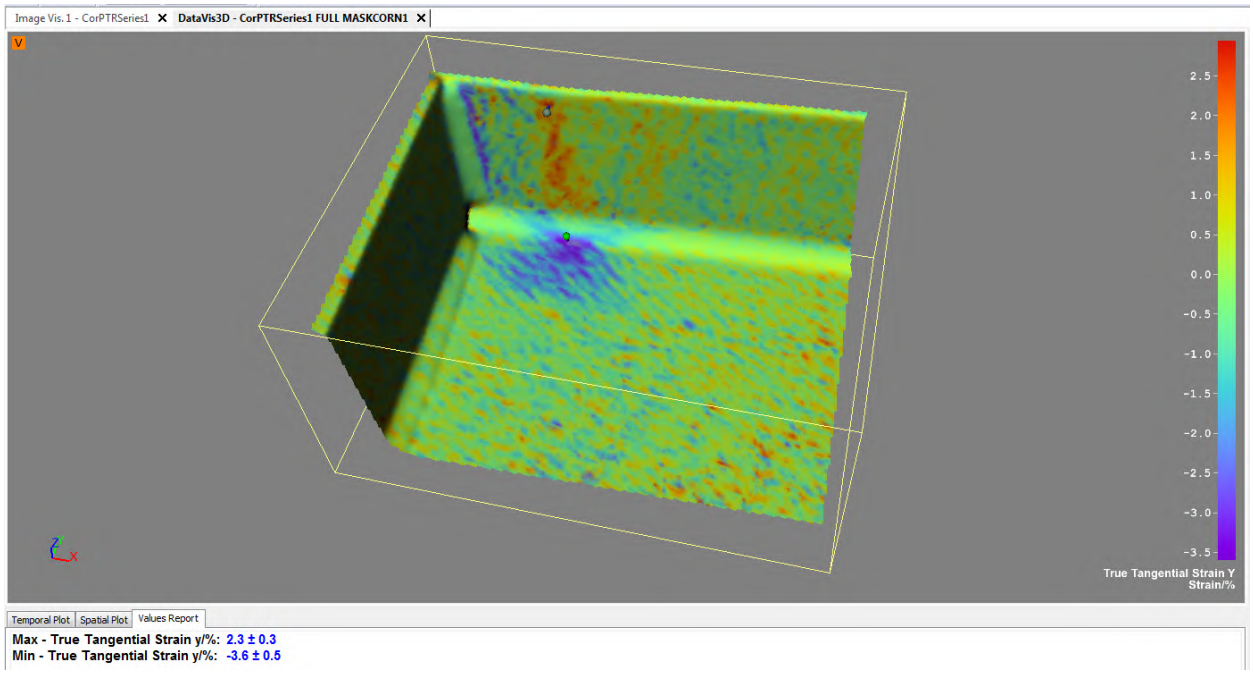

Figure C-62: W12X26-DC-E2 showing true tangential strain Y at a load of 86.4 kips

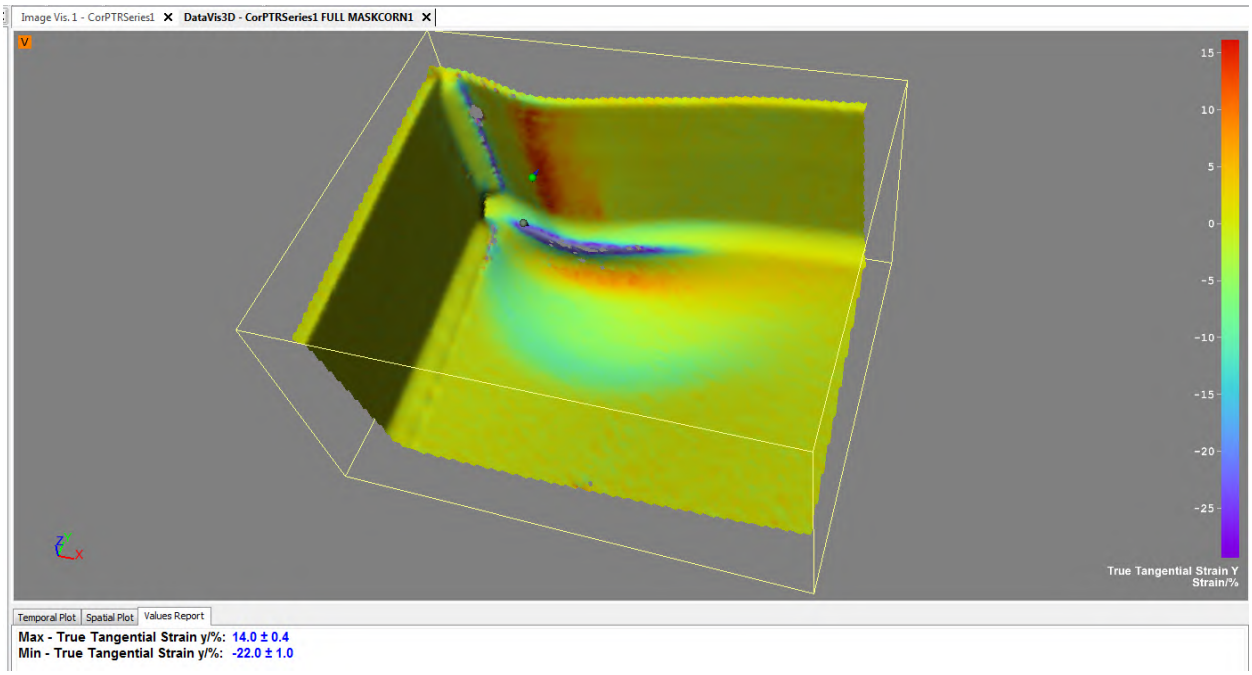

Figure C-63: W12X26-DC-E2 showing true tangential strain Y at its maximum load of 110.9 kips

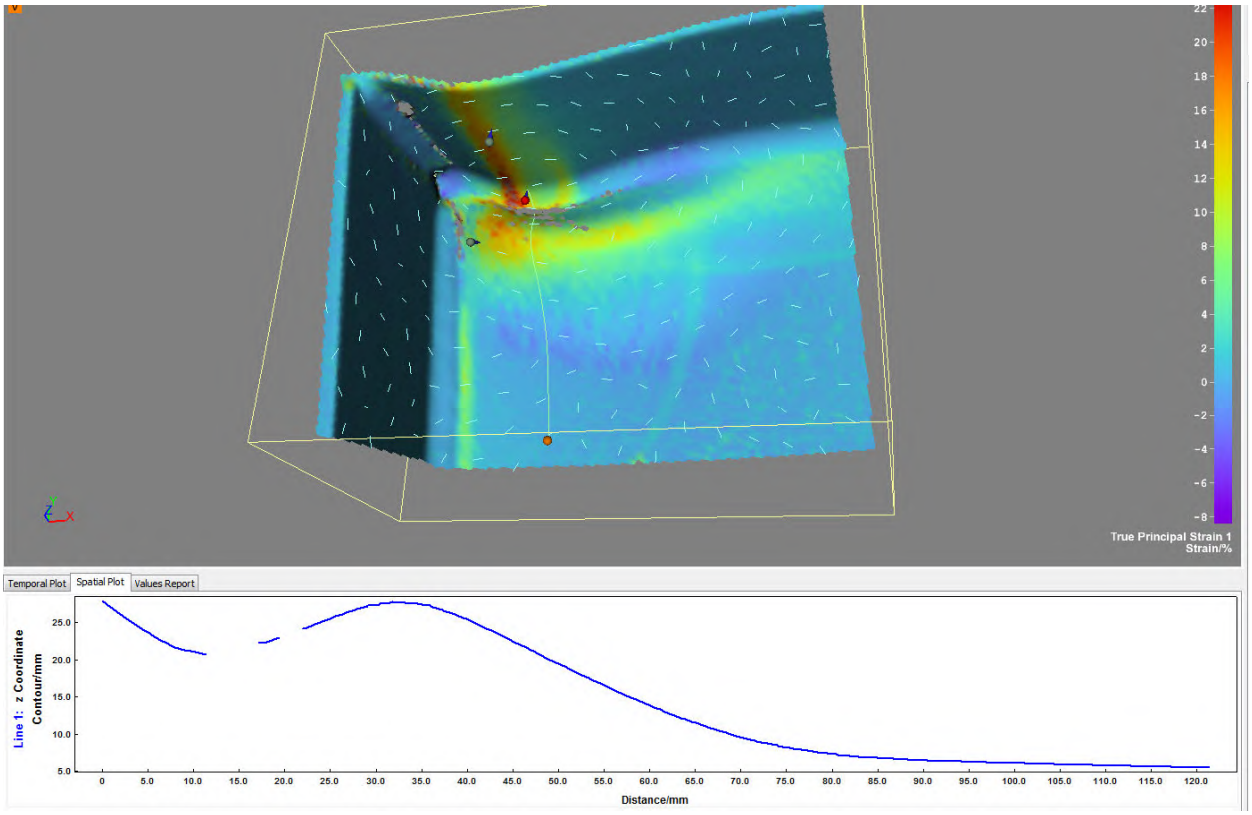

Figure C-64: W12X26-DC-E2 showing out of plane displacement at its maximum load of 110.9 kips

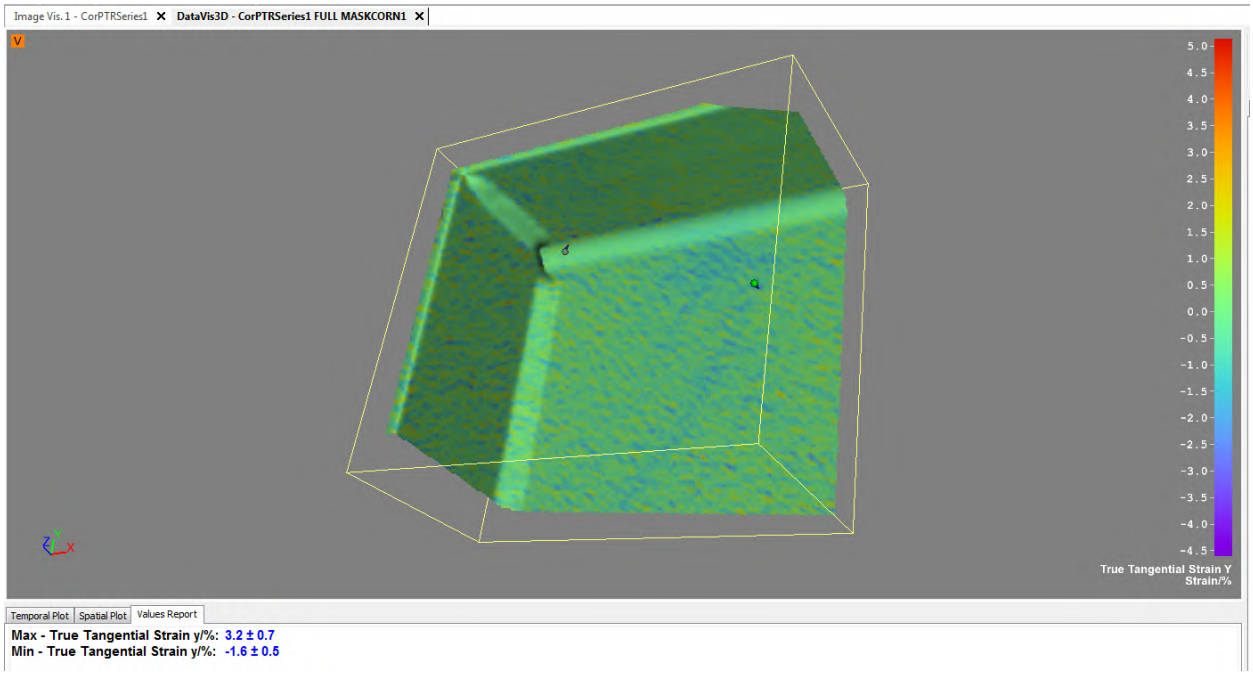

Figure C-65: W12X26-DC-E4 showing true tangential strain Y at a load of 59 kips

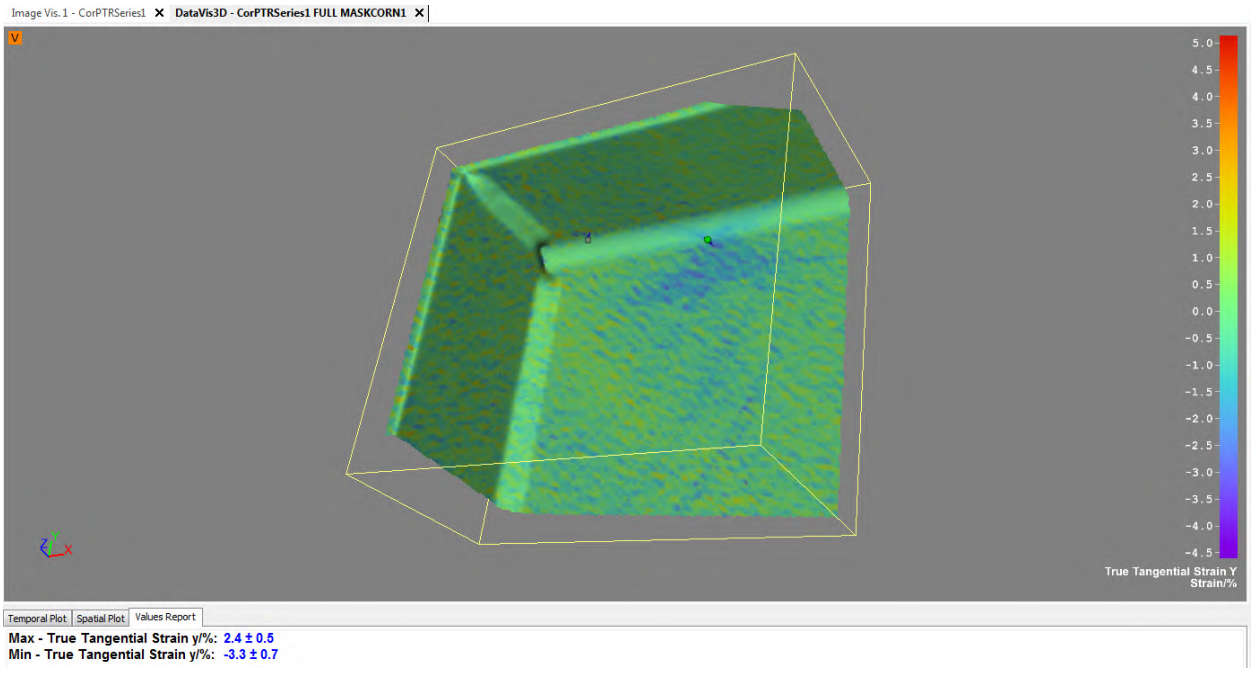

Figure C-66: W12X26-DC-E4 showing true tangential strain Y at a load of 70 kips

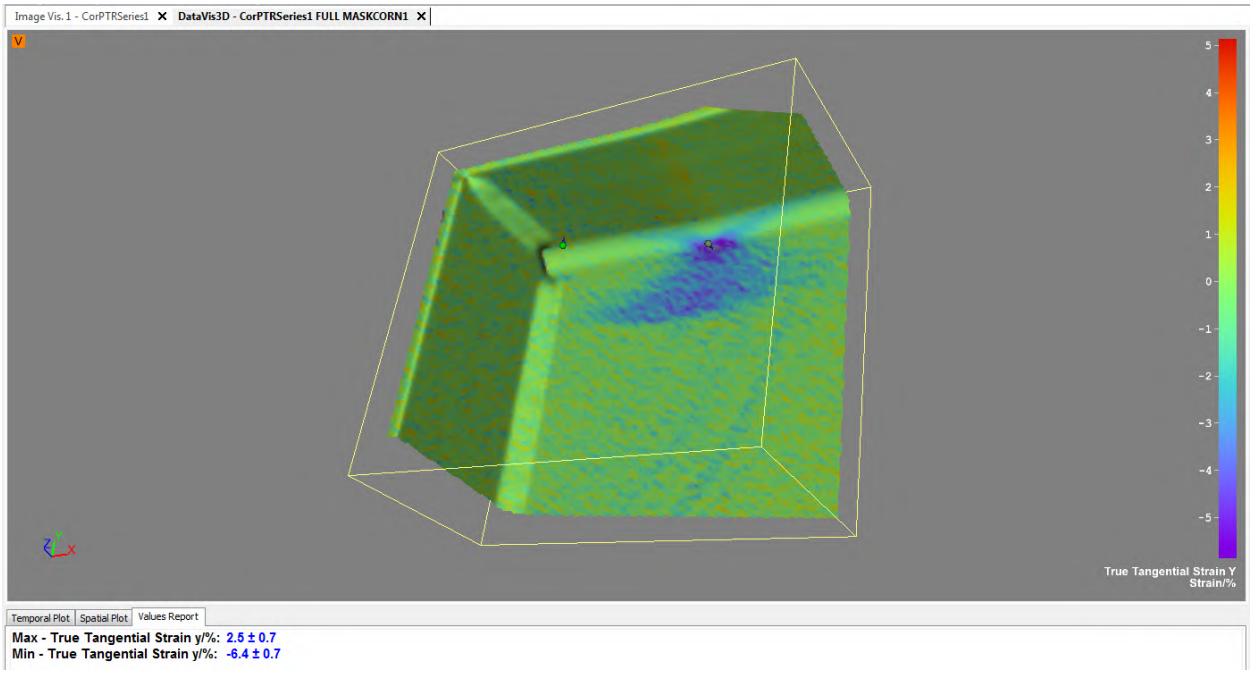

Figure C-67: W12X26-DC-E4 showing true tangential strain Y at a load of 86.4 kips

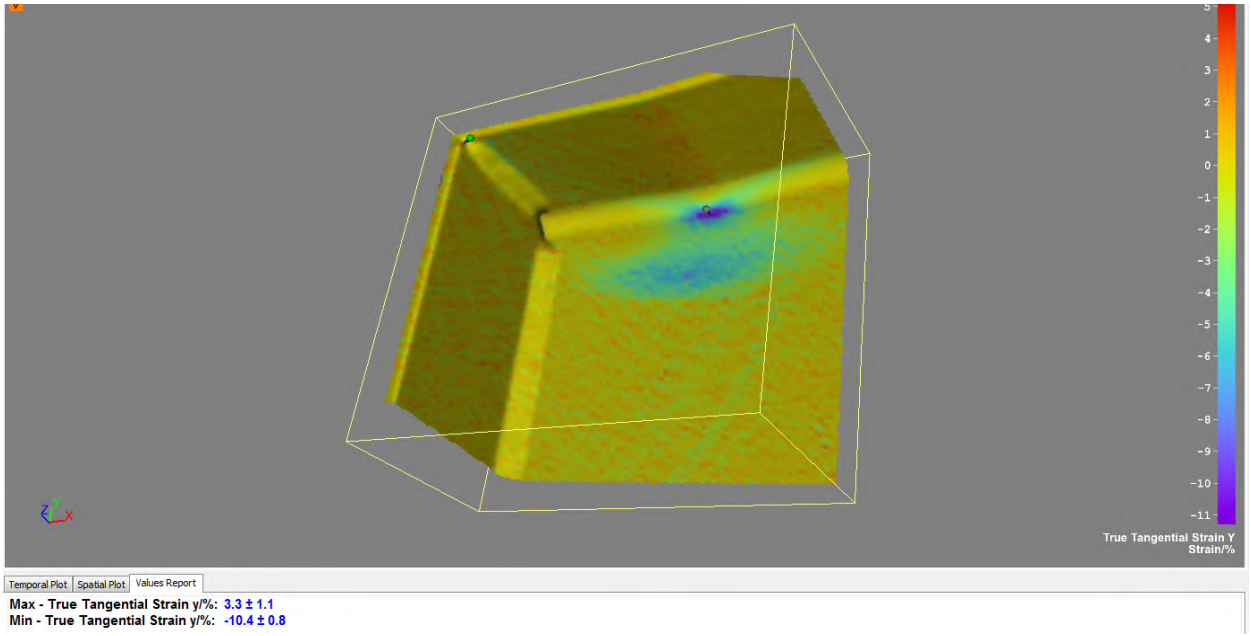

Figure C-68: W12X26-DC-E4 showing true tangential strain Y at its maximum load of 90.6 kips

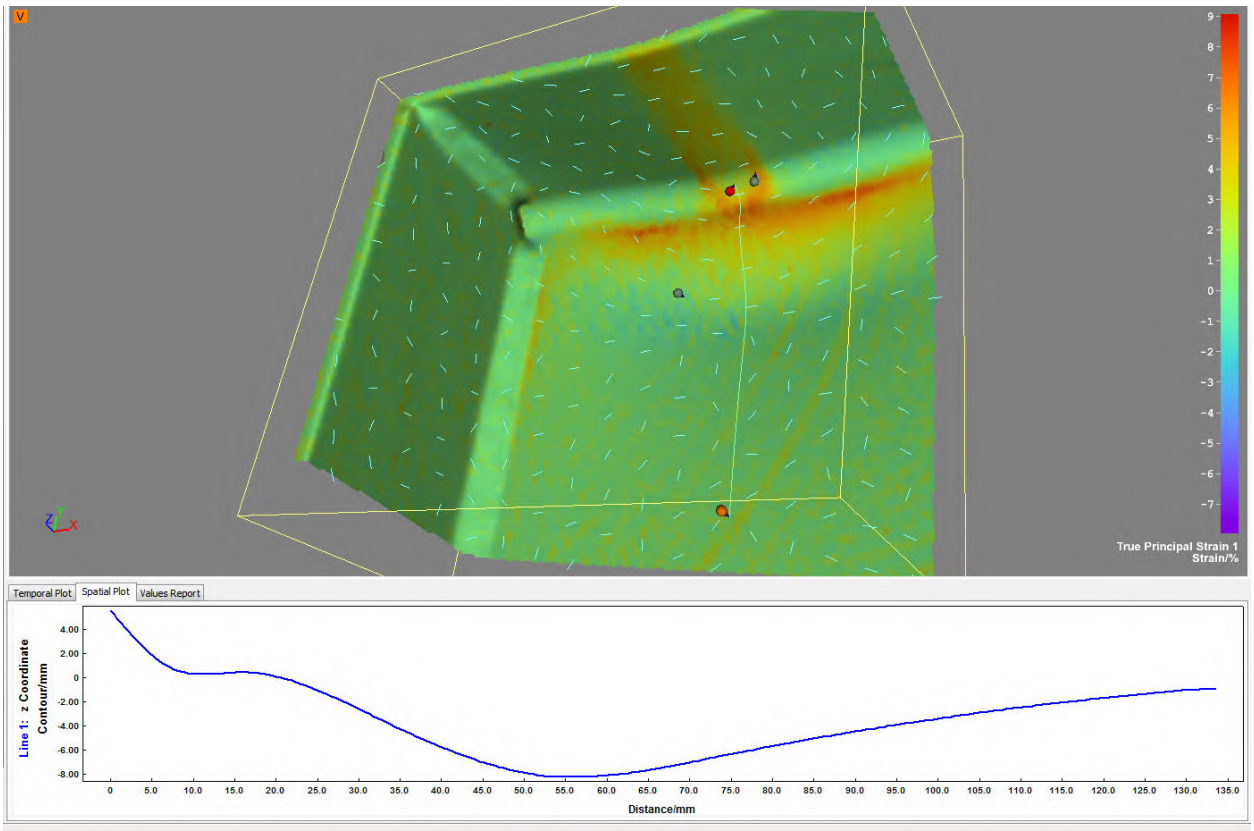

Figure C-69: W12X26-DC-E4 showing out of plane displacement at its maximum load of 90.6 kips

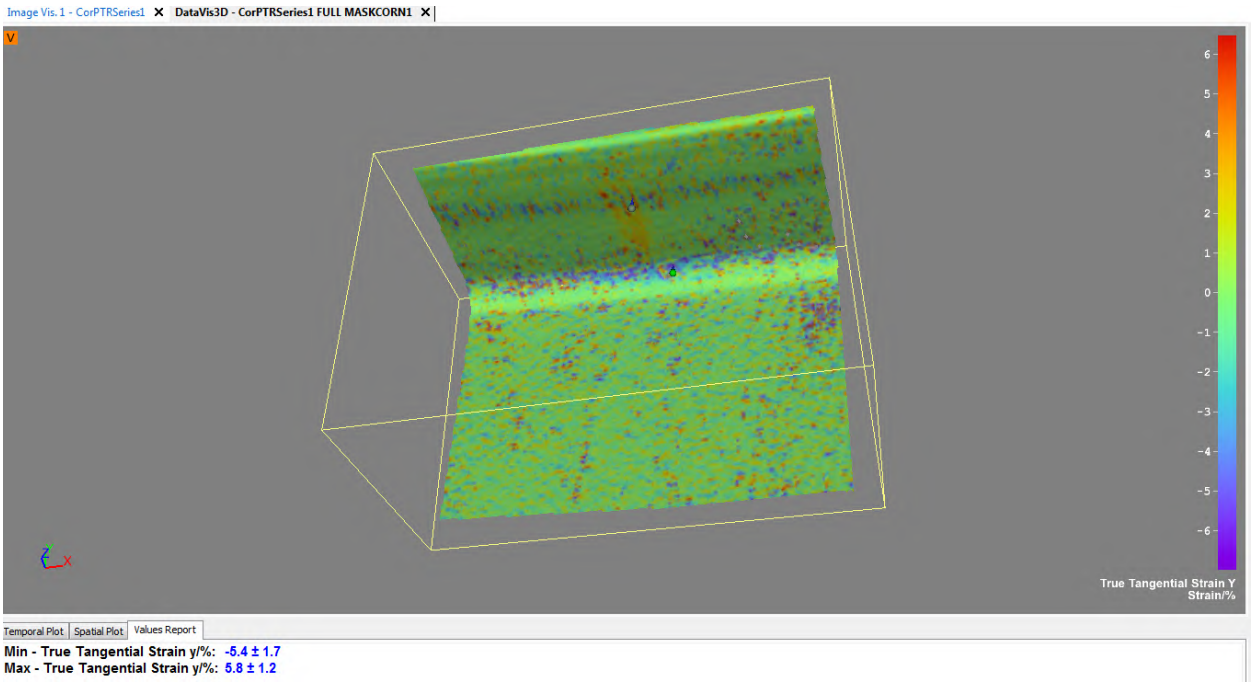

Figure C-70: W12X26-DC-NA showing true tangential strain Y at a load of 59 kips

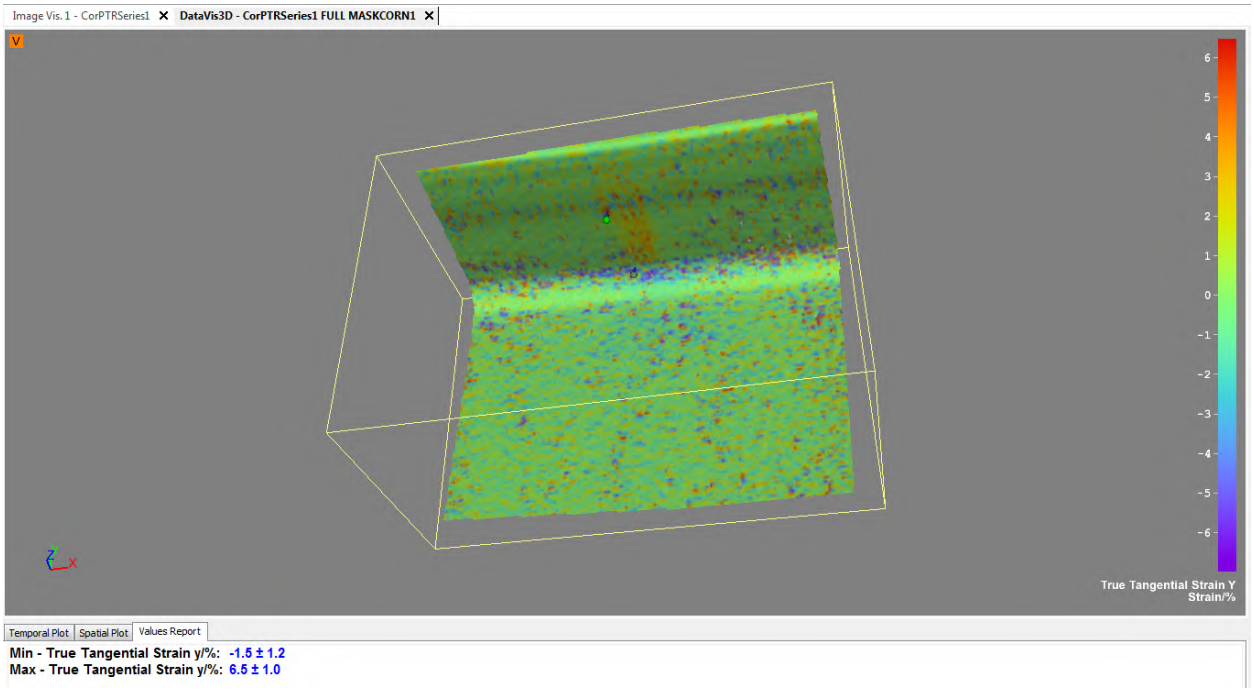

Figure C-71: W12X26-DC-NA showing true tangential strain Y at a load of 70 kips

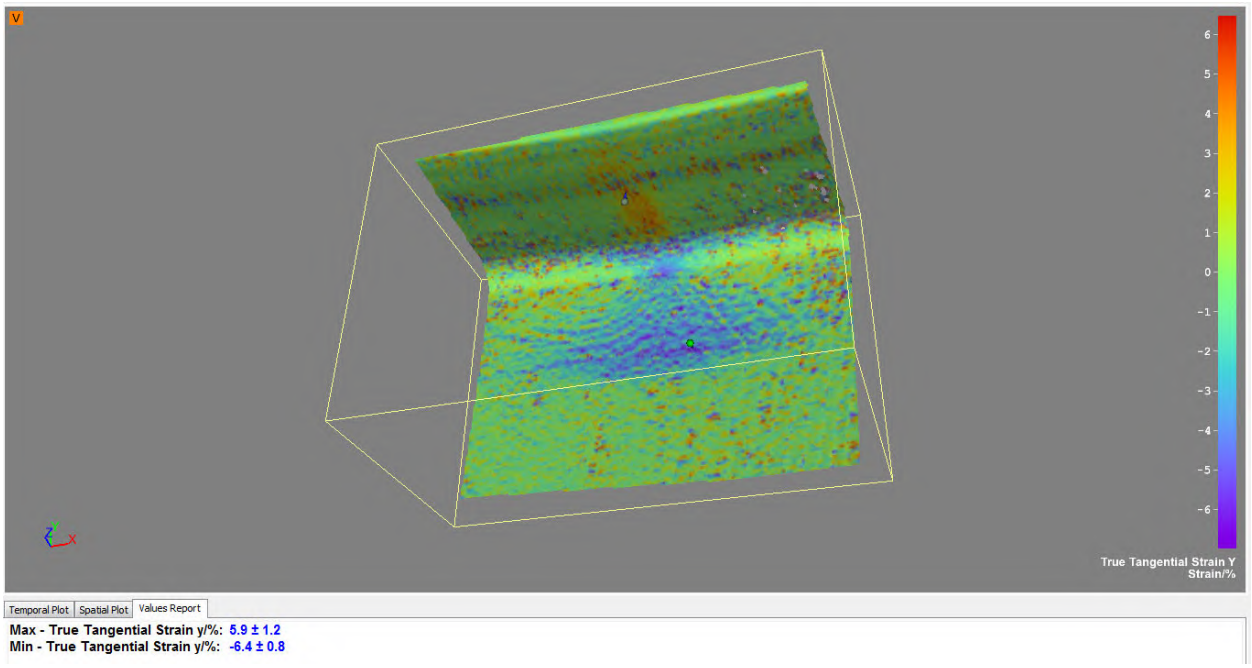

Figure C-72: W12X26-DC-NA showing true tangential strain Y at its maximum load of 86.4 kips

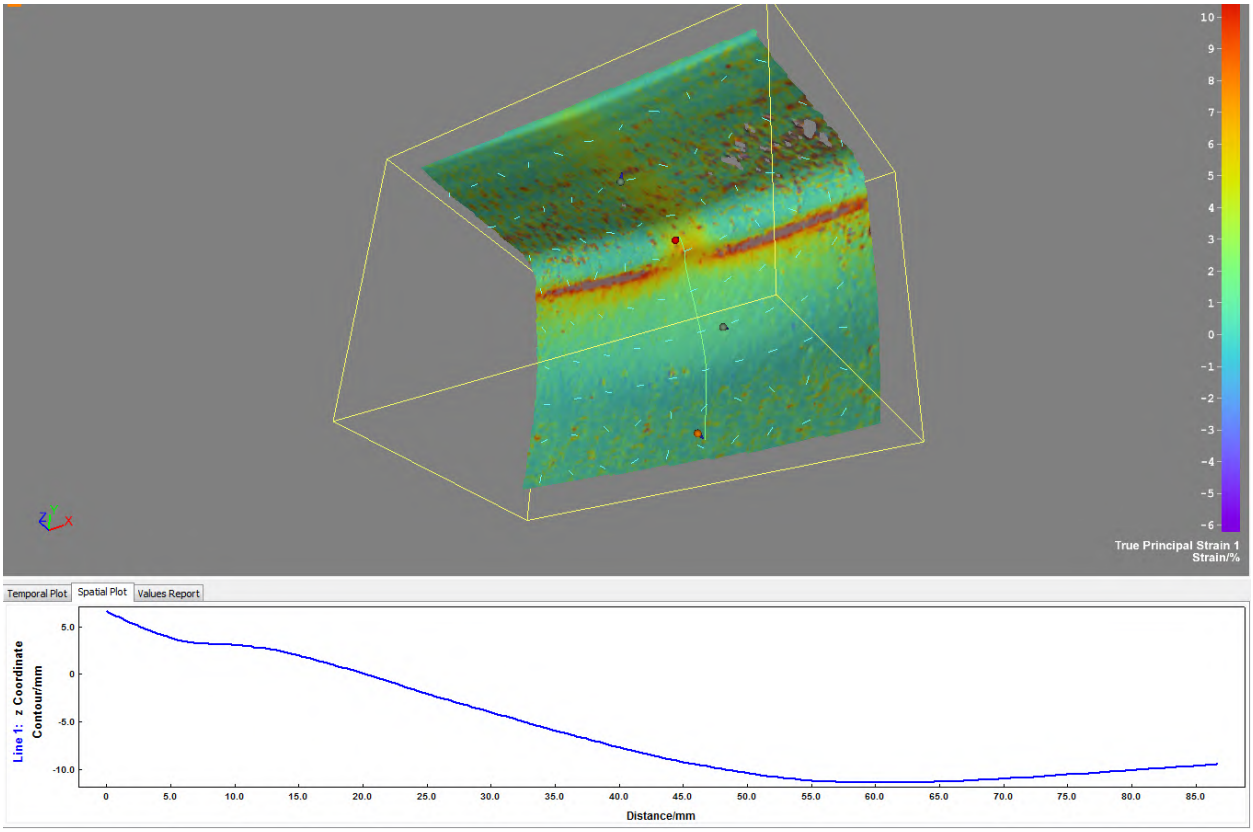

Figure C-73: W12X26-DC-NA showing out of plane displacement at its maximum load of 86.4 kips

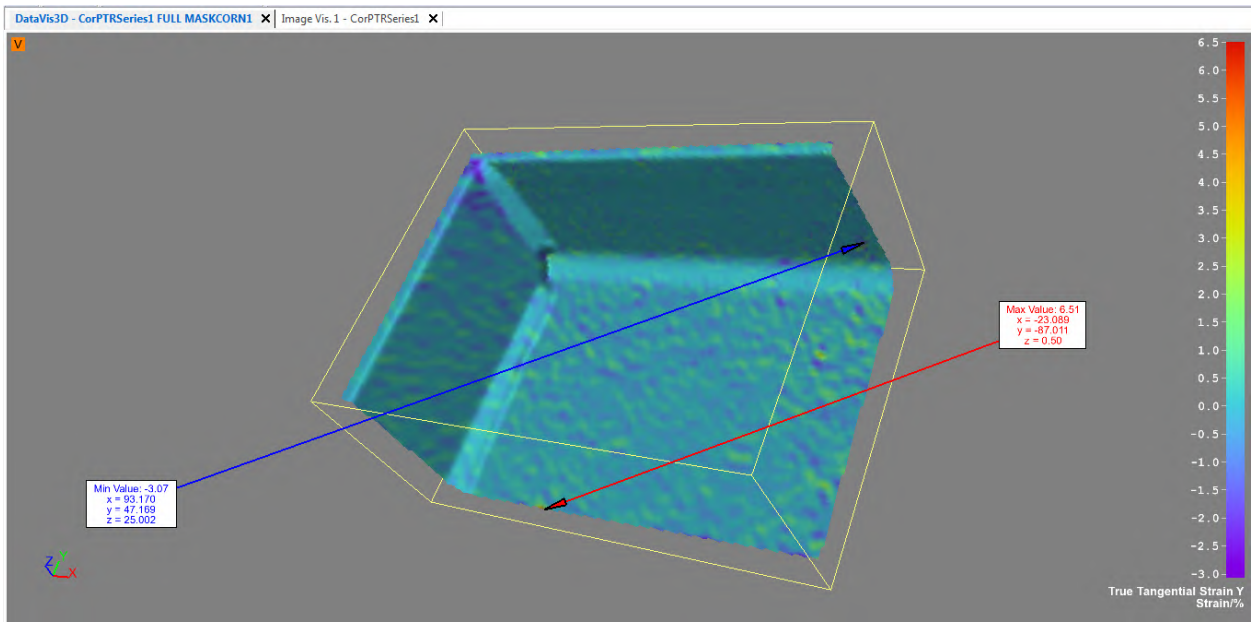

Figure C-74: W12X26-SC-E0 showing true tangential strain Y at a load of 59 kips

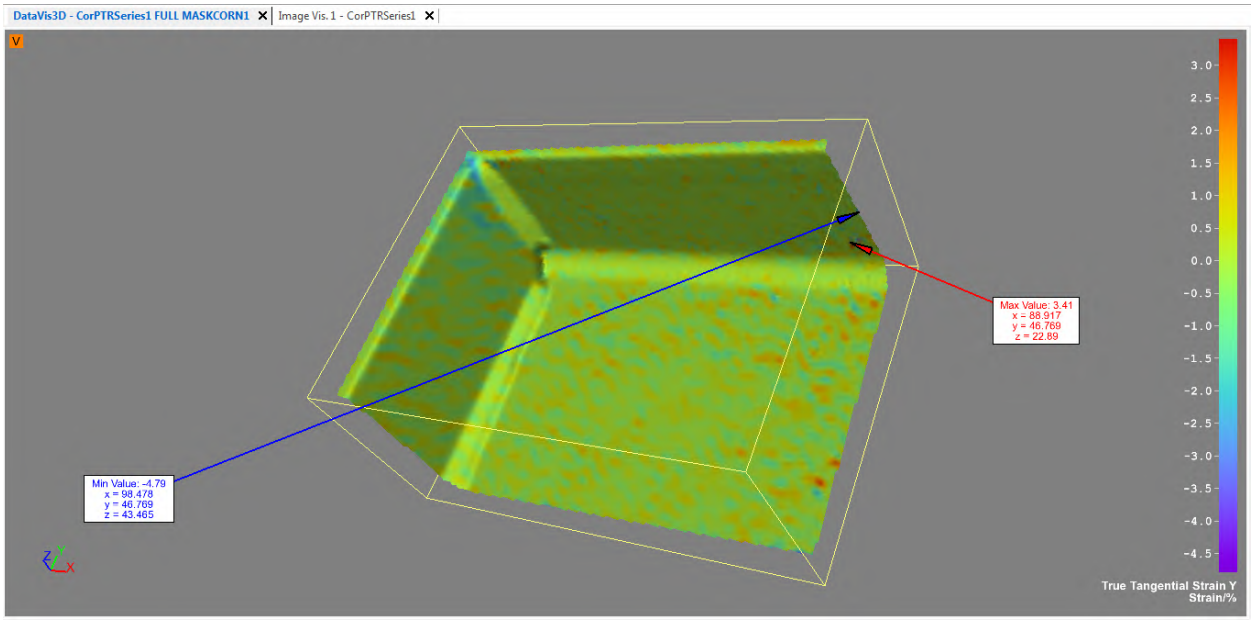

Figure C-75: W12X26-SC-E0 showing true tangential strain Y at a load of 70 kips

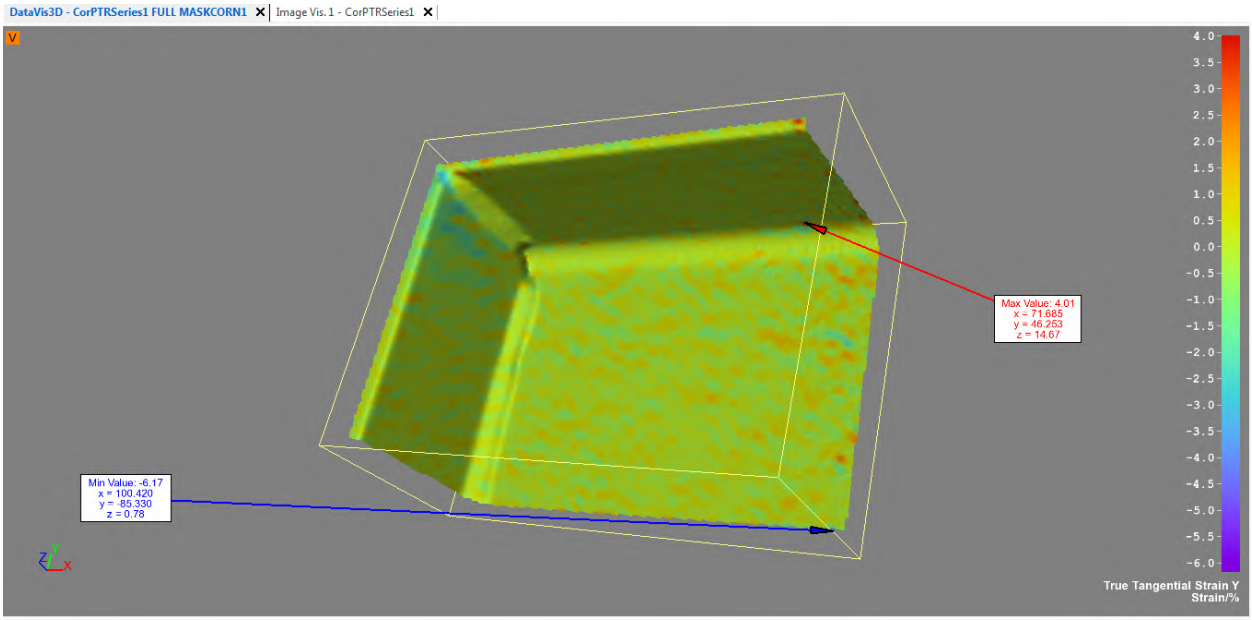

Figure C-76: W12X26-SC-E0 showing true tangential strain Y at a load of 78.2 kips

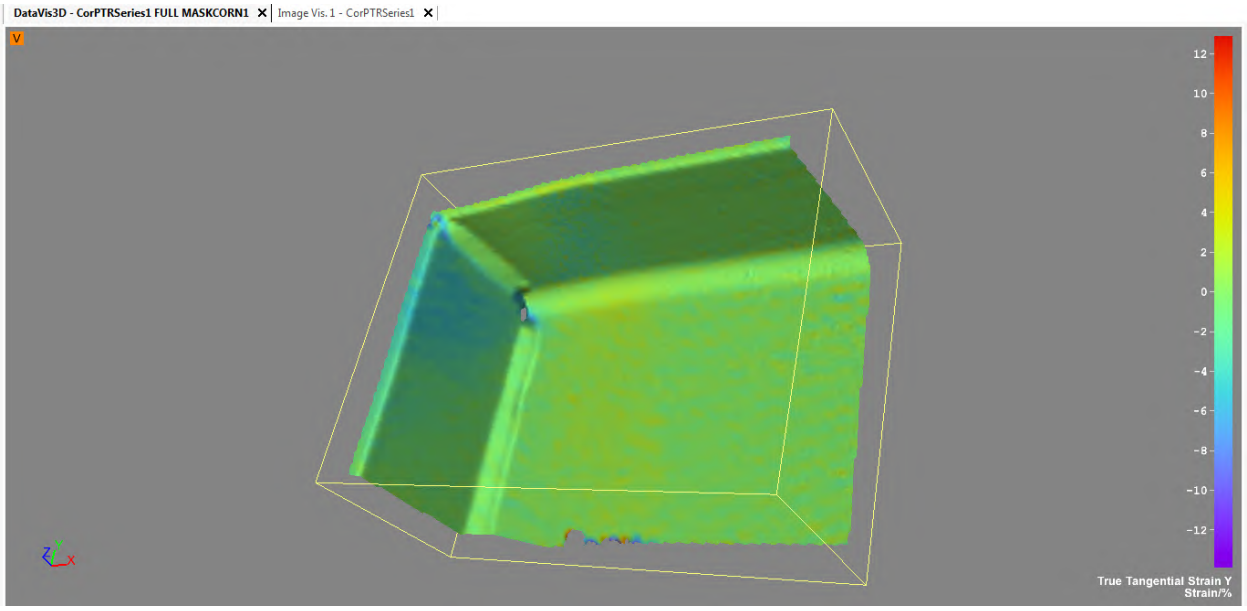

Figure C-77: W12X26-SC-E0 showing true tangential strain Y at its maximum load of 148.3 kips

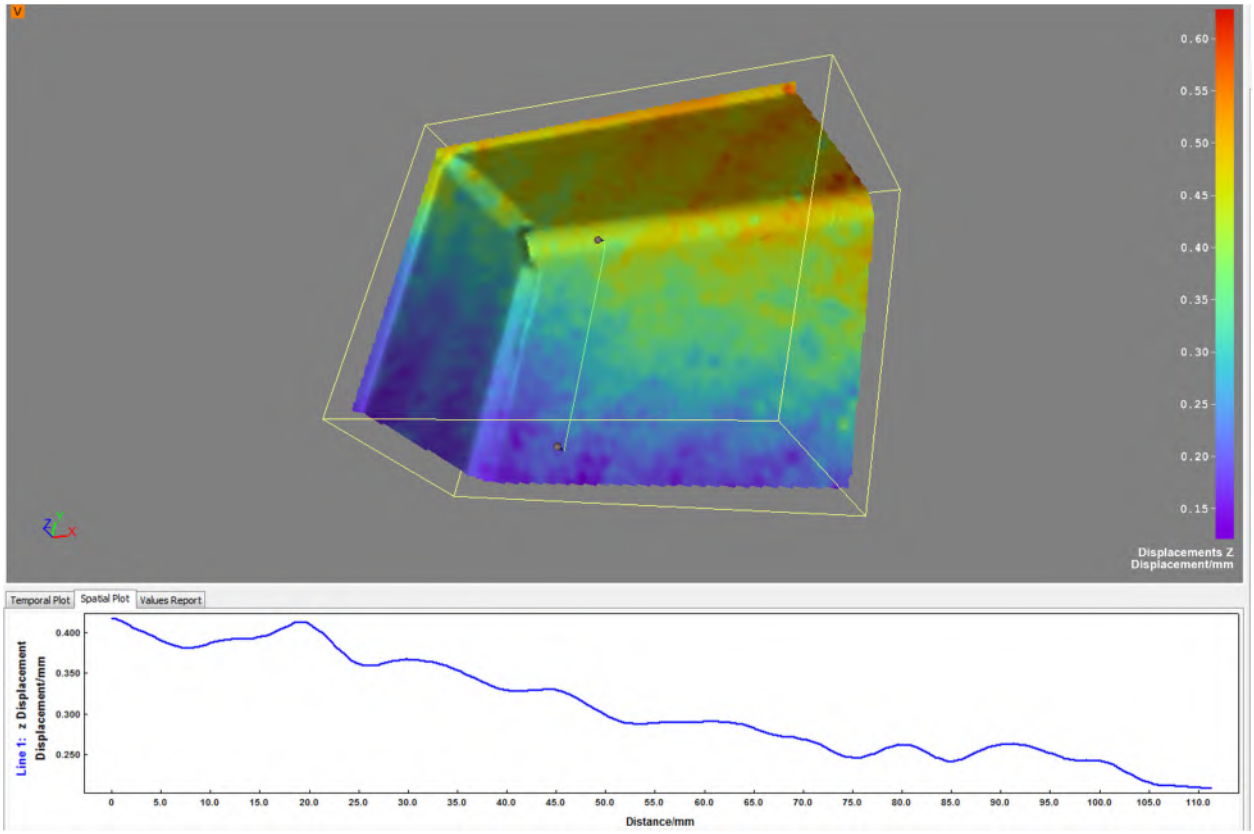

Figure C-78: W12X26-SC-E0 showing out of plane displacement Z a load of 78.2 kips

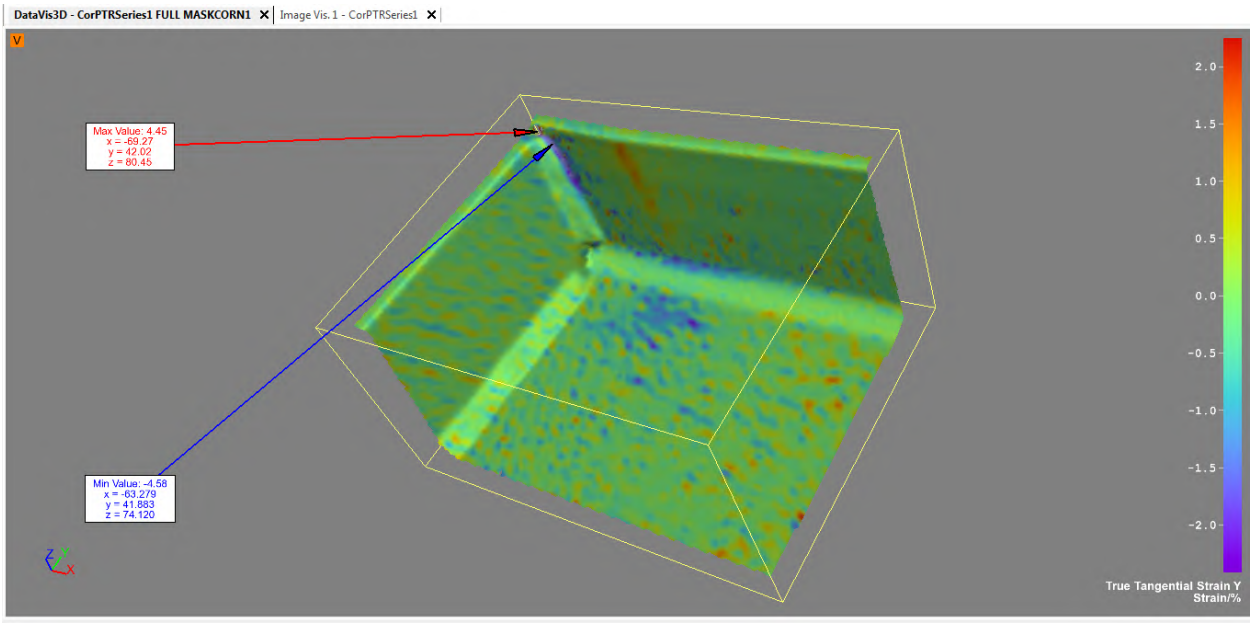

Figure C-79: W12X26-SC-E2 showing true tangential strain Y at a load of 59 kips

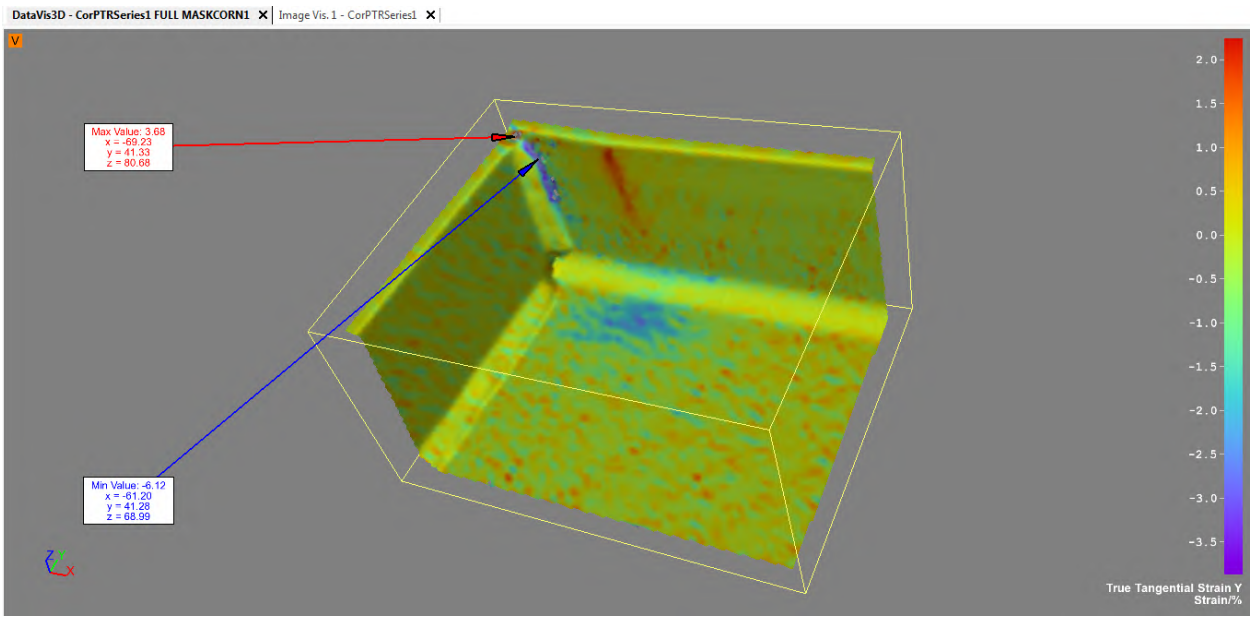

Figure C-80: W12X26-SC-E2 showing true tangential strain Y at a load of 70 kips

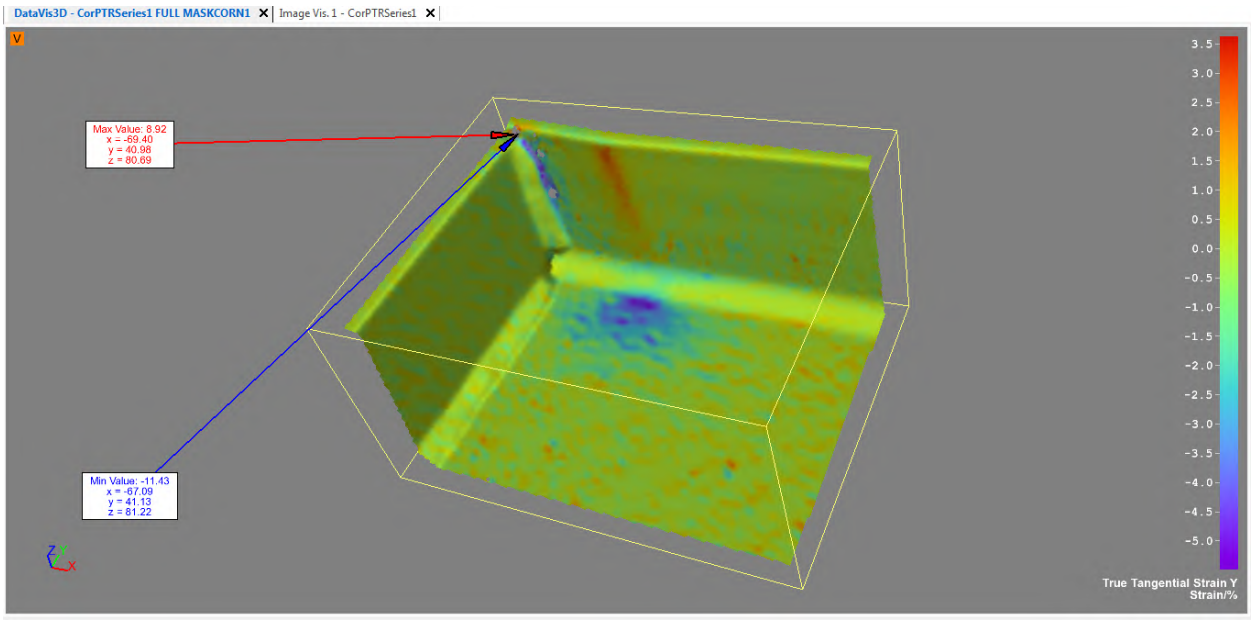

Figure C-81: W12X26-SC-E2 showing true tangential strain Y at a load of 78.2 kips

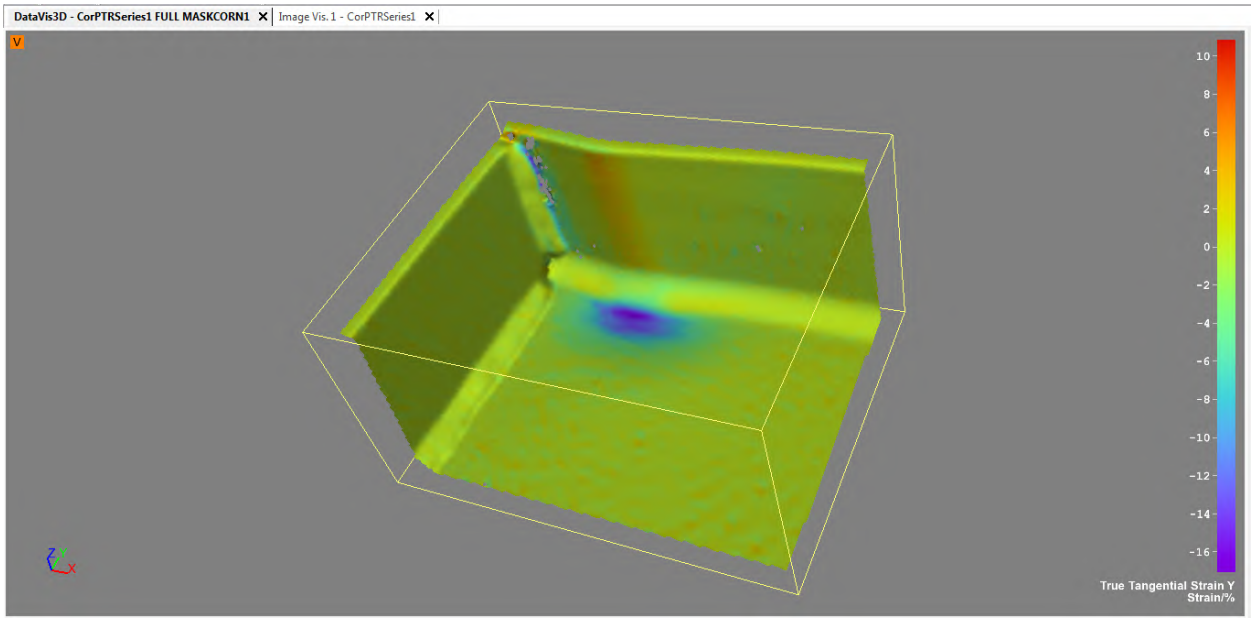

Figure C-82: W12X26-SC-E2 showing true tangential strain Y at its maximum load of 87.1 kips

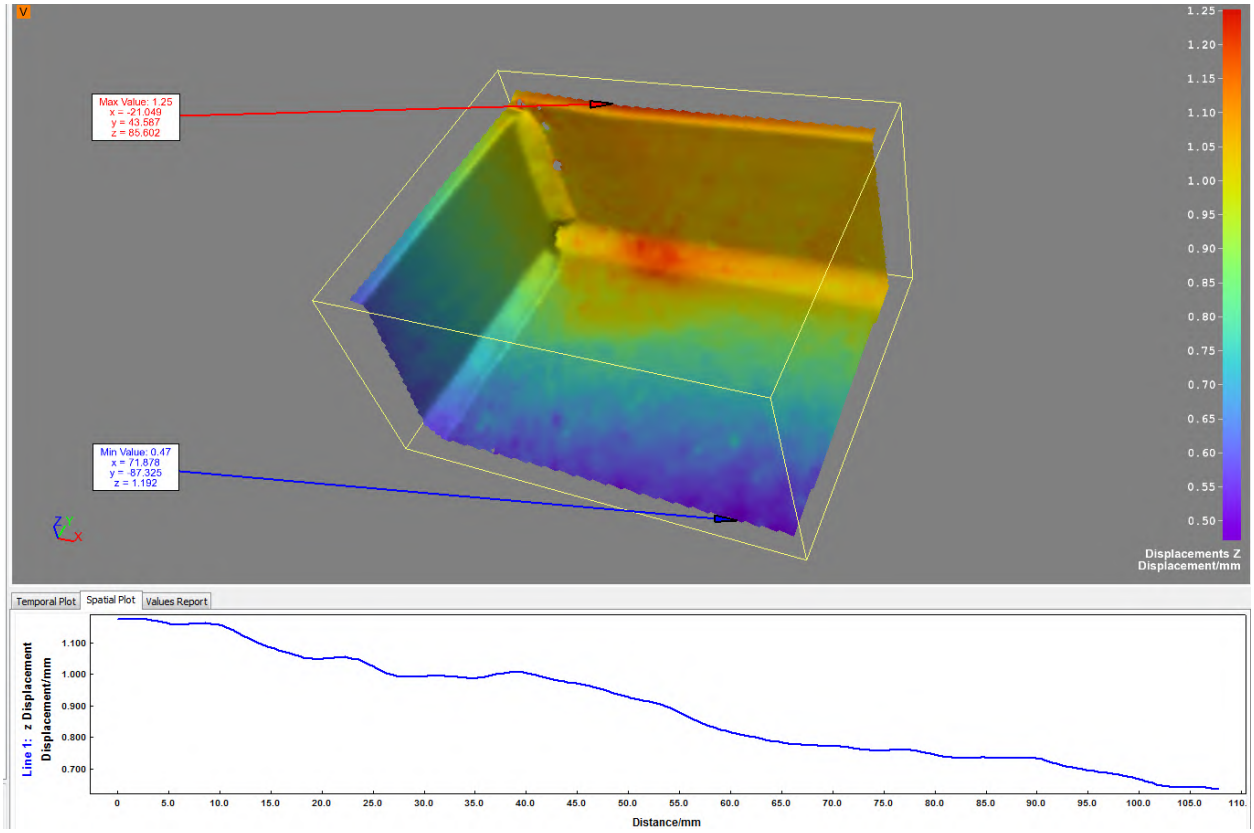

Figure C-83: W12X26-SC-E2 showing out of plane displacement Z at a load of 78.2 kips

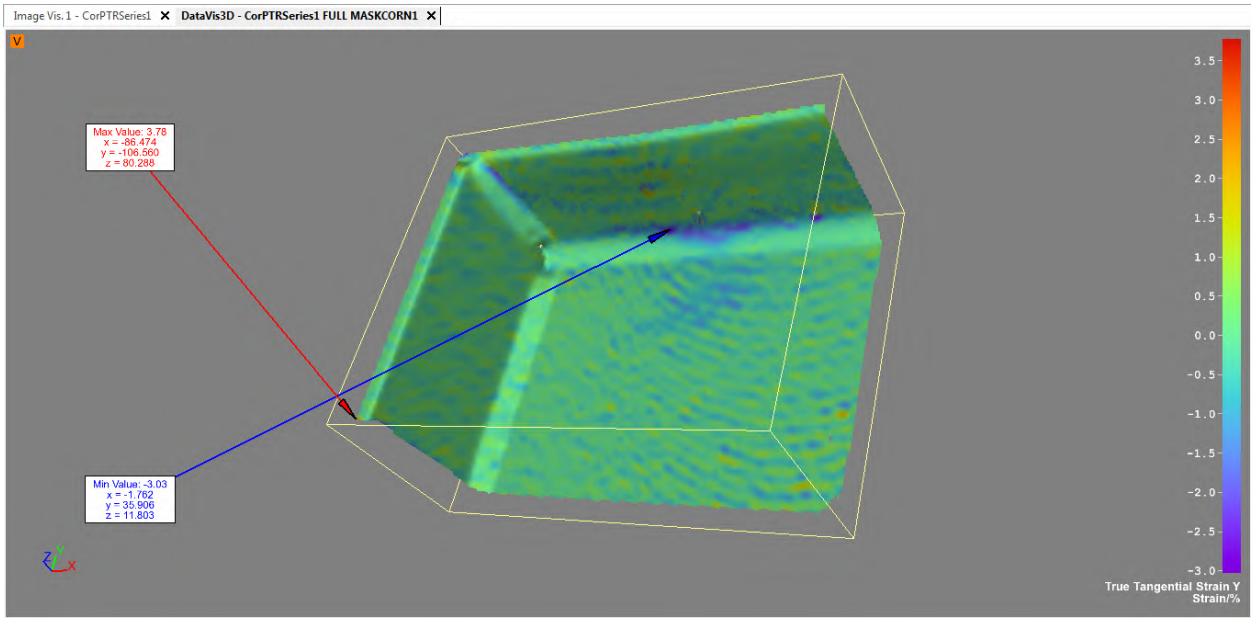

Figure C-84: W12X26-SC-E4 showing true tangential strain Y at a load of 59 kips

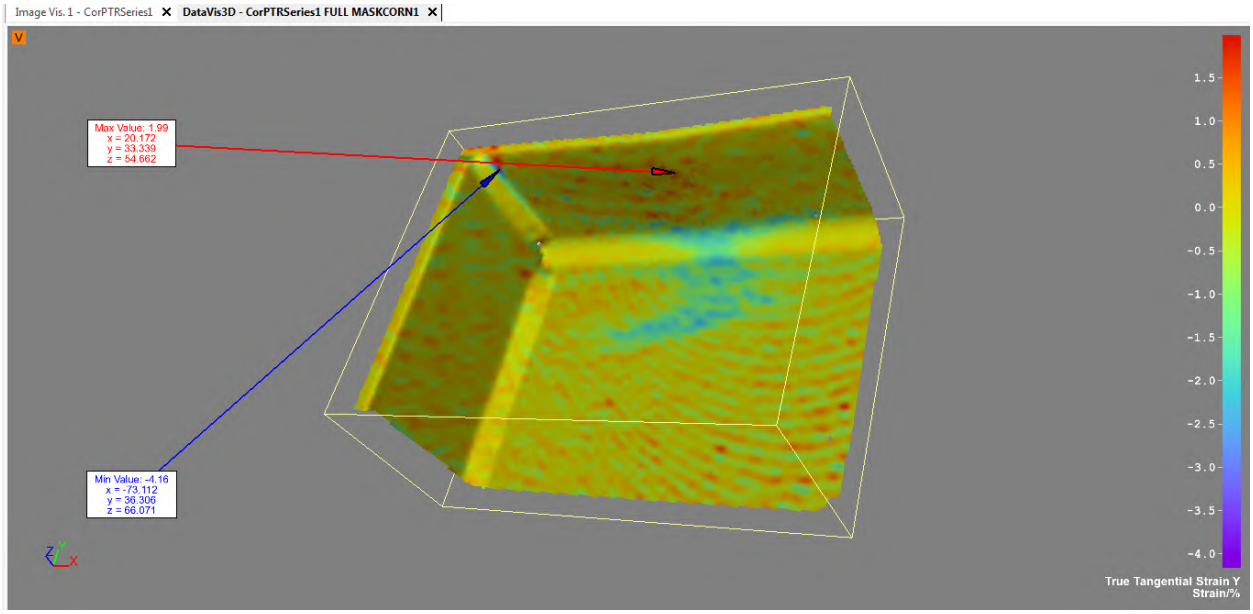

Figure C-85: W12X26-SC-E4 showing true tangential strain Y at a load of 70 kips

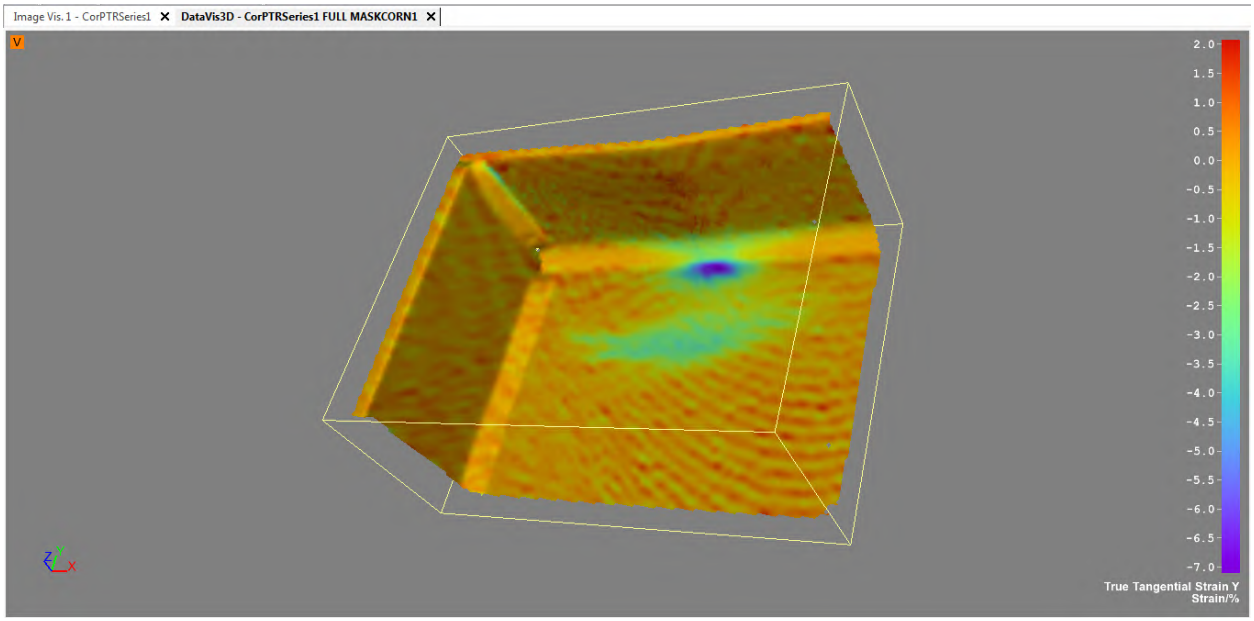

Figure C-86: W12X26-SC-E4 showing true tangential strain Y at a load of 78.2 kips

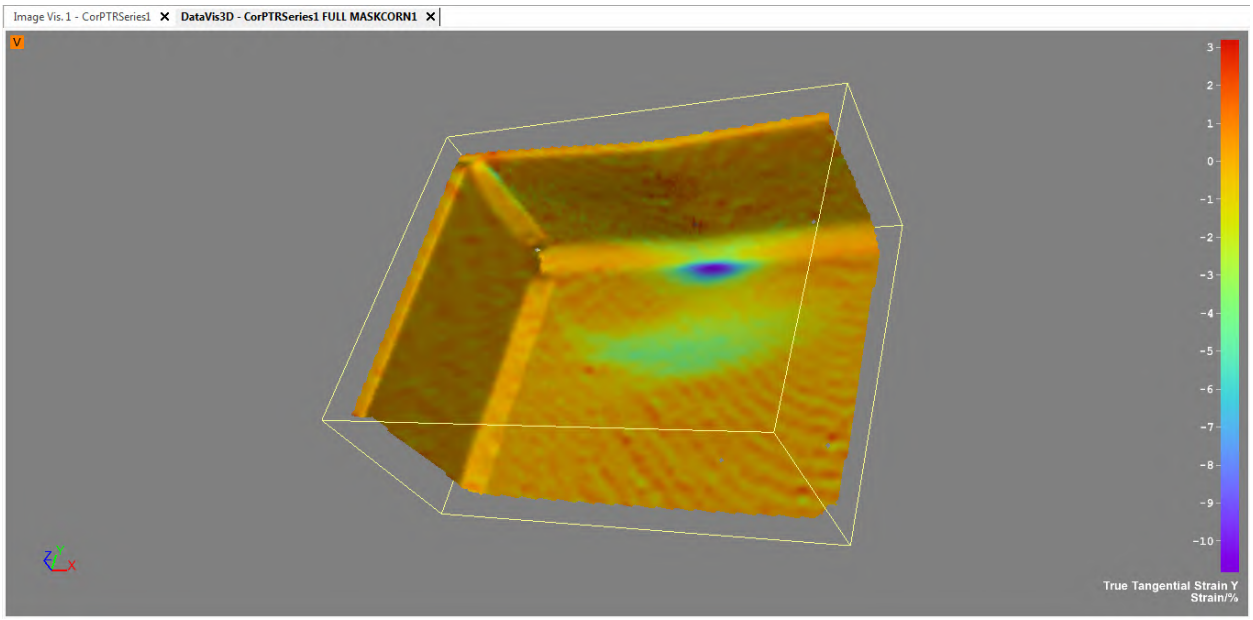

Figure C-87: W12X26-SC-E4 showing true tangential strain Y at its maximum load of 79.2 kips

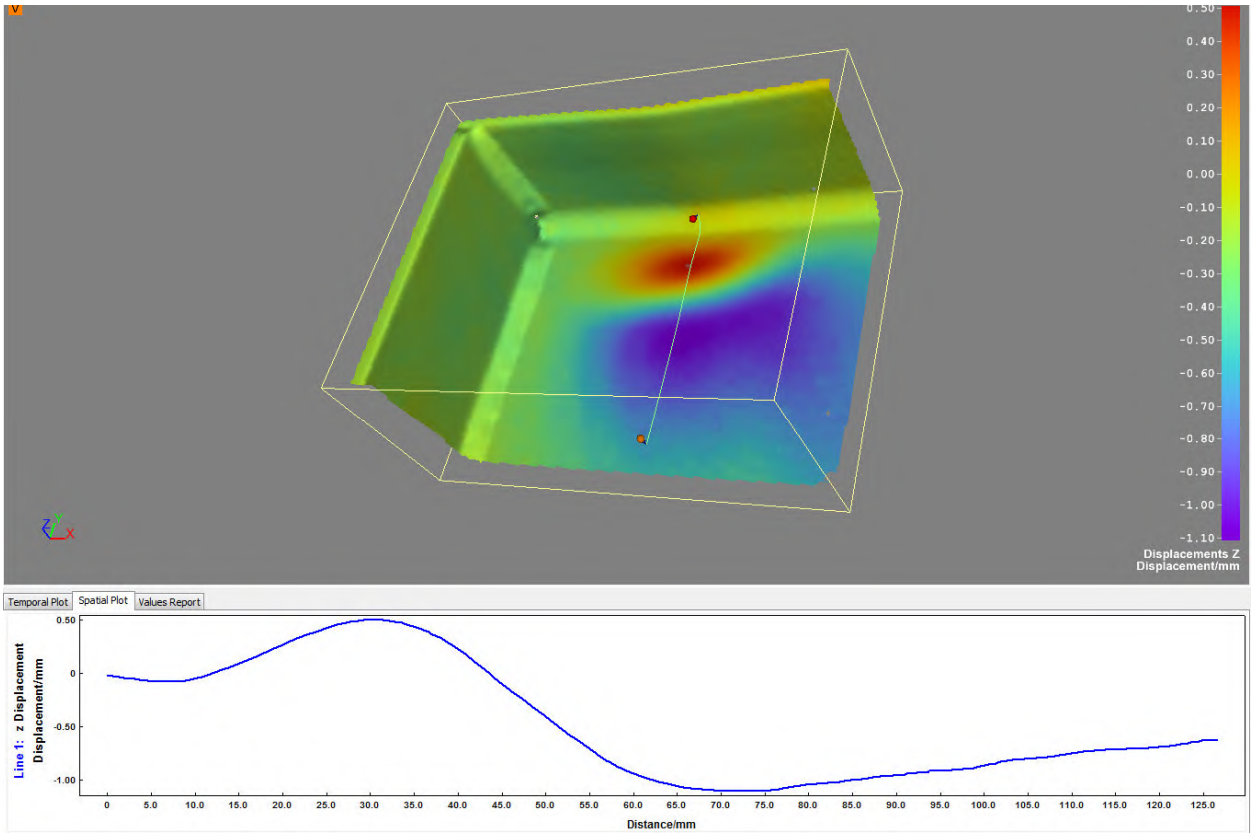

Figure C-88: W12X26-SC-E4 showing out of plane displacement Z at a load of 78.2 kips

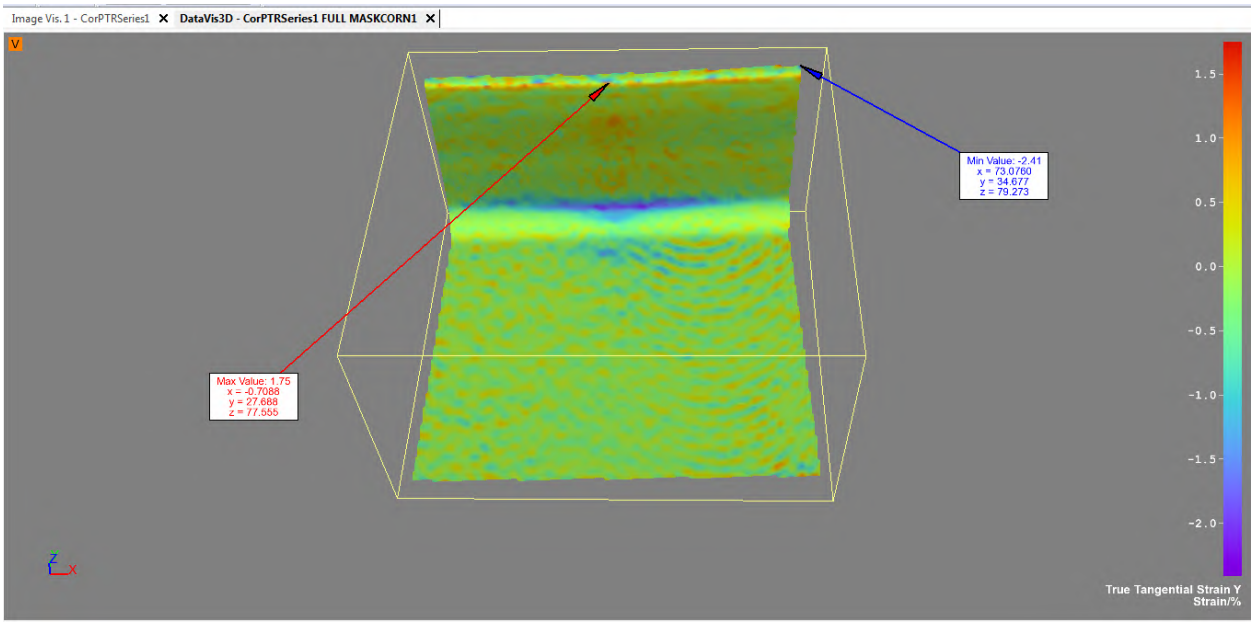

Figure C-89: W12X26-SC-NA showing true tangential strain Y at a load of 59 kips

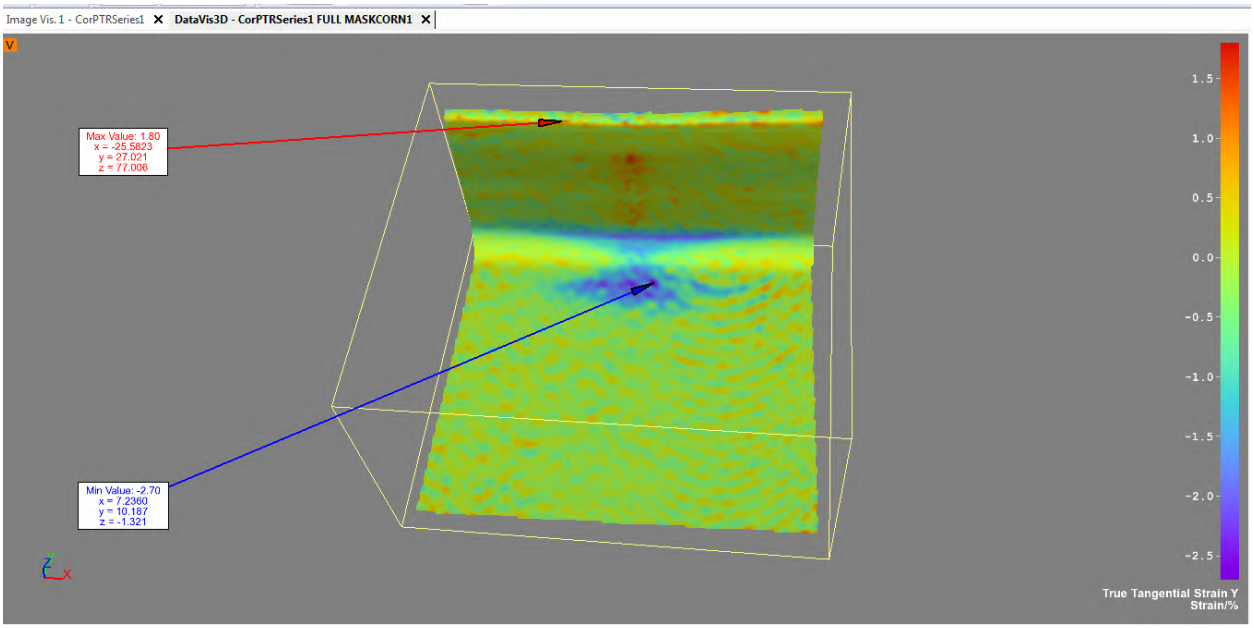

Figure C-90: W12X26-SC-NA showing true tangential strain Y at a load of 70 kips

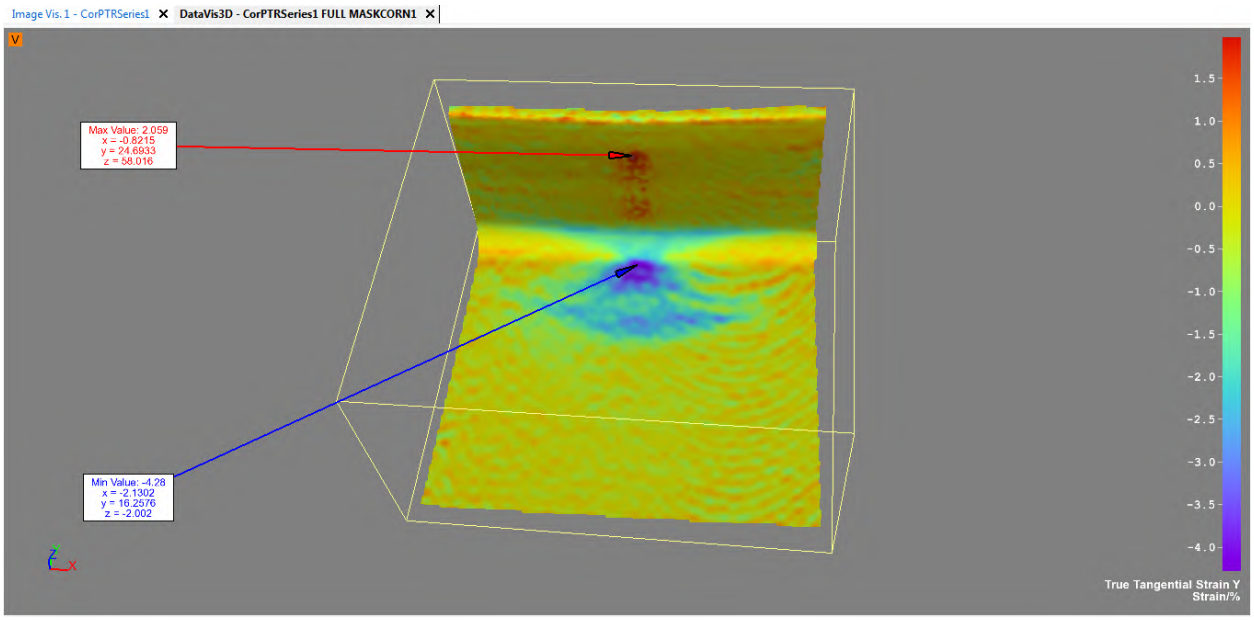

Figure C-91: W12X26-SC-NA showing true tangential strain Y at its maximum load of 78.2 kips

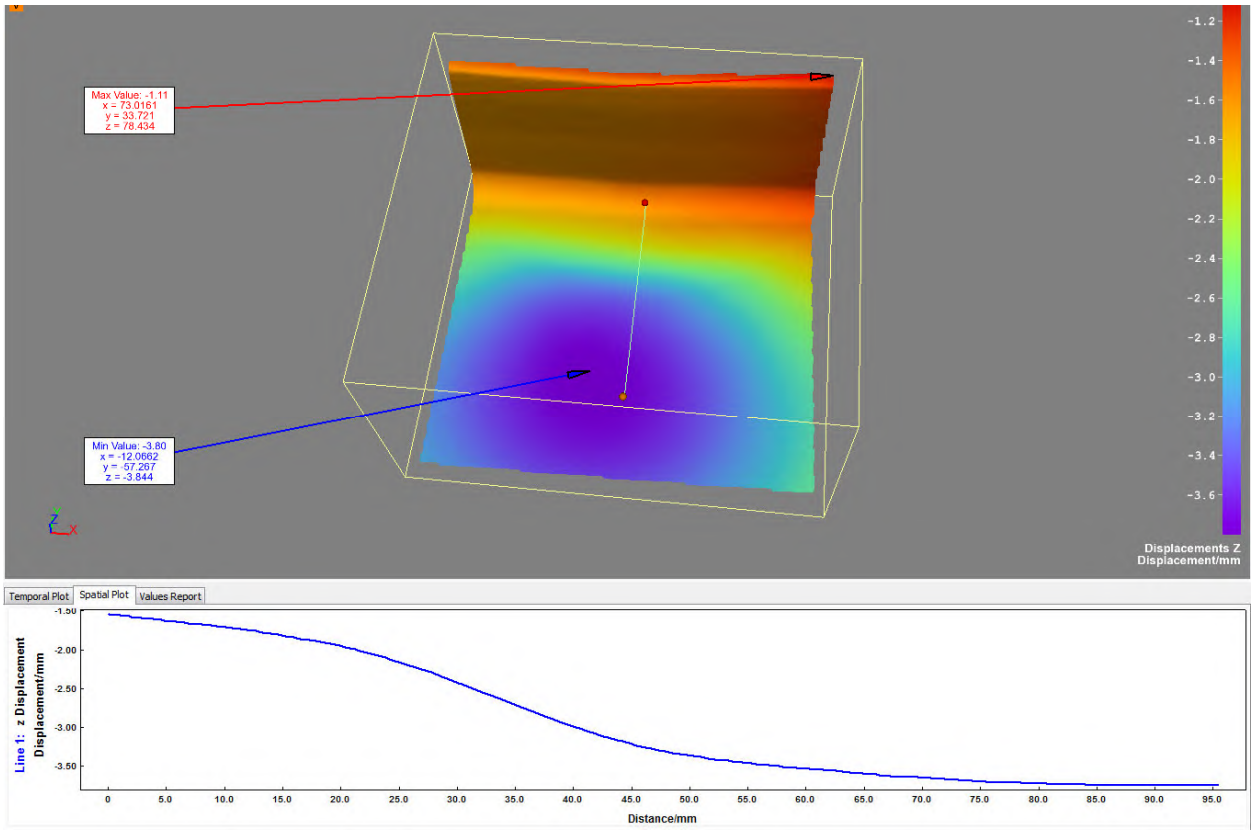

Figure C-92: W12X26-SC-NA showing out of plane displacement Z at its maximum load of 78.2 kips

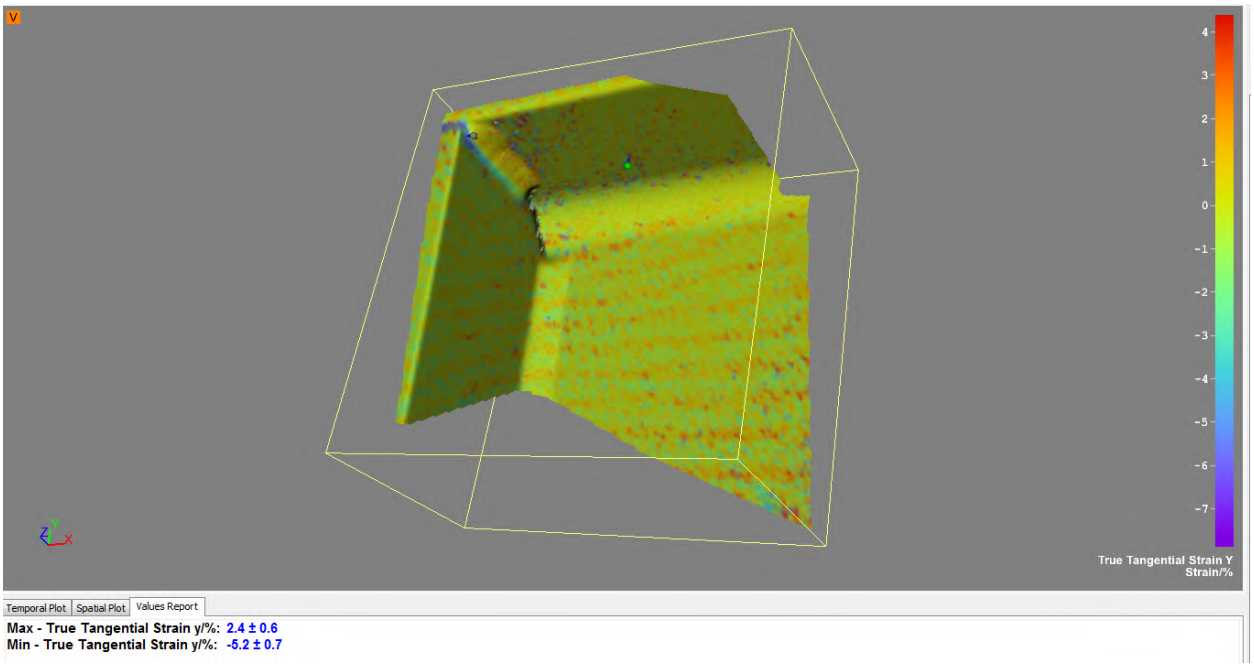

Figure C-93: W16X31-DC-E0 showing true tangential strain Y at a load of 82 kips

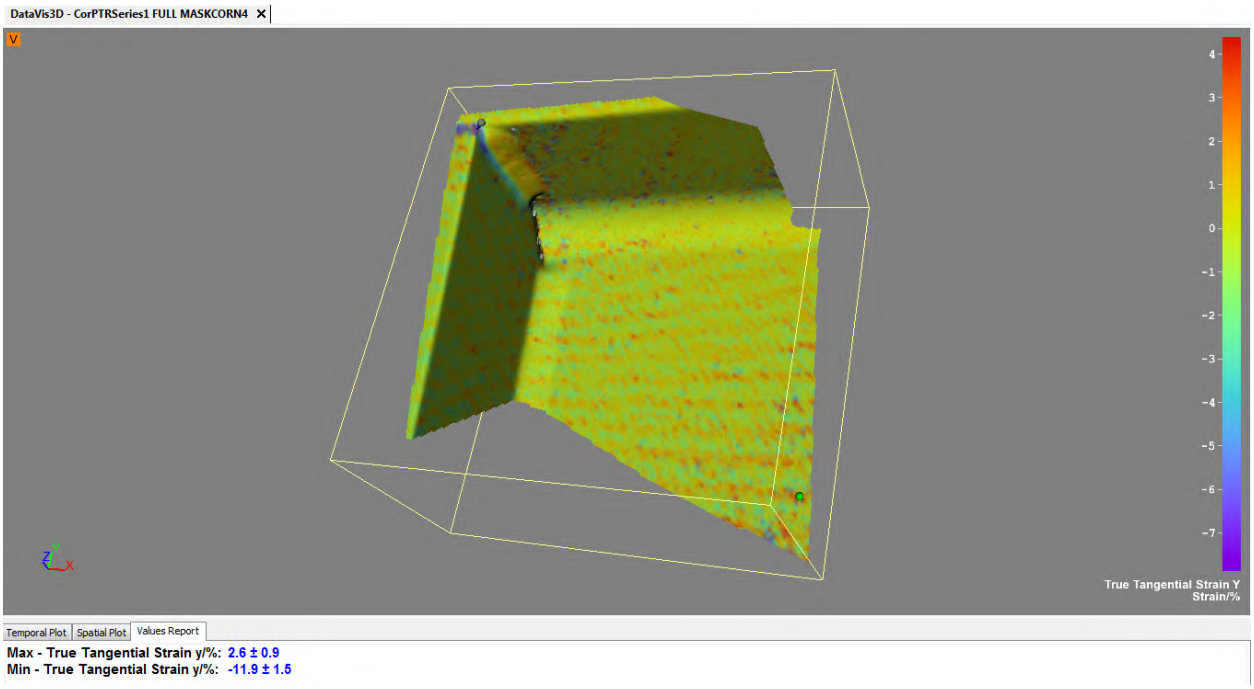

Figure C-94: W16X31-DC-E0 showing true tangential strain Y at a load of 101 kips

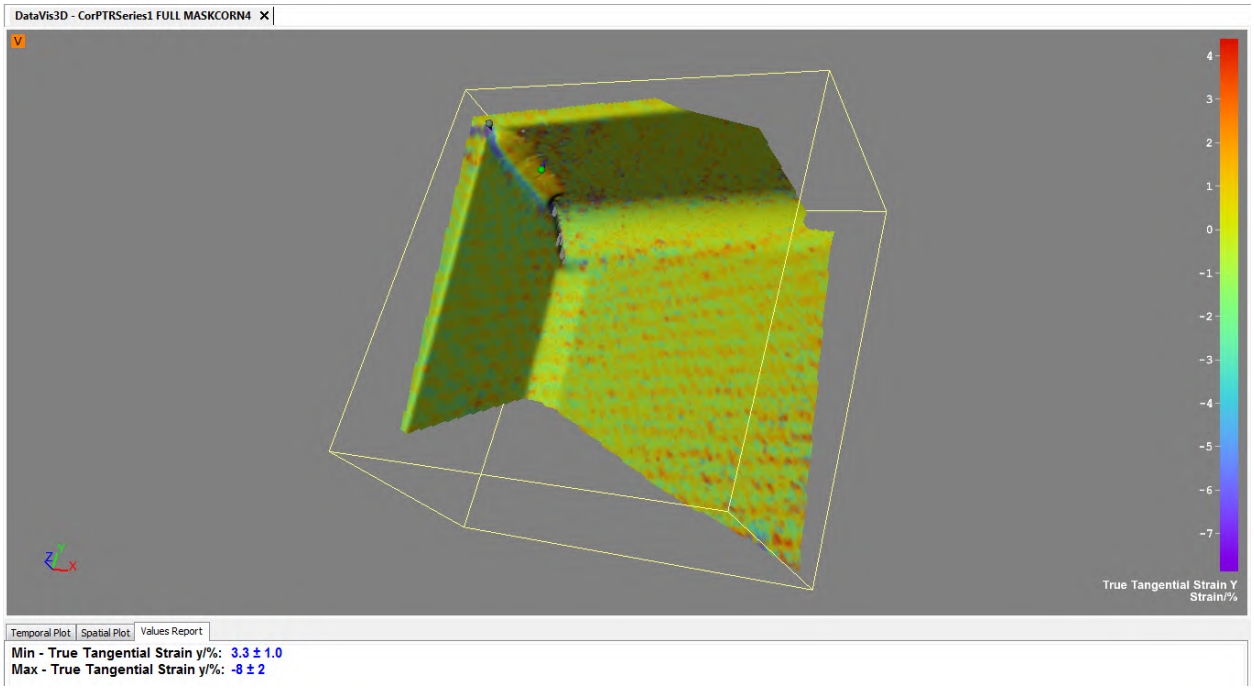

Figure C-95: W16X31-DC-E0 showing true tangential strain Y at a load of 119.7 kips

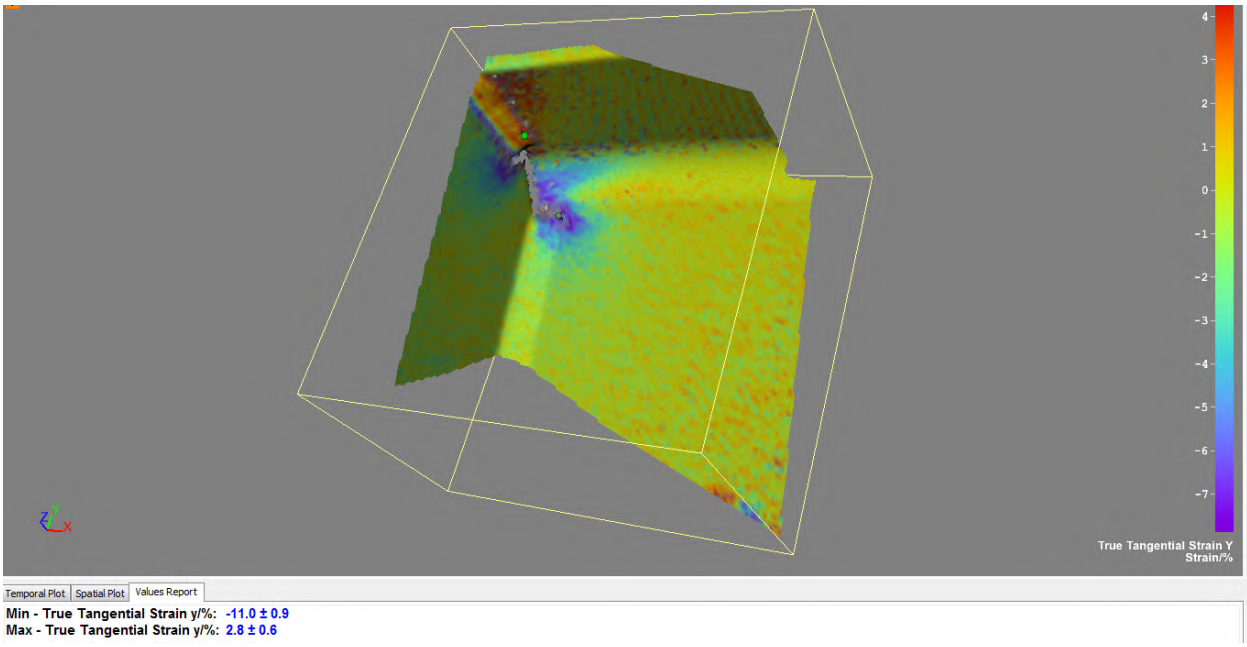

Figure C-96: W16X31-DC-E0 showing true tangential strain Y at its maximum load of 163.2 kips

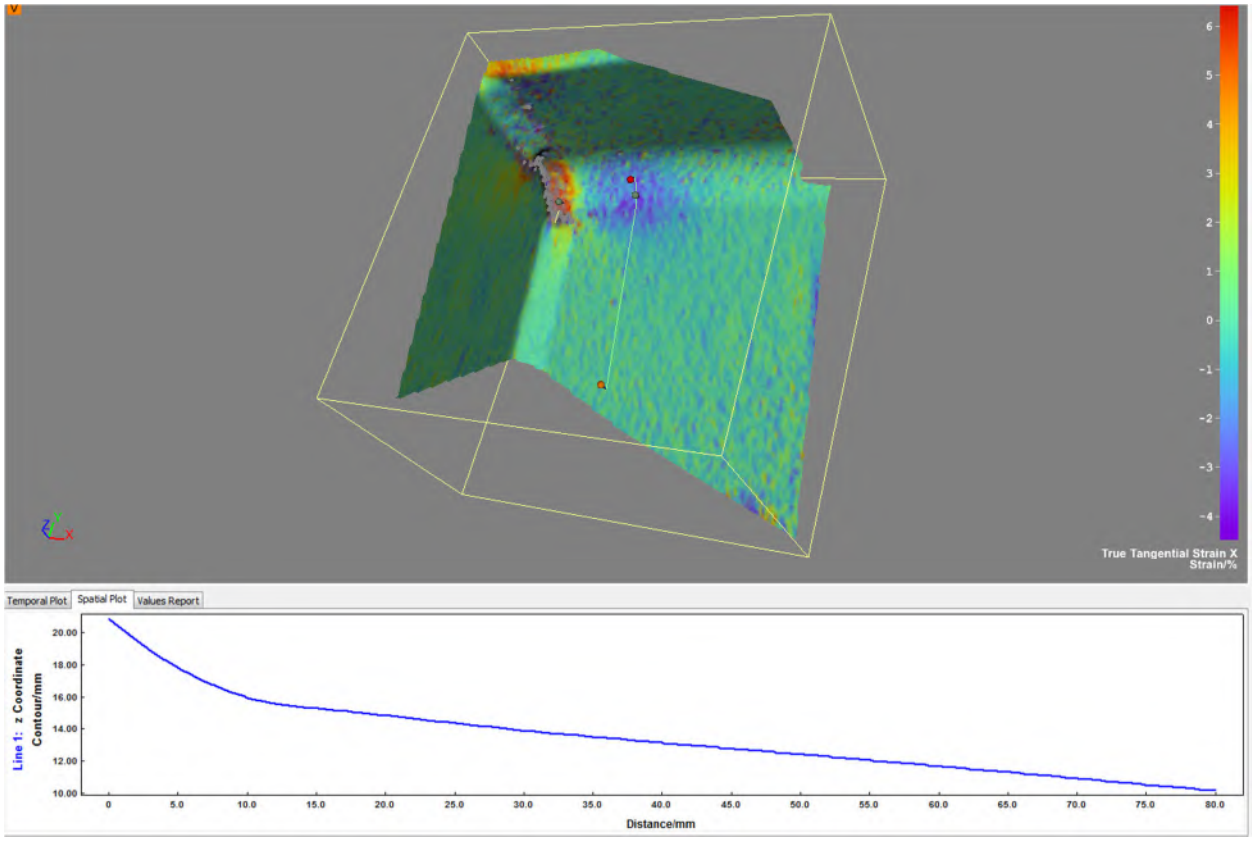

Figure C-97: W16X31-DC-E0 showing out of plane displacement at its maximum load of 163.2 kips

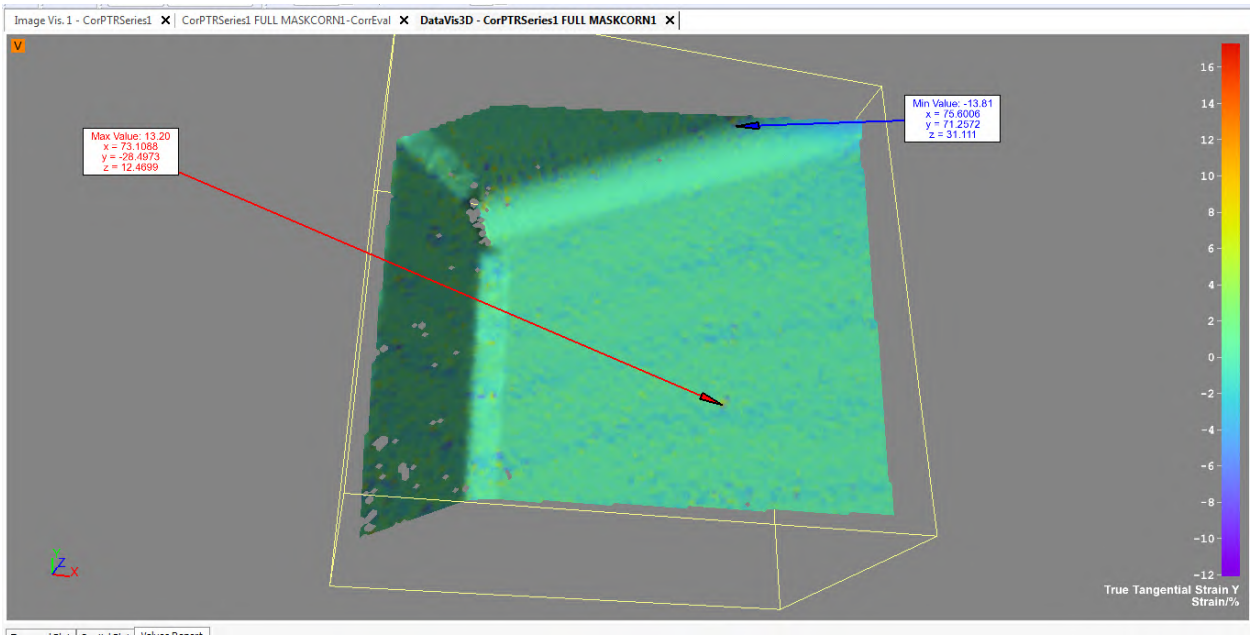

Figure C-98: W16X31-DC-E6 showing true tangential strain Y at a load of 82 kips

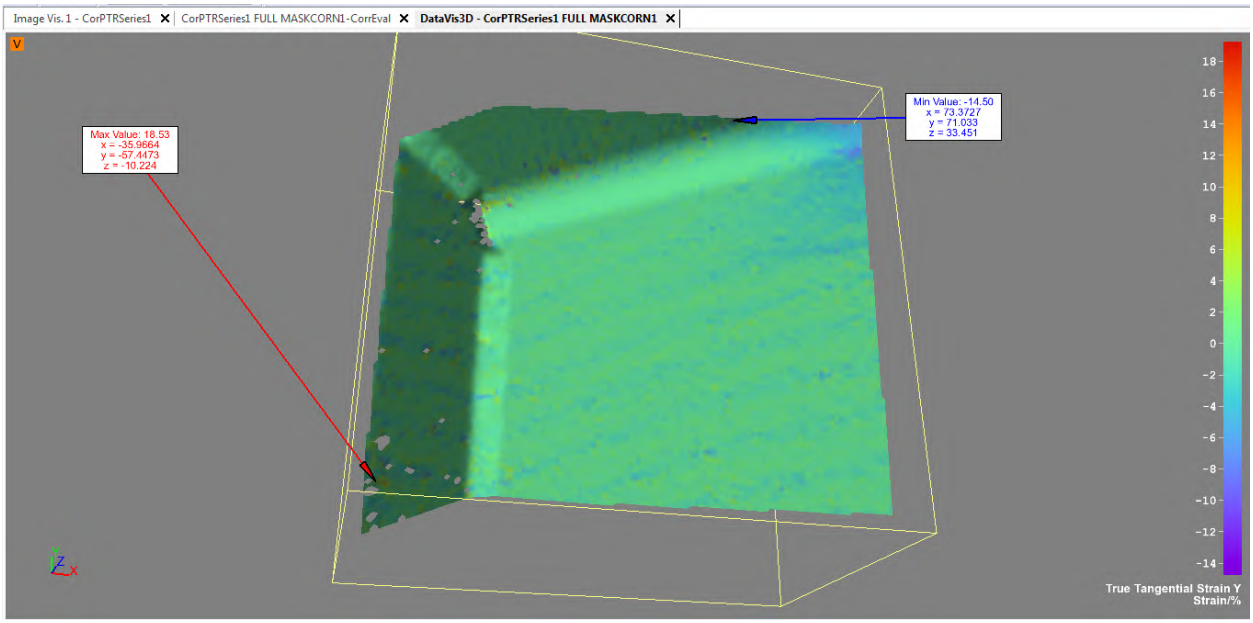

Figure C-99: W16X31-DC-E6 showing true tangential strain Y at a load of 101 kips

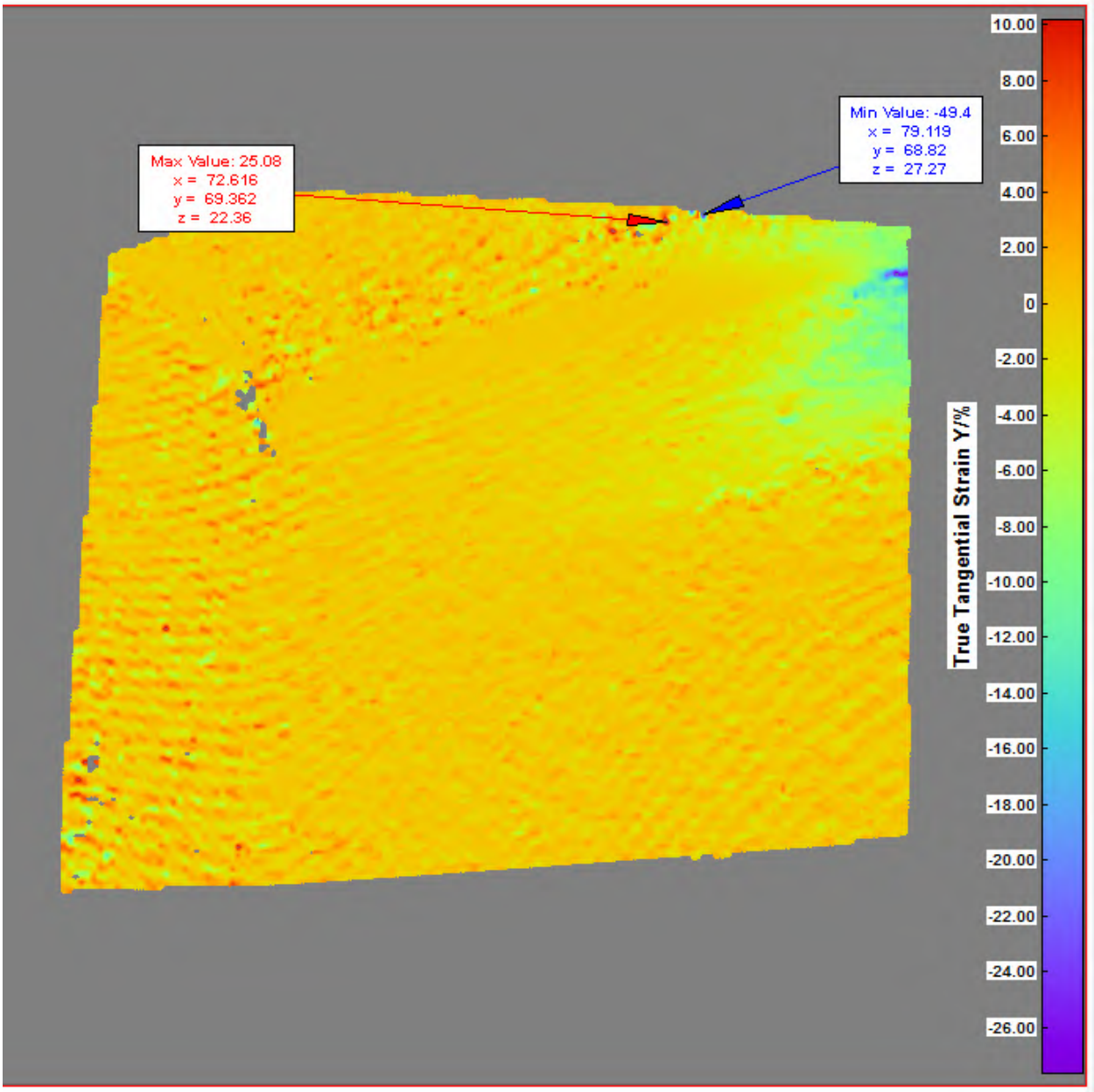

Figure C-100: W16X31-DC-E6 showing true tangential strain Y at its maximum load of 117.4 kips

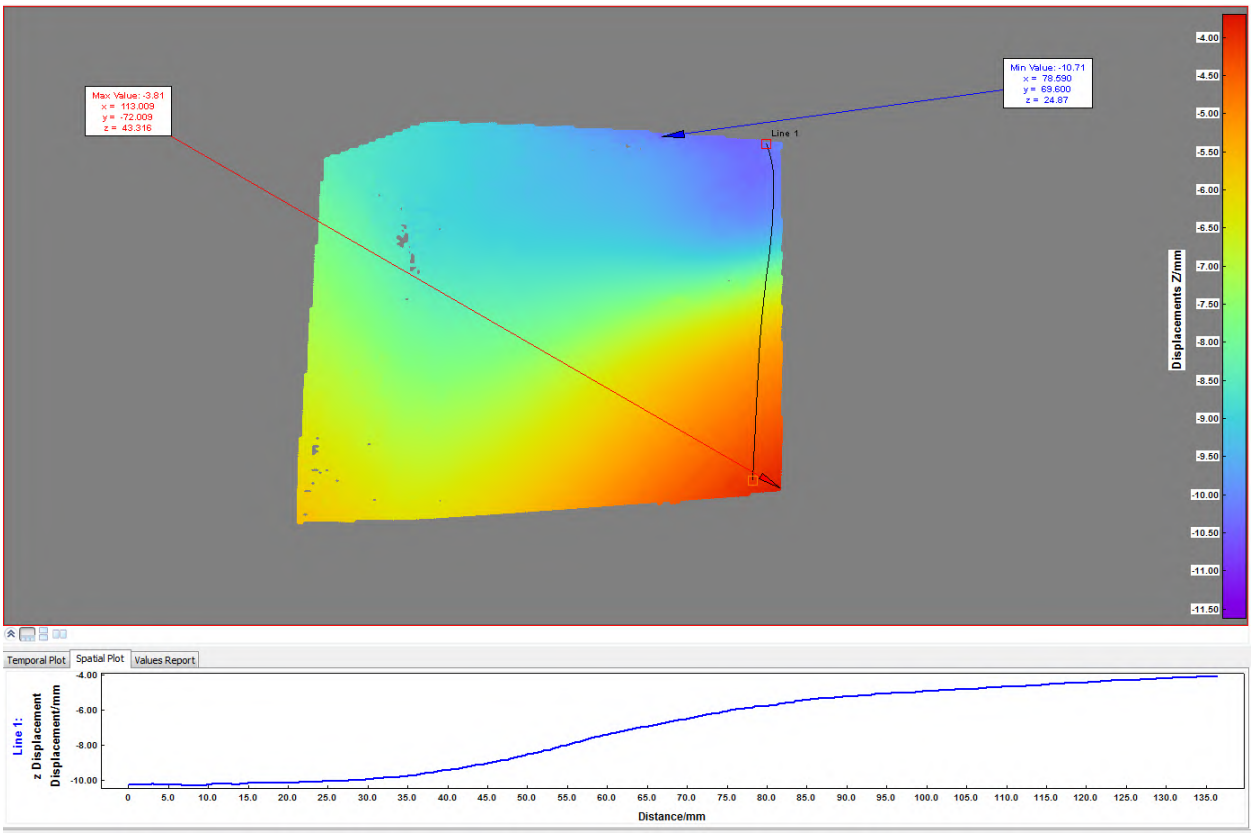

Figure C-101: W16X31-DC-E6 showing out of plane displacement at its maximum load of 117.4 kips

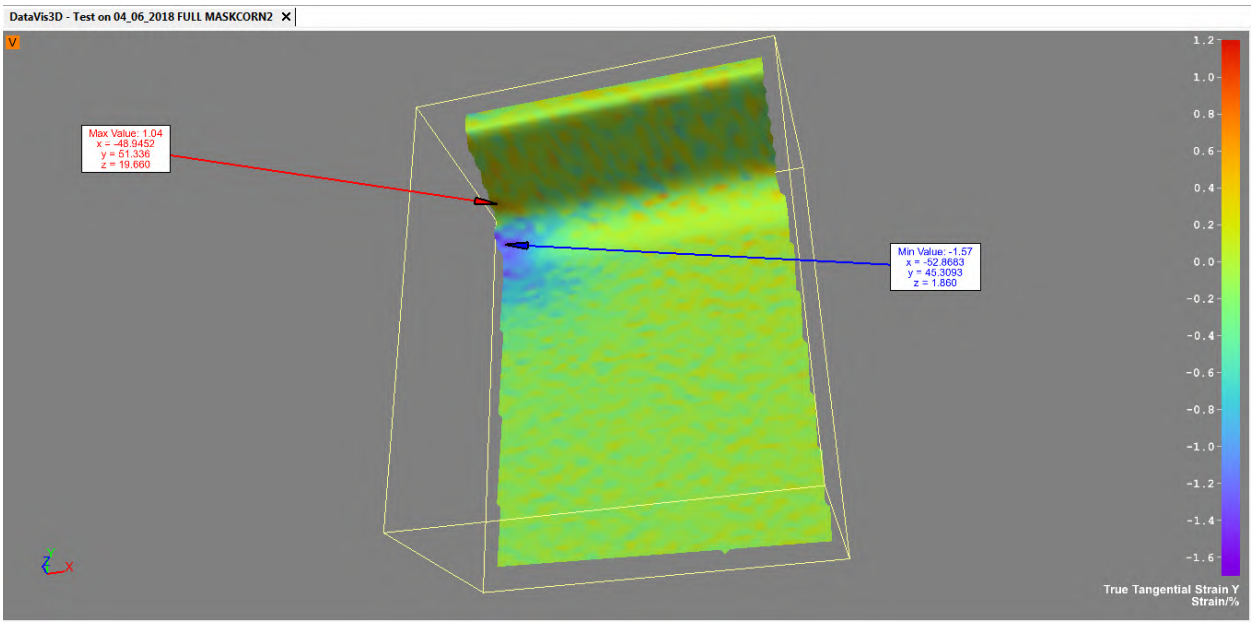

Figure C-102: W16X31-DC-NA showing true tangential strain Y at a load of 82 kips

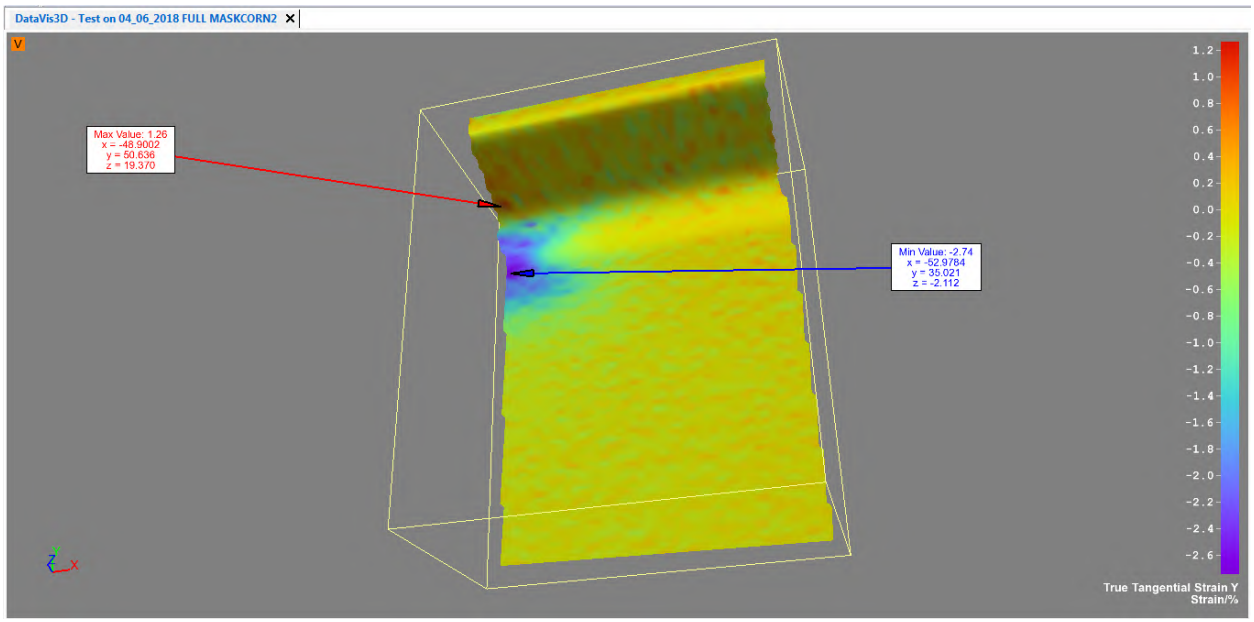

Figure C-103: W16X31-DC-NA showing true tangential strain Y at a load of 101 kips

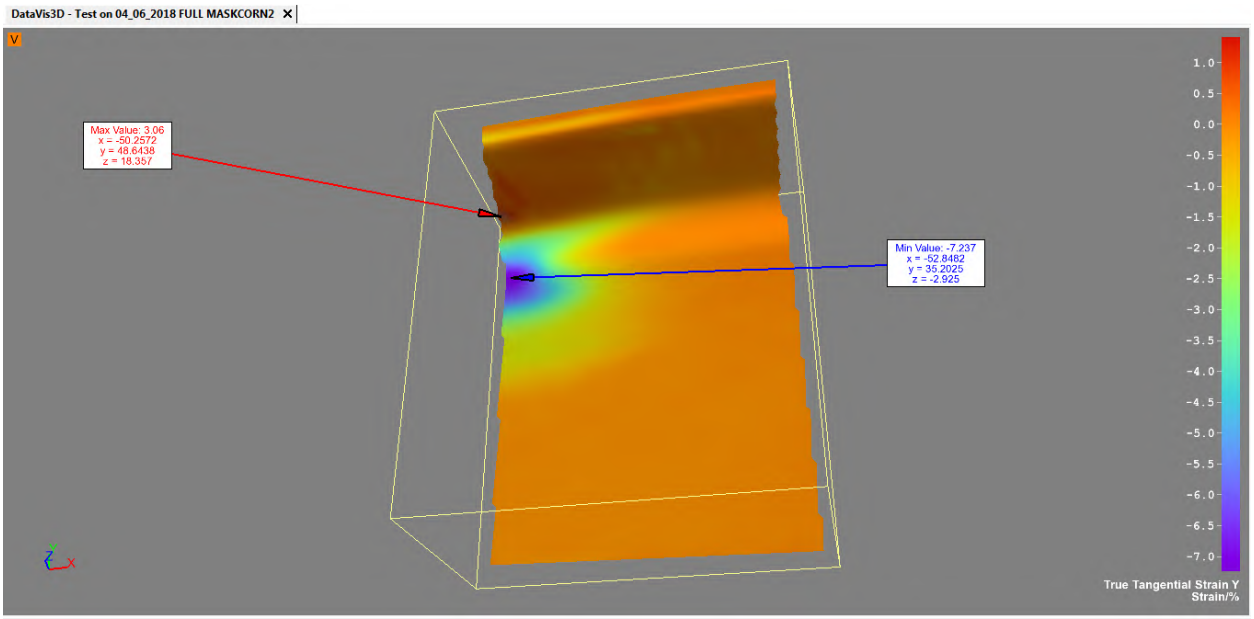

Figure C-104: W16X31-DC-NA showing true tangential strain Y at its maximum load of 119.7 kips

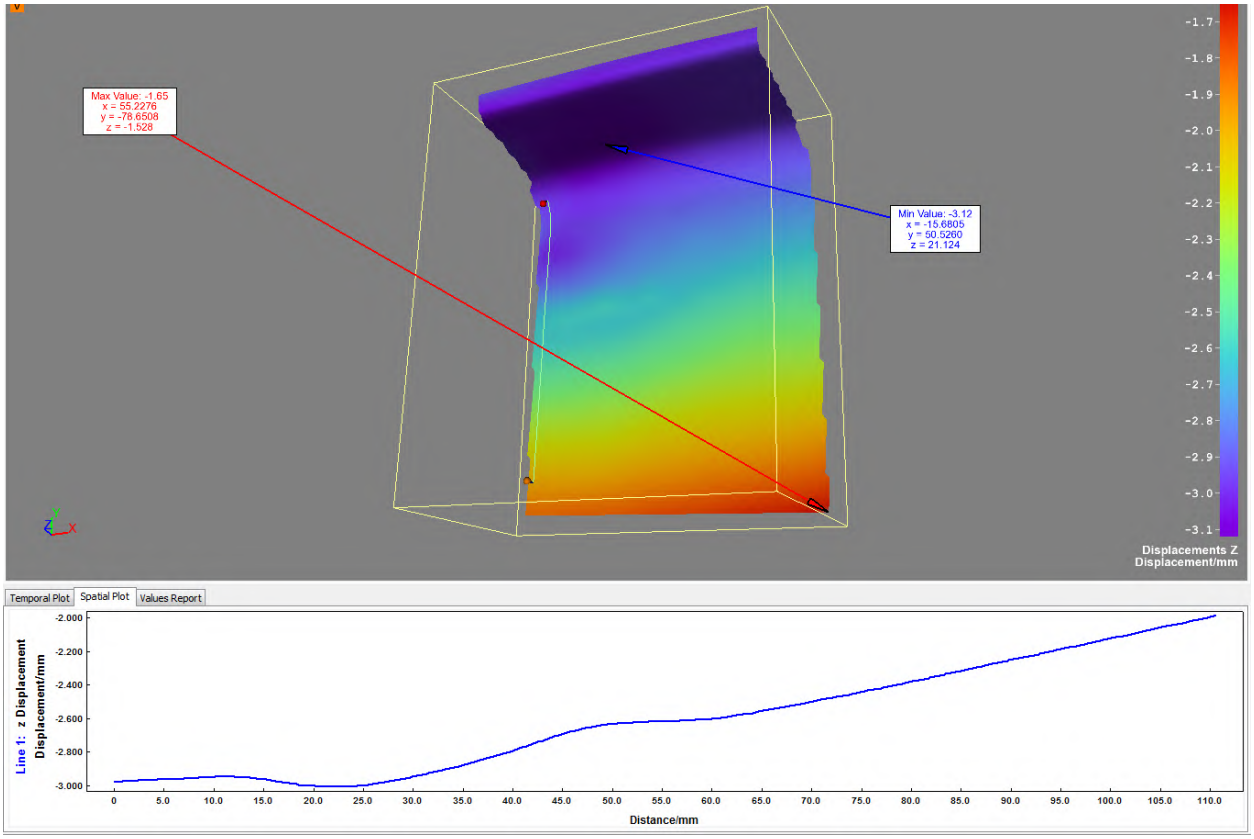

Figure C-105: W16X31-DC-NA showing out of plane displacement at its maximum load of 119.7 kips

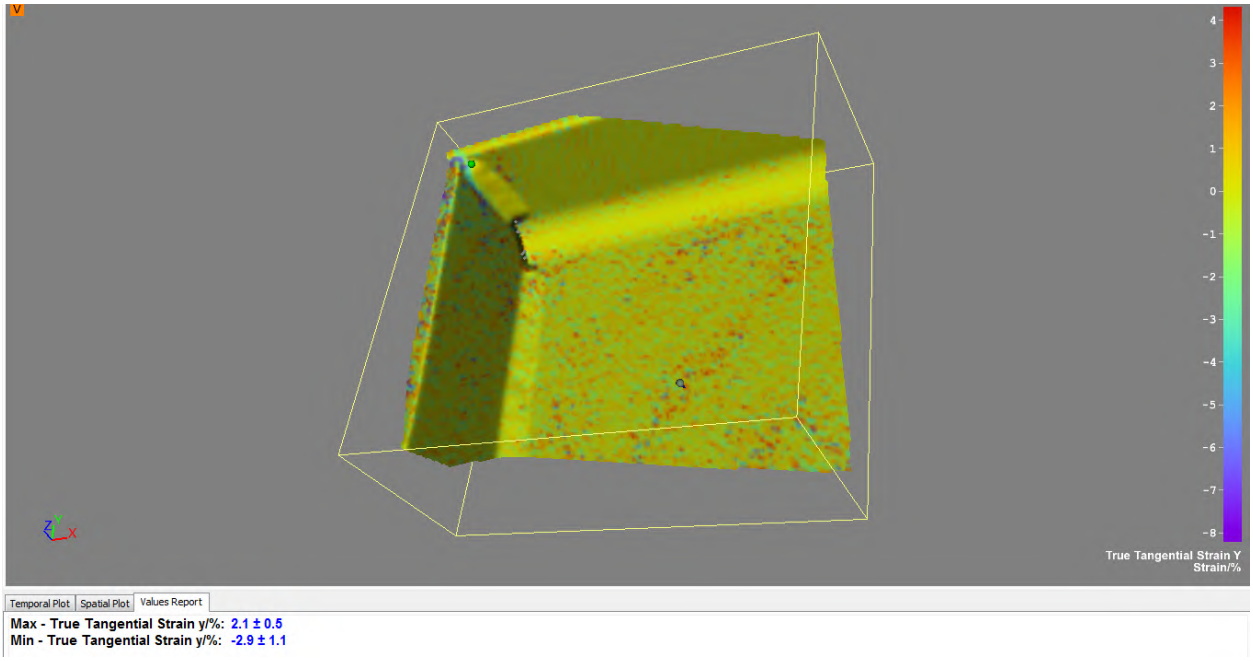

Figure C-106: W16X31-SC-E0 showing true tangential strain Y at a load of 82 kips

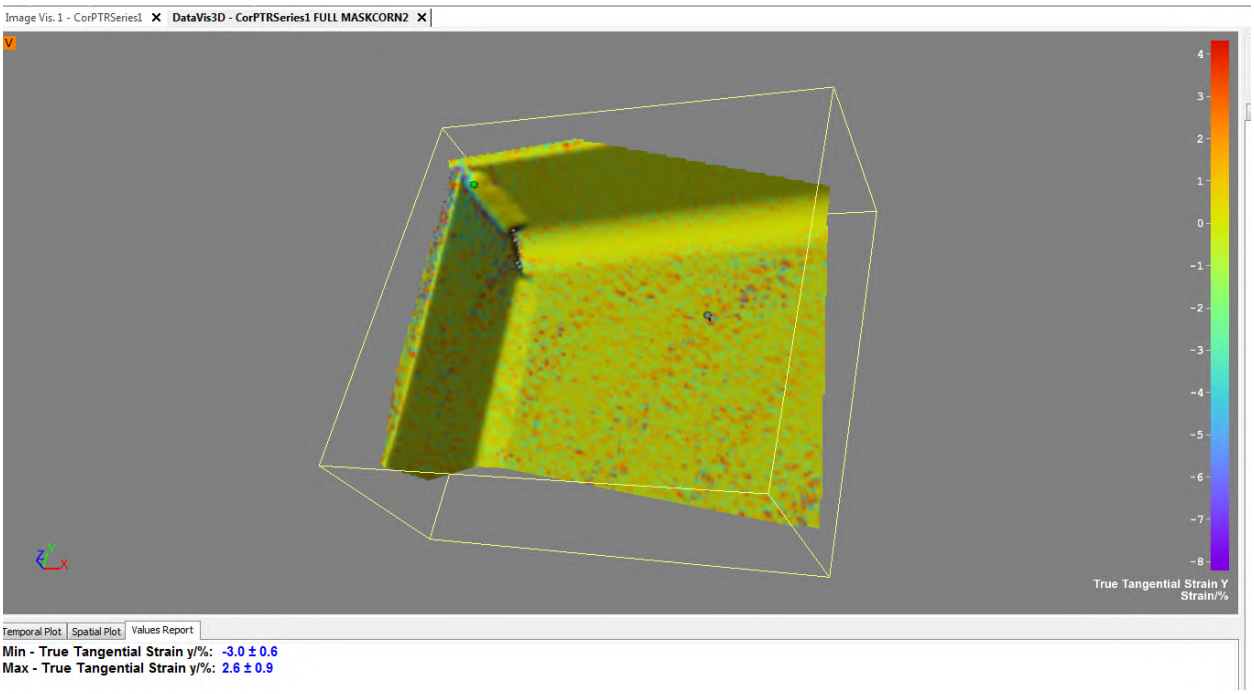

Figure C-107: W16X31-SC-E0 showing true tangential strain Y at a load of 96 kips

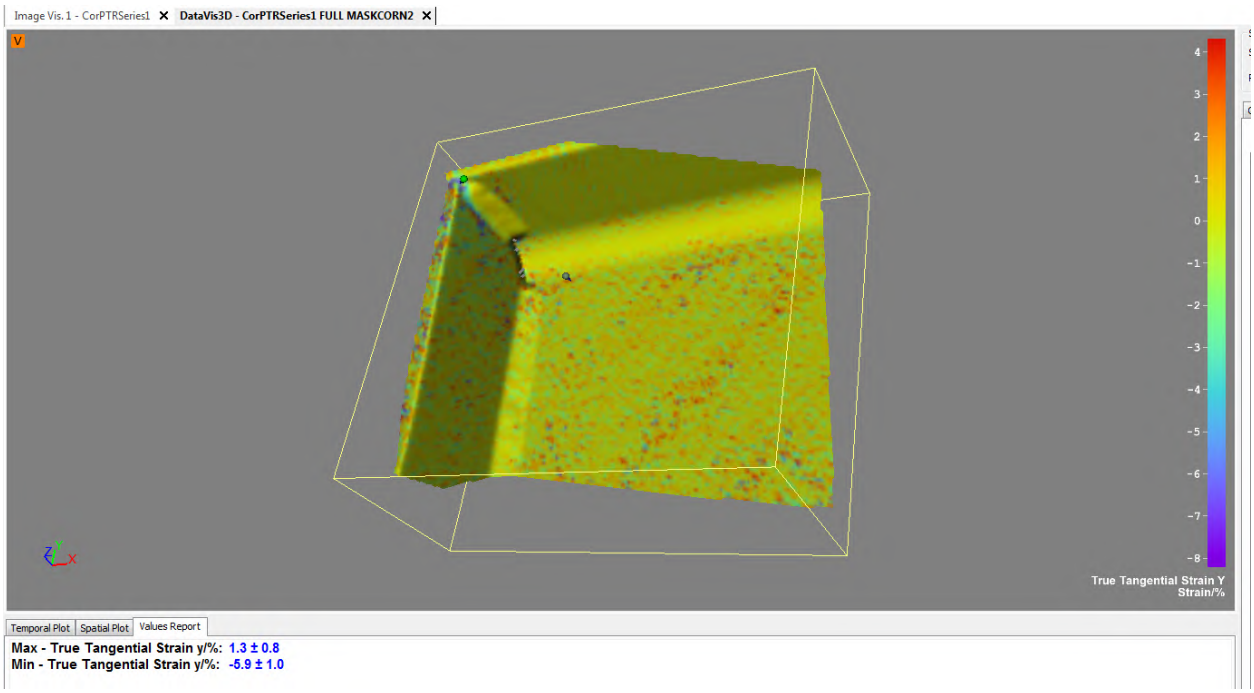

Figure C-108: W16X31-SC-E0 showing true tangential strain Y at a load of 112.4 kips

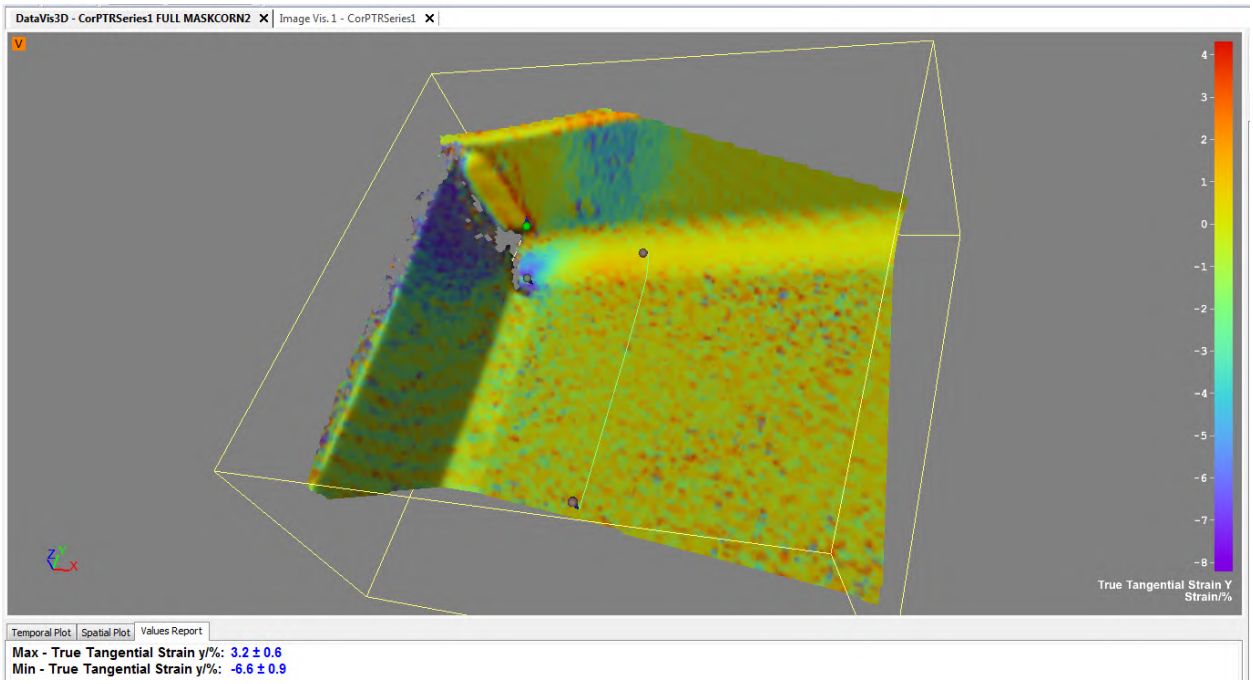

Figure C-109: W16X31-SC-E0 showing true tangential strain Y at its maximum load of 176.8 kips

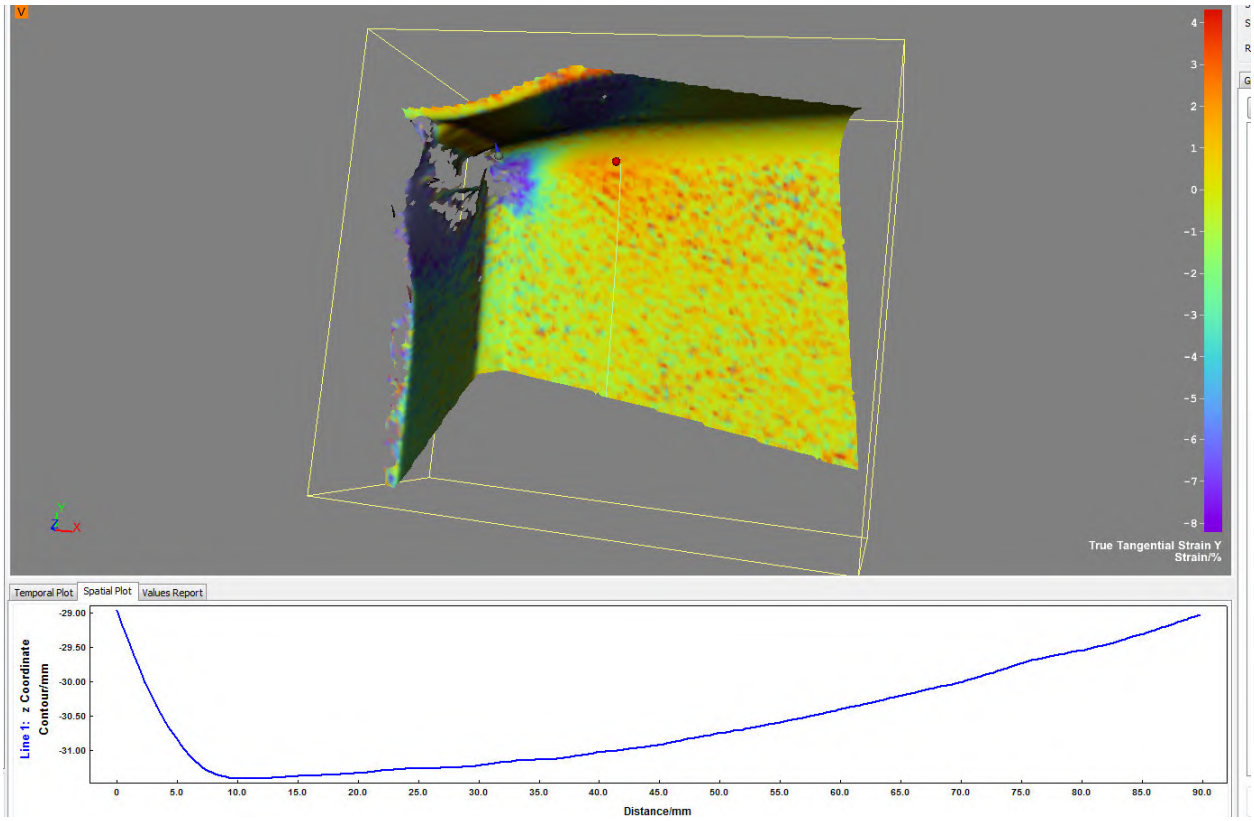

Figure C-110: W16X31-SC-E0 showing out of plane displacement at its maximum load of

176.8 kips

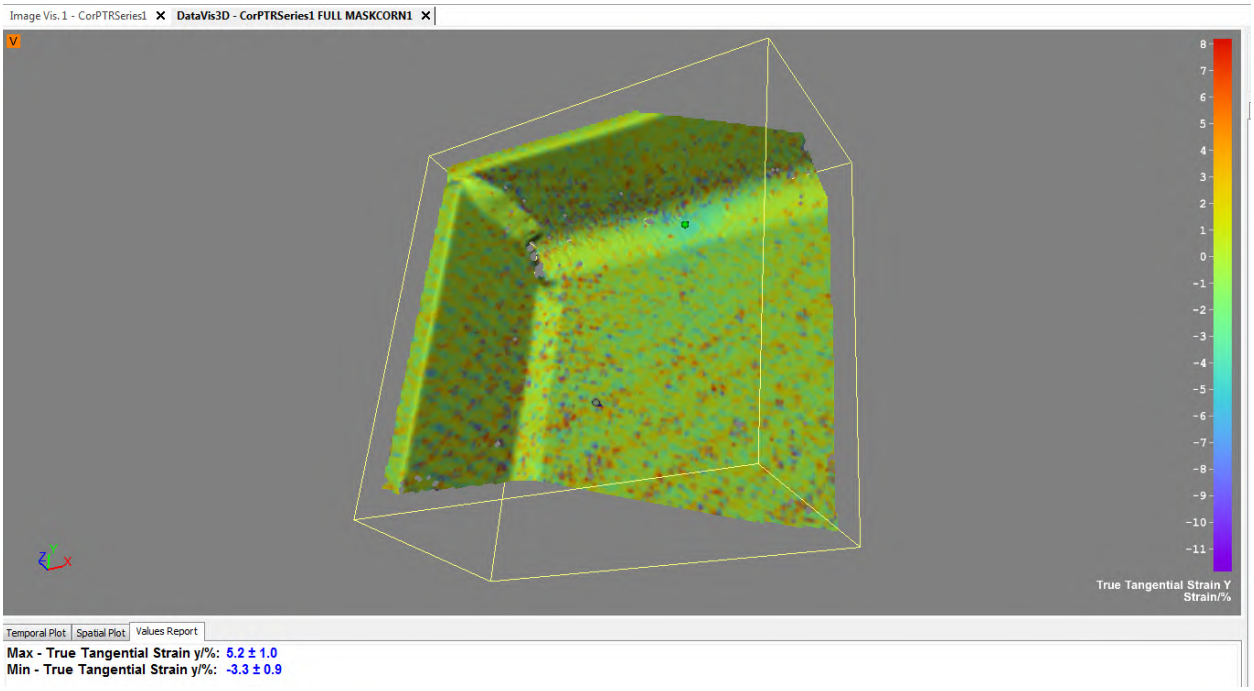

Figure C-111: W16X31-SC-E3 showing true tangential strain Y at a load of 82 kips

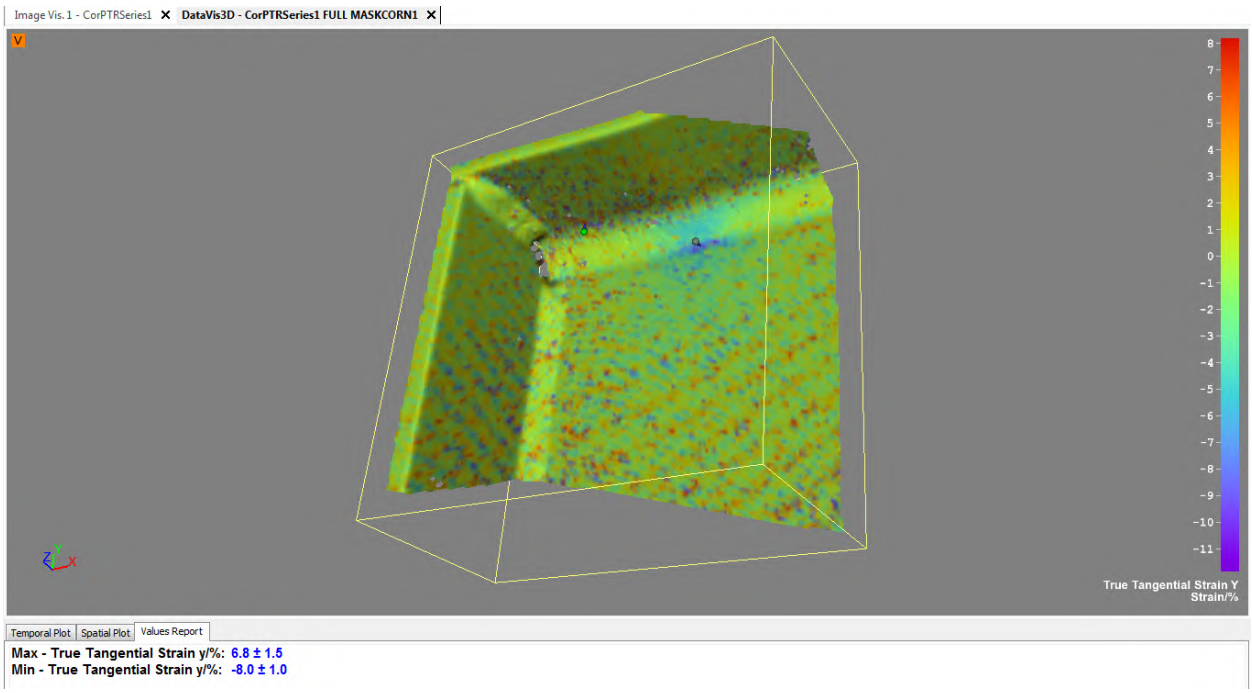

Figure C-112: W16X31-SC-E3 showing true tangential strain Y at a load of 96 kips

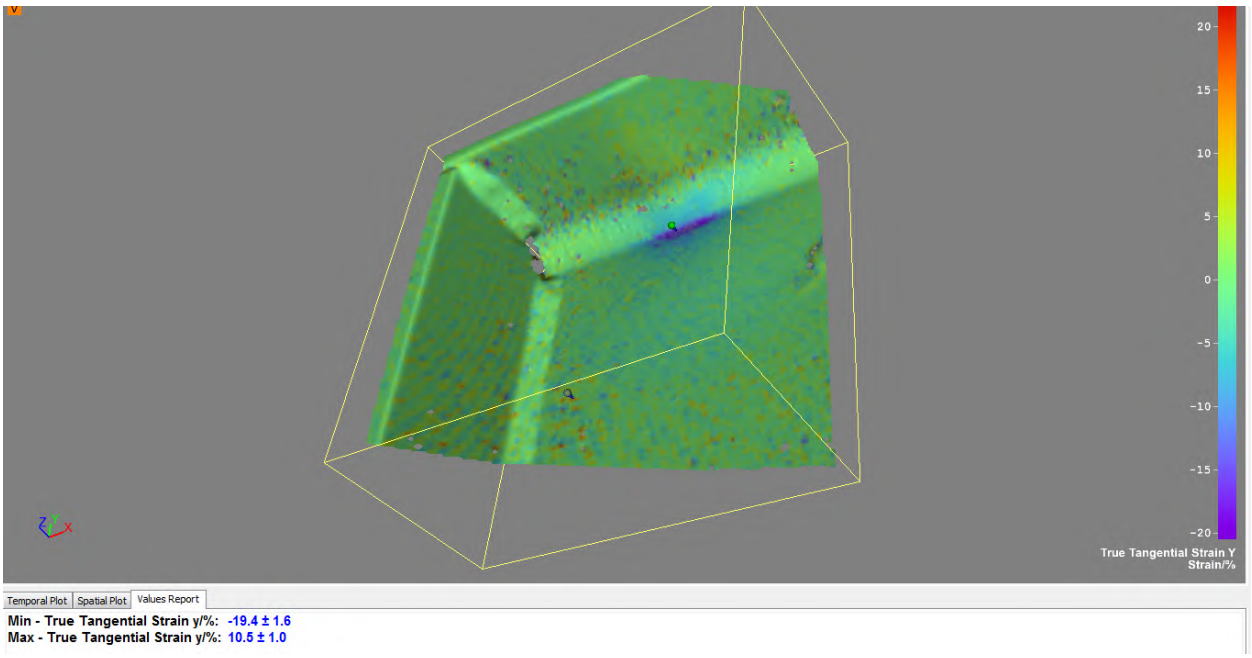

Figure C-113: W16X31-SC-E3 showing true tangential strain Y at its maximum load of 111.2 kips

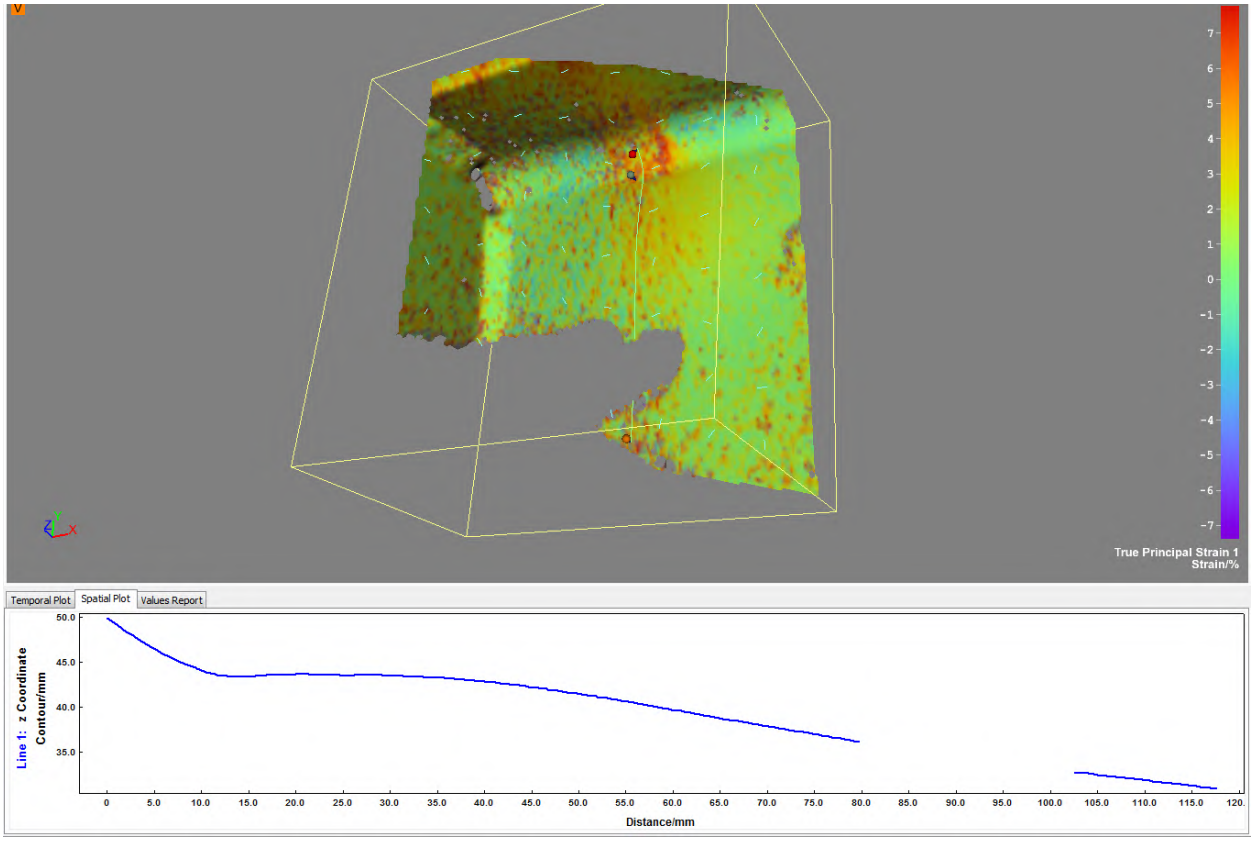

Figure C-114: W16X31-SC-E3 showing out of plane displacement at its maximum load of

111.2 kips

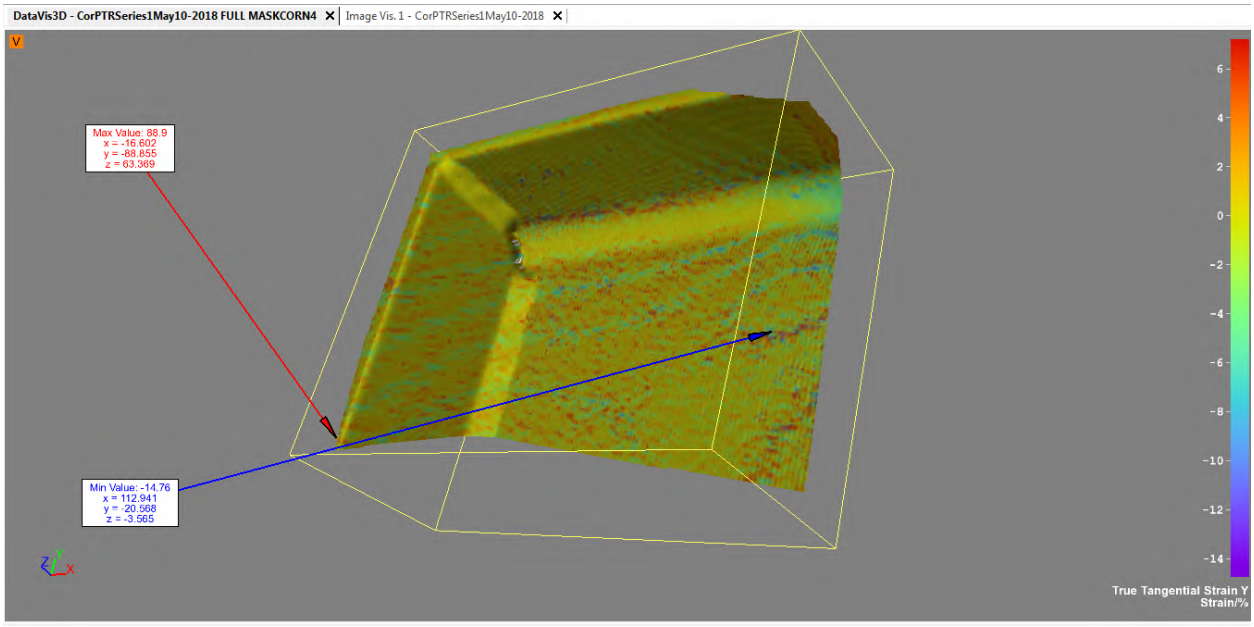

Figure C-115: W16X31-SC-E6 showing true tangential strain Y at a load of 82 kips

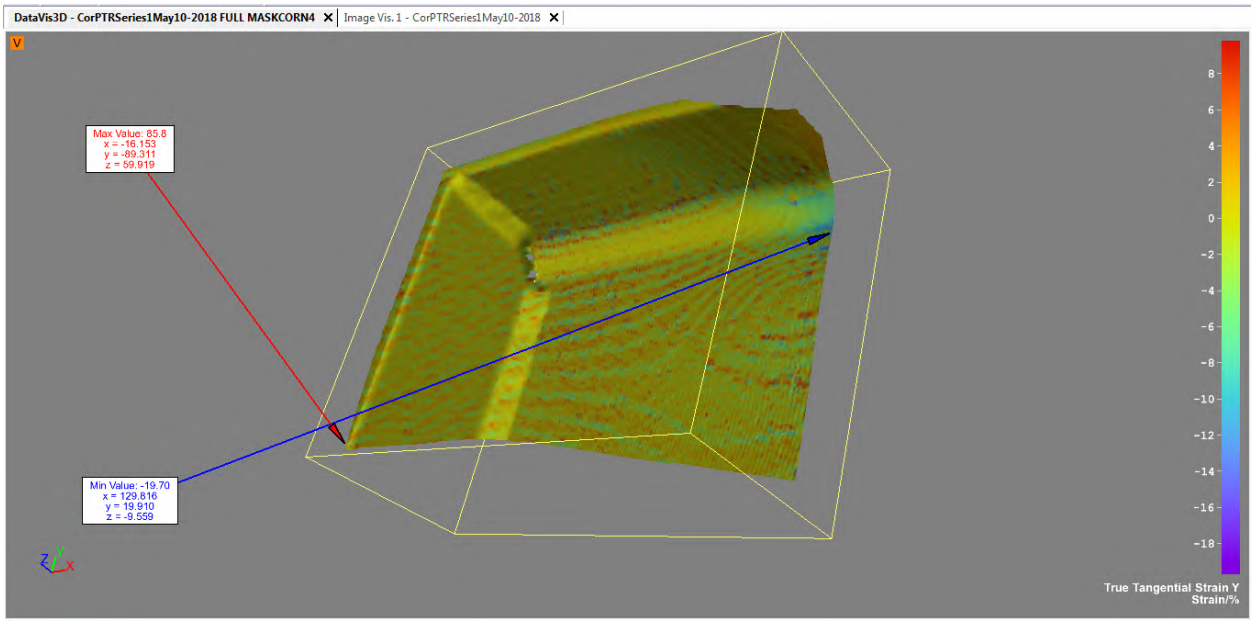

Figure C-116: W16X31-SC-E6 showing true tangential strain Y at a load of 96 kips

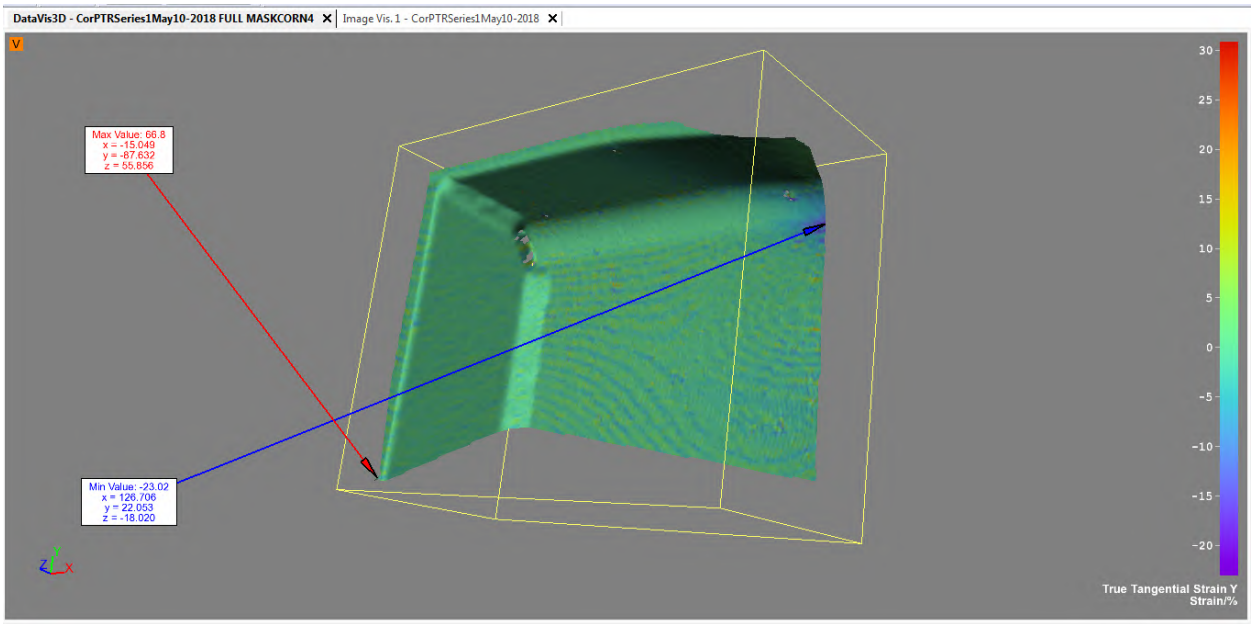

Figure C-117: W16X31-SC-E6 showing true tangential strain Y at its maximum load of 99.3 kips

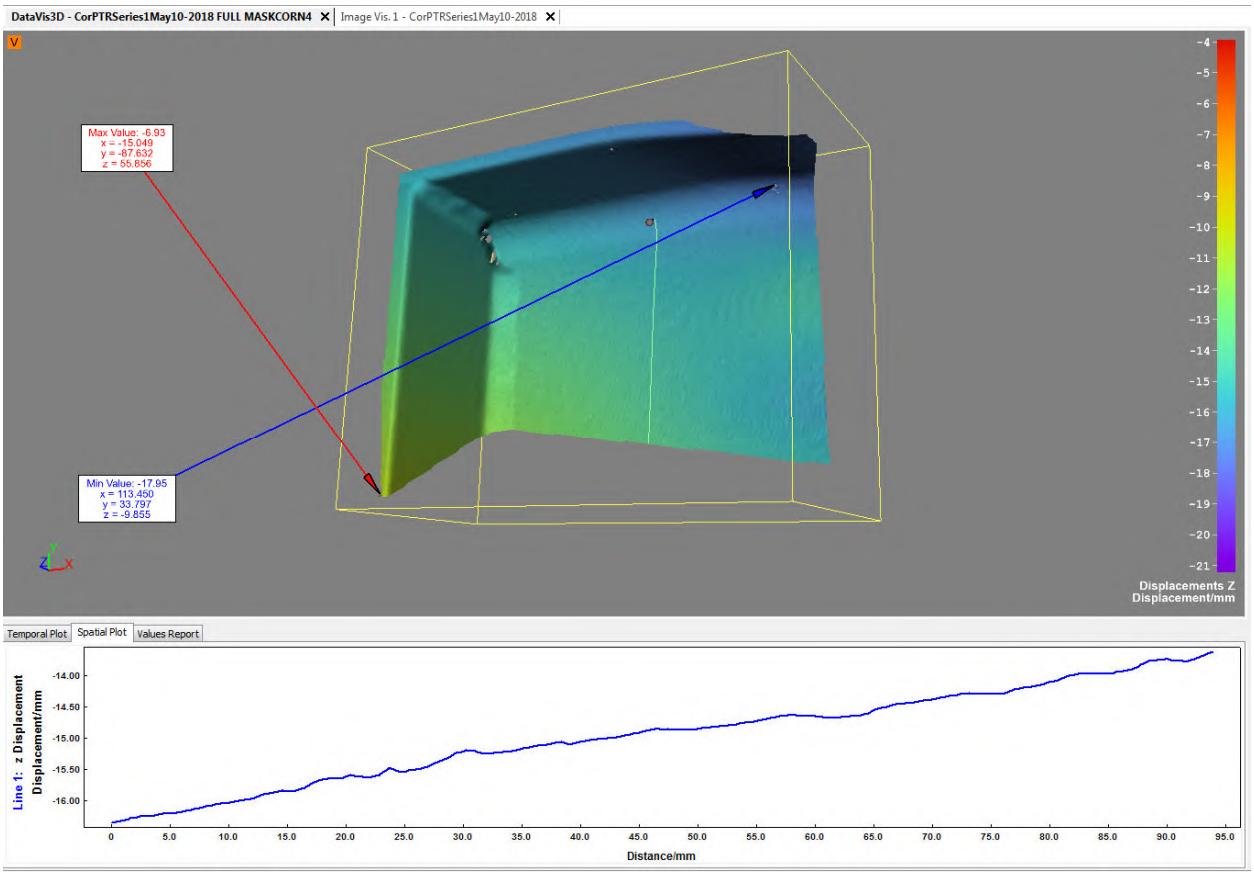

Figure C-118: W16X31-SC-E6 showing out of plane displacement at its maximum load of

99.3 kips

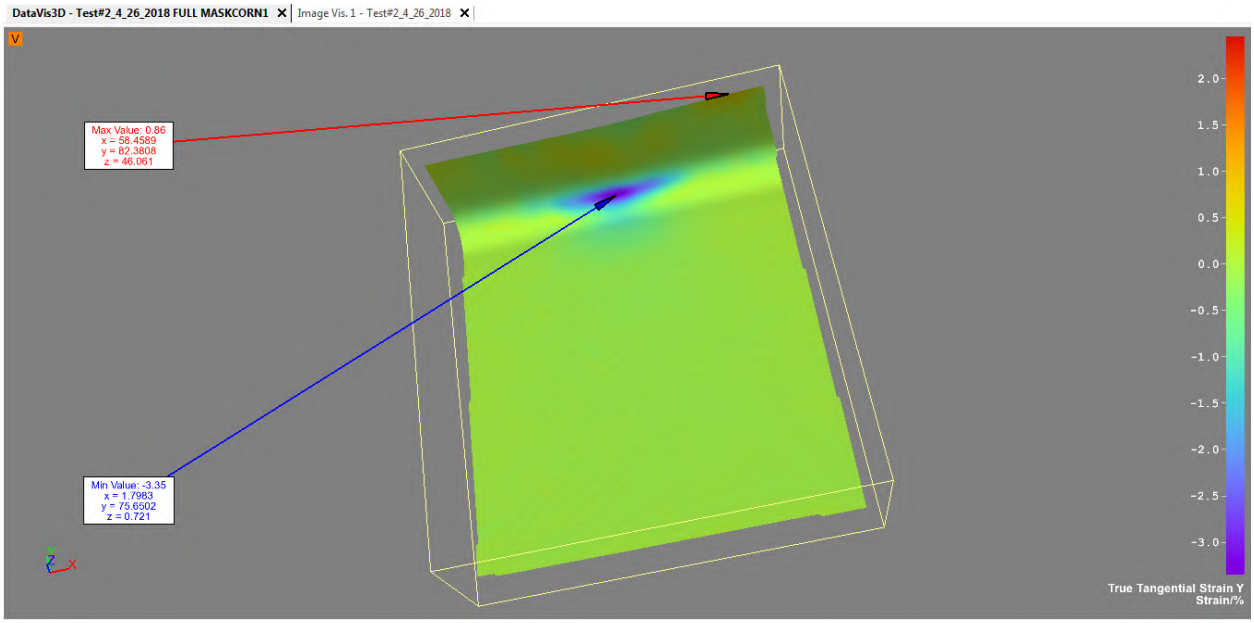

Figure C-119: W16X31-SC-NA showing true tangential strain Y at a load of 82 kips

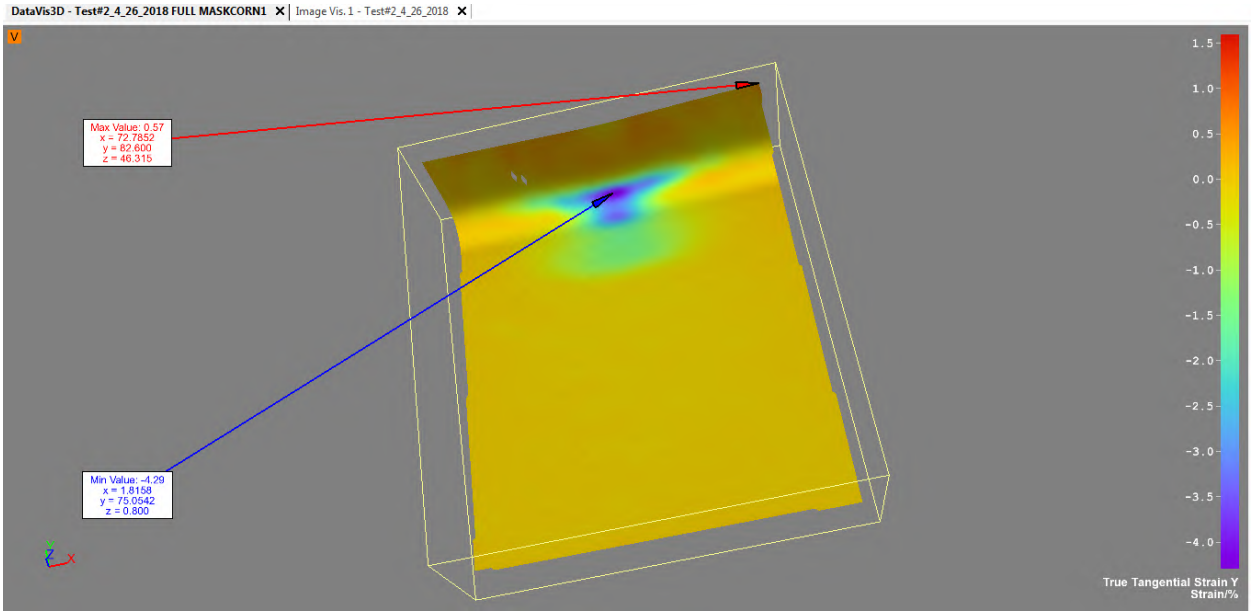

Figure C-120: W16X31-SC-NA showing true tangential strain Y at a load of 96 kips

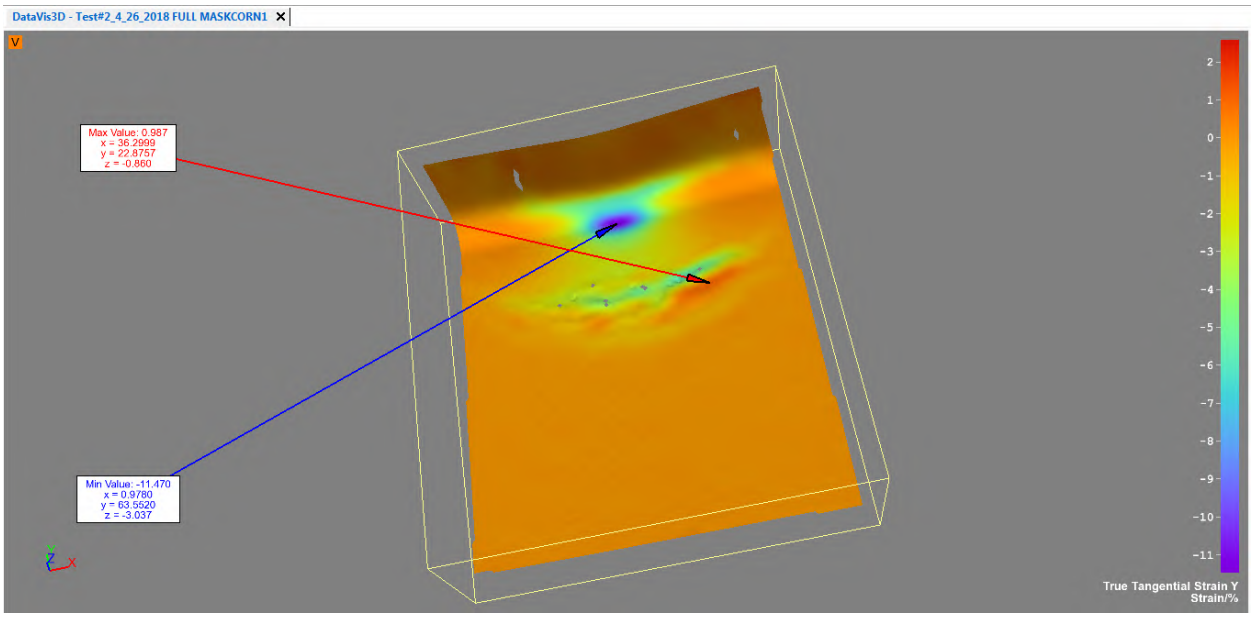

Figure C-121: W16X31-SC-NA showing true tangential strain Y at its maximum load of 112.4 kips

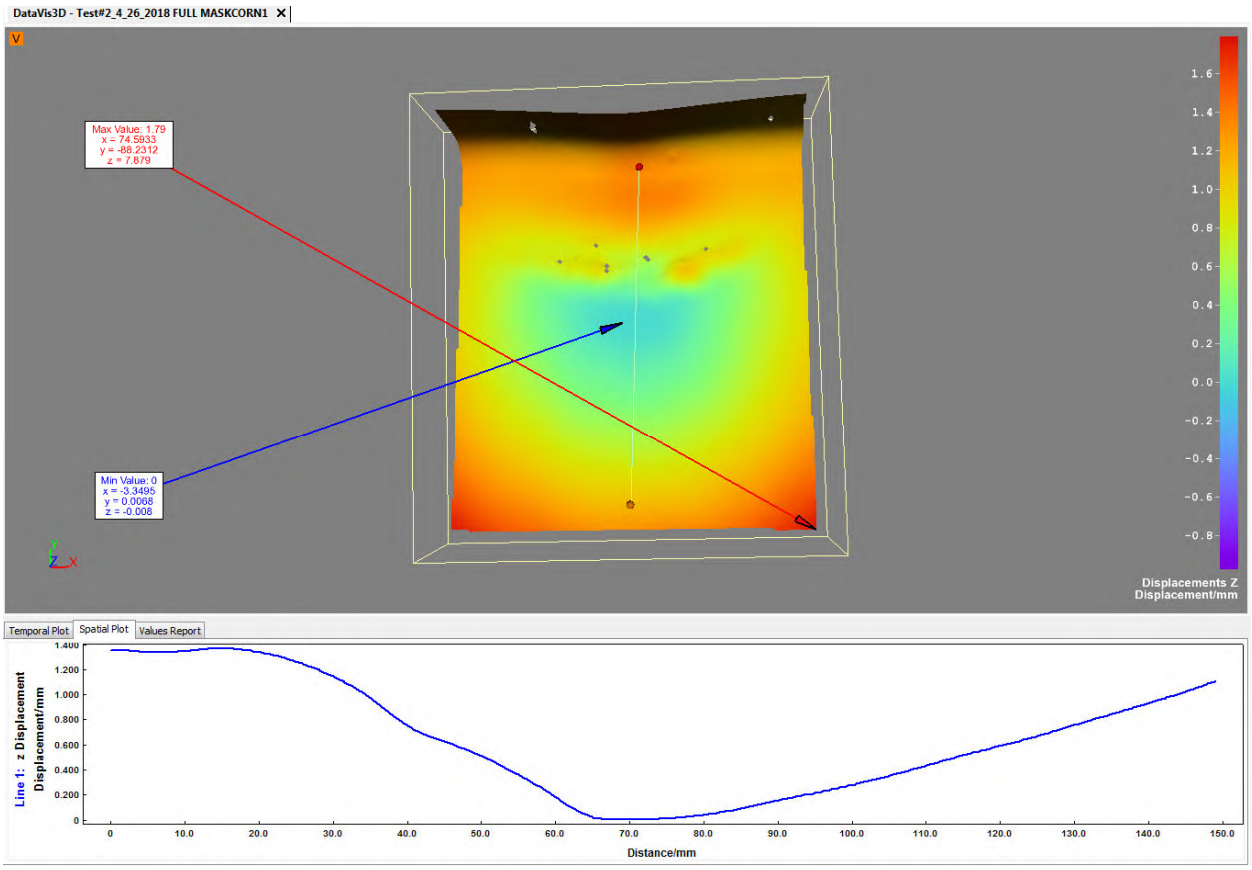

Figure C-122: W16X31-SC-NA showing out of plane displacement at its maximum load of 112.4 kips

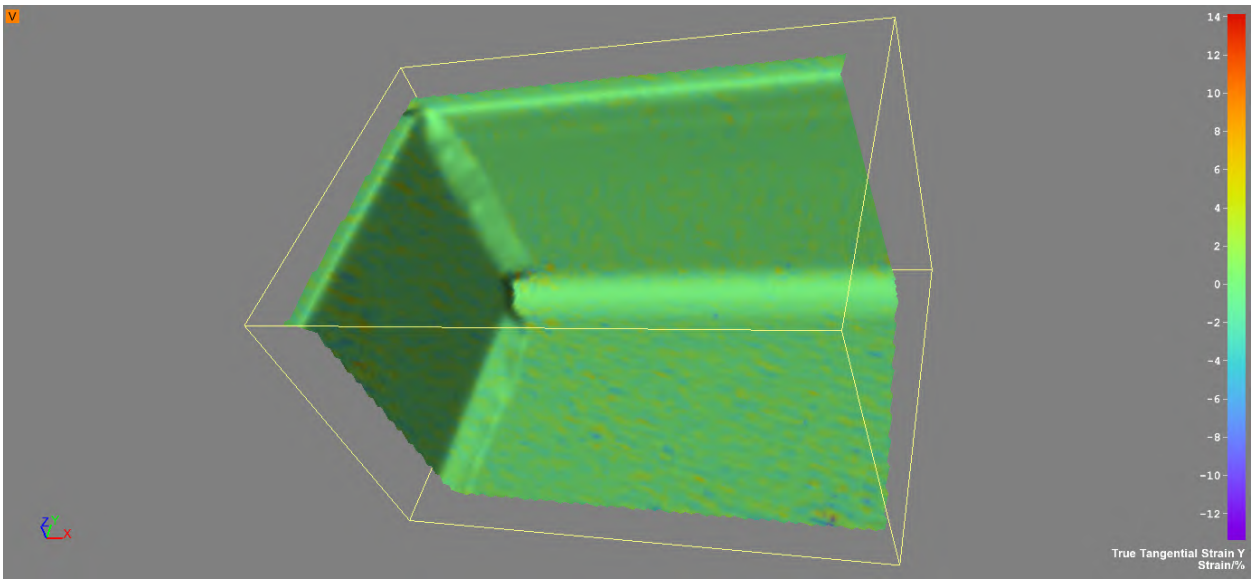

Figure C-123: W10X39-ST-E0 showing true tangential strain Y at a load of 111 kips

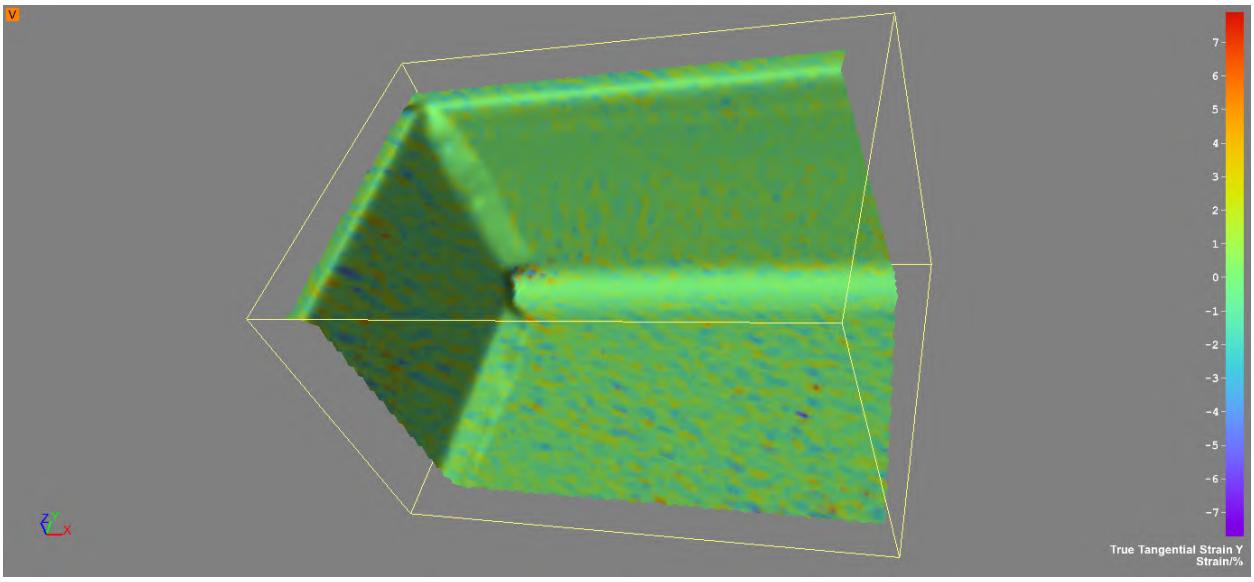

Figure C-124: W10X39-ST-E0 showing true tangential strain Y at a load of 142.3 kips

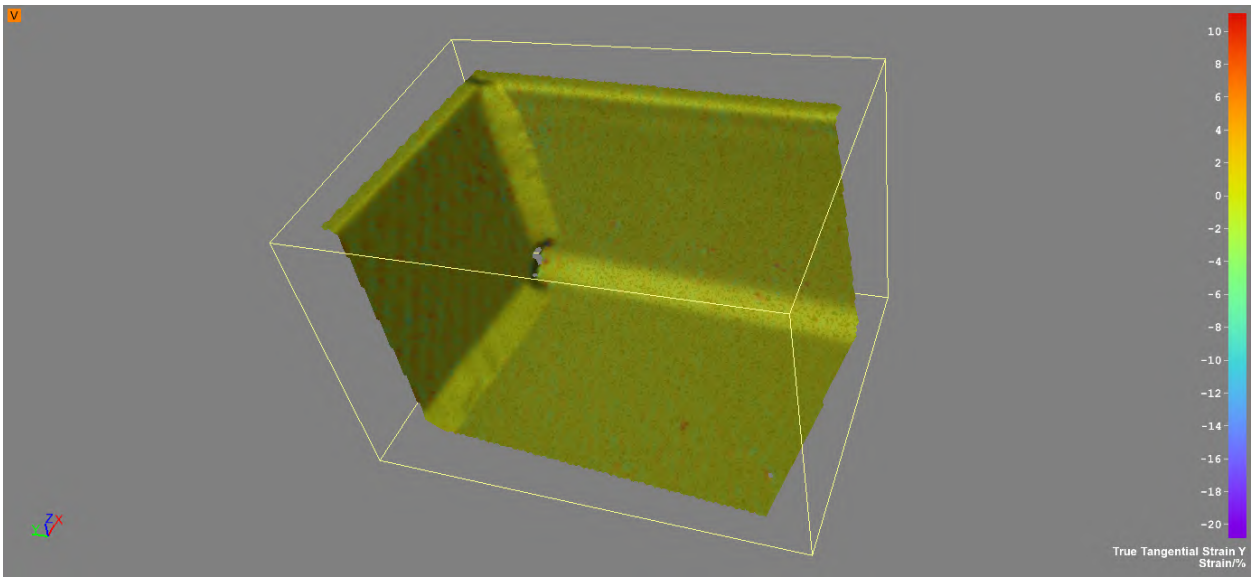

Figure C-125: W10X39-ST-E2 showing true tangential strain Y at a load of 111 kips

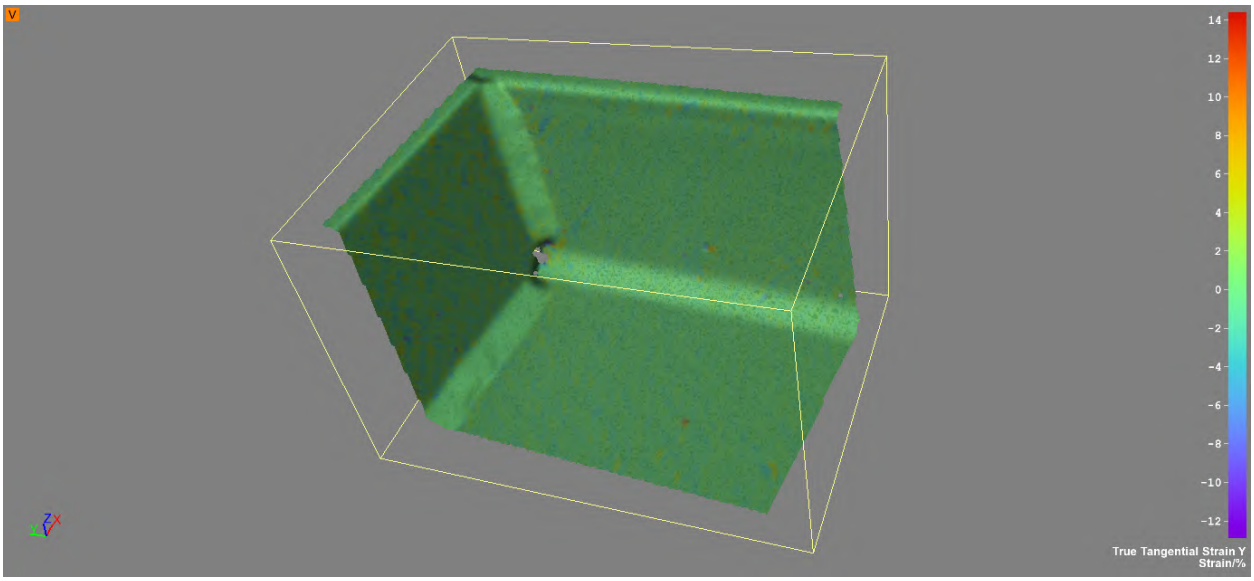

Figure C-126: W10X39-ST-E2 showing true tangential strain Y at a load of 142.3 kips

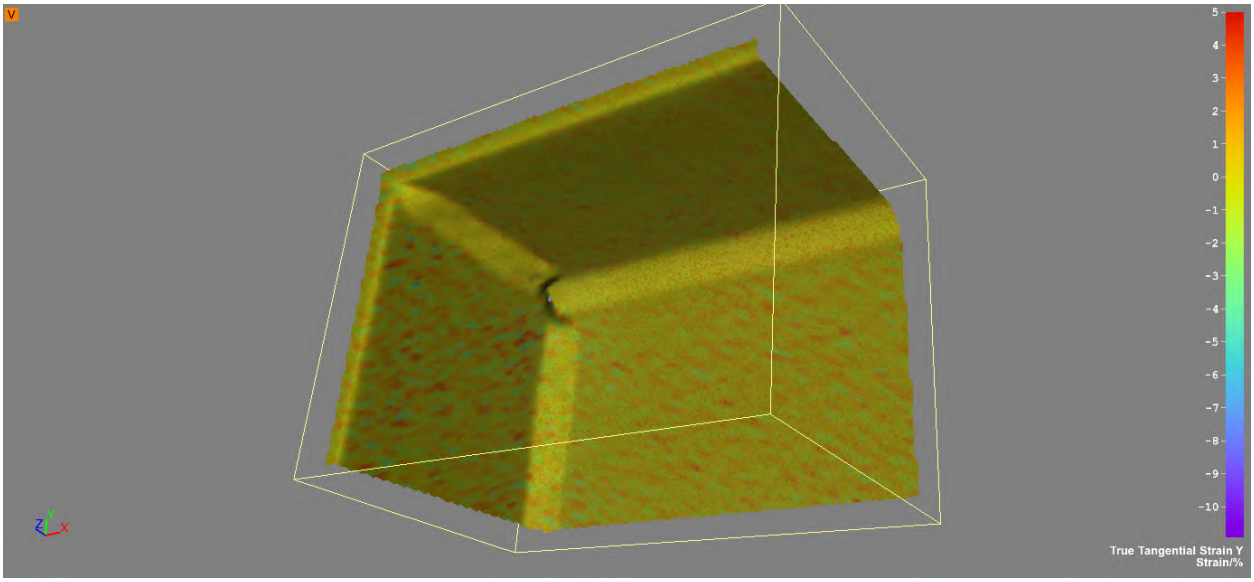

Figure C-127: W10X39-ST-E4 showing true tangential strain Y at a load of 111 kips

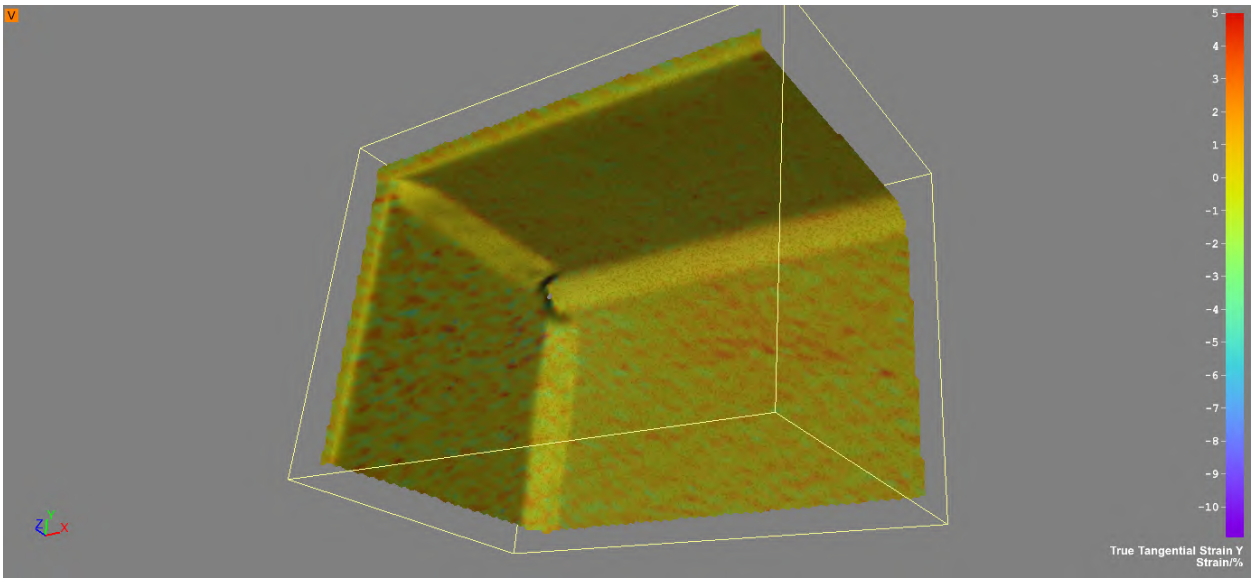

Figure C-128: W10X39-ST-E4 showing true tangential strain Y at a load of 142.3 kips

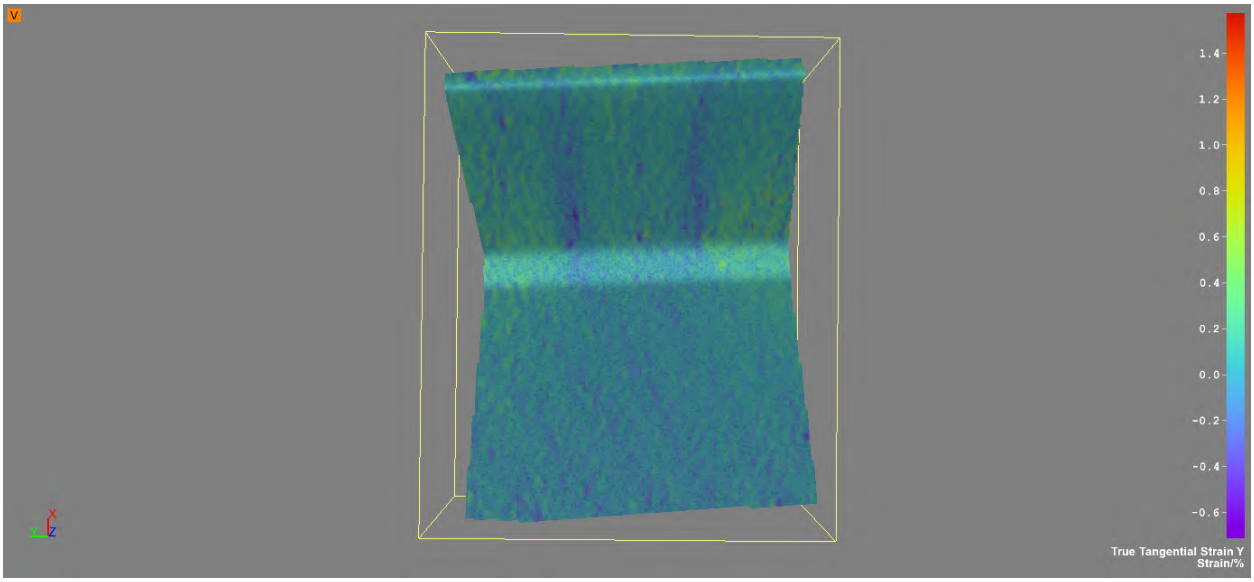

Figure C-129: W10X39-ST-NA showing true tangential strain Y at a load of 111 kips

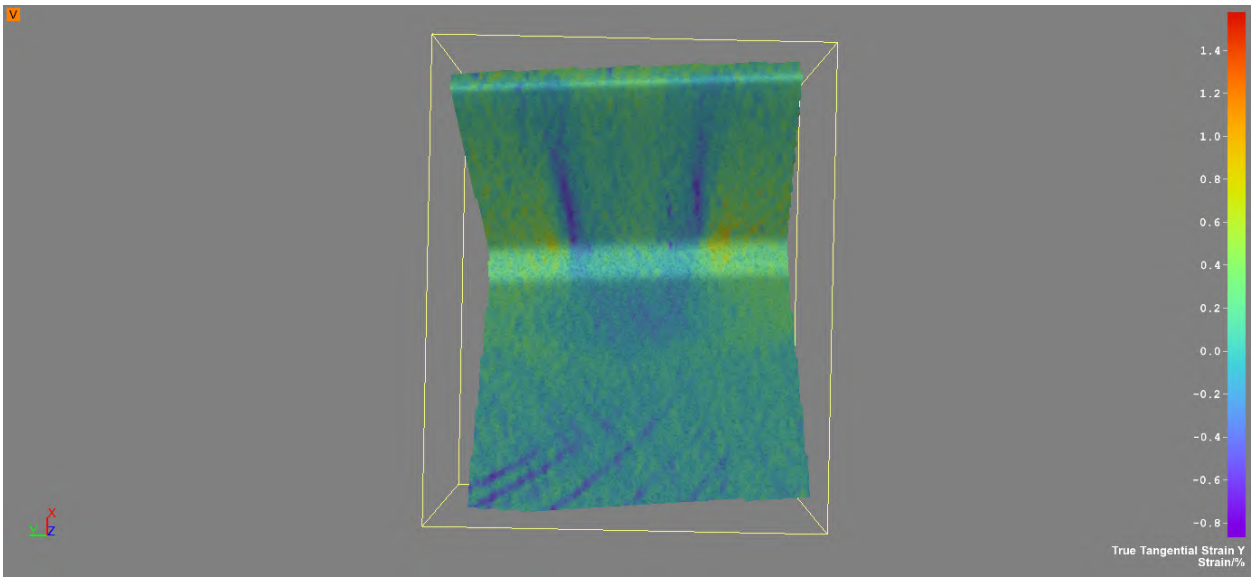

Figure C-130: W10X39-ST-NA showing true tangential strain Y at a load of 142.3 kips

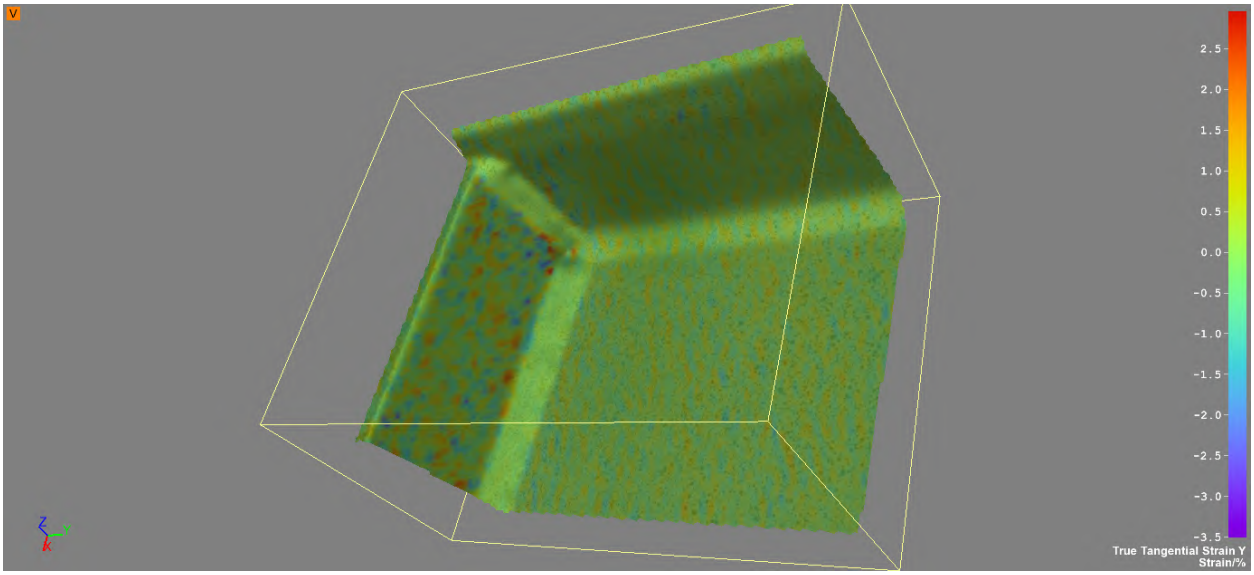

Figure C-131: W12X26-ST-E0 showing true tangential strain Y at a load of 111 kips

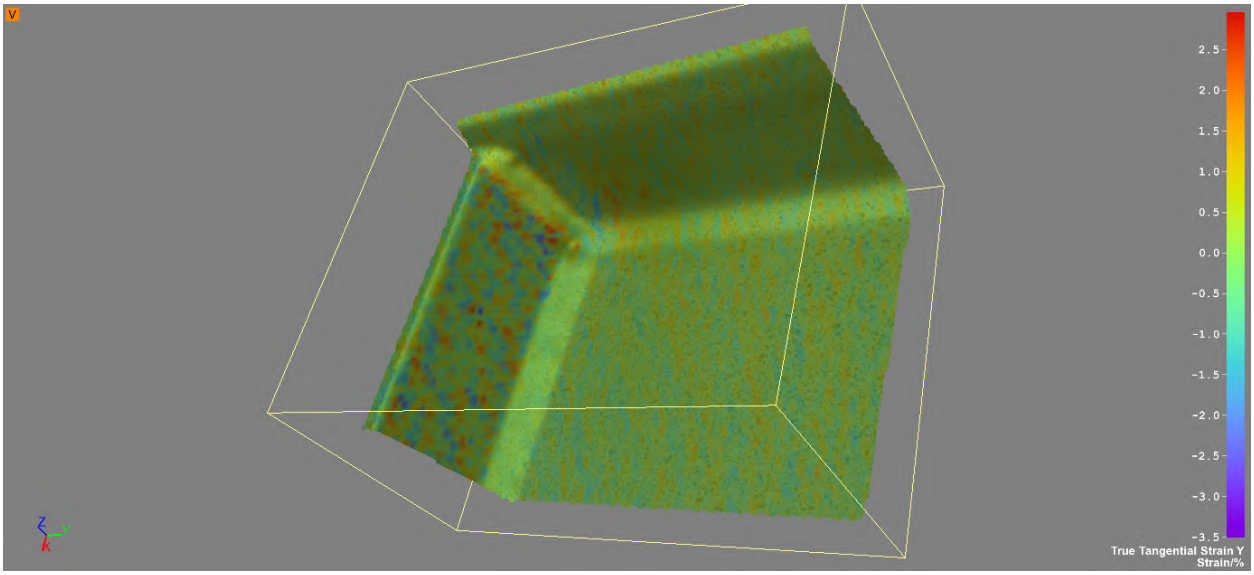

Figure C-132: W12X26-ST-E0 showing true tangential strain Y at a load of 79.2 kips

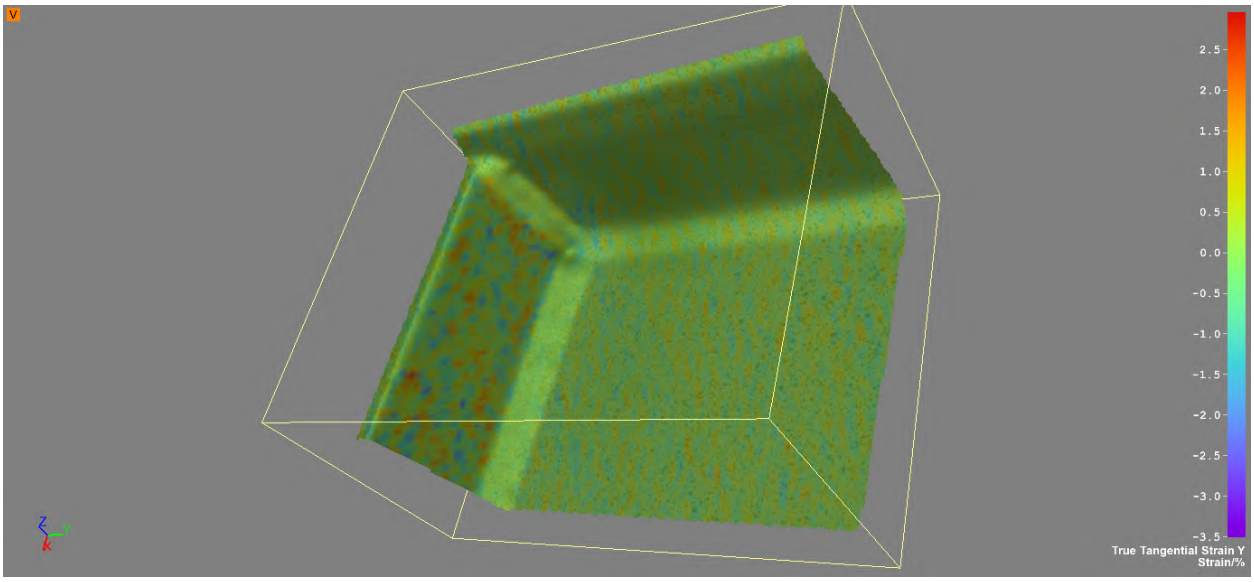

Figure C-133: W12X26-ST-E0 showing true tangential strain Y at a load of 142.3 kips

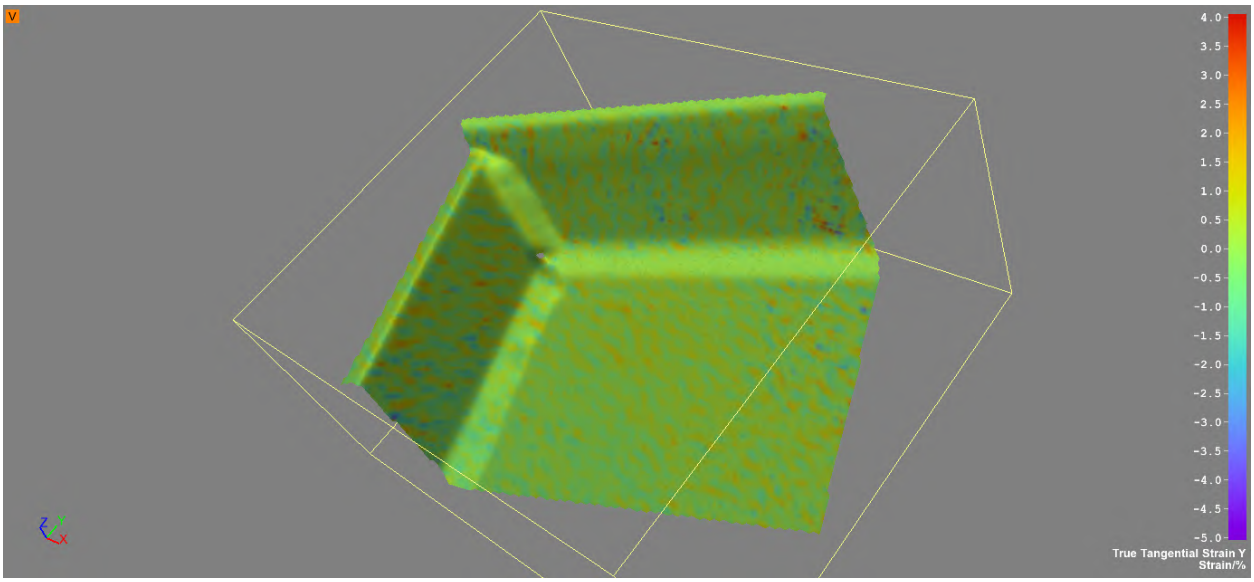

Figure C-134: W12X26-ST-E2 showing true tangential strain Y at a load of 59 kips

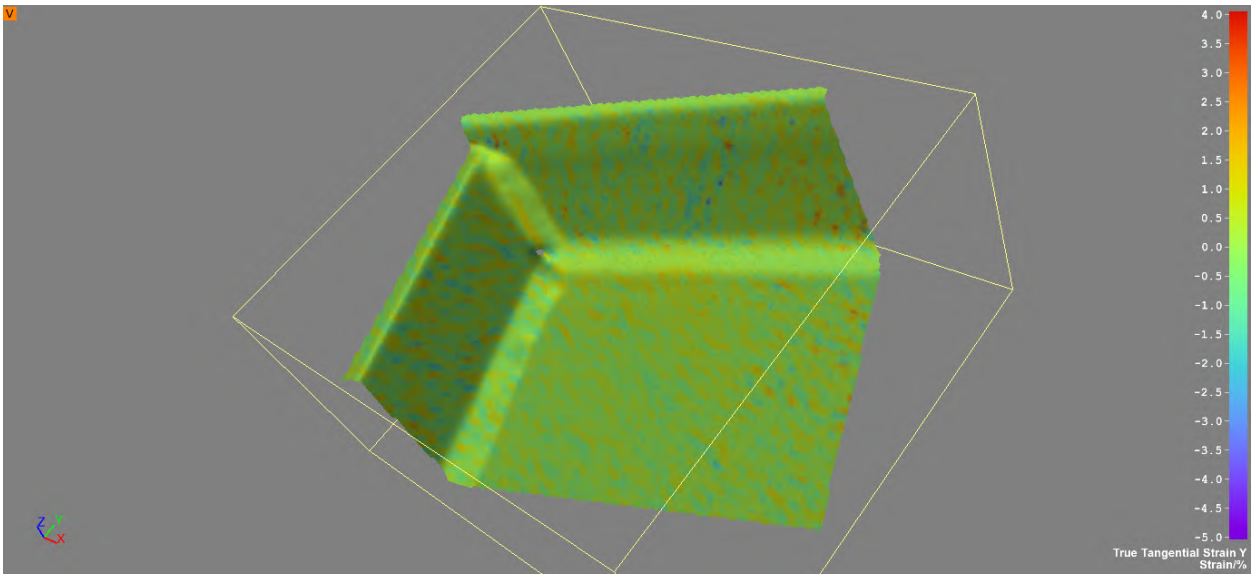

Figure C-135: W12X26-ST-E2 showing true tangential strain Y at a load of 79.2 kips

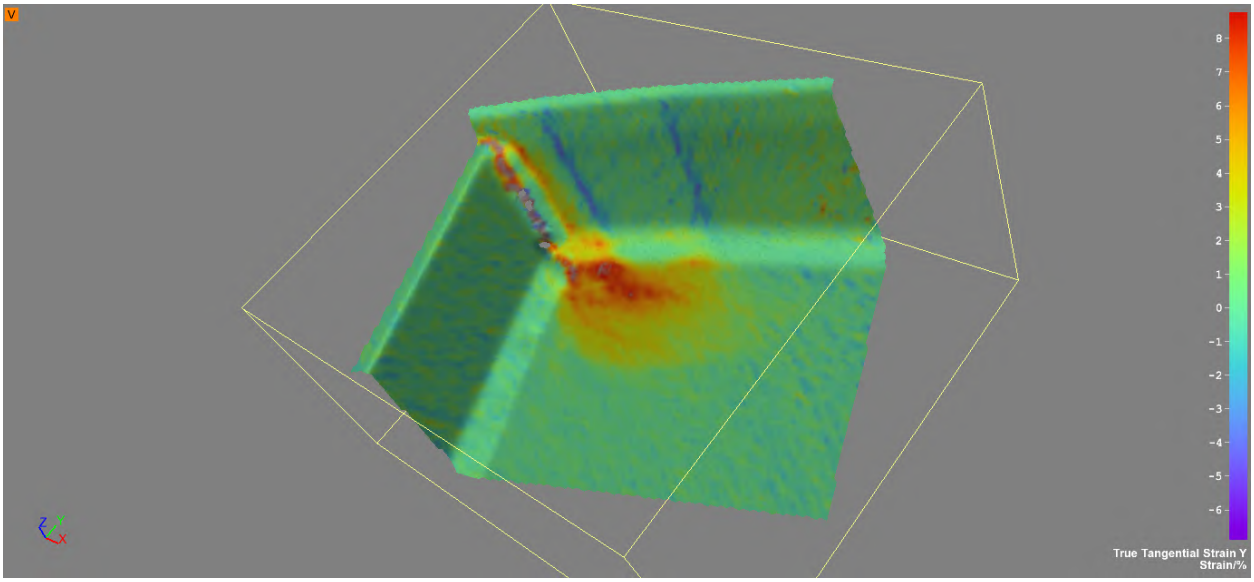

Figure C-136: W12X26-ST-E2 showing true tangential strain Y at its maximum load of 133.7 kips

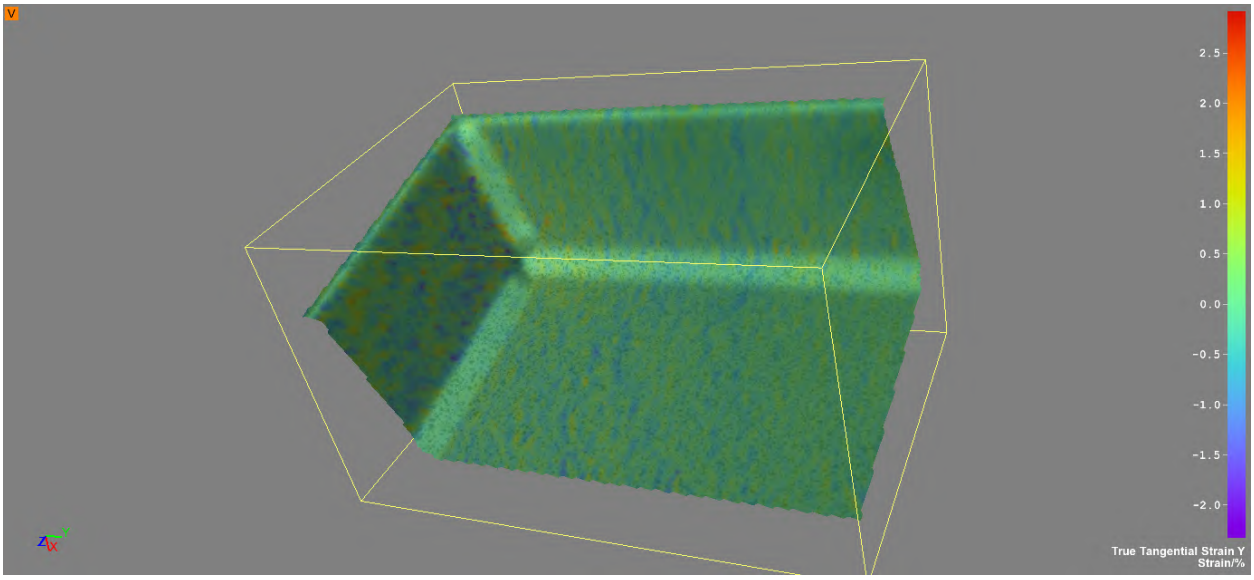

Figure C-137: W12X26-ST-E4 showing true tangential strain Y at a load of 59 kips

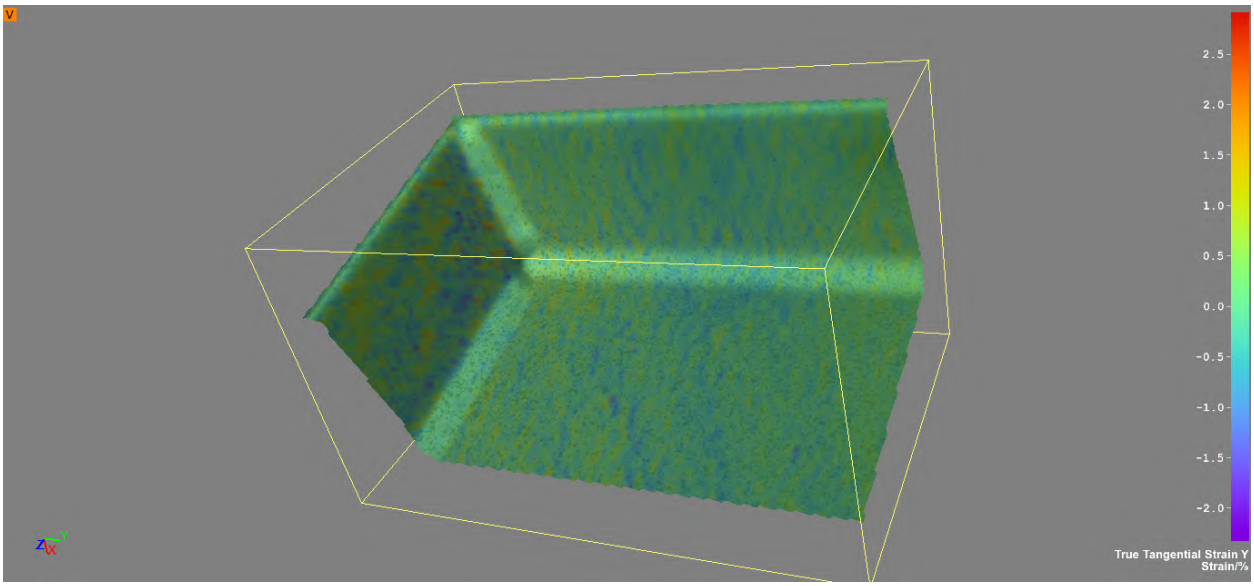

Figure C-138: W12X26-ST-E4 showing true tangential strain Y at a load of 79.2 kips

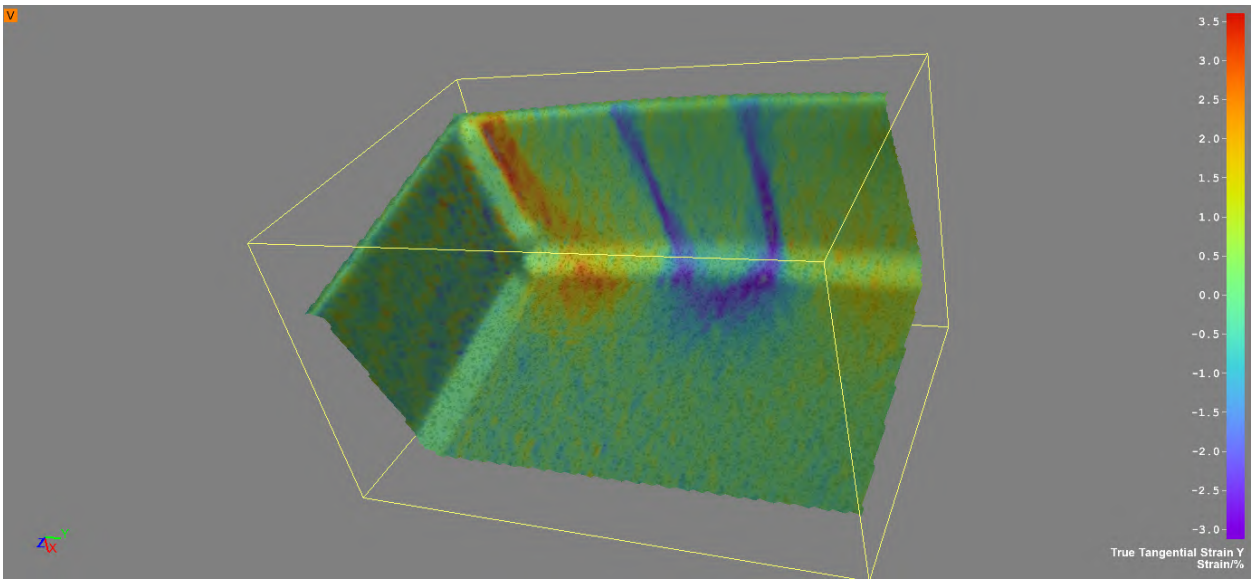

Figure C-139: W12X26-ST-E4 showing true tangential strain Y at its maximum load of 115.1 kips

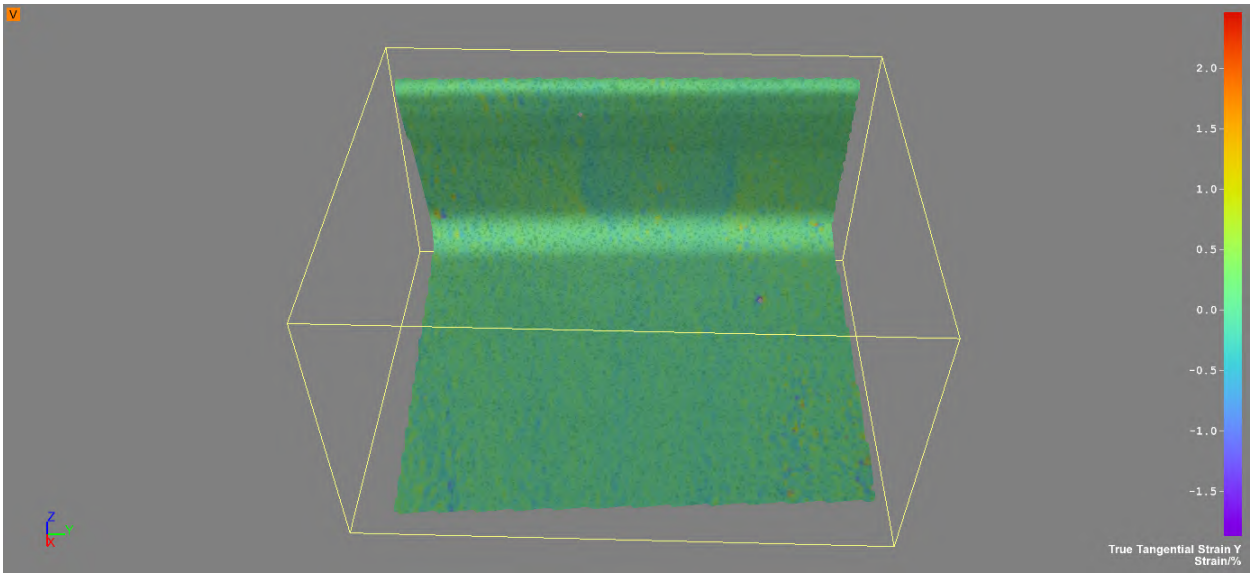

Figure C-140: W12X26-ST-NA showing true tangential strain Y at a load of 59 kips

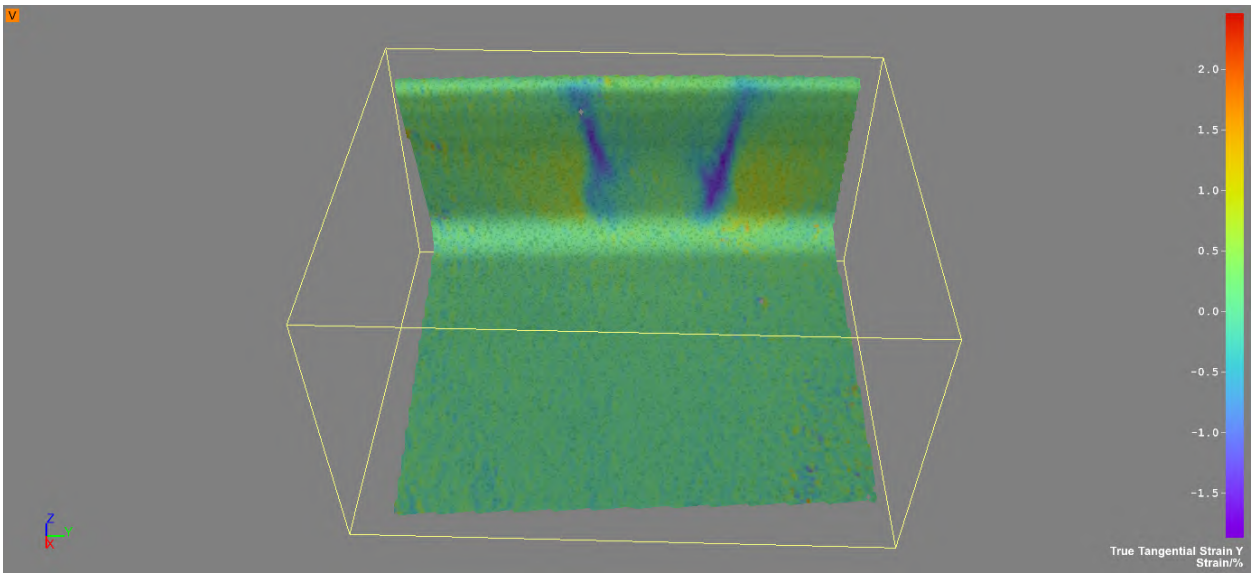

Figure C-141: W12X26-ST-NA showing true tangential strain Y at its maximum load of 79.2 kips

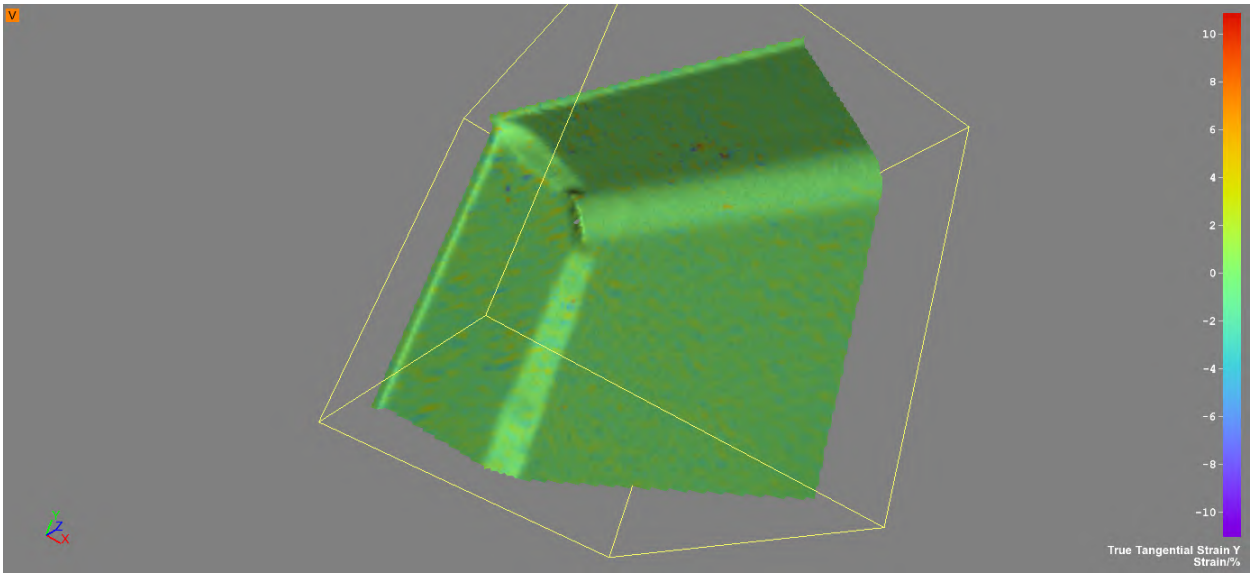

Figure C-142: W16X31-ST-E0 showing true tangential strain Y at a load of 82 kips

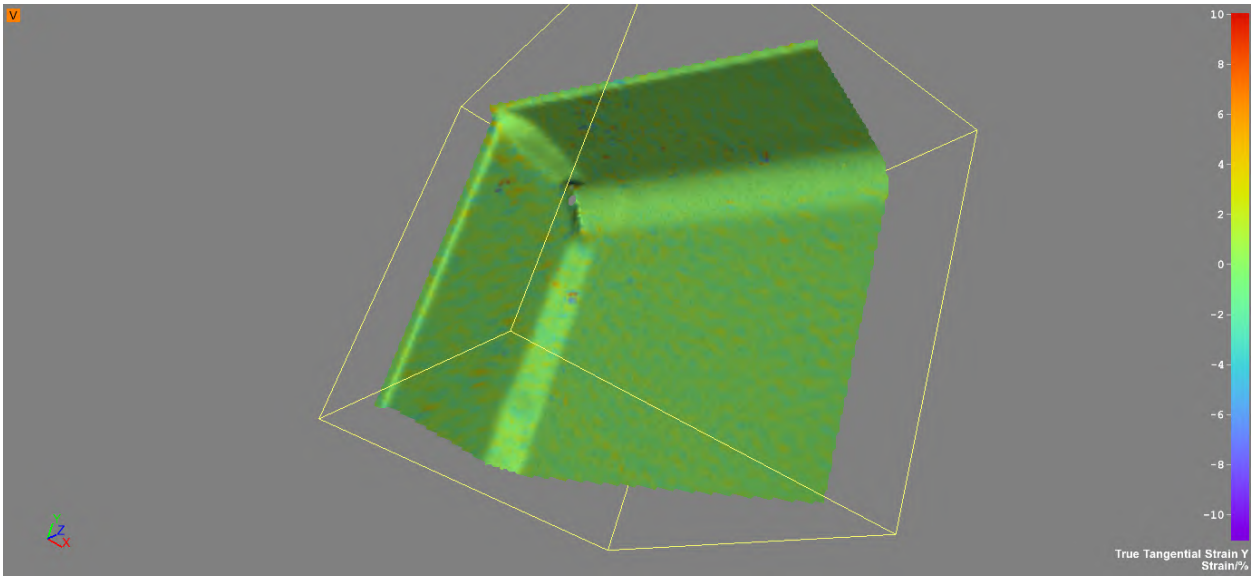

Figure C-143: W16X31-ST-E0 showing true tangential strain Y at a load of 127 kips

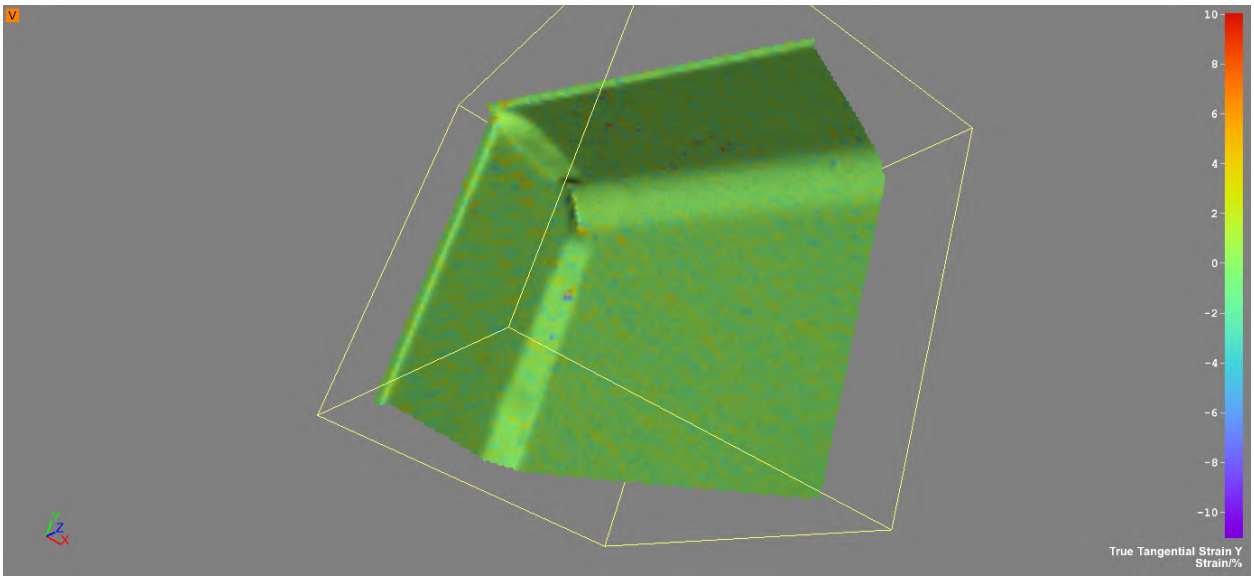

Figure C-144: W16X31-ST-E0 showing true tangential strain Y at a load of 142.3 kips

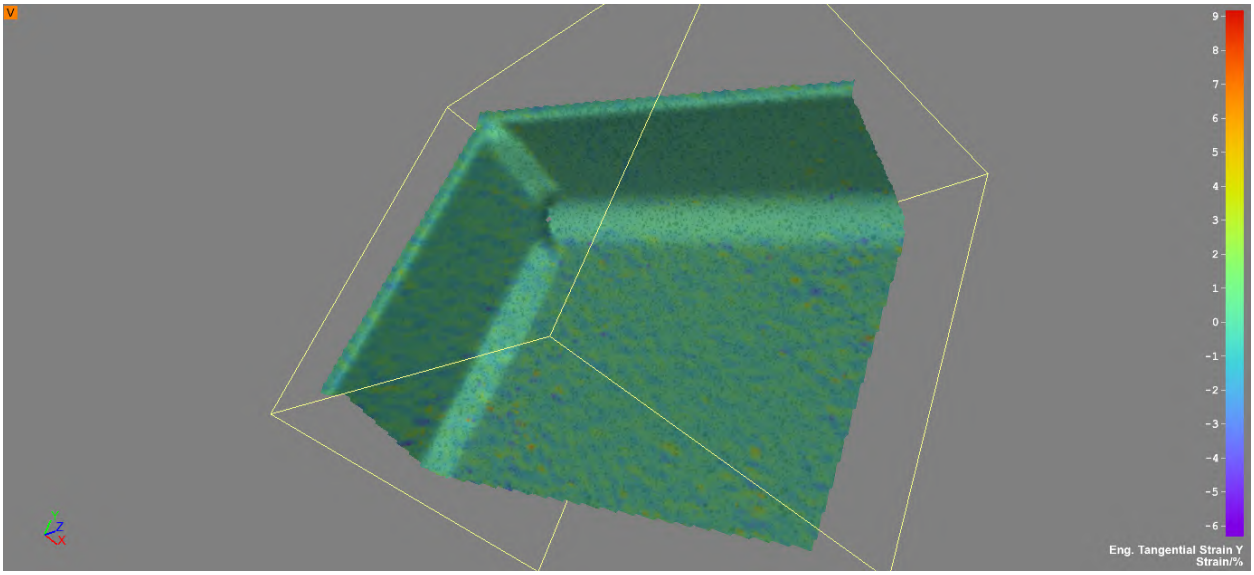

Figure C-145: W16X31-ST-E3 showing true tangential strain Y at a load of 82 kips

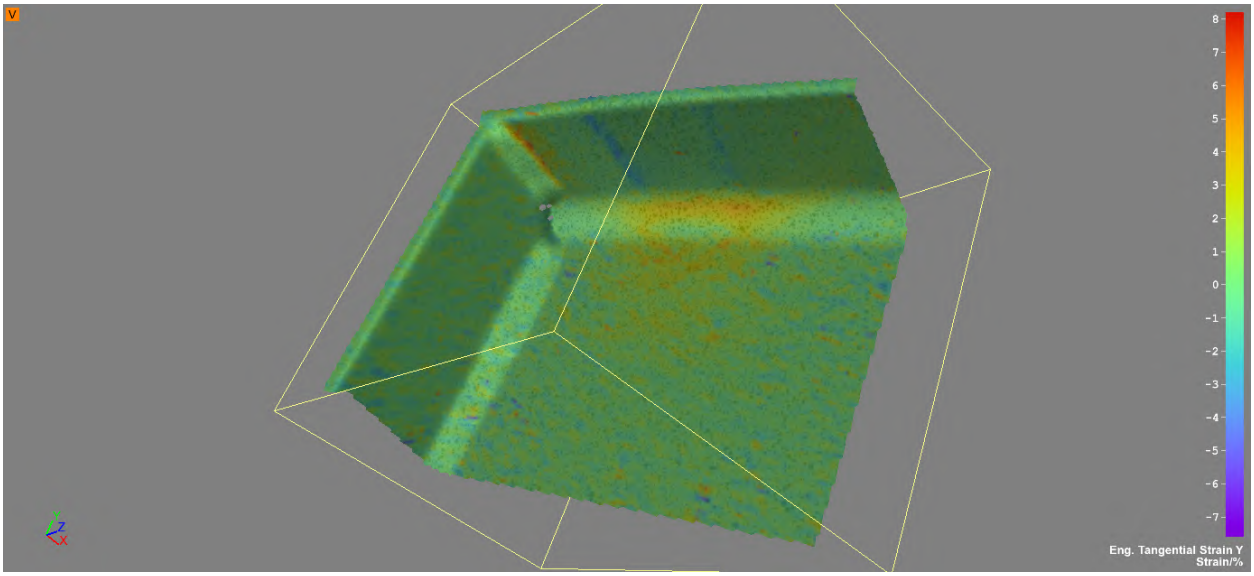

Figure C-146: W16X31-ST-E3 showing true tangential strain Y at a load of 127 kips

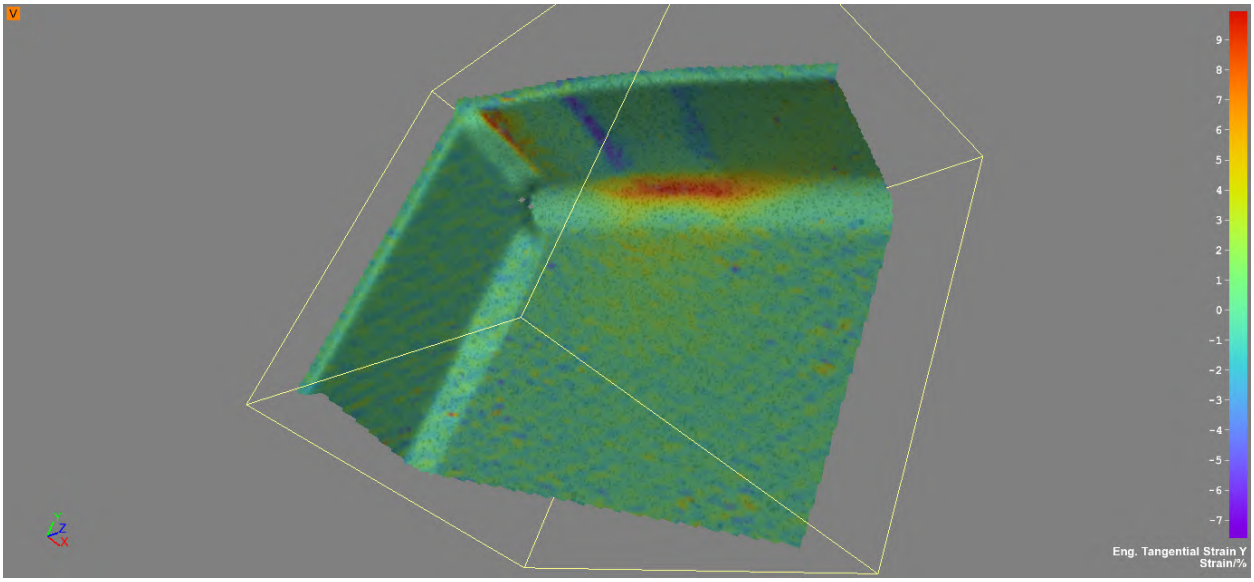

Figure C-147: W16X31-ST-E3 showing true tangential strain Y at its maximum load of 129 kips

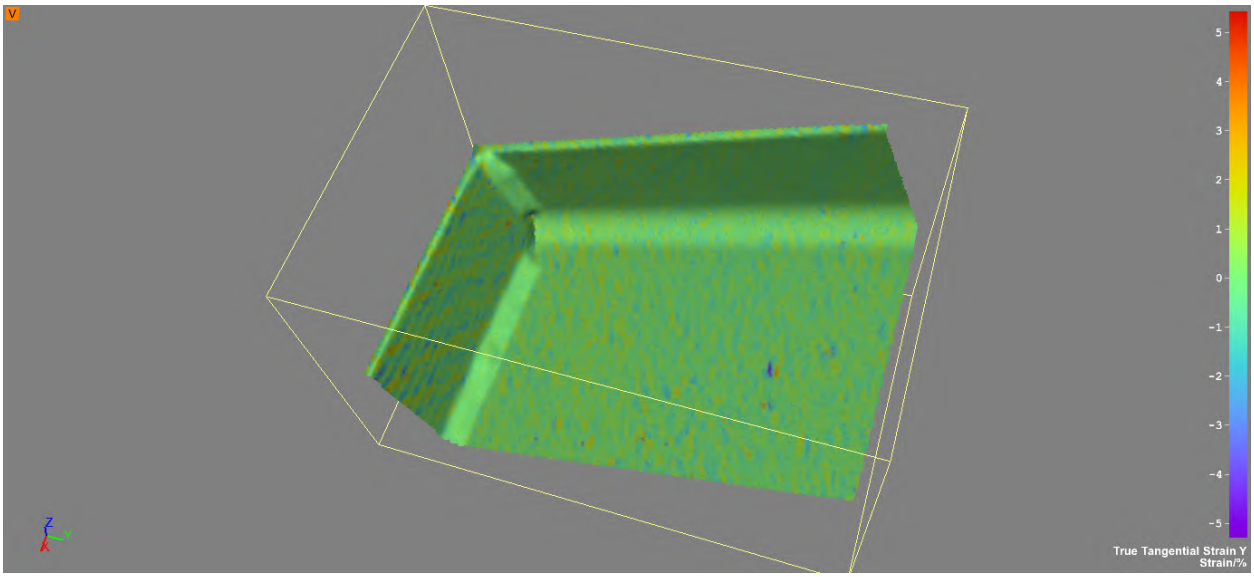

Figure C-148: W16X31-ST-E6 showing true tangential strain Y at a load of 82 kips

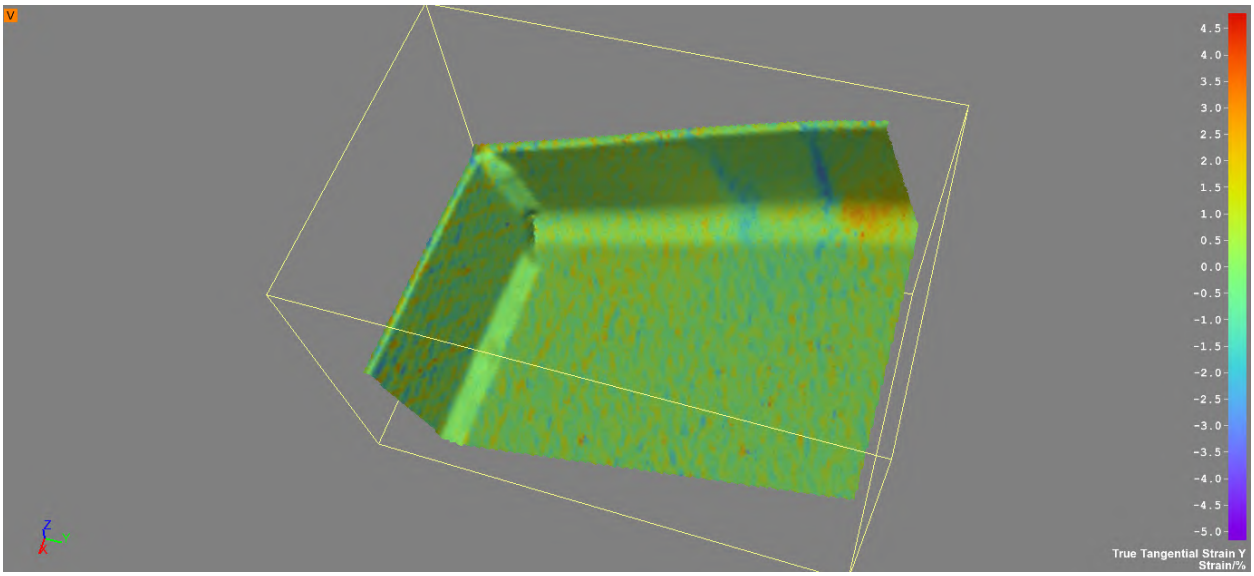

Figure C-149: W16X31-ST-E6 showing true tangential strain Y at a load of 125.5 kips

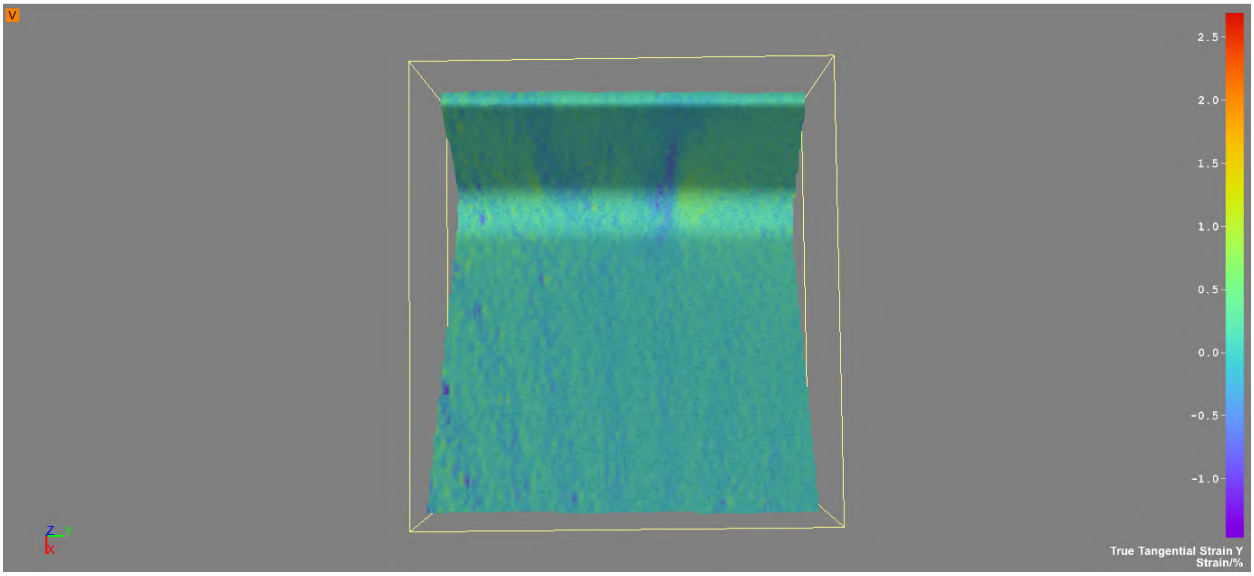

Figure C-150: W16X31-ST-NA showing true tangential strain Y at a load of 82 kips

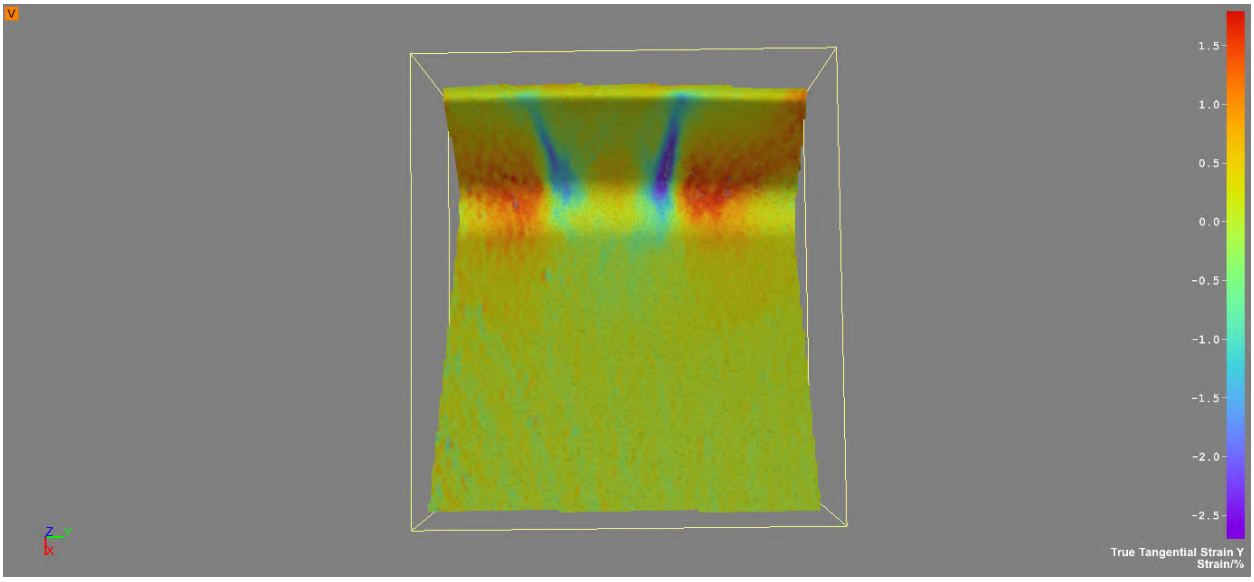

Figure C-151: W16X31-ST-NA showing true tangential strain Y at its maximum load of 127 kips

APPENDIX D: CONCENTRATED LOAD THEORETICAL CAPACITIES FOR EXPERIMENTAL COLUMN SPECIMENS AND ANALYTICAL MODELS

LIMIT STATE CAPACITIES FOR BEAMS STUDIED IN THIS RESEARCH

Note: All calculations assume expected yield = 1.1 x minimum yield stress per grade.

W10X19

$d := 10.2$ in $b_f := 4.02$ in $t_f := 0.395$ in $t_w := 0.25$ in $k_{des} := 0.695$ in $F_y := 55$ ksi

For Compression: $l_{bc} := 0.75$ in For Tension: $l_{bt} := 0.875$ in $k_1 := 0.625$ in

Tension Checks:

Flange Bending: $R_{n1} := 6.25 \cdot F_y \cdot t_f^2$ $R_{n1} = 53.634$ kips

Web Yielding: $R_{n2} := \left(5 \cdot k_{des} + l_{bt}\right) \cdot F_y \cdot t_w$ $R_{n2} = 59.812$ kips

Compression Checks:

Web Yielding: $R_{n3} := \left(5 \cdot k_{des} + l_{bc}\right) \cdot F_y \cdot t_w$ $R_{n3} = 58.094$ kips

Web Crippling: $R_{n4} := 0.8 \cdot t_w^2 \cdot \left[1 + 3 \cdot \left(\frac{l_{bc}}{d}\right) \cdot \left(\frac{t_w}{t_f}\right)^{1.5}\right] \cdot \sqrt{\frac{29000 \cdot F_y \cdot t_f}{t_w}}$ $R_{n4} = 88.19$ kips

Web Compression Buckling: $h := d - 2 \cdot k_{des}$ $h = 8.81$ in

$$R_{n5} := \frac{24 \cdot t_w^3 \cdot \sqrt{29000 \cdot F_y}}{h}$$ $R_{n5} = 53.757$ kips

Stiffener capacity: All experimental stiffeners clipped 1/2 in.

$t_s := 0.25$ in $b_s := \frac{b_f}{2} - \frac{t_w}{2} - \frac{1}{2} = 1.385$ in $F_{ys} := 39$ ksi

For two stiffeners: $R_n := F_{ys} \cdot t_s \cdot b_s \cdot 2 = 27.007$ kips

W10X39

$d := 9.92$ in $b_f := 7.99$ in $t_f := 0.530$ in $t_w := 0.315$ in $k_{des} := 1.03$ in $F_y := 55$ ksi

For Compression: $l_{bc} := 0.75$ in For Tension: $l_{bt} := 0.875$ in $k_1 := \frac{13}{16}$ in

Tension Checks:

Flange Bending: $R_{n1} := 6.25 \cdot F_y \cdot t_f^{\,2}$ $R_{n1} = 96.559$ kips

Web Yielding: $R_{n2} := \left(5 \cdot k_{des} + l_{bt}\right) \cdot F_y \cdot t_w$ $R_{n2} = 104.383$ kips

Compression Checks:

Web Yielding: $R_{n3} := \left(5 \cdot k_{des} + l_{bc}\right) \cdot F_y \cdot t_w$ $R_{n3} = 102.218$ kips

Web Crippling: $R_{n4} := 0.8 \cdot t_w^{\,2} \cdot \left[1 + 3 \cdot \left(\frac{l_{bc}}{d}\right) \cdot \left(\frac{t_w}{t_f}\right)^{1.5}\right] \cdot \sqrt{\frac{29000 \cdot F_y \cdot t_f}{t_w}}$ $R_{n4} = 143.554$ kips

Web Compression Buckling: $h := d - 2 \cdot k_{des}$ $h = 7.86$ in

$$R_{n5} := \frac{24 \cdot t_w^{\,3} \cdot \sqrt{29000 \cdot F_y}}{h}$$ $R_{n5} = 120.532$ kips

Stiffener capacity: All experimental stiffeners clipped 1/2 in.

$t_s := 0.375$ in $b_s := \frac{b_f}{2} - \frac{t_w}{2} - \frac{1}{2} = 3.337$ in $F_{ys} := 39$ ksi

For two stiffeners: $R_n := F_{ys} \cdot t_s \cdot b_s \cdot 2 = 97.622$ kips

W12X26

$d := 12.2$ in $b_f := 6.49$ in $t_f := 0.38$ in $t_w := 0.23$ in $k_{des} := 0.68$ in $F_y := 55$ ksi

For Compression: $l_{bc} := 0.75$ in For Tension: $l_{bt} := 0.875$ in $k_1 := 0.75$ in

Tension Checks:

Flange Bending: $R_{n1} := 6.25 \cdot F_y \cdot t_f^{\,2}$ $R_{n1} = 49.638$ kips

Web Yielding: $R_{n2} := \left(5 \cdot k_{des} + l_{bt}\right) \cdot F_y \cdot t_w$ $R_{n2} = 54.079$ kips

Compression Checks:

Web Yielding: $R_{n3} := \left(5 \cdot k_{des} + l_{bc}\right) \cdot F_y \cdot t_w$ $R_{n3} = 52.498$ kips

Web Crippling: $R_{n4} := 0.8 \cdot t_w^{\,2} \cdot \left[1 + 3 \cdot \left(\frac{l_{bc}}{d}\right) \cdot \left(\frac{t_w}{t_f}\right)^{1.5}\right] \cdot \sqrt{\frac{29000 \cdot F_y \cdot t_f}{t_w}}$ $R_{n4} = 74.666$ kips

Web Compression Buckling: $h := d - 2 \cdot k_{des}$ $h = 10.84$ in

$$R_{n5} := \frac{24 \cdot t_w^{\,3} \cdot \sqrt{29000 \cdot F_y}}{h}$$ $R_{n5} = 34.021$ kips

Stiffener capacity: All experimental stiffeners clipped 1/2 in.

$t_s := 0.375$ in $b_s := \frac{b_f}{2} - \frac{t_w}{2} - \frac{1}{2} = 2.63$ in $F_{ys} := 39$ ksi

For two stiffeners: $R_n := F_{ys} \cdot t_s \cdot b_s \cdot 2 = 76.927$ kips

W16X31

$d := 15.9$ in $b_f := 5.53$ in $t_f := 0.44$ in $t_w := 0.275$ in $k_{des} := 0.842$ in $F_y := 55$ ksi

For Compression: $l_{bc} := 0.75$ in For Tension: $l_{bt} := 0.875$ in $k_1 := 0.75$ in

Tension Checks:

Flange Bending: $R_{n1} := 6.25 \cdot F_y \cdot t_f^{\,2}$ $R_{n1} = 66.55$ kips

Web Yielding: $R_{n2} := \left(5 \cdot k_{des} + l_{bt}\right) \cdot F_y \cdot t_w$ $R_{n2} = 76.911$ kips

Compression Checks:

Web Yielding: $R_{n3} := \left(5 \cdot k_{des} + l_{bc}\right) \cdot F_y \cdot t_w$ $R_{n3} = 75.02$ kips

Web Crippling: $R_{n4} := 0.8 \cdot t_w^{\,2} \cdot \left[1 + 3 \cdot \left(\frac{l_{bc}}{d}\right) \cdot \left(\frac{t_w}{t_f}\right)^{1.5}\right] \cdot \sqrt{\frac{29000 \cdot F_y \cdot t_f}{t_w}}$ $R_{n4} = 103.406$ kips

Web Compression Buckling: $h := d - 2 \cdot k_{des}$ $h = 14.216$ in

$$R_{n5} := \frac{24 \cdot t_w^{\,3} \cdot \sqrt{29000 \cdot F_y}}{h}$$ $R_{n5} = 44.342$ kips

Stiffener capacity: All experimental stiffeners clipped 1/2 in.

$t_s := 0.375$ in $b_s := \frac{b_f}{2} - \frac{t_w}{2} - \frac{1}{2} = 2.127$ in $F_{ys} := 39$ ksi

For two stiffeners: $R_n := F_{ys} \cdot t_s \cdot b_s \cdot 2 = 62.229$ kips

For double compression, only stiffeners on one side used:

$R_n := F_{ys} \cdot t_s \cdot b_s = 31.115$ kips

W14X68

$d := 14$ in $b_f := 10$ in $t_f := 0.72$ in $t_w := 0.415$ in $k_{des} := 1.31$ in $F_y := 50$ ksi

For Compression: $l_{bc} := 0.75$ in $k_1 := 1.0625$ in

Tension Checks:

Flange Bending: $R_{n1} := 6.25 \cdot F_y \cdot t_f^{\,2}$ $R_{n1} = 162$ kips

Web Yielding, 0.75 in. plate: $l_{bt} := 0.75$ in $R_{n2} := \left(5 \cdot k_{des} + l_{bt}\right) \cdot F_y \cdot t_w$ $R_{n2} = 151.475$ kips

Web Yielding, 1.5 in. plate: $l_{bt} := 1.5$ in $R_{n2} := \left(5 \cdot k_{des} + l_{bt}\right) \cdot F_y \cdot t_w$ $R_{n2} = 167.038$ kips

Web Yielding, 2.25 in. plate: $l_{bt} := 2.25$ in $R_{n2} := \left(5 \cdot k_{des} + l_{bt}\right) \cdot F_y \cdot t_w$ $R_{n2} = 182.6$ kips

Compression Checks:

Web Yielding: $R_{n3} := \left(5 \cdot k_{des} + l_{bc}\right) \cdot F_y \cdot t_w$ $R_{n3} = 151.475$ kips

Web Crippling: $R_{n4} := 0.8 \cdot t_w^{\,2} \cdot \left[1 + 3 \cdot \left(\frac{l_{bc}}{d}\right) \cdot \left(\frac{t_w}{t_f}\right)^{1.5}\right] \cdot \sqrt{\frac{29000 \cdot F_y \cdot t_f}{t_w}}$ $R_{n4} = 233.899$ kips

Web Compression Buckling: $h := d - 2 \cdot k_{des}$ $h = 11.38$ in

$$R_{n5} := \frac{24 \cdot t_w^{\,3} \cdot \sqrt{29000 \cdot F_y}}{h}$$ $R_{n5} = 181.509$ kips

Stiffener capacity: $t_s := 0.375$ in $b_s := \frac{b_f}{2} - k_1 = 3.938$ in $F_{ys} := 50$ ksi

For two stiffeners: $R_n := F_{ys} \cdot t_s \cdot b_s \cdot 2 = 147.656$ kips

W14X120

$d := 14.5$ in $b_f := 14.7$ in $t_f := 0.94$ in $t_w := 0.59$ in $k_{des} := 1.54$ in $F_y := 50$ ksi

For Compression: $l_{bc} := 0.75$ in $k_1 := 1.5$ in

Tension Checks:

Flange Bending: $R_{n1} := 6.25 \cdot F_y \cdot t_f^{\,2}$ $R_{n1} = 276.125$ kips

Web Yielding, 0.75 in. plate: $l_{bt} := 0.75$ in $R_{n2} := \left(5 \cdot k_{des} + l_{bt}\right) \cdot F_y \cdot t_w$ $R_{n2} = 249.275$ kips

Web Yielding, 1.5 in. plate: $l_{bt} := 1.5$ in $R_{n2} := \left(5 \cdot k_{des} + l_{bt}\right) \cdot F_y \cdot t_w$ $R_{n2} = 271.4$ kips

Web Yielding, 2.25 in. plate: $l_{bt} := 2.25$ in $R_{n2} := \left(5 \cdot k_{des} + l_{bt}\right) \cdot F_y \cdot t_w$ $R_{n2} = 293.525$ kips

Compression Checks:

Web Yielding: $R_{n3} := \left(5 \cdot k_{des} + l_{bc}\right) \cdot F_y \cdot t_w$ $R_{n3} = 249.275$ kips

Web Crippling: $R_{n4} := 0.8 \cdot t_w^{\,2} \cdot \left[1 + 3 \cdot \left(\frac{l_{bc}}{d}\right) \cdot \left(\frac{t_w}{t_f}\right)^{1.5}\right] \cdot \sqrt{\frac{29000 \cdot F_y \cdot t_f}{t_w}}$ $R_{n4} = 455.929$ kips

Web Compression Buckling: $h := d - 2 \cdot k_{des}$ $h = 11.42$ in

$$R_{n5} := \frac{24 \cdot t_w^{\,3} \cdot \sqrt{29000 \cdot F_y}}{h} \qquad R_{n5} = 519.739 \text{ kips}$$

Stiffener capacity: $t_s := 0.375$ in $b_s := \frac{b_f}{2} - k_1 = 5.85$ in $F_{ys} := 50$ ksi

For two stiffeners: $R_n := F_{ys} \cdot t_s \cdot b_s \cdot 2 = 219.375$ kips

W14X176

$d := 15.2$ in $b_f := 15.7$ in $t_f := 1.31$ in $t_w := 0.83$ in $k_{des} := 1.91$ in $F_y := 50$ ksi

For Compression: $l_{bc} := 0.75$ in $k_1 := 1.625$ in

Tension Checks:

Flange Bending: $R_{n1} := 6.25 \cdot F_y \cdot t_f^2$ $R_{n1} = 536.281$ kips

Web Yielding, 0.75 in. plate: $l_{bt} := 0.75$ in $R_{n2} := \left(5 \cdot k_{des} + l_{bt}\right) \cdot F_y \cdot t_w$ $R_{n2} = 427.45$ kips

Web Yielding, 1.5 in. plate: $l_{bt} := 1.5$ in $R_{n2} := \left(5 \cdot k_{des} + l_{bt}\right) \cdot F_y \cdot t_w$ $R_{n2} = 458.575$ kips

Web Yielding, 2.25 in. plate: $l_{bt} := 2.25$ in $R_{n2} := \left(5 \cdot k_{des} + l_{bt}\right) \cdot F_y \cdot t_w$ $R_{n2} = 489.7$ kips

Compression Checks:

Web Yielding: $R_{n3} := \left(5 \cdot k_{des} + l_{bc}\right) \cdot F_y \cdot t_w$ $R_{n3} = 427.45$ kips

Web Crippling: $R_{n4} := 0.8 \cdot t_w^2 \cdot \left[1 + 3 \cdot \left(\frac{l_{bc}}{d}\right) \cdot \left(\frac{t_w}{t_f}\right)^{1.5}\right] \cdot \sqrt{\frac{29000 \cdot F_y \cdot t_f}{t_w}}$ $R_{n4} = 895.973$ kips

Web Compression Buckling: $h := d - 2 \cdot k_{des}$ $h = 11.38$ in

$$R_{n5} := \frac{24 \cdot t_w^3 \cdot \sqrt{29000 \cdot F_y}}{h} \qquad R_{n5} = 1.452 \times 10^3 \text{ kips}$$

Stiffener capacity: $t_s := 0.375$ in $b_s := \frac{b_f}{2} - k_1 = 6.225$ in $F_{ys} := 50$ ksi

For two stiffeners: $R_n := F_{ys} \cdot t_s \cdot b_s \cdot 2 = 233.438$ kips

W14X233

$d := 16$ in $b_f := 15.9$ in $t_f := 1.72$ in $t_w := 1.07$ in $k_{des} := 1.75$ in $F_y := 50$ ksi

For Compression: $l_{bc} := 0.75$ in $k_1 := 1.75$ in

Tension Checks:

Flange Bending: $R_{n1} := 6.25 \cdot F_y \cdot t_f^{\,2}$ $R_{n1} = 924.5$ kips

Web Yielding, 0.75 in. plate: $l_{bt} := 0.75$ in $R_{n2} := \left(5 \cdot k_{des} + l_{bt}\right) \cdot F_y \cdot t_w$ $R_{n2} = 508.25$ kips

Web Yielding, 1.5 in. plate: $l_{bt} := 1.5$ in $R_{n2} := \left(5 \cdot k_{des} + l_{bt}\right) \cdot F_y \cdot t_w$ $R_{n2} = 548.375$ kips

Web Yielding, 2.25 in. plate: $l_{bt} := 2.25$ in $R_{n2} := \left(5 \cdot k_{des} + l_{bt}\right) \cdot F_y \cdot t_w$ $R_{n2} = 588.5$ kips

Compression Checks:

Web Yielding: $R_{n3} := \left(5 \cdot k_{des} + l_{bc}\right) \cdot F_y \cdot t_w$ $R_{n3} = 508.25$ kips

Web Crippling: $R_{n4} := 0.8 \cdot t_w^{\,2} \cdot \left[1 + 3 \cdot \left(\frac{l_{bc}}{d}\right) \cdot \left(\frac{t_w}{t_f}\right)^{1.5}\right] \cdot \sqrt{\frac{29000 \cdot F_y \cdot t_f}{t_w}}$ $R_{n4} = 1.495 \times 10^3$ kips

Web Compression Buckling: $h := d - 2 \cdot k_{des}$ $h = 12.5$ in

$$R_{n5} := \frac{24 \cdot t_w^{\,3} \cdot \sqrt{29000 \cdot F_y}}{h} \qquad R_{n5} = 2.832 \times 10^3 \text{ kips}$$

Stiffener capacity: $t_s := 0.375$ in $b_s := \frac{b_f}{2} - k_1 = 6.2$ in $F_{ys} := 50$ ksi

For two stiffeners: $R_n := F_{ys} \cdot t_s \cdot b_s \cdot 2 = 232.5$ kips

W24X131

$d := 24.5$ in $b_f := 12.9$ in $t_f := 0.96$ in $t_w := 0.605$ in $k_{des} := 1.46$ in $F_y := 50$ ksi

For Compression: $l_{bc} := 0.75$ in $k_1 := 1.125$ in

Tension Checks:

Flange Bending: $R_{n1} := 6.25 \cdot F_y \cdot t_f^{\,2}$ $R_{n1} = 288$ kips

Web Yielding, 0.75 in. plate: $l_{bt} := 0.75$ in $R_{n2} := \left(5 \cdot k_{des} + l_{bt}\right) \cdot F_y \cdot t_w$ $R_{n2} = 243.513$ kips

Web Yielding, 1.5 in. plate: $l_{bt} := 1.5$ in $R_{n2} := \left(5 \cdot k_{des} + l_{bt}\right) \cdot F_y \cdot t_w$ $R_{n2} = 266.2$ kips

Web Yielding, 2.25 in. plate: $l_{bt} := 2.25$ in $R_{n2} := \left(5 \cdot k_{des} + l_{bt}\right) \cdot F_y \cdot t_w$ $R_{n2} = 288.888$ kips

Compression Checks:

Web Yielding: $R_{n3} := \left(5 \cdot k_{des} + l_{bc}\right) \cdot F_y \cdot t_w$ $R_{n3} = 243.513$ kips

Web Crippling: $R_{n4} := 0.8 \cdot t_w^{\,2} \cdot \left[1 + 3 \cdot \left(\frac{l_{bc}}{d}\right) \cdot \left(\frac{t_w}{t_f}\right)^{1.5}\right] \cdot \sqrt{\frac{29000 \cdot F_y \cdot t_f}{t_w}}$ $R_{n4} = 464.571$ kips

Web Compression Buckling: $h := d - 2 \cdot k_{des}$ $h = 21.58$ in

$$R_{n5} := \frac{24 \cdot t_w^{\,3} \cdot \sqrt{29000 \cdot F_y}}{h}$$ $R_{n5} = 296.558$ kips

Stiffener capacity: $t_s := 0.375$ in $b_s := \frac{b_f}{2} - k_1 = 5.325$ in $F_{ys} := 50$ ksi

For two stiffeners: $R_n := F_{ys} \cdot t_s \cdot b_s \cdot 2 = 199.688$ kips

W24X229

$d := 26$ in $b_f := 13.1$ in $t_f := 1.73$ in $t_w := 0.96$ in $k_{des} := 2.23$ in $F_y := 50$ ksi

For Compression: $l_{bc} := 0.75$ in $k_1 := 1.3125$ in

Tension Checks:

Flange Bending: $R_{n1} := 6.25 \cdot F_y \cdot t_f^{\,2}$ $R_{n1} = 935.281$ kips

Web Yielding, 0.75 in. plate: $l_{bt} := 0.75$ in $R_{n2} := \left(5 \cdot k_{des} + l_{bt}\right) \cdot F_y \cdot t_w$ $R_{n2} = 571.2$ kips

Web Yielding, 1.5 in. plate: $l_{bt} := 1.5$ in $R_{n2} := \left(5 \cdot k_{des} + l_{bt}\right) \cdot F_y \cdot t_w$ $R_{n2} = 607.2$ kips

Web Yielding, 2.25 in. plate: $l_{bt} := 2.25$ in $R_{n2} := \left(5 \cdot k_{des} + l_{bt}\right) \cdot F_y \cdot t_w$ $R_{n2} = 643.2$ kips

Compression Checks:

Web Yielding: $R_{n3} := \left(5 \cdot k_{des} + l_{bc}\right) \cdot F_y \cdot t_w$ $R_{n3} = 571.2$ kips

Web Crippling: $R_{n4} := 0.8 \cdot t_w^{\,2} \cdot \left[1 + 3 \cdot \left(\frac{l_{bc}}{d}\right) \cdot \left(\frac{t_w}{t_f}\right)^{1.5}\right] \cdot \sqrt{\frac{29000 \cdot F_y \cdot t_f}{t_w}}$ $R_{n4} = 1.234 \times 10^3$ kips

Web Compression Buckling: $h := d - 2 \cdot k_{des}$ $h = 21.54$ in

$$R_{n5} := \frac{24 \cdot t_w^{\,3} \cdot \sqrt{29000 \cdot F_y}}{h} \qquad R_{n5} = 1.187 \times 10^3 \text{ kips}$$

Stiffener capacity: $t_s := 0.375$ in $b_s := \frac{b_f}{2} - k_1 = 5.237$ in $F_{ys} := 50$ ksi

For two stiffeners: $R_n := F_{ys} \cdot t_s \cdot b_s \cdot 2 = 196.406$ kips

APPENDIX E: SCREENSHOTS OF FINITE ELEMENT MODELS

Table E-1: Index of photographs for finite element model screenshots

Column Specimen or Column Specimen Group	Figures	Starting Page	Column Specimen or Column Specimen Group	Figures	Starting Page
W10X19-DC-NA	E-1 to E-3	E-3	W24X229-DC-3/4	E-167 to E-175	E-86
W10X19-DC-E0	E-4 to E-6	E-4	W24X229-DC-NA	E-176 to E-178	E-90
W12X26-DC-NA	E-7 to E-9	E-6	W14X68-DC-3/8	E-179 to E-187	E-92
W12X26-DC-E0	E-10 to E-13	E-7	W14X68-DC-3/4	E-188 to E-196	E-96
W12X26-DC-E4	E-14 to E-16	E-9	W14X68-DC-NA	E-197 to E-199	E-101
W16X31-DC-NA	E-17 to E-19	E-11	W14X120-DC-3/8	E-200 to E-208	E-102
W10X39-SC-NA	E-20 to E-22	E-12	W14X120-DC-3/4	E-209 to E-217	E-107
W10X39-SC-E0	E-23 to E-25	E-14	W14X120-DC-NA	E-218 to E-220	E-111
W12X26-SC-NA	E-26 to E-28	E-15	W14X176-DC-3/8	E-221 to E-229	E-113
W12X26-SC-E0	E-29 to E-31	E-17	W14X176-DC-3/4	E-230 to E-238	E-117
W12X26-SC-E4	E-32 to E-34	E-18	W14X176-DC-NA	E-239 to E-241	E-122
W12X26-ST-E0	E-35 to E-37	E-20	W14X233-DC-3/8	E-242 to E-250	E-123
W12X26-ST-E4	E-38 to E-40	E-21	W14X233-DC-3/4	E-251 to E-259	E-128
W16X31-ST-E0	E-41 to E-43	E-23	W14X233-DC-NA	E-260 to E-262	E-132
W16X31-ST-NA	E-44 to E-46	E-24	W24X131-ST-1/4	E-263 to E-274	E-134
W24X131-SC-3/8	E-47 to E-55	E-25	W24X229-ST-1/4	E-275 to E-286	E-140
W24X131-SC-NA	E-56 to E-58	E-30	W14X68-ST-1/4	E-287 to E-298	E-146
W24X229-SC-3/8	E-59 to E-67	E-32	W14X120-ST-1/4	E-299 to E-310	E-152
W24X229-SC-3/4	E-68 to E-76	E-36	W14X176-ST-1/4	E-311 to E-322	E-158
W24X229-SC-NA	E-77 to E-79	E-41	W14X233-ST-1/4	E-323 to E-334	E-164
W14X68-SC-3/8	E-80 to E-88	E-42	W24X131-ST-9/16	E-335 to E-346	E-170
W14X68-SC-NA	E-89 to E-91	E-47	W24X229-ST-9/16	E-347 to E-358	E-176
W14X120-SC-3/8	E-92 to E-100	E-48	W14X68-ST-9/16	E-359 to E-370	E-182
W14X120-SC-NA	E-101 to E-103	E-53	W14X120-ST-9/16	E-371 to E-382	E-188
W14X176-SC-3/8	E-104 to E-112	E-54	W14X176-ST-9/16	E-383 to E-394	E-194
W14X176-SC-NA	E-113 to E-115	E-59	W14X233-ST-9/16	E-395 to E-406	E-200
W14X233-SC-3/8	E-116 to E-124	E-60	W24X131-ST-7/8	E-407 to E-418	E-206
W14X233-SC-3/4	E-125 to E-133	E-65	W24X229-ST-7/8	E-419 to E-430	E-212
W14X233-SC-NA	E-134 to E-136	E-69	W14X68-ST-7/8	E-431 to E-442	E-218
W24X131-DC-3/8	E-137 to E-145	E-71	W14X120-ST-7/8	E-443 to E-454	E-224
W24X131-DC-3/4	E-146 to E-154	E-75	W14X176-ST-7/8	E-455 to E-466	E-230
W24X131-DC-NA	E-155 to E-157	E-80	W14X233-ST-7/8	E-467 to E-478	E-236
W24X229-DC-3/8	E-158 to E-166	E-81			

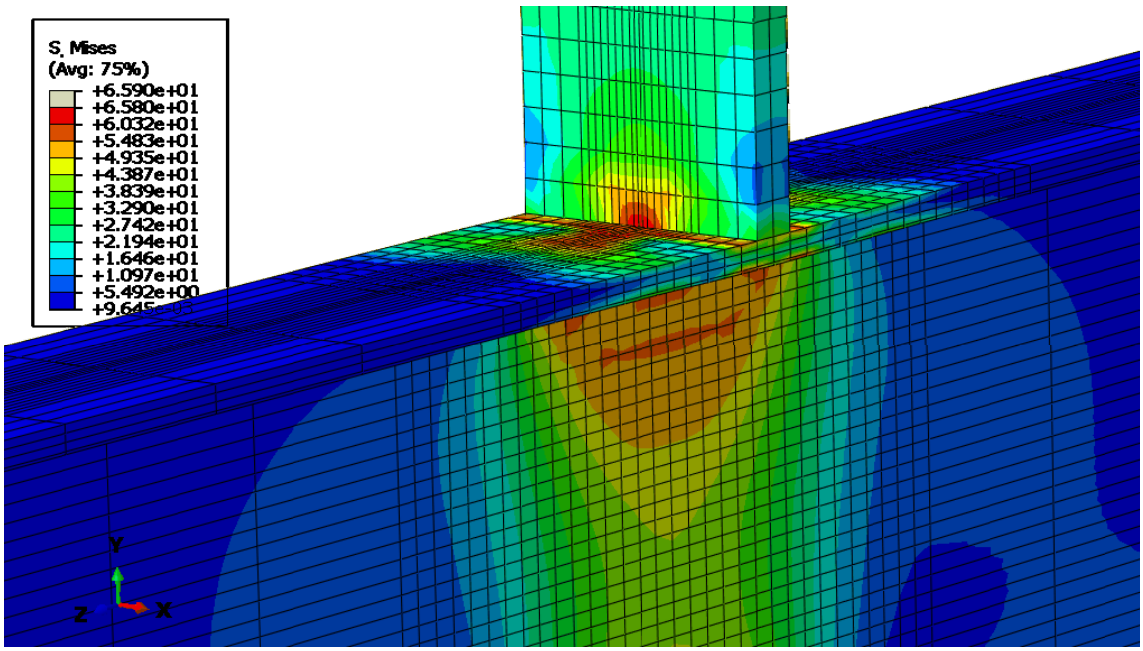

Figure E-1: Finite element model of W10X19-DC-NA during elastic behavior

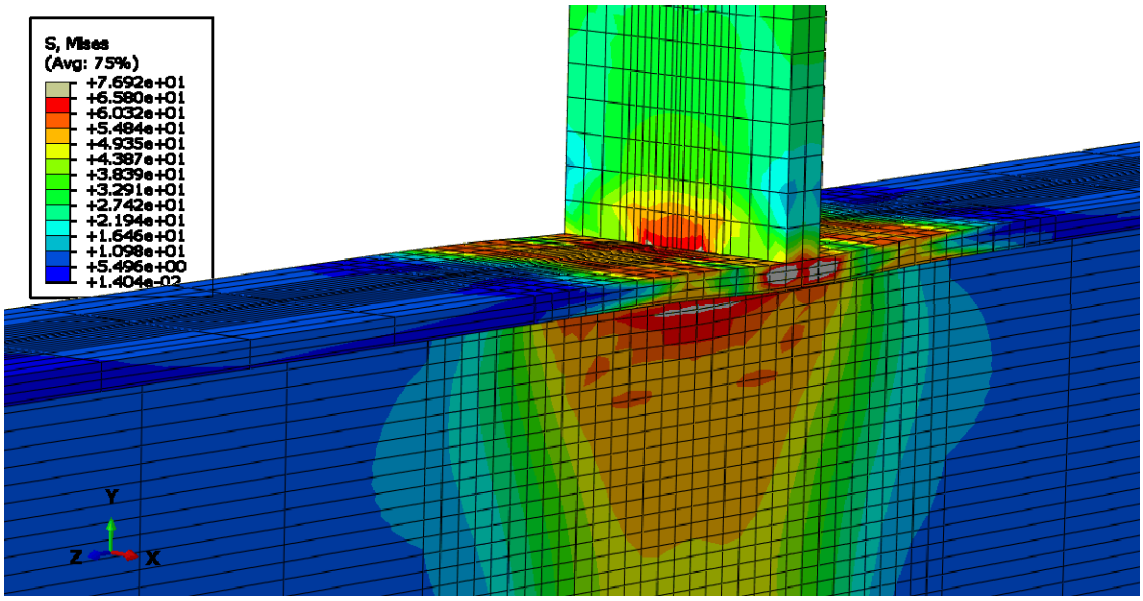

Figure E-2: Finite element model of W10X19-DC-NA during inelastic behavior

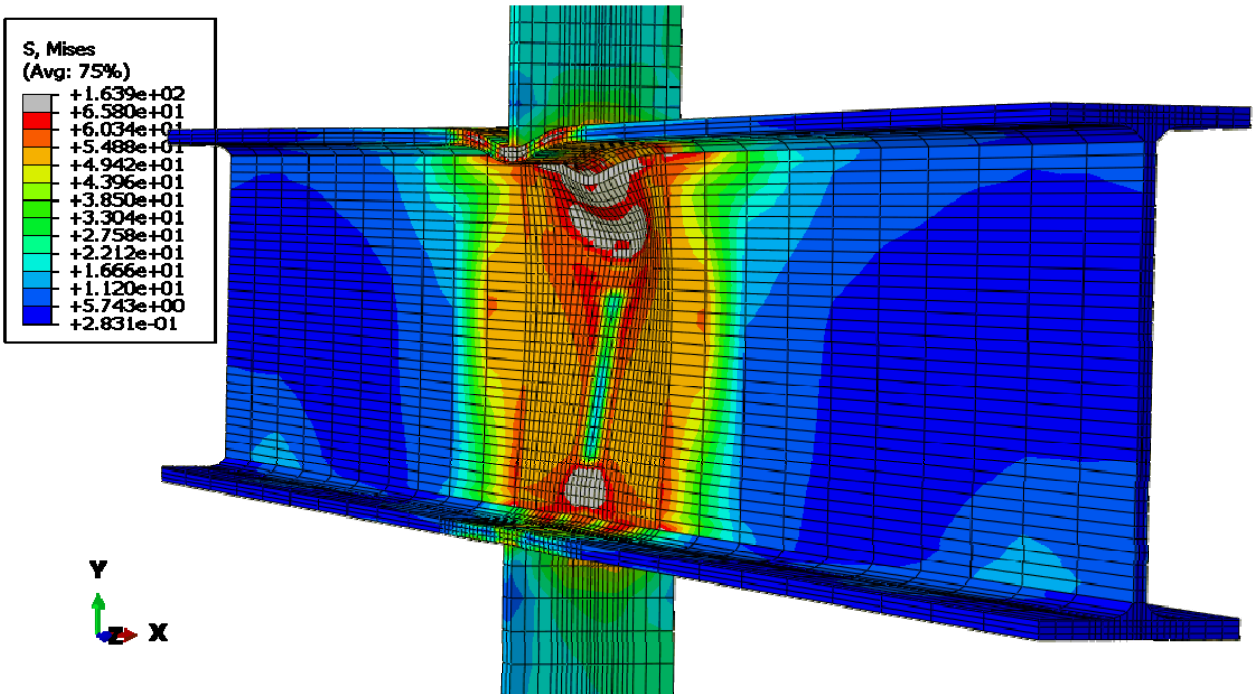

Figure E-3: Finite element model of W10X19-DC-NA emphasizing inelastic deformations

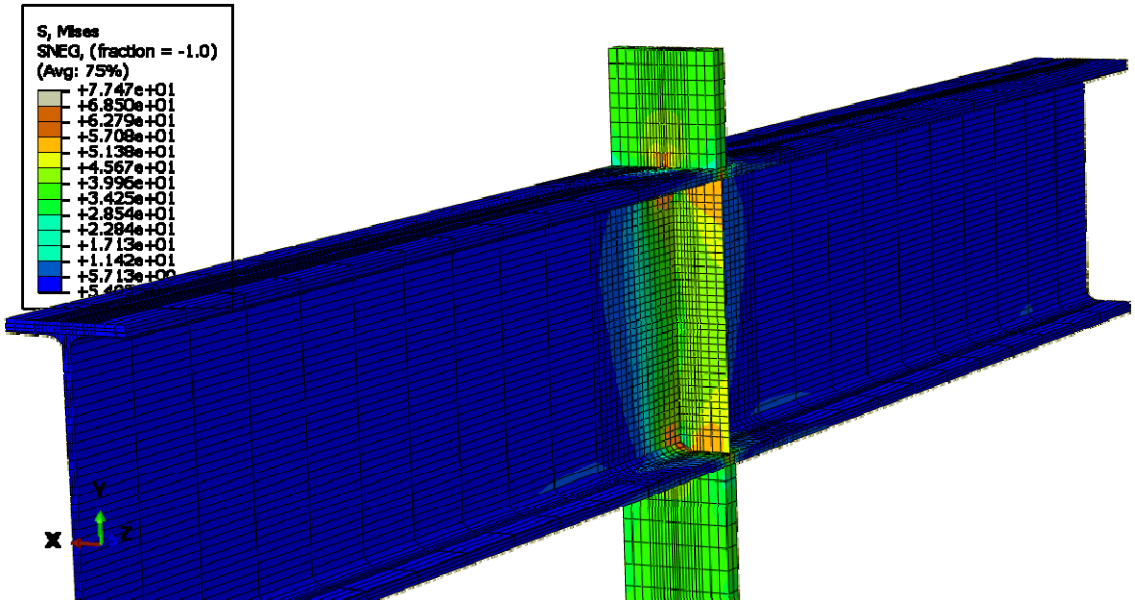

Figure E-4: Finite element model of W10X19-DC-E0 during elastic behavior

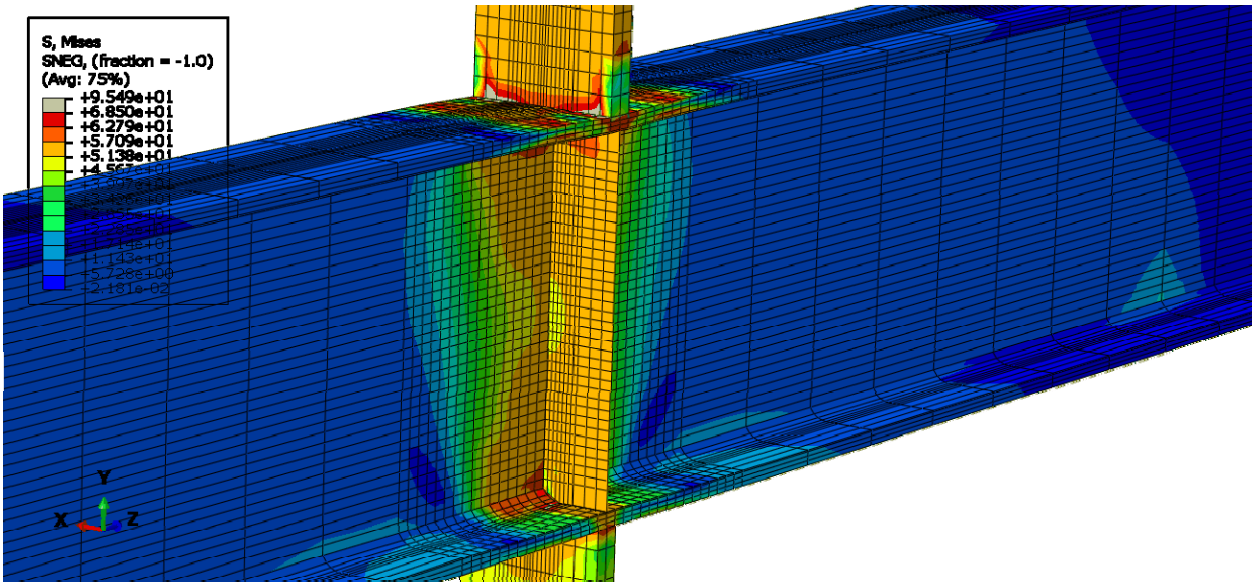

Figure E-5: Finite element model of W10X19-DC-E0 during inelastic behavior

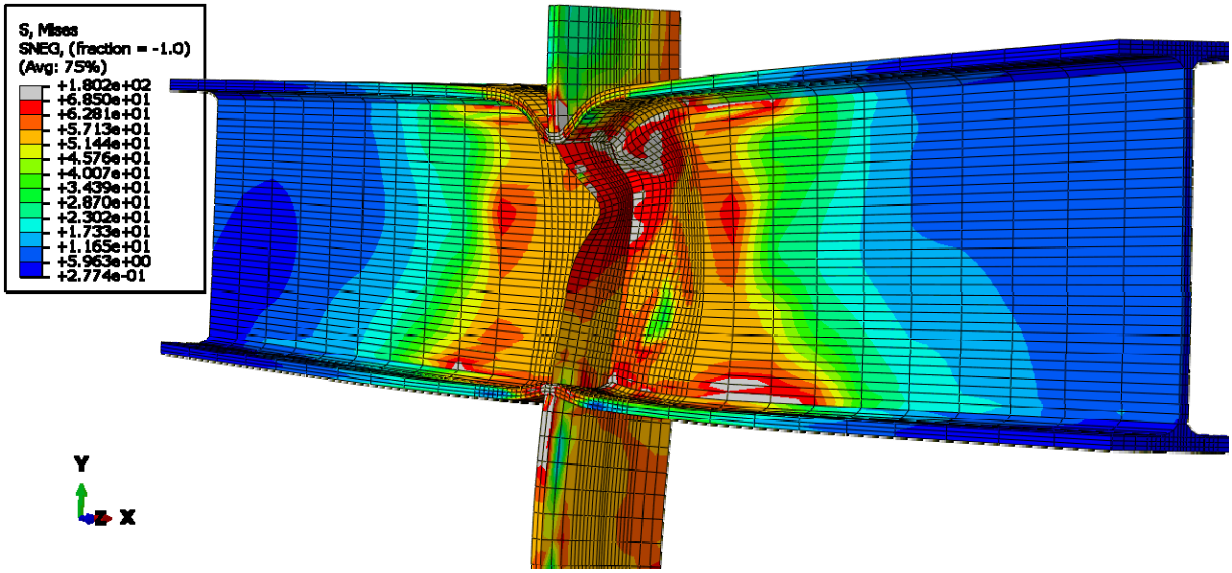

Figure E-6: Finite element model of W10X19-SC-E0 near maximum load

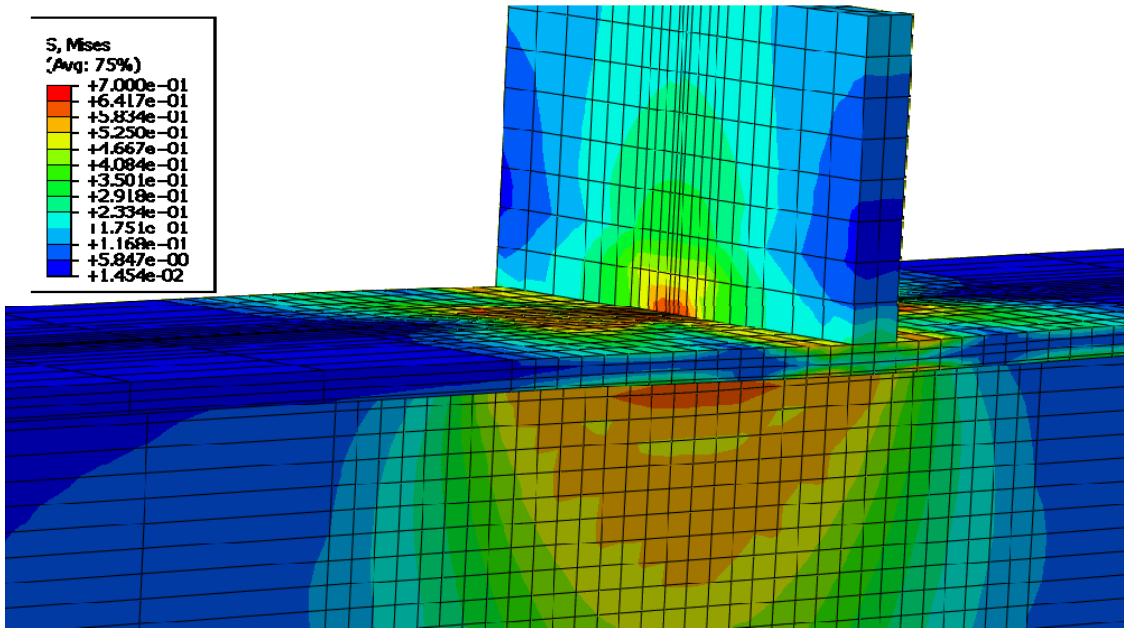

Figure E-7: Finite element model of W12X26-DC-NA during elastic behavior

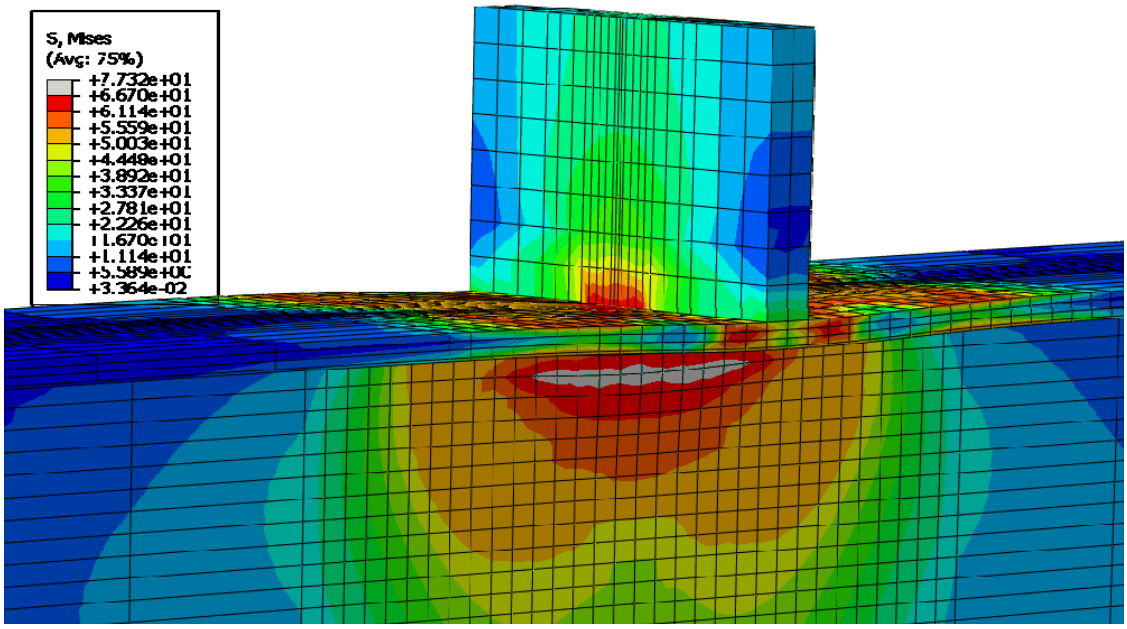

Figure E-8: Finite element model of W12X26-DC-NA during inelastic behavior

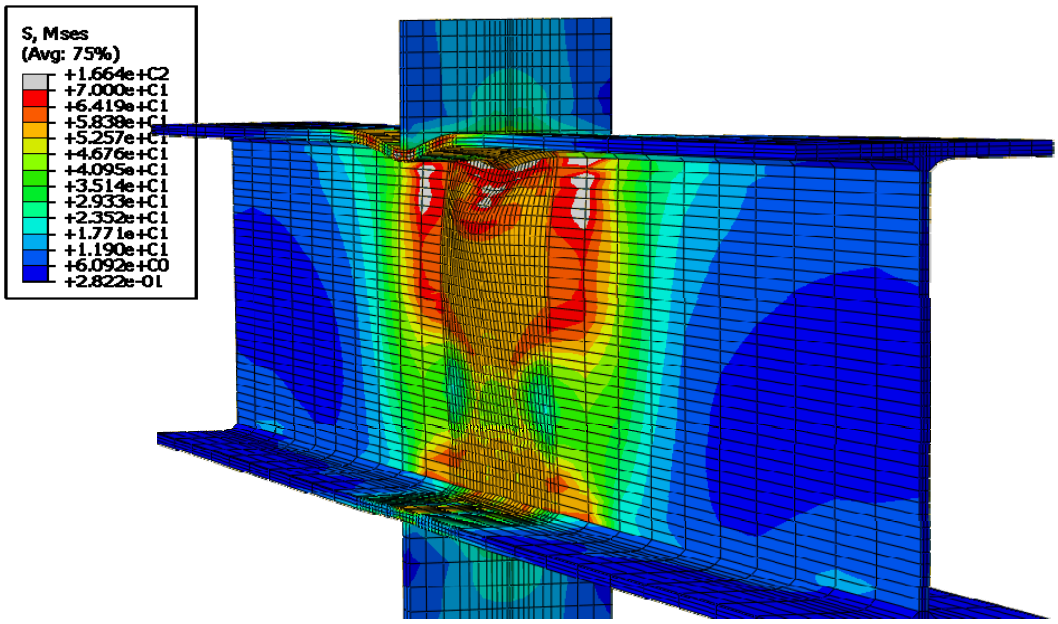

Figure E-9: Finite element model of W12X26-DC-NA after web crippling occurred

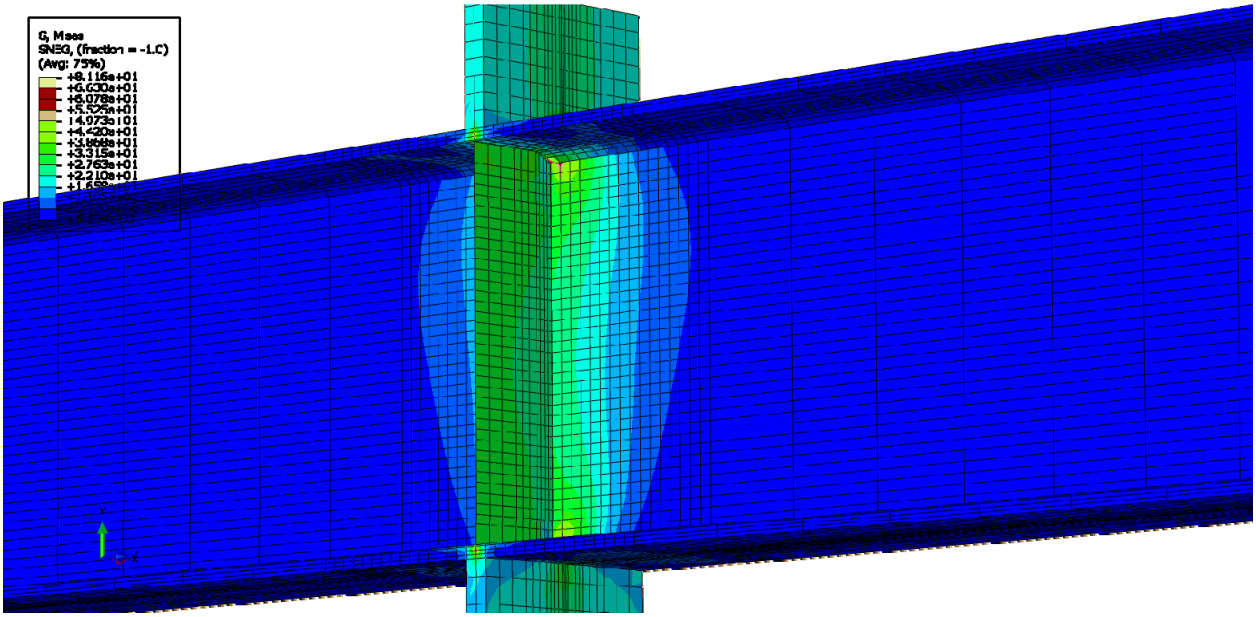

Figure E-10: Finite element model of W12X26-DC-E0 during elastic behavior

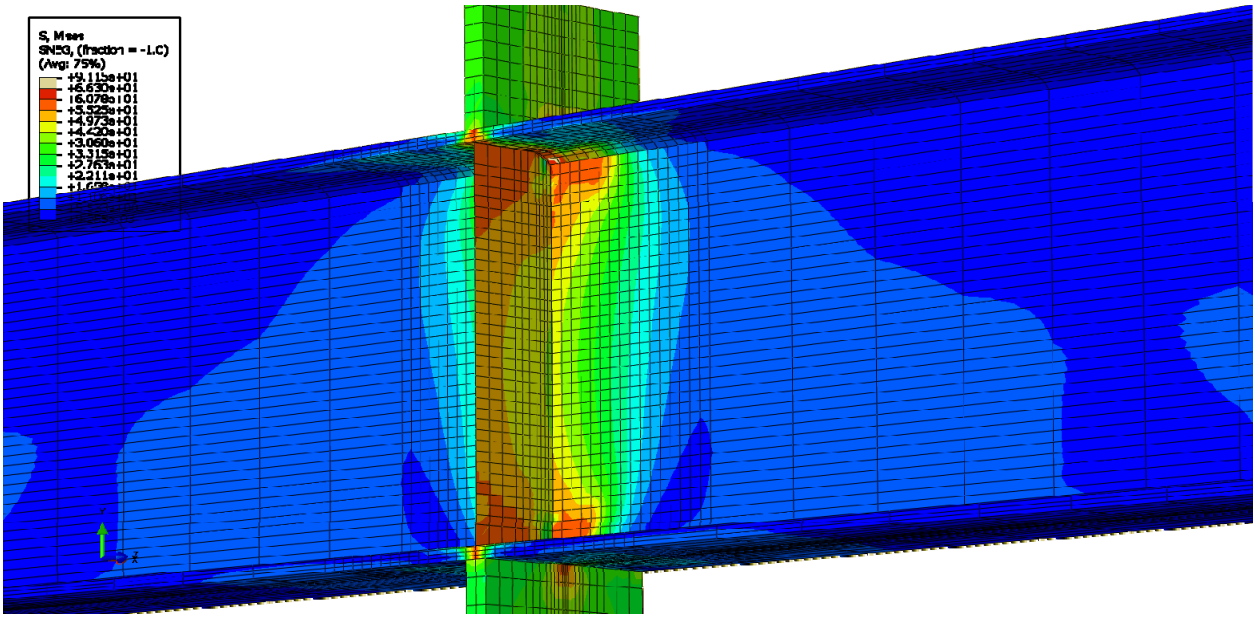

Figure E-11: Finite element model of W12X26-DC-E0 during inelastic behavior

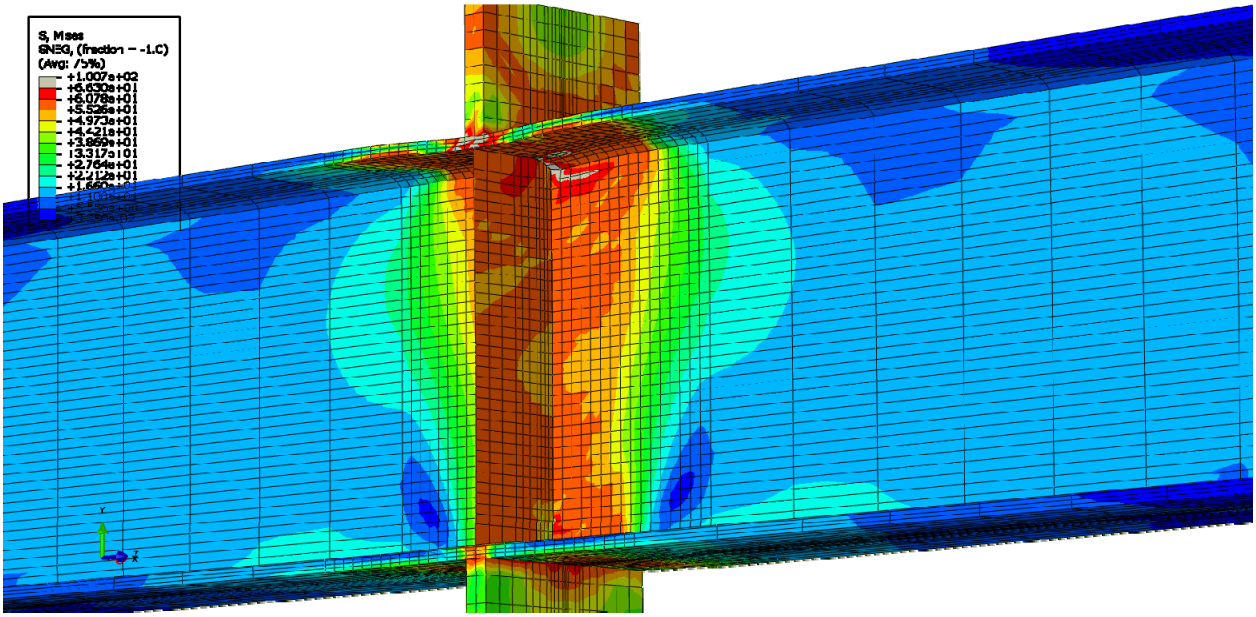

Figure E-12: Finite element model of W12X26-DC-E0 with more inelastic behavior

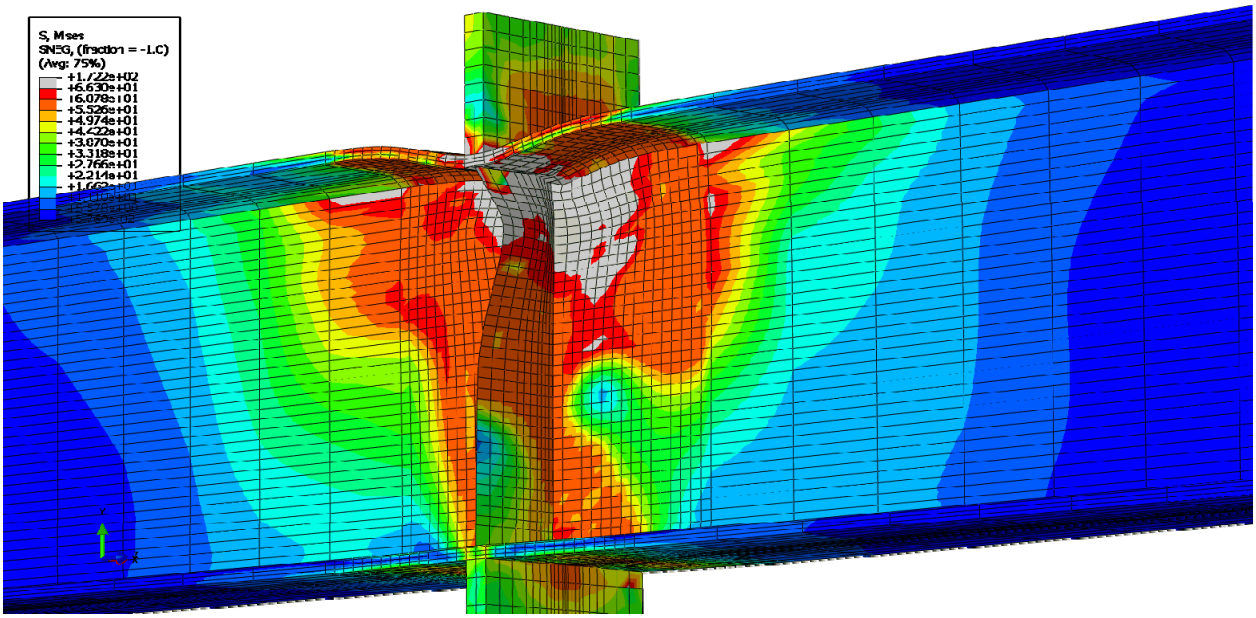

Figure E-13: Finite element model of W12X26-DC-E0 after stiffener buckling

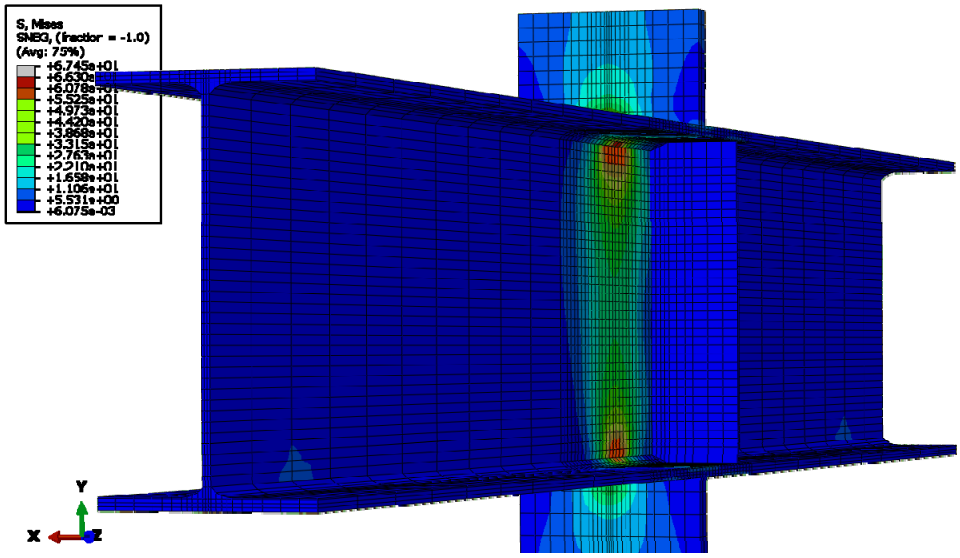

Figure E-14: Finite element model of W12X26-DC-E4 during elastic behavior

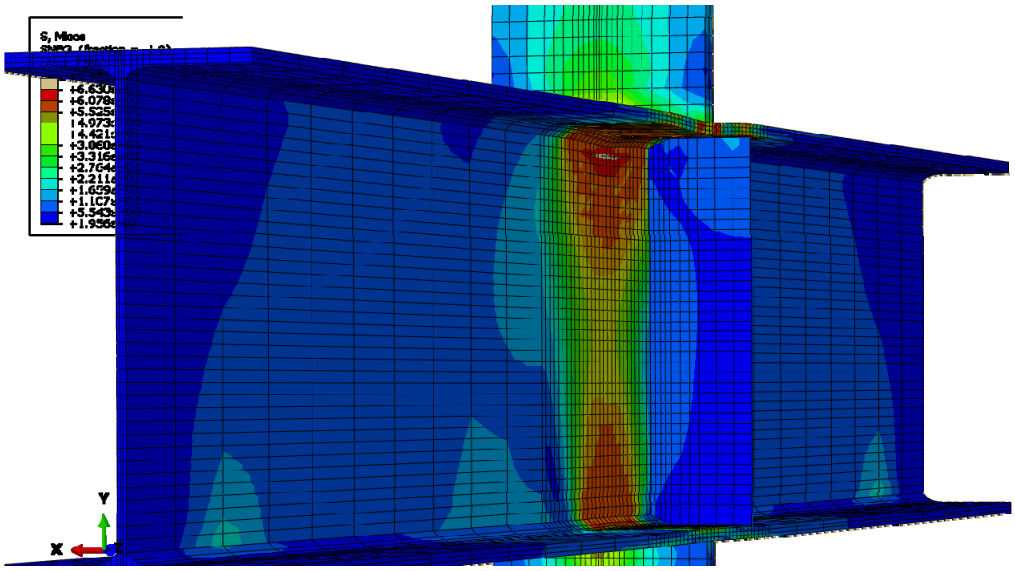

Figure E-15: Finite element model of W12X26-DC-E4 during inelastic behavior

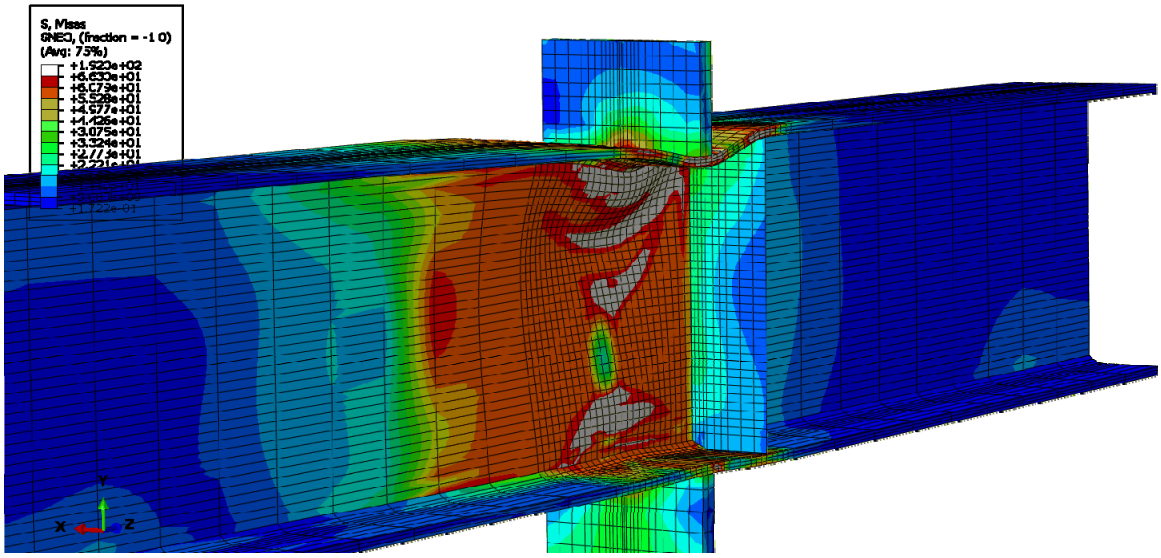

Figure E-16: Finite element model of W12X26-DC-E4 after web crippling

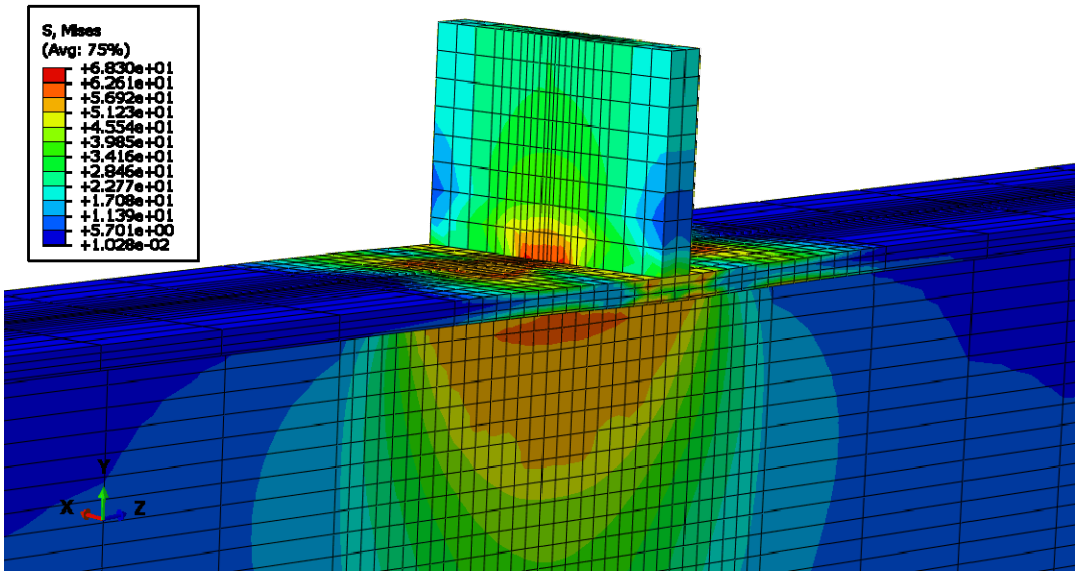

Figure E-17: Finite element model of W16X31-DC-NA during elastic behavior

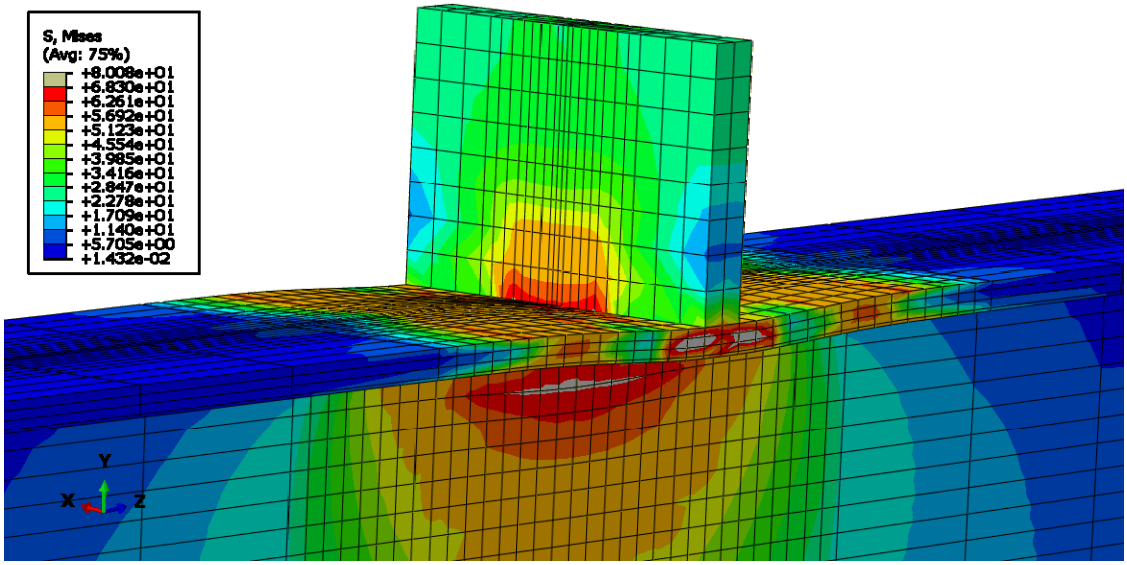

Figure E-18: Finite element model of W16X31-DC-NA during inelastic behavior

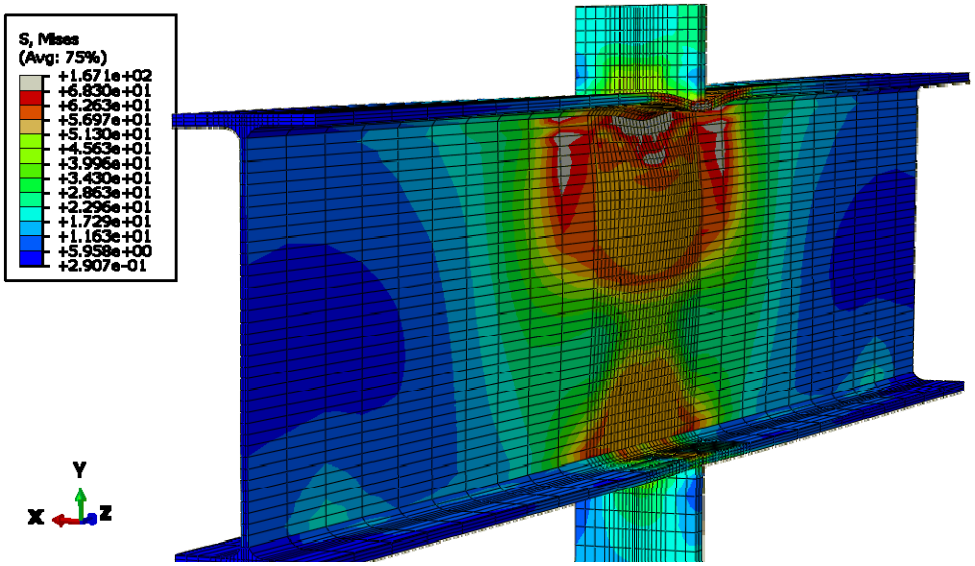

Figure E-19: Finite element model of W12X26-DC-NA showing web crippling

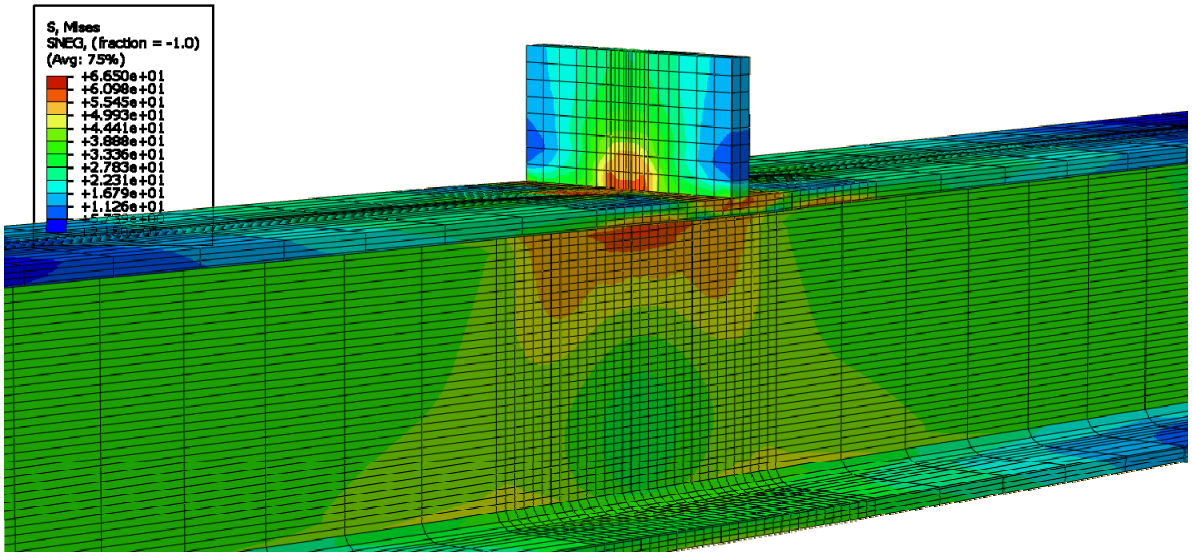

Figure E-20: Finite element model of W10X39-SC-NA during elastic behavior

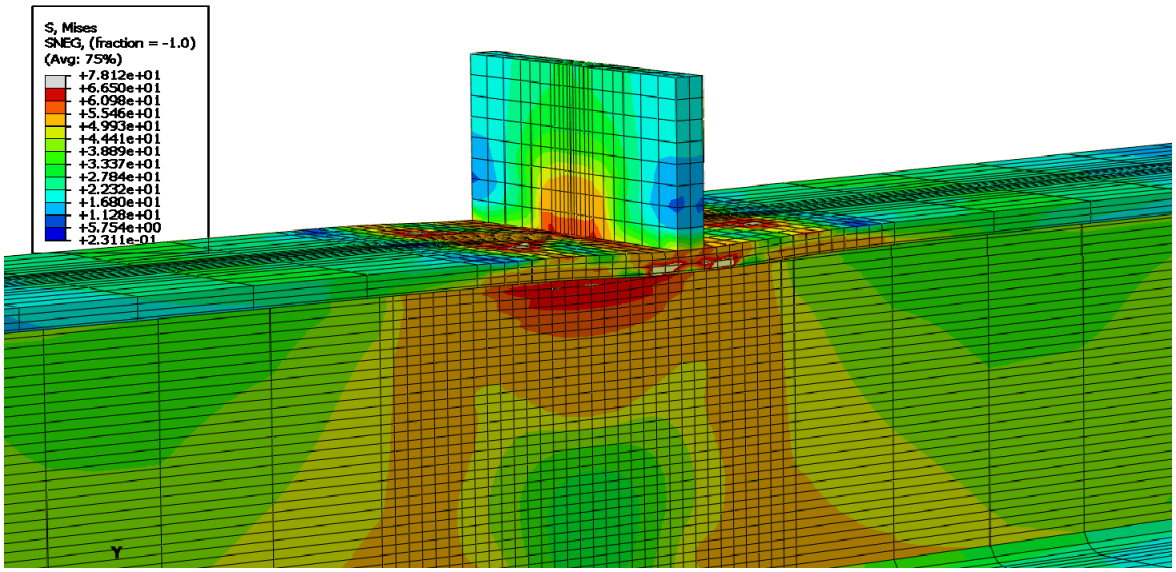

Figure E-21: Finite element model of W10X39-SC-NA during inelastic behavior

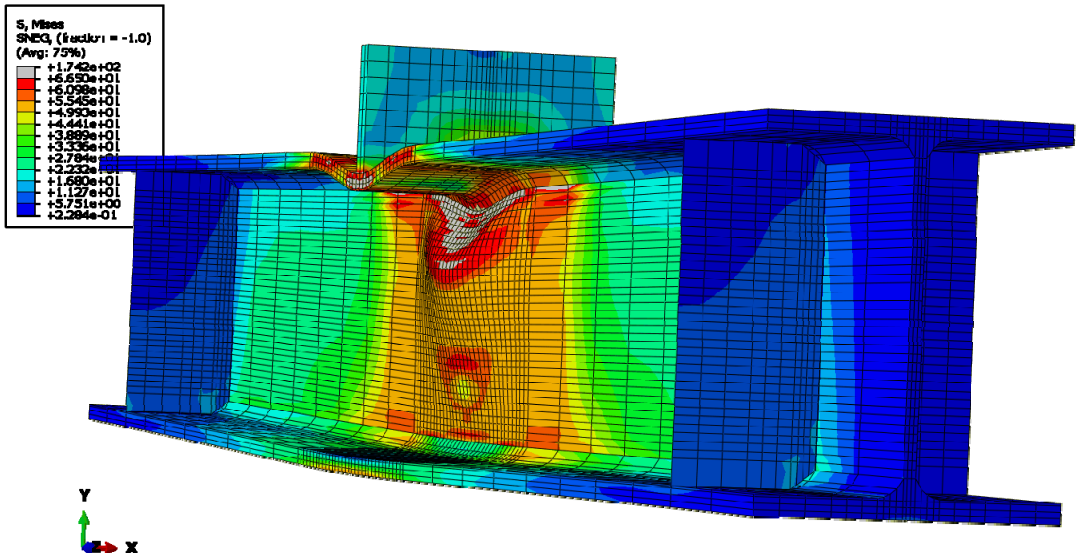

Figure E-22: Finite element model of W10X39-SC-NA after web crippling occurs

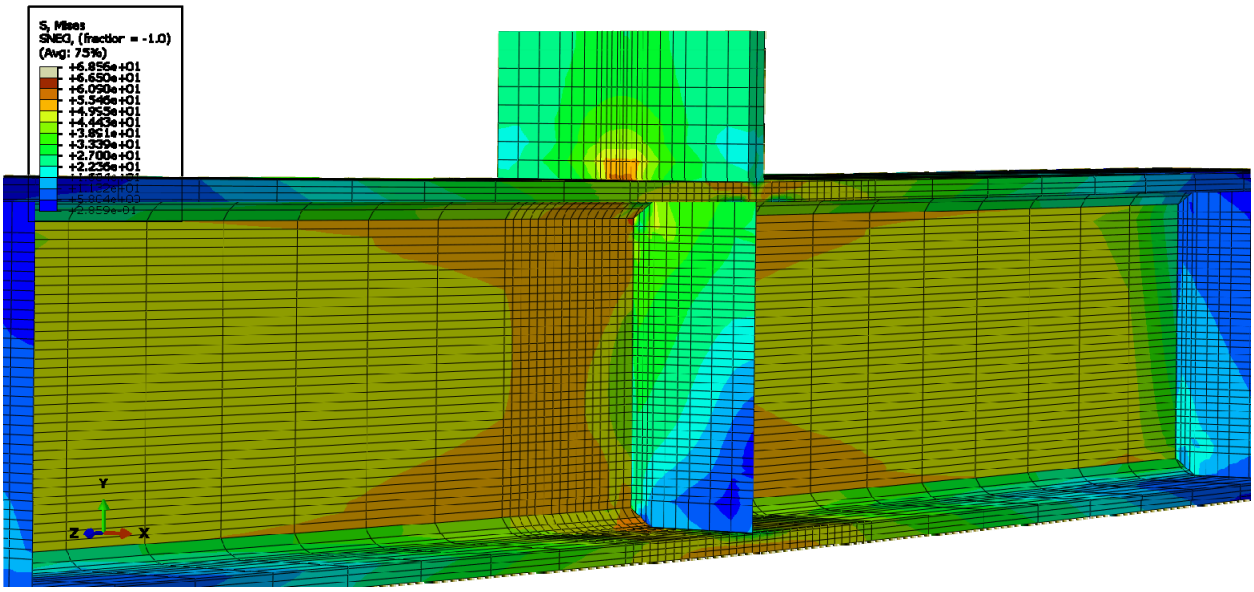

Figure E-23: Finite element model of W10X39-SC-E0 during elastic behavior

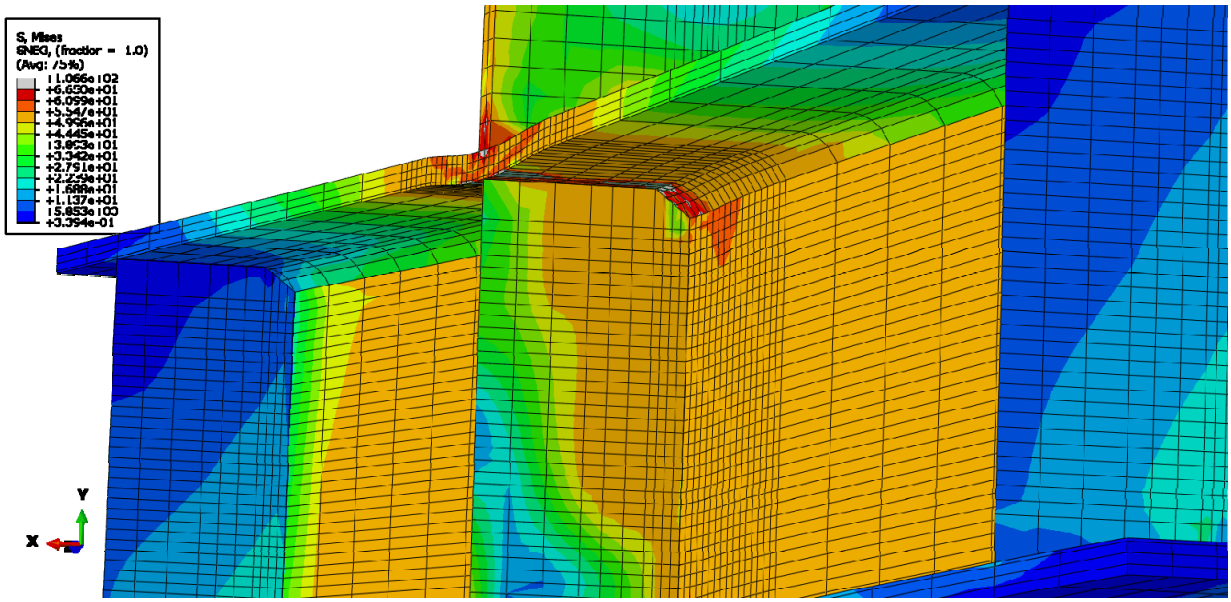

Figure E-24: Finite element model of W10X39-SC-E0 during inelastic behavior

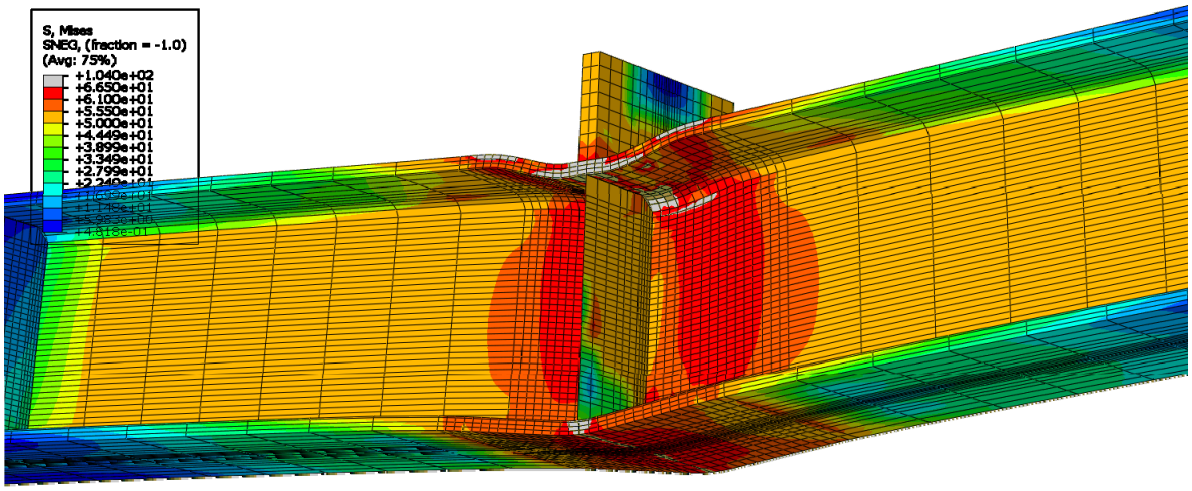

Figure E-25: Finite element model of W10X39-SC-E0 after maximum load

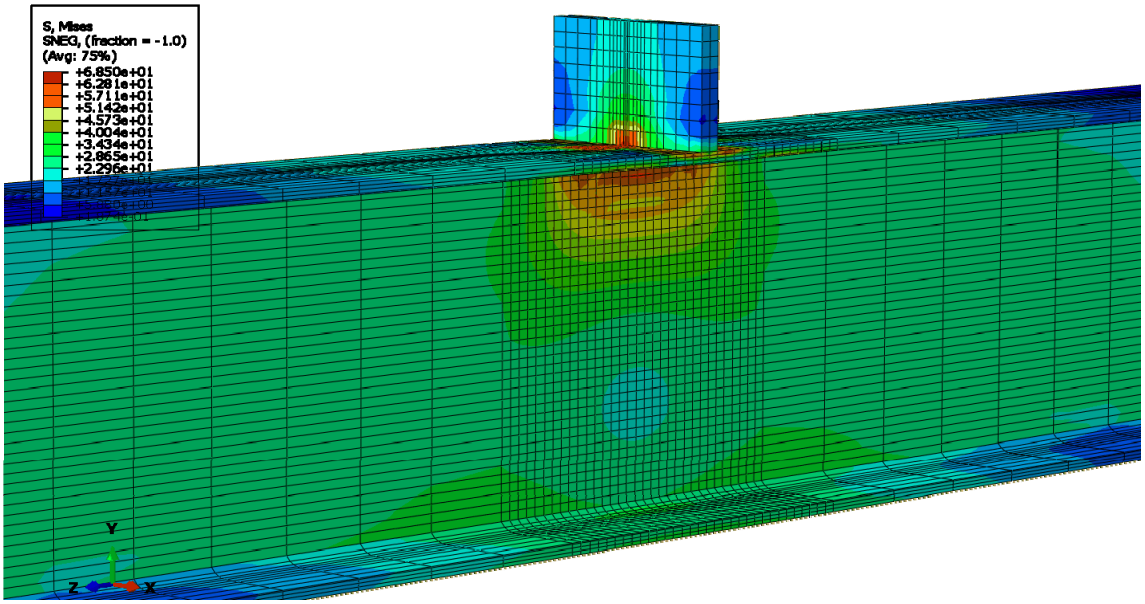

Figure E-26: Finite element model of W12X26-SC-NA during elastic behavior

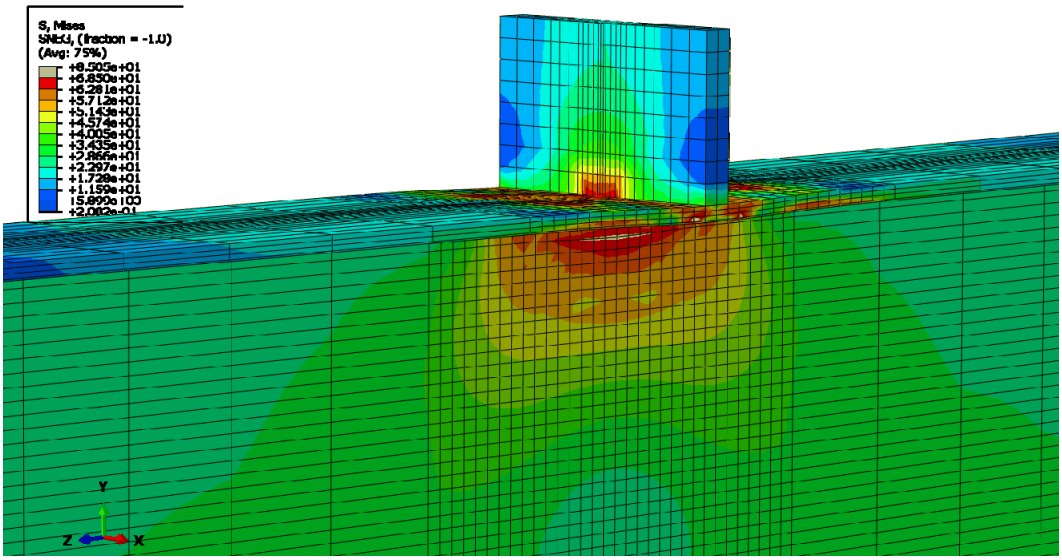

Figure E-27: Finite element model of W12X26-SC-NA during inelastic behavior

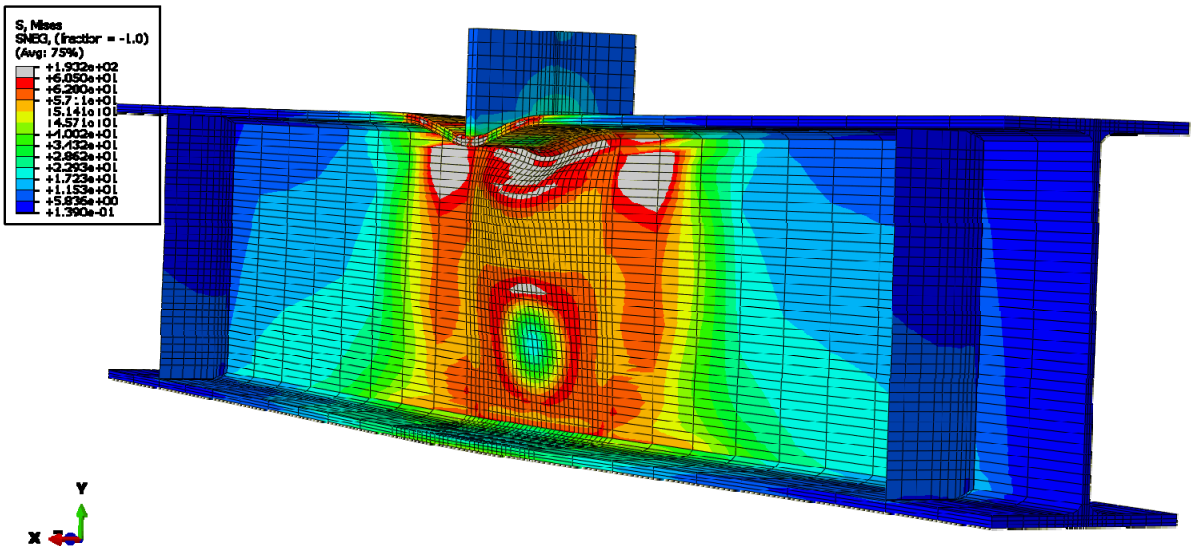

Figure E-28: Finite element model of W12X26-SC-NA after web crippling

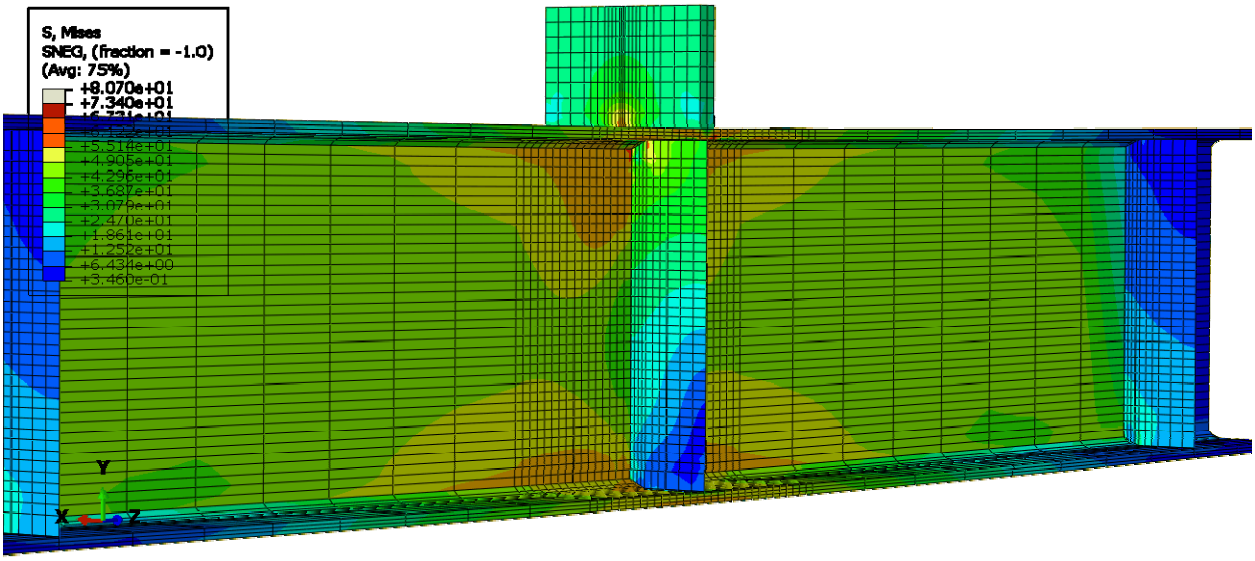

Figure E-29: Finite element model of W12X26-SC-E0 during elastic behavior

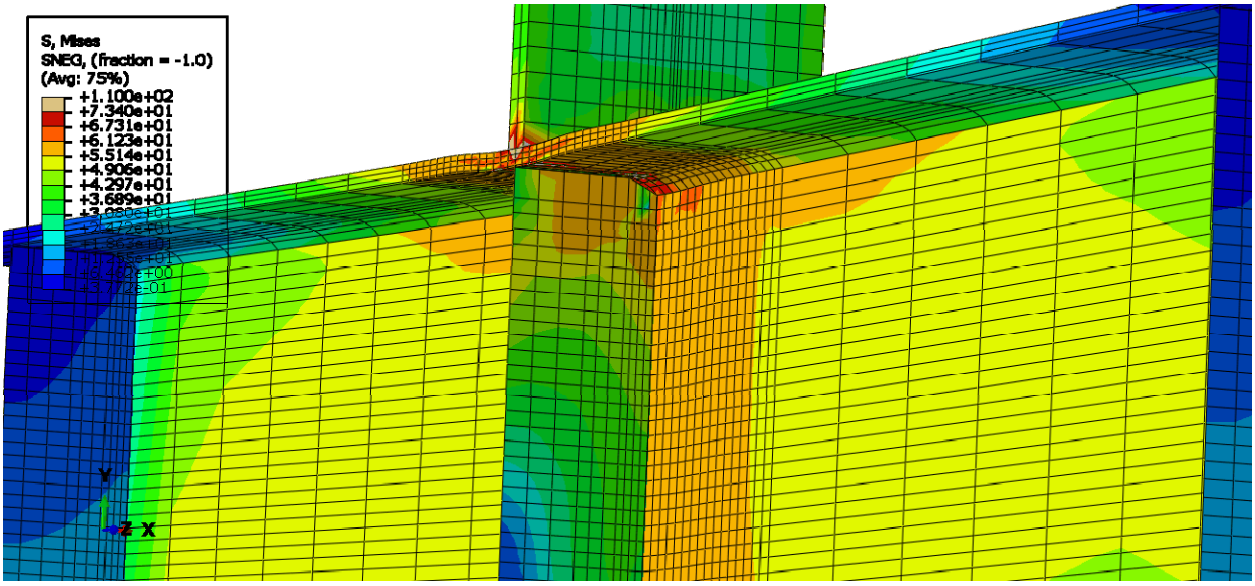

Figure E-30: Finite element model of W12X26-SC-E0 during inelastic behavior

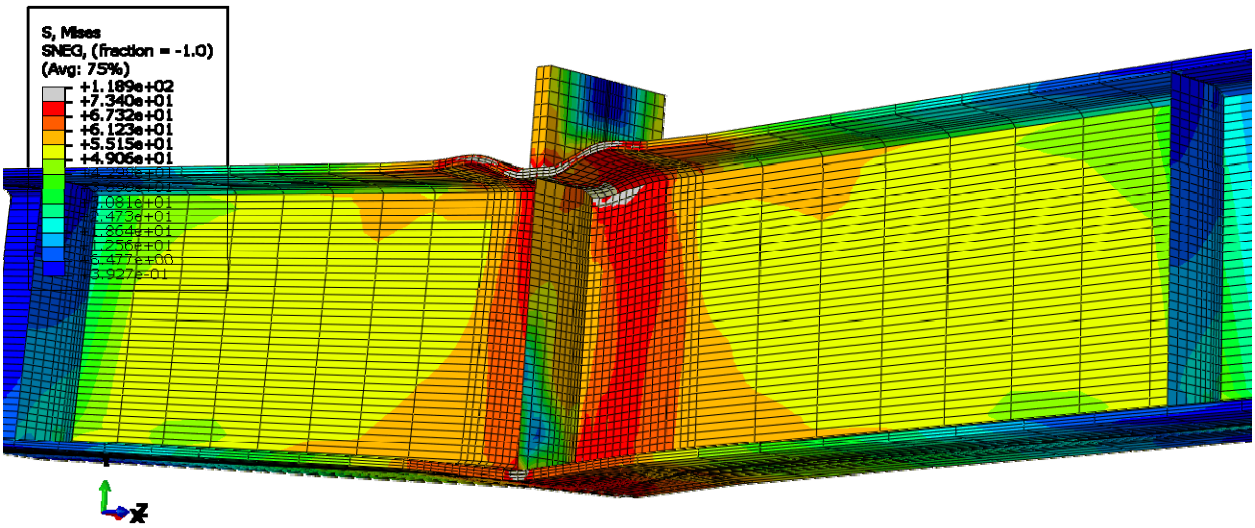

Figure E-31: Finite element model of W12X26-SC-E0 after the maximum load

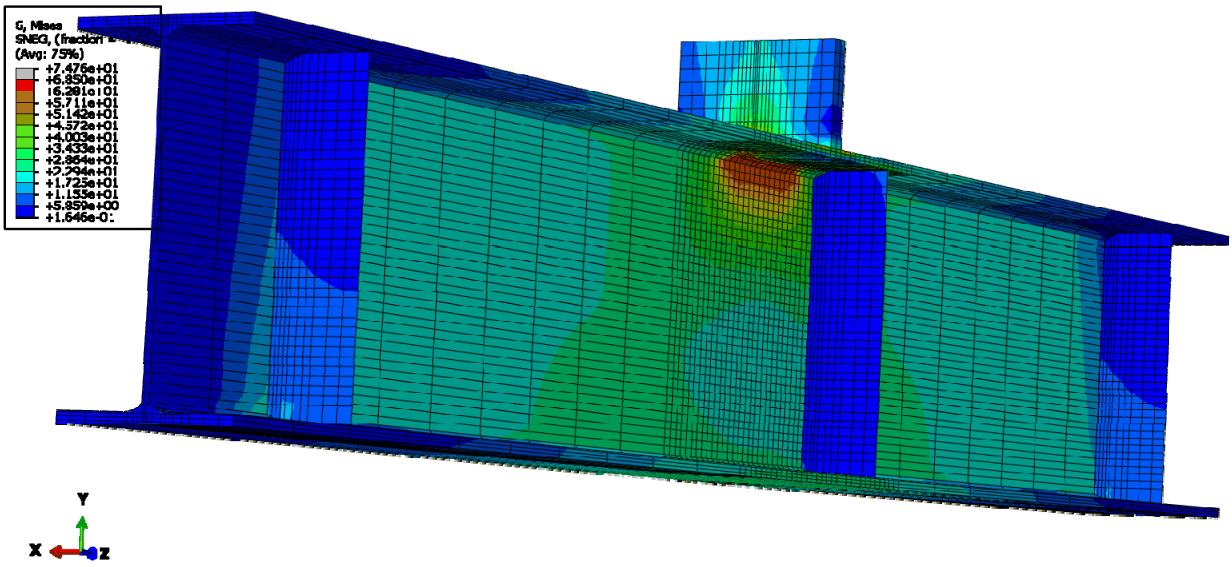

Figure E-32: Finite element model of W12X26-SC-E4 during elastic behavior

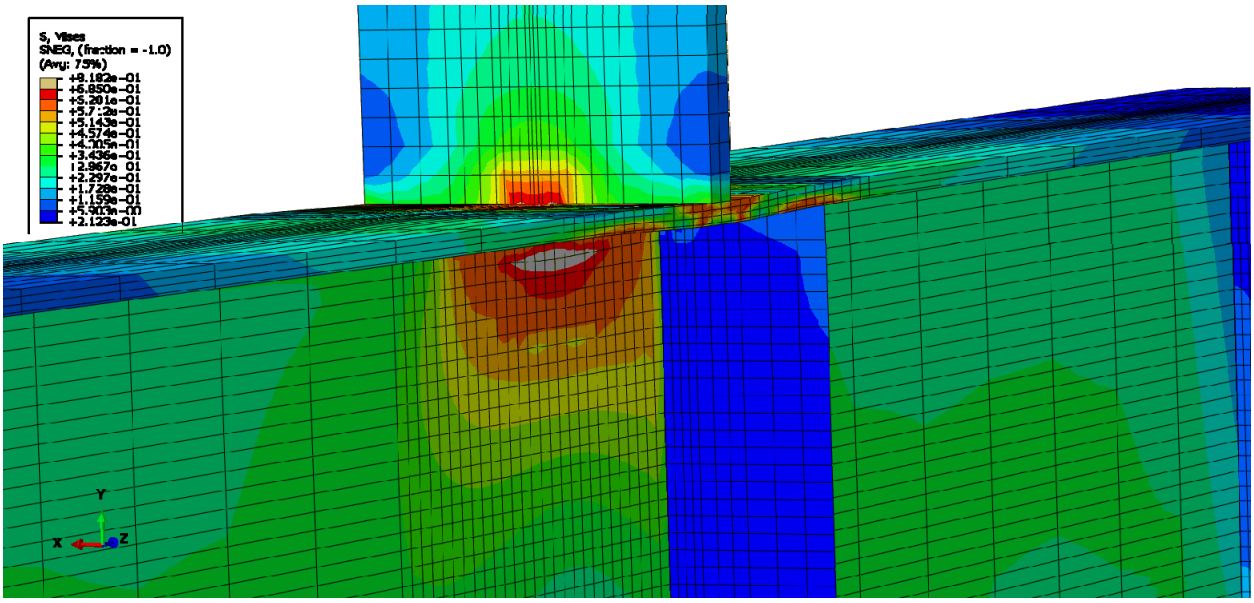

Figure E-33: Finite element model of W12X26-SC-E4 during inelastic behavior

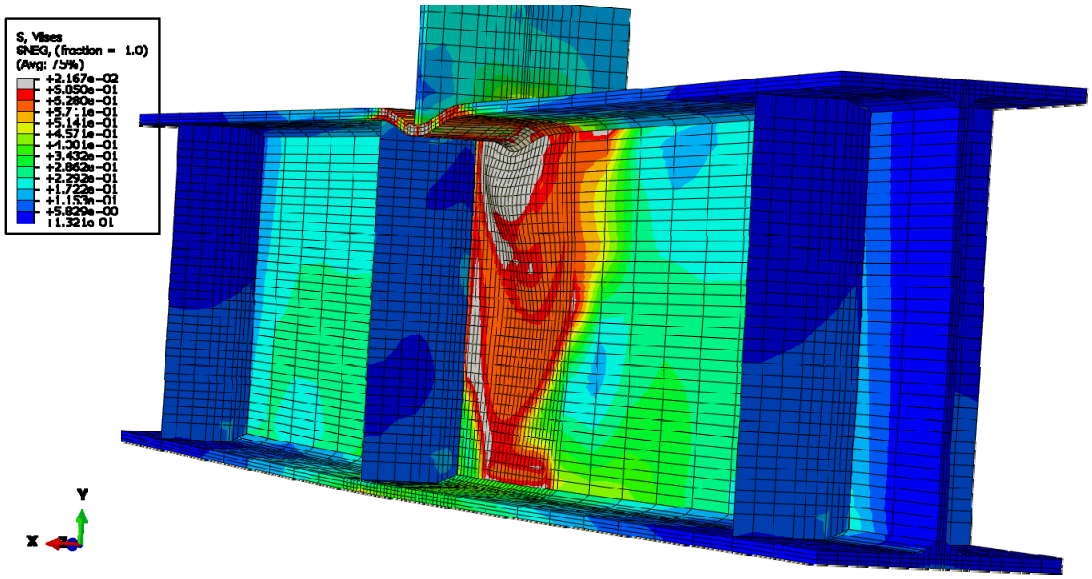

Figure E-34: Finite element model of W12X26-SC-E4 after web crippling

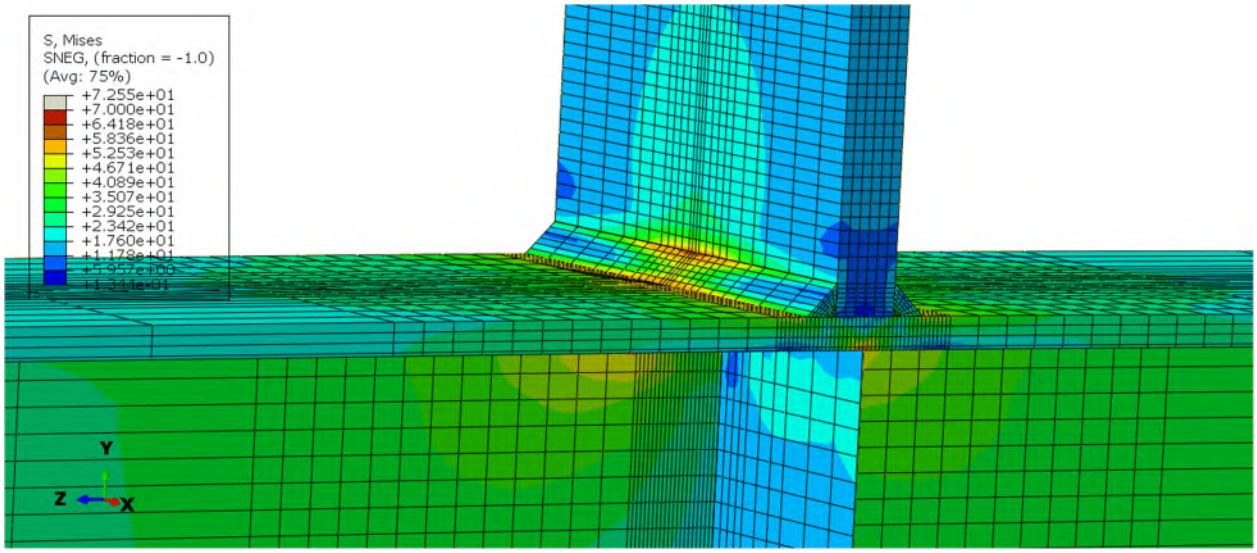

Figure E-35: Finite element model of W12X26-ST-E0 while remaining elastic

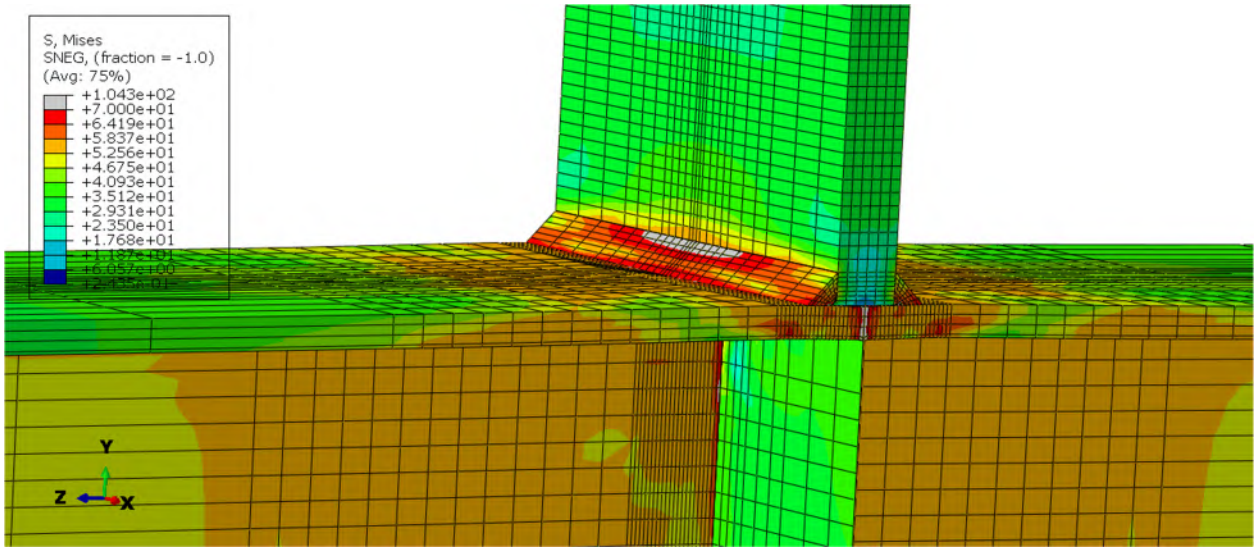

Figure E-36: Finite element model of W12X26-ST-E0 while behaving inelastic

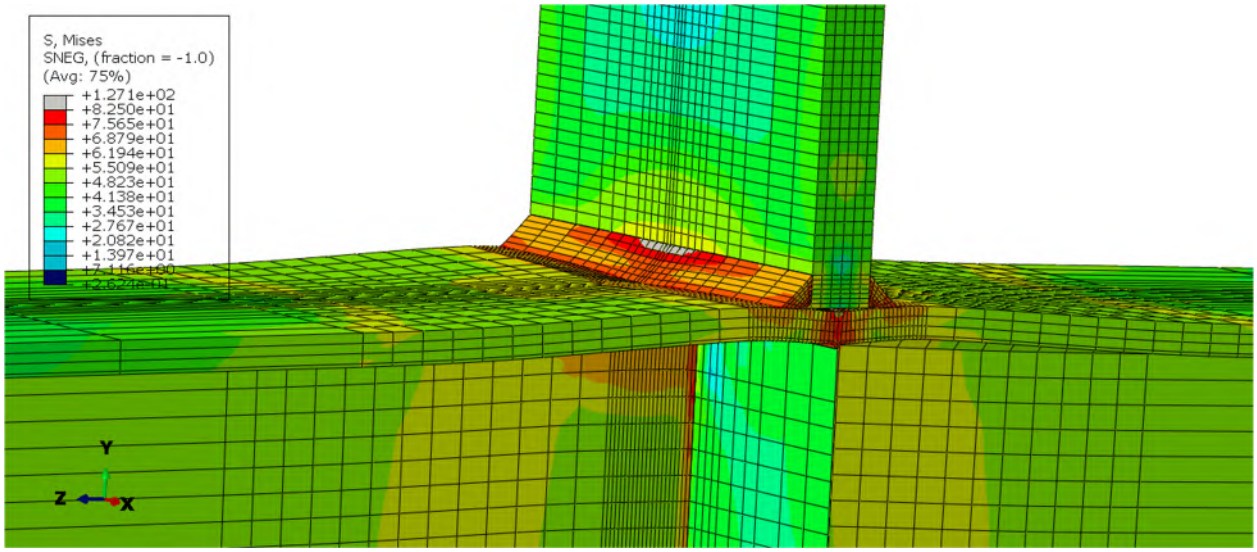

Figure E-37: Finite element model of W12X26-ST-E0 at assumed failure load of 155 kip

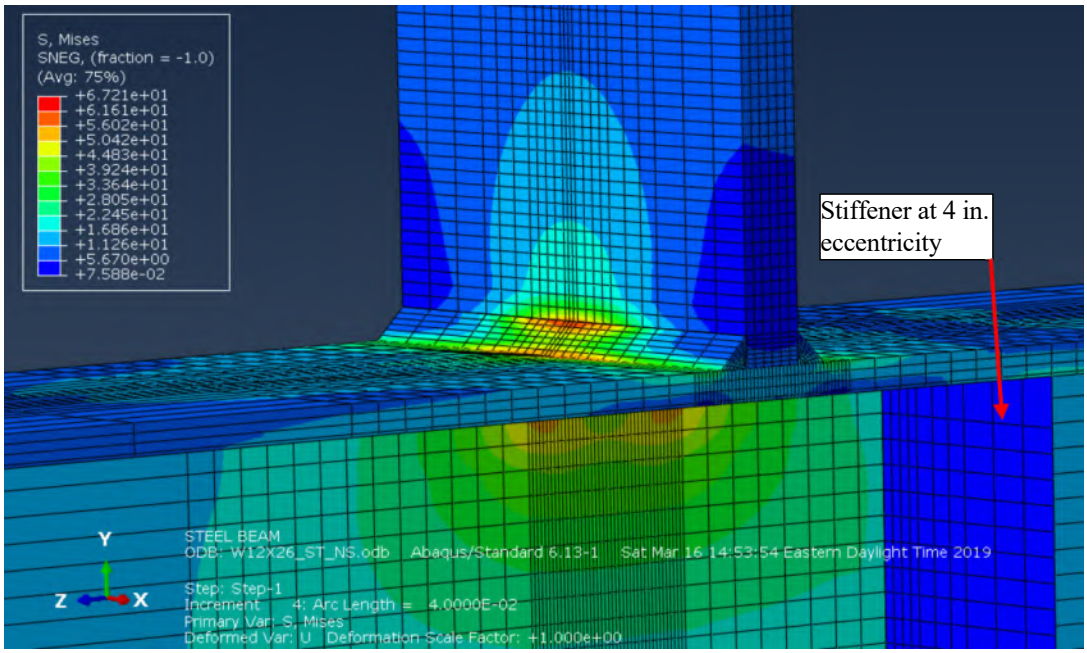

Figure E-38: Finite element model of W12X26-ST-E4 while remaining elastic

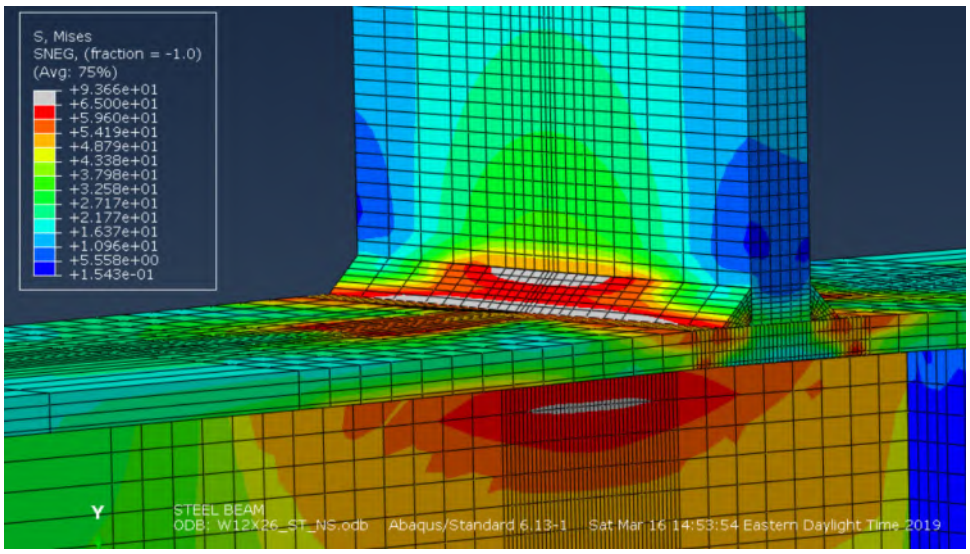

Figure E-39: Finite element model of W12X26-ST-E4 while behaving inelastic

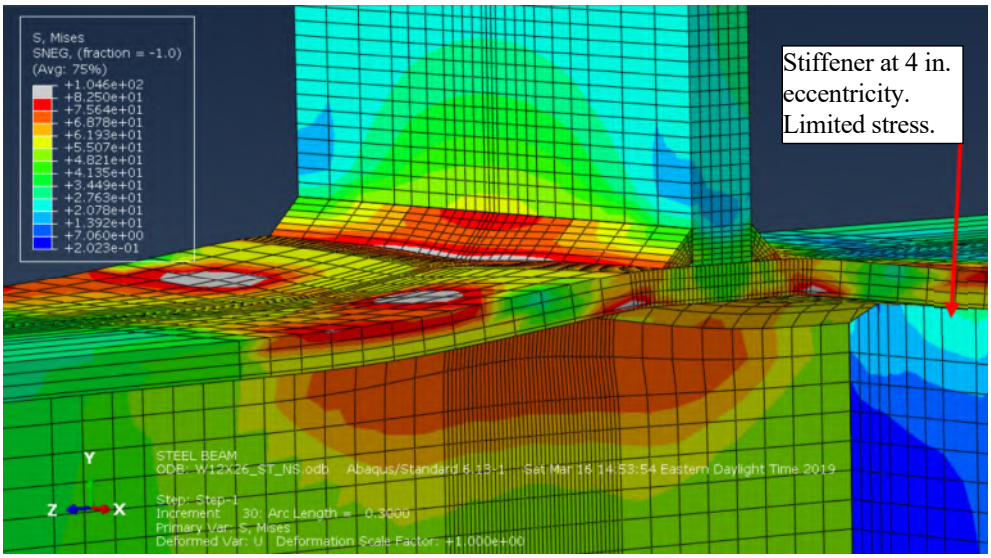

Figure E-40: Finite element model of W12X26-ST-E4 at assumed failure load of 111 kips

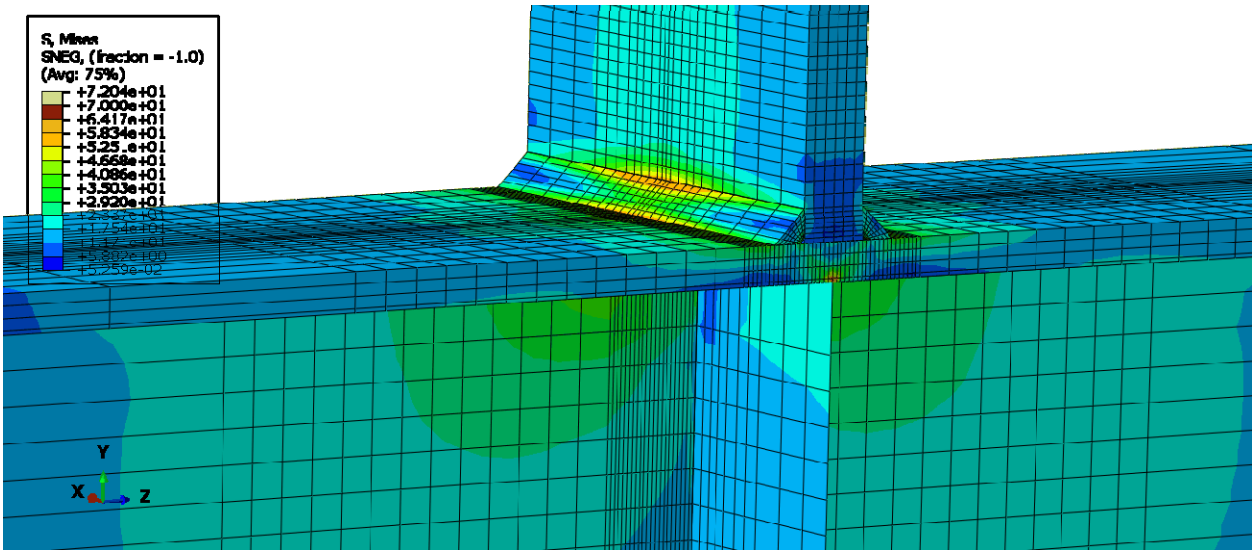

Figure E-41: Finite element model of W16X31-ST-E0 while remaining elastic

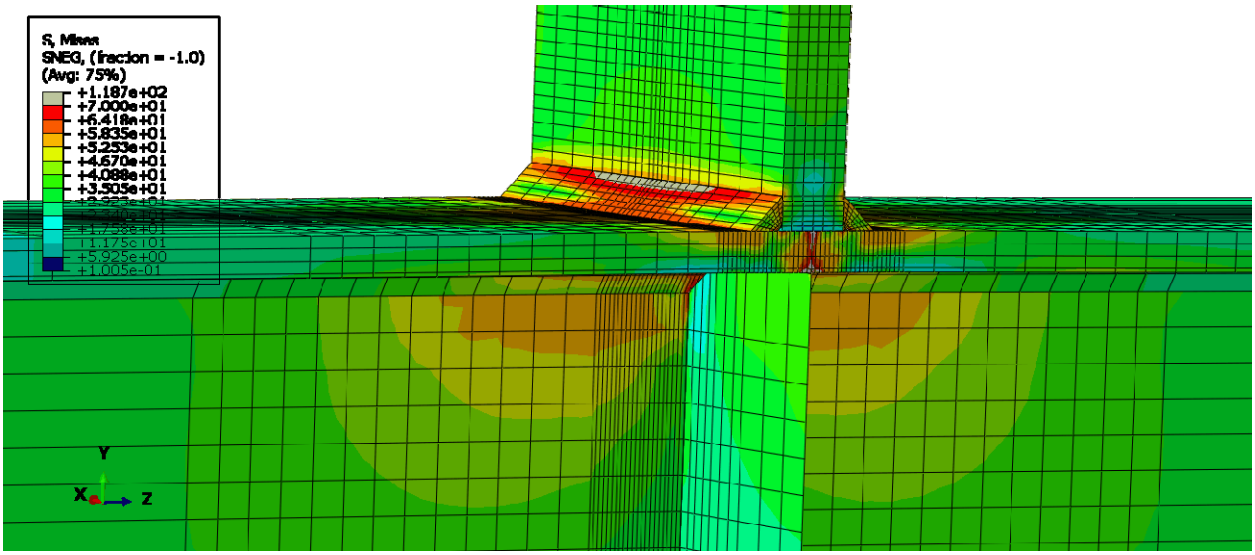

Figure E-42: Finite element model of W16X31-ST-E0 while behaving inelastic

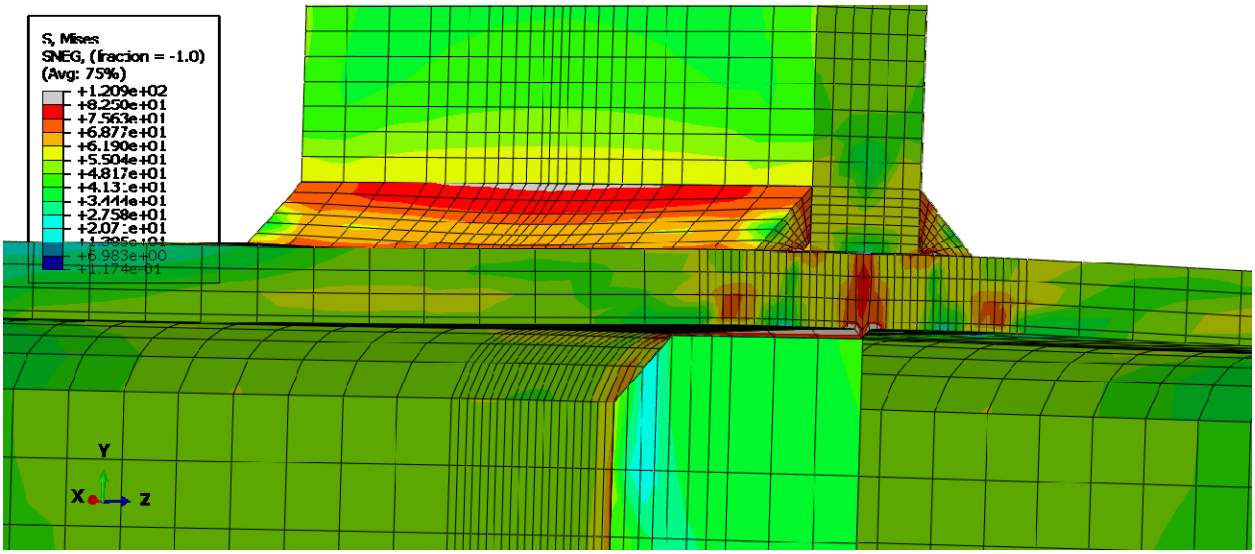

Figure E-43: Finite element model of W16X31-ST-E0 at assumed failure load of 157.5 kip

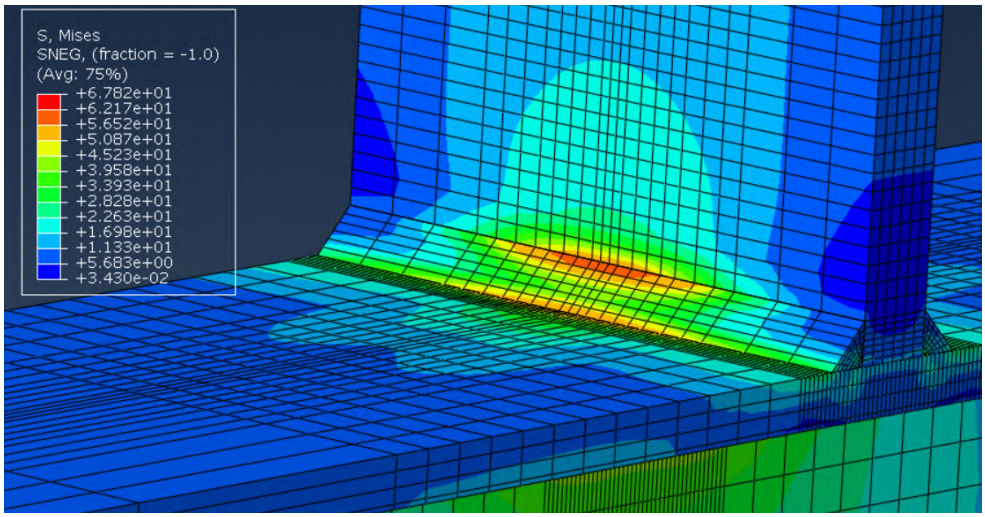

Figure E-44: Finite element model of W16X31-ST-NA during elastic behavior

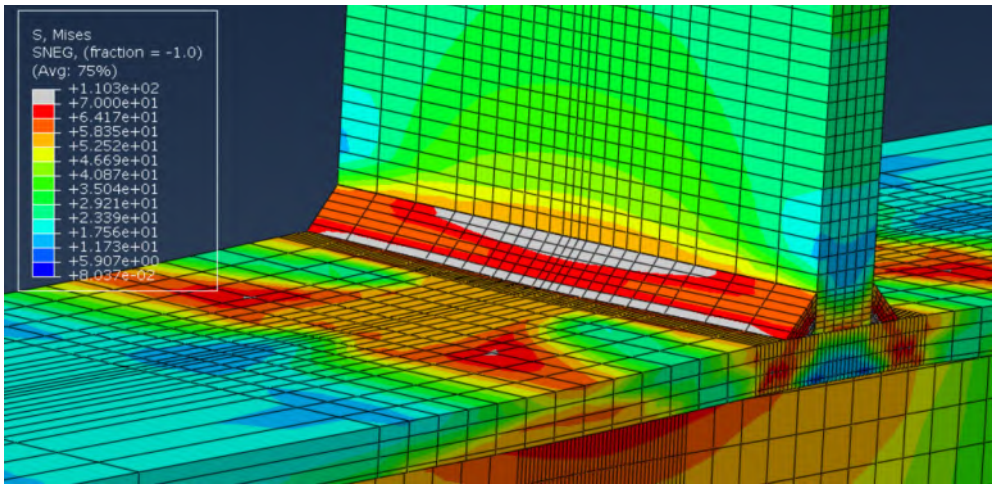

Figure E-45: Finite element model of W16X31-ST-NA during inelastic behavior

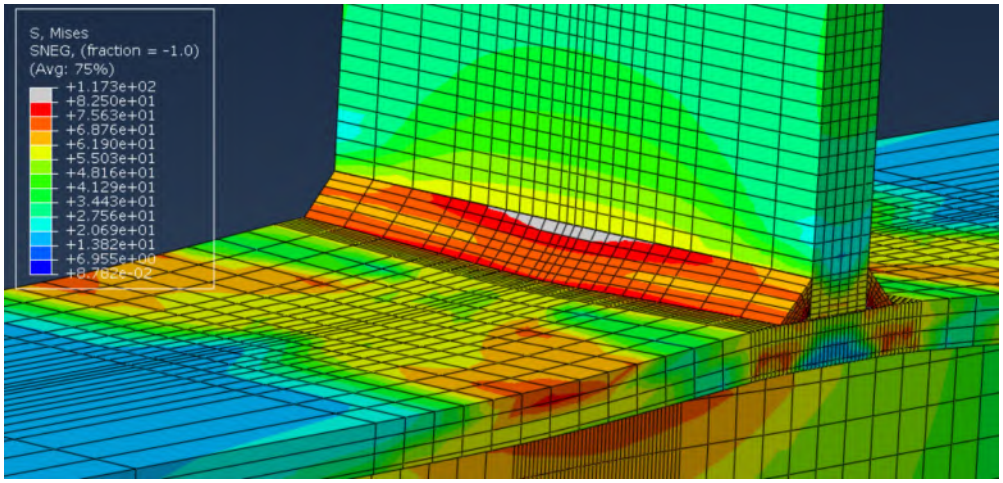

Figure E-46: Finite element model of W16X31-ST-NA at assumed failure load of 122 kips

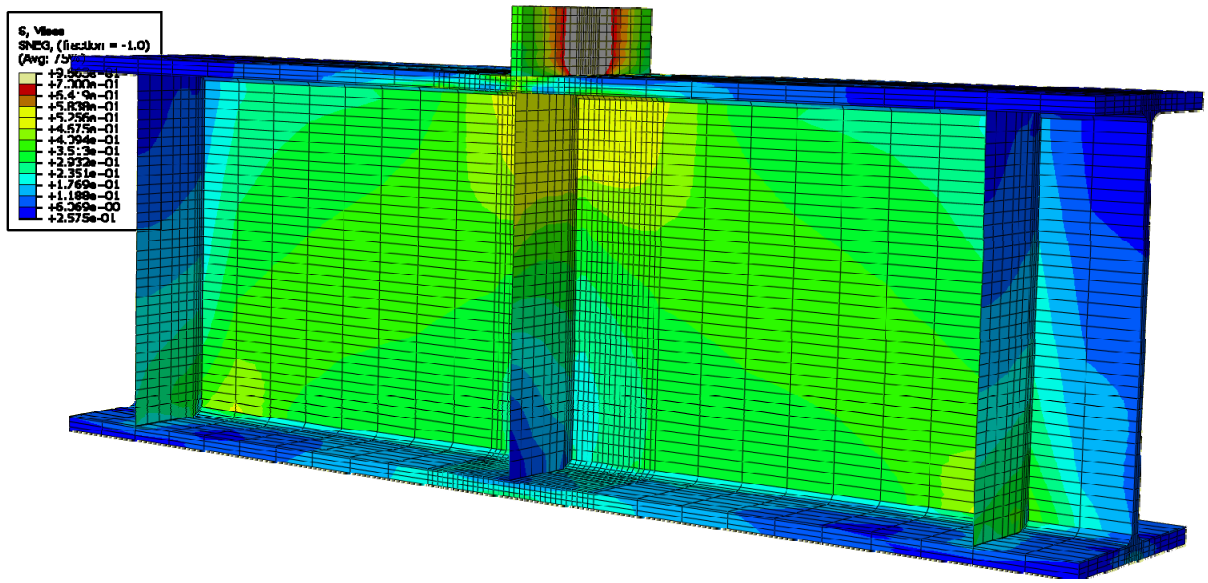

Figure E-47: Finite element model of W24X131-SC-E0 with 3/8 in. stiffeners during elastic behavior

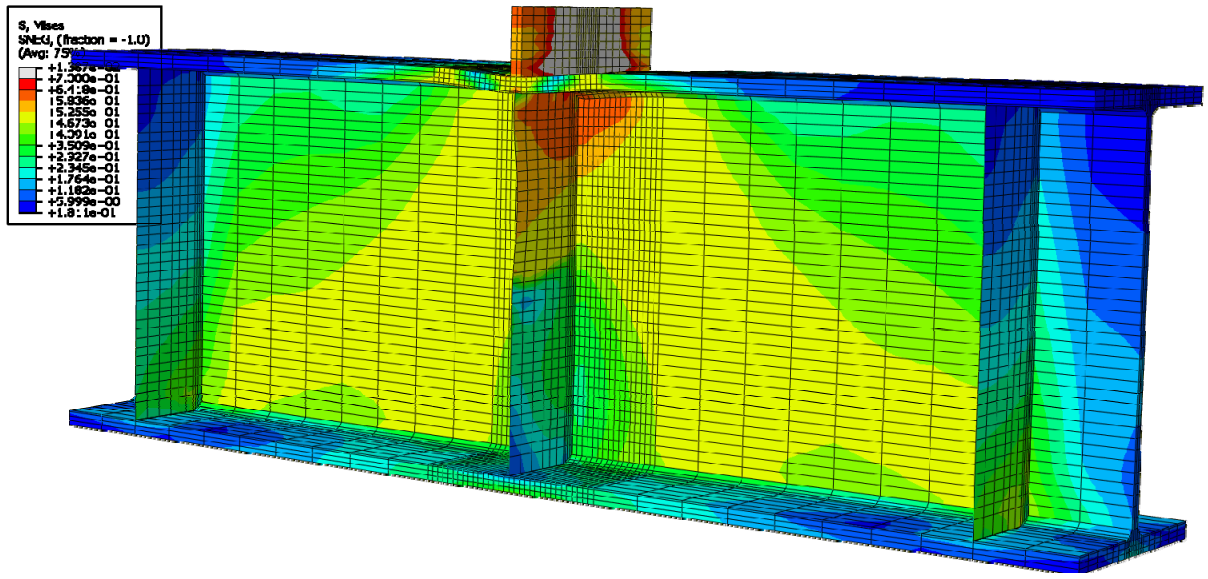

Figure E-48: Finite element model of W24X131-SC-E0 with 3/8 in. stiffeners during inelastic behavior

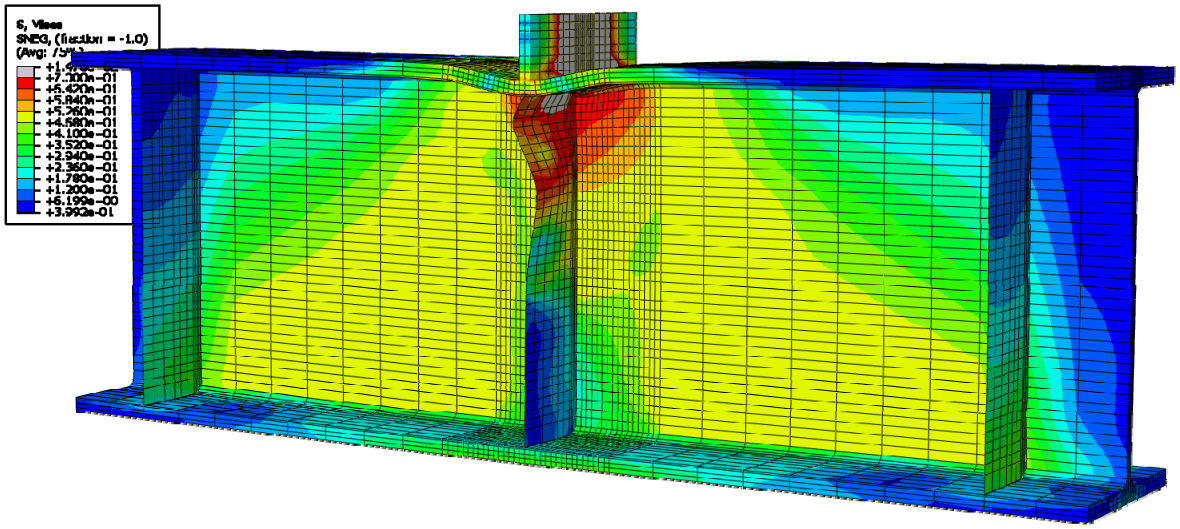

Figure E-49: Finite element model of W21X131-SC-E0 with 3/8 in. stiffeners emphasizing stiffener buckling

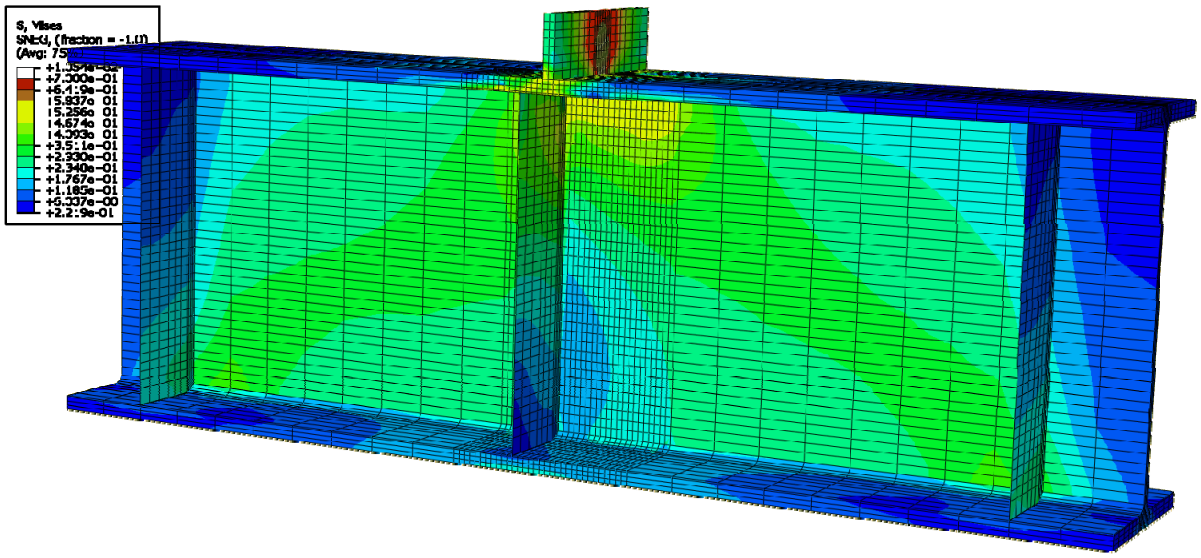

Figure E-50: Finite element model of W24X131-SC-E2 with 3/8 in. stiffeners during elastic behavior

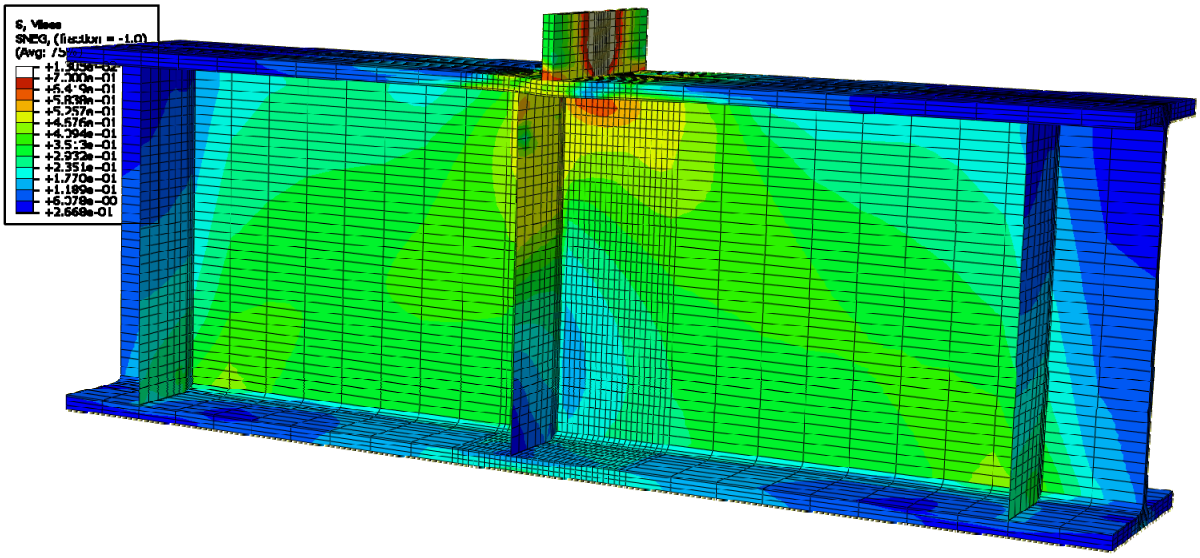

Figure E-51: Finite element model of W24X131-SC-E2 with 3/8 in. stiffeners during inelastic behavior

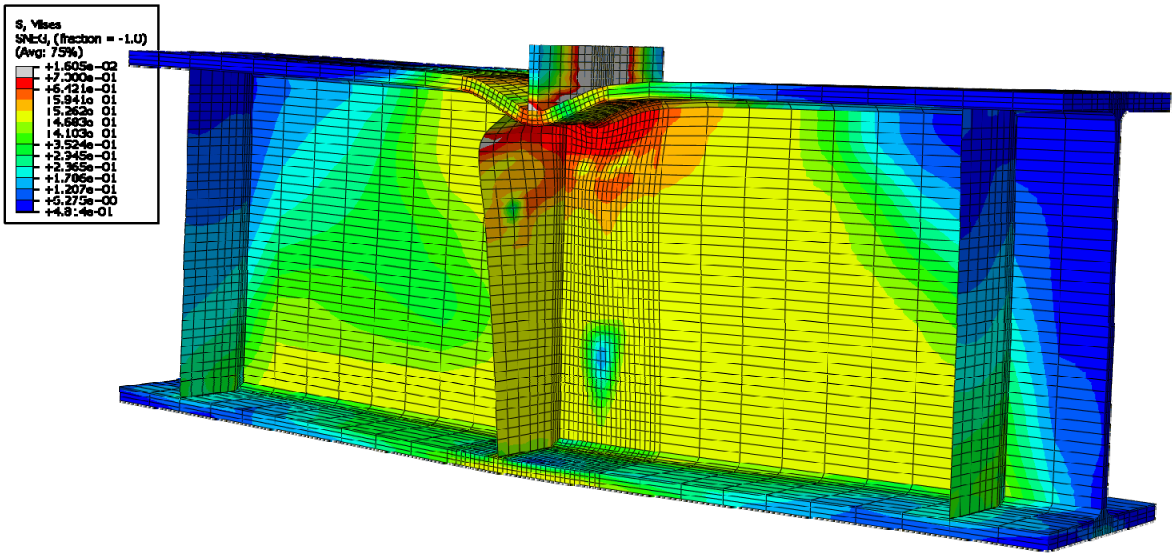

Figure E-52: Finite element model of W24X131-SC-E2 with 3/8 in. stiffeners after the maximum load

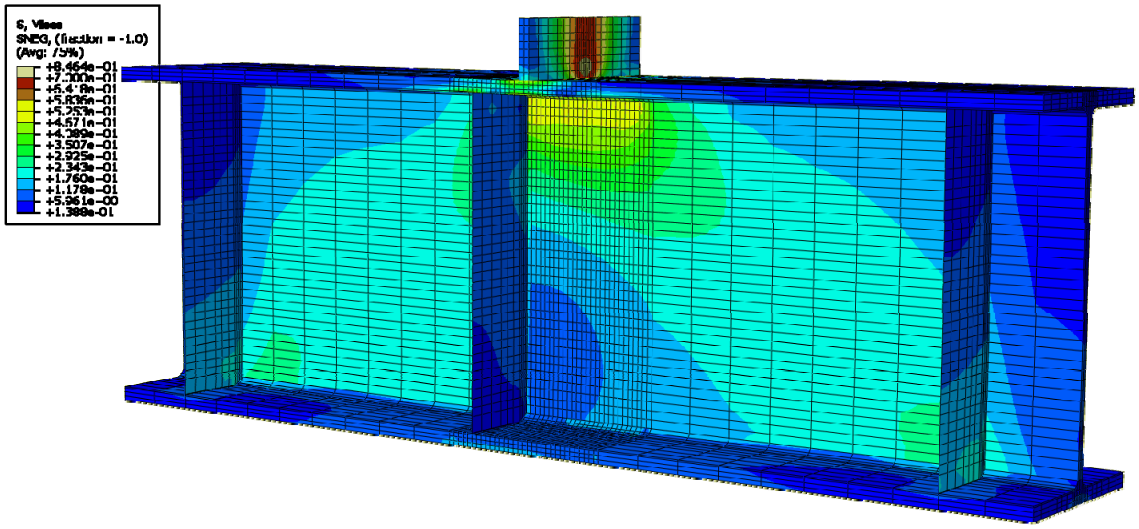

Figure E-53: Finite element model of W24X131-SC-E4 with 3/8 in. stiffeners during elastic behavior

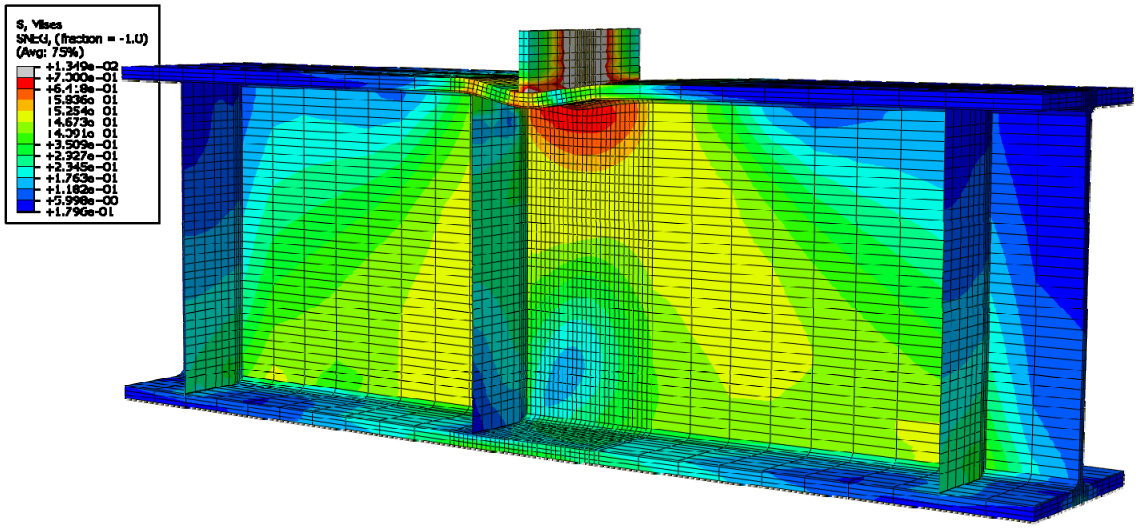

Figure E-54: Finite element model of W24X131-SC-E4 with 3/8 in. stiffeners during inelastic behavior

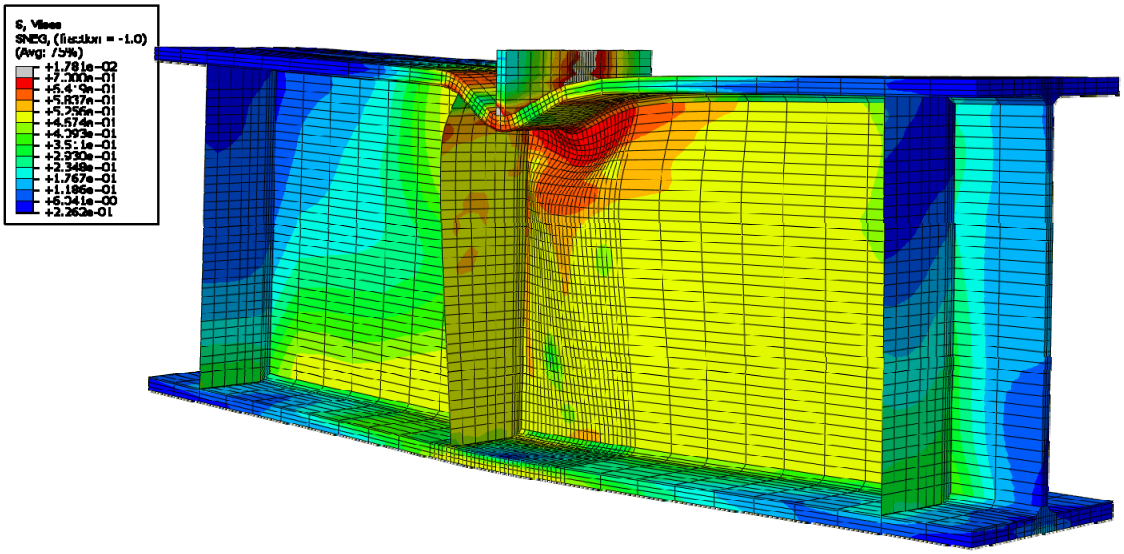

Figure E-55: Finite element model of W24X131-SC-E4 with 3/8 in. stiffeners after the maximum load

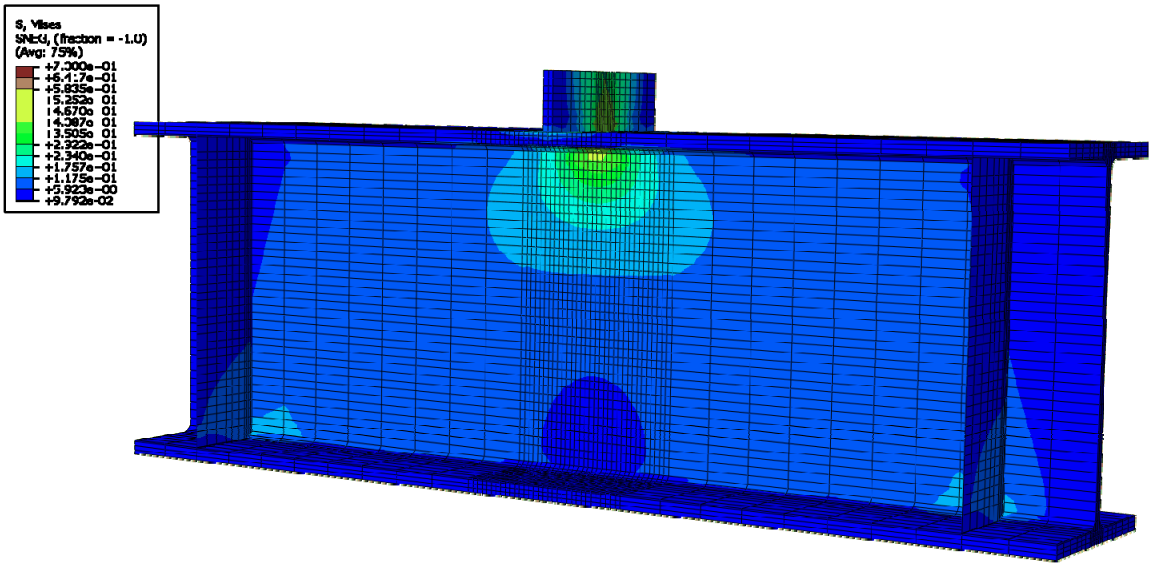

Figure E-56: Finite element model of W24X131-SC-NA during elastic behavior

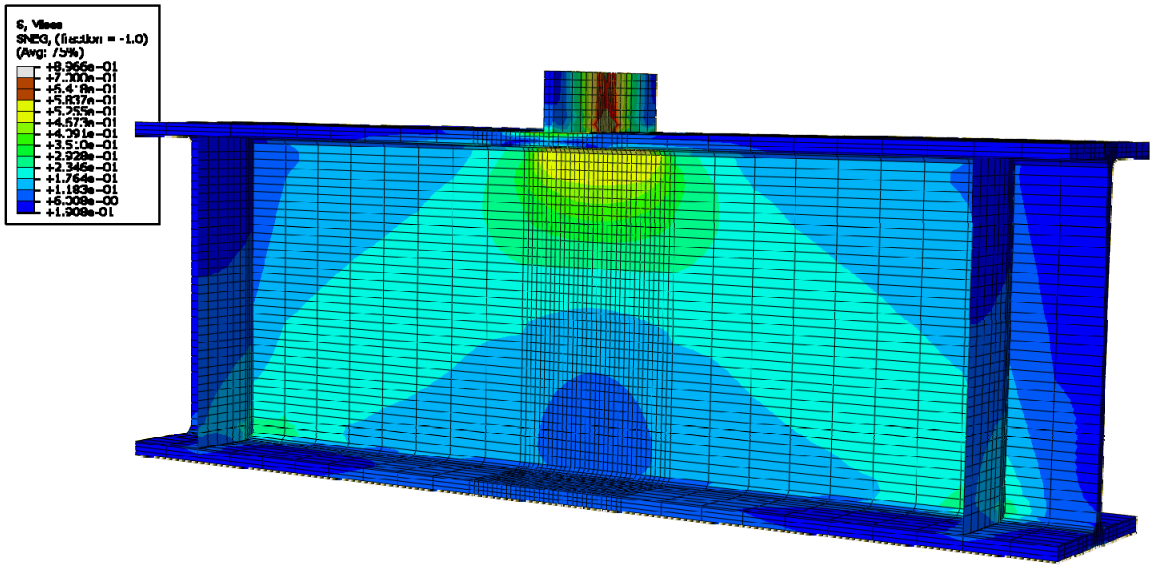

Figure E-57: Finite element model of W24X131-SC-NA during inelastic behavior

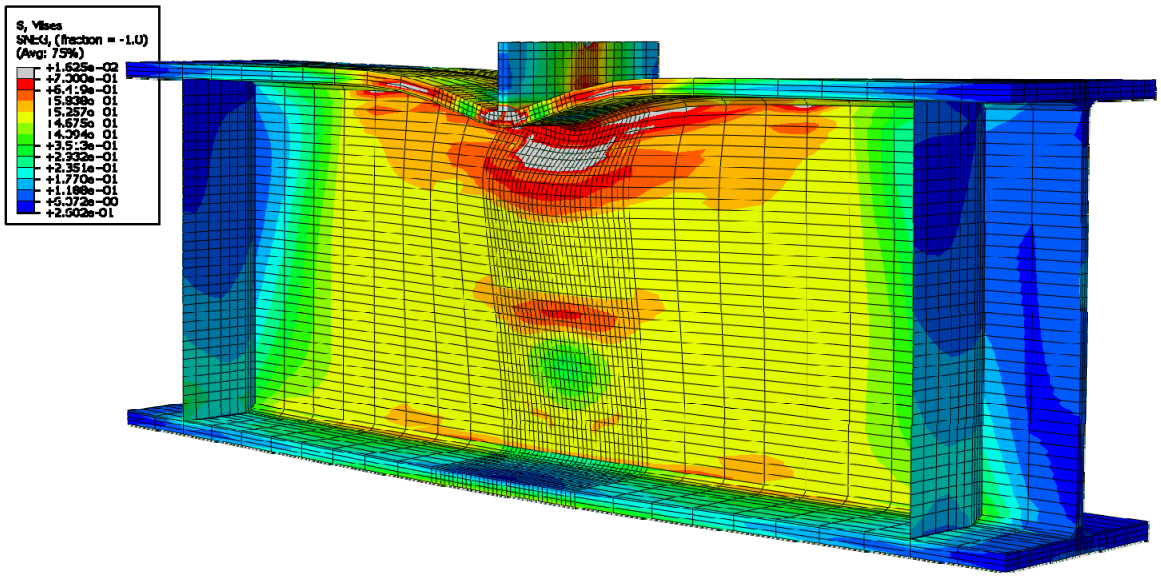

Figure E-58: Finite element model of W24X131-SC-NA after the maximum load emphasizing web crippling

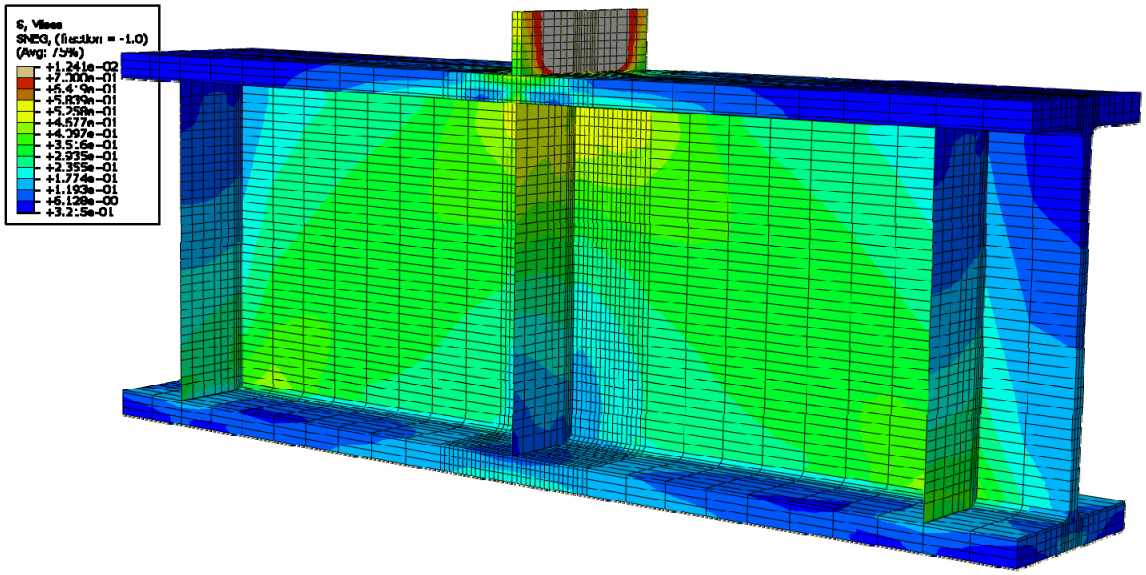

Figure E-59: Finite element model of W24X229-SC-E0 with 3/8 in. stiffeners during elastic behavior

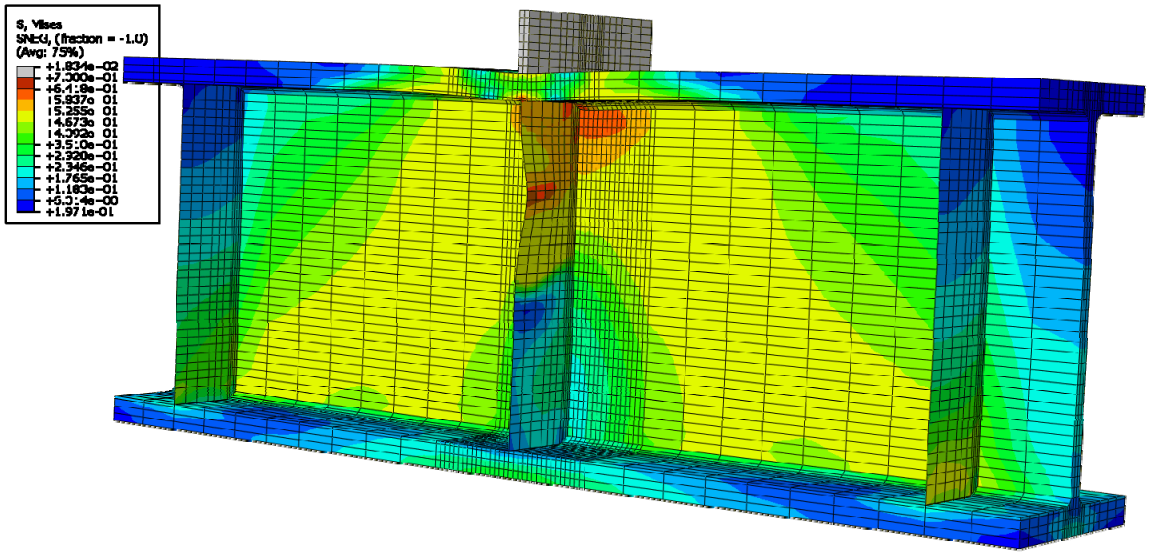

Figure E-60: Finite element model of W24X229-SC-E0 with 3/8 in. stiffeners during inelastic behavior

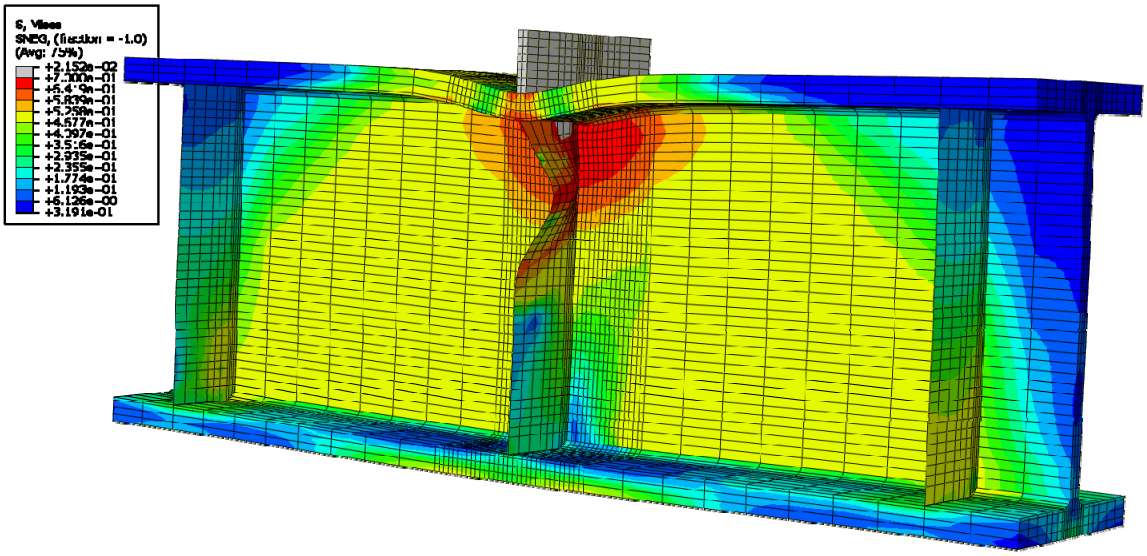

Figure E-61: Finite element model of W24X229-SC-E0 with 3/8 in. stiffeners after the maximum load emphasizing stiffener buckling

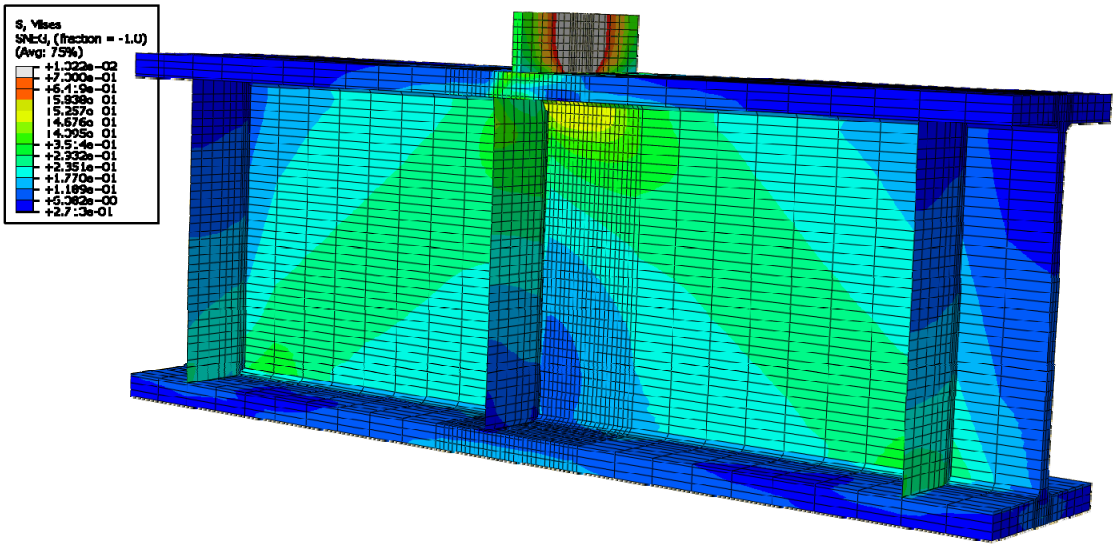

Figure E-62: Finite element model of W24X229-SC-E2 with 3/8 in. stiffeners during elastic behavior

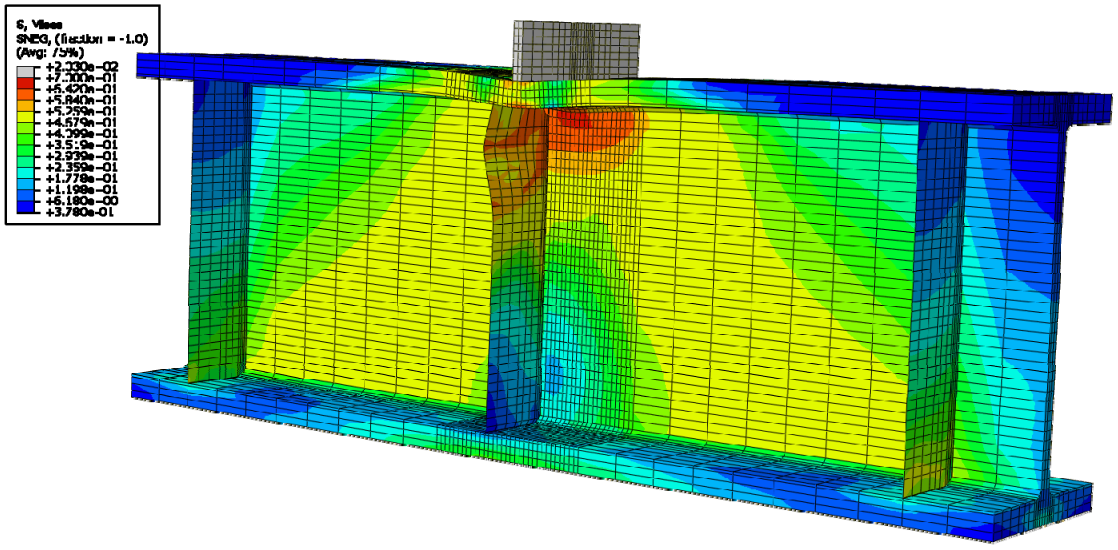

Figure E-63: Finite element model of W24X229-SC-E2 with 3/8 in. stiffeners during inelastic behavior

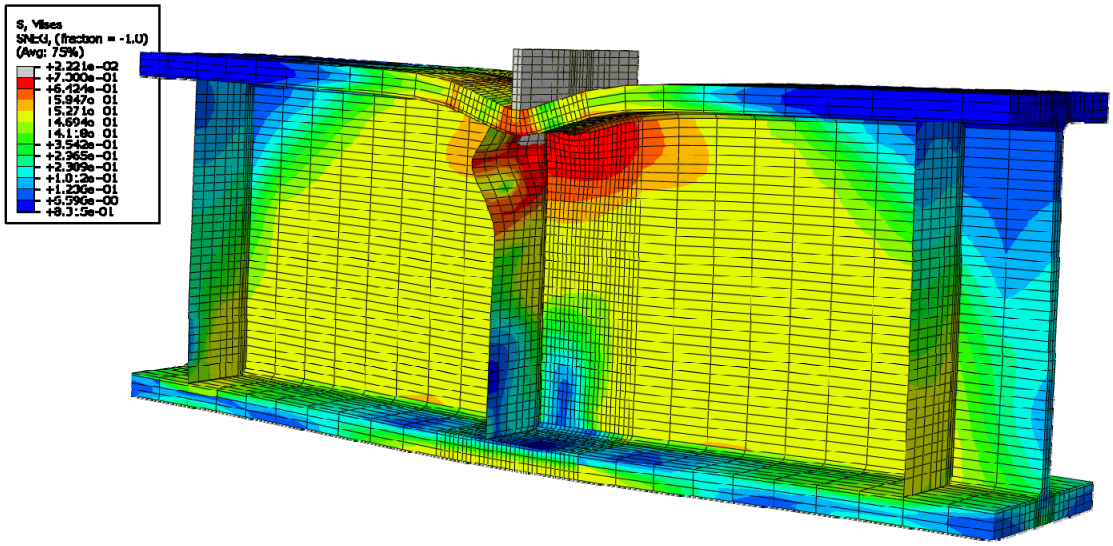

Figure E-64: Finite element model of W24X229-SC-E2 with 3/8 in. stiffeners after the maximum load

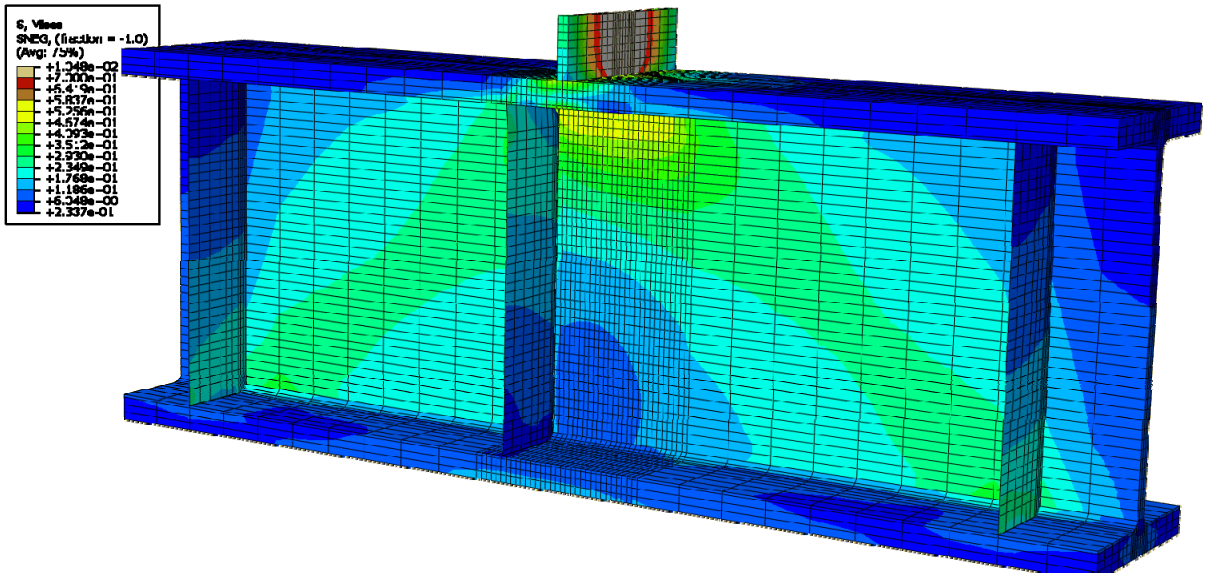

Figure E-65: Finite element model of W24X229-SC-E4 with 3/8 in. stiffeners during elastic behavior

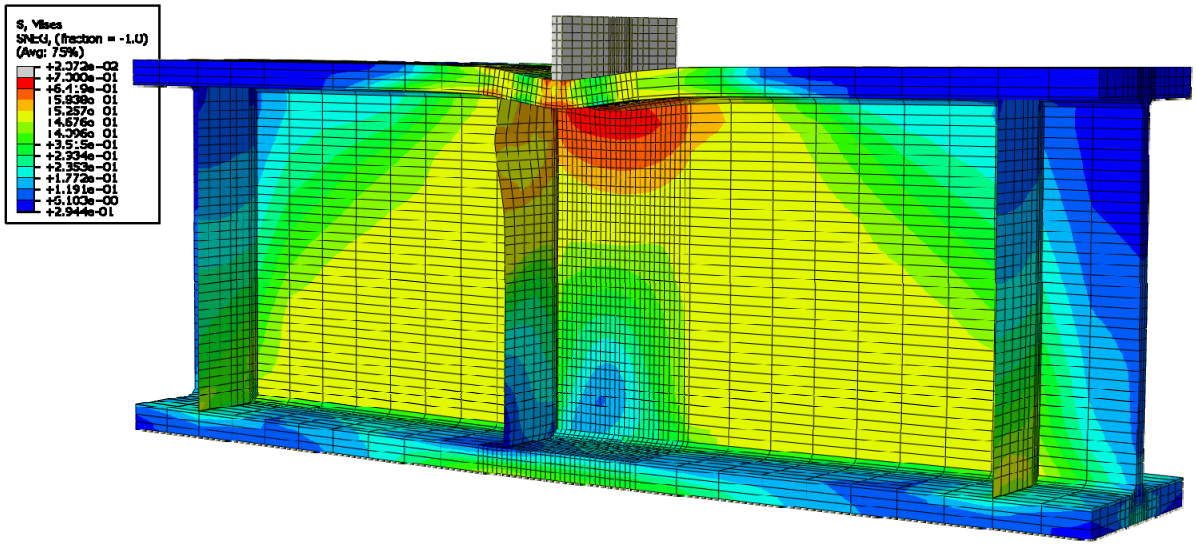

Figure E-66: Finite element model of W24X229-SC-E4 with 3/8 in. stiffeners during inelastic behavior

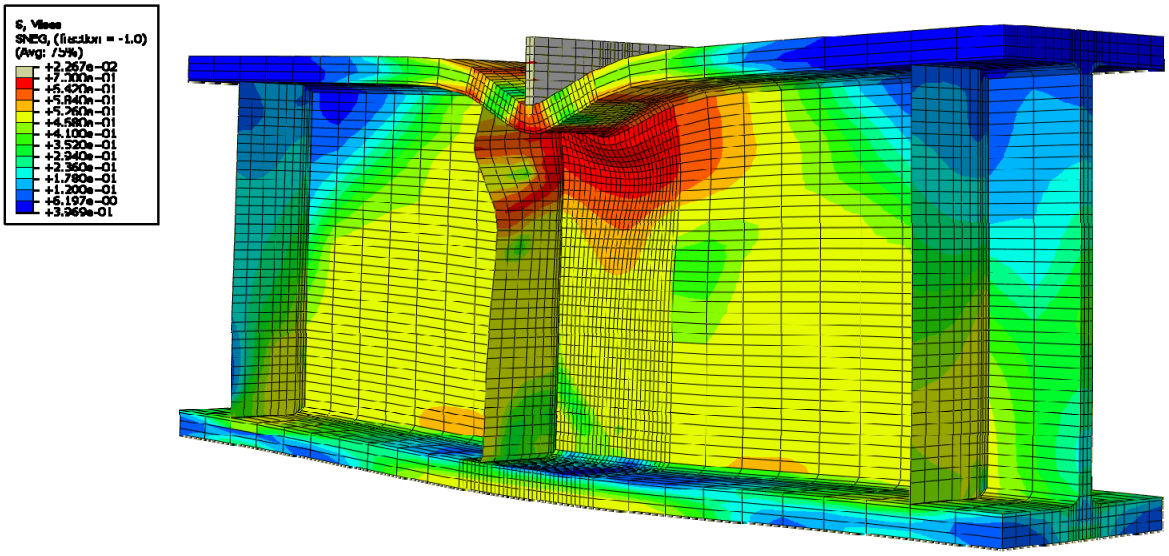

Figure E-67: Finite element model of W24X229-SC-E4 with 3/8 in. stiffeners after the maximum load

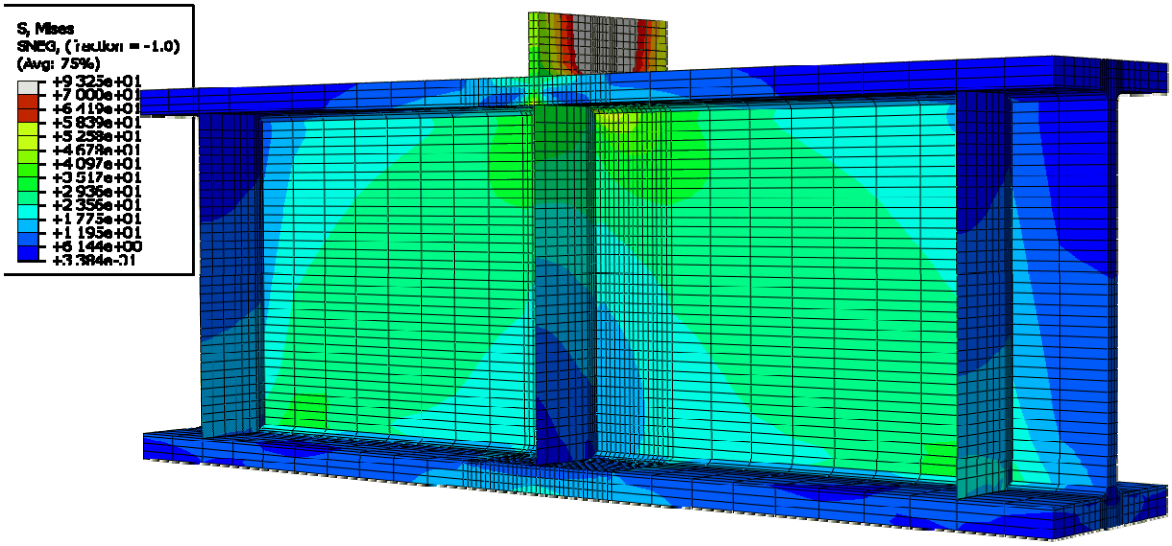

Figure E-68: Finite element model of W24X229-SC-E0 with 3/4 in. stiffeners during elastic behavior

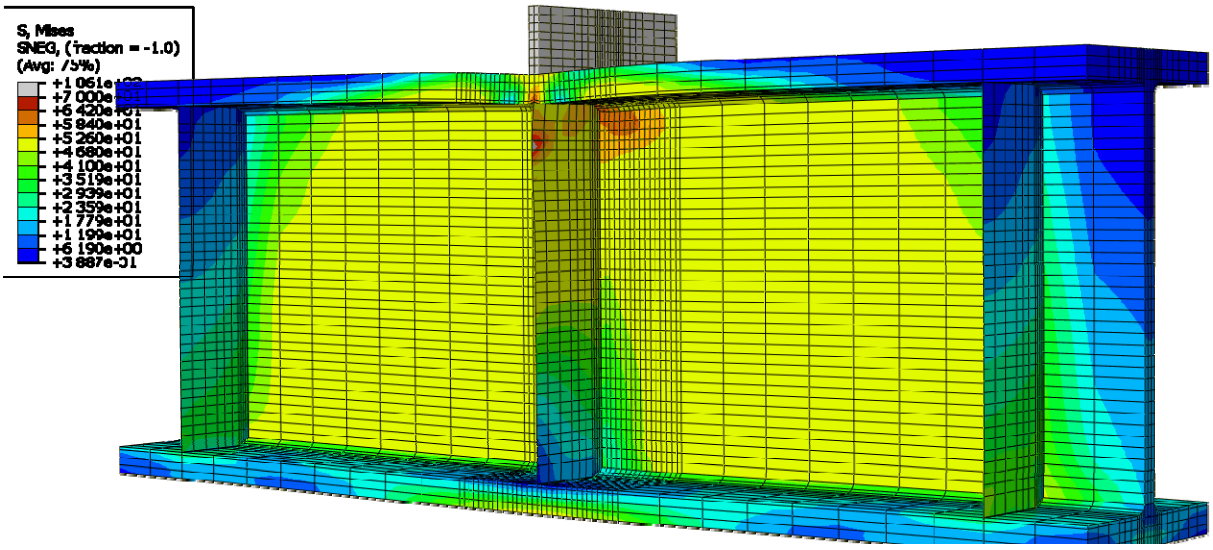

Figure E-69: Finite element model of W24X229-SC-E0 with 3/4 in. stiffeners during inelastic behavior

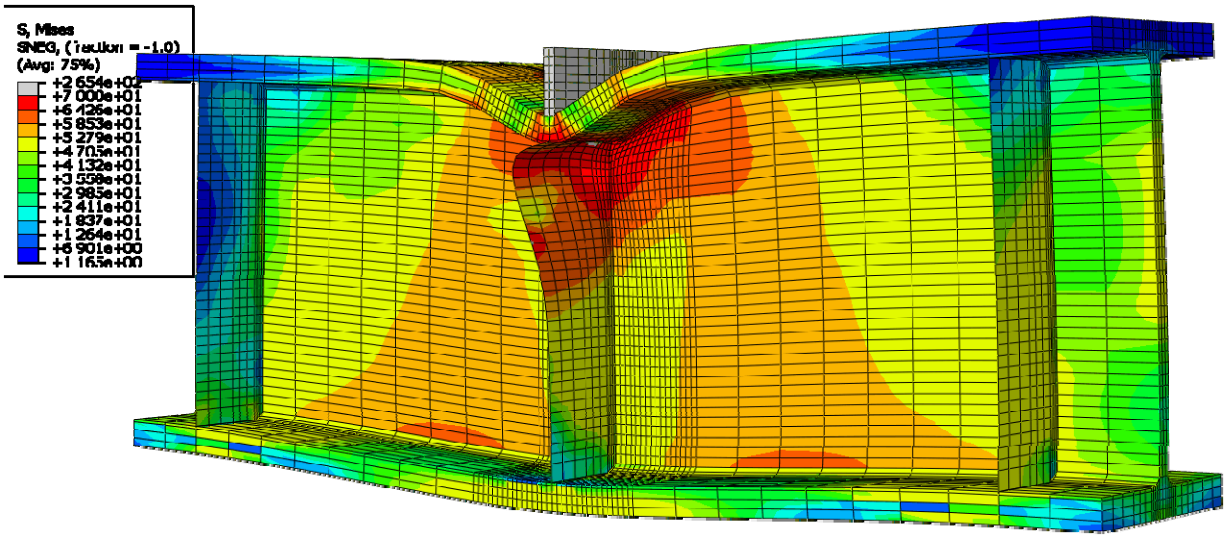

Figure E-70: Finite element model of W24X229-SC-E0 with 3/4 in. stiffeners after the maximum load emphasizing stiffener buckling

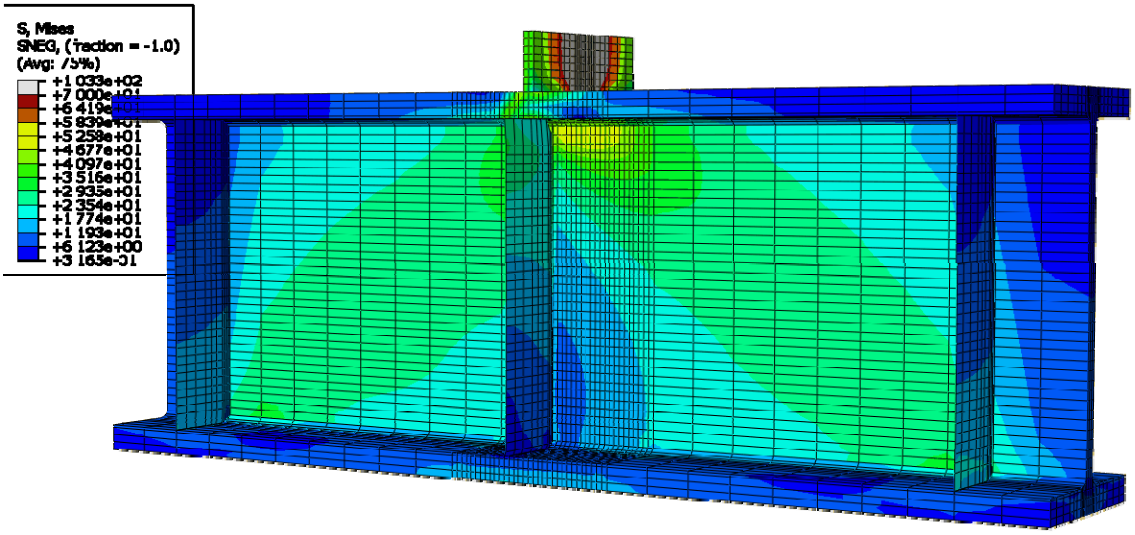

Figure E-71: Finite element model of W24X229-SC-E2 with 3/4 in. stiffeners during elastic behavior

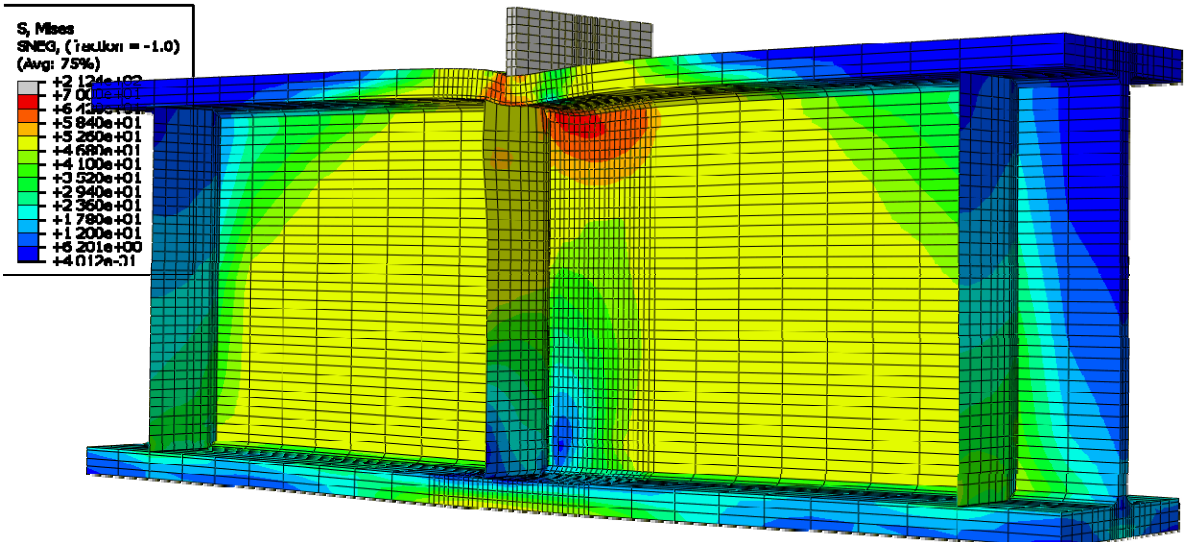

Figure E-72: Finite element model of W24X229-SC-E2 with 3/4 in. stiffeners during inelastic behavior

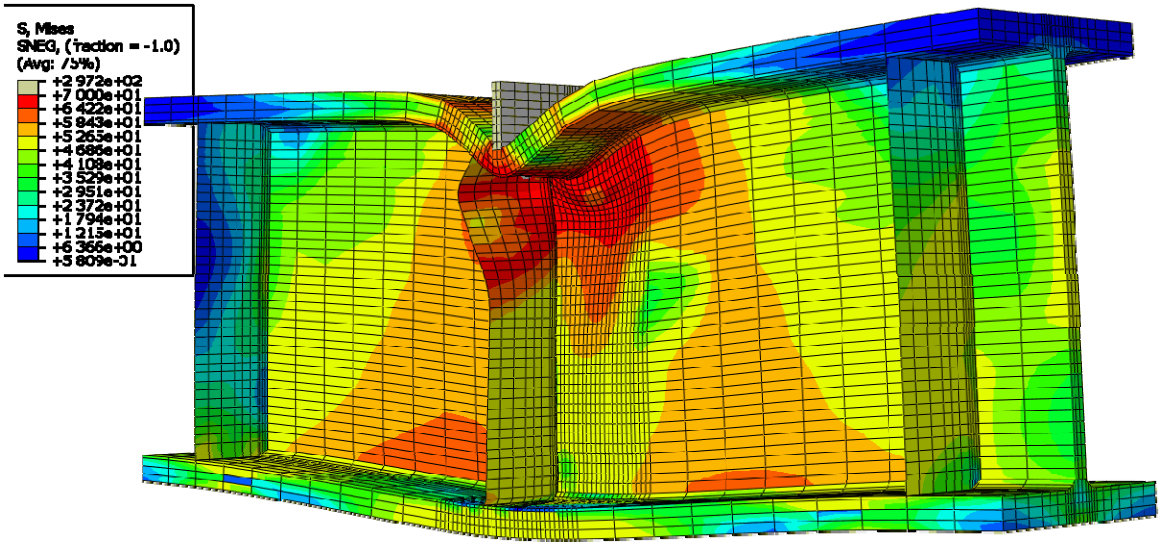

Figure E-73: Finite element model of W24X229-SC-E2 with 3/4 in. stiffeners after the maximum load

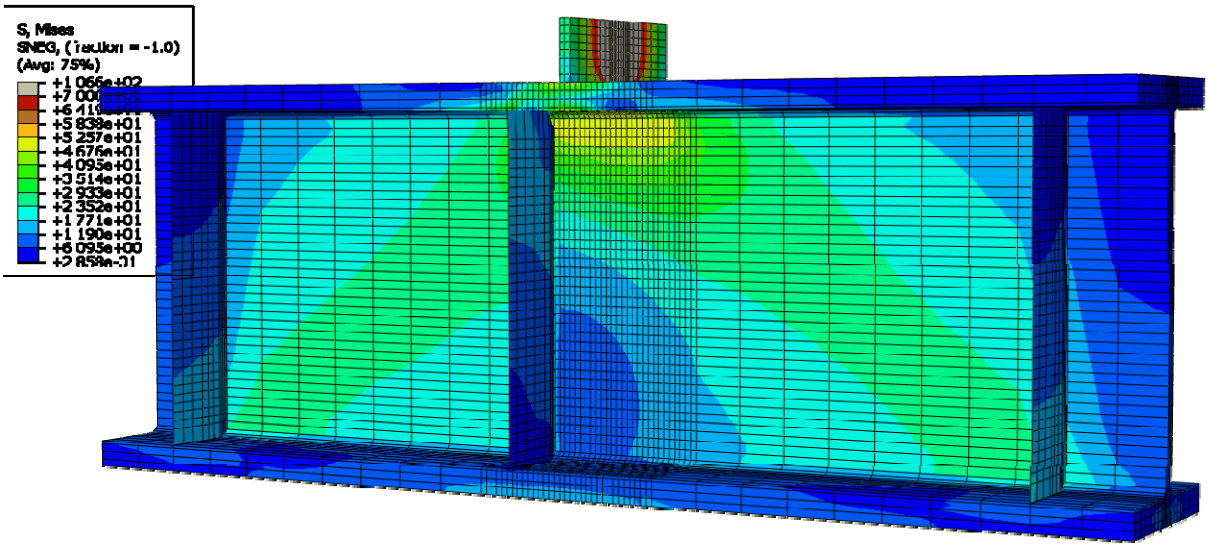

Figure E-74: Finite element model of W24X229-SC-E4 with 3/4 in. stiffeners during elastic behavior

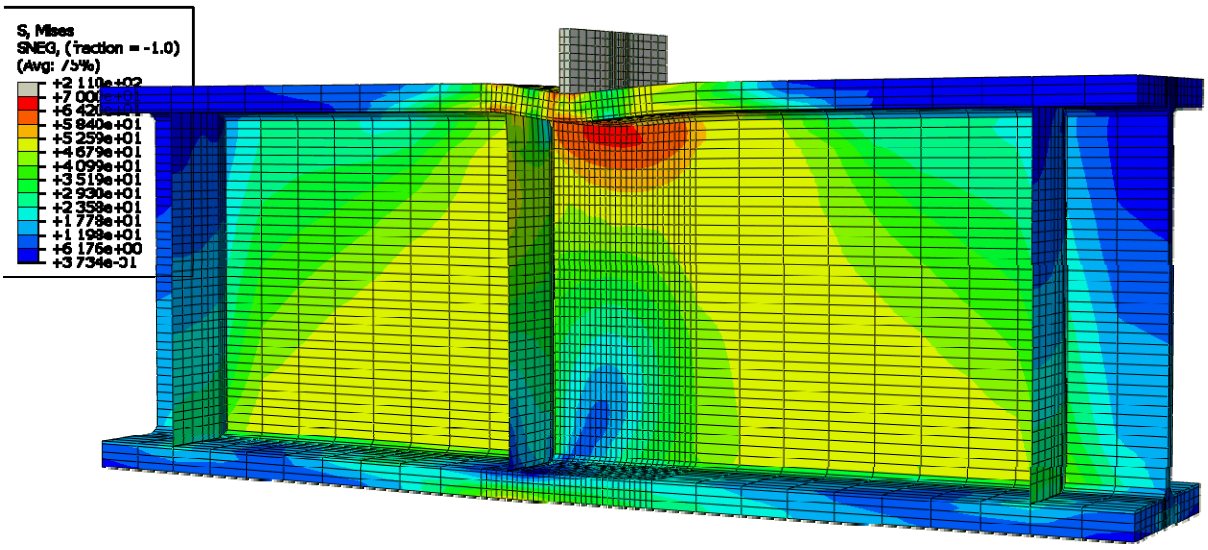

Figure E-75: Finite element model of W24X229-SC-E4 with 3/4 in. stiffeners during inelastic behavior

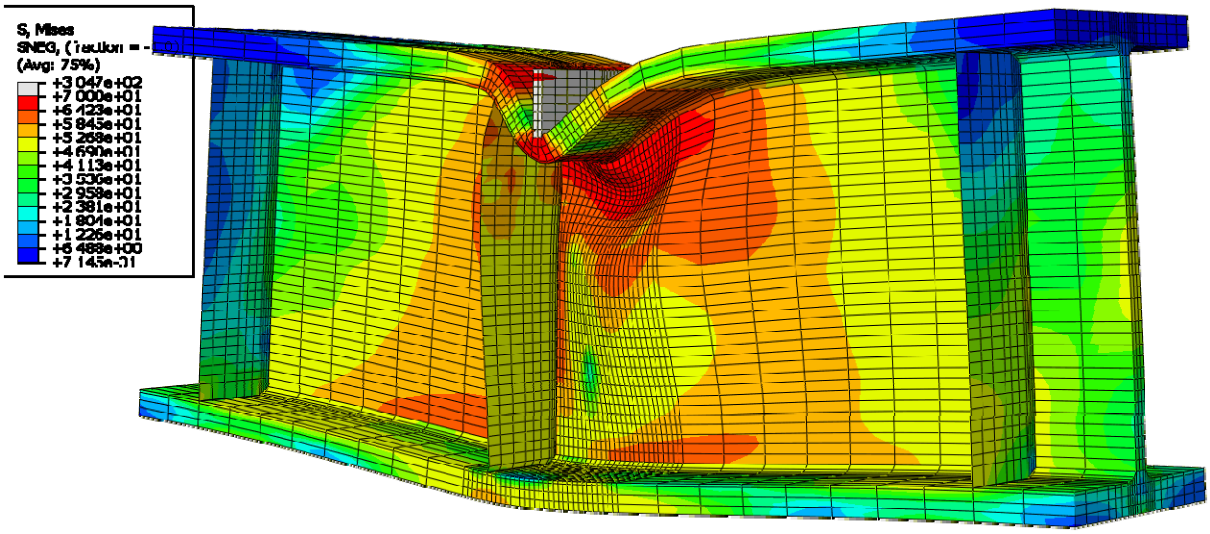

Figure E-76: Finite element model of W24X229-SC-E4 with 3/4 in. stiffeners after the maximum load

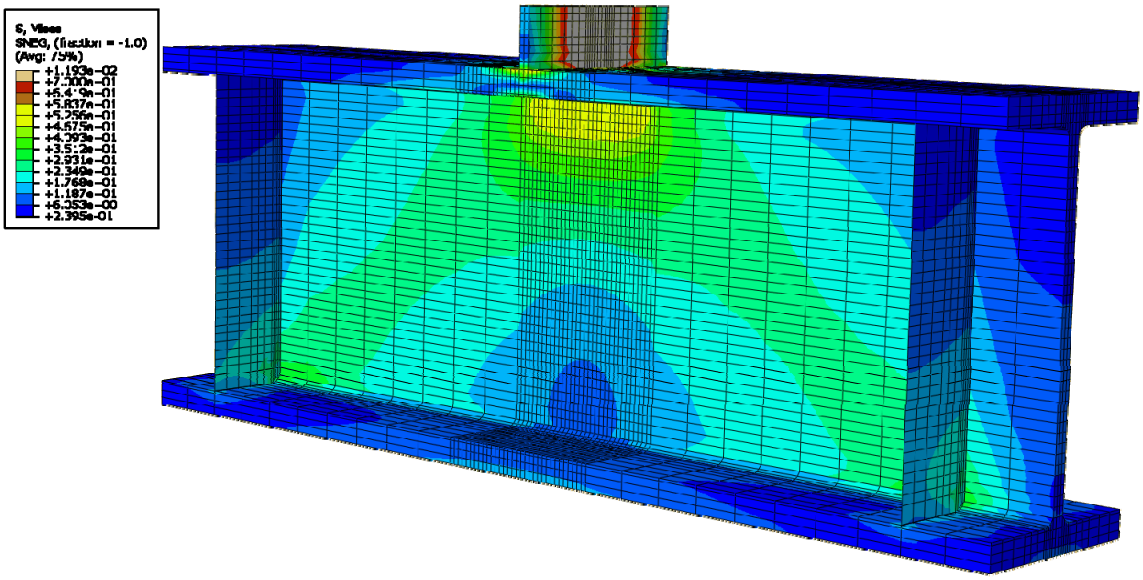

Figure E-77: Finite element model of W24X229-SC-NA during elastic behavior

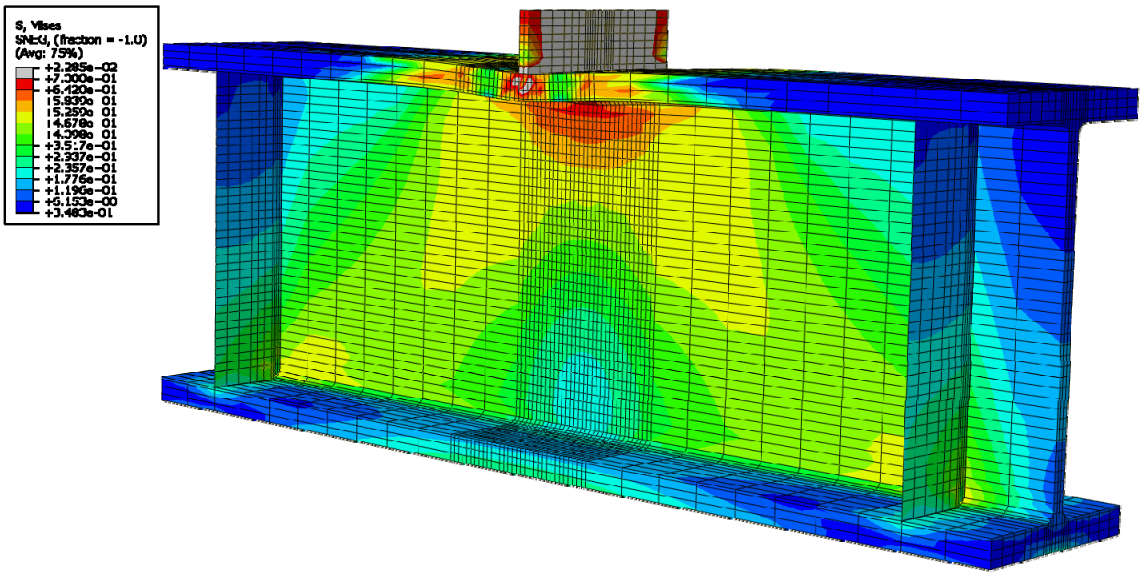

Figure E-78: Finite element model of W24X229-SC-NA during inelastic behavior

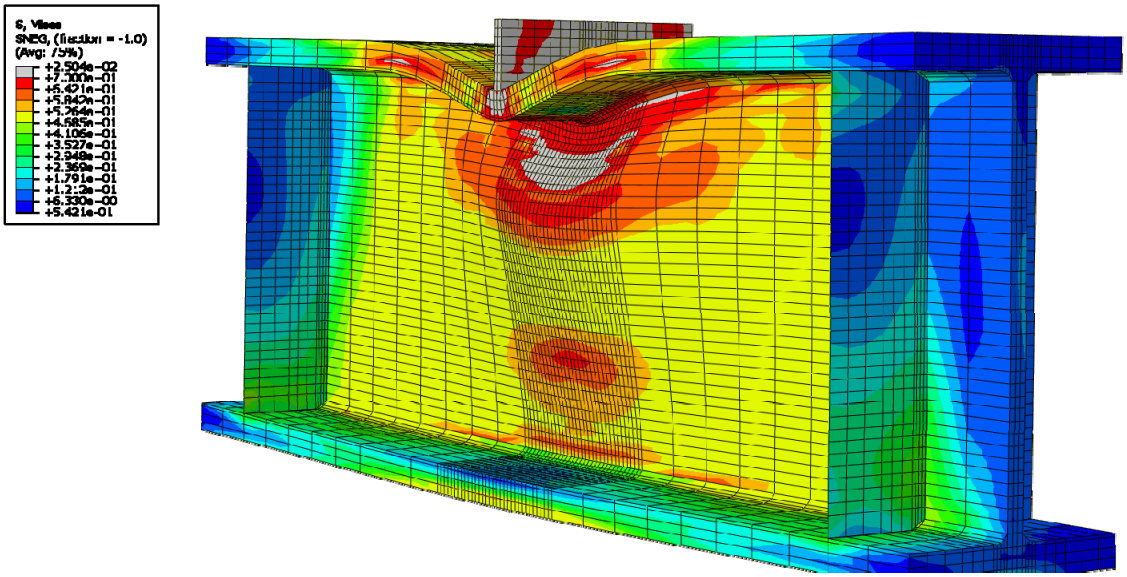

Figure E-79: Finite element model of W24X229-SC-NA after the maximum load emphasizing web crippling

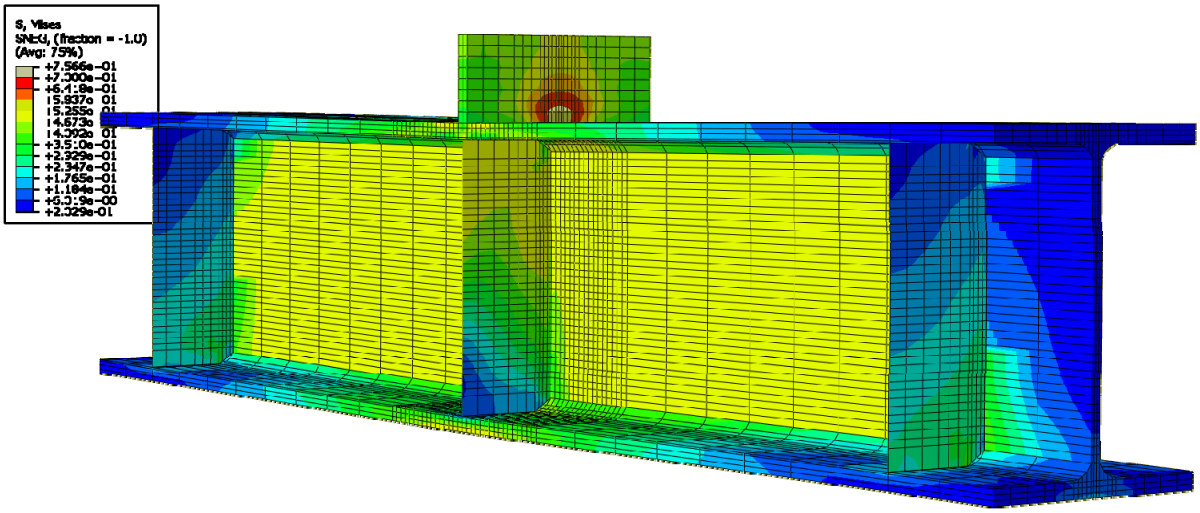

Figure E-80: Finite element model of W14X68-SC-E0 with 3/8 in. stiffeners during elastic behavior

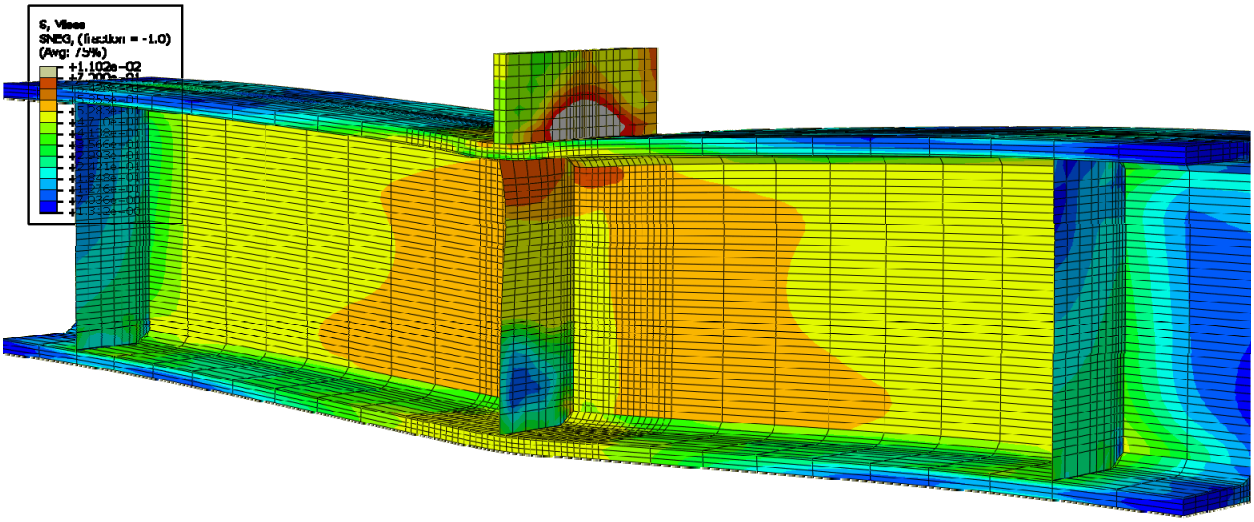

Figure E-81: Finite element model of W14X68-SC-E0 with 3/8 in. stiffeners during inelastic behavior

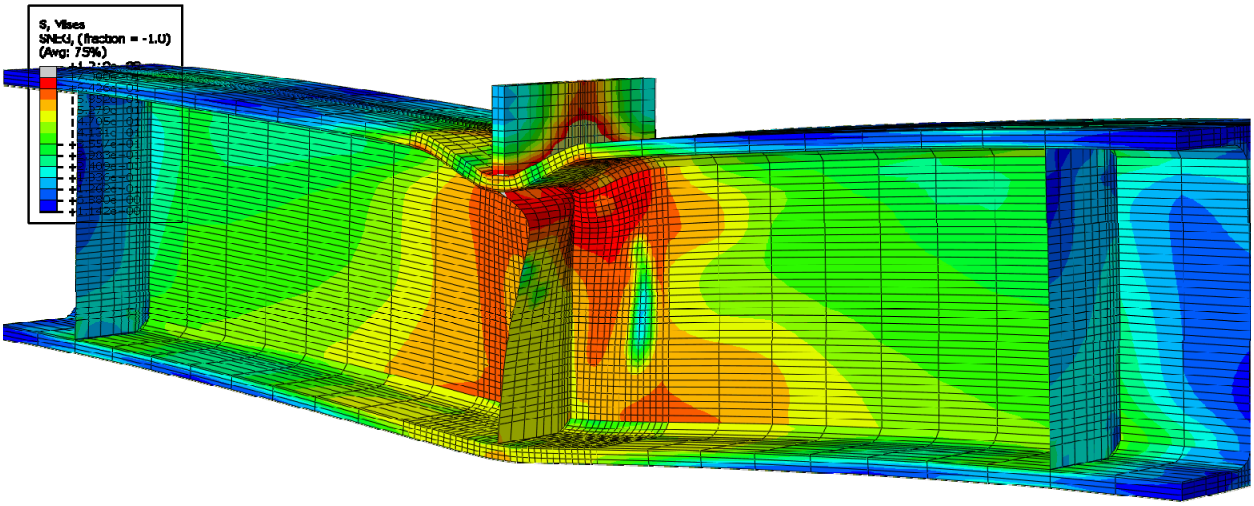

Figure E-82: Finite element model of W14X68-SC-E0 with 3/8 in. stiffeners after the maximum load emphasizing stiffener buckling

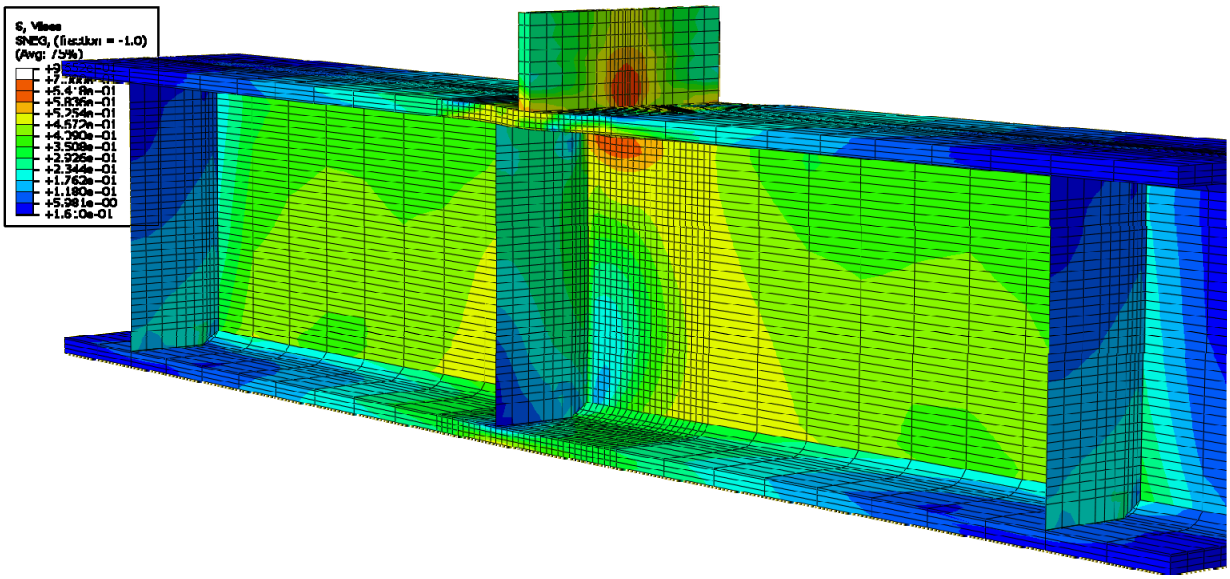

Figure E-83: Finite element model of W14X68-SC-E2 with 3/8 in. stiffeners during elastic behavior

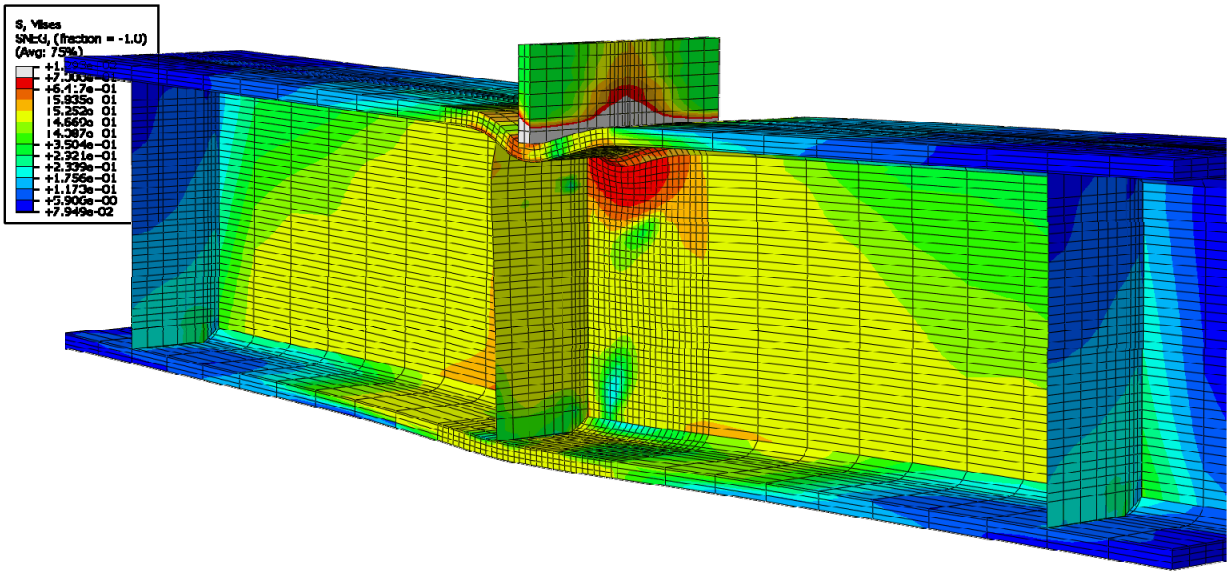

Figure E-84: Finite element model of W14X68-SC-E2 with 3/8 in. stiffeners during inelastic behavior

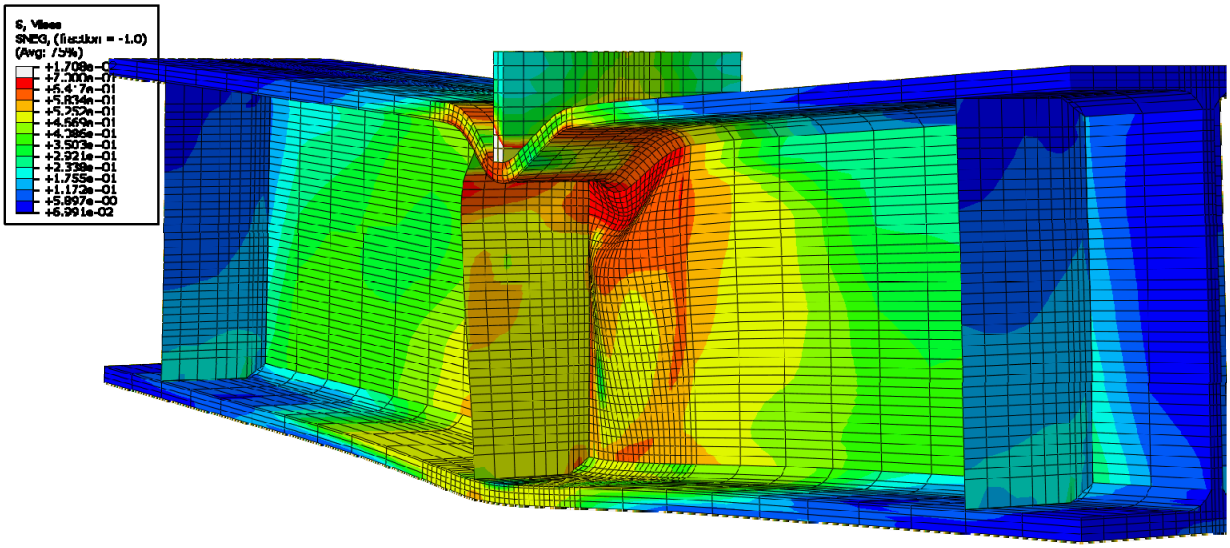

Figure E-85: Finite element model of W14X68-SC-E2 with 3/8 in. stiffeners after the maximum load

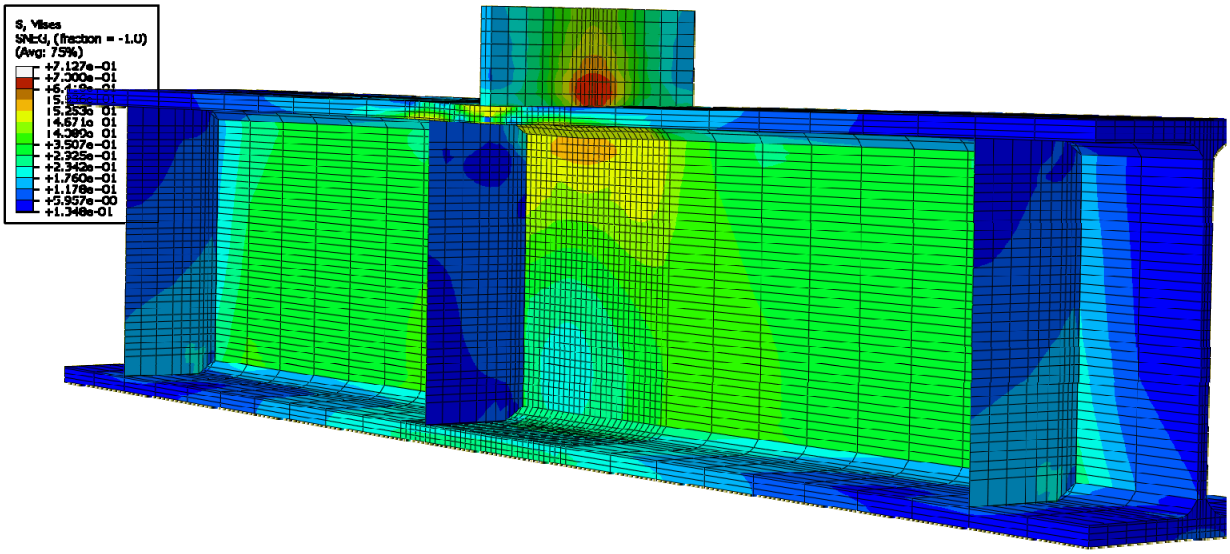

Figure E-86: Finite element model of W14X68-SC-E4 with 3/8 in. stiffeners during elastic behavior

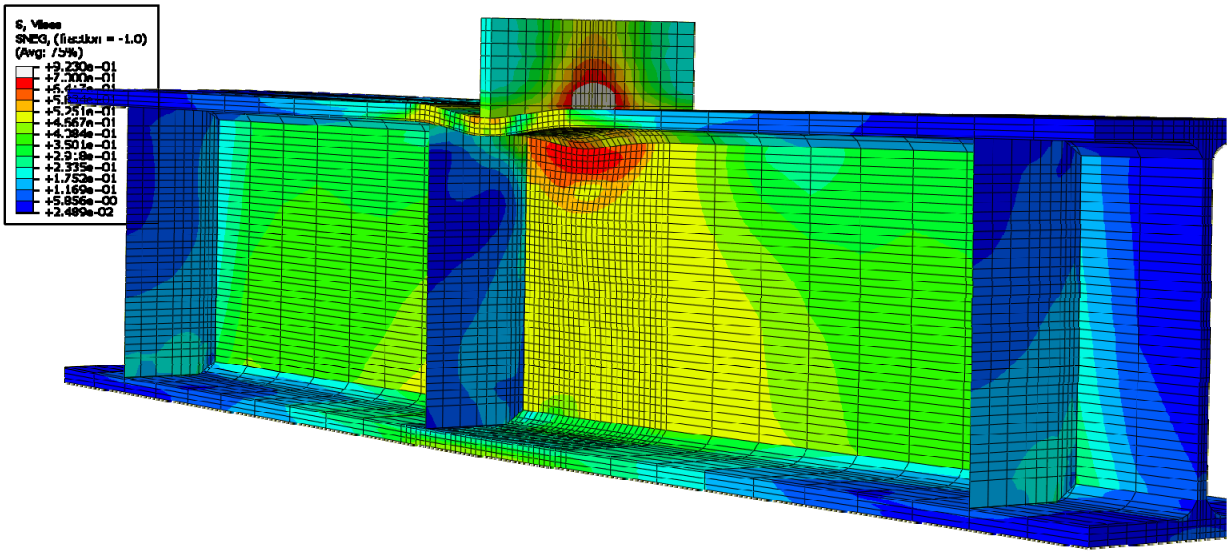

Figure E-87: Finite element model of W14X68-SC-E4 with 3/8 in. stiffeners during inelastic behavior

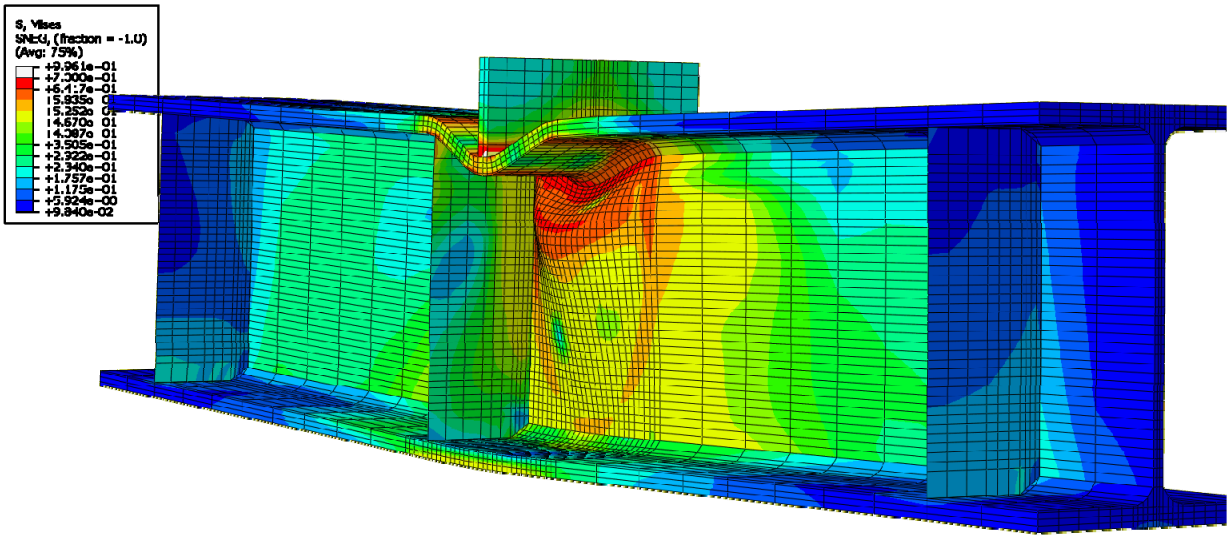

Figure E-88: Finite element model of W14X68-SC-E4 with 3/8 in. stiffeners after the maximum load

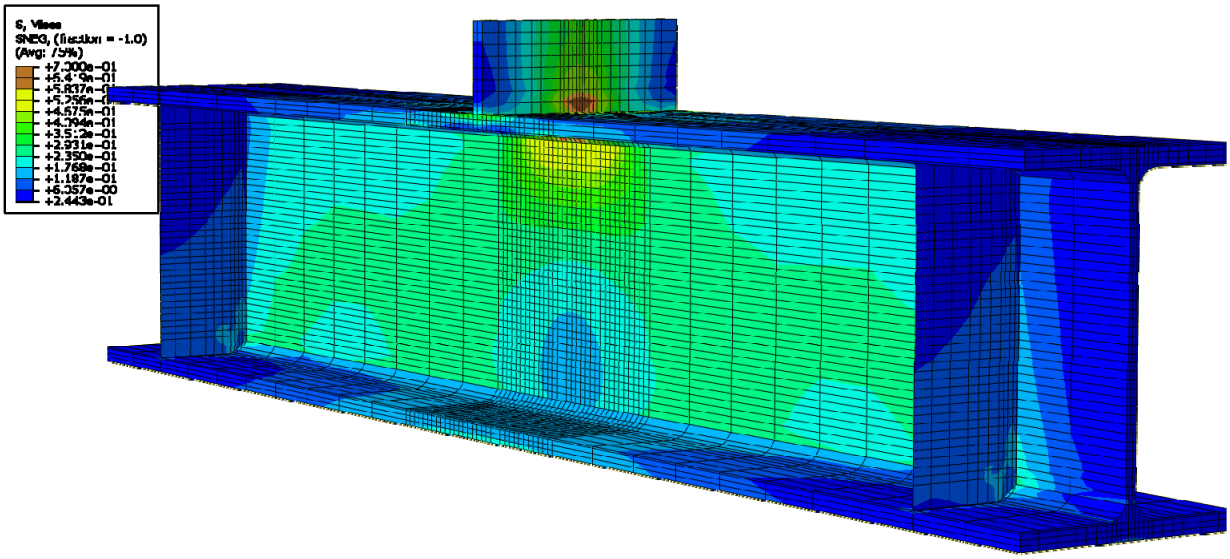

Figure E-89: Finite element model of W14X68-SC-NA during elastic behavior

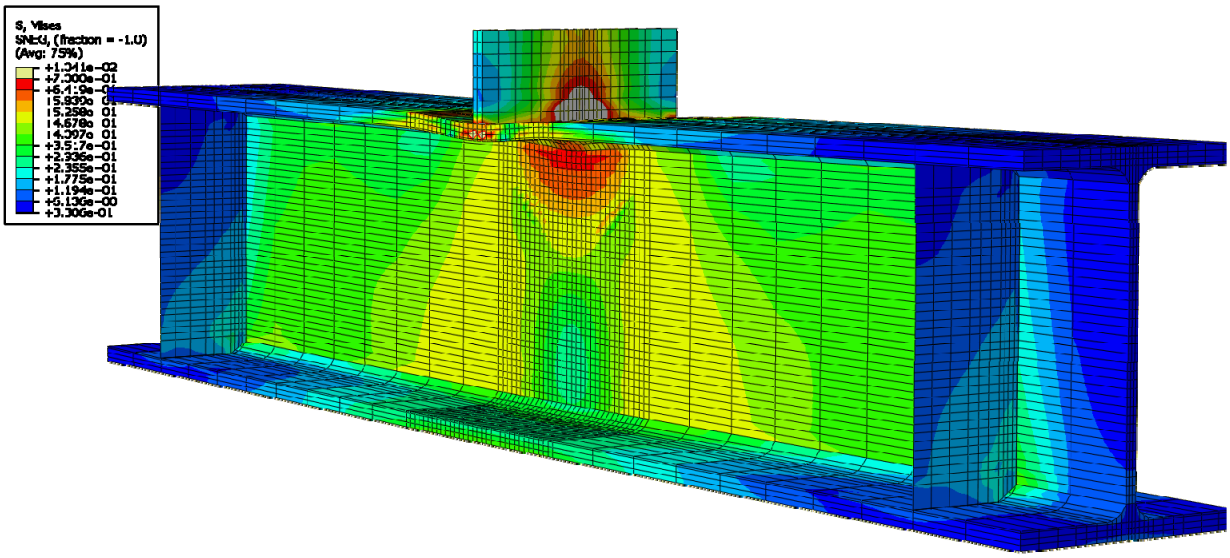

Figure E-90: Finite element model of W14X68-SC-NA during inelastic behavior

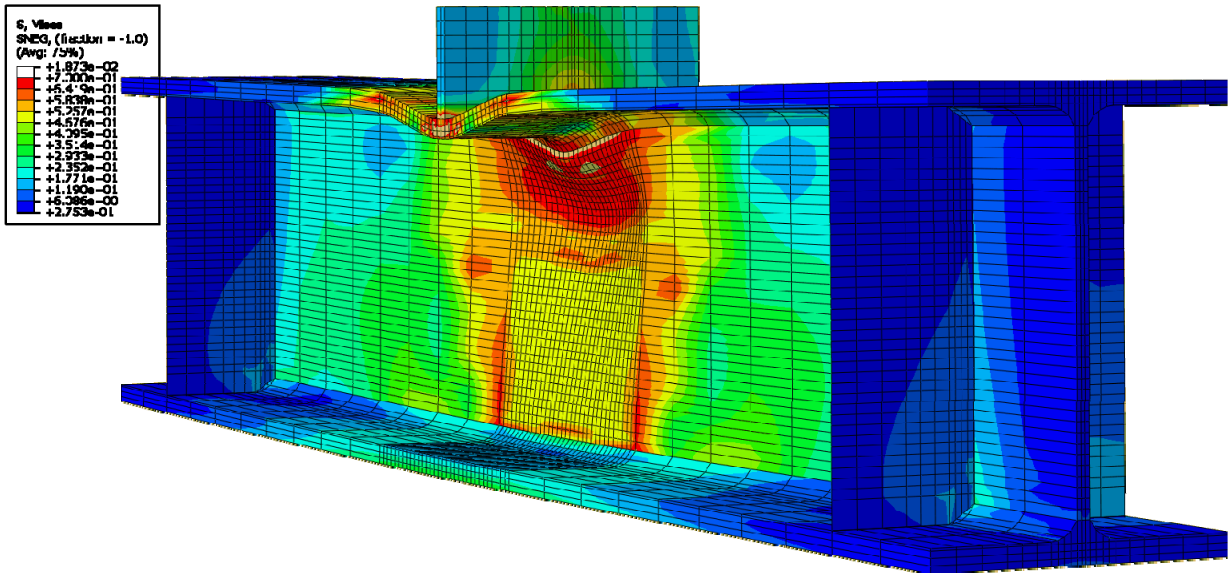

Figure E-91: Finite element model of W14X68-SC-NA after web crippling

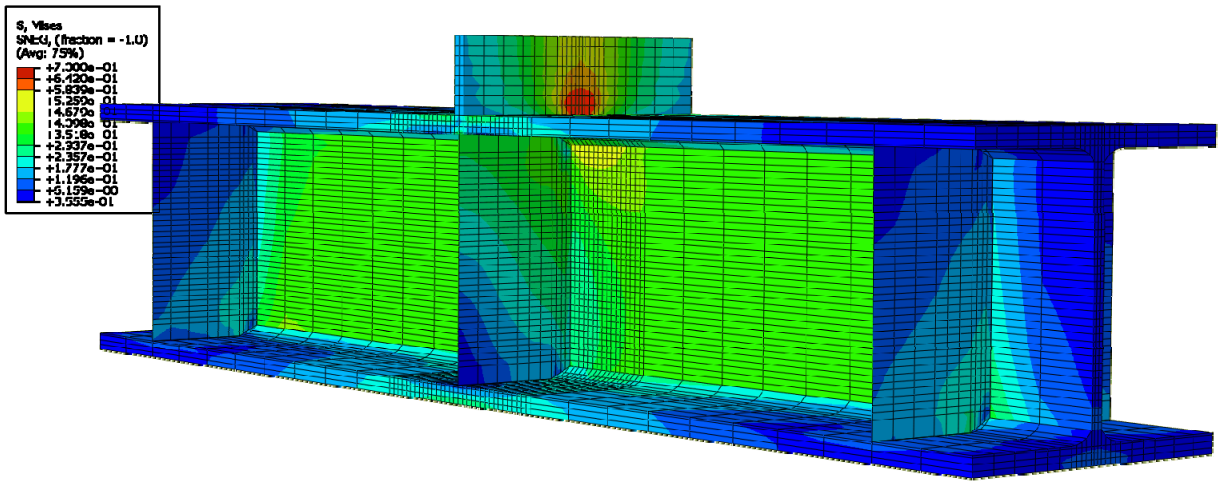

Figure E-92: Finite element model of W14X120-SC-E0 with 3/8 in. stiffeners during elastic behavior

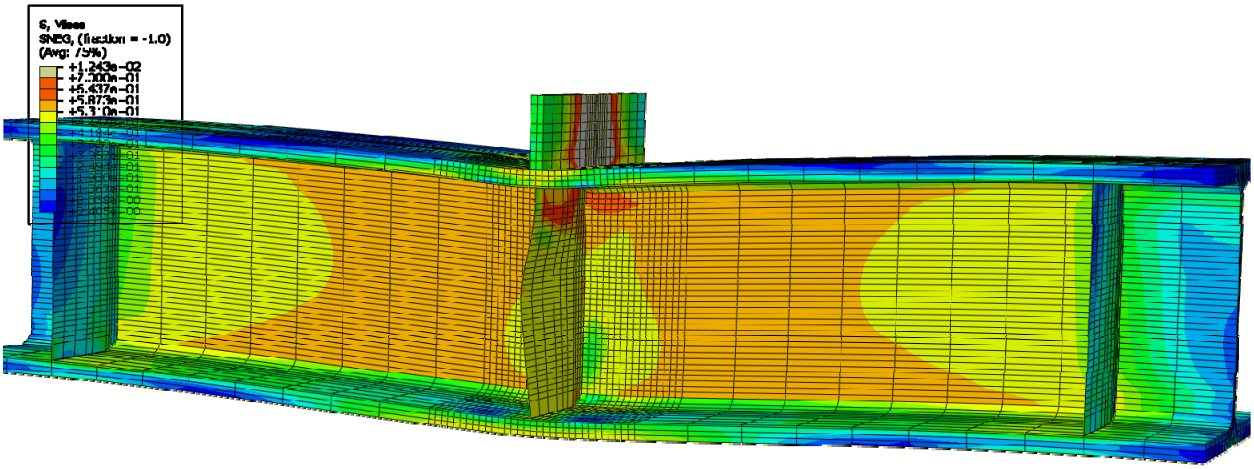

Figure E-93: Finite element model of W14X120-SC-E0 with 3/8 in. stiffeners during inelastic behavior

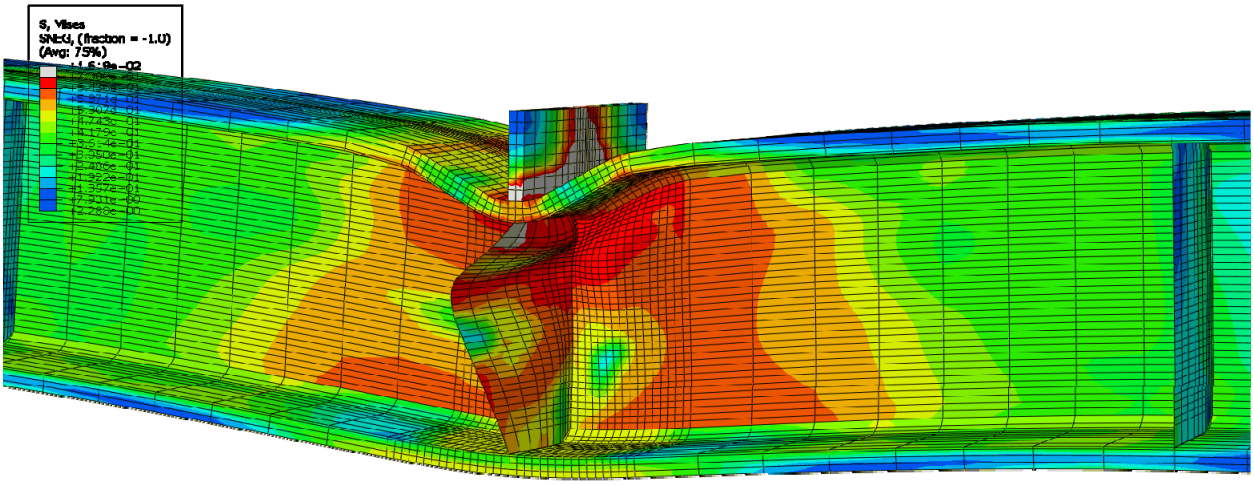

Figure E-94: Finite element model of W14X120-SC-E0 with 3/8 in. stiffeners after the maximum load showing stiffener buckling

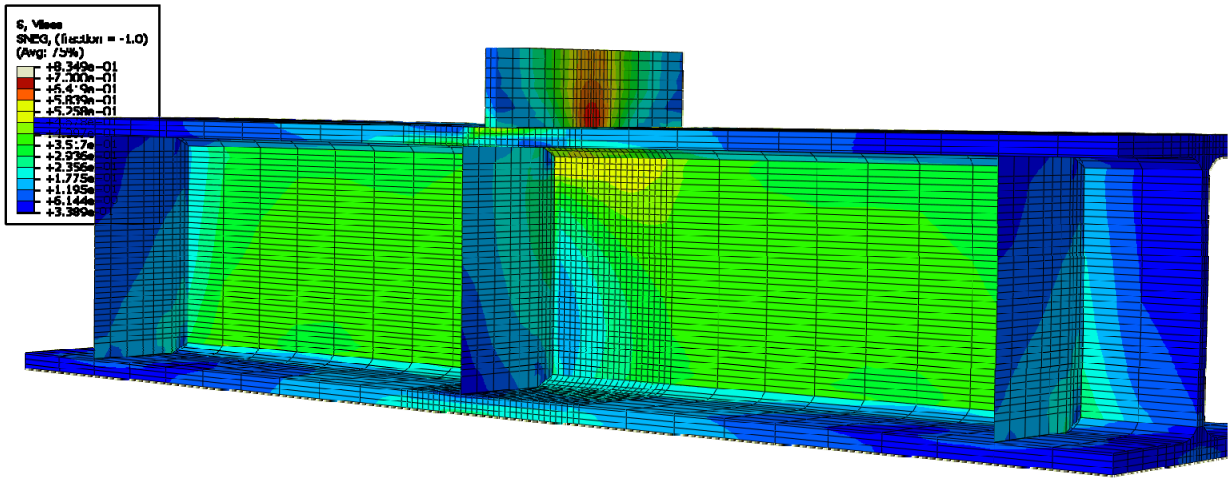

Figure E-95: Finite element model of W14X120-SC-E2 with 3/8 in. stiffeners during elastic behavior

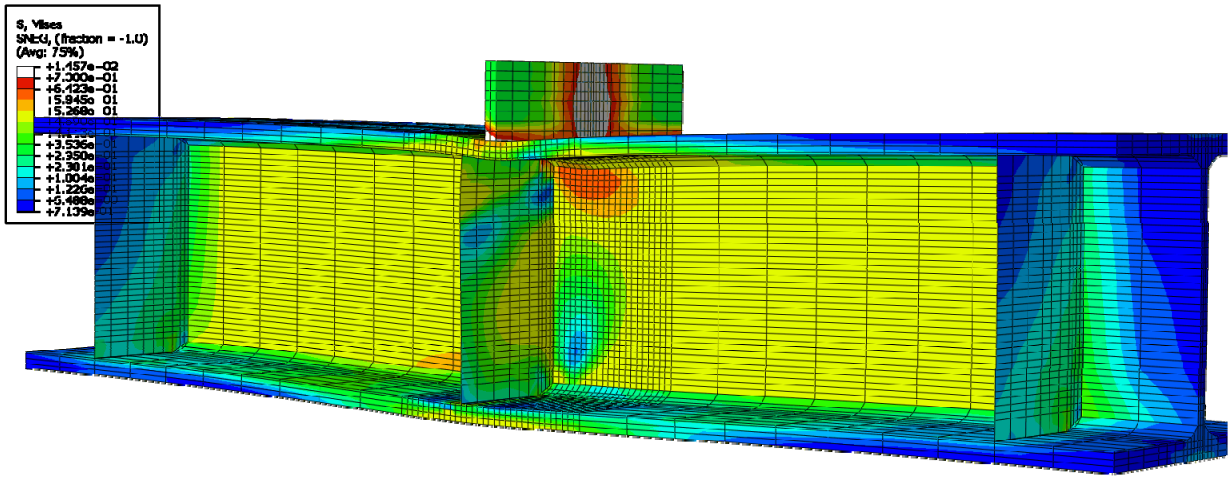

Figure E-96: Finite element model of W14X120-SC-E2 with 3/8 in. stiffeners during inelastic behavior

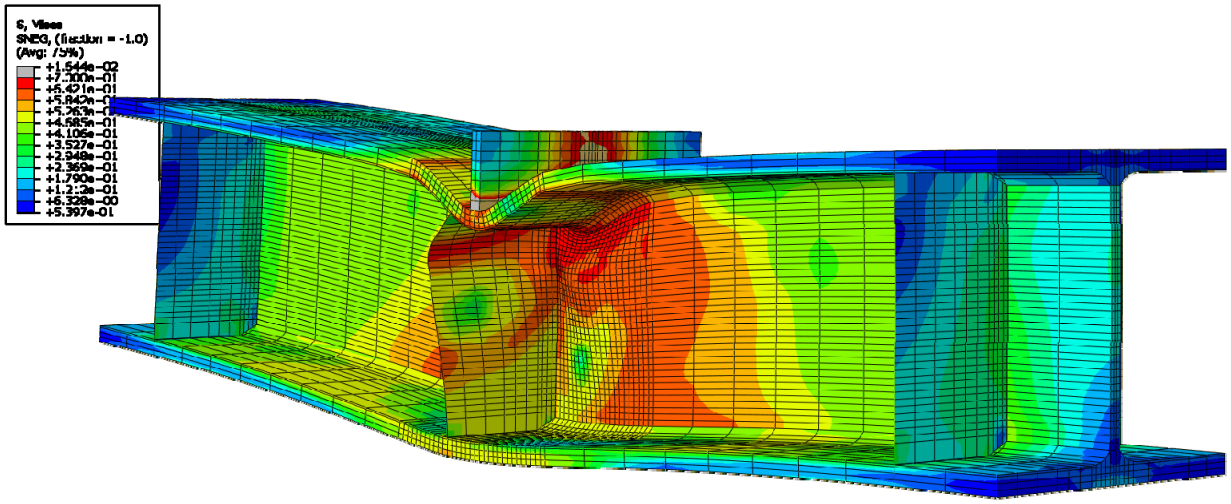

Figure E-97: Finite element model of W14X120-SC-E2 with 3/8 in. stiffeners after the maximum load

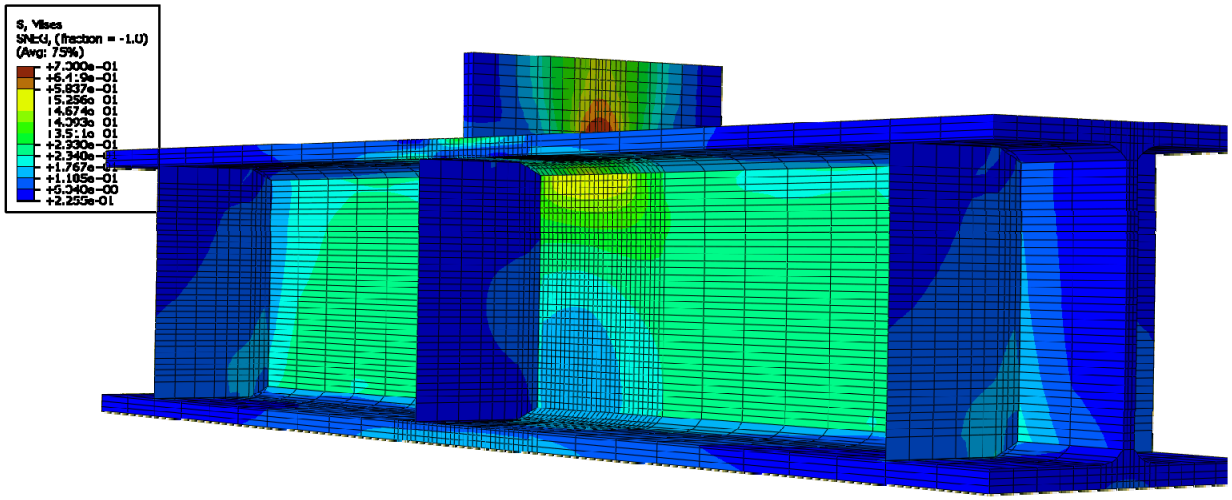

Figure E-98: Finite element model of W14X120-SC-E4 with 3/8 in. stiffeners during elastic behavior

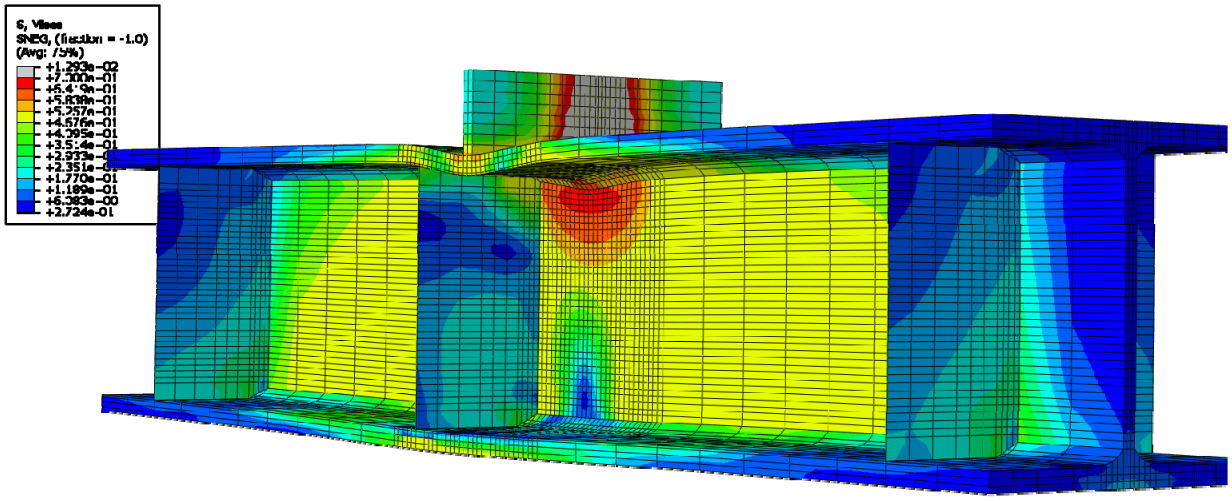

Figure E-99: Finite element model of W14X120-SC-E4 with 3/8 in. stiffeners during inelastic behavior

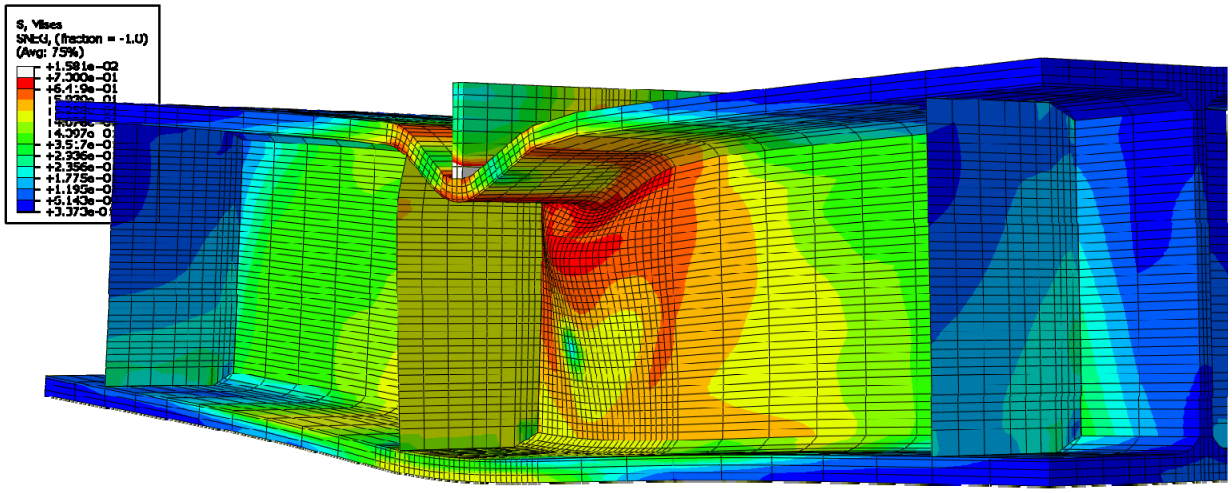

Figure E-100: Finite element model of W14X120-SC-E4 with 3/8 in. stiffeners after the maximum load

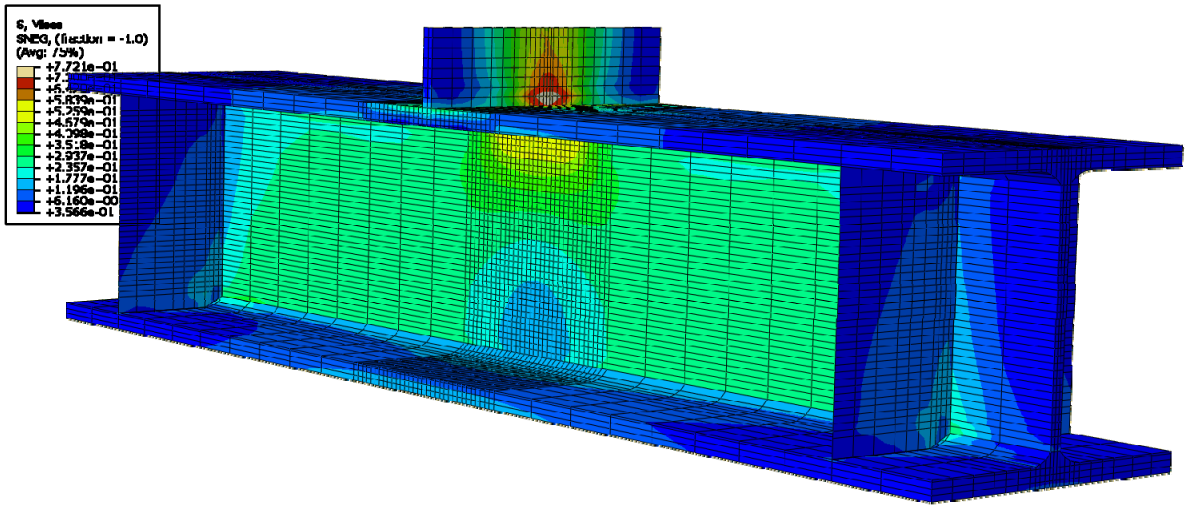

Figure E-101: Finite element model of W14X120-SC-NA during elastic behavior

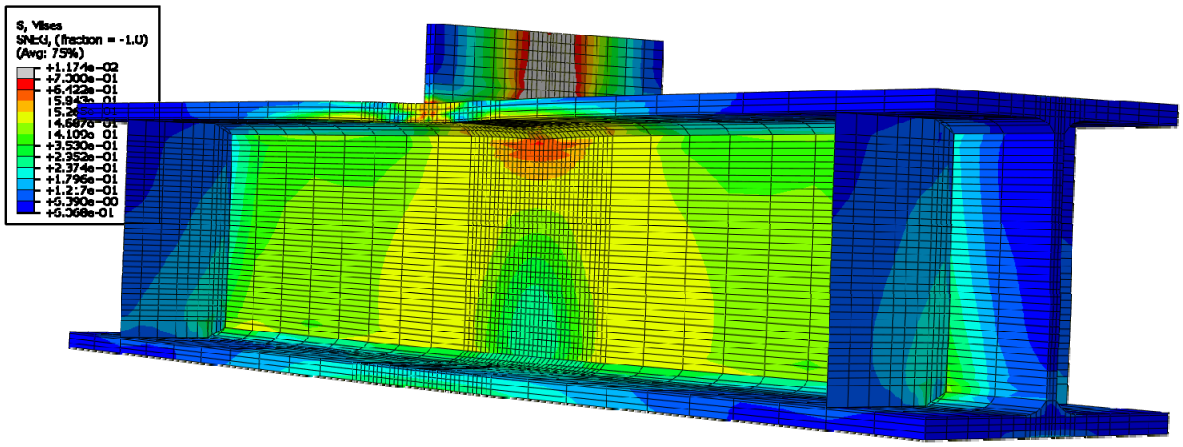

Figure E-102: Finite element model of W14X120-SC-NA during inelastic behavior

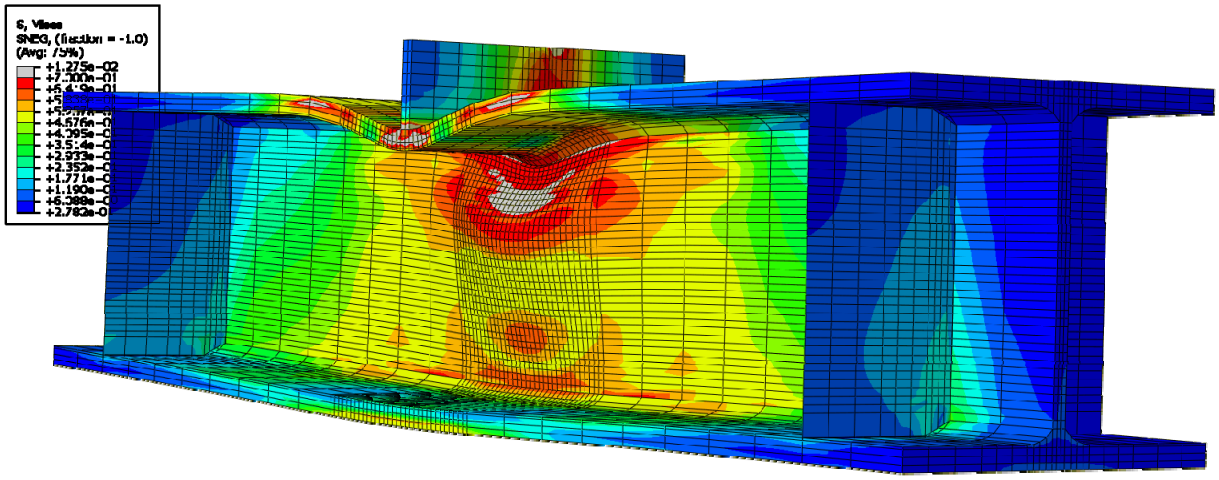

Figure E-103: Finite element model of W14X120-SC-NA after the maximum load emphasizing web crippling

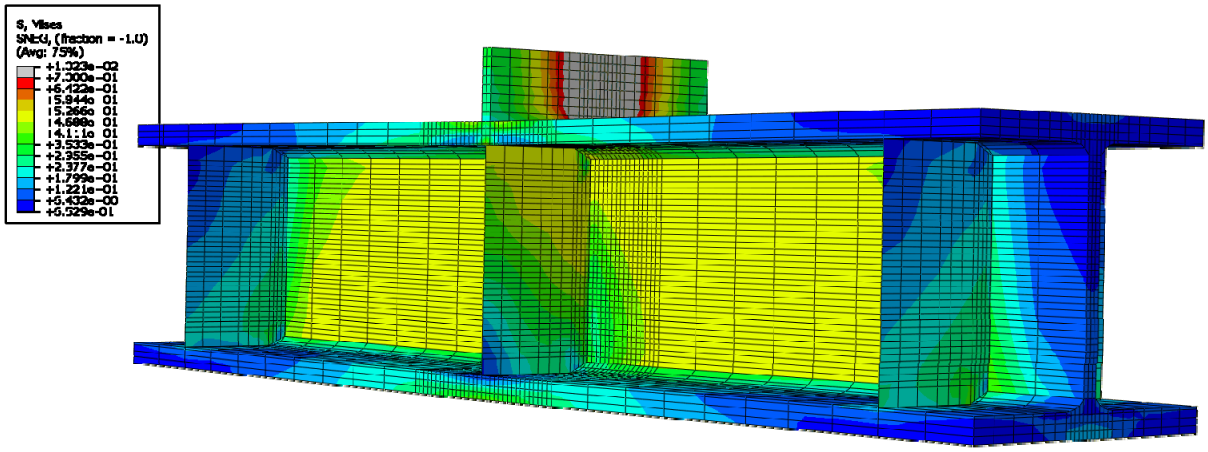

Figure E-104: Finite element model of W14X176-SC-E0 with 3/8 in. stiffeners during elastic behavior

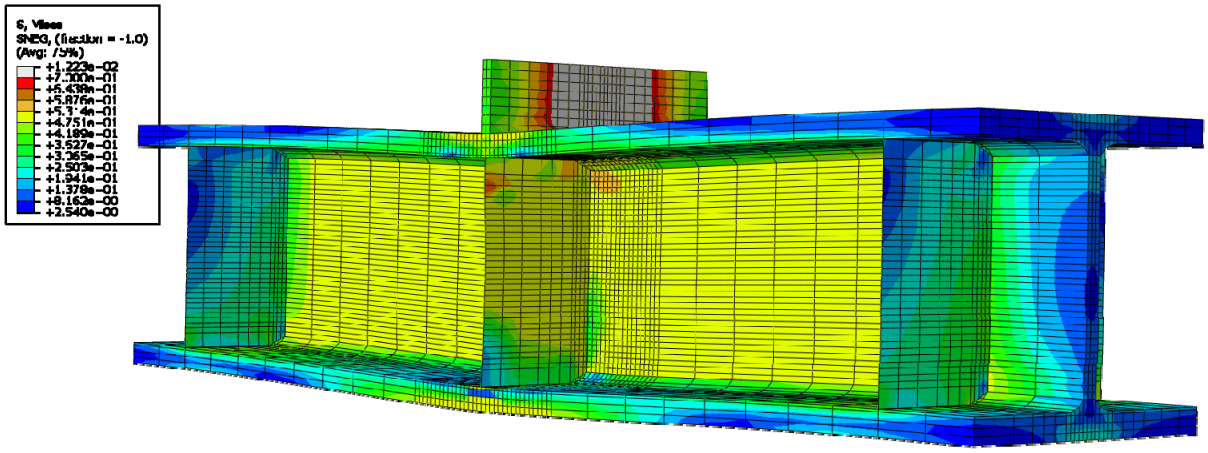

Figure E-105: Finite element model of W14X176-SC-E0 with 3/8 in. stiffeners during inelastic behavior

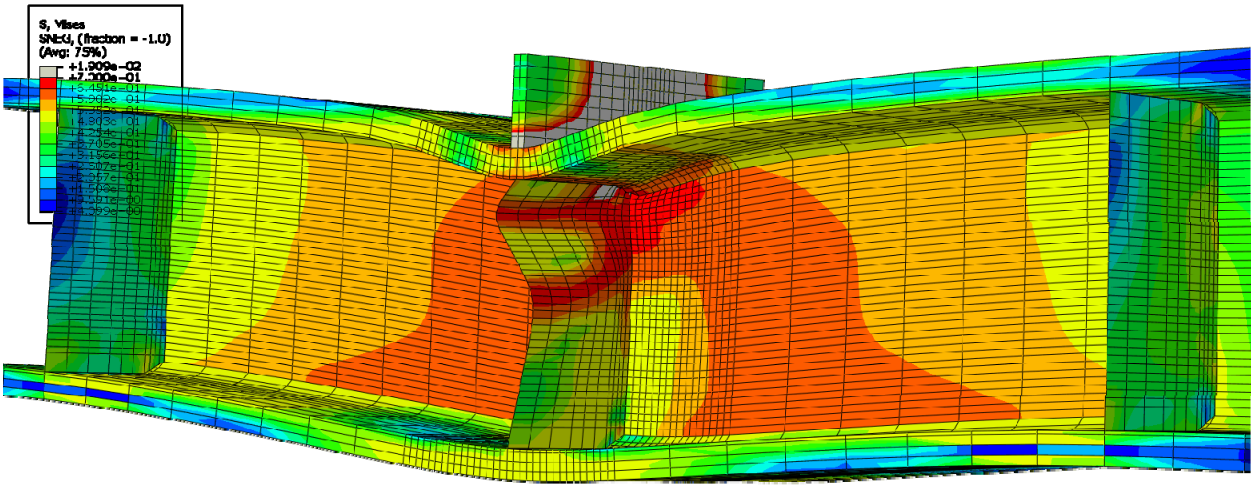

Figure E-106: Finite element model of W14X176-SC-E0 with 3/8 in. stiffeners after the maximum load

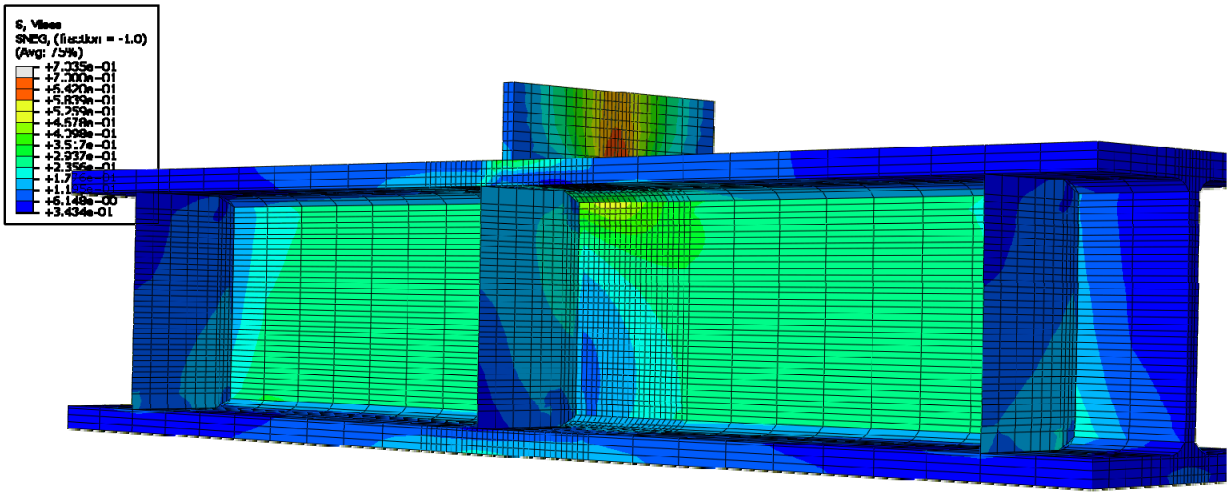

Figure E-107: Finite element model of W14X176-SC-E2 with 3/8 in. stiffeners during elastic behavior

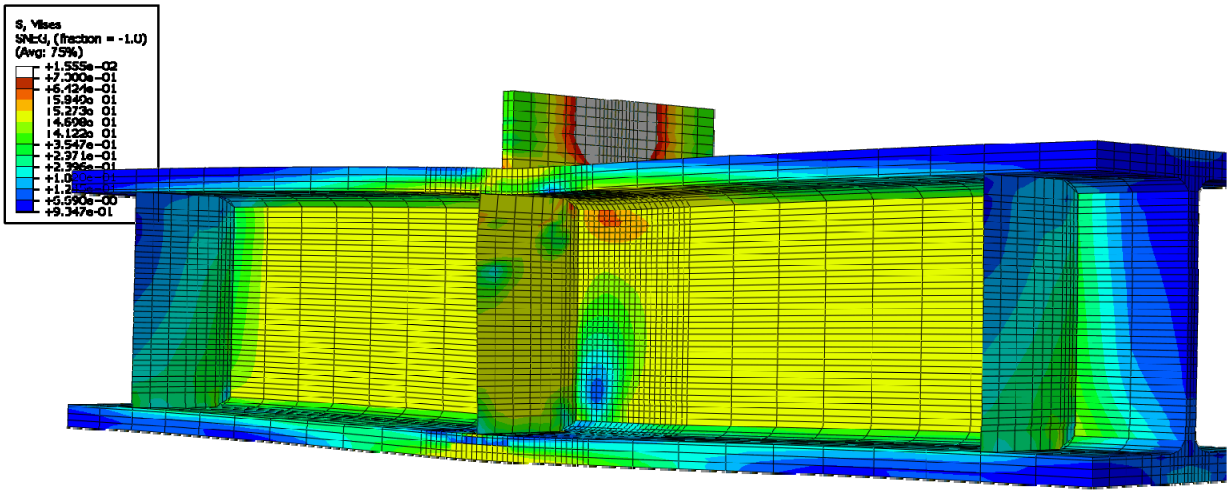

Figure E-108: Finite element model of W14X176-SC-E2 with 3/8 in. stiffeners during inelastic behavior

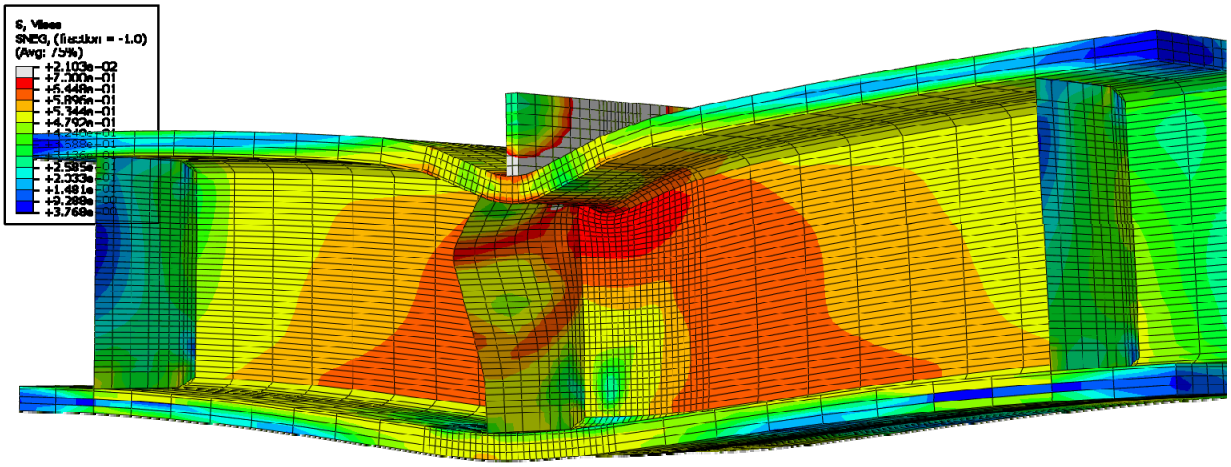

Figure E-109: Finite element model of W14X176-SC-E2 with 3/8 in. stiffeners after the maximum load

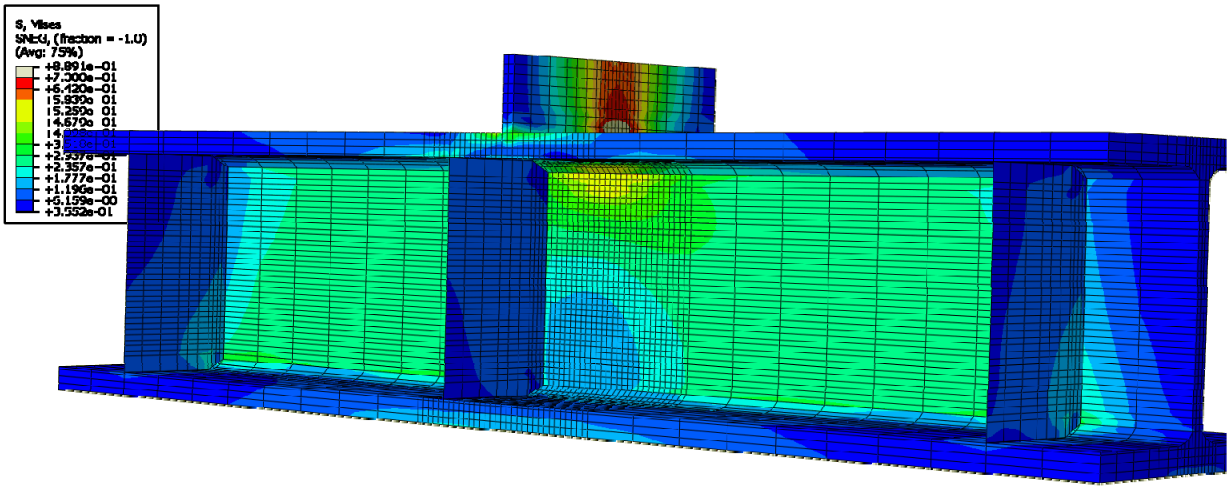

Figure E-110: Finite element model of W14X176-SC-E4 with 3/8 in. stiffeners during elastic behavior

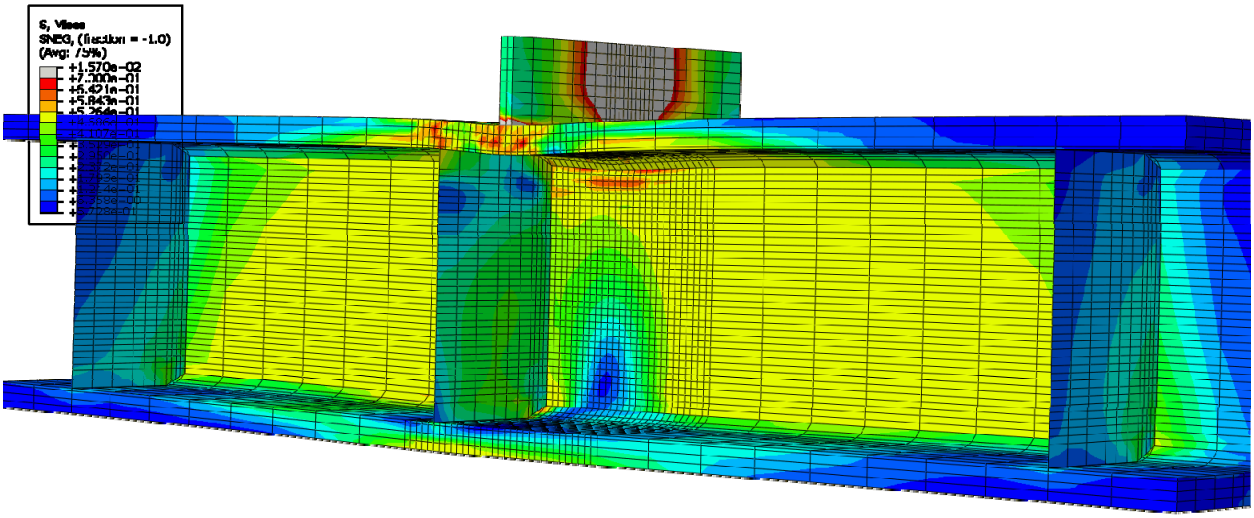

Figure E-111: Finite element model of W14X176-SC-E4 with 3/8 in. stiffeners during inelastic behavior

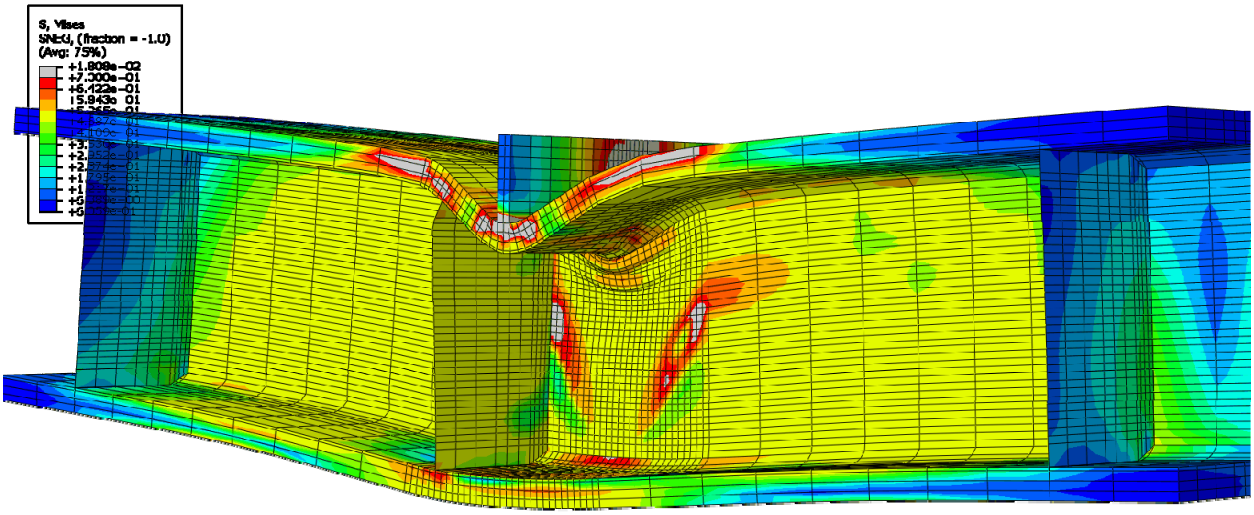

Figure E-112: Finite element model of W14X176-SC-E4 with 3/8 in. stiffeners after the maximum load

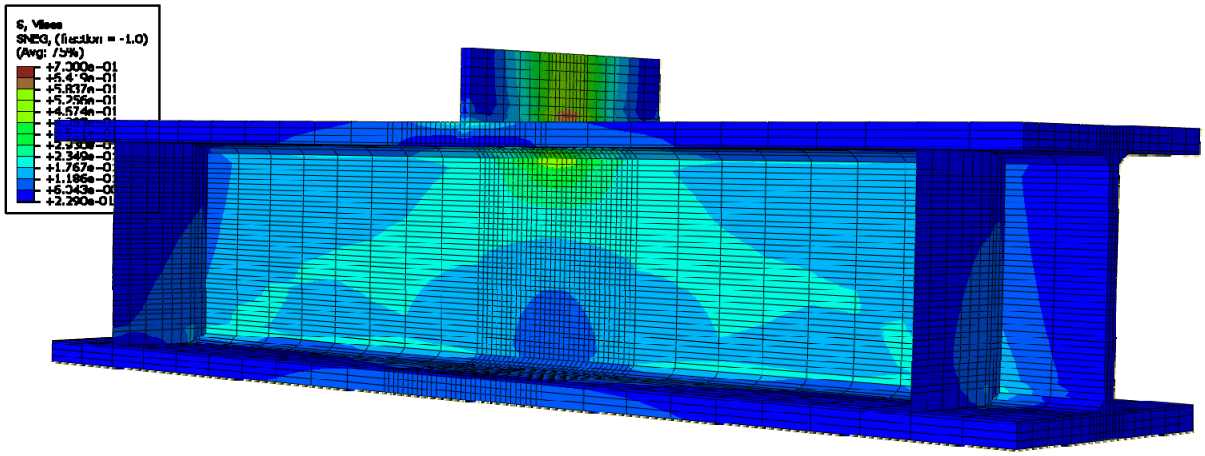

Figure E-113: Finite element model of W14X176-SC-NA during elastic behavior

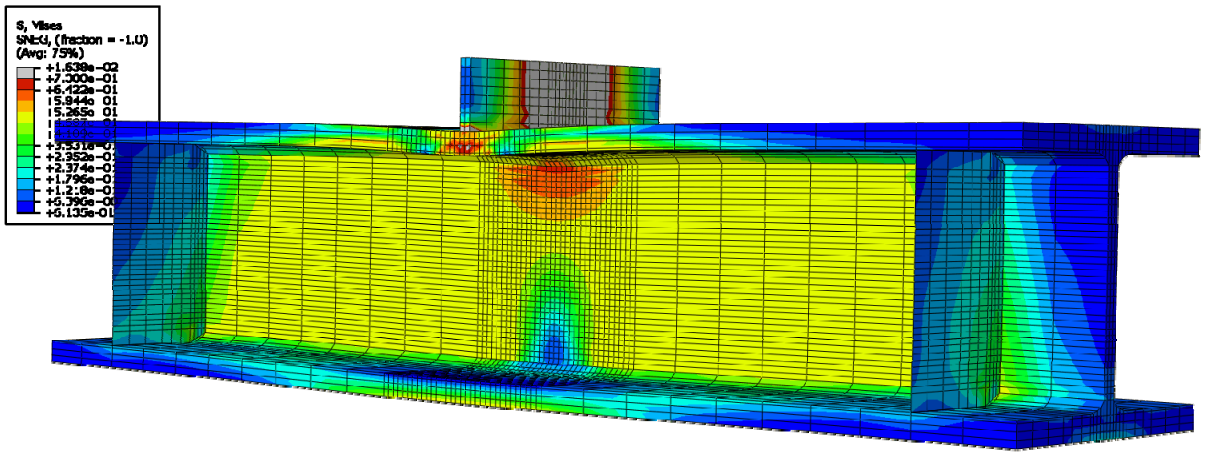

Figure E-114: Finite element model of W14X176-SC-NA during inelastic behavior

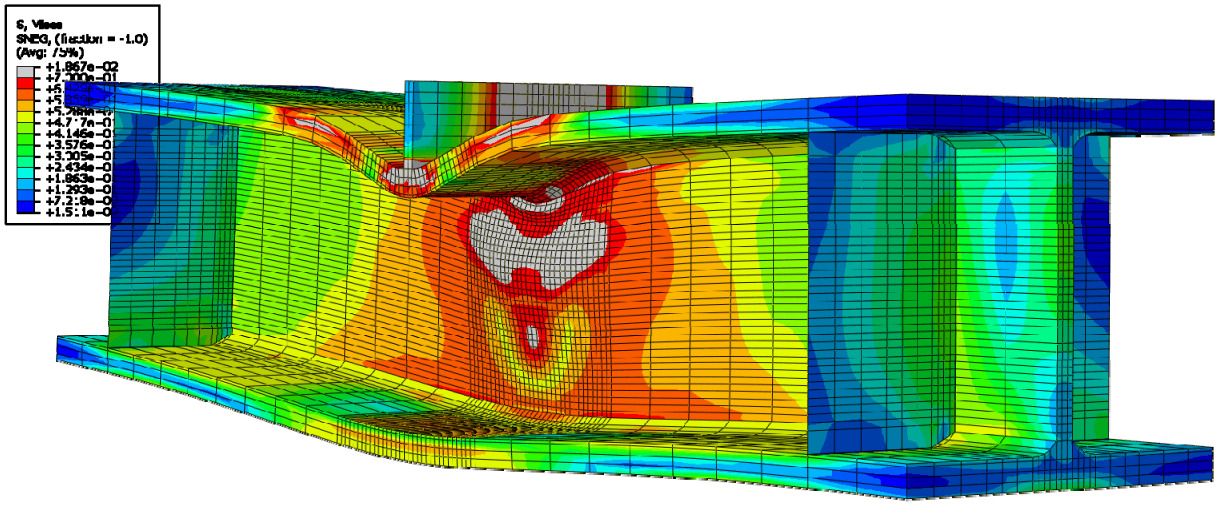

Figure E-115: Finite element model of W14X176-SC-NA after the maximum load

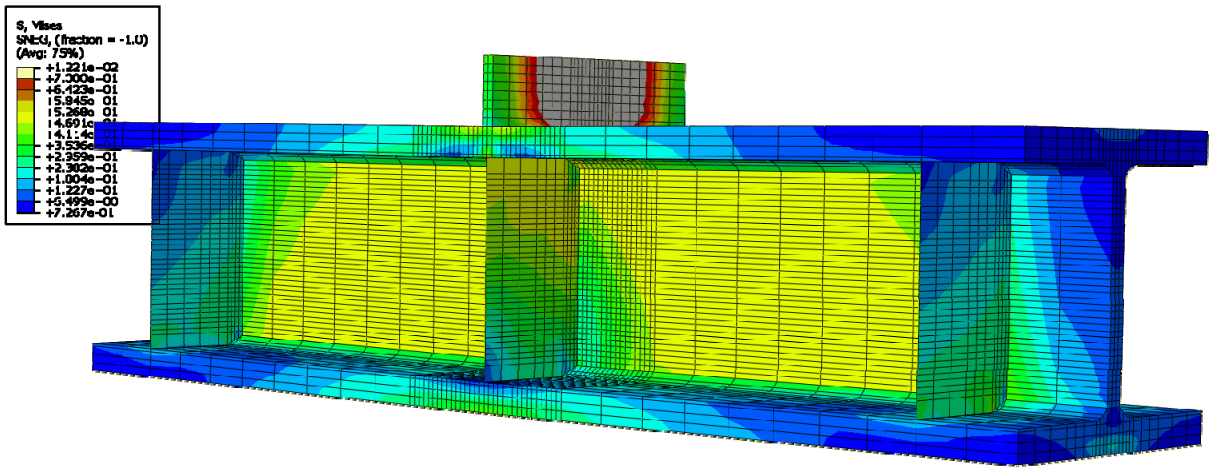

Figure E-116: Finite element model of W14X233-SC-E0 with 3/8 in. stiffeners during elastic behavior

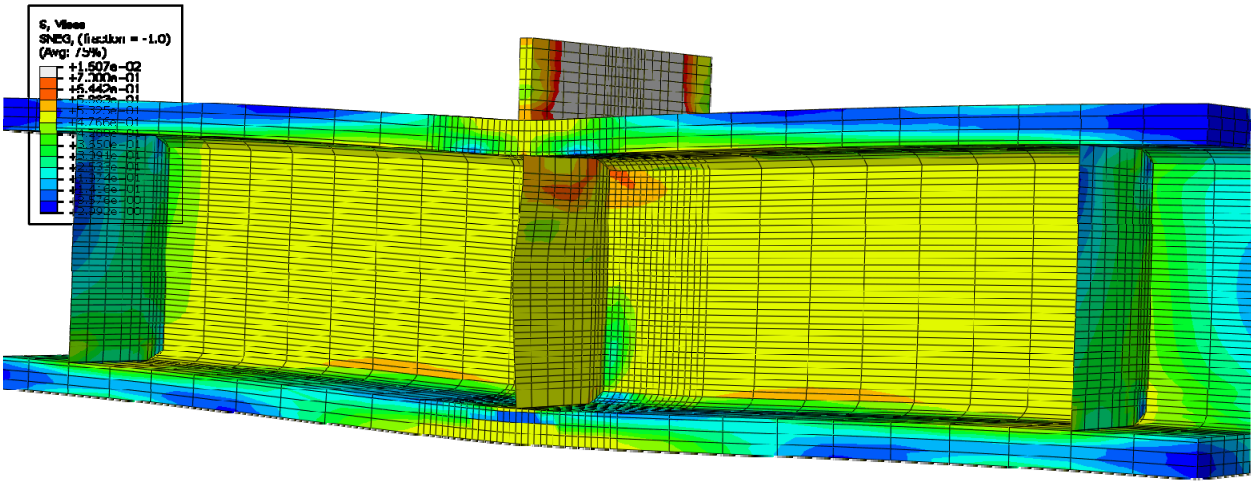

Figure E-117: Finite element model of W14X233-SC-E0 with 3/8 in. stiffeners during inelastic behavior

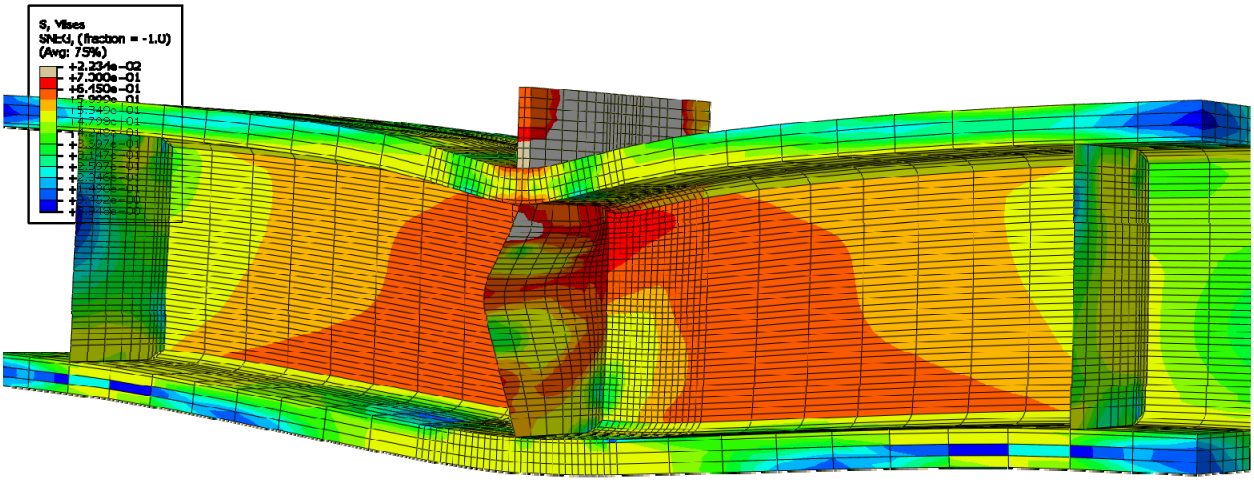

Figure E-118: Finite element model of W14X233-SC-E0 with 3/8 in. stiffeners after the maximum load emphasizing stiffener buckling

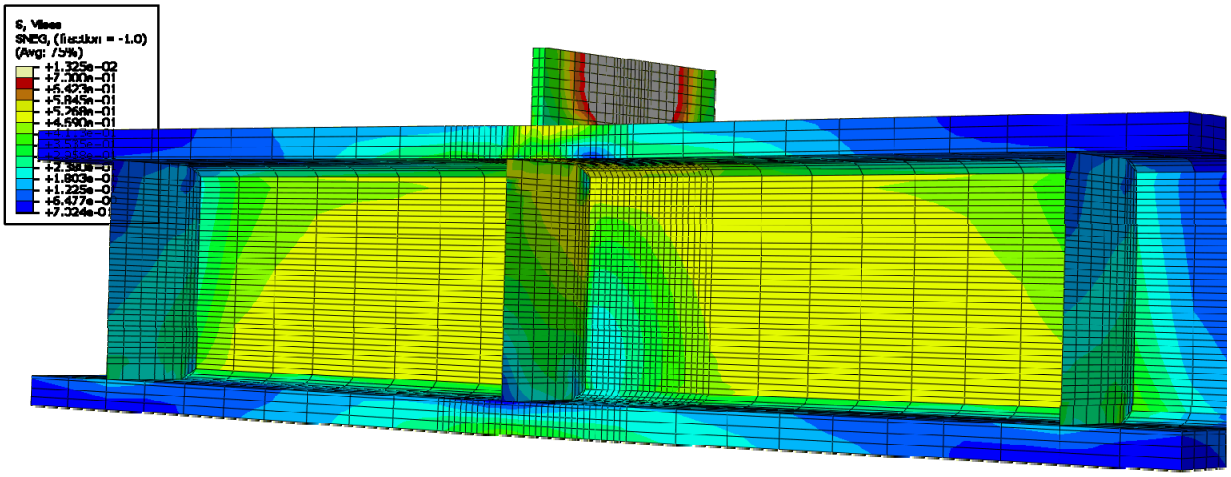

Figure E-119: Finite element model of W14X233-SC-E2 with 3/8 in. stiffeners during elastic behavior

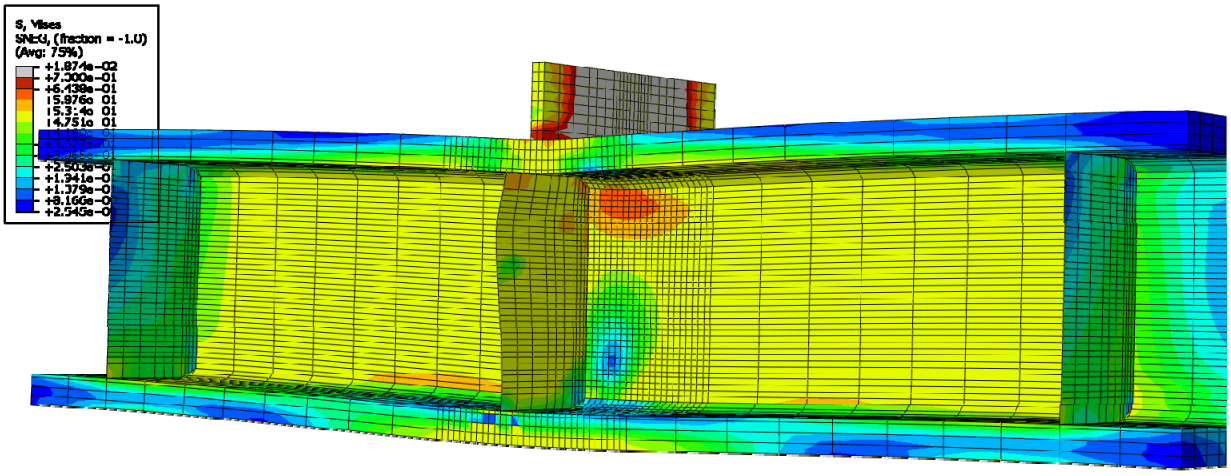

Figure E-120: Finite element model of W14X233-SC-E2 with 3/8 in. stiffeners during inelastic behavior

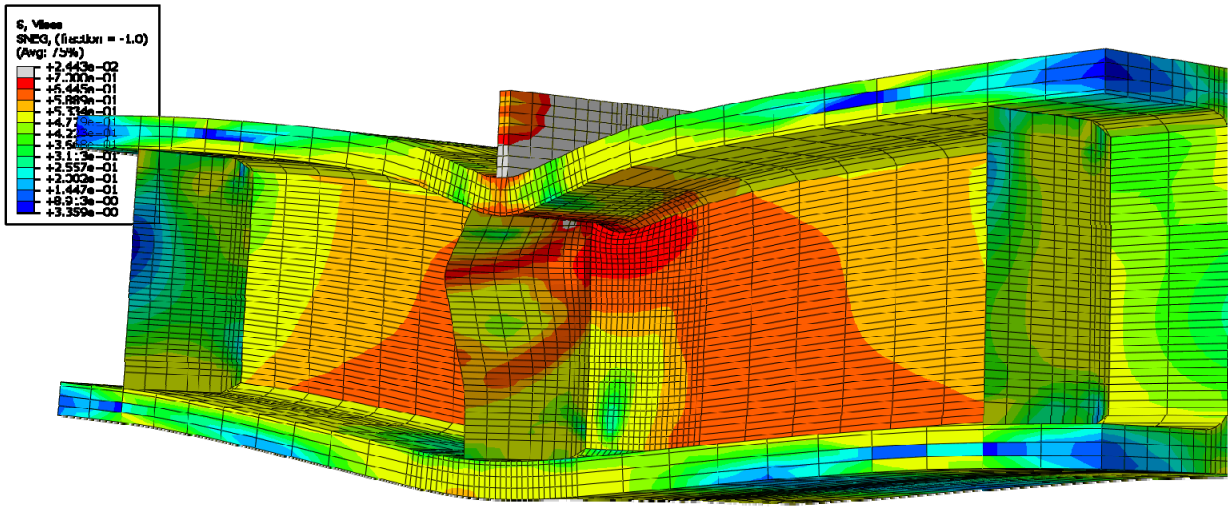

Figure E-121: Finite element model of W14X233-SC-E2 with 3/8 in. stiffeners after the maximum load

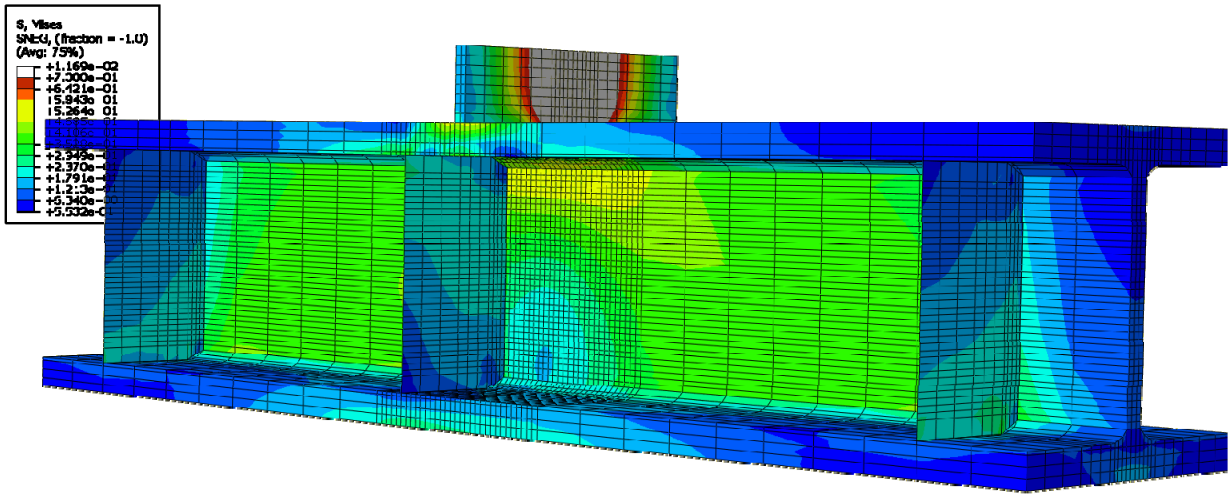

Figure E-122: Finite element model of W14X233-SC-E4 with 3/8 in. stiffeners during elastic behavior

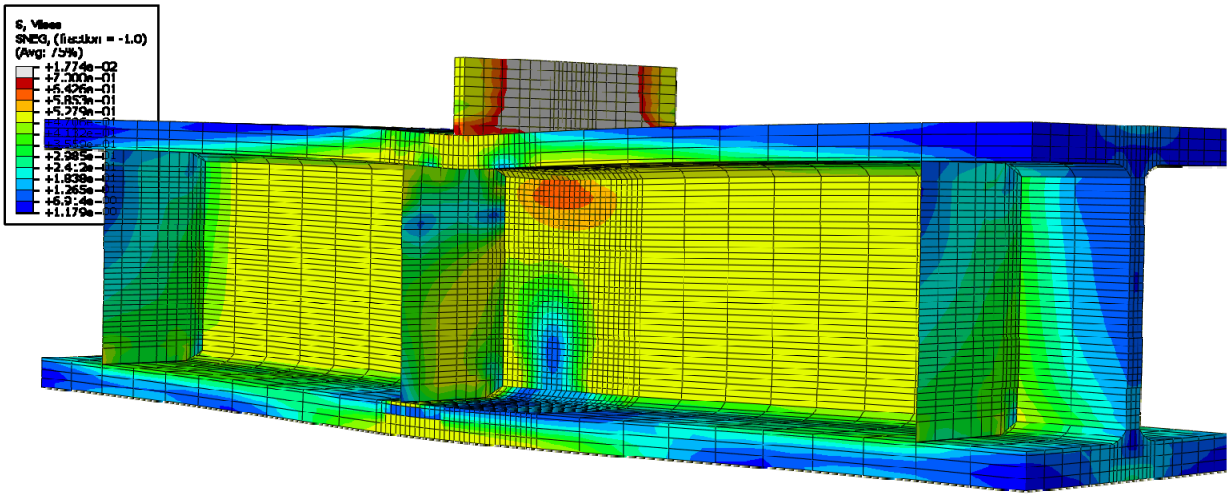

Figure E-123: Finite element model of W14X233-SC-E4 with 3/8 in. stiffeners during inelastic behavior

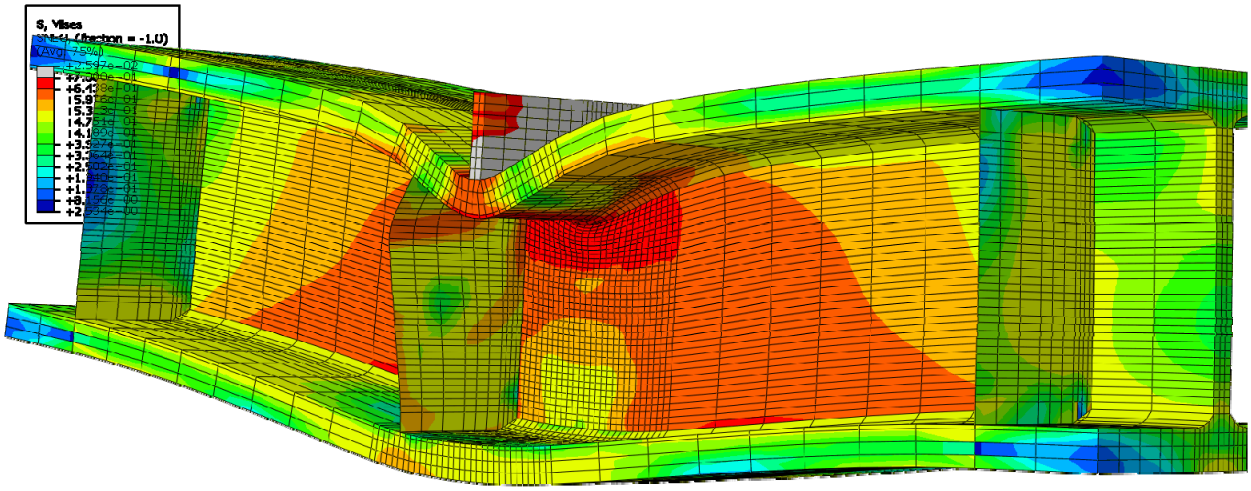

Figure E-124: Finite element model of W14X233-SC-E4 with 3/8 in. stiffeners after the maximum load

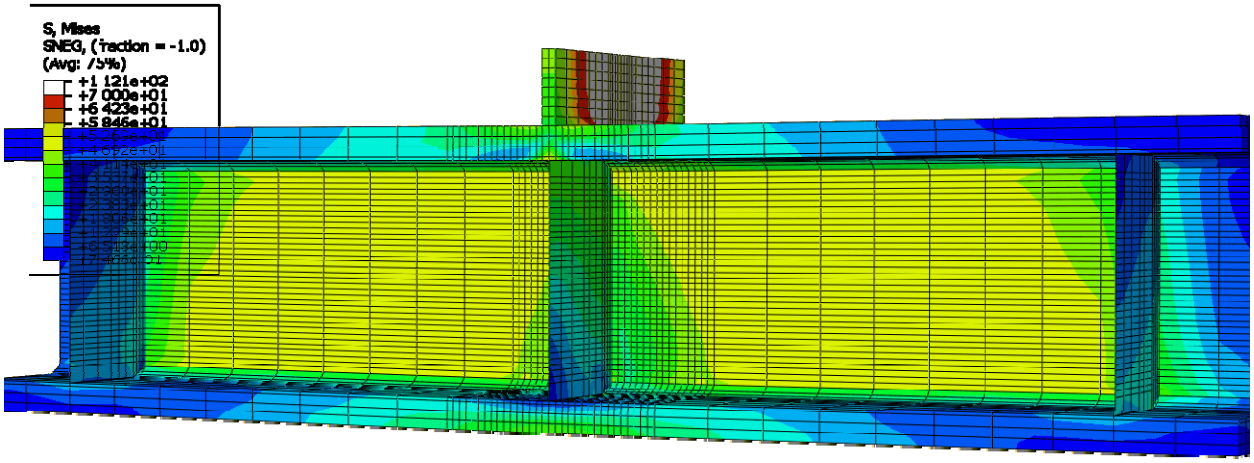

Figure E-125: Finite element model of W14X233-SC-E0 with 3/4 in. stiffeners during elastic behavior

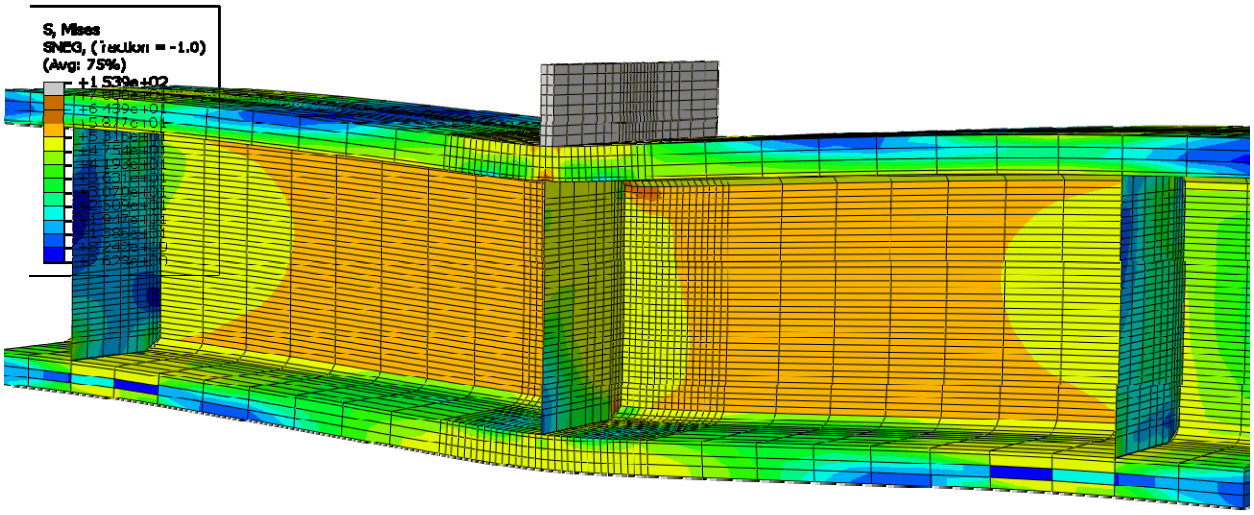

Figure E-126: Finite element model of W14X233-SC-E0 with 3/4 in. stiffeners during inelastic behavior

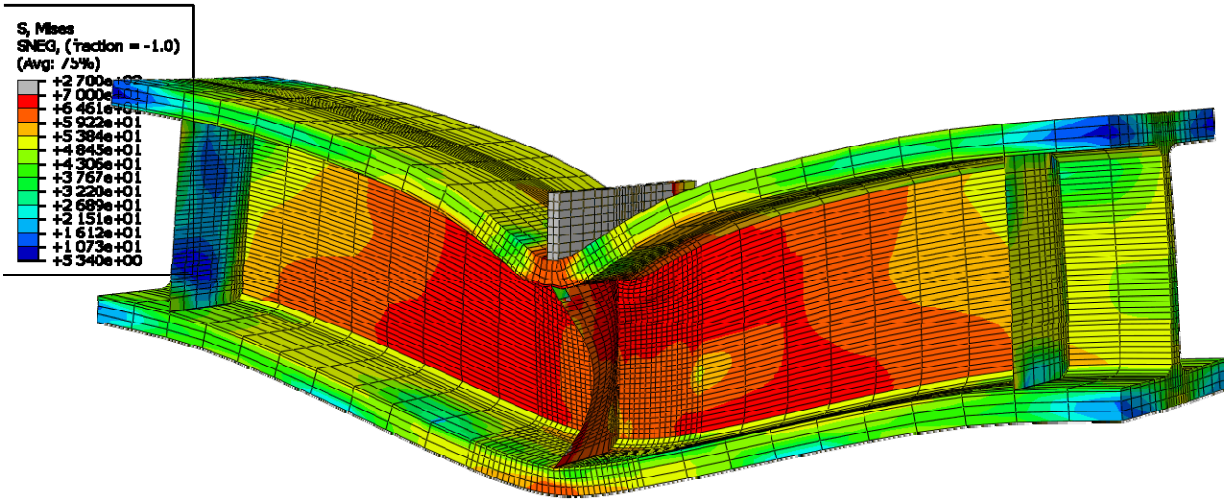

Figure E-127: Finite element model of W14X233-SC-E0 with 3/4 in. stiffeners after the maximum load emphasizing stiffener buckling

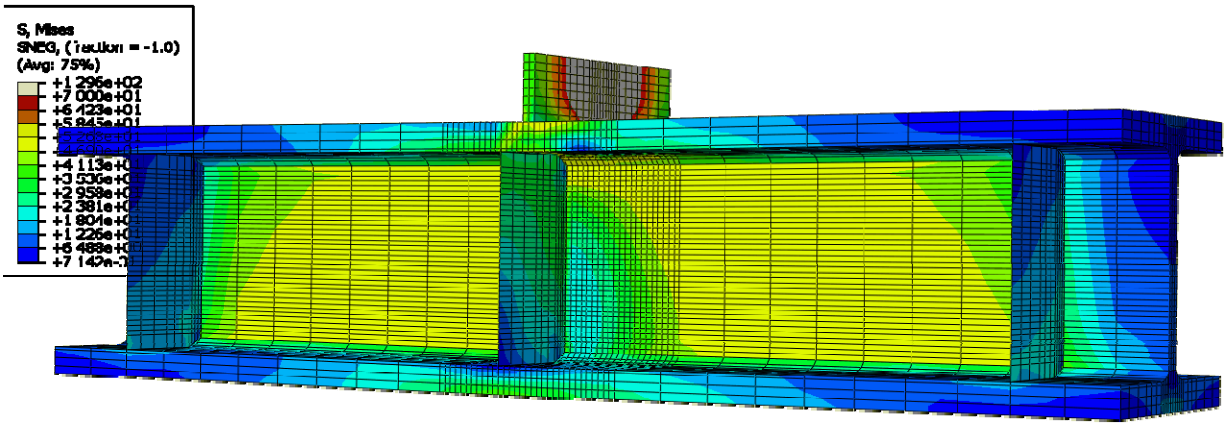

Figure E-128: Finite element model of W14X233-SC-E2 with 3/4 in. stiffeners during elastic behavior

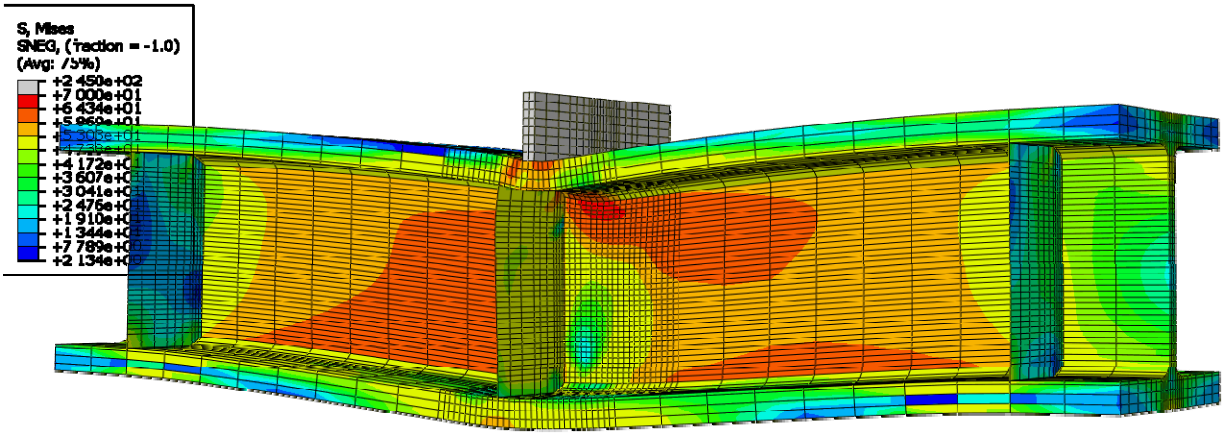

Figure E-129: Finite element model of W14X233-SC-E2 with 3/4 in. stiffeners during inelastic behavior

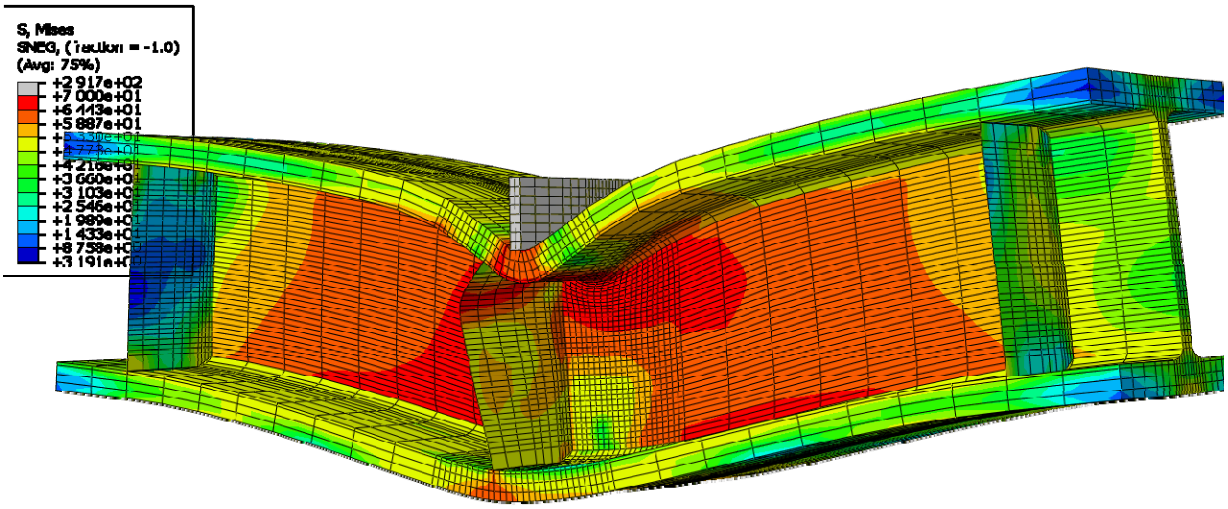

Figure E-130: Finite element model of W14X233-SC-E2 with 3/4 in. stiffeners after the maximum load

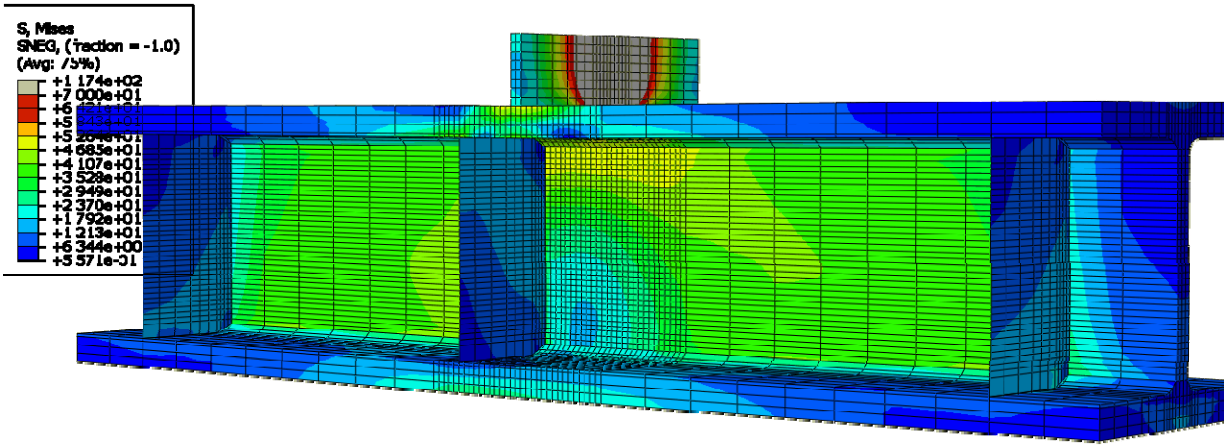

Figure E-131: Finite element model of W14X233-SC-E4 with 3/4 in. stiffeners during elastic behavior

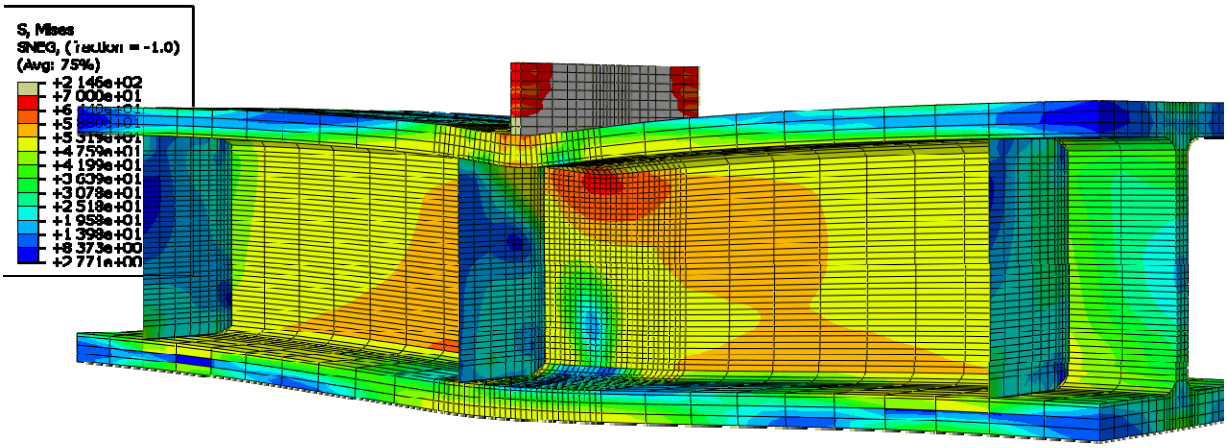

Figure E-132: Finite element model of W14X233-SC-E4 with 3/4 in. stiffeners during inelastic behavior

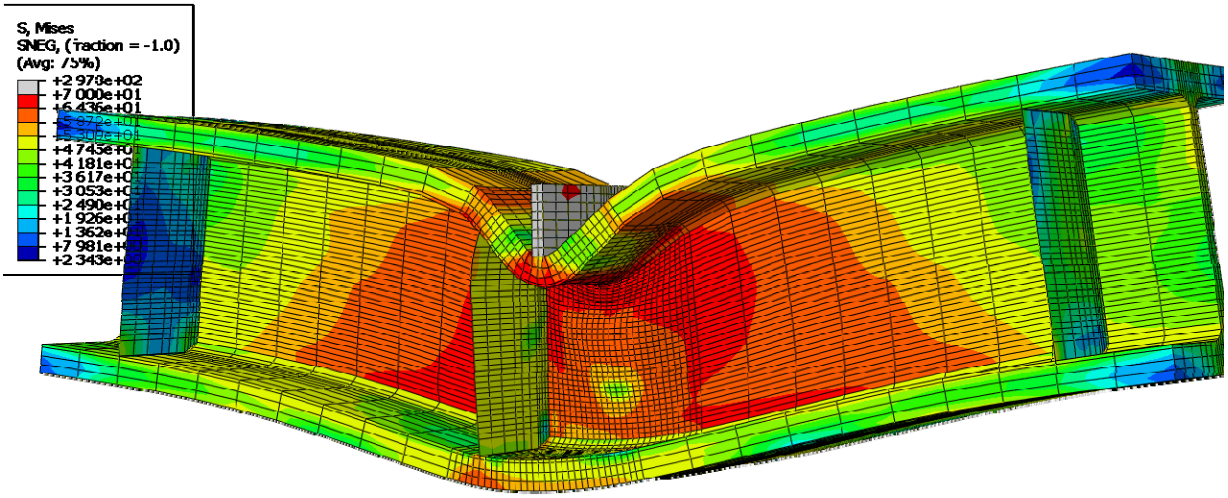

Figure E-133: Finite element model of W14X233-SC-E4 with 3/4 in. stiffeners after the maximum load

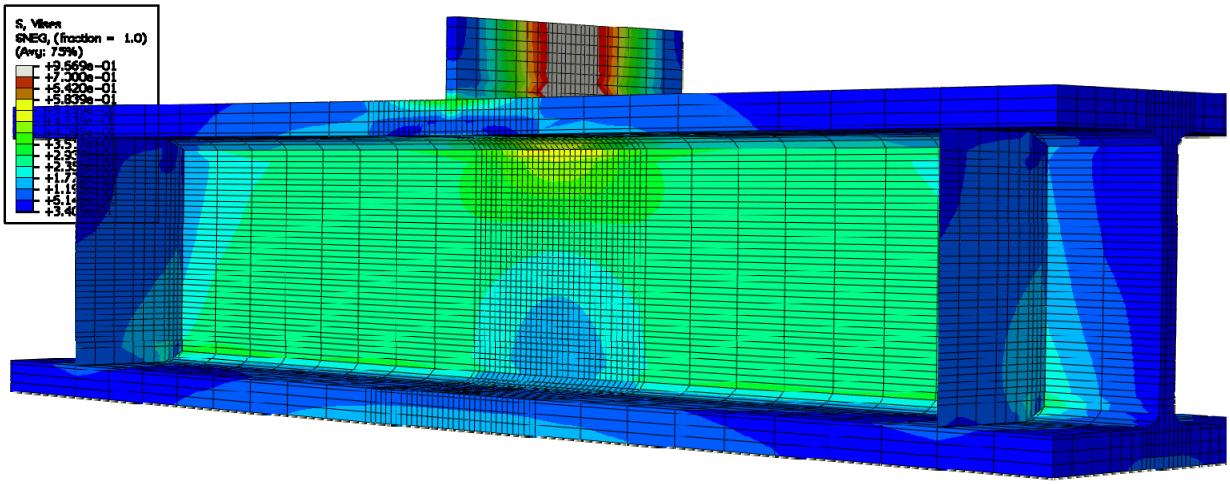

Figure E-134: Finite element model of W14X233-SC-NA during elastic behavior

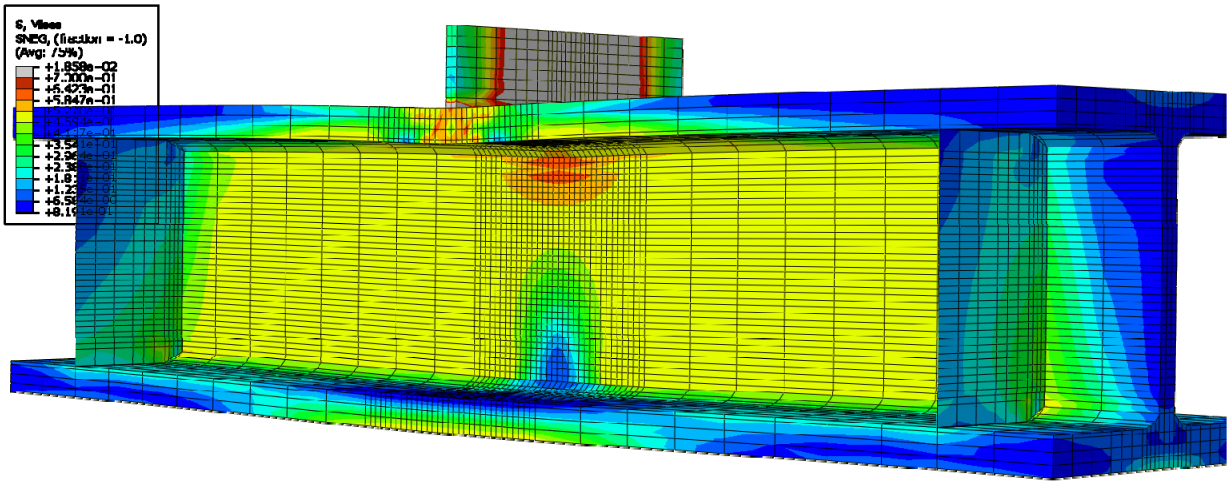

Figure E-135: Finite element model of W14X233-SC-NA during inelastic behavior

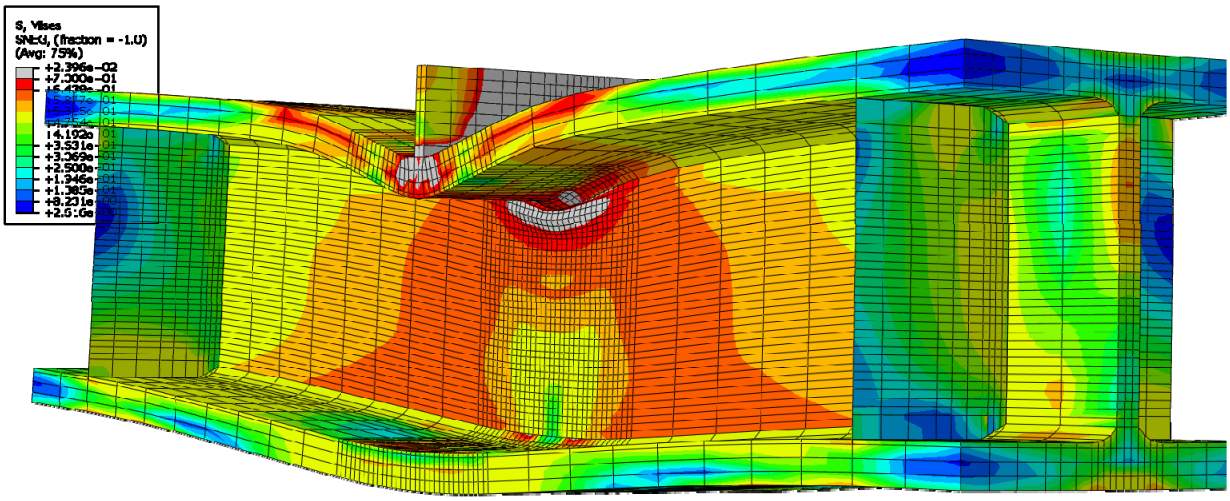

Figure E-136: Finite element model of W14X233-SC-NA after the maximum load

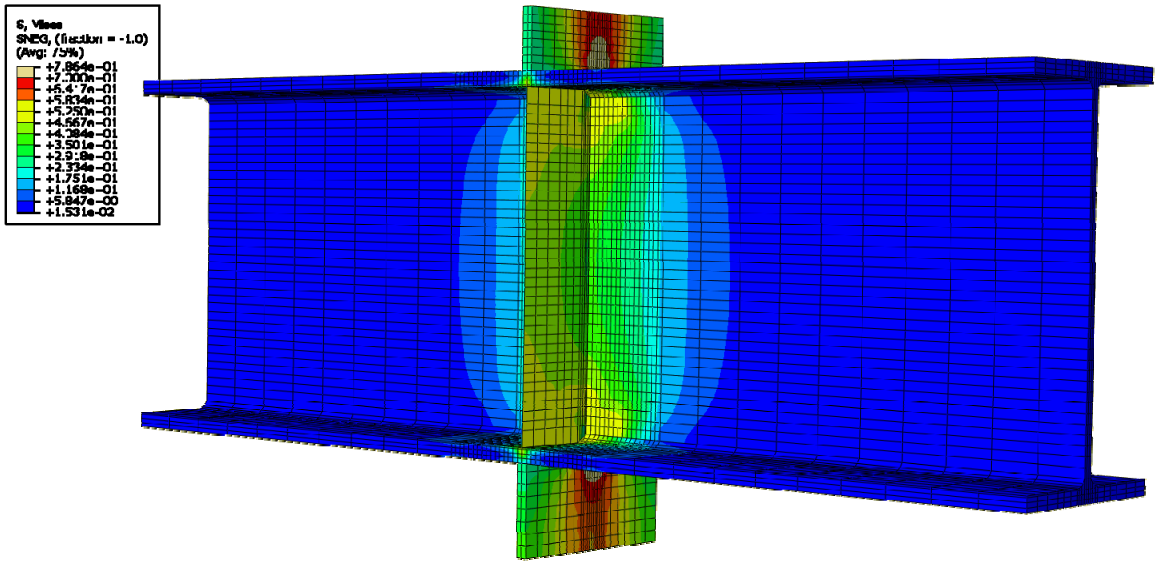

Figure E-137: Finite element model of W24X131-DC-E0 with 3/8 in. stiffeners during elastic behavior

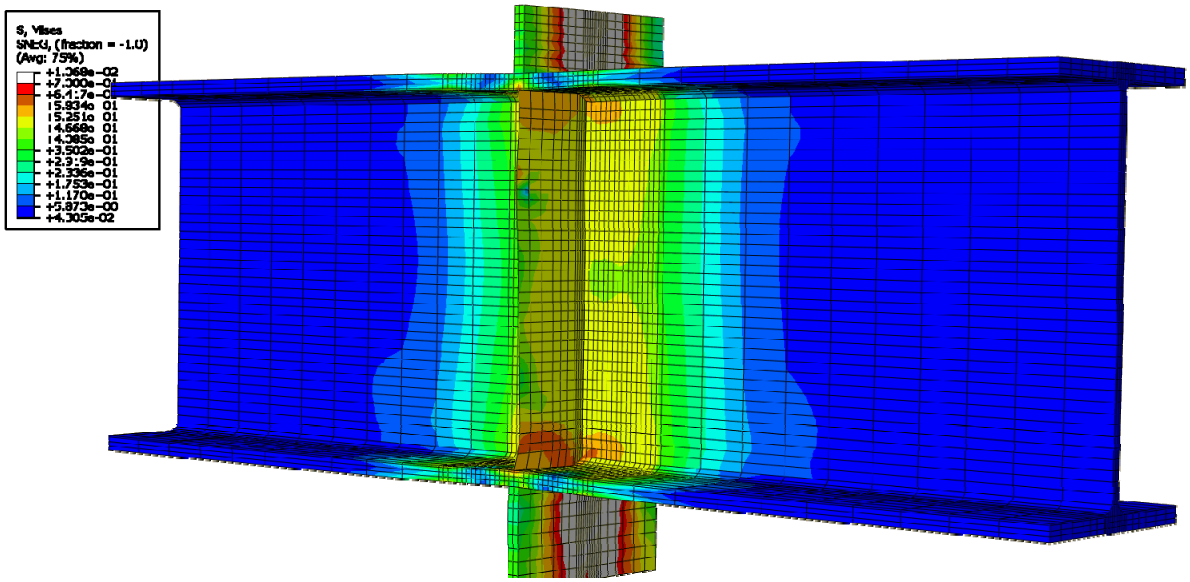

Figure E-138: Finite element model of W24X131-DC-E0 with 3/8 in. stiffeners during inelastic behavior

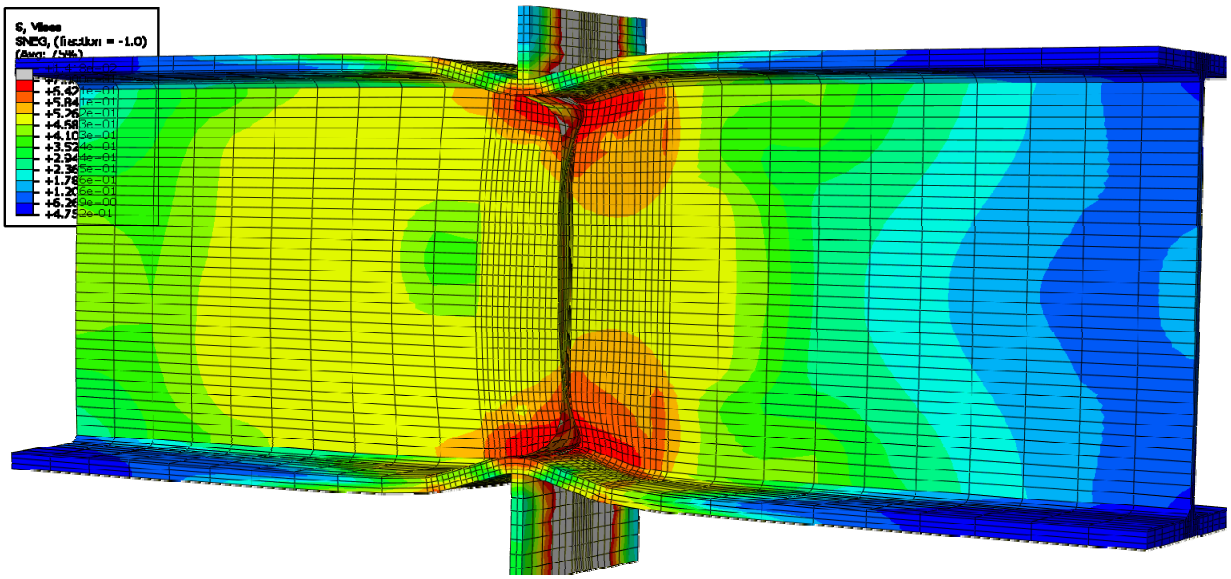

Figure E-139: Finite element model of W24X131-DC-E0 with 3/8 in. stiffeners after the maximum load

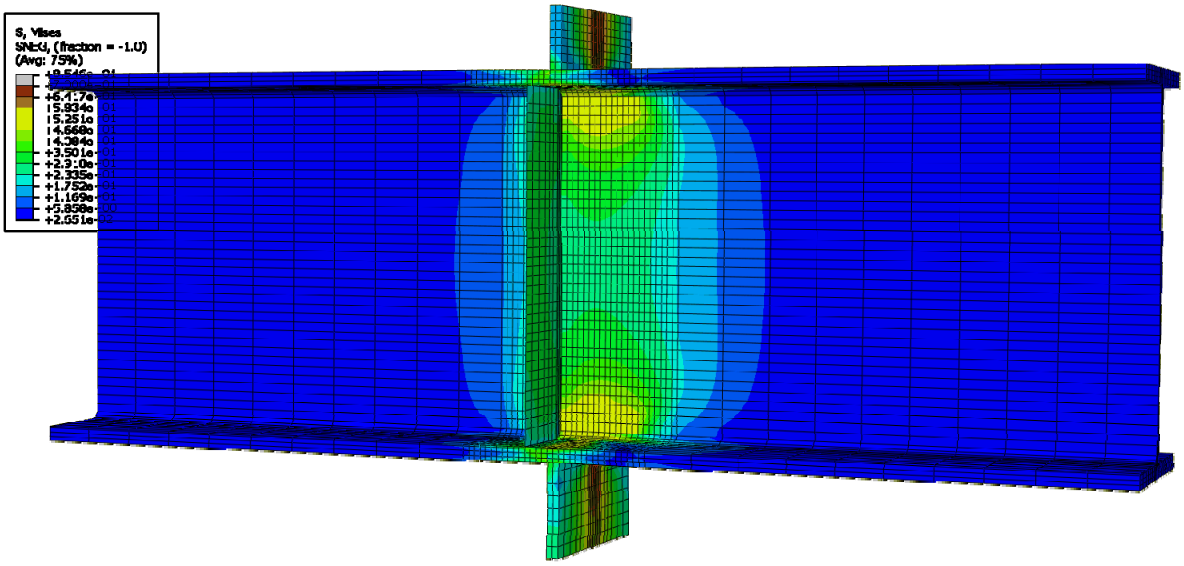

Figure E-140: Finite element model of W24X131-DC-E2 with 3/8 in. stiffeners during elastic behavior

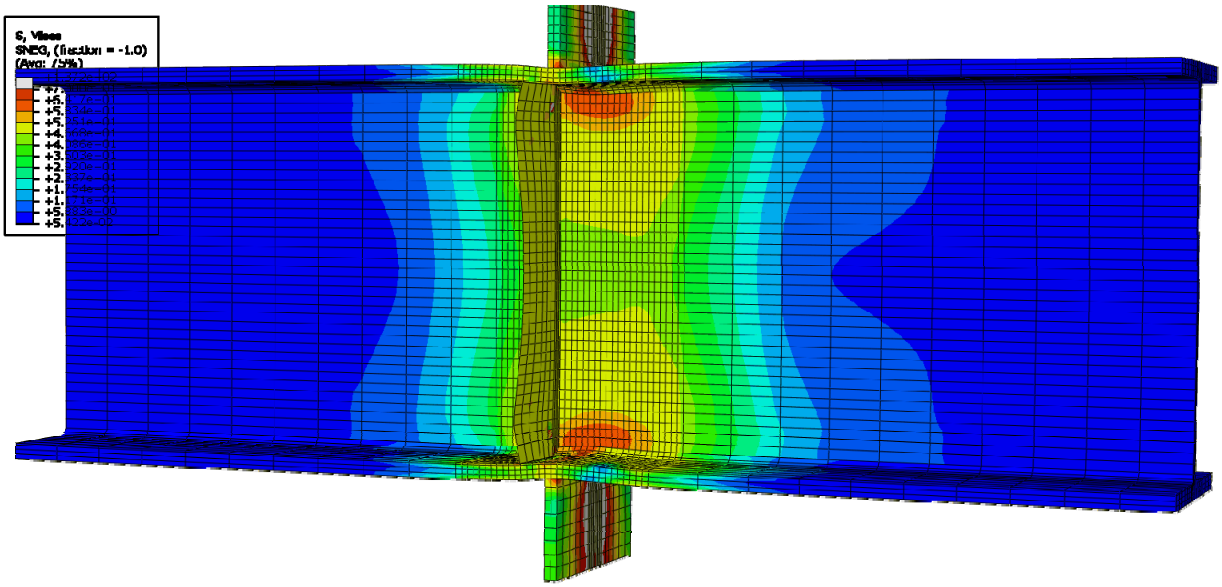

Figure E-141: Finite element model of W24X131-DC-E2 with 3/8 in. stiffeners during inelastic behavior

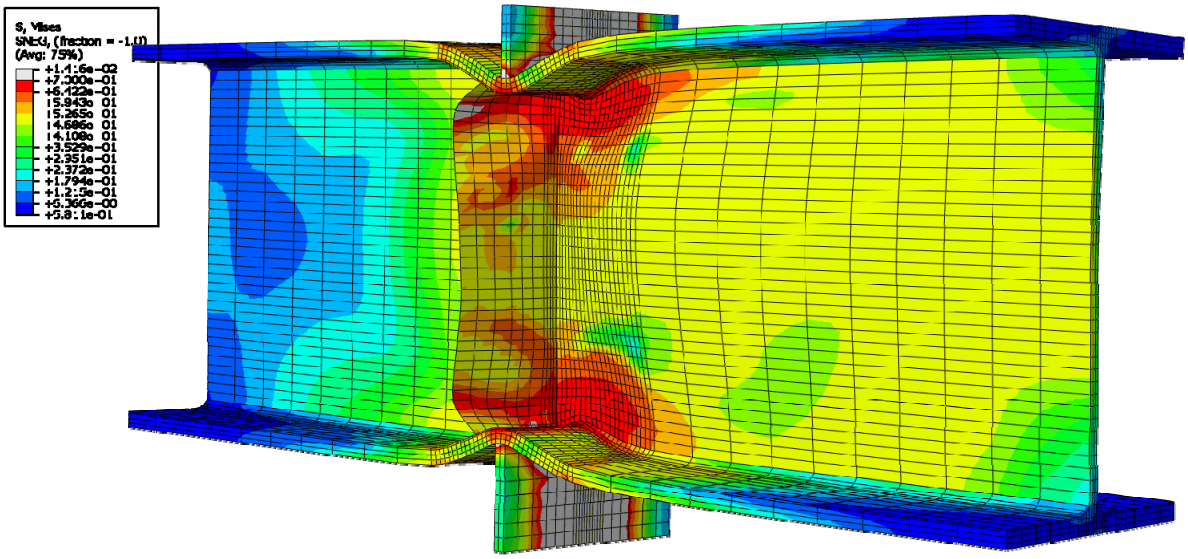

Figure E-142: Finite element model of W24X131-DC-E2 with 3/8 in. stiffeners after the maximum load

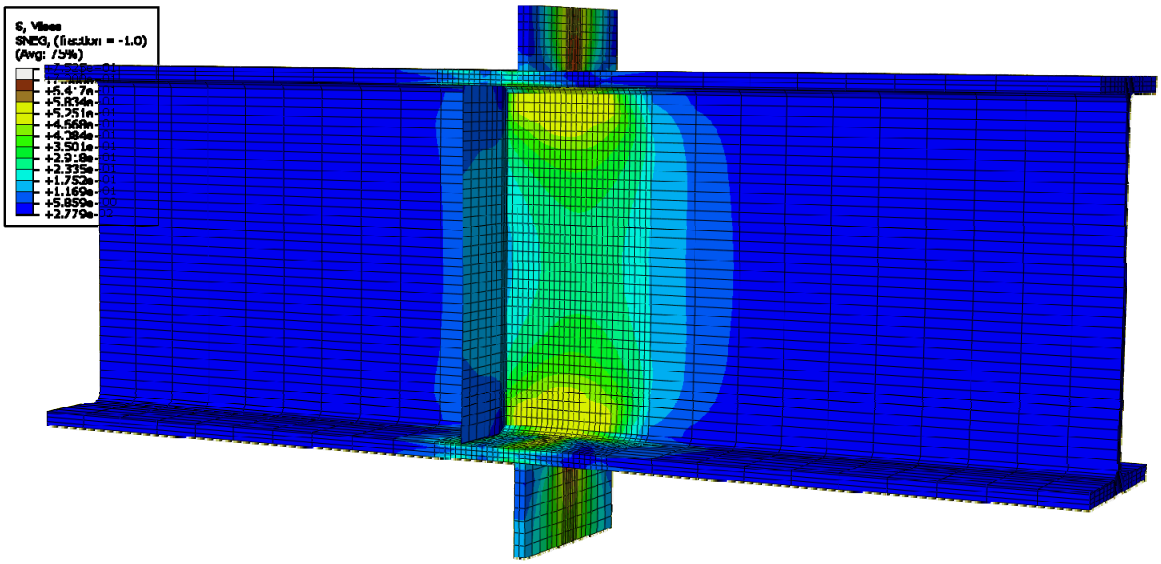

Figure E-143: Finite element model of W24X131-DC-E4 with 3/8 in. stiffeners during elastic behavior

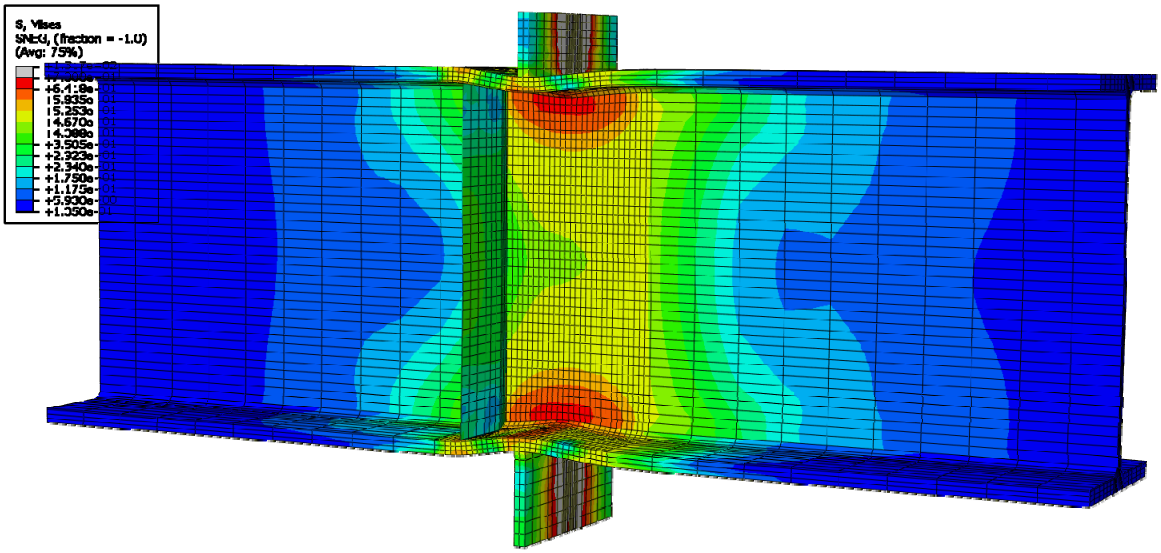

Figure E-144: Finite element model of W24X131-DC-E4 with 3/8 in. stiffeners during inelastic behavior

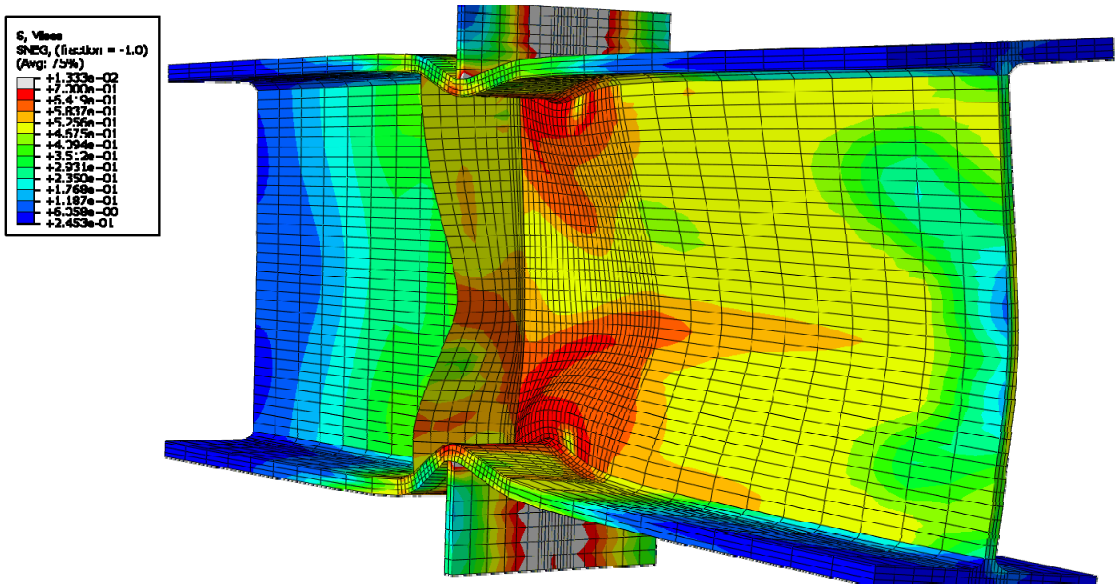

Figure E-145: Finite element model of W24X131-DC-E4 with 3/8 in. stiffeners after the maximum load

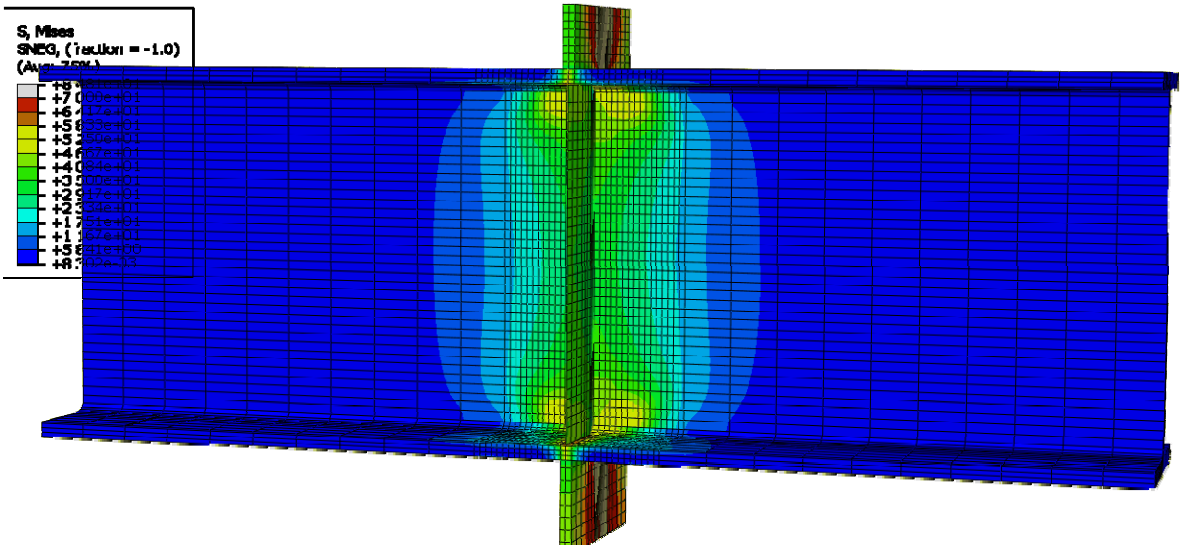

Figure E-146: Finite element model of W24X131-DC-E0 with 3/4 in. stiffeners during elastic behavior

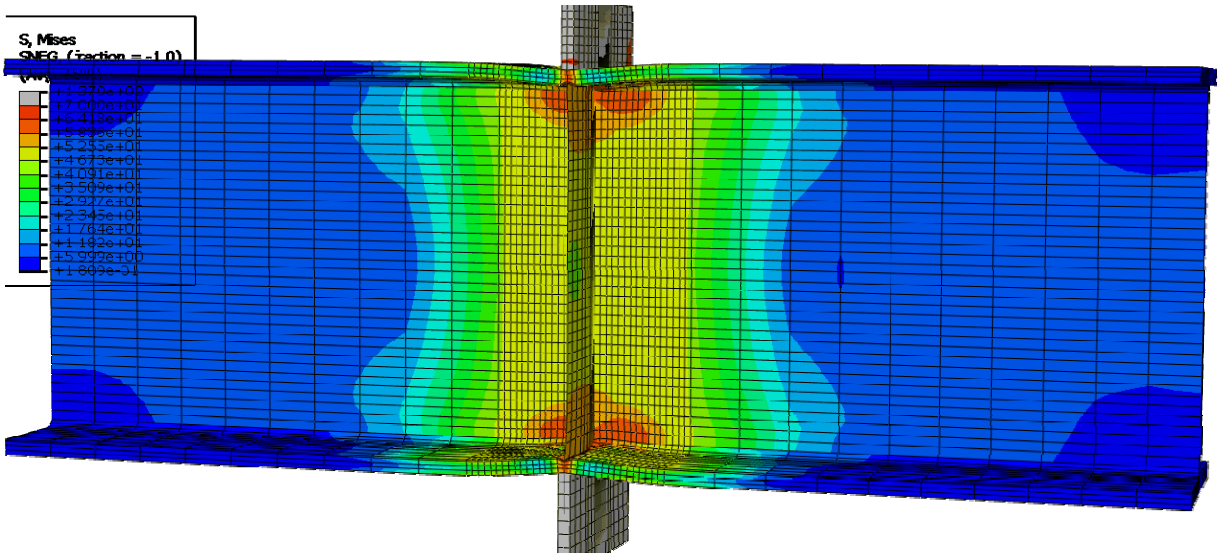

Figure E-147: Finite element model of W24X131-DC-E0 with 3/4 in. stiffeners during inelastic behavior

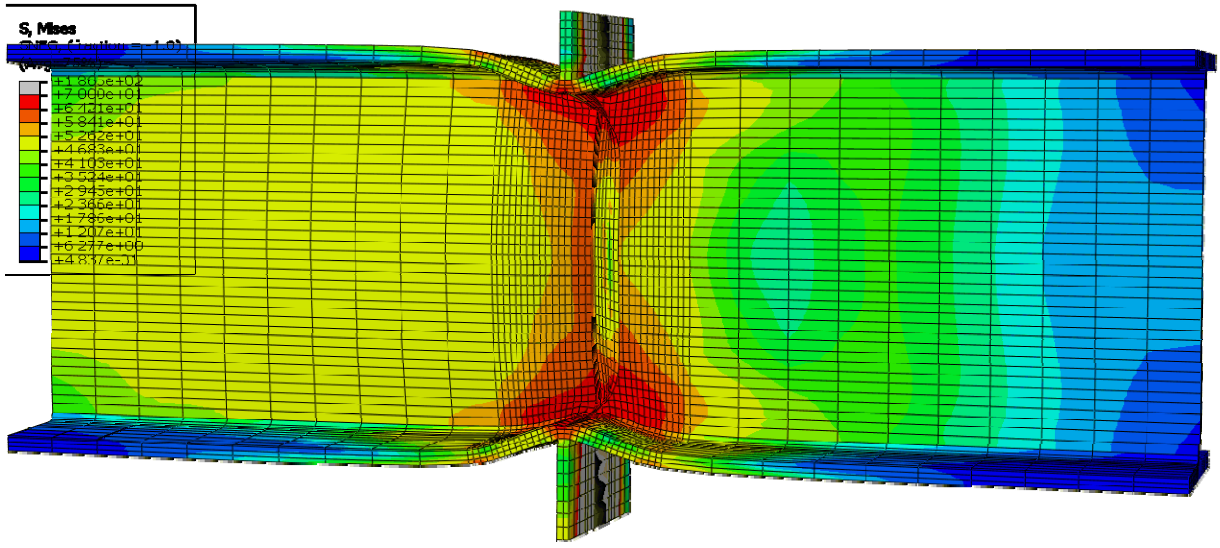

Figure E-148: Finite element model of W24X131-DC-E0 with 3/4 in. stiffeners after the maximum load

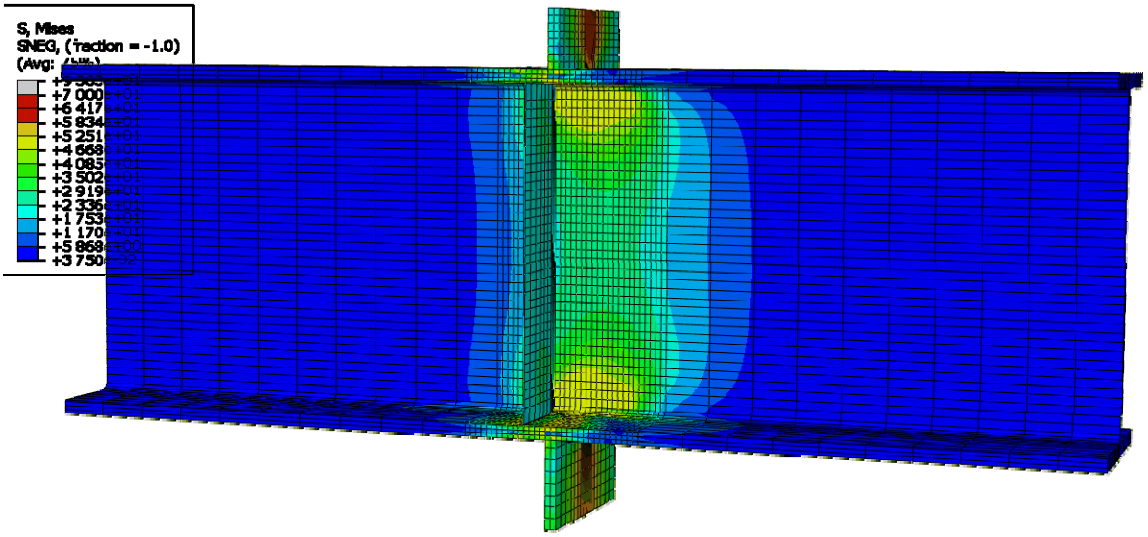

Figure E-149: Finite element model of W24X131-DC-E2 with 3/4 in. stiffeners during elastic behavior

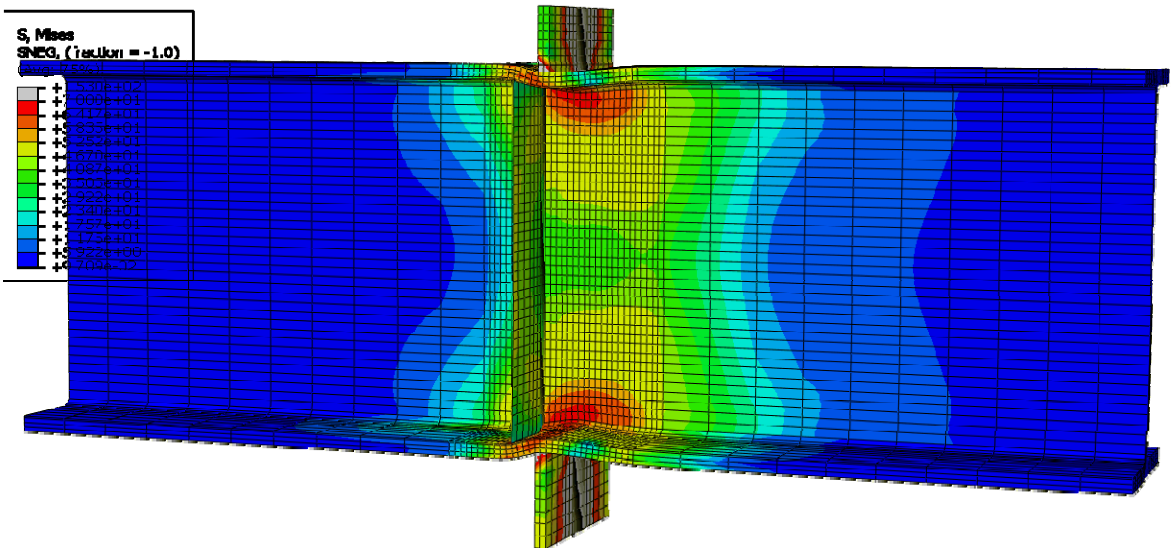

Figure E-150: Finite element model of W24X131-DC-E2 with 3/4 in. stiffeners during inelastic behavior

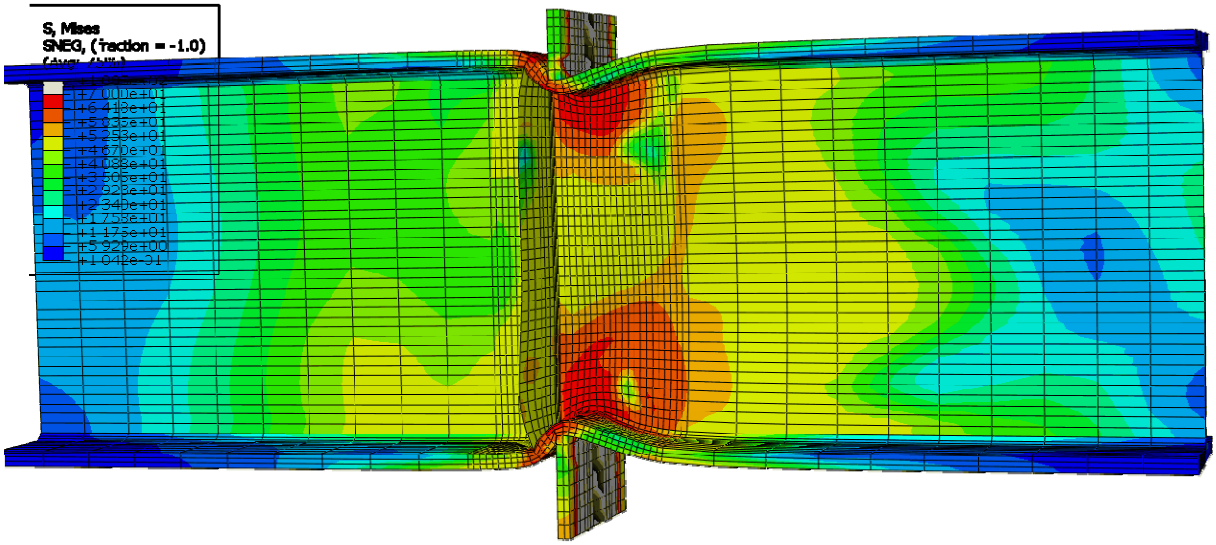

Figure E-151: Finite element model of W24X131-DC-E2 with 3/4 in. stiffeners after the maximum load

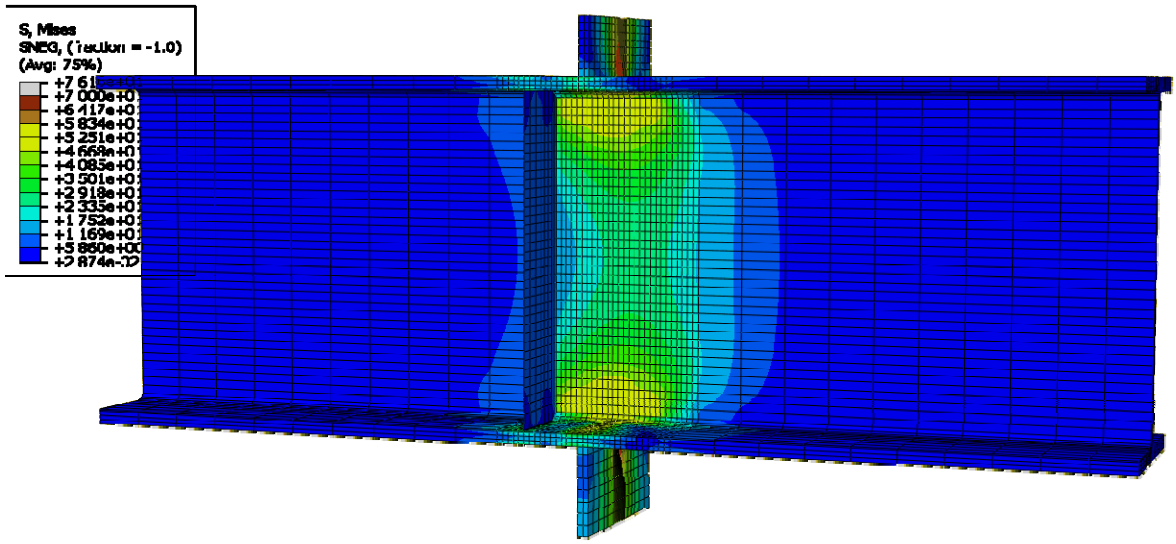

Figure E-152: Finite element model of W24X131-DC-E4 with 3/4 in. stiffeners during elastic behavior

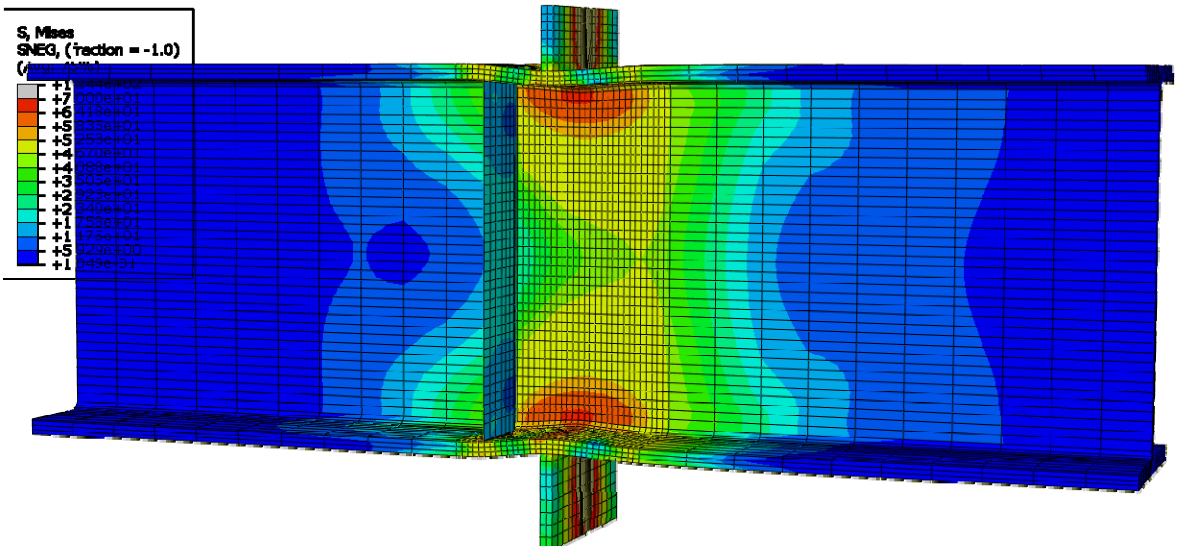

Figure E-153: Finite element model of W24X131-DC-E4 with 3/4 in. stiffeners during inelastic behavior

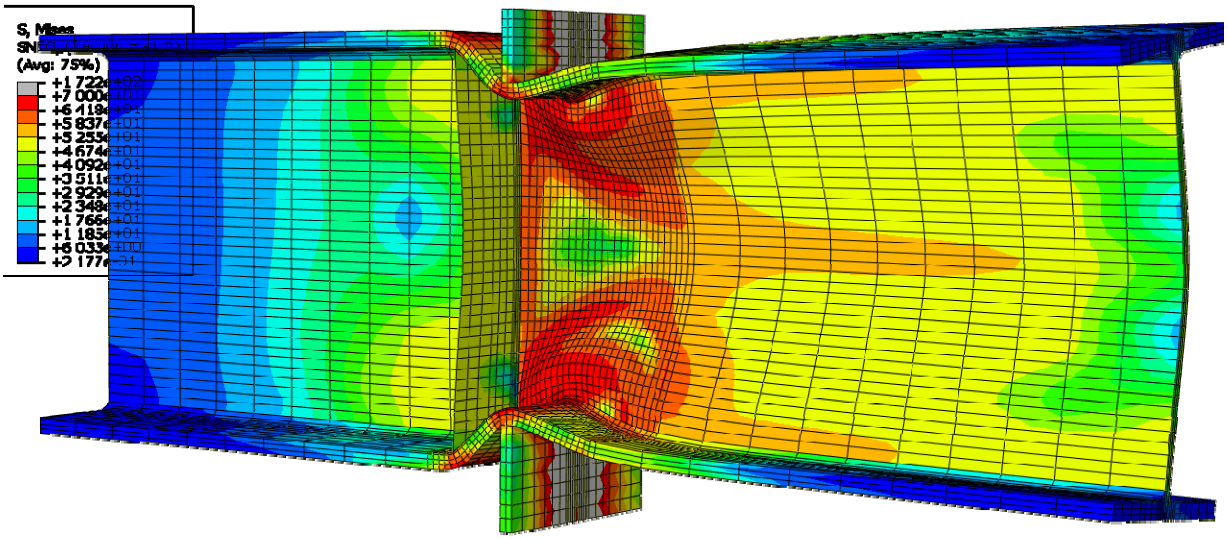

Figure E-154: Finite element model of W24X131-DC-E4 with 3/4 in. stiffeners after the maximum load

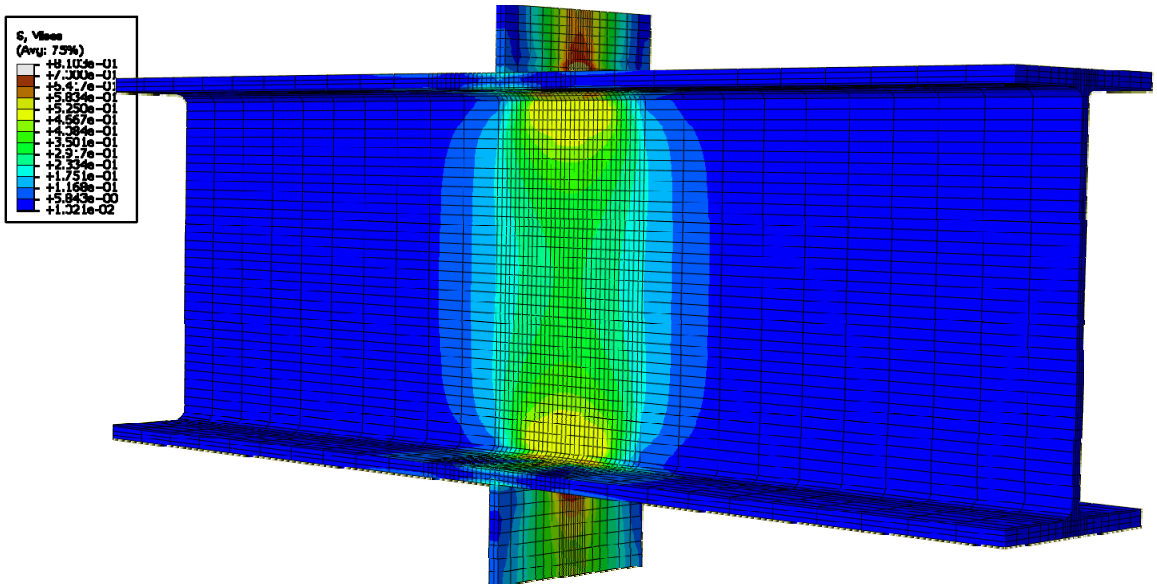

Figure E-155: Finite element model of W24X131-DC-NA during elastic behavior

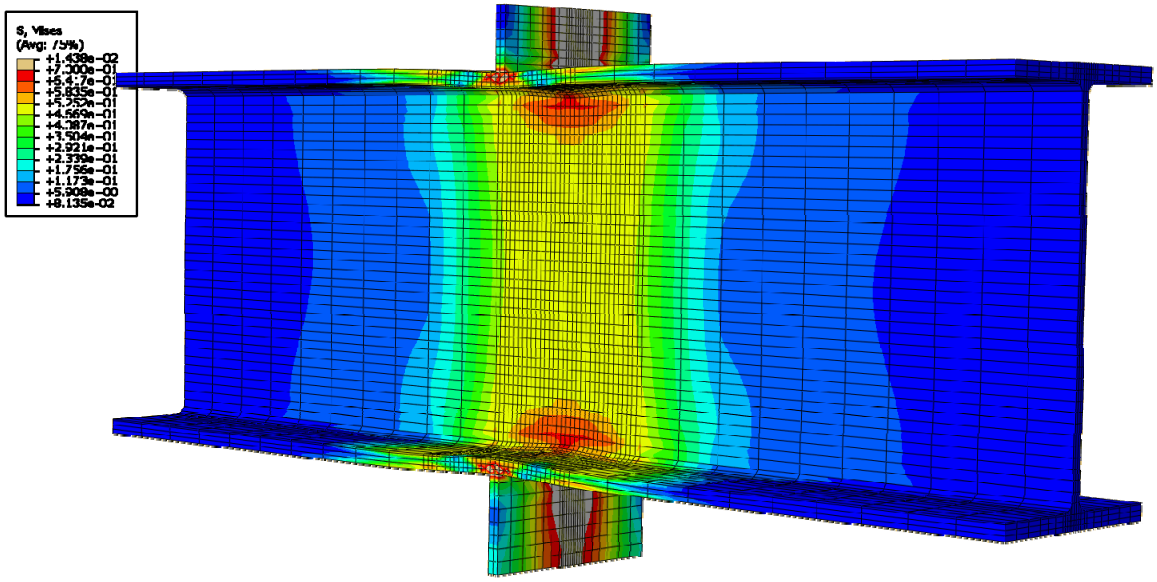

Figure E-156: Finite element model of W24X131-DC-NA during inelastic behavior

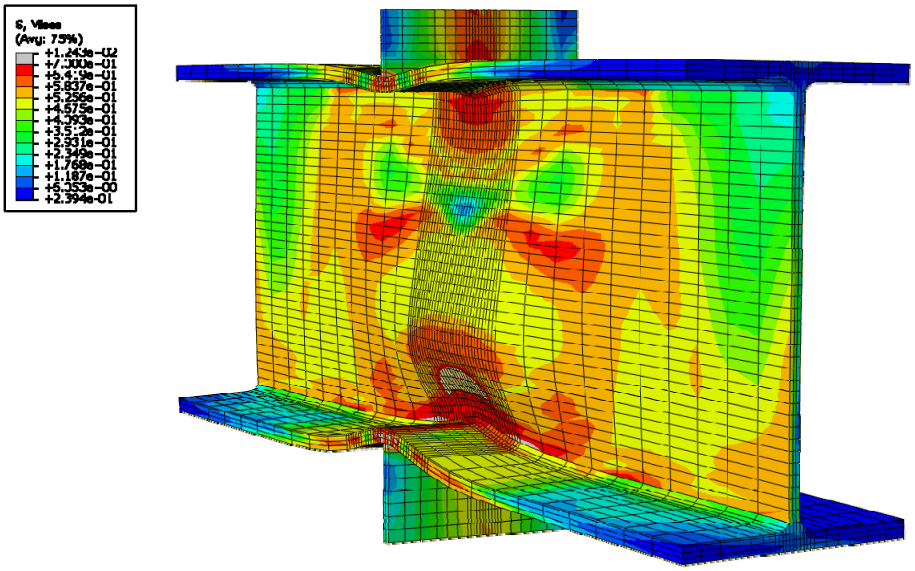

Figure E-157: Finite element model of W24X131-DC-NA after the maximum load

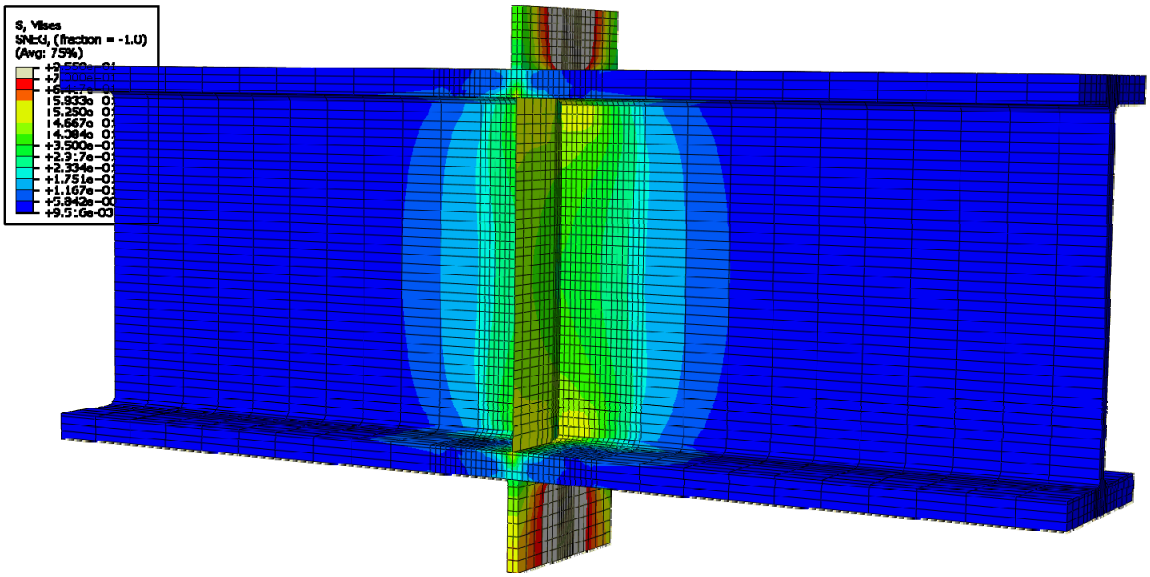

Figure E-158: Finite element model of W24X229-DC-E0 with 3/8 in. stiffeners during elastic behavior

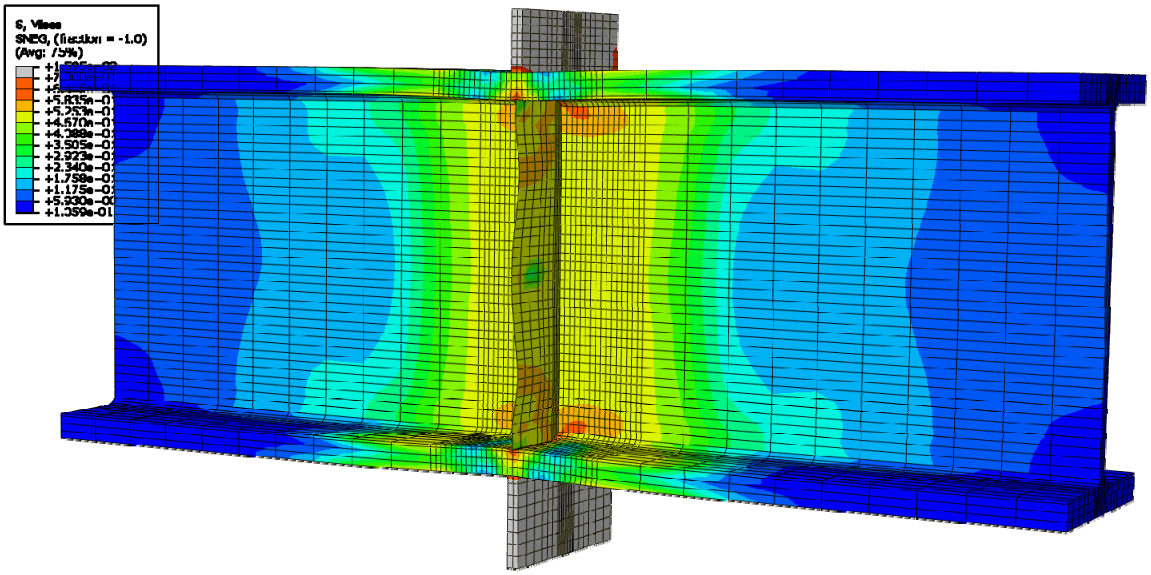

Figure E-159: Finite element model of W24X229-DC-E0 with 3/8 in. stiffeners during inelastic behavior

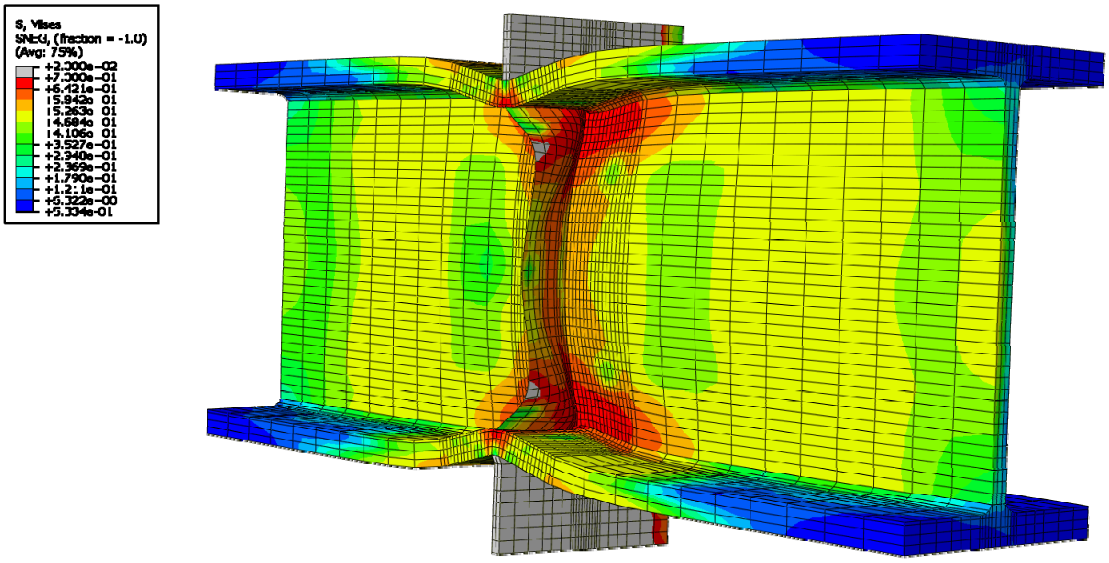

Figure E-160: Finite element model of W24X229-DC-E0 with 3/8 in. stiffeners after the maximum load

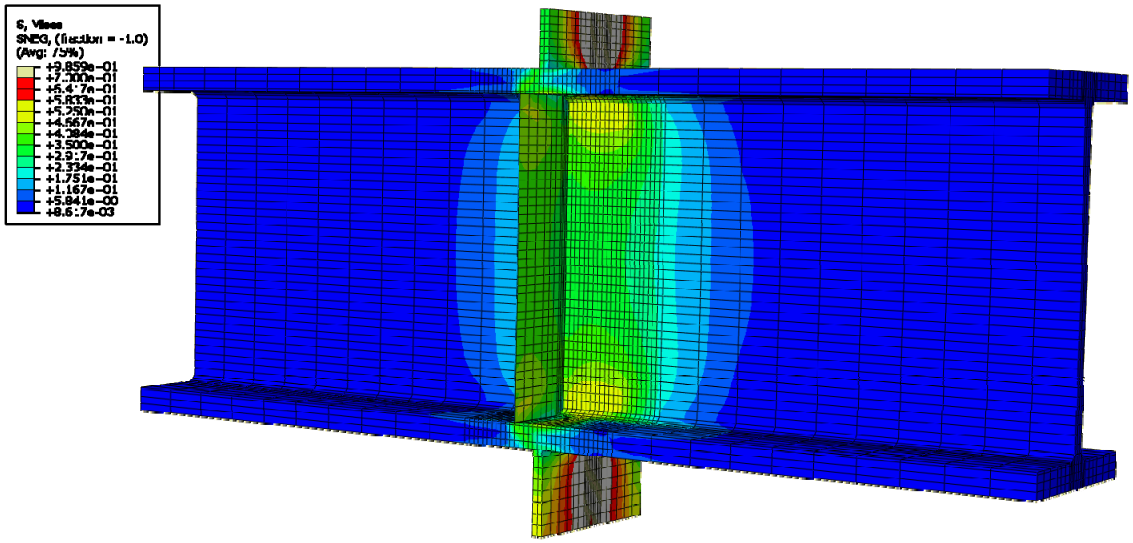

Figure E-161: Finite element model of W24X229-DC-E2 with 3/8 in. stiffeners during elastic behavior

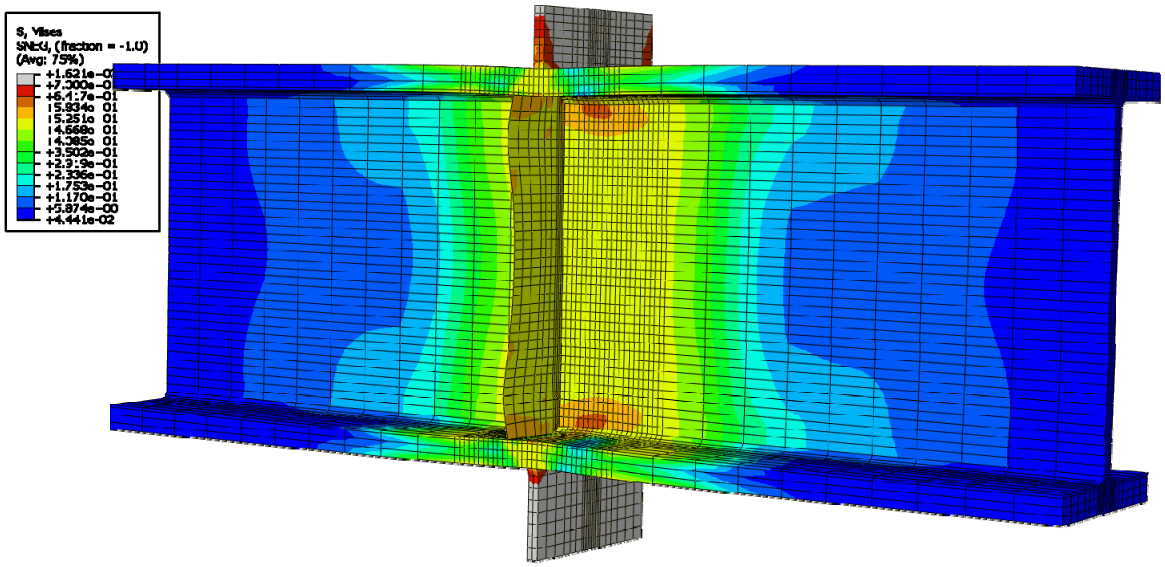

Figure E-162: Finite element model of W24X229-DC-E2 with 3/8 in. stiffeners during inelastic behavior

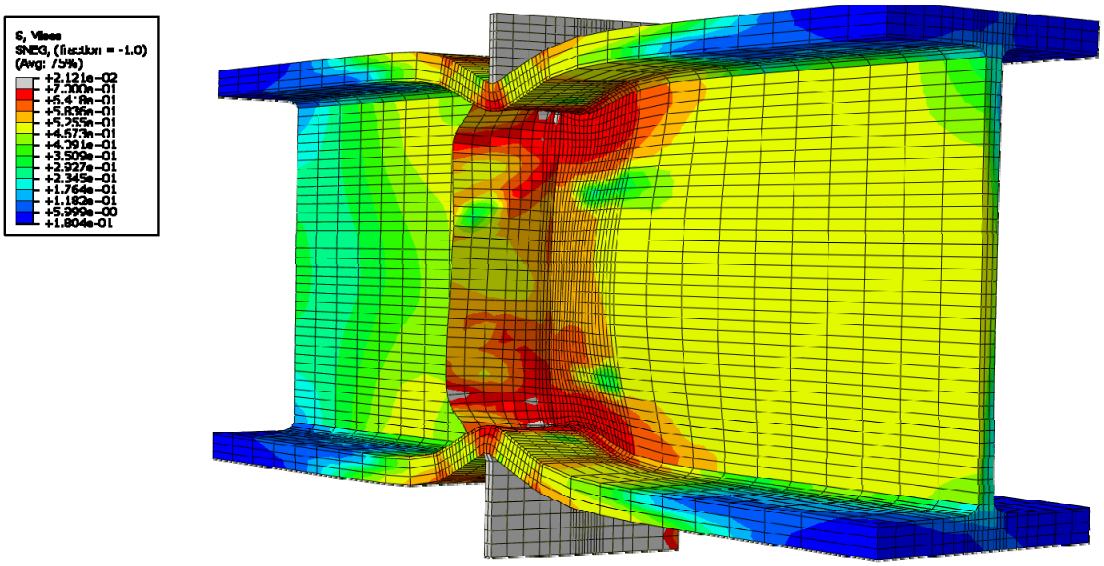

Figure E-163: Finite element model of W24X229-DC-E2 with 3/8 in. stiffeners after the maximum load

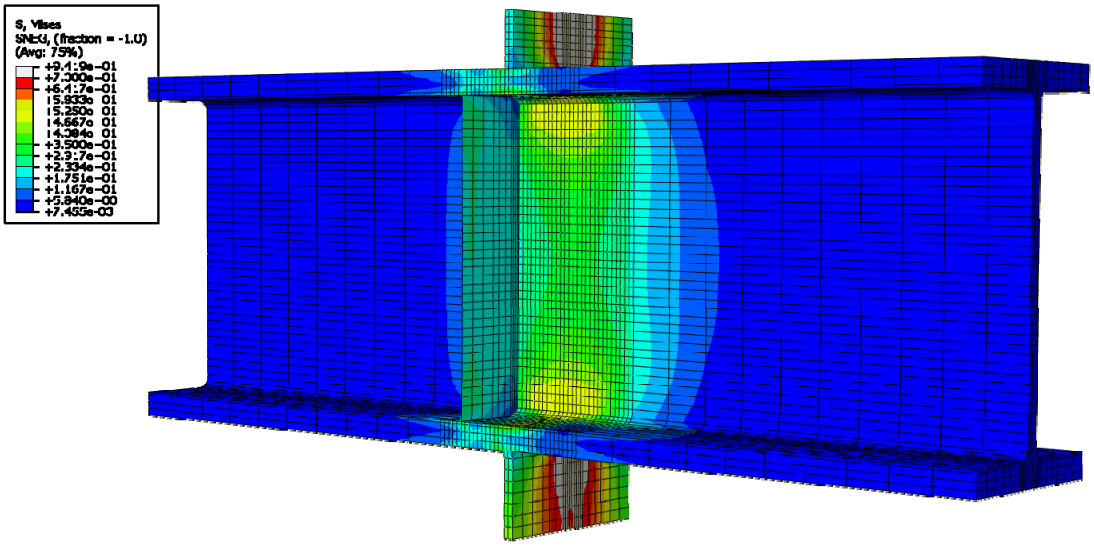

Figure E-164: Finite element model of W24X229-DC-E4 with 3/8 in. stiffeners during elastic behavior

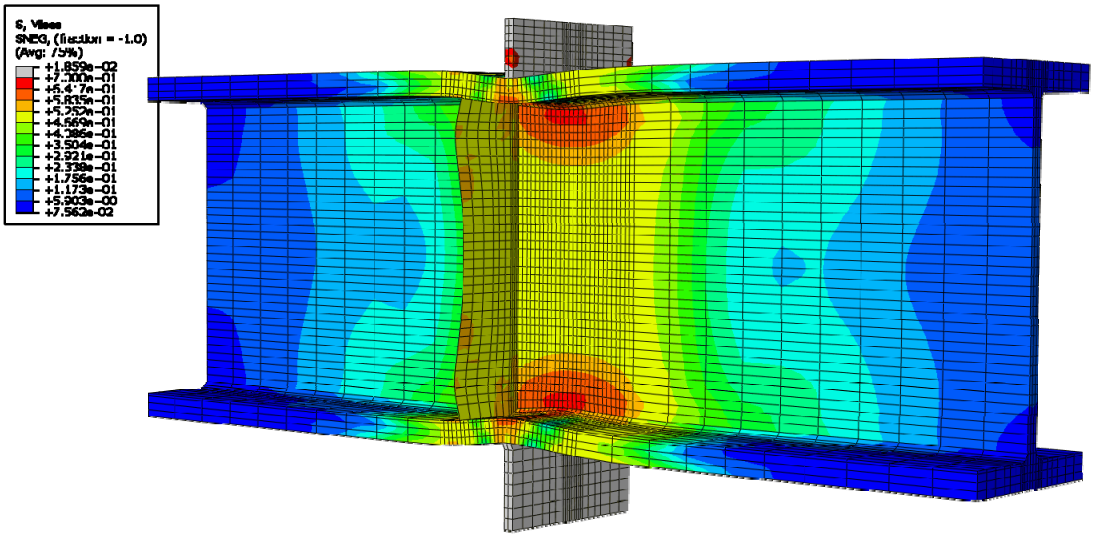

Figure E-165: Finite element model of W24X229-DC-E4 with 3/8 in. stiffeners during inelastic behavior

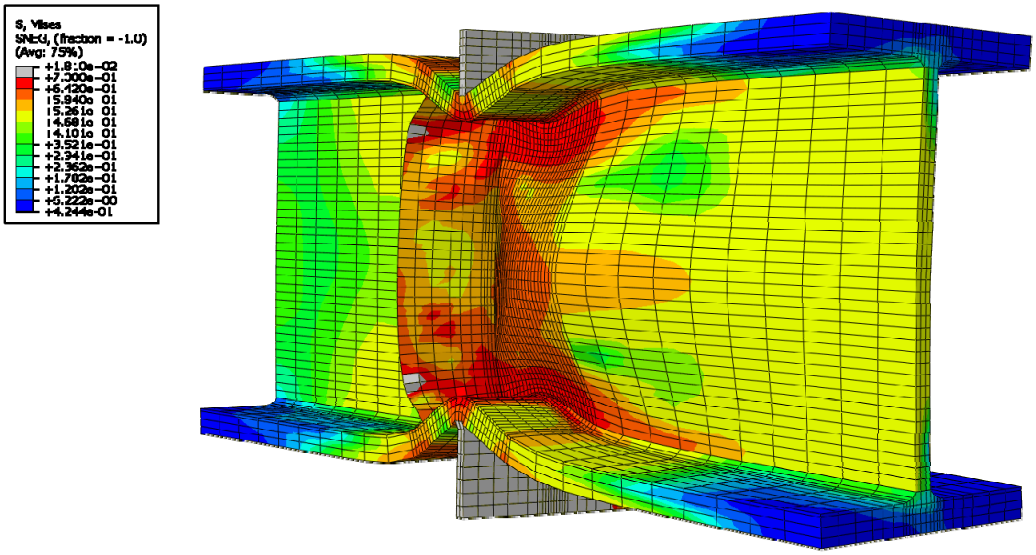

Figure E-166: Finite element model of W24X229-DC-E4 with 3/8 in. stiffeners after the maximum load

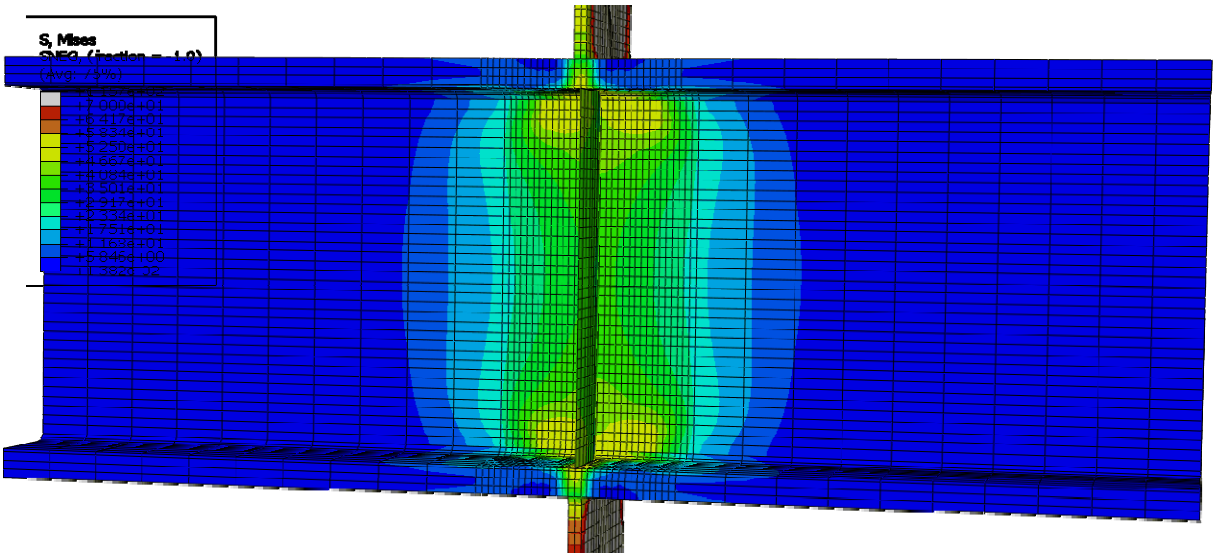

Figure E-167: Finite element model of W24X229-DC-E0 with 3/4 in. stiffeners during elastic behavior

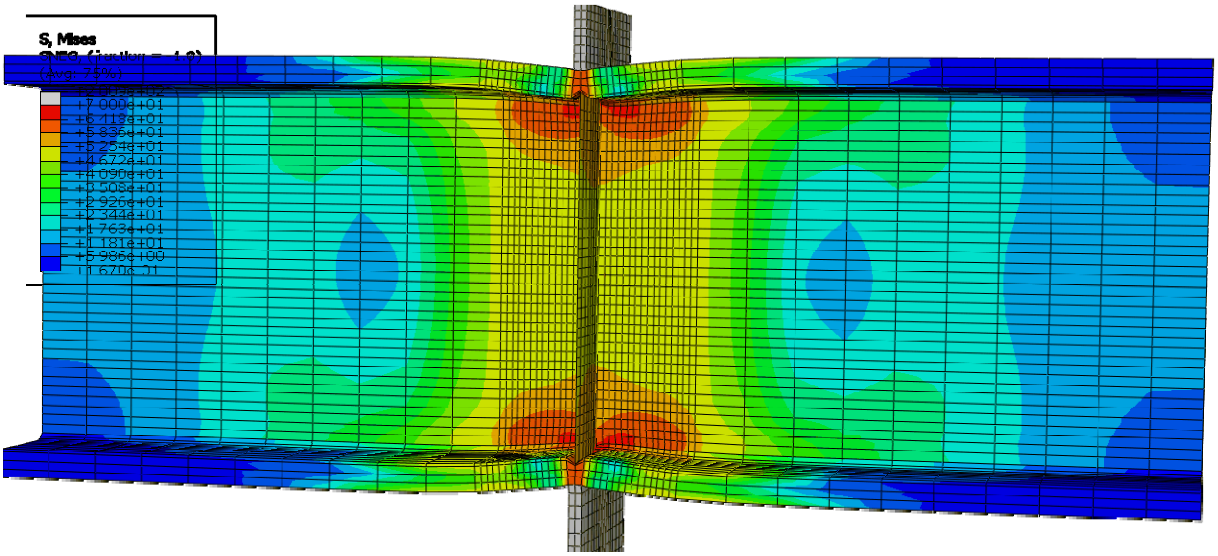

Figure E-168: Finite element model of W24X229-DC-E0 with 3/4 in. stiffeners during inelastic behavior

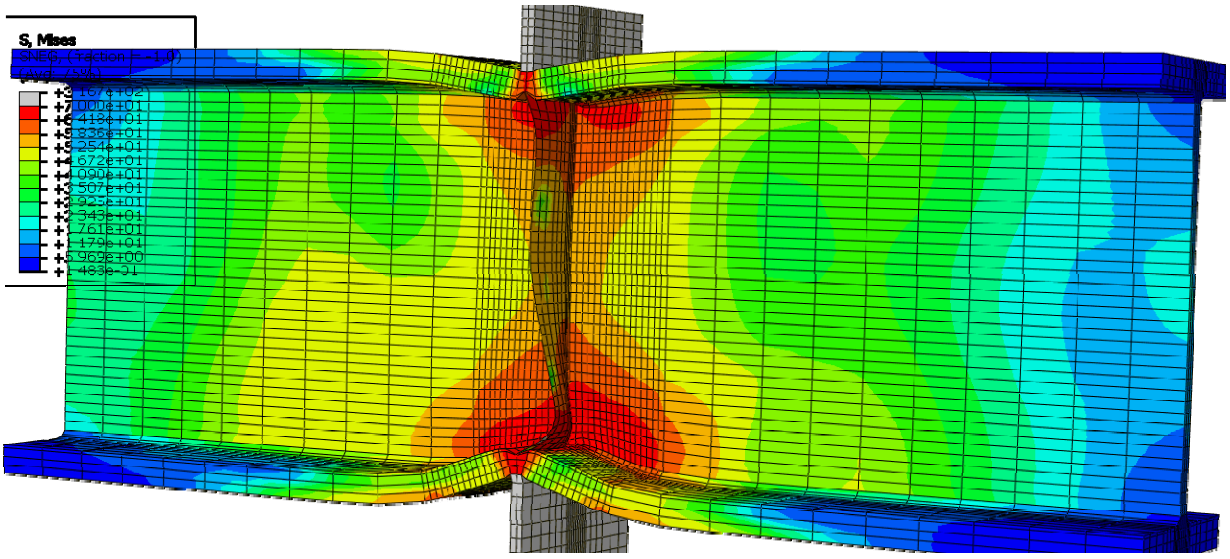

Figure E-169: Finite element model of W24X229-DC-E0 with 3/4 in. stiffeners after the maximum load

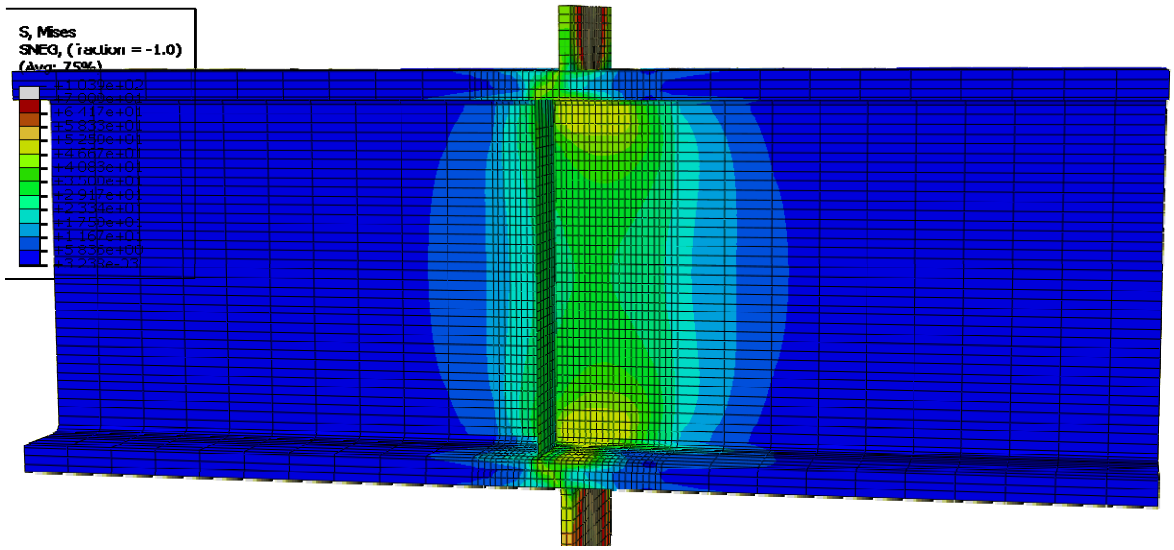

Figure E-170: Finite element model of W24X229-DC-E2 with 3/4 in. stiffeners during elastic behavior

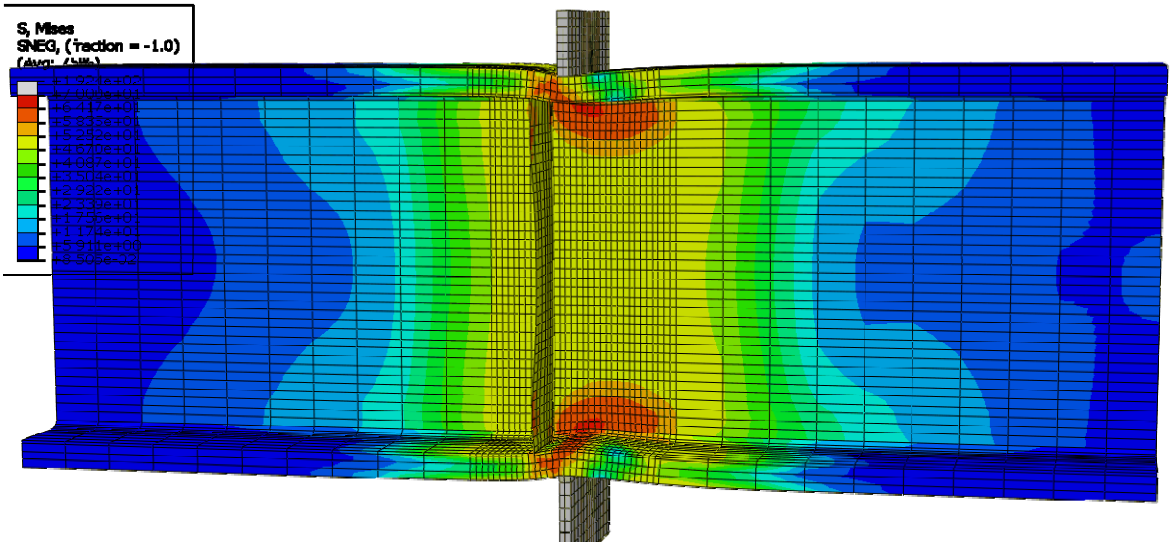

Figure E-171: Finite element model of W24X229-DC-E2 with 3/4 in. stiffeners during inelastic behavior

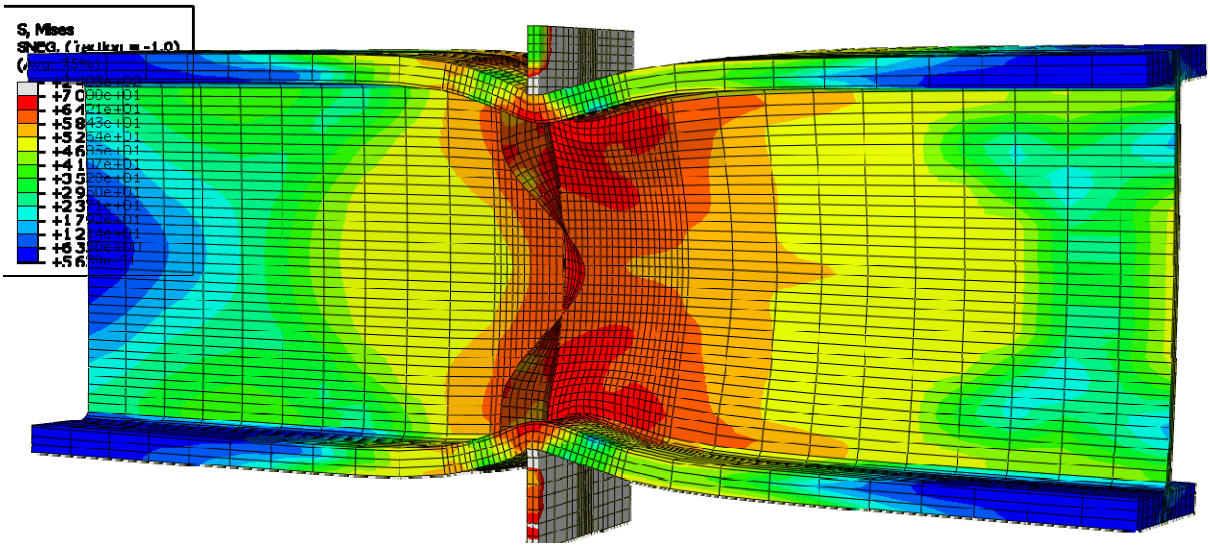

Figure E-172: Finite element model of W24X229-DC-E2 with 3/4 in. stiffeners after the maximum load

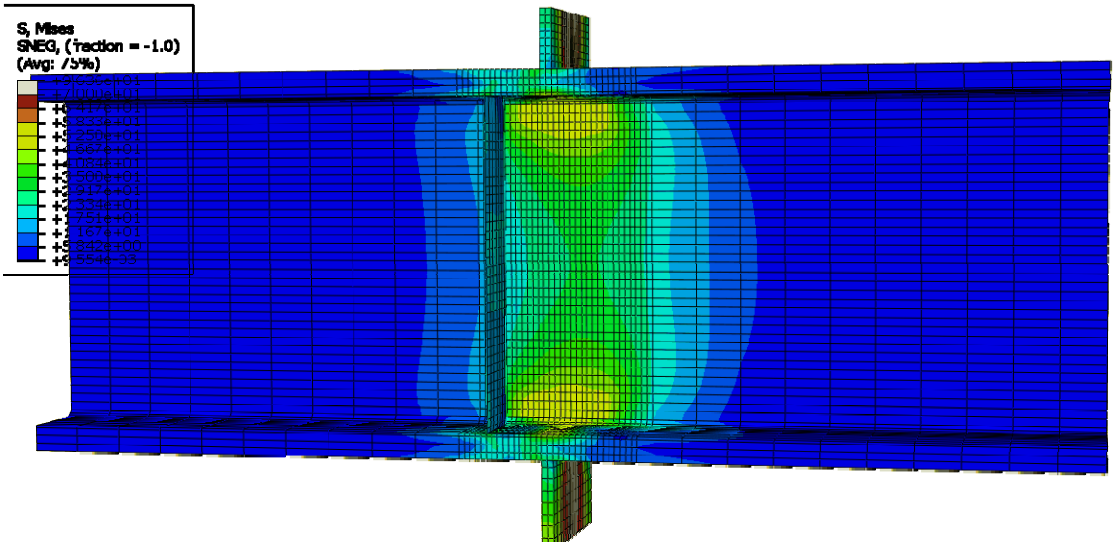

Figure E-173: Finite element model of W24X229-DC-E4 with 3/4 in. stiffeners during elastic behavior

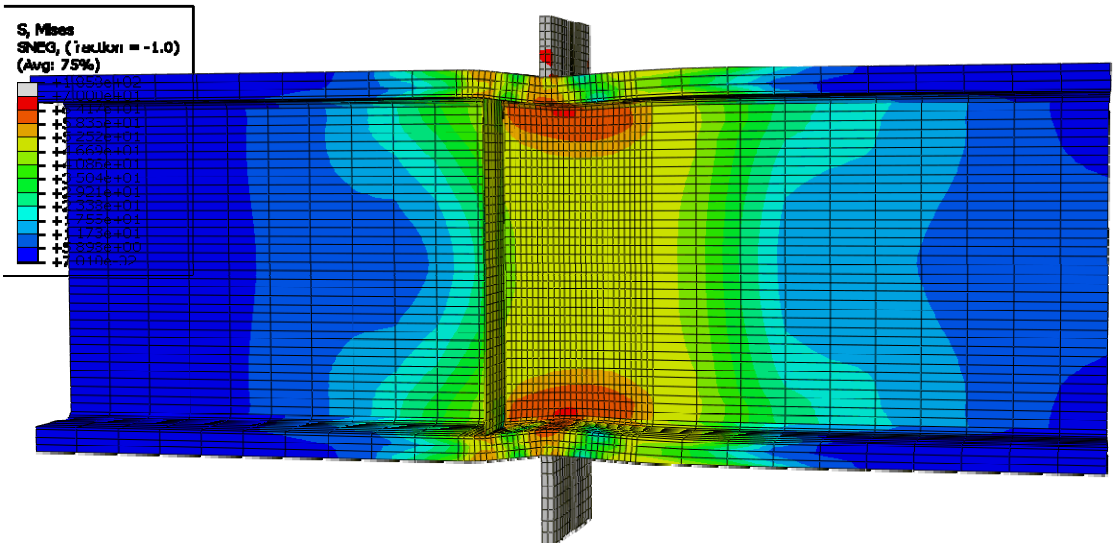

Figure E-174: Finite element model of W24X229-DC-E4 with 3/4 in. stiffeners during inelastic behavior

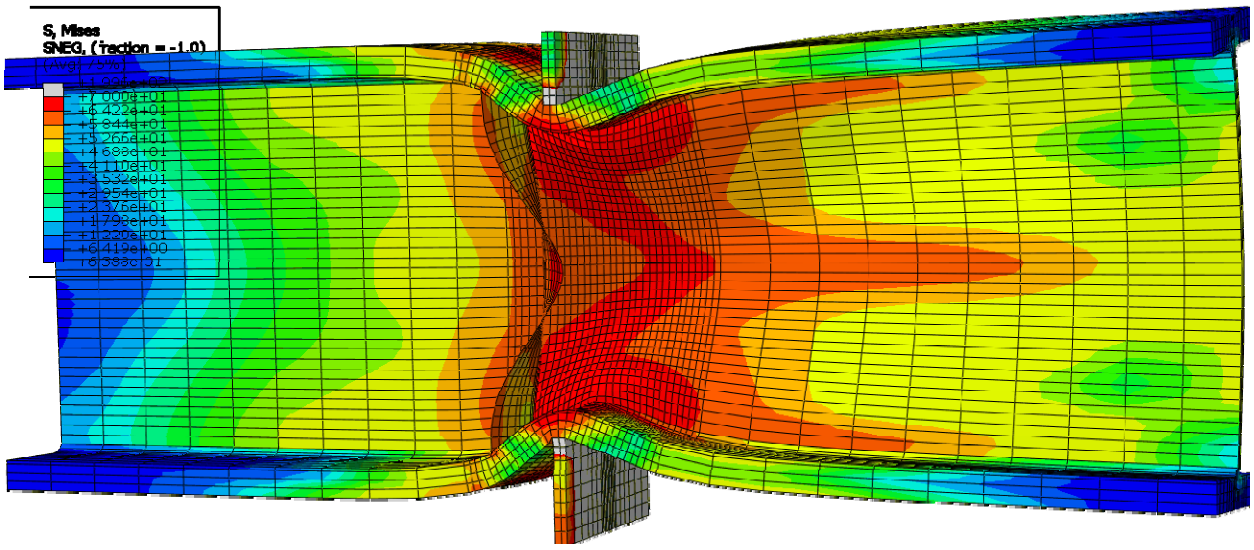

Figure E-175: Finite element model of W24X229-DC-E4 with 3/4 in. stiffeners after the maximum load

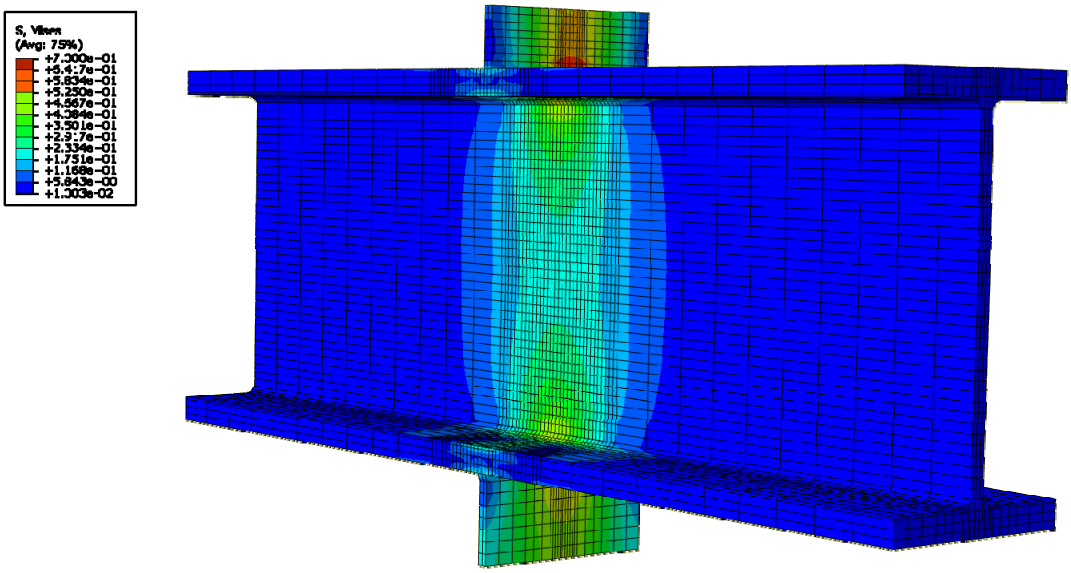

Figure E-176: Finite element model of W24X229-DC-NA during elastic behavior

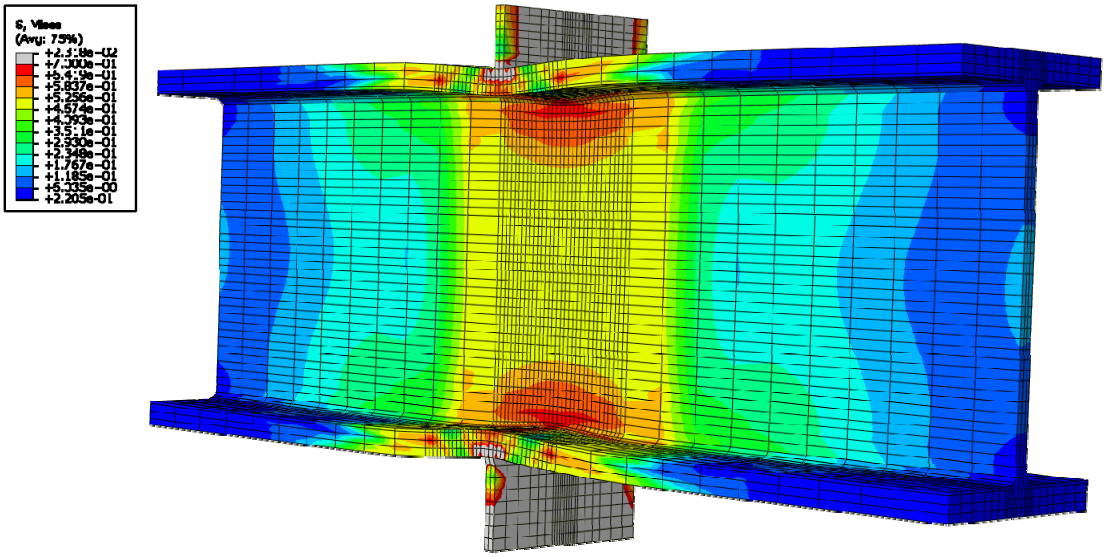

Figure E-177: Finite element model of W24X229-DC-NA during inelastic behavior

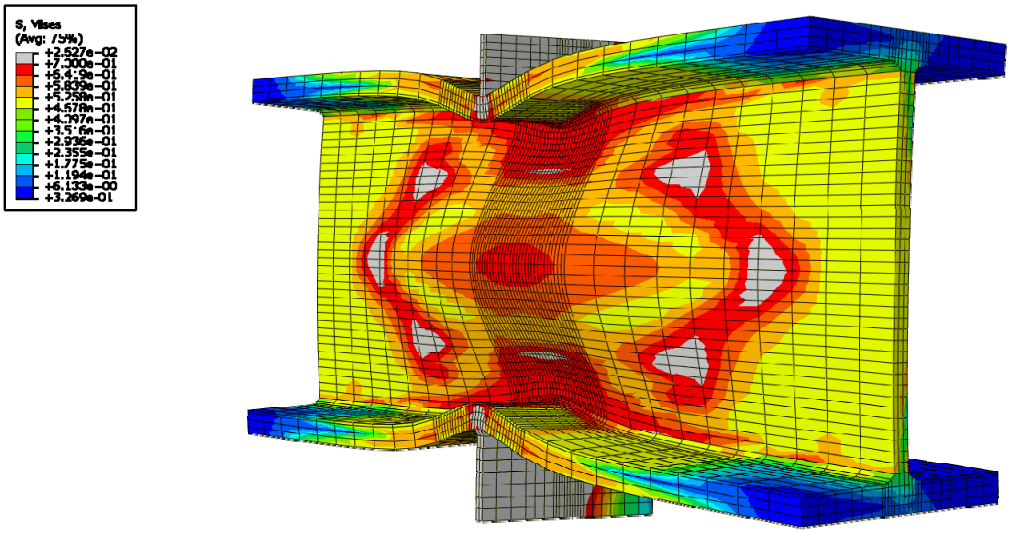

Figure E-178: Finite element model of W24X229-DC-Na after the maximum load emphasizing web compression buckling

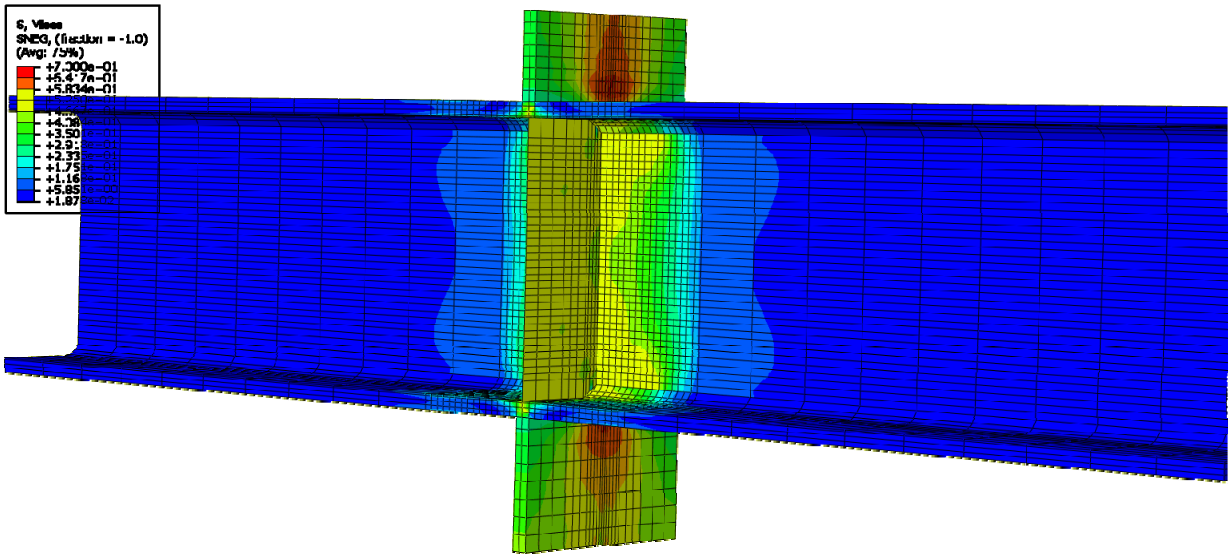

Figure E-179: Finite element model of W14X68-DC-E0 with 3/8 in. stiffeners during elastic behavior

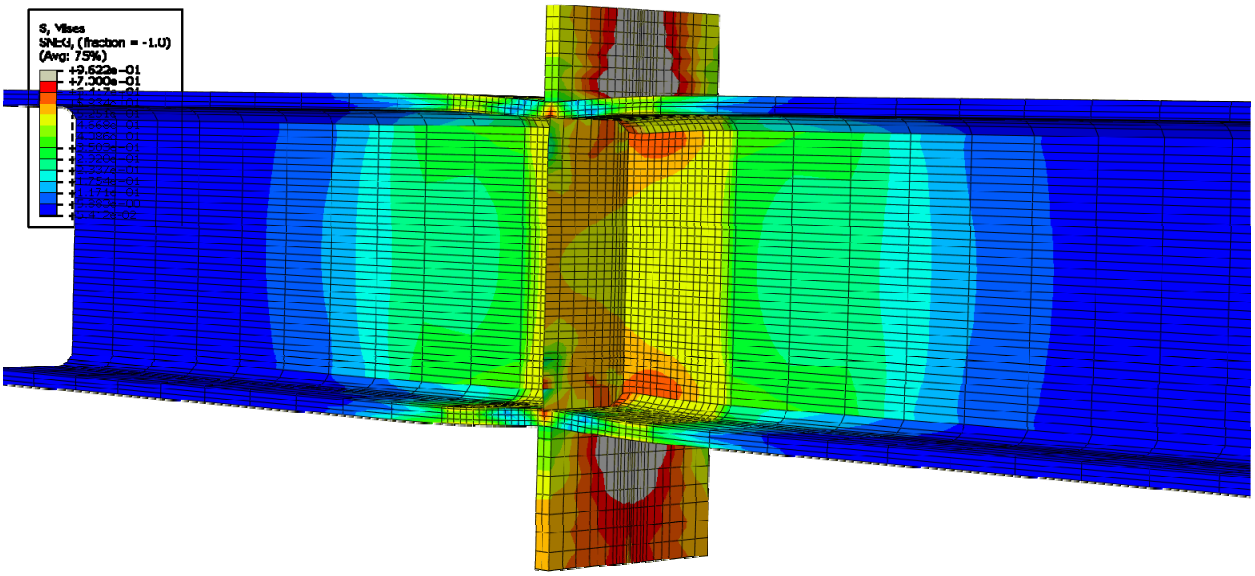

Figure E-180: Finite element model of W14X68-DC-E0 with 3/8 in. stiffeners during inelastic behavior

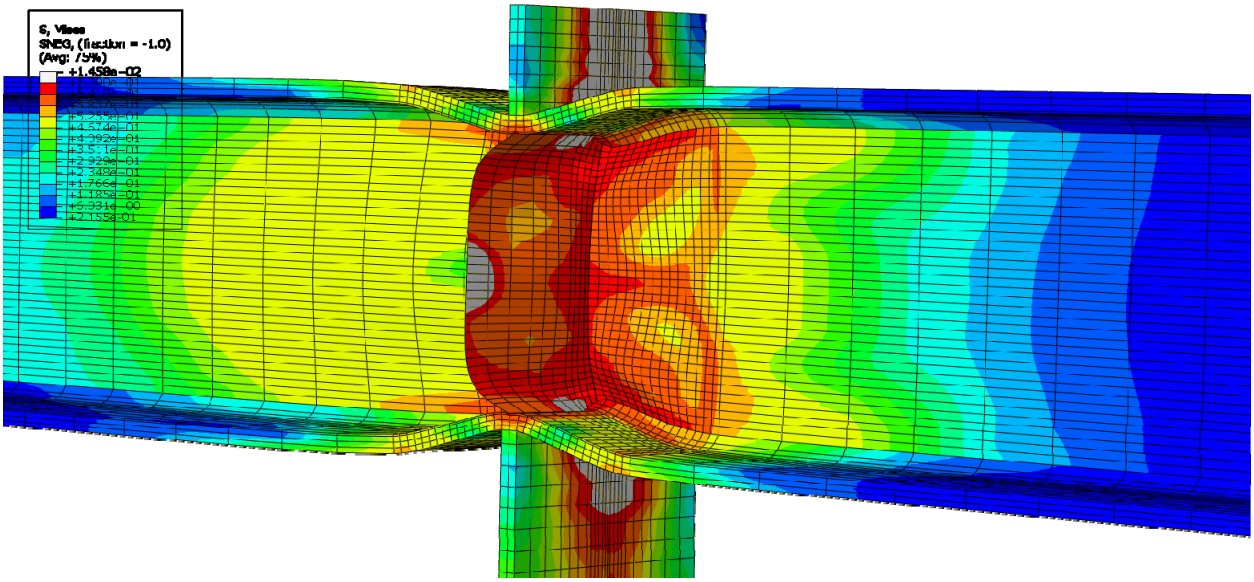

Figure E-181: Finite element model of W14X68-DC-E0 with 3/8 in. stiffeners after the maximum load

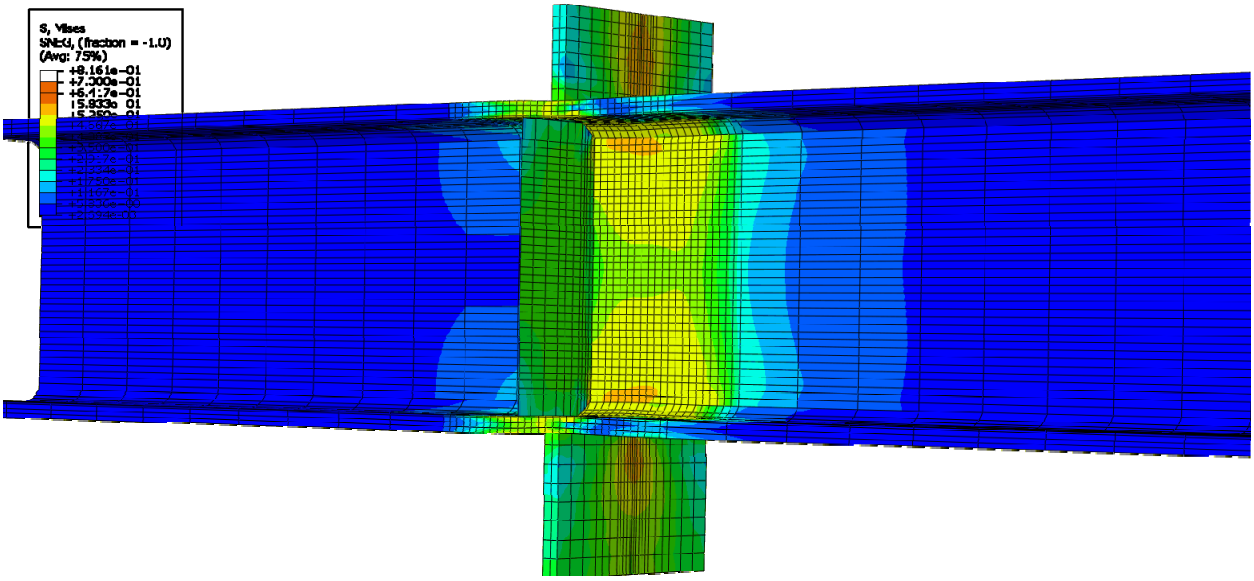

Figure E-182: Finite element model of W14X68-DC-E2 with 3/8 in. stiffeners during elastic behavior

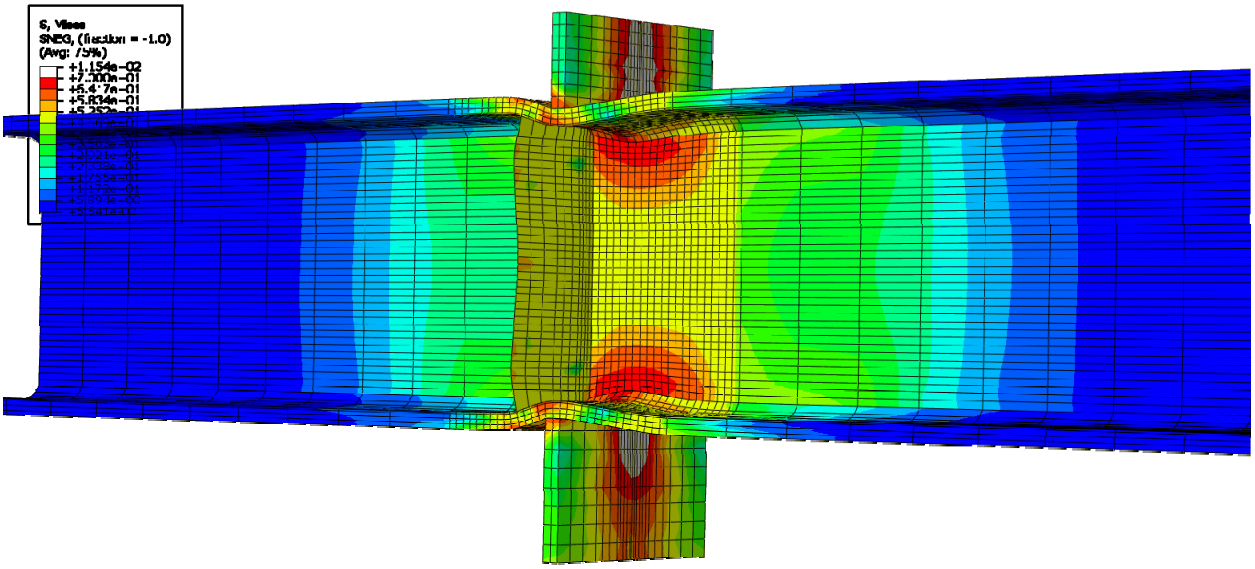

Figure E-183: Finite element model of W14X68-DC-E2 with 3/8 in. stiffeners during inelastic behavior

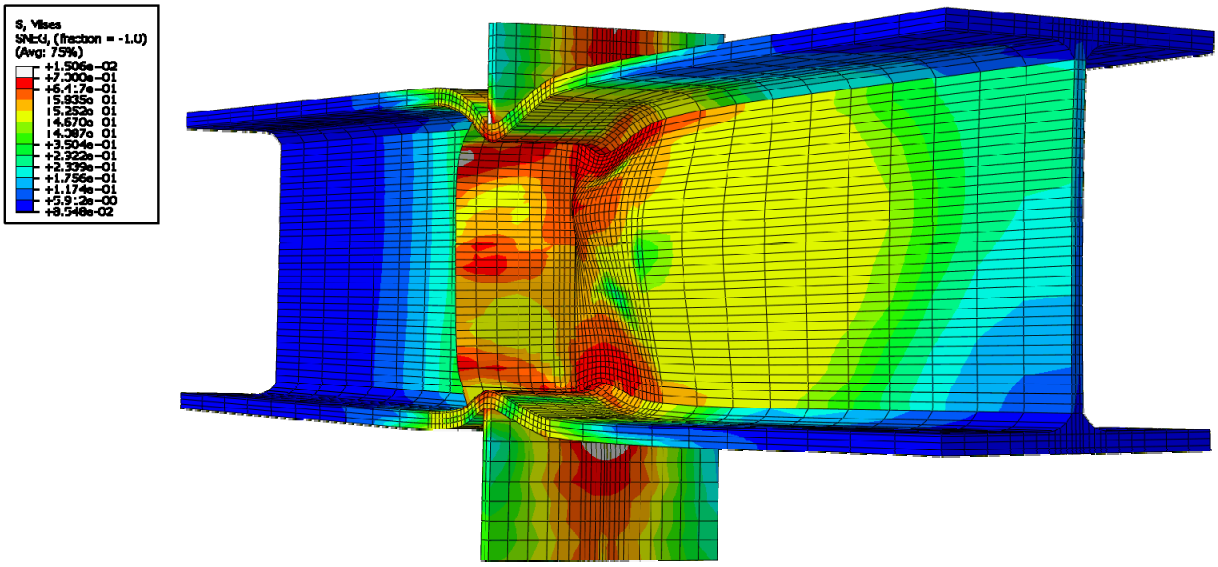

Figure E-184: Finite element model of W14X68-DC-E2 with 3/8 in. stiffeners after the maximum load

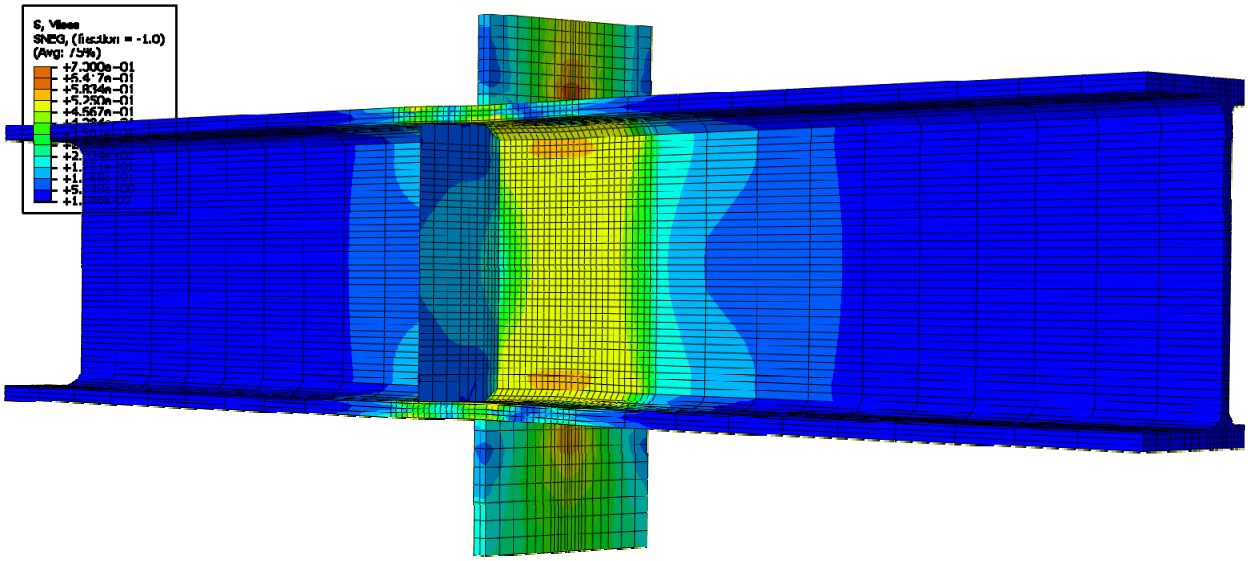

Figure E-185: Finite element model of W14X68-DC-E4 with 3/8 in. stiffeners during elastic behavior

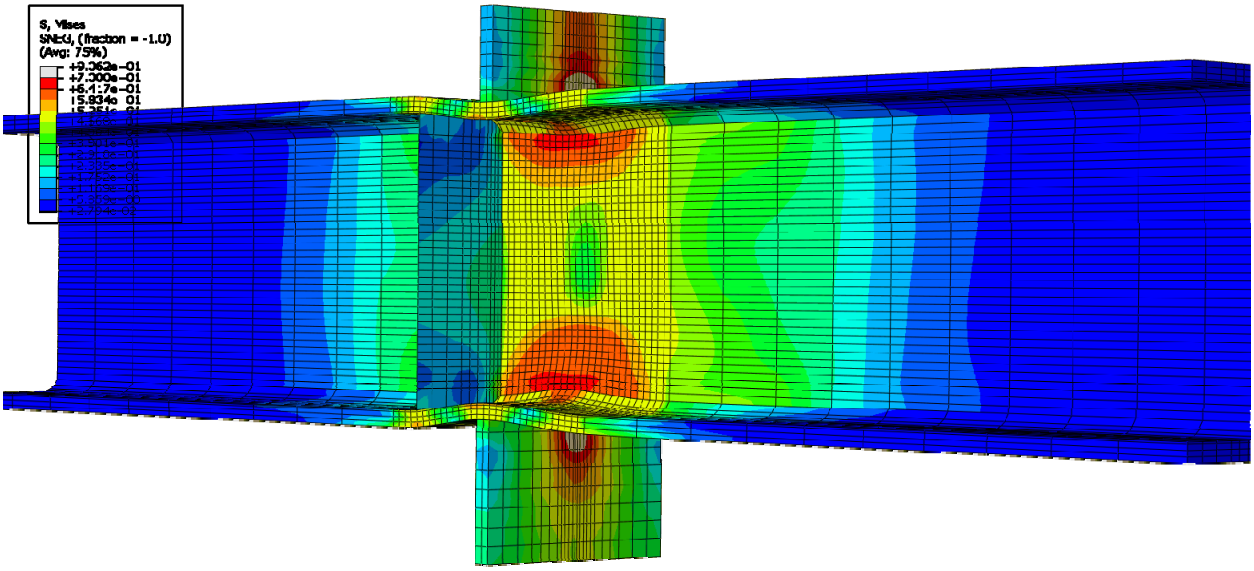

Figure E-186: Finite element model of W14X68-DC-E4 with 3/8 in. stiffeners during inelastic behavior

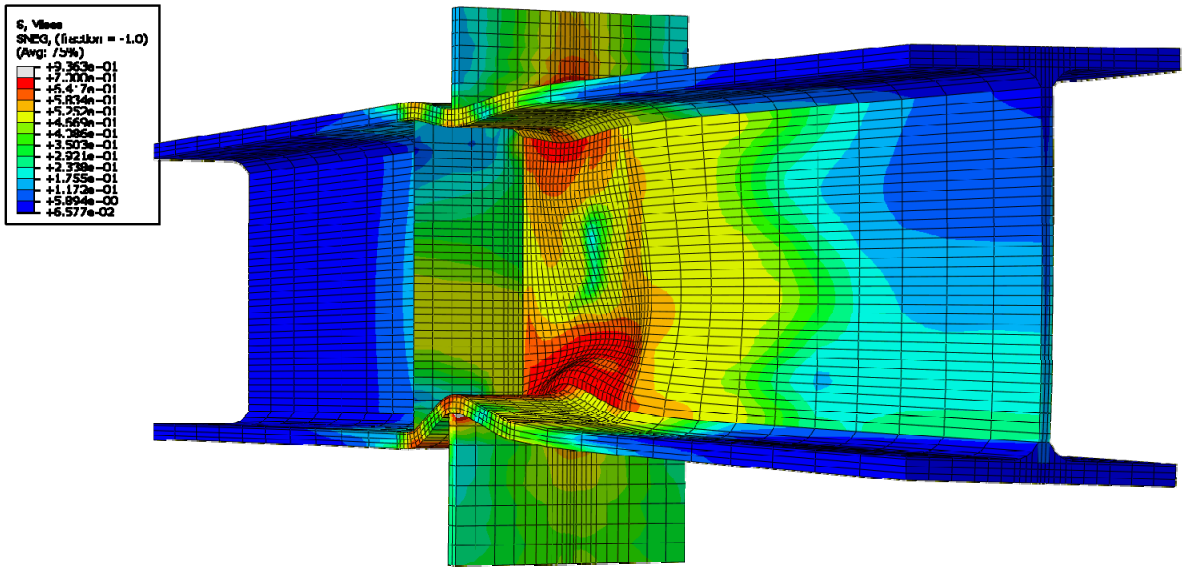

Figure E-187: Finite element model of W14X68-DC-E4 with 3/8 in. stiffeners after the maximum load

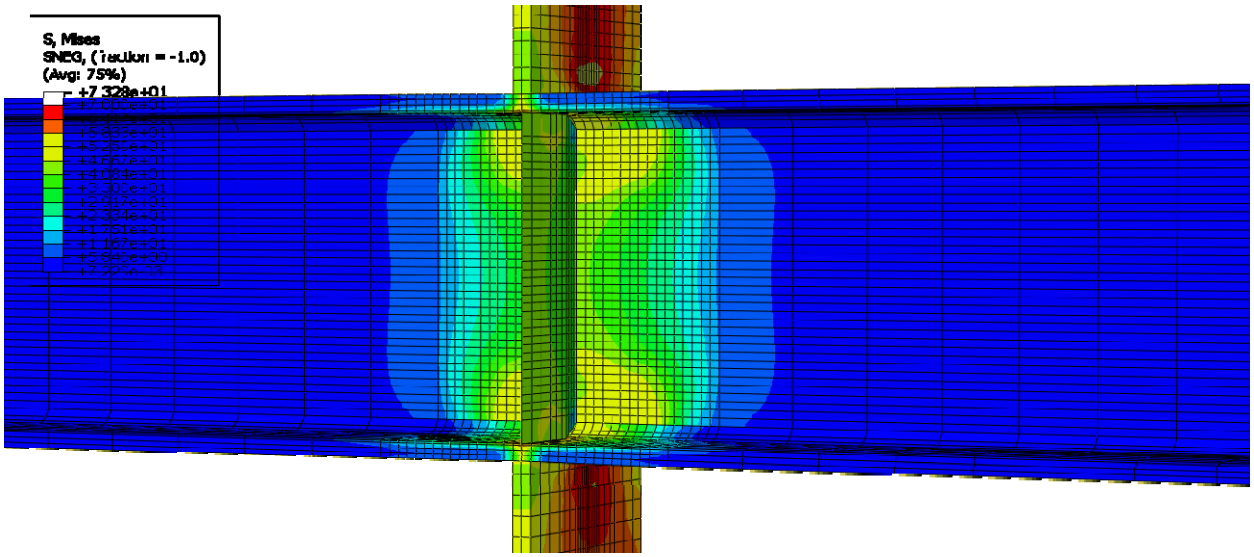

Figure E-188: Finite element model of W14X68-DC-E0 with 3/4 in. stiffeners during elastic behavior

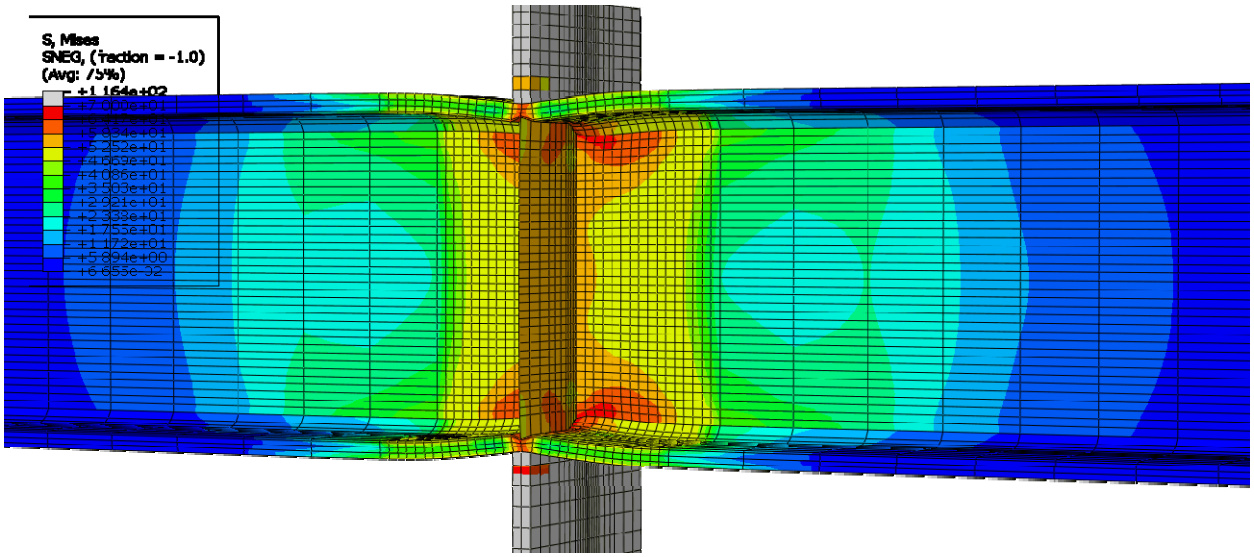

Figure E-189: Finite element model of W14X68-DC-E0 with 3/4 in. stiffeners during inelastic behavior

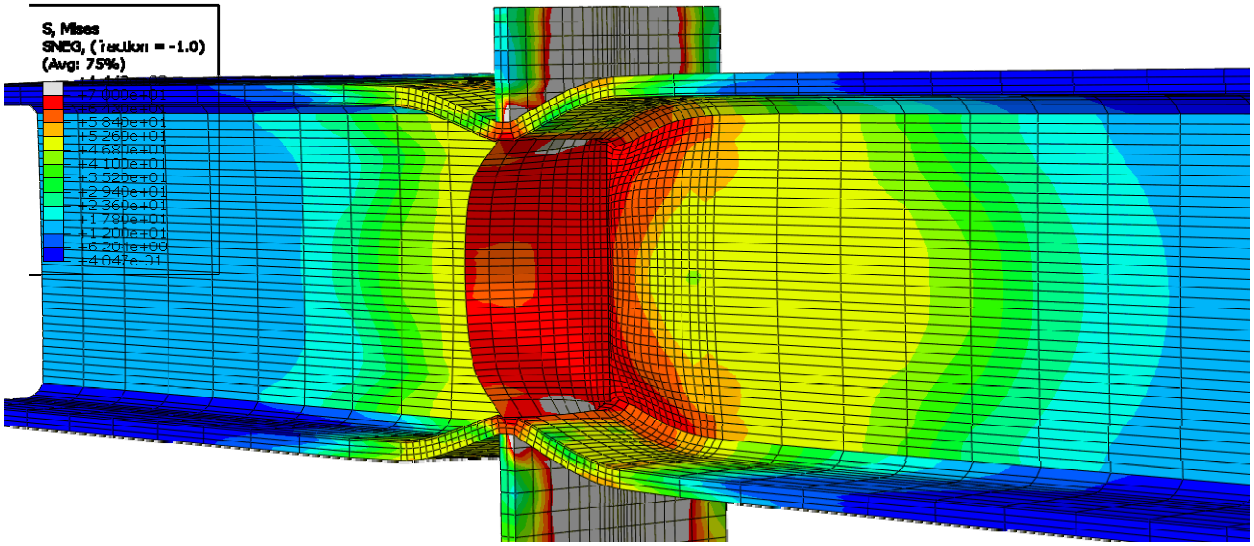

Figure E-190: Finite element model of W14X68-DC-E0 with 3/4 in. stiffeners after the maximum load

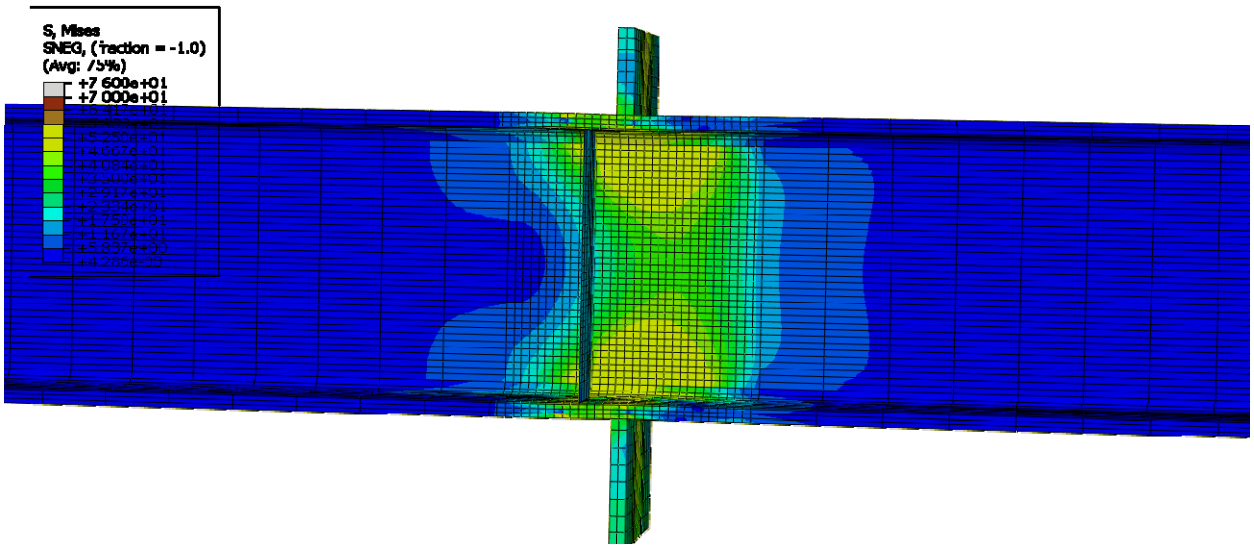

Figure E-191: Finite element model of W14X68-DC-E2 with 3/4 in. stiffeners during elastic behavior

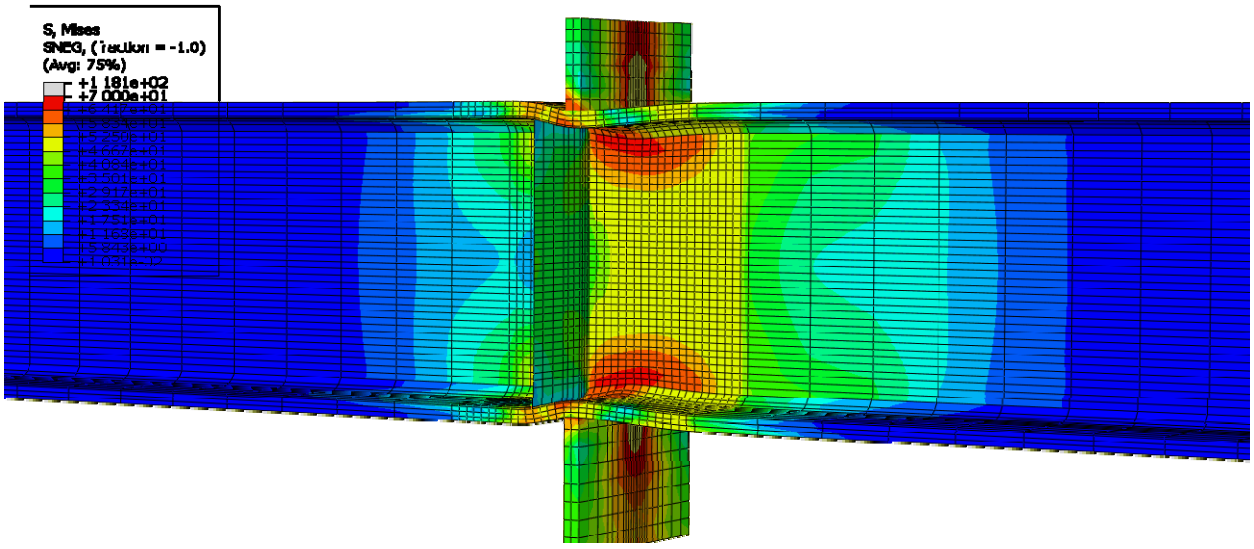

Figure E-192: Finite element model of W14X68-DC-E2 with 3/4 in. stiffeners during inelastic behavior

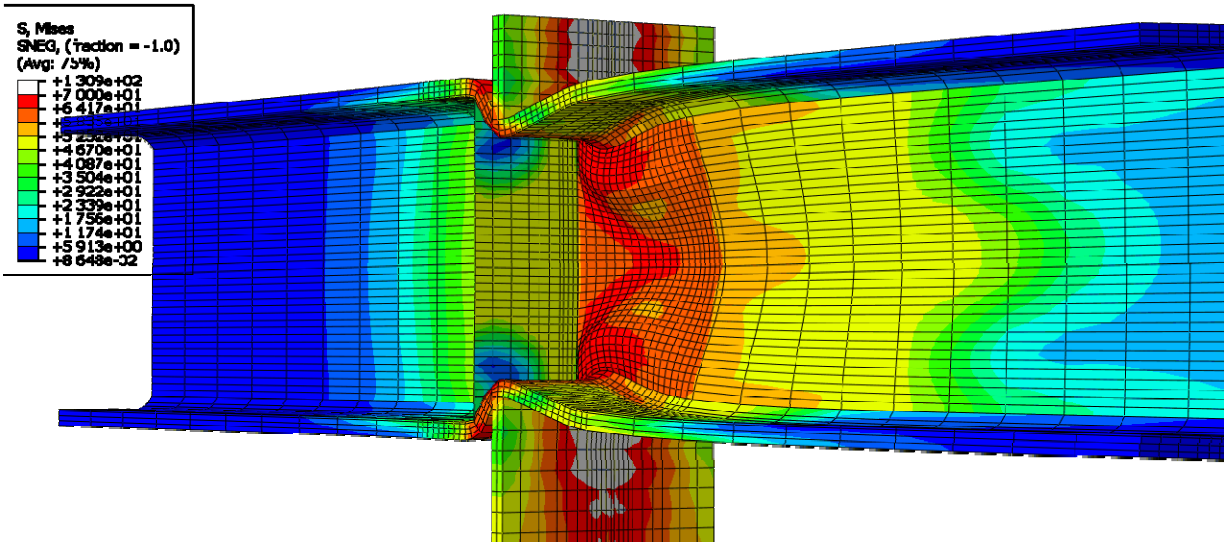

Figure E-193: Finite element model of W14X68-DC-E2 with 3/4 in. stiffeners after the maximum load

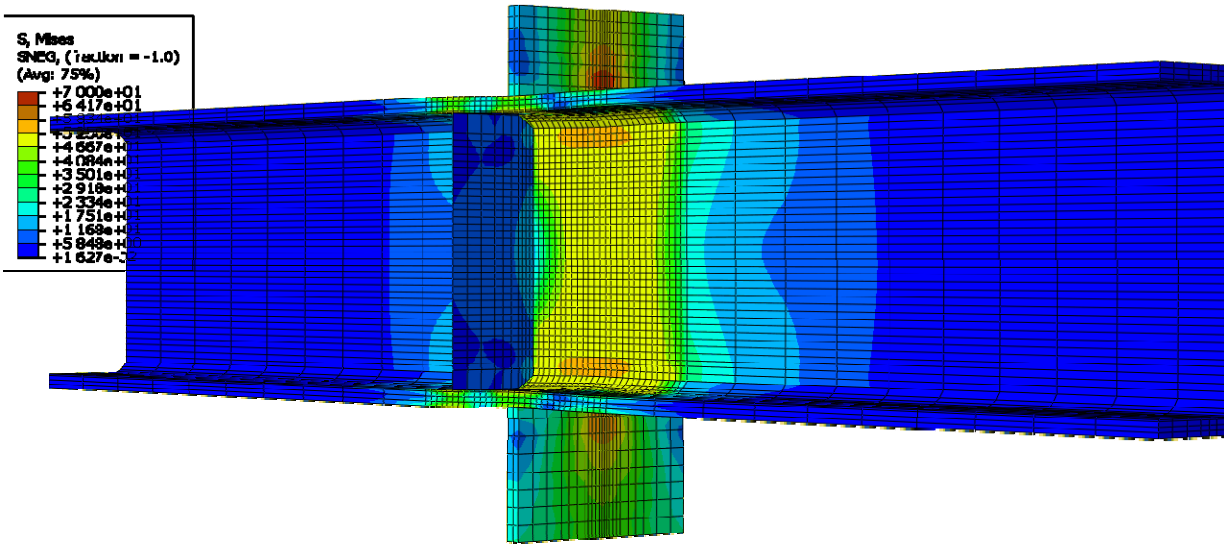

Figure E-194: Finite element model of W14X68-DC-E4 with 3/4 in. stiffeners during elastic behavior

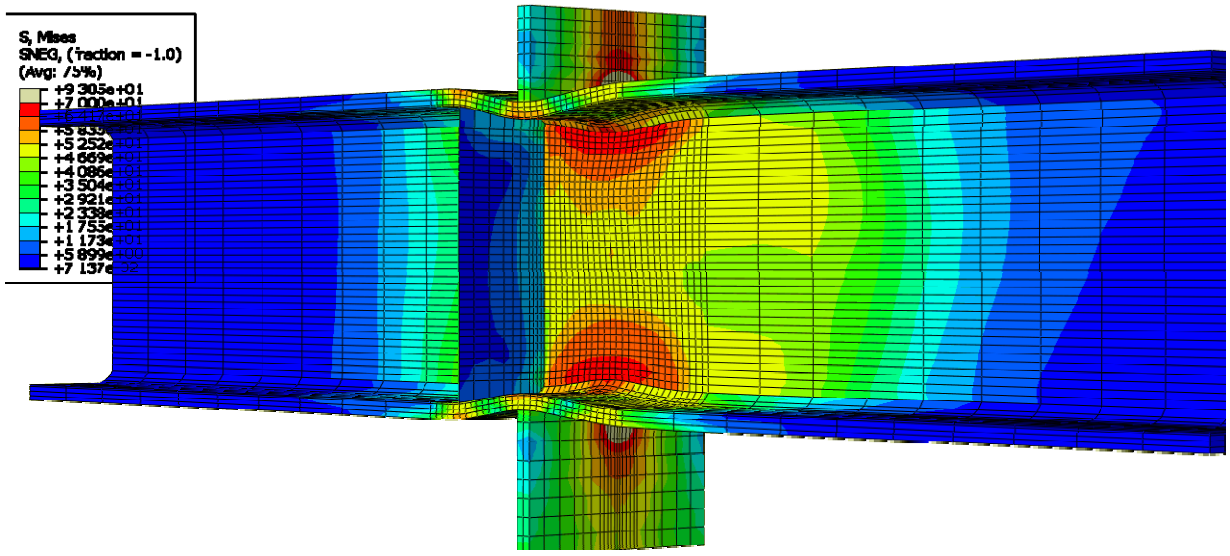

Figure E-195: Finite element model of W14X68-DC-E4 with 3/4 in. stiffeners during inelastic behavior

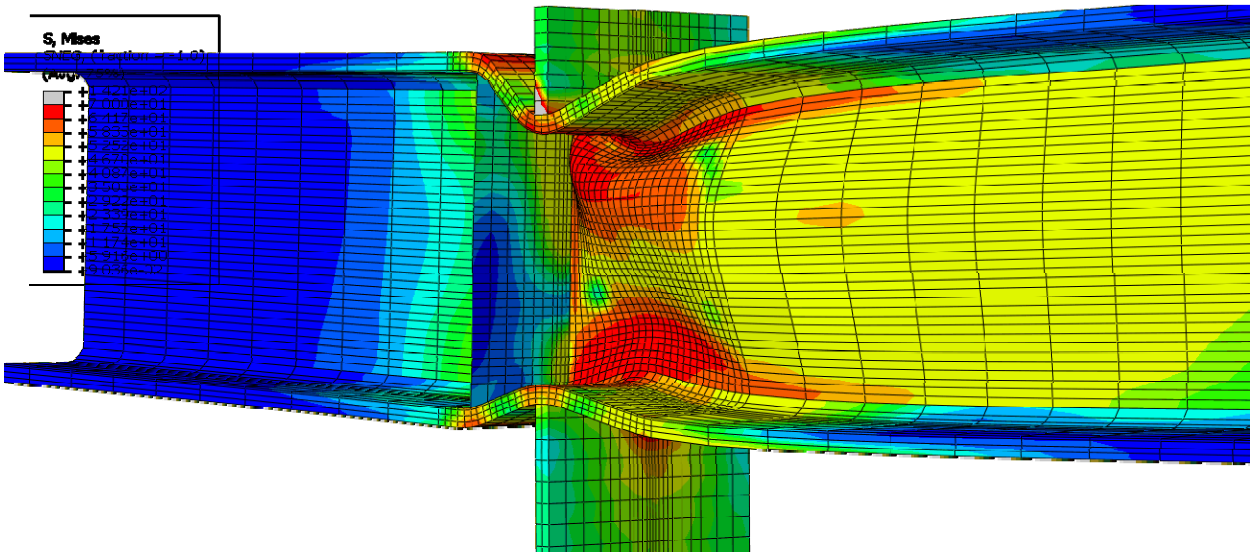

Figure E-196: Finite element model of W14X68-DC-E4 with 3/4 in. stiffeners after the maximum load

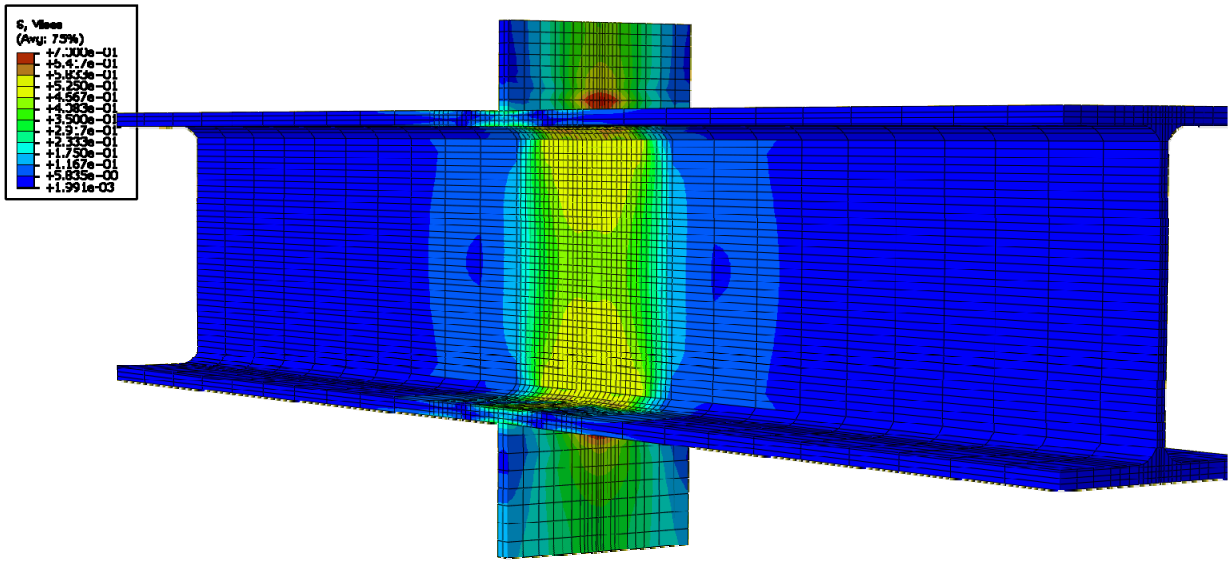

Figure E-197: Finite element model of W14X68-DC-NA during elastic behavior

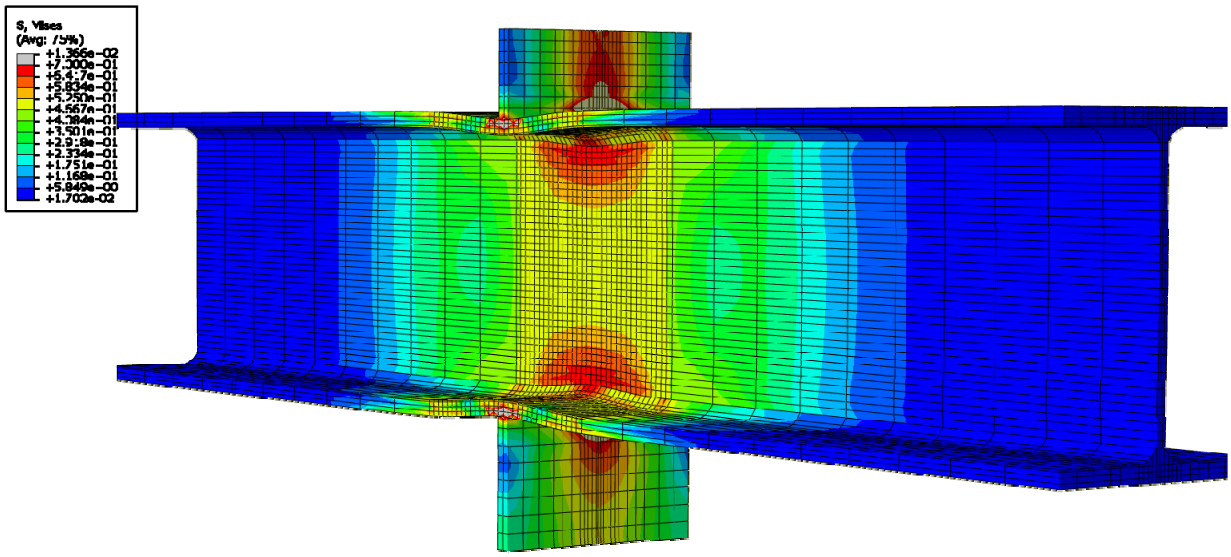

Figure E-198: Finite element model of W14X68-DC-NA during inelastic behavior

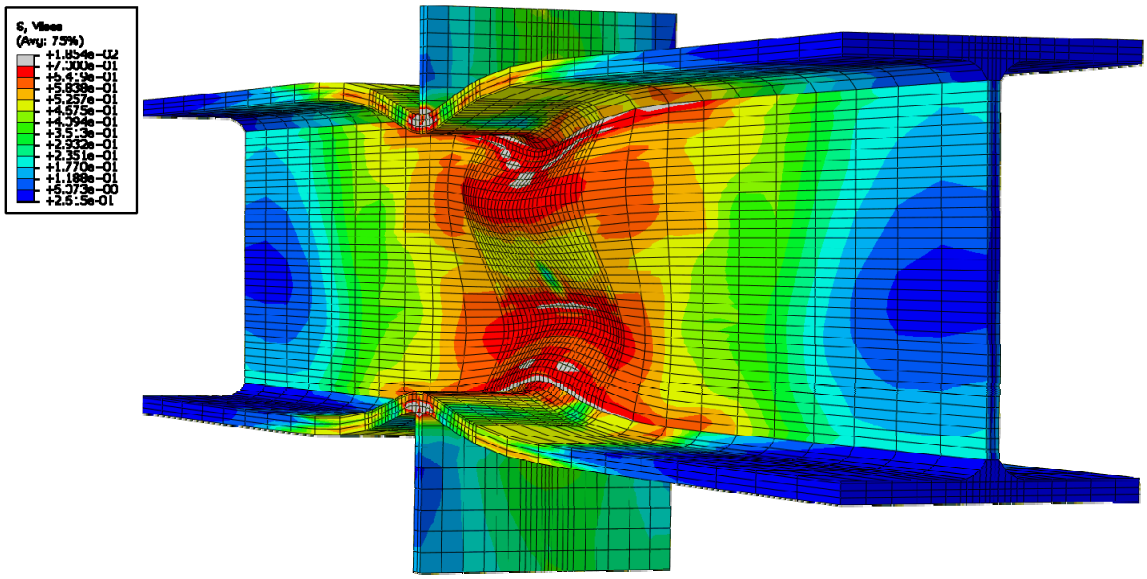

Figure E-199: Finite element model of W14X68-DC-NA after the maximum load emphasizing web compression buckling

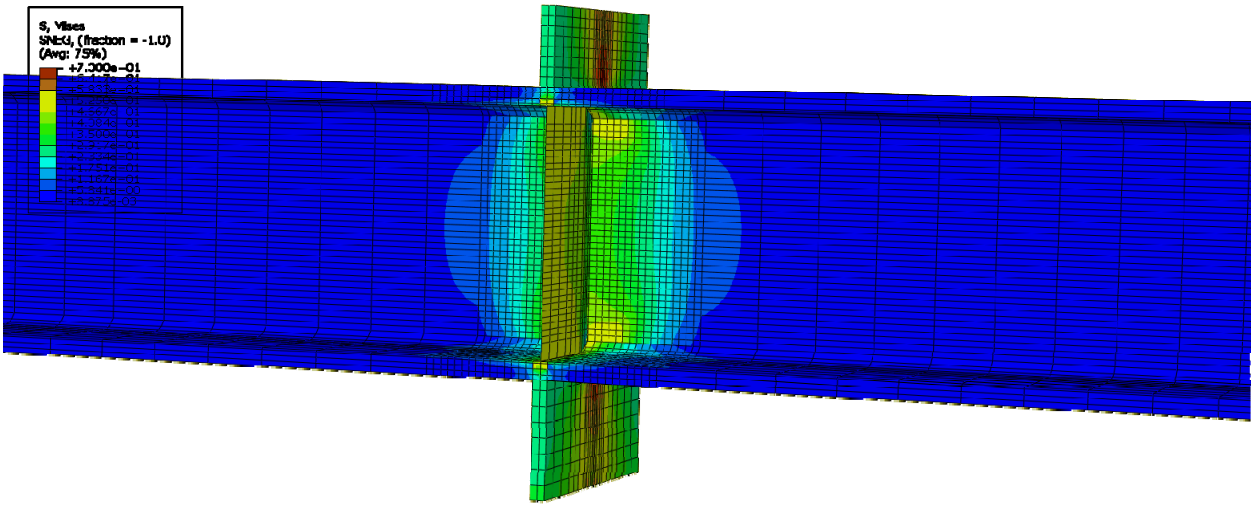

Figure E-200: Finite element model of W14X120-DC-E0 with 3/8 in. stiffeners during elastic behavior

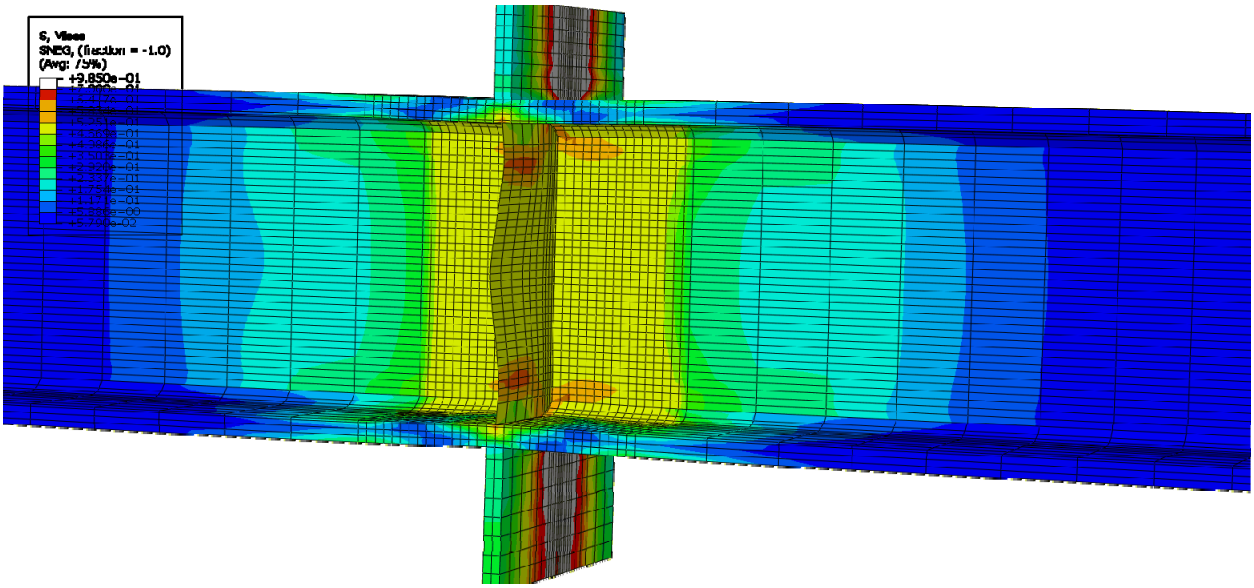

Figure E-201: Finite element model of W14X120-DC-E0 with 3/8 in. stiffeners during inelastic behavior

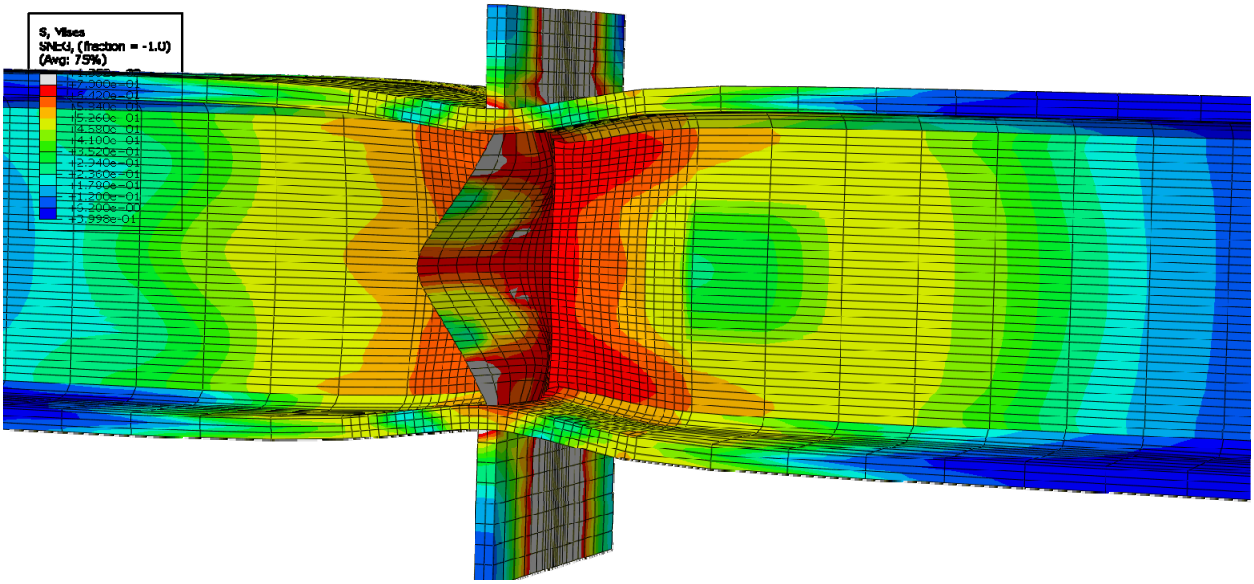

Figure E-202: Finite element model of W14X120-DC-E0 with 3/8 in. stiffeners after the maximum load emphasizing stiffener buckling

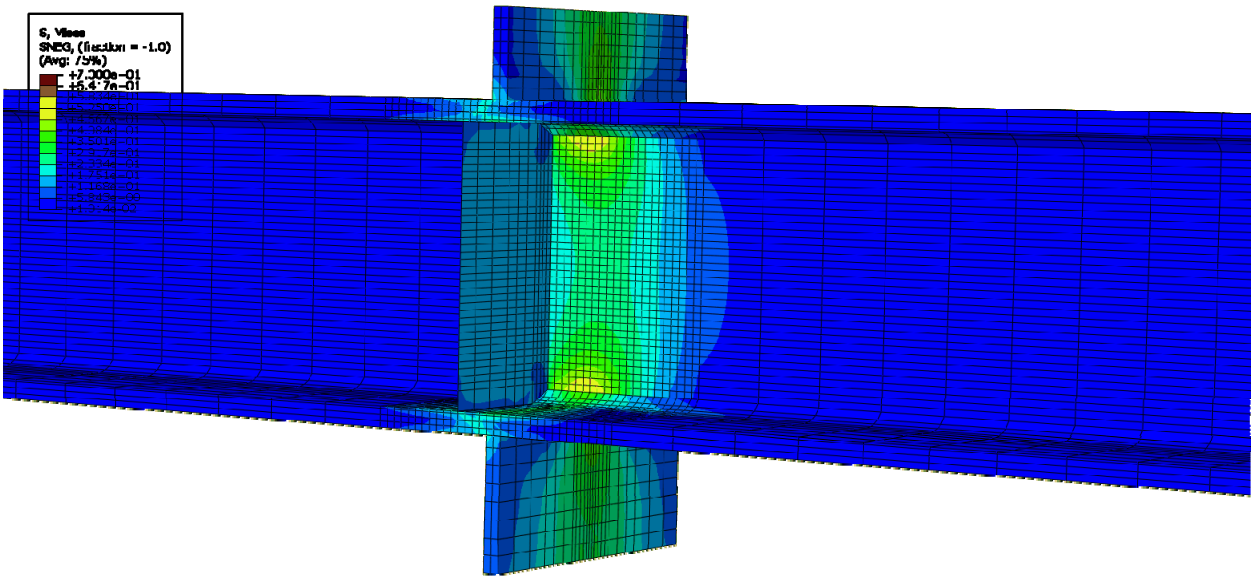

Figure E-203: Finite element model of W14X120-DC-E2 with 3/8 in. stiffeners during elastic behavior

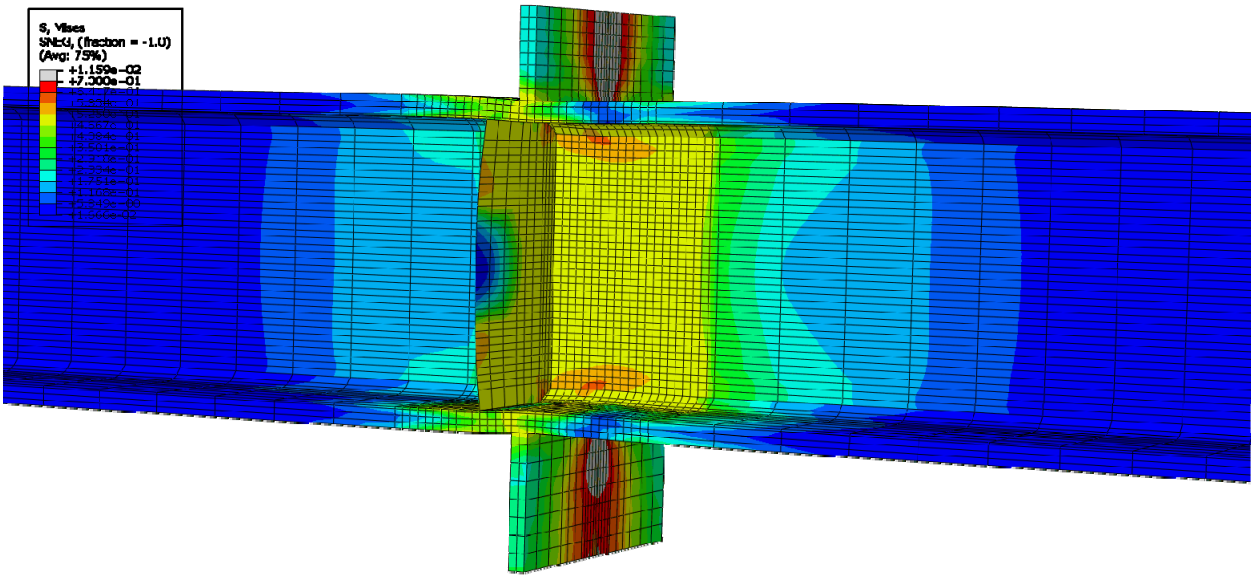

Figure E-204: Finite element model of W14X120-DC-E2 with 3/8 in. stiffeners during inelastic behavior

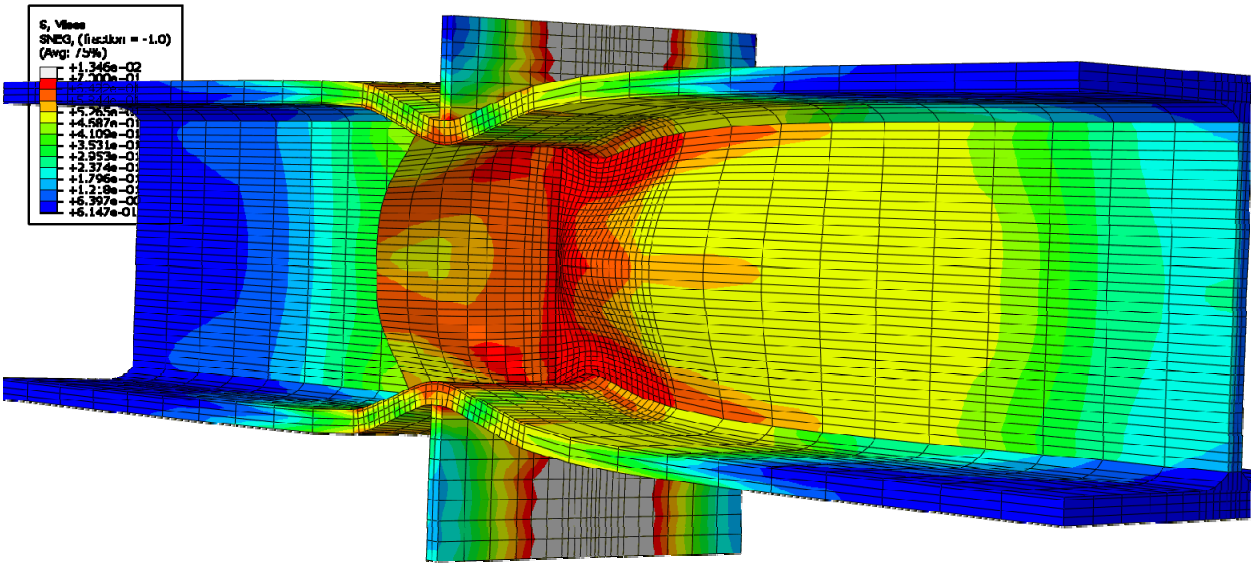

Figure E-205: Finite element model of W14X120-DC-E2 with 3/8 in. stiffeners after the maximum load

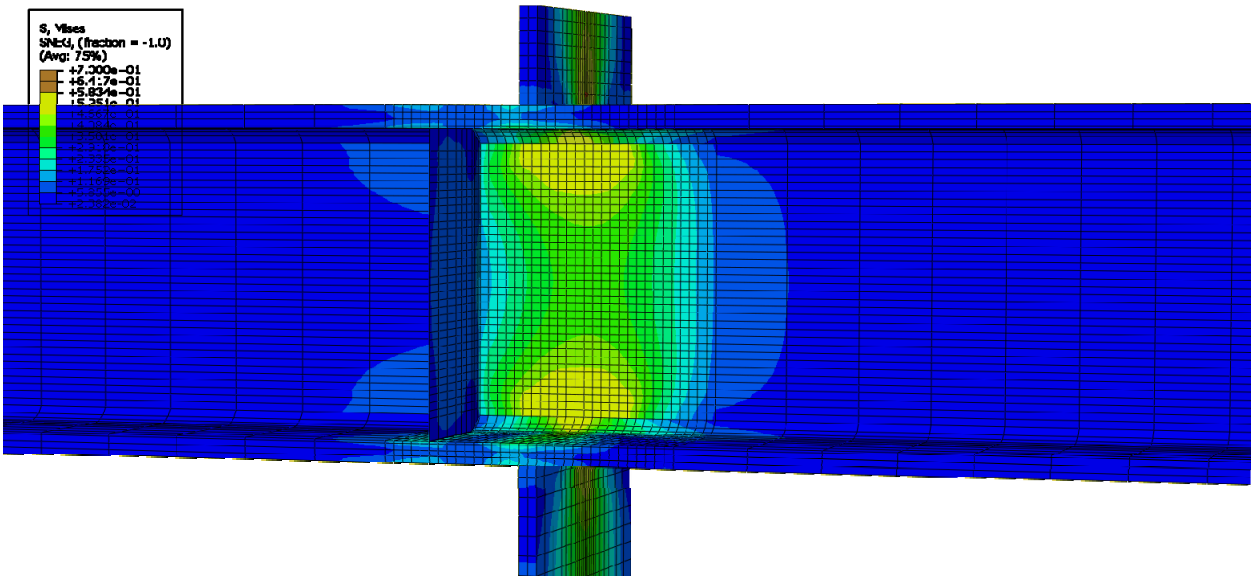

Figure E-206: Finite element model of W14X120-DC-E4 with 3/8 in. stiffeners during elastic behavior

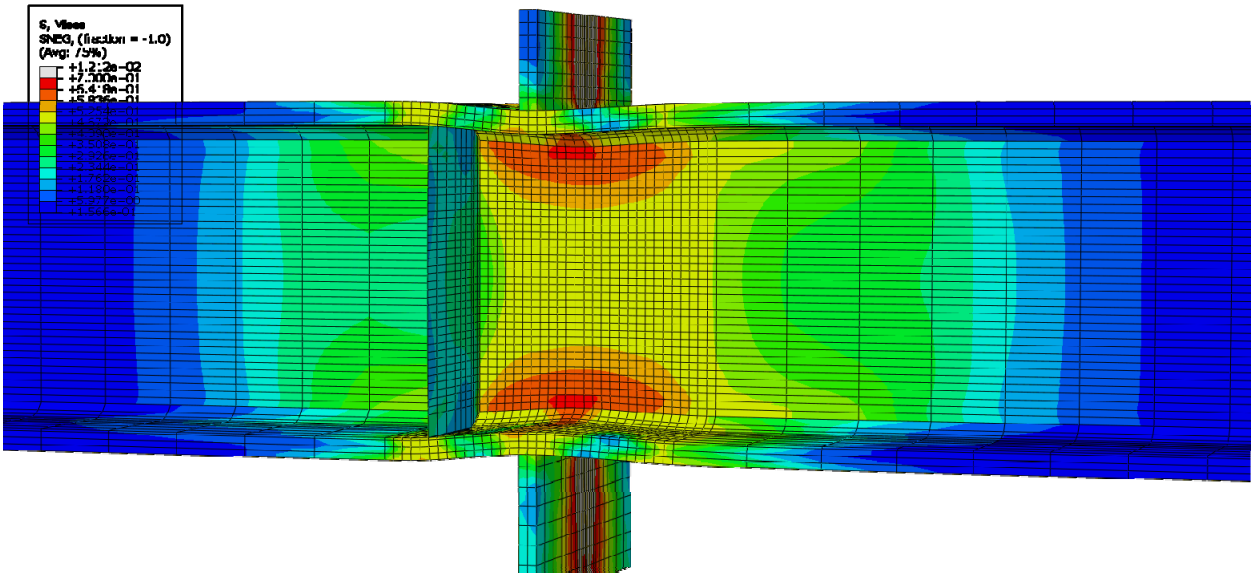

Figure E-207: Finite element model of W14X120-DC-E4 with 3/8 in. stiffeners during inelastic behavior

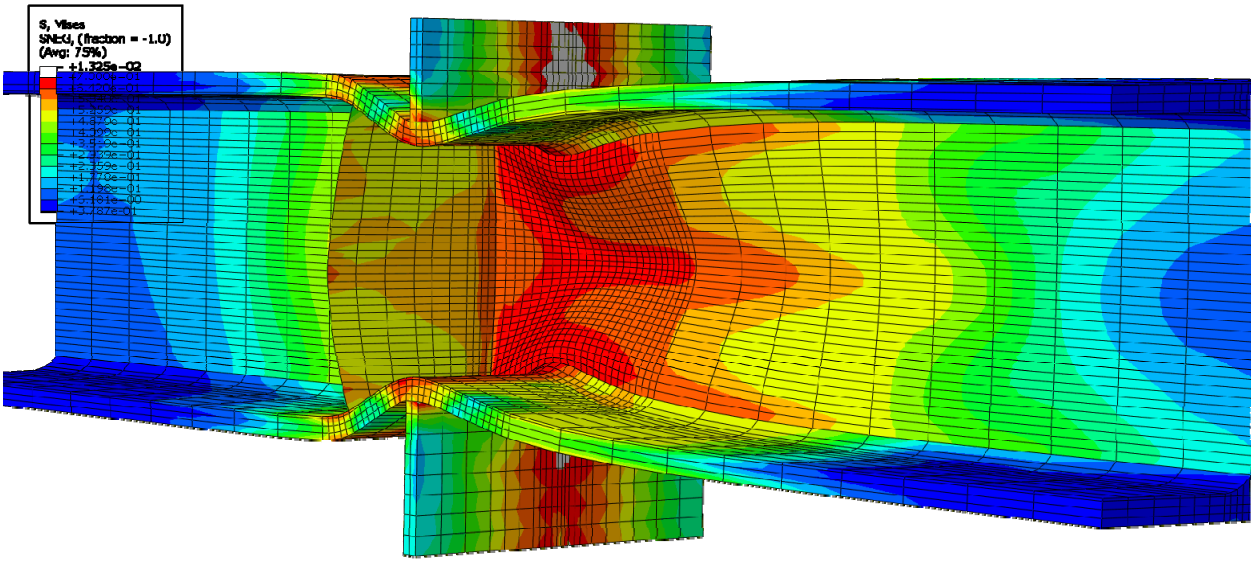

Figure E-208: Finite element model of W14X120-DC-E4 with 3/8 in. stiffeners after the maximum load

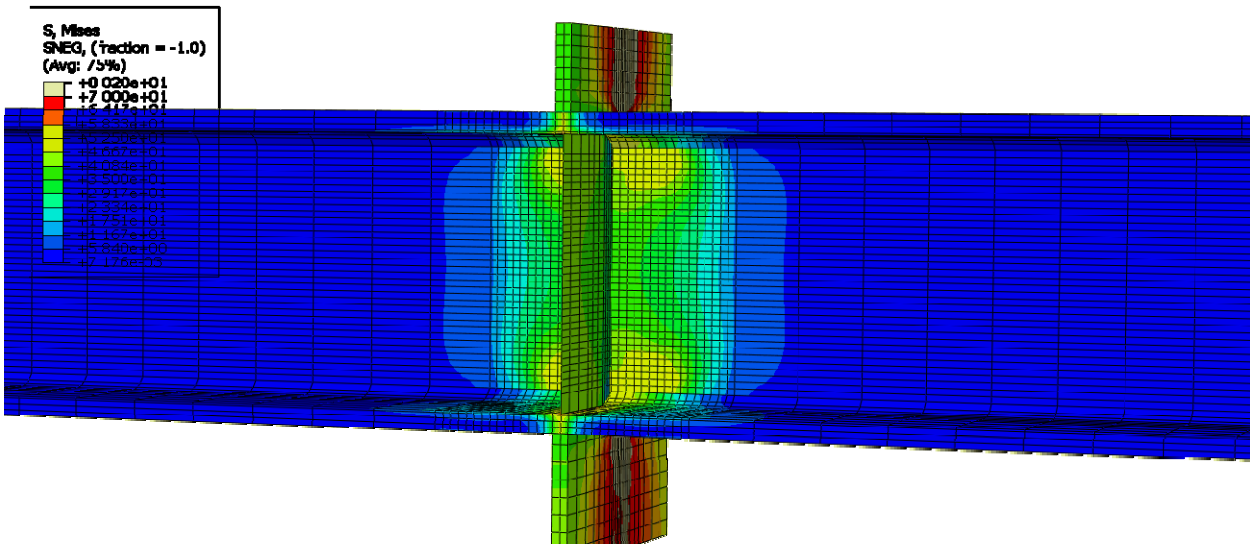

Figure E-209: Finite element model of W14X120-DC-E0 with 3/4 in. stiffeners during elastic behavior

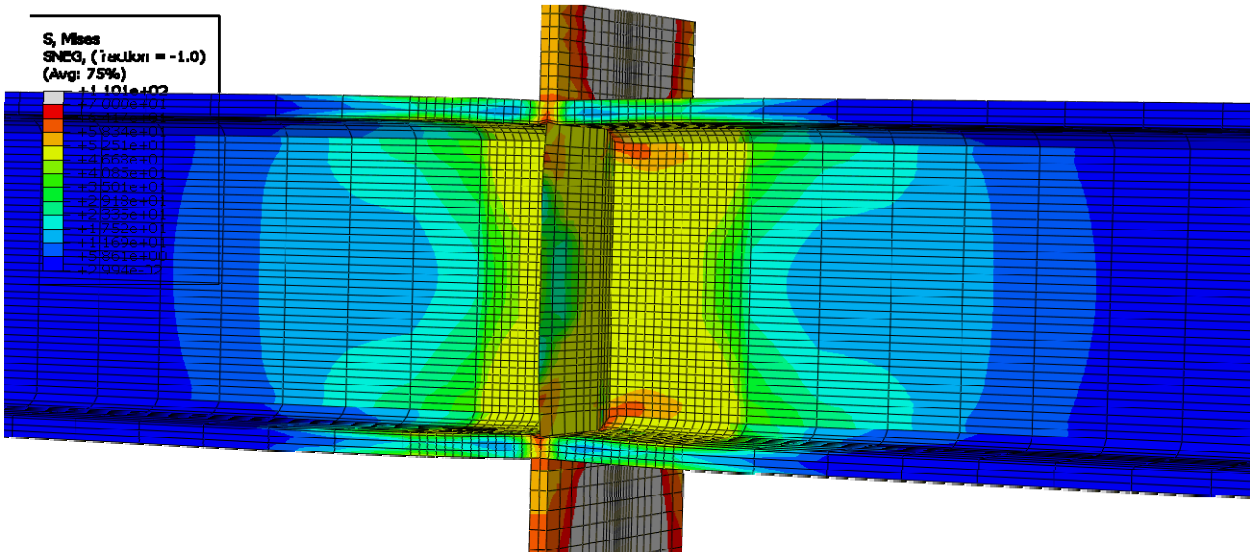

Figure E-210: Finite element model of W14X120-DC-E0 with 3/4 in. stiffeners during inelastic behavior

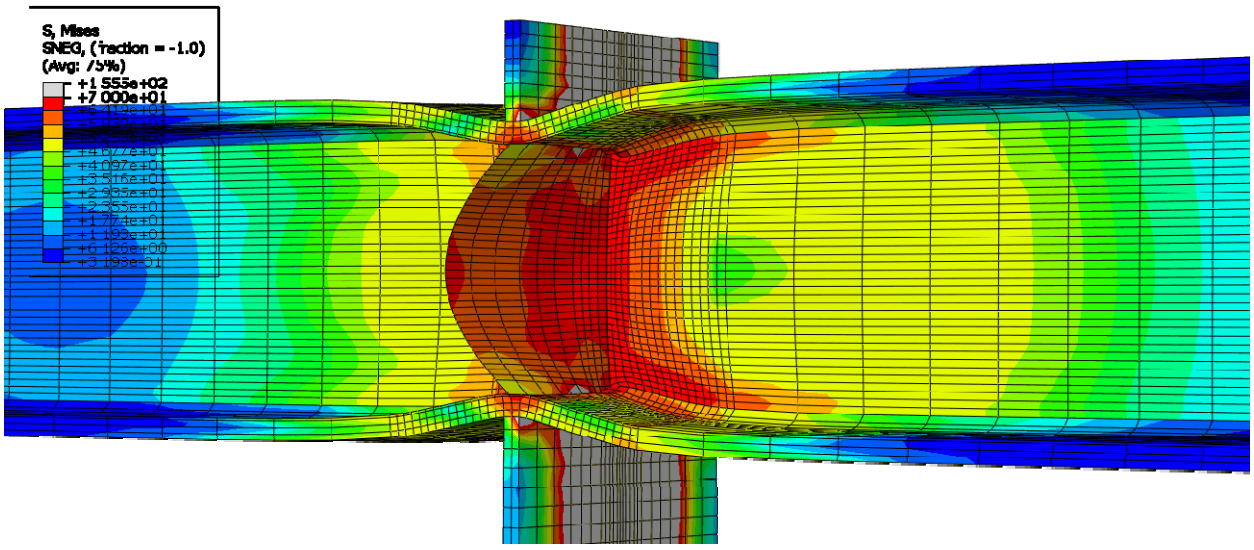

Figure E-211: Finite element model of W14X120-DC-E0 with 3/4 in. stiffeners after the maximum load emphasizing stiffener buckling

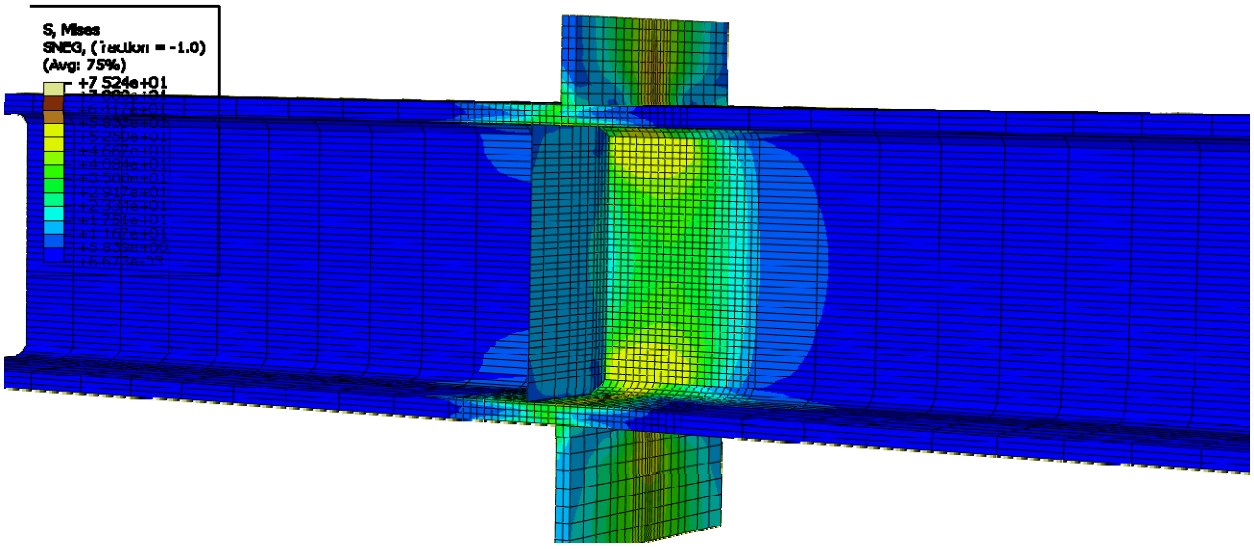

Figure E-212: Finite element model of W14X120-DC-E2 with 3/4 in. stiffeners during elastic behavior

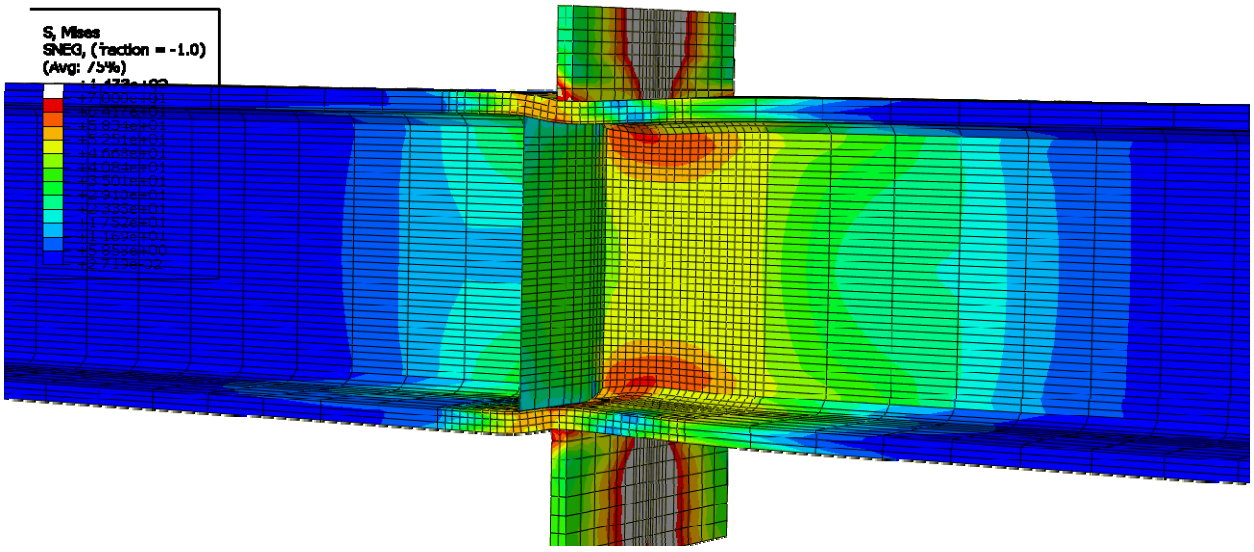

Figure E-213: Finite element model of W14X120-DC-E2 with 3/4 in. stiffeners during inelastic behavior

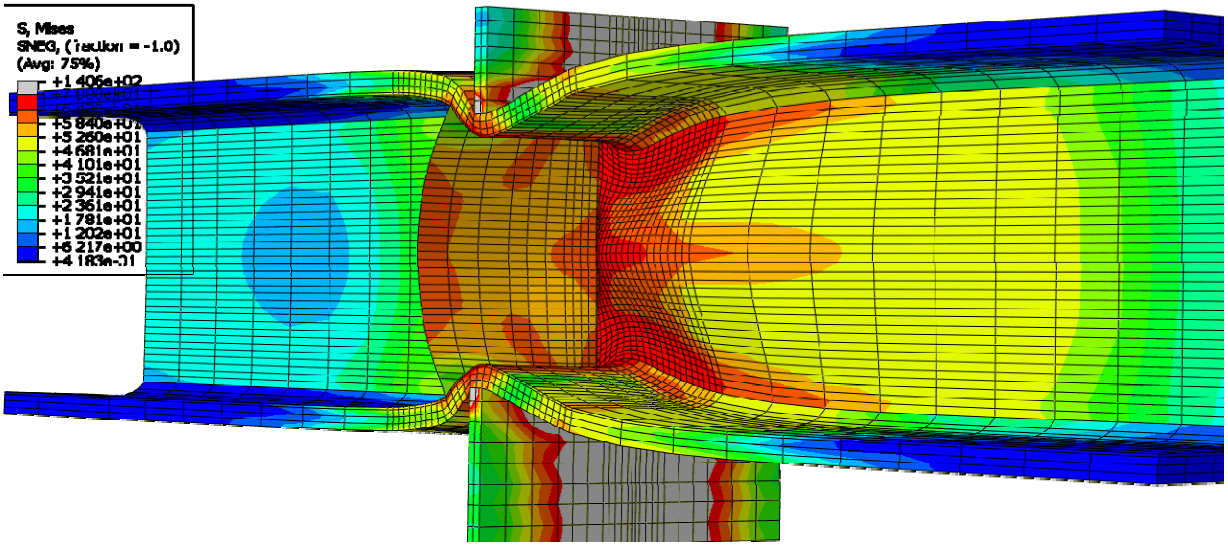

Figure E-214: Finite element model of W14X120-DC-E2 with 3/4 in. stiffeners after the maximum load

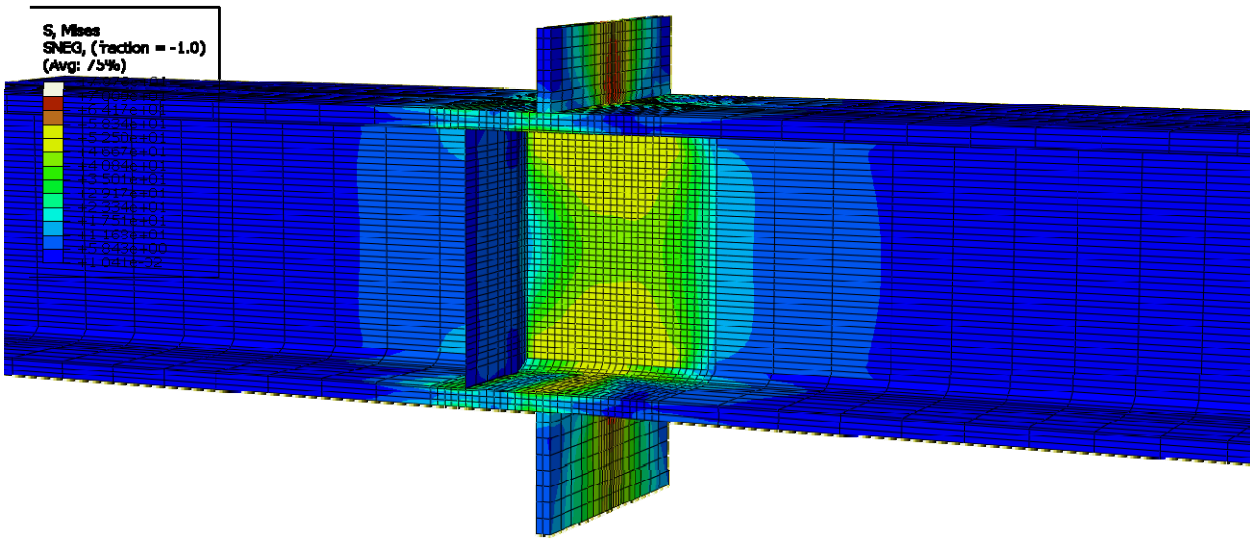

Figure E-215: Finite element model of W14X120-DC-E4 with 3/4 in. stiffeners during elastic behavior

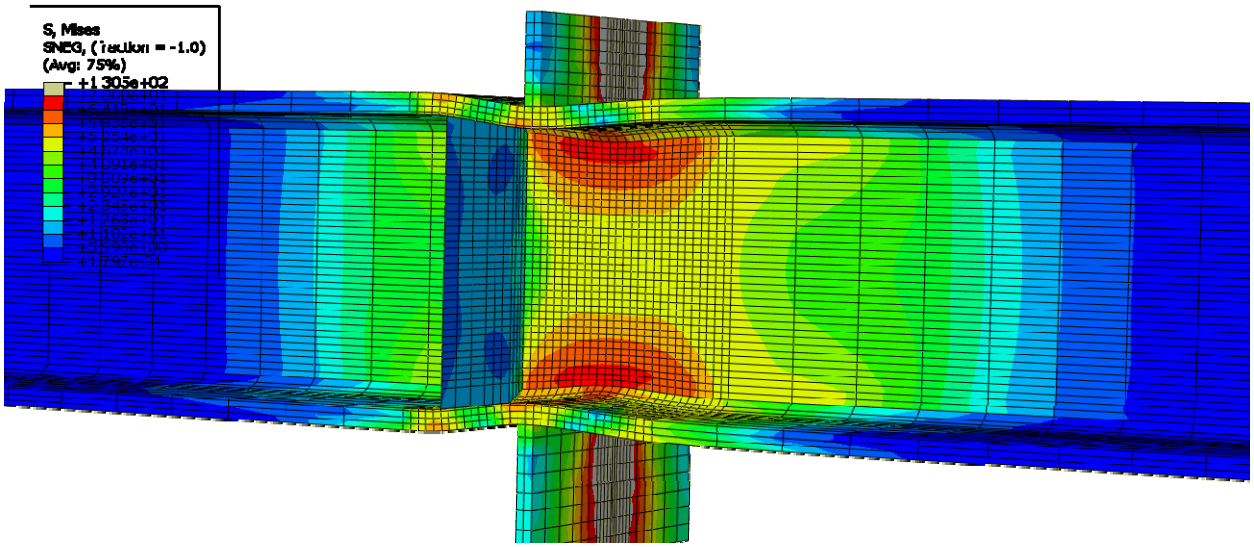

Figure E-216: Finite element model of W14X120-DC-E4 with 3/4 in. stiffeners during inelastic behavior

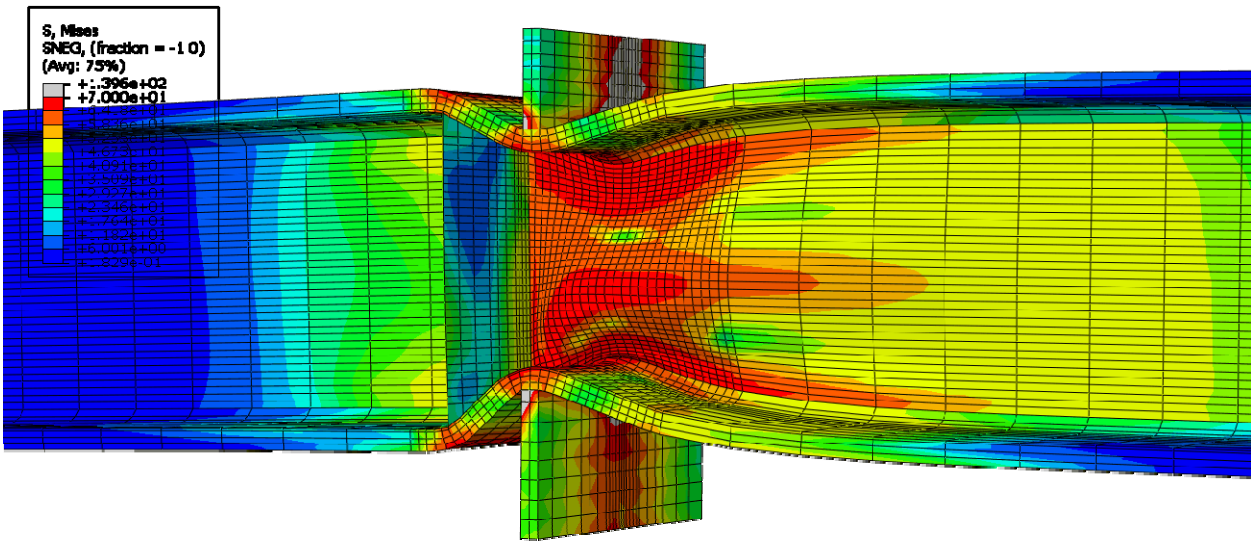

Figure E-217: Finite element model of W14X120-DC-E4 with 3/4 in. stiffeners after the maximum load

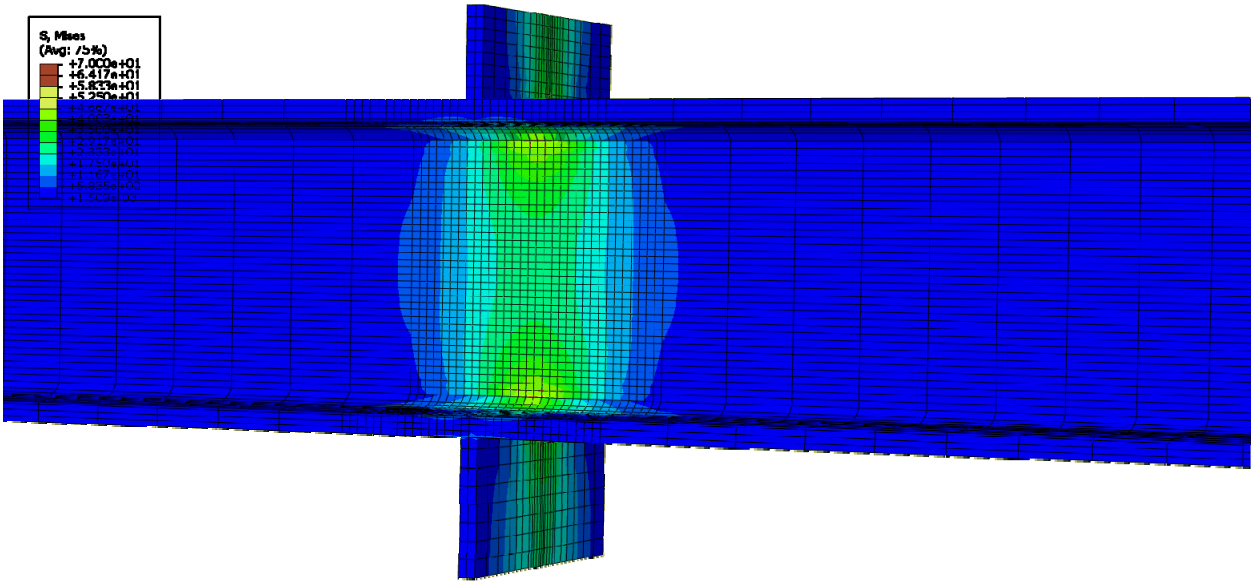

Figure E-218: Finite element model of W14X120-DC-NA during elastic behavior

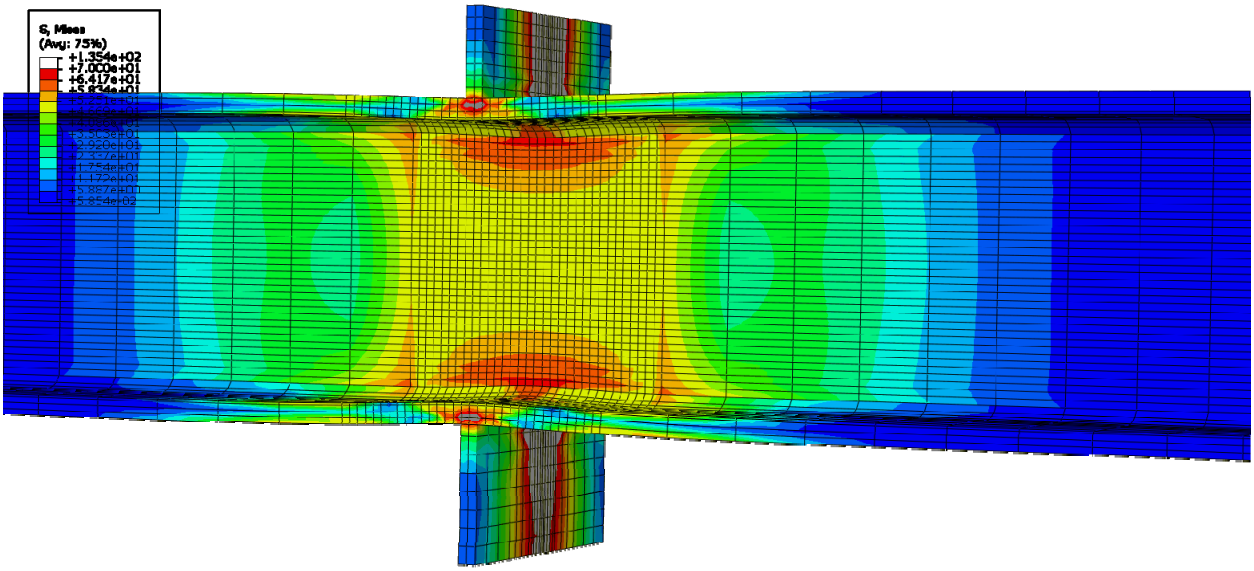

Figure E-219: Finite element model of W14X120-DC-NA during inelastic behavior

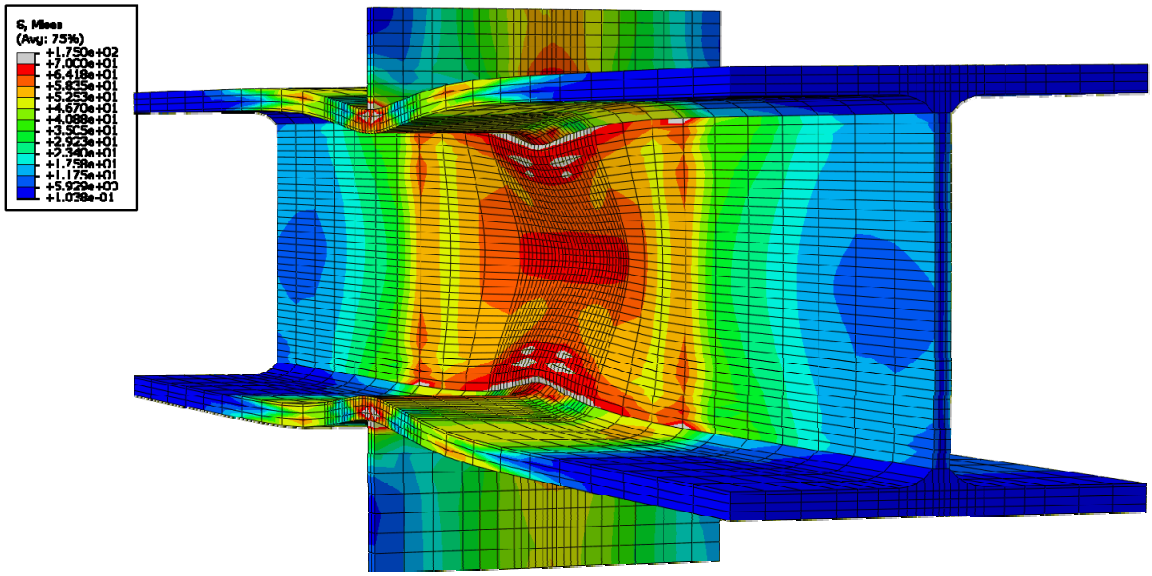

Figure E-220: Finite element model of W14X120-DC-NA after the maximum load emphasizing web compression buckling

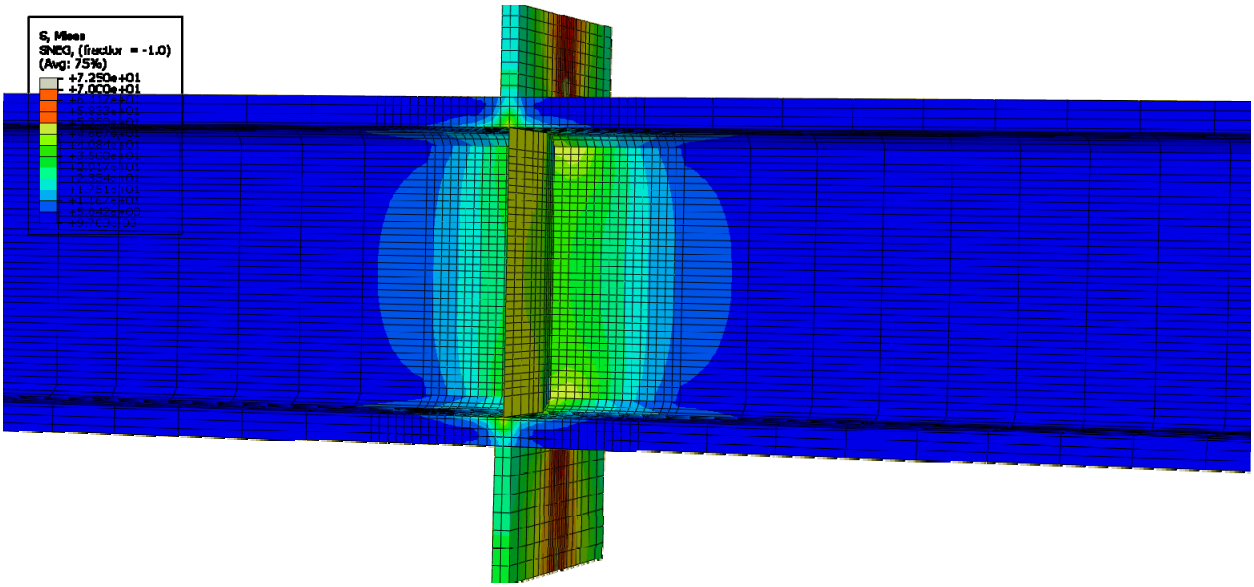

Figure E-221: Finite element model of W14X176-DC-E0 with 3/8 in. stiffeners during elastic behavior

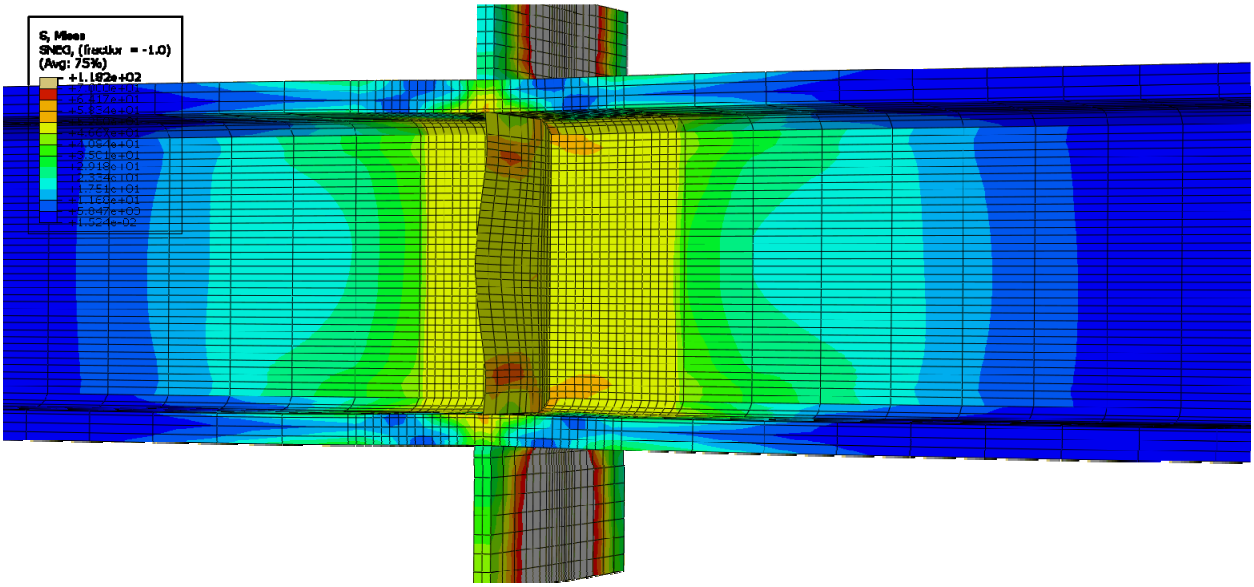

Figure E-222: Finite element model of W14X176-DC-E0 with 3/8 in. stiffeners during inelastic behavior

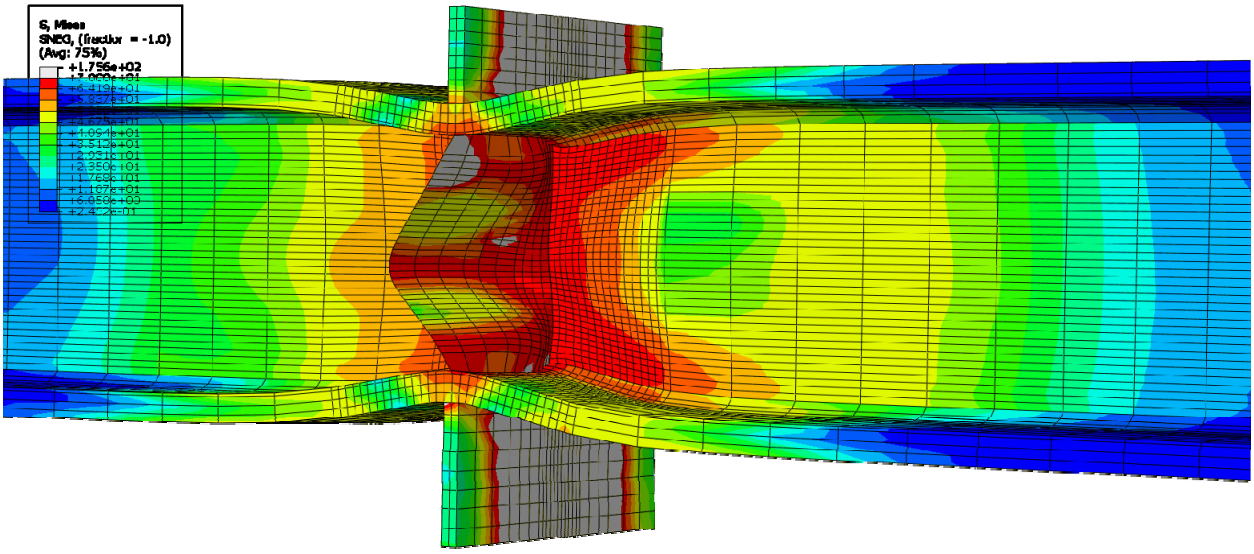

Figure E-223: Finite element model of W14X176-DC-E0 with 3/8 in. stiffeners after the maximum load showing stiffener buckling

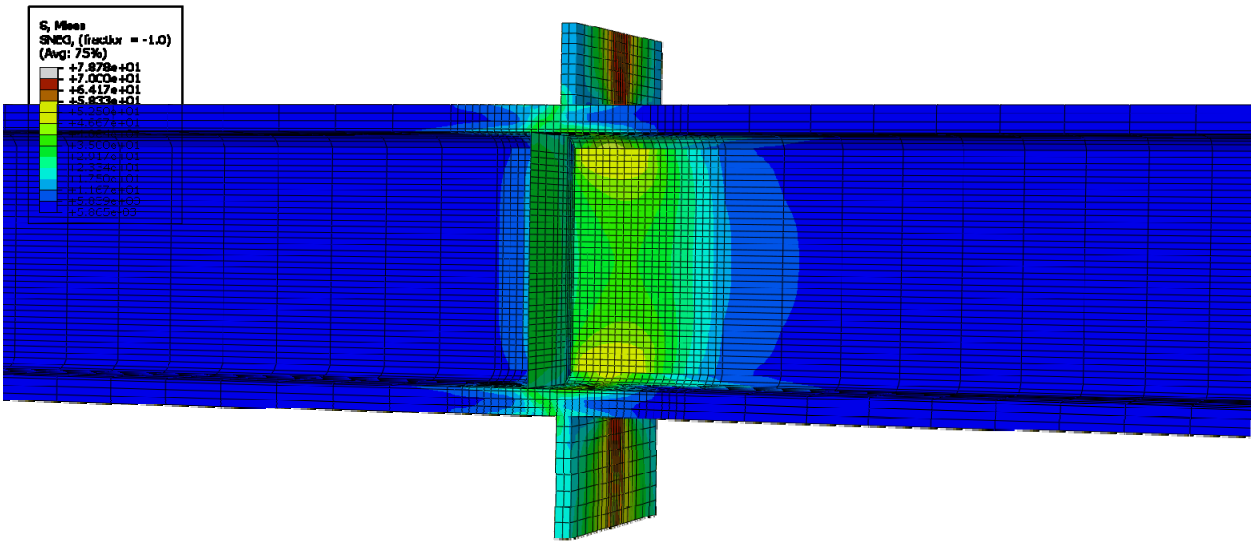

Figure E-224: Finite element model of W14X176-DC-E2 with 3/8 in. stiffeners during elastic behavior

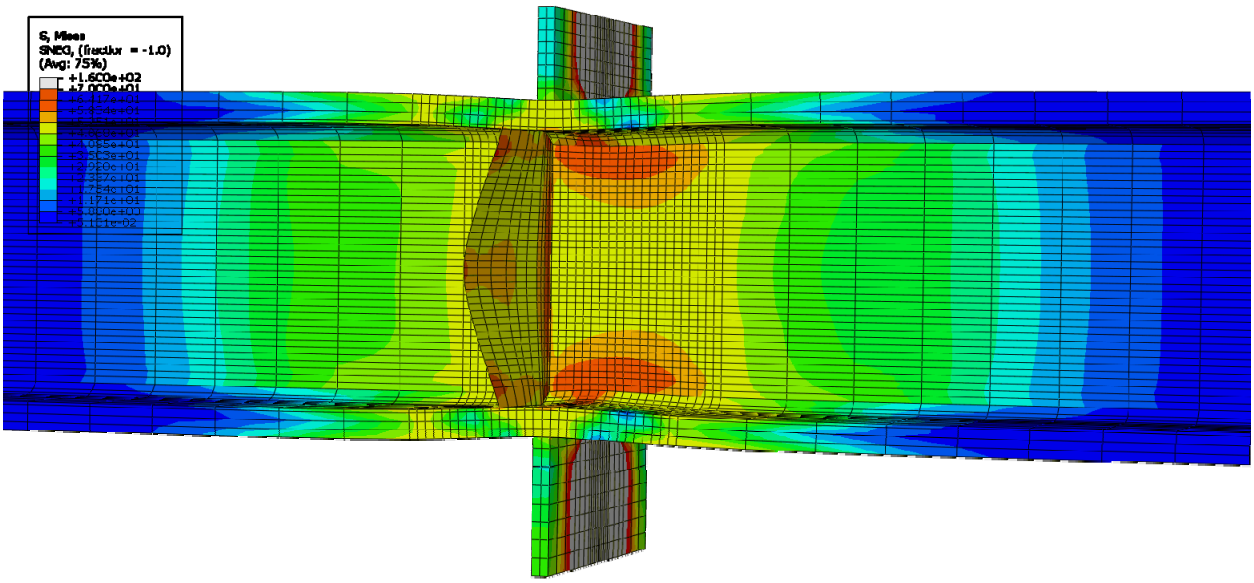

Figure E-225: Finite element model of W14X176-DC-E2 with 3/8 in. stiffeners during inelastic behavior

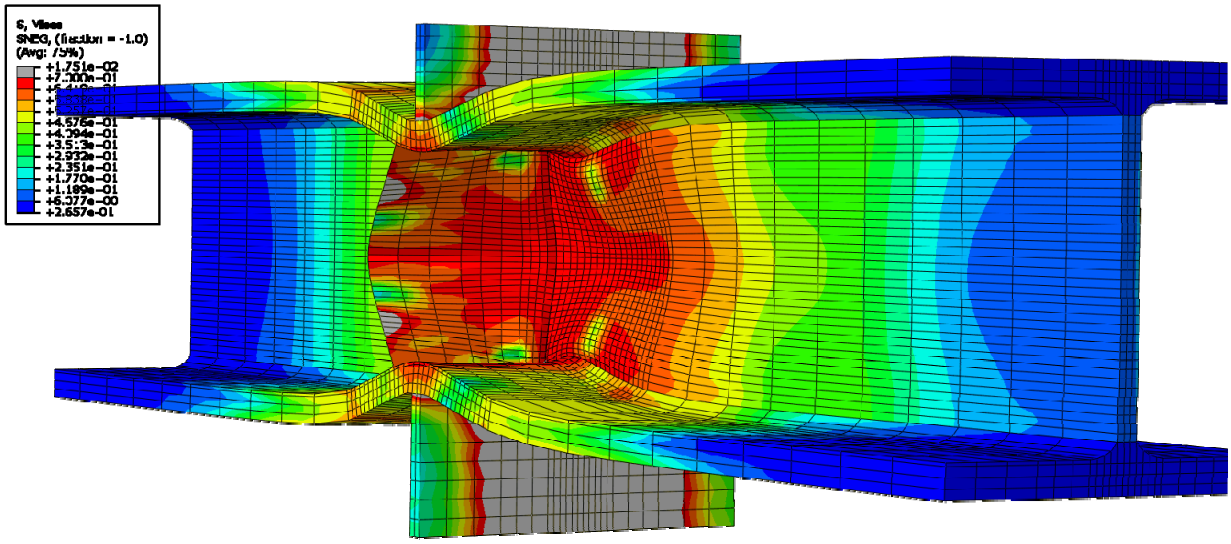

Figure E-226: Finite element model of W14X176-DC-E2 with 3/8 in. stiffeners after the maximum load

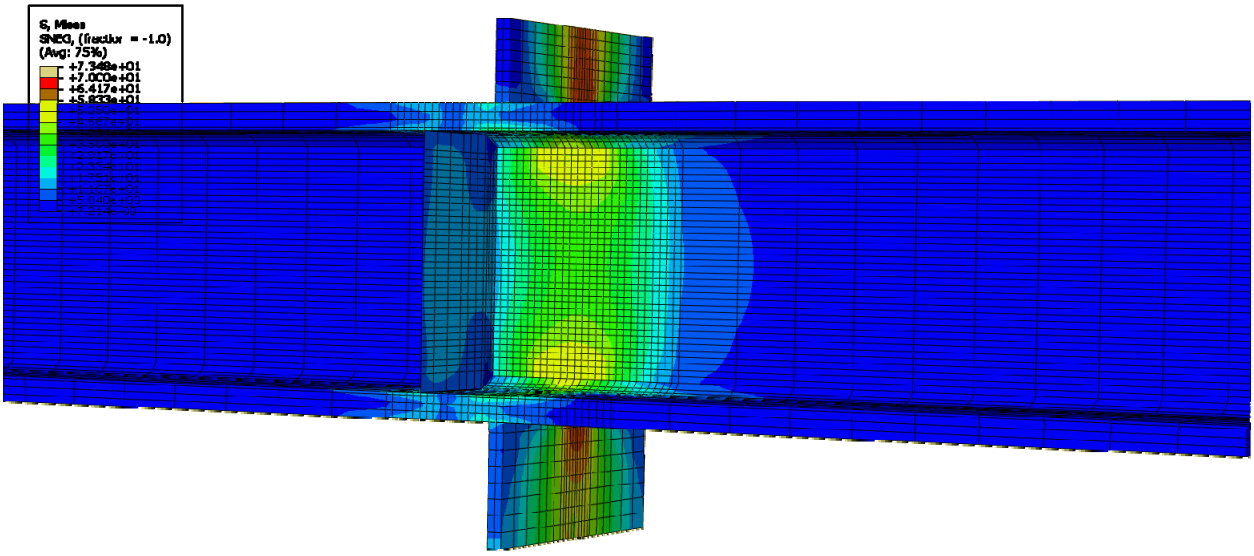

Figure E-227: Finite element model of W14X176-DC-E4 with 3/8 in. stiffeners during elastic behavior

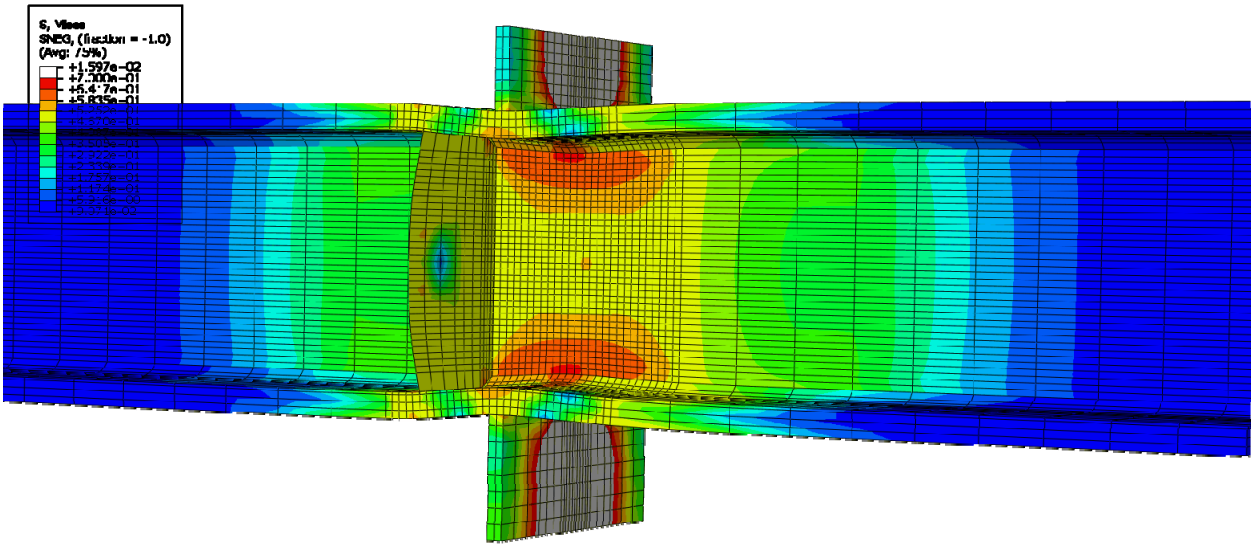

Figure E-228: Finite element model of W14X176-DC-E4 with 3/8 in. stiffeners during inelastic behavior

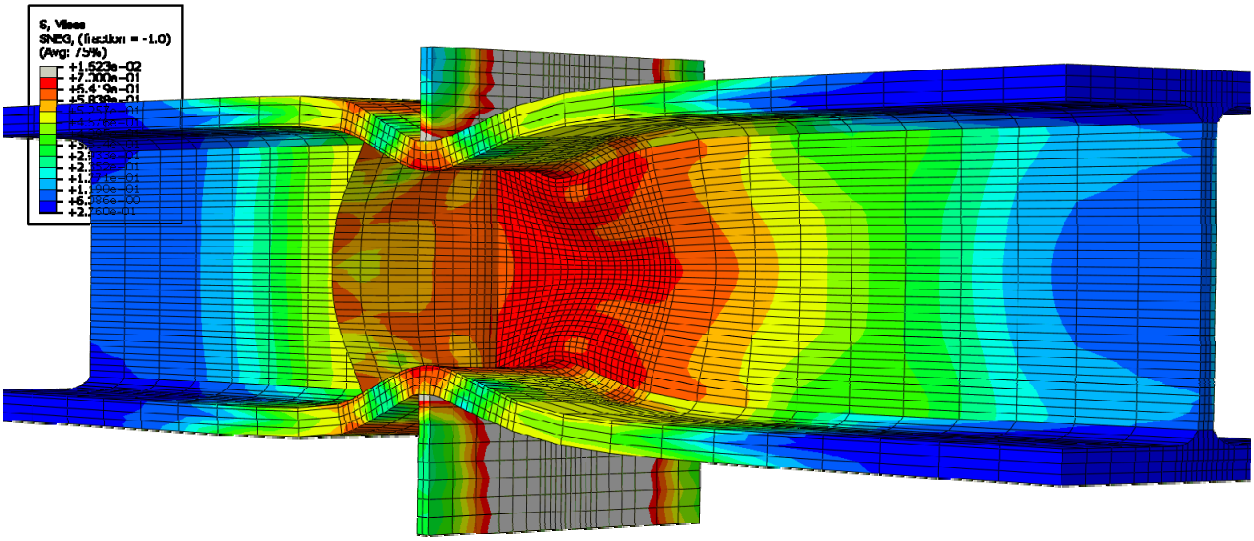

Figure E-229: Finite element model of W14X176-DC-E4 with 3/8 in. stiffeners after the maximum load

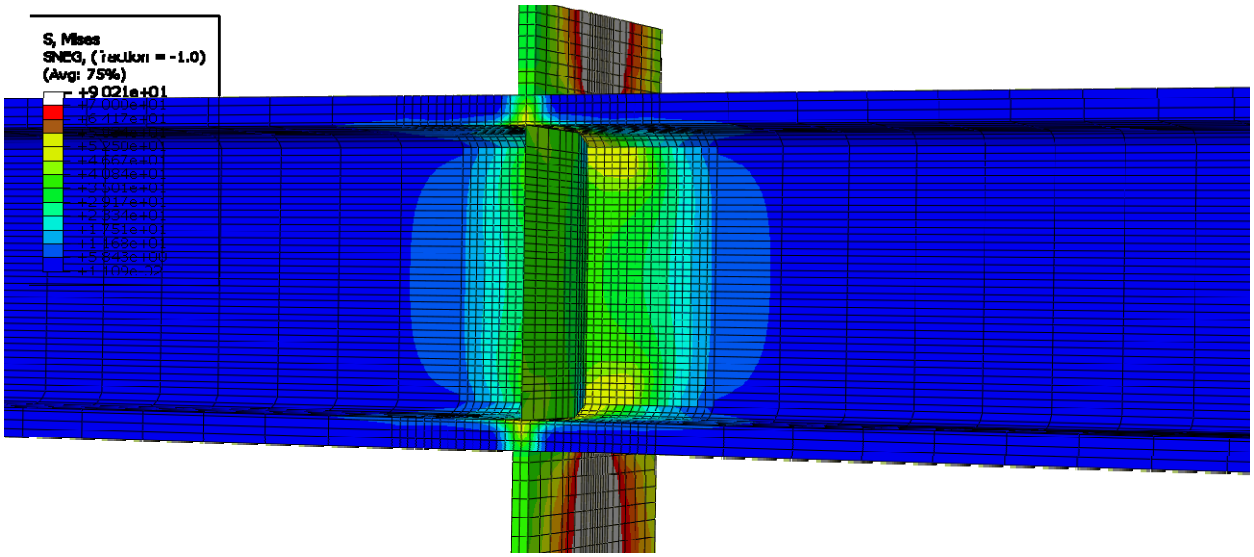

Figure E-230: Finite element model of W14X176-DC-E0 with 3/4 in. stiffeners during elastic behavior

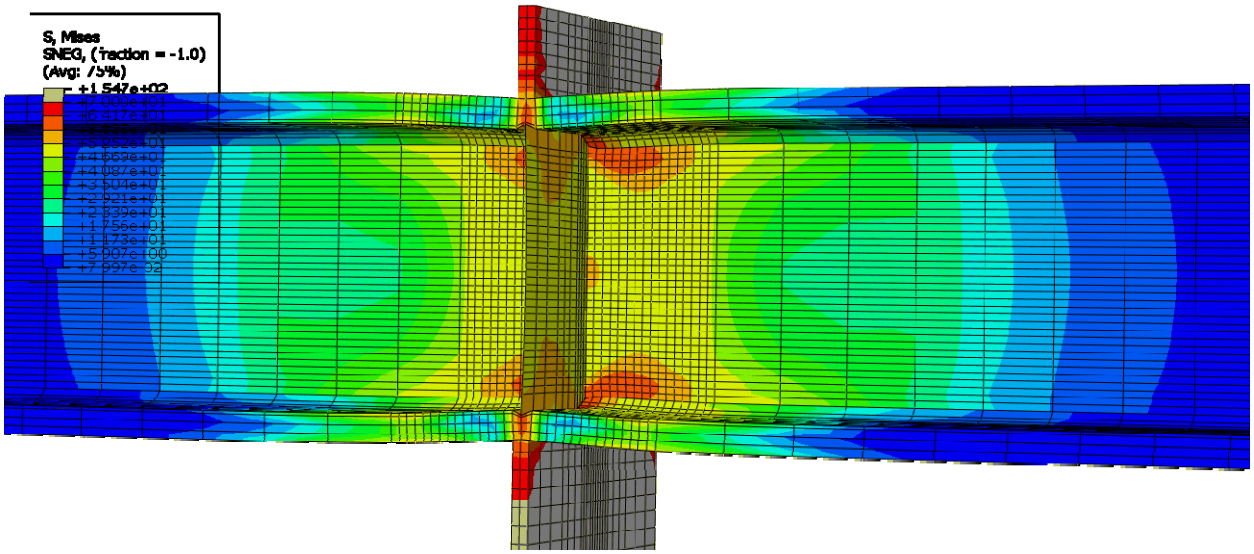

Figure E-231: Finite element model of W14X176-DC-E0 with 3/4 in. stiffeners during inelastic behavior

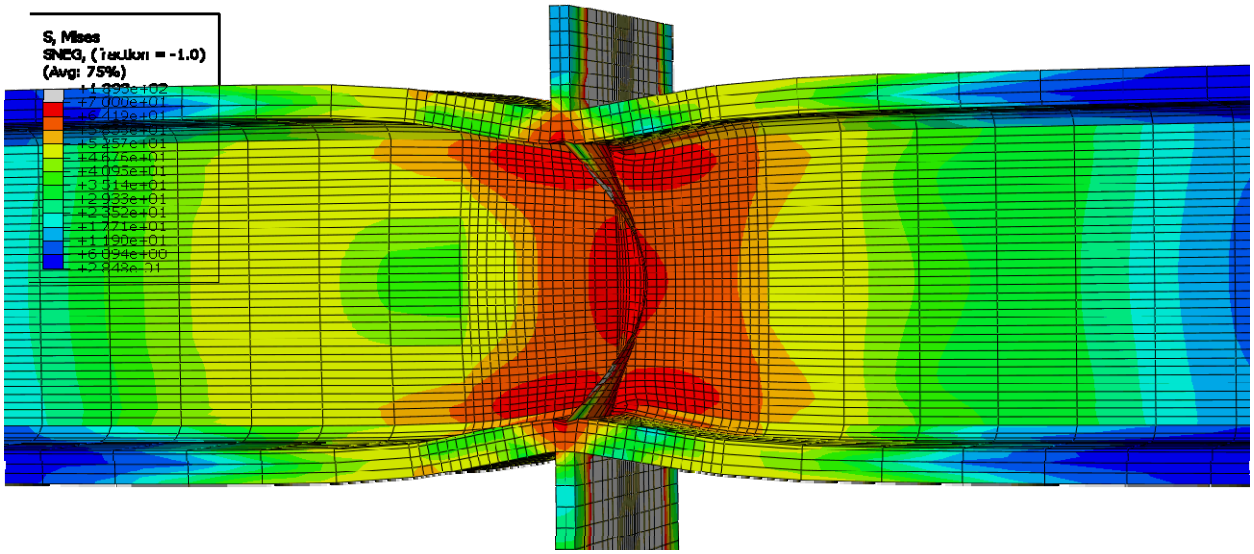

Figure E-232: Finite element model of W14X176-DC-E0 with 3/4 in. stiffeners after the maximum load showing stiffener buckling

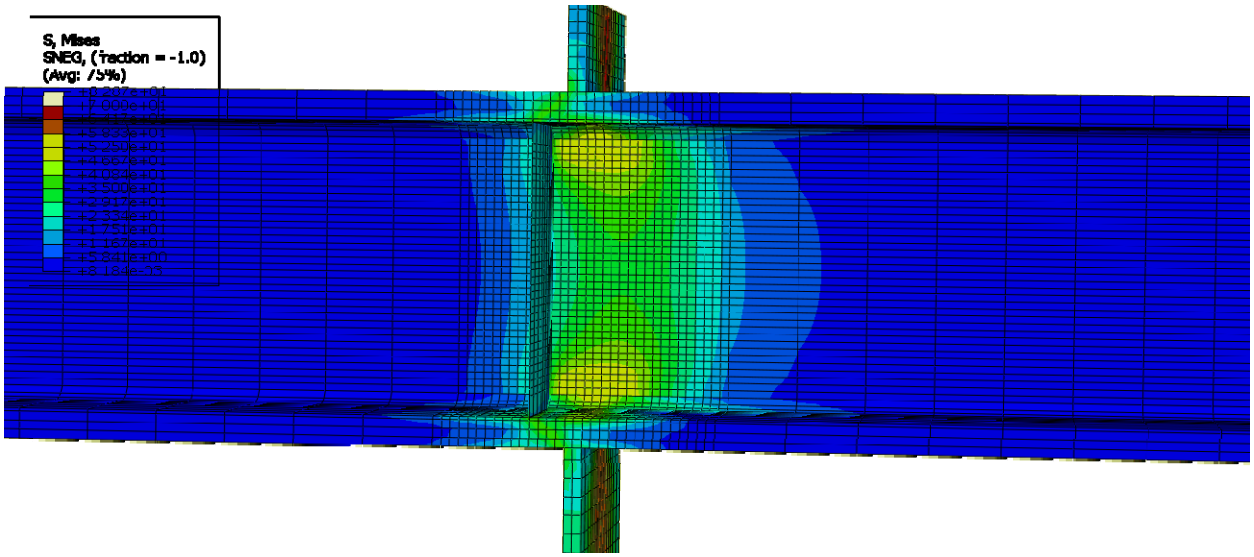

Figure E-233: Finite element model of W14X176-DC-E2 with 3/4 in. stiffeners during elastic behavior

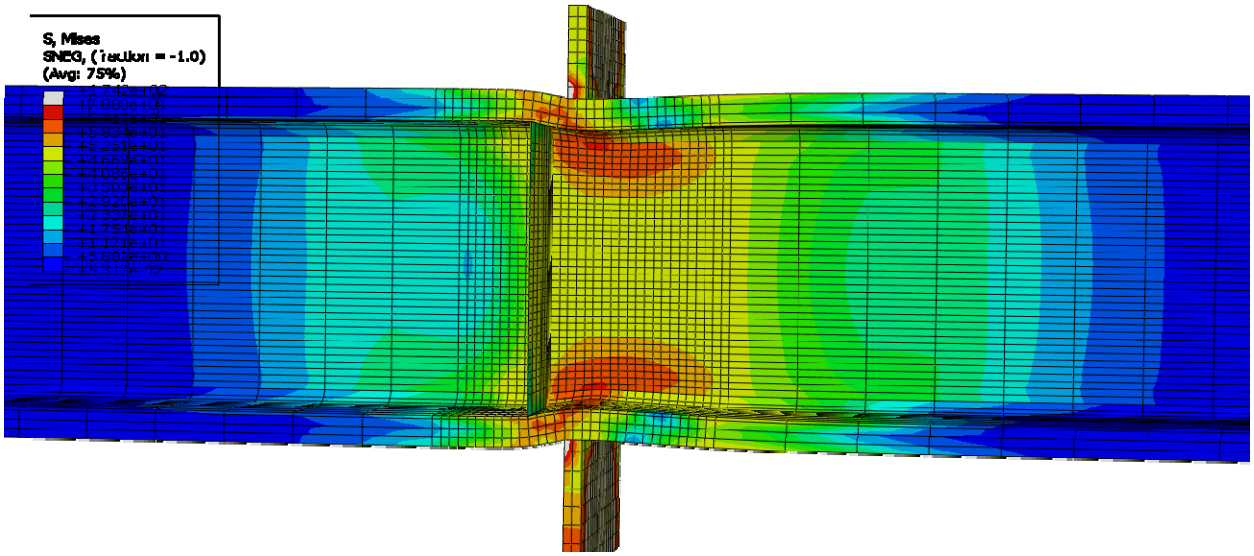

Figure E-234: Finite element model of W14X176-DC-E2 with 3/4 in. stiffeners during inelastic behavior

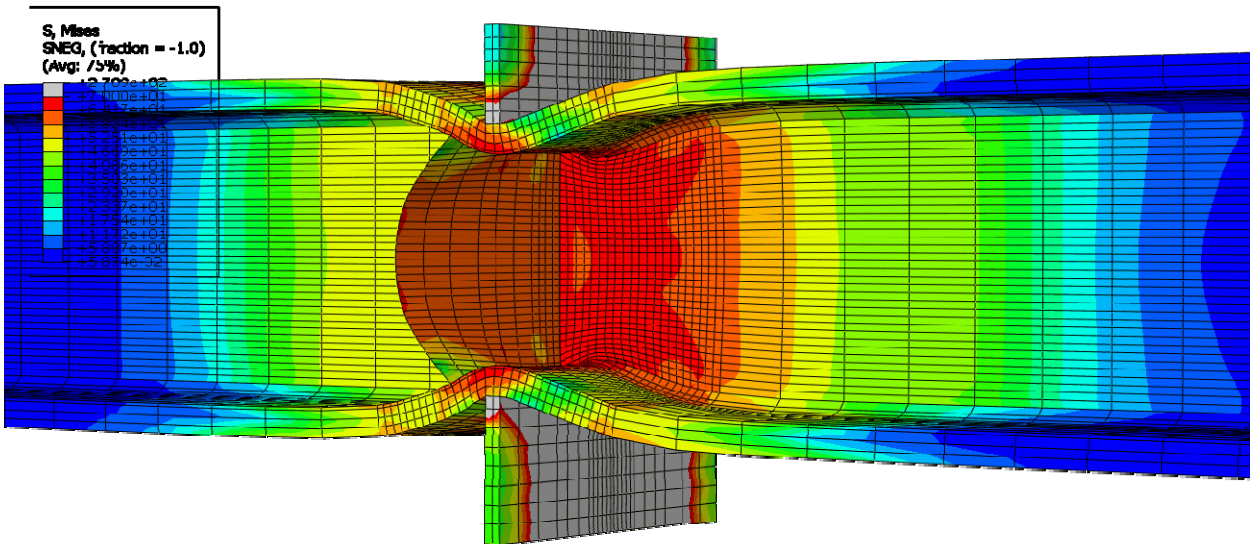

Figure E-235: Finite element model of W14X176-DC-E2 with 3/4 in. stiffeners after the maximum load

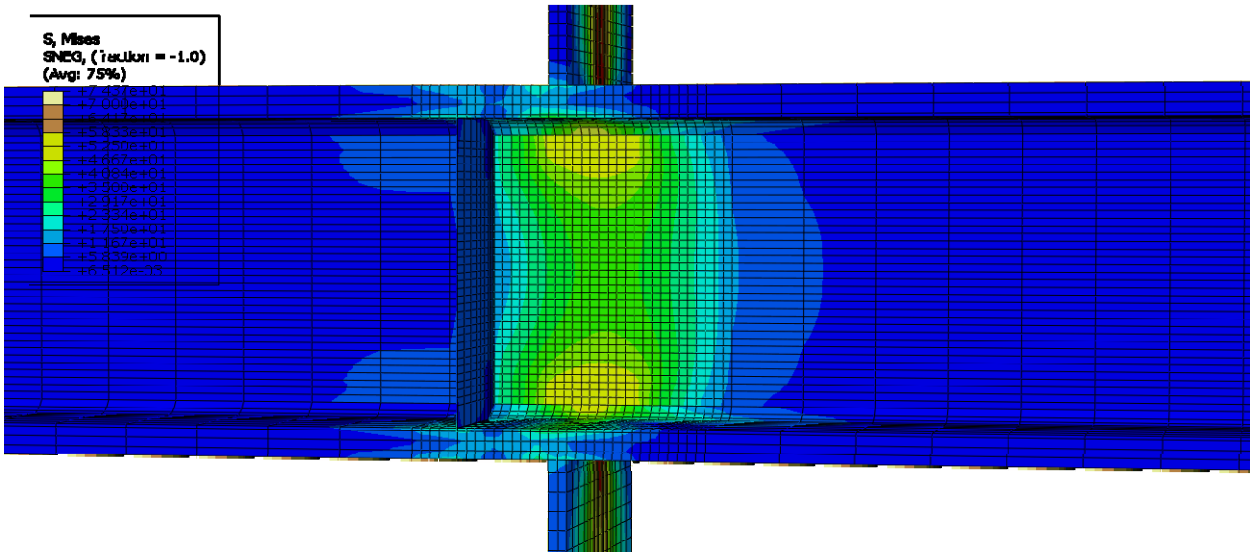

Figure E-236: Finite element model of W14X176-DC-E4 with 3/4 in. stiffeners during elastic behavior

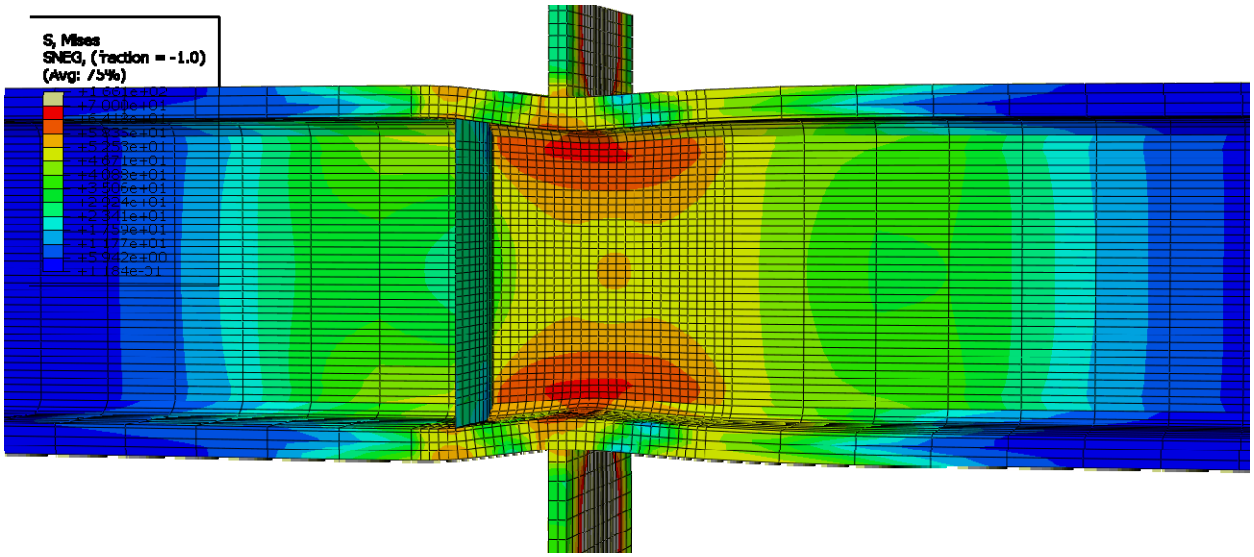

Figure E-237: Finite element model of W14X176-DC-E4 with 3/4 in. stiffeners during inelastic behavior

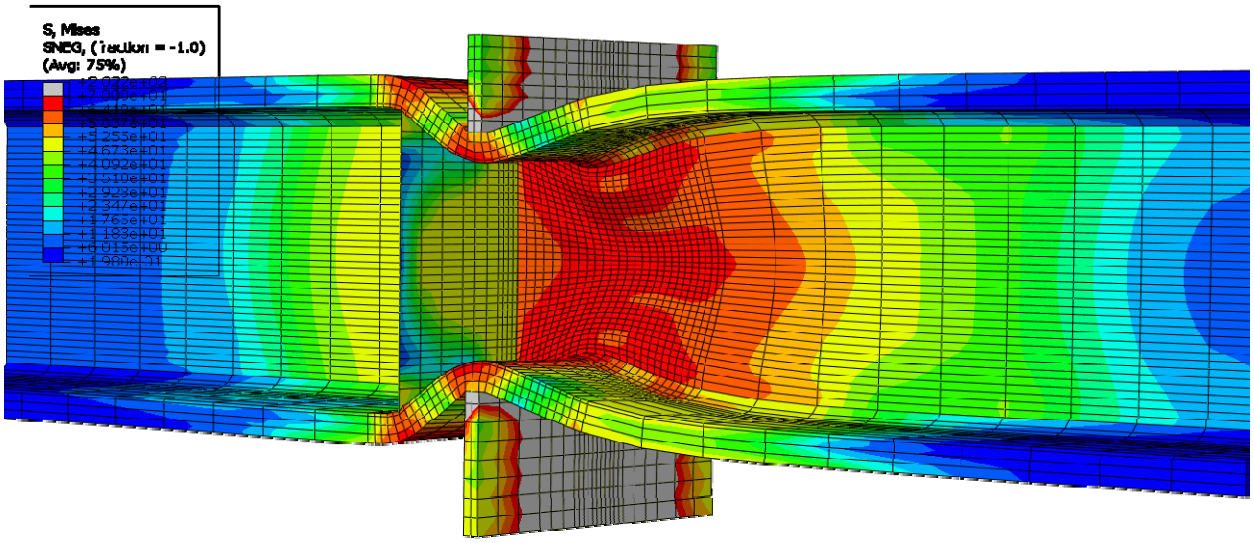

Figure E-238: Finite element model of W14X176-DC-E4 with 3/4 in. stiffeners after the maximum load

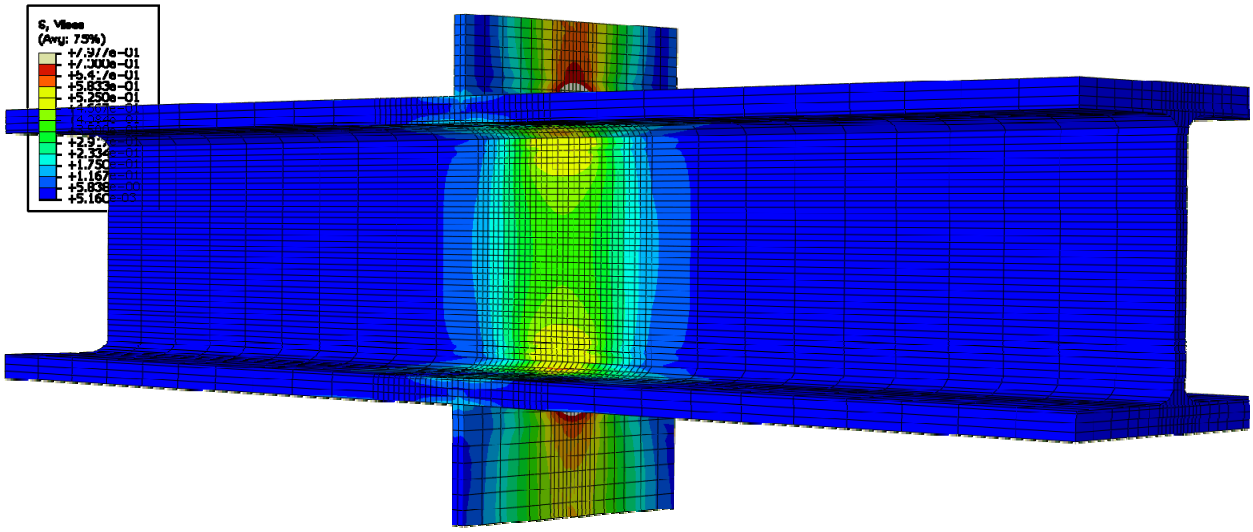

Figure E-239: Finite element model of W14X176-DC-NA during elastic behavior

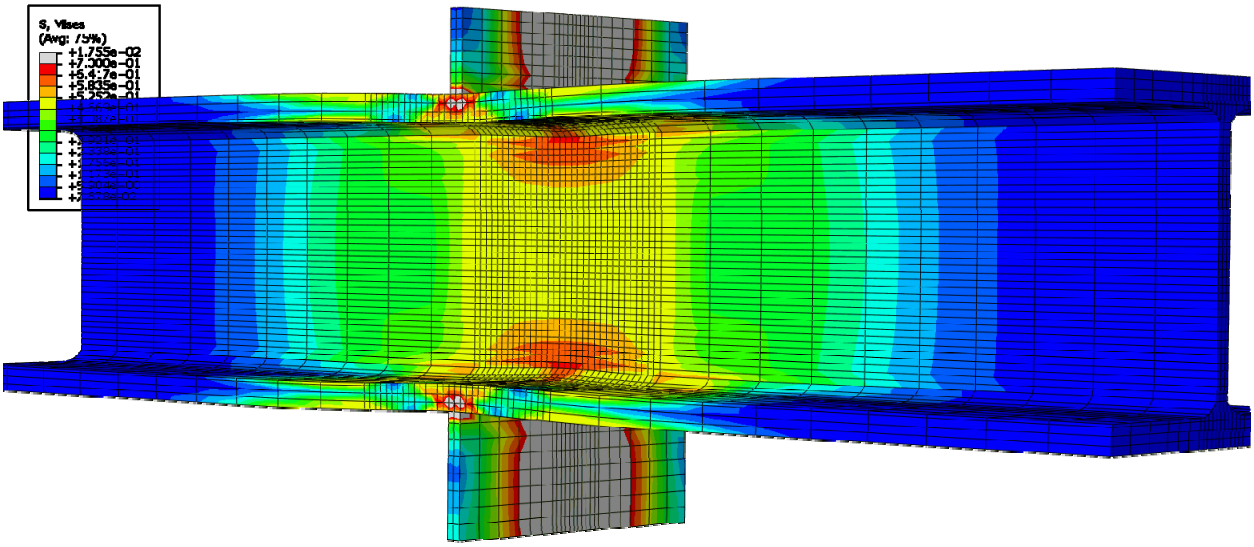

Figure E-240: Finite element model of W14X176-DC-NA during inelastic behavior

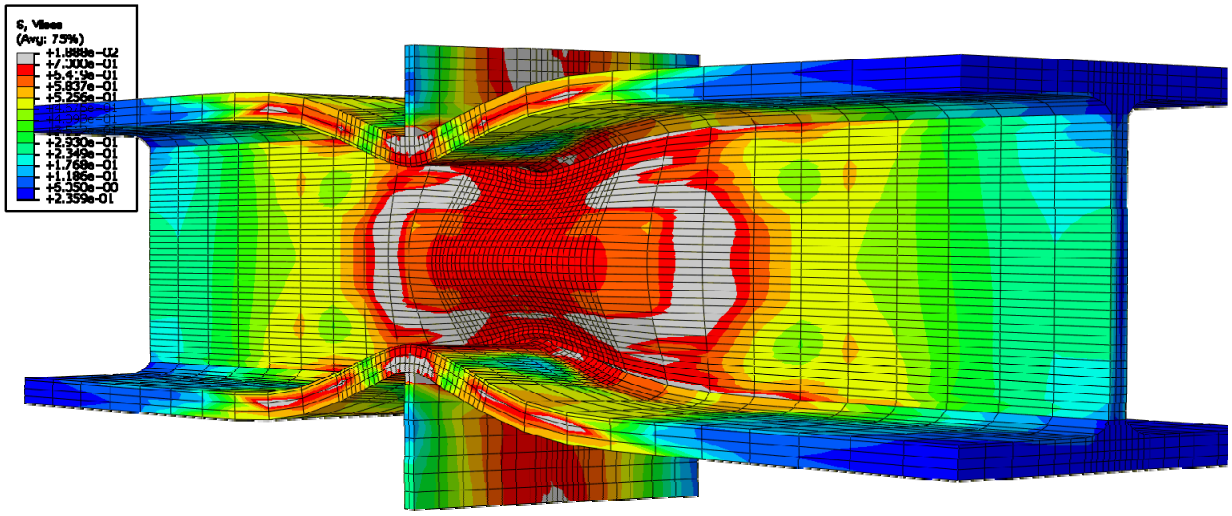

Figure E-241: Finite element model of W14X176-DC-NA after the maximum load showing web compression buckling

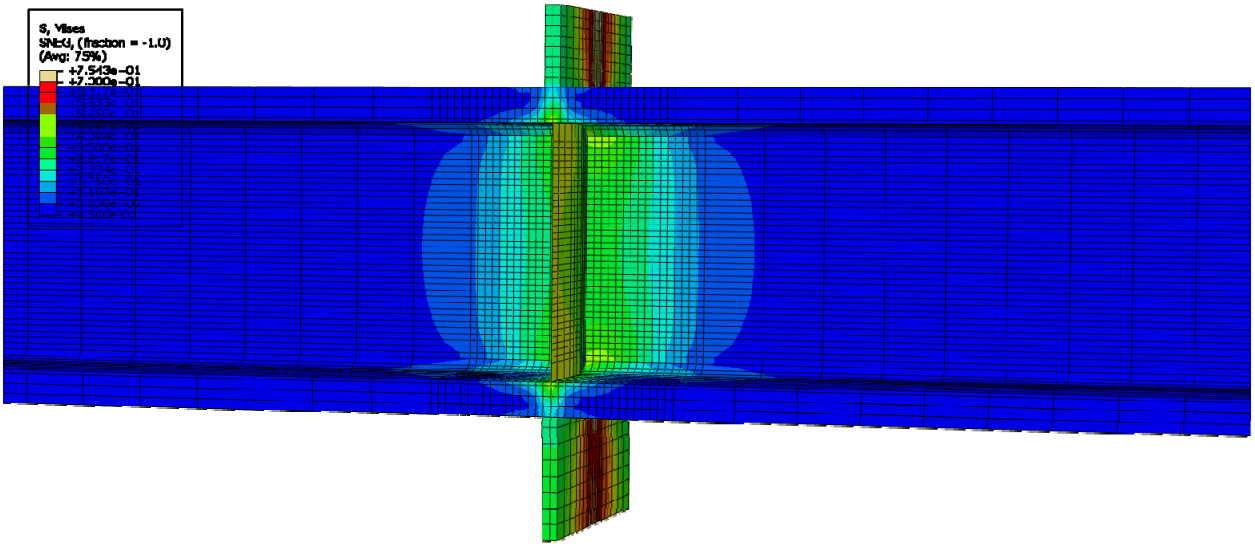

Figure E-242: Finite element model of W14X233-DC-E0 with 3/8 in. stiffeners during elastic behavior

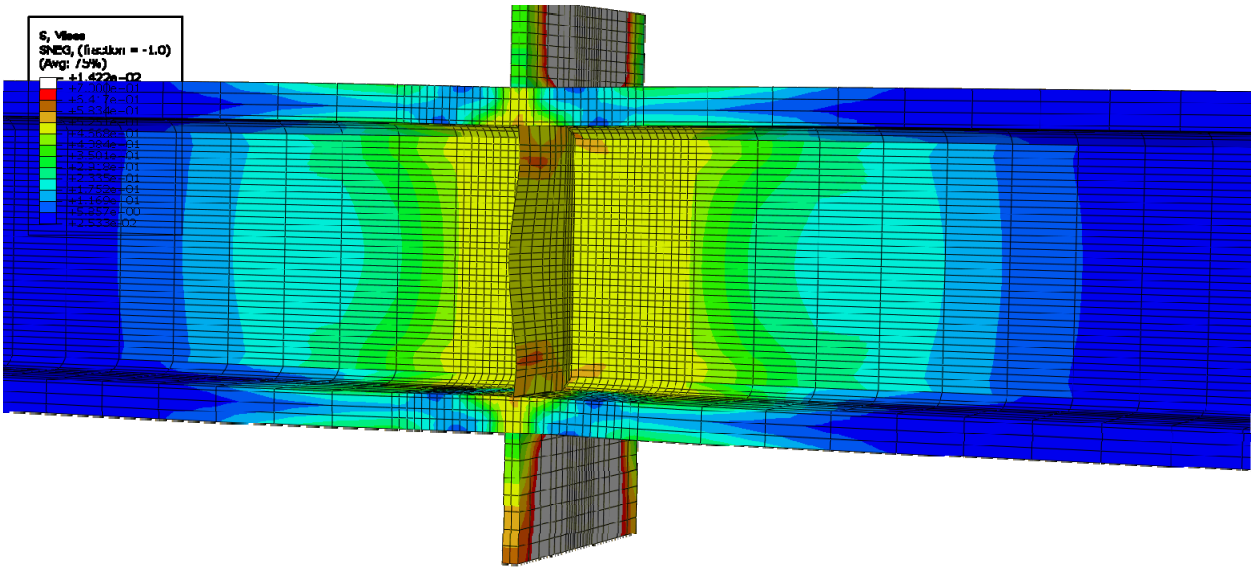

Figure E-243: Finite element model of W14X233-DC-E0 with 3/8 in. stiffeners during inelastic behavior

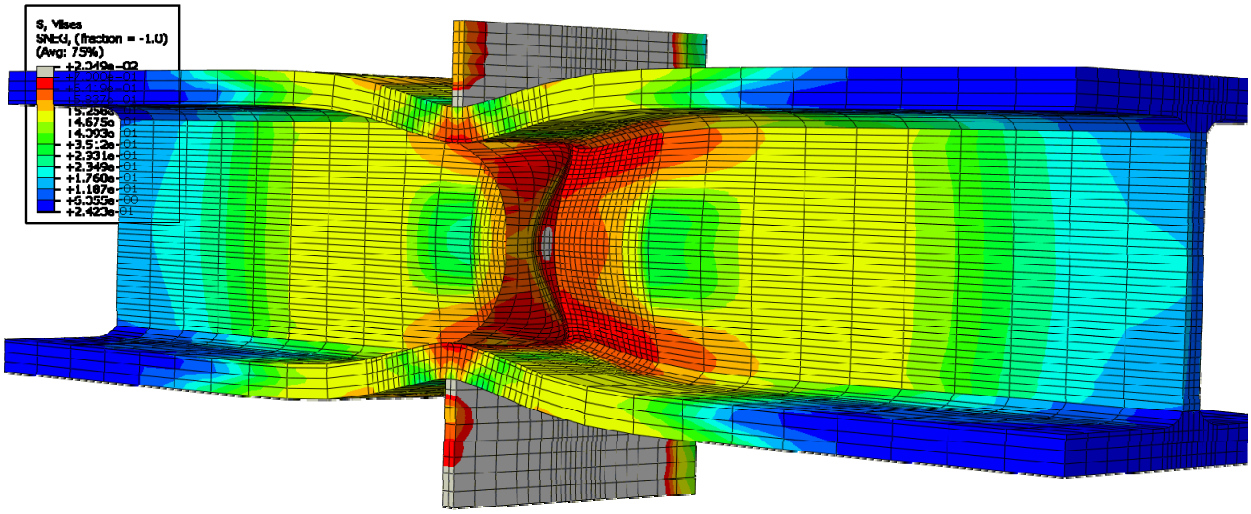

Figure E-244: Finite element model of W14X233-DC-E0 with 3/8 in. stiffeners after the maximum load

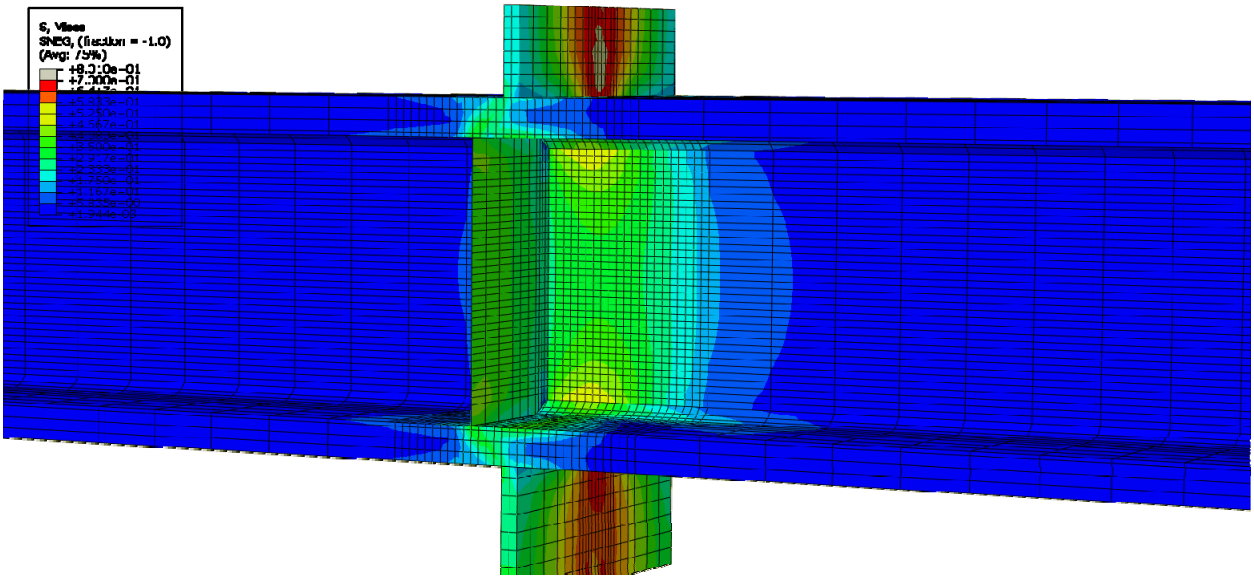

Figure E-245: Finite element model of W14X233-DC-E2 with 3/8 in. stiffeners during elastic behavior

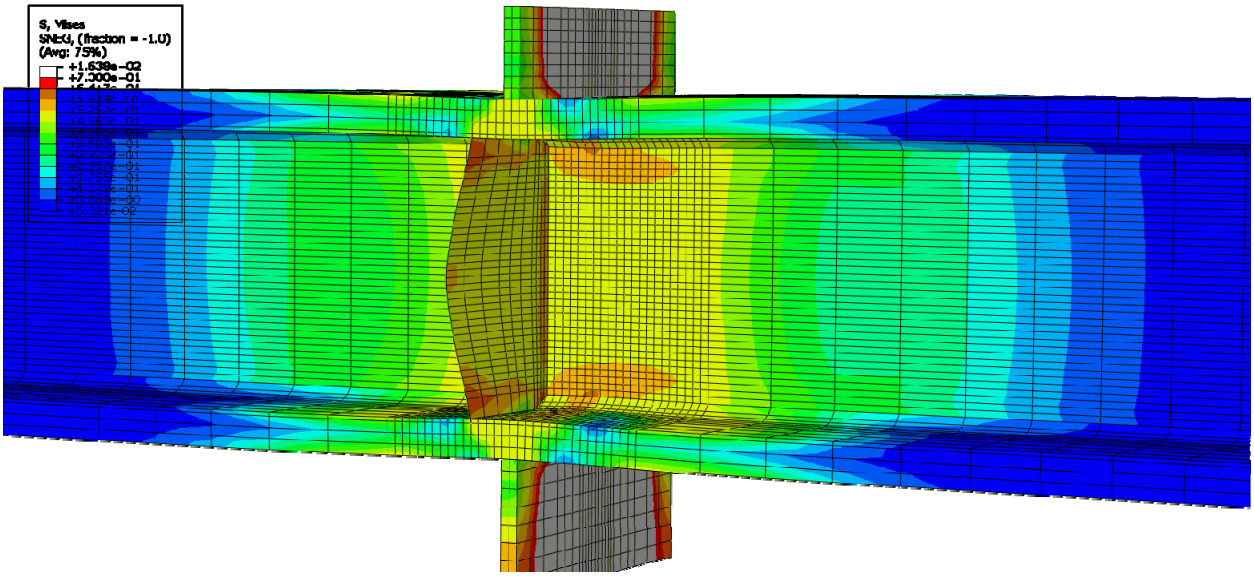

Figure E-246: Finite element model of W14X233-DC-E2 with 3/8 in. stiffeners during inelastic behavior

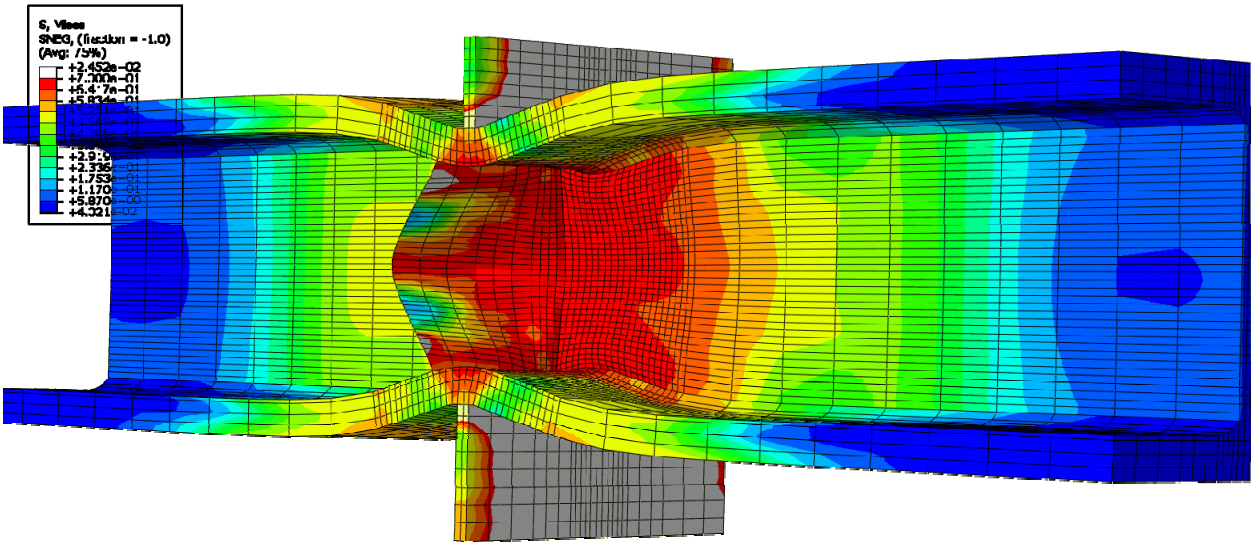

Figure E-247: Finite element model of W14X233-DC-E2 with 3/8 in. stiffeners after the maximum load

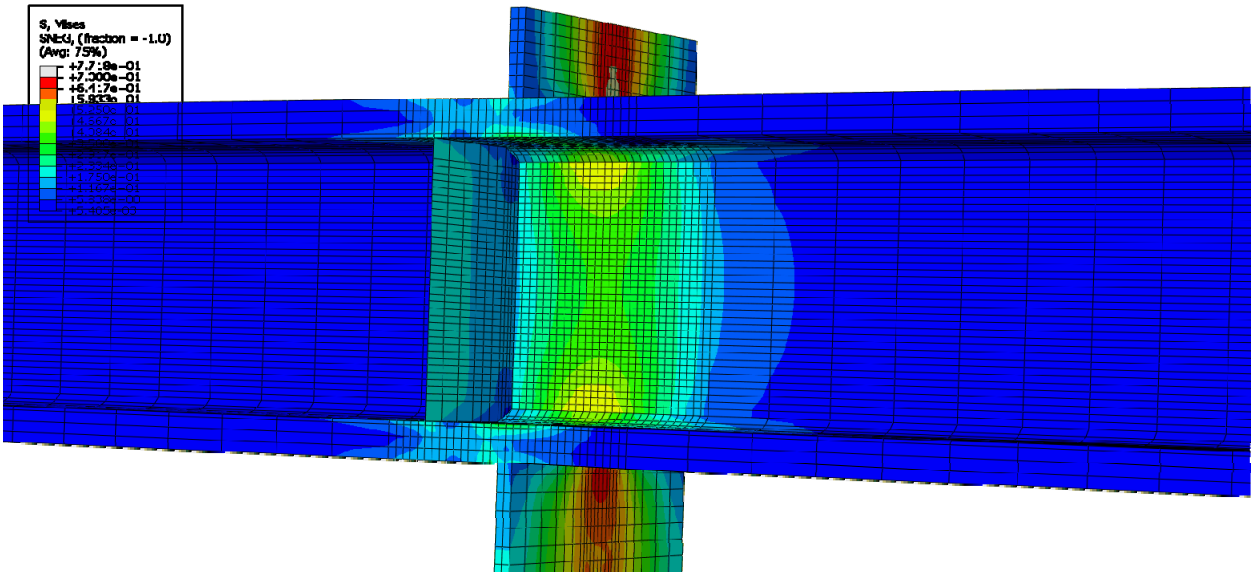

Figure E-248: Finite element model of W14X233-DC-E4 with 3/8 in. stiffeners during elastic behavior

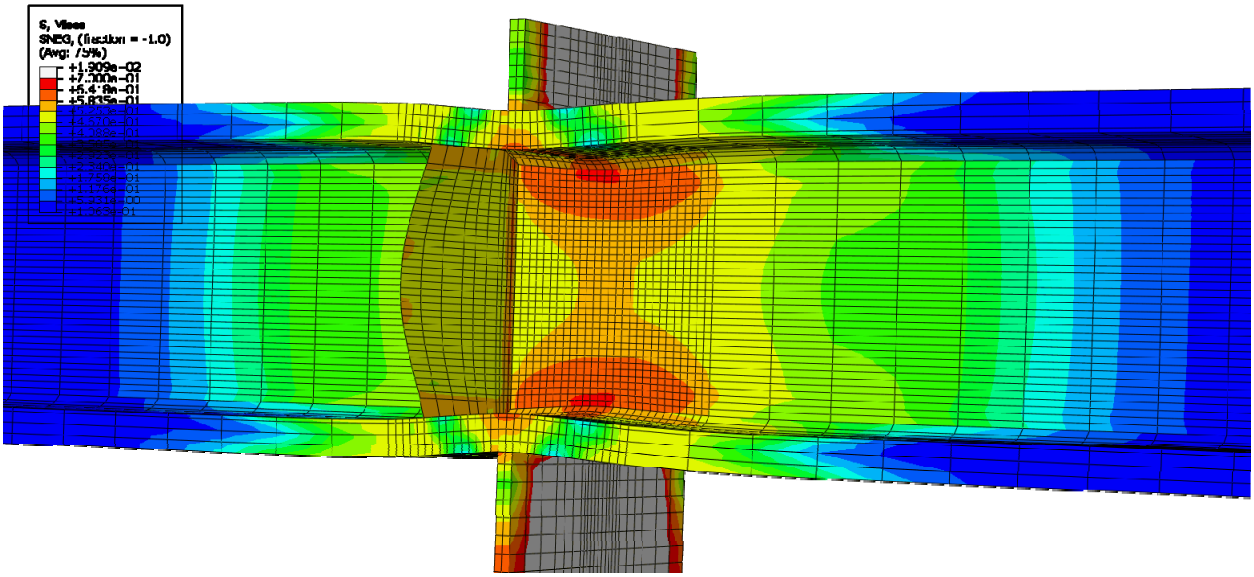

Figure E-249: Finite element model of W14X233-DC-E4 with 3/8 in. stiffeners during inelastic behavior

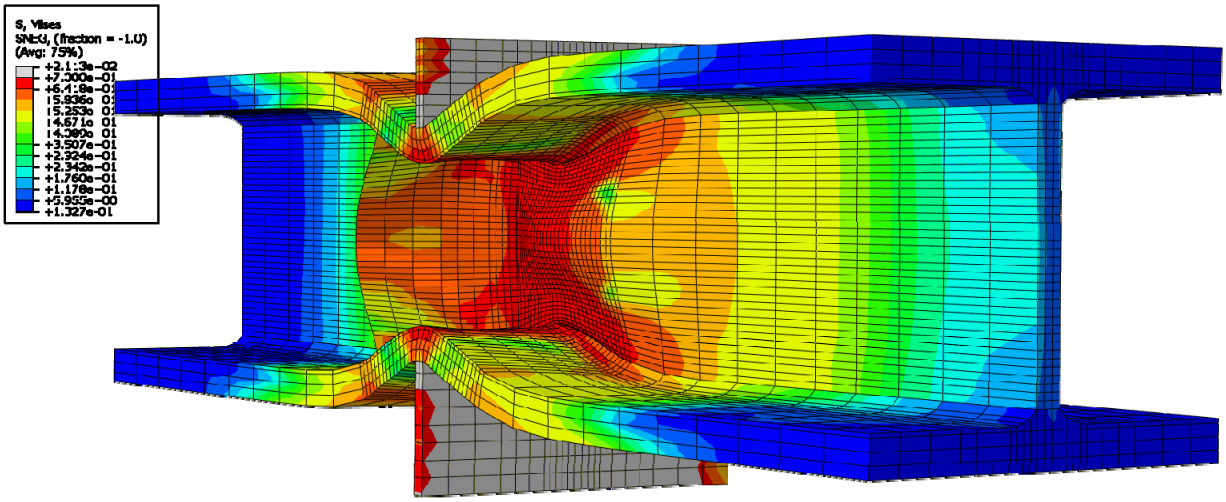

Figure E-250: Finite element model of W14X233-DC-E4 with 3/8 in. stiffeners after the maximum load

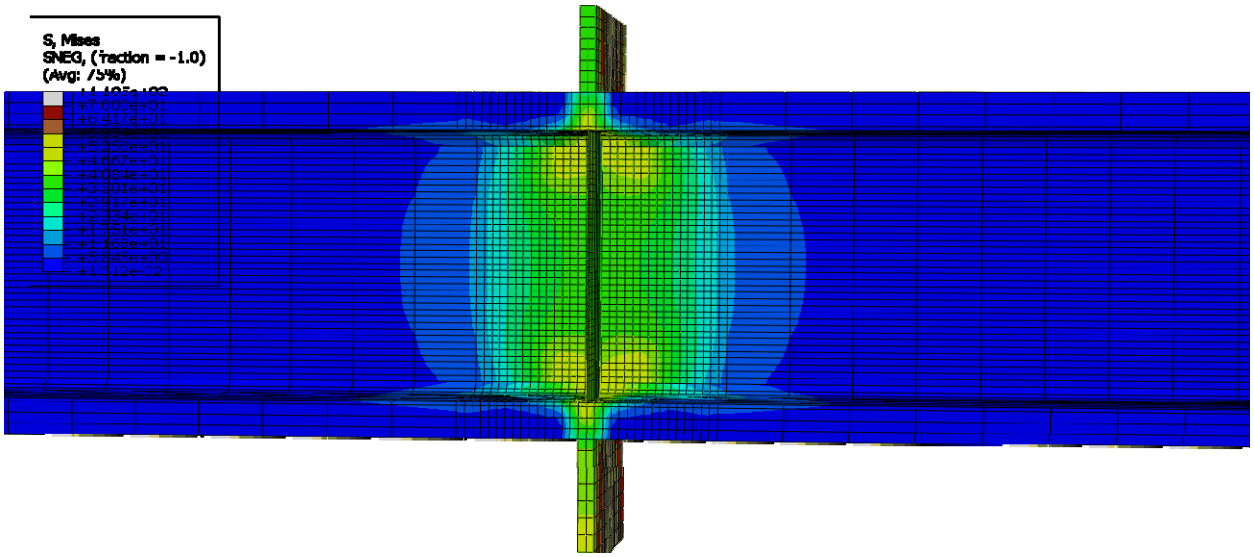

Figure E-251: Finite element model of W14X233-DC-E0 with 3/4 in. stiffeners during elastic behavior

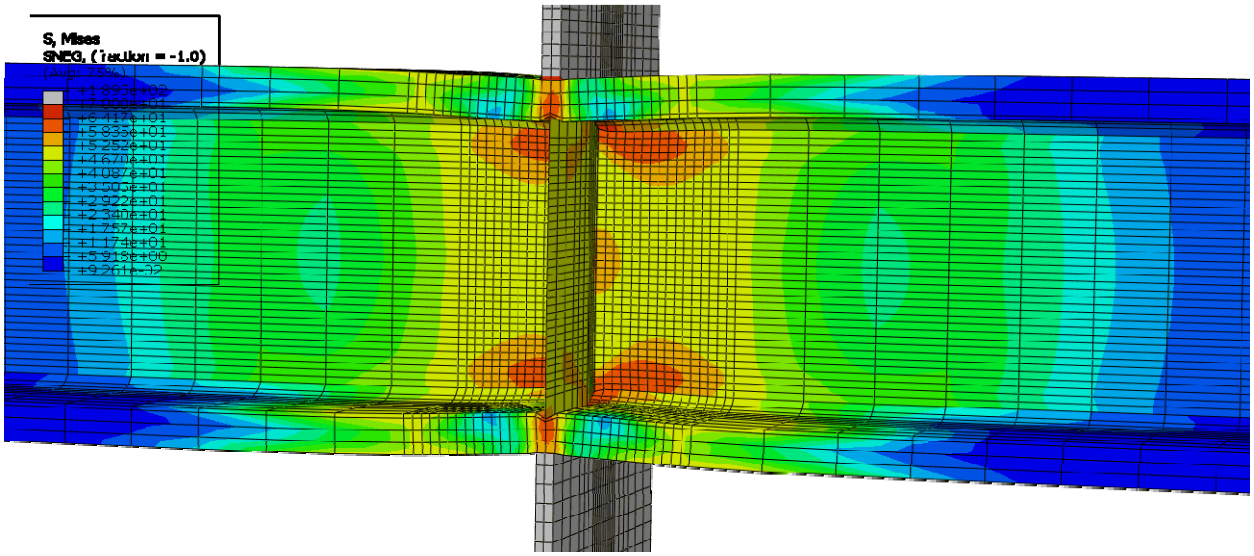

Figure E-252: Finite element model of W14X233-DC-E0 with 3/4 in. stiffeners during inelastic behavior

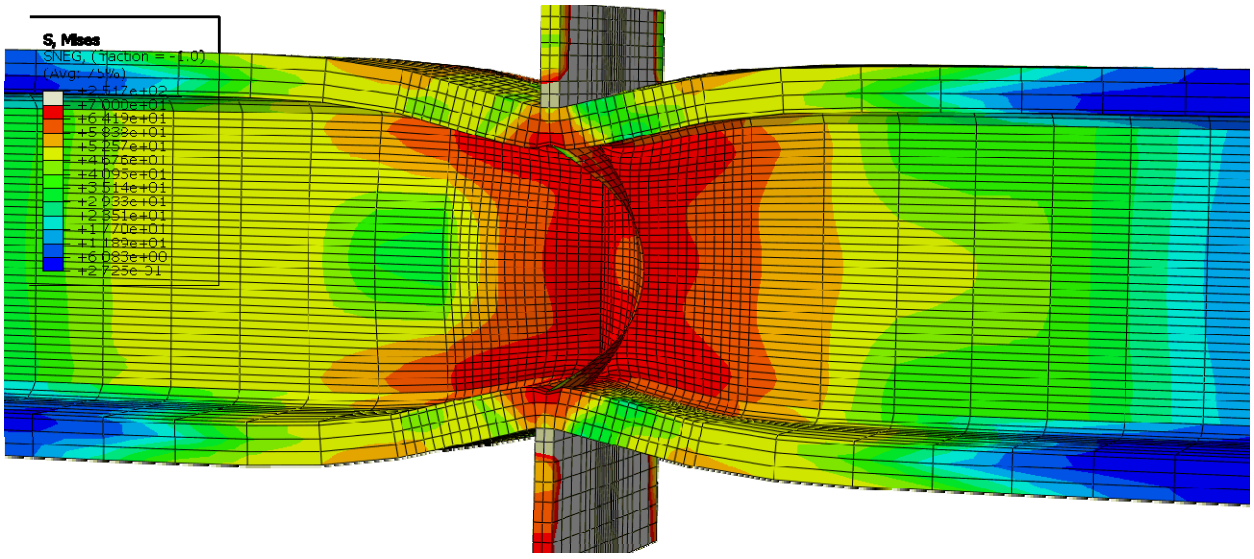

Figure E-253: Finite element model of W14X233-DC-E0 with 3/4 in. stiffeners after the maximum load

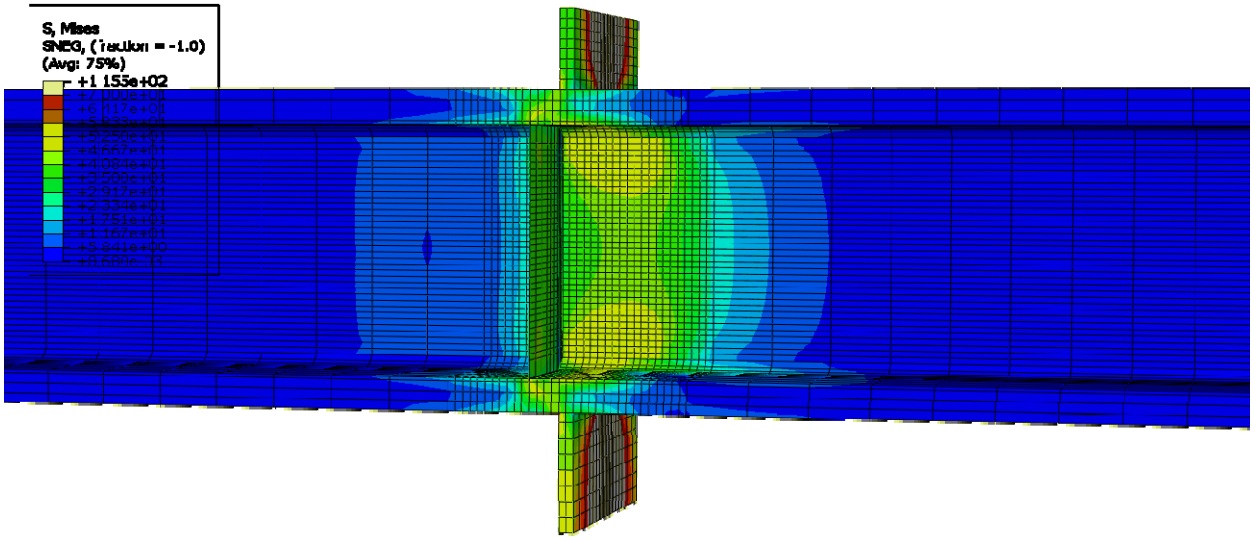

Figure E-254: Finite element model of W14X233-DC-E2 with 3/4 in. stiffeners during elastic behavior

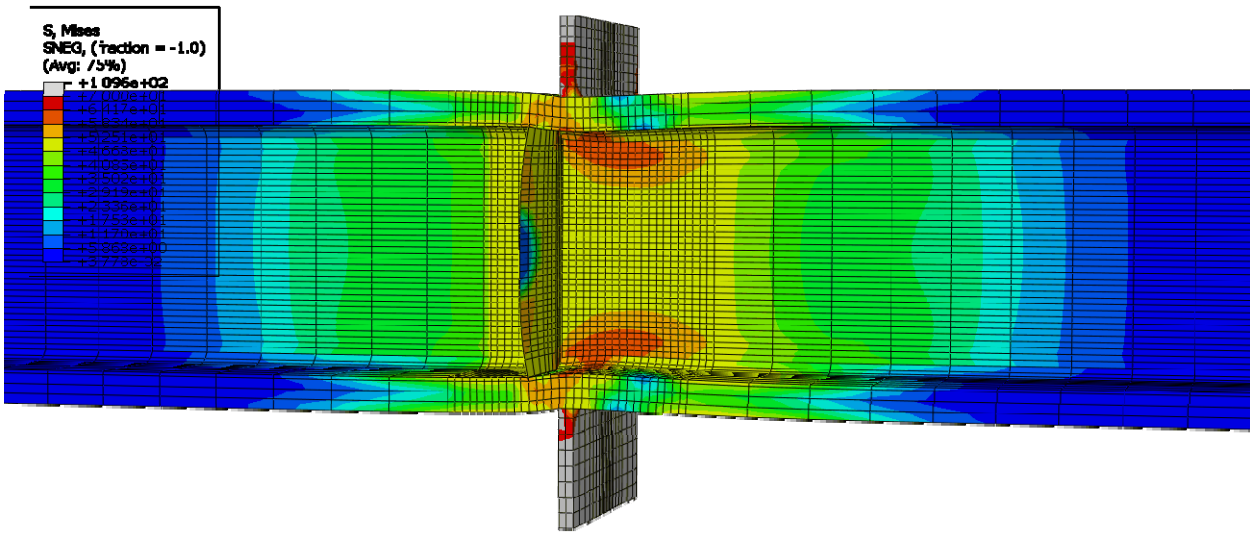

Figure E-255: Finite element model of W14X233-DC-E2 with 3/4 in. stiffeners during inelastic behavior

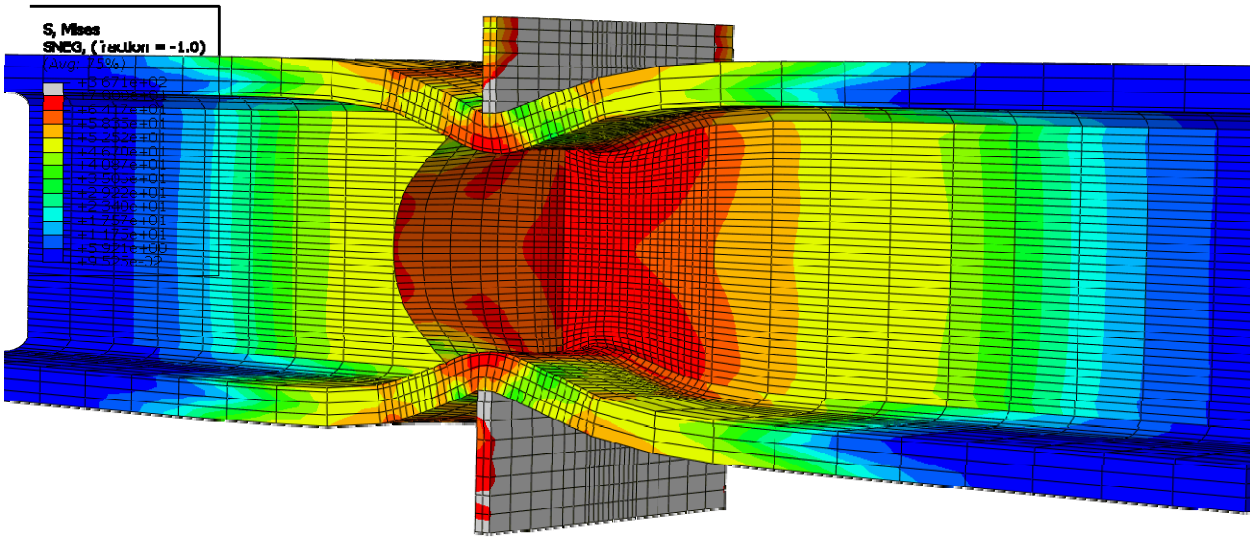

Figure E-256: Finite element model of W14X233-DC-E2 with 3/4 in. stiffeners after the maximum load

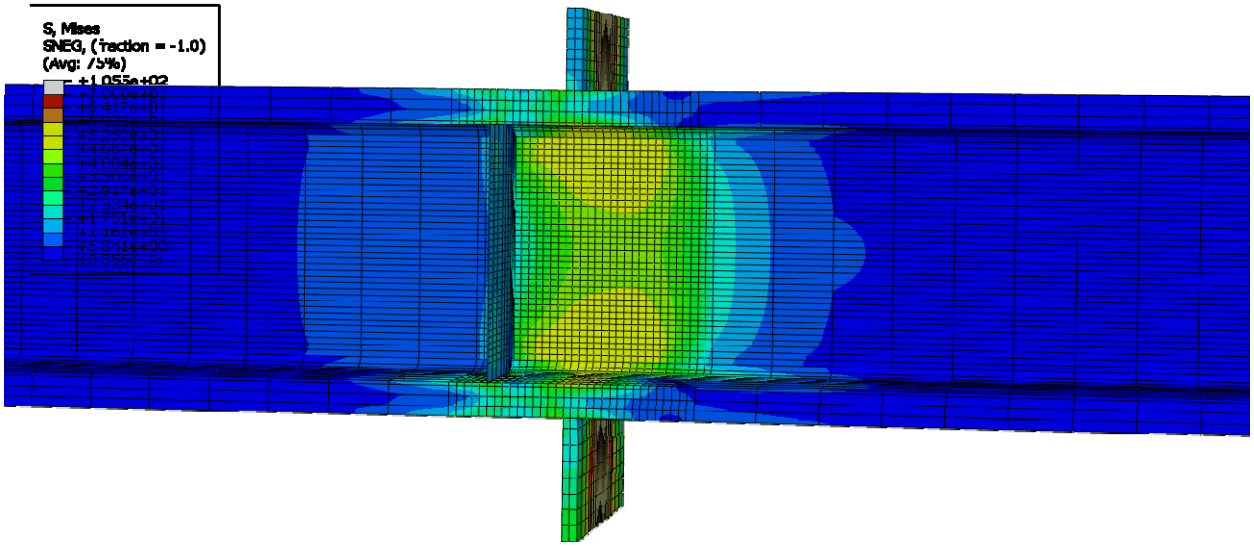

Figure E-257: Finite element model of W14X233-DC-E4 with 3/4 in. stiffeners during elastic behavior

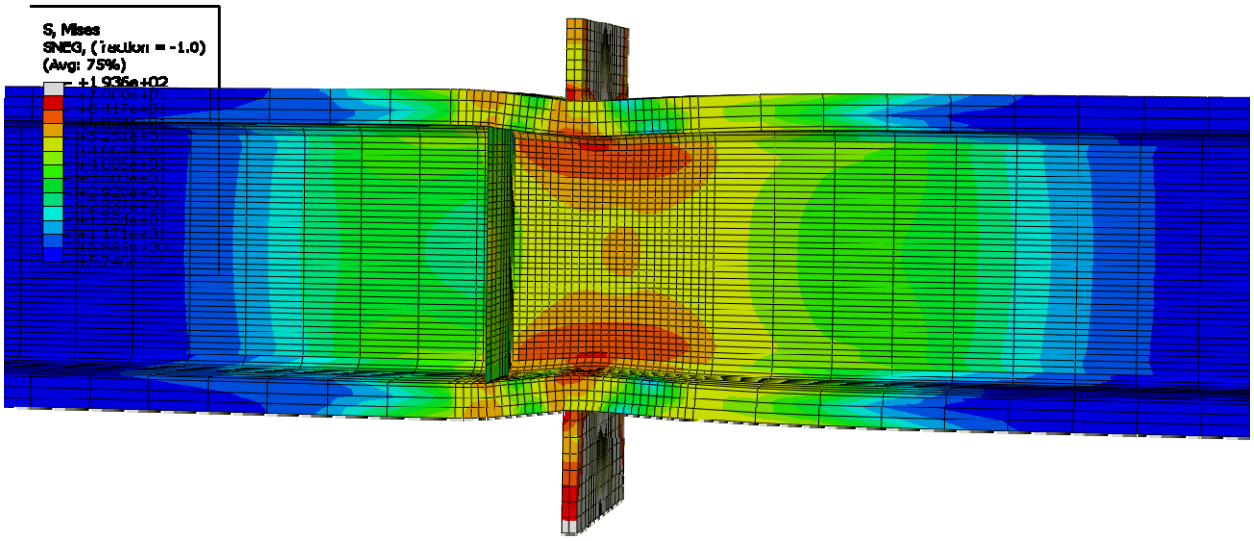

Figure E-258: Finite element model of W14X233-DC-E4 with 3/4 in. stiffeners during inelastic behavior

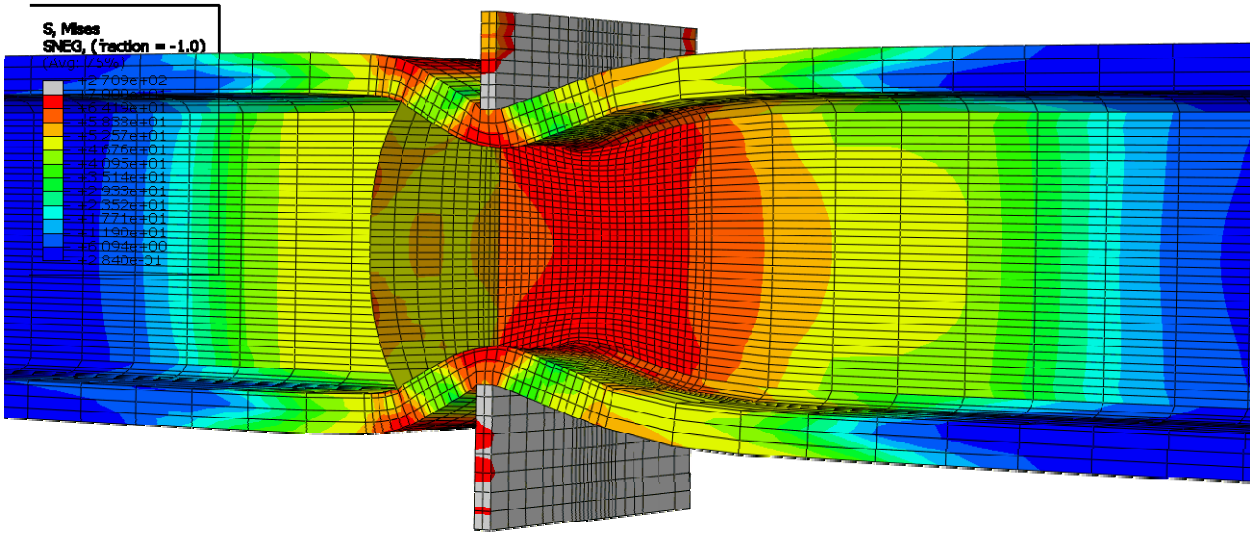

Figure E-259: Finite element model of W14X233-DC-E4 with 3/4 in. stiffeners after the maximum load

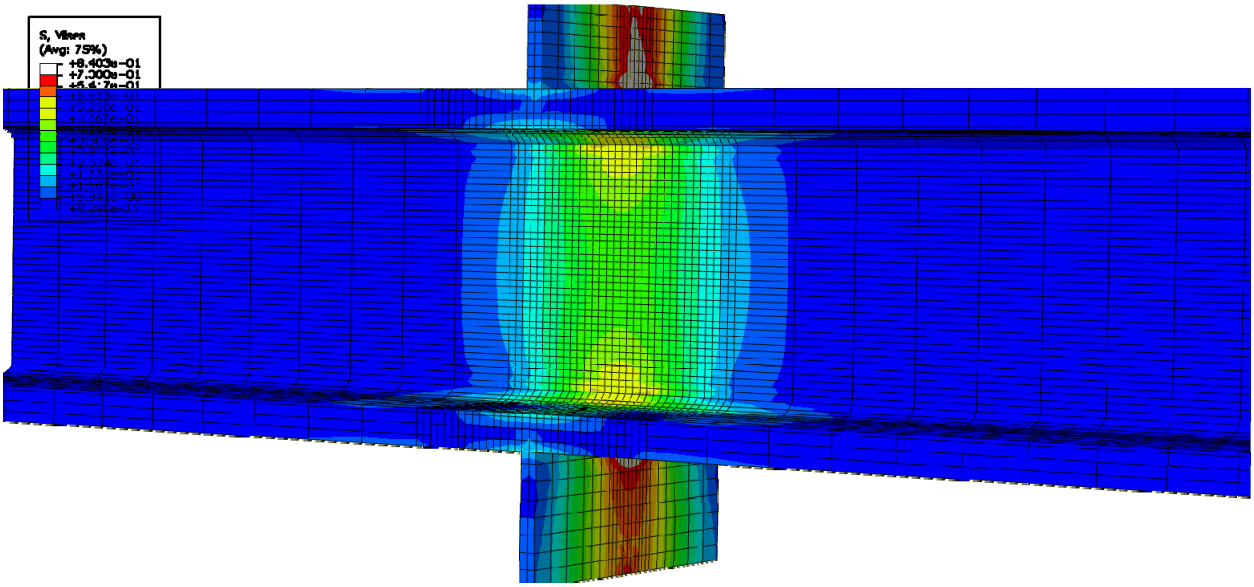

Figure E-260: Finite element model of W14X233-DC-NA during elastic behavior

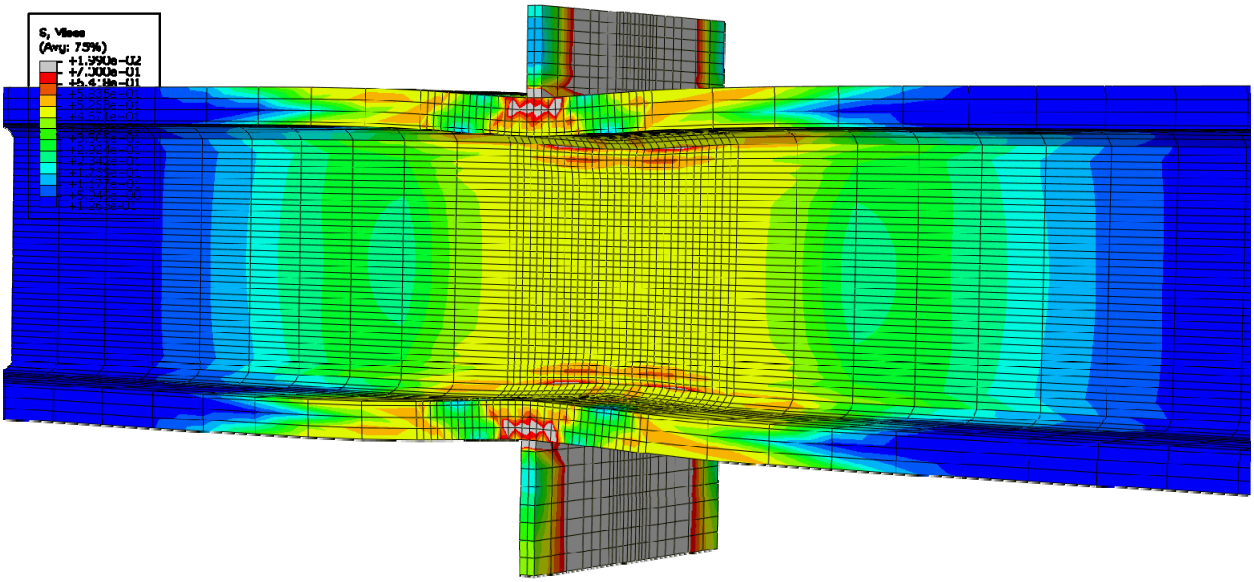

Figure E-261: Finite element model of W14X233-DC-NA during inelastic behavior

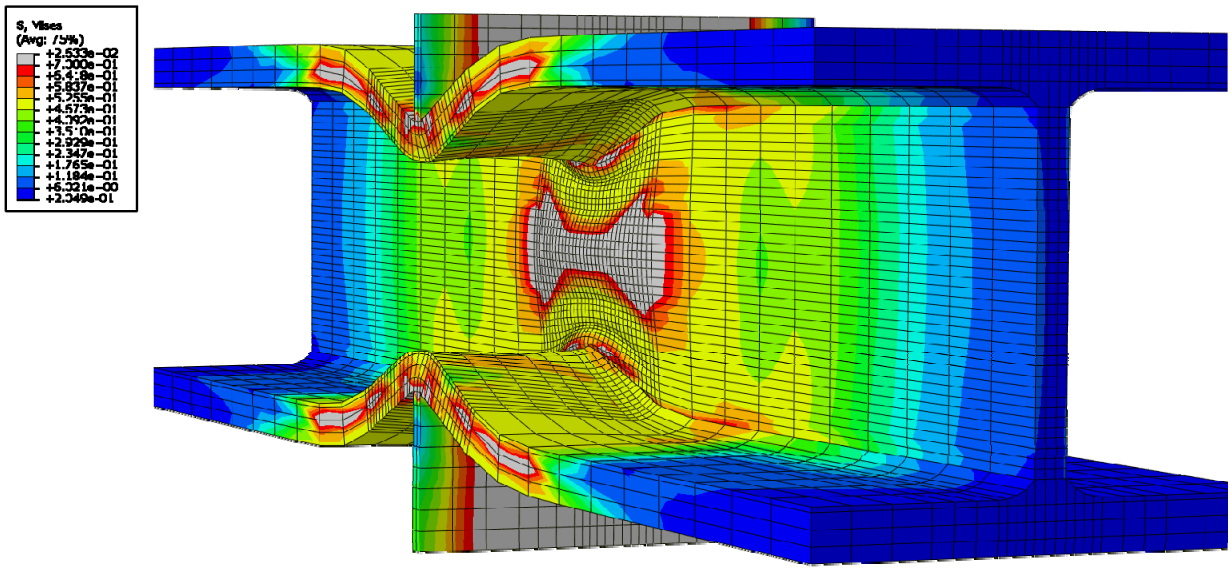

Figure E-262: Finite element model of W14X233-DC-NA after the maximum load showing inelastic web compression buckling

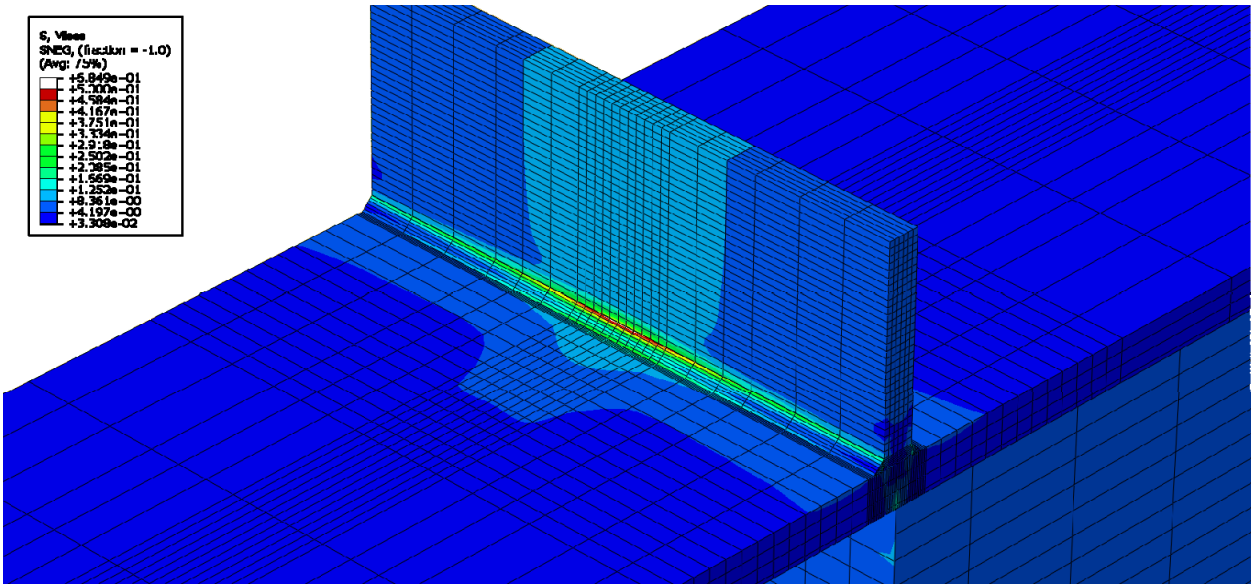

Figure E-Error! No text of specified style in document.**263: Finite element model of W24X131-ST-E0 with 1/4 in. welds while remaining elastic**

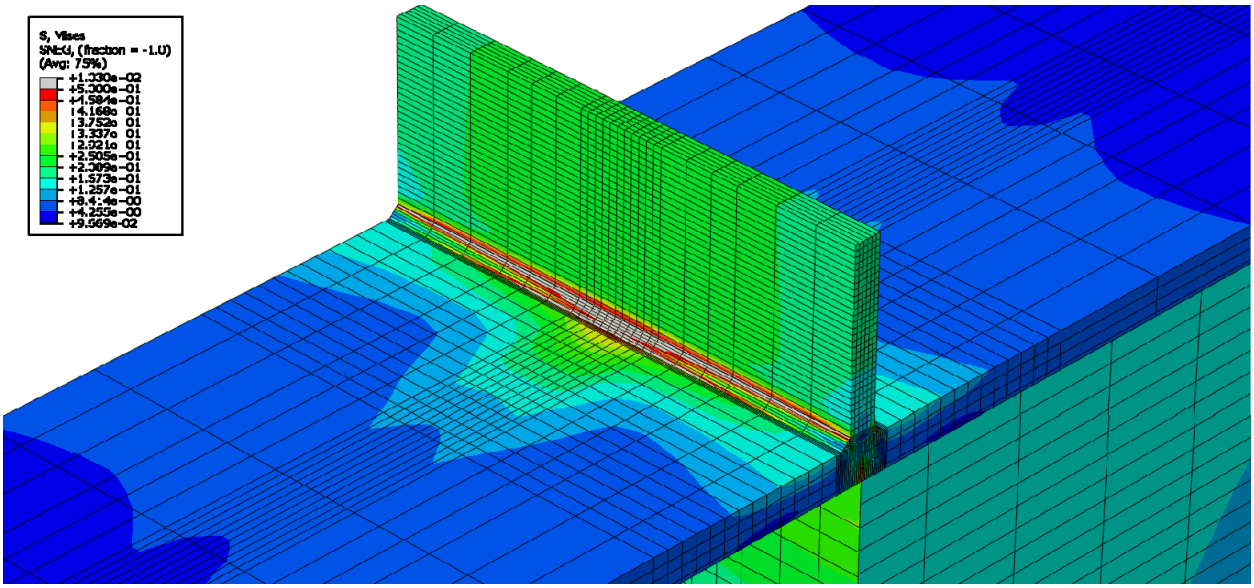

Figure E-264: Finite element model of W24X131-ST-E0 with 1/4 in. welds during inelastic behavior

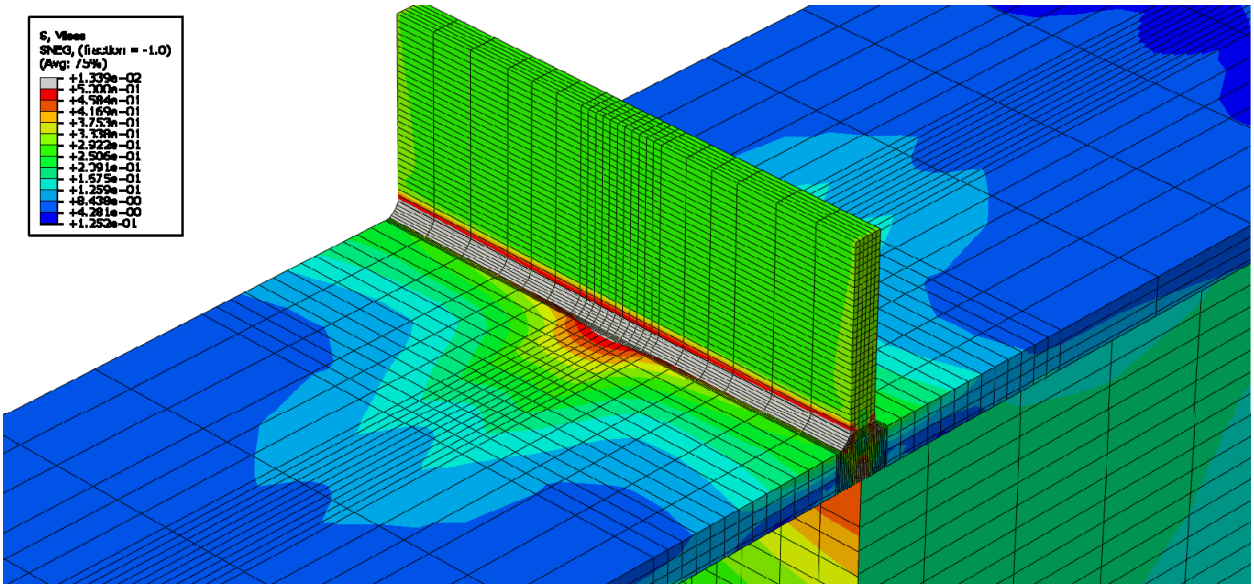

Figure E-265: Finite element model of W24X131-ST-E0 with 1/4 in. welds at its load capacity of 215.58 kips

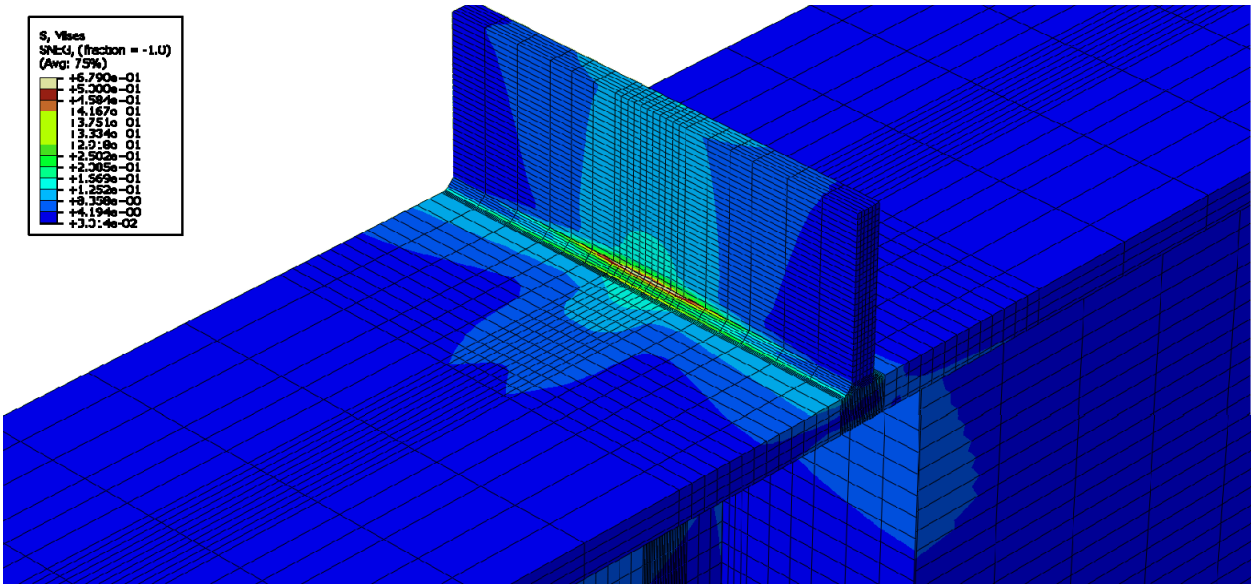

Figure E-266: Finite element model of W24X131-ST-E2 with 1/4 in. welds while remaining elastic

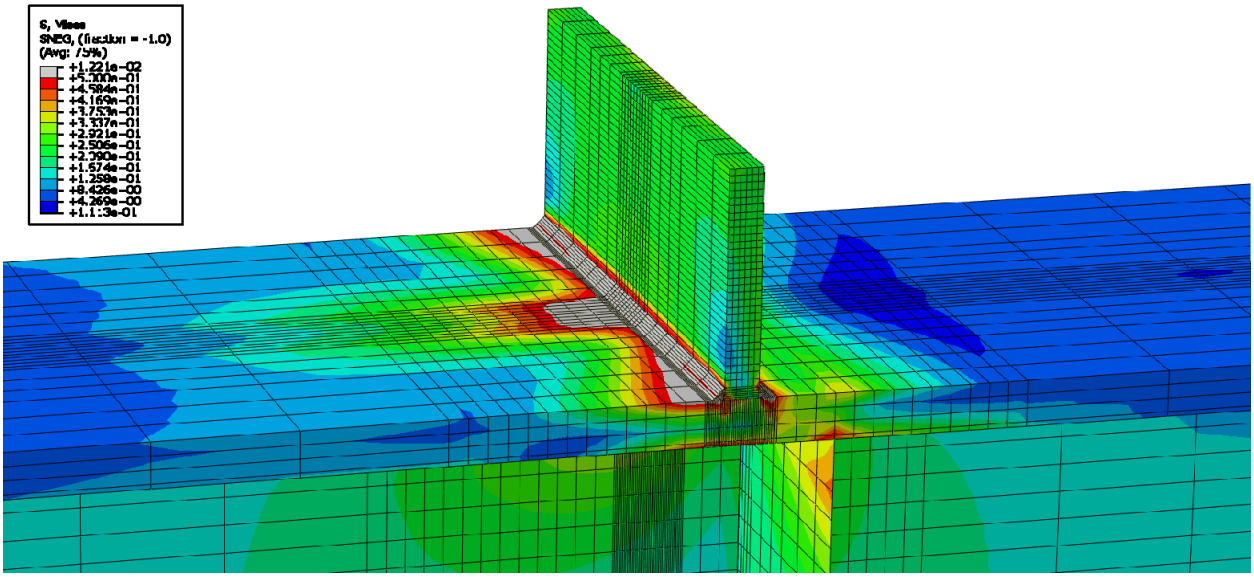

Figure E-267: Finite element model of W24X131-ST-E2 with 1/4 in. welds during inelastic behavior

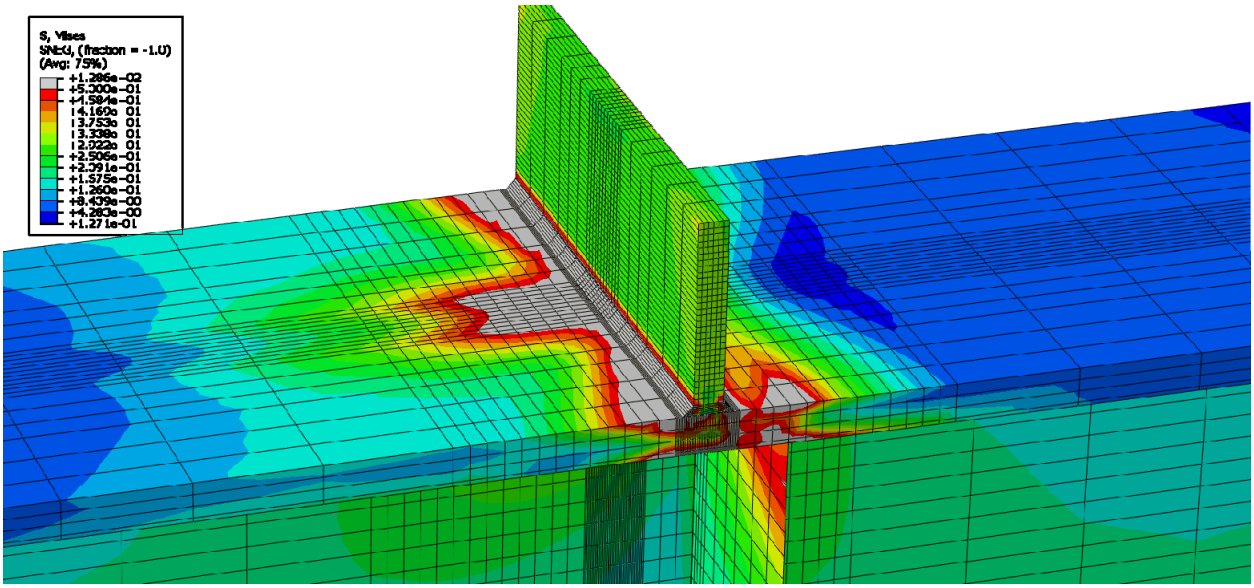

Figure E-268: Finite element model of W24X131-ST-E0 with 1/4 in. welds at its load capacity of 257.88 kips

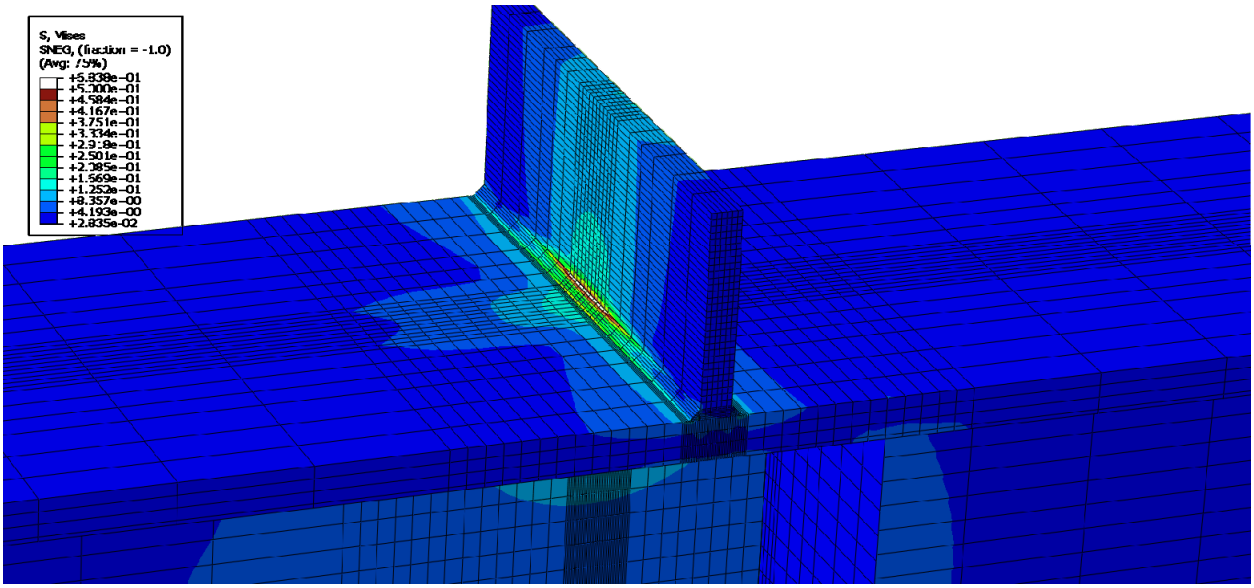

Figure E-269: Finite element model of W24X131-ST-E4 with 1/4 in. welds while remaining elastic

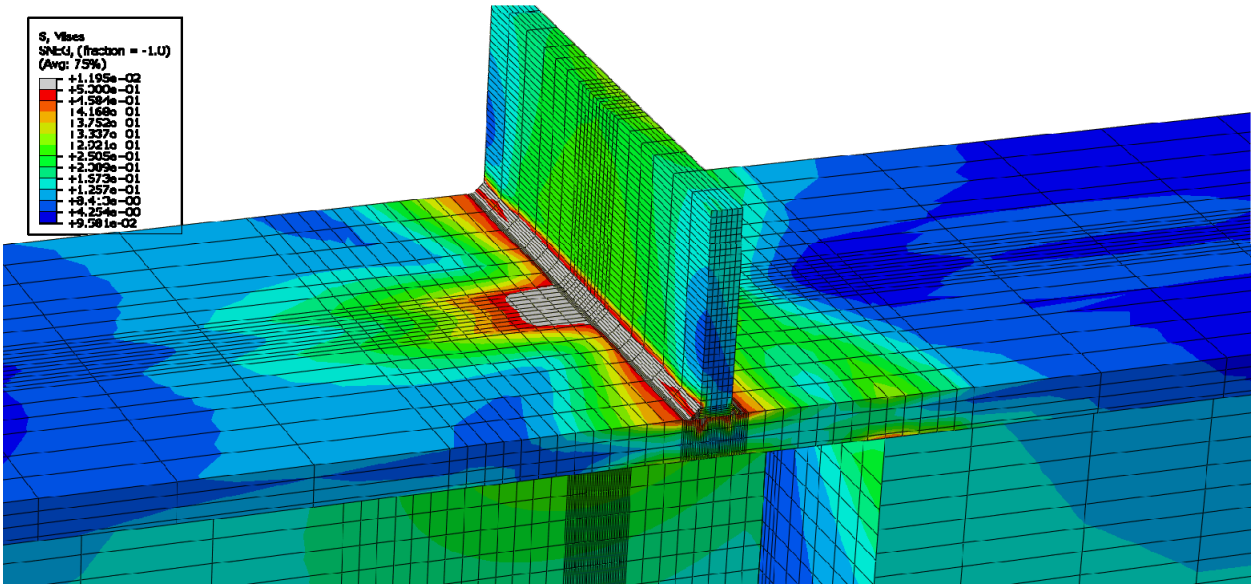

Figure E-270: Finite element model of W24X131-ST-E4 with 1/4 in. welds during inelastic behavior

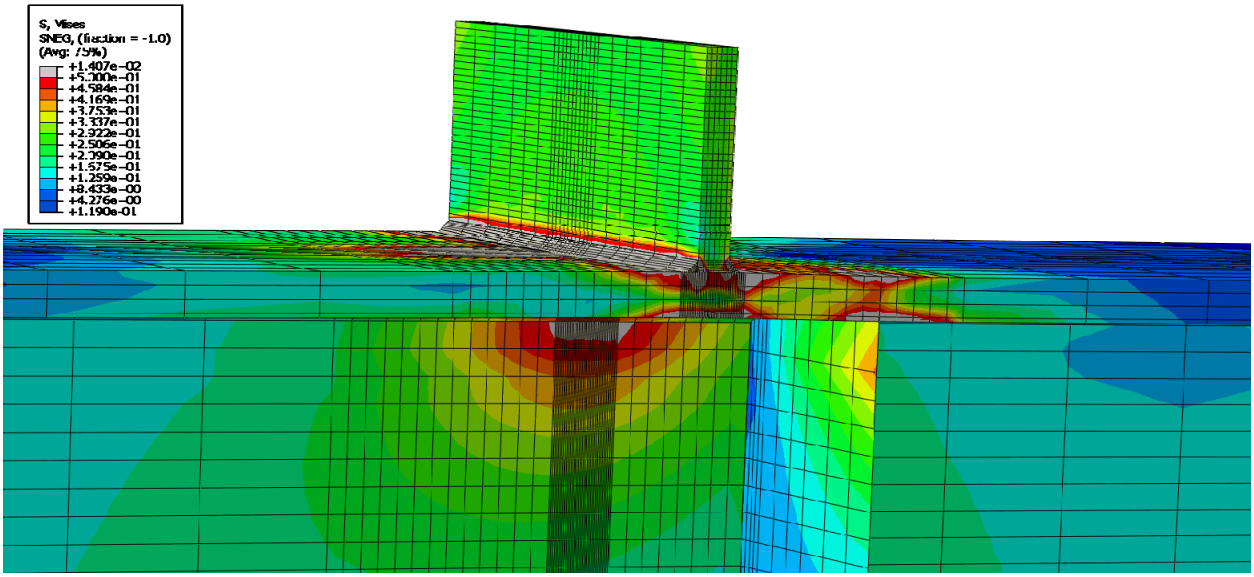

Figure E-271: Finite element model of W24X131-ST-E4 with 1/4 in. welds at its load capacity of 235.43 kips

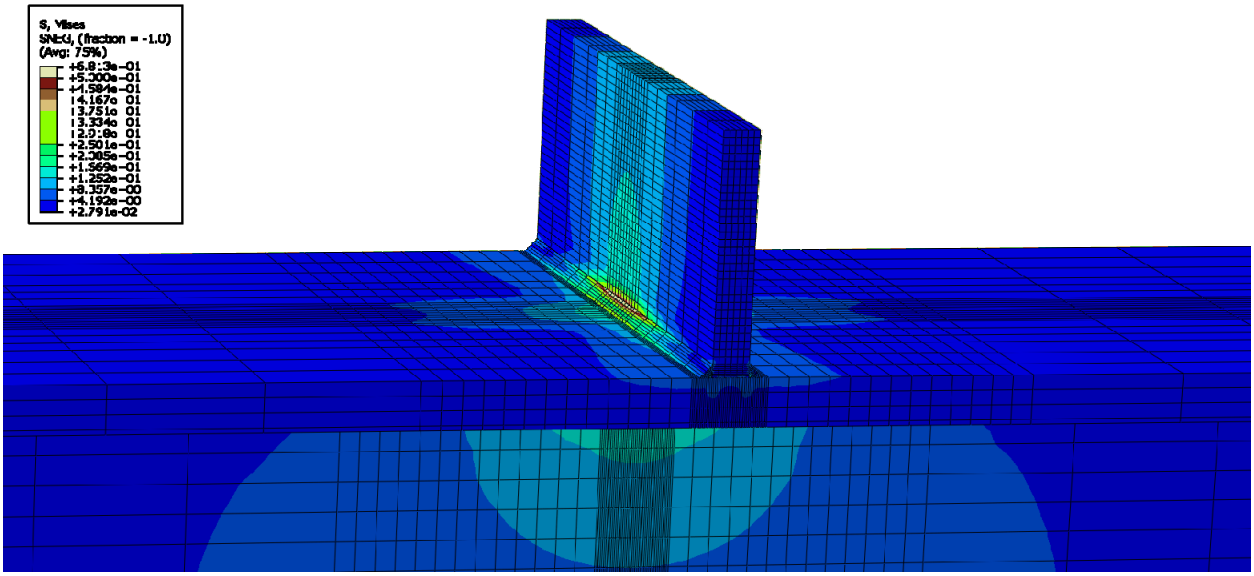

Figure E-272: Finite element model of W24X131-ST-NA with 1/4 in. welds while remaining elastic

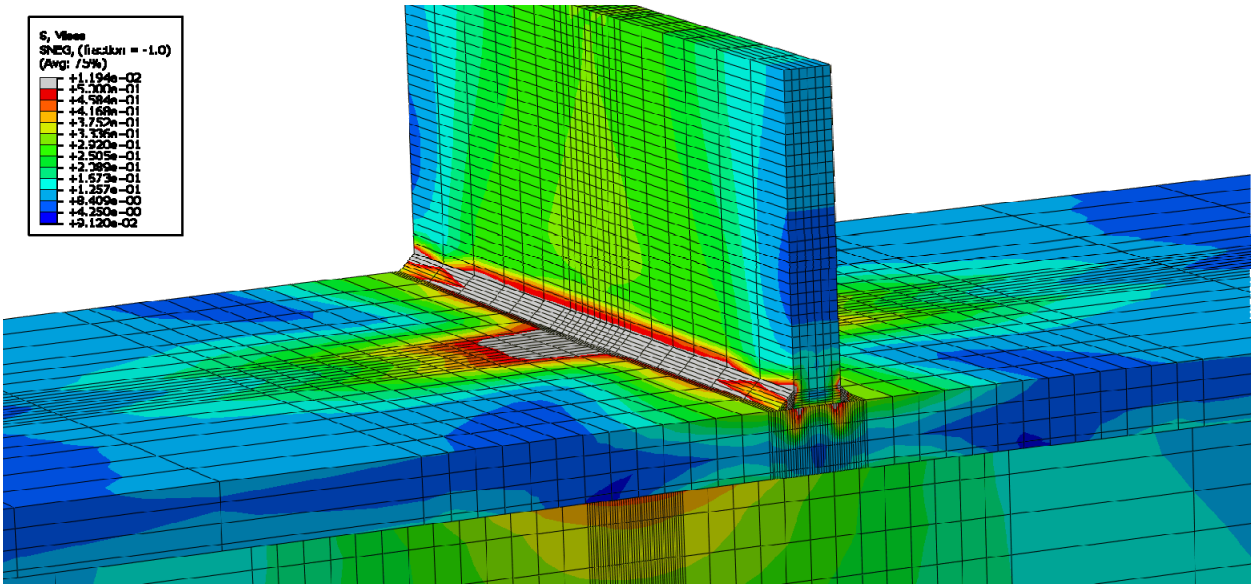

Figure E-273: Finite element model of W24X131-ST-NA with 1/4 in. welds during inelastic behavior

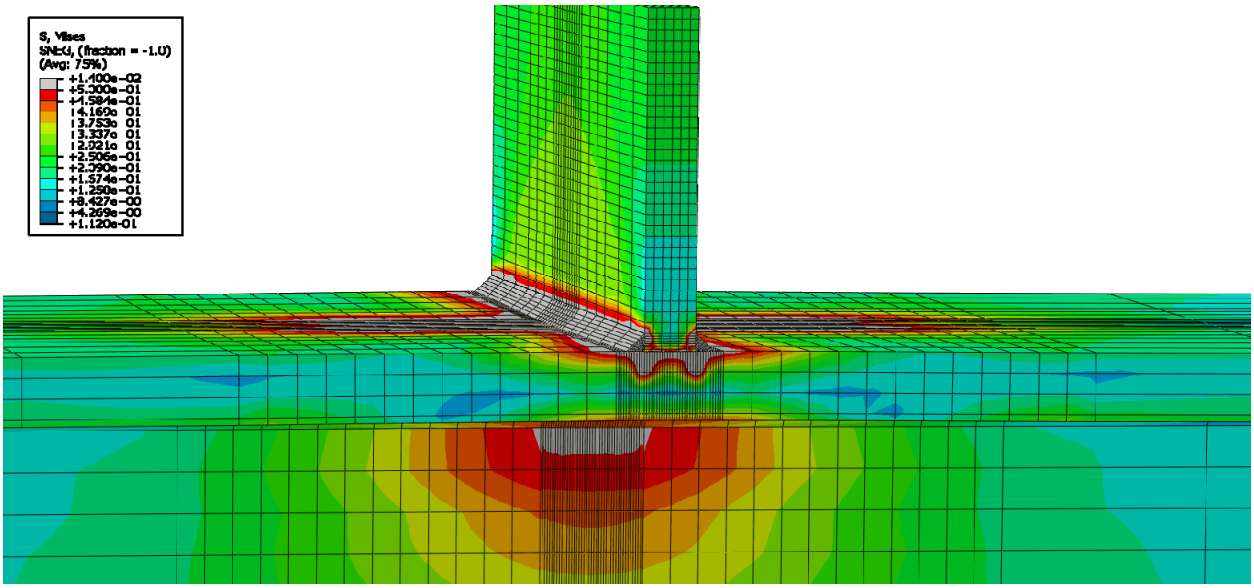

Figure E-274: Finite element model of W24X131-ST-NA with 1/4 in. welds at its load capacity of 215.58 kips

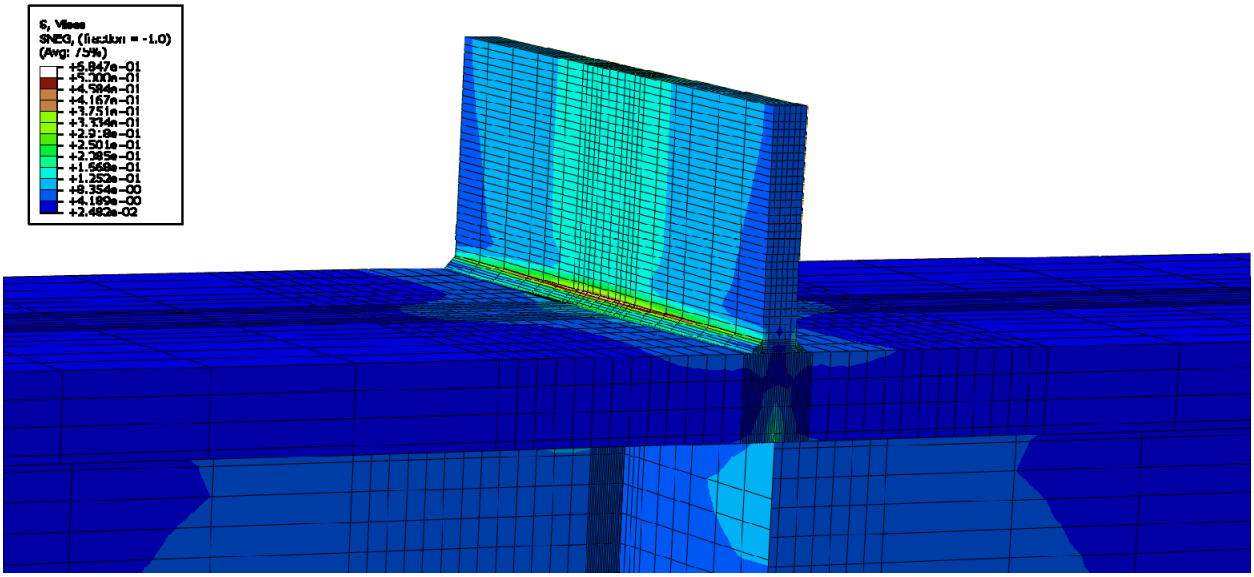

Figure E-275: Finite element model of W24X229-ST-E0 with 1/4 in. welds while remaining elastic

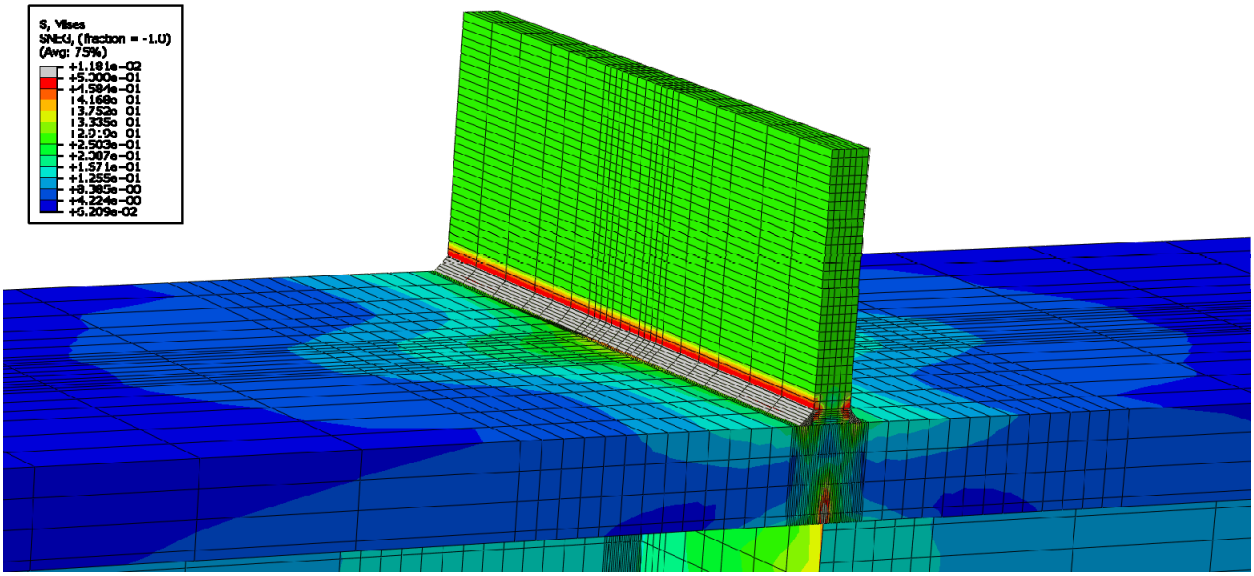

Figure E-276: Finite element model of W24X229-ST-E0 with 1/4 in. welds during inelastic behavior

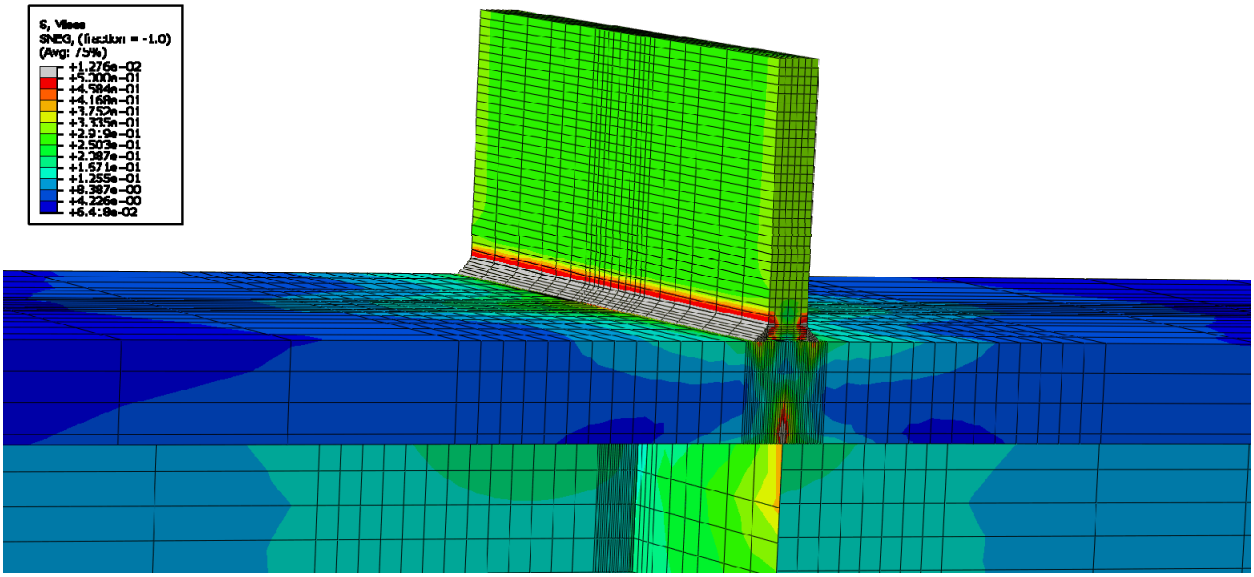

Figure E-277: Finite element model of W24X229-ST-E0 with 1/4 in. welds at its load capacity of 263.57 kips

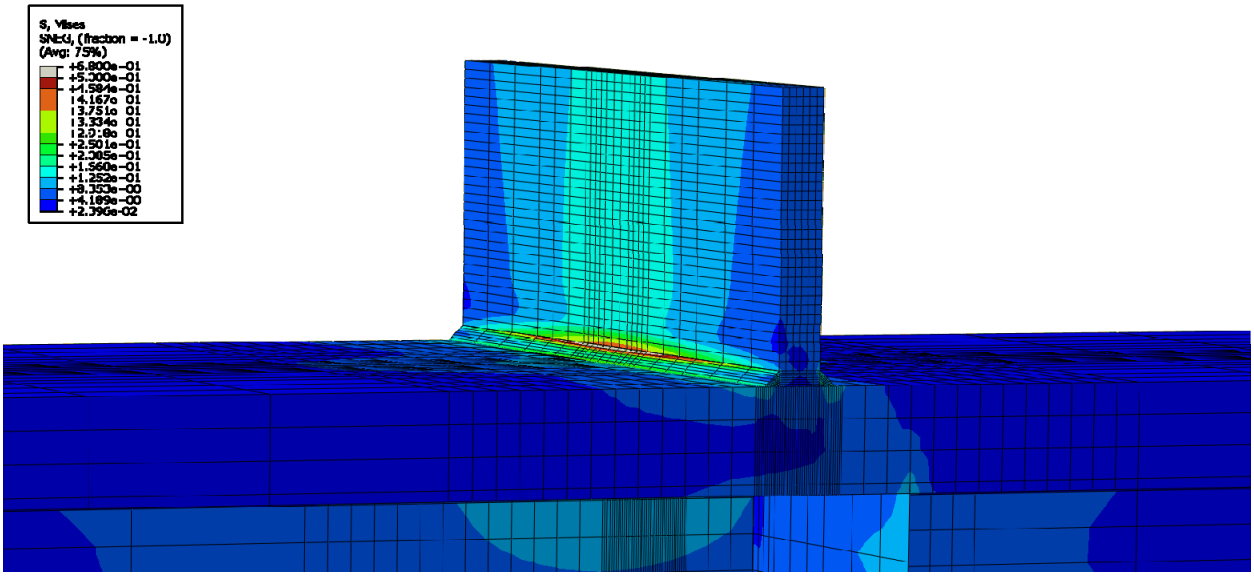

Figure E-278: Finite element model of W24X229-ST-E2 with 1/4 in. welds while remaining elastic

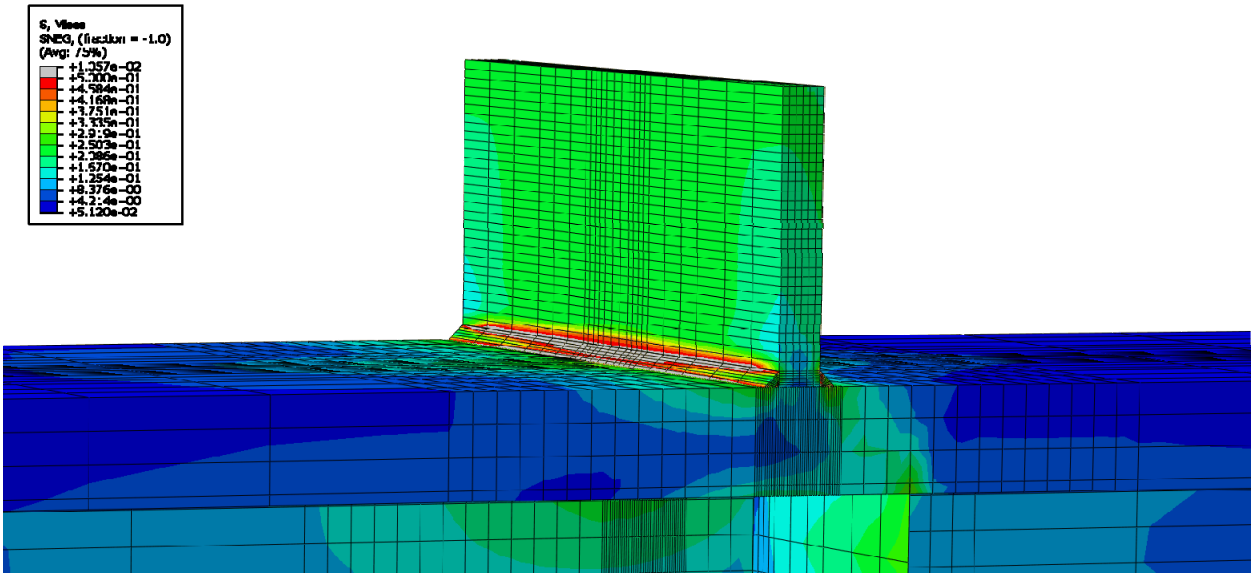

Figure E-279: Finite element model of W24X229-ST-E2 with 1/4 in. welds during inelastic behavior

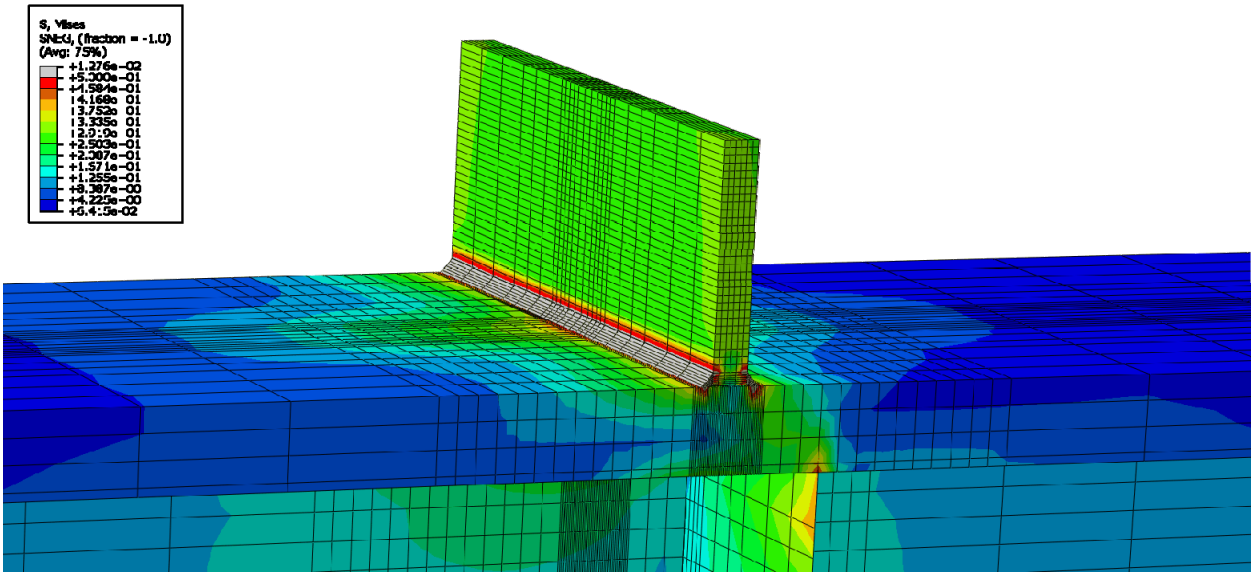

Figure E-280: Finite element model of W24X229-ST-E2 with 1/4 in. welds at its load capacity of 263.15 kips

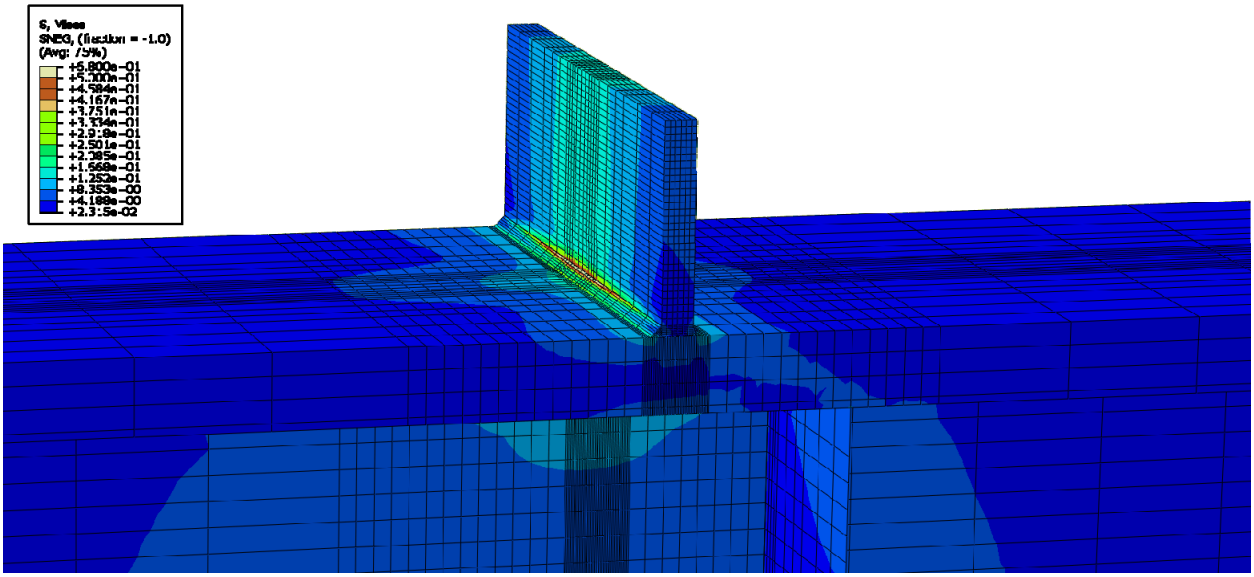

Figure E-281: Finite element model of W24X229-ST-E4 with 1/4 in. welds while remaining elastic

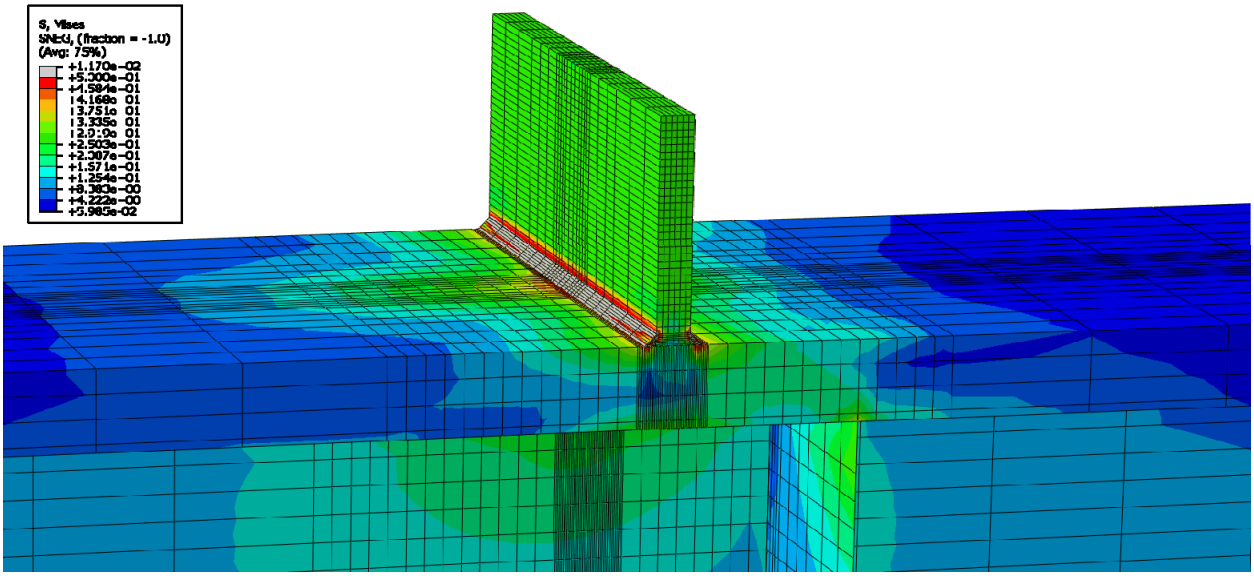

Figure E-282: Finite element model of W24X229-ST-E4 with 1/4 in. welds during inelastic behavior

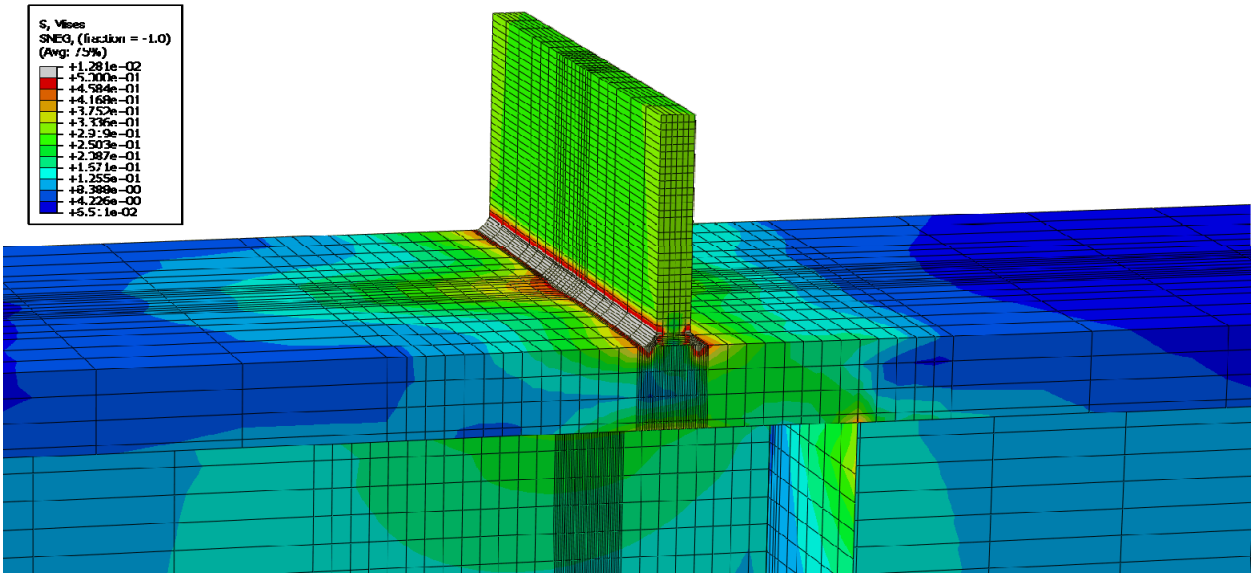

Figure E-283: Finite element model of W24X229-ST-E0 with 1/4 in. welds at its load capacity of 263.11 kips

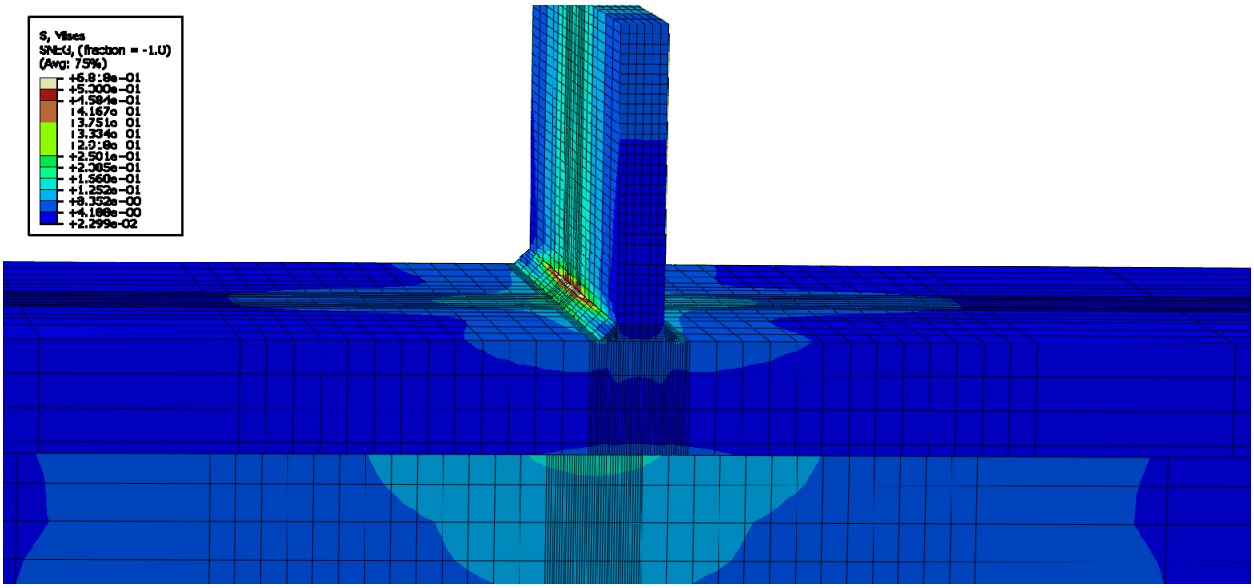

Figure E-284: Finite element model of W24X229-ST-NA with 1/4 in. welds while remaining elastic

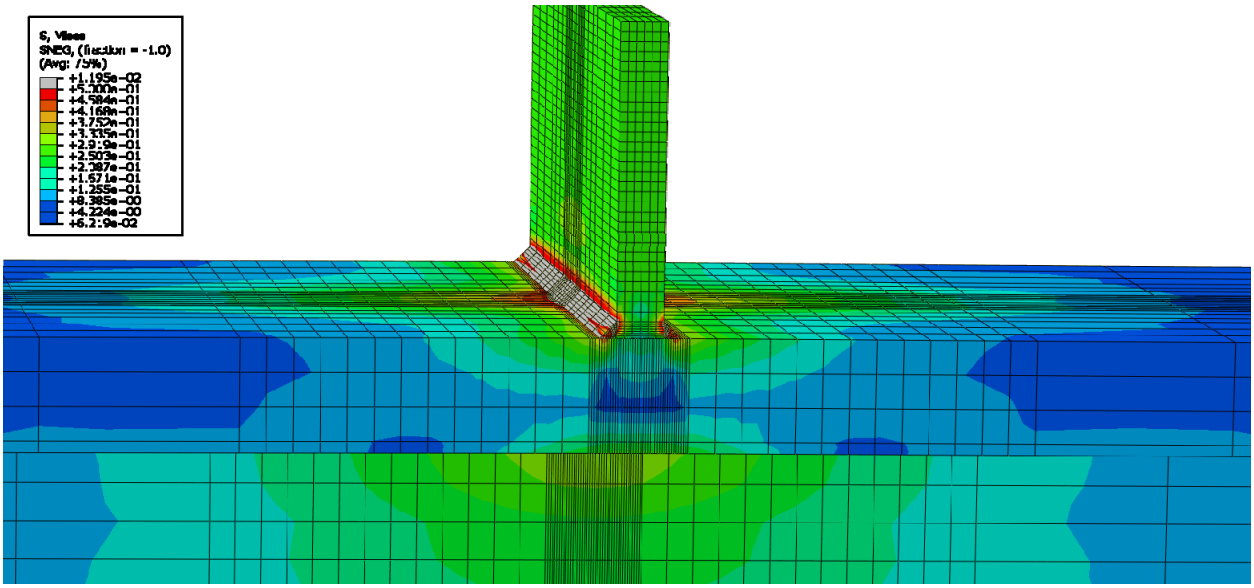

Figure E-285: Finite element model of W24X229-ST-E0 with 1/4 in. welds during inelastic behavior

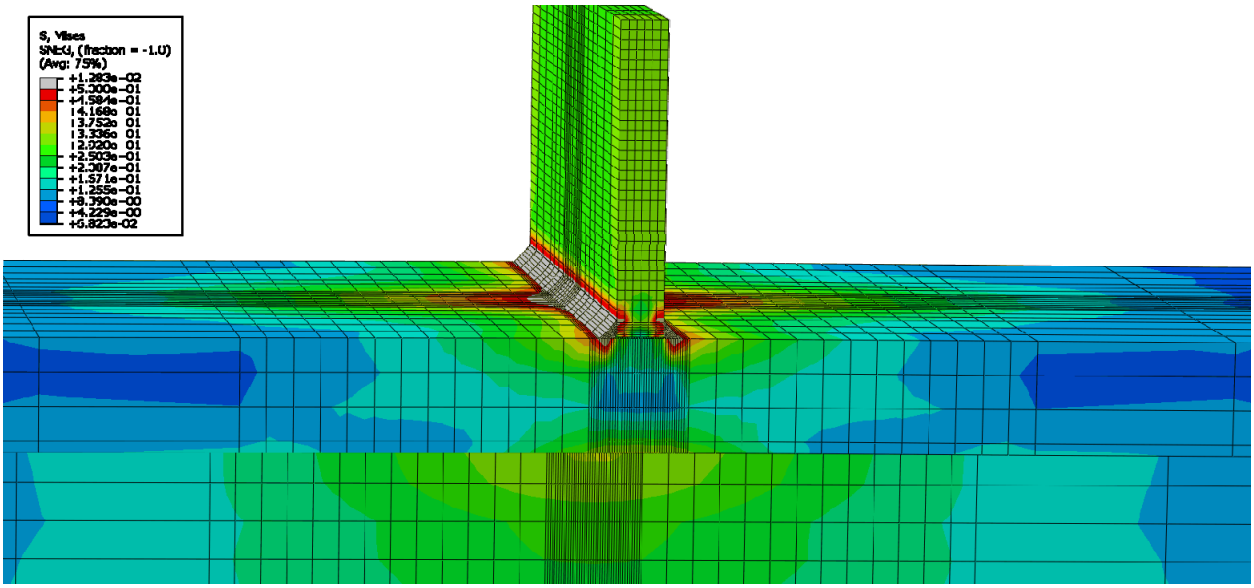

Figure E-286: Finite element model of W24X229-ST-E0 with 1/4 in. welds at its load capacity of 262.99 kips

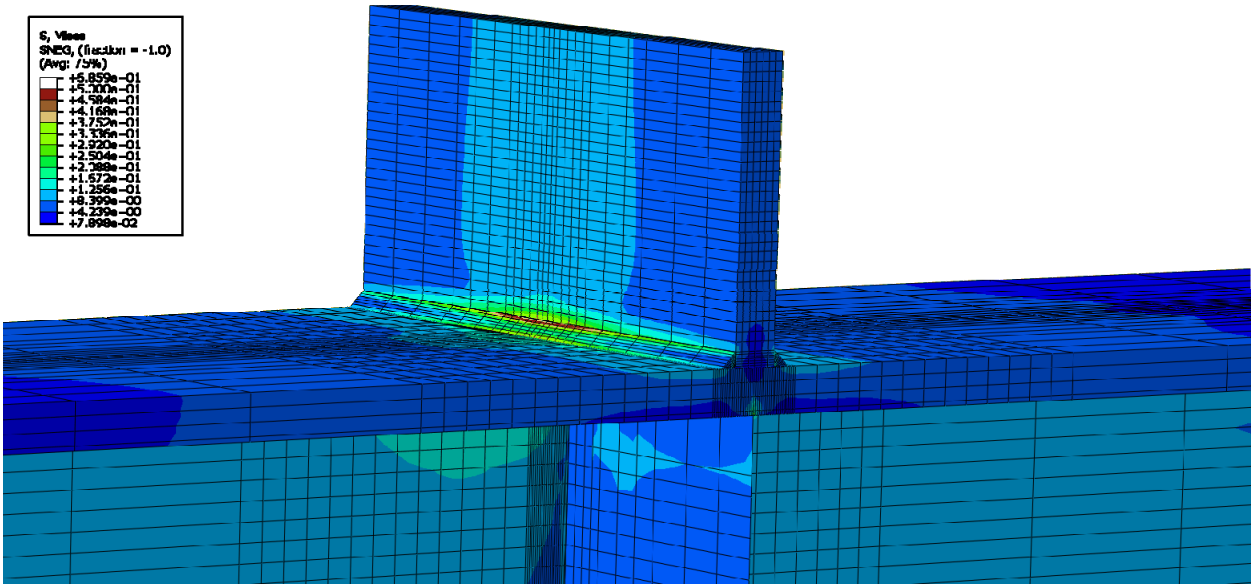

Figure E-287: Finite element model of W14X68-ST-E0 with 1/4 in. welds while remaining elastic

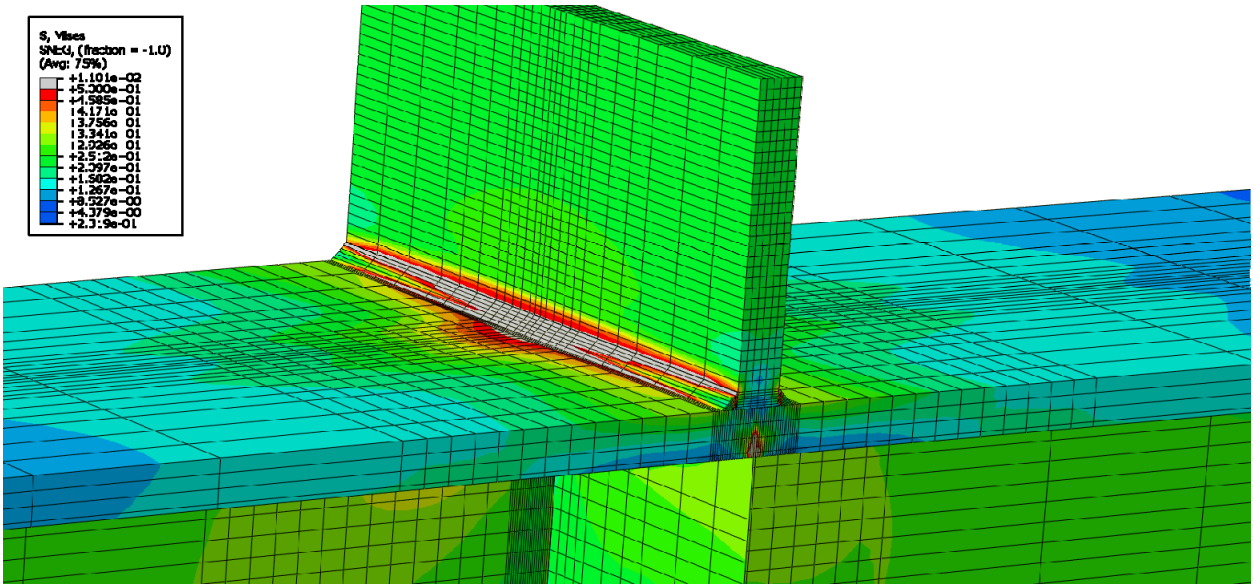

Figure E-288: Finite element model of W14X68-ST-E0 with 1/4 in. welds during inelastic behavior

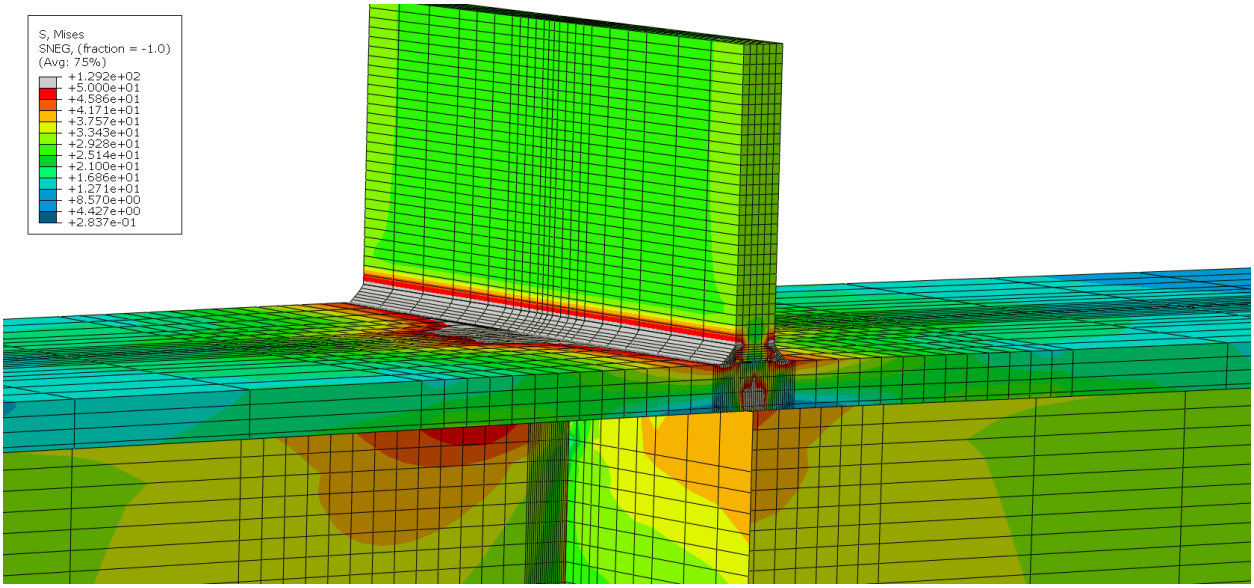

Figure E-289: Finite element model of W14X68-ST-E0 with 1/4 in. welds at its load capacity of 200.37 kips

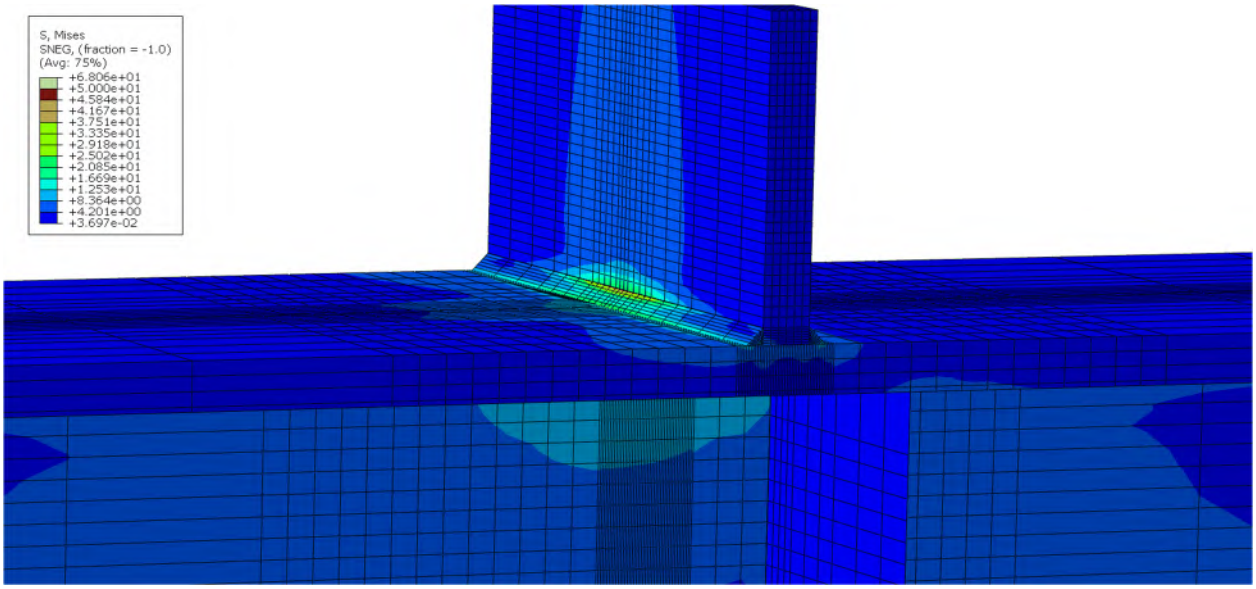

Figure E-290: Finite element model of W14X68-ST-E2 with 1/4 in. welds while remaining elastic

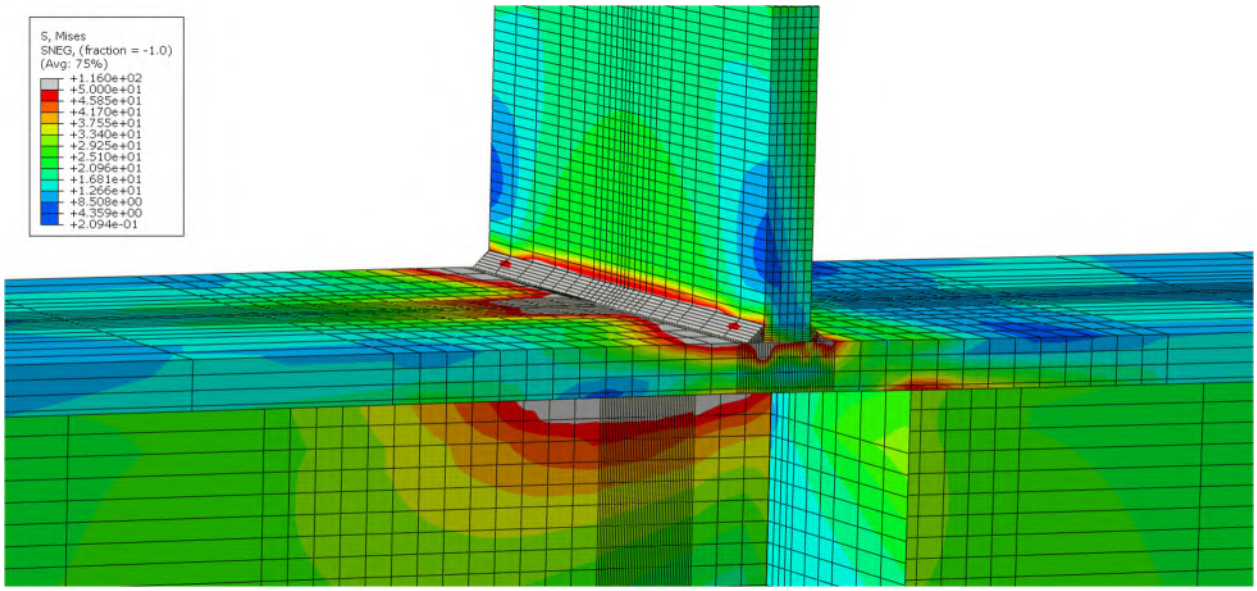

Figure E-291: Finite element model of W14X68-ST-E2 with 1/4 in. welds during inelastic behavior

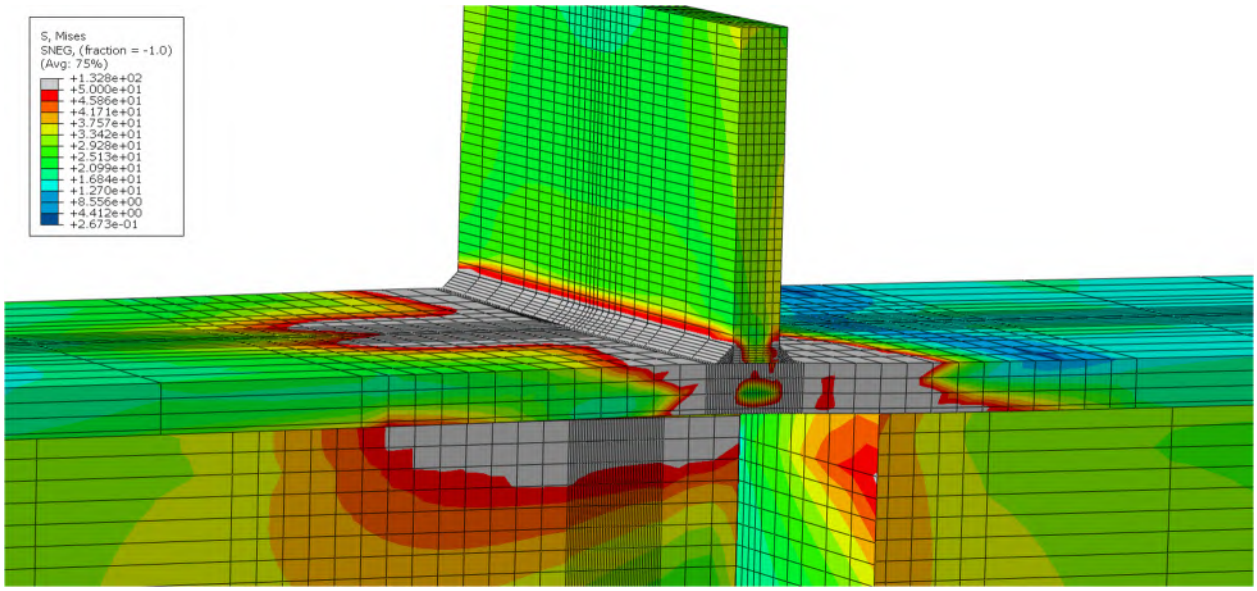

Figure E-292: Finite element model of W14X68-ST-E2 with 1/4 in. welds at its load capacity of 190.57 kips

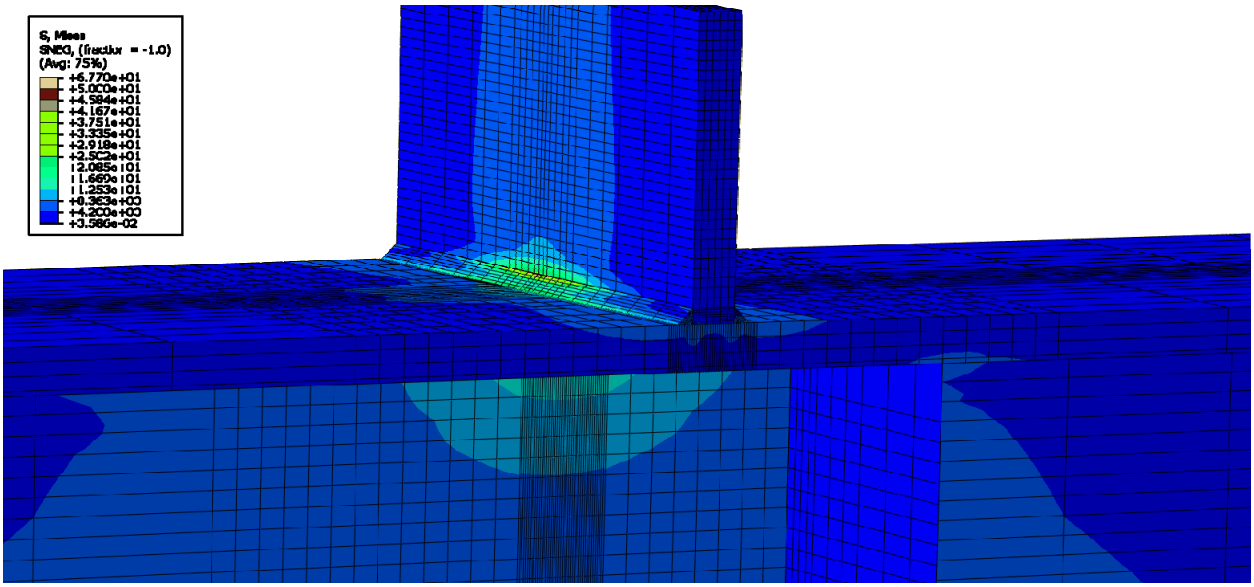

Figure E-293: Finite element model of W14X68-ST-E4 with 1/4 in. welds while remaining elastic

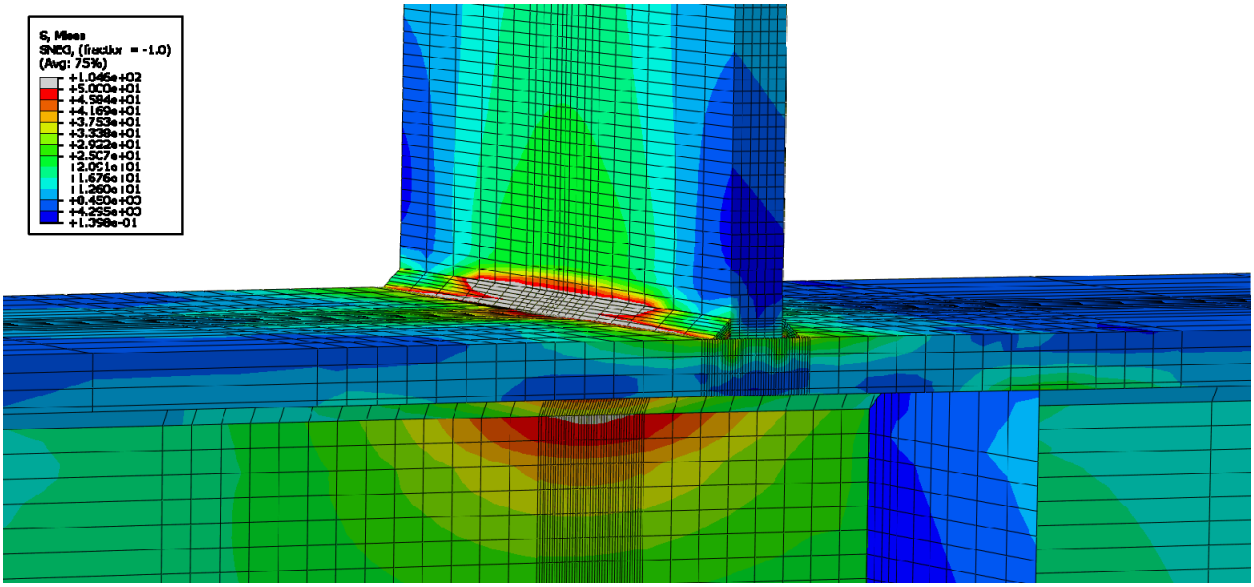

Figure E-294: Finite element model of W14X68-ST-E4 with 1/4 in. welds during inelastic behavior

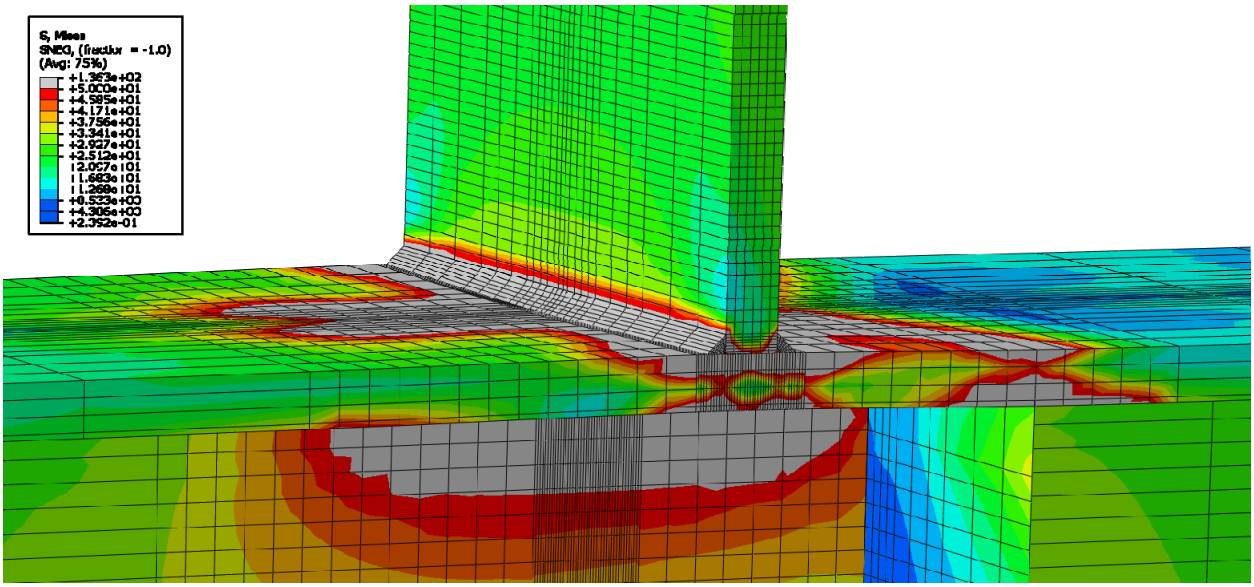

Figure E-295: Finite element model of W14X68-ST-E4 with 1/4 in. welds at its load capacity of 169.42 kips

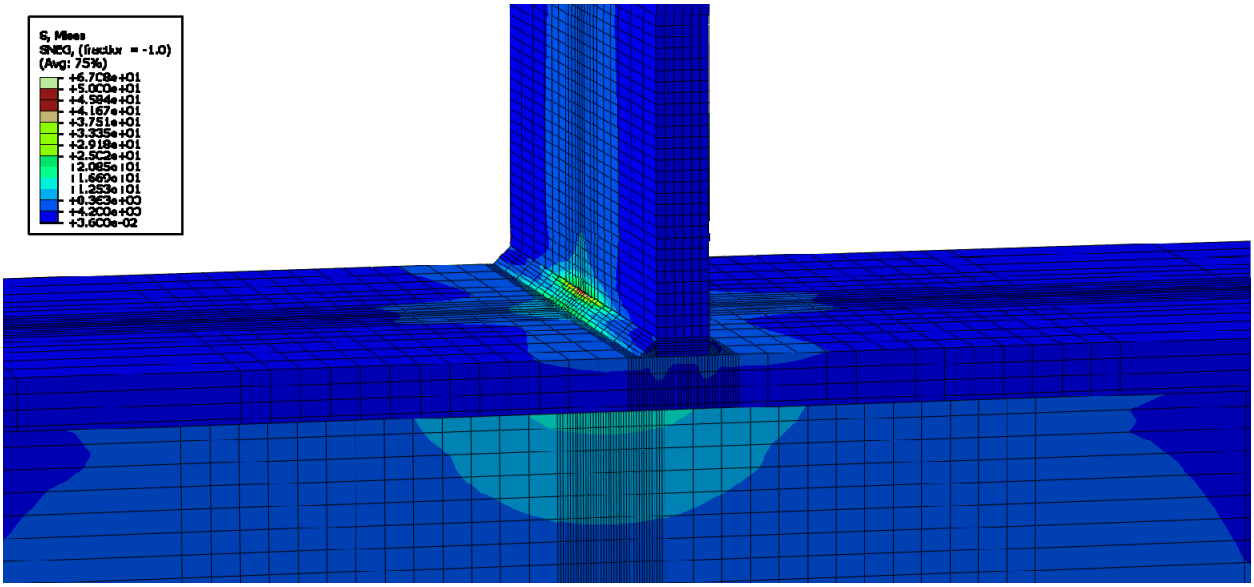

Figure E-296: Finite element model of W14X68-ST-NA with 1/4 in. welds while remaining elastic

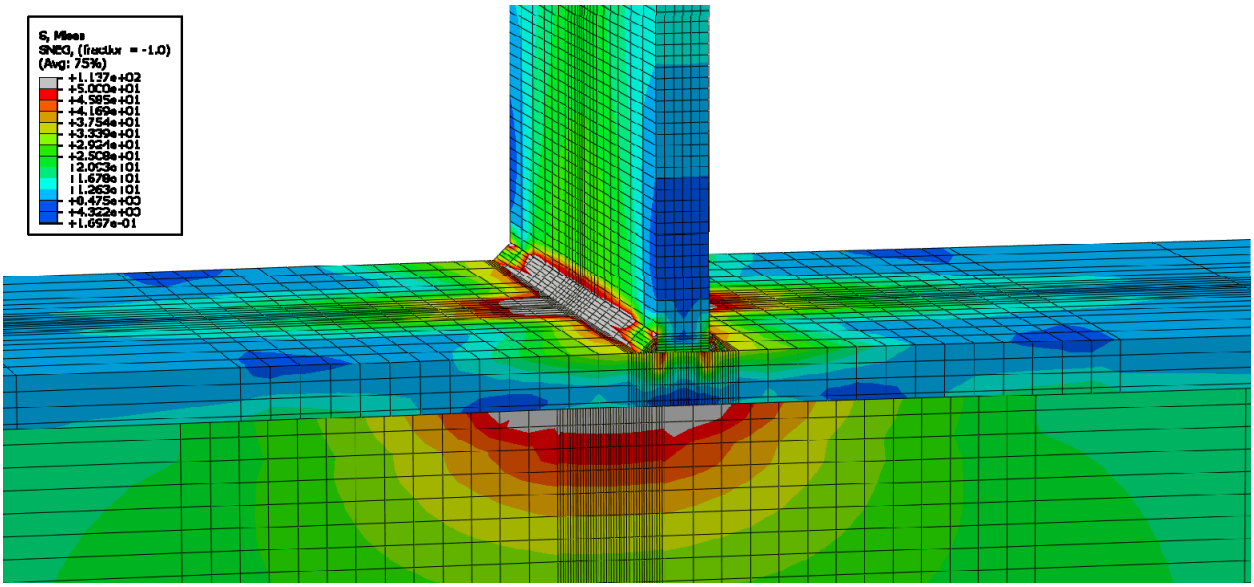

Figure E-297: Finite element model of W14X68-ST-NA with 1/4 in. welds during inelastic behavior

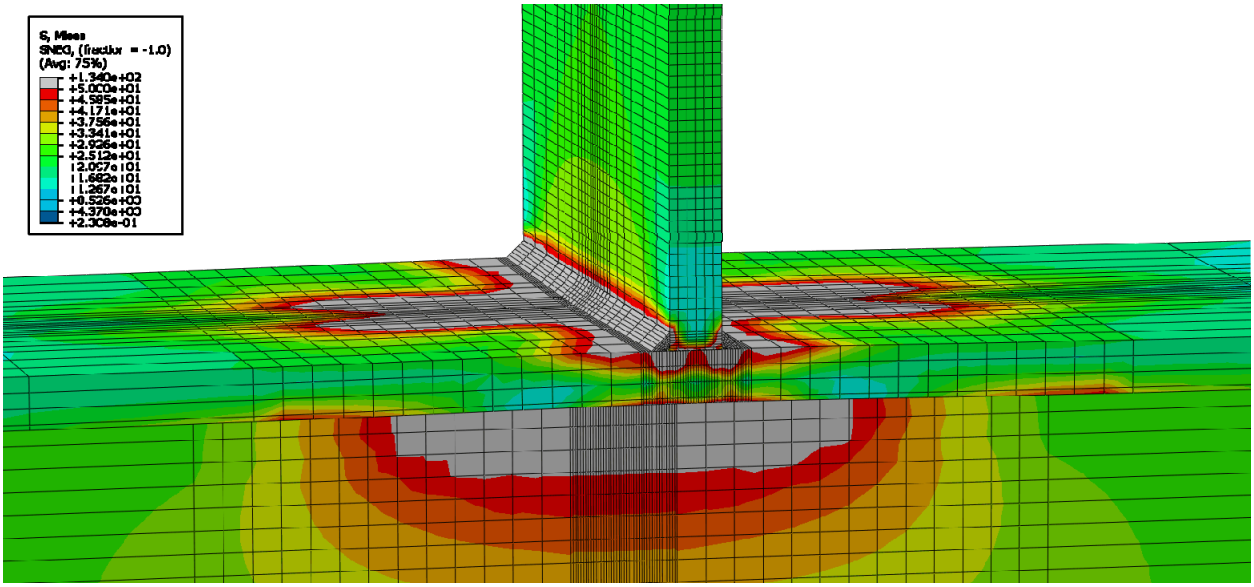

Figure E-298: Finite element model of W14X68-ST-NA with 1/4 in. welds at its load capacity of 159.44 kips

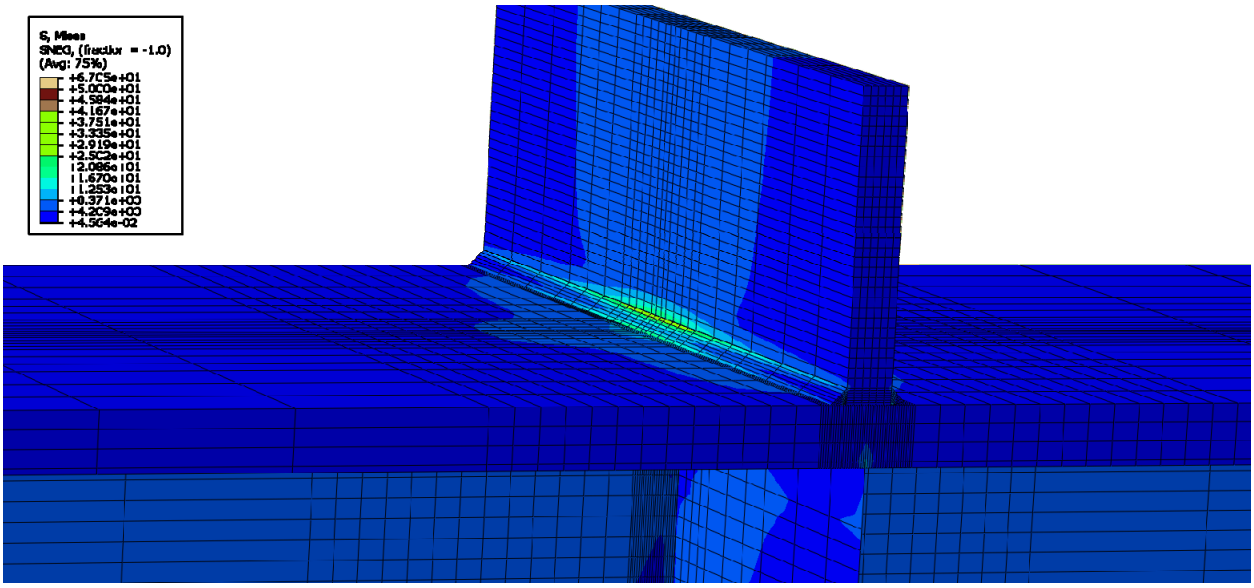

Figure E-299: Finite element model of W14X120-ST-E0 with 1/4 in. welds while remaining elastic

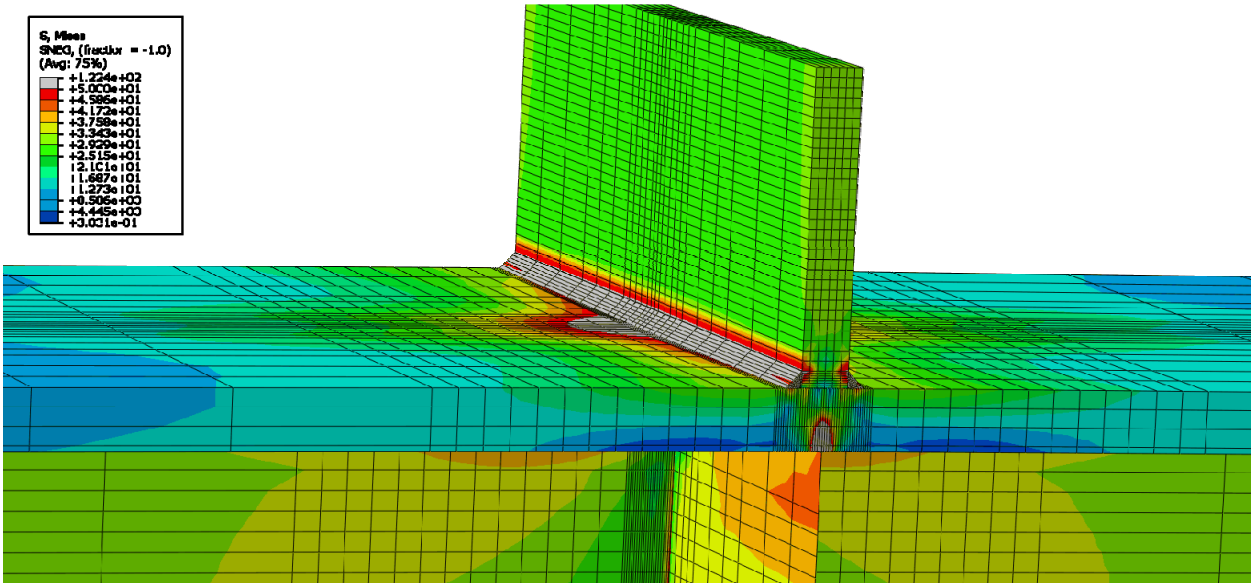

Figure E-300: Finite element model of W14X120-ST-E0 with 1/4 in. welds during inelastic behavior

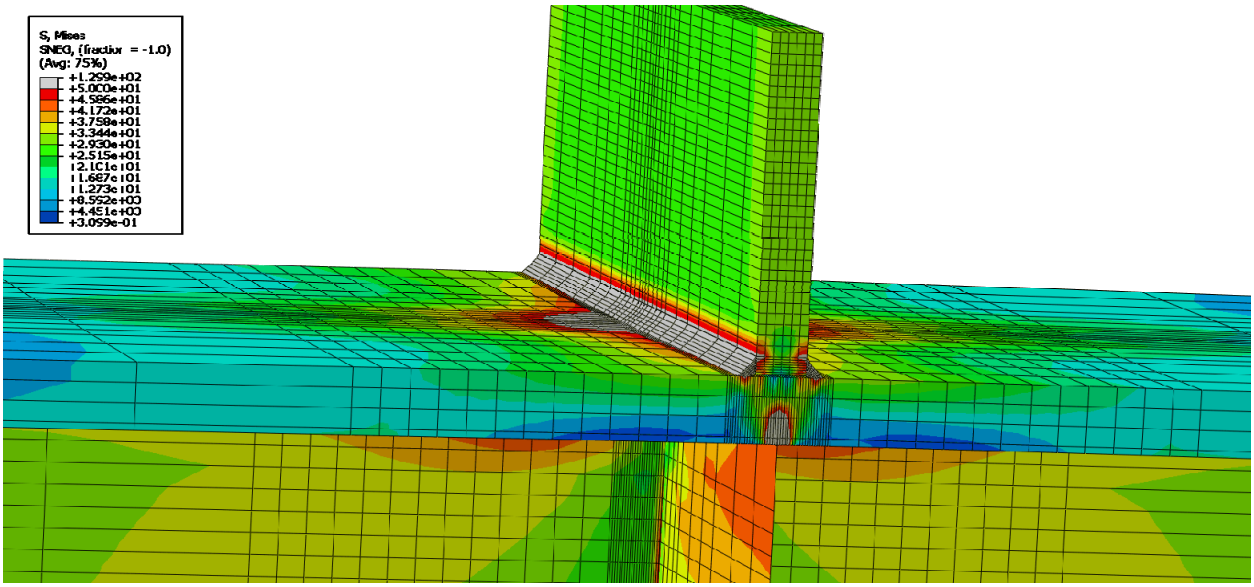

Figure E-301: Finite element model of W14X120-ST-E0 with 1/4 in. welds at its load capacity of 294.65 kips

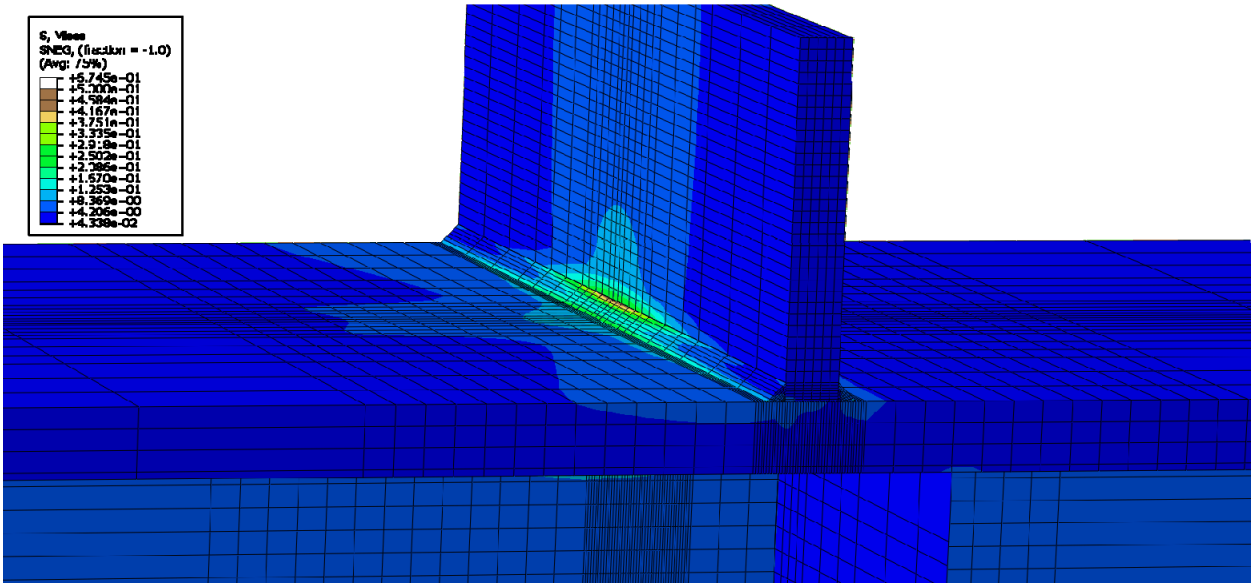

Figure E-302: Finite element model of W14X120-ST-E2 with 1/4 in. welds while remaining elastic

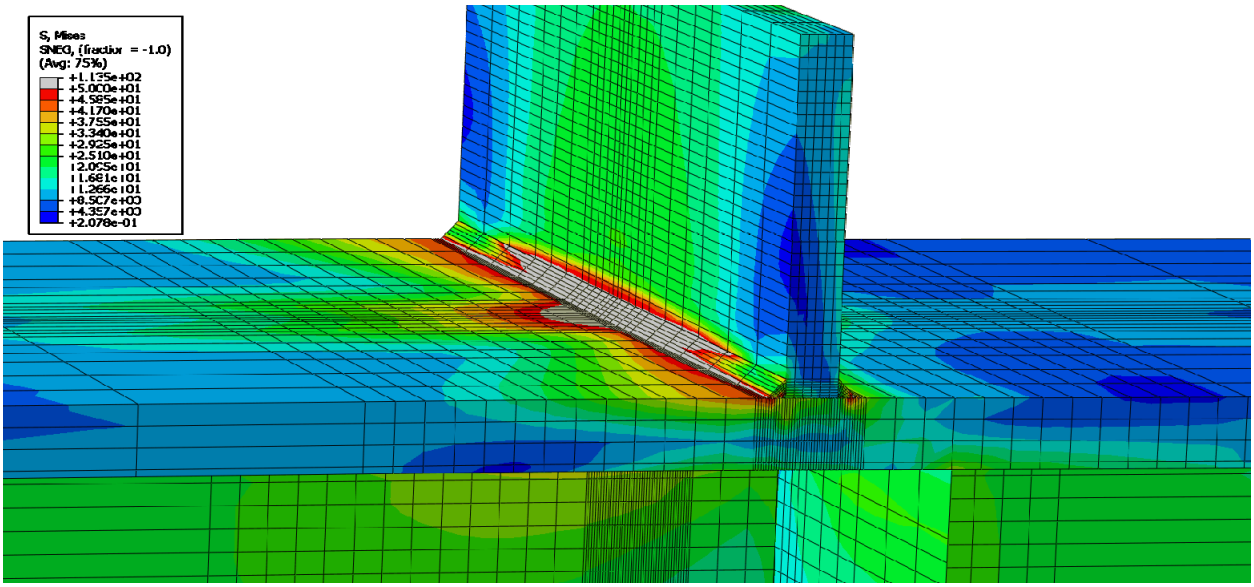

Figure E-303: Finite element model of W14X120-ST-E2 with 1/4 in. welds during inelastic behavior

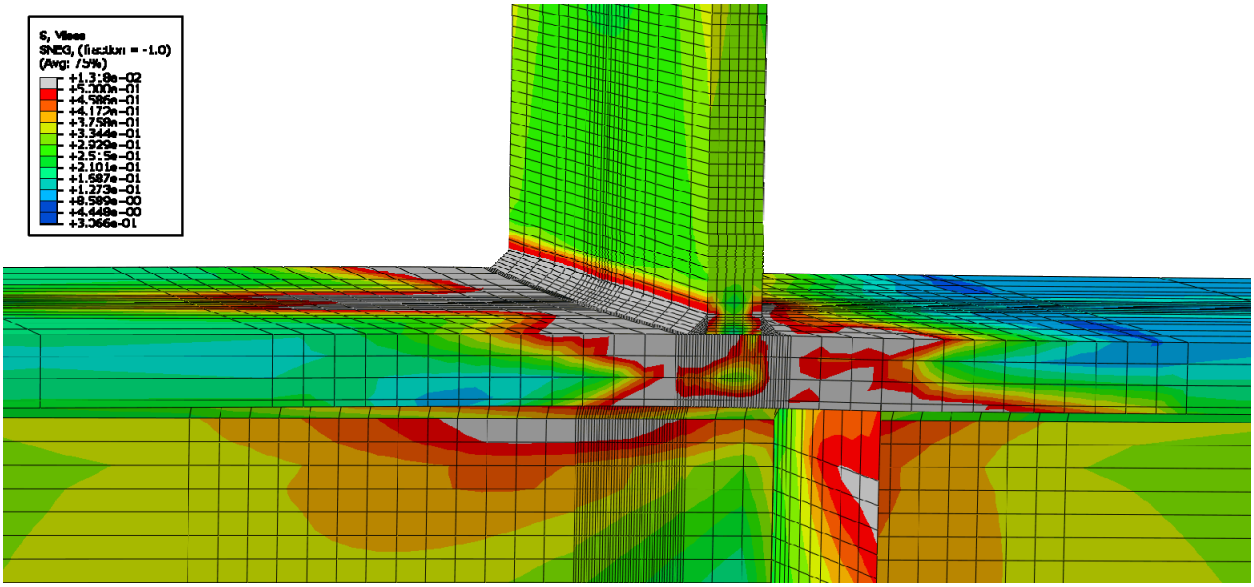

Figure E-304: Finite element model of W14X120-ST-E2 with 1/4 in. welds at its load capacity of 290.55 kips

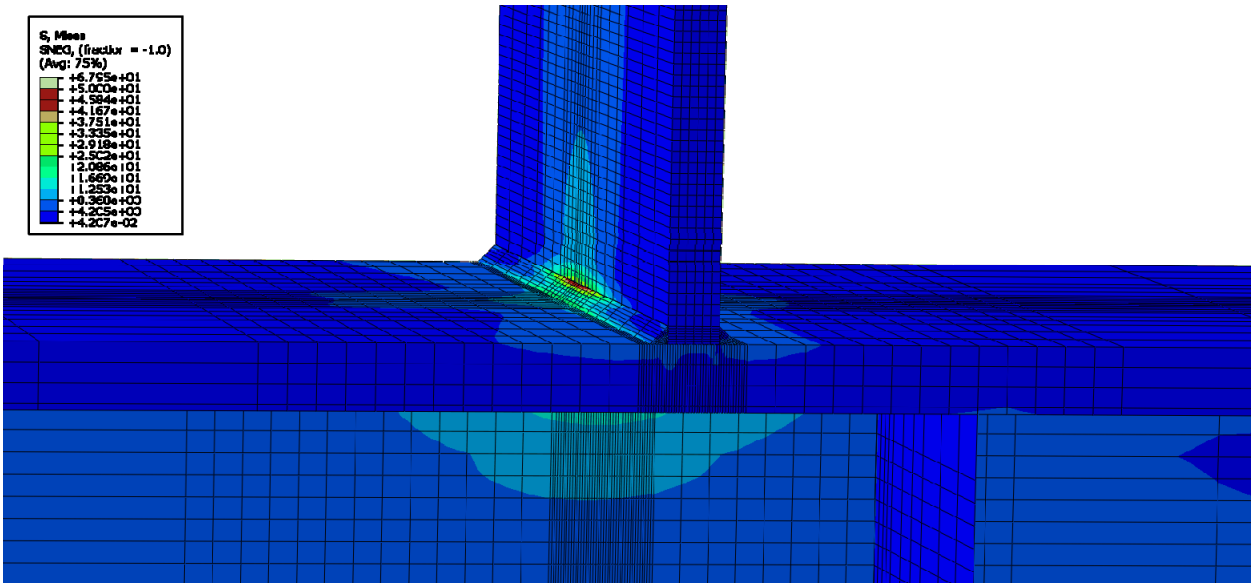

Figure E-305: Finite element model of W14X120-ST-E4 with 1/4 in. welds while remaining elastic

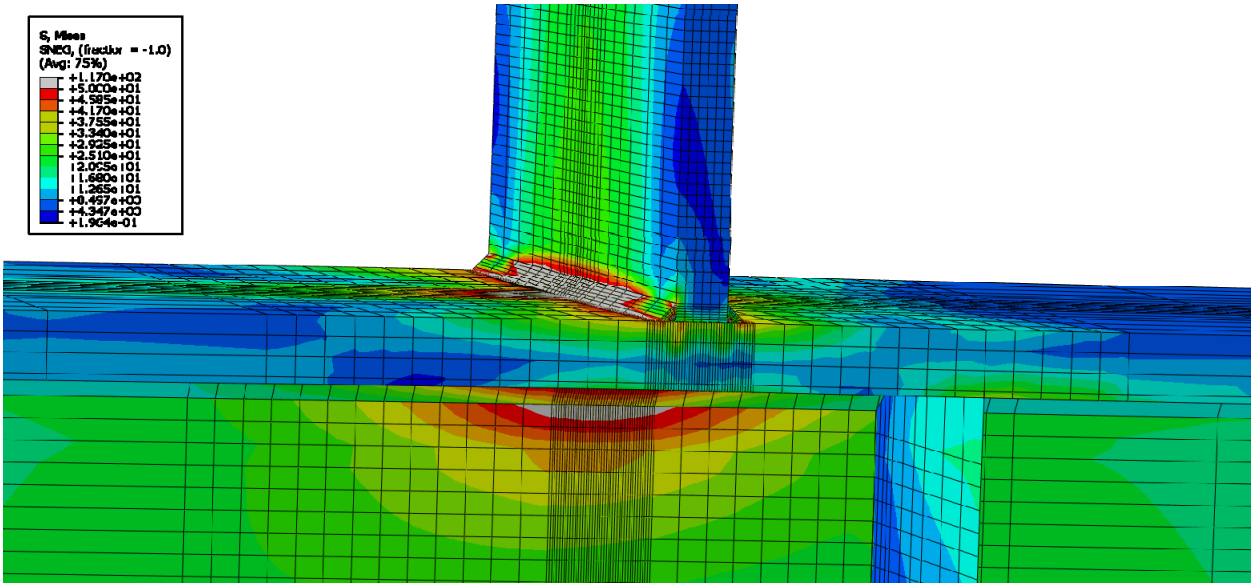

Figure E-306: Finite element model of W14X120-ST-E4 with 1/4 in. welds during inelastic behavior

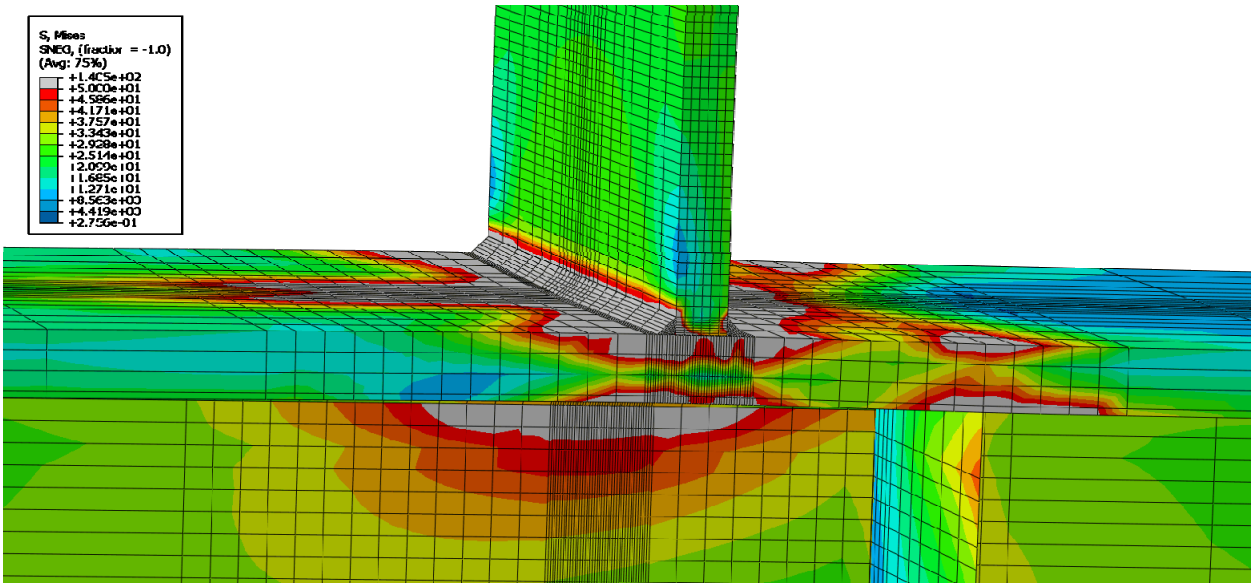

Figure E-307: Finite element model of W14X120-ST-E4 with 1/4 in. welds at its load capacity of 252.60 kips

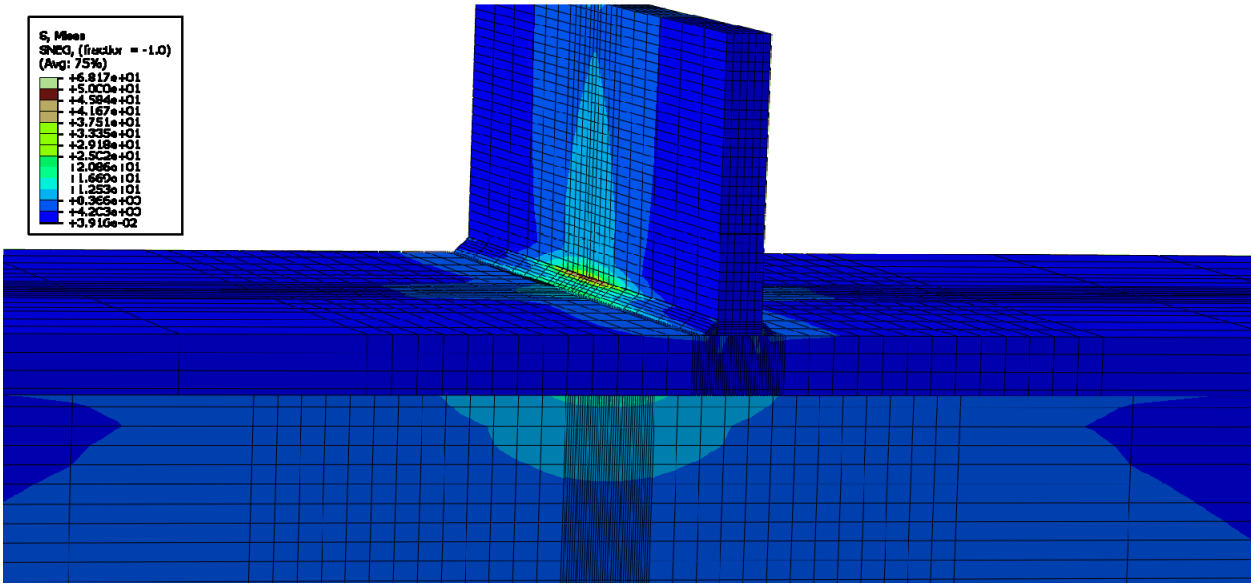

Figure E-308: Finite element model of W14X120-ST-NA with 1/4 in. welds while remaining elastic

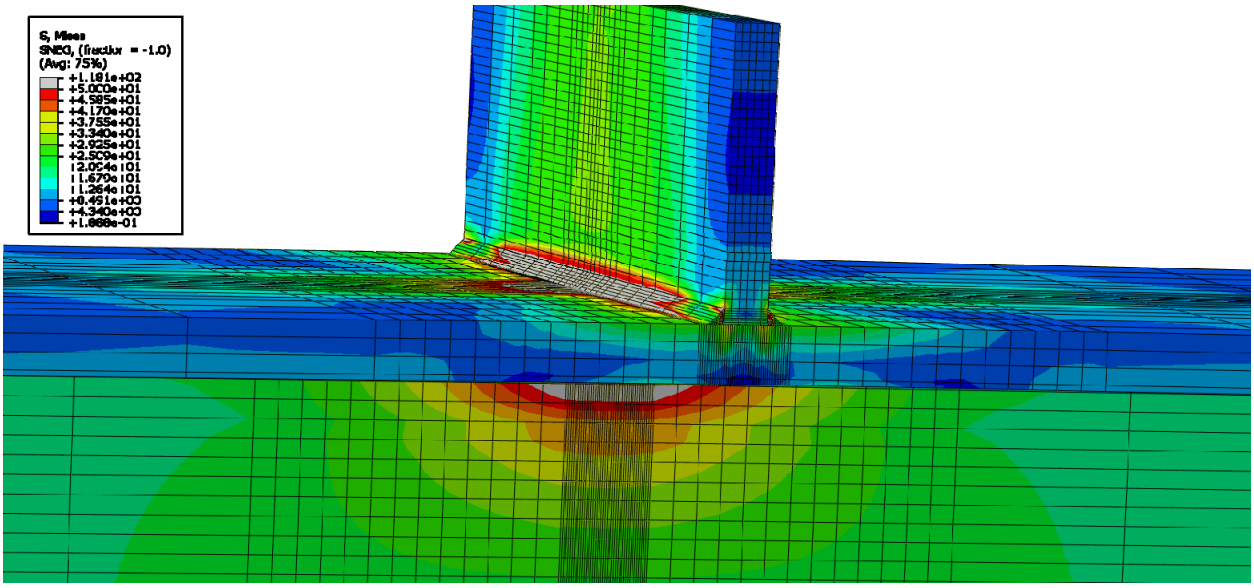

Figure E-309: Finite element model of W14X120-ST-NA with 1/4 in. welds during inelastic behavior

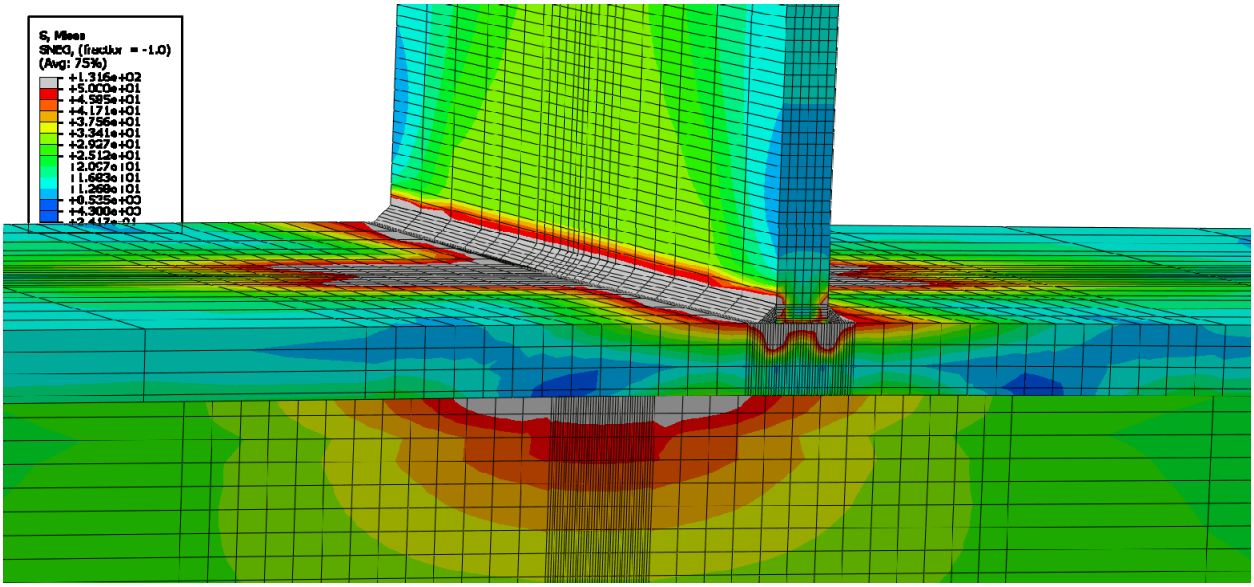

Figure E-310: Finite element model of W14X120-ST-NA with 1/4 in. welds at its load capacity of 221.27 kips

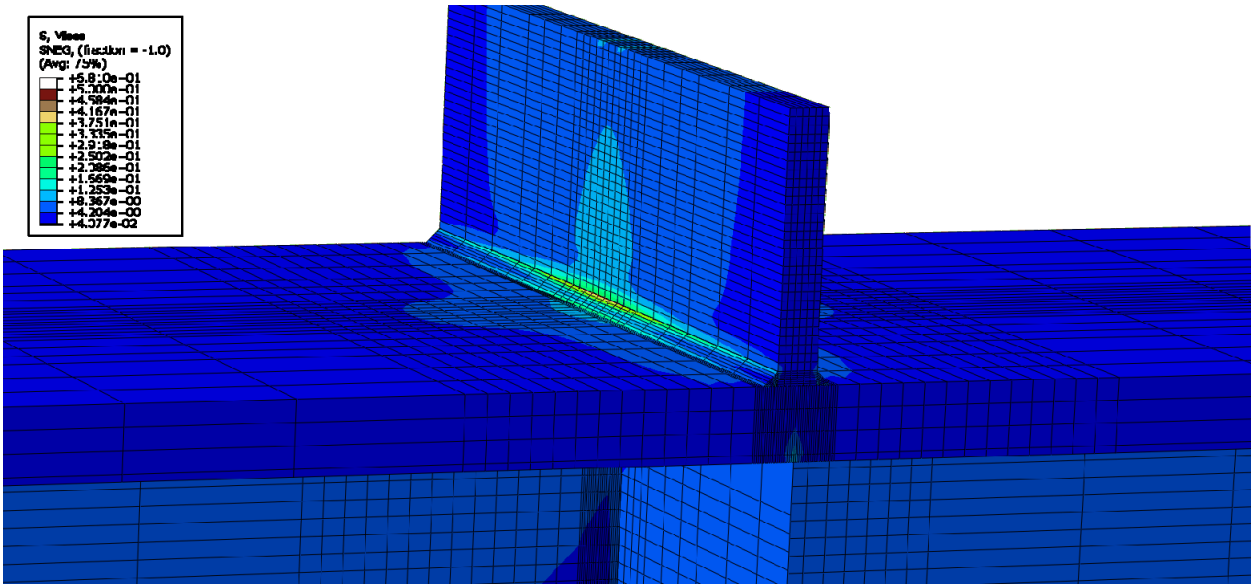

Figure E-311: Finite element model of W14X176-ST-E0 with 1/4 in. welds while remaining elastic

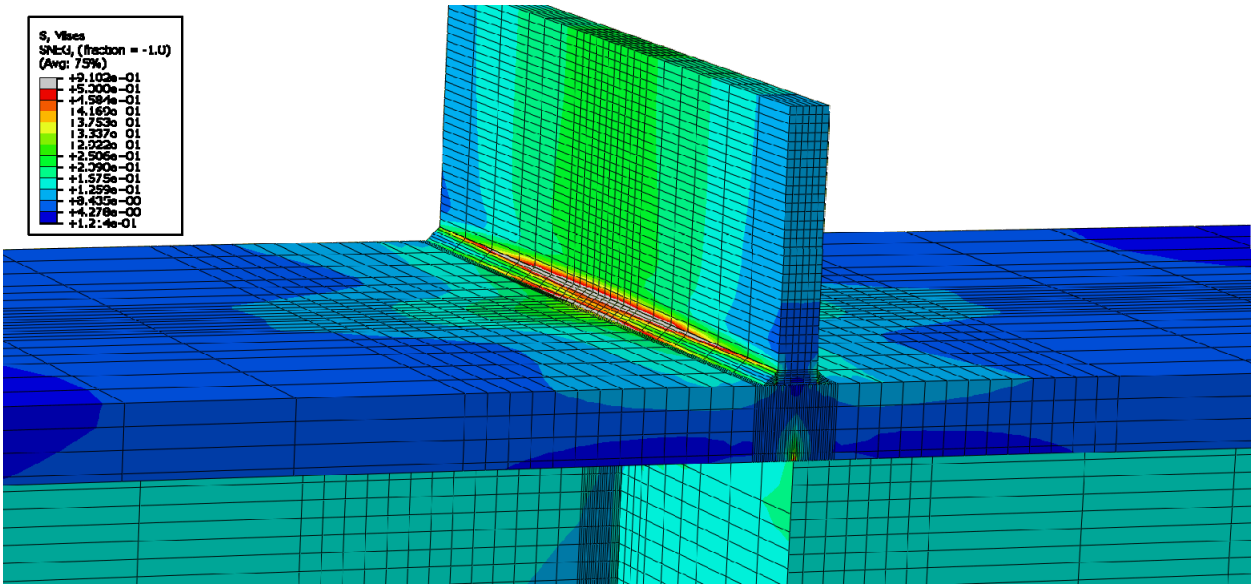

Figure E-312: Finite element model of W14X176-ST-E0 with 1/4 in. welds during inelastic behavior

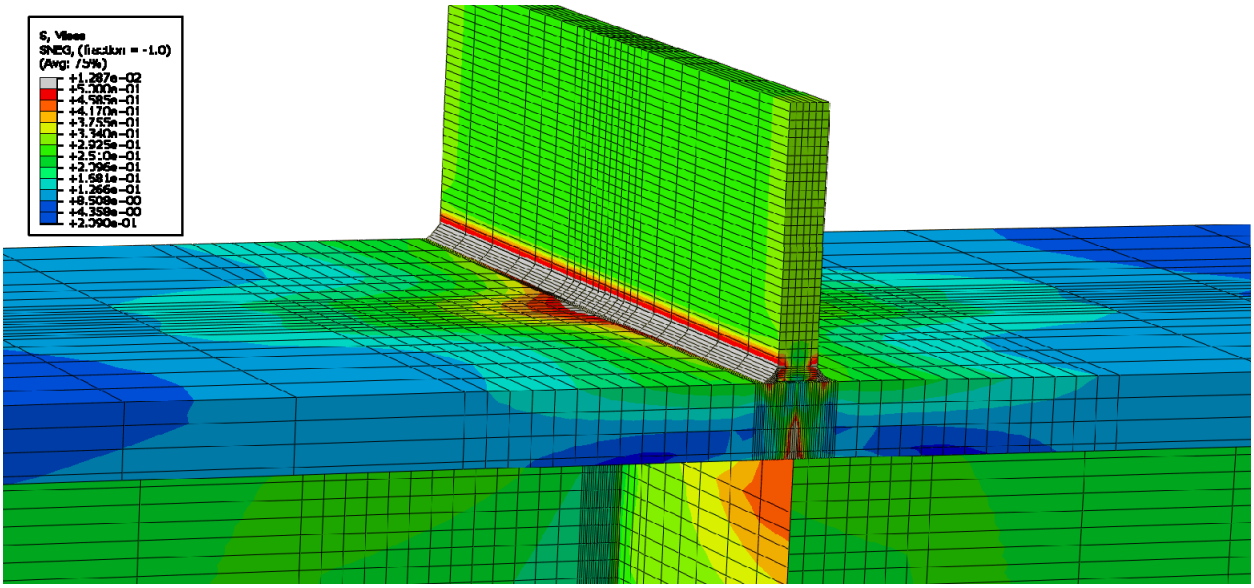

Figure E-313: Finite element model of W14X176-ST-E0 with 1/4 in. welds at its load capacity of 315.47 kips

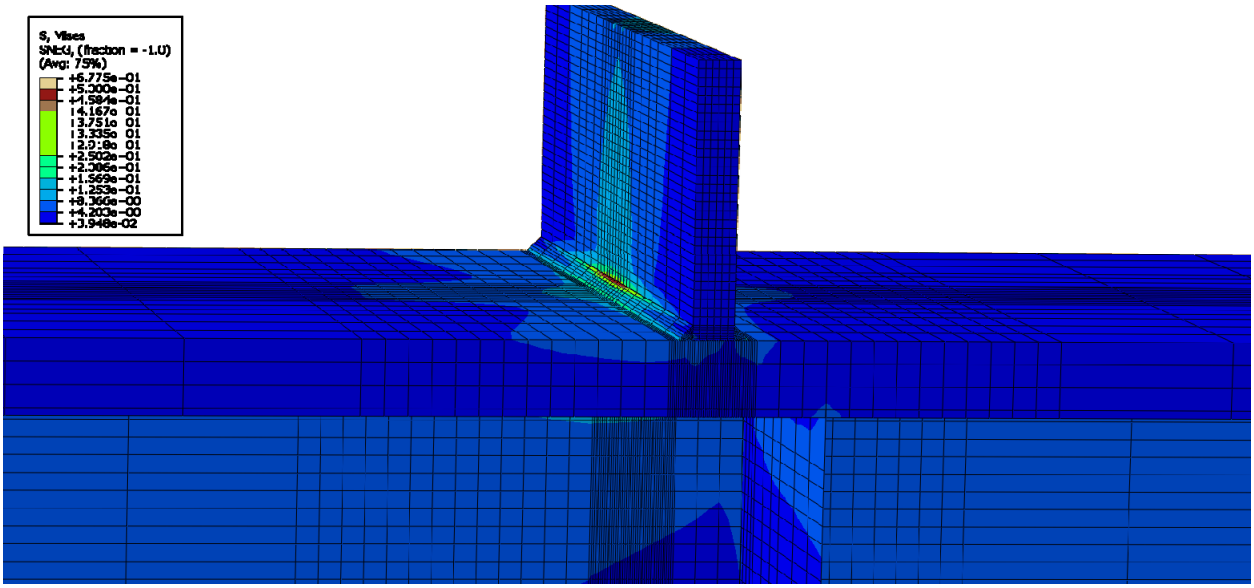

Figure E-314: Finite element model of W14X176-ST-E2 with 1/4 in. welds while remaining elastic

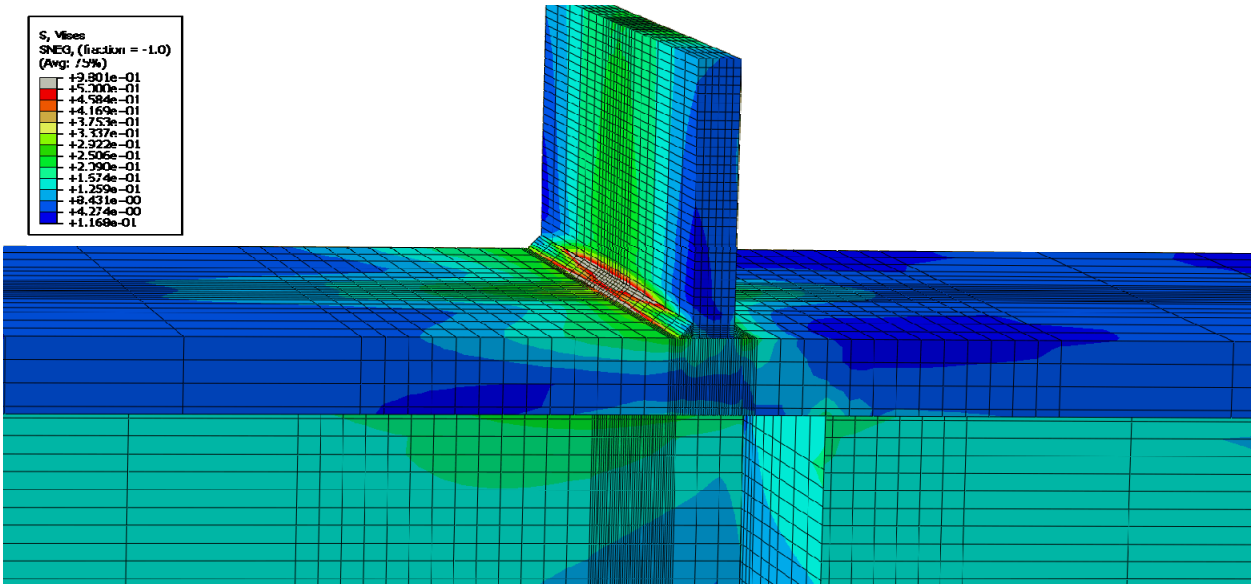

Figure E-315: Finite element model of W14X176-ST-E2 with 1/4 in. welds during inelastic behavior

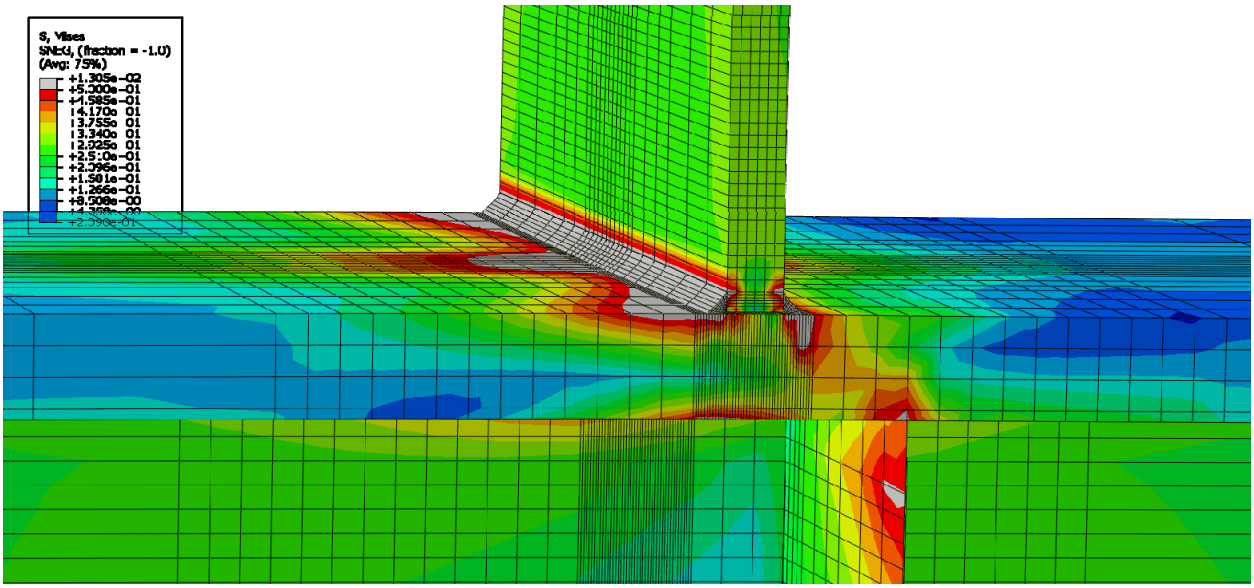

Figure E-316: Finite element model of W14X176-ST-E2 with 1/4 in. welds at its load capacity of 314.33 kips

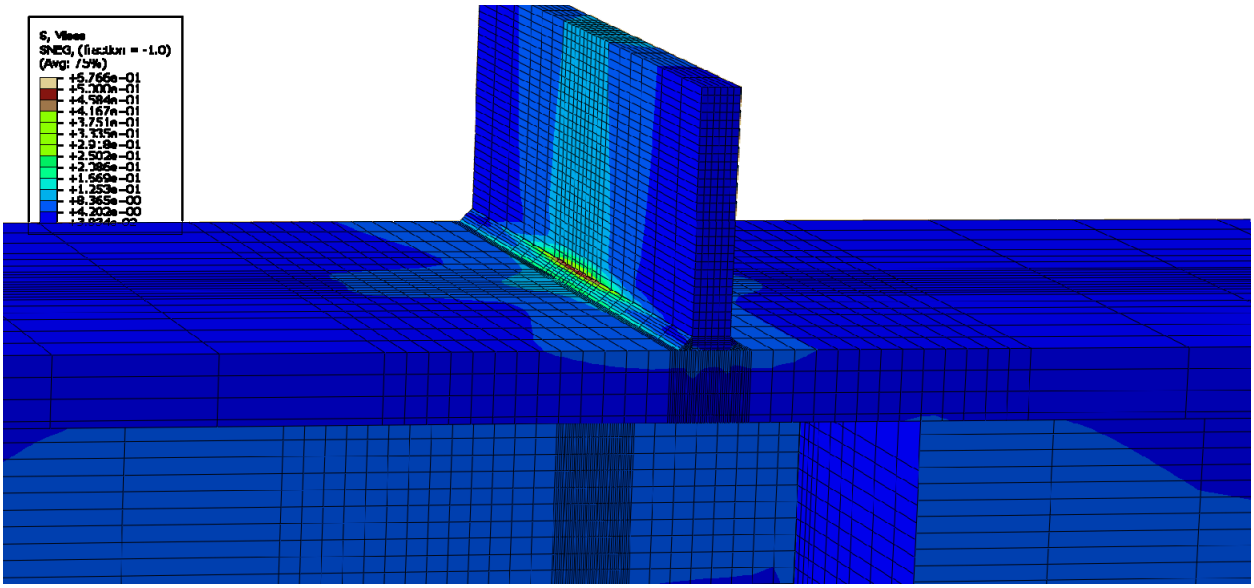

Figure E-317: Finite element model of W14X176-ST-E4 with 1/4 in. welds while remaining elastic

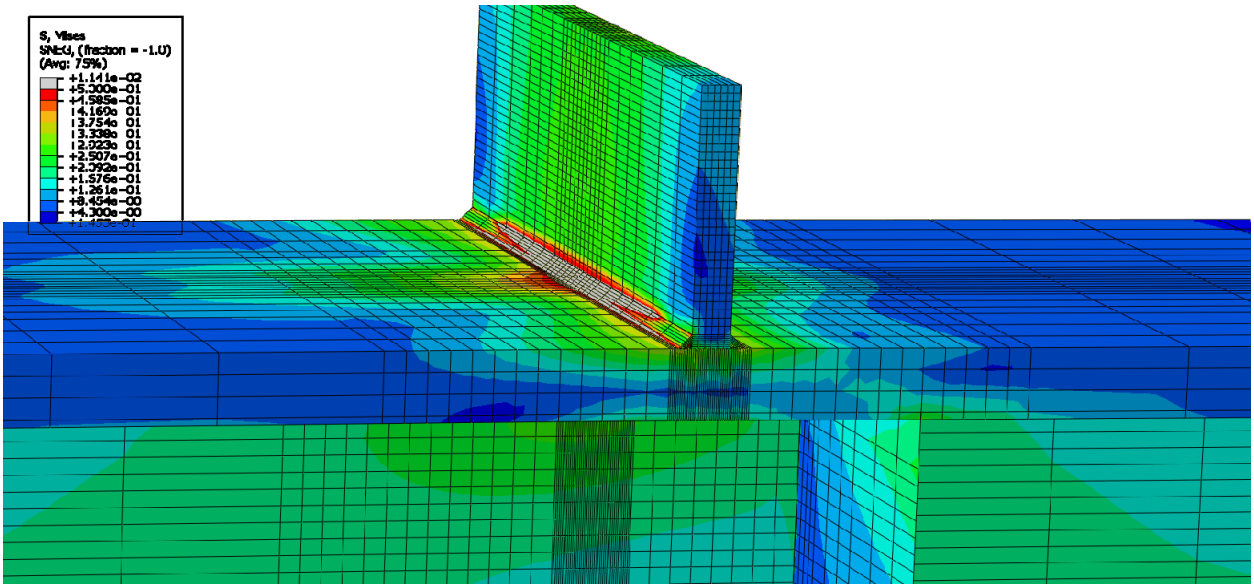

Figure E-318: Finite element model of W14X176-ST-E4 with 1/4 in. welds during inelastic behavior

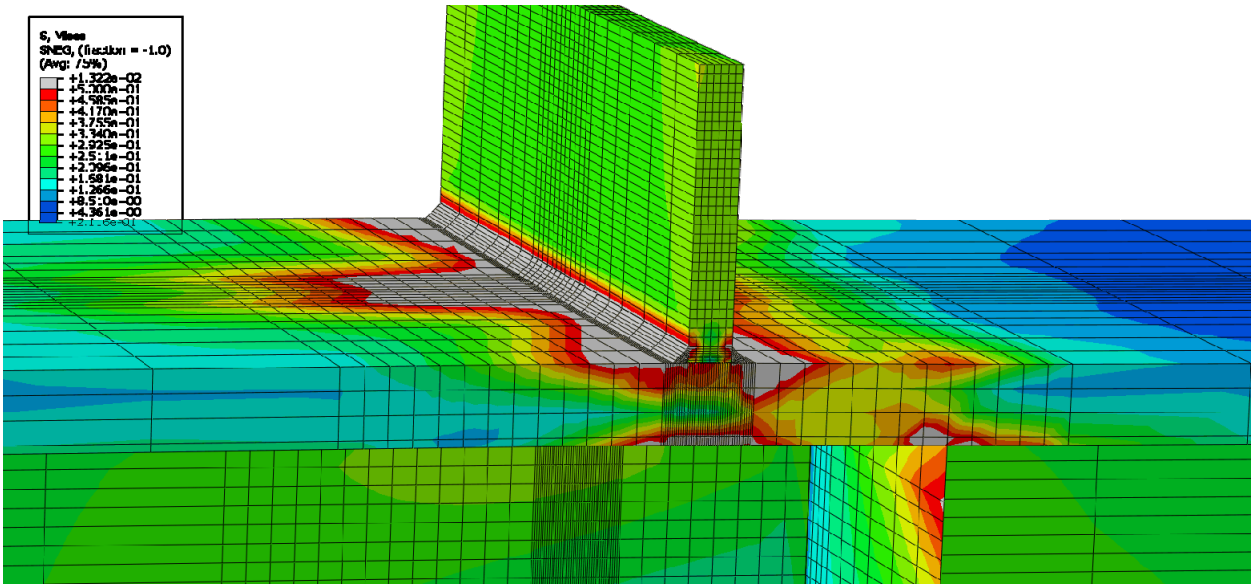

Figure E-319: Finite element model of W14X176-ST-E4 with 1/4 in. welds at its load capacity of 312.11 kips

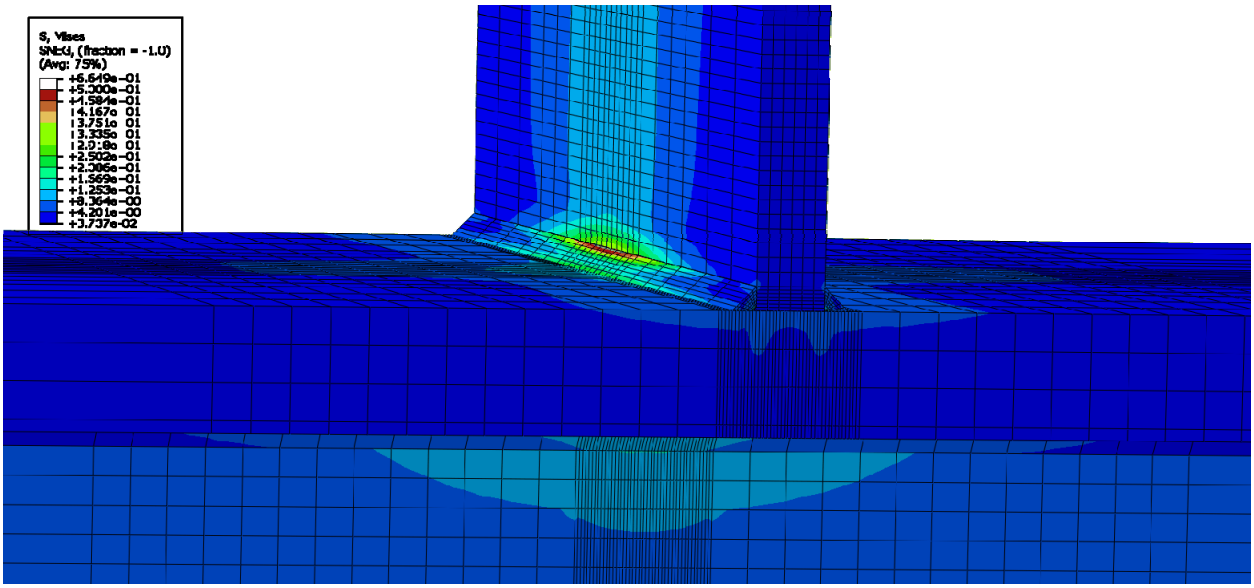

Figure E-320: Finite element model of W14X176-ST-NA with 1/4 in. welds while remaining elastic

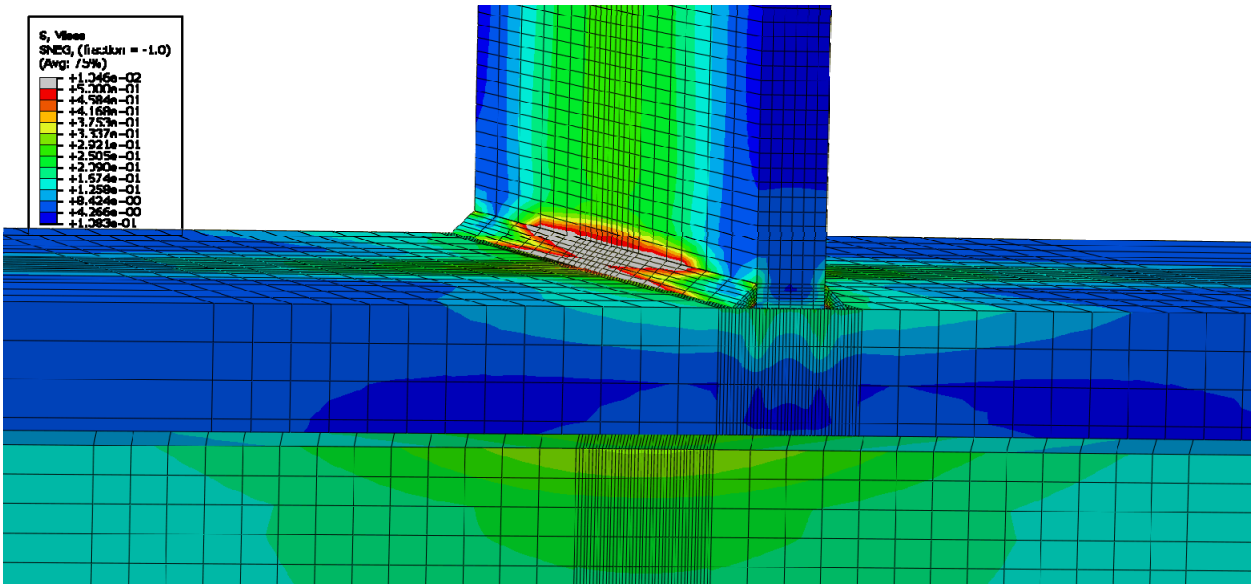

Figure E-321: Finite element model of W14X176-ST-NA with 1/4 in. welds during inelastic behavior

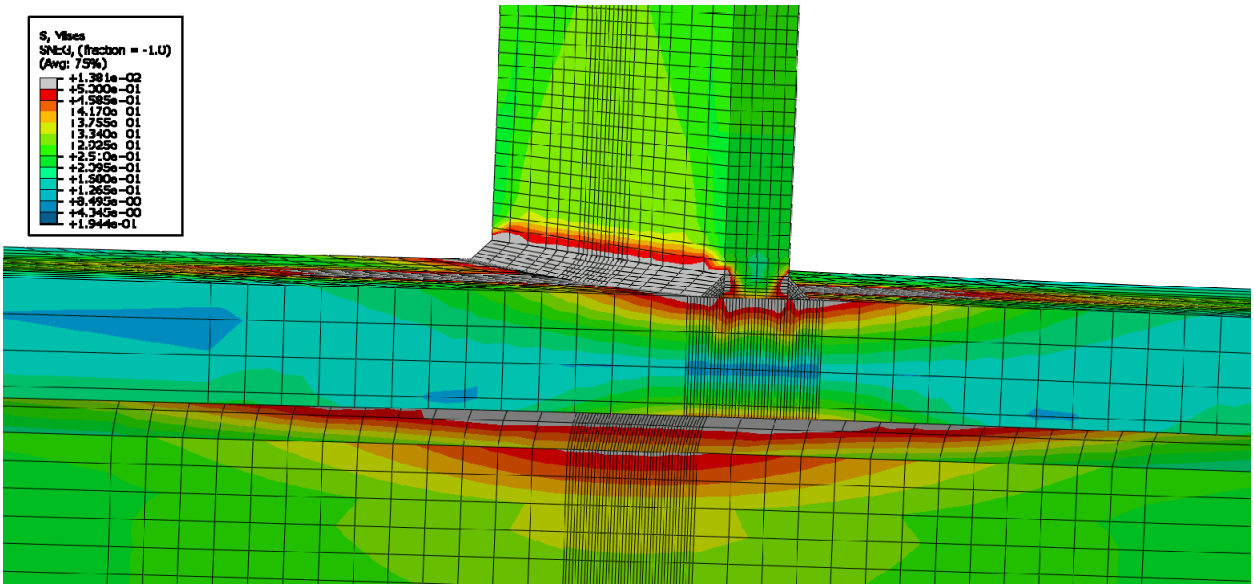

Figure E-322: Finite element model of W14X176-ST-NA with 1/4 in. welds at its load capacity of 283.51 kips

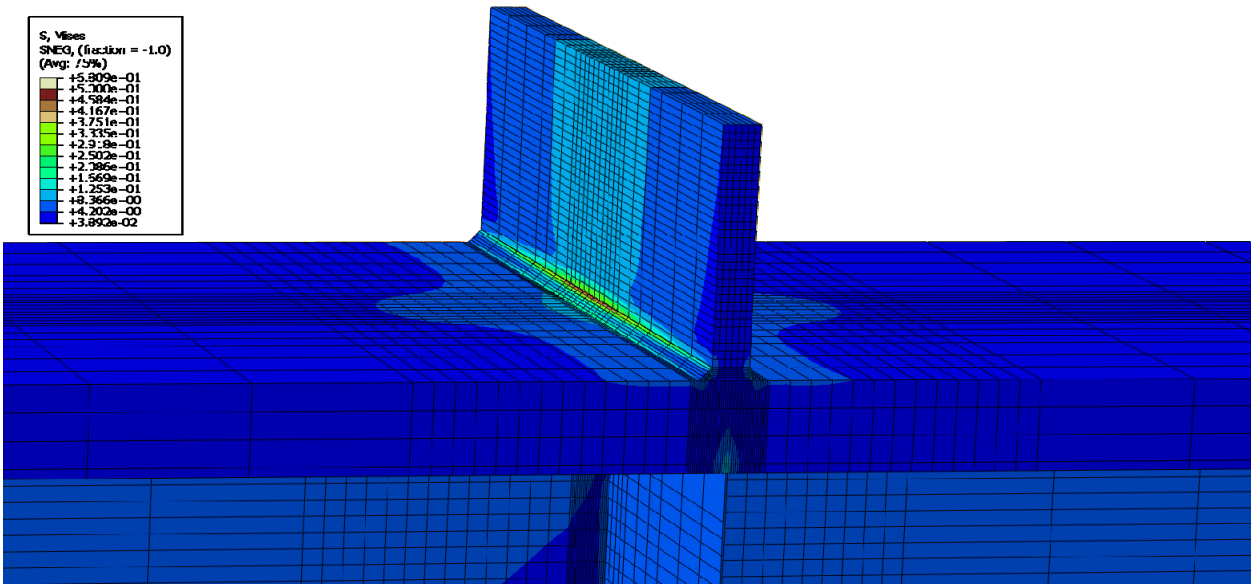

Figure E-323: Finite element model of W14X233-ST-E0 with 1/4 in. welds while remaining elastic

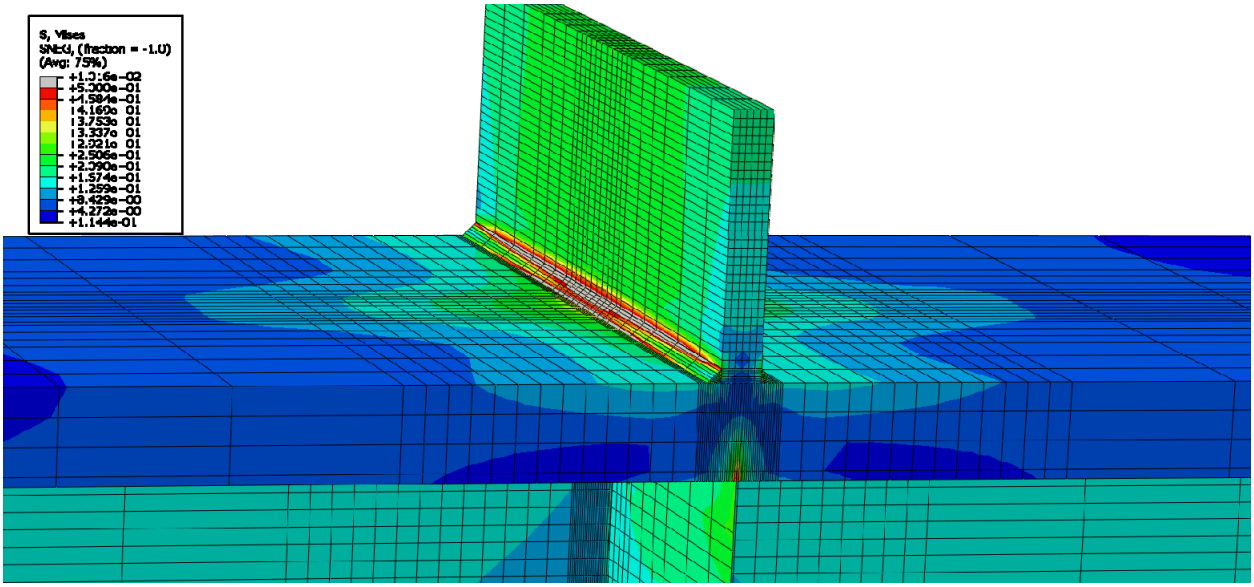

Figure E-324: Finite element model of W14X233-ST-E0 with 1/4 in. welds during inelastic behavior

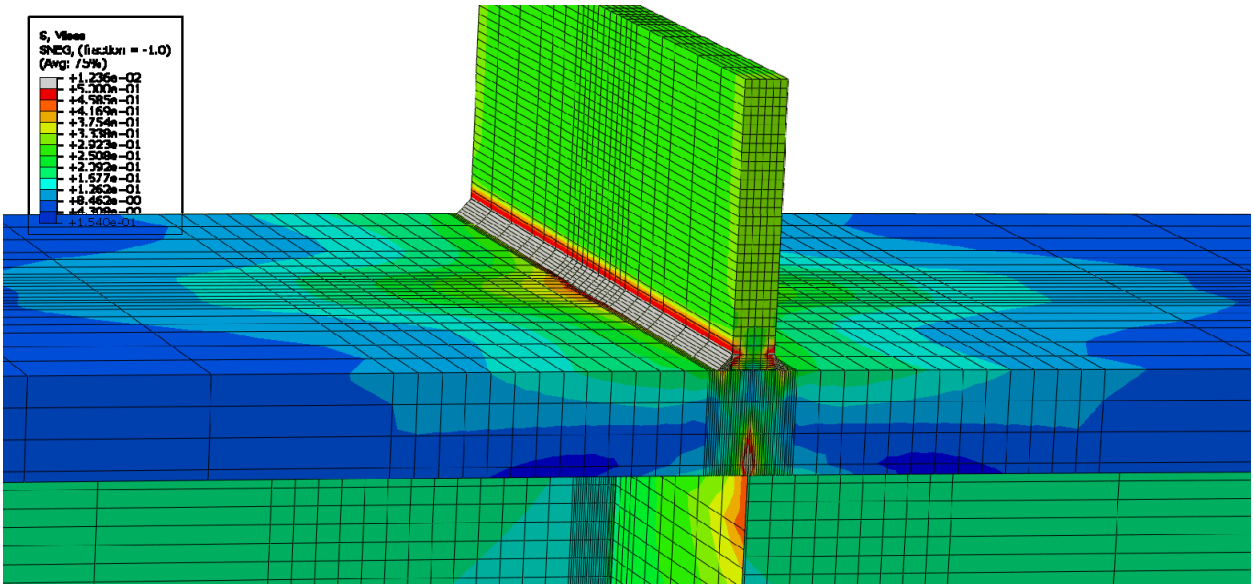

Figure E-325: Finite element model of W14X233-ST-E0 with 1/4 in. welds at its load capacity of 319.56 kips

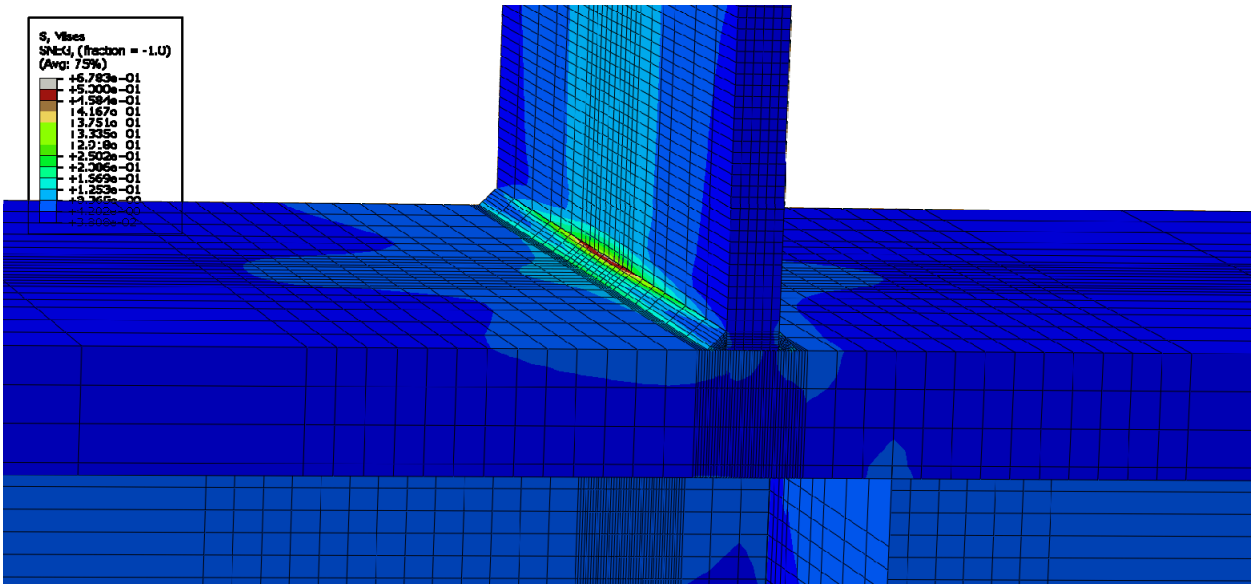

Figure E-326: Finite element model of W14X233-ST-E2 with 1/4 in. welds while remaining elastic

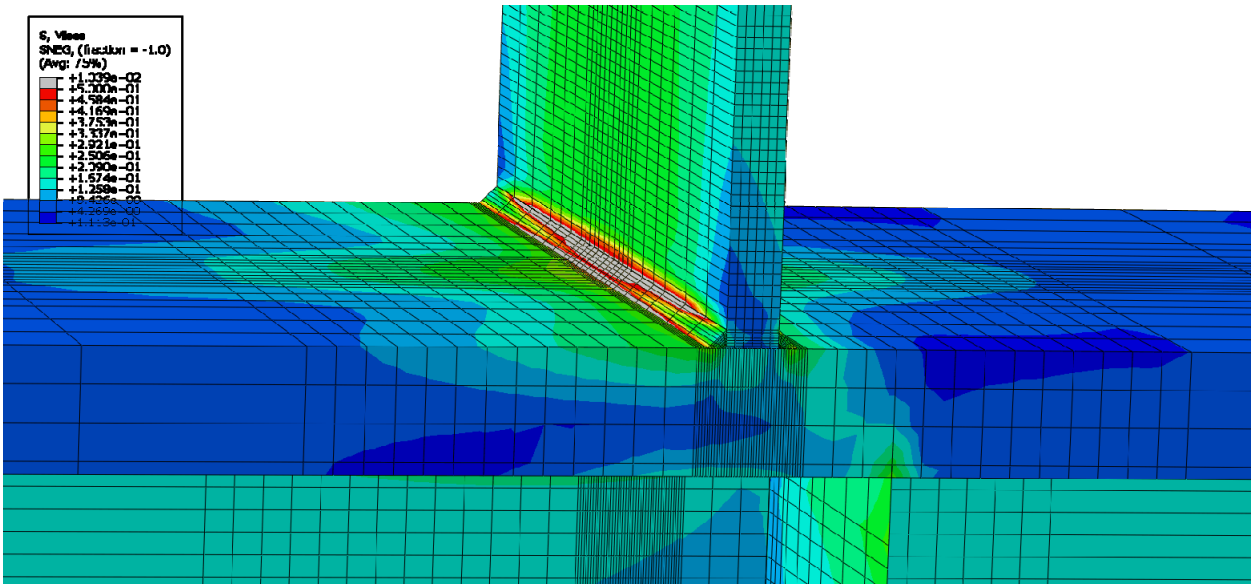

Figure E-327: Finite element model of W14X233-ST-E2 with 1/4 in. welds during inelastic behavior

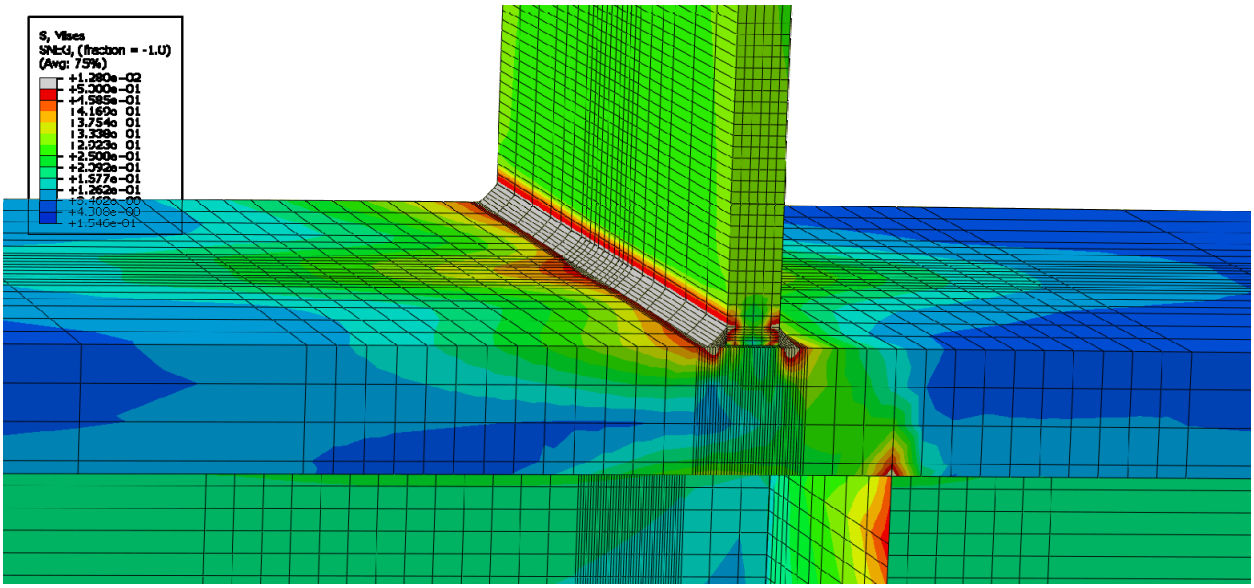

Figure E-328: Finite element model of W14X233-ST-E2 with 1/4 in. welds at its load capacity of 319.34 kips

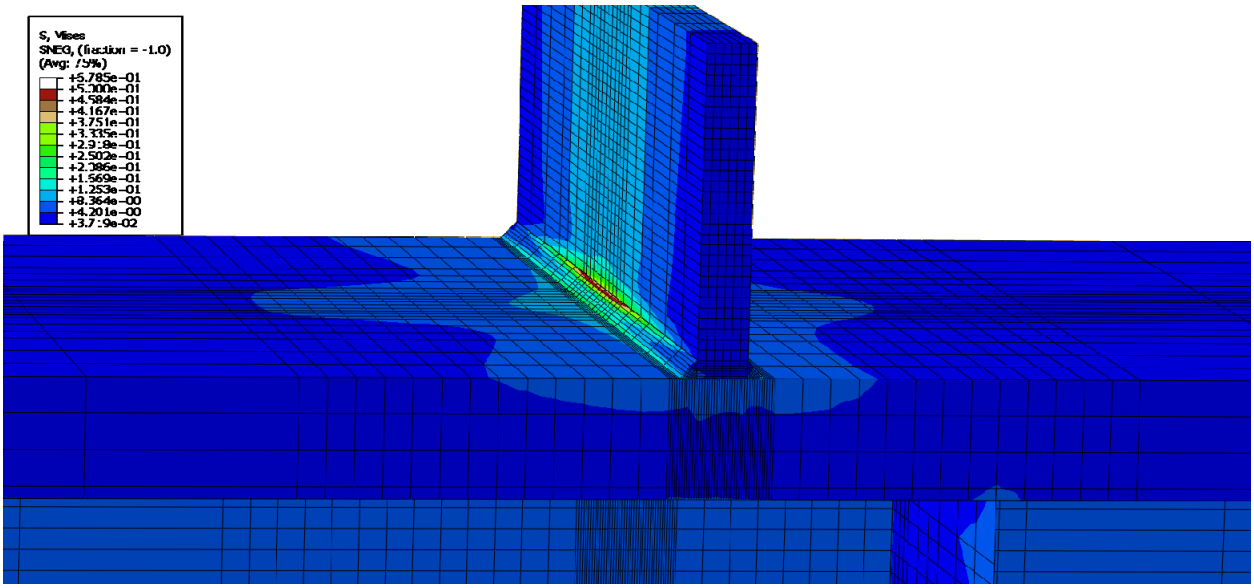

Figure E-329: Finite element model of W14X233-ST-E4 with 1/4 in. welds while remaining elastic

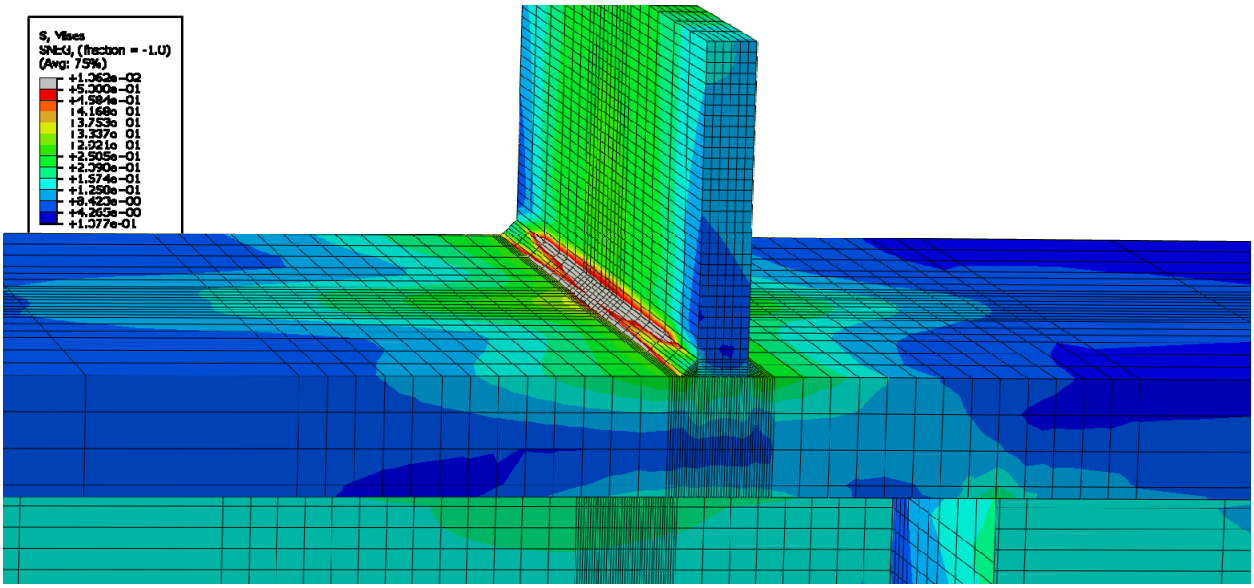

Figure E-330: Finite element model of W14X233-ST-E4 with 1/4 in. welds during inelastic behavior

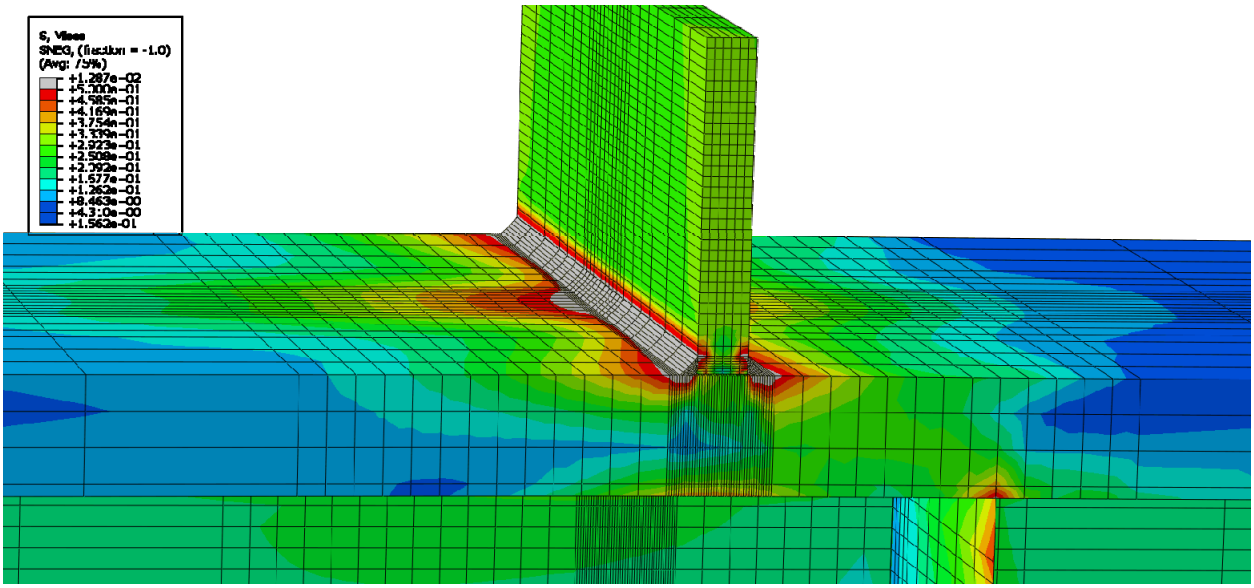

Figure E-331: Finite element model of W14X233-ST-E4 with 1/4 in. welds at its load capacity of 319.05 kips

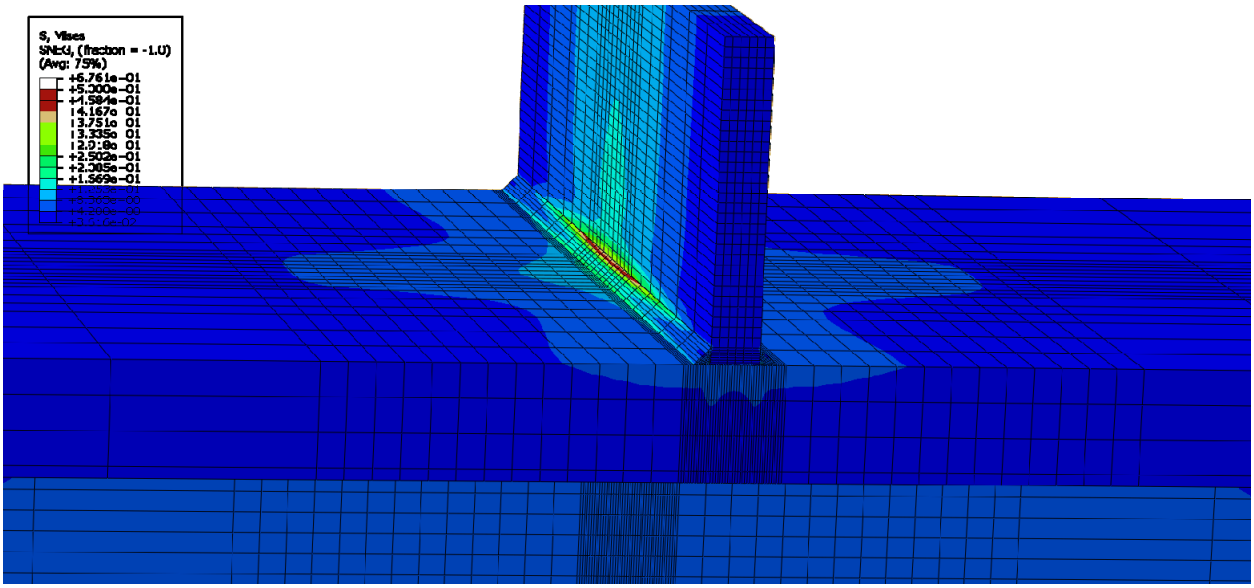

Figure E-332: Finite element model of W14X233-ST-NA with 1/4 in. welds while remaining elastic

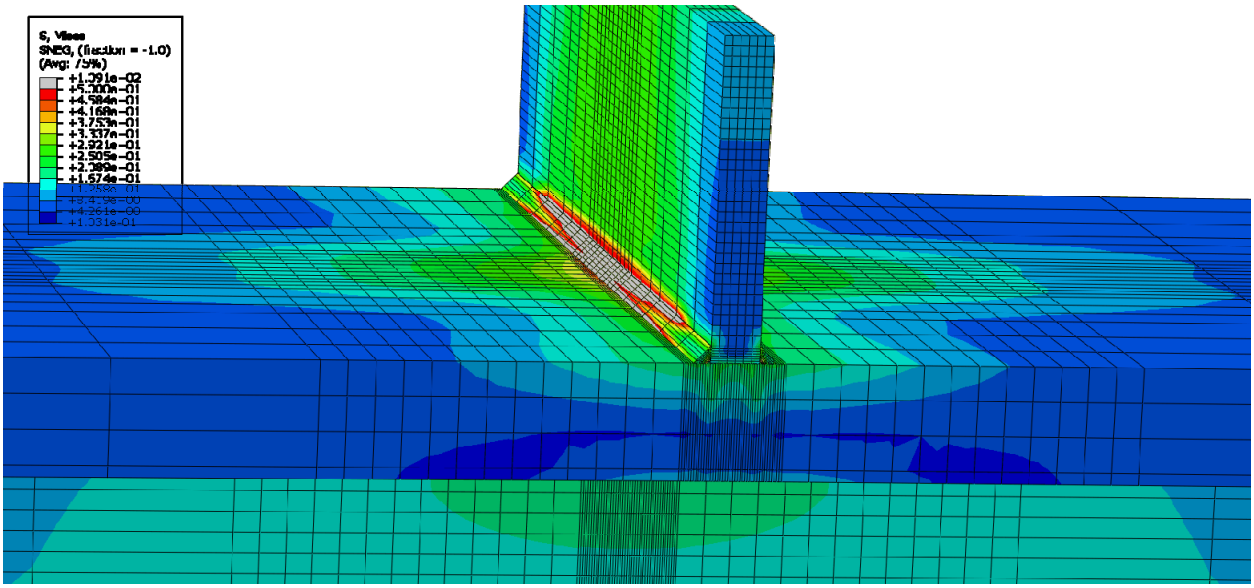

Figure E-333: Finite element model of W14X233-ST-NA with 1/4 in. welds during inelastic behavior

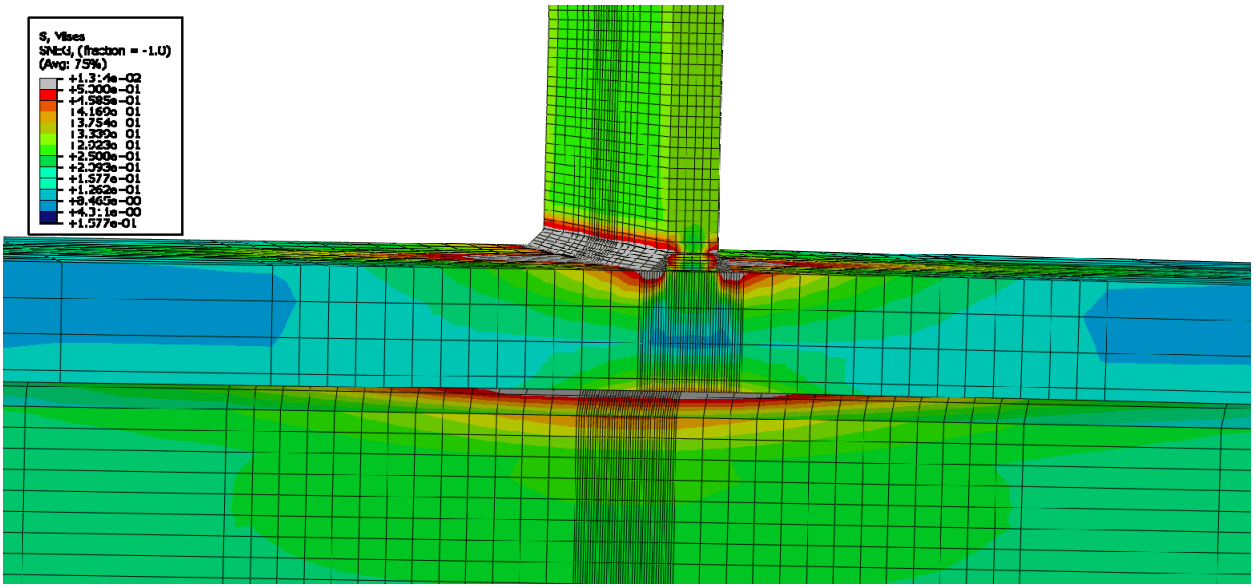

Figure E-334: Finite element model of W14X233-ST-NA with 1/4 in. welds at its load capacity of 317.85 kips

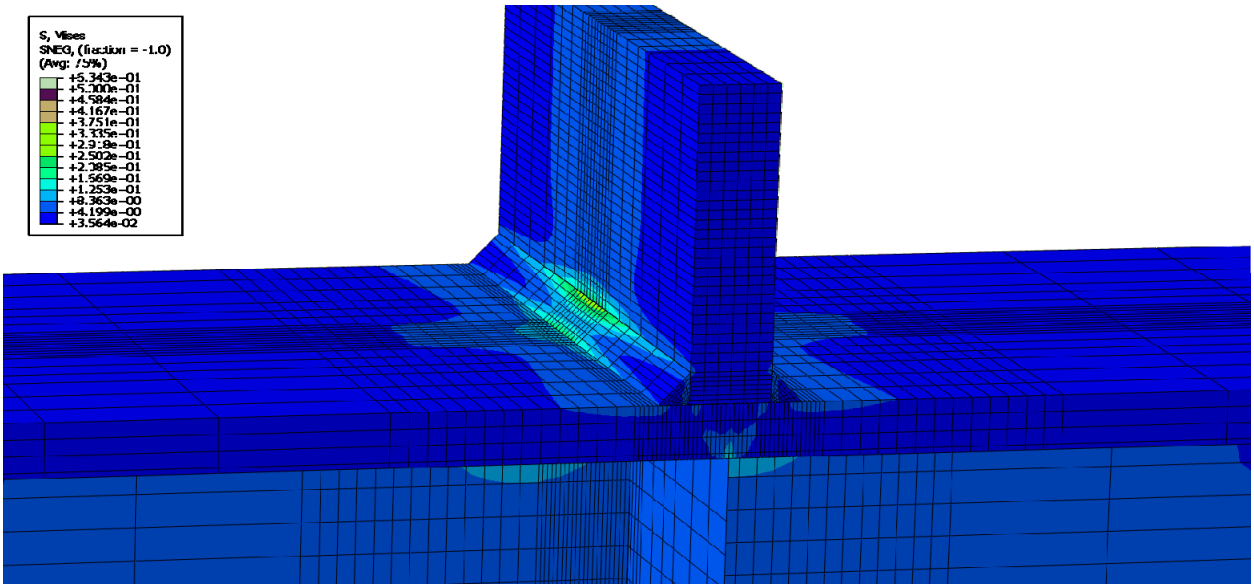

Figure E-335: Finite element model of W24X131-ST-E0 with 9/16 in. welds while remaining elastic

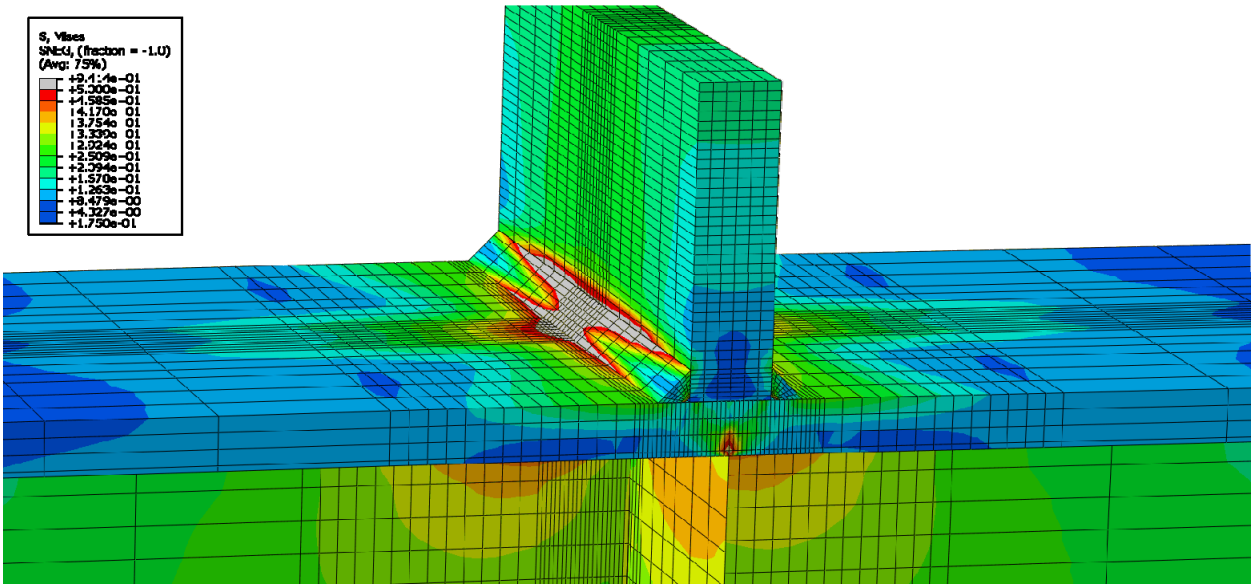

Figure E-336: Finite element model of W24X131-ST-E0 with 9/16 in. welds during inelastic behavior

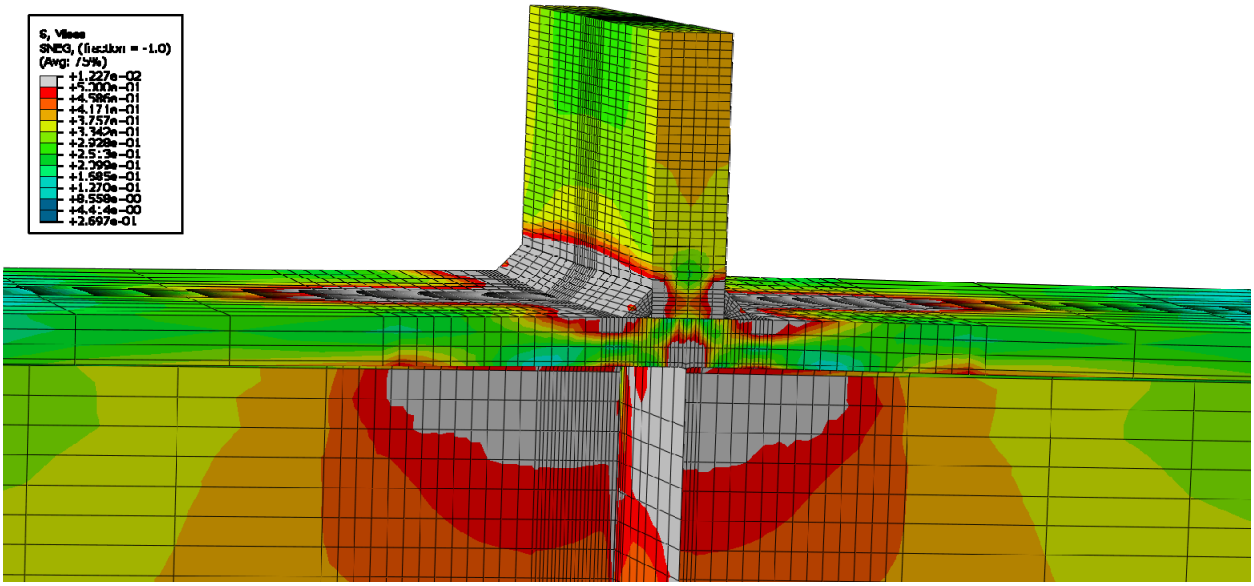

Figure E-337: Finite element model of W24X131-ST-E0 with 9/16 in. welds at its load capacity of 542.02 kips

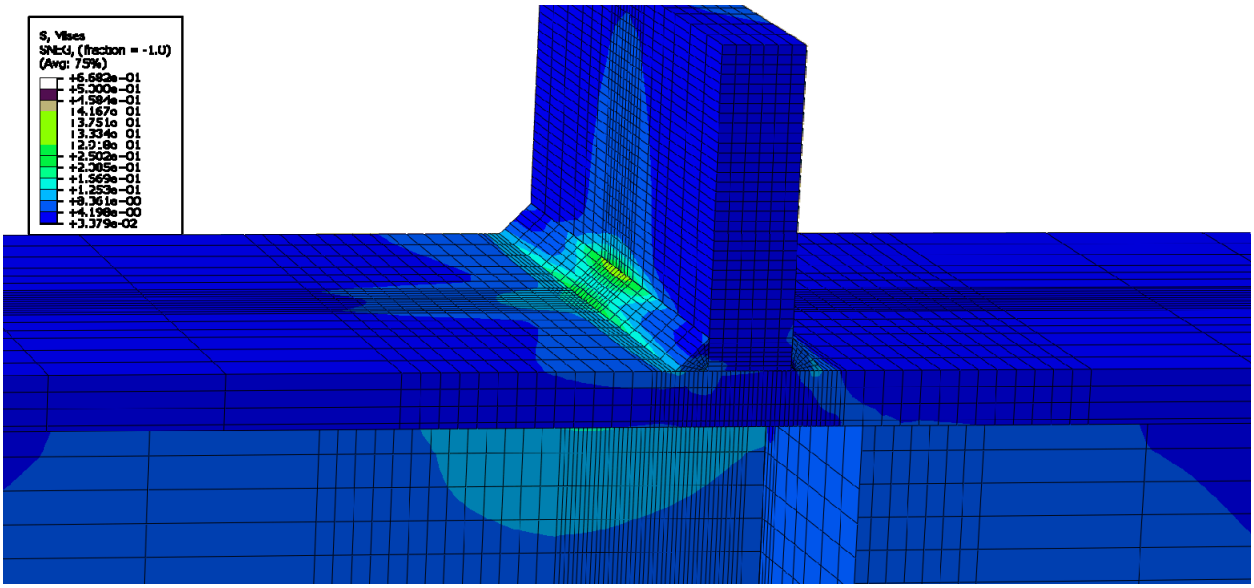

Figure E-338: Finite element model of W24X131-ST-E2 with 9/16 in. welds while remaining elastic

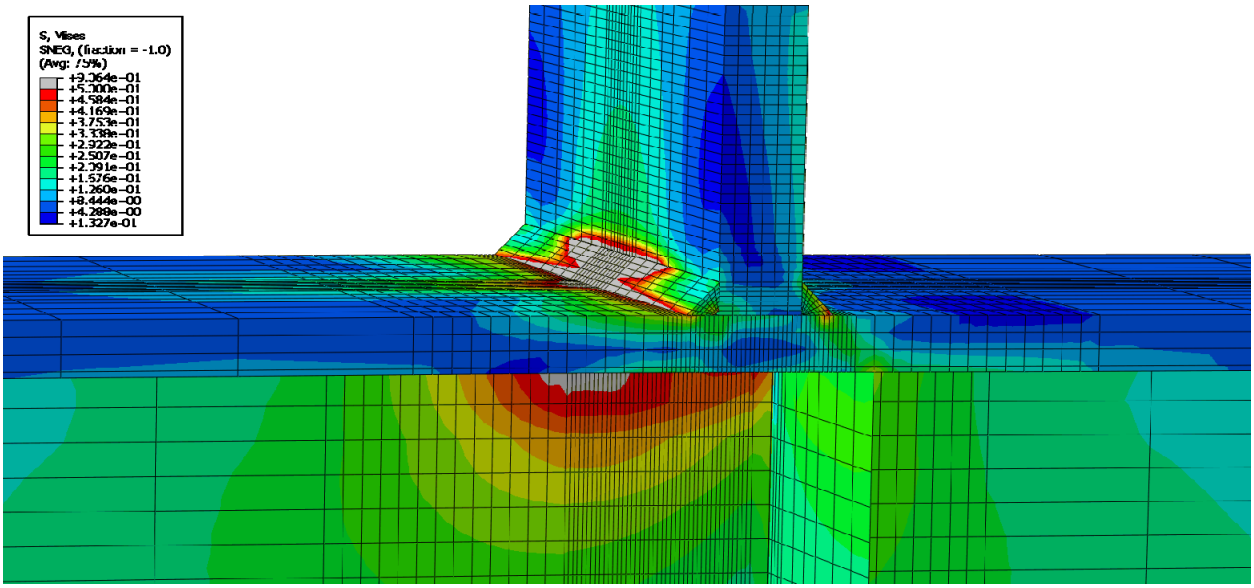

Figure E-339: Finite element model of W24X131-ST-E2 with 9/16 in. welds during inelastic behavior

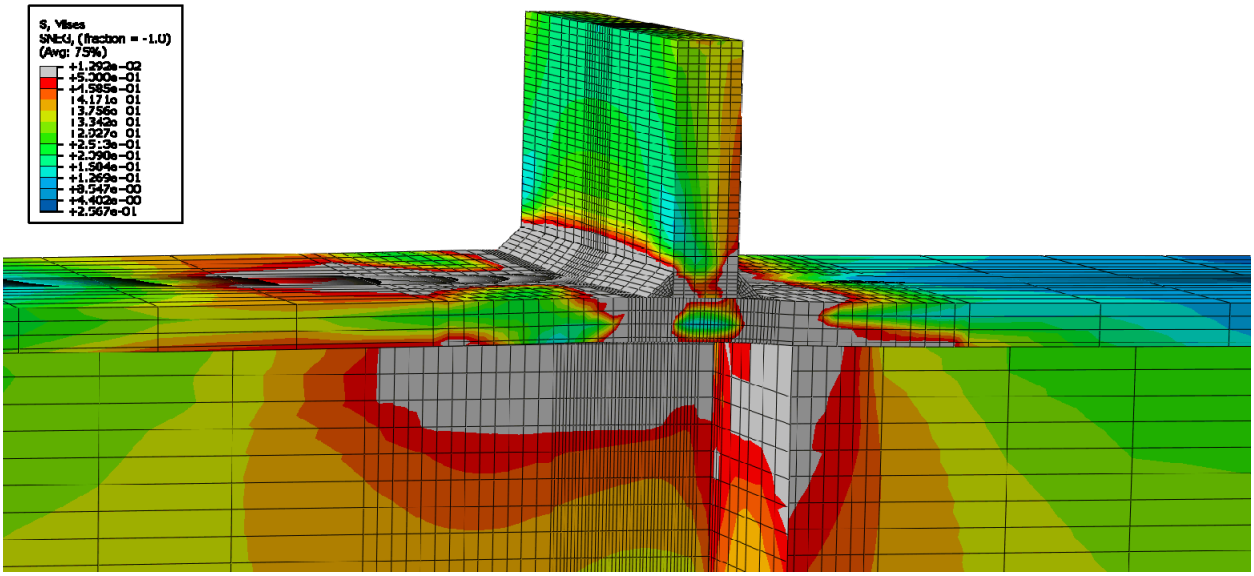

Figure E-340: Finite element model of W24X131-ST-E2 with 9/16 in. welds at its load capacity of 512.77 kips

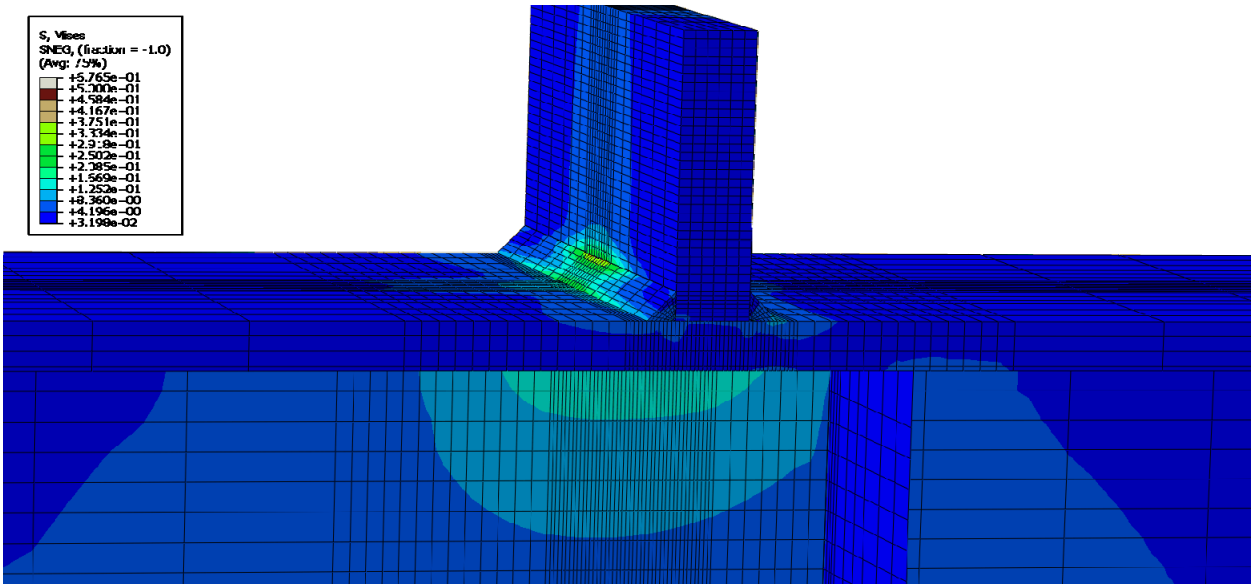

Figure E-341: Finite element model of W24X131-ST-E4 with 9/16 in. welds while remaining elastic

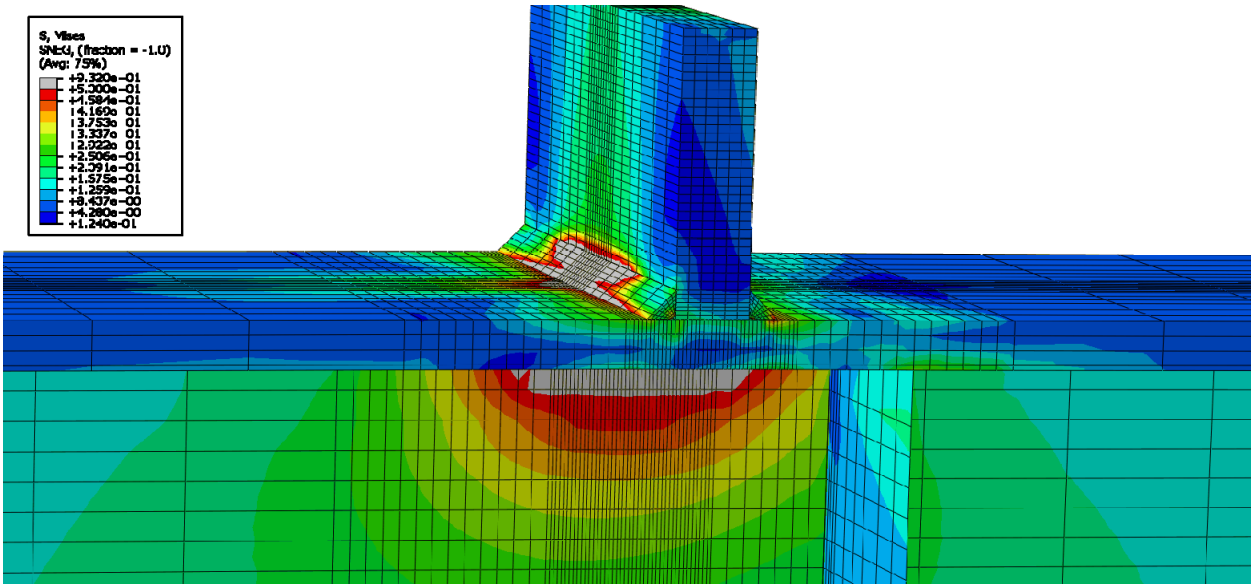

Figure E-342: Finite element model of W24X131-ST-E4 with 9/16 in. welds during inelastic behavior

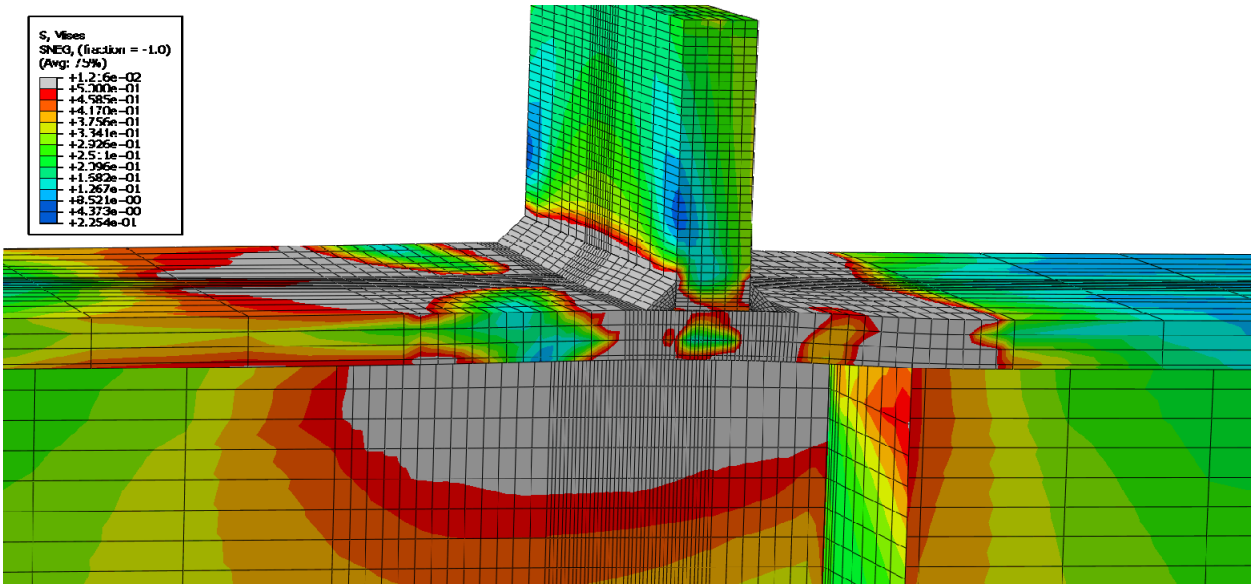

Figure E-343: Finite element model of W24X131-ST-E4 with 9/16 in. welds at its load capacity of 445.15 kips

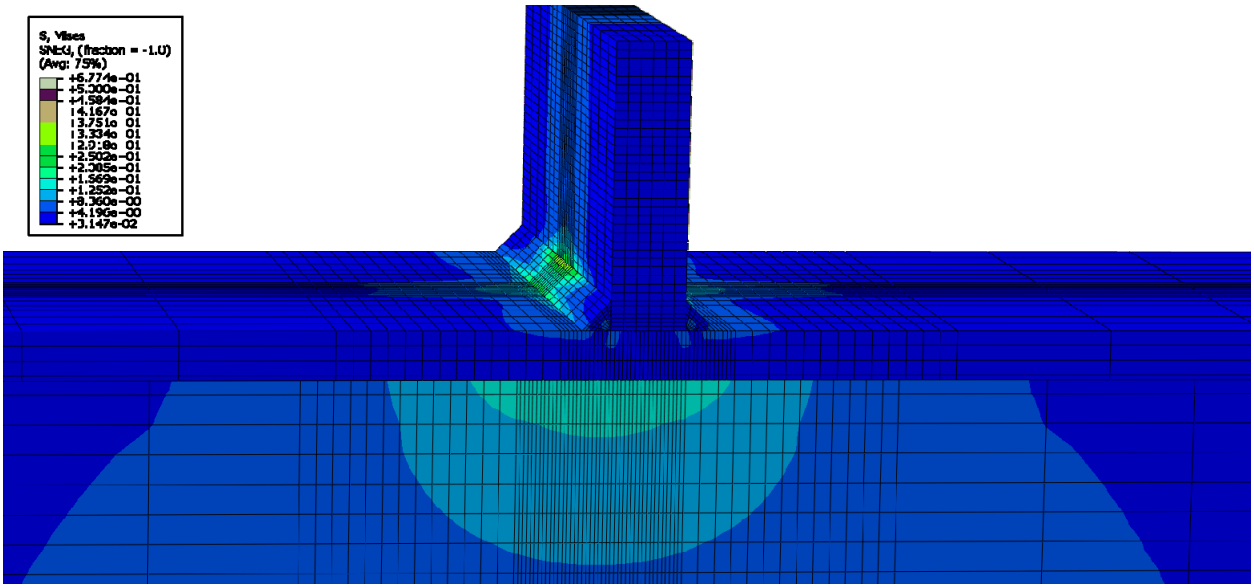

Figure E-344: Finite element model of W24X131-ST-NA with 9/16 in. welds while remaining elastic

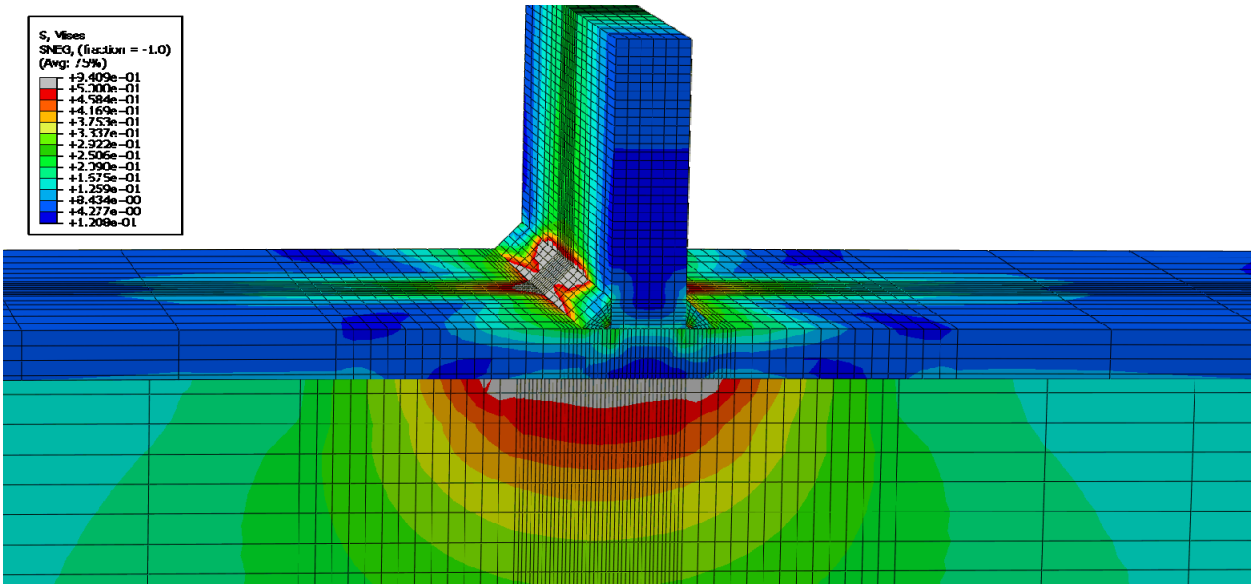

Figure E-345: Finite element model of W24X131-ST-NA with 9/16 in. welds during inelastic behavior

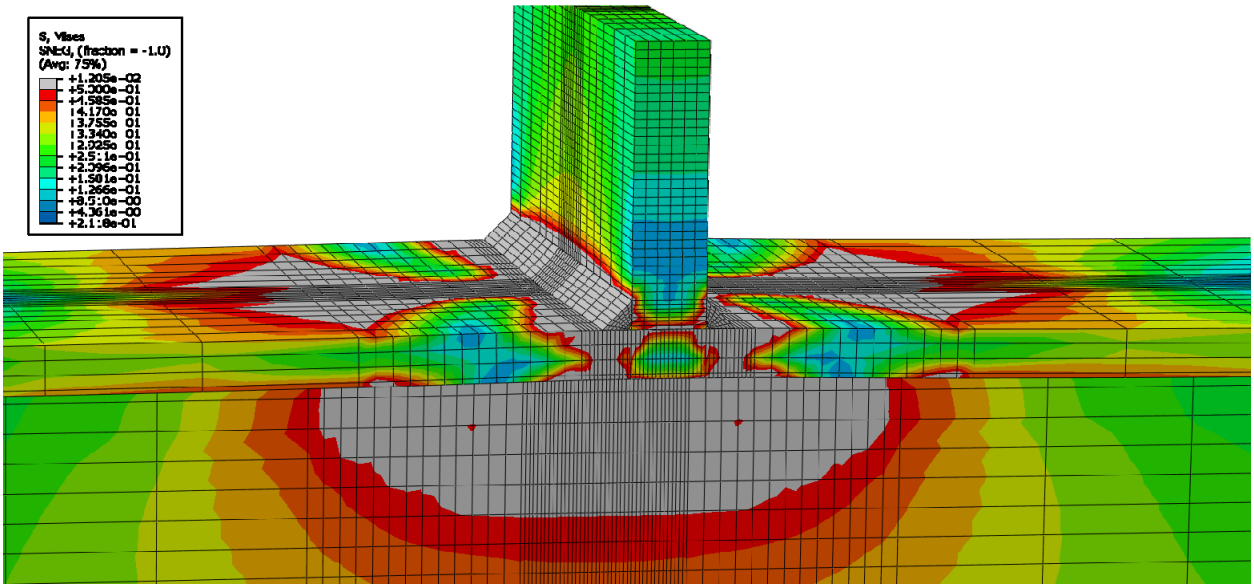

Figure E-346: Finite element model of W24X131-ST-NA with 9/16 in. welds at its load capacity of 402.30 kips

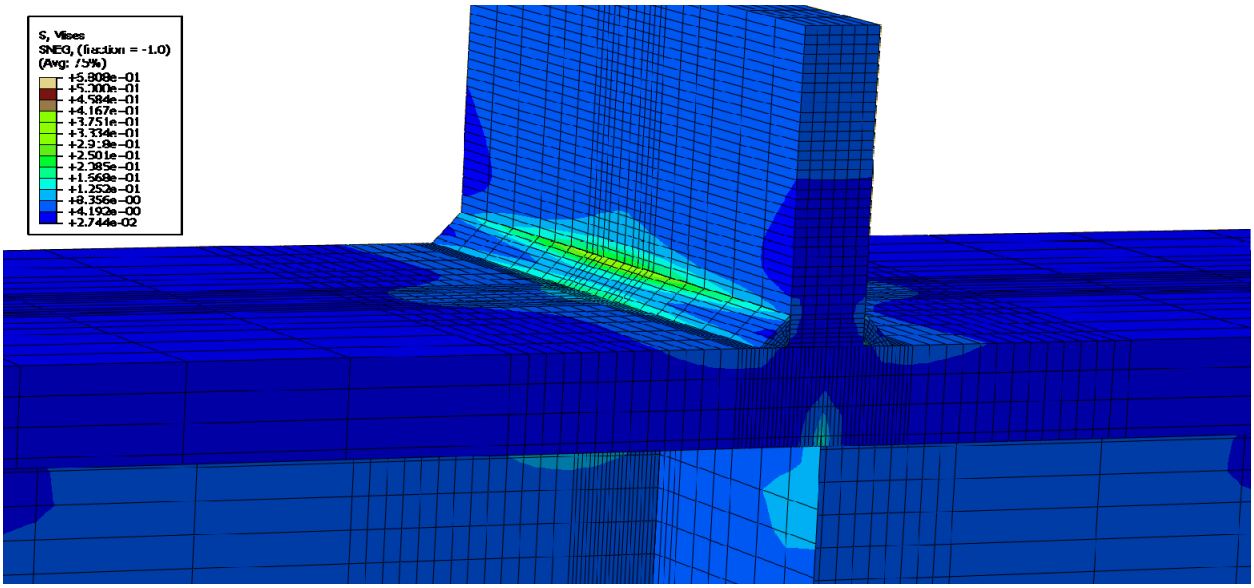

Figure E-347: Finite element model of W24X229-ST-E0 with 9/16 in. welds while remaining elastic

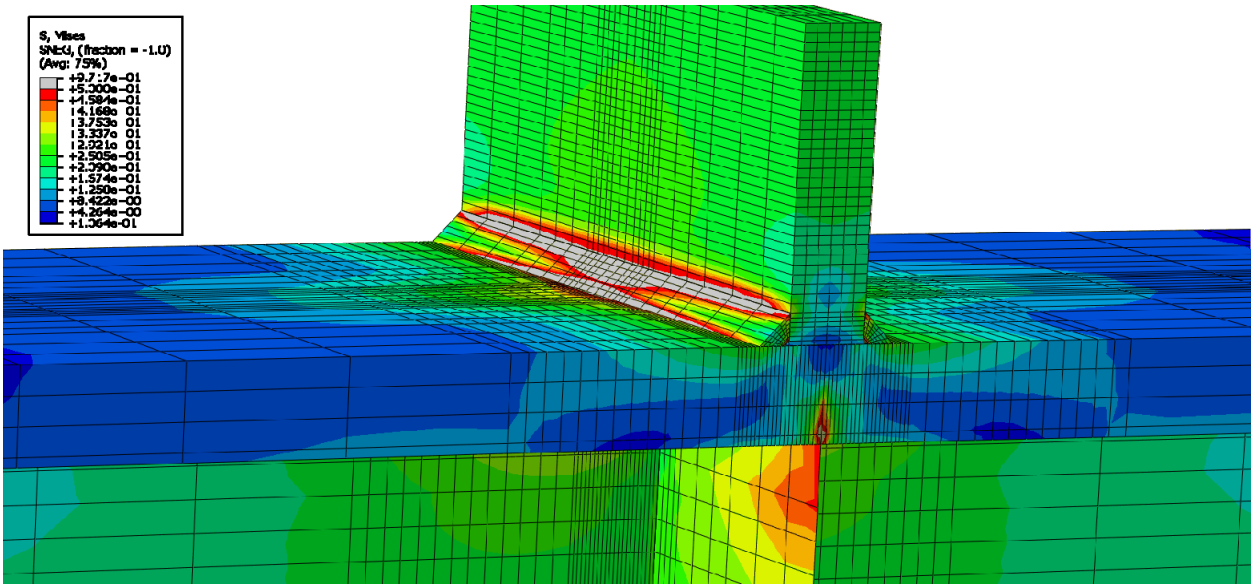

Figure E-348: Finite element model of W24X229-ST-E0 with 9/16 in. welds during inelastic behavior

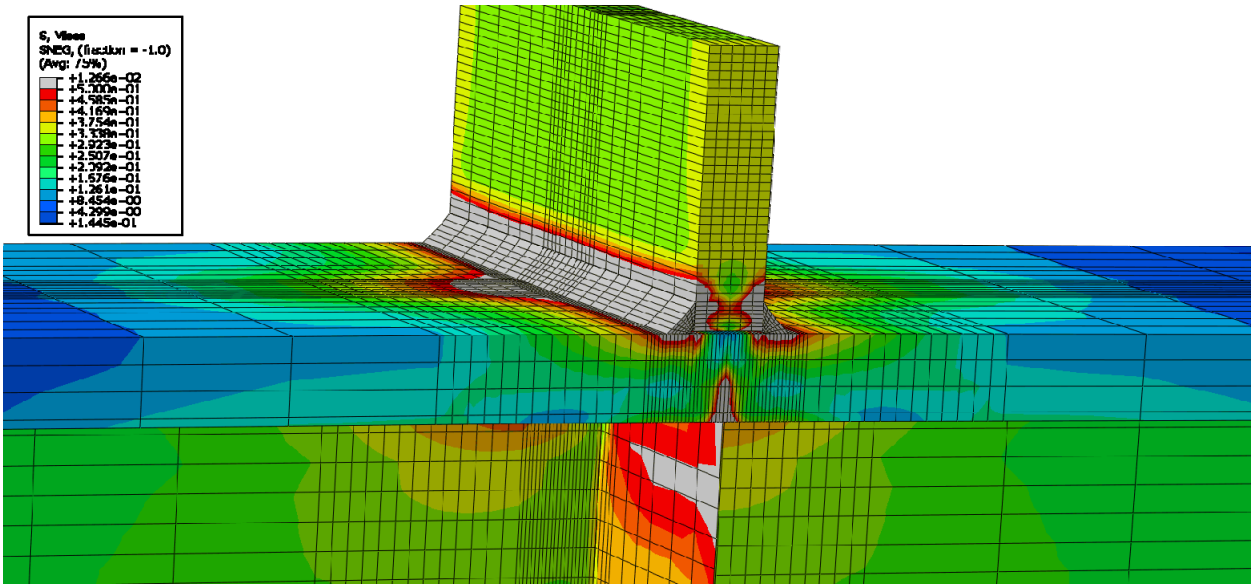

Figure E-349: Finite element model of W24X229-ST-E0 with 9/16 in. welds at its load capacity of 591.02 kips

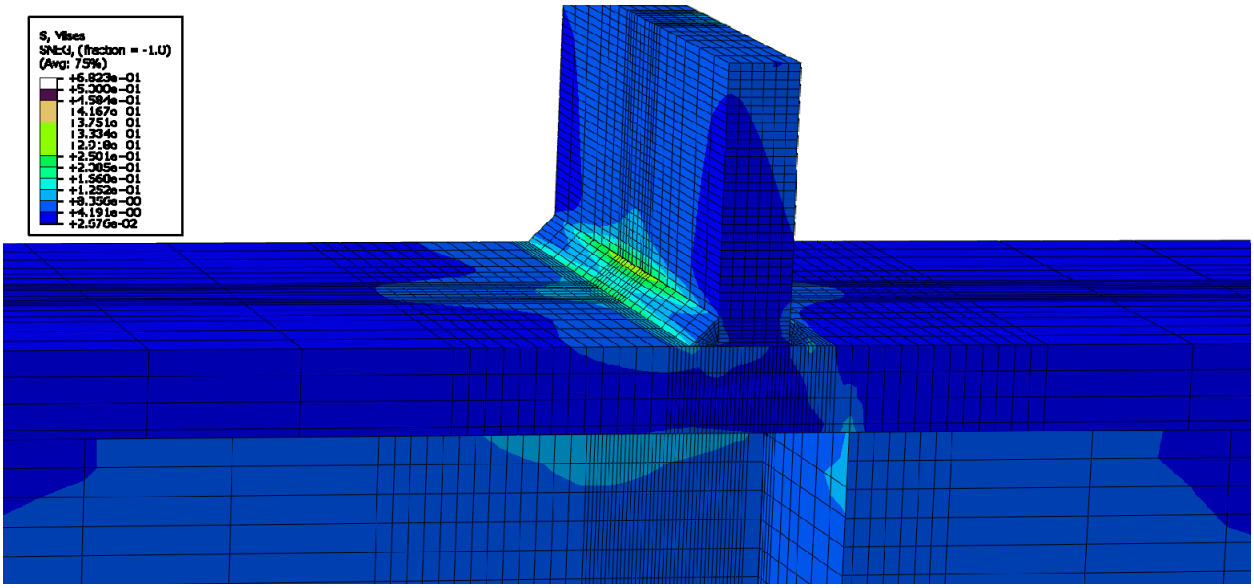

Figure E-350: Finite element model of W24X229-ST-E2 with 9/16 in. welds while remaining elastic

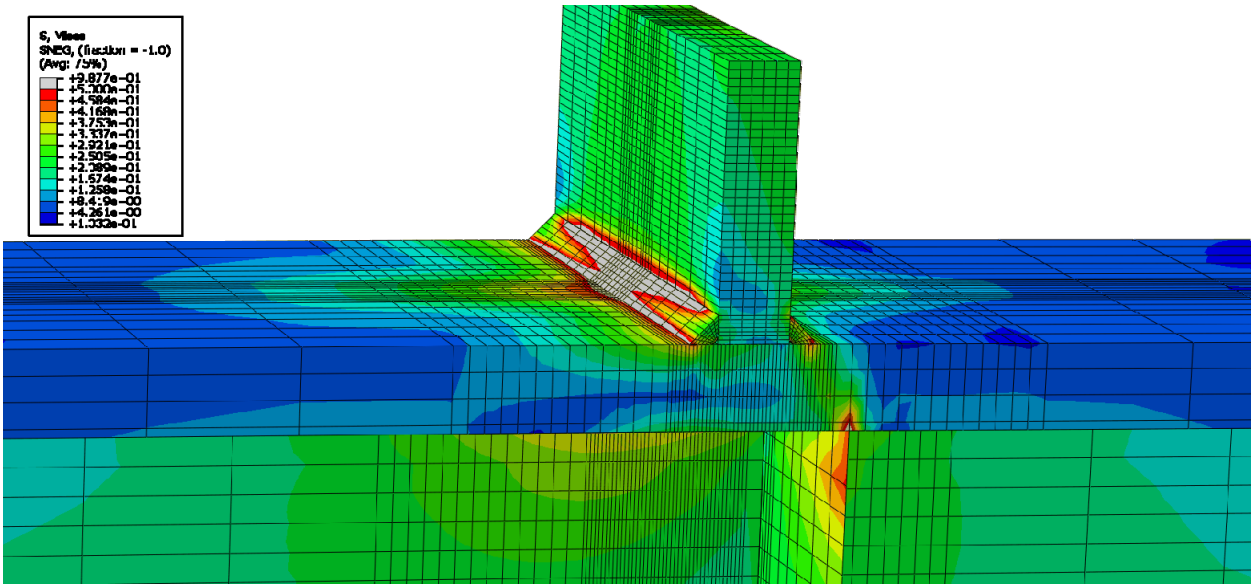

Figure E-351: Finite element model of W24X229-ST-E2 with 9/16 in. welds during inelastic behavior

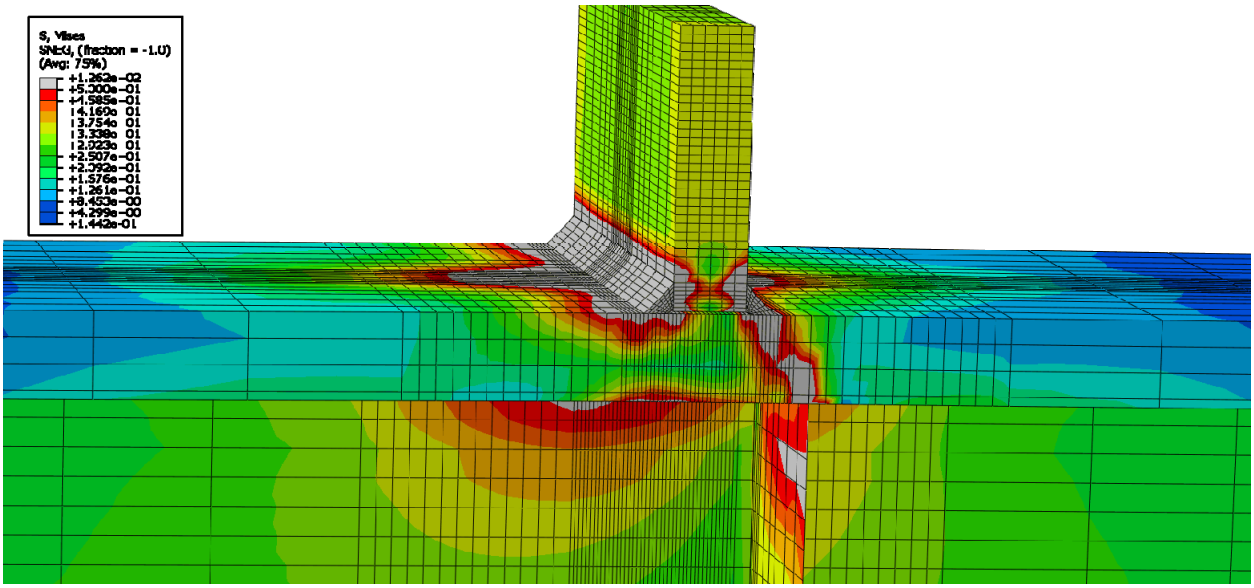

Figure E-352: Finite element model of W24X229-ST-E2 with 9/16 in. welds at its load capacity of 590.48 kips

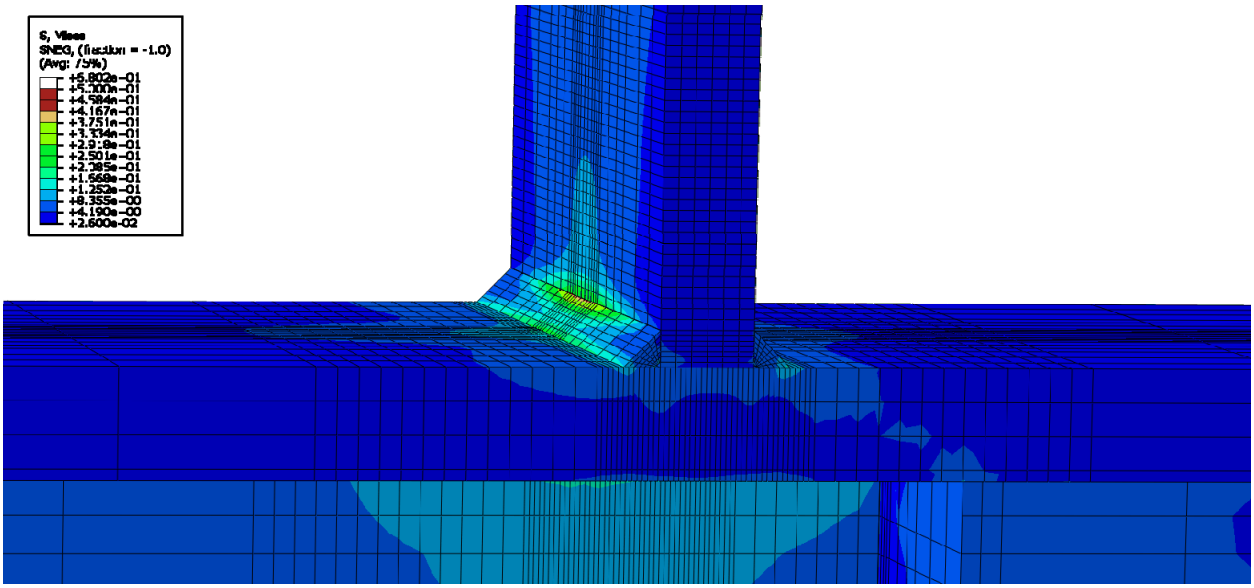

Figure E-353: Finite element model of W24X229-ST-E4 with 9/16 in. welds while remaining elastic

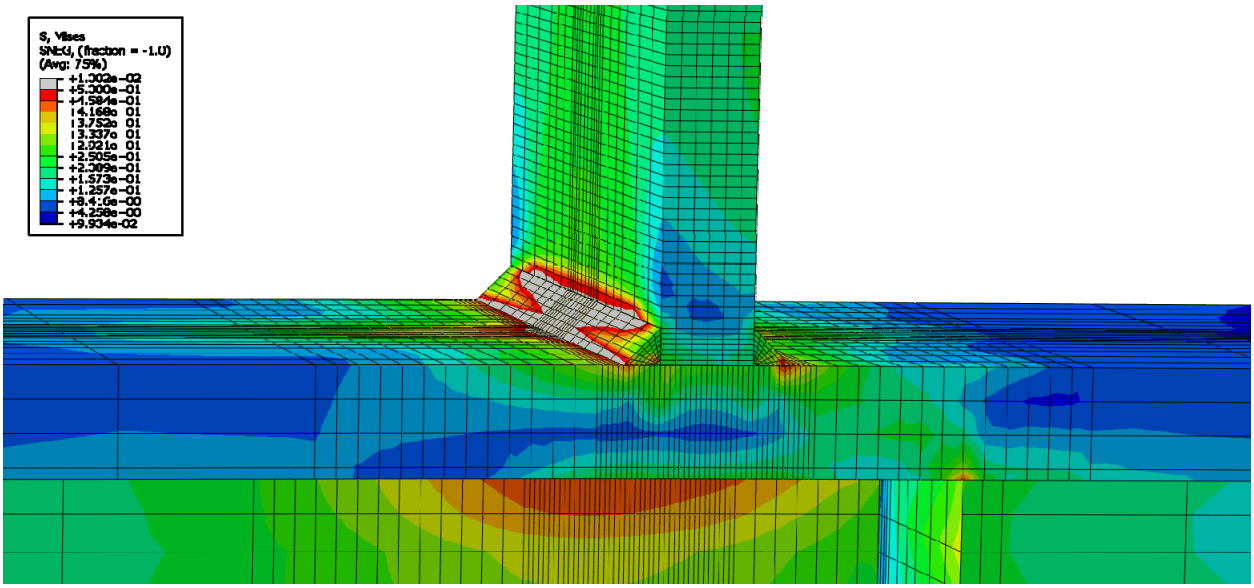

Figure E-354: Finite element model of W24X229-ST-E4 with 9/16 in. welds during inelastic behavior

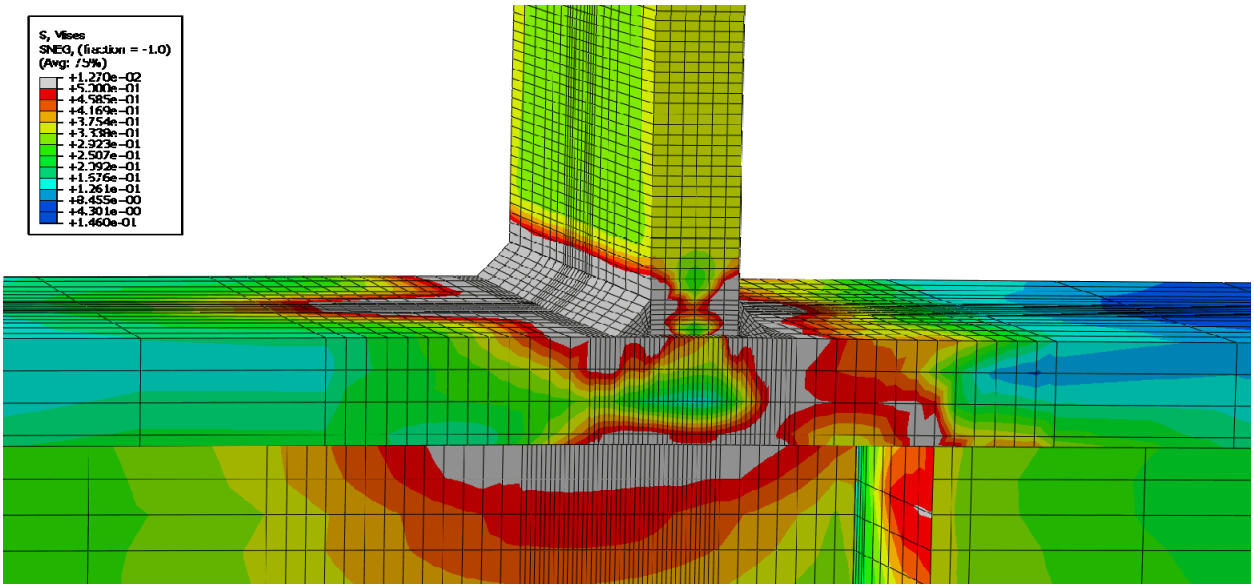

Figure E-355: Finite element model of W24X229-ST-E4 with 9/16 in. welds at its load capacity of 590.36 kips

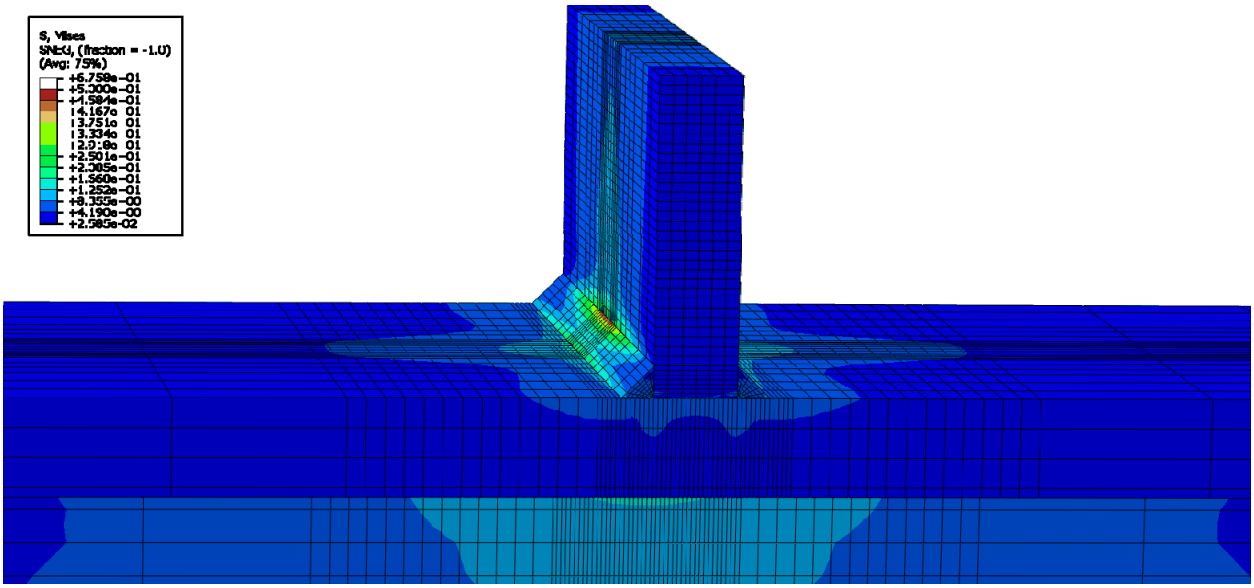

Figure E-356: Finite element model of W24X229-ST-NA with 9/16 in. welds while remaining elastic

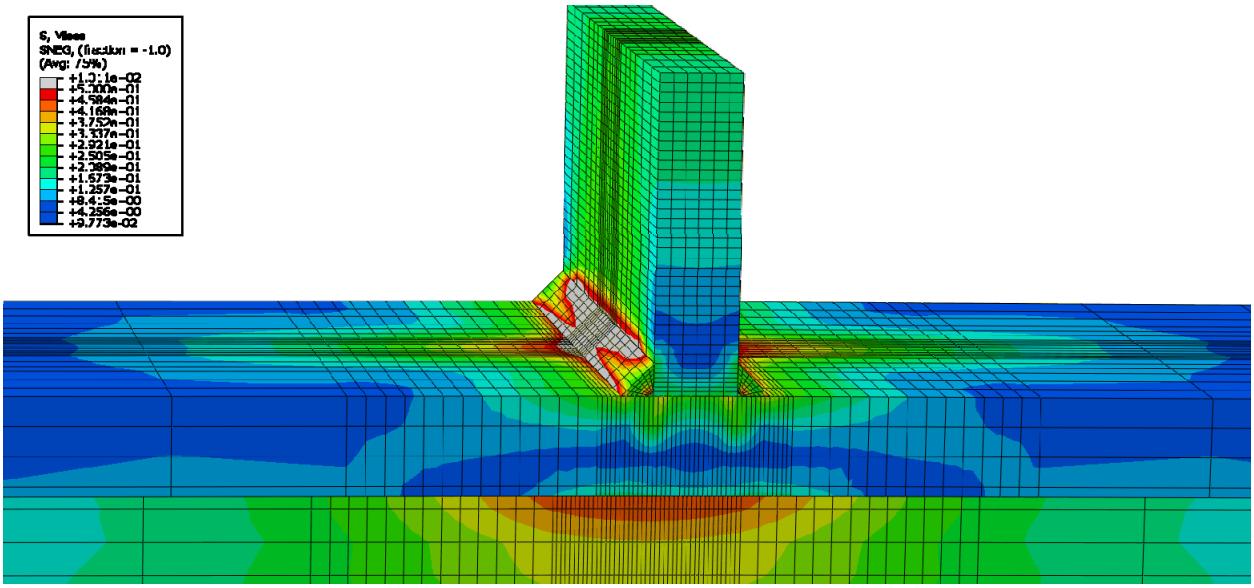

Figure E-357: Finite element model of W24X229-ST-NA with 9/16 in. welds during inelastic behavior

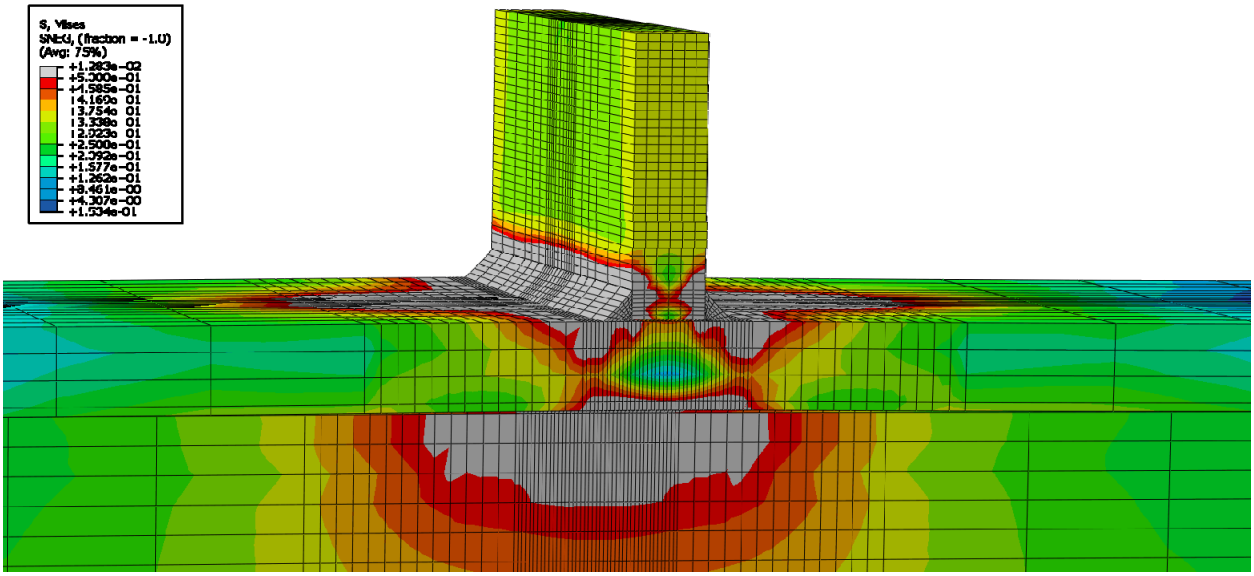

Figure E-358: Finite element model of W24X229-ST-NA with 9/16 in. welds at its load capacity of 589.70 kips

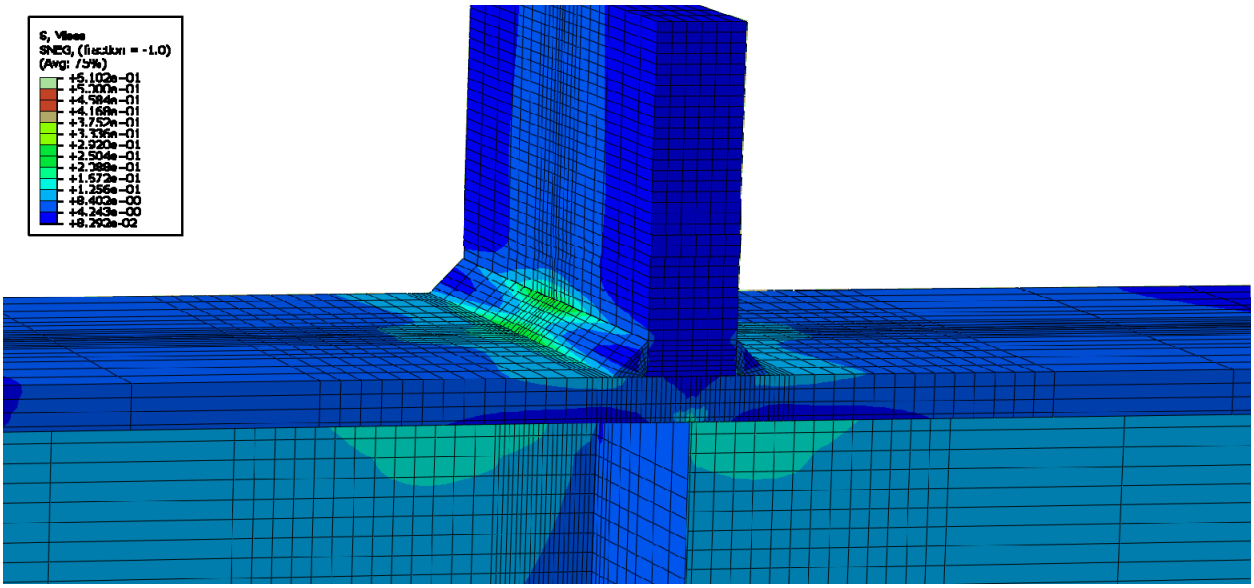

Figure E-359: Finite element model of W14X68-ST-E0 with 9/16 in. welds while remaining elastic

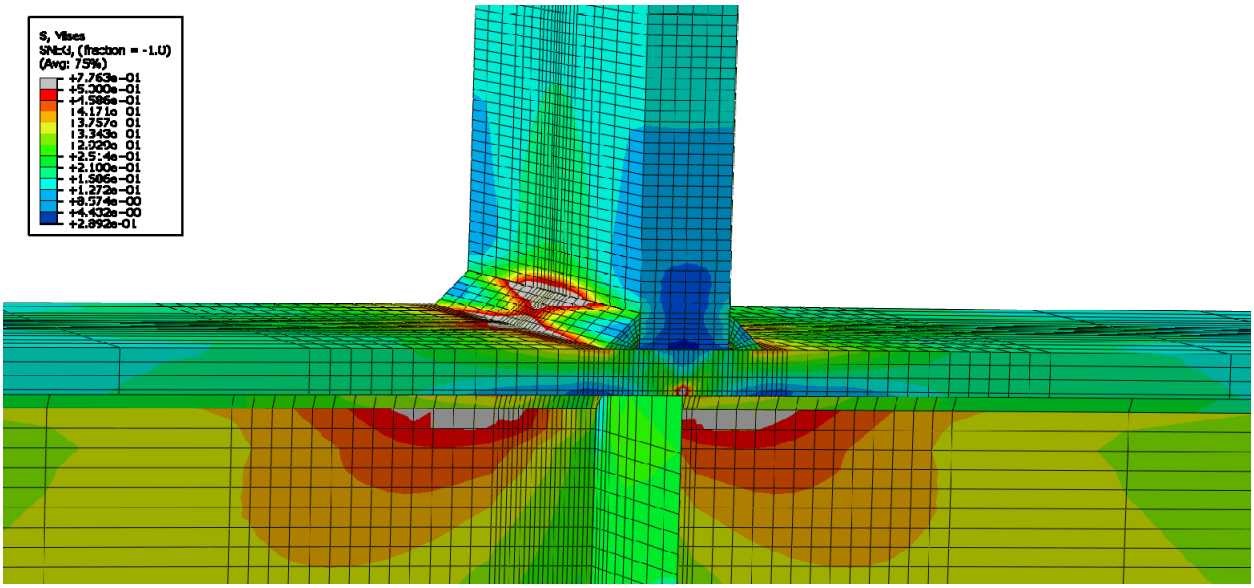

Figure E-360: Finite element model of W14X68-ST-E0 with 9/16 in. welds during inelastic behavior

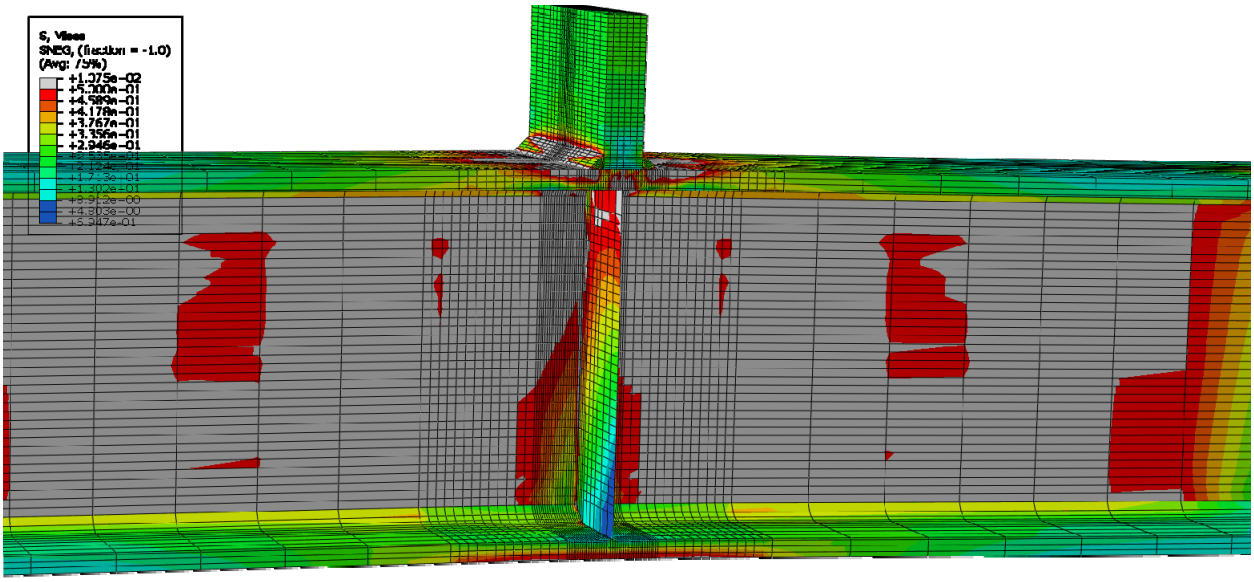

Figure E-361: Finite element model of W14X68-ST-E0 with 9/16 in. welds at its load capacity of 342.72 kips

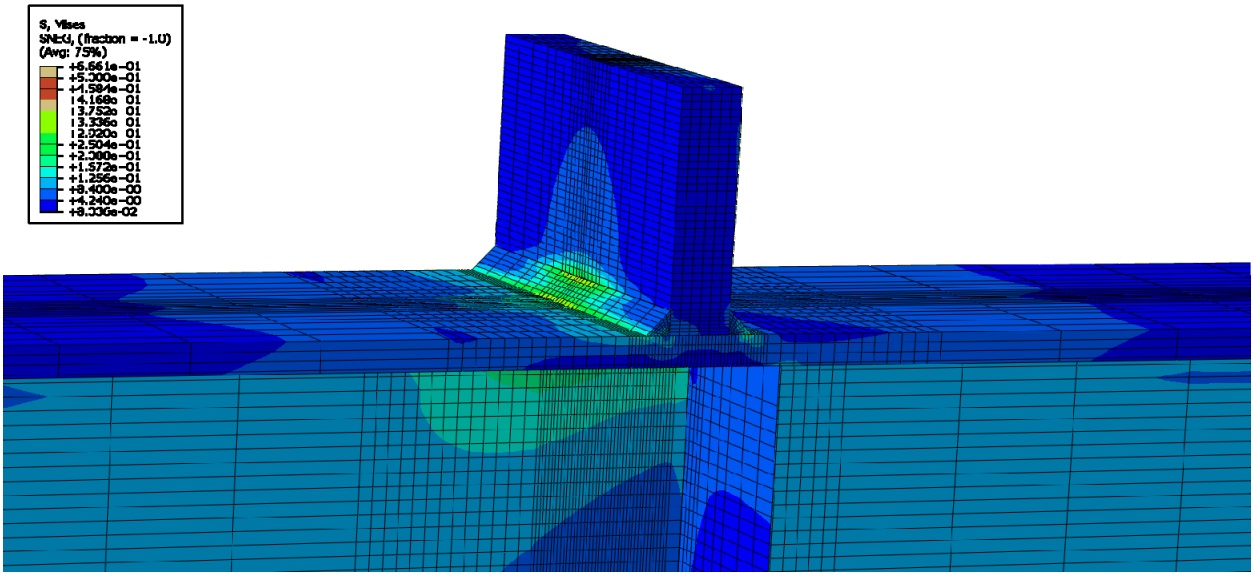

Figure E-362: Finite element model of W14X68-ST-E2 with 9/16 in. welds while remaining elastic

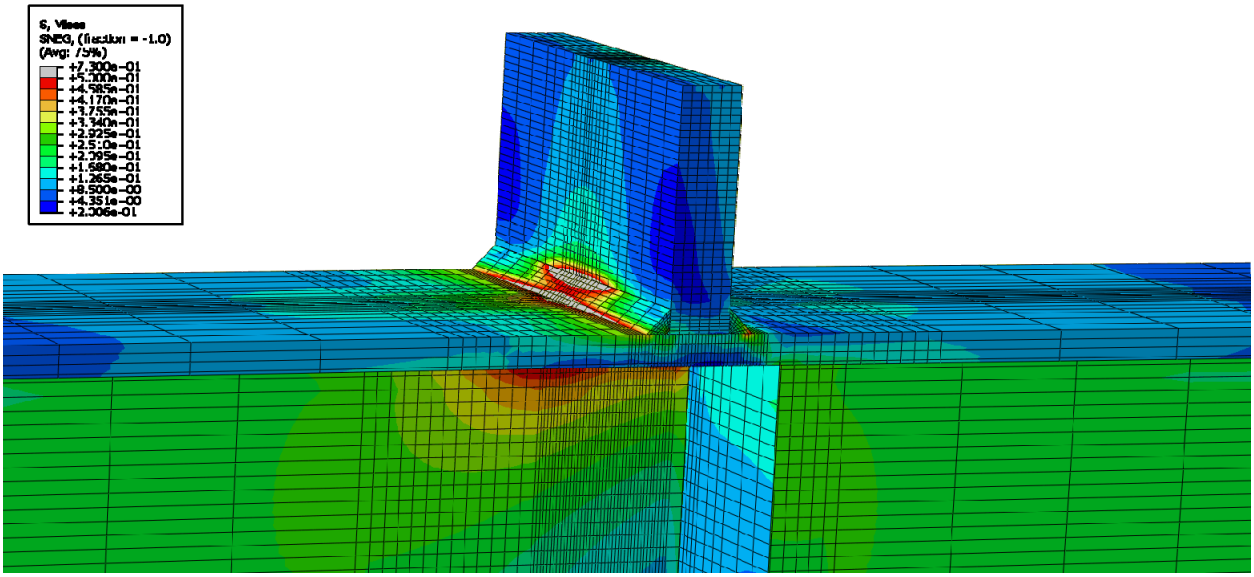

Figure E-363: Finite element model of W14X68-ST-E2 with 9/16 in. welds during inelastic behavior

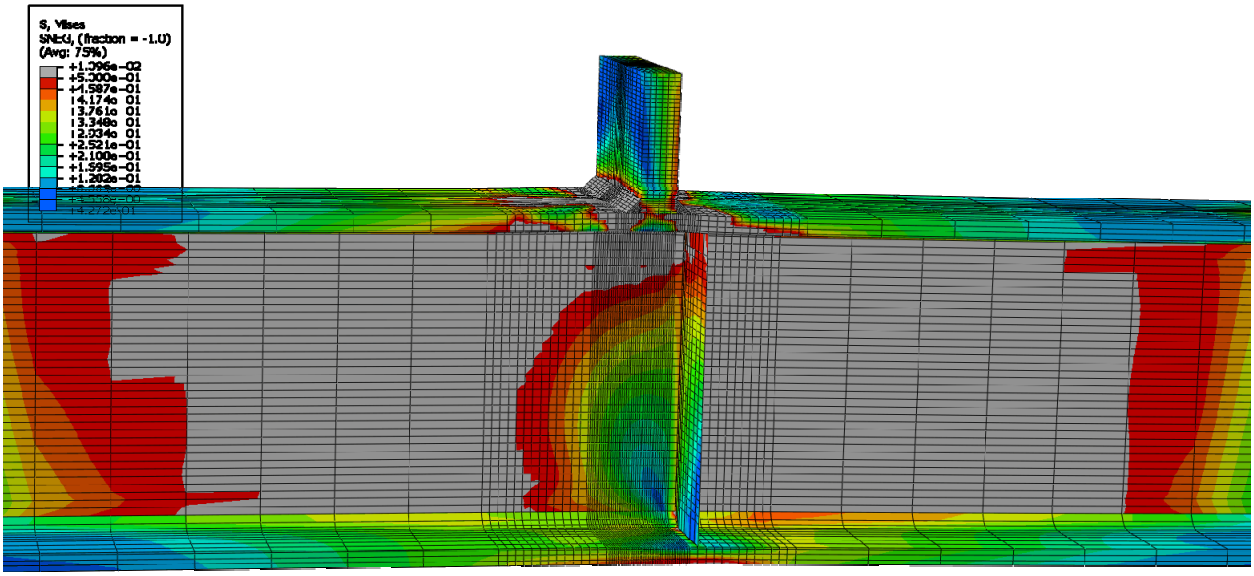

Figure E-364: Finite element model of W14X68-ST-E2 with 9/16 in. welds at its load capacity of 308.41 kips

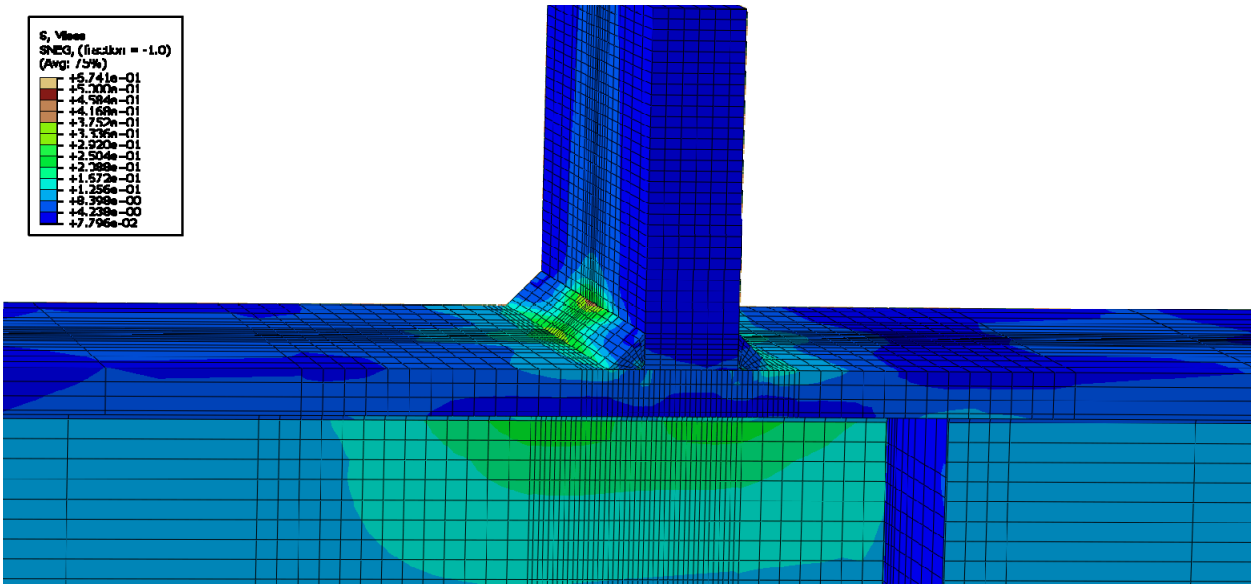

Figure E-365: Finite element model of W14X68-ST-E4 with 9/16 in. welds while remaining elastic

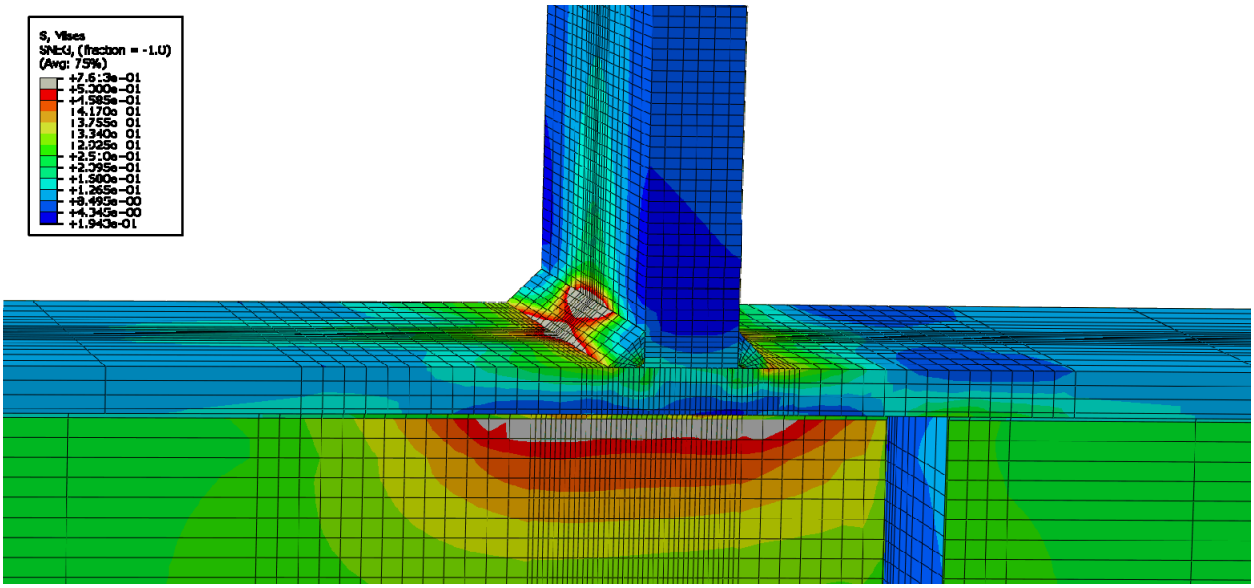

Figure E-366: Finite element model of W14X68-ST-E4 with 9/16 in. welds during inelastic behavior

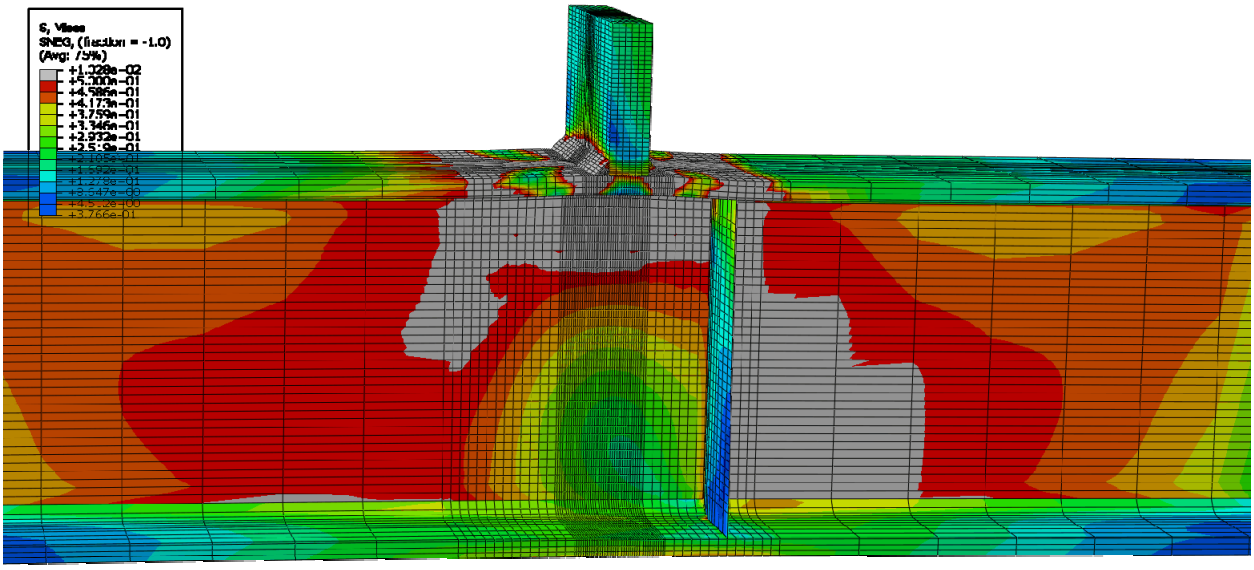

Figure E-367: Finite element model of W14X68-ST-E4 with 9/16 in. welds at its load capacity of 274.97 kips

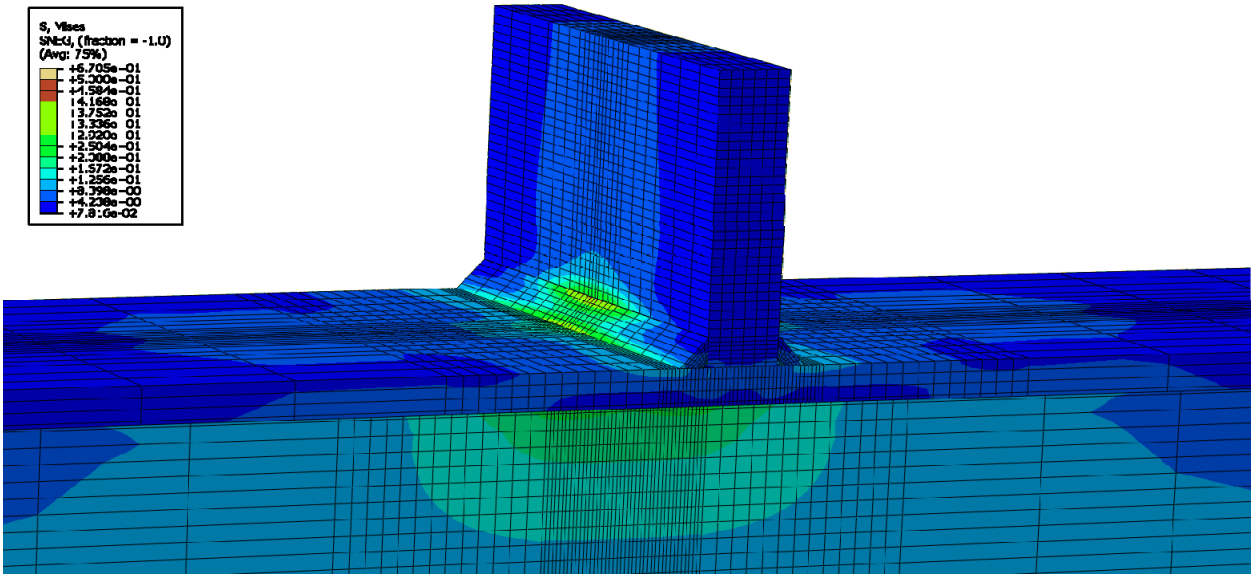

Figure E-368: Finite element model of W14X68-ST-NA with 9/16 in. welds while remaining elastic

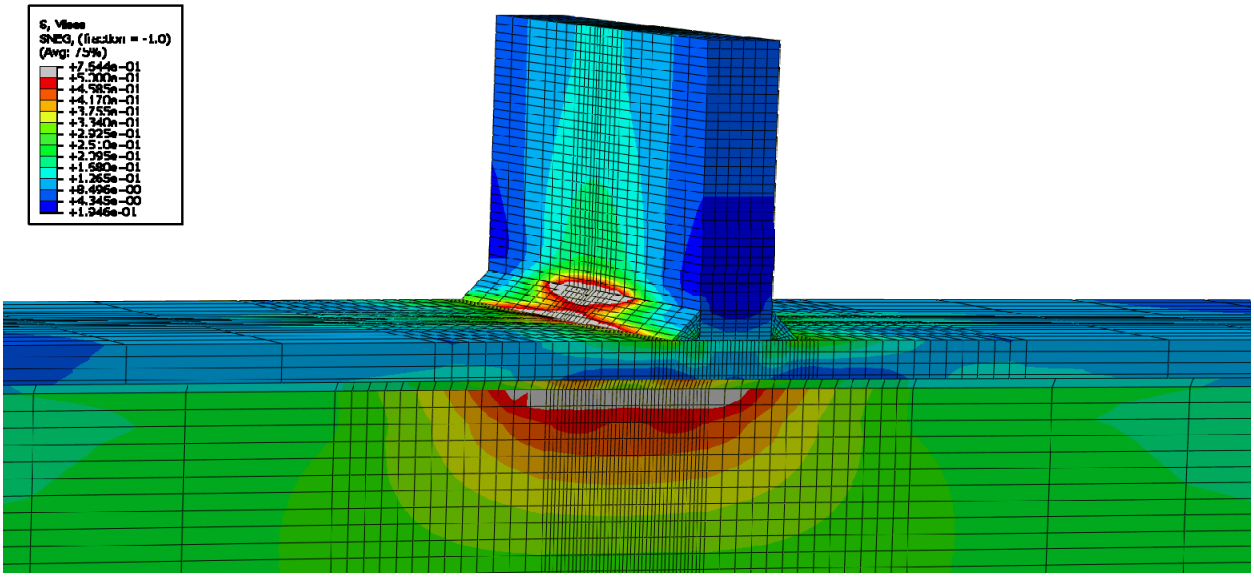

Figure E-369: Finite element model of W14X68-ST-NA with 9/16 in. welds during inelastic behavior

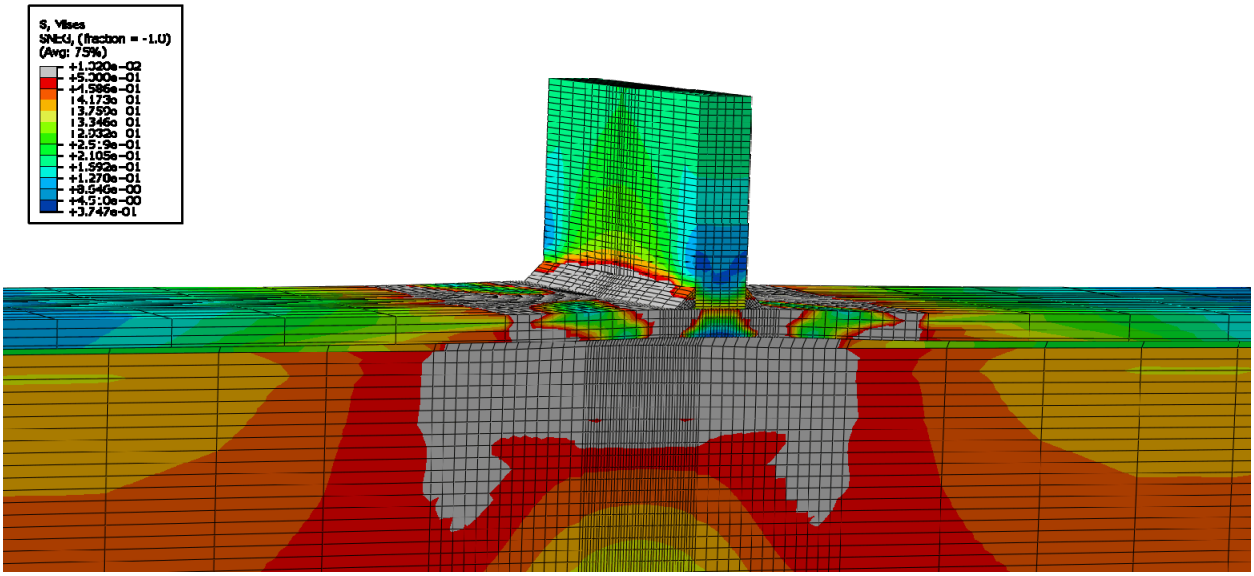

Figure E-370: Finite element model of W14X68-ST-NA with 9/16 in. welds at its load capacity of 259.47 kips

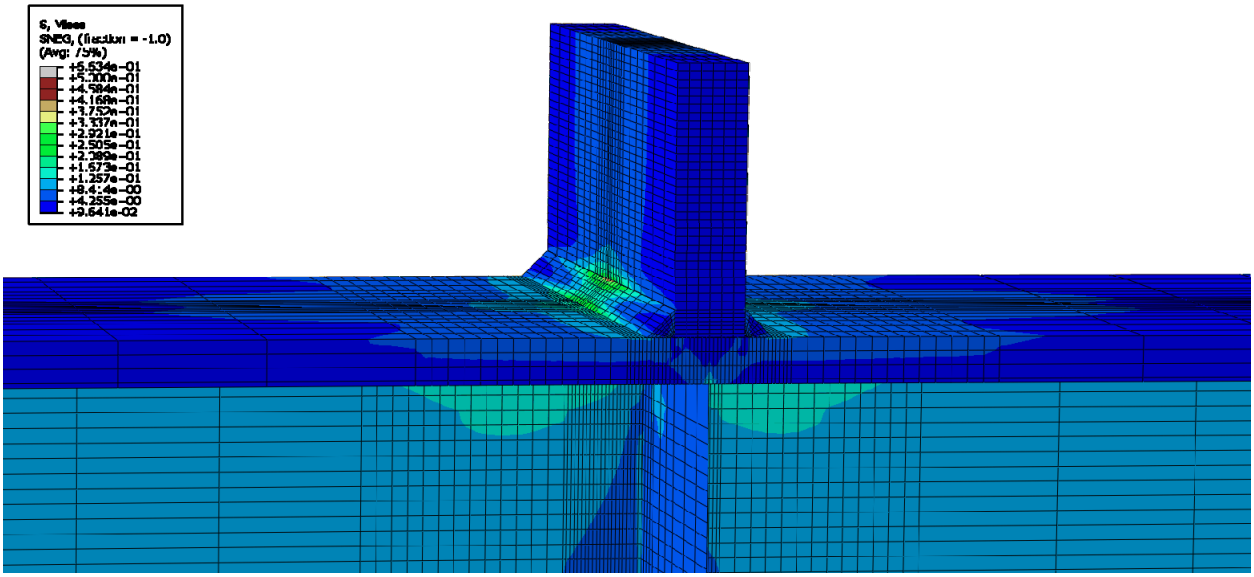

Figure E-371: Finite element model of W14X120-ST-E0 with 9/16 in. welds while remaining elastic

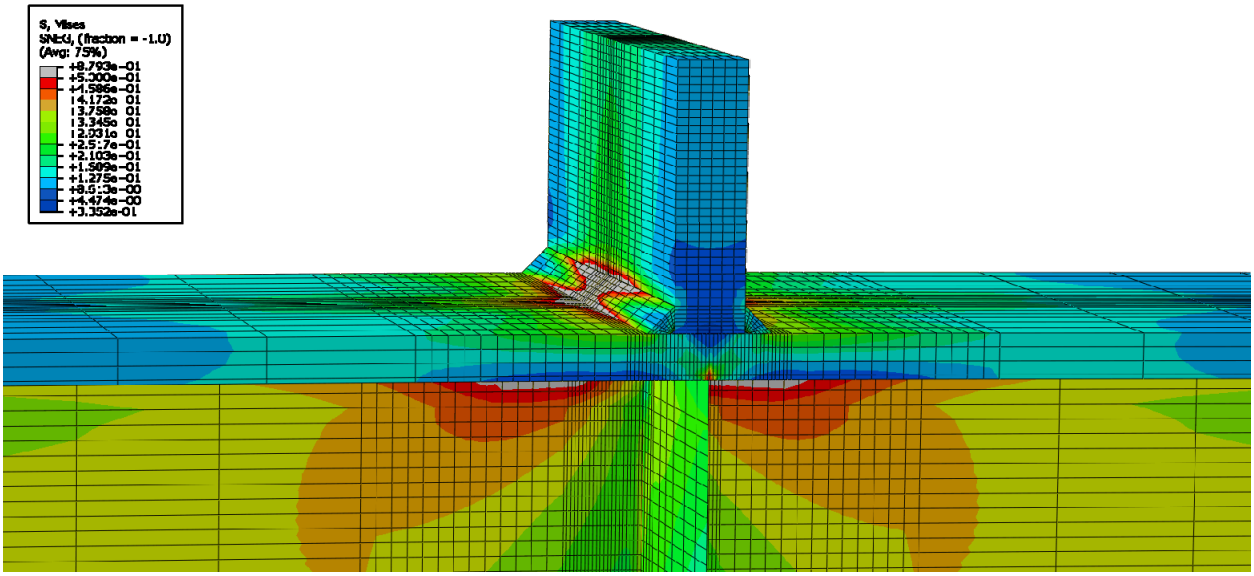

Figure E-372: Finite element model of W14X120-ST-E0 with 9/16 in. welds during inelastic behavior

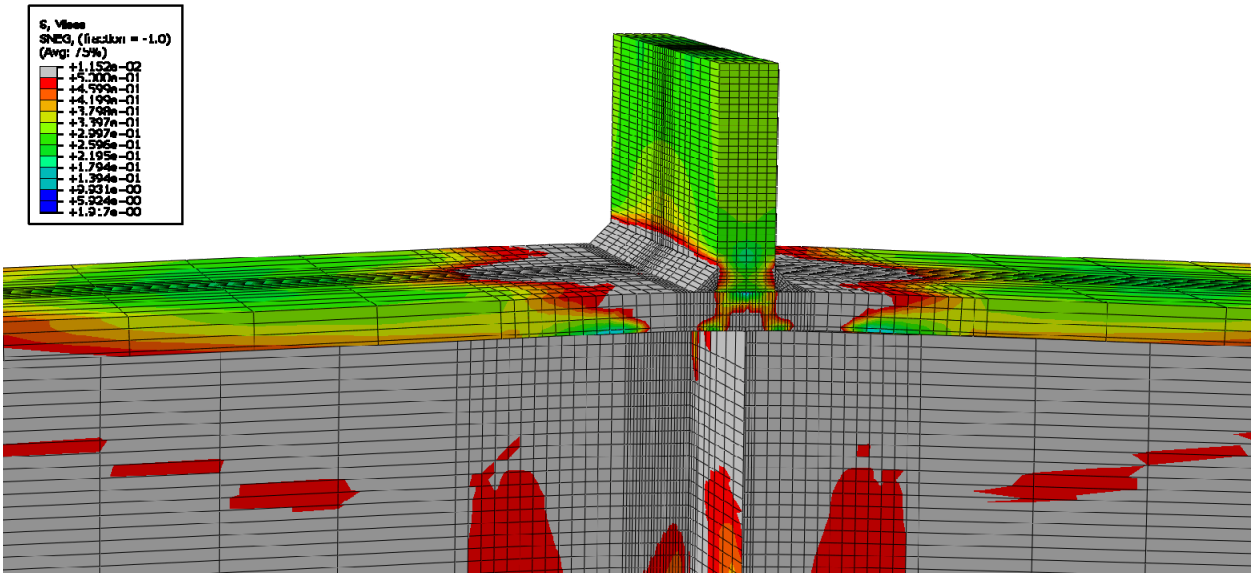

Figure E-373: Finite element model of W14X120-ST-E0 with 9/16 in. welds at its load capacity of 621.02 kips

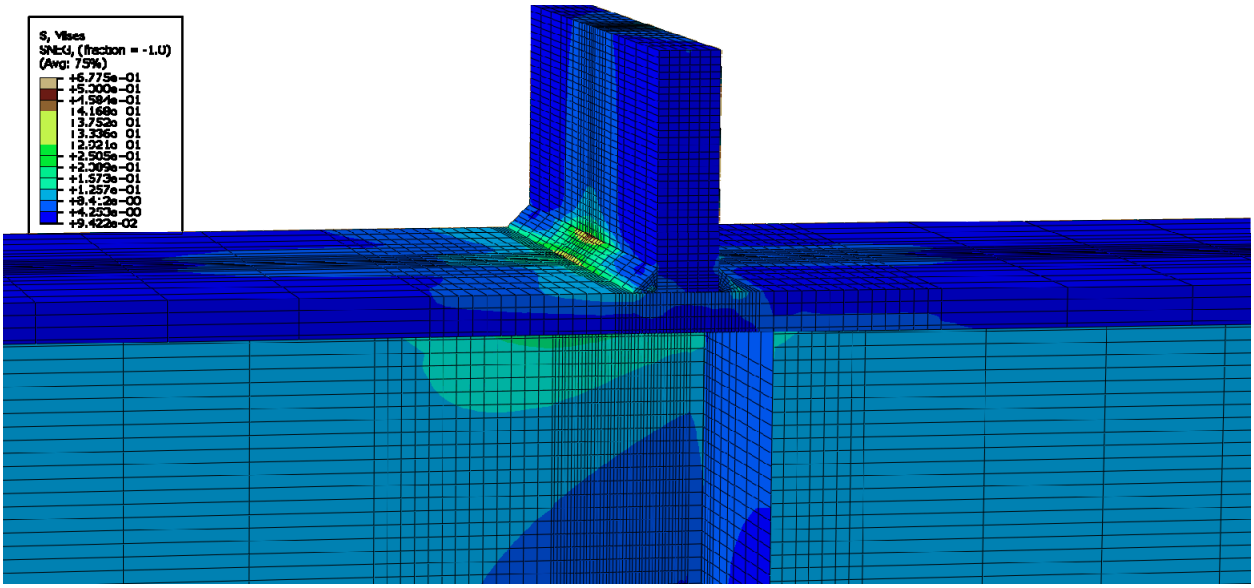

Figure E-374: Finite element model of W14X120-ST-E2 with 9/16 in. welds while remaining elastic

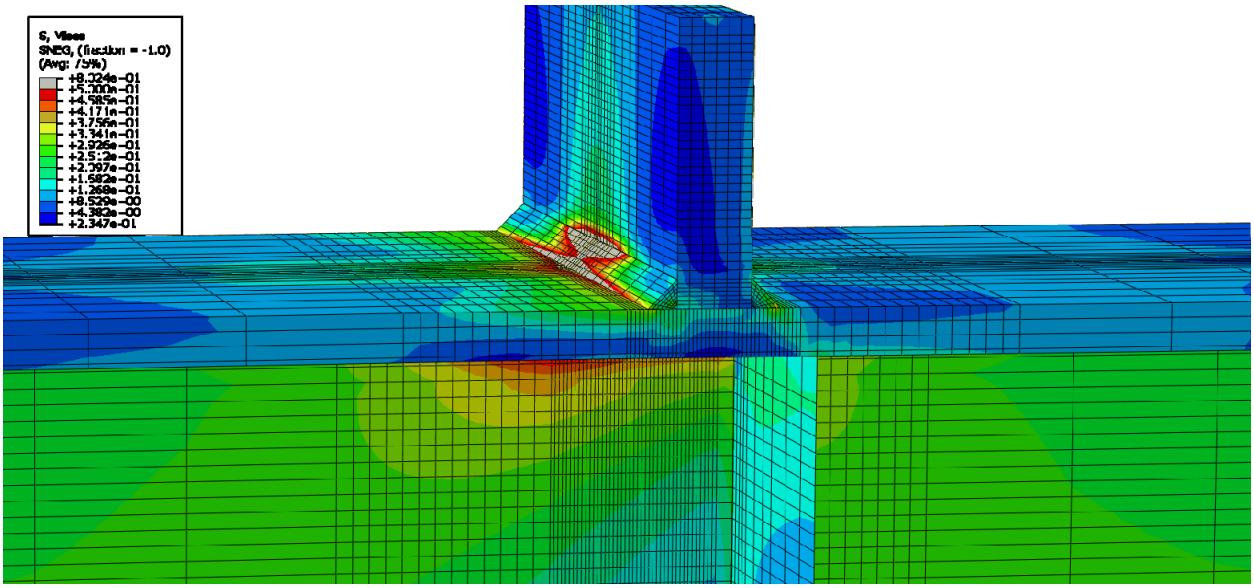

Figure E-375: Finite element model of W14X120-ST-E2 with 9/16 in. welds during inelastic behavior

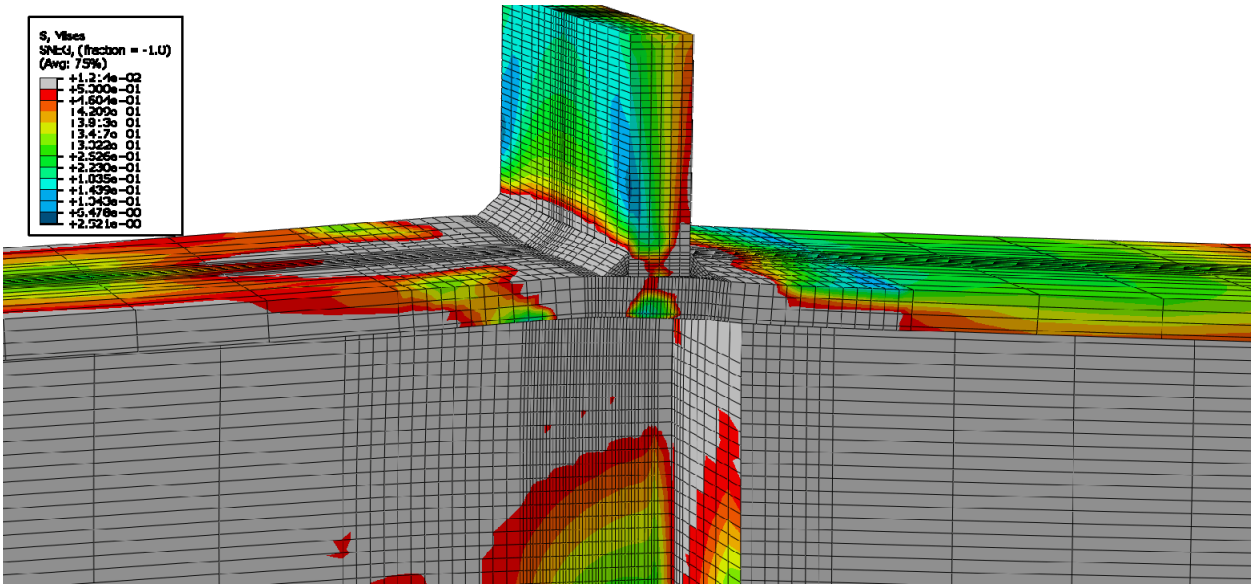

Figure E-376: Finite element model of W14X120-ST-E2 with 9/16 in. welds at its load capacity of 562.15 kips

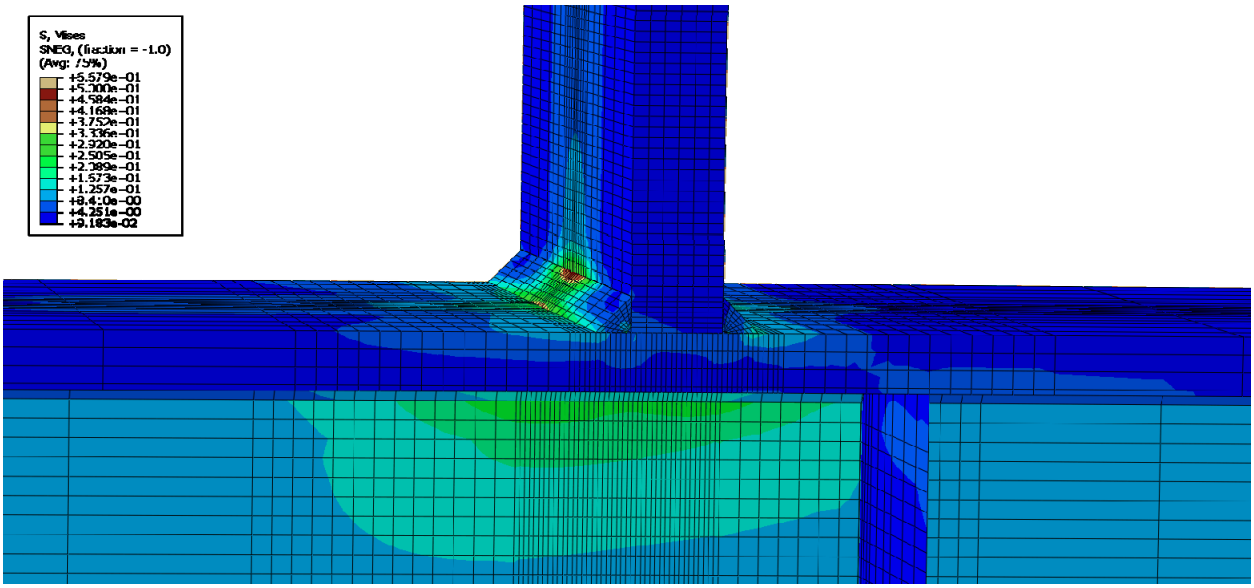

Figure E-377: Finite element model of W14X120-ST-E4 with 9/16 in. welds while remaining elastic

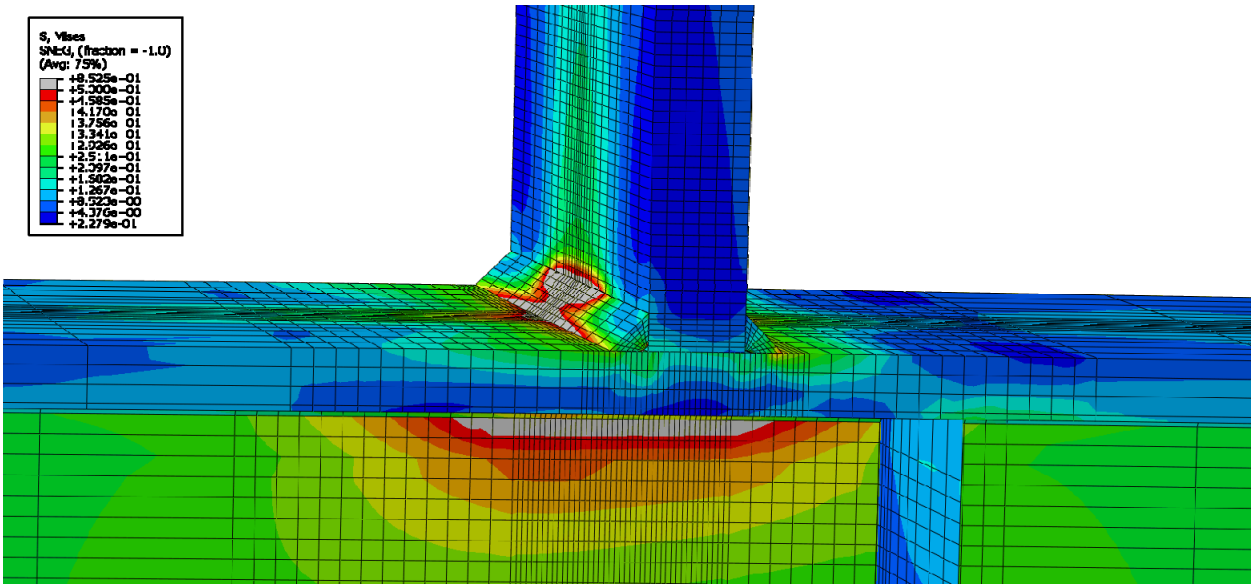

Figure E-378: Finite element model of W14X120-ST-E4 with 9/16 in. welds during inelastic behavior

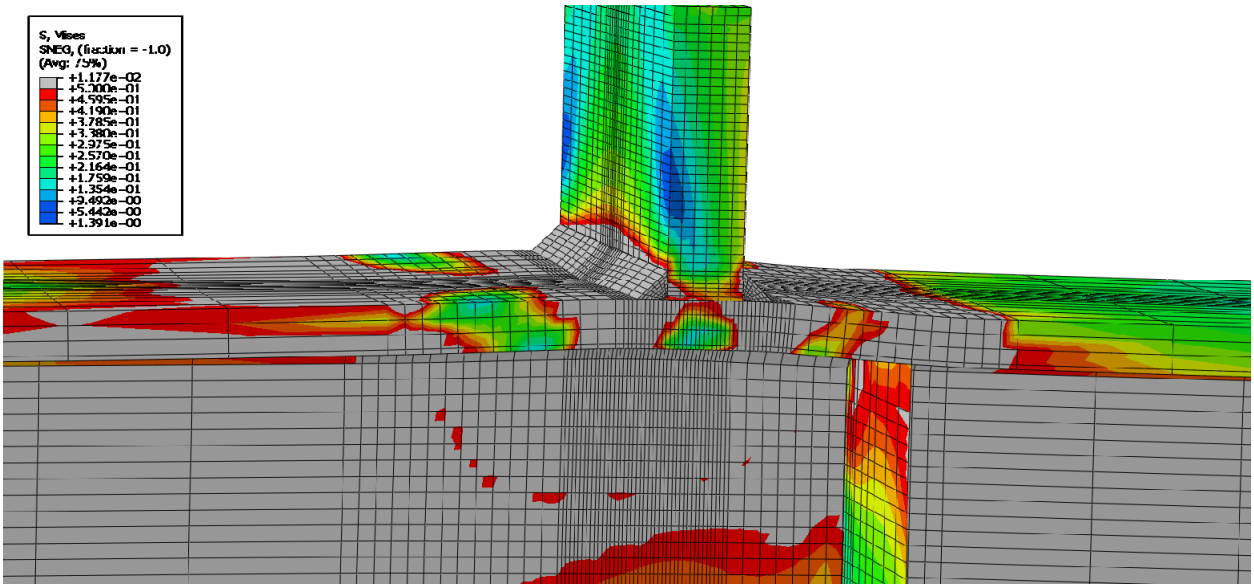

Figure E-379: Finite element model of W14X120-ST-E4 with 9/16 in. welds at its load capacity of 485.25 kips

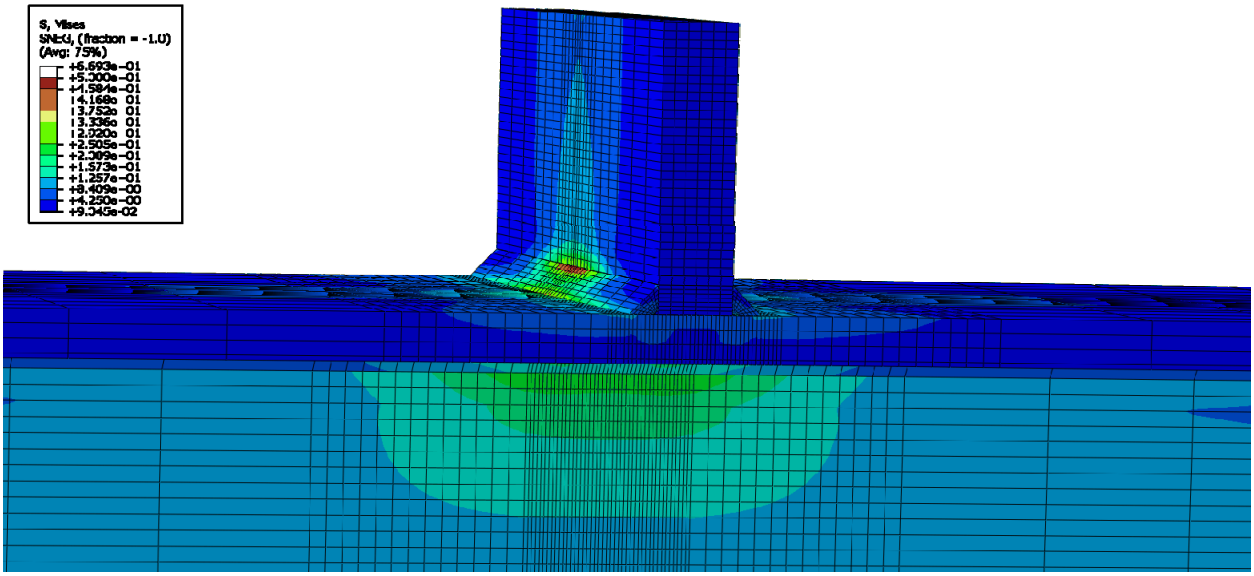

Figure E-380: Finite element model of W14X120-ST-NA with 9/16 in. welds while remaining elastic

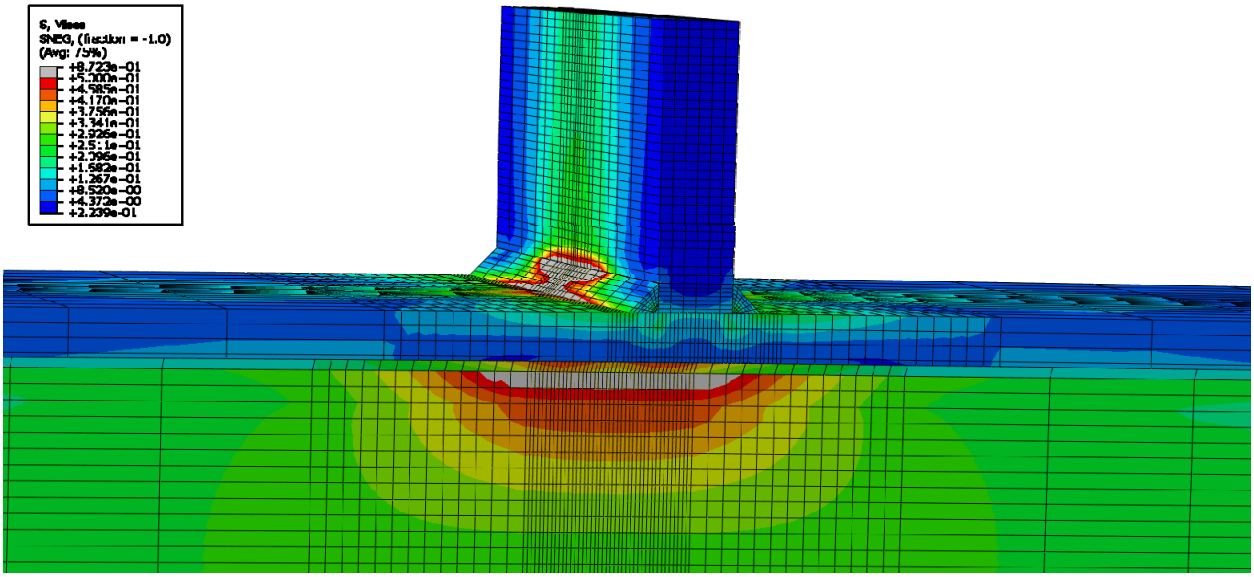

Figure E-381: Finite element model of W14X120-ST-NA with 9/16 in. welds during inelastic behavior

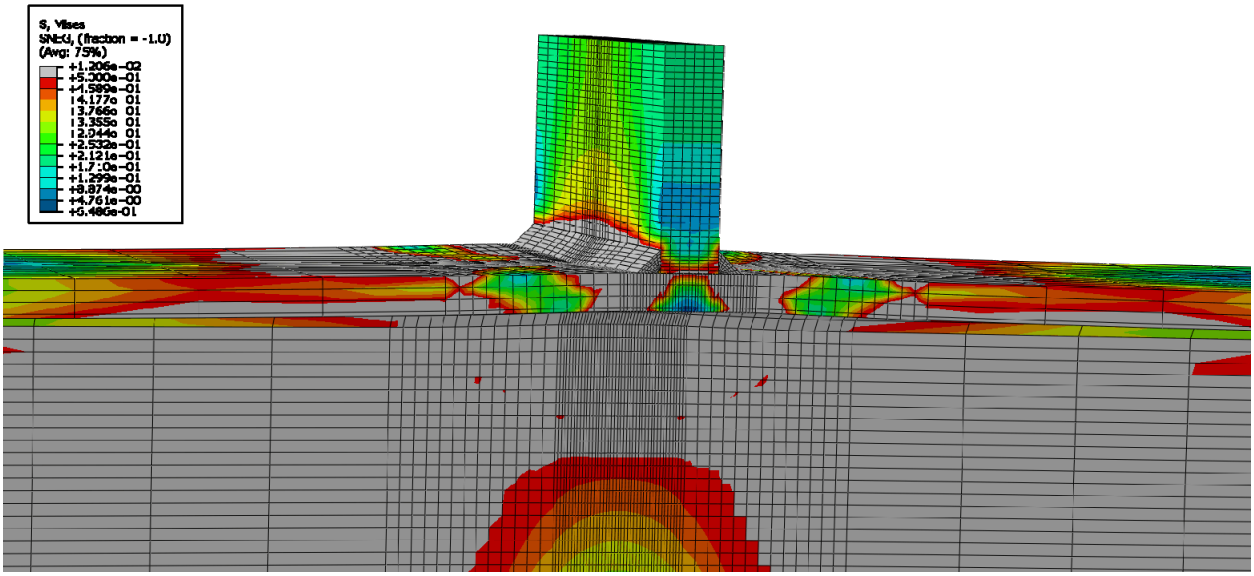

Figure E-382: Finite element model of W14X120-ST-NA with 9/16 in. welds at its load capacity of 449.53 kips

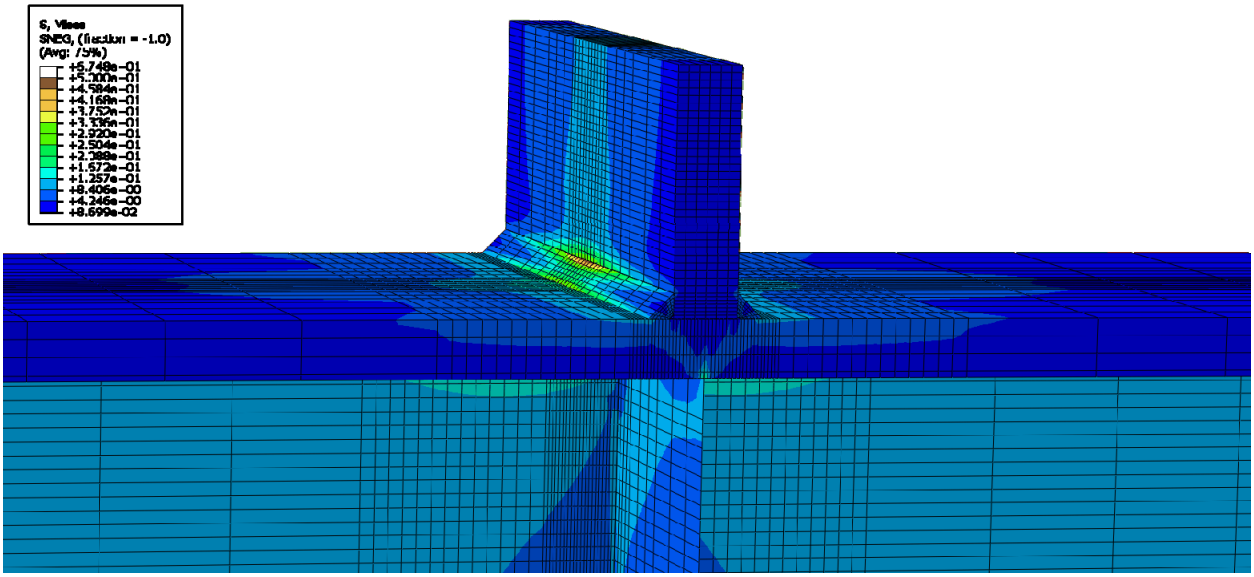

Figure E-383: Finite element model of W14X176-ST-E0 with 9/16 in. welds while remaining elastic

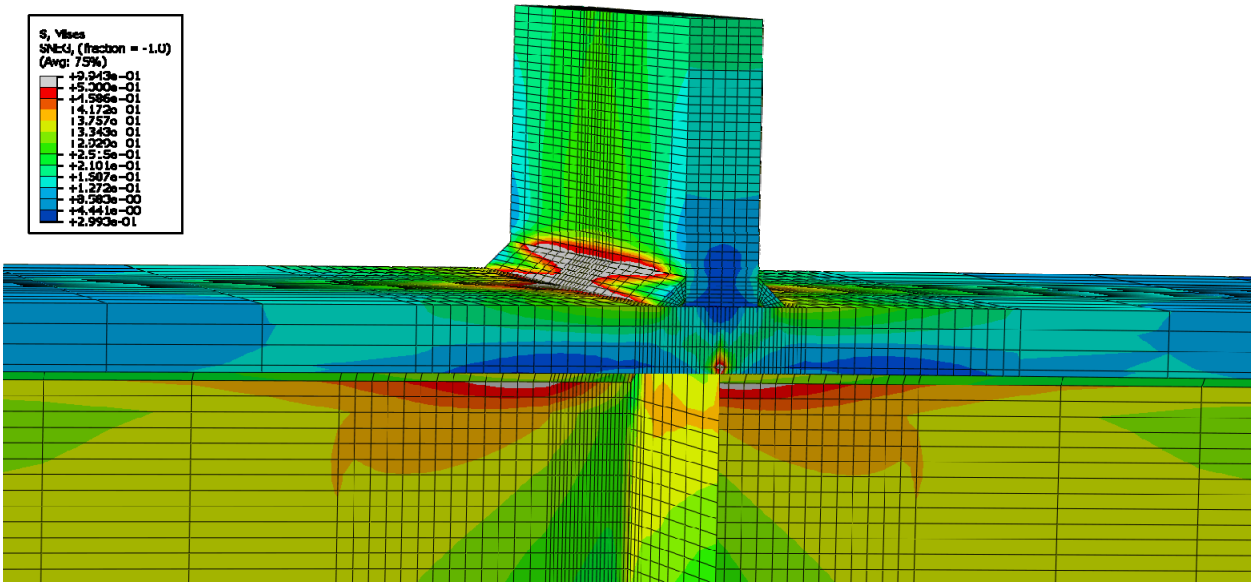

Figure E-384: Finite element model of W14X176-ST-E0 with 9/16 in. welds during inelastic behavior

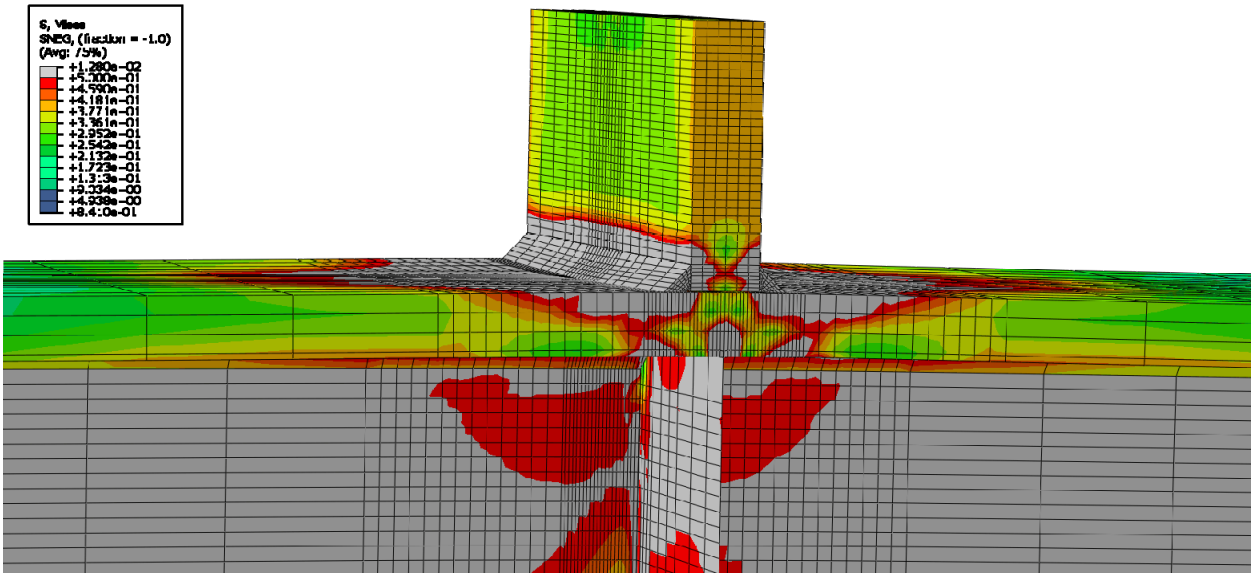

Figure E-385: Finite element model of W14X176-ST-E0 with 9/16 in. welds at its load capacity of 699.53 kips

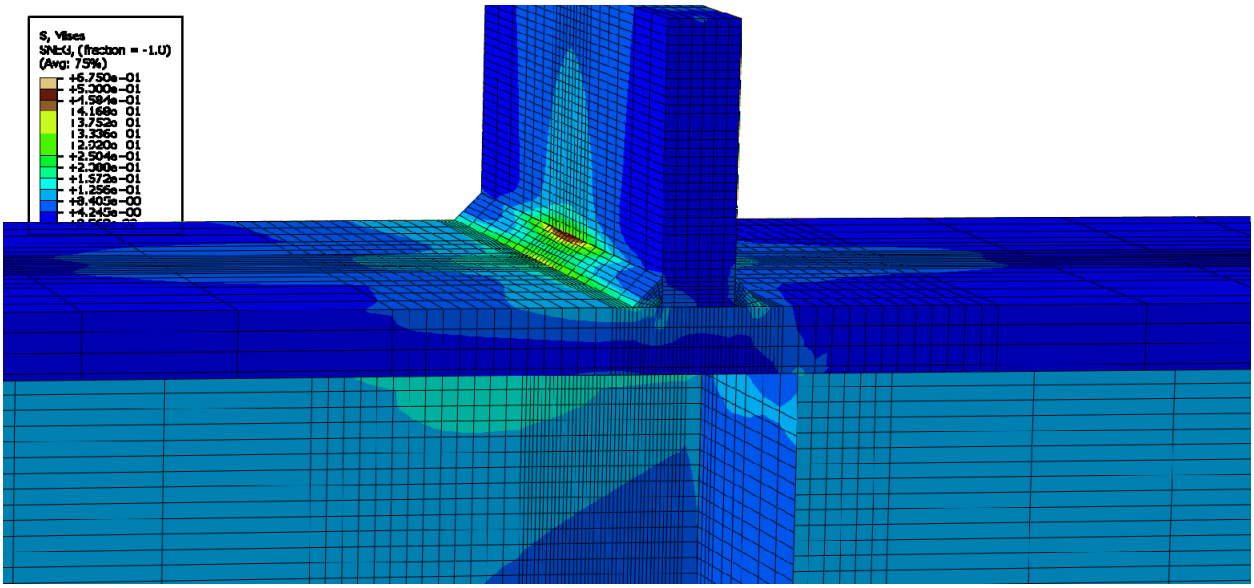

Figure E-386: Finite element model of W14X176-ST-E2 with 9/16 in. welds while remaining elastic

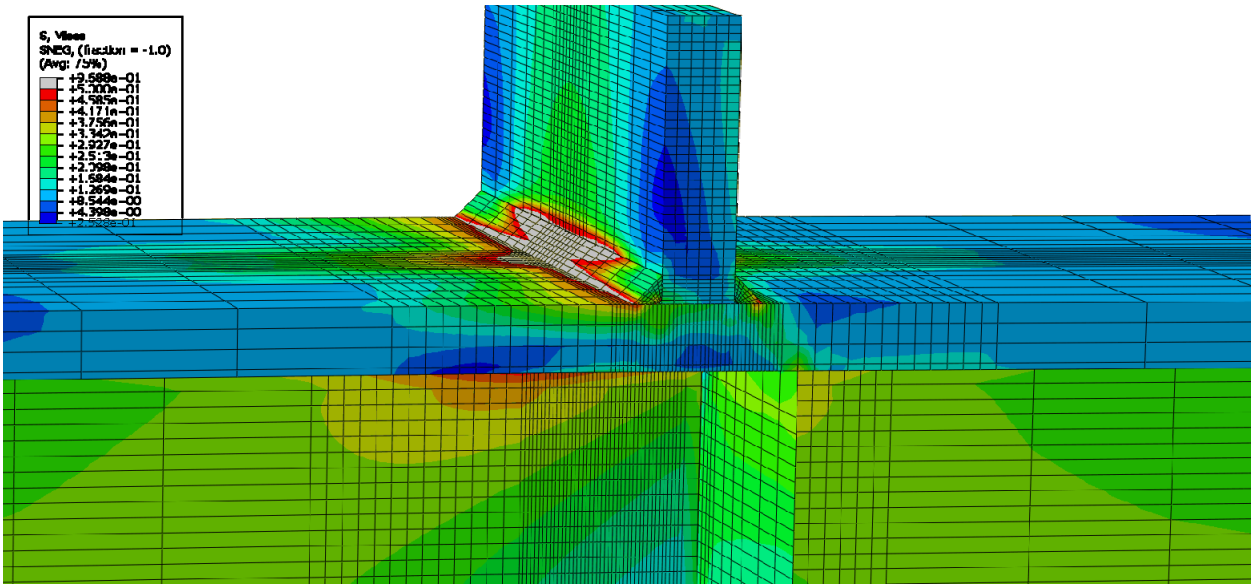

Figure E-387: Finite element model of W14X176-ST-E2 with 9/16 in. welds during inelastic behavior

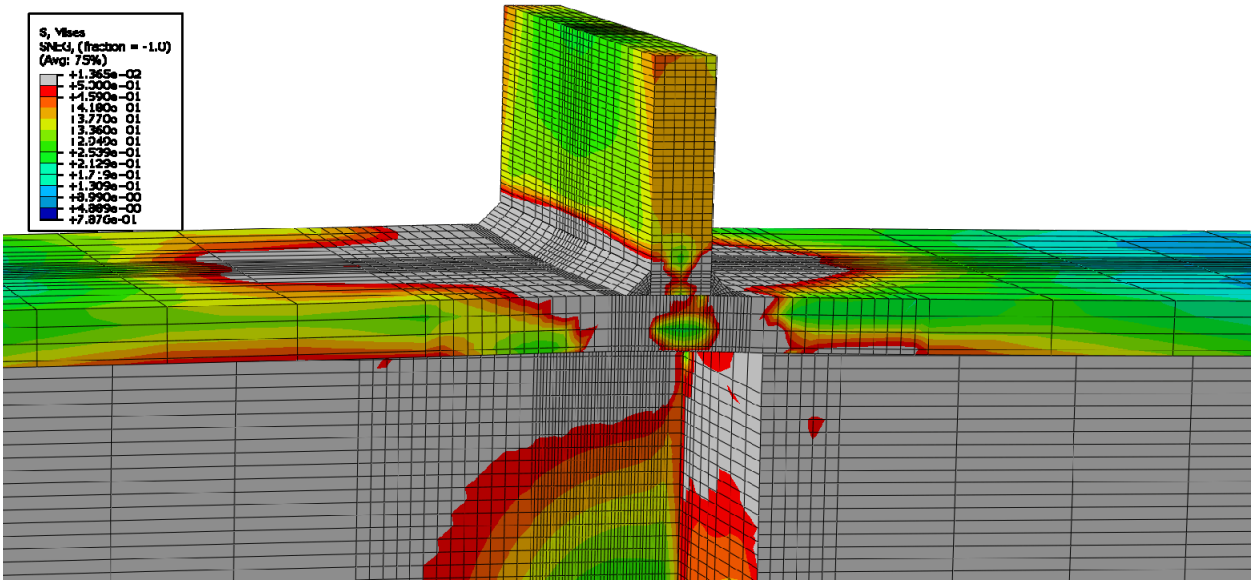

Figure E-388: Finite element model of W14X176-ST-E2 with 9/16 in. welds at its load capacity of 685.71 kips

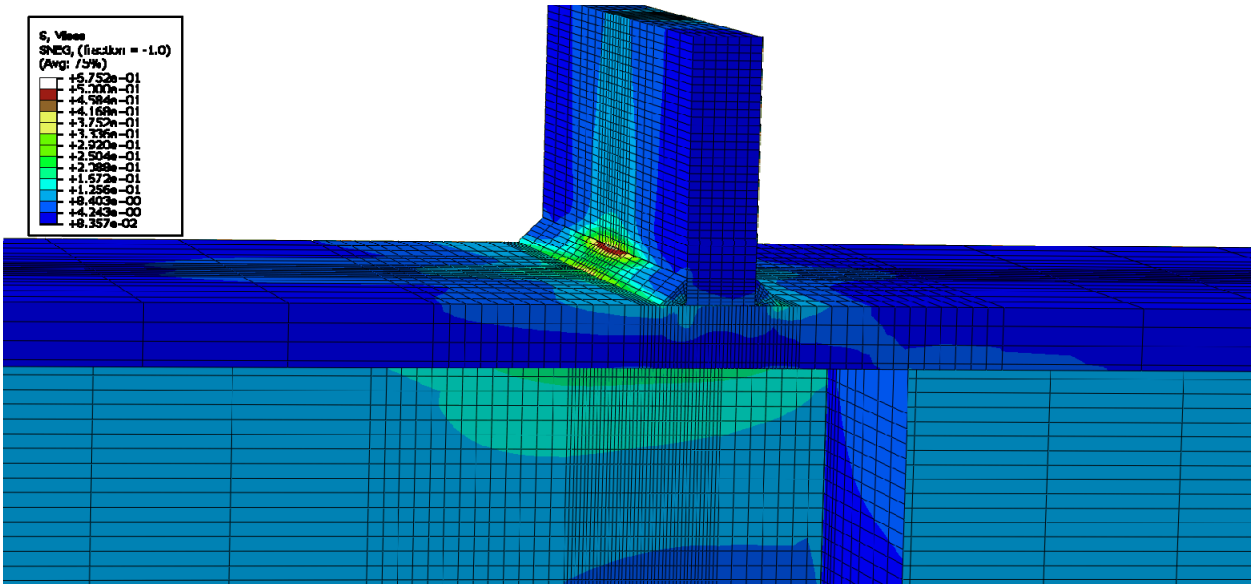

Figure E-389: Finite element model of W14X176-ST-E4 with 9/16 in. welds while remaining elastic

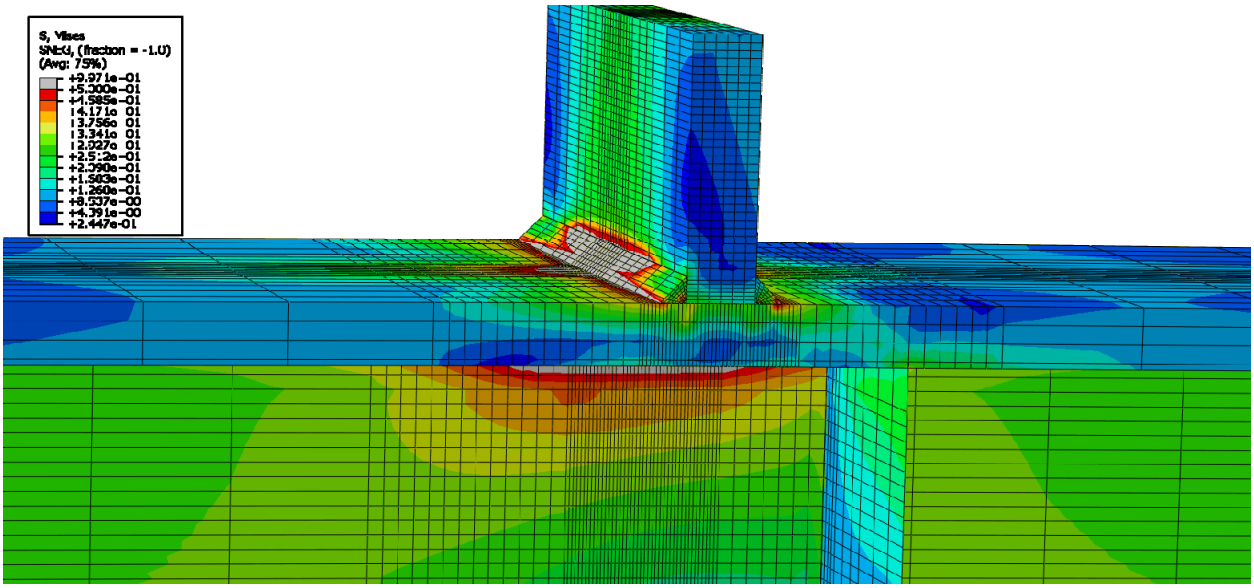

Figure E-390: Finite element model of W14X176-ST-E4 with 9/16 in. welds during inelastic behavior

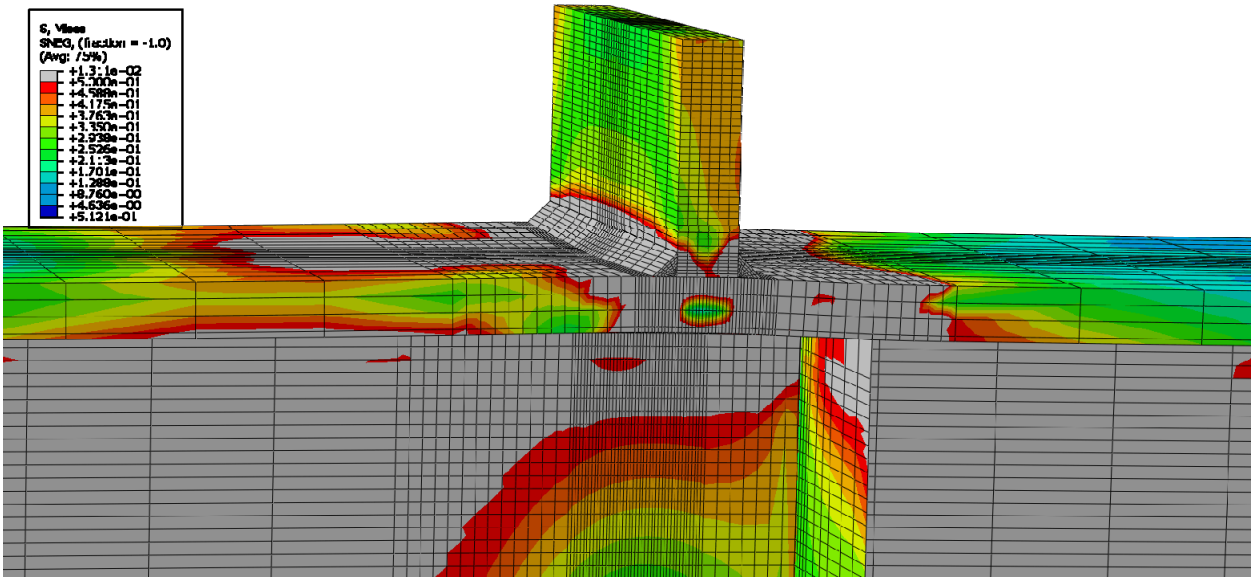

Figure E-391: Finite element model of W14X176-ST-E4 with 9/16 in. welds at its load capacity of 652.26 kips

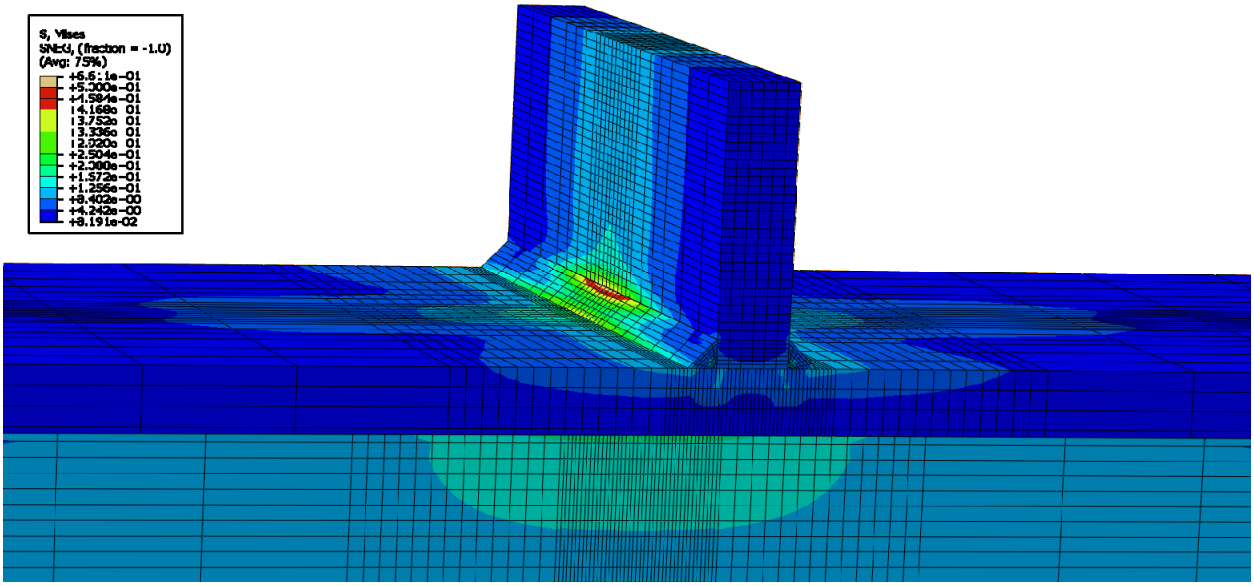

Figure E-392: Finite element model of W14X176-ST-NA with 9/16 in. welds while remaining elastic

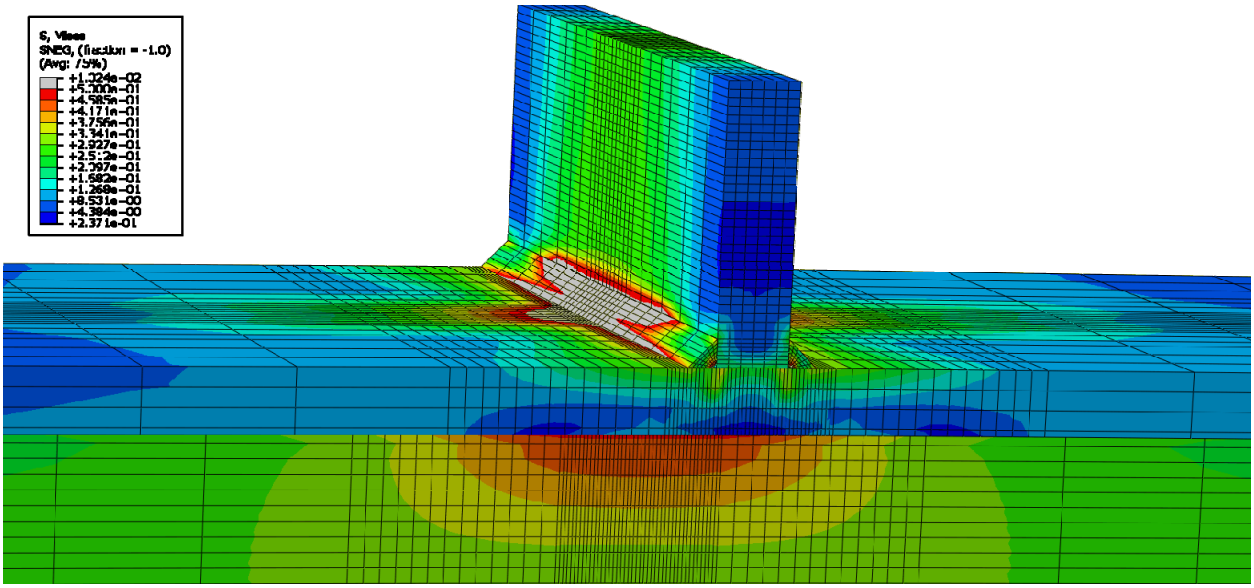

Figure E-393: Finite element model of W14X176-ST-NA with 9/16 in. welds during inelastic behavior

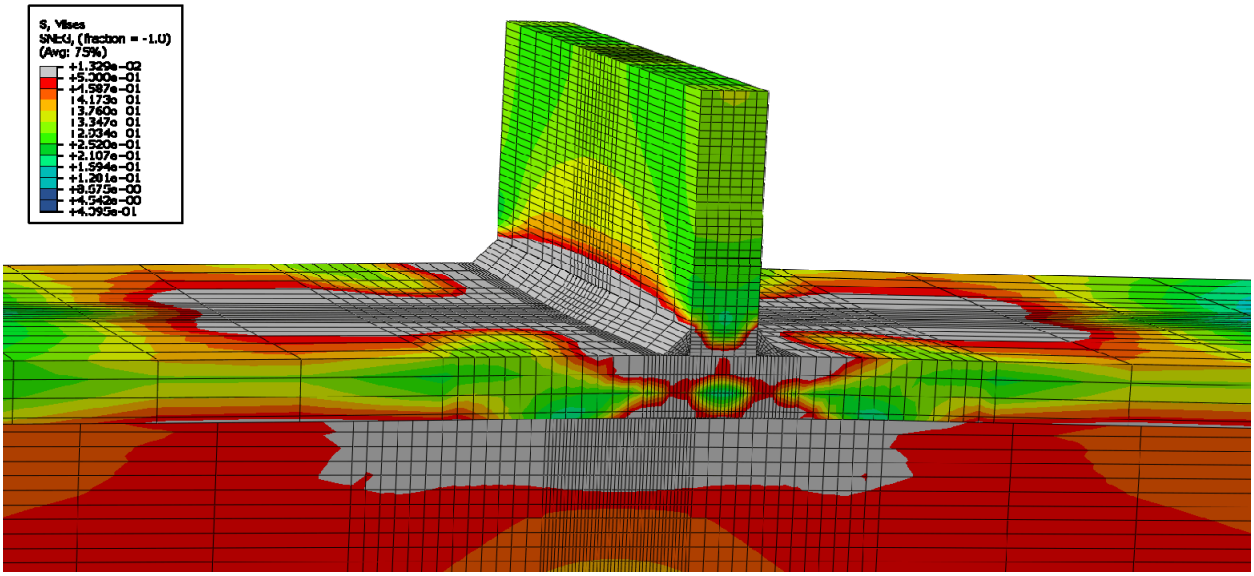

Figure E-394: Finite element model of W14X176-ST-NA with 9/16 in. welds at its load capacity of 590.42 kips

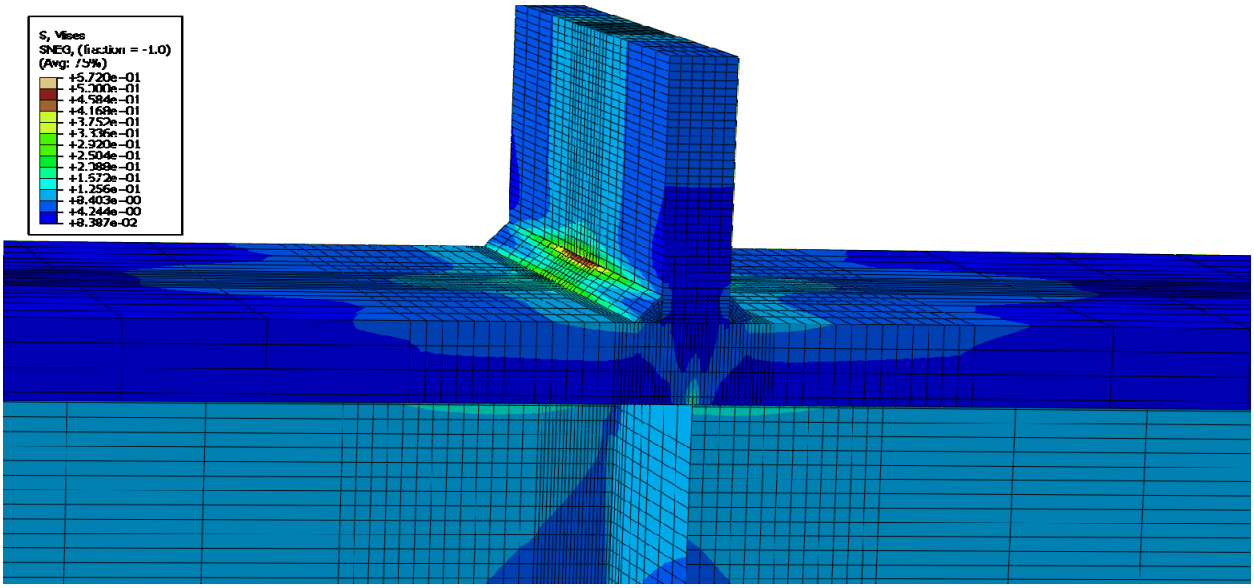

Figure E-395: Finite element model of W14X233-ST-E0 with 9/16 in. welds while remaining elastic

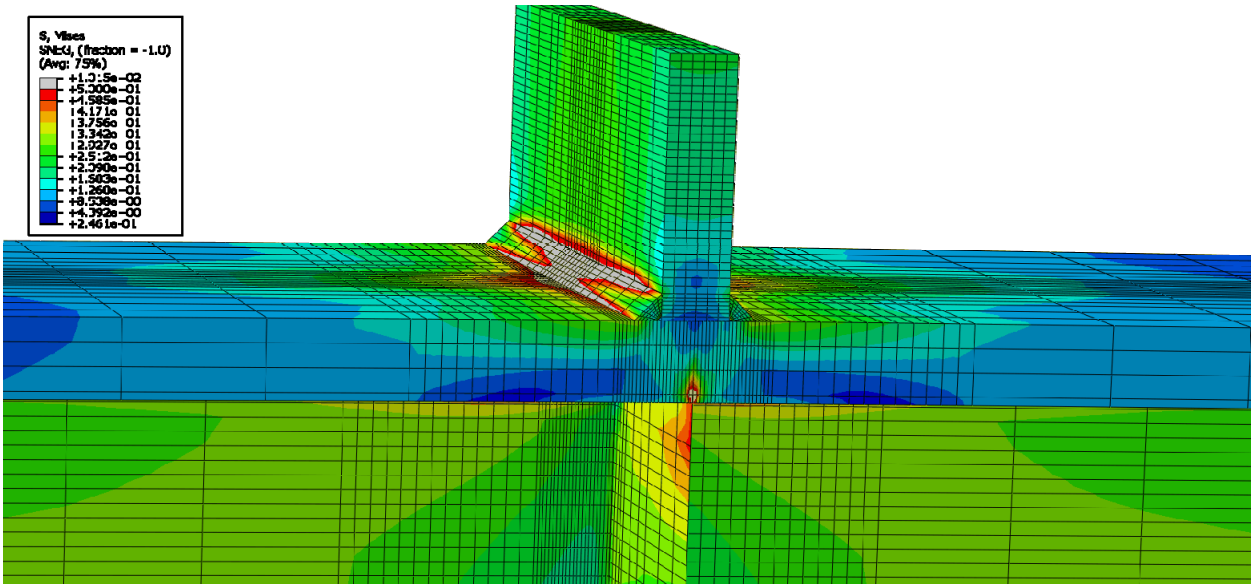

Figure E-396: Finite element model of W14X233-ST-E0 with 9/16 in. welds during inelastic behavior

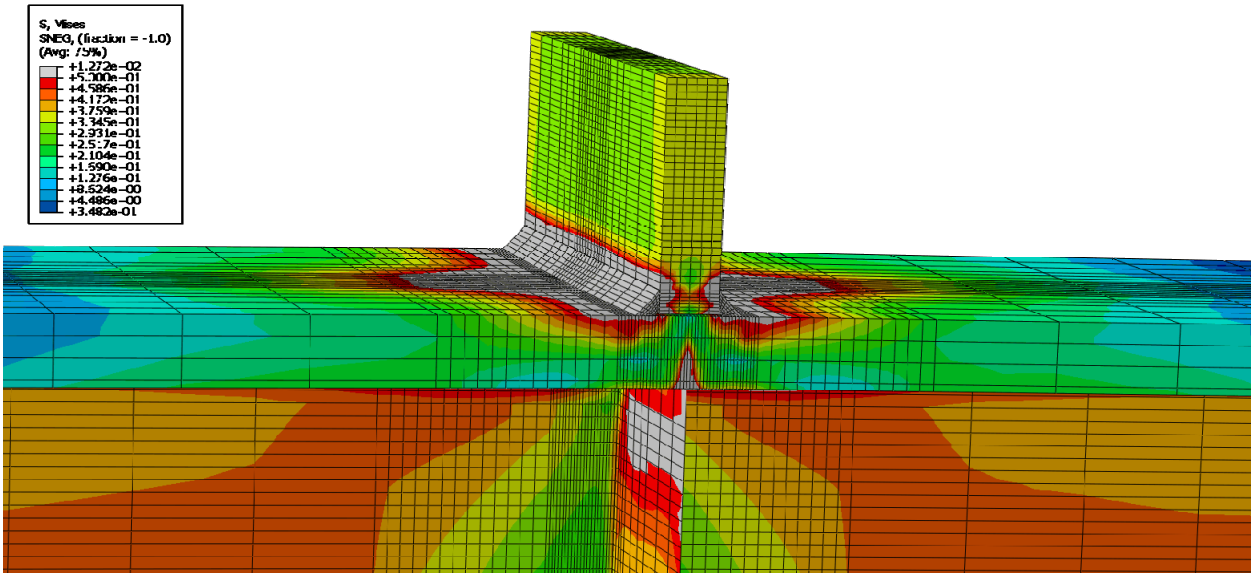

Figure E-397: Finite element model of W14X233-ST-E0 with 9/16 in. welds at its load capacity of 716.69 kips

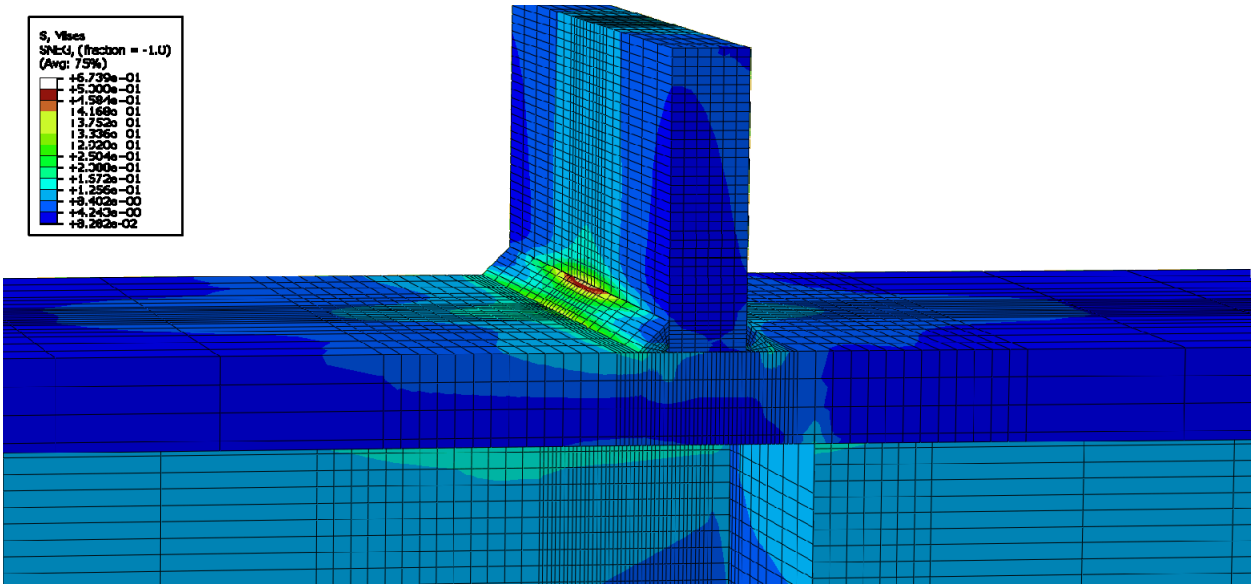

Figure E-398: Finite element model of W14X233-ST-E2 with 9/16 in. welds while remaining elastic

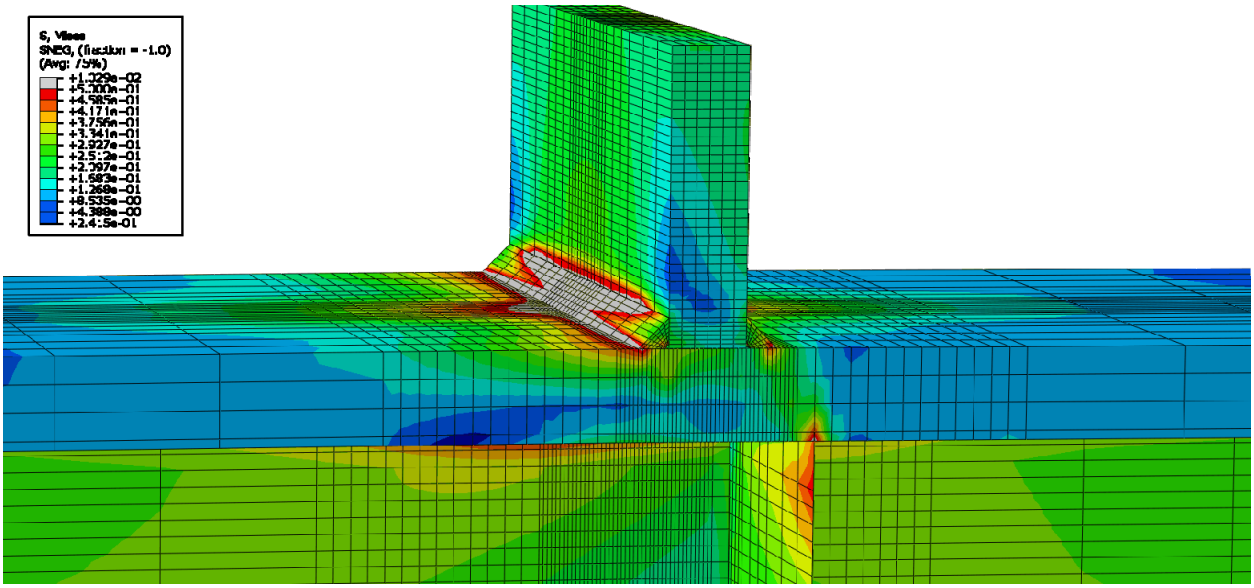

Figure E-399: Finite element model of W14X233-ST-E2 with 9/16 in. welds during inelastic behavior

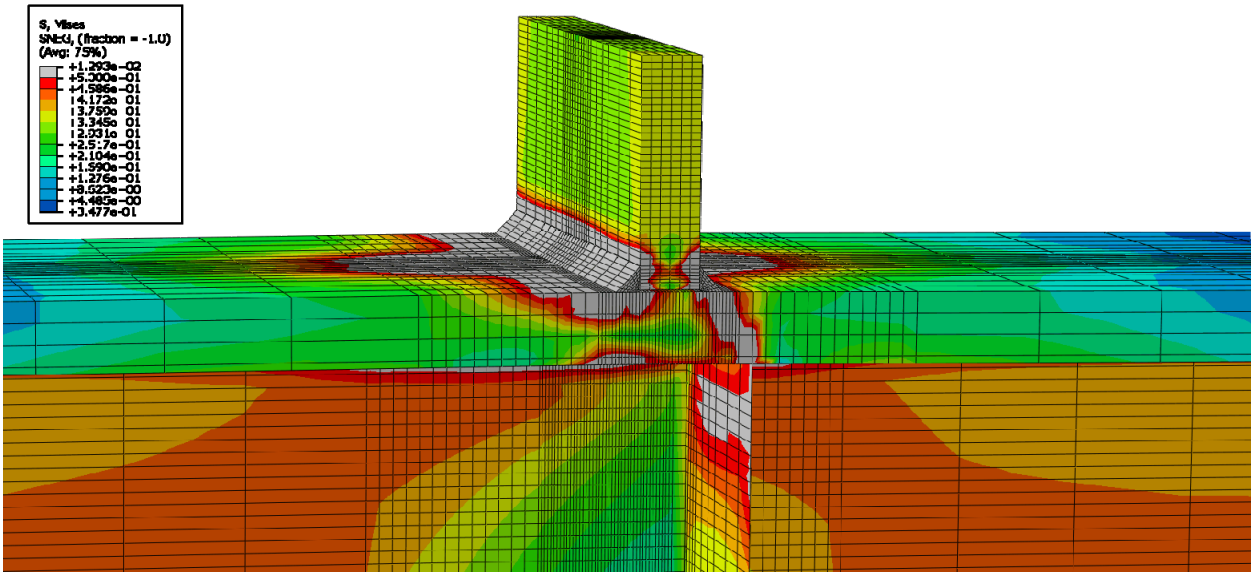

Figure E-400: Finite element model of W14X233-ST-E2 with 9/16 in. welds at its load capacity of 715.79 kips

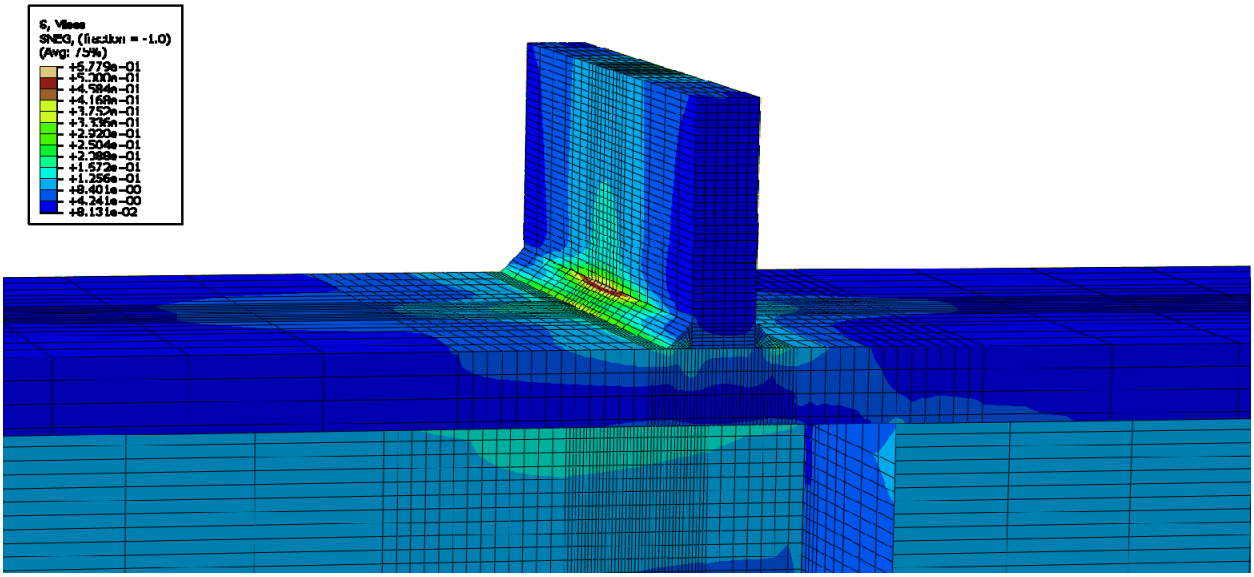

Figure E-401: Finite element model of W14X233-ST-E4 with 9/16 in. welds while remaining elastic

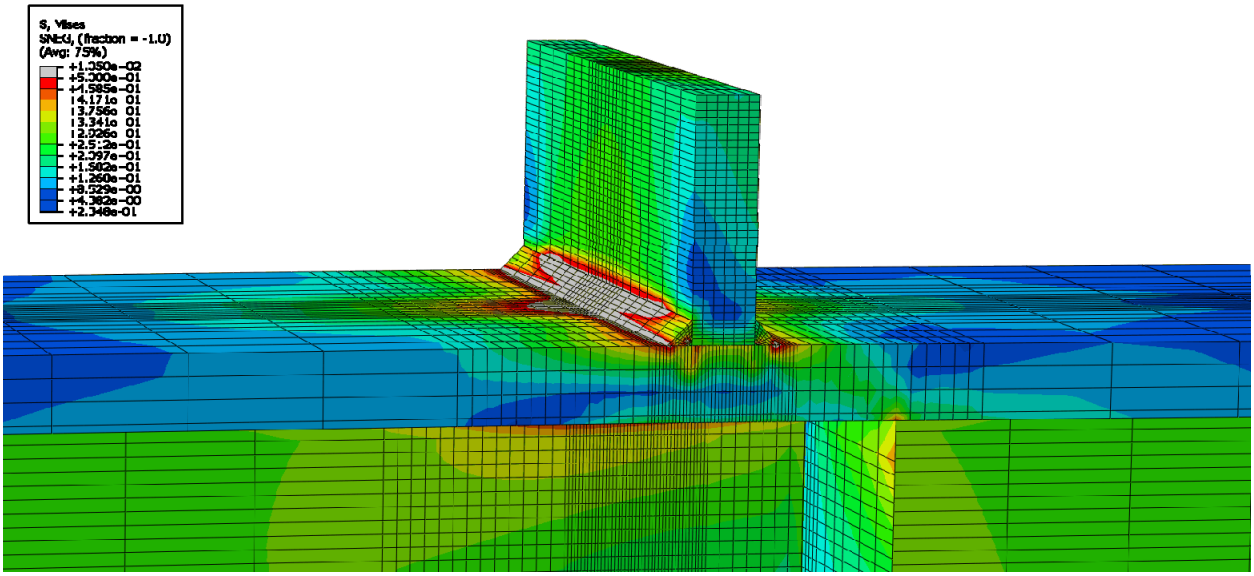

Figure E-402: Finite element model of W14X233-ST-E4 with 9/16 in. welds during inelastic behavior

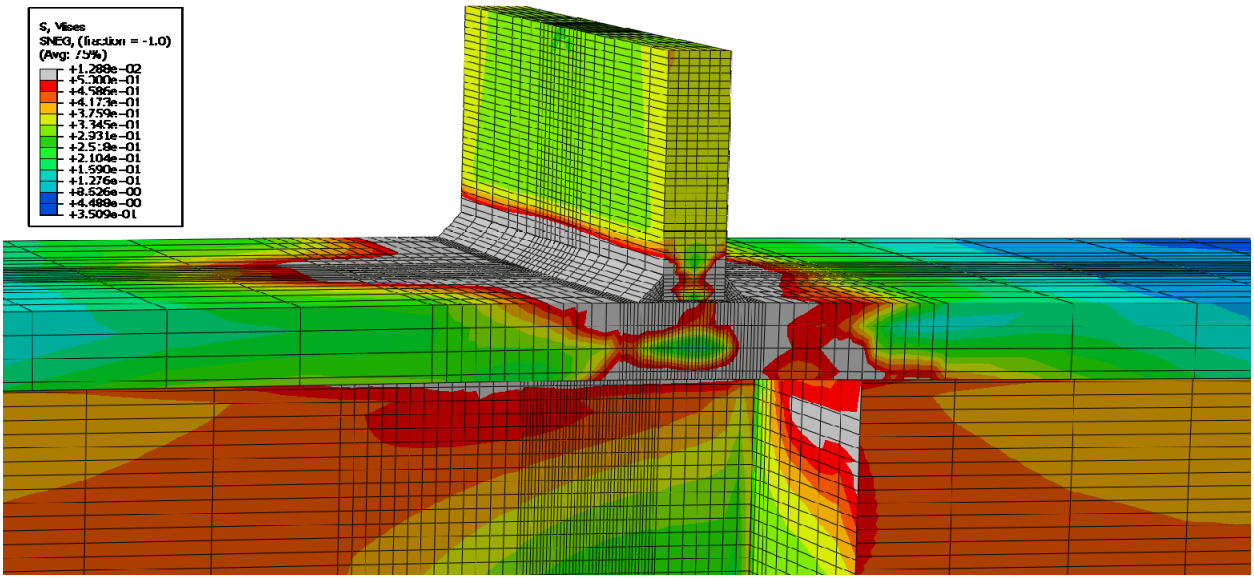

Figure E-403: Finite element model of W14X233-ST-E4 with 9/16 in. welds at its load capacity of 714.84 kips

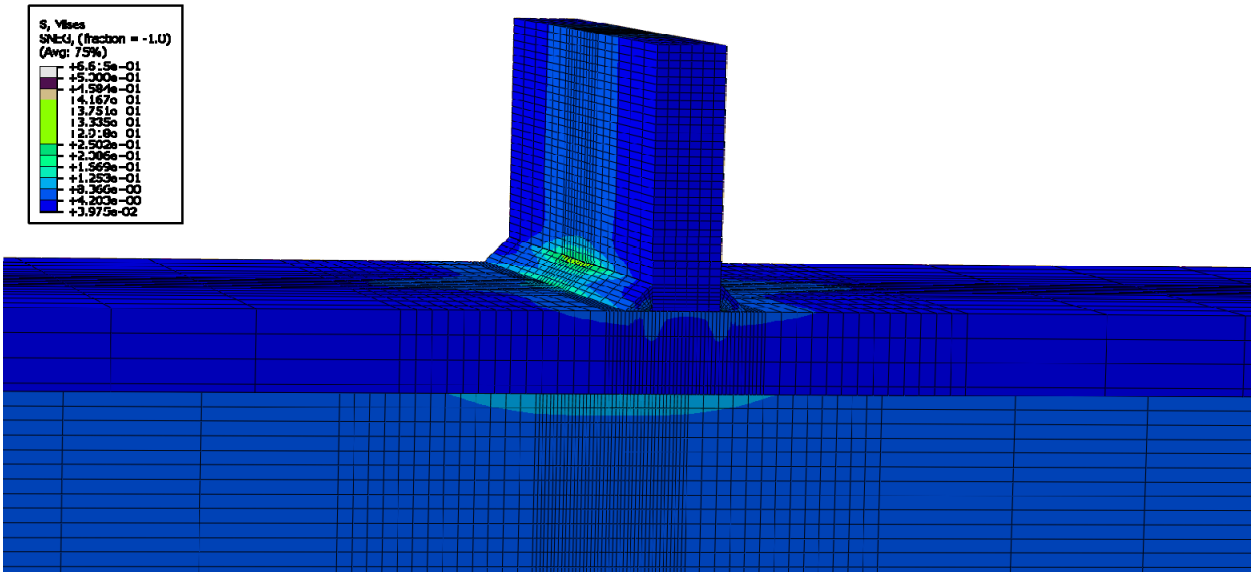

Figure E-404: Finite element model of W14X233-ST-NA with 9/16 in. welds while remaining elastic

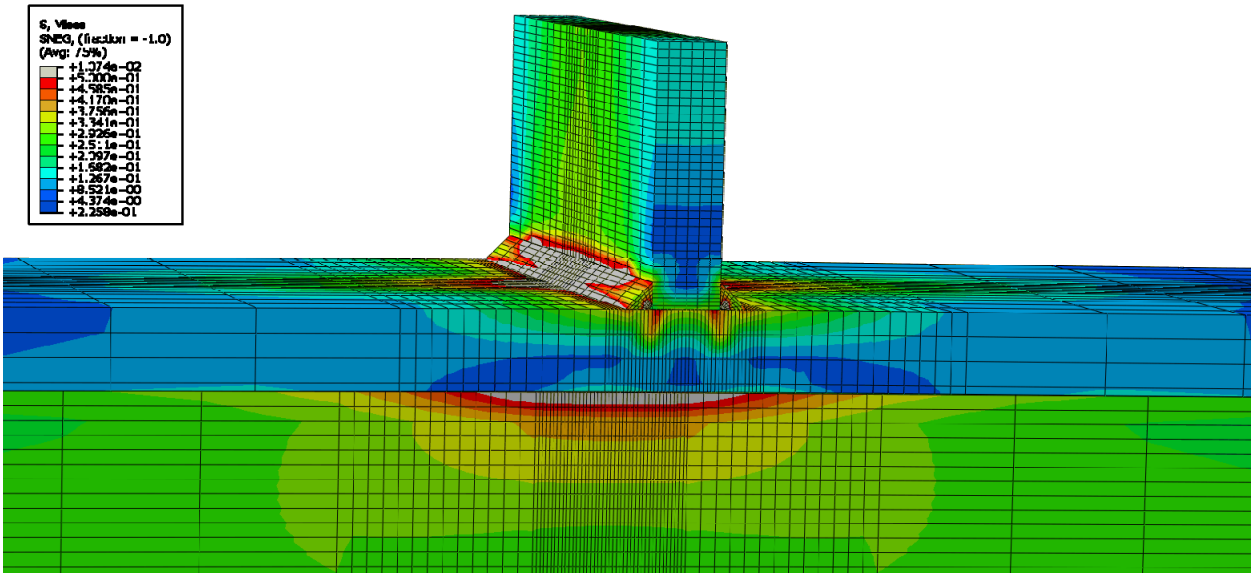

Figure E-405: Finite element model of W14X233-ST-NA with 9/16 in. welds during inelastic behavior

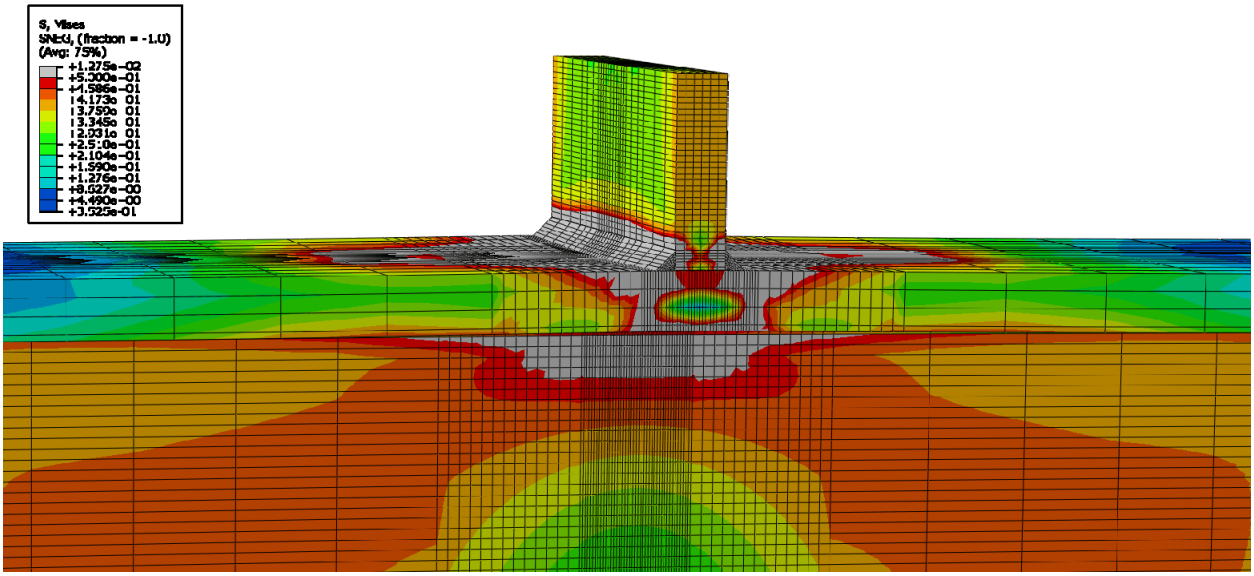

Figure E-406: Finite element model of W14X233-ST-NA with 9/16 in. welds at its load capacity of 704.44 kips

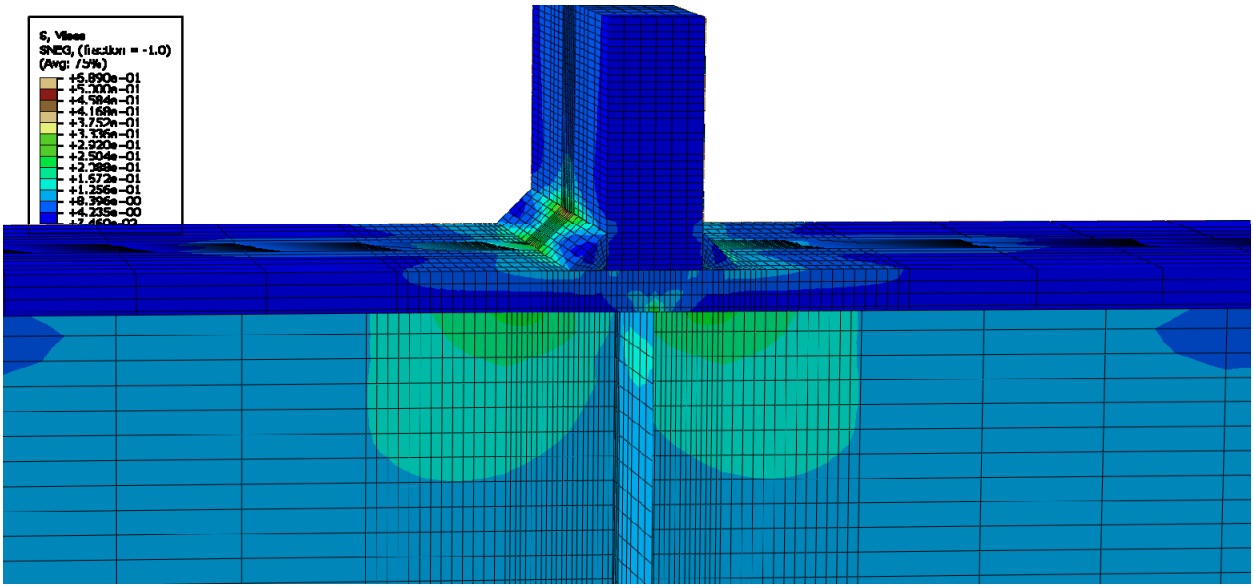

Figure E-407: Finite element model of W24X131-ST-E0 with 7/8 in. welds while remaining elastic

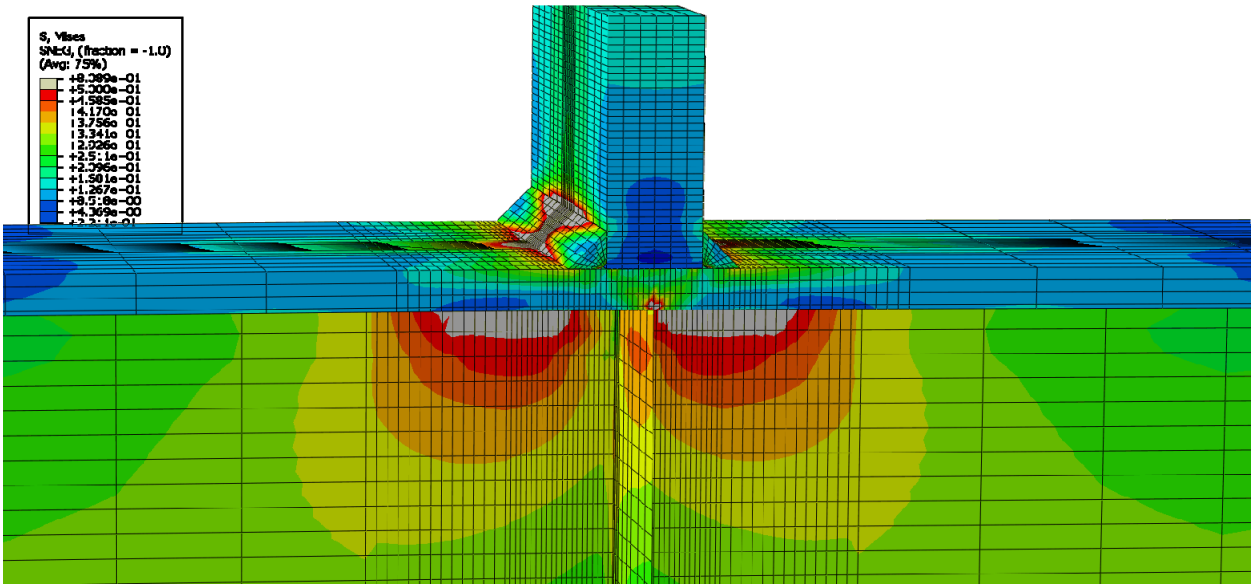

Figure E-408: Finite element model of W24X131-ST-E0 with 7/8 in. welds during inelastic behavior

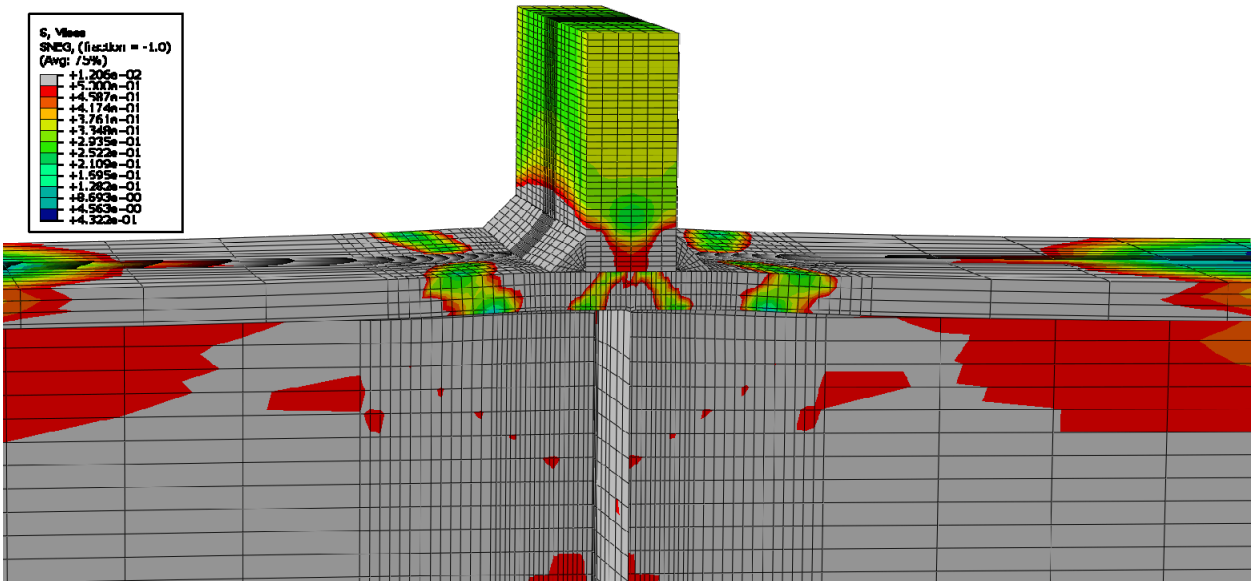

Figure E-409: Finite element model of W24X131-ST-E0 with 7/8 in. welds at its load capacity of 772.19 kips

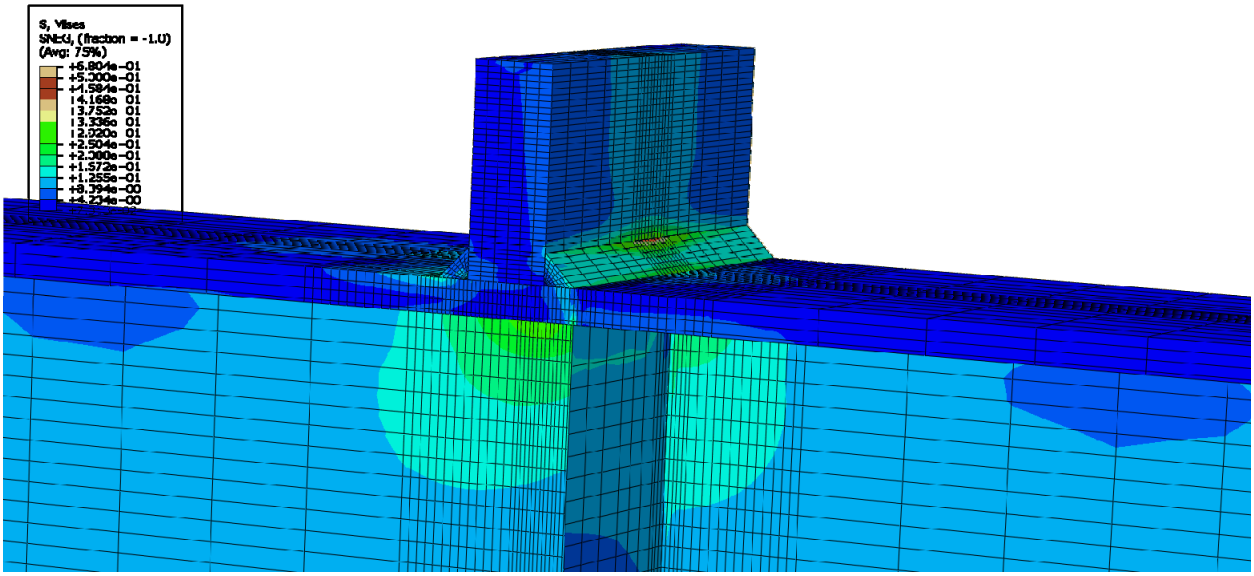

Figure E-410: Finite element model of W24X131-ST-E2 with 7/8 in. welds while remaining elastic

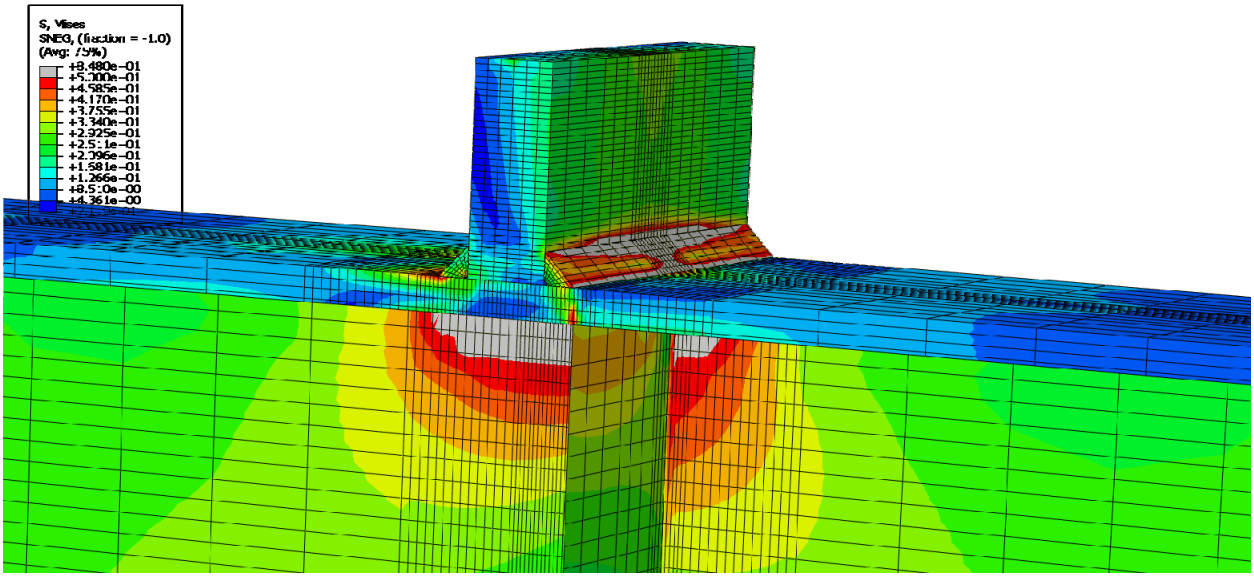

Figure E-411: Finite element model of W24X131-ST-E2 with 7/8 in. welds during inelastic behavior

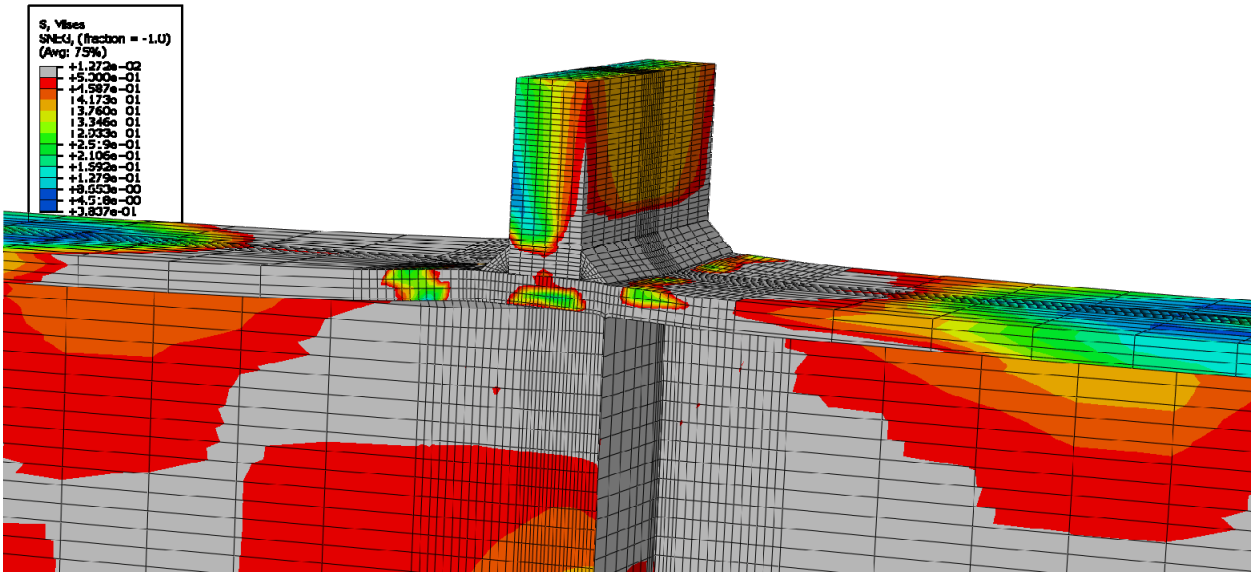

Figure E-412: Finite element model of W24X131-ST-E2 with 7/8 in. welds at its load capacity of 742.09 kips

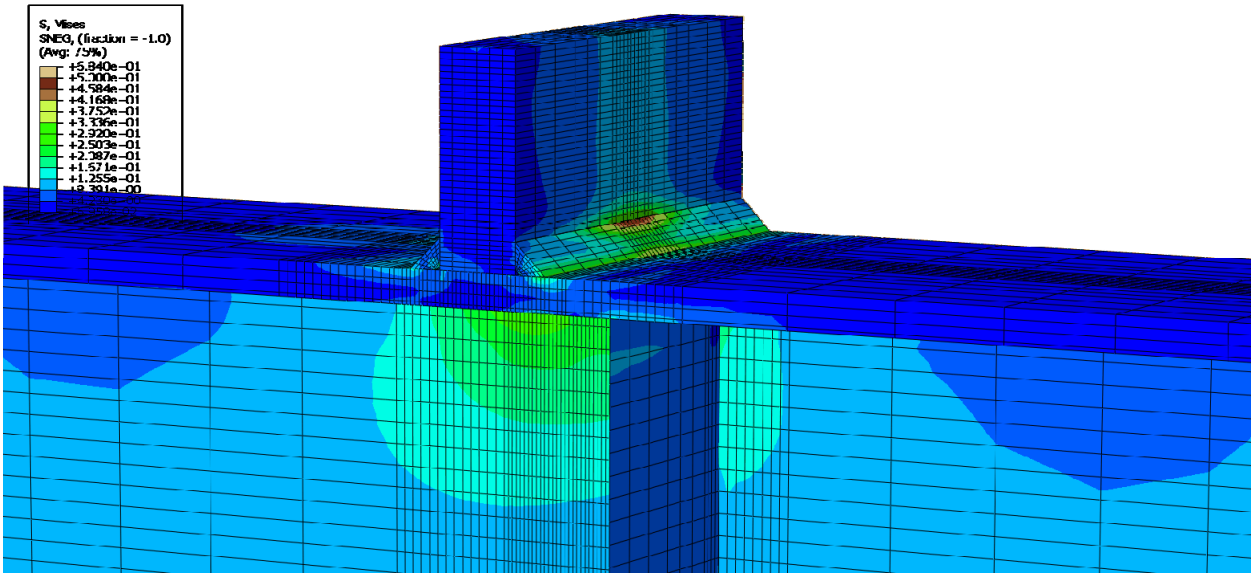

Figure E-413: Finite element model of W24X131-ST-E4 with 7/8 in. welds while remaining elastic

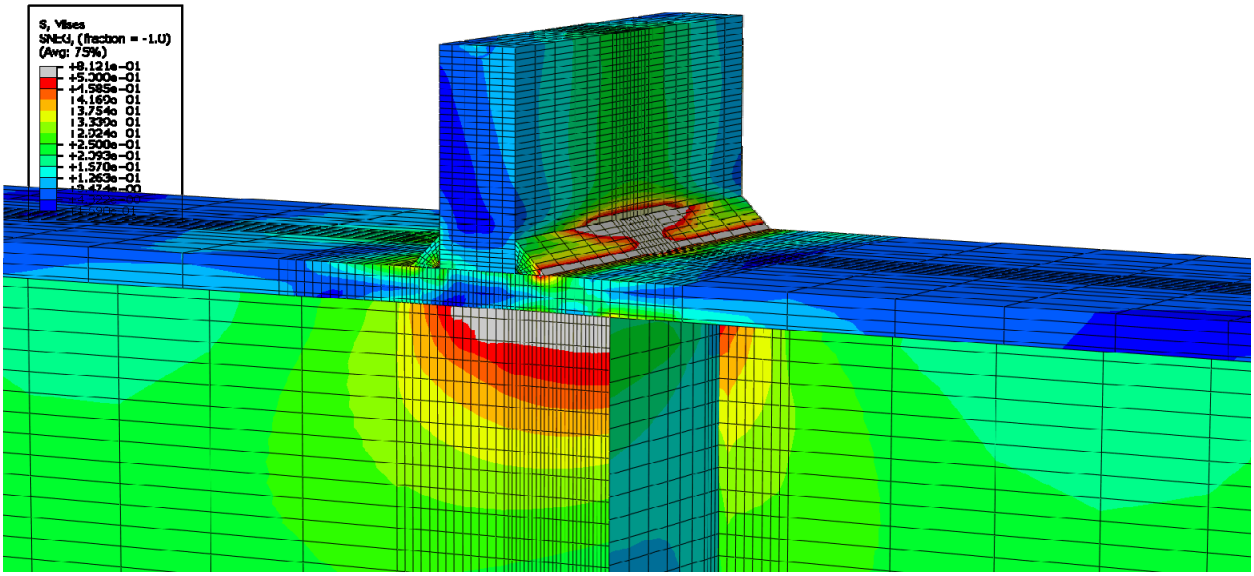

Figure E-414: Finite element model of W24X131-ST-E4 with 7/8 in. welds during inelastic behavior

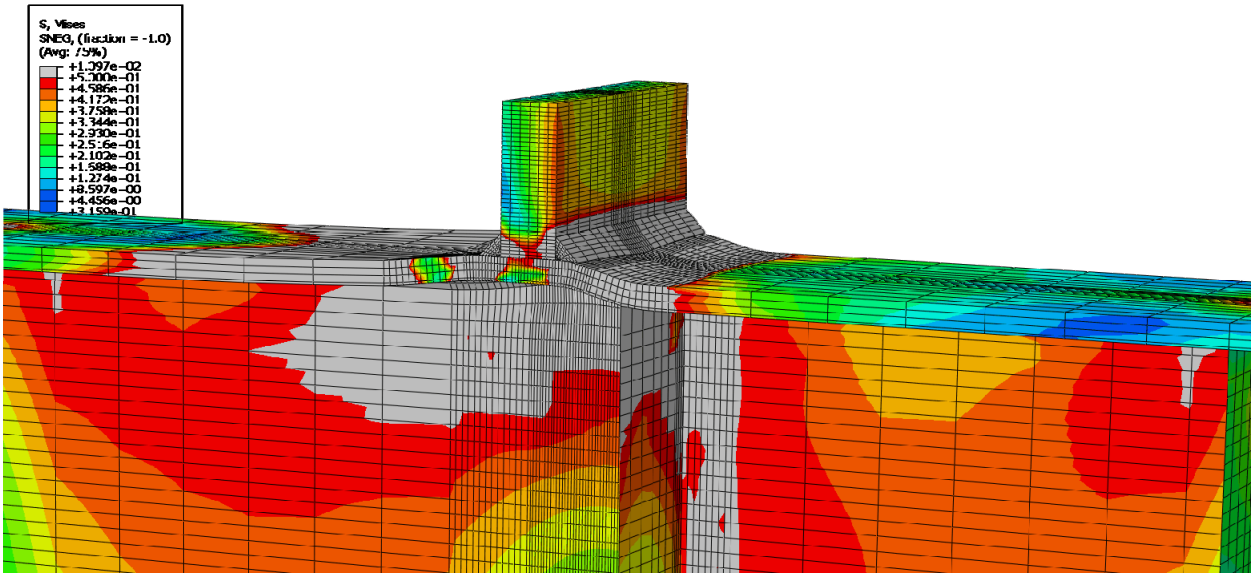

Figure E-415: Finite element model of W24X131-ST-E4 with 7/8 in. welds at its load capacity of 666.19 kips

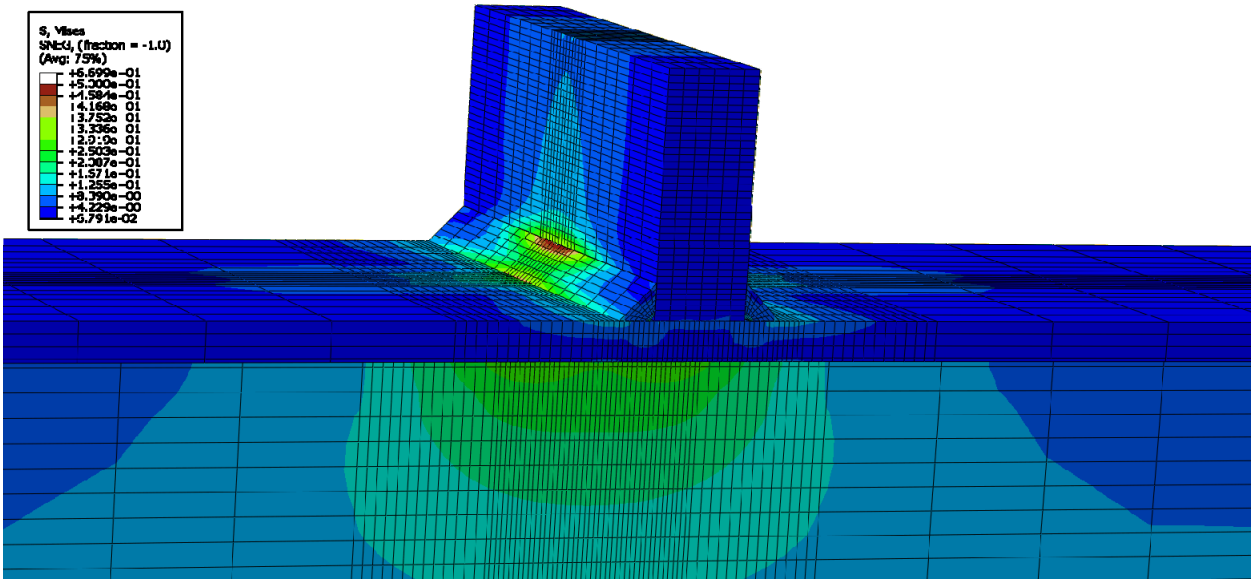

Figure E-416: Finite element model of W24X131-ST-NA with 7/8 in. welds while remaining elastic

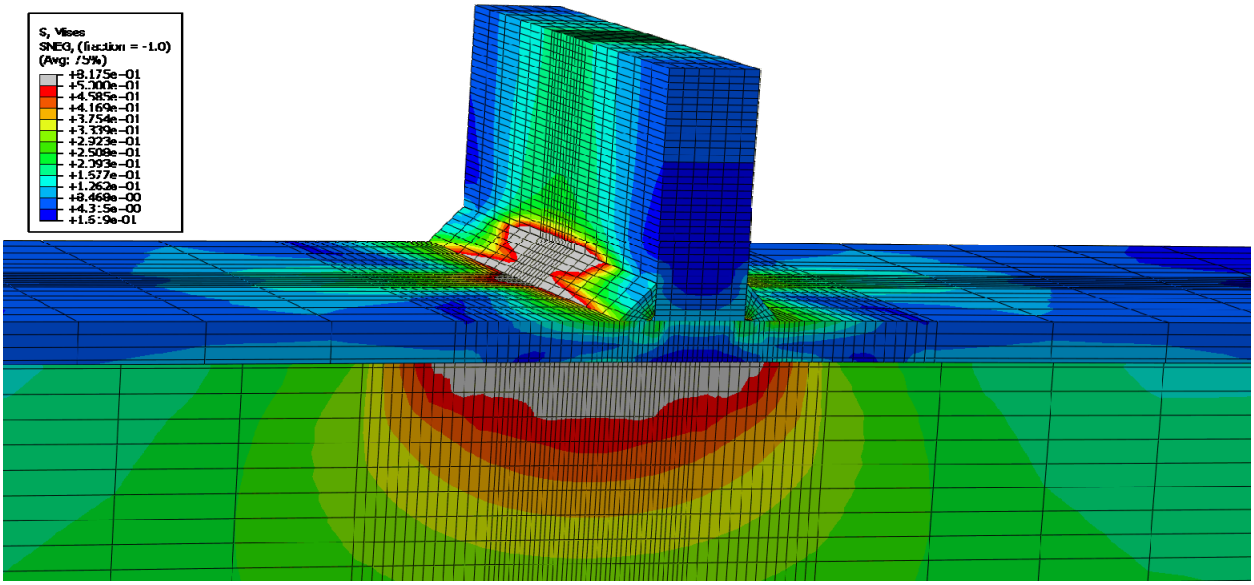

Figure E-417: Finite element model of W24X131-ST-NA with 7/8 in. welds during inelastic behavior

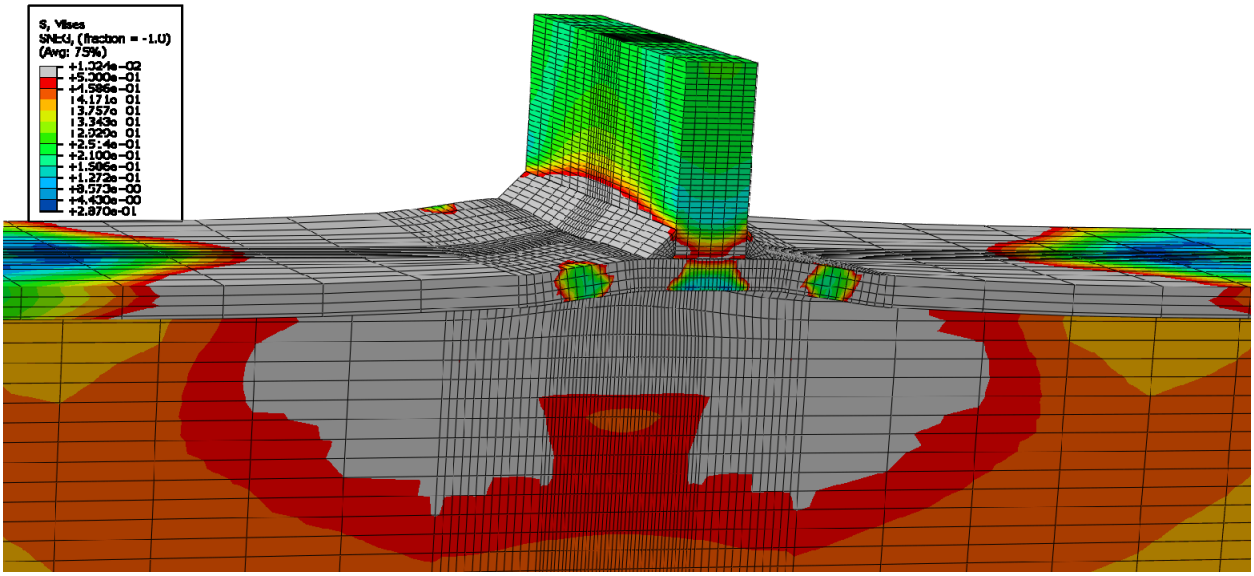

Figure E-418: Finite element model of W24X131-ST-NA with 7/8 in. welds at its load capacity of 581.92 kips

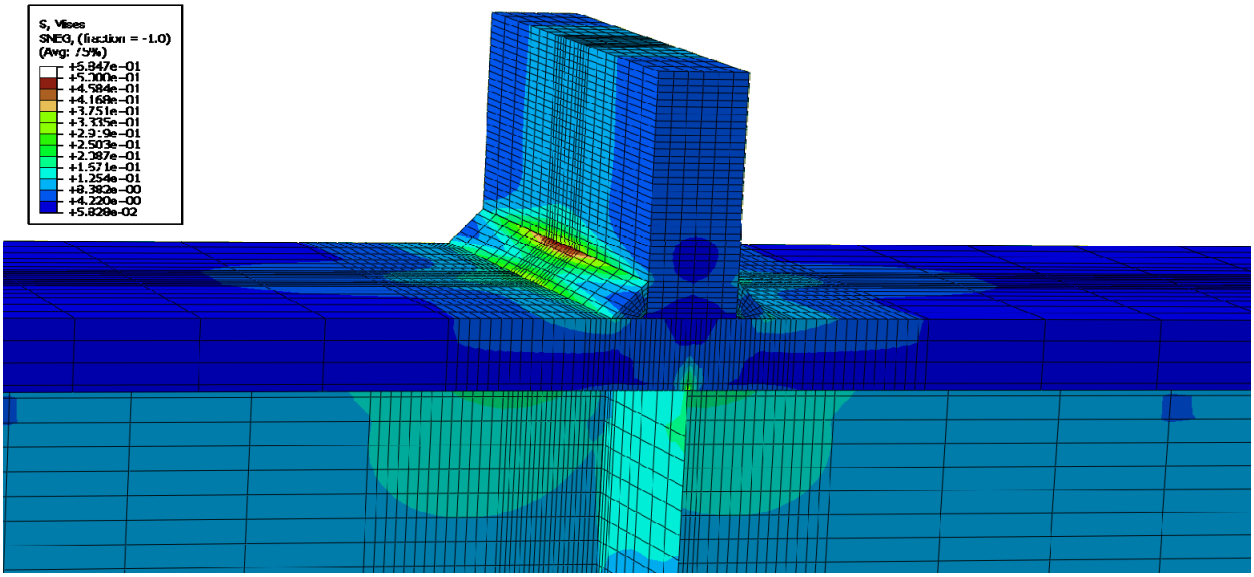

Figure E-419: Finite element model of W24X229-ST-E0 with 7/8 in. welds while remaining elastic

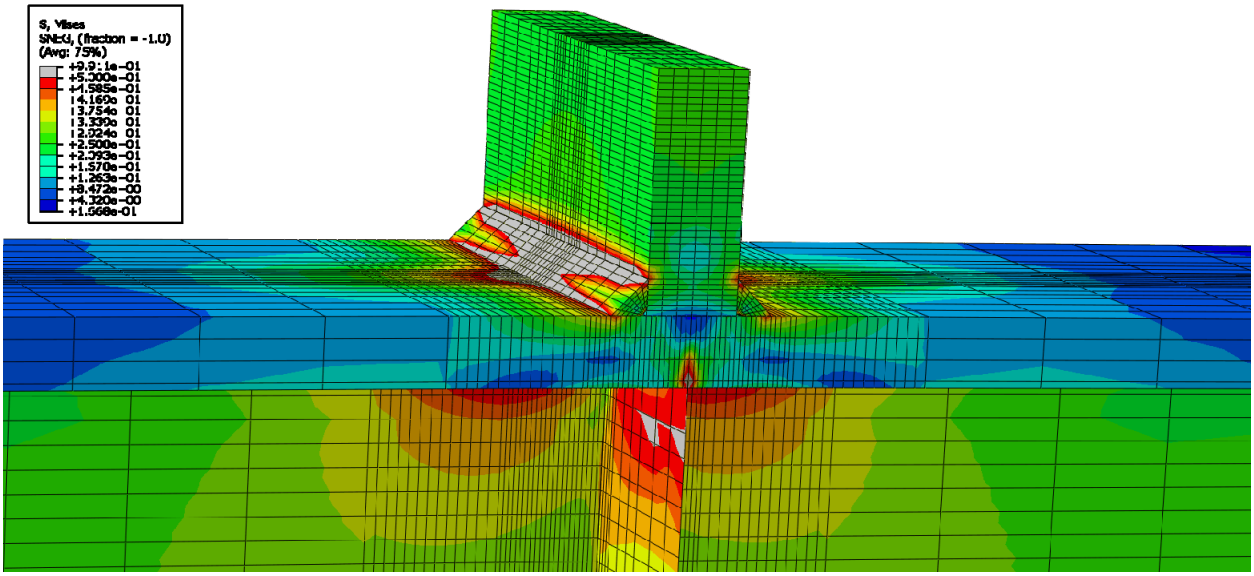

Figure E-420: Finite element model of W24X229-ST-E0 with 7/8 in. welds during inelastic behavior

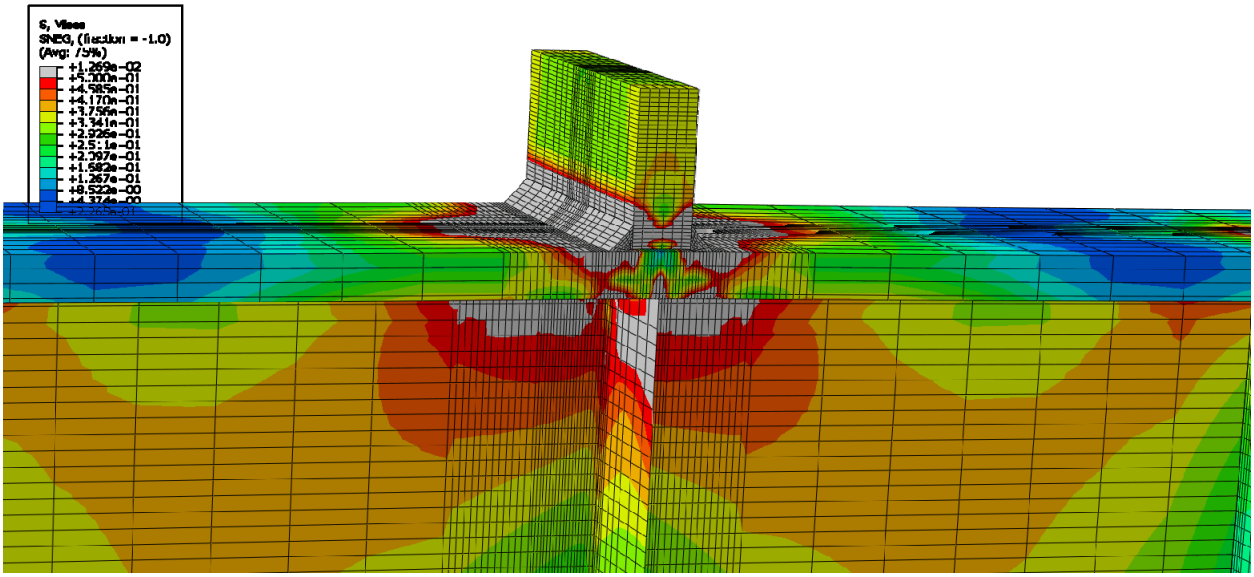

Figure E-421: Finite element model of W24X229-ST-E0 with 7/8 in. welds at its load capacity of 916.04 kips

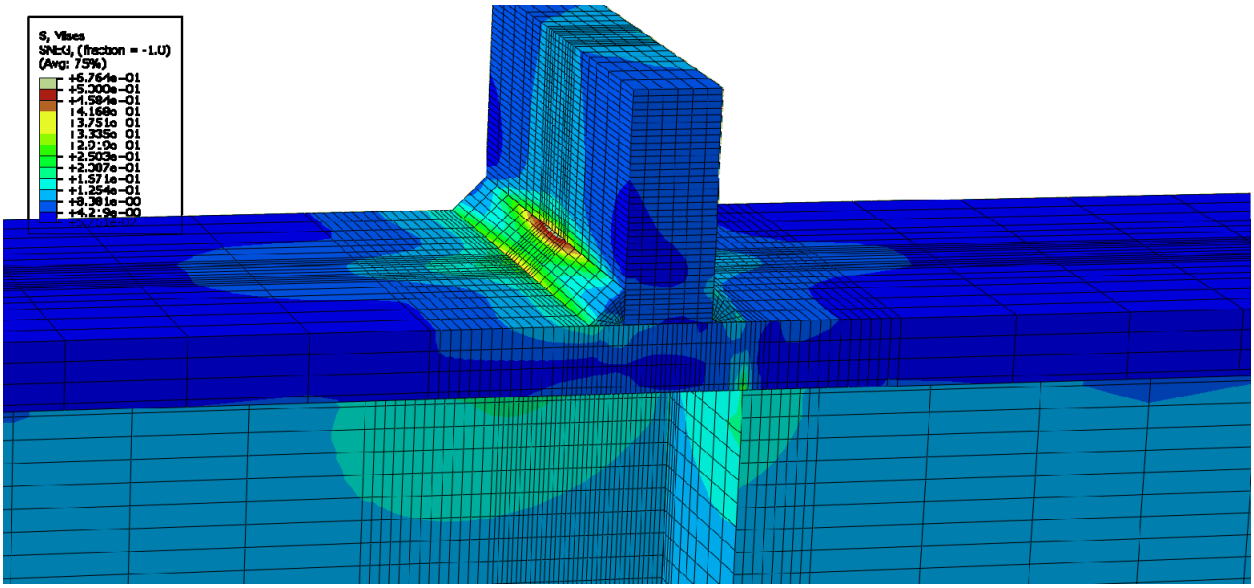

Figure E-422: Finite element model of W24X229-ST-E2 with 7/8 in. welds while remaining elastic

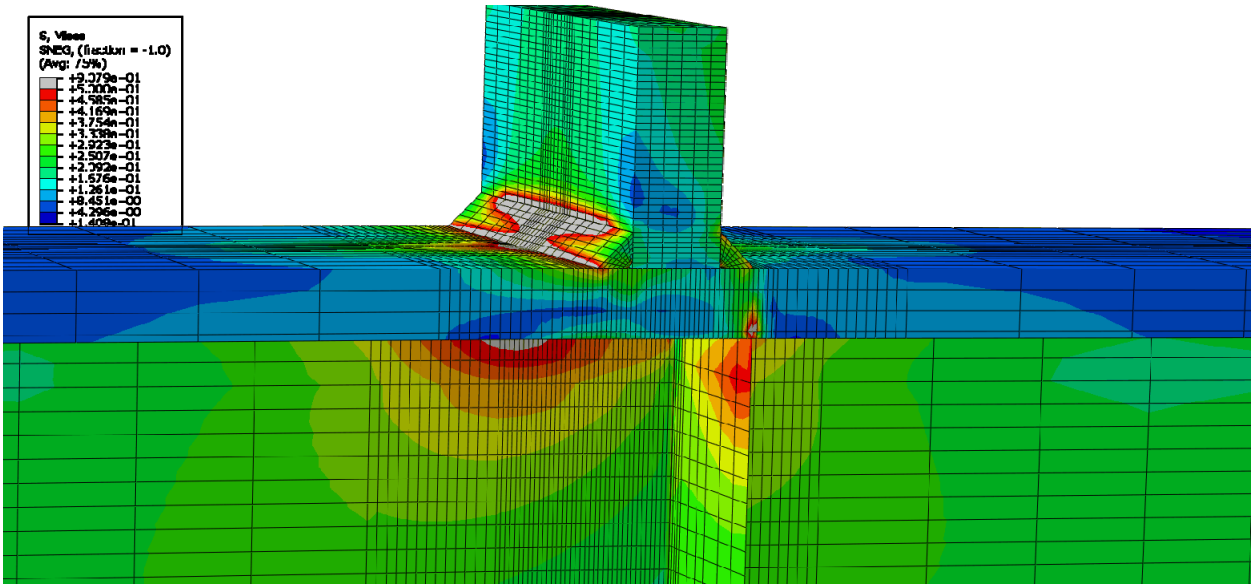

Figure E-423: Finite element model of W24X229-ST-E2 with 7/8 in. welds during inelastic behavior

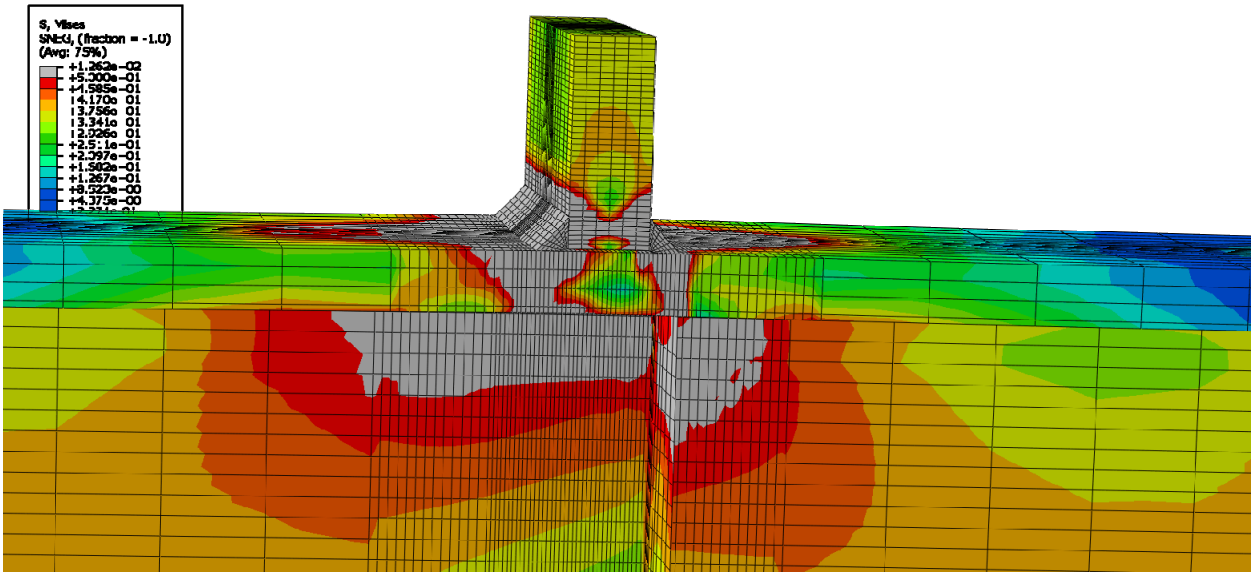

Figure E-424: Finite element model of W24X229-ST-E2 with 7/8 in. welds at its load capacity of 915.08 kips

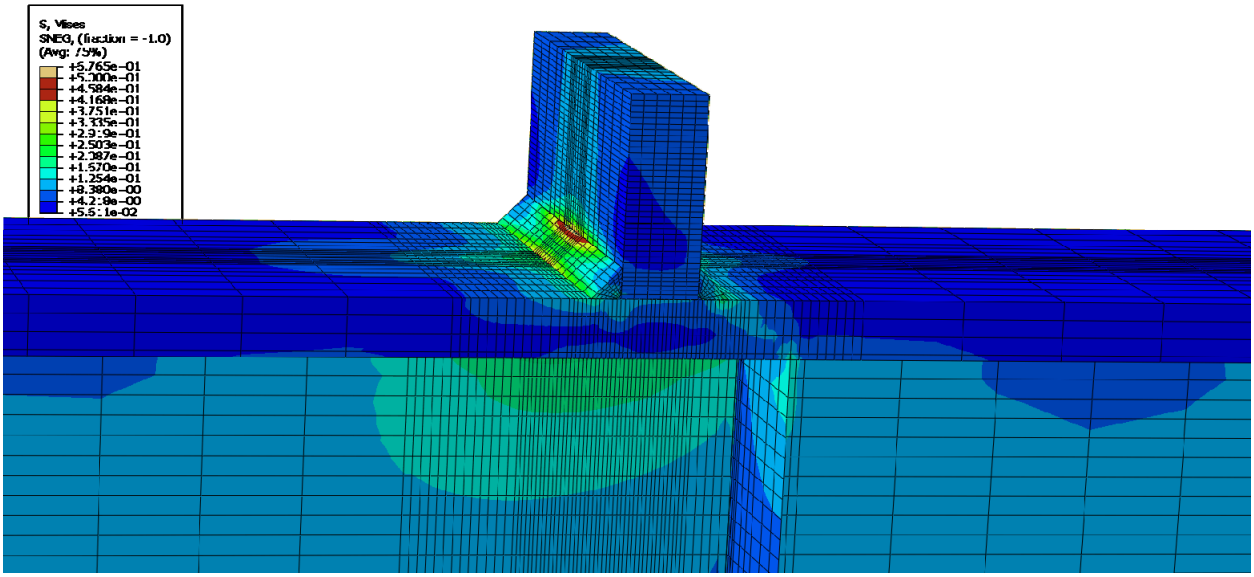

Figure E-425: Finite element model of W24X229-ST-E4 with 7/8 in. welds while remaining elastic

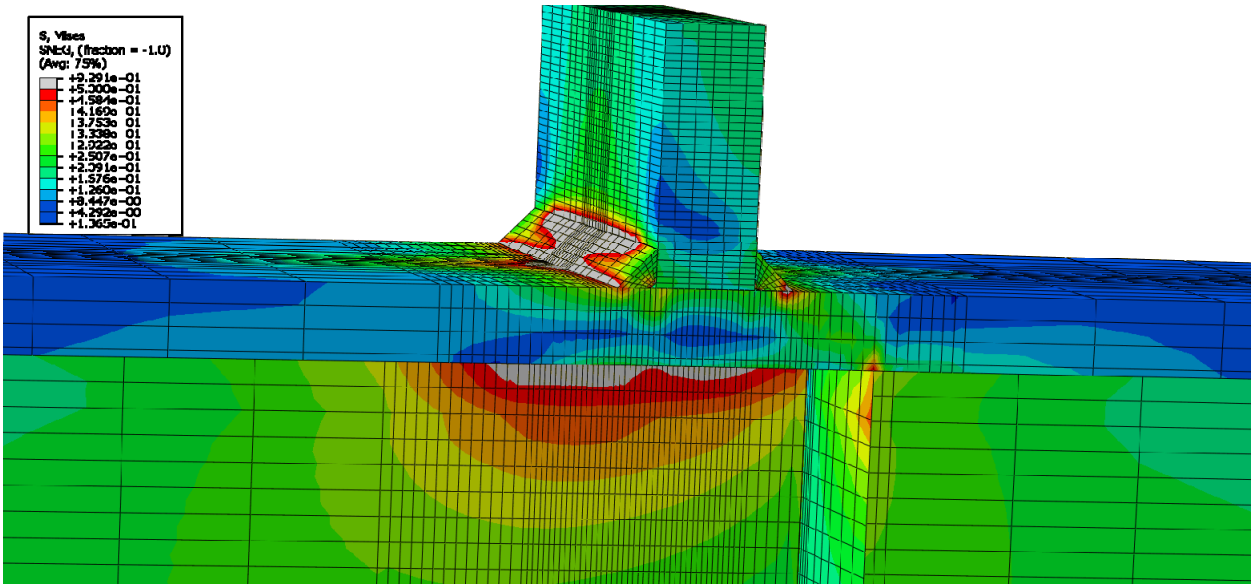

Figure E-426: Finite element model of W24X229-ST-E4 with 7/8 in. welds during inelastic behavior

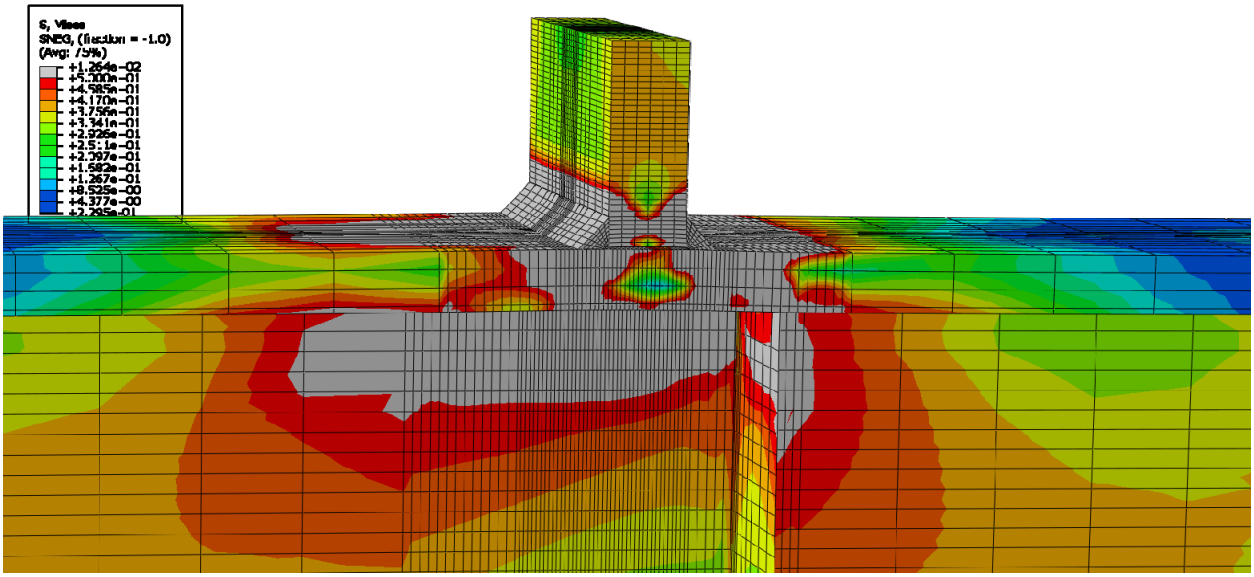

Figure E-427: Finite element model of W24X229-ST-E4 with 7/8 in. welds at its load capacity of 913.18 kips

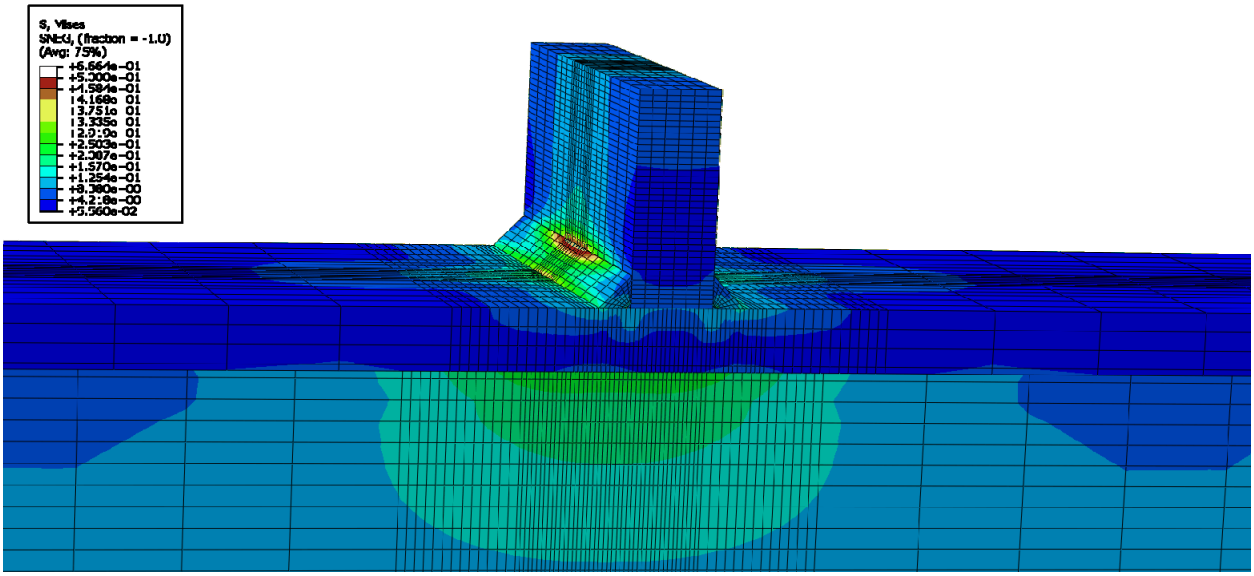

Figure E-428: Finite element model of W24X229-ST-NA with 7/8 in. welds while remaining elastic

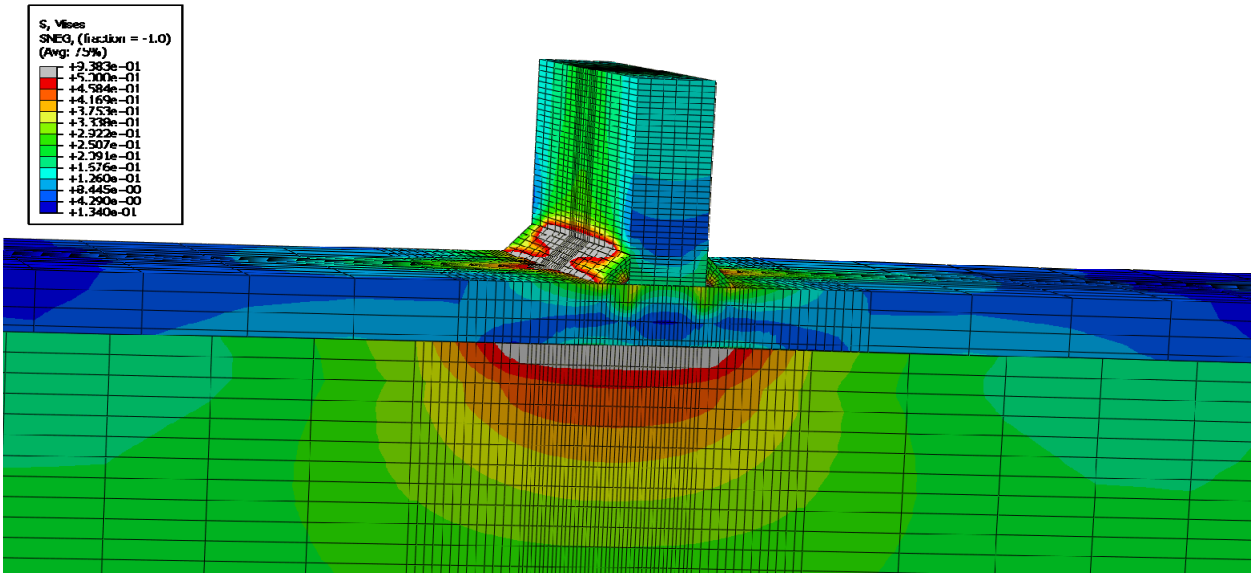

Figure E-429: Finite element model of W24X229-ST-NA with 7/8 in. welds during inelastic behavior

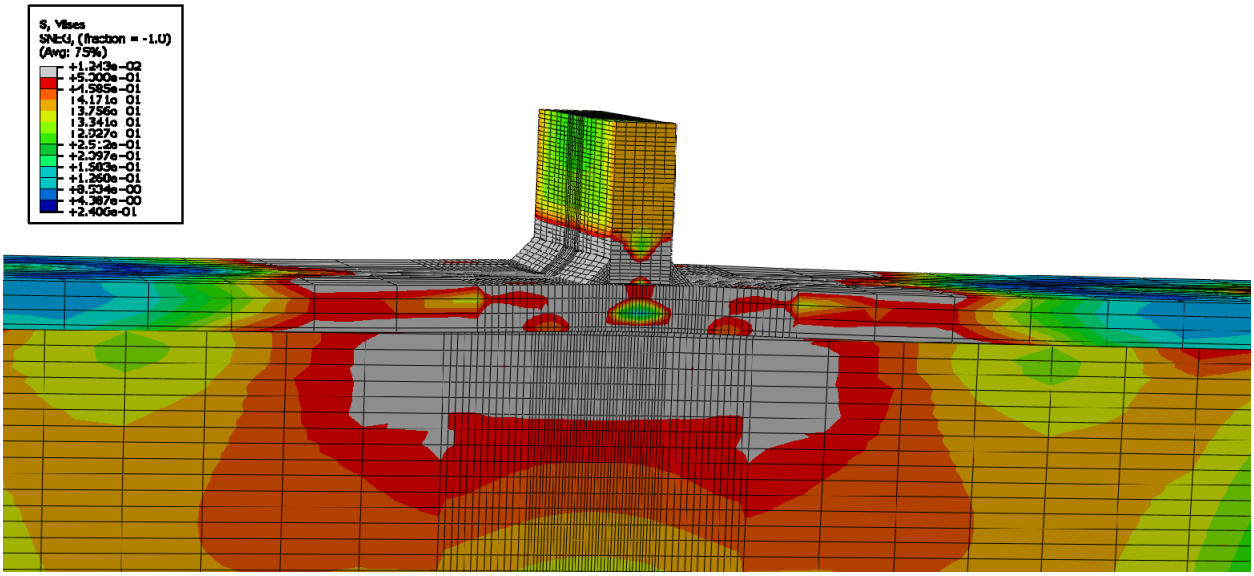

Figure E-430: Finite element model of W24X229-ST-NA with 7/8 in. welds at its load capacity of 903.42 kips

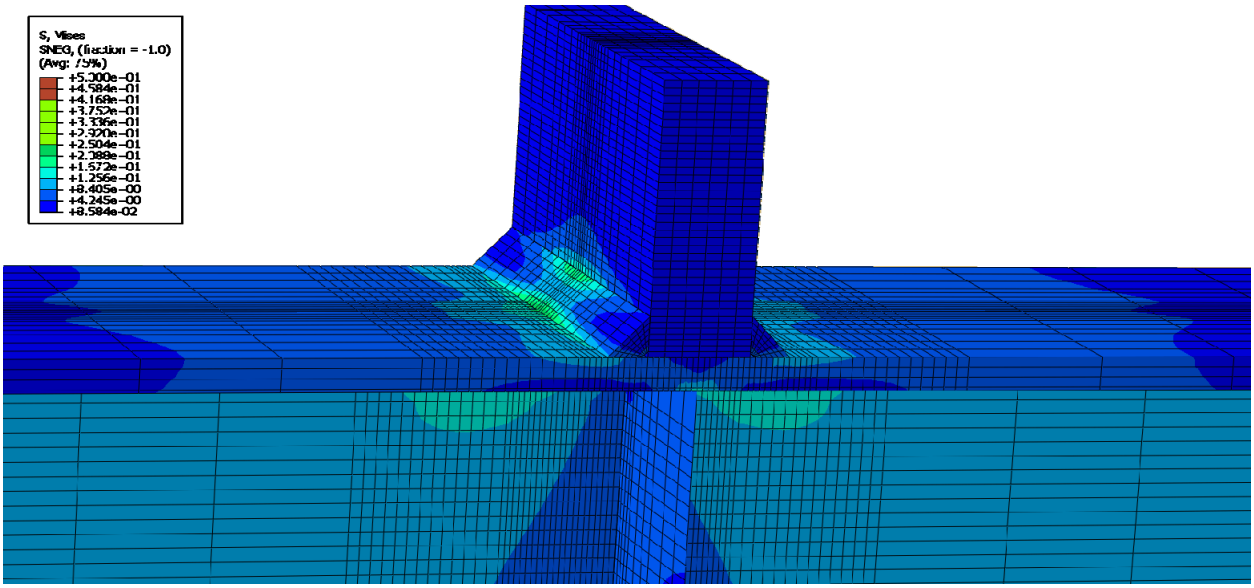

Figure E-431: Finite element model of W14X68-ST-E0 with 7/8 in. welds while remaining elastic

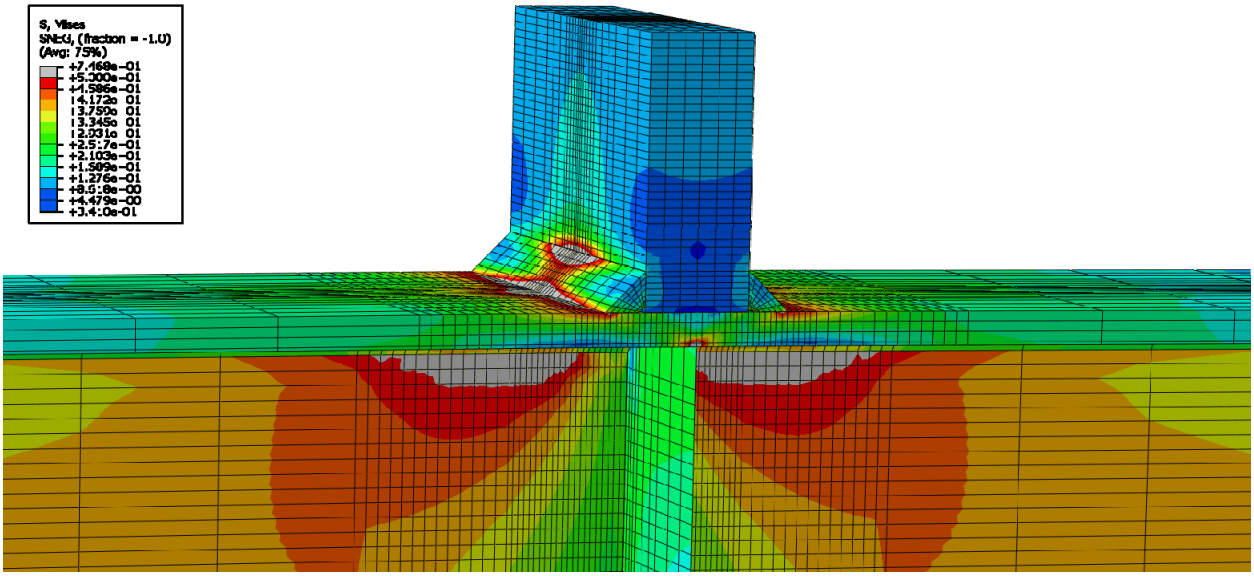

Figure E-432: Finite element model of W14X68-ST-E0 with 7/8 in. welds during inelastic behavior

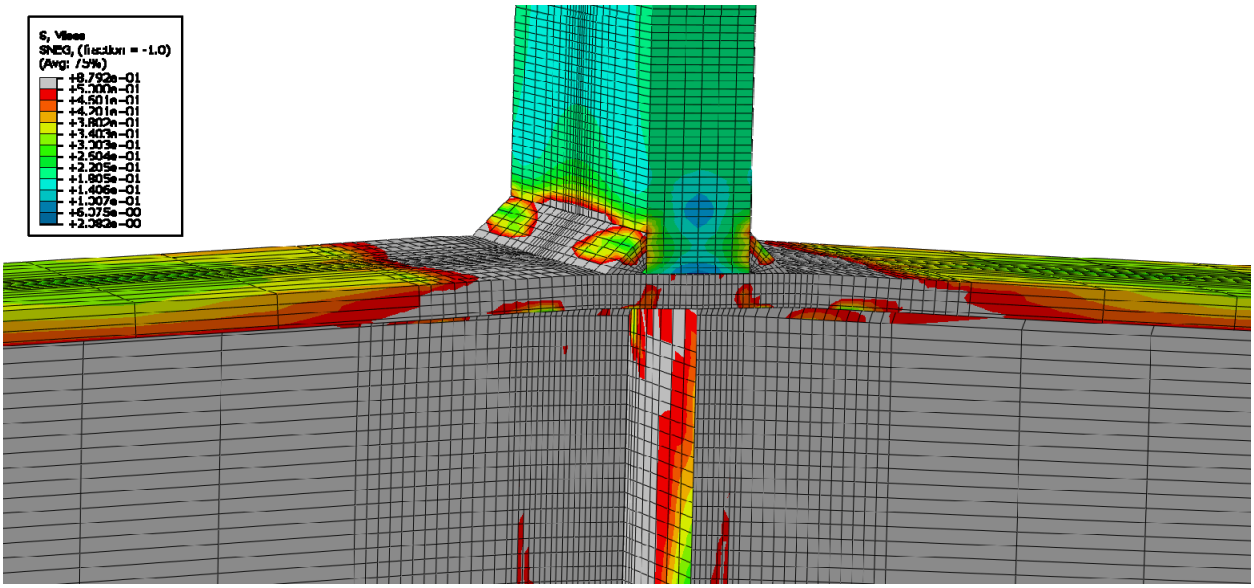

Figure E-433: Finite element model of W14X68-ST-E0 with 7/8 in. welds at its load capacity of 433.69 kips

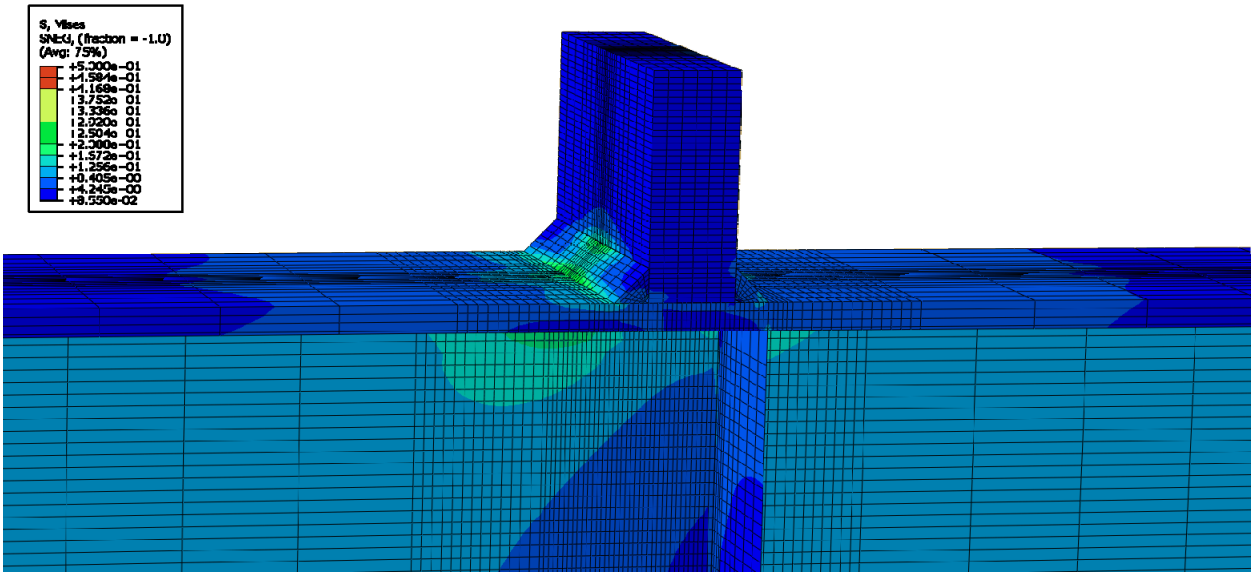

Figure E-434: Finite element model of W14X68-ST-E2 with 7/8 in. welds while remaining elastic

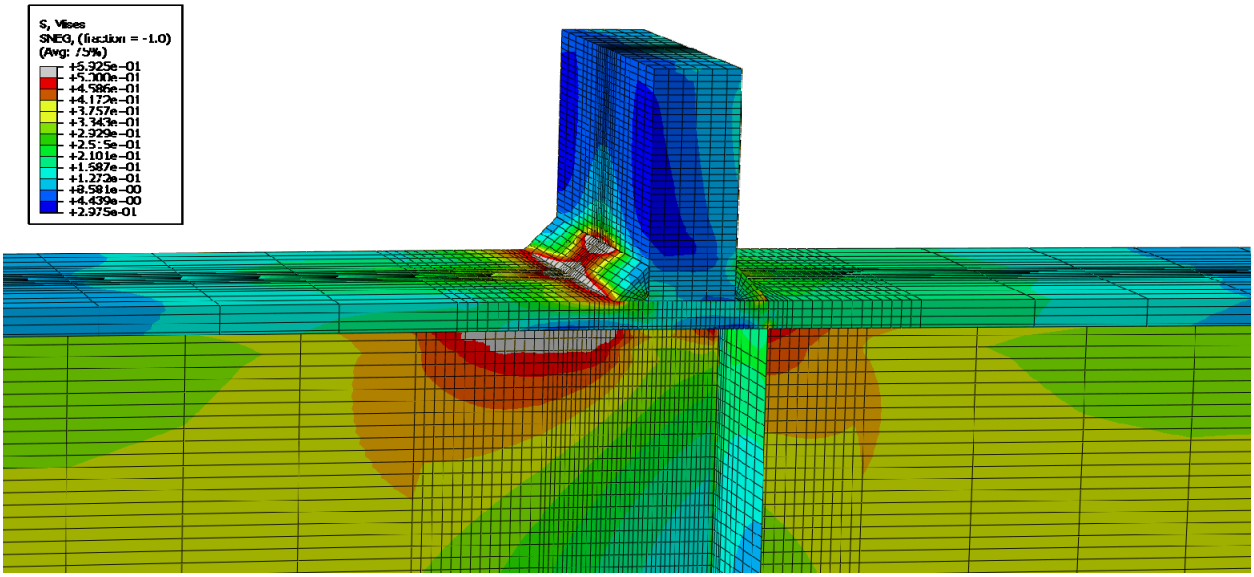

Figure E-435: Finite element model of W14X68-ST-E2 with 7/8 in. welds during inelastic behavior

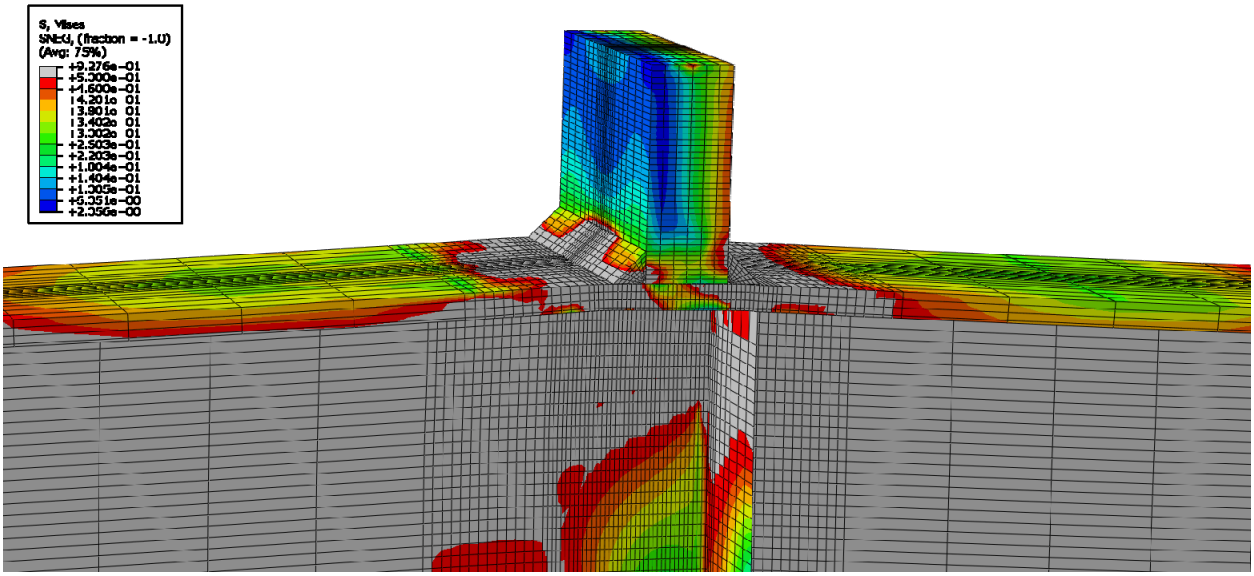

Figure E-436: Finite element model of W14X68-ST-E2 with 7/8 in. welds at its load capacity of 429.62 kips

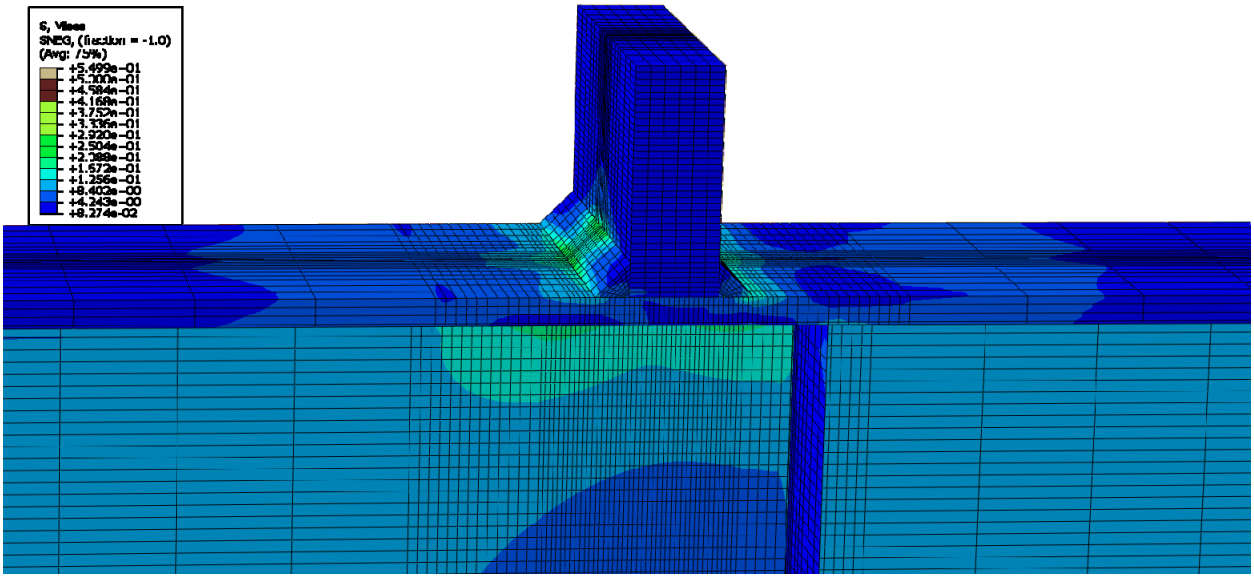

Figure E-437: Finite element model of W14X68-ST-E4 with 7/8 in. welds while remaining elastic

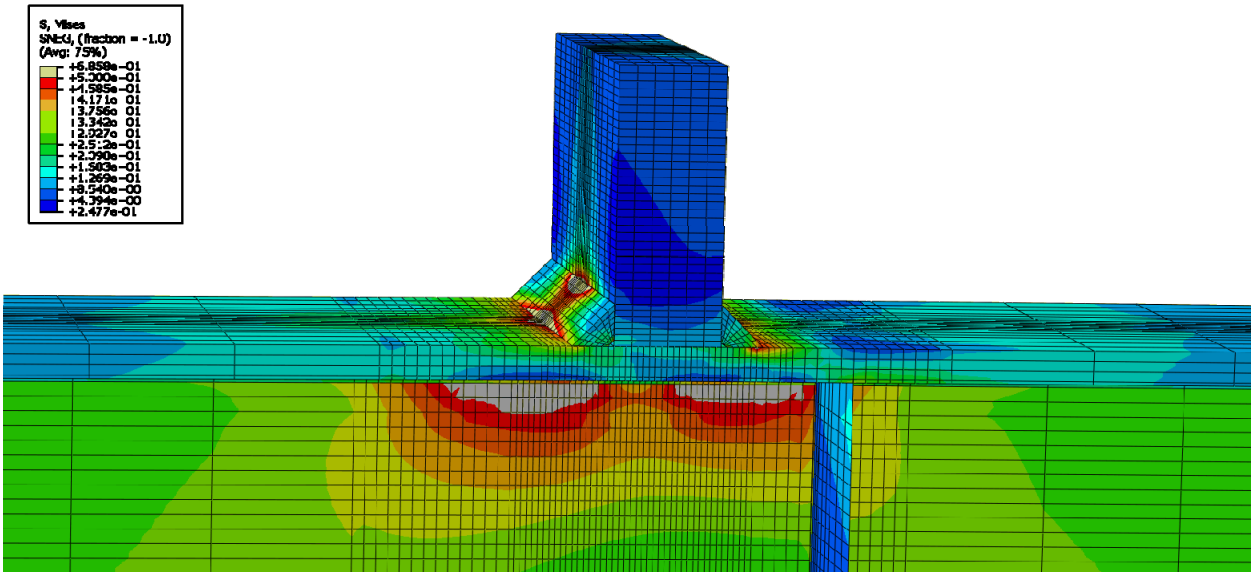

Figure E-438: Finite element model of W14X68-ST-E4 with 7/8 in. welds during inelastic behavior

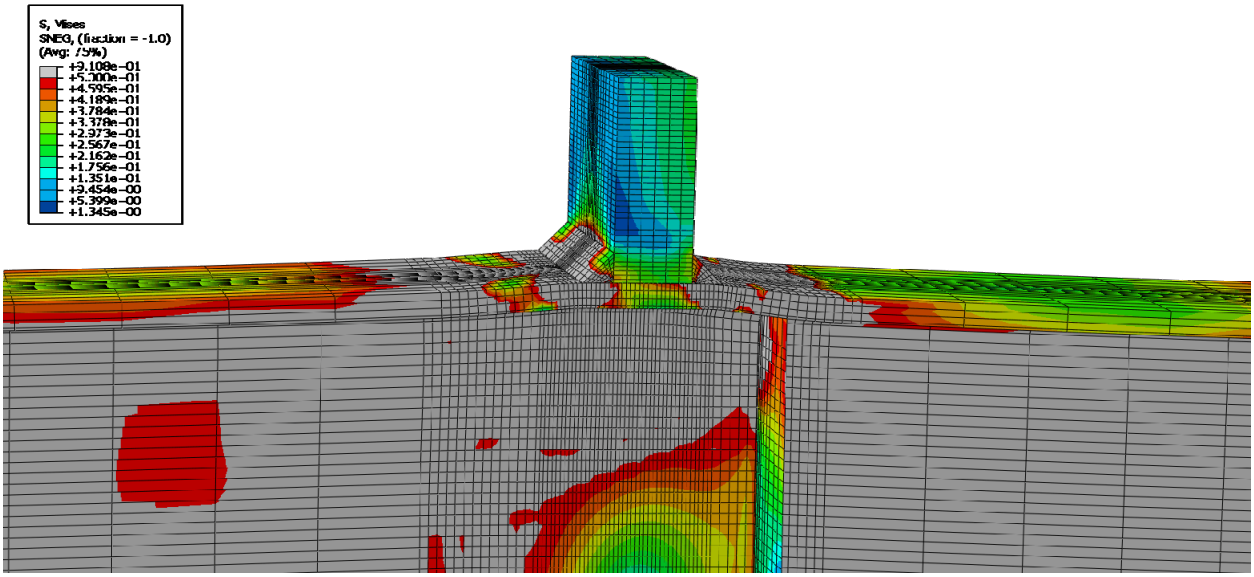

Figure E-439: Finite element model of W14X68-ST-E4 with 7/8 in. welds at its load capacity of 399.51 kips

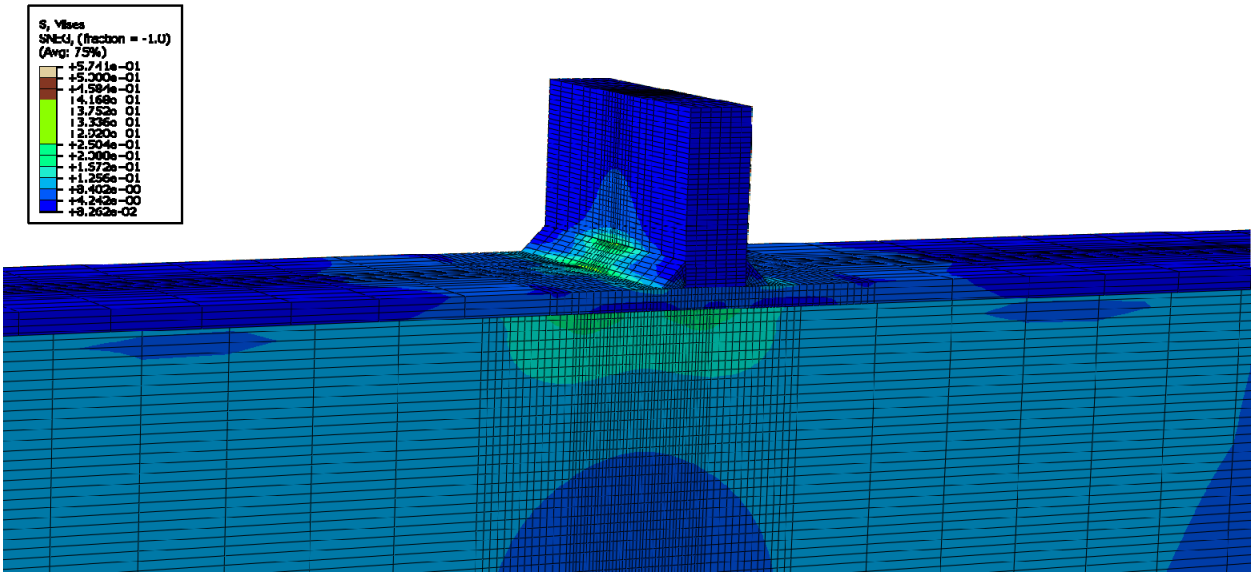

Figure E-440: Finite element model of W14X68-ST-NA with 7/8 in. welds while remaining elastic

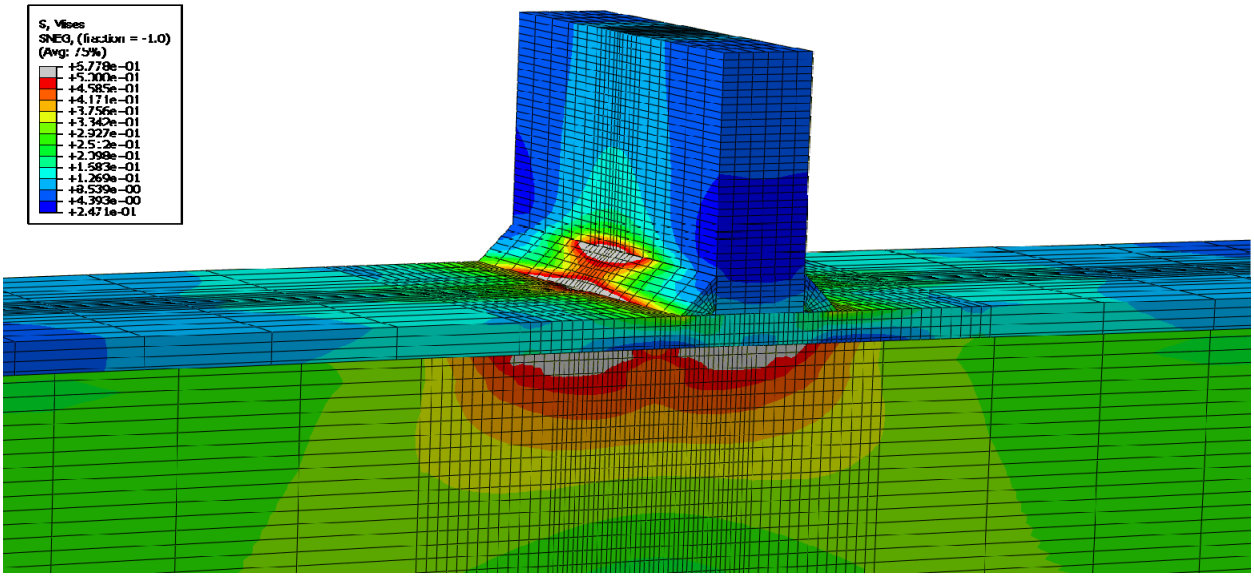

Figure E-441: Finite element model of W14X68-ST-NA with 7/8 in. welds during inelastic behavior

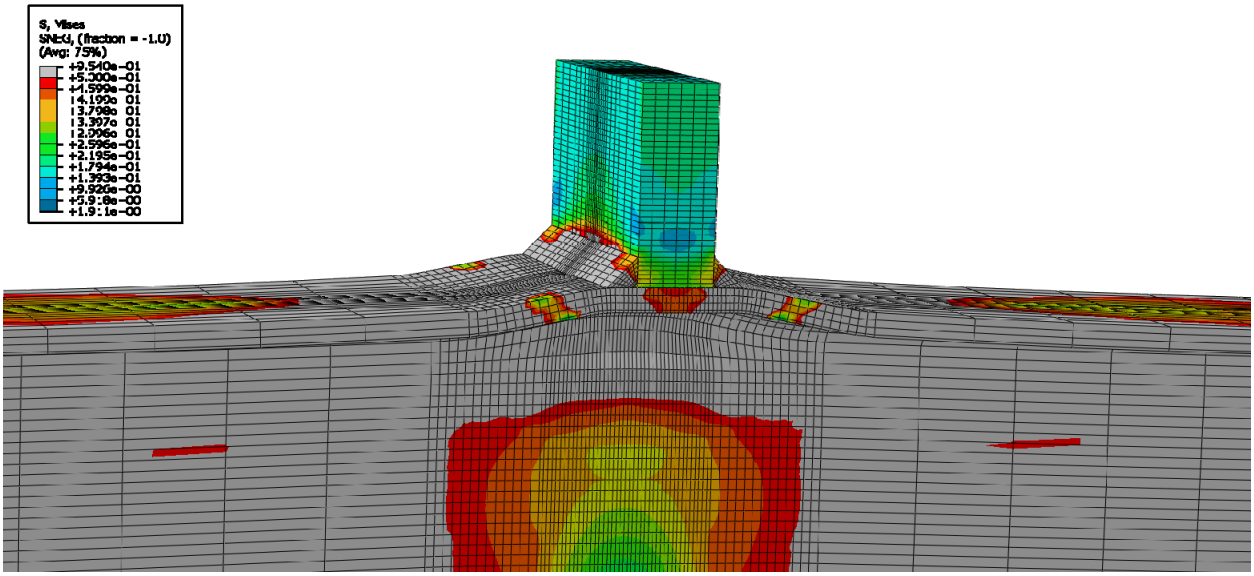

Figure E-442: Finite element model of W14X68-ST-NA with 7/8 in. welds at its load capacity of 347.86 kips

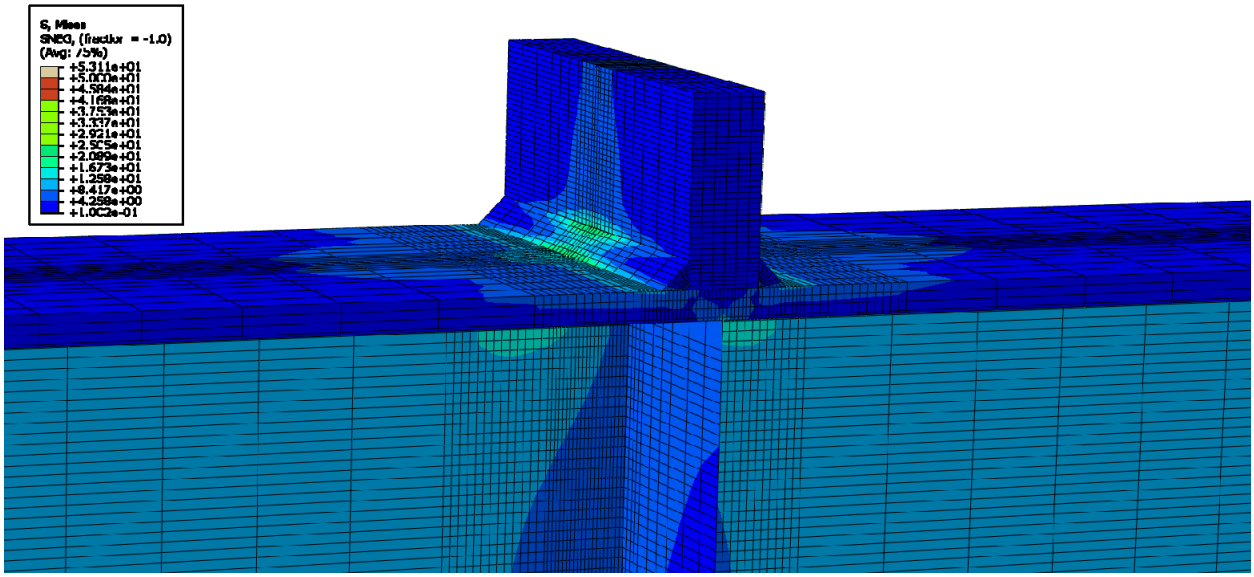

Figure E-443: Finite element model of W14X120-ST-E0 with 7/8 in. welds while remaining elastic

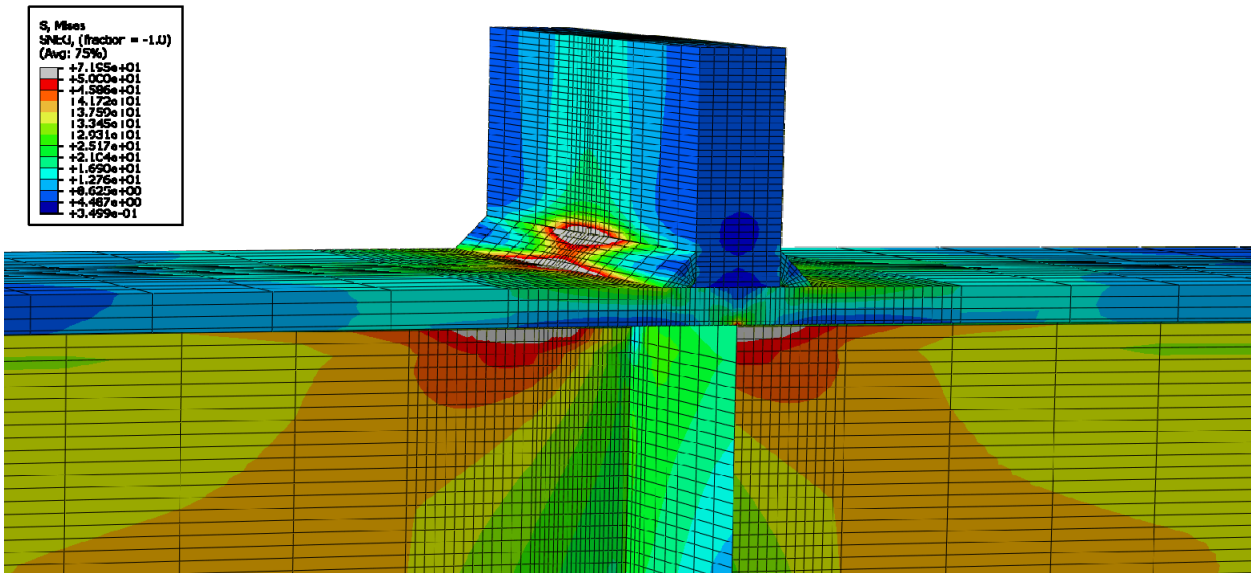

Figure E-444: Finite element model of W14X120-ST-E0 with 7/8 in. welds during inelastic behavior

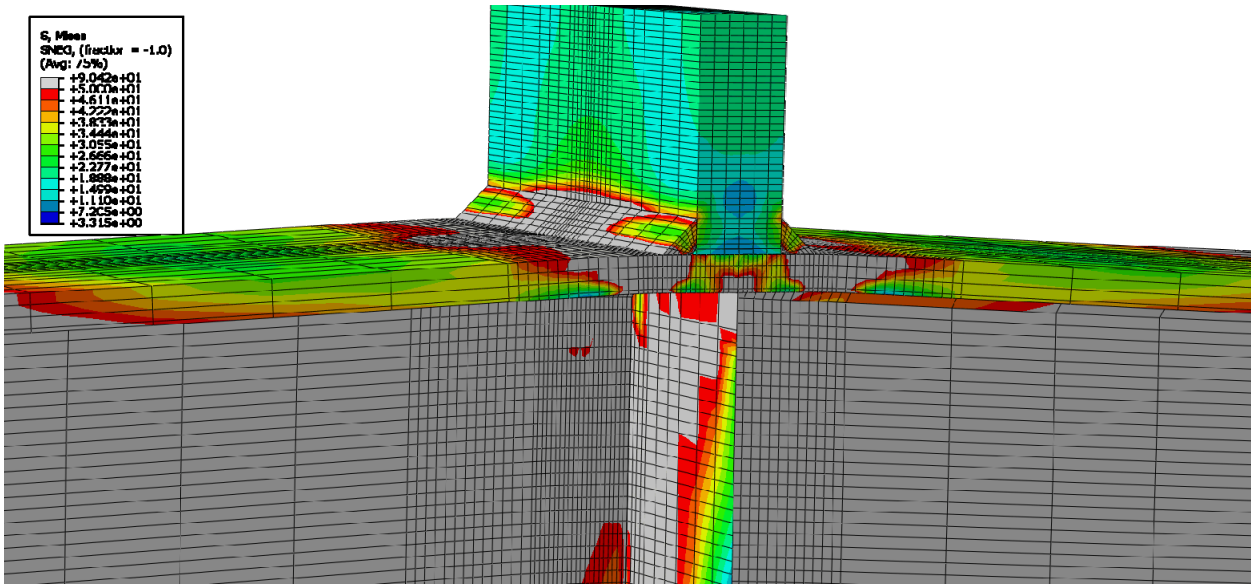

Figure E-445: Finite element model of W14X120-ST-E0 with 7/8 in. welds at its load capacity of 672.39 kips

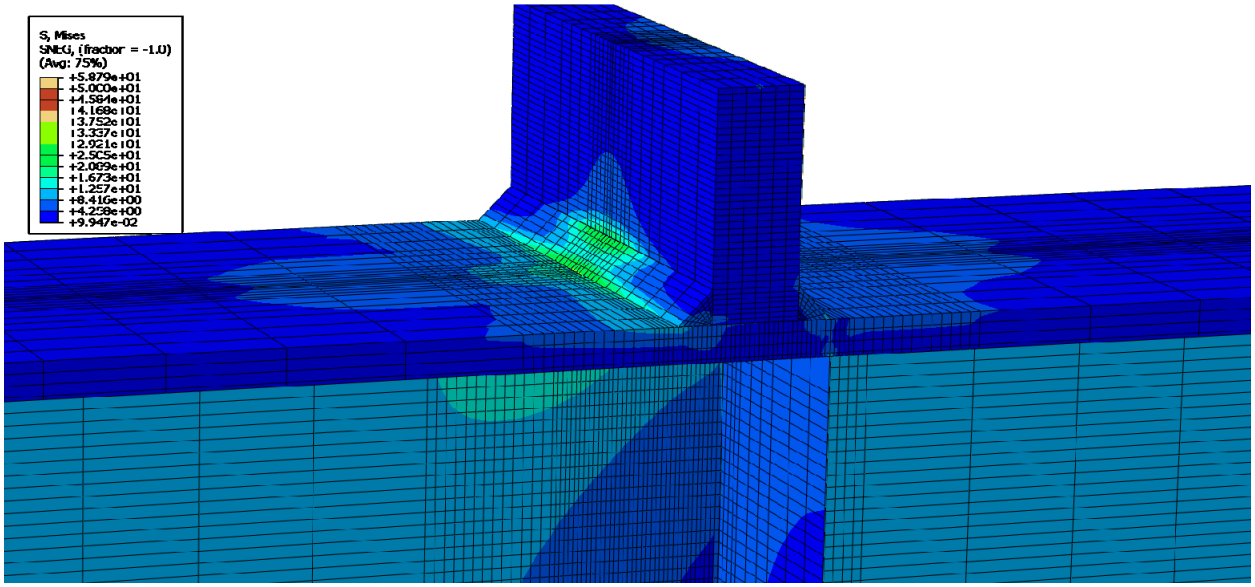

Figure E-446: Finite element model of W14X120-ST-E2 with 7/8 in. welds while remaining elastic

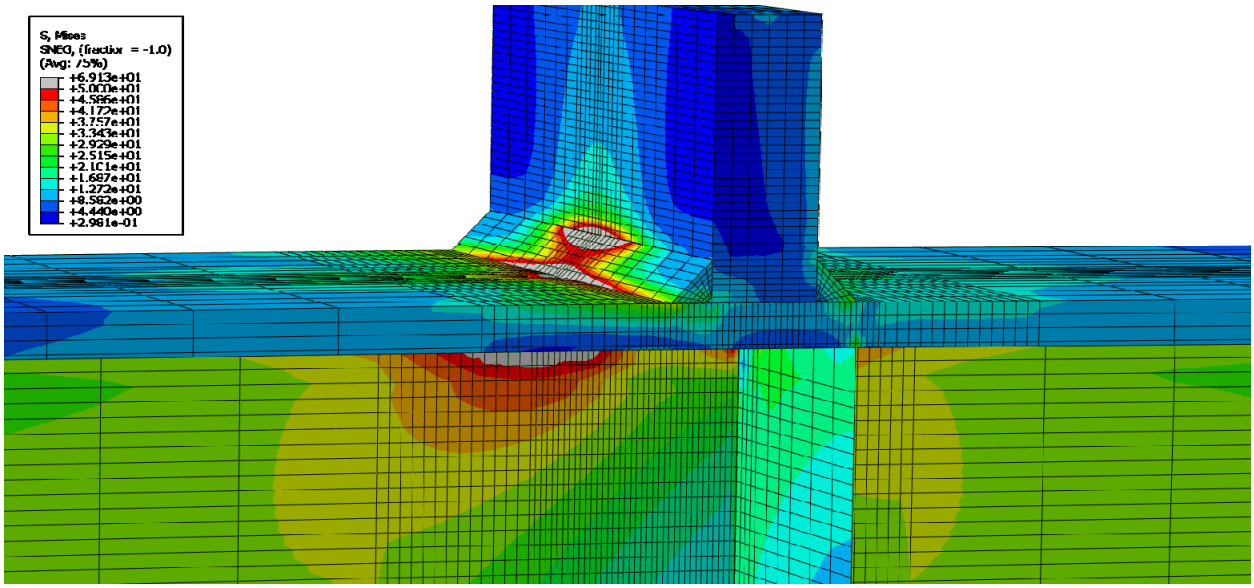

Figure E-447: Finite element model of W14X120-ST-E2 with 7/8 in. welds during inelastic behavior

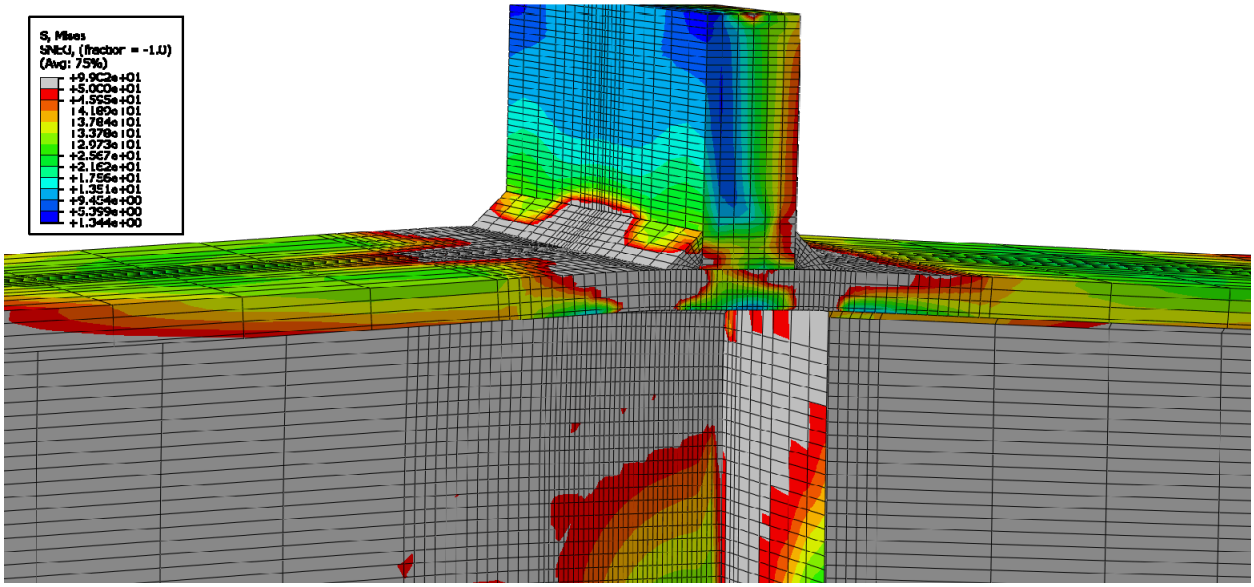

Figure E-448: Finite element model of W14X120-ST-E2 with 7/8 in. welds at its load capacity of 669.06 kips

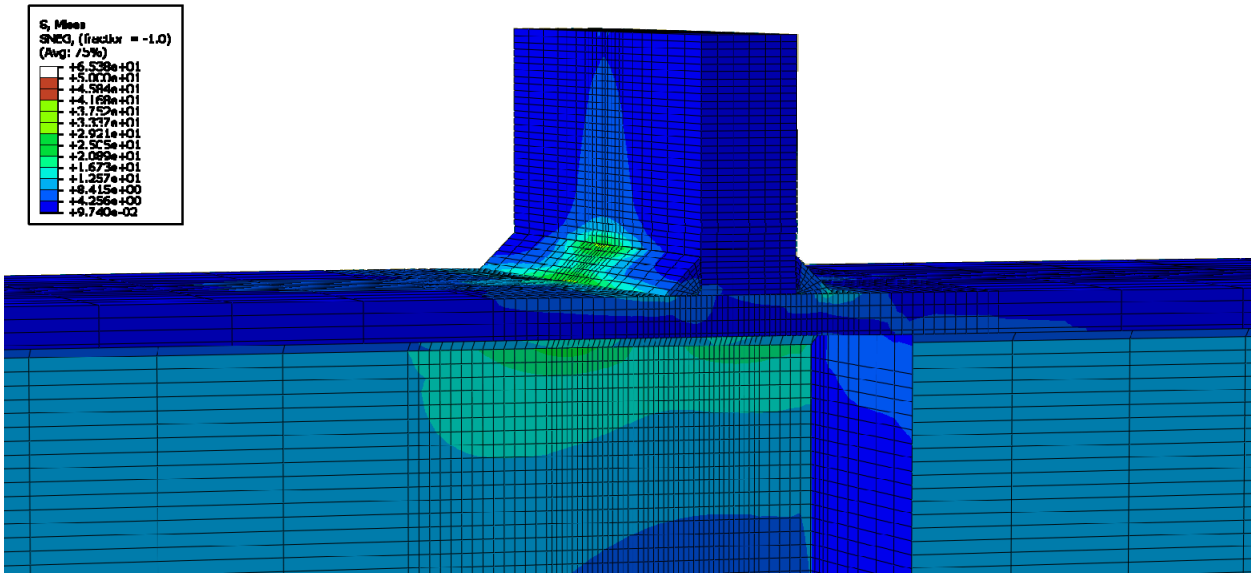

Figure E-449: Finite element model of W14X120-ST-E4 with 7/8 in. welds while remaining elastic

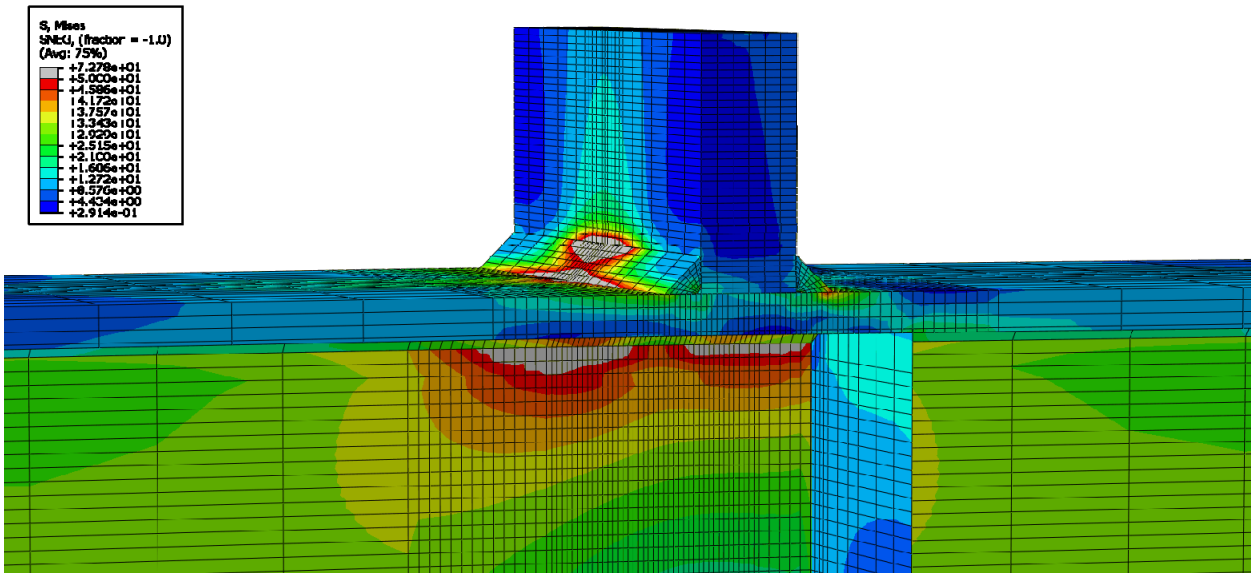

Figure E-450: Finite element model of W14X120-ST-E4 with 7/8 in. welds during inelastic behavior

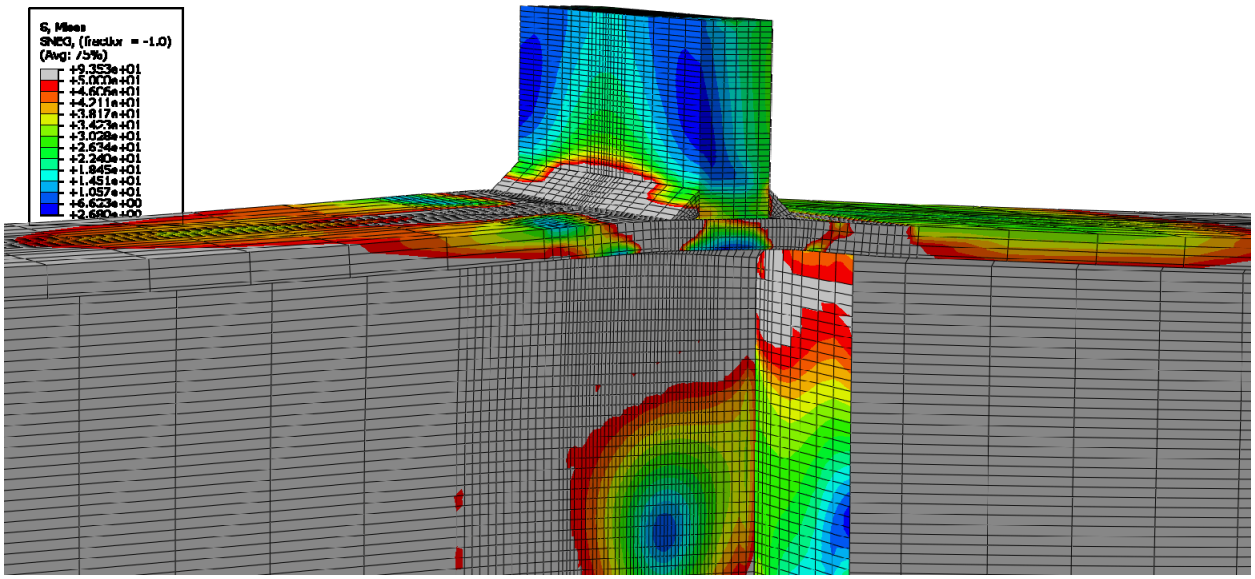

Figure E-451: Finite element model of W14X120-ST-E4 with 7/8 in. welds at its load capacity of 661.09 kips

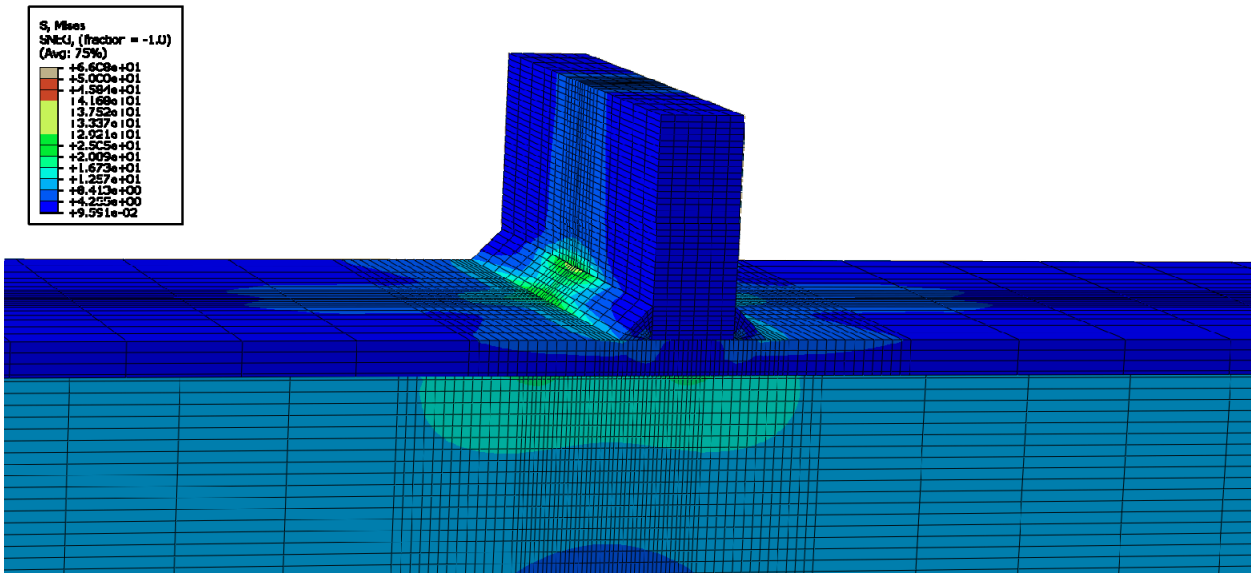

Figure E-452: Finite element model of W14X120-ST-NA with 7/8 in. welds while remaining elastic

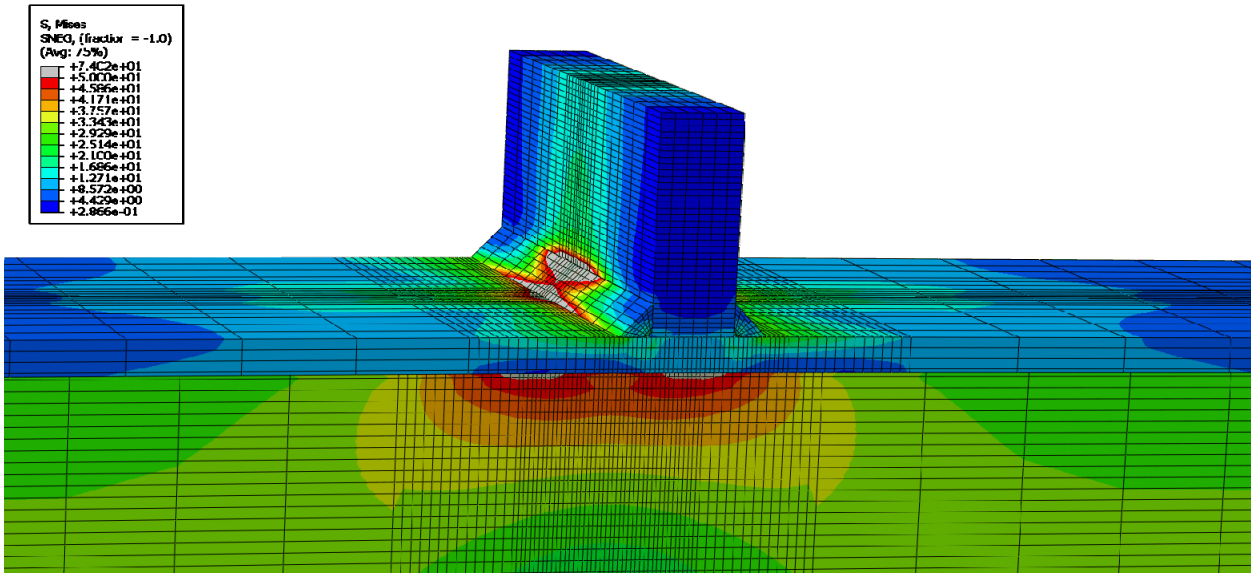

Figure E-453: Finite element model of W14X120-ST-NA with 7/8 in. welds during inelastic behavior

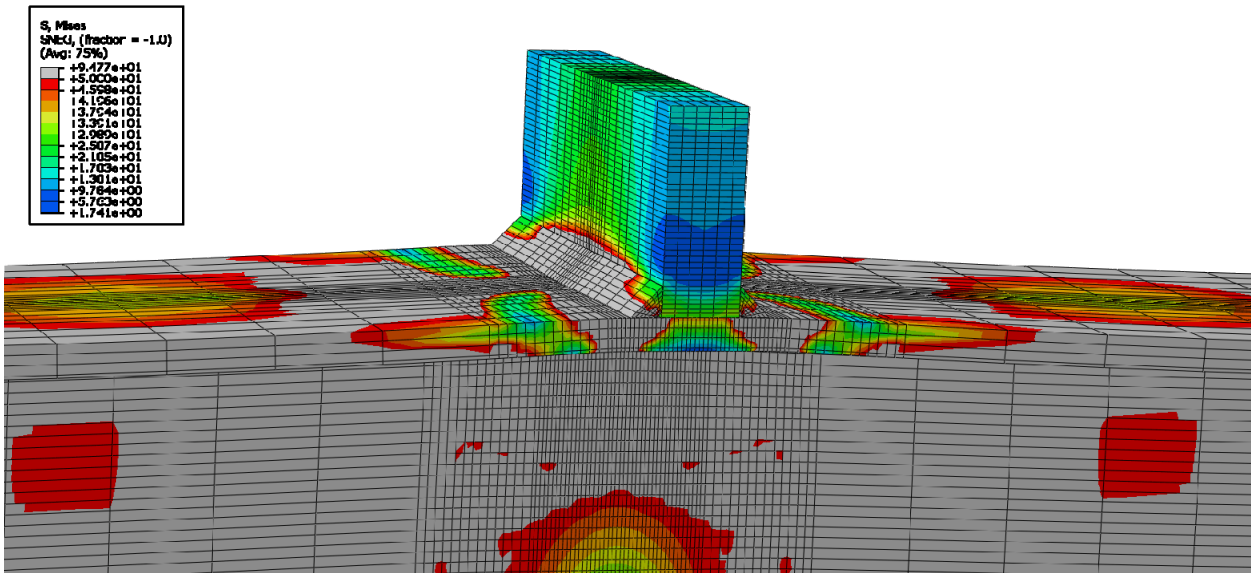

Figure E-454: Finite element model of W14X120-ST-NA with 7/8 in. welds at its load capacity of 612.88 kips

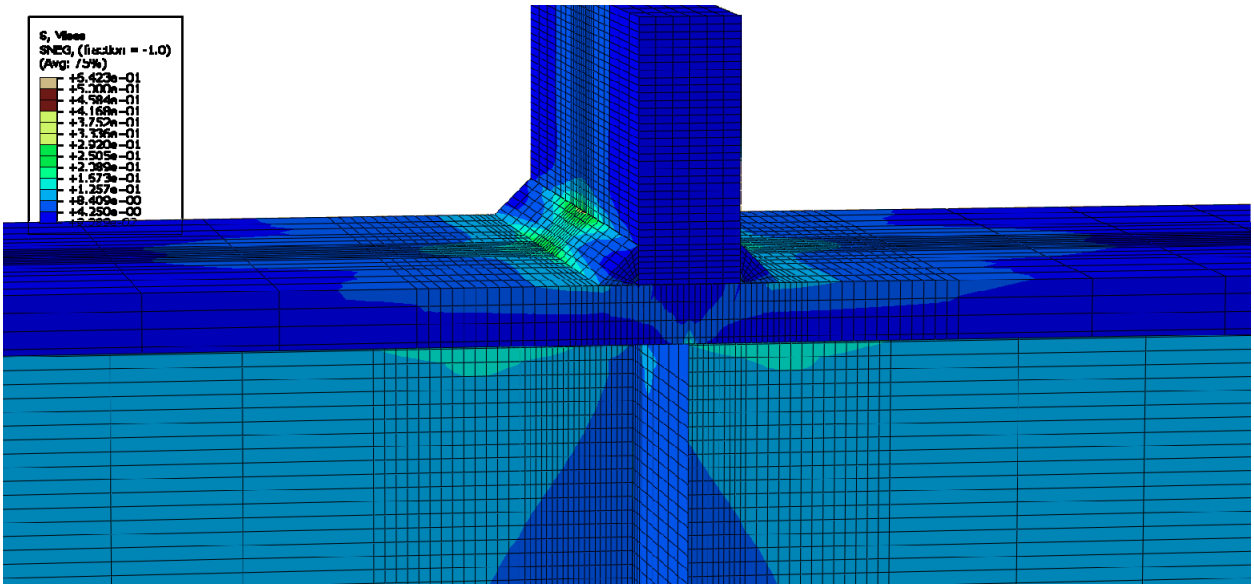

Figure E-455: Finite element model of W14X176-ST-E0 with 7/8 in. welds while remaining elastic

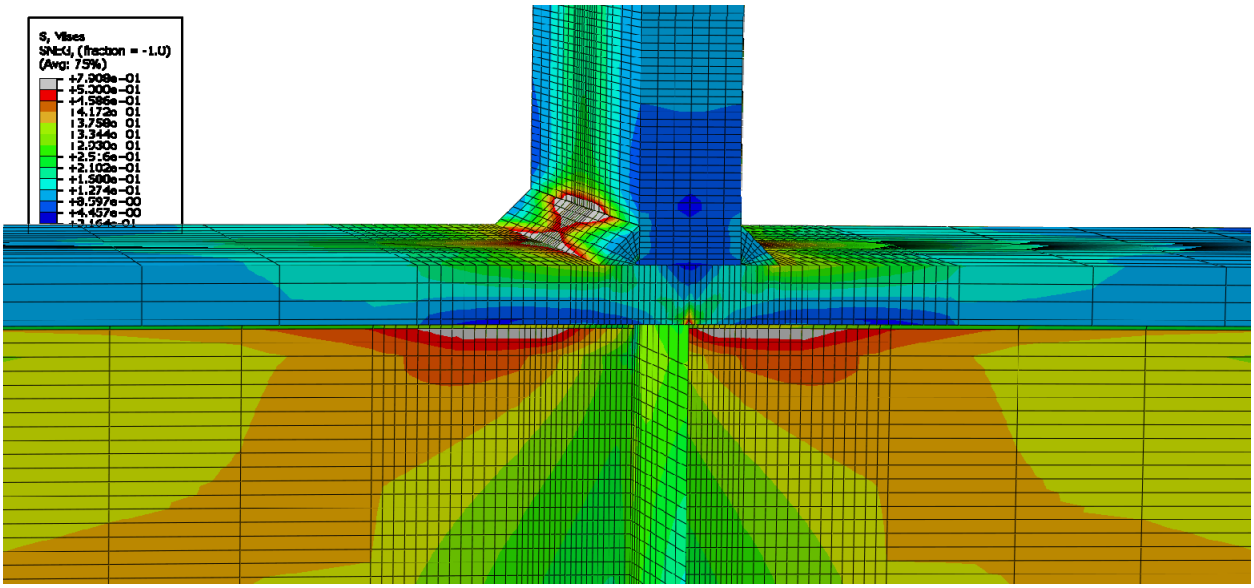

Figure E-456: Finite element model of W14X176-ST-E0 with 7/8 in. welds during inelastic behavior

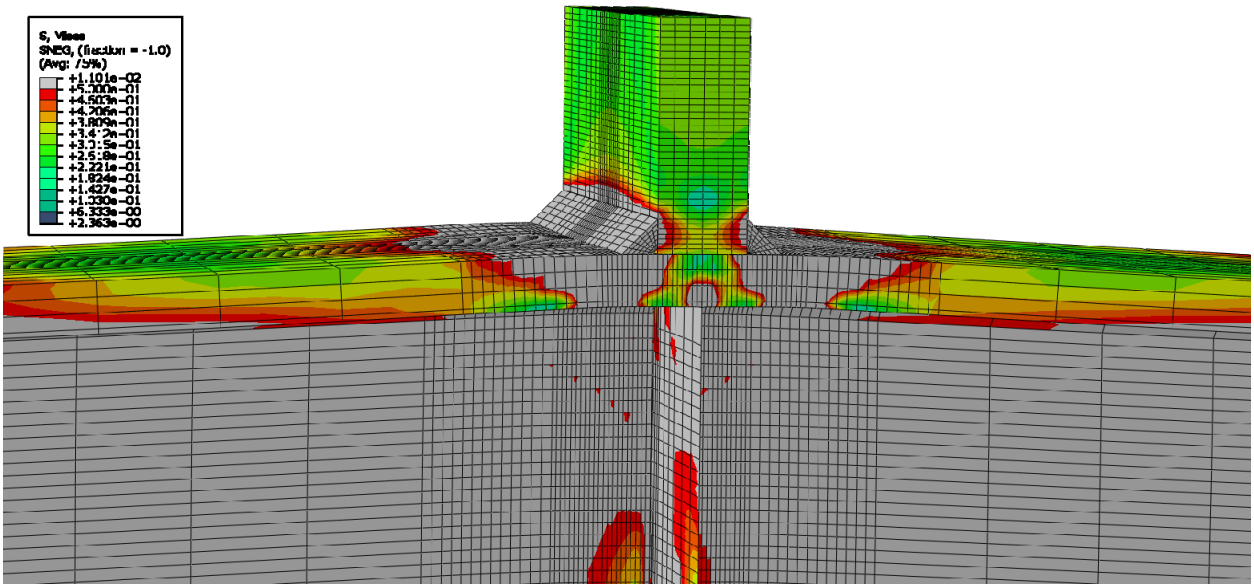

Figure E-457: Finite element model of W14X176-ST-E0 with 7/8 in. welds at its load capacity of 993.34 kips

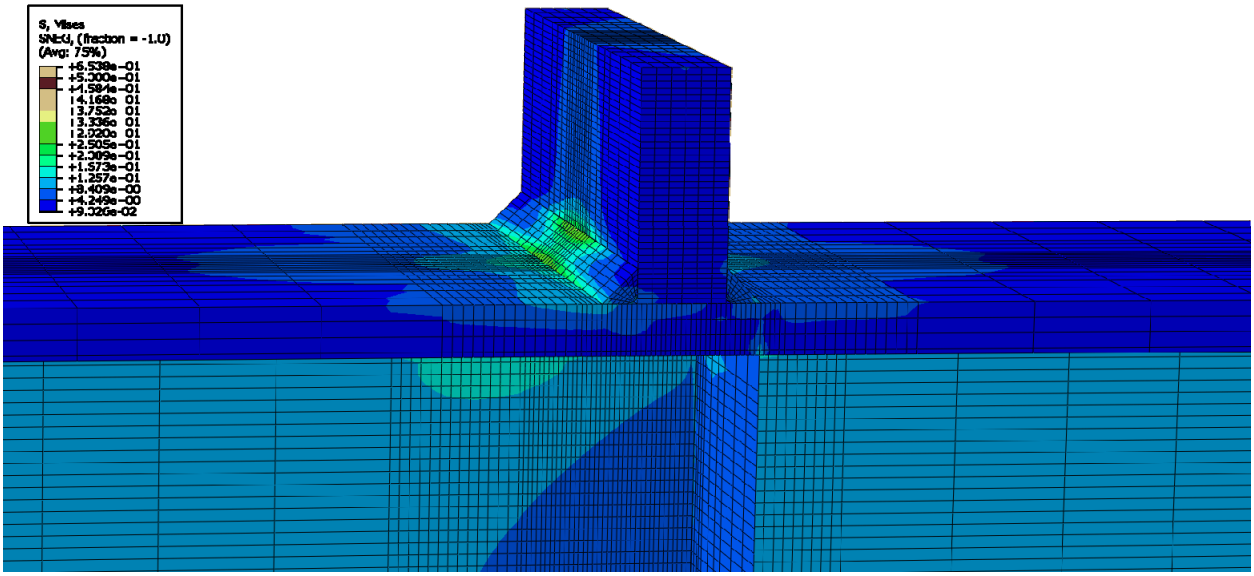

Figure E-458: Finite element model of W14X176-ST-E2 with 7/8 in. welds while remaining elastic

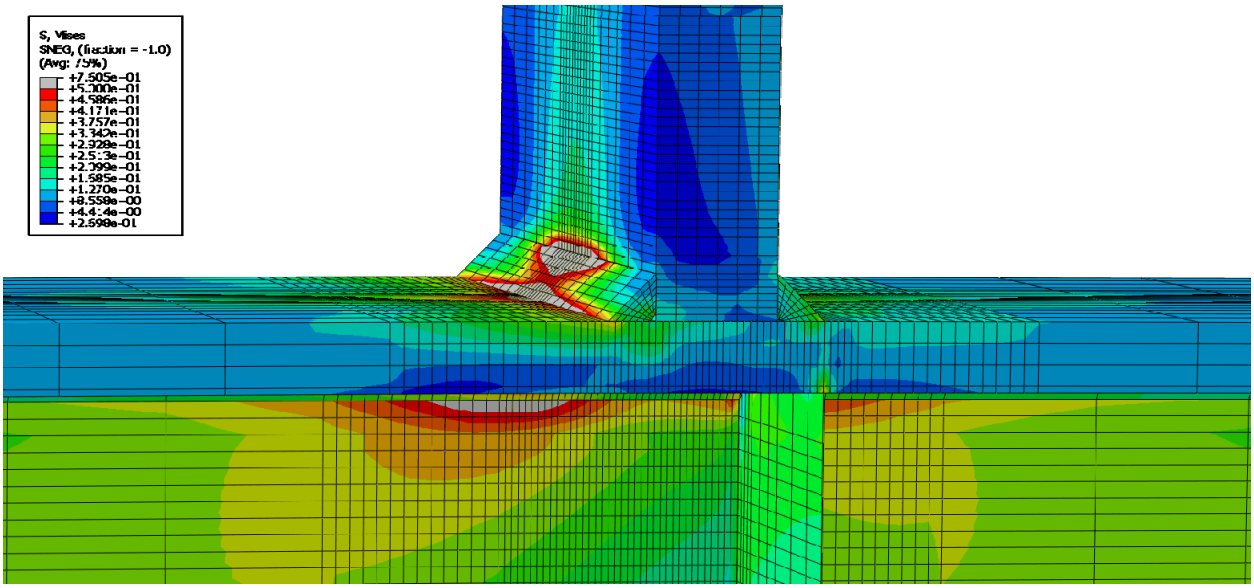

Figure E-459: Finite element model of W14X176-ST-E2 with 7/8 in. welds during inelastic behavior

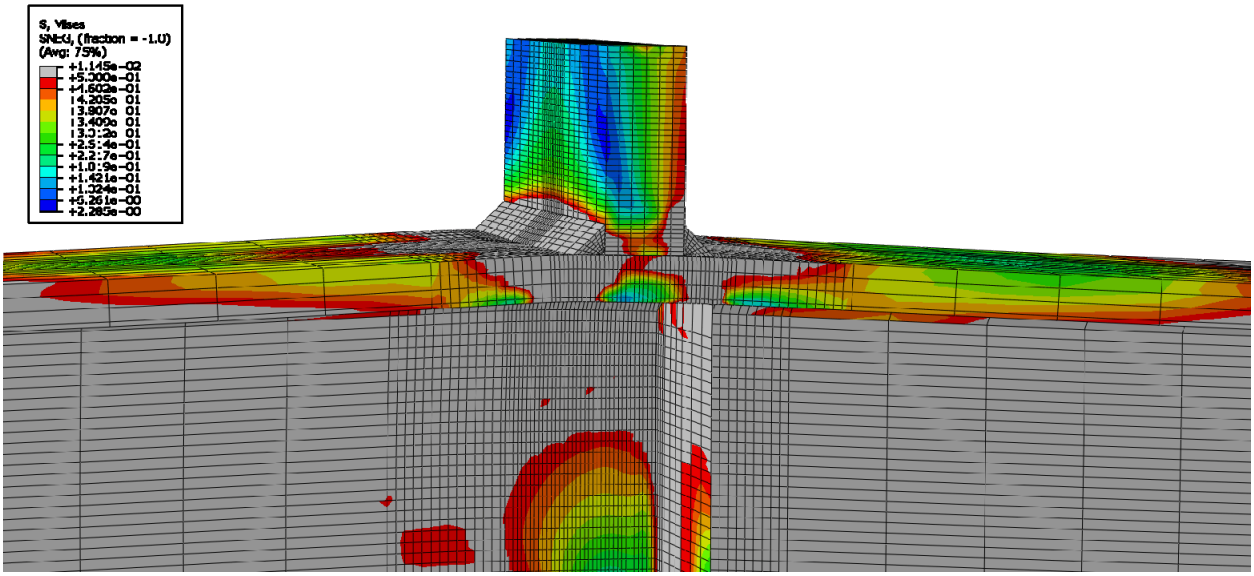

Figure E-460: Finite element model of W14X176-ST-E2 with 7/8 in. welds at its load capacity of 978.65 kips

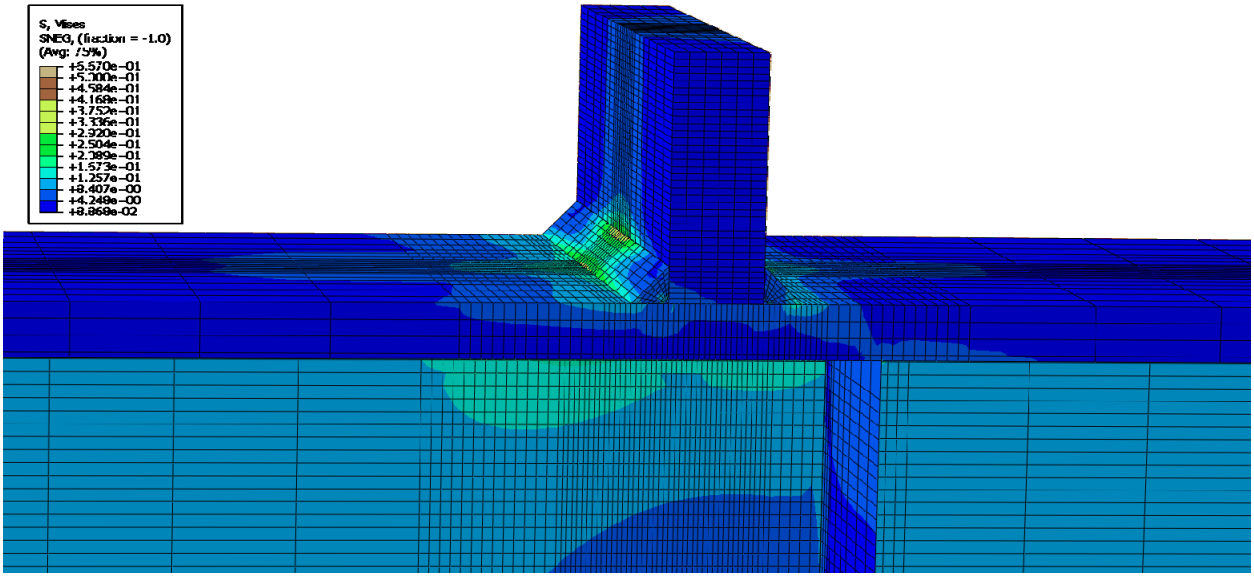

Figure E-461: Finite element model of W14X176-ST-E4 with 7/8 in. welds while remaining elastic

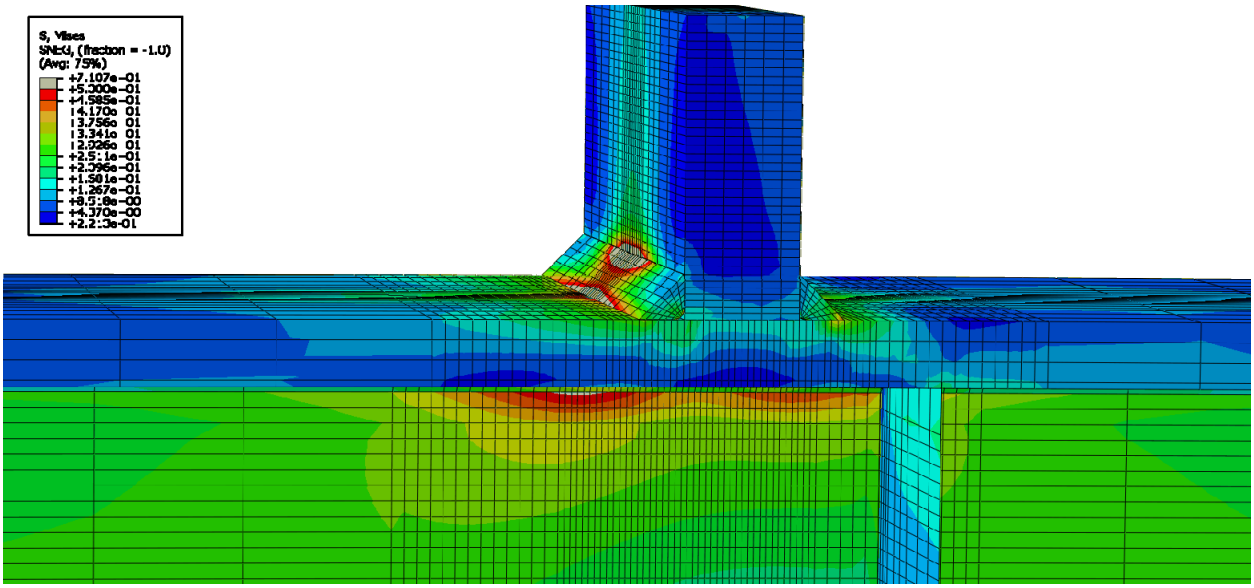

Figure E-462: Finite element model of W14X176-ST-E4 with 7/8 in. welds during inelastic behavior

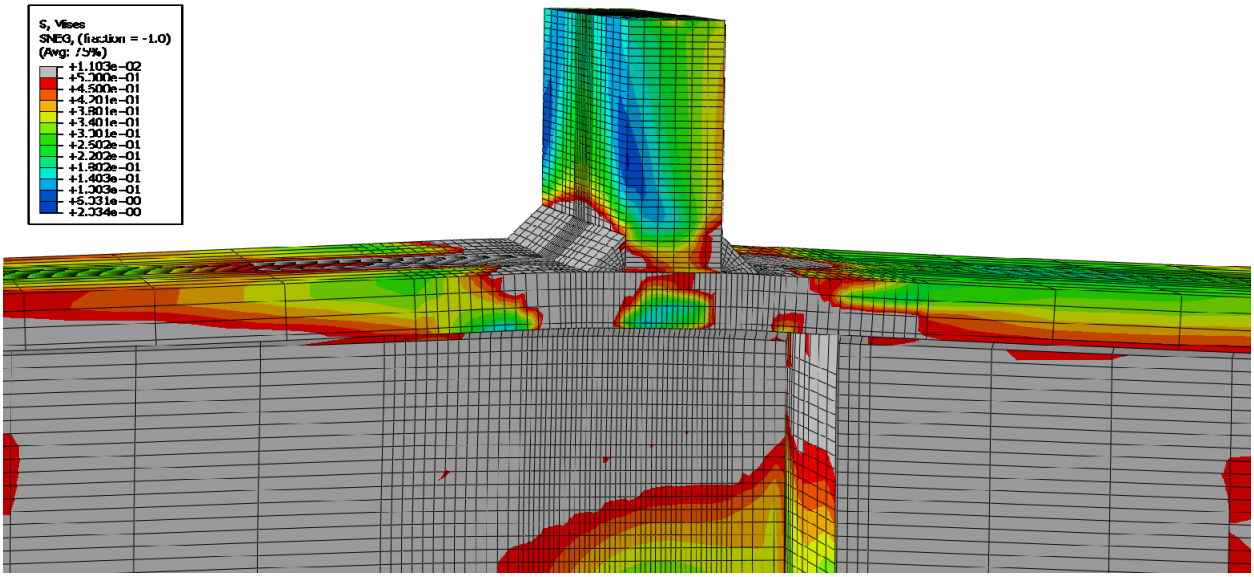

Figure E-463: Finite element model of W14X176-ST-E4 with 7/8 in. welds at its load capacity of 930.03 kips

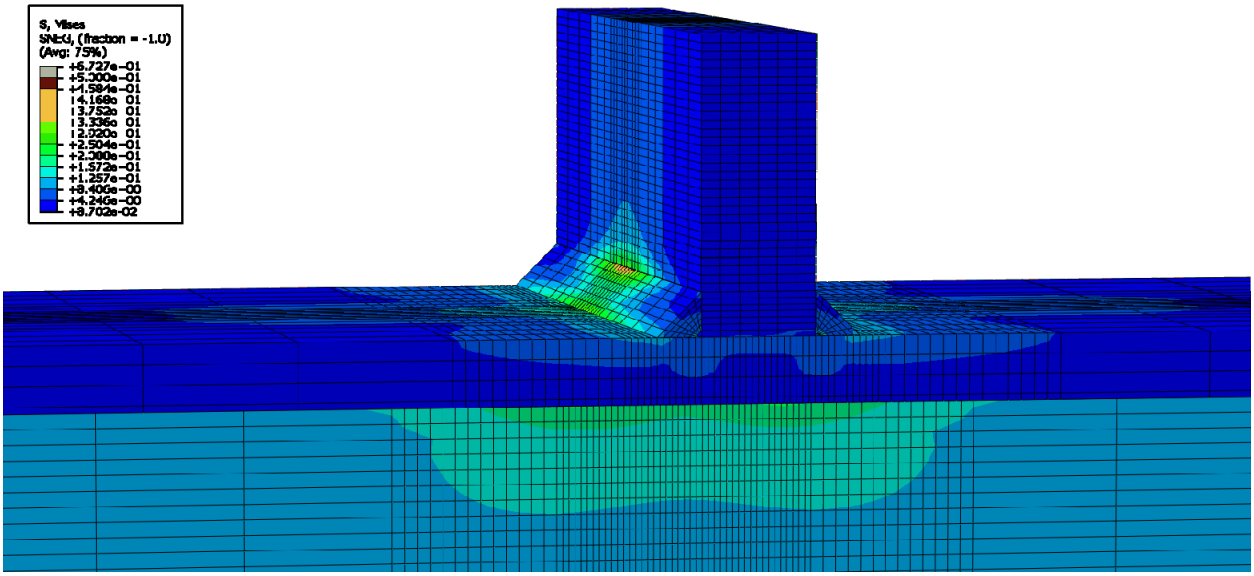

Figure E-464: Finite element model of W14X176-ST-NA with 7/8 in. welds while remaining elastic

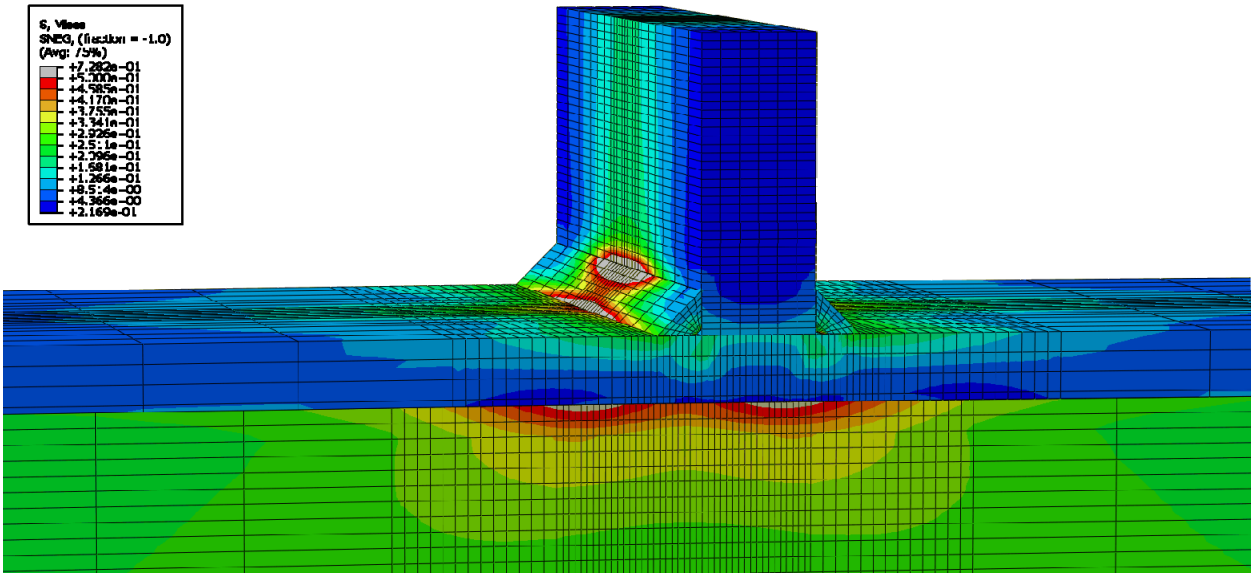

Figure E-465: Finite element model of W14X176-ST-NA with 7/8 in. welds during inelastic behavior

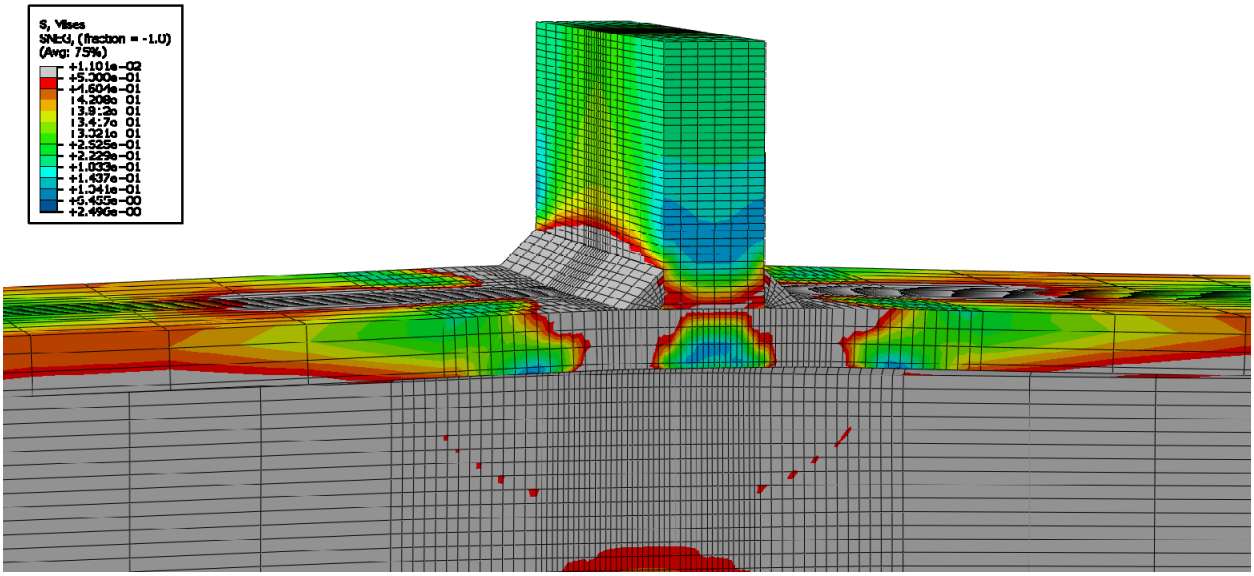

Figure E-466: Finite element model of W14X176-ST-NA with 7/8 in. welds at its load capacity of 855.01 kips

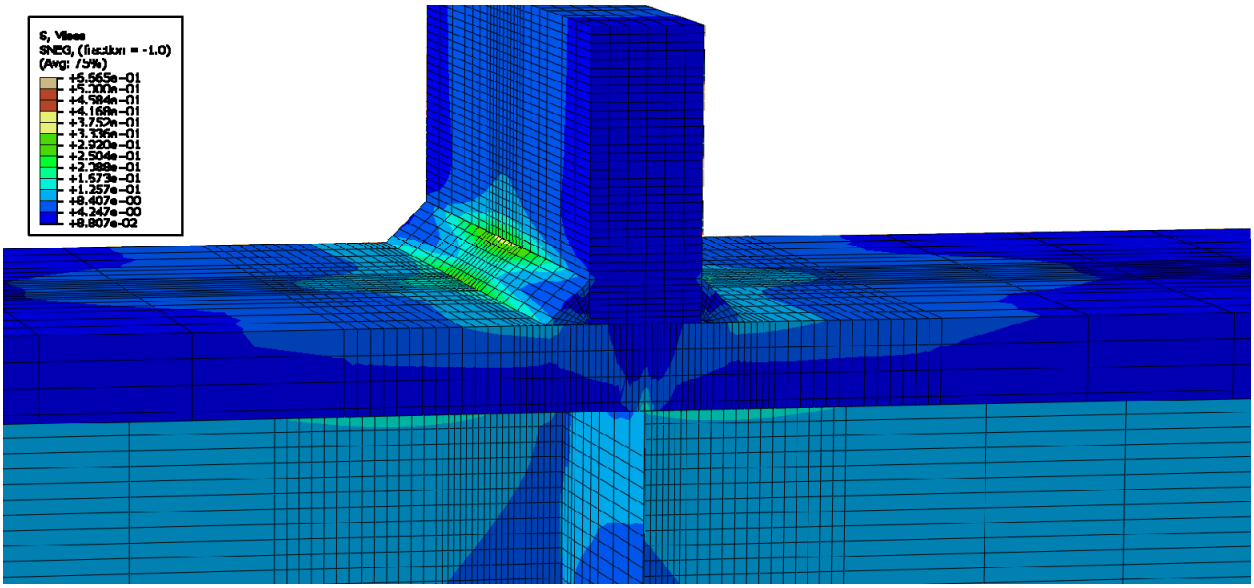

Figure E-467: Finite element model of W14X233-ST-E0 with 7/8 in. welds while remaining elastic

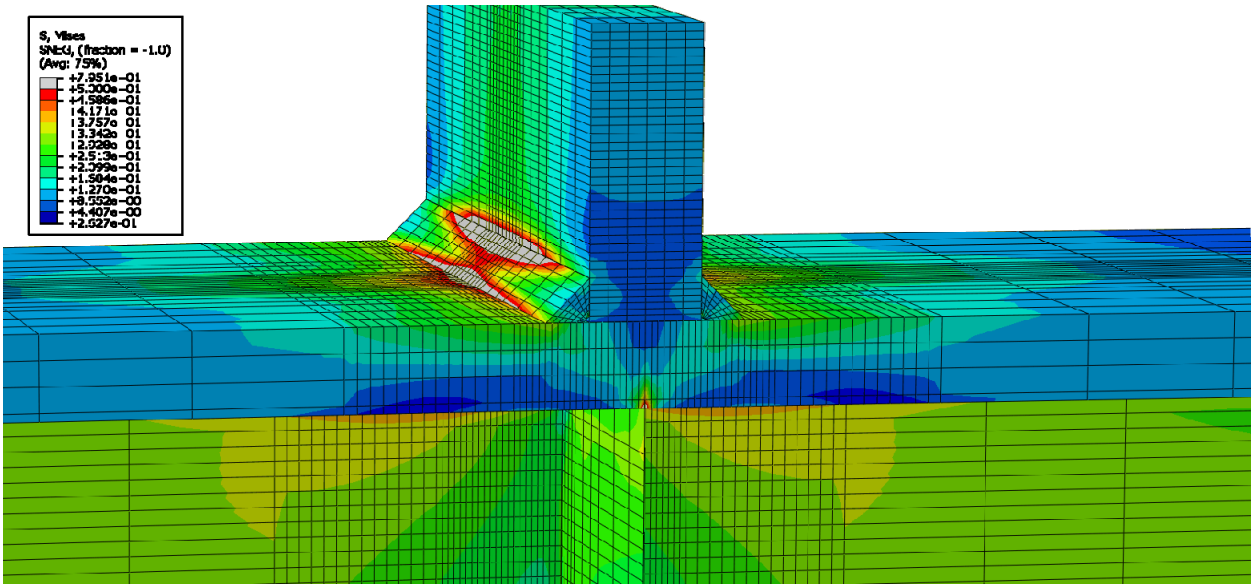

Figure E-468: Finite element model of W14X233-ST-E0 with 7/8 in. welds during inelastic behavior

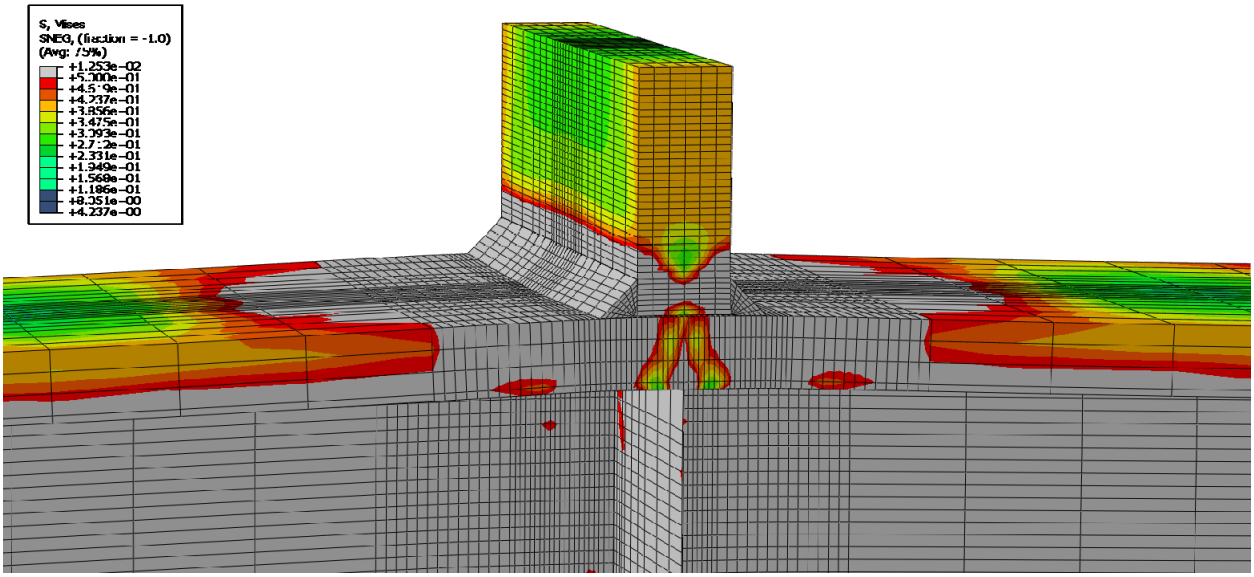

Figure E-469: Finite element model of W14X233-ST-E0 with 7/8 in. welds at its load capacity of 1095.60 kips

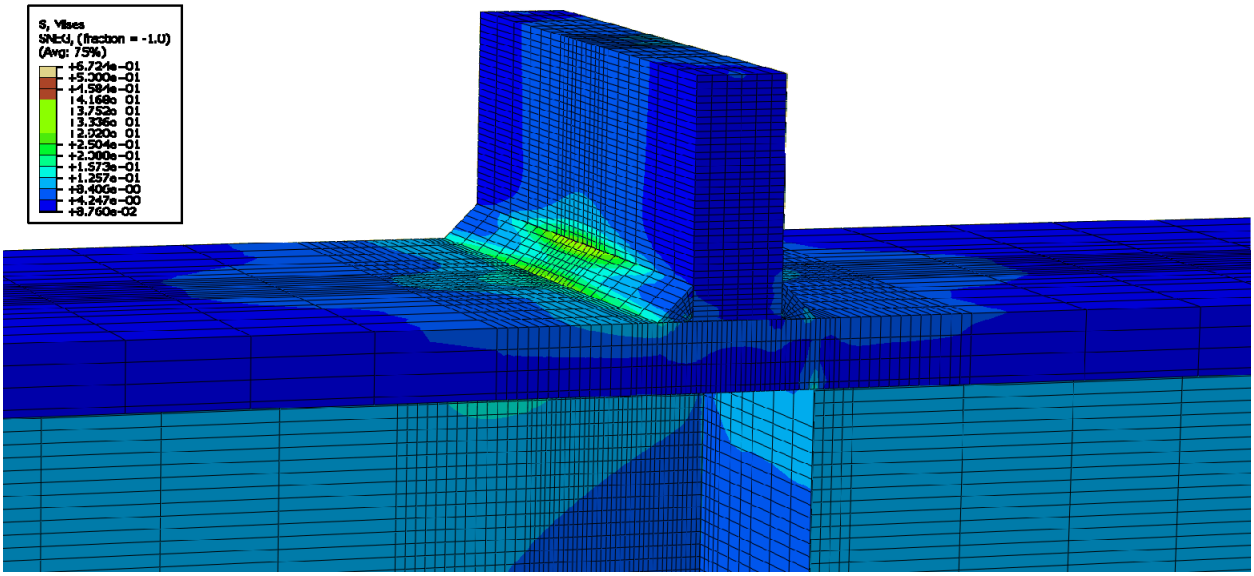

Figure E-470: Finite element model of W14X233-ST-E2 with 7/8 in. welds while remaining elastic

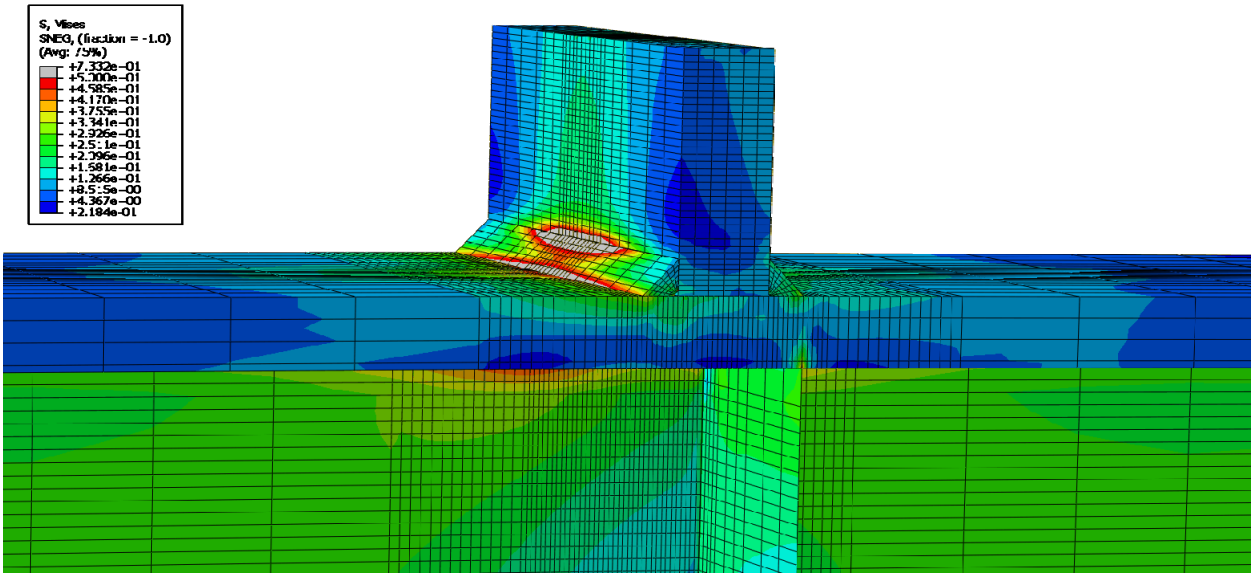

Figure E-471: Finite element model of W14X233-ST-E2 with 7/8 in. welds during inelastic behavior

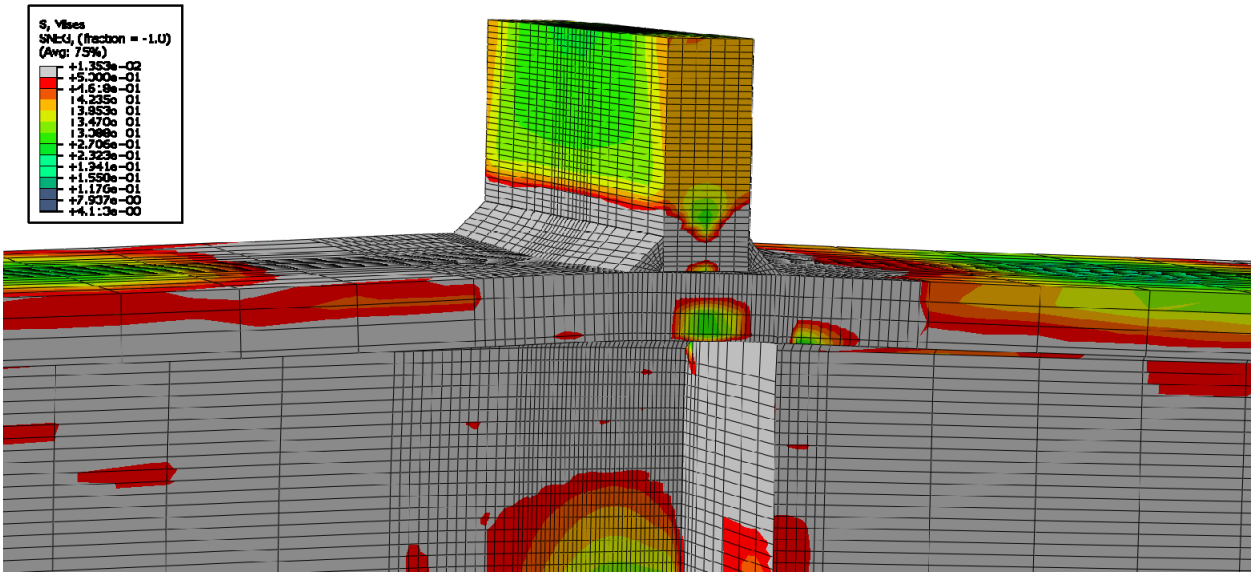

Figure E-472: Finite element model of W14X233-ST-E2 with 7/8 in. welds at its load capacity of 1087.56 kips

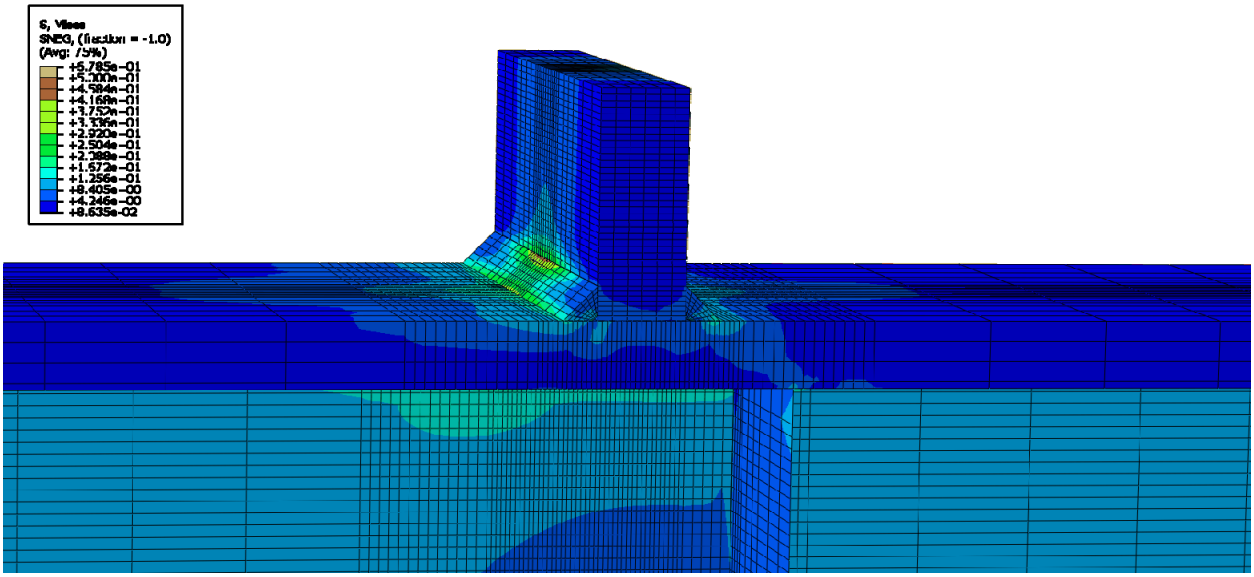

Figure E-473: Finite element model of W14X233-ST-E4 with 7/8 in. welds while remaining elastic

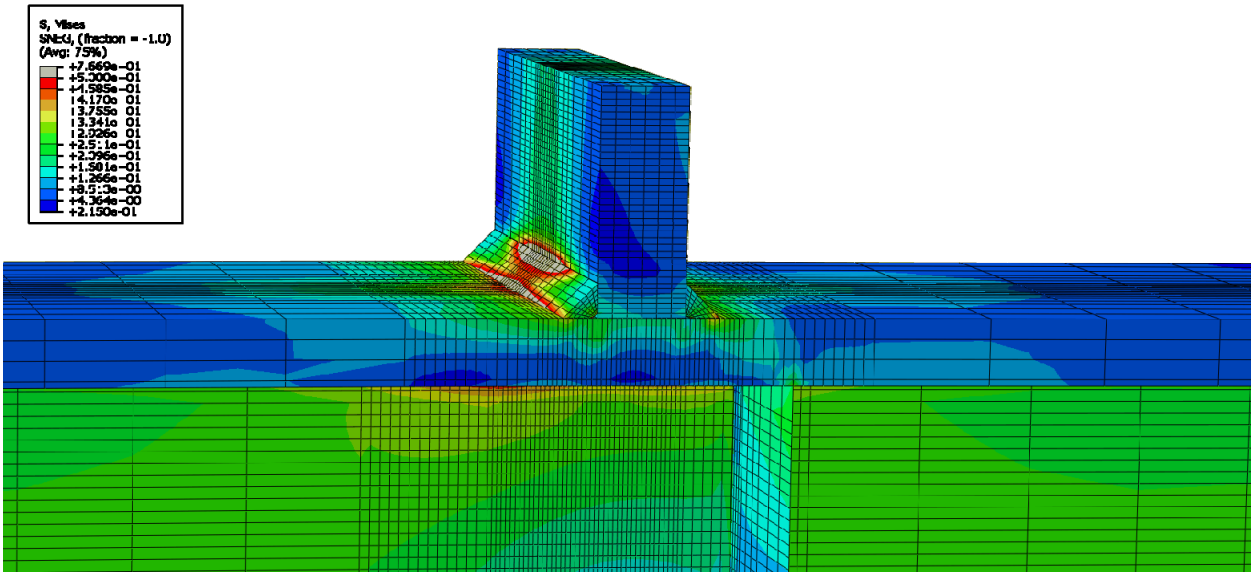

Figure E-474: Finite element model of W14X233-ST-E4 with 7/8 in. welds during inelastic behavior

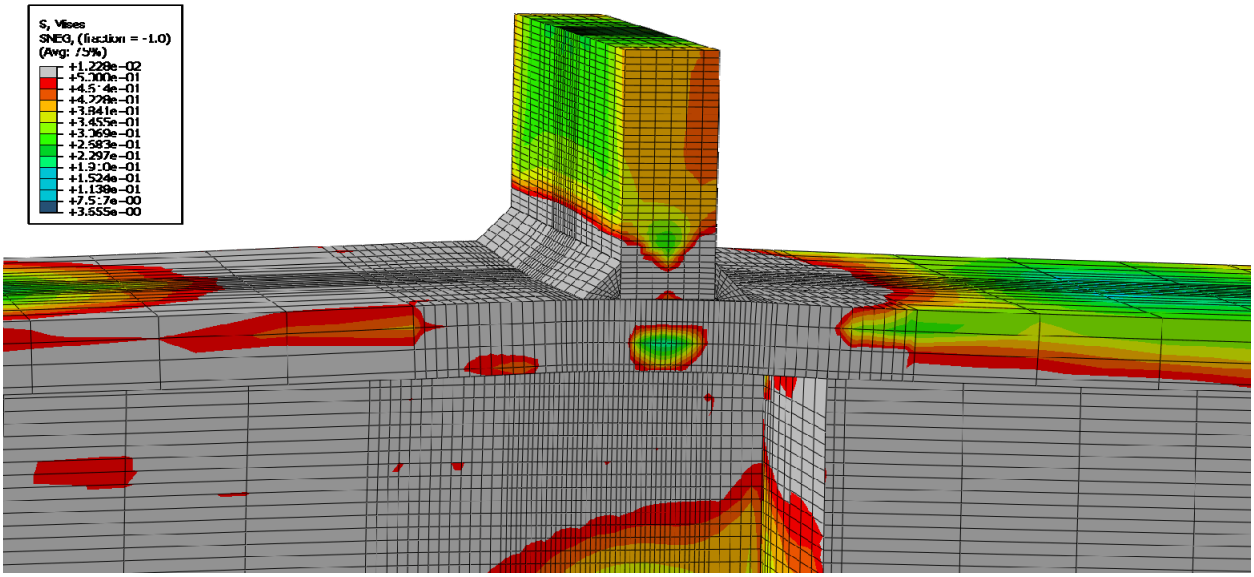

Figure E-475: Finite element model of W14X233-ST-E4 with 7/8 in. welds at its load capacity of 1063.92 kips

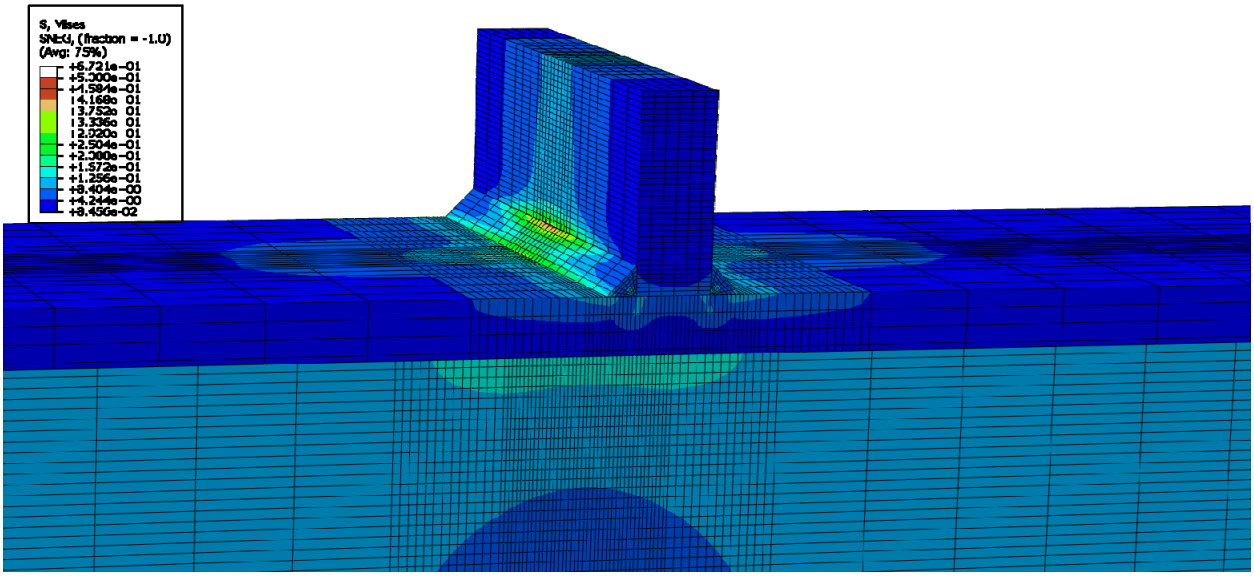

Figure E-476: Finite element model of W14X233-ST-NA with 7/8 in. welds while remaining elastic

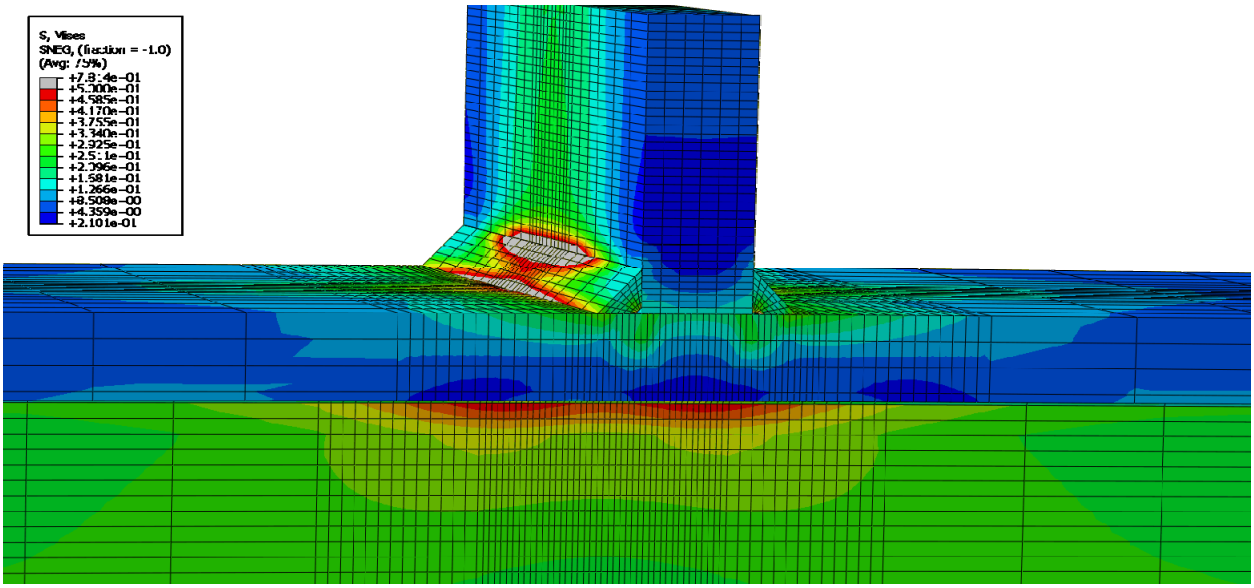

Figure E-477: Finite element model of W14X233-ST-NA with 7/8 in. welds during inelastic behavior

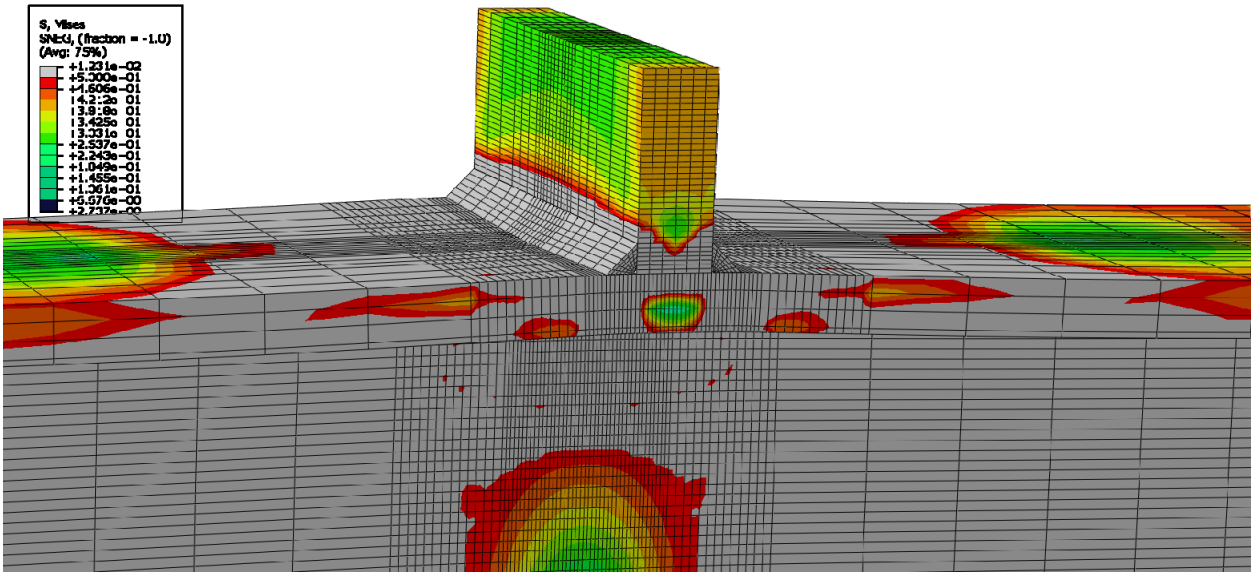

Figure E-478: Finite element model of W14X233-ST-NA with 7/8 in. welds at its load capacity of 1012.98 kips